

Reinhold Kleiner and Werner Buckel

# Superconductivity

An Introduction

Third Updated Edition



# Table of Contents

[Cover](#)

[Title Page](#)

[Copyright](#)

[Related Titles](#)

[Preface to the Third Edition](#)

[Introduction 1: Introduction](#)

[References](#)

[Chapter 1: Fundamental Properties of Superconductors](#)

[1.1 The Vanishing of the Electrical Resistance](#)

[1.2 Ideal Diamagnetism, Flux Lines, and Flux Quantization](#)

[1.3 Flux Quantization in a Superconducting Ring](#)

[1.4 Superconductivity: A Macroscopic Quantum Phenomenon](#)

[1.5 Quantum Interference](#)

[References](#)

[Chapter 2: Superconducting Elements, Alloys, and Compounds](#)

[2.1 Introductory Remarks](#)

[2.2 Superconducting Elements](#)

[2.3 Superconducting Alloys and Metallic Compounds](#)

[2.4 Fullerides](#)

[2.5 Chevrel Phases and Boron Carbides](#)

[2.6 Heavy-Fermion Superconductors](#)

[2.7 Natural and Artificial Layered Superconductors](#)

[2.8 The Superconducting Oxides](#)

[2.9 Iron Pnictides and Related Compounds](#)

[2.10 Organic Superconductors](#)

[2.11 Superconductivity at Interfaces](#)

[References](#)

[Chapter 3: Cooper Pairing](#)

[3.1 Conventional Superconductivity](#)

[3.2 Unconventional Superconductivity](#)

[References](#)

## [Chapter 4: Thermodynamics and Thermal Properties of the Superconducting State](#)

[4.1 General Aspects of Thermodynamics](#)

[4.2 Specific Heat](#)

[4.3 Thermal Conductivity](#)

[4.4 Ginzburg–Landau Theory](#)

[4.5 Characteristic Lengths of the Ginzburg–Landau Theory](#)

[4.6 Type-I Superconductors in a Magnetic Field](#)

[4.7 Type-II Superconductors in a Magnetic Field](#)

[4.8 Fluctuations above the Transition Temperature](#)

[4.9 States Outside Thermodynamic Equilibrium](#)

[References](#)

## [Chapter 5: Critical Currents in Type-I and Type-II Superconductors](#)

[5.1 Limit of the Supercurrent Due to Pair Breaking](#)

[5.2 Type-I Superconductors](#)

[5.3 Type-II Superconductors](#)

[References](#)

## [Chapter 6: Josephson Junctions and Their Properties](#)

[6.1 Current Transport across Interfaces in a Superconductor](#)

[6.2 The RCSJ Model](#)

[6.3 Josephson Junctions under Microwave Irradiation](#)

[6.4 Vortices in Long Josephson Junctions](#)

[6.5 Quantum Properties of Superconducting Tunnel Junctions](#)

[References](#)

## [Chapter 7: Applications of Superconductivity](#)

[7.1 Superconducting Magnetic Coils](#)

[7.2 Superconducting Permanent Magnets](#)

[7.3 Applications of Superconducting Magnets](#)

[7.4 Superconductors for Power Transmission: Cables, Transformers, and Current Fault Limiters](#)

[7.5 Superconducting Resonators and Filters](#)

[7.6 Superconducting Detectors](#)

[7.7 Superconductors in Microelectronics](#)

[References](#)

## [Monographs and Article Collections](#)

[History of Superconductivity](#)

[General Books](#)

[Special Materials](#)

[Tunnel Junctions, Josephson Junctions, and Vortices](#)

[Nonequilibrium Superconductivity](#)

[Applications of Superconductivity](#)

[General Overview](#)

[Magnets, Cables, Power Applications](#)

[Microwaves, Magnetic Field Sensors, Electronics](#)

[Low Temperature Physics and Technology](#)

[Index](#)

[End User License Agreement](#)

## List of Illustrations

Introduction 1: Introduction

[Figure 1 Schematics of the temperature dependence of electrical resistance at low temperatures. See text for details of curves.](#)

[Figure 2 The superconductivity of mercury.](#)

[Figure 3 The magnetic susceptibility of two samples of the Ba–La–Cu–O system versus temperature \[11\].](#)

[Figure 4 Evolution of the superconducting transition temperature since the discovery of superconductivity.](#)

Chapter 1: Fundamental Properties of Superconductors

[Figure 1.1 The generation of a permanent current in a superconducting ring.](#)

[Figure 1.2 Arrangement for the observation of a permanent current. \(a\) side view, \(b\) top view. \(After \[2\].\) Ring 1 is attached to the cryostat.](#)

[Figure 1.3 The “levitated magnet” for demonstrating the permanent currents that are generated in superconducting lead by induction during the lowering of the magnet. \(a\) Starting position. \(b\) Equilibrium position.](#)

[Figure 1.4 Application of free levitation by means of the permanent currents in a superconductor. The Sumo wrestler \(including the plate at the bottom\) weighs 202 kg. The superconductor is  \$\text{YBa}\_2\text{Cu}\_3\text{O}\_7\$ .](#)

[Figure 1.5 Energy–momentum relation for an electron in a periodic potential. The relation \(Eq. \(1.2\)\) valid for free electrons is shown as the dashed parabolic line.](#)

Figure 1.6 Fermi function.  $E_F$  is a few electronvolts, whereas thermal smearing is only a few  $10^{-3}$  eV. To indicate this, the abscissa is interrupted.

Figure 1.7 “Levitated magnet” for demonstrating the Meissner–Ochsenfeld effect in the presence of an applied magnetic field. (a) Starting position at  $T > T_c$ . (b) Equilibrium position at  $T < T_c$ .

Figure 1.8 Schematic diagram of the Shubnikov phase. The magnetic field and the supercurrents are shown only for two flux lines.

Figure 1.9 Image of the vortex lattice obtained with an electron microscope following the decoration with iron colloid. Frozen-in flux after the magnetic field has been reduced to zero. Material: Pb +6.3 at% In; temperature: 1.2 K; sample shape: cylinder, 60 mm long, 4 mm diameter; and magnetic field  $\mathbf{B}_a$  parallel to the axis. Magnification: 8300 $\times$ .

Figure 1.10 Methods for the imaging of flux lines. (a) Neutron diffraction pattern of the vortex lattice in niobium (Figure kindly provided by Institute Max von Laue-Paul Langevin, Grenoble; Authors: E. M. Forgan (Univ. Birmingham), S. L. Lee (Univ. St. Andrews), D. McK.Paul (Univ. Warwick), H. A. Mook (Oak Ridge) and R. Cubitt (ILL)). (b) Magneto-optical image of vortices in NbSe<sub>2</sub> [11]. (c) Lorentz microscopy of niobium (Figure kindly provided by A. Tonomura, Fa. Hitachi Ltd.). (d) Electron holography of Pb [12]. (e) Low-temperature scanning electron microscopy of YBa<sub>2</sub>Cu<sub>3</sub>O<sub>7</sub> [13]. (f) Scanning tunneling microscopy of NbSe<sub>2</sub>

Figure 1.11 Hanging toy train [20] (Leibniz Institute for Solid State and Materials Research, Dresden).

Figure 1.12 Schematics of the experimental setup of Doll and N  bauer. (From [22].) The quartz rod carries a small lead cylinder formed as a thin layer by evaporation. The rod vibrates in liquid helium.

Figure 1.13 Results of Doll and N  bauer on the magnetic flux quantization in a Pb cylinder ( $1 \text{ G} = 10^{-4} \text{ T}$ ).

Figure 1.14 Results of Deaver and Fairbank on the magnetic flux quantization in a Sn cylinder. The cylinder was about 0.9 mm long, and had an inner diameter of 13 µm and a wall thickness of 1.5 µm ( $1 \text{ G} = 10^{-4} \text{ T}$ ).

Figure 1.15 Decrease in the magnetic field within the superconductor near the planar surface.

Figure 1.16 Spatial dependence of the magnetic field in a thin superconducting layer of thickness  $d$ . For the assumed ratio  $d/\lambda_L = 3$ , the magnetic field only decreases to about half of its outside value.

Figure 1.17 Generation of the supercurrent. Four electrons in a wire bent to a ring are shown.

[Figure 1.18 Generation of the supercurrent: current transport and decay of the permanent current illustrated with the Fermi sphere.](#)

[Figure 1.19 The optical Sagnac interferometer.](#)

[Figure 1.20 Sandwich geometry of two superconductors separated from each other by a thin barrier.](#)

[Figure 1.21 Derivation of the Josephson equations. We consider a thin superconducting wire with a weakened location at  \$z = 0\$ , at which the Cooper pair density  \$n\_s\$  is strongly reduced. Due to current conservation, we have  \$n\_s\(z\)\gamma'\(z\) = \text{constant}\$ , leading to a peak in  \$\gamma'\(z\)\$  and to a step in  \$\gamma\$ . For illustration we have used the following “test function”:  \$n\_s\(z\) = 1/\gamma'\(z\) = 1/\[1.001 - \tanh^2\(x\)\]\$ , constant = 0.001. For  \$\gamma\(z\)\$  one finds  \$\gamma\(z\) = \tanh\(z\) + 0.001z\$ . At the weakened location,  \$\gamma\(z\)\$  changes very rapidly from  \$-1\$  to  \$+1\$ .](#)

[Figure 1.22 Schematics of the different possibilities for producing a weak coupling between two superconductors: \(a\) SIS junction with an oxide layer as a barrier; \(b\) SNS junction with a normal conducting barrier; \(c\) point contact; \(d\) microbridge; \(e\)  \$\text{YBa}\_2\text{Cu}\_3\text{O}\_7\$  grain boundary junction; and \(f\) intrinsic Josephson junction in  \$\text{Bi}\_2\text{Sr}\_2\text{CaCu}\_2\text{O}\_8\$ .](#)

[Figure 1.23 Arrangement for the experimental demonstration of the alternating Josephson current according to Giaever: layers 1–3 are Sn layers; layers a and b are oxide layers. The thicknesses of layers a and b are chosen such that layers 1 and 2 form a Josephson junction, and such that no Josephson currents are possible between layers 2 and 3.](#)

[Figure 1.24 Characteristic of the junction 2–3 from Figure 1.22. Curve 1: no voltage at junction 1–2. Curve 2: 0.055 mV applied to junction 1–2.](#)

[Figure 1.25 Generation of spatial interferences of the superconducting wave function in a ring structure. \(a\) Schematics of the wave. \(b\) Notation for the derivation of the quantum interference.](#)

[Figure 1.26 Modulation of the maximum supercurrent of a superconducting quantum interferometer as a function of the magnetic flux through the ring. The curves are shown for three different values of the inductance parameter  \$\beta\_L\$ .](#)

[Figure 1.27 Geometry of the spatially extended Josephson junction.](#)

[Figure 1.28 Dependence of the maximum Josephson current on the magnetic field parallel to the barrier layer. \(a\) Theoretical curve according to Eq. \(1.73\). \(b\) Measured data for a Sn–SnO–Sn tunnel junction \( \$1 \text{ G} = 10^{-4} \text{ T}\$ \).](#)

[Figure 1.29 Variation of the Josephson supercurrent density for three different values of the magnetic flux penetrating through the Josephson junction.](#)

[Figure 1.30 Magnetic field dependence of the maximum supercurrent of a SQUID](#)

structure made of  $\text{YBa}_2\text{Cu}_3\text{O}_7$ . The two Josephson junctions are  $9 \mu\text{m}$  wide, such that the  $I_c$  modulation of the individual junctions appears as the envelope of the SQUID oscillations [51].

Figure 1.31 Phase change of electron waves caused by a vector potential. (a) Beam geometry. (b) Interference pattern during a change of the magnetic field. The biprisms are quartz threads covered by a metal. The coil with  $20 \mu\text{m}$  diameter was fabricated from tungsten wire.

## Chapter 2: Superconducting Elements, Alloys, and Compounds

Figure 2.1 Distribution of the superconductors and their transition temperatures in kelvin within the Periodic Table [4]. The elements, which are superconducting only in the high-pressure phase, are shown with a dark background. (\*): C is superconducting only in the form of carbon nanotubes ( $T_C = 15 \text{ K}$ ) or in the form of boron-doped diamond films ( $T_C = 4 \text{ K}$ ), Cr in the form of thin films, Pd after irradiation with  $\text{He}^+$ -ions.

Figure 2.2 Transition temperature of some alloys of the transition metals plotted versus the average number of valence electrons

Figure 2.3 The unit cell of the  $\beta$ -tungsten (A15) structure of the binary compounds  $\text{A}_3\text{B}$ .

Figure 2.4 The crystal structure of  $\text{MgB}_2$ .

Figure 2.5 Maximum transition temperature of Pd–noble metal alloys after charging with hydrogen by means of ion implantation at low temperatures plotted versus the noble metal concentration.

Figure 2.6 (a) Fullerene molecule  $\text{C}_{60}$ . (b) Crystal structure of the fullerides [32].

Figure 2.7 The crystal structure of the Chevrel phases [37].

Figure 2.8 The crystal structure of the boron carbide  $\text{LuNi}_2\text{B}_2\text{C}$ .

Figure 2.9 Temperature dependence of the normalized resistivity of  $\text{HoNi}_{1-x}\text{Co}_x\text{B}_2\text{C}$ . For  $x = 0.005$  reentrant superconductivity is observed.

Figure 2.10 Crystal structure of the heavy-fermion superconductor  $\text{UPt}_3$  [48].

Figure 2.11 Crystal structure of the layered superconductor  $2\text{H}-\text{TaS}_2$ .

Figure 2.12 General crystal structure of the perovskite compounds.

Figure 2.13 Crystal structures of the two high-temperature superconductors  $\text{YBa}_2\text{Cu}_3\text{O}_7$  and  $\text{Bi}_2\text{Sr}_2\text{CaCu}_2\text{O}_8$ .

Figure 2.14 Phase diagram (temperature vs oxygen content  $x$ ) of the cuprate  $\text{YBa}_2\text{Cu}_3\text{O}_{6+x}$ . In the state “AF,” the material is ordered antiferromagnetically and is electrically insulating. In the region “SC” the material is superconducting [49].

[Figure 2.15 Phase diagram \(temperature vs Sr content  \$x\$ \) of the cuprate  \$\text{La}\_{2-x}\text{Sr}\_x\text{CuO}\_4\$  \[69\].](#)

[Figure 2.16 Crystal structure of strontium ruthenate compared with the crystal structure of  \$\(\text{La},\text{Ba}\)\_2\text{CuO}\_4\$ .](#)

[Figure 2.17 Crystal structure of  \$\text{La}\(\text{O}\_{1-x}\text{F}\_x\)\text{FeAs}\$  \(a\) and  \$\text{Ba}\_{1-x}\text{K}\_x\text{Fe}\_2\text{As}\_2\$  \(b\).](#)

[Figure 2.18 Phase diagram of  \$\text{La}\(\text{O}\_{1-x}\text{F}\_x\)\text{FeAs}\$ .](#)

[Figure 2.19 Structural formulas of organic superconductors: \(a\) tetramethyltetraselenofulvalene \(TMTSF\) and \(b\) bis\(ethylenedithia\)tetra-thiafulvalene \(BEDT-TTF\).](#)

[Figure 2.20 Crystal structure of the organic superconductor  \$\kappa-\(\text{BEDT-TTF}\)\_2\text{Cu}\(\text{NCS}\)\_2\$ .](#)

[Figure 2.21 Formula](#)

## Chapter 3: Cooper Pairing

[Figure 3.1 Polarization of the lattice of atomic ions due to the electrons. Within a static model, this polarization cannot overcompensate the repulsion between the electrons because of their equal charge. It can only strongly reduce the repulsion.](#)

[Figure 3.2 Attraction between two small balls on an elastic membrane. The configuration \(a\) is unstable and changes into configuration \(b\).](#)

[Figure 3.3 Binding of the  \$\text{H}\_2^+\$  molecule. The scales are arbitrary. \(a\), \(b\): Two possible electron distributions for a large distance between the protons. \(c\) electron distribution for a small distance between the protons.](#)

[Figure 3.4 Electron-electron interaction via phonons.](#)

[Figure 3.5 The functions  \$|u\_{\mathbf{k}}|^2\$  and  \$|v\_{\mathbf{k}}|^2\$ , indicating the probability that a pair state  \$\{\mathbf{k}\uparrow, -\mathbf{k}\downarrow\}\$  is occupied \( \$|v\_{\mathbf{k}}|^2\$ \) or unoccupied \( \$|u\_{\mathbf{k}}|^2\$ \). For the figure, the values  \$E\_F = 1 \text{ eV}\$  and  \$\Delta\_0 = 1 \text{ meV}\$  were used.](#)

[Figure 3.6 Energy of an unpaired electron \(quasiparticle\) in a superconductor, plotted versus the energy the electron would have without the pair interaction.](#)

[Figure 3.7 Normalized density of states  \$N\_s\(E\)/N\_n\(E\_F\)\$  of the quasiparticles in a superconductor according to the BCS theory. The ratio  \$\Delta\_0/E\_F\$  was taken as  \$10^{-3}\$ . At the temperature  \$T = 0\$ , all states below the Fermi energy are occupied \(hatched region\).](#)

[Figure 3.8 Isotope effect in tin:  \$\circ\$  Maxwell;  \$\square\$  Lock, Pippard, and Shoenberg; and  \$\Delta\$  Serin, Reynolds, and Lohman.](#)

[Figure 3.9 Absorption of electromagnetic waves with frequency  \$f\$  in superconductors. Transition temperatures  \$T\_c\$  are V, 5.3 K; In, 3.42 K; and Sn, 3.72 K. Measurement](#)

temperature is 1.4 K. In vanadium for  $f < 2\Delta_0/h$ , a frequency dependence is observed, the possible origin of which cannot be discussed here.

Figure 3.10 Ultrasound absorption in superconducting tin and indium. The solid line indicates the behavior expected from the BCS theory for the energy gap  $2\Delta_0 = 3.5k_B T_c$ .

Figure 3.11 (a) The arrangement for measuring a tunneling current. (b) The allowed energy values (black areas) and their occupation (gray shaded areas).

Figure 3.12 Tunneling current between normal metals for three values of applied voltage, (a)  $U = 0$ , (b)  $U = U_1$  and (c)  $U = U_2 > U_1$ . For simplicity, the distribution for  $T = 0$  is shown. Near the energy  $E_F$  there are no states in the insulating barrier.

Figure 3.13 Current–voltage characteristic of tunnel junctions: curve 1, normal conductor/normal conductor (Figure 3.12); curve 2, normal conductor/superconductor,  $T = 0$  K (Figure 3.14); and curve 3, normal conductor/superconductor,  $0 < T < T_c$ .

Figure 3.14 Tunneling current between a normal conductor and a superconductor for  $T = 0$  and three values of applied voltage, (a)  $U = 0$ , (b)  $U = U_1$  and (c)  $U = U_2 > U_1$ .

Figure 3.15 Tunneling current between two superconductors;  $0 < T < T_c$ . (a) and (b) show the density of states and (c) displays the current voltage characteristic.

Figure 3.16 Tunnel junction between two layers. Layer 1 was oxidized before the deposition of layer 2. The thicknesses of the layers are strongly exaggerated. Mostly they are below 1  $\mu\text{m}$ . Usually, the oxide barriers are about 3 nm thick.

Figure 3.17 Voltage–current characteristic of an Al–Al<sub>2</sub>O<sub>3</sub>–Pb tunnel junction.

Measuring temperature: curve 1,  $T = 10$  K; curve 2,  $T = 4.2$  K; curve 3,  $T = 1.64$  K; curve 4,  $T = 1.05$  K. At 1.05 K the Al is also superconducting. The steep rise at  $eU = \Delta_I + \Delta_{II}$  can clearly be seen. Transition temperatures are: Pb, 7.2 K and Al, 1.2 K.

Figure 3.18 Current–voltage characteristic of a Nb–insulator–Sn tunnel junction at  $T = 3.38$  K. The solid line is the experimentally recorded curve. The dots are calculated from Eq. (3.13) using the values  $2\Delta_{\text{Sn}} = 0.74$  meV and  $2\Delta_{\text{Nb}} = 2.98$  meV.

Figure 3.19 Temperature dependence of the energy gap of tantalum;  $\Delta(0) = 1.3$  meV.

Figure 3.20 Plot showing  $\alpha^2 F(\omega)$  obtained from tunneling measurements and  $F(\omega)$  from neutron diffraction experiments as functions of the phonon energy  $\omega$  for Pd–D samples (see Section 2.3.3).

Figure 3.21 Tunneling effect between superconductors in the picture of Cooper pairs and “excited” single electrons:  $\circ\circ$  Cooper pairs and  $\bullet$  single electrons (excitations). Graphs (a) to (c) are for different values of applied voltage.

Figure 3.22 Shift of the transition temperature of Sn due to impurity atoms. Graph (b) is an enlargement of the region indicated in (a).

Figure 3.23 Shift of the transition temperature of thallium due to the implantation of lattice defects. Residual resistance ratio of the defect-free sample:  $\sigma^* = 0.4 \times 10^{-3}$ .

Figure 3.24 Temperature dependence of the resistance of a tin layer produced by condensation from the vapor. Condensation temperature 4 K, layer thickness 50 nm, length 10 mm, width 1 mm. The black dots show the data observed during cooling after an annealing process.

Figure 3.25 Temperature dependence of the resistance of a tin layer produced by quench condensation together with 10 at% copper acting as impurity. Layer thickness about 50 nm, width 5 mm, length 10 mm, condensation temperature 10 K.

Figure 3.26 Transition temperatures of lanthanum alloys each containing 1 at% admixture of a rare-earth element (open circles), and effective magnetic moment of the admixture (black dots).

Figure 3.27 (a) to (d): Influence of paramagnetic ions on the transition temperature of lead. In part (d) the results are plotted in reduced units. The solid line is obtained from the theory for the following critical concentrations: Mn, 0.26 at%; Fe, 1.2 at%; Cr, about 1 at%; Gd, 2.8 at%; Co, 6.3 at%. All results, except for curve 1 in part (a), were obtained with quench-condensed films. Curve 1 in part (a) was observed in alloys produced at liquid-helium temperatures by means of ion implantation. Data sources as follows: Pb + Fe, Pb + Cr, Pb + Co [58]; Pb + Mn [59–61]; and Pb + Gd [62].

Figure 3.28 Transition curves of  $(La_{1-x}Ce_x)Al_2$ , with  $x = 0.63$  at%.

Figure 3.29 Density of states of unpaired electrons in a superconductor containing paramagnetic ions at  $T = 0$ . The curves 1–5 correspond to increasing concentrations of the paramagnetic ions; curve 4 corresponds to the critical concentration.

Figure 3.30 Normalized conductivity  $\sigma_s/\sigma_n$  (proportional to the density of states of the electrons) of lead with an admixture of manganese. (From [61].) Temperature 200 mK. Curve 0, pure lead; curve 1, Pb + 25 ppm Mn; and curve 2, Pb + 250 ppm Mn. The dotted line is calculated from the MHZB theory [76].

Figure 3.31 Measurement of the Knight shift: (a) for the high-temperature superconductor  $YBa_2Cu_3O_7$  [79] and (b) for  $Sr_2RuO_4$  [80]. (© 1998 Nature.) The lines indicate the expected behavior for a superconductor with spin-singlet pairing and  $d_{x^2-y^2}$  symmetry of the pair wave function.

Figure 3.32 Conventional superconductor with s-wave symmetry: (a) amplitude of the pair wave function in  $k$ -space and (b) dependence of the magnitude of the energy gap  $\Delta_0$  upon  $k$ .

Figure 3.33 The value of the function  $x^2 - y^2$  on the unit circle. In (a)  $f$  is plotted versus the angle  $\phi$  between the  $y$  axis and a radius vector on the unit circle:  $f(\phi) = -\cos(2\phi)$ . In (b)  $|f(x,y)|$  is plotted in the  $(x,y)$  plane. The distance vector between the origin and  $f(x,y)$  is proportional to  $|f(x,y)|$ . The sign of the function is indicated as “+” or “-.”

Figure 3.34 (a) Amplitude of the pair wave function and (b) energy gap in  $\mathbf{k}$ -space for  $d_{x^2-y^2}$  symmetry. In (a) the distance from the origin to the function is proportional to  $|\Psi_0|$ . The sign of  $\Psi_0$  is indicated explicitly.

Figure 3.35 A section of the  $\text{CuO}_2$  plane of a high-temperature superconductor consisting of four unit cells ( $\bullet$  copper;  $\circ$  oxygen). On the lower right the relevant atomic orbitals of copper and of oxygen are sketched. The symbol “ $U$ ” indicates the electrostatic repulsion between two electrons on the same copper ion; the symbol “ $t$ ” (for “transfer”) indicates the kinetic energy of the electron, when it hops between neighboring copper ions.

Figure 3.36 Quasiparticle density of states  $N_s(E)$  in a superconductor with  $d_{x^2-y^2}$  symmetry of the pair wave function.

Figure 3.37 Conductivity of tunnel junctions between the Ir tip of a scanning tunneling microscope and  $\text{Bi}_2\text{Sr}_2\text{CaCu}_2\text{O}_{8+x}$  single crystals with different doping levels. For clarity the curves are shifted vertically. The two upper curves show overdoped crystals, the third curve from the top shows an optimally doped crystal, and the curve at the bottom an underdoped crystal. The inset shows the superposition of 200 tunneling measurements for an overdoped crystal with  $T_c = 71.4$  K. The measurements were performed at different locations of the crystal surface [95].

Figure 3.38 ARPES measurements of the energy gap in  $\text{Bi}_2\text{Sr}_2\text{CaCu}_2\text{O}_8$  in the  $(k_x, k_y)$  plane. The main Figure shows  $\Delta_0$  as a function of the angle to the Cu–O bonds. The inset shows the section of the Fermi surface for which the energy gap was determined ( $\bullet$  raw data,  $\circ$  corrected data) [98].

Figure 3.39 Conductivity of a tunnel junction between the Ir tip of a scanning tunneling microscope and an underdoped  $\text{Bi}_2\text{Sr}_2\text{CaCu}_2\text{O}_{8+x}$  single crystal for different temperatures (see also Figure 3.37). For clarity, the experimental curves are shifted vertically [95].

Figure 3.40 (a), (b): Two interferometer geometries between an unconventional superconductor with  $d_{x^2-y^2}$  symmetry of the pair wave function and a conventional superconductor. The two superconductors are connected with each other by means of the Josephson junctions “1” and “2.”

Figure 3.41 Magnetic field or magnetic flux dependence of a Josephson junction between  $\text{YBa}_2\text{Cu}_3\text{O}_7$  and Pb for the geometry indicated in the inset in part (b). (a) The theoretical curve calculated from Eq. (25); the curve is normalized with the supercurrent  $j_c A$  expected through the junction area  $A$  in the case of homogeneous current flow. (b) The measured curve [106] ( $1 \text{ G} = 10^{-4} \text{ T}$ ).

Figure 3.42 Geometry of the tricrystal experiment for detecting the half-integer magnetic flux quanta. The (100) and (010) directions indicate the directions of the

crystallographic  $a$  and  $b$  axes, respectively. Inner (outer) ring diameters: 48  $\mu\text{m}$  (68  $\mu\text{m}$ ).

Figure 3.43 Magnetic flux passing through the  $\text{YBa}_2\text{Cu}_3\text{O}_7$  rings shown in Figure 3.42 in the absence of an applied magnetic field. The reference rings are free of magnetic flux, whereas the ring around the tricrystalline point carries the flux  $\Phi_0/2$  [103].

Figure 3.44 Imaging of the magnetic flux distribution in a  $\text{Bi}_2\text{Sr}_2\text{CaCu}_2\text{O}_8$  thin film deposited on a tricrystal as shown in Figure 3.42. Applied magnetic field: 0.37  $\mu\text{T}$ . At the tricrystalline point, indicated by the arrow, a half-integer magnetic flux quantum has appeared [109]. Image section about 1 mm  $\times$  0.7 mm.

Figure 3.45 Grain-boundary interferometer geometry for demonstrating the  $d_{x^2-y^2}$  symmetry in high-temperature superconductors [113].

Figure 3.46 Maximum supercurrent across the Josephson junctions denoted by “0” and “ $\pi$ ” in Figure 3.45 plotted versus the magnetic field. Graph (b) is an enlargement of the low-field region of graph (a). The negative values of  $I_c$  were measured for a negative transport current across the interferometer [113].

Figure 3.47 Josephson junction between a  $\text{YBa}_2\text{Cu}_3\text{O}_7$  single crystal and Pb with the current flow perpendicular to the  $\text{CuO}_2$  planes. The observed supercurrent indicates that the pair wave function must contain a small s component. Main figure: Maximum supercurrent plotted versus the magnetic field. Inset on left: Current–voltage characteristic. Inset on right: Josephson current plotted versus the temperature. (From [102].) ( $1\text{G} = 10^{-4}\text{ T}$ ).

Figure 3.48 (a) The three phases of  $\text{UPt}_3$  in a magnetic field-temperature diagram. (b) One of the discussed energy-gap functions of the B phase, plotted on a spherical Fermi surface. However, the actual Fermi surface of  $\text{UPt}_3$  is much more complicated.

Figure 3.49 Electrical conductivity of a tunnel junction between  $\text{UPd}_2\text{Al}_3$  and Pb with  $\text{AlO}_x$  as the tunneling barrier ( $T = 0.3\text{ K}$ ,  $B = 0.3\text{ T}$ ). The thinner gray line shows a theoretical fit using  $\Delta_{\max} = 235\text{ }\mu\text{eV}$ . The fit takes into account the finite lifetime of the quasiparticles. However, it does not contain structures due to the exchange boson [127].

Figure 3.50 Spectra of the neutron intensity of inelastic neutron scattering as a function of the energy transfer between the neutrons and  $\text{UPd}_2\text{Al}_3$  for different temperatures. The magnetic exciton appears as a peak at about 1.4 meV. The inset shows the resulting dependence of the frequency of the magnetic exciton upon the wave vector for  $T = 2.5\text{ K}$  (x) and  $T = 0.15\text{ K}$  (•) [126].

Figure 3.51 (a) Calculated density of states of  $\text{UPd}_2\text{Al}_3$  taking into account the magnetic exciton for different temperatures. (b) An enlarged section, in which one can see the structure caused by the exciton [126].

[Figure 3.52 \(a\) Structure of the 3K phase of  \$\text{Sr}\_2\text{RuO}\_4\$  developing at the interface with the Ru inclusions. \(b\) Appearance of phase jumps of  \$\pi\$  between three such inclusions.](#)

[Figure 3.53 Fermi surfaces of  \$\text{MgB}\_2\$ . The method of calculation is described in \[138\].](#)

## Chapter 4: Thermodynamics and Thermal Properties of the Superconducting State

[Figure 4.1 Specific heat of tin plotted versus the temperature. Open circles: without a magnetic field; solid dots: with a magnetic field  \$B > B\_c\$ ; dashed line: contribution of the electrons for  \$B > B\_c\$ ; dashed-dotted line: lattice contribution for  \$B > B\_c\$  \( \$1 \text{ cal} \approx 4.18 \text{ J}\$ \). \(From \[6\].\).](#)

[Figure 4.2 Electronic component of the specific heat of tin and vanadium. The straight line represents the relation predicted by the BCS theory. The dashed curve indicates a  \$T^3\$  law according to Eq. \(4.15\). \(From \[7\].\)](#)

[Figure 4.3 Sommerfeld coefficient  \$\gamma = c\_{\text{el}}/T\$  plotted versus temperature  \$T\$  for  \$\text{YBa}\_2\text{Cu}\_3\text{O}\_{6+x}\$  crystals with different doping levels \[12\].](#)

[Figure 4.4 Thermal conductivity of pure tin and mercury. \(From \[16\].\) The left scale is for Sn.](#)

[Figure 4.5 Thermal conductivity of lead and lead–bismuth alloys. Solid lines: normal state; dashed lines: superconducting state. \(From \[18\].\)](#)

[Figure 4.6 Variation of the function  \$\psi\(x\)\$  according to Eq. \(4.39\) at the edge of a superconducting half-space.](#)

[Figure 4.7 Temperature dependence of the penetration depth of Hg \[23\]. The solid line corresponds to the exponent  \$a = 4\$  in the bracket of Eq. \(4.40\). For comparison, the cases  \$a = 3\$  and  \$a = 6\$  are also shown by the dashed curves.](#)

[Figure 4.8 Temperature dependence of the magnetic penetration depth in highly pure  \$\text{YBa}\_2\text{Cu}\_3\text{O}\_7\$ . The circles indicate the penetration depth along the  \$a\$ -direction of the crystal, and the squares indicate the penetration depth along the  \$b\$ -direction. At low temperatures, the measurement yielded the values  \$\lambda\_a\(0\) = 160 \text{ nm}\$  and  \$\lambda\_b\(0\) = 80 \text{ nm}\$  \[24\].](#)

[Figure 4.9 Magnetic field expulsion for a rod-shaped sample. The sample is cooled down in the field  \$B\$ .](#)

[Figure 4.10 Magnetization of a rod-shaped sample \( \$N\_M = 0\$ \) in a magnetic field parallel to the axis. During a reversible transition, the same curve is followed for increasing and decreasing field  \$B\$ .](#)

[Figure 4.11 Magnetic field in the interior of a rod-shaped sample \( \$N\_M = 0\$ \) in a magnetic field parallel to the axis. During a reversible transition, the same curve is followed for increasing and decreasing field  \$B\$ .](#)

Figure 4.12 Critical magnetic field plotted versus the temperature for different type-I superconductors (1 G =  $10^{-4}$  T).

Figure 4.13 Gibbs functions  $G_n$  and  $G_s$ , entropy difference  $S_n - S_s$ , and heat of transition  $Q$  plotted versus the temperature. Numerical example for 1 mol Sn:  $T_c = 3.72$  K;  $(G_n - G_s)_{T=0} = 5 \times 10^{-3}$  W s;  $(S_n - S_s)_{\max} = 2.28 \times 10^{-3}$  W s/K; and  $Q_{\max} = 5 \times 10^{-3}$  W s.

Figure 4.14 Expulsion of magnetic field (solid field lines) from a superconducting sphere. In the absence of the sphere, the field is homogeneous (dashed field lines).

Figure 4.15 Magnetic flux  $\Phi$  passing through the equatorial plane of a sphere plotted versus the external field  $B_a$ .

Figure 4.16 Intermediate state structure of an indium plate. The dark regions represent the superconducting domains. In purity: 99.999 at%; thickness: 11.7 mm; diameter: 38 mm;  $B_a/B_{c\text{th}} = 0.1$ ;  $T = 1.98$  K;  $T_c$  of indium: 3.42 K; transition N → S; magnification: 5×. Because of its high demagnetization coefficient, the plate enters the intermediate state already at  $B_a/B_{c\text{th}} = 1$  [33].

Figure 4.17 Intermediate state structure imaged by means of the Faraday effect. Pb layer with 7 μm thickness; thickness of the magneto-optic film of EuS and EuF<sub>2</sub>: about 100 nm; magnetic field  $B_a = 0.77 B_c$  perpendicular to the layer. The dark regions represent the superconducting domains. The imaged area is about 0.5 mm × 0.5 mm [34]. (By courtesy of Dr Kirchner, Siemens, Munich.)

Figure 4.18 Spatial variation of  $B$  and  $n_s$  at an interface between a normal conducting domain and a superconducting domain within a homogeneous material at temperature  $T$ . (Here,  $x_{Gm}$  = “magnetic boundary” and  $x_{GK}$  = “condensate boundary.”)

Figure 4.19 Spatial variation of the expulsion energy  $\epsilon_B$  and of the condensation energy  $\epsilon_C$  per unit volume at the boundary. We have  $\int_0^{x_{GK}} (\epsilon_B - \epsilon_C) F dx = (\xi_{GL} - \lambda_L) F \frac{1}{2\mu_0} B_{c\text{th}}^2$ .

Figure 4.20 Pressure dependence of the transition temperature of tin [36].

Figure 4.21 Temperature dependence of the critical field (1 G =  $10^{-4}$  T) of cadmium at atmospheric pressure (curve 1) and at 1550 bar (curve 2). (From [39].) The original curves have many more data points than this reproduction.

Figure 4.22 Relative length change  $(l_s - l_n)/l_s$  of a tin rod at the transition into the superconducting state. (From [41].)

Figure 4.23 Magnetization curve of a type-II superconductor. Rod-shaped sample with  $N_M = 0$ . Because of the definition of  $B_{c\text{th}}$ , the shaded areas must be equal.

Figure 4.24 Average magnetic field in the interior of a type-II superconductor plotted versus the external field.

Figure 4.25 Magnetization curve of lead with 13.9 at% of indium (solid line). Rod-shaped sample with a small demagnetization coefficient. The dashed line shows the ideal curve of pure lead ( $1 \text{ G} = 10^{-4} \text{ T}$ ). (From [52].)

Figure 4.26 Schematics of the phase diagram of a type-II superconductor.

Figure 4.27 The critical fields ( $1 \text{ G} = 10^{-4} \text{ T}$ ) of an indium bismuth alloy, In + 4 at% Bi. (From [54].)

Figure 4.28 Upper critical field of some high-field superconductors:  $\circ$  Nb<sub>3</sub>Sn, wire diameter 0.5 mm [59];  $\Delta$  V<sub>3</sub>Ga, sintered sample [59];  $\times$  Nb<sub>50</sub>Ti<sub>50</sub> [60];  $\blacksquare$  PbMo<sub>6.35</sub>S<sub>8</sub> [61];  $\bullet$  PbGd<sub>0.3</sub>Mo<sub>6</sub>S<sub>8</sub> [61]. (See also Ref. [62].)

Figure 4.29 Upper critical field  $B_{c2} = \mu_0 H_{c2}$  of the two high-temperature superconductors YBa<sub>2</sub>Cu<sub>3</sub>O<sub>7</sub> ( $T_c = 91.2 \text{ K}$ , a) and Bi<sub>2</sub>Sr<sub>2</sub>CaCu<sub>2</sub>O<sub>8</sub> ( $T_c \approx 85 \text{ K}$ , b) obtained from resistance measurements plotted versus the angle between the CuO<sub>2</sub> planes and the applied field. The main plots show the angles near the parallel orientation. The insets refer to the full range of angles. Measuring temperatures: for YBa<sub>2</sub>Cu<sub>3</sub>O<sub>7</sub>, 89 K (upper curve) and 84.5 K (lower curve); for Bi<sub>2</sub>Sr<sub>2</sub>CaCu<sub>2</sub>O<sub>8</sub>, 80.4 K. The sharply peaked curves correspond to Eq. (4.91) for the angle dependence of the upper critical field of a thin plate. The rounded curves refer to Eq. (4.92) for a strongly anisotropic, but spatially homogeneous, superconductor. (From [64].)

Figure 4.30 Spatial variations of Cooper pair density, magnetic field, and supercurrent density for a planar cut across a vortex, shown schematically.

Figure 4.31 Spatial variations of Cooper pair density and magnetic field in the Shubnikov phase, shown schematically. Between the vortices the Cooper pair density attains the equilibrium value corresponding to the given values of  $T$  and  $B$ . Since  $\lambda_L > \xi_{GL}$ , with increasing field the magnetic field between the vortices is not completely expelled any more.

Figure 4.32 Coexistence of the Meissner phase and of the Shubnikov phase in a type-II superconductor with  $\kappa$  close to  $1/\sqrt{2}$ . Material: Pb + 1.89 at% Tl,  $\kappa = 0.73$ ,  $T = 1.2 \text{ K}$ ; sample: disk with 2 mm diameter and 1 mm thickness; external field  $B_a = 36.5 \text{ mT}$ ; magnification 4800 $\times$ . This state can be established in samples with a finite value of the demagnetization coefficient. (By courtesy of Dr U. Essmann.)

Figure 4.33 Possible phases of the so-called vortex matter in a spatially homogeneous superconductor in the case where thermal fluctuations play an important role [75]. (A) We see schematically different vortex configurations: (a) vortex lattice, (b) a liquid phase where the vortices still remain separated, and (c) a liquid phase with entangled vortices. (B) A schematic phase diagram is shown [76]. In the liquid phase a certain amount of short-range order is possible (“hexatic vortex liquid”). One must note also that the liquid phase is inserted between the Meissner phase and the vortex lattice.

Figure 4.34 Experimental phase diagram of the vortex state in  $\text{YBa}_2\text{Cu}_3\text{O}_7$  in magnetic fields  $\mu_0 H$  perpendicular to the  $\text{CuO}_2$  planes. The plot shows the melting line  $H_m$  ending in the critical point “CP.” The line  $H_{\text{ft}}$  separates the vortex lattice from a glassy state caused by defects in the vortex crystal. Above the line  $H^*$  the magnetization curves are reversible, and below  $H^*$  there appears hysteresis. The dashed line corresponds to a theoretical curve of the melting of the vortex lattice. (From [80], © 2001 Nature.)

Figure 4.35 Vortex phase diagrams of  $\text{Bi}_2\text{Sr}_2\text{CaCu}_2\text{O}_{8+x}$  single crystals with different doping. The diagrams were obtained from measurements of the muon-spin rotation ( $\mu\text{SR}$ ) and of the magnetization. (a) Over-doped crystal,  $T_c = 64$  K and (b,c) under-doped crystal,  $T_c = 77$  K [86].

Figure 4.36 (a) Schematic of the circulating currents around a “Josephson vortex” in a superconducting layered structure. The superconducting layers are the hatched regions extending along the  $(x,y)$  planes. The vortex axis runs along the  $x$ -direction, that is, perpendicular to the paper. (b) The supercurrent density in the  $z$ -direction between the two layers, between which the vortex axis is located. (From [91].)

Figure 4.37 Staircase pattern of flux lines in a magnetic field applied at an angle  $\theta$  to the superconducting layers [95]. The flux lines pass across the planes in the form of pancake vortices joined together by short segments (of length  $L$ ) of Josephson vortices.

Figure 4.38 Phase diagram of a  $\text{Bi}_2\text{Sr}_2\text{CaCu}_2\text{O}_8$  single crystal as a function of the magnetic field components  $H_c (=H_\perp)$  and  $H_\parallel$ . The vortex phases were observed by means of Hall probe microscopy. Measuring temperature: 77–88 K. The two Figure on the right schematically indicate two of the vortex phases (From [96], © 2001 Nature.)

Figure 4.39 Transition curve of an amorphous bismuth film of 47 nm thickness: (a) resistance and (b) conductance. The solid lines correspond to Eqs. (4.97) and (4.98). (From [102].)

Figure 4.40 Additional conductance for seven different films plotted versus the reduced temperature. (From [102].)

Figure 4.41 Recombination time in Al films plotted versus the reduced temperature. Transition temperature  $T_c = 1.27$  K;  $\Delta_0(0) = 0.195$  meV; thickness values: 102, 76, and 64 nm. Full circles, stationary measurement; open circles, pulse technique. (From [110].)

Figure 4.42 (a) Transition curves and (b) critical currents of Al films without and with high-frequency irradiation ( $f = 3 \times 10^9$  Hz);  $\circ$  without irradiation (solid line) and  $\bullet$  with irradiation (dashed line). (From [114].) The dimensions of the films are as listed below:

Figure 5.1 Distribution of the current density and of the magnetic field in a current-carrying superconducting wire. The surface layer has the thickness of only the penetration depth  $\lambda_L$ .

Figure 5.2 Critical current of a tin wire with 1 mm diameter plotted versus the temperature.

Figure 5.3 (a) Field distribution around a superconducting wire in the Meissner phase without a transport current. (b) Critical current of a wire with circular cross-section in external field  $B_a$  oriented perpendicular to the wire axis.

Figure 5.4 Intermediate-state structure of a wire with circular cross-section at the critical current. Hatched domains are normal conducting. The structure shows rotational symmetry around the cylinder axis. For a transport current  $I > I_c$ , the superconducting domains shrink (dashed lines).

Figure 5.5 Intermediate-state structure of a current-carrying In cylinder. The bright stripes indicate normal conducting domains. Length 38 mm, diameter 6 mm, transport current 30 A, external field  $B_a$  perpendicular to the cylinder axis 0.01 T, temperature  $T = 2.1$  K ( $T_c$  of In: 3.42 K), normal conducting → superconducting transition.

Figure 5.6 Electrical resistance plotted against the transport current.

Figure 5.7 Shubnikov phase in the presence of a transport current density  $j$ . The flux lines experience a force  $F$  driving them along the  $y$ -direction. The magnetic field distribution around the flux lines is indicated by the shading.

Figure 5.8 Generation of an electrical voltage  $U$  during vortex motion. A and B are superconductors, C is an insulating layer. All layer thicknesses are strongly exaggerated.

Figure 5.9 Pinning effect of normal conducting precipitates. In location “a” the effective length of the vortex is shorter compared to that in location “b,” since there are no circulating currents in the normal conducting region.

Figure 5.10 Vortex configuration in a hard superconductor. The hatched regions represent pinning centers. The dots indicate atomic defects.

Figure 5.11 Magnetization curves of a  $\text{Nb}_{55}\text{Ta}_{45}$  alloy: curve a, well annealed; curve b, with many lattice defects

Figure 5.12 Complete magnetization cycle of a Pb–Bi alloy (53 at% Bi). The dashed curve is expected if there are no flux jumps

Figure 5.13 Dendritic flux avalanches, which have penetrated into an  $\text{MgB}_2$  thin film. Sample area:  $5 \times 5 \text{ mm}^2$ , film thickness: 200 nm. The magnetic field (8 mT) was applied perpendicular to the thin film. Temperature: 10 K.

Figure 5.14 Glass-like vortex phases in the cuprates in the presence of pinning centers

[31]. BrG, Bragg glass; VG, vortex glass; VL, vortex liquid. The small insets indicate how the Gibbs energy in the corresponding phases changes as a function of the dislocation density in the vortex lattice.

Figure 5.15 Magnetization curve of a  $\text{YBa}_2\text{Cu}_3\text{O}_{7-\delta}$  single crystal at temperatures between 60 and 72 K. At fields above 4 T, we note a second peak [32].

Figure 5.16 Magnetization curve of a PbGe film (a) in which a regular lattice of microholes was fabricated (b). The magnetization (being proportional to the critical current density in the film) shows a very large hysteresis. Distinct maxima appear at the magnetic field values at which the number of vortices is an integer multiple of the number of microholes. For comparison, the magnetization curve of a PbGe film without antidots is also shown. In the latter case, the magnetization strongly decreases already at small fields. Measuring temperature: 6 K.

Figure 5.17 Magnetic field distribution in a hollow cylinder of a hard superconductor for increasing (left) and decreasing (right) applied magnetic fields. At  $B_{a4}$  the decrease in  $j_c$  with increasing  $B$  is indicated by a less steep field slope [36]. fp = field probe.

Figure 5.18 Magnetic shielding of a hollow cylinder made from  $\text{V}_3(\text{Ga}_{0.54}\text{Al}_{0.46})$ . Inner field  $B_i$  plotted versus the external field  $B_a$  (1 kG = 0.1 T). Measuring temperature: 4.2 K; transition temperature: 12.2 K.

Figure 5.19 Temporal decay of the magnetization of different superconductors. The magnetization is normalized to its value  $m_0$  observed 10 s after the supercurrents were turned on [40]. ▪ NbTi at 4.2 K; ○, •  $\text{YBa}_2\text{Cu}_3\text{O}_7$  with oriented grains at 77 K; □  $\text{YBa}_2\text{Cu}_3\text{O}_7$  single crystal at 60 K.

Figure 5.20 Current–voltage characteristics of an  $\text{Nb}_{50}\text{Ta}_{50}$  alloy in the Shubnikov phase.  $T = 3.0$  K; external field  $B_a = 0.2$  T;  $T_c$  in zero field: 6.25 K.

Figure 5.21 Current–voltage characteristics of a Pb–In alloy in the Shubnikov phase. Material: Pb + 17 at% In;  $T = 2.0$  K; transition temperature in zero field: about 7.1 K.

Figure 5.22 Critical current of an  $\text{Nb}_{55}\text{Ta}_{45}$  alloy in an external magnetic field (1 kG = 0.1 T) oriented perpendicular to the current. Wire diameter: 0.38 mm; measuring temperature: 4.2 K. Curve 1, immediately after cold working; curve 2, after 24 h at 1800 K; curve 3, after 48 h at 1800 K.

Figure 5.23 Critical currents of thin wires of metallic high-field superconductors (1 kG = 0.1 T). Measuring temperature: 4.2 K. Curve 1:  $\text{V}_3\text{Si}$ ; curve 2:  $\text{Nb}_3\text{Sn}$ ; curve 3:  $\text{V}_3\text{Ga}$ . Wire diameter of all three samples: 0.5 mm. In each case the compound exists only within a surface layer obtained by diffusion of the second component into the base material Nb or V. Curve 4, Nb–Ti; wire diameter 0.15 mm.

Figure 5.24 Critical current density of a  $\text{YBa}_2\text{Cu}_3\text{O}_7$  thin film for three temperatures

plotted versus the applied magnetic field. The field was oriented either perpendicular to the layered structure (i.e., parallel to the crystallographic  $c$ -axis) or parallel to it.

## Chapter 6: Josephson Junctions and Their Properties

Figure 6.1 Temperature dependence of the critical current of Sn–SnO<sub>x</sub>–Sn and Pb–PbO<sub>x</sub>–Sn tunnel junctions [4].

Figure 6.2 Current–voltage characteristic of a Sn–SnO<sub>x</sub>–Sn tunnel junction. Measuring temperature: 1.8 K; current scale: 0.5 mA/division; voltage scale: 1 mV/division.

Figure 6.3 Current–voltage characteristic of an intrinsic Josephson junction between the CuO<sub>2</sub> planes of a Bi<sub>2</sub>Sr<sub>2</sub>Ca<sub>2</sub>Cu<sub>3</sub>O<sub>10</sub> thin film. Junction area: 2 × 2 μm<sup>2</sup>; measuring temperature: 4.2 K.

Figure 6.4 Current–voltage characteristic of a mesa structure with 2 × 2 μm<sup>2</sup> area and 65 nm thickness on a Bi<sub>2</sub>Sr<sub>2</sub>CaCu<sub>2</sub>O<sub>8</sub> single crystal. The thickness of the mesa corresponds to a stack of 43 intrinsic Josephson junctions. At higher currents, the outer branch of the characteristic continues similarly as the current–voltage characteristic shown in Figure 6.3.

Figure 6.5 Transition temperature of double layers of lead and copper. Deposition temperature: 10 K; thickness of the Cu layers  $d_{\text{Cu}} = \xi_N$ ; electron mean free path: about 5.5 nm in Pb, and about 4.5 nm (curve 1) and 80 nm (curve 2) in Cu.

Figure 6.6 Transition temperature of double layers of lead and copper. Deposition temperature: 10 K; thickness of the Pb films: (○) 100 nm, (Δ) 50 nm, (▽) 30 nm, (□) 15 nm, (●) 10 nm, and (■) 7 nm.

Figure 6.7 Current–voltage characteristic of a Pb–(CuAl)–Pb junction for different temperatures. Junction area: 4 × 10<sup>4</sup> μm<sup>2</sup>; thickness of the CuAl layer: about 0.5 μm [19].

Figure 6.8 (a) Critical current  $I_c$  of an SFS-Josephson contact (thickness of the ferromagnetic barrier: 22 nm) plotted versus the temperature for two samples (a) and (b). (Printed with permission of [29], © 2001 American Physical Society.) The inset shows the magnetic field dependence of  $I_c$ , measured at points 1, 2, and 3 of the main graph. Part (b) shows the product of the critical current  $I_c$  and the normal resistance  $R_n$  for an SIFS-Josephson contact as a function of the temperature. (Printed with permission of [31], © 2002 American Physical Society.) Solid line: Theoretical curve. Inset: Current–voltage characteristic of the SIFS-contact compared with a traditional SIS-tunnel contact. Superconducting layers: Nb, ferromagnet: PdNi, insulator: Al<sub>2</sub>O<sub>3</sub>.

Figure 6.9 (a) Replacement circuit of a Josephson junction carrying an applied current. (b) The pendulum as an analogous model satisfying the same equation of motion as the Josephson junction. The acting torque  $M$  is indicated by a hanging weight.

[Figure 6.10 Current–voltage characteristics of Josephson junctions calculated from the RCSJ model.](#)

[Figure 6.11 Current–voltage characteristics of  \$24^\circ\$   \$\text{YBa}\_2\text{Cu}\_3\text{O}\_7\$  grain-boundary junctions: \(a\) at 4.2 K \[34\] and \(b\) at 77 K. Junction width: 2.3  \$\mu\text{m}\$ ; film thickness: 120 nm.](#)

[Figure 6.12 Current–voltage characteristics of Josephson junctions under microwave irradiation calculated from the RCSJ model. \(a\)  \$\beta\_c = 0.5\$  and \(b\)  \$\beta\_c = 10\$ . The inset in \(a\) shows the critical current \( \$\bullet\$ \) and the height of the first Shapiro step \( \$\circ\$ \) plotted versus the a.c. amplitude. All currents are given in units of the critical current  \$I\_c\$  in the absence of microwave irradiation.](#)

[Figure 6.13 Measured current–voltage characteristics of Josephson junctions under microwave irradiation. \(a\) Overdamped  \$\text{YBa}\_2\text{Cu}\_3\text{O}\_7\$  grain-boundary junction \[37\]. \(Courtesy of C. Schneider and J. Mannhart.\) \(b\) Underdamped Nb tunnel junction \[38\]; microwave frequency: 94 GHz.](#)

[Figure 6.14 Schematics of a Josephson junction extended in the  \$x\$  direction.](#)

[Figure 6.15 A “vortex” in a chain of pendulums \(a\) or in a Josephson junction \(b\). The chain of pendulums is realized by means of pins stuck into a rubber band. For a vortex at rest \(vortex center at  \$x\_0\$ \), the solution of the sine-Gordon equation is  \$y\(x\) = 4 \arctan \{\exp\[-\(x - x\_0\)/\lambda\_J\]\}\$ .](#)

[Figure 6.16 \(a\) Current–voltage characteristic of a Sn–SnO–Sn junction in a magnetic field of 0.52 mT parallel to the barrier layer. \(b\) Superposition of current–voltage characteristics for magnetic fields between 0 and 0.8 mT. Vertical scale: 200  \$\mu\text{A}/\text{cm}\$ ; horizontal scale: 100  \$\mu\text{V}/\text{cm}\$ . Measuring temperature: 1.93 K \[44\].](#)

[Figure 6.17 Fluxons that are reflected back and forth cause zero-field steps in an Nb–Pb tunnel junction. Length of the junction: 1 mm, width: 15  \$\mu\text{m}\$ . Josephson penetration depth: about 29  \$\mu\text{m}\$ . Measuring temperature: 4.2 K. Neighboring branches each correspond to one additional fluxon \[47\].](#)

[Figure 6.18 Superimposed current–voltage characteristics of a ring-shaped Nb–Pb Josephson tunnel junction, into which nine fluxons were injected sequentially by means of an electron beam. The numbers indicate the number of fluxons within the ring. Inner diameter of the ring: 100  \$\mu\text{m}\$ ; outer diameter: 150  \$\mu\text{m}\$  \[48\].](#)

[Figure 6.19 Imaging of fluxons in a ring-shaped Josephson tunnel junction by means of low-temperature scanning electron microscopy. \(a\) Geometry of the ring \(inner diameter: 100  \$\mu\text{m}\$ ; outer diameter: 120  \$\mu\text{m}\$ ; circumference in units of  \$\lambda\_J\$ : 5.8\).](#)

[Measuring temperature: 5 K. In the ring there are two moving fluxon–antifluxon pairs. The locations where the collisions between the fluxons and the antifluxons happen are indicated by the bright signal. Image \(b\) shows the collisions for a small bias current and a low fluxon velocity. Image \(c\) refers to a fluxon velocity near the Swihart](#)

velocity  $\bar{c}$  [51].

Figure 6.20 Current–voltage characteristic of a long Josephson junction in an external magnetic field calculated from Eq. (6.20) (applied magnetic flux:  $5\Phi_0$ ). Junction length:  $10\lambda_J$ . Damping parameter  $\beta_c = (f_c/f_p)^{1/2} = 50$ .

Figure 6.21 Coulomb blockade and Coulomb staircase shown for the example of the current–voltage characteristic of a tunnel junction with an extremely small capacity between a Pt–Ir tip and the surface of a granular Au film. Measuring temperature: 4.2 K. Curve A: large distance between tip and surface; curve B: short distance between tip and surface [57].

Figure 6.22 Schematics of the “Cooper pair box.” (a) A superconducting island is connected with a superconducting counter-electrode by means of a tunnel junction (capacity  $C_j$ ). The number of electrons on the island can be controlled by means of a gate electrode (capacity  $C_g$ ). (b) Charging energy of the island plotted versus the charge  $C_g U$  induced by the gate electrode.

Figure 6.23 Measurement of the time-averaged charge  $\langle n \rangle$  induced by the gate electrode shown in Figure 6.21 plotted versus the gate voltage. The superconductor is Al. The dashed line indicates the behavior of  $\langle n \rangle$  in the absence of the quantum mechanical interaction between neighboring states  $|n\rangle$  and  $|n+1\rangle$ . The behavior of  $\langle n \rangle$  of a normal conducting reference island, where the charge varies in units of  $e$ , is also shown.

Figure 6.24 Observation of Rabi oscillations by means of a Cooper pair box. Used superconductor: Al; measuring temperature: 30 mK. The two states differing by one Cooper pair are denoted by  $|0\rangle$  and  $|1\rangle$ . In the upper left diagram, the electrostatic energies of these states are shown as crossing dotted lines as a function of the charge  $Q_t$  induced on the island by the gate voltage. The crossing point is located at  $Q_t = e$ . The quantum mechanical coupling due to the Josephson effect splits the energetically degenerate states (parabolic solid lines), and at  $Q_t = e$  the splitting takes the value  $E_J$  (Josephson coupling energy). Initially, at  $Q_t = Q_0$  the system is in the state  $|0\rangle$ . By means of a short pulse (see the lower left graph) the gate voltage and, hence,  $Q_t$  is raised up to the value  $e$  within a few picoseconds. Now the system oscillates for a time  $\Delta t$  with frequency  $f = E_J/h = 1/T_{coh}$  between  $|0\rangle$  and  $|1\rangle$ . Subsequently  $Q_t$  is reduced very quickly again to its starting value. Depending on the pulse width  $\Delta t$ , with a certain probability the Cooper pair box exists either in the state  $|0\rangle$  or in the state  $|1\rangle$ . The state  $|1\rangle$  with the higher energy is unstable. The excess charge  $2e$  flows off in the form of two quasiparticles via the tunnel junction. If  $\Delta t$  is varied, this tunneling current oscillates as a function of  $\Delta t$  with the period being just  $T_{coh}$ . The experimental result is shown in the graph on the right-hand side. In the experiment the Josephson coupling energy could be controlled by a magnetic field or a flux  $\Phi$ . The inset of this graph

shows the value of  $E_J$  determined from  $T_{coh} = h/E_J$  for various values of  $\Phi$  and compares these values with measurements from independent studies (“microwave spectroscopy”).

Figure 6.25 Macroscopic quantum tunneling (MQT) in a Josephson junction. The potential normalized to  $E_J$  (Eq. (6.25)) is shown for  $I/I_c = 1/4$ .

Figure 6.26 Double-well potential for the generation of quantum mechanically superimposed states: (a) symmetric potential with energetically degenerate energy levels (horizontal lines; only a few levels are shown schematically) and (b) tilted potential with nondegenerate ground state.

Figure 6.27 Circuit quantum electrodynamics based on a Cooper-pair box coupled to a superconducting resonator. A: Scheme of the superconducting chip. (Reprinted with permission of [74], © 2004 American Physical Society.) B: Measurements of the transmission probability of a microwave through the circuit ([75], © 2004 Nature). In the upper part, the energy levels of the Cooper-pair box are adjusted such that they are far from the energy levels of the resonator. In the lower part, both qubit levels coincide with the energy levels of the resonator. The dashed curve in part (b) is the theoretical curve in the uncoupled case.

## Chapter 7: Applications of Superconductivity

Figure 7.1 (a) Strongly overstabilized Nb–Ti conductor in a Cu matrix. Seven such tapes were electron-beam-welded together along their flat surface, and then were used as the conductor material in the bubble chamber magnet at CERN (see Figure 7.4). At 5 T,  $I_c$  amounts to 110 A. (b) Scanning electron microscope image of a multifilamentary conductor made of Nb–Ti. The superconducting material is embedded into a matrix made from Cu and CuNi. To obtain the image, the Cu was removed by etching.

Figure 7.4 Cross-section of a “cable in conduit.” (a) Whole cable; the individual wires are grouped around a central opening of 1 cm diameter. (b) Individual wire (diameter 0.81 mm) consisting of Nb<sub>3</sub>Sn filaments within a Cu matrix.

Figure 7.2 Superconducting laboratory magnets. The coil diameter ranges from a few centimeters up to decimeters.

Figure 7.3 Pancake coil of the superconducting bubble chamber magnet of the European Nuclear Research Center (CERN) in Geneva.

Figure 7.5 Critical current densities at 4.2 K of Nb–Ti, Nb<sub>3</sub>Sn, and Bi<sub>2</sub>Sr<sub>2</sub>CaCu<sub>2</sub>O<sub>8</sub> conductor tapes plotted versus the magnetic field.

Figure 7.6 (a) Cross-section of a (Bi,Pb)<sub>2</sub>Sr<sub>2</sub>Ca<sub>2</sub>Cu<sub>3</sub>O<sub>10</sub> conductor tape. (By courtesy of O. Eibl, University of Tübingen.) (b) Schematic of a YBa<sub>2</sub>Cu<sub>3</sub>O<sub>7</sub> film prepared using the RABiTS/MOD process on a nickel alloy substrate.

Figure 7.7 Superconducting tapes made of YBa<sub>2</sub>Cu<sub>3</sub>O<sub>7</sub> (right) compared with a copper

cable (left), which can carry the same amount of current.

Figure 7.8 Schematics of a twisted superconducting cable for applications in the case of temporally changing currents and fields. The three arrangements (a) rope, braid, and Rutherford design – require a flexible wire. ([26], © IEEE.) The schematics (b) (Röbel-design) is suitable also in the case of tape conductors made of high-temperature superconductors.

Figure 7.9 Three examples (a),(b) and (c) of electric coil protection:  $N$  = current supply;  $r$  = internal resistance of the coil;  $R$  = protective resistance;  $S$  = switch, which is automatically activated at a disturbance. The dashed lines surround the parts located within the He bath.

Figure 7.10 Schematic diagram of nuclear magnetic resonance: (a) energy levels and (b) absorption signal.

Figure 7.11 Comparison between the NMR spectra of estradiol acetate in fields of 9.4 T (a), 14.1 T (b), and 21.1 T (c).

Figure 7.12 NMR spectrometer: (a) modern 1000 MHz NMR spectrometer with a highly homogeneous 21.1 T magnetic field and (b) principle of construction of an NMR magnet system cooled with superfluid helium.

Figure 7.13 View into the 3 T whole-body nuclear spin tomography with a superconducting magnet, installed in the Radiology Clinic at the University of Tübingen (Siemens Magnetom Trio). In the foreground we see the table that is moved into the tube of the tomography.

Figure 7.14 Magnetic resonance image of a human head and brain.

Figure 7.15 View of the dipole magnets within the LHC circular tunnel.

Figure 7.16 Two dipole magnets of the LHC are joined together.

Figure 7.17 Schematic of the fusion reactor ITER, which is presently under construction. The toroidal plasma chamber (with a kidney-shaped cross-section) is enclosed by 18 field coils (each 14 m high and 8 m wide). At the torus axis (center of the picture), the central coil (12 m high, 4 m diameter) is placed vertically. The torus is surrounded by six poloidal coils and by smaller correcting coils.

Figure 7.18 Magnetic energy storage device consisting of 10 Nb–Ti coils (diameter of each coil: 36 cm). Up to 420 kJ can be stored.

Figure 7.19 The rotating part of the magnetic bearing of a flywheel (a). Courtesy of IOP. The layer made of  $\text{YBa}_2\text{Cu}_3\text{O}_7$ -pellets, above which the flywheel rotates (b).

Figure 7.20 A 5 MW ship's engine having superconducting rotor coils [55].

Figure 7.21 Schematics of the construction of a current generator in the case of a wind power plant [56].

Figure 7.22 1.75 MVA generator for operation in a hydroelectric power plant.

Figure 7.23 Schematic construction of a magnetic separator [57].

Figure 7.24 Magnetic block-heating facility (induction heater) containing superconducting HTS-magnets.

Figure 7.25 Magnetically levitated Maglev MLX 01 train on the test track near Tokyo.

Figure 7.26 Superconducting cable as it is operated in the Long Island project. Around an inner core made of copper, two layers of  $\text{Bi}_2\text{Sr}_2\text{Ca}_2\text{Cu}_3\text{O}_{10}$ -tape conductors, which are separated from each other by dielectric layers, are wound in a spiral. The outer spiral layer is made of copper and serves for stabilization. The corrugated tubes constitute the cryostat system. Liquid nitrogen passes through the inner tube. The space between both corrugated tubes is evacuated and contains insulating layers.

Figure 7.27 The cable system of the Long Island project.

Figure 7.28 A resistive 42 MVA to 31 kV current fault limiter. (a) Whole system and (b) coil system.

Figure 7.29 Sectional view of an inductive 15 MVA to 10 kV current fault limiters

Figure 7.30 Surface resistance of aluminum plotted versus the reduced temperature. (From [68].) Curve 1:  $f = 15.7 \text{ GHz}$ ,  $hf = 0.64k_B T_c$ ; Curve 2:  $f = 60 \text{ GHz}$ ,  $hf = 2.46k_B T_c$ ; Curve 3:  $f = 76 \text{ GHz}$ ,  $hf = 3.08k_B T_c$ ; Curve 4:  $f = 89 \text{ GHz}$ ,  $hf = 3.63k_B T_c$ ; and Curve 5:  $f = 94.5 \text{ GHz}$ ,  $hf = 3.91k_B T_c$ .

Figure 7.31 Surface resistance of (a)  $\text{YBa}_2\text{Cu}_3\text{O}_7$  compared to Cu at 77 K [72] and (b) Nb at 1.8 and 4.16 K. The residual resistance at low temperatures is also shown [77].

Figure 7.32 Critical high-frequency fields  $H = B/\mu_0$  in the superconductors Nb and  $\text{Nb}_3\text{Sn}$  plotted versus the temperature. Above this field the surface resistance strongly increases. The thermodynamic critical fields  $H_c$  and the superheating fields  $H_{sh}$  are also shown. In the case of  $\text{Nb}_3\text{Sn}$ ,  $H_{c1}$  is also indicated.

Figure 7.33 Principle of the acceleration of charged particles in a cylindrical resonating cavity. The resonator is excited in the “ $\text{TM}_{010}$  mode,” in which the electric field is oriented parallel to the z-axis, and the magnetic field in azimuthal direction.

Figure 7.34 Resonator structure for the acceleration of electrons at CEBAF (Jefferson Laboratory, Newport News, Virginia, USA). (a) Cross-sectional drawing. (b) Real structure. The structure consists of five resonators covered with a Nb layer and placed in series. Its active length is 50 cm. The resonance frequency is 1.5 GHz. The electron beam traverses the resonator during one half-wave, whereas it traverses the opening between the resonators during the second half-wave. Therefore, within the resonators the electrons always experience an electric field that accelerates them in the forward direction.

Figure 7.35 Different designs of planar resonator structures: (a) quasilumped element, (b) microstrip, (c) coplanar waveguide, (d) folded microstrip with integrated capacitors, and (e) ring resonator.

Figure 7.36 Eight-pole elliptic bandpass filter consisting of meandering  $\text{YBa}_2\text{Cu}_3\text{O}_7$  resonators on a  $\text{MgO}$  substrate and the transmission curve [87].

Figure 7.37 SEM image of an  $8 \times 8$  microcalorimeter array and a magnified detail of the  $\text{Si}_3\text{N}_4$  membranes, which allow a freely hanging mount of each calorimeter. The magnified detail also shows part of the thermometer [98].

Figure 7.38 The cartridge of the seventh frequency band of the ALMA telescope.

Figure 7.39 HEB mixer made from NbN. Scanning electron microscope image of three microbridges integrated into a dipole antenna ((A) the bridges can just be seen in the form of very narrow lines in the slit between the wide contact areas) and the current-voltage characteristic of a bridge (a) without and (b) with high-frequency irradiation with a local oscillator. The bridges are  $0.4 \mu\text{m}$  long and  $0.8 \mu\text{m}$  wide [113].

Figure 7.40 Integrated superconducting receiver for frequencies up to 600 GHz. (a) Photograph of the central part of the chip with  $4 \times 4 \text{ mm}^2$  total area. (b) Magnification of the part with the SIS-mixer. The section shown represents an area of about  $100 \times 150 \mu\text{m}^2$  and is rotated by  $90^\circ$  relative to the photograph (a).

Figure 7.41 Realized geometries of planar d.c. SQUIDs made of high-temperature superconductors (mainly from  $\text{YBa}_2\text{Cu}_3\text{O}_7$ ). The Josephson junctions are generated at the grain boundary within the substrate (often  $\text{SrTiO}_3$ ), indicated by the dashed line. The current input is located at the upper or lower edges of the structures indicated as the extensions [125].

Figure 7.42 Different  $\text{YBa}_2\text{Cu}_3\text{O}_7$  SQUID magnetometer designs together with a flux transformer. (a) and (b) Show a directly coupled magnetometer, in which a large input loop (b) within a single superconducting layer is connected with the SQUID (a). (c) Shows a single-layer transformer fabricated on a separate substrate, placed on top of the SQUID in the flip-chip technology. (d) Shows a magnetometer in which the transformer and the SQUID are integrated on the same chip using a two-layer technology. The input coil of the transformer consists of 12 windings, and the washer SQUID located below has an edge length of  $0.5 \text{ mm}$  [125].

Figure 7.43 Multiloop or “cartwheel” SQUID magnetometer: (a) schematic representation; (b) 16-loop magnetometer made of  $\text{YBa}_2\text{Cu}_3\text{O}_7$  on a bicrystal substrate with  $1 \times 1 \text{ cm}^2$  area [125, 128]; and (c) 8-loop magnetometer made of Nb [129]. The two differently hatched areas in (a) indicate two different superconducting layers. The two Josephson junctions in each loop are indicated by crosses.

Figure 7.44 Signal-reading principle of the d.c. SQUID: (a) equivalent circuit of the SQUID; (b) schematic current–voltage characteristic; and (c) voltage modulation at

constant applied current [125].

Figure 7.45 Flux noise and energy resolution of a  $\text{YBa}_2\text{Cu}_3\text{O}_7$  SQUID operated at 77 K for the application only of the flux modulation technique (static bias) and of the double modulation technique (bias reversal). The peaks visible above 1 kHz are caused by the bias reversal technique itself. At low frequencies perturbing signals caused by the a.c. environment (at harmonics of 60 Hz) and due to other sources can be seen [125].

Figure 7.46 Functional principle of the r.f. SQUID: total flux through the ring plotted versus the external flux.

Figure 7.47 Superconducting quantum interference filter (SQIF). (a) Equivalent circuit and (b) voltage response of a 30-junction interferometer compared with a d.c. SQUID of the same size.

Figure 7.48 Comparison between environmental noise sources and important biomagnetic fields.

Figure 7.49 Realizations of single-layer planar gradiometers measuring the gradient  $\frac{dB_z}{dy}$  [124]. In (a) the field gradient generates a current in strip “3,” which is coupled to the SQUID “4” [144]. The gradiometer of  $1 \times 1 \text{ cm}^2$  area shown in (b) is coupled to the SQUID in the center and, in turn, is coupled to the larger gradiometer (c) [145].

Figure 7.50 Different gradiometers constructed from wires. The wire connections between the windings are not shown. (a,b) Symmetric or antisymmetric gradiometer of second order for  $\frac{d^2B_z}{dz^2}$ . (c,d) Symmetric or antisymmetric gradiometer of third order for  $\frac{d^3B_z}{dz^3}$ . The curved arrows indicate the current direction in the gradiometer; the straight arrows show the direction of the magnetic fields generated by the currents.

Figure 7.51 SQUID multichannel system for magneto-encephalography. (a) Whole system with a test person within a magnetically shielded chamber (CTF MEG system, installed at Riken, Japan). (b) View into the helmet-like SQUID arrangement of 275 sensors in the form of radial gradiometers.

Figure 7.52 Low-field nuclear spin tomography of a pepper–vegetable. (a) “Free” sample. (b) The pepper–vegetable was kept in an aluminum can.

Figure 7.53 Different types of SQUID microscopes: (a–c) The SQUID including the flux transformer is scanned over the surface of the cooled sample. (d–f) The SQUID and the sample are thermally insulated from each other, where the sample perhaps can remain in air at room temperature. (f) The magnetic field signal is coupled into the SQUID by means of a ferromagnetic tip.

Figure 7.54 Section of the portrait of George Washington on a \$1 bill imaged with the SQUID microscope [162].

Figure 7.55 Schematic diagram of the arrangement of Josephson junctions and of the microwave input in a voltage standard [171].(a) layout, (b) array schematic.

Figure 7.56 The 10 V voltage standard consisting of 20 208 Josephson tunnel junctions. The series-connected junctions are supplied with direct current. The microwaves (75 GHz) are coupled into the chip via a finline antenna and there are distributed to the branches of the meander [171].

Figure 7.57 Establishing a quantized voltage level on the characteristic of a voltage standard. A given voltage  $V_s$  can distribute itself along the load line  $V_s/R$  in different ways over the Josephson junctions and the resistors  $R$  inserted in the circuit [171].

Figure 7.58 Locations of the current input at a programmable voltage standard containing nonhysteretic Josephson junctions [171].

Figure 7.59 Sequence of voltage or current pulses across a Josephson junction. Numerical calculation based on Eq. (6.13), RCSJ model.

Figure 7.60 Basic principle of the RSFQ logic. (a) elementary numerical call, (b) scheme of an “or” gate.

Figure 7.61 Basic circuits from the RSFQ logic: (a) pulse-splitter and (b) set-reset flip-flop.

Figure 7.62 A 20 GHz microprocessor containing about 65 000 Nb Josephson junctions [187].

Figure 7.63 Circuit consisting of four qubits coupled together. (a) schematic circuit, (b) image of chip. The capacitive coupling structure is located within the dashed square. The qubits are located in the center of the dark regions and are inductively coupled to the bias connections and the read-out SQUIDs.

## List of Tables

Chapter 2: Superconducting Elements, Alloys, and Compounds

Table 2.1 Selected superconducting elements, crystal structure, melting point, and some properties of the superconducting state

Table 2.2 Superconducting compounds with the  $\beta$ -tungsten structure [24, 13]

Table 2.3 Superconducting properties of the Chevrel phases [[38], M7]

Table 2.4 Superconducting properties of some boron carbides

Table 2.5 Superconducting properties of some heavy-fermion superconductors

Table 2.6 Properties of the superconducting state of some dichalcogenides and their intercalates

Table 2.7 Characteristic data of different cuprate superconductors

Table 2.8 Data of some iron pnictides

Table 2.9 Data of some organic superconductors based on the BEDT molecule

## Chapter 3: Cooper Pairing

[Table 3.1 Isotope effect in mercury \[13\]](#)

[Table 3.2 Isotope effect](#)

[Table 3.3 Energy gap  \$2\Delta\_0\$  in units of  \$k\_B T\_c\$  for some superconducting elements](#)

[Table 3.4 Energy gap  \$2\Delta\_0\$  for selected superconducting compounds \(s-wave Cooper pairing\)](#)

[Table 3.5 Reduction of the transition temperature of some superconductors due to paramagnetic ions](#)

## Chapter 4: Thermodynamics and Thermal Properties of the Superconducting State

[Table 4.1 Values of  \$\(c\_s - c\_n\)\_{T=T\_c}\$  obtained from thermal and magnetic data](#)

[Table 4.2 The  \$\kappa\$  values<sup>a</sup> of In–Bi alloys](#)

[Table 4.3 The  \$\kappa\_0\$  values<sup>a</sup> of superconducting elements](#)

*Reinhold Kleiner and Werner Buckel*

# **Superconductivity**

## **An Introduction**

*Third, Updated Edition*

**WILEY-VCH**  
Verlag GmbH & Co. KGaA

## **The Authors**

### **Professor Dr. Werner Buckel deceased**

Technische Universität Karlsruhe  
Kösliner Str. 87  
76139 Karlsruhe  
Germany

### **Professor Dr. Reinhold Kleiner**

Physikalisches Institut  
Auf der Morgenstelle 14  
72076 Tübingen  
Germany

### **Translator**

### **Professor Dr. Rudolf Hübener**

Physikalisches Institut  
Auf der Morgenstelle 14  
72076 Tübingen  
Germany

Translation of the 7th German edition

## **Cover**

Photo courtesy: © Kiyoshi Takahase Segundo/Stockami

All books published by **Wiley-VCH** are carefully produced. Nevertheless, authors, editors, and publisher do not warrant the information contained in these books, including this book, to be free of errors. Readers are advised to keep in mind that statements, data, illustrations, procedural details or other items may inadvertently be inaccurate.

### **Library of Congress Card No.:** applied for

### **British Library Cataloguing-in-Publication Data**

A catalogue record for this book is available from the British Library.

### **Bibliographic information published by the Deutsche Nationalbibliothek**

The Deutsche Nationalbibliothek lists this publication in the Deutsche Nationalbibliografie; detailed bibliographic data are available on the Internet at <<http://dnb.d-nb.de>>.

© 2016 Wiley-VCH Verlag GmbH & Co. KGaA,

Boschstr. 12, 69469 Weinheim, Germany

All rights reserved (including those of translation into other languages). No part of this book may be reproduced in any form – by photoprinting, microfilm, or any other means – nor transmitted or translated into a machine language without written permission from the publishers. Registered names, trademarks, etc. used in this book, even when not specifically marked as such, are not to be considered unprotected by law.

**Print ISBN:** 978-3-527-41162-7

**ePDF ISBN:** 978-3-527-68652-0

**ePub ISBN:** 978-3-527-68654-4

**Mobi ISBN:** 978-3-527-68653-7

**oBook ISBN:** 978-3-527-68651-3

**Cover Design** Schulz Grafik-Design, Fußgönheim, Germany

**Printing and Binding** Markono Print Media Pte Ltd., Singapore

## **Related Titles**

Bhattacharya, R., Paranthaman, M. (eds.)

### **High Temperature Superconductors**

2010

Print ISBN: 978-3-527-40827-6, also available in electronic formats

Bezryadin, A.

### **Superconductivity in Nanowires**

### **Fabrication and Quantum Transport**

2012

Print ISBN: 978-3-527-40832-0, also available in electronic formats

Altomare, F., Chang, A.M.

### **One-Dimensional Superconductivity in Nanowires**

2013

Print ISBN: 978-3-527-40995-2, also available in electronic formats

Buzdin, A.I., Ryazanov, V.V.

### **Superconductor-Ferromagnet Hybrid Structures**

2015

Print ISBN: 978-3-527-41033-0, also available in electronic formats

Hofmann, P.

### **Solid State Physics**

### **An Introduction, 2nd Edition**

2015

Print ISBN: 978-3-527-41282-2, also available in electronic formats

# Preface to the Third Edition

Because 8 years have passed since the last edition of this book, it was time to revise the text and to cover new developments. With the iron-pnictides a new class of superconductors has been found. Among the physicists, this discovery generated almost the same excitement as the discovery of the cuprate superconductors in the 1980s. Furthermore, there were many interesting applications, say, in the area of superconducting cables or magnets, or with the qubits in the area of microelectronics. In order to keep the size of this book within reasonable limits, by far not all results could be included. For this I apologize.

As in the previous editions, the guiding principle, followed by Werner Buckel, remained to explain superconductivity as simple as possible. Also the nonexperts should be able to gain insight into this exciting field at its age of 100 years by now.

I am thanking all colleagues who have contributed to the new edition by means of ideas and suggestions, in particular Vera Palmer, Ulrike Werner, as well as Harald Reiss, Paul Seidel, and Peter Kes. Particularly I want to thank Rudolf Huebener for his excellent translation of the 7th German edition. I thank Klaus Schlenga, Bruker EST, for helping with the text of Section Nuclear Magnetic Resonance. For allowing to reproduce unpublished figures I thank Mrs. van Bühl, Nexans, Cheri Hart, AMSC, as well as Joachim Albrecht, Hochschule Aalen, Alexander Henning, Bruker ASC, Tom H. Johansen, Superconductivity Laboratory of Oslo University, Hans Henning Klauss, TU Dresden, Hubertus Lütkens, Paul Scherrer Institut, S. Mahieu, IRAM, Xiaofeng Qian, MIT, Daniel Schmickler, Zenergy GmbH, and Converteam UK Ltd, Wolfgang Schmidt, Siemens AG, Michael Strasik, Boeing, and CERN.

*Reinhold Kleiner*

Tübingen

July 2015

# Introduction

In physics, many phenomena result from the activity of specific mutual interactions. An important example is the relation between the uncorrelated thermal motion of the atomic building blocks of matter and the ordering forces between these building blocks. With increasing temperature, the thermal motional energy eventually becomes sufficiently large compared to some relevant ordering interaction energy that the ordered state of matter, established at low temperatures, breaks down. All phase transitions, say, from the liquid to the gaseous state, as well as the construction of the atoms themselves from the elementary constituents of matter, follow this rule. Therefore, it is not surprising that often unexpected new properties of matter, which subsequently also may become important for technology, are discovered in experiments performed under extreme conditions. Superconductivity is an example of such a discovery.

In the year 1908, Kamerlingh-Onnes [1],<sup>1</sup> Director of the Low-Temperature Laboratory at the University of Leiden, finally achieved the liquefaction of helium as the last of the noble gases. He had founded this laboratory, which became world-famous under his leadership. At atmospheric pressure the boiling point of helium is 4.2 K. It can be reduced further by pumping. The liquefaction of helium extended the available temperature range near to the absolute zero point. The first successful experiment still needed the total combined manpower of the Institute. However, earlier Kamerlingh-Onnes was able to perform extended experiments at these low temperatures. At first, he started an investigation of the electrical resistance of metals.

At that time, ideas about the mechanism of electrical conduction were only poorly developed. It was known that it must be electrons affecting the charge transport. Also the temperature dependence of the electrical resistance of many metals had been measured, and it had been found that near room temperature the resistance decreases linearly with decreasing temperature. However, at low temperatures, this decrease was found to become weaker and weaker. In principle, there were three possibilities to be discussed:

1. The resistance could approach zero value with decreasing temperature (James Dewar, 1904; [Figure 1](#), curve 1).
2. It could approach a finite limiting value (Heinrich Friedrich Ludwig Matthiesen, 1864; [Figure 1](#), curve 2).
3. It could pass through a minimum and approach infinity at very low temperatures (William Thomson = Lord Kelvin, 1902; [Figure 1](#), curve 3).

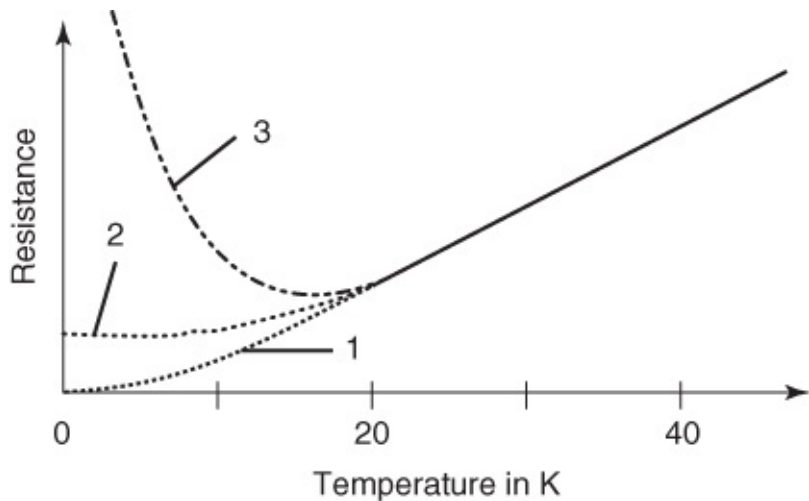


**Figure 1** Schematics of the temperature dependence of electrical resistance at low temperatures. See text for details of curves.

In particular, the third possibility was favored by the idea that at sufficiently low temperatures, the electrons are likely to be bound to their respective atoms. Hence, their free mobility was expected to vanish. The first possibility, according to which the resistance would approach zero at very low temperatures, was suggested by the strong decrease with decreasing temperature.

Initially, Kamerlingh-Onnes studied platinum and gold samples, since at that time he could obtain these metals with high purity. He found that during the approach to zero temperature, the electrical resistance of his samples reached a finite limiting value, the so-called residual resistance, a behavior corresponding to the second possibility discussed earlier. The value of this residual resistance depended on the purity of the samples. The purer the samples, the smaller was the residual resistance. After these results, Kamerlingh-Onnes expected that in the temperature range of liquid helium ideally pure platinum or gold should have a vanishingly small resistance. In a lecture at the Third International Congress of Refrigeration in Chicago in 1913, he reported on these experiments and arguments. There he said [2]: “Allowing a correction for the additive resistance I came to the conclusion that probably the resistance of absolutely pure platinum would have vanished at the boiling point of helium.” These ideas were supported further by the quantum physics rapidly developing at that time. Albert Einstein had proposed a model of crystals, according to which the vibrational energy of the crystal atoms should decrease exponentially at very low temperatures. Since the resistance of highly pure samples, according to the view of Kamerlingh-Onnes (which turned out to be perfectly correct, as we know today), is only due to this motion of the atoms, his hypothesis mentioned above appeared obvious.

In order to test these ideas, Kamerlingh-Onnes decided to study mercury, the only metal at the time that he hoped could be extremely well purified by means of multiple distillation. He estimated that at the boiling point of helium he could barely just detect the resistance of mercury with his equipment, and that at still lower temperatures it should rapidly approach a zero value.

The initial experiments carried out by Kamerlingh-Onnes, together with his coworkers Gerrit Flim, Gilles Holst, and Gerrit Dorsman, appeared to confirm these concepts. At temperatures below 4.2 K the resistance of mercury, indeed, became immeasurably small. In his lecture of 1913, Kamerlingh-Onnes summarized this phase of his experiments and ideas as follows: "With this beautiful prospect before me there was no more question of reckoning with difficulties. They were overcome and the result of the experiment was as convincing as could be."

However, during his further experiments using improved apparatus, he soon recognized that the observed effect could not be identical to the expected decrease in resistance. The resistance change took place within a temperature interval of only a few hundredths of a degree and, hence, it resembled more of a resistance jump than a continuous decrease.

[Figure 2](#) shows the curve published by Kamerlingh-Onnes [3]. As he himself commented [2]: "At this point (slightly below 4.2 K) within some hundredths of a degree came a sudden fall not foreseen by the vibrator theory of resistance, bringing the resistance at once to less than a millionth of its original value at the melting point. ... Mercury had passed into a new state, which on account of its extraordinary electrical properties may be called the superconductive state."

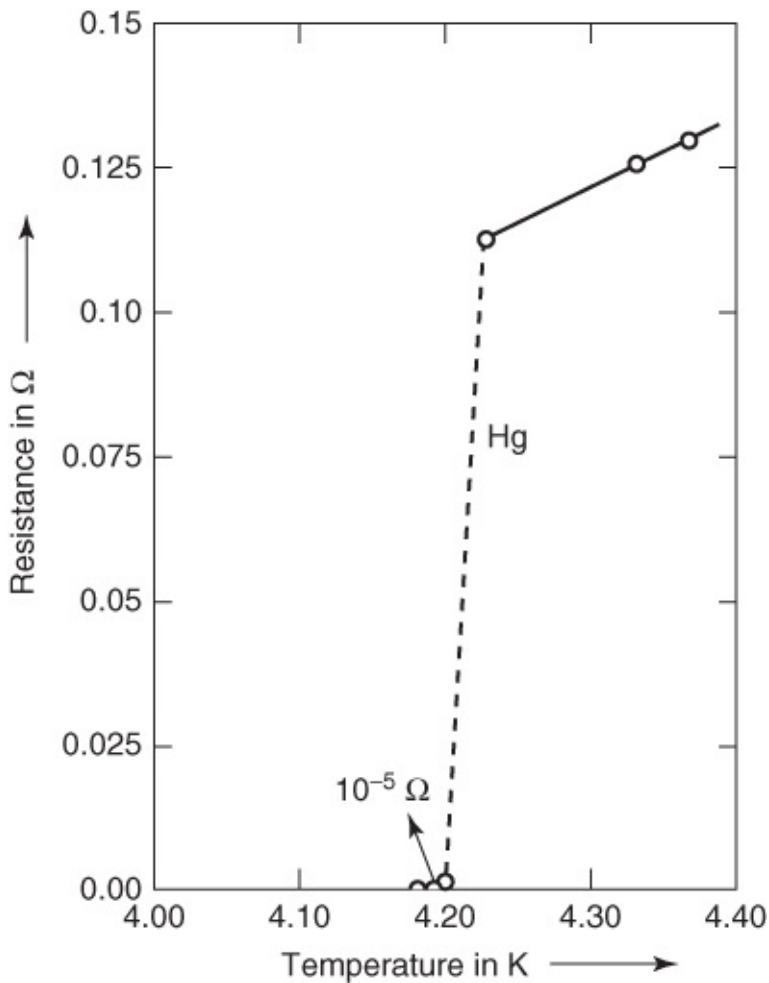


[Figure 2](#) The superconductivity of mercury.

(After Ref. [3].)

In this way, also the name for this new phenomenon had been found. The discovery came unexpectedly during experiments that were meant to test some well-founded ideas. Soon it became clear that the purity of the samples was unimportant for the vanishing of the resistance. The carefully performed experiment had uncovered a new state of matter.

Today we know that superconductivity represents a widespread phenomenon. In the Periodic Table of the elements, superconductivity occurs in many metals. Here, at atmospheric pressure, niobium is the element with the highest transition temperature of about 9 K. Thousands of superconducting compounds have been found, and this development is by no means closed.

The scientific importance of the discovery of superconductivity can be seen from the fact that in 1913 Kamerlingh-Onnes was awarded the Nobel Prize in physics. At that time, hardly anybody could have foreseen the richness in fundamental questions and interesting concepts resulting from this observation, and it took nearly half a century until superconductivity was understood at least in principle.<sup>2</sup>

The vanishing of the electrical resistance below a “critical temperature” or “transition temperature”  $T_c$  is not the only unusual property of superconductors. An externally applied magnetic field can be expelled from the interior of superconductors except for a thin outer layer (“ideal diamagnetism” or “Meissner–Ochsenfeld effect”), or superconductors can concentrate the magnetic field in the form of “flux tubes.” Here, the magnetic flux is quantized<sup>3</sup> in units of the “magnetic flux quantum,”  $\Phi_0 = 2.07 \times 10^{-15}$  Wb. The ideal diamagnetism of superconductors was discovered by Walther Meissner and Robert Ochsenfeld in 1933. It was a big surprise, since based on the induction law one would only have expected that an ideal conductor conserves its interior magnetic field and does not expel it.

The breakthrough in the theoretical understanding of superconductivity was achieved in 1957 by the theory of John Bardeen, Leon Neil Cooper, and John Robert Schrieffer (“BCS theory”) [4]. In 1972, they were awarded the Nobel Prize in physics for their theory. They recognized that at the transition to the superconducting state the electrons condense pairwise into a new state, in which they form a coherent matter wave with a well-defined phase, following the rules of quantum mechanics. Here the interaction of the electrons is mediated by the “phonons,” the quantized vibrations of the crystal lattice.

The formation of a coherent matter wave, often referred to as a “macroscopic wave function,” represents the key property of the superconducting state. We know similar phenomena from other branches of physics. The laser is based on a coherent wave represented by photons. In the phenomenon of superfluidity below the so-called lambda point, the helium atoms condense into a coherent matter wave [5, 6]. For the isotope  $^4\text{He}$  the lambda point is 2.17 K, and for  $^3\text{He}$  it is about 3 mK. Under the proper conditions, these superfluids can flow without any friction. Furthermore, recently the condensation of gases of alkali atoms such as rubidium or potassium into a coherent quantum state has also been achieved. This “Bose–Einstein condensation” was predicted by Bose and Einstein in 1925. Only in 1995 could such condensates consisting of a few thousand atoms be prepared by means of special optical and magnetic refrigeration techniques at temperatures below 1  $\mu\text{K}$  [7]. Also the discoveries of the laser, of superfluidity,

and of the Bose–Einstein condensation were honored by the awards of Nobel Prizes.<sup>4</sup>

For more than 75 years, superconductivity represented specifically a low-temperature phenomenon. This changed in 1986, when J. G. Bednorz and K. A. Müller discovered superconductors based on copper oxide. For their discovery, the two scientists were awarded the Nobel Prize in physics in 1987 [8]. In the September 1986 issue of the journal *Zeitschrift für Physik B*, Bednorz and Müller published a paper with the cautionary title “Possible high  $T_c$  superconductivity in the Ba–La–CuO system” [9]. In this paper the authors reported that this material loses its resistance at about 30 K. Surprisingly, the paper received only little attention. There were doubts that superconductivity was really observed. The samples consisted of mixtures of several phases among which there were also electrically insulating substances. Therefore, they had large values of the specific electrical resistance. It could well be possible that some phase transition within the texture caused the drop in resistance.<sup>5</sup> Hence, a convincing proof of superconductivity in these samples was still needed.

This proof was achieved by Bednorz, *et al.* [11] by demonstrating the existence of the Meissner–Ochsenfeld effect. [Figure 3](#) shows the key measurement of this paper. Above 40 K both samples displayed the well-known paramagnetism of metals, which is nearly independent of temperature. Around 30 K, that is, in the same temperature range where the drop in resistance appears, during cooling in a magnetic field, an increasing diamagnetism due to the Meissner–Ochsenfeld effect can be seen, and the magnetic susceptibility turns negative.

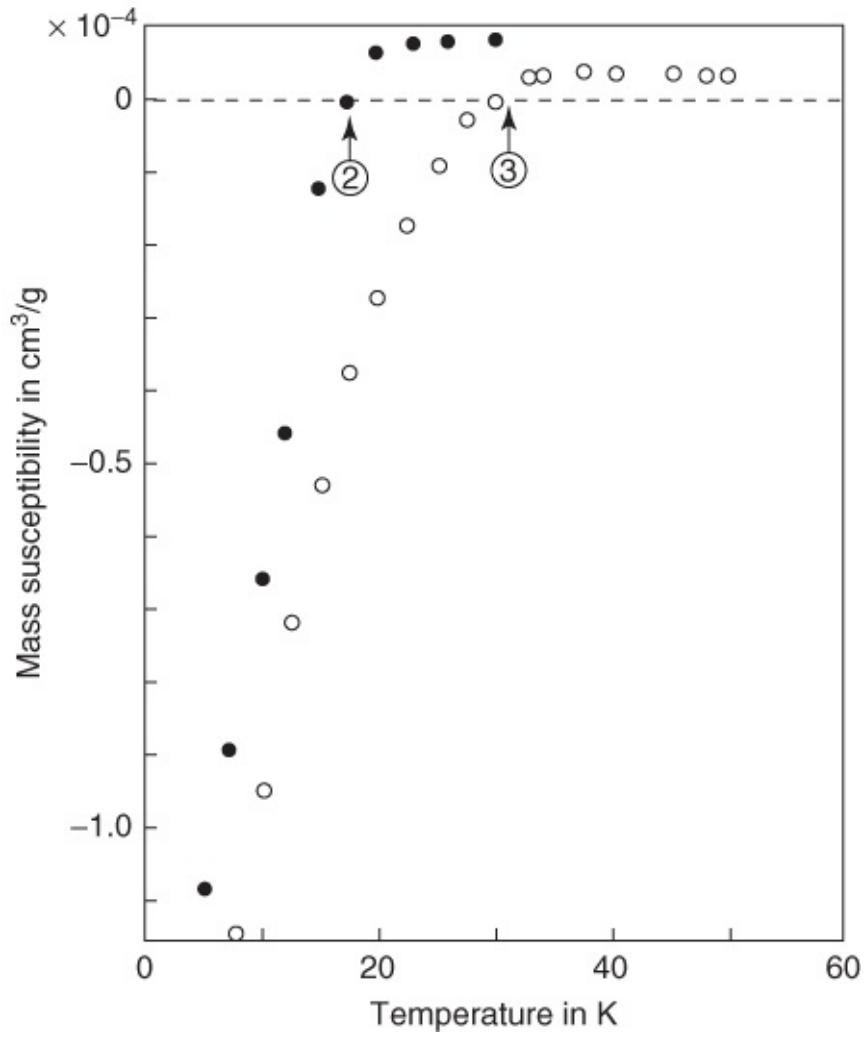


**Figure 3** The magnetic susceptibility of two samples of the Ba–La–Cu–O system versus temperature [11].

This result was highly surprising for the scientific community, because already in the mid-1960s Bernd Matthias and his coworkers had started a systematic study of the metallic oxides (see [12]). They searched among the substances based on the transition metal oxides, such as W, Ti, Mo, and Bi. They found extremely interesting superconductors, for example, in the Ba–Pb–Bi–O system; however, no particularly high transition temperatures were found.

During the turn of 1986/1987 the “gold rush” set in, when it became known that the group of S. Tanaka in Japan could exactly reproduce the results of Bednorz and Müller. Now scientists in countless laboratories all over the world began to study these new oxides. Soon this extraordinary scientific effort yielded successful results. One could show that within the La–Sr–Cu–O system, superconductors with transition temperatures above 40 K could be produced [13]. Only a few weeks later, transition temperatures above 80 K were observed in the Y–Ba–Cu–O system [14, 15]. During this phase, new results were more often reported in press conferences than in scientific journals. The media anxiously followed this development. With superconductivity at temperatures above the boiling point of liquid nitrogen ( $T = 77$  K), one could envision many important technical applications of this phenomenon.

Today we are familiar with a large series of “high-temperature superconductors” based on

copper oxide. Here the most studied compounds are  $\text{YBa}_2\text{Cu}_3\text{O}_7$  (also “YBCO” or “Y123”) and  $\text{Bi}_2\text{Sr}_2\text{CaCu}_2\text{O}_8$  (also “BSCCO” or “Bi2212”), which display maximum transition temperatures around 90 K. Many compounds have transition temperatures even above 100 K. The record value is claimed by  $\text{HgBa}_2\text{Ca}_2\text{Cu}_3\text{O}_8$ , having a  $T_c$  value of 135 K at atmospheric pressure and a value as high as  $T_c = 164$  K at a pressure of 30 GPa. [Figure 4](#) shows the evolution of transition temperatures since the discovery by Kamerlingh-Onnes. The jump-like increase due to the discovery of the copper oxides is particularly impressive.

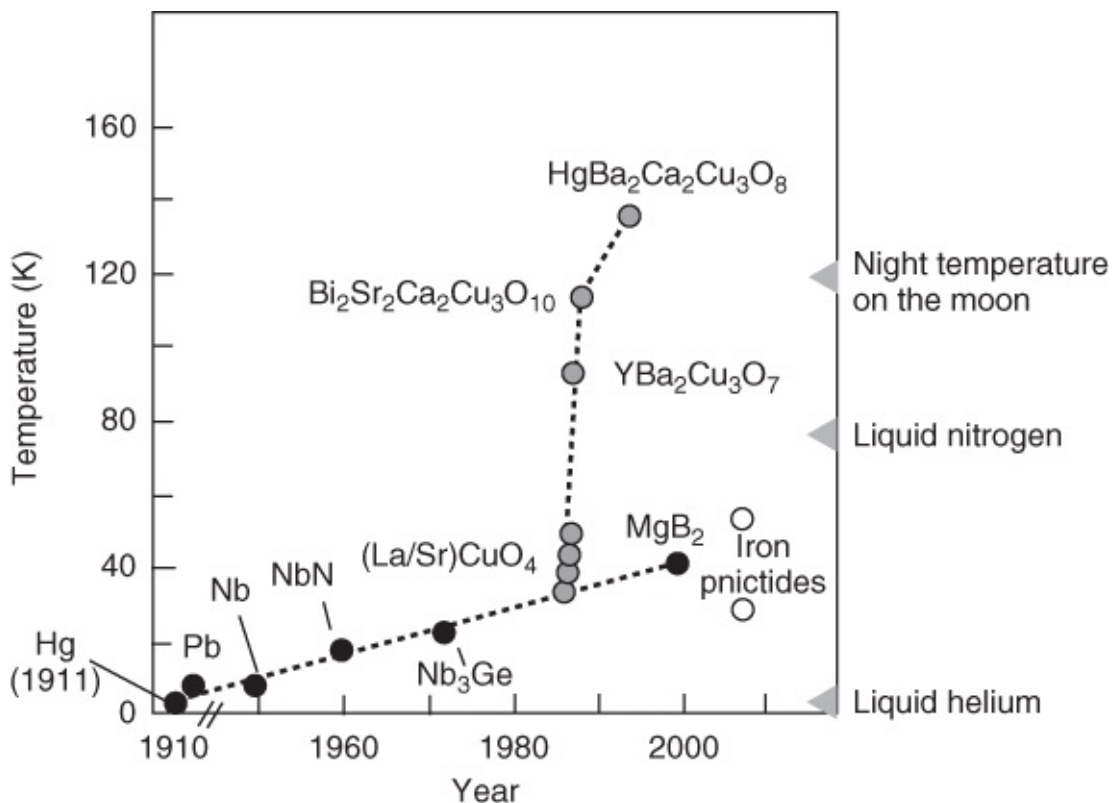


[Figure 4](#) Evolution of the superconducting transition temperature since the discovery of superconductivity.

(After Ref. [16].)

In this figure, we have included the metallic compound  $\text{MgB}_2$ , as well as the group of the iron pnictides. It is surprising that in the case of  $\text{MgB}_2$  superconductivity with a transition temperature of 39 K was discovered only in the beginning of 2000, although this material has been commercially available for a long time [17]. This discovery also generated much activity in the physics community, and in the two following years important properties of this material were clarified.  $\text{MgB}_2$  shows similar behavior as the “classical” metallic superconductors. The excitement at the discovery of the iron pnictides in 2008 was also large [18]. These are compounds in the form  $\text{LaFeAsO}_{0.89}\text{F}_{0.11}$  or  $\text{Ba}_{0.6}\text{KFe}_2\text{As}_2$ , showing transition temperatures up to 55 K. In the case of these materials, layers of iron–arsenic represent the central building block, analogous to the copper-oxide planes in the case of the cuprates.

Many properties of the cuprates, and also of other superconducting compounds, are very

unusual, as we will see during the course of this book. More than 25 years after their discovery, it is still unclear how Cooper pairing is accomplished in these materials. However, magnetic interactions are likely to play an important role. Perhaps we can learn more from a comparison with the iron pnictides.

Another important aspect concerns the maximum electric current, the “critical current,” which a superconductor can carry without electrical resistance. We will see that the property “zero resistance” is not always valid. In the case of AC, the resistance remains finite and increases with increasing frequency of the alternating current. However, the critical current is limited also in the case of DC. It depends on the temperature and the magnetic field, and also on the material and the geometry of the conductor. Even today, it is still a special art to develop a conductor that hundreds of amperes can flow without resistance.

Due to the discovery of the high-temperature superconductors, the phenomenon of superconductivity is not restricted anymore to a temperature range far away from that relevant for all organic life. One hopes that one day materials are found showing this phenomenon at room temperature or even above it.

On the other hand, low temperatures become more and more accessible for day-to-day utilization. Refrigerators and cold boxes are regular household items. Just recently, large advances have been achieved in refrigeration techniques. Modern cryo-coolers today reliably reach temperatures of 30 K, or in some cases even 4.2 K and lower [19].<sup>6</sup> Also cooling with liquid nitrogen is a standard procedure in many branches of industry. Hence, superconductivity will enter our daily lives more and more in the fields of energy technology or microelectronics, for example.

By using liquid helium as a cooling liquid, for sometime one uses metallic superconductors in medical applications, say, for the generation of high magnetic fields in nuclear-spin tomographs or in magnetic-field sensoric. Also voltage standards are based on superconducting devices. In the case of these applications, the compounds NbTi, Nb<sub>3</sub>Sn, and the elementary superconductor Nb are particularly important. Also the high-temperature superconductors are more and more utilized. In the field of energy technology, the first superconducting cables are operating. Superconducting motors, say, for the driving of ships are being fabricated. Superconducting filters made of YBa<sub>2</sub>Cu<sub>3</sub>O<sub>7</sub> are applied in communication technology. Magnetic-field sensors made of this material are utilized in the field for the detection of minerals or for nondestructive testing of materials. High-temperature superconductors can levitate above magnets or can hang even under the magnets. This provides the possibility of a contact-free and nearly frictionless mounting and motion, which is attractive in the case of many areas of technology.

This book is meant to provide an initial exposure to the phenomenon of superconductivity. Only selected aspects could be dealt with. Some subjects have had to be summarized only briefly in order to keep the size of the book within reasonable limits. However, it is hoped that the book transmits some of the fascination that superconductivity has offered now for nearly a century.

## References

1. H. Kamerlingh-Onnes: *Proc. Roy. Acad. Amsterdam* **11**, 168 (1908).
2. H. Kamerlingh-Onnes: *Comm. Leiden*, Suppl. No. **34** (1913).
3. H. Kamerlingh-Onnes: *Comm. Leiden* **120b** (1911).
4. J. Bardeen, L. N. Cooper, J. R. Schrieffer: *Phys. Rev.* **108**, 1175 (1957).
5. D. R. Tilley, J. Tilley: “*Superfluidity and Superconductivity*”, Van Nostrand Reinhold Company, New York (1974).
6. D. M. Lee: *Rev. Mod. Phys.* **69**, 645 (1997); D. D. Osheroff, *Rev. Mod. Phys.* **69**, 667 (1997); R. C. Richardson: *Rev. Mod. Phys.* **69**, 683 (1997).
7. E. A. Cornell, C. E. Wieman: *Rev. Mod. Phys.* **74**, 875 (2002); W. Ketterle: *Rev. Mod. Phys.* **74**, 1131 (2002).
8. J. Bednorz, K. A. Müller, *Rev. Mod. Phys.* **60**, 585 (1988).
9. J. G. Bednorz, K. A. Müller: *Z. Phys. B* **64**, 189 (1986).
10. R. A. Ogg Jr. *Phys. Rev.* **69**, 243 and 668 (1946); **70**, 93 (1946).
11. J. G. Bednorz, M. Takashige, K. A. Müller: *Europhys. Lett.* **3**, 379 (1987).
12. Ch. J. Raub: *J. Less-Common Met.* **137**, 287 (1988).
13. R. J. Cava, R. B. van Dover, B. Batlogg, E. A. Rietmann: *Phys. Rev. Lett.* **58**, 408 (1987); C. W. Chu, P. H. Hor, R. L. Meng, L. Gao, Z. J. Huang, Y. Q. Wang: *Phys. Rev. Lett.* **58**, 405 (1987).
14. M. K. Wu, J. R. Ashburn, C. J. Torng, P. H. Hor, R. L. Meng, L. Gao, Z. J. Huang, Y. O. Wang, C. W. Chu: *Phys. Rev. Lett.* **58**, 908 (1987).
15. Z. X. Zhao: *Int. J. Mod. Phys. B* **1**, 179 (1987).
16. Kirtley, J.R. and Tsuei, C.C. (1996) Spektrum der Wissenschaft, p. 58 (German edition of Scientific American).
17. J. Nagamatsu, N. Nakagawa, T. Muranaka, Y. Zenitani, J. Akimitsu: *Nature* **410**, 63 (2001).
18. H. Takahashi, K. Igawa, K. Arii, Y. Kamihara, M. Hirano, H. Hosono: *Nature* **453**, 376 (2008).
19. C. Heiden: In monograph [M26], S. 289; C. Lienert, G. Thummes, C. Heiden: *IEEE Trans. Appl. Supercond.* **11**, 832 (2002).

- <sup>1</sup> A biography can be found in Spektrum der Wissenschaft, May 1997, pp. 84–89 (German edition of Scientific American).
- <sup>2</sup> For a summary of the history of superconductivity, we refer to monograph [M1].
- <sup>3</sup> The magnetic flux  $\Phi$  through a loop of area  $F$  carrying a perpendicular and spatially homogeneous flux density  $B$  is given by  $\Phi = BF$ . In the following, we denote  $B$  simply by “magnetic field.” In the general case of an arbitrarily oriented and spatially inhomogeneous magnetic field  $\mathbf{B}$  one must integrate over the area of the loop,  $\Phi = \int_F \mathbf{B} d\mathbf{f}$ . The unit of magnetic flux is the weber (Wb), and the unit of magnetic field is the tesla (T). Frequently, the unit gauss (G) is used also ( $1 \text{ G} = 10^{-4} \text{ T}$ ). We have  $1 \text{ Wb} = 1 \text{ T m}^2$ . If a loop is placed at a large distance around the axis of an isolated flux tube, we have  $\Phi = \Phi_0$ .
- <sup>4</sup> To Landau in 1962 ( ${}^4\text{He}$ ); to Townes, Basov, and Prokhorov in 1964 (laser); to Lee, Osheroff, and Richardson in 1996 ( ${}^3\text{He}$ ); and to Cornell, Wieman, and Ketterle in 2001 (Bose–Einstein condensation).
- <sup>5</sup> In the mid-1940s during cooling below about 70 K, sharp drops of the resistance in metallic sodium ammonia solutions were observed, which initially were interpreted in terms of superconductivity. However, in fact, they were due to sodium threads precipitating from the solution [10].
- <sup>6</sup> In the laboratory, by means of various refrigeration methods, temperatures down to only a few millikelvins can be sustained continuously. Based on nuclear spin demagnetization, final temperatures in the microkelvins range and below are reached. For a summary, see the monographs [M32] and [M33].

# Chapter 1

## Fundamental Properties of Superconductors

The vanishing of the electrical resistance, the observation of ideal diamagnetism, or the appearance of quantized magnetic flux lines represent characteristic properties of superconductors that we will discuss in detail in this chapter. We will see that all of these properties can be understood, if we associate the superconducting state with a macroscopic coherent matter wave. In this chapter, we will also learn about experiments convincingly demonstrating this wave property. First we turn to the feature providing the name “superconductivity.”

### 1.1 The Vanishing of the Electrical Resistance

The initial observation of the superconductivity of mercury raised a fundamental question about the magnitude of the decrease in resistance on entering the superconducting state. Is it correct to talk about the *vanishing* of the electrical resistance?

During the first investigations of superconductivity, a standard method for measuring electrical resistance was used. The electrical voltage across a sample carrying an electric current was measured. Here, one could only determine that the resistance dropped by more than a factor of a thousand when the superconducting state was entered. One could only talk about the vanishing of the resistance in that the resistance fell below the sensitivity limit of the equipment and, hence, could no longer be detected. Here, we must realize that in principle it is impossible to prove experimentally that the resistance has exactly zero value. Instead, experimentally, we can only find an upper limit of the resistance of a superconductor.

Of course, to understand such a phenomenon, it is highly important to test with the most sensitive methods to see whether a finite residual resistance can also be found in the superconducting state. So we are dealing with the problem of measuring extremely small values of the resistance. Already in 1914 Kamerlingh-Onnes used by far the best technique for this purpose. He detected the decay of an electric current flowing in a closed superconducting ring. If an electrical resistance exists, the stored energy of such a current is transformed gradually into joule heat. Hence, we need to only monitor such a current. If it decays as a function of time, we can be certain that a resistance still exists. If such a decay is observed, one can deduce an upper limit of the resistance from the temporal change and from the geometry of the superconducting circuit.

This method is more sensitive by many orders of magnitude than the usual current–voltage measurement. It is shown schematically in [Figure 1.1](#). A ring made from a superconducting material, say, from lead, is held in the normal state above the transition temperature  $T_c$ . A magnetic rod serves for applying a magnetic field penetrating the ring opening. Now we cool the ring below the transition temperature  $T_c$  at which it becomes superconducting. The

magnetic field<sup>1</sup> penetrating the opening practically remains unchanged. Subsequently we remove the magnet. This induces an electric current in the superconducting ring, since each change of the magnetic flux  $\Phi$  through the ring causes an electrical voltage along the ring. This induced voltage then generates the current.

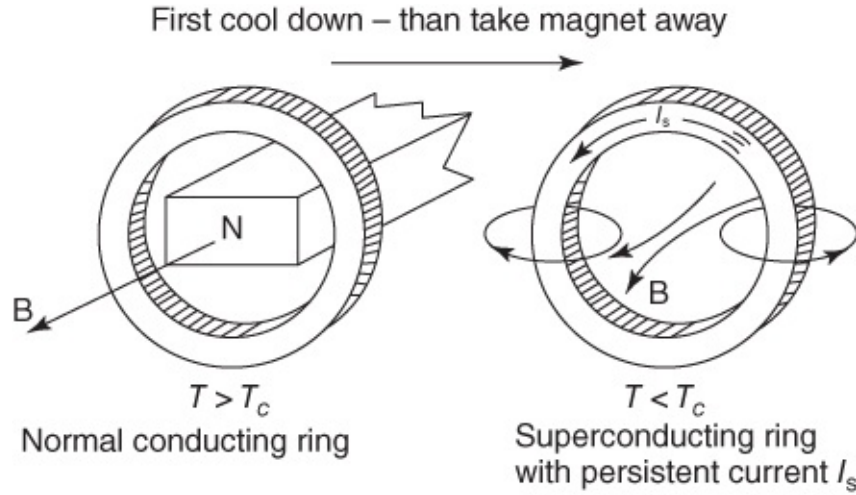


**Figure 1.1** The generation of a permanent current in a superconducting ring.

If the resistance had exactly zero value, this current would flow without any change as a “permanent current” as long as the lead ring remained superconducting. However, if there exists a finite resistance  $R$ , the current would decrease with time, following an exponential decay law. We have

$$I(t) = I_0 e^{-(R/L)t} \quad \text{1.1}$$

Here,  $I_0$  denotes the current at some time that we take as time zero;  $I(t)$  is the current at time  $t$ ;  $R$  is the resistance; and  $L$  is the self-induction coefficient, depending only upon the geometry of the ring.<sup>2</sup>

For an estimate, we assume that we are dealing with a ring of 5 cm diameter made from a wire with a thickness of 1 mm. The self-induction coefficient  $L$  of such a ring is about  $1.3 \times 10^{-7}$  H. If the permanent current in such a ring decreases by less than 1% within an hour, we can conclude that the resistance must be smaller than  $4 \times 10^{-13}$   $\Omega$ .<sup>3</sup>

$$R \leq \frac{-\ln 0.99 \times 1.3 \times 10^{-7}}{3.6 \times 10^3} \frac{\text{Vs}}{\text{Am}} \cong 3.6 \times 10^{-13} \Omega$$

This means that in the superconducting state the resistance has changed by more than 8 orders of magnitude.

During such experiments the magnitude of the permanent current must be monitored. Initially [1] this was simply accomplished by means of a magnetic needle, its deflection in the magnetic field of the permanent current being observed. A more sensitive setup was used by Kamerlingh-Onnes and somewhat later by Tuyn [2]. It is shown schematically in [Figure 1.2](#). In both superconducting rings 1 and 2, a permanent current is generated by an induction process. Because of this current both rings are kept in a parallel position. If one of the rings (here the

inner one) is suspended from a torsion thread and is slightly turned away from the parallel position, the torsion thread experiences a force originating from the permanent current. As a result, an equilibrium position is established in which the angular moments of the permanent current and of the torsion thread balance each other. This equilibrium position can be observed very sensitively using a light beam. Any decay of the permanent current within the rings would be indicated by the light beam as a change in its equilibrium position. During all such experiments, no change of the permanent current has ever been observed.

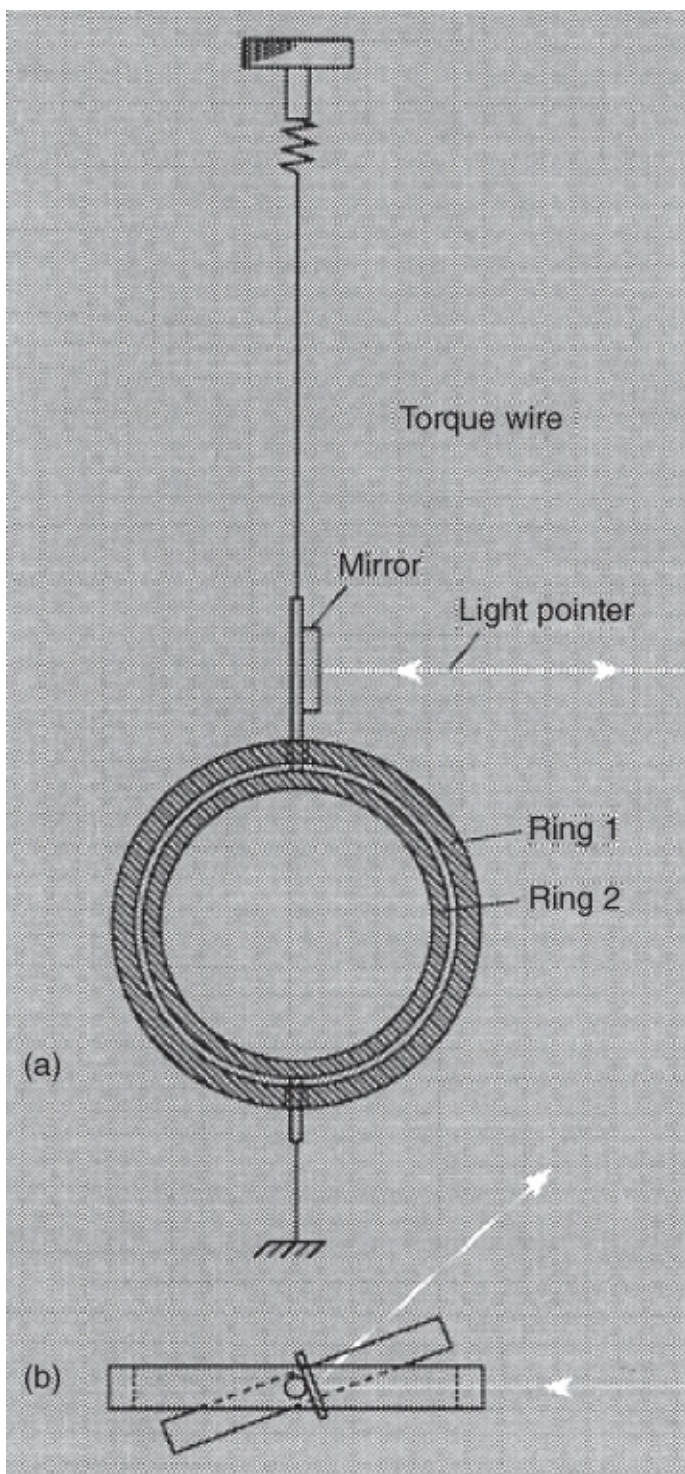


**Figure 1.2** Arrangement for the observation of a permanent current. (a) side view, (b) top view. (After [2].) Ring 1 is attached to the cryostat.

A nice demonstration of superconducting permanent currents is shown in [Figure 1.3](#). A small permanent magnet that is lowered toward a superconducting lead bowl generates induction currents according to Lenz's rule, leading to a repulsive force acting on the magnet. The induction currents support the magnet at an equilibrium height. This arrangement is referred to as a ***levitated magnet***. The magnet is supported as long as the permanent currents are flowing within the lead bowl, that is, as long as the lead remains superconducting. For high-temperature superconductors such as  $\text{YBa}_2\text{Cu}_3\text{O}_7$ , the levitation can easily be performed using liquid nitrogen in regular air. Furthermore, it can also serve for levitating freely real heavyweights such as the Sumo wrestler shown in [Figure 1.4](#).

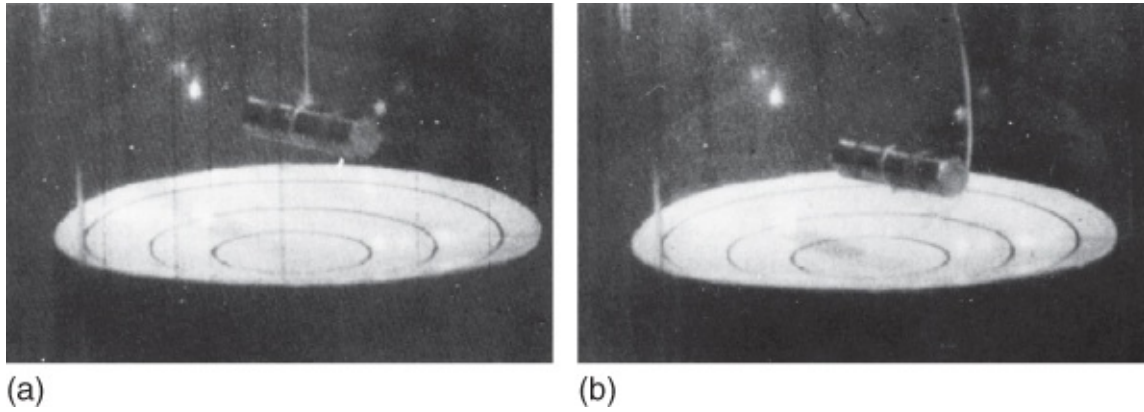


[Figure 1.3](#) The “levitated magnet” for demonstrating the permanent currents that are generated in superconducting lead by induction during the lowering of the magnet. (a) Starting position. (b) Equilibrium position.



**Figure 1.4** Application of free levitation by means of the permanent currents in a superconductor. The Sumo wrestler (including the plate at the bottom) weighs 202 kg. The superconductor is  $\text{YBa}_2\text{Cu}_3\text{O}_7$ .

(Photograph kindly supplied by the International Superconductivity Research Center (ISTEC) and Nihon-SUMO Kyokai, Japan, 1997.)

The most sensitive arrangements for determining an upper limit of the resistance in the superconducting state are based on geometries having an extremely small self-induction coefficient  $L$ , in addition to an increase in the observation time. In this way, the upper limit can be lowered further. A further increase in the sensitivity is accomplished by the modern superconducting magnetic field sensors (see [Section 7.6.4](#)). Today, we know that the jump in resistance during entry into the superconducting state amounts to at least 14 orders of magnitude [3]. Hence, in the superconducting state, a metal can have a specific electrical resistance that is at most about 17 orders of magnitude smaller than the specific resistance of copper, one of our best metallic conductors, at 300 K. Since hardly anyone has a clear idea about “17 orders of magnitude,” we also present another comparison: the difference in resistance of a metal between the superconducting and normal states is at least as large as that between copper and a standard electrical insulator.

Following this discussion, it appears justified at first to assume that in the superconducting state the electrical resistance actually vanishes. However, we must point out that this statement is valid only under specific conditions. So the resistance can become finite even in the case of small transport currents, if magnetic flux lines exist within the superconductor. Furthermore, alternating currents experience a resistance that is different from zero. We return to this subject in more detail in subsequent chapters.

This totally unexpected behavior of the electric current, flowing without resistance through a metal and at the time contradicting all well-supported concepts, becomes even more surprising if we look more closely at charge transport through a metal. In this way, we can also appreciate more strongly the problem confronting us in terms of an understanding of superconductivity.

We know that electric charge transport in metals takes place through the electrons. The concept that, in a metal, a definite number of electrons per atom (for instance, in the alkalis, one electron, the valence electron) exist freely, rather like a gas, was developed at an early time (by Paul Drude in 1900, and Hendrik Anton Lorentz in 1905). These “free” electrons also mediate the binding of the atoms in metallic crystals. In an applied electric field the free electrons are accelerated. After a specific time, the mean collision time  $\tau$ , they collide with atoms and lose the energy they have taken up from the electric field. Subsequently, they are accelerated again. The existence of the free charge carriers, interacting with the lattice of the metallic crystal, results in the high electrical conductivity of metals.

Also the increase in the resistance (decrease in the conductivity) with increasing temperature can be understood immediately. With increasing temperature, the uncorrelated thermal motion of the atoms in a metal (each atom is vibrating with a characteristic amplitude about its equilibrium position) becomes more pronounced. Hence, the probability for collisions between the electrons and the atoms increases, that is, the time  $\tau$  between two collisions becomes smaller. Since the conductivity is directly proportional to this time, in which the electrons are freely accelerated because of the electric field, it decreases with increasing temperature and the resistance increases.

This “free-electron model,” according to which electron energy can be delivered to the crystal lattice only due to the collisions with the atomic ions, provides a plausible understanding of electrical resistance. However, within this model, it appears totally inconceivable that, within a very small temperature interval at a finite temperature, these collisions with the atomic ions should abruptly become forbidden. Which mechanism(s) could have the effect that, in the superconducting state, energy exchange between electrons and lattice is not allowed any more? This appears to be an extremely difficult question.

Based on the classical theory of matter, another difficulty appeared with the concept of the free-electron gas in a metal. According to the general rules of classical statistical thermodynamics, each degree of freedom<sup>4</sup> of a system on average should contribute  $k_B T/2$  to the internal energy of the system. Here,  $k_B = 1.38 \times 10^{-23} \text{ W s/K}$  is Boltzmann's constant. This also means that the free electrons are expected to contribute the amount of energy  $3k_B T/2$  per

free electron, characteristic for a monatomic gas. However, specific heat measurements of metals have shown that the contribution of the electrons to the total energy of metals is about a thousand times smaller than expected from the classical laws.

Here, one can see clearly that the classical treatment of the electrons in metals in terms of a gas of free electrons does not yield a satisfactory understanding. On the other hand, the discovery of energy quantization by Max Planck in 1900 started a totally new understanding of physical processes, particularly on the atomic scale. The following decades then demonstrated the overall importance of quantum theory and of the new concepts resulting from the discovery made by Max Planck. Also the discrepancy between the observed contribution of the free electrons to the internal energy of a metal and the amount expected from the classical theory was resolved by Arnold Sommerfeld in 1928 by means of the quantum theory.

The quantum theory is based on the fundamental idea that each physical system is described in terms of discrete states. A change of physical quantities such as the energy can only take place by a transition of the system from one state to another. This restriction to discrete states becomes particularly clear for atomic objects. In 1913, Niels Bohr proposed the first stable model of an atom, which could explain a large number of facts hitherto not understood. Bohr postulated the existence of discrete stable states of atoms. If an atom in some way interacts with its environment, say, by the gain or loss of energy (e.g., due to the absorption or emission of light), then this is possible only within discrete steps in which the atom changes from one discrete state to another. If the amount of energy (or that of another quantity to be exchanged) required for such a transition is not available, the state remains stable.

In the final analysis, this relative stability of quantum mechanical states also yields the key to the understanding of superconductivity. As we have seen, we need some mechanism(s) forbidding the interaction between the electrons carrying the current in a superconductor and the crystal lattice. If one assumes that the “superconducting” electrons occupy a quantum state, some stability of this state can be understood. Already in about 1930, the concept became accepted that superconductivity represents a typical quantum phenomenon. However, there was still a long way to go for a complete understanding. One difficulty originated from the fact that quantum phenomena were expected for atomic systems, but not for macroscopic objects. In order to characterize this peculiarity of superconductivity, one often referred to it as a ***macroscopic quantum phenomenon***. Below we will understand this notation even better.

In modern physics another aspect has also been developed, which must be mentioned at this stage, since it is needed for a satisfactory understanding of some superconducting phenomena. We have learned that the particle picture and the wave picture represent complementary descriptions of one and the same physical object. Here, one can use the simple rule that propagation processes are suitably described in terms of the wave picture and exchange processes during the interaction with other systems in terms of the particle picture.

We illustrate this important point with two examples. Light appears to us as a wave because of many diffraction and interference effects. On the other hand, during the interaction with matter, say, in the photoelectric effect (knocking an electron out of a crystal surface), we clearly notice the particle aspect. One finds that independently of the light intensity the energy transferred to

the electron only depends upon the light frequency. However, the latter is expected if light represents a current of particles where all particles have an energy depending on the frequency.

For electrons, we are more used to the particle picture. Electrons can be deflected by means of electric and magnetic fields, and they can be thermally evaporated from metals (glowing cathode). All these are processes where the electrons are described in terms of particles. However, Louis de Broglie proposed the hypothesis that each moving particle also represents a wave, where the wavelength  $\lambda$  is equal to Planck's constant  $h$  divided by the magnitude  $p$  of the particle momentum, that is,  $\lambda = h/p$ . The square of the wave amplitude at the location  $(x, y, z)$  then is a measure of the probability of finding the particle at this location.

We see that the particle is spatially “smeared” over some distance. If we want to favor a specific location of the particle within the wave picture, we must construct a wave with a pronounced maximum amplitude at this location. Such a wave is referred to as a **wave packet**. The velocity with which the wave packet spatially propagates is equal to the particle velocity.

Subsequently, this hypothesis was brilliantly confirmed. With electrons we can observe diffraction and interference effects. Similar effects also exist for other particles, say, for neutrons. The diffraction of electrons and neutrons has developed into important techniques for structural analysis. In an electron microscope, we generate images by means of electron beams and achieve a spatial resolution much higher than that for visible light because of the much smaller wavelength of the electrons.

For the matter wave associated with the moving particle, there exists, like for each wave process, a characteristic differential equation, the fundamental Schrödinger equation. This deeper insight into the physics of electrons must also be applied to the description of the electrons in a metal. The electrons within a metal also represent waves. Using a few simplifying assumptions, from the Schrödinger equation we can calculate the discrete quantum states of these electron waves in terms of a relation between the allowed energies  $E$  and the so-called wave vector  $\mathbf{k}$ . The magnitude of  $\mathbf{k}$  is given by  $2\pi/\lambda$ , and the spatial direction of  $\mathbf{k}$  is the propagation direction of the wave. For a completely free electron, this relation is very simple. We have in this case

$$E = \frac{\hbar^2 \mathbf{k}^2}{2m} \quad 1.2$$

where  $m$  is the electron mass and  $\hbar = h/2\pi$ .

However, within a metal the electrons are not completely free. First, they are confined to the volume of the piece of metal, like in a box. Therefore, the allowed values of  $\mathbf{k}$  are discrete, simply because the allowed electron waves must satisfy specific boundary conditions at the walls of the box. For example, the amplitude of the electron wave may have to vanish at the boundary.

Second, within the metal the electrons experience the electrostatic forces originating from the positively charged atomic ions, in general arranged periodically. This means that the electrons exist within a periodic potential. Near the positively charged atomic ions, the potential energy

of the electrons is lower than between these ions. As a result of this periodic potential, in the relation between  $E$  and  $\mathbf{k}$ , not all energies are allowed any more. Instead, there exist different energy ranges separated from each other by ranges with forbidden energies. An example of such an  $E$ - $\mathbf{k}$  dependence, modified because of a periodic potential, is shown schematically in [Figure 1.5](#).

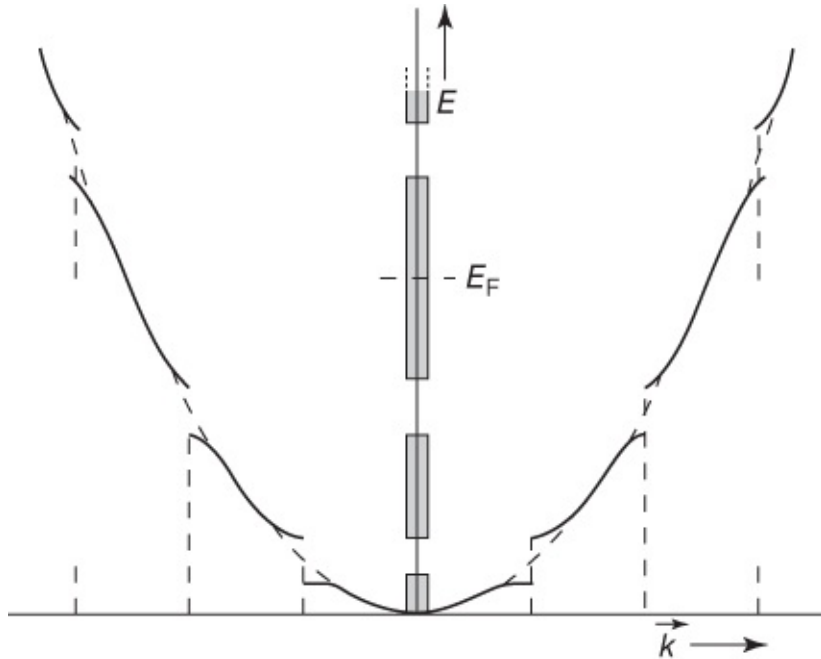


**Figure 1.5** Energy–momentum relation for an electron in a periodic potential. The relation (Eq. (1.2)) valid for free electrons is shown as the dashed parabolic line.

So now we are dealing with energy bands. The electrons must be filled into these bands. Here, we have to pay attention to another important principle formulated by Wolfgang Pauli in 1924. This “Pauli principle” requires that in quantum physics each discrete state can be occupied only by a single electron (or more generally by a single particle with a half-integer spin, a so-called “fermion”). Since the angular momentum (spin) of the electrons represents another quantum number with two possible values, according to the Pauli principle each of the discrete  $\mathbf{k}$ -values can be occupied by only two electrons. In order to accommodate all the electrons of a metal, the states must be filled up to relatively high energies. The maximum energy up to which the states are being filled is referred to as the **Fermi energy  $E_F$** . The density of states per energy interval and per unit volume is referred to simply as the **density of states  $N(E)$** . In the simplest case, in momentum space the filled states represent a sphere, the so-called Fermi sphere. However, in general, one finds more complex objects. In a metal the Fermi energy is located within an allowed energy band, that is, the band is only partly filled.<sup>5</sup> In [Figure 1.5](#), the Fermi energy is indicated for this case.

The occupation of the states is determined by the distribution function for a system of fermions, the Fermi function. This Fermi function takes into account the Pauli principle and is given by

$$f = \frac{1}{e^{(E-E_F)/k_B T} + 1} \quad 1.3$$

where  $k_B$  is Boltzmann's constant and  $E_F$  is the Fermi energy. This Fermi function is shown in [Figure 1.6](#) for the case  $T = 0$  (dashed line) and for the case  $T > 0$  (solid line). For finite temperatures, the Fermi function is slightly smeared out. This smearing is equal to about the average thermal energy of the fermions. At room temperature, it amounts to about  $\frac{1}{40}$  eV.<sup>6</sup> At finite temperatures, the Fermi energy is the energy at which the distribution function has the value 1/2. In a typical metal, it amounts to about a few electronvolts. This has the important consequence that at normal temperatures the smearing of the Fermi edge is very small. Such an electron system is referred to as a ***degenerate electron gas***.

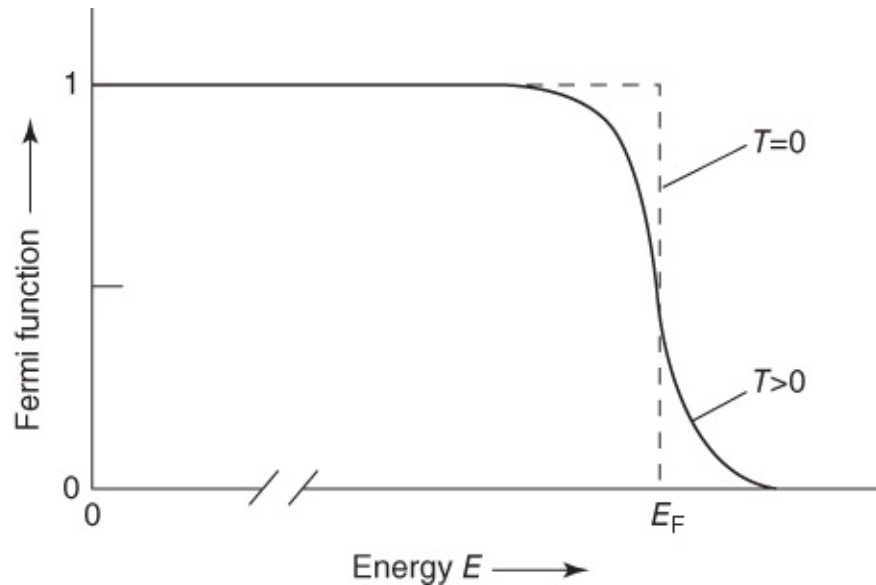


**Figure 1.6** Fermi function.  $E_F$  is a few electronvolts, whereas thermal smearing is only a few  $10^{-3}$  eV. To indicate this, the abscissa is interrupted.

At this stage, we can also understand the very small contribution of the electrons to the internal energy. According to the concepts we have discussed earlier, only very few electrons, namely those within the energy smearing of the Fermi edge, can participate in the thermal energy exchange processes. All other electrons cannot be excited with thermal energies, since they do not find empty states that they could occupy after their excitation.

We have to become familiar with the concept of quantum states and their occupation if we want to understand modern solid-state physics. This is also necessary for an understanding of superconductivity. In order to get used to the many new ideas, we will briefly discuss the mechanism generating electrical resistance. The electrons are described in terms of waves propagating in all directions through the crystal. An electric current results if slightly more waves propagate in one direction than in the opposite direction. The electron waves are scattered because of their interaction with the atomic ions. This scattering corresponds to collisions in the particle picture. What is new in the wave picture is the fact that this scattering cannot take place for a strongly periodic crystal lattice. The states of the electrons resulting as the solutions of the Schrödinger equation represent stable quantum states. Only a perturbation of the periodic potential, caused by thermal vibrations of the atoms, by defects in the crystal lattice, or by chemical impurities, can lead to a scattering of the electron waves, that is, to a

change in the occupation of the quantum states. The scattering due to the thermal vibrations yields a temperature-dependent component of the resistance, whereas that at crystal defects and chemical impurities yields the residual resistance.

After this brief and simplified excursion into the modern theoretical treatment of electronic conduction, we return to our central problem, charge transport with zero resistance in the superconducting state. Also the new wave mechanical ideas do not yet provide an easy access to the appearance of a permanent current. We have only changed the language. Now we must ask: Which mechanisms completely eliminate any energy exchange with the crystal lattice by means of scattering at finite temperatures within a very narrow temperature interval? It turns out that an additional new aspect must be taken into account, namely a particular interaction between the electrons themselves. In our previous discussion we have treated the quantum states of the individual electrons, and we have assumed that these states do not change when they become occupied with electrons. However, if an interaction exists between the electrons, this treatment is no longer correct. Now we must ask instead: What are the states of the system of electrons with an interaction, that is, what collective states exist? Here, we encounter the understanding and also the difficulty of superconductivity. It is a typical collective quantum phenomenon characterized by the formation of a coherent matter wave, propagating through the superconductor without any friction.

## 1.2 Ideal Diamagnetism, Flux Lines, and Flux Quantization

It has been known for a long time that the characteristic property of the superconducting state is that it shows no measurable resistance for direct current. If a magnetic field is applied to such an *ideal conductor*, permanent currents are generated by induction, which screen the magnetic field from the interior of the sample. In [Section 1.1](#) we have seen this principle already for the levitated magnet.

What happens if a magnetic field  $\mathbf{B}_a$  is applied to a *normal conductor* and if subsequently, by cooling below the transition temperature  $T_c$ , ideal superconductivity is reached? At first, in the normal state, on application of the magnetic field, eddy currents flow because of induction. However, as soon as the magnetic field reaches its final value and no longer changes with time, these currents decay according to Eq. (1.1), and finally the magnetic fields within and outside the superconductor become equal.

If now the ideal conductor is cooled below  $T_c$ , this magnetic state simply remains, since further induction currents are generated only during *changes* of the field. Exactly this is expected, if the magnetic field is turned off below  $T_c$ . In the interior of the ideal conductor, the magnetic field remains conserved.

Hence, depending on the way in which the final state, namely temperature below  $T_c$  and applied magnetic field  $\mathbf{B}_a$ , has been reached, within the interior of the ideal conductor we have completely different magnetic fields.

An experiment by Kamerlingh-Onnes from 1924 appeared to confirm exactly this complicated behavior of a superconductor. Kamerlingh-Onnes [4] cooled a hollow sphere made of lead below the transition temperature in the presence of an applied magnetic field and subsequently turned off the external magnetic field. Then he observed permanent currents and a magnetic moment of the sphere, as expected for the case  $R = 0$ .

Accordingly, a material with the property  $R = 0$ , for the same external variables  $T$  and  $\mathbf{B}_a$ , could be transferred into completely different states, depending on the previous history. Therefore, for the same given thermodynamic variables, we would not have just one well-defined superconducting phase, but, instead, a continuous manifold of superconducting phases with arbitrary shielding currents, depending on the previous history. However, the existence of a manifold of superconducting phases appeared so unlikely that, before 1933, one referred to only a single superconducting phase [5] even without experimental verification.

However, a superconductor behaves quite differently from an ideal electrical conductor. Again, we imagine that a sample is cooled below  $T_c$  in the presence of an applied magnetic field. If this magnetic field is very small, one finds that the field is completely expelled from the interior of the superconductor except for a very thin layer at the sample surface. In this way, one obtains an ideal diamagnetic state, independent of the temporal sequence in which the magnetic field was applied and the sample was cooled.

This ideal diamagnetism was discovered in 1933 by Meissner and Ochsenfeld for rods made of lead or tin [6]. This expulsion effect, similar to the property  $R = 0$ , can be nicely demonstrated using the “levitated magnet.”<sup>7</sup> In order to show the property  $R = 0$ , in [Figure 1.3](#) we have lowered the permanent magnet toward the superconducting lead bowl, in this way generating permanent currents by induction. To demonstrate the Meissner–Ochsenfeld effect, we place the permanent magnet into the lead bowl at  $T > T_c$  ([Figure 1.7a](#)) and then cool down further. The field expulsion appears at the superconducting transition: the magnet is repelled from the diamagnetic superconductor, and it is raised up to the equilibrium height ([Figure 1.7b](#)). In the limit of ideal magnetic field expulsion, the same levitation height is reached as in [Figure 1.3](#).

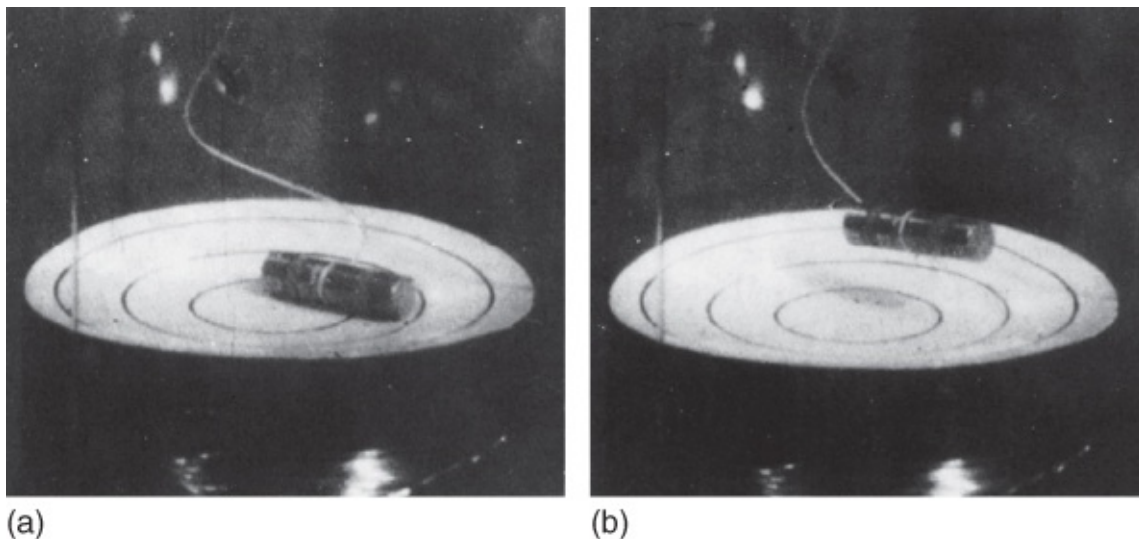


**Figure 1.7** “Levitated magnet” for demonstrating the Meissner–Ochsenfeld effect in the presence of an applied magnetic field. (a) Starting position at  $T > T_c$ . (b) Equilibrium position at  $T < T_c$ .

What went wrong during the original experiment of Kamerlingh-Onnes? He used a hollow sphere in order to consume a smaller amount of liquid helium for cooling. The observations for this sample were correct. However, he had overlooked the fact that during cooling of a hollow sphere a closed ring-shaped superconducting object can be formed, which keeps the magnetic flux penetrating its open area constant. Hence, a hollow sphere can act like a superconducting ring ([Figure 1.1](#)), leading to the observed result.

Above, we had assumed that the magnetic field applied to the superconductor would be “small.” Indeed, one finds that ideal diamagnetism only exists within a finite range of magnetic fields and temperatures, which, furthermore, also depends on the sample geometry.

Next, we consider a long, rod-shaped sample where the magnetic field is applied parallel to the axis. For other shapes, the magnetic field can often be distorted. For an ideal diamagnetic sphere, at the “equator” the magnetic field is 1.5 times larger than the externally applied field. In [Section 4.6.4](#), we will discuss these geometric effects in more detail.

One finds that there exist two different types of superconductors:

- The first type, referred to as ***type-I superconductors*** or ***superconductors of the first kind***, expels the magnetic field up to a maximum value  $B_c$ , the critical field. For larger fields, superconductivity breaks down, and the sample assumes the normal conducting state. Here, the critical field depends on the temperature and reaches zero at the transition temperature  $T_c$ . Mercury and lead are examples of a type-I superconductor.
- The second type, referred to as ***type-II superconductors*** or ***superconductors of the second kind***, shows ideal diamagnetism for magnetic fields smaller than the “lower critical magnetic field”  $B_{c1}$ . Superconductivity completely vanishes for magnetic fields larger than the “upper critical magnetic field”  $B_{c2}$ , which often is much larger than  $B_{c1}$ .

Both critical fields reach zero at  $T_c$ . This behavior is found in many alloys and also in the high-temperature superconductors. In the latter,  $B_{c2}$  can reach even values larger than 100 T.

What happens in type-II superconductors in the “Shubnikov phase” between  $B_{c1}$  and  $B_{c2}$ ? In this regime, the magnetic field only partly penetrates into the sample. Now shielding currents flow within the superconductor and concentrate the magnetic field lines, such that a system of flux lines, also referred to as **Abrikosov vortices**, is generated. For the prediction of quantized flux lines, A. A. Abrikosov received the Nobel Prize in physics in 2003. In an ideal homogeneous superconductor in general, these vortices arrange themselves in the form of a triangular lattice. In [Figure 1.8](#) we show schematically this structure of the Shubnikov phase. The superconductor is penetrated by magnetic flux lines, each of which carries a magnetic flux quantum and is located at the corners of equilateral triangles. Each flux line consists of a system of circulating currents, which in [Figure 1.8](#) are indicated for two flux lines. These currents together with the external magnetic field generate the magnetic flux within the flux line and reduce the magnetic field between the flux lines. Hence, one also talks about flux vortices. With increasing external field  $\mathbf{B}_a$ , the distance between the flux lines becomes smaller.

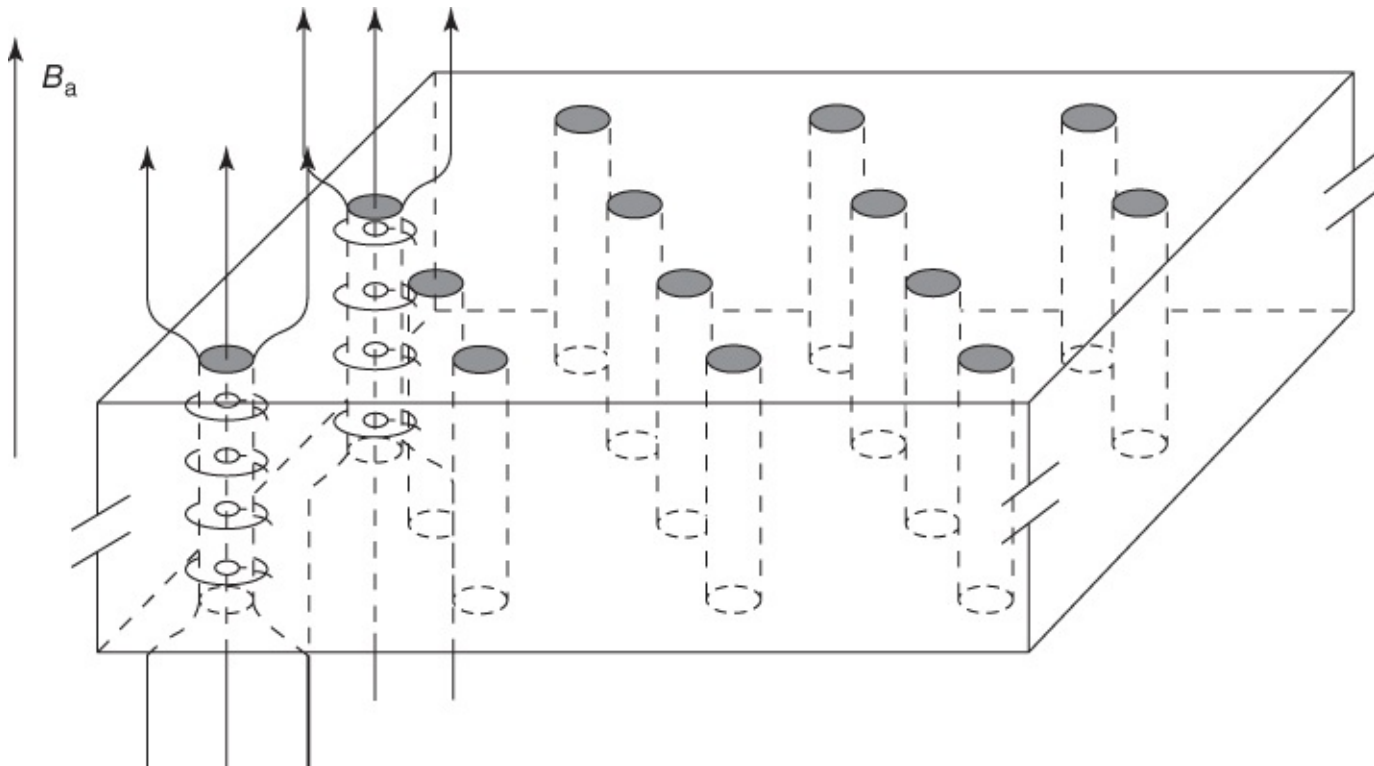


[Figure 1.8](#) Schematic diagram of the Shubnikov phase. The magnetic field and the supercurrents are shown only for two flux lines.

The first experimental proof of a periodic structure of the magnetic field in the Shubnikov phase was given in 1964 by a group at the Nuclear Research Center in Saclay using neutron diffraction [8]. However, they could only observe a basic period of the structure. Beautiful neutron diffraction experiments with this magnetic structure were performed by a group at the Nuclear Research Center, Jülich [9]. Real images of the Shubnikov phase were generated by

Essmann and Träuble [10] using an ingenious decoration technique. In [Figure 1.9](#), we show a lead–indium alloy as an example. These images of the magnetic flux structure were obtained as follows: Above the superconducting sample, iron atoms are evaporated from a hot wire. During their diffusion through the helium gas in the cryostat, the iron atoms coagulate to form iron colloids. These colloids have a diameter of less than 50 nm, and they slowly approach the surface of the superconductor. At this surface, the flux lines of the Shubnikov phase exit from the superconductor. In [Figure 1.8](#), this is shown for two flux lines. The ferromagnetic iron colloid is collected at the locations where the flux lines exit from the surface, since here they find the largest magnetic field gradients. In this way, the flux lines can be decorated. Subsequently, the structure can be observed in an electron microscope. The image shown in [Figure 1.9](#) was obtained in this way. Such experiments convincingly confirmed the vortex structure predicted theoretically by Abrikosov.

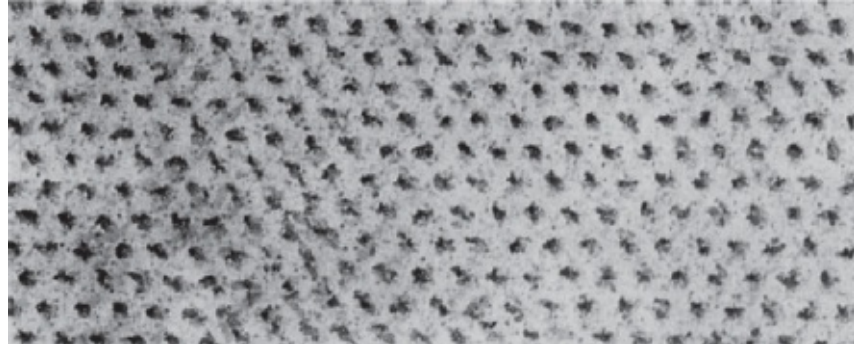


**Figure 1.9** Image of the vortex lattice obtained with an electron microscope following the decoration with iron colloid. Frozen-in flux after the magnetic field has been reduced to zero. Material: Pb +6.3 at% In; temperature: 1.2 K; sample shape: cylinder, 60 mm long, 4 mm diameter; and magnetic field  $\mathbf{B}_a$  parallel to the axis. Magnification: 8300 $\times$ .

(Reproduced by courtesy of Dr Essmann.)

The question remains whether the decorated locations at the surface indeed correspond to the ends of the flux lines carrying only a single flux quantum. In order to answer this question, we just have to count the number of flux lines and also have to determine the total flux, say, by means of an induction experiment. Then we find the value of the magnetic flux of a flux line by dividing the total flux  $\Phi_{\text{tot}}$  through the sample by the number of flux lines. Such evaluations exactly confirmed that in highly homogeneous type-II superconductors, each flux line contains a single flux quantum  $\Phi_0 = 2.07 \times 10^{-15} \text{ T m}^2$ .

Today, we know different methods for imaging magnetic flux lines. Often, the methods supplement each other and provide valuable information about superconductivity. Therefore, we will discuss some of them in more detail.

Neutron diffraction and decoration still represent important techniques. [Figure 1.10a](#) shows a diffraction pattern observed at the Institute Laue-Langevin in Grenoble by means of neutron diffraction at the vortex lattice in niobium. The triangular structure of the vortex lattice can clearly be seen from the diffraction pattern.

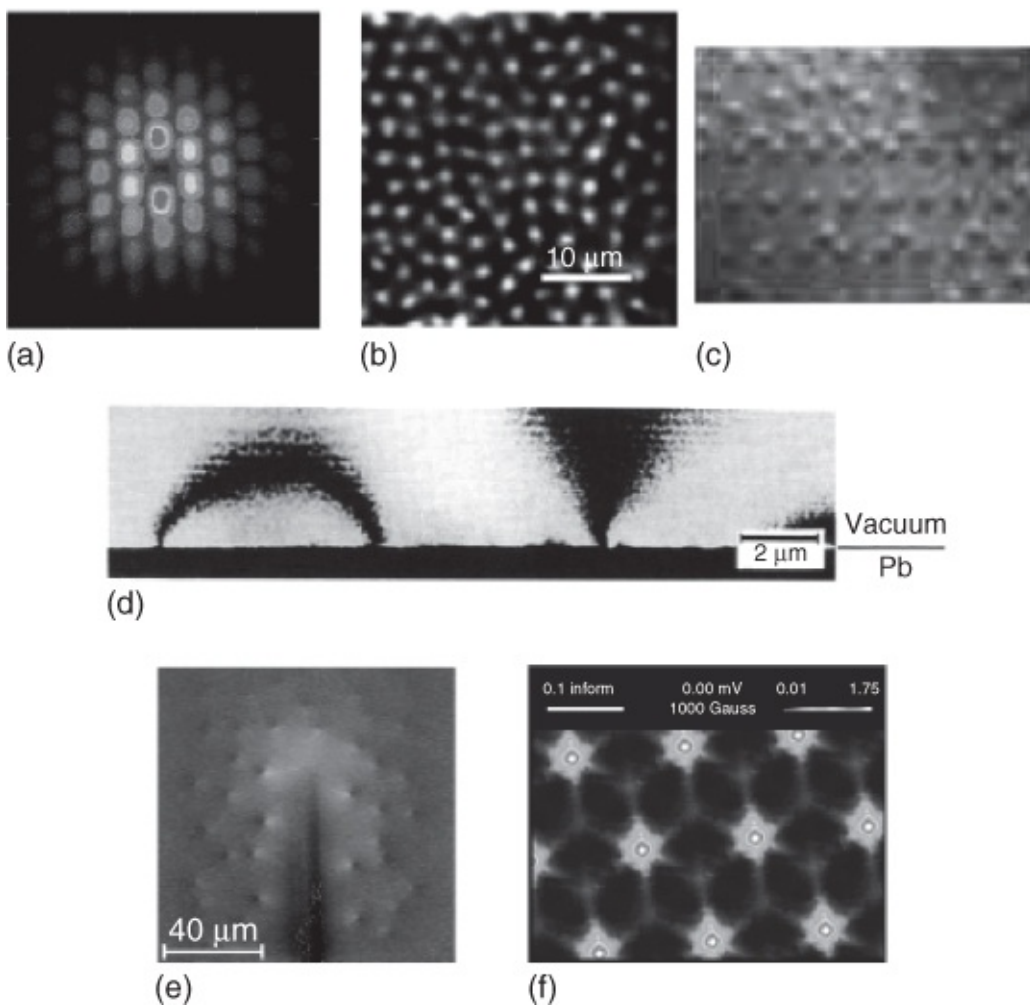


**Figure 1.10** Methods for the imaging of flux lines. (a) Neutron diffraction pattern of the vortex lattice in niobium (Figure kindly provided by Institute Max von Laue-Paul Langevin, Grenoble; Authors: E. M. Forgan (Univ. Birmingham), S. L. Lee (Univ. St. Andrews), D. McK.Paul (Univ. Warwick), H. A. Mook (Oak Ridge) and R. Cubitt (ILL)). (b) Magneto-optical image of vortices in  $\text{NbSe}_2$  [11]. (c) Lorentz microscopy of niobium (Figure kindly provided by A. Tonomura, Fa. Hitachi Ltd.). (d) Electron holography of Pb [12]. (e) Low-temperature scanning electron microscopy of  $\text{YBa}_2\text{Cu}_3\text{O}_7$  [13]. (f) Scanning tunneling microscopy of  $\text{NbSe}_2$

(Figure kindly provided by Fa. Lucent Technologies Inc./Bell labs).

Magneto-optics represents another method for spatially imaging magnetic structures. Here, one utilizes the Faraday effect. If linearly polarized light passes through a thin layer of a “Faraday-active” material such as a ferrimagnetic garnet film, the plane of polarization of the light will be rotated due to a magnetic field within the garnet film. A transparent substrate, covered with a thin ferrimagnetic garnet film, is placed on top of a superconducting sample and is irradiated with polarized and well-focused light. The light is reflected at the superconductor, passes through the ferrimagnetic garnet film again, and is then focused into a CCD camera. The magnetic field from the vortices in the superconductor penetrates into the ferrimagnetic garnet film and there causes a rotation of the plane of polarization of the light. An analyzer located in front of the CCD camera only transmits light whose polarization is rotated away from the original direction. In this way, the vortices appear as bright dots, as shown in Figure 1.10b for

the compound  $\text{NbSe}_2$  [11].<sup>8</sup> This method yields a spatial resolution of more than  $1 \mu\text{m}$ . Presently, one can take about 10 images/s, also allowing the observation of dynamic processes. Unfortunately, at this time, the method is restricted to superconductors with a very smooth and highly reflecting surface.

For Lorentz microscopy, an electron beam is transmitted through a thin superconducting sample. The samples must be very thin, and the electron energy must be high in order that the beam penetrates through the sample. Near a flux line the transmitted electrons experience an additional Lorentz force, and the electron beam is slightly defocused due to the magnetic field gradient of a flux line. The phase contrast caused by the flux lines can be imaged beyond the focus of the transmission electron microscope. Because of the deflection, each vortex appears as a circular signal: one half of which is bright, and the other half is dark. This alternation between bright and dark also yields the polarity of the vortex. Lorentz microscopy allows a very rapid imaging of the vortices, such that motion pictures can be taken, clearly showing the vortex motion, similar to the situation for magneto-optics [14]. [Figure 1.10c](#) shows such an image obtained for niobium by A. Tonomura (Hitachi Ltd). This sample carried small micro-holes (antidots) arranged as a square lattice. In the image, most of the micro-holes are occupied by vortices, and some vortices are located between the antidots. The vortices enter the sample from the top side. Then they are hindered from further penetration into the sample by the antidots and by the vortices already existing in the superconductor.

Electron holography [14] is based on the wave nature of electrons. Similar to optical holography, a coherent electron beam is split into a reference wave and an object wave, which subsequently interfere with each other. The relative phase position of the two waves can be influenced by a magnetic field, or more accurately by the magnetic flux enclosed by both waves. The effect utilized for imaging is closely related to the magnetic flux quantization in superconductors. In [Section 1.5.2](#), we will discuss this effect in more detail. In [Figure 1.10d](#), the magnetic stray field generated by vortices near the surface of a lead film is shown [12]. The alternation from bright to dark in the interference stripes corresponds to the magnetic flux of one flux quantum. On the left side the magnetic stray field between two vortices of opposite polarity joins together, whereas on the right side the stray field turns away from the superconductor.

For imaging by means of low-temperature scanning electron microscopy (LTSEM), an electron beam is scanned along the surface of the sample to be studied. As a result, the sample is heated locally by a few kelvin within a spot of about  $1 \mu\text{m}$  diameter. An electronic property of the superconductor, which changes due to this local heating, is then measured. With this method, many superconducting properties, such as, the transition temperature  $T_c$ , can be spatially imaged [15]. In the special case of the imaging of vortices, the magnetic field of the vortex is detected using a superconducting quantum interferometer (or superconducting quantum interference device, “SQUID,” see [Section 1.5.2](#)) [13]. If the electron beam passes close to a vortex, the supercurrents flowing around the vortex axis are distorted, resulting in a small displacement of the vortex axis toward the electron beam. This displacement also changes the magnetic field of the vortex detected by the quantum interferometer, and this magnetic field

change yields the signal to be imaged. A typical image of vortices in the high-temperature superconductor  $\text{YBa}_2\text{Cu}_3\text{O}_7$  is shown in [Figure 1.10e](#). Here, the vortices are located within the quantum interferometer itself. Similar to Lorentz microscopy, each vortex is indicated as a circular bright/dark signal, generated by the displacement of the vortex in different directions. The dark vertical line in the center indicates a slit in the quantum interferometer, representing the proper sensitive part of the magnetic field sensor. We note the highly irregular arrangement of the vortices. A specific advantage of this technique is the fact that very small displacements of the vortices from their equilibrium position can also be observed, since the SQUID already detects a change of the magnetic flux of only a few millionths of a magnetic flux quantum. Such changes occur, for example, if the vortices statistically jump back and forth between two positions due to thermal motion. Since such processes can strongly reduce the resolution of SQUIDs, they are being carefully investigated using LTSEM.

As the last group of imaging methods, we wish to discuss the scanning probe techniques, in which a suitable detector is moved along the superconductor. The detector can be a magnetic tip [16], a micro-Hall probe [17], or a SQUID [18]. In particular, the latter method has been used in a series of key experiments for clarifying our understanding of high-temperature superconductors. These experiments will be discussed in [Section 3.2.2](#). Finally, the scanning tunneling microscope yielded similarly important results. Here, a non-magnetic metallic tip is scanned along the sample surface. The distance between the tip and the sample surface is so small that electrons can flow from the sample surface to the tip because of the quantum mechanical tunneling process.

Contrary to the methods mentioned earlier, (all of which detect the magnetic field of vortices), with the scanning tunneling microscope one images the spatial distribution of the electrons, or more exactly of the density of the allowed quantum mechanical states of the electrons [19]. This technique can reach atomic resolution. In [Figure 1.10f](#) we show an example. This image was obtained by H. F. Hess and coworkers (Bell Laboratories, Lucent Technologies Inc.) using an  $\text{NbSe}_2$  single crystal. The applied magnetic field was  $1000 \text{ G} = 0.1 \text{ T}$ . Later, we will discuss the fact that, near the vortex axis, the superconductor is normal conducting. It is this region where the tunneling currents between the tip and the sample reach their maximum values. Hence, the vortex axis appears as a bright spot.

In addition to the imaging methods, there exists a series of other techniques for characterizing the vortex state. In the case of muon-spin-resonance ( $\mu\text{SR}$ ), the superconductor is irradiated with spin-polarized, usually positively charged muons, which are generated by a particle accelerator. The muons are rapidly stopped within the superconductor. In the local magnetic fields, the spin of the muon precesses. After about  $2 \mu\text{s}$ , the muon decays into two neutrinos and one positron. During the decay, the positron is emitted along the direction of the muon spin. Hence, its detection yields information about the local magnetic fields in the interior of the superconductor and thereby also about the structure of the flux-line lattice. Other indirect methods are based, for example, on the analysis of the specific heat or of transport phenomena such as the thermal conductivity or the electric conductivity, which becomes finite at sufficiently large currents (see [Chapter 5](#)).

Finally, we note that a superconductor can also levitate in the state of the Shubnikov phase. The superconductor  $\text{YBa}_2\text{Cu}_3\text{O}_7$  shown in [Figure 1.4](#) had been cooled in the field of the permanent magnets and was penetrated by magnetic flux lines. It is essential that the flux lines can be pinned at defects within the superconductor. The corresponding physics will be discussed in [Section 5.3.2](#).

In the case of the “hard” superconductors, this pinning phenomenon is particularly effective. If they are pinned, the flux lines cannot move as long as the maximum pinning force of the pinning centers is not exceeded. As a result, the hard superconductor will keep the field in its interior at the value at which it had been cooled down.

If the superconductor is cooled down at a certain distance above a permanent magnet, an *attractive* force is acting if one tries to move the superconductor away from the magnet. Similarly, a *repulsive* force is generated if the superconductor is moved closer to the permanent magnet. In the end, the hard superconductor tries to keep exactly the distance to the magnet in which it was cooled down. The same applies to any other motional direction. As soon as the external field changes, shielding currents are generated in the hard superconductor in such a way that the field (and the flux-line lattice) in its interior does not change. Therefore, a hard superconductor including a heavy load can not only levitate above a magnet as shown in [Figure 1.4](#), but it can also hang freely below a magnet, or it can be positioned at an arbitrary angle. This effect is demonstrated in [Figure 1.11](#). In this case suitably prepared small blocks made of  $\text{YBa}_2\text{Cu}_3\text{O}_7$  were mounted within a toy train, and the blocks were cooled down at a certain distance from the magnets, which represented the “train tracks.” The train can move along the tracks practically without friction, since the magnetic field remains constant along this direction.



[Figure 1.11](#) Hanging toy train [20] (Leibniz Institute for Solid State and Materials Research, Dresden).

With this toy train a special trick was demonstrated, which keeps the hanging train from falling

down after heating above  $T_c$ . Permanent magnets were installed in the train in such a way that in the absence of the superconductor the train would be pulled to the track. This happens exactly, if the superconductor heats up. However, in the superconducting state, against the attraction by the permanent magnets the train is kept away from the track and can move freely along it.

## 1.3 Flux Quantization in a Superconducting Ring

Again we look at the experiment shown in [Figure 1.1](#). A permanent current has been generated in a superconducting ring by induction. How large is the magnetic flux through the ring?

The flux is given by the product of the self-inductance  $L$  of the ring and the current  $I$  circulating in the ring:  $\Phi = LI$ . From our experience with macroscopic systems, we would expect that we could generate by induction any value of the permanent current by the proper choice of the magnetic field. Then also the magnetic flux through the ring could take any arbitrary value. On the other hand, we have seen that in the interior of type-II superconductors magnetic fields are concentrated in the form of flux lines, each of which carries a single flux quantum  $\Phi_0$ . Now the question arises whether the flux quantum also plays a role in a superconducting ring. Already in 1950 such a presumption was expressed by Fritz London [21].

In 1961, two groups, namely Doll and N  bauer [22] in Munich and Deaver and Fairbank [23] in Stanford, published the results of flux quantization measurements using superconducting hollow cylinders, which clearly showed that the magnetic flux through the cylinder only appears in multiples of the flux quantum  $\Phi_0$ . These experiments had a strong impact on the development of superconductivity. Because of their importance and their experimental excellence, we will discuss these experiments in more detail.

For testing the possible existence of flux quantization in a superconducting ring or hollow cylinder, permanent currents had to be generated using different magnetic fields, and the resulting magnetic flux had to be determined with a resolution of better than a flux quantum  $\Phi_0$ . Due to the small value of the flux quantum, such experiments are extremely difficult. To achieve a relatively large change of the magnetic flux in different states, one must try to keep the flux through the ring in the order of only a few  $\Phi_0$ . Hence, one needs very small superconducting rings, since otherwise the magnetic fields required to generate the permanent currents become too small. We refer to these fields as “freezing fields,” since the generated flux through the opening of the ring is “frozen-in” during the onset of superconductivity. For example, in an opening of only  $1 \text{ mm}^2$ , one flux quantum already exists in a field of only  $2 \times 10^{-9} \text{ T}$ .

Therefore, both groups used very small samples in the form of thin tubes with a diameter of only about  $10 \mu\text{m}$ . For this diameter, one flux quantum  $\Phi_0 = h/2e = 2.07 \times 10^{-15} \text{ T m}^2$  is generated in a field of only  $\Phi_0/\pi r^2 = 2.6 \times 10^{-5} \text{ T}$ . With careful shielding of perturbing magnetic fields, for example, of the Earth's magnetic field, such fields can be well controlled

experimentally.

Doll and N  bauer utilized lead cylinders evaporated onto little quartz rods ([Figure 1.12](#)). Within these lead cylinders, a permanent current is generated by cooling in a freezing field  $B_f$  oriented parallel to the cylinder axis and by turning off this field after the onset of superconductivity at  $T < T_c$ . The permanent current turns the lead cylinder into a magnet. In principle, the magnitude of the frozen-in flux can be determined from the torque exerted upon the sample due to the measuring field  $B_M$  oriented perpendicular to the cylinder axis.

Therefore, the sample is attached to a quartz thread. The deflection can be indicated by means of a light beam and a mirror. However, the attained torque values were too small to be detected in a static experiment using extremely thin quartz threads. Doll and N  bauer circumvented this difficulty using an elegant technique, which may be called a ***self-resonance method***.

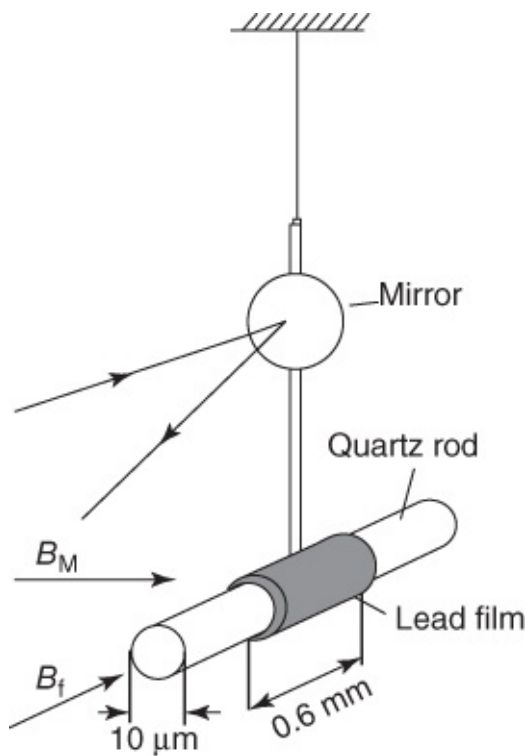


**Figure 1.12** Schematics of the experimental setup of Doll and N  bauer. (From [22].) The quartz rod carries a small lead cylinder formed as a thin layer by evaporation. The rod vibrates in liquid helium.

They utilized the small torque exerted upon the lead cylinder by the measuring field to excite a torsional oscillation of the system. At resonance, the amplitudes become sufficiently large that they can be recorded without difficulty. At resonance, the amplitude is proportional to the acting torque to be measured. For the excitation, the magnetic field  $B_M$  must be reversed periodically at the frequency of the oscillation. To ensure that the excitation always follows the resonance frequency, the reversal of the field was controlled by the oscillating system itself using the light beam and a photocell.

In [Figure 1.13](#) we show the results of Doll and N  bauer. On the ordinate the resonance

amplitude is plotted, divided by the measuring field, that is, a quantity proportional to the torque to be determined. The abscissa indicates the freezing field. If the flux in the superconducting lead cylinder varied continuously, the observed resonance amplitude also should vary proportional to the freezing field (dashed straight line in [Figure 1.13](#)). The experiment clearly indicates a different behavior. Up to a freezing field of about  $1 \times 10^{-5}$  T, no flux at all is frozen-in. The superconducting lead cylinder remains in the energetically lowest state with  $\Phi = 0$ . Only for freezing fields larger than  $1 \times 10^{-5}$  T does a state appear containing frozen-in flux. For all freezing fields between  $1 \times 10^{-5}$  and about  $3 \times 10^{-5}$  T, the state remains the same. In this range, the resonance amplitude is constant. The flux calculated from this amplitude and from the parameters of the apparatus corresponds approximately to a flux quantum  $\Phi_0 = h/2e$ . For larger freezing fields, additional quantum steps are observed. This experiment clearly demonstrates that the magnetic flux through a superconducting ring can take up only discrete values  $\Phi = n\Phi_0$ .

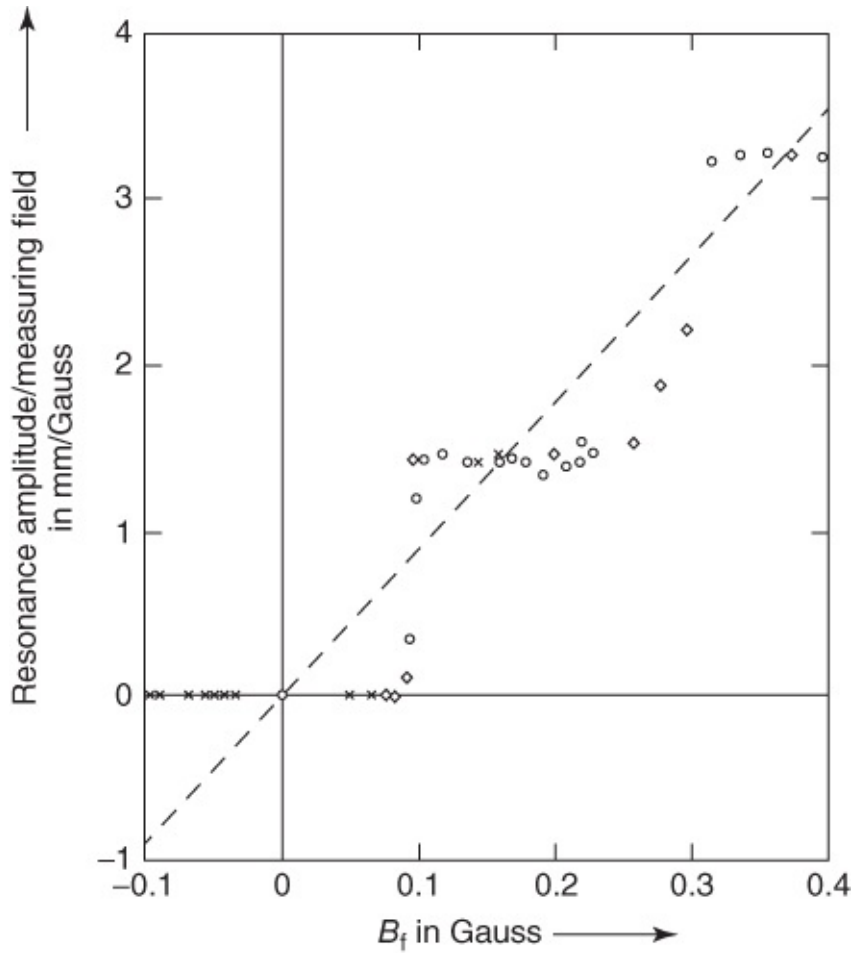


[Figure 1.13](#) Results of Doll and N  bauer on the magnetic flux quantization in a Pb cylinder ( $1$  G =  $10^{-4}$  T).

(From [22].)

An example of the results of Deaver and Fairbank is shown in [Figure 1.14](#). Their results also demonstrated the quantization of magnetic flux through a superconducting hollow cylinder and

confirmed the elementary flux quantum  $\Phi_0 = h/2e$ . Deaver and Fairbank used a completely different method for detecting the frozen-in flux. They moved the superconducting cylinder back and forth by 1 mm along its axis at a frequency of 100 Hz. As a result, in two small detector coils surrounding the two ends of the little cylinder, respectively, an inductive voltage was generated, which could be measured after sufficient amplification. In [Figure 1.14](#) the flux through the little tube is plotted in multiples of the elementary flux quantum  $\Phi_0$  versus the freezing field. The states with 0, 1, and 2 flux quanta can clearly be seen.

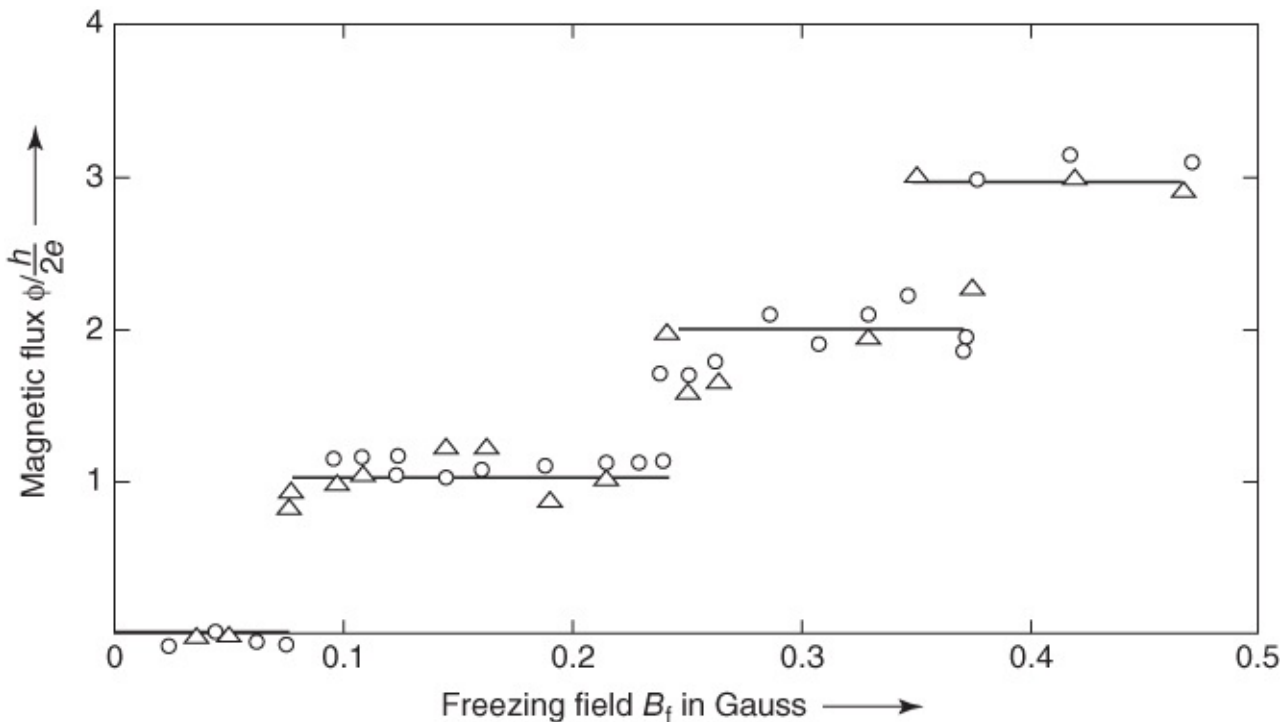


[Figure 1.14](#) Results of Deaver and Fairbank on the magnetic flux quantization in a Sn cylinder. The cylinder was about 0.9 mm long, and had an inner diameter of 13  $\mu\text{m}$  and a wall thickness of 1.5  $\mu\text{m}$  ( $1 \text{ G} = 10^{-4} \text{ T}$ ).

(From [23].)

## 1.4 Superconductivity: A Macroscopic Quantum Phenomenon

Next, we will deal with the conclusions to be drawn from the quantization of the magnetic flux in units of the flux quantum  $\Phi_0$ .

For atoms we are well used to the appearance of discrete states. For example, the stationary atomic states are distinguished due to a quantum condition for the angular momentum appearing in multiples of  $\hbar = h/2\pi$ . This quantization of the angular momentum is a result of the condition that the quantum mechanical wave function, indicating the probability of finding the electron, be single-valued. If we move around the atomic nucleus starting from a specific point, the wave function must reproduce itself exactly if we return to this starting point. Here, the phase of the wave function can change by an integer multiple of  $2\pi$ , since this does not affect the

wave function.

We can have the same situation also on a macroscopic scale. Imagine that we have an arbitrary wave propagating without damping in a ring with radius  $R$ . The wave can become stationary if an integer number  $n$  of wavelengths  $\lambda$  exactly fit into the ring. Then we have the condition  $n\lambda = 2\pi R$  or  $kR = n$ , using the wavenumber  $k = 2\pi/\lambda$ . If this condition is violated, after a few revolutions the wave disappears due to interference.

Next we apply these ideas to an electron wave propagating around the ring. For an exact treatment, we would have to solve the Schrödinger equation for the relevant geometry. However, we refrain from this and, instead, we restrict ourselves to a semiclassical treatment, also yielding the essential results.

We start with the relation between the wave vector of the electron and its momentum.

According to de Broglie, for an uncharged quantum particle we have  $\mathbf{p}_{\text{kin}} = \hbar\mathbf{k}$ , where  $\mathbf{p}_{\text{kin}} = m\mathbf{v}$  denotes the “kinetic momentum” (where  $m$  is the mass and  $\mathbf{v}$  is the velocity of the particle). This yields the kinetic energy of the particle:  $E_{\text{kin}} = (\mathbf{p}_{\text{kin}})^2/2m$ . For a charged particle as the electron, according to the rules of quantum mechanics, the wave vector  $\mathbf{k}$  depends on the so-called vector potential  $\mathbf{A}$ . This vector potential is connected with the magnetic field through the relation<sup>9</sup>

$$(\text{curl } \mathbf{A})_x = \frac{\partial A_z}{\partial y} - \frac{\partial A_y}{\partial z}; \quad (\text{curl } \mathbf{A})_y = \frac{\partial A_x}{\partial z} - \frac{\partial A_z}{\partial x}, \quad (\text{curl } \mathbf{A})_z = \frac{\partial A_y}{\partial x} - \frac{\partial A_x}{\partial y}.$$

$$\text{curl } \mathbf{A} = \mathbf{B} \quad 1.4$$

We define the “canonical momentum”

$$\mathbf{p}_{\text{can}} = m\mathbf{v} + q\mathbf{A} \quad 1.5$$

where  $m$  is the mass and  $q$  is the charge of the particle. Then the relation between the wave vector  $\mathbf{k}$  and  $\mathbf{p}_{\text{can}}$  is

$$\mathbf{p}_{\text{can}} = \hbar\mathbf{k} \quad 1.6$$

Now we require that an integer number of wavelengths exists within the ring. We integrate  $\mathbf{k}$  along an integration path around the ring, and we set this integral equal to an integer multiple of  $2\pi$ . Then we have

$$n \cdot 2\pi = \oint \mathbf{k} \cdot d\mathbf{r} = \frac{1}{\hbar} \oint \mathbf{p}_{\text{can}} \cdot d\mathbf{r} = \frac{m}{\hbar} \oint \mathbf{v} \cdot d\mathbf{r} + \frac{q}{\hbar} \oint \mathbf{A} \cdot d\mathbf{r} \quad 1.7$$

According to Stokes' theorem, the second integral ( $\oint \mathbf{A} \cdot d\mathbf{r}$ ) on the right-hand side can be replaced by the area integral  $\int_F \text{curl } \mathbf{A} \cdot d\mathbf{f}$  taken over the area  $F$  enclosed by the ring. However, this integral is nothing other than the magnetic flux  $\int_F \text{curl } \mathbf{A} \cdot d\mathbf{f} = \int_F \mathbf{B} \cdot d\mathbf{f} = \Phi$  enclosed by the ring. Hence, Eq. (1.7) can be changed into

$$n \frac{h}{q} = \frac{m}{q} \oint \mathbf{v} d\mathbf{r} + \Phi$$

Here, we have multiplied Eq. (1.7) by  $\hbar/q$  and used  $\hbar = h/2\pi$ .

In this way, we have found a quantum condition connecting the magnetic flux through the ring with Planck's constant and the charge of the particle. If the path integral on the right-hand side of Eq. (1.8) is constant, the magnetic flux through the ring changes exactly by a multiple of  $h/q$ .

So far we have discussed only a single particle. However, what happens if all or at least many charge carriers occupy the same quantum state? Also in this case, we can describe these charge carriers in terms of a single coherent matter wave with a well-defined phase, and where all charge carriers jointly change their quantum states. In this case, Eq. (1.8) is also valid for this coherent matter wave.

However, now we are confronted with the problem that electrons must satisfy the Pauli principle and must occupy different quantum states, like all quantum particles having half-integer spin. Here, the solution comes from the pairing of two electrons, forming Cooper pairs in an ingenious way. In [Chapter 3](#), we will discuss this pairing process in more detail. Then each pair has an integer spin that is equal to zero for most superconductors. The coherent matter wave can be constructed from these pairs. The wave is connected with the motion of the center of mass of the pairs, which is identical for all pairs.

Next, we will further discuss Eq. (1.8) and see what conclusions can be drawn regarding the superconducting state. We start by connecting the velocity  $\mathbf{v}$  with the supercurrent density  $\mathbf{j}_s$  via  $\mathbf{j}_s = q n_s \mathbf{v}$ . Here,  $n_s$  denotes the density of the superconducting charge carriers. For generality, we keep the notation  $q$  for the charge. Now Eq. (1.8) can be rewritten as

$$n \frac{h}{q} = \frac{m}{q^2 n_s} \oint \mathbf{j}_s d\mathbf{r} + \Phi \quad 1.9$$

Furthermore, we introduce the abbreviation  $m/(q^2 n_s) = \mu_0 \lambda_L^2$ . The length

$$\lambda_L = \sqrt{m/(\mu_0 q^2 n_s)} \quad 1.10$$

is the London penetration depth (where  $q$  is the charge,  $m$  is the particle mass,  $n_s$  is the particle density, and  $\mu_0$  is the permeability). In the following, we will deal with the penetration depth  $\lambda_L$  many times. With Eq. (1.10), we find

$$n \frac{h}{q} = \mu_0 \lambda_L^2 \oint \mathbf{j}_s d\mathbf{r} + \Phi \quad 1.11$$

Equation (1.11) represents the quantization of the fluxoid. The expression on the right-hand side denotes the “fluxoid.” In many cases, the supercurrent density and, hence, the line integral on the right-hand side of Eq. (1.11) are negligibly small. This happens in particular if we deal with a thick-walled superconducting cylinder or with a ring made of a type-I superconductor.

Because of the Meissner–Ochsenfeld effect, the magnetic field is expelled from the superconductor. The shielding supercurrents only flow near the surface of the superconductor and decay exponentially toward the interior, as we will discuss further below. We can place the integration path, along which Eq. (1.11) must be evaluated, deep in the interior of the ring. In this case, the integral over the current density is exponentially small, and we obtain in good approximation

$$\Phi \approx n \frac{h}{q} \quad 1.12$$

However, this is exactly the condition for the quantization of the magnetic flux, and the experimental observation  $\Phi = n(h/2|e|) = n\Phi_0$  clearly shows that the super-conducting charge carriers have the charge  $|q| = 2e$ . The sign of the charge carriers cannot be found from the observation of the flux quantization, since the direction of the particle current is not determined in this experiment. In many superconductors, the Cooper pairs are formed by electrons, that is,  $q = -2e$ . On the other hand, in many high-temperature superconductors, we have hole conduction similar to that found in p-doped semiconductors. Here, we have  $q = +2e$ .

Next, we turn to a massive superconductor without any hole in its geometry. We assume that the superconductor is superconducting everywhere in its interior. Then we can imagine an integration path with an arbitrary radius placed around an arbitrary point, and again we obtain Eq. (1.11) similar to the case of the ring. However, now we can consider an integration path having a smaller and smaller radius  $r$ . It is reasonable to assume that on the integration path the supercurrent density cannot become infinitely large. However, then the line integral over  $\mathbf{j}_s$  approaches zero, since the circumference of the ring vanishes. Similarly, the magnetic flux  $\Phi$ , which integrates the magnetic field  $\mathbf{B}$  over the area enclosed by the integration path, approaches zero, since this area becomes smaller and smaller. Here, we have assumed that the magnetic field cannot become infinite. As a result, the right-hand side of Eq. (1.11) vanishes, and we have to also conclude that the left-hand side must vanish, that is,  $n = 0$ , if we are dealing with a continuous superconductor.

Now we assume again a finite integration path, and with  $n = 0$  we have the condition

$$\mu_0 \lambda_L^2 \oint \mathbf{j}_s \cdot d\mathbf{r} = -\Phi = - \int_F \mathbf{B} \cdot d\mathbf{f} \quad 1.13$$

Using Stokes' theorem again, this condition can also be written as

$$\mathbf{B} = -\mu_0 \lambda_L^2 \operatorname{curl} \mathbf{j}_s \quad 1.14$$

Equation (1.14) is the second London equation, which we will derive below in a slightly different way. It is one of two fundamental equations with which the two brothers F. London and H. London already in 1935 had constructed a successful theoretical model of superconductivity [24].

Next, we turn to the Maxwell equation  $\operatorname{curl} \mathbf{H} = \mathbf{j}$ , which we change to

$$\operatorname{curl} \mathbf{B} = \mu_0 \mathbf{j}_s$$

[1.15](#)

using  $\mathbf{B} = \mu\mu_0\mathbf{H}$ ,  $\mu \approx 1$  for non-magnetic superconductors and  $\mathbf{j} = \mathbf{j}_s$ . Again we take the curl of both sides of Eq. (1.15), replace  $\operatorname{curl} \mathbf{j}_s$  with the help of Eq. (1.14), and continue to use the relation<sup>10</sup>  $\operatorname{curl}(\operatorname{curl} \mathbf{B}) = \operatorname{grad}(\operatorname{div} \mathbf{B}) - \Delta \mathbf{B}$  and Maxwell's equation  $\operatorname{div} \mathbf{B} = 0$ . Thereby we obtain

$$\Delta \mathbf{B} = \frac{1}{\lambda_L^2} \mathbf{B} \quad \text{1.16}$$

This differential equation produces the Meissner–Ochsenfeld effect, as we can see from a simple example. For this purpose, we consider the surface of a very large superconductor, located at the coordinate  $x = 0$  and extended infinitely along the  $(x, y)$  plane. The superconductor occupies the half-space  $x > 0$  (see [Figure 1.15](#)). An external magnetic field  $\mathbf{B}_a = (0, 0, B_a)$  is applied to the superconductor. Due to the symmetry of our problem, we can assume that within the superconductor only the  $z$ -component of the magnetic field is different from zero and is only a function of the  $x$ -coordinate. Equation (1.16) then yields for  $B_z(x)$  within the superconductor, that is, for  $x > 0$ :

$$\frac{d^2 B_z(x)}{dx^2} = \frac{1}{\lambda_L^2} B_z(x) \quad \text{1.17}$$

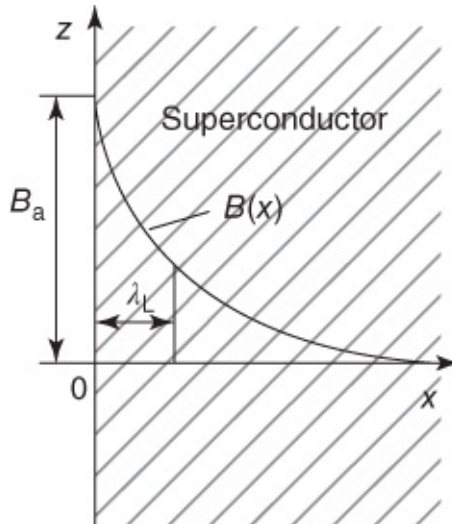


[Figure 1.15](#) Decrease in the magnetic field within the superconductor near the planar surface.

This equation has the solution

$$B_z(x) = B_z(0) \times \exp(-x/\lambda_L) \quad \text{1.18}$$

which is shown in [Figure 1.15](#). Within the length  $\lambda_L$  the magnetic field is reduced by the factor  $1/e$ , and the field vanishes deep within the superconductor.

We note that Eq. (1.17) also yields a solution increasing with  $x$ :

$$B_z(x) = B_z(0) \times \exp(+x/\lambda_L)$$

However, this solution leads to an arbitrarily large magnetic field in the superconductor and, hence, is not meaningful.

From Eq. (1.10) we can obtain a rough estimate of the London penetration depth with the simplifying assumption that one electron per atom with free-electron mass  $m_e$  contributes to the supercurrent. For tin, for example, such an estimate yields  $\lambda_L = 26$  nm. This value deviates only little from the measured value, which at low temperatures falls in the range 25–36 nm.

Only a few nanometers away from its surface, the superconducting half-space is practically free of the magnetic field and displays the ideal diamagnetic state. The same can be found for samples with a more realistic geometry, for example, a superconducting rod, as long as the radii of curvature of the surfaces are much larger than  $\lambda_L$  and the superconductor is also much thicker than  $\lambda_L$ . Then on a length scale of  $\lambda_L$ , the superconductor closely resembles a superconducting half-space. Of course, for an exact solution, Eq. (1.16) must be solved.

The London penetration depth depends on temperature. From Eq. (1.10) we see that  $\lambda_L$  is proportional to  $1/n_s^{1/2}$ . We can assume that the number of electrons combined into Cooper pairs decreases with increasing temperature and vanishes at  $T_c$ . Above the transition temperature, no stable Cooper pairs should exist anymore.<sup>11</sup> Hence, we expect that  $\lambda_L$  increases with increasing temperature and diverges at  $T_c$ . Correspondingly, the magnetic field penetrates further and further into the superconductor until it homogeneously fills the sample above the transition temperature.

We consider now in some detail a superconducting plate with thickness  $d$ . The plate is arranged parallel to the  $(y, z)$  plane, and a magnetic field  $B_a$  is applied parallel to the  $z$ -direction. This geometry is shown in Figure 1.16. Also in this case, we can calculate the spatial variation of the magnetic field within the superconductor using the differential equation (1.17). However, now the magnetic field is equal to the applied field  $B_a$  at both surfaces, that is, at  $x = \pm d/2$ . To find the solution, we have to also take into account the exponential function increasing with  $x$ . As an ansatz we chose the linear combination

$$B_z(x) = B_1 e^{-x/\lambda_L} + B_2 e^{+x/\lambda_L} \quad 1.19$$

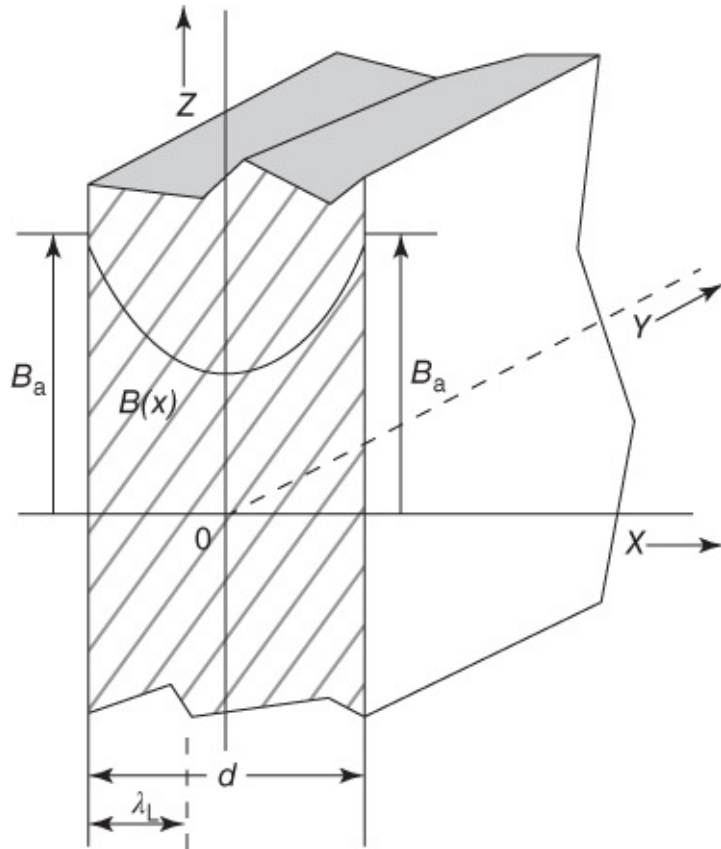


**Figure 1.16** Spatial dependence of the magnetic field in a thin superconducting layer of thickness  $d$ . For the assumed ratio  $d/\lambda_L = 3$ , the magnetic field only decreases to about half of its outside value.

For  $x = d/2$ , we find

$$B_a = B_z \left( \frac{d}{2} \right) = B_1 e^{-d/2\lambda_L} + B_2 e^{+d/2\lambda_L} \quad 1.20$$

Since our problem is symmetric for  $x$  and  $-x$  for the chosen coordinate system, we have  $B_1 = B_2 = B^*$  and we obtain

$$B_a = B^* (e^{d/2\lambda_L} + e^{-d/2\lambda_L}), \quad \text{with } B^* = \frac{B_a}{2 \cosh(d/2\lambda_L)} \quad 1.21$$

Hence, we find within the superconductor

$$B_z(x) = B_a \frac{\cosh(x/\lambda_L)}{\cosh(d/\lambda_L)} \quad 1.22$$

This result is shown in [Figure 1.16](#). For  $d \gg \lambda_L$ , the field decays exponentially in the superconductor away from the two surfaces, and the interior of the plate is nearly free of magnetic field. However, for decreasing thickness  $d$  the variation of the magnetic field becomes smaller and smaller, since the shielding layer cannot develop completely anymore. Finally, for  $d \ll \lambda_L$ , the field varies only little over the thickness. Now the field penetrates

practically homogeneously through the superconducting layer.

For the cases of the superconducting half-space and of the superconducting plate, we also calculate the shielding current flowing within the superconductor. From the variation of the magnetic field, we find the density of the shielding current using the first Maxwell equation ([1.15](#)), which reduces to the equation  $\mu_0 j_{s,y} = -(dB_z/dx)$  for  $\mathbf{B} = (0, 0, B_z(x))$ . Hence, the current density only has a  $y$ -component, which decreases from the surface toward the interior of the superconductor, similar to the magnetic field.

For the case of the superconducting half-space, one finds  $j_{s,y} = (B_a/\mu_0\lambda_L)e^{-x/\lambda_L}$ . Therefore, at the surface the current density is  $B_a/\mu_0\lambda_L$ . For the case of the thin plate we obtain  $j_{s,y} = -(B_a/\mu_0\lambda_L)(\sinh(x/\lambda_L)/\cosh(d/\lambda_L))$ , which reduces to  $j_{s,y}(-d/2) = (B_a/\mu_0\lambda_L)\tanh(d/2\lambda_L)$  at the surface at  $x = -d/2$ . At  $x = d/2$ , the supercurrent density is the negative of this value.

We see that at  $x = -d/2$  the supercurrents flow into the plane of the paper, and at  $x = d/2$  they flow out of this plane. Noting that for a plate with finite size these currents must join together, we are dealing with a circulating current flowing near the surface around the plate. The magnetic field generated by this current is oriented in the direction opposite to that of the applied field. Hence, the plate behaves like a diamagnet.

How can one measure the London penetration depth? In principle, one must determine the influence of the thin shielding layer upon the diamagnetic behavior. This has been done using several different methods.

For example, one can determine the magnetization of thinner and thinner plates [25]. As long as the thickness of the plate is much larger than the penetration depth, one will find a nearly ideal diamagnetic result, which will decrease, however, if the plate thickness approaches the range of  $\lambda_L$ . Another method is  $\mu$ SR, which is sensitive to local magnetic fields, as discussed in [Section 1.2](#). In order to determine the penetration depth in the Meissner state, the muons are implanted into different depths by varying the implantation energy. In this way, one finds  $\lambda_L$  [26].

Other methods are based on the Shubnikov phase and determine  $\lambda_L$  from the diameter of the flux lines.

To determine the temperature dependence of  $\lambda_L$ , only relative measurements are needed. One can determine the resonance frequency of a cavity fabricated from a superconducting material. The resonance frequency depends sensitively on the geometry. If the penetration depth varies with the temperature, this is equivalent to a variation of the geometry of the cavity and, hence, of the resonance frequency, yielding the change of  $\lambda_L$  [27]. We will present experimental results in [Section 4.5](#).

A strong interest in the exact measurement of the penetration depth, say, as a function of temperature, magnetic field, or the frequency of the microwaves for excitation, arises because of its dependence on the density of the superconducting charge carriers. It yields important information on the superconducting state and can serve as a sensor for studying

superconductors.

Let us now return to our discussion of the macroscopic wave function. The concept of the coherent matter wave formed by the charge carriers in the superconducting state has already provided the explanation of ideal diamagnetism and of the fluxoid quantization or of flux quantization. Furthermore, we have found a fundamental length scale of superconductivity, namely the London penetration depth.

What causes the difference between type-I and type-II superconductivity and the generation of vortices? From the assumption of a continuous superconductor, we have obtained the second London equation and ideal diamagnetism. In type-I superconductors, this state is established as long as the applied magnetic field does not exceed a critical value. At higher fields superconductivity breaks down. For a discussion of the critical magnetic field, we must treat the energy of a superconductor more accurately. This will be done in [Chapter 4](#). We will see that it is the competition between two energies, the energy gain from the condensation of Cooper pairs and the energy loss due to the magnetic field expulsion, which causes the transition between the superconducting and the normal conducting state.

At small magnetic fields, the Meissner phase is also established in type-II superconductors. However, at the lower critical field, vortices appear within the material. Turning again to Eq. [\(1.11\)](#), we see that the separation of the magnetic flux into units<sup>12</sup> of  $\pm 1\Phi_0$  corresponds to states with quantum number  $n = \pm 1$ . However, the discussion of the Meissner state has also shown that the superconductor cannot display continuous superconductivity anymore. Instead, we must assume that the vortex axis is not superconducting, similar to the ring geometry. In this case, the integration path cannot be contracted to a point anymore, and the derivation of the second London equation with  $n = 0$ , resulting in the Meissner–Ochsenfeld effect, is no longer valid. A more accurate treatment based on the Ginzburg–Landau theory shows that, on a length scale  $\xi_{\text{GL}}$ , the Ginzburg–Landau coherence length, superconductivity vanishes as one approaches the vortex axis (see also [Section 4.7.2](#)). Depending on the superconducting material, this length ranges between a few and a few hundred nanometers. Similar to the London penetration depth, it is temperature dependent, in particular close to  $T_c$ .

In the Shubnikov phase, the superconductor is penetrated by many normal conducting lines. However, why does each vortex carry exactly one flux quantum  $\Phi_0$ ? Again we must look at the energy of a superconductor. Essentially we find that in a type-II superconductor, it is energetically favorable if it generates a superconductor/normal conductor interface above the lower critical magnetic field (see [Section 4.7](#)). Therefore, as many of these interfaces as possible are generated. This is achieved by choosing the smallest quantum state with  $n = \pm 1$ , since in this case the maximum number of vortices and the largest interface area near the vortex axis is established.

We could use Eq. [\(1.11\)](#) for calculating how far the magnetic field of a flux line extends into the superconductor. However, we refrain from presenting this calculation. It turns out that also in this case the field decreases nearly exponentially with the distance from the vortex axis on the length scale  $\lambda_L$ . Hence, we can say that the flux line has a magnetic radius of  $\lambda_L$ .

Now we can also estimate the lower critical field  $B_{c1}$ . Each flux line carries a flux quantum  $\Phi_0$ , and one needs at least a magnetic field  $B_{c1} \approx \Phi_0 / (\text{cross-sectional area of the flux line}) \approx \Phi_0 / (\pi \lambda_L^2)$  to generate this amount of flux. With a value of  $\lambda_L = 100 \text{ nm}$ , one finds  $B_{c1} \approx 66 \text{ mT}$ .

For increasing magnetic field, the flux lines are packed closer and closer to each other, until near  $B_{c2}$  their distance is about equal to the Ginzburg–Landau coherence length  $\xi_{\text{GL}}$ . For a simple estimate of  $B_{c2}$ , we assume a cylindrical normal conducting vortex core. Then superconductivity is expected to vanish if the distance between the flux quanta becomes equal to the core diameter, that is, at  $B_{c2} \approx \Phi_0 / (\pi \xi_{\text{GL}}^2)$ . An exact theory yields a value smaller by a factor of 2.<sup>13</sup> We note that, depending on the value of  $\xi_{\text{GL}}$ ,  $B_{c2}$  can become very large. With the value  $\xi_{\text{GL}} = 2 \text{ nm}$ , one obtains a field larger than 80 T. Such high values of the upper critical magnetic field are reached or even exceeded in high-temperature superconductors.

At the end of this section, we wish to ask how permanent current and zero resistance, the key phenomena of superconductivity, can be explained in terms of the macroscopic wave function. Therefore, we look at the second London equation (1.14),  $\mathbf{B} = -\mu_0 \lambda_L^2 \text{curl} \mathbf{j}_s$ , and in addition we use Maxwell's equation

$$\text{curl} \mathbf{E} = -\frac{d\mathbf{B}}{dt} = -\dot{\mathbf{B}} \quad 1.23$$

connecting the curl of the electric field with the temporal change of the magnetic field. We take the time derivative of Eq. (1.14) and insert the result into Eq. (1.23). Then we obtain  $\text{curl} \mathbf{E} = \mu_0 \lambda_L^2 \text{curl} \mathbf{j}_s$  and, except for an integration constant,

$$\mathbf{E} = \mu_0 \lambda_L^2 \dot{\mathbf{j}}_s \quad 1.24$$

This is the first London equation. For a temporally constant supercurrent, the right-hand side of Eq. (1.24) is zero. Hence, we obtain current flow without an electric field and zero resistance.

Equation (1.24) also indicates that in the presence of an electric field the supercurrent density continues to increase with time. For a superconductor this seems reasonable, since the superconducting charge carriers are accelerated more and more due to the electric field. On the other hand, the supercurrent density cannot increase up to infinity. Therefore, additional energy arguments are needed to find the maximum supercurrent density that can be reached. In [Section 5.1](#), we will present these arguments using the Ginzburg–Landau theory.

We could have derived the first London equation also from classical arguments, if we note that for current flow without resistance the superconducting charge carriers cannot experience (inelastic) collision processes. Then, in the presence of an electric field, we have the force equation  $m\ddot{\mathbf{v}} = q\mathbf{E}$ . We use  $\dot{\mathbf{j}} = qn_s \mathbf{v}$  and find  $\mathbf{E} = (m/q^2 n_s) \dot{\mathbf{j}}_s$ . The latter equation can be turned into Eq. (1.24) using the definition (1.10) of the London penetration depth.

This argument indicates at least formally that the zero value of the resistance is also a consequence of the macroscopic wave function. However, we may also ask what processes

lead to a finite resistance or cause the decay of a permanent current. For simplicity, we restrict our discussion to direct currents in a type-I superconductor, that is, we do not consider dissipative effects caused by vortex motion or by the acceleration of unpaired electrons in an alternating electric field.

We look at the strongly simplified situation shown in [Figure 1.17](#). We assume the geometry of a metallic ring containing only four electrons. The electrons can move only along the ring. In this figure, the ring is shown after being cut and straightened into a piece of wire, the two ends of which are identical. Such a case is also referred to as a ***periodic boundary condition***. An electron leaving the ring, say, on the left end, reappears again on the right end.

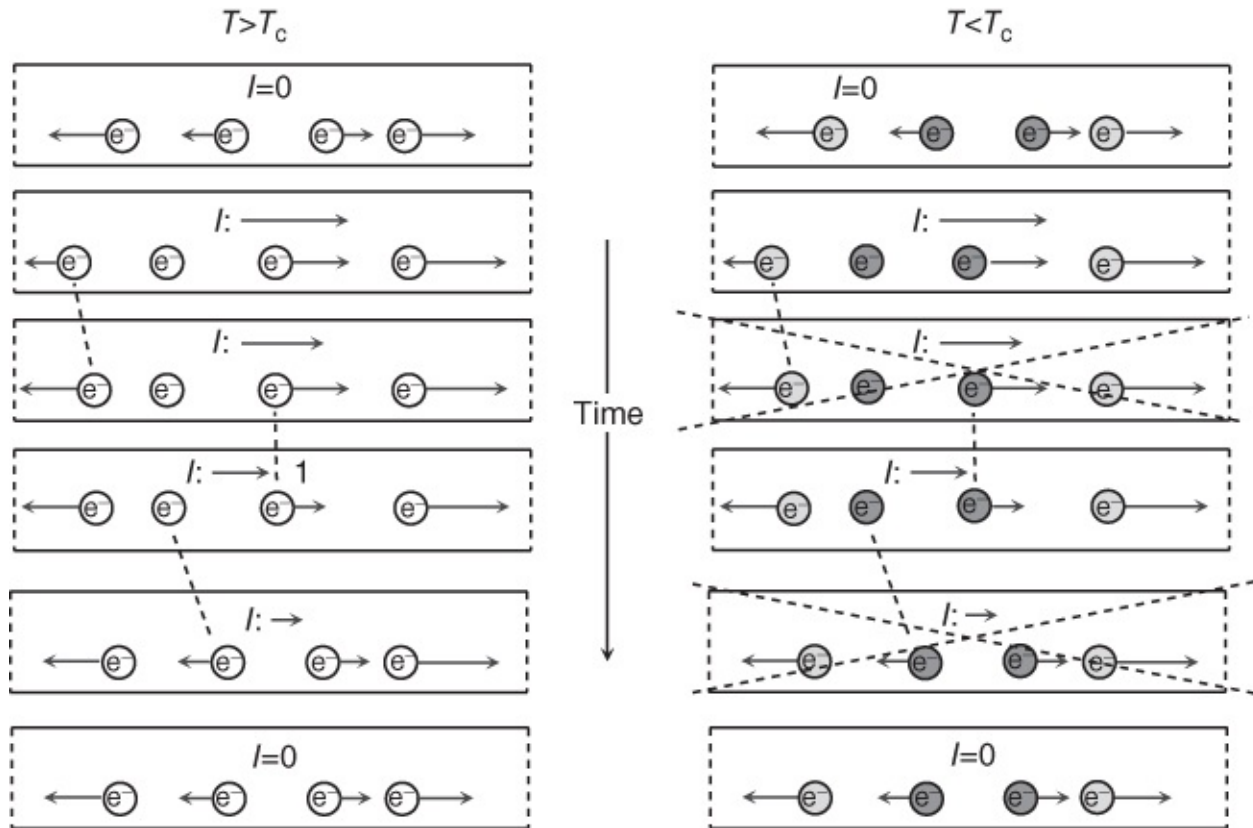


[Figure 1.17](#) Generation of the supercurrent. Four electrons in a wire bent to a ring are shown.

In the normal conducting state ( $T > T_c$ ), the circulating current is assumed to be zero. However, this does not mean that the electrons are completely at rest. Because of the Pauli principle, the electrons must occupy different quantum states. If we neglect the electron spin, the four electrons must have different wave vectors and, hence, different velocities. We have marked these velocities by arrows with different lengths and different directions, which are attached to the electrons. As required by quantum mechanics, the wave numbers and, hence, the velocities of the electrons can change only in integer steps. This is indicated by the length of the arrows. If no net circulating current is assumed to flow, the velocities of the four electrons must cancel each other exactly. This is the situation shown in the upper left of the figure. On the other hand, if we have generated a circulating current, the electrons are moving predominantly in one direction. This is shown in the second picture from the top. Here, we have added one unit to the velocity of each electron, and the total current is indicated by the arrow of the sum.<sup>14</sup>

If we leave the system alone, the electrons will change their quantum state very rapidly by means of collision processes toward the state with the smallest possible total energy. Hence, the circulating current will have decayed after a short time. In the figure a few collision processes are indicated, where we have marked the scattered electrons by a dashed line. Here, the total current can change in steps of one unit.

The macroscopic wave function is distinguished by the fact that the centers of mass of all Cooper pairs have the same momentum and the same wave vector. For illustration, on the right-hand side of [Figure 1.17](#), the four electrons are combined into two Cooper pairs and are marked by dark or light gray color. We note that in the two upper pictures of the right-hand side, both pairs have the same velocity of the center of mass, respectively. For current  $I = 0$ , this velocity is zero. In the second picture the velocity vector of both pairs points to the right by one unit. Now a number of collision processes, resulting in the decay of the current at  $T > T_c$ , do not function anymore, since they violate the condition that the velocity of the centers of mass of both pairs must be the same. During a transition of one electron, the other electrons must adjust their quantum states in such a way that all pairs continue to have the same velocity of the centers of mass. The total current must change in steps of at least two units, until the state  $I = 0$  is reached again. Similarly, for  $N$  pairs, the total current must change in steps of  $N$  units. For  $N = 2$  such events clearly would not be very unlikely. However, for  $10^{20}$  electrons or Cooper pairs, the probability of such simultaneous processes would be extremely small, and the current does not decay.

We can illustrate the above arguments also more realistically with the Fermi sphere. In [Figure 1.18](#) two dimensions  $k_x$  and  $k_y$  of  $\mathbf{k}$ -space are shown. The allowed discrete values of  $\mathbf{k}$  are indicated by the individual dots (which are shown at a strongly exaggerated distance). At least for  $T = 0$ , the electrons occupy the states with the lowest energy, yielding the Fermi sphere for 3D and correspondingly a circle in the  $(k_x, k_y)$  plane. For zero net current flow, this sphere is centered around the origin of the coordinate system. If a net current is flowing in the  $x$ -direction, the Fermi sphere is slightly displaced parallel to  $k_x$ , since a net motion in the direction of the current must remain, if we sum over all electrons.<sup>15</sup> In [Figure 1.18](#), this displacement is highly exaggerated.

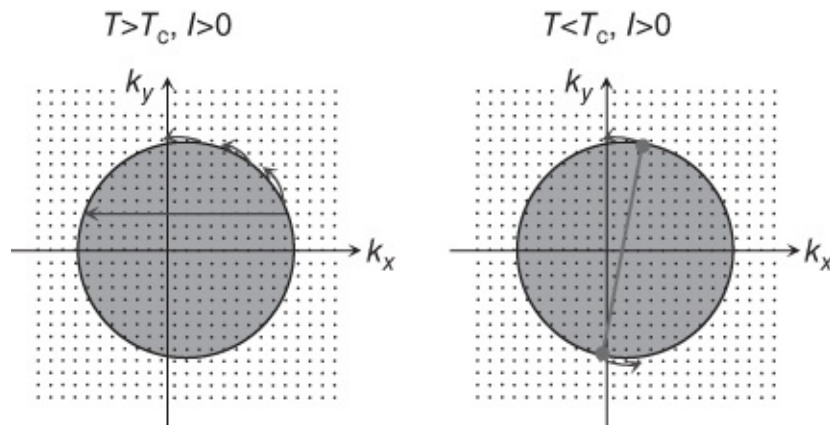


**Figure 1.18** Generation of the supercurrent: current transport and decay of the permanent current illustrated with the Fermi sphere.

In the normal conducting state with the observation of the Pauli principle, electrons can scatter into lower energy states essentially independently of each other (as indicated by the arrows), and the Fermi sphere rapidly relaxes back to the origin, that is, the circulating current decays quickly. However, in the superconducting state, the pairs are correlated with respect to the center of the Fermi sphere. They can only scatter around the sphere, without affecting the center of the sphere. Hence, the circulating current does not decay and we have a permanent current.

The simplest possibility for slowing down the circulating current in a ring containing many electrons arises by briefly eliminating the pair correlation in the smallest possible volume element of the ring by means of a fluctuation. This volume element would briefly be normal conducting, and the circulating current could decrease easily. We wish to estimate roughly the probability of such a process.

The length scale over which the superconductivity can be suppressed is the Ginzburg–Landau coherence length  $\xi_{\text{GL}}$ , which we have discussed already in conjunction with the vortices in type-II superconductors. The smallest volume that can briefly become normal is then given by the cross-section of the wire multiplied by  $\xi_{\text{GL}}$ , if the wire diameter does not exceed  $\xi_{\text{GL}}$ . We assume that the volume to become normal is  $V_c = \xi_{\text{GL}}^3$ . How many Cooper pairs are contained in this volume? The electron density is taken as  $n$ , and we assume that the fraction  $a$  of all electrons are paired. Then within the volume  $\xi_{\text{GL}}^3$ , there are  $N_c = a n \xi_{\text{GL}}^3 / 2$  pairs. According to the Bardeen–Cooper–Schrieffer (BCS) theory, the fraction  $a$  of electrons effectively participating in Cooper pairing is approximately given by  $\Delta_0/E_F$ , where  $E_F$  is the Fermi energy and  $\Delta_0$  the energy gap. For metallic superconductors such as Nb or Pb, we have  $\Delta_0 \approx 1 \text{ meV}$  and  $E_F \approx 1 \text{ eV}$ . Hence, we find for the fraction  $a \approx 10^{-3}$ . If we take  $n = 10^{23} \text{ cm}^{-3}$  and  $\xi_{\text{GL}} \approx 100 \text{ nm}$ , we obtain about  $10^5$  Cooper pairs to be transferred into the normal state by means of a fluctuation. The condensation energy per pair is also about 1 meV. Hence, the energy cost  $E_c$  of the above process is at least about  $10^2 \text{ eV}$ . From thermodynamics we know that the probability for this process is proportional to the Boltzmann factor  $\exp(-E_c/k_B T)$ . For a temperature of 1 K, we have  $k_B T \approx 0.08 \text{ meV}$ , and for the ratio  $E_c/k_B T$  we obtain about  $10^6$ . Hence, the Boltzmann factor is only about  $\exp(-10^6)$ .

Here, we note that an exact analysis of the fluctuation effects leading to the appearance of a finite resistance in a thin superconducting wire is much more complicated than just described [28, 29]. However, the exponential dependence on the condensation energy within a coherence volume remains. This dependence has been tested by measurements of the resistance of very thin single-crystalline tin wires (so-called whiskers) near  $T_c = 3.7 \text{ K}$  [30, 31]. Within 1 mK, the resistance dropped exponentially by 6 orders of magnitude. If we extrapolate this behavior to lower temperatures, we find the probability for a brief breakdown of superconductivity so extremely small that with good reason we can speak of the zero resistance.

For high-temperature superconductors, the condensation energy per pair is about 1 order of magnitude larger than for Nb or Pb. However, the volume  $V_c$  is much smaller. Here, the Ginzburg–Landau coherence length is anisotropic. In two spatial directions it is about 1–2 nm,

and in the third direction it is smaller than 0.3 nm. Here, at low temperatures, the volume  $V_c$  may contain less than 10 Cooper pairs. In this case at  $T = 1$  K, the Boltzmann factor is about  $\exp(-10^2)$ .

Indeed, in high-temperature superconductors, fluctuation effects often are not negligible and can lead to a number of interesting phenomena, in particular in conjunction with vortices. We will discuss this in more detail in Chapters 4 and 5.

## 1.5 Quantum Interference

How can we directly demonstrate the coherent matter wave in a superconductor? In optics this is elegantly done by means of diffraction experiments or interference. Everybody is familiar with the interference stripes produced, for example, by laser light passing through a double slit and then focused on a screen.

In [Figure 1.19](#), a special optical interferometer, the Sagnac interferometer, is shown schematically. A laser beam is split in two by means of a semi-transparent mirror in such a way that the two partial waves travel along a “circular” path in opposite directions due to three additional mirrors. If two partial waves with the same phase reach the detector, the waves interfere constructively, and a large signal can be observed. It is the sensitivity with respect to a rotation of the measurement setup that makes the Sagnac interferometer so interesting. If the setup rotates, say, clockwise in the diagram, the mirrors move against the beam coming from the opposite direction. However, the mirrors move away from the beam coming along the same direction. Hence, the beam running clockwise must travel a larger distance before it hits the detector than the beam running counterclockwise. As a result, a phase difference between the partial waves appears at the detector. The detected signal is smaller. With faster and faster rotational velocity of the measurement setup, the signal is expected to vary periodically between a maximum and a minimum value. Because of this dependence of the detector signal upon the rotational velocity of the setup, one can use the Sagnac interferometer as a gyroscope for detecting rotational motion.

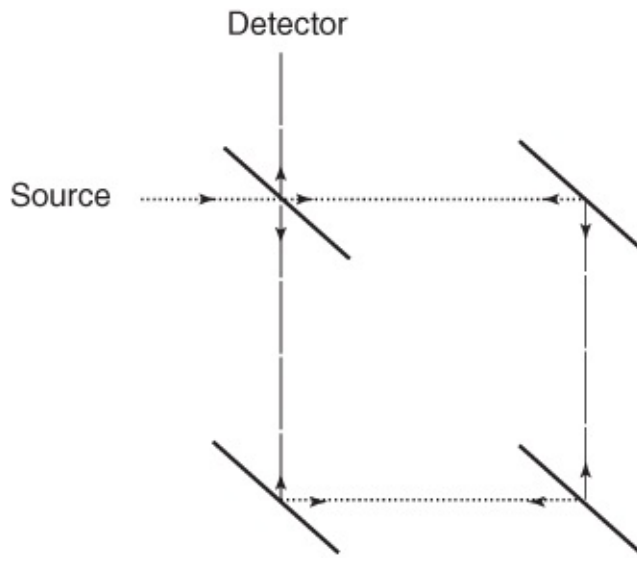


**Figure 1.19** The optical Sagnac interferometer.

In principle, wave nature can be demonstrated also using *temporal* interference. Imagine that two waves having different frequencies interfere with each other, and that we observe the total amplitude of the two waves at a specific location, say, at  $x = 0$ . Each time when both waves are exactly in phase, the total amplitude of the wave is equal to the sum of the amplitudes of both partial waves. If both waves are exactly in the opposite phase, the total amplitude is equal to the difference of the amplitudes of the two partial waves. Hence, we observe that the amplitude of the total wave oscillates periodically with time, where the frequency is given by the difference of the oscillation frequencies of both partial waves.

Can similar phenomena occur in superconductors based on the coherent matter wave? The answer is yes: both phenomena, spatial and temporal interferences, can be observed and are utilized in many applications. For a more exact treatment, we must go a little further and first discuss the Josephson effect.

### 1.5.1 Josephson Currents

Imagine two superconductors placed on top of each other in the form of a sandwich structure. This arrangement is shown schematically in [Figure 1.20](#). Between the two superconductors we imagine a non-superconducting barrier, for instance, an electrical insulator. If the barrier is sufficiently thin, about a few nanometers, electrons can pass from one superconductor to the other, although a non-conducting layer exists between the two metals. The reason is the quantum mechanical tunneling effect. The wave function, describing the probability of finding an electron, leaks out from the metallic region. If a second metal is brought into this zone, the electron can tunnel from metal 1 to metal 2, and a current can flow across this sandwich structure. This tunneling process is a highly fundamental phenomenon in quantum mechanics. For instance, it plays an important role in the alpha decay of atomic nuclei.

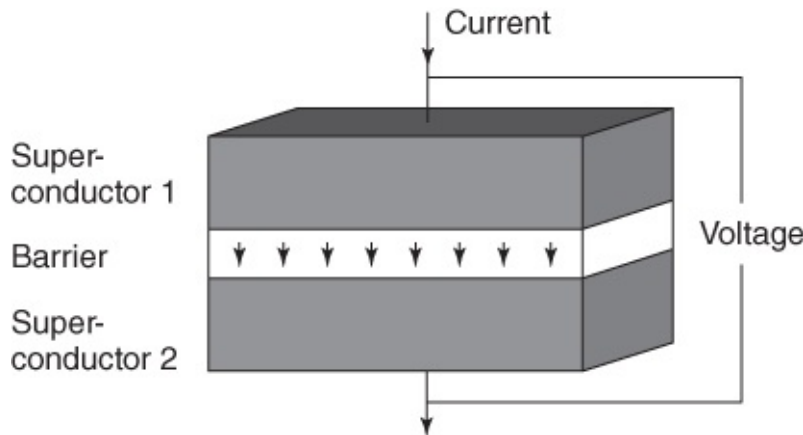


**Figure 1.20** Sandwich geometry of two superconductors separated from each other by a thin barrier.

Due to the tunneling electrons or Cooper pairs, the two superconductors are coupled to each other, and a weak supercurrent, the Josephson current, can flow across the barrier. This current was theoretically predicted for the first time in 1962 by Josephson [32]. The Josephson current displays a number of surprising properties, which are closely connected with the phase of the macroscopic wave function in the superconducting state. In 1973, Josephson received the Nobel Prize for his discovery.

We will see that the Josephson current is proportional to the sine of the phase difference  $\phi_1 - \phi_2$  of the macroscopic wave function of the two superconductors. More exactly, we have

$$I_c = I_c \sin \gamma \quad \text{1.25}$$

where  $\gamma$  is the gauge-invariant phase difference

$$\gamma = \varphi_2 - \varphi_1 - \frac{2\pi}{\Phi_0} \int_1^2 \mathbf{A} d\mathbf{l} \quad \text{1.26}$$

Here, the path integral of the vector potential is taken from superconductor 1 to superconductor 2 across the barrier.

Equation (1.25) is the first Josephson equation. The constant  $I_c$  is denoted as the critical current. Divided by the contact area, we have the critical current density  $j_c$ . At low temperatures, it typically falls in the range  $10^2$ – $10^4$  A/cm<sup>2</sup>.

If a direct voltage  $U$  can be applied to the sandwich, as shown in Figure 1.20, the gauge-invariant phase difference increases as a function of time, as will be discussed in more detail below. In this case, we observe a high-frequency alternating current, the frequency of which is given by

$$f_J = \frac{U}{\Phi_0} = U \frac{2e}{h} \quad \text{1.27}$$

The alternating Josephson current represents the temporal interference of the wave functions of

the two superconductors. The exact relation between the gauge-invariant phase difference  $\gamma$  and the applied voltage  $U$  is described by the second Josephson equation

$$\dot{\gamma} = \frac{2\pi}{\Phi_0} U \quad \underline{1.28}$$

Below, the two Josephson equations will be derived in detail.

The frequency of the alternating Josephson current is proportional to the applied direct voltage, and the proportionality constant is the inverse of the flux quantum  $\Phi_0$ . One finds a value of about 483.6 GHz/mV of applied voltage. This high value, and the fact that the oscillation frequency can be tuned using the applied voltage, makes Josephson junctions interesting as oscillators at frequencies in the high gigahertz range or even in the terahertz range. On the other hand, the fact that Eq. (1.27) connects voltage and frequency through the two fundamental constants  $h$  and  $e$  allows us to define voltage using the frequency of the alternating Josephson current and to utilize Josephson junctions as voltage standards. In Chapters 6 and 7, we will return to the many applications of Josephson junctions.

Now we look more exactly at the properties of the Josephson junction in terms of the macroscopic wave function. Similar to the case of individual electrons discussed earlier, we can imagine here also that the coherent matter wave is leaking out of the superconductor and in this way couples both superconducting parts.

Because of the great significance of the Josephson effect, we will derive the underlying “Josephson equations” in two different ways.

(1) The first derivation goes back to Feynman *et al.* [33]. One considers two weakly coupled quantum mechanical systems and solves the Schrödinger equation for this problem by means of an approximation. The magnetic field is neglected at this stage. The two *separate* systems will be described by the two wave functions  $\Psi_1$  and  $\Psi_2$ . According to the time-dependent Schrödinger equation, for the temporal change of both wave functions, we have

$$\frac{\partial\Psi_1}{\partial t} = \frac{-i}{\hbar}E_1\Psi_1; \quad \frac{\partial\Psi_2}{\partial t} = \frac{-i}{\hbar}E_2\Psi_2 \quad \underline{1.29}$$

If there is weak coupling between the systems, the temporal change of  $\Psi_1$  will also be affected by  $\Psi_2$  and vice versa. This situation can be taken into account by introducing an additional coupling into Eq. (1.29):

$$\frac{\partial\Psi_1}{\partial t} = \frac{-i}{\hbar}(E_1\Psi_1 + K\Psi_2) \quad \underline{1.30a}$$

$$\frac{\partial\Psi_2}{\partial t} = \frac{-i}{\hbar}(E_2\Psi_2 + K\Psi_1) \quad \underline{1.30b}$$

In our case, the coupling means that Cooper pairs can be exchanged between the superconductors 1 and 2. The coupling strength is symmetric and is fixed by the constant  $K$ .

Compared to other quantum mechanical systems with two states (for instance, the  $\text{H}_2^+$  molecule), a peculiarity of the two weakly coupled superconductors is the fact that  $\Psi_1$  and  $\Psi_2$  describe macroscopic states occupied by a large number of particles. Then we can interpret the square of the amplitude in terms of the particle density  $n_s$  of the Cooper pairs. Hence, we can write

$$\Psi_1 = \sqrt{n_{s1}} e^{i\varphi_1}; \quad \Psi_2 = \sqrt{n_{s2}} e^{i\varphi_2} \quad 1.31$$

Here,  $\phi_1$  and  $\phi_2$  are the phases of the wave functions  $\Psi_1$  and  $\Psi_2$ , respectively. Inserting these wave functions into Eqs. (1.30a) and (1.30b), we obtain

$$\frac{\dot{n}_{s1}}{2\sqrt{n_{s1}}} e^{i\varphi_1} + i\sqrt{n_{s1}} e^{i\varphi_1} \times \dot{\varphi}_1 = -\frac{i}{\hbar} \{E_1 \sqrt{n_{s1}} e^{i\varphi_1} + K \sqrt{n_{s2}} e^{i\varphi_2}\} \quad 1.32\text{a}$$

$$\frac{\dot{n}_{s2}}{2\sqrt{n_{s2}}} e^{i\varphi_2} + i\sqrt{n_{s2}} e^{i\varphi_2} \times \dot{\varphi}_2 = -\frac{i}{\hbar} \{E_2 \sqrt{n_{s2}} e^{i\varphi_2} + K \sqrt{n_{s1}} e^{i\varphi_1}\} \quad 1.32\text{b}$$

By separating the real and the imaginary parts, we find

$$\frac{1}{2} \frac{\dot{n}_{s1}}{\sqrt{n_{s1}}} = \frac{K}{\hbar} \sqrt{n_{s2}} \sin(\varphi_2 - \varphi_1) \quad 1.33\text{a}$$

$$\frac{1}{2} \frac{\dot{n}_{s2}}{\sqrt{n_{s2}}} = \frac{K}{\hbar} \sqrt{n_{s1}} \sin(\varphi_1 - \varphi_2) \quad 1.33\text{b}$$

$$i\sqrt{n_{s1}} \dot{\varphi}_1 = -\frac{i}{\hbar} \{E_1 \sqrt{n_{s1}} + K \sqrt{n_{s2}} \cos(\varphi_2 - \varphi_1)\} \quad 1.34\text{a}$$

$$i\sqrt{n_{s2}} \dot{\varphi}_2 = -\frac{i}{\hbar} \{E_2 \sqrt{n_{s2}} + K \sqrt{n_{s1}} \cos(\varphi_1 - \varphi_2)\} \quad 1.34\text{b}$$

If we also take into account that, because of the exchange of Cooper pairs between 1 and 2, we must always have  $\dot{n}_{s1} = -\dot{n}_{s2}$ , and if for simplicity we assume two identical superconductors (i.e.,  $n_{s1} = n_{s2}$ ), from Eqs. (1.33a) and (1.33b) we obtain the differential equation

$$\dot{n}_{s1} = \frac{2K}{\hbar} n_{s1} \sin(\varphi_2 - \varphi_1) = -\dot{n}_{s2} \quad 1.35$$

The temporal change of the particle density in 1 multiplied with the volume  $V$  of 1 yields the change of the particle number and, hence, the particle current across the junction. The electric current  $I_s$  is obtained by multiplication of the particle current with the charge  $2e$  of each individual particle. Then we find

$$I_s = I_c \sin(\varphi_2 - \varphi_1) \quad 1.36$$

with

$$I_c = \frac{2K \times 2e}{\hbar} V n_s = \frac{4\pi K}{\Phi_0} V n_s \quad 1.37$$

This is the first Josephson equation, if we set the vector potential  $\mathbf{A} = 0$ . We recall that we had neglected magnetic fields. Therefore, this step is justified. Turning from  $n_s$  to the current within the junction, we must remember that both superconductors are connected to a current source, which serves to keep  $n_s$  constant within the superconductors by supplying or accepting the charges.

From Eqs. (1.34a) and (1.34b) one obtains a differential equation for the temporal change of the phase difference. With  $n_{s1} = n_{s2}$  and  $E_2 - E_1 = 2eU$ , we have

$$\frac{d}{dt}(\varphi_2 - \varphi_1) = \frac{2eU}{\hbar} = \frac{2\pi}{\Phi_0} U \quad 1.38$$

This is the second Josephson equation for the case  $\mathbf{A} = 0$ . We see that, for a temporally constant voltage  $U = \text{constant}$ , the phase difference increases linearly with time:

$$\varphi_2 - \varphi_1 = \frac{2\pi}{\Phi_0} Ut + \varphi(t = 0) \quad 1.39$$

However, this means that according to the first Josephson equation an alternating current appears in the junction, the frequency  $f$  of which is given by Eq. (1.27).

(2) The second derivation of the Josephson equations that we want to discuss in part goes back to Landau and Lifschitz [34]. It is based only on very general symmetry and invariance principles and thereby emphasizes the wide range of validity of the Josephson effect.

We start by considering qualitatively how supercurrent density and phase are connected to each other within a homogeneous superconducting wire.<sup>16</sup> The current is assumed to flow in the  $z$ -direction. It is convenient to write the supercurrent density as  $j_{s,z} = 2en_s v_z$ . We have used this relation already for the derivation of the fluxoid quantization. If we eliminate  $v_z$  by using the canonical momentum, Eq. (1.5), we obtain

$$j_{s,z} = \frac{q}{m} n_s (p_{\text{can},z} - qA_z)$$

or by using  $\mathbf{p}_{\text{can}} = \hbar\mathbf{k}$

$$j_{s,z} = \frac{q}{m} n_s (\hbar k_z - qA_z)$$

We consider a matter wave of the form  $\Psi = \Psi_0 e^{i\phi} = \Psi_0 e^{i\mathbf{k} \cdot \mathbf{x}}$  and, instead of  $k_z$ , we write the expression  $\phi' \equiv d\phi/dz$  (the derivative of the phase  $\phi = \mathbf{k} \cdot \mathbf{x}$  with respect to  $z$  yields  $k_z$ ). Then we obtain

$$j_{s,z} = \frac{q}{m} n_s (\hbar\phi' - qA_z) \quad 1.40$$

Now we define

$$\gamma(z) = \varphi(z) - \frac{q}{\hbar} \int_0^z A_z dz \quad \text{1.41}$$

yielding

$$j_{s,z} = \frac{q\hbar}{m} n_s \times \gamma' \quad \text{1.42}$$

What happens if our superconducting wire has a weakened location, where the Cooper pair density is strongly reduced? This geometry is shown schematically in [Figure 1.21](#). The current passing through the wire must have the same value everywhere. If we assume a constant supercurrent density over the cross-section of the wire, in Eq. (1.42) the product  $n_s \gamma'$  must have the same value everywhere. However, if  $n_s$  is strongly reduced at the weakened location, there  $\gamma'$  must be much larger than in the remainder of the wire. If at the weakened location  $\gamma'$  displays a sharp peak,  $\gamma(z)$  changes there very rapidly from a value  $\gamma_1$  to a much larger value  $\gamma_2$ .

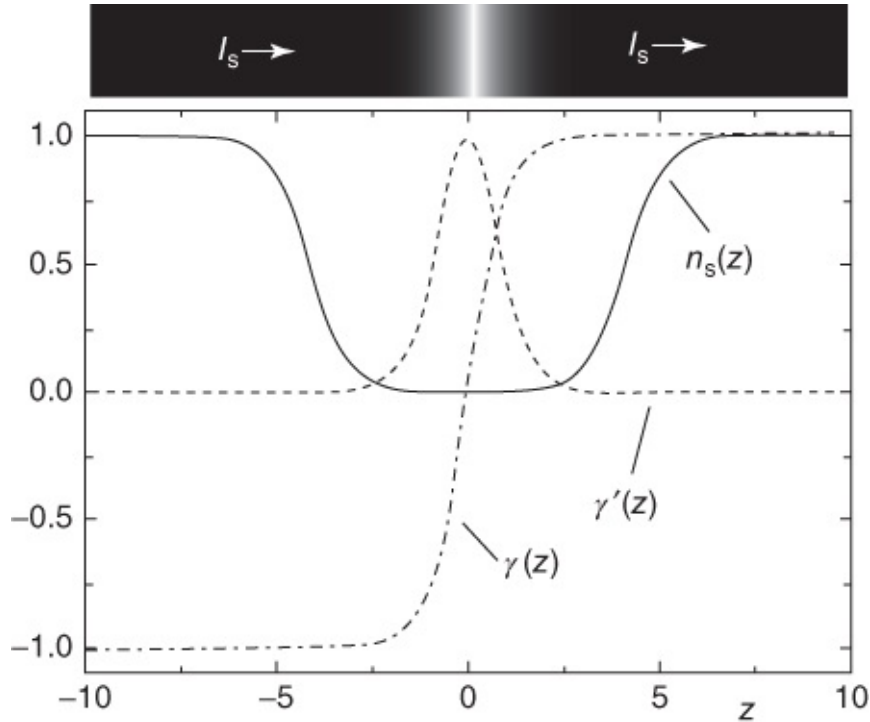


[Figure 1.21](#) Derivation of the Josephson equations. We consider a thin superconducting wire with a weakened location at  $z = 0$ , at which the Cooper pair density  $n_s$  is strongly reduced. Due to current conservation, we have  $n_s(z)\gamma'(z) = \text{constant}$ , leading to a peak in  $\gamma'(z)$  and to a step in  $\gamma$ . For illustration we have used the following “test function”:  $n_s(z) = 1/\gamma'(z) = 1/[1.001 - \tanh^2(x)]$ ,  $\text{constant} = 0.001$ . For  $\gamma(z)$  one finds  $\gamma(z) = \tanh(z) + 0.001z$ . At the weakened location,  $\gamma(z)$  changes very rapidly from  $-1$  to  $+1$ .

Using Eq. (1.41), we can write the jump of the phase at the barrier as

$$\gamma = \gamma(z_2) - \gamma(z_1) = \varphi(z_2) - \varphi(z_1) - \frac{q}{\hbar} \int_{z_1}^{z_2} A_z dz \quad 1.43$$

where  $z_1$  denotes a coordinate in superconductor 1 in front of the barrier and  $z_2$  a coordinate in superconductor 2 behind the barrier. Equation (1.43) has exactly the same form as Eq. (1.26).

If we specify the spatial dependence  $n_s(z)$ , the supercurrent across the barrier is a function of the jump  $\gamma$  of the phase, that is,  $I_s = I_s(\gamma)$ . However, a change of the phase difference of  $2\pi$  should yield the same wave function and, hence, the same value of the supercurrent across the barrier. Therefore, we can expand  $I_s$  as a sum of sine and cosine terms (a Fourier series):

$$I_s(\gamma) = \sum_{n=0}^{\infty} I_{cn} \sin(n\gamma) + \sum_{n=0}^{\infty} \tilde{I}_{cn} \cos(n\gamma) \quad 1.44$$

Here,  $I_{cn}$  and  $\tilde{I}_{cn}$  are the expansion coefficients of the function  $I_s(\gamma)$ . We note that microscopic details such as the structure of the barrier or the temperature dependence of the Cooper pair density are contained in these expansion coefficients. However, the periodicity of  $I_s(\gamma)$  is independent of this.

Now we utilize the principle of time inversion symmetry. Many fundamental phenomena in Nature are reversible. If we record such a phenomenon with a camera and then run the motion picture backward, we see again a process that is physically possible.<sup>17</sup> Now we assume that this principle also applies to the Josephson current. If the time is reversed, the current flows backward, that is, we have a current  $-I_s$ . The macroscopic wave functions oscillate according to  $\exp(-i\omega t)$ . If the time is reversed here also, we see that also the sign of the phase of the wave function must be reversed. So if we request that the Josephson current be invariant under time reversal, we have the condition  $I_s(\gamma) = -I_s(-\gamma)$ . This eliminates all the cosine terms in Eq. (1.44).

Under time inversion symmetry, the supercurrent across the barrier is described by

$$I_s(\gamma) = \sum_{n=0}^{\infty} I_{cn} \sin(n\gamma) \quad 1.45$$

Very often, but not necessarily, one finds that this series converges very rapidly, that is, the expansion coefficients become smaller very quickly. Then the series can be restricted to the first term, and we obtain the first Josephson equation.

At this stage, we note that there are situations for which the first expansion coefficient  $I_{c1}$  vanishes, for example. In this case, the relation between the supercurrent and the phase difference  $\gamma$  has period  $\pi$  instead of  $2\pi$ .

To obtain the second Josephson equation, we take the time derivative of Eq. (1.43), and we obtain

$$\dot{\gamma} = \dot{\phi}(z_2) - \dot{\phi}(z_1) - \frac{q}{\hbar} \int_{z_1}^{z_2} \dot{A}_z dz$$

According to the laws of electrodynamics, the integral over the time derivative of the vector potential yields exactly the voltage induced across the barrier by a temporally changing magnetic field. The time derivative of the difference  $\phi(z_2) - \phi(z_1)$ , with

$\Psi \propto \exp(-i\omega t) = \exp(-iEt/\hbar)$ , yields the difference  $[E(z_2) - E(z_1)]/\hbar$  between the two superconductors on both sides of the barrier. We can write this difference as  $q U_{21}$ , with the voltage difference  $U_{21}$ . So we have

$$\dot{\gamma} = \frac{q}{\hbar} (U_{21} + U_{\text{ind}}) = \frac{q}{\hbar} U_{\text{total}} \quad 1.47$$

With  $q = 2e$ , this yields the second Josephson equation (1.28).

The second derivation of the Josephson equations is very general. It was assumed that there exists a macroscopic wave function with a well-defined phase  $\phi$ , and that the system satisfies time inversion symmetry. Equations (1.40)–(1.47) are also gauge-invariant.

The gauge invariance represents a highly fundamental principle. In the force and field equations of electrodynamics, only the electric and magnetic fields appear, not the corresponding potentials, the vector potential  $\mathbf{A}$  and the scalar potential  $\Phi$ . From the latter, one obtains the (negative) electric field by forming the gradient. We have mentioned already that  $\text{curl } \mathbf{A} = \mathbf{B}$ . However, the magnetic field is source-free, that is, we have  $\text{div } \mathbf{B} = 0$ . Therefore, a vector  $\mathbf{V}(x,y,z,t)$ , obtained from the gradient of a function  $\chi(x, y, z, t)$ , can be added to  $\mathbf{A}$ . This corresponds to a different scaling of  $\mathbf{A}$ . The curl of  $\mathbf{V}$  always vanishes, and, hence, the magnetic field remains unaffected. However, in order also to keep the electric field unchanged during this transformation, at the same time we must subtract the quantity  $\chi(x,y,z,t)$  from the scalar potential. Finally, in the Schrödinger equation, the phase  $\phi$  of the wave function must be rescaled to  $\phi + (2\pi/\Phi_0)\chi$ . The gauge invariance of Eqs. ((1.40)–(1.47)) can be shown by explicitly inserting these relations.

Often, equations showing gauge invariance are of fundamental importance in physics and cannot be affected easily by microscopic details. Hence, we can expect that the Josephson equations are generally valid in the case of many different types of barriers and superconductors.

In Figure 1.22, some types of junctions are shown schematically. For the superconductor–insulator–superconductor (SIS) junction (Figure 1.22a), the insulating barrier must be only 1–2 nm thick. The superconductor–normal conductor–superconductor (SNS) junction (Figure 1.22b) can function with a much larger thickness of the normal conductor, simply because the Cooper pairs can penetrate much deeper into a normal conducting metal than into an oxide layer. Here, in the normal metal, the decay length of the Cooper pair concentration depends among other things on the electron mean free path. For very large values of the electron mean free path (small amount of perturbations), normal conducting layers with a thickness up to a few hundred nanometers can be used. An important difference between the oxide and the

normal conductor junctions is the value of the resistance per square (normal resistance/area of the barrier). For the oxide junctions, the value of the resistance per square is typically  $10^{-4}$ – $10^{-3} \Omega \text{ cm}^2$ . However, for the SNS junctions, this value is about  $10^{-8} \Omega \text{ cm}^2$  or below. In addition to the SIS and SNS junctions, one often also uses junctions with a more complicated structure of the barrier, for instance, the so-called SINIS junctions where the barrier is formed by two insulators and one normal conducting layer.

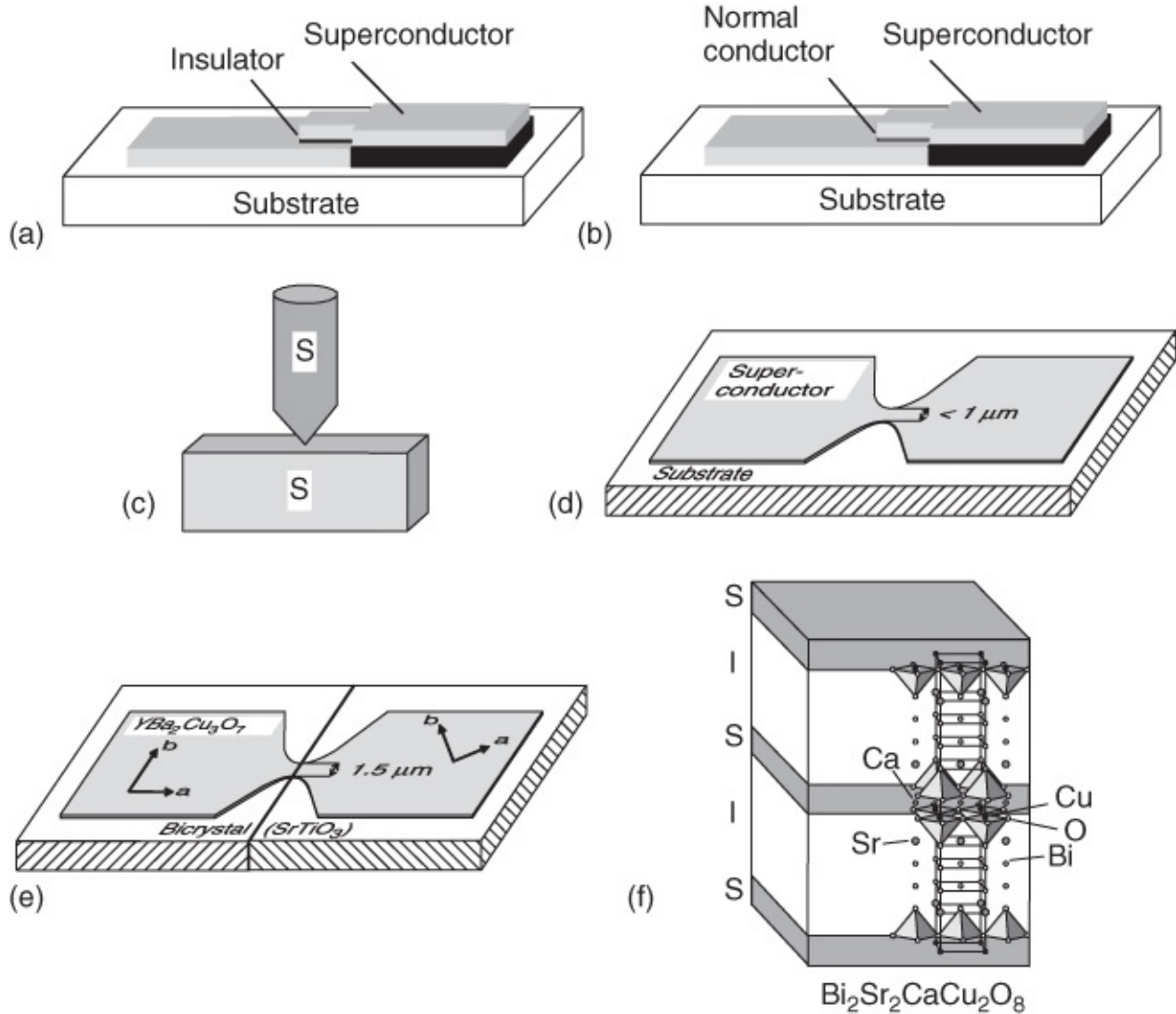


**Figure 1.22** Schematics of the different possibilities for producing a weak coupling between two superconductors: (a) SIS junction with an oxide layer as a barrier; (b) SNS junction with a normal conducting barrier; (c) point contact; (d) microbridge; (e) YBa<sub>2</sub>Cu<sub>3</sub>O<sub>7</sub> grain boundary junction; and (f) intrinsic Josephson junction in Bi<sub>2</sub>Sr<sub>2</sub>CaCu<sub>2</sub>O<sub>8</sub>.

The point contacts ([Figure 1.22c](#)) are particularly simple. In this case, a metal tip is pressed against a surface. The cross-section of the bridge depends on the applied pressure. In this way, the desired junction properties can be produced easily and can be adjusted if necessary. The microbridge ([Figure 1.22d](#)) only consists of a narrow constriction that limits the exchange of Cooper pairs because of its very small cross-section. Here, it is necessary to fabricate reproducibly bridges with a width of only 1 μm or smaller, which requires advanced

structuring techniques such as electron beam lithography.

For the high-temperature superconductors, one can use grain boundaries as weak coupling regions because of the small values of the coherence length [35, 36]. One can deposit a thin film, say, of  $\text{YBa}_2\text{Cu}_3\text{O}_7$  on a “bicrystal substrate,” consisting of two single-crystalline parts joined together at a specific angle. The grain boundary of the substrate is then transferred also into the deposited film, which otherwise is grown single-crystalline (epitaxially, [Figure 1.22e](#)). Well-defined grain boundaries can also be produced at steps in the substrate or at the edges of buffer layers epitaxially deposited on a substrate. The strength of the Josephson coupling can be varied over a large range by means of the grain boundary angle.

In some high-temperature superconductors such as, for instance,  $\text{Bi}_2\text{Sr}_2\text{CaCu}_2\text{O}_8$ , even intrinsic Josephson junctions exist simply because of their crystal structure ([Figure 1.22f](#)). Here, the superconductivity is restricted only to the copper oxide layers with about 0.3 nm thickness. Between these layers, there are electrically insulating bismuth oxide and strontium oxide planes. Hence, such materials form stacks of SIS Josephson junctions, where each junction has a thickness of only 1.5 nm, the distance between two neighboring copper oxide layers [37].

These highly different types of Josephson junctions only represent a small selection of the many possibilities. Each type of junction has its advantages and disadvantages. Depending on the specific application, quite different types can be utilized.

At this stage, we are confronted with the following question: How similar are the Josephson effects in these junctions, in particular, with respect to the connection between the oscillation frequency of the alternating Josephson currents and the applied voltage? The proportionality factor  $1/\Phi_0$ , which is also referred to<sup>18</sup> as the “**Josephson constant**”  $K_J = 2e/h = 483.5979$  GHz/mV, has been determined for many different types of Josephson junctions. For example, a Josephson junction made of indium with its weak location realized by a constriction (microbridge) has been compared directly with a Josephson junction made of niobium where the barrier consisted of a thin gold layer [38]. The Josephson constants measured for both junctions were equal within an uncertainty of only  $2 \times 10^{-16}$  or less. In the meantime, this accuracy could be increased even to about  $10^{-19}$ . Therefore, Josephson junctions are now applied for representing the voltage standard [39].

How can we demonstrate alternating Josephson currents experimentally? A very direct method is the observation of the electromagnetic radiation generated by the oscillating Josephson currents in the frequency range of microwaves. We want to estimate the order of magnitude of the microwave power emitted from the junction.

We assume a voltage of 100 µV applied to the junction, corresponding to an emitted frequency of about 48 GHz. The critical current  $I_c$  of the junction is assumed to be 100 µA. Then the d.c. power applied to the junction is  $10^{-8}$  W, and the emitted power is expected to be much smaller than this value.

The difficulty of direct experimental demonstration did not so much arise because of the small power of this radiation, but, instead, it had to do with the problem of coupling the high-

frequency power from the tiny tunnel junction into a proper high-frequency waveguide. Therefore, the first confirmation of the alternating Josephson current came in an indirect way [40]. If such a junction is placed within the high-frequency field of an oscillating microwave cavity, characteristic, equidistant steps of constant voltage are observed in the voltage–current characteristic (see [Section 6.3](#)). On the voltage axis, their distance  $\Delta U$  is given by

$$\Delta U_S = \Phi_0 \times f_{HF} \quad 1.48$$

where  $f_{HF}$  is the frequency of the high-frequency field. These “Shapiro steps” result from the superposition of the alternating Josephson current and the microwave field. Each time that the frequency of the alternating Josephson current corresponds to an integer multiple of the microwave frequency, the superposition produces an additional d.c. Josephson current, causing the step structure of the characteristic.

Another indirect confirmation of the existence of an alternating Josephson current was found for junctions placed within a small static magnetic field. Here, at small voltages  $U_s$ , equidistant steps in the characteristic could be observed without irradiation by an external high-frequency field (see [Section 6.4](#)). The sandwich geometry of a Josephson tunnel junction by itself represents a resonating cavity, and the structures observed in the characteristic, the “Fiske steps,” correspond to resonances within the junction. For the proper values of the voltage  $U_s$  and of the field  $B$ , the Josephson oscillations of the current density exactly fit a cavity mode of the junction. For such a resonance, the current becomes particularly large.

A more accurate description of the Shapiro and Fiske modes requires a mathematical treatment beyond the scope of this first chapter. However, in [Chapter 6](#), we will return to these structures.

In 1965 Ivar Giaever<sup>[19](#)</sup> achieved a more direct confirmation of the alternating Josephson current [41]. As we have seen, the main difficulty with the direct confirmation, say, with a typical high-frequency apparatus, arose from the extraction of power out of the small tunnel junction. Giaever had the idea that a second tunnel junction, placed immediately on top of the Josephson junction, would be quite favorable for such an extraction ([Figure 1.23](#)).

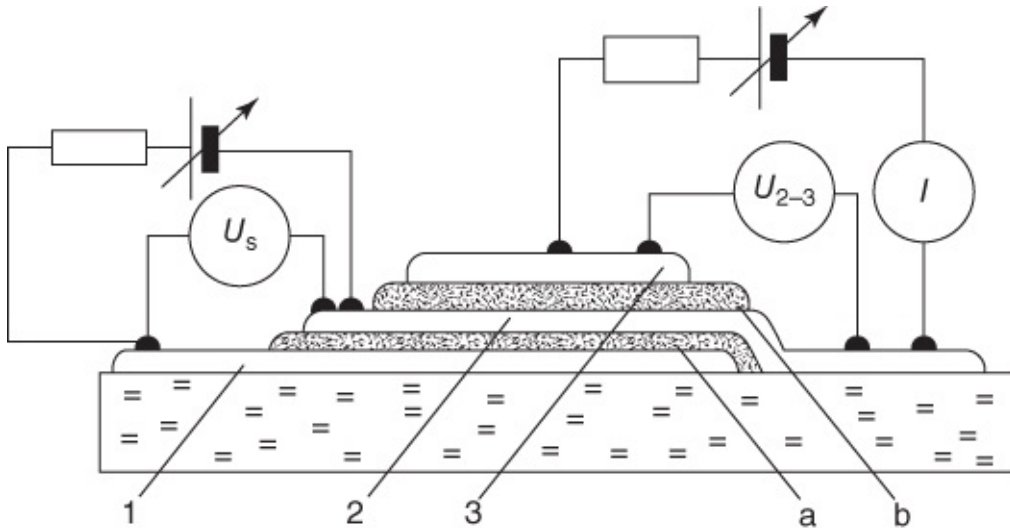


**Figure 1.23** Arrangement for the experimental demonstration of the alternating Josephson current according to Giaever: layers 1–3 are Sn layers; layers a and b are oxide layers. The thicknesses of layers a and b are chosen such that layers 1 and 2 form a Josephson junction, and such that no Josephson currents are possible between layers 2 and 3.

(From [40].)

Here, the confirmation of the extracted power happens in the second tunnel junction by means of the change of the characteristic of the tunneling current for individual electrons, this change being caused by the irradiating high-frequency field generated in the Josephson junction. In the years prior to this, it had been shown that a high-frequency field generates a structure in the characteristic of the single-electron-tunneling current [42]. The electrons can interact with the high-frequency field by absorbing or emitting photons with energy  $E = hf_{\text{HF}}$ .

In [Section 3.1.3](#) we will see that, in the absence of a high-frequency field, individual electrons can tunnel in large numbers between the two superconductors only after the voltage  $(\Delta_1 + \Delta_2)/e$  has been reached. Here,  $\Delta_1$  and  $\Delta_2$  denote the energy gaps of the two superconductors, respectively, the magnitudes of which depend on the material. In other words, during the tunneling process, the electrons must take up at least the energy  $eU = (\Delta_1 + \Delta_2)$ . Then at the voltage  $(\Delta_1 + \Delta_2)/e$ , the voltage–current characteristic displays a sharp step as seen in [Figure 1.23](#).

In a high-frequency field, a tunneling process assisted by photons can set in already at the voltage  $U_s = (\Delta_1 + \Delta_2 - hf_{\text{HF}})/e$ . If during a tunneling process an electron absorbs several photons, one obtains a structure in the characteristic with the specific interval of the voltage  $U_s$

$$\Delta U_s = \frac{hf_{\text{HF}}}{e} \quad 1.49$$

where  $h$  is the Planck's constant,  $f_{\text{HF}}$  is the frequency of the high-frequency field, and  $e$  is the elementary charge. Such processes can happen at high photon densities, that is, at high power of the high-frequency field. We note that for single-electron tunneling, the elementary charge  $e$

of single electrons appears.

At the junction 2–3, one observes a typical single-electron characteristic if no voltage is applied to the junction 1–2 (curve 1 in [Figure 1.24](#)). For performing the key experiment, a small voltage  $U_s$  is applied to the Josephson junction 1–2. If the expected high-frequency alternating current appears in this junction, in the junction 2–3 the well-known structure of the tunneling characteristic should be observed, because of the close coupling between the two junctions. Giaever, indeed, could observe this expected effect. Such a characteristic is shown by curve 2 in [Figure 1.24](#). Here a voltage  $U_s$  of 0.055 mV was applied to junction 1–2, acting as the generator of the high-frequency field. The frequency of the alternating Josephson current is  $f_J = 2eU_s/h$ , and the structure of the characteristic of junction 2–3 should display the voltage steps with the distance between them  $\Delta U_s = hf_J/e = 2U_s$ . For the curve shown in [Figure 1.24](#), this yields  $\Delta U_{2,3} = 0.11$  mV, which was observed by Giaever.

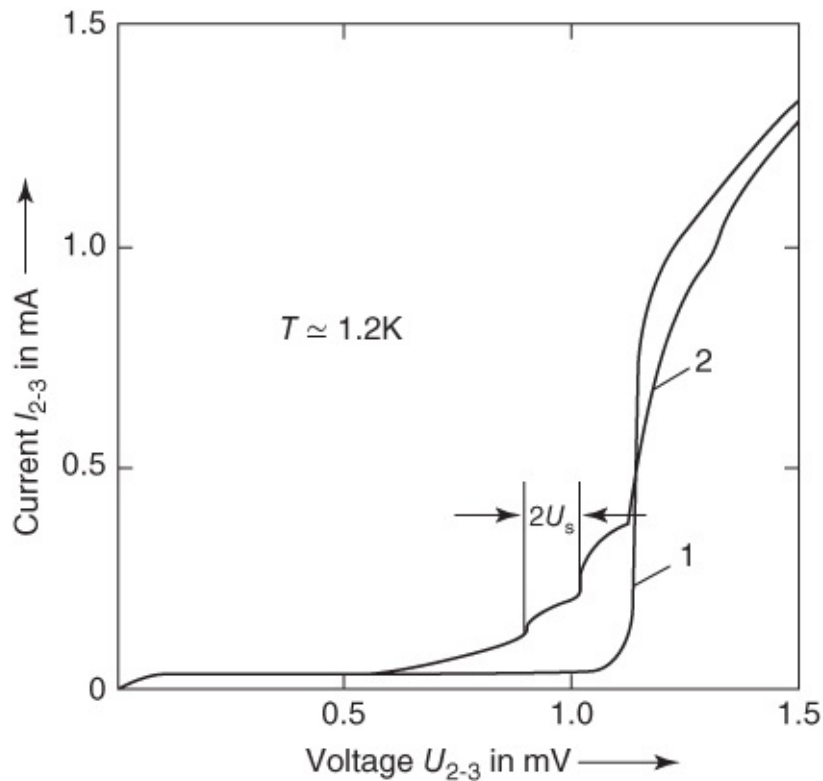


**Figure 1.24** Characteristic of the junction 2–3 from [Figure 1.22](#). Curve 1: no voltage at junction 1–2. Curve 2: 0.055 mV applied to junction 1–2.

The most direct detection of the alternating Josephson current by coupling the power into a high-frequency waveguide has been achieved by an American and a Russian group. The Americans [43] could detect the high-frequency power of the Josephson junction by placing the junction into a tuned resonating cavity, which was operated at a resonance frequency of the junction by choosing a proper value of the magnetic field. However, this still required an extremely high detection sensitivity. The detected power was about  $10^{-11}$  W, whereas the sensitivity limit for detection could be increased up to  $10^{-16}$  W. The Russian group, Yanson *et al.* [44], could detect a radiation power of about  $10^{-13}$  W of a Josephson junction. The relation

$f_J = 2eU_s/h$  has always been found between the frequency of the alternating Josephson current and the voltage applied to the junction. The experimental accuracy has been increased by the American group sufficiently far that a precision measurement of  $2e/h$  could be carried out [45]. This represented further convincing proof of the importance of electron pairs in superconductivity.

Today, the techniques for the detection of electromagnetic radiation are improved to such an extent that the alternating Josephson current can be extracted without any difficulty up to the 100 GHz range. However, there are still problems at frequencies in the terahertz range, which play an important role, for instance, in the intrinsic Josephson junctions of high-temperature superconductors. In the meantime, also this emission was detected. [54, 55]

In the future, Josephson junctions are expected to play an important role in the terahertz range. On the one hand, this frequency range is too high to be covered by semiconductor devices, and on the other, it is too low to be handled by optical methods.

### 1.5.2 Quantum Interference in a Magnetic Field

In the alternating Josephson currents, the macroscopic wave function manifests itself in the form of a *temporal* interference between the matter waves in the two superconducting electrodes. What can we say about the *spatial* interference, say, analogous to the optical double-slit experiment or to the Sagnac interferometer?

Let us look at the structure shown in [Figure 1.25](#). It consists of a superconducting ring into which two Josephson junctions are integrated. The ring is located in a magnetic field oriented perpendicular to the area of the ring. A transport current  $I$  flows along the ring. By measuring the voltage drop across the Josephson junctions, we can determine the maximum supercurrent that can be carried by the ring. We will see that this maximum supercurrent  $I_{s,\max}$  oscillates as a function of the magnetic flux through the ring, similar to the light intensity, or more exactly the light amplitude, on the screen of the double-slit experiment, and also similar to the Sagnac interferometer with its dependence on the rotational frequency.

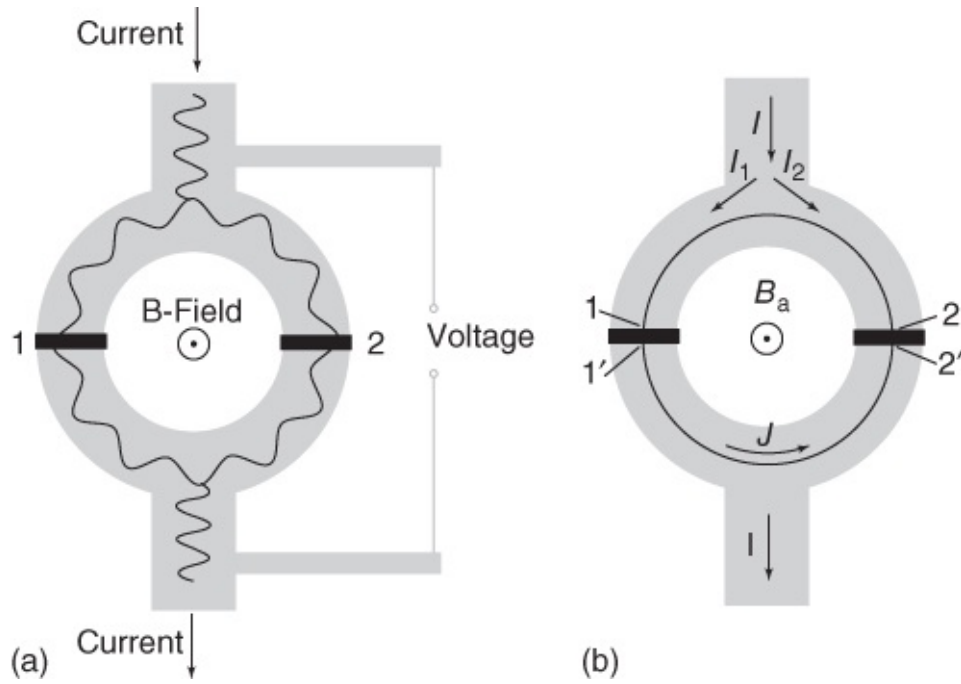


**Figure 1.25** Generation of spatial interferences of the superconducting wave function in a ring structure. (a) Schematics of the wave. (b) Notation for the derivation of the quantum interference.

In [Section 1.3](#), we looked at a superconducting ring placed in a magnetic field and we found that the magnetic flux through the ring appears in multiples of the flux quantum  $\Phi_0$ . An arbitrary magnetic field  $\mathbf{B}_a$  could be applied to the ring, generating an arbitrary magnetic flux  $\Phi_a$  through the ring. However, in this case, a circulating current  $J$  flows along the ring. It also generates a magnetic flux  $\Phi_{\text{ind}} = LJ$ , such that the total flux amounts to a multiple of  $\Phi_0$ :  $\Phi_{\text{tot}} = \Phi_a + LJ$ . The circulating current results in a shift of  $\Phi_a$  upward or downward to the next integer value of  $\Phi_{\text{tot}}/\Phi_0$ . Apparently,  $LJ$  must then reach a maximum value up to  $\Phi_0/2$ .

This picture is changed because of the insertion of the two Josephson junctions. At both Josephson junctions, the phase of the superconducting wave function can jump by amounts  $\gamma_1$  or  $\gamma_2$ , which must be taken into account in the integration of the phase gradient around the ring (integral  $\oint k dx$ ). The jumps of the phase are connected with the current across the junctions because of the first Josephson equation ([1.25](#)).

Next, we derive the dependence  $I_{s,\max}(\Phi_a)$  using the notation of [Figure 1.25b](#). We assume that the width of the Josephson junctions is much smaller than the diameter of the ring. The current  $I$  separates into the currents  $I_1$  and  $I_2$ , flowing along the two halves of the ring, respectively.

Because of current conservation, we have

$$I = I_1 + I_2 \quad 1.50$$

The currents  $I_1$  and  $I_2$  can also be written in terms of the circulating current  $J$  flowing in the ring yielding

$$I_1 = \frac{I}{2} + J; \quad I_2 = \frac{I}{2} - J \quad 1.51$$

The current  $I_1$  flows through the Josephson junction 1, and the current  $I_2$  through the Josephson junction 2. Therefore, we have

$$I_1 = I_c \sin \gamma_1; \quad I_2 = I_c \sin \gamma_2 \quad 1.52$$

Here, for simplicity, we have assumed that the critical currents  $I_c$  of the two Josephson junctions are identical. Therefore, we find

$$\frac{I}{2} + J = I_c \sin \gamma_1 \quad 1.53a$$

$$\frac{I}{2} - J = I_c \sin \gamma_2 \quad 1.53b$$

Next, we need a relation connecting the gauge-invariant phase differences  $\gamma_1$  and  $\gamma_2$  with the applied magnetic field. We proceed analogously to the derivation of the quantization of the fluxoid (Eq. (1.11)), but we do not integrate the wave vector  $\mathbf{k}$  over the complete ring, as in Eq. (1.7). Instead, we integrate separately over the lower and upper halves, that is, from  $1'$  to  $2'$  or from  $2$  to  $1$  in [Figure 1.25b](#). Then we obtain

$$\int_{1'}^{2'} \mathbf{k} d\mathbf{r} = \mu_0 \lambda_L^2 \int_{1'}^{2'} \mathbf{j}_s d\mathbf{r} + \frac{2\pi}{\Phi_0} \int_{1'}^{2'} \mathbf{A} d\mathbf{r} \quad 1.54a$$

$$\int_2^1 \mathbf{k} d\mathbf{r} = \mu_0 \lambda_L^2 \int_2^1 \mathbf{j}_s d\mathbf{r} + \frac{2\pi}{\Phi_0} \int_2^1 \mathbf{A} d\mathbf{r} \quad 1.54b$$

Here, we have used the definition (1.10) of the London penetration depth and  $\Phi_0 = h/q = h/2e$ .

The integral  $\int_{1'}^{2'} \mathbf{k} d\mathbf{r}$  yields the difference between the phase  $\phi_2$  of the wave function of the lower half of the ring,  $\Psi_2 \sim \exp(ik \cdot r) = \exp(i\phi_2)$  at the locations  $2'$  and  $1'$ ,

$\int_{1'}^{2'} \mathbf{k} d\mathbf{r} = \varphi_2(2') - \varphi_2(1')$ . Analogously, one finds  $\int_2^1 \mathbf{k} d\mathbf{r} = \varphi_1(1) - \varphi_1(2)$ . By adding Eqs. (1.54a) and (1.54b), we obtain

$$\varphi_2(2') - \varphi_1(2) - [\varphi_2(1') - \varphi_1(1)] = \mu_0 \lambda_L^2 \left( \int_{1'}^{2'} \mathbf{j}_s d\mathbf{r} + \int_2^1 \mathbf{j}_s d\mathbf{r} \right) + \frac{2\pi}{\Phi_0} \oint_{C'} \mathbf{A} d\mathbf{r} \quad 1.55$$

Here, the integral over the curve  $C'$  does not include the barriers of the two Josephson junctions. Otherwise, the integral would run over the complete ring, and by using Stokes' theorem we could turn it into the magnetic flux through the ring. However, we can accomplish this by adding the integrals over the corresponding distances on both sides of Eq. (1.55). Then we find

$$\oint_C \mathbf{A} d\mathbf{r} + \int_{2'}^2 \mathbf{A} d\mathbf{r} + \int_1^{1'} \mathbf{A}_r d\mathbf{r} = \oint_C \mathbf{A} d\mathbf{r} = \int_F \mathbf{B} df = \Phi \quad 1.56$$

On the left-hand side of Eq. (1.55), the term

$$\varphi_2(2') - \varphi_1(2) + \frac{2\pi}{\Phi_0} \int_{2'}^2 \mathbf{A} d\mathbf{r}$$

yields the gauge-invariant phase difference  $\gamma_2$  across the Josephson junction 2. Analogously, the expression

$$\varphi_2(1') - \varphi_1(1) - \frac{2\pi}{\Phi_0} \int_1^{1'} \mathbf{A} d\mathbf{r}$$

yields the gauge-invariant phase difference  $\gamma_1$  across the Josephson junction 1. In this way, we find

$$\gamma_2 - \gamma_1 = \mu_0 \lambda_L^2 \left( \int_{1'}^{2'} \mathbf{j}_s d\mathbf{r} + \int_2^1 \mathbf{j}_s d\mathbf{r} \right) + \frac{2\pi}{\Phi_0} \Phi \quad 1.57$$

Similar to the case of a massive circular ring, the magnetic flux  $\Phi$  is given by the sum of the applied flux  $\Phi_a$  and the self-field of the circulating currents  $J$ :  $\Phi = \Phi_a + LJ$ . The contributions of the current densities are proportional to the circulating current  $J$  and can be included in the term  $LJ$ .<sup>20</sup> Finally, we obtain the relation we had been looking for

$$\gamma_2 - \gamma_1 = \frac{2\pi}{\Phi_0} \Phi = \frac{2\pi}{\Phi_0} (\Phi_a + LJ) \quad 1.58$$

From Eqs. (1.53a), (1.53b) and (1.58), we can calculate the maximum supercurrent along the ring as a function of the applied magnetic field or of the flux.

Let us start by assuming that we can neglect the contribution of the term  $LJ$  to the magnetic flux. The circulating current  $J$  clearly cannot become larger than the critical current  $I_c$  of the Josephson junctions. Hence, the flux generated by the term  $LJ$  is smaller than  $LI_c$ . We assume also that this flux is much smaller than half a flux quantum, yielding the condition  $2LI_c/\Phi_0 \ll 1$ . The quantity  $2LI_c/\Phi_0$  is referred to as the **inductance parameter**  $\beta_L$ ,

$$\beta_L = \frac{2LI_c}{\Phi_0} \quad 1.59$$

If we neglect the magnetic flux generated by the circulating current, we have  $\Phi = \Phi_a$ . Using Eq. (1.58), we eliminate  $\gamma_2$  from Eqs. (1.53a) and (1.53b). Then, by adding Eqs. (1.53a) and (1.53b), we obtain

$$I = I_c \left[ \sin \gamma_1 + \sin \left( 2\pi \frac{\Phi_a}{\Phi_0} + \gamma_1 \right) \right] \quad 1.60$$

Now it is advantageous to use the variable  $\delta = \gamma_1 + \pi(\Phi_a/\Phi_0)$  instead of  $\gamma_1$ . Then Eq. (1.60) can be changed into

$$I = I_c \left[ \sin \left( \delta - \pi \frac{\Phi_a}{\Phi_0} \right) + \sin \left( \delta + \pi \frac{\Phi_a}{\Phi_0} \right) \right] \quad 1.61$$

By using the trigonometric identity for the summation of sines, we obtain the expression

$$I = 2I_c \sin \delta \cos \left( \pi \frac{\Phi_a}{\Phi_0} \right) \quad 1.62$$

If we specify the flux  $\Phi_a$  and the current  $I$ , the variable  $\delta$  will adjust itself such that Eq. (1.62) is satisfied. For increasing current, this is possible at most up to the point where  $\sin \delta$  becomes equal to  $+1$  or  $-1$ , depending on the current direction and on the sign of the cosine factor. Hence, the maximum supercurrent that can flow through this circular structure is given by

$$I_{s,\max} = 2I_c \left| \cos \left( \pi \frac{\Phi_a}{\Phi_0} \right) \right| \quad 1.63$$

The quantity  $I_{s,\max}$  reaches a maximum if the flux corresponds to an integer multiple of a flux quantum. Then the cosine factor is equal to 1, and we obtain  $I_{s,\max} = 2I_c$ . This is the maximum supercurrent that can be carried by the parallel configuration of the two Josephson junctions. In this case, we have  $\sin \gamma_1 = \sin \gamma_2 = 1$ . In this case, the circulating current  $J$ , obtained as

$$J = \frac{I_c}{2} (\sin \gamma_1 - \sin \gamma_2) \quad 1.64$$

by subtraction of Eqs. (1.53a) and (1.53b), vanishes. The current  $I_{s,\max}$  vanishes each time that  $\Phi_a$  reaches the value  $(n + 1/2)\Phi_0$  with  $n = 0, \pm 1, \pm 2, \dots$  Now the circulating current attains its maximum value, becoming equal to  $+I_c$  or  $-I_c$  depending on the value of  $n$ .

The maximum supercurrent flowing within the circular structure also oscillates periodically as a function of the applied magnetic field. Here, the period of the magnetic flux generated by the field is the magnetic flux quantum. This effect was first demonstrated experimentally by Mercereau and coworkers [46]. It is the analogy of the diffraction of light by a double slit, and it represents the foundation of the application of such circular structures as a superconducting quantum interferometer (SQUID). We note that SQUIDs can measure an applied magnetic field continuously.

SQUIDs will be discussed in detail in [Section 7.6.4](#). However, at this stage, we point out already that SQUIDs can resolve changes of the magnetic flux down to about  $10^{-6}\Phi_0$ . If the area of the SQUID is about  $1 \text{ mm}^2$ , then this corresponds to field changes  $\Delta B$  of about  $10^{-6}\Phi_0/\text{mm}^2 = 10^{-15} \text{ T}$ , which can be detected with a SQUID.

This value is smaller than the Earth's magnetic field by 11 orders of magnitude, and

approximately corresponds to the magnetic fields generated at the surface of the skull by the electric currents within the human brain. SQUIDs belong to the group of most sensitive detectors by far. Since the measurement of many physical quantities can be transformed into a magnetic field or flux measurement, SQUIDs find very wide applications.

Again, we can briefly discuss the analogy with the Sagnac interferometer. If in a constant external magnetic field the SQUID is rotating around an axis perpendicular to the area of the ring, a phase shift of  $(2m/\hbar)2\pi R^2\Omega = 4\pi^2 R^2(2m/h)\Omega$  results in the interferometer. Here,  $\Omega$  is the angular velocity and  $2m$  is the mass of a Cooper pair. We have assumed a circular SQUID with radius  $R$ . Hence,  $I_{s,\max}$  oscillates with a period depending on the ratio  $m/h$ . Already by 1950, Fritz London had pointed out the equivalence of a rotating superconductor and an externally applied magnetic field [47]. A similar rotational effect can also be observed with other coherent matter waves, for instance, with superfluid helium [48]. However, since the mass of helium atoms is much larger than that of Cooper pairs, for helium the sensitivity against rotation is much larger than for SQUIDs.

Next, we discuss briefly the approximations leading us to Eq. (1.63). We had assumed that the critical currents  $I_c$  of both Josephson junctions are identical. Without this assumption, we would find that  $I_{s,\max}$  varies between  $I_{c1} + I_{c2}$  and  $|I_{c1} - I_{c2}|$ , where again the period is one flux quantum. So compared to Eq. (1.63), there is no qualitative change. Furthermore, the period of the oscillation remains unchanged if the finite inductance is taken into account. As before, the maximum value  $I_{s,\max}$  is again given by  $I_{c1} + I_{c2}$ . However, the minimum value of  $I_{s,\max}(\Phi)$  more and more approaches the maximum value. In [Figure 1.26](#), we show this effect for three different values of the inductance parameter  $\beta_L$ .

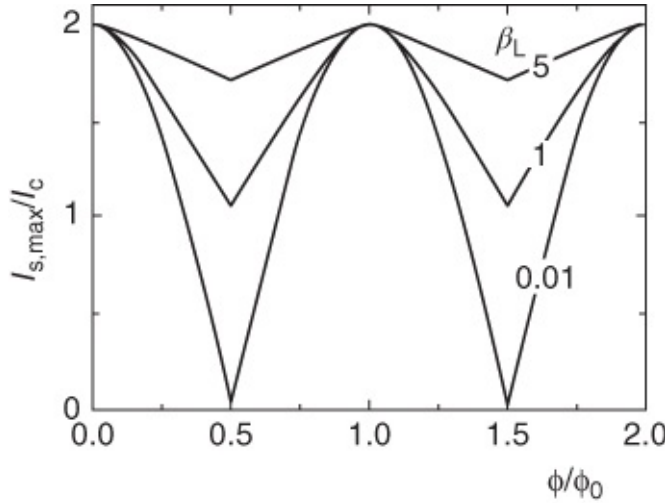


**Figure 1.26** Modulation of the maximum supercurrent of a superconducting quantum interferometer as a function of the magnetic flux through the ring. The curves are shown for three different values of the inductance parameter  $\beta_L$ .

For large values of the inductance parameter  $\beta_L$ , the relative modulation amplitude decreases proportional to  $1/\beta_L$ . In order to see this, we must remember that for a massive

superconducting ring, a shielding current with a maximum value of  $J = \Phi_0/2L$  was sufficient to supplement the applied flux until it reached the next integer value of  $\Phi_0$ . If we apply this principle to the SQUID, the circulating current must not exceed the value  $\Phi_0/2L$ . For large values of the inductance, this circulating current is smaller than  $I_c$ , and  $I_{s,\max}$  is reduced to the value  $2(I_c - J)$ . Therefore, we obtain a relative modulation amplitude of  $[2I_c - 2(I_c - J)]/2I_c = J/I_c = \Phi_0/(2LI_c) = 1/\beta_L$ . Hence, the effect of the quantum interference decreases with increasing inductance.

If we include thermal fluctuation effects, one can show that the optimum sensitivity of SQUIDs against flux changes is reached for  $\beta_L = 1$ . However, for a given value of the critical current, this also limits the area of the SQUID ring, since the inductance increases with increasing circumference of the ring. Hence, on the one hand, one desires an area as large as possible in order to achieve a large change of flux with a small change of the magnetic field. On the other hand, this area cannot be too large, because otherwise the inductance would become too large. This conflict has resulted in a number of highly special SQUID geometries, which deviate strongly from the simple ring structure shown in [Figure 1.25](#). We will discuss these geometries in [Section 7.6.4](#).

Finally, we turn to the effects resulting from the finite size of the Josephson junctions. We will see that also the critical current of the junctions depends on the magnetic field or on the magnetic flux through the junction, in analogy to the diffraction of light at a double slit.

Let us look at the geometry of a spatially extended Josephson junction shown schematically in [Figure 1.27](#). We assume that this junction is penetrated by a magnetic field along the z-direction parallel to the barrier layer. We look for an equation describing the dependence of the gauge-invariant phase difference  $\gamma$  on the applied magnetic field. For the superconducting ring of [Figure 1.25](#), we saw that the difference  $\gamma_2 - \gamma_1$  of the two phases of the Josephson junctions, assumed to represent point junctions, is proportional to the magnetic flux enclosed between these junctions.

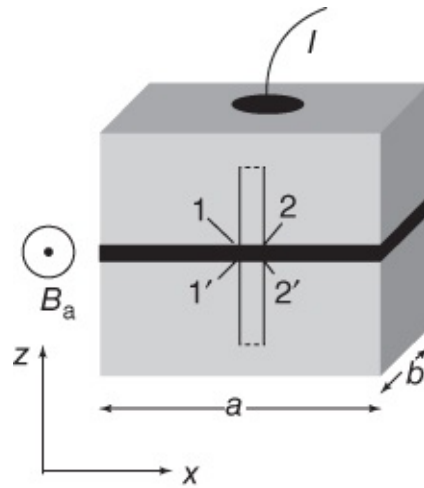


[Figure 1.27](#) Geometry of the spatially extended Josephson junction.

In analogy to the earlier derivation of the relevant equations, we look at the path along which

we want to integrate the wave vector of the superconducting wave function. In [Figure 1.27](#), this path is shown as the dotted line. Along the  $x$ -axis the path extends from point  $x$  to point  $x + dx$ , where  $dx$  denotes an infinitesimally small distance. Along the  $y$ -direction the path extends deeply into the interior of both superconductors, for which we assume that they are much thicker than the London penetration depth. In analogy to Eq. (1.57), we find

$$\gamma(x + dx) - \gamma(x) = \mu_0 \lambda_L^2 \left( \int_{1'}^{2'} \mathbf{j}_s dr + \int_2^1 \mathbf{j}_s dr \right) + \frac{2\pi}{\Phi_0} \Phi_1 \quad 1.65$$

Here,  $\Phi_1$  denotes the total flux enclosed by the integration path. Beyond a layer of depth  $\lambda_L$ , the shielding currents in the superconducting electrodes are exponentially small. Therefore, we can neglect the two integrals taken over the supercurrent densities. Furthermore, we assume that the supercurrents and the magnetic fields vary along the  $x$ -direction, but not along the  $y$ -direction. Then we write for the magnetic flux

$$\Phi_1 = B t_{\text{eff}} dx \quad 1.66$$

We find the “effective thickness”  $t_{\text{eff}}$  by integrating the magnetic field along the  $z$ -direction. Since the magnetic field decays exponentially in the two superconductors within a characteristic length  $\lambda_L$ , this integration yields

$$t_{\text{eff}} = \lambda_{L,1} + \lambda_{L,2} + t_b \quad 1.67$$

Here,  $\lambda_{L,1}$  and  $\lambda_{L,2}$  are the London penetration depths in the two superconductors, respectively. They do not have to be identical. The thickness of the barrier layer is denoted by  $t_b$ . In general, it is much smaller than  $\lambda_{L,1}$  and  $\lambda_{L,2}$ . Hence, mostly it can be neglected.

With these assumptions and notations, from Eq. (1.65) we obtain the differential equation

$$\gamma' \equiv \frac{dy}{dx} = \frac{2\pi}{\Phi_0} B t_{\text{eff}} \quad 1.68$$

yielding the connection we had been looking for.

Furthermore, we assume that we can neglect the self-field generated by the Josephson currents. This assumption represents a condition about the spatial extension of the junction along the  $x$  and  $y$  directions. In [Section 6.4](#), we will see that it is necessary that the lengths  $a$  and  $b$  of the edges of the junction do not exceed the so-called Josephson penetration depth

$$\lambda_J = \sqrt{\frac{\Phi_0}{2\pi\mu_0 j_c l_{\text{eff}}}} \quad 1.69$$

Here,  $j_c$  is the critical supercurrent density, assumed to be spatially homogeneous, and the length  $l_{\text{eff}}$  is equal to  $t_{\text{eff}}$  if the superconducting electrodes are much thicker than  $\lambda_L$ , as we had assumed. Typically, the Josephson penetration depth is a few micrometers. However, it can

also increase up to the millimeter scale if the critical supercurrent density is very small.

With the assumptions indicated earlier, the magnetic field  $B$  is equal to the externally applied field  $B_a$ . Then we can integrate Eq. (1.68) and obtain

$$\gamma(x) = \gamma(0) + \frac{2\pi}{\Phi_0} B_a t_{\text{eff}} x \quad 1.70$$

The gauge-invariant phase difference is seen to increase linearly with the  $x$ -coordinate. Inserting this function  $\gamma(x)$  into the first Josephson equation, we obtain for the spatial dependence of the supercurrent density across the barrier layer

$$j_s(x) = j_c \sin \left[ \gamma(0) + \frac{2\pi}{\Phi_0} B_a t_{\text{eff}} x \right] \quad 1.71$$

We see that the supercurrent density oscillates along the  $x$ -coordinate, that is, perpendicular to the applied field. Here, the wavelength of the oscillation is determined by the applied magnetic field.

Now we want to calculate the maximum Josephson current that can flow across the Josephson junction. For this we integrate Eq. (1.71) over the area of the junction:

$$I_s = \int_0^b dy \int_0^a dx j_c \sin \left[ \gamma(0) + \frac{2\pi}{\Phi_0} B_a t_{\text{eff}} x \right] \quad 1.72a$$

Next we assume that the critical supercurrent density  $j_c$  is spatially homogeneous, that is, it is independent of  $x$  and  $y$ . Then the integration yields

$$I_s = j_c b \int_0^a dx \sin \left[ \gamma(0) + \frac{2\pi}{\Phi_0} B_a t_{\text{eff}} x \right] = -j_c b \frac{\cos \left[ \gamma(0) + \frac{2\pi}{\Phi_0} B_a t_{\text{eff}} a \right]}{\frac{2\pi}{\Phi_0} B_a t_{\text{eff}}} \Big|_0^a \quad 1.72b$$

Inserting the integration limits, we obtain

$$I_s = j_c b \frac{\cos \gamma(0) - \cos \left[ \gamma(0) + \frac{2\pi}{\Phi_0} B_a t_{\text{eff}} a \right]}{\frac{2\pi}{\Phi_0} B_a t_{\text{eff}}} \quad 1.72c$$

With the variable  $\delta = \gamma(0) + (\pi/\Phi_0) B_a t_{\text{eff}} a$  and using the relation  $\cos(\alpha \pm \beta) = \cos \alpha \cos \beta \mp \sin \alpha \sin \beta$ , finally we find

$$I_s = j_c ab \sin \delta \frac{\sin \left[ \frac{\pi}{\Phi_0} B_a t_{\text{eff}} a \right]}{\frac{\pi}{\Phi_0} B_a t_{\text{eff}} a} \quad 1.72d$$

Similar to Eq. (1.62), for a given current  $I$  and magnetic field  $B_a$ , the quantity  $\delta$  will adjust itself in such a way that Eq. (1.72d) will be satisfied. This is possible up to the value for

which  $\sin \delta = \pm 1$ , and finally we obtain the magnetic field dependence of the critical current of the Josephson junction

$$I_c(\Phi_J) = I_c(0) \left| \frac{\sin \left[ \pi \frac{\Phi_J}{\Phi_0} \right]}{\pi \frac{\Phi_J}{\Phi_0}} \right| \quad 1.73$$

where  $\Phi_J = B_a t_{\text{eff}} a$  and  $I_c(0) = j_c ab$ . The quantity  $\Phi_J$  corresponds to the magnetic flux penetrating the Josephson junction.

The function (1.73) is shown in [Figure 1.28a](#). In analogy to the diffraction of light by a slit, it is referred to as a **Fraunhofer pattern**. In [Figure 1.28b](#), we see the measured dependence  $I_c(B_a)$  for a Sn–SnO–Sn tunnel junction. With a value of the London penetration depth of 30 nm, one obtains for  $t_{\text{eff}}$  a value of about 60 nm. The width of the junction was 250  $\mu\text{m}$ . Hence, we expect zero values of the critical current within a distance  $\Delta B_a = \Phi_0/(at_{\text{eff}}) \approx 1.4$  G. This agrees well with the experimental result  $\Delta B_a = 1.25$  G.

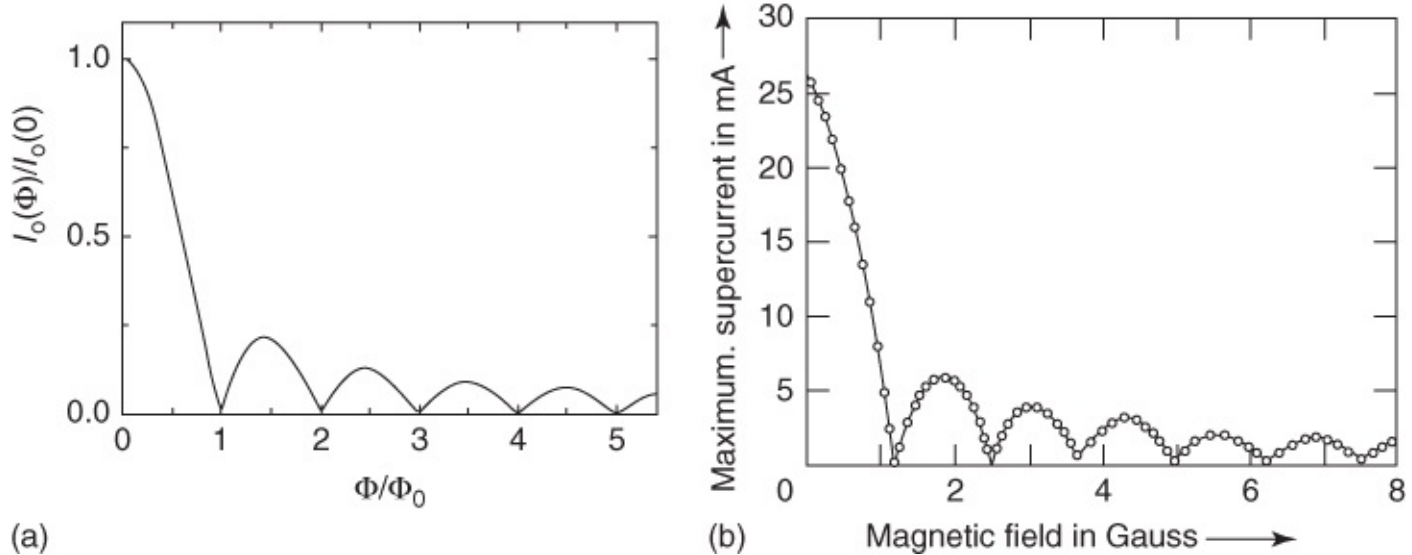


**Figure 1.28** Dependence of the maximum Josephson current on the magnetic field parallel to the barrier layer. (a) Theoretical curve according to Eq. (1.73). (b) Measured data for a Sn–SnO–Sn tunnel junction ( $1 \text{ G} = 10^{-4} \text{ T}$ ).

(From [49].)

If the critical current density  $j_c$  had been inhomogeneous, that is, depending upon the spatial coordinates  $x$  and  $y$ , the function  $I_c(B_a)$  would have deviated strongly from the form of the Fraunhofer pattern. Therefore, the measurement of  $I_c(B_a)$  often serves as a simple test of the homogeneity of the barrier layer.

What about the physics behind the Fraunhofer pattern? For light diffraction by a slit, minima in the interference stripes appear at locations where the waves passing through the slit interfere

destructively with each other. According to Eq. (1.70), in the Josephson junction the magnetic field causes an increase in the gauge-invariant phase difference along the barrier, and the supercurrent density spatially oscillates in the  $x$ -directions.<sup>21</sup> At the zero values of  $I_c(\Phi)$ , the wavelength of these oscillations is an integer fraction of the width  $a$  of the junction. Hence, equal amounts of the supercurrent flow across the barrier in both directions, and the integral over the supercurrent density is zero, independent of the value of the initial phase  $\gamma(0)$  in Eq. (1.70). However, away from the zero values, the wavelength of the supercurrent density is incommensurable with the width of the junction. In this case the supercurrent can attain a finite value, which is adjustable up to a certain maximum value by means of the phase shift  $\gamma(0)$ . This maximum value becomes smaller for smaller wavelengths of the oscillations of the supercurrent density, since the supercurrents more and more average to zero over an increasing number of periods.

In [Figure 1.29](#), we show this effect for three different spatial distributions of the current density at values of the flux  $\Phi_0/2$ ,  $\Phi_0$ , and  $3\Phi_0/2$ . For the values  $\Phi_0/2$  and  $3\Phi_0/2$ , the phase  $\gamma(0)$  is chosen such that the supercurrent across the junction reaches a maximum value. For the value  $\Phi_0$  the supercurrent across the junction is always zero, independent of  $\gamma(0)$ . Furthermore, we note that the fraction of the Josephson current not flowing in the forward direction across the junction must flow in a closed loop within the superconducting electrodes. In [Figure 1.29](#), this is indicated by the “horizontal” arrows.

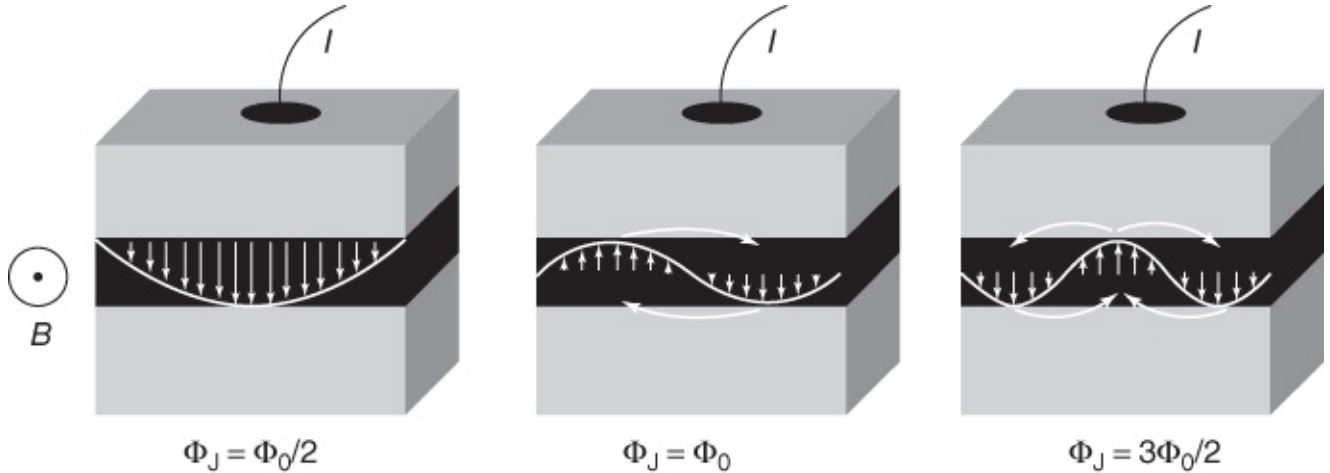


**Figure 1.29** Variation of the Josephson supercurrent density for three different values of the magnetic flux penetrating through the Josephson junction.

What happens, finally, if the self-field generated by the Josephson current is taken into account? If the effect of the self-field is small, such that the magnetic flux generated by this field is much smaller than  $\Phi_0$ , the correction of the applied field remains small. However, if the magnetic flux generated by the supercurrents circulating across the barrier approaches the value  $\Phi_0$ , vortices can appear with their axis located within the barrier layer. These vortices are also referred to as **Josephson flux quanta** or **fluxons**. They display many interesting properties, which we will discuss in more detail in [Section 6.4](#). In particular, based on moving Josephson vortices, high-frequency oscillators can be built that are utilized in the application

of Josephson junctions for the detection of microwaves (see [Section 7.6.3](#)).

Let us go back to the circular structure of [Figure 1.25](#). If here the finite extension of both Josephson junctions is taken into account, the magnetic field dependence of their critical currents and the periodic modulation of the maximum supercurrent that can pass through the circular structure are superimposed on each other. Formally, we can account for this, for example, by replacing  $I_c$  in Eq. (1.62) by Eq. (1.72d). For a typical SQUID, the area  $a t_{\text{eff}}$  of both Josephson junctions is smaller than that of the SQUID itself by several orders of magnitude. The maximum supercurrent oscillates on a field scale of a few microtesla, whereas the critical current of the Josephson junctions decreases appreciably only at fields of about 1 m T. So sometimes one can observe thousands of oscillations with nearly the same maximum amplitude  $I_{c1} + I_{c2}$ . However, in some cases, geometric structures have been investigated in which the SQUID area and the dimension of the Josephson junctions were similar. In [Figure 1.30](#), we show an example obtained with a circular structure made of  $\text{YBa}_2\text{Cu}_3\text{O}_7$ , for which the area  $a t_{\text{eff}}$  of the Josephson junctions was just barely by a factor 10 smaller than the ring area [51]. Here, we can clearly see the superposition of the SQUID modulation and of the Fraunhofer pattern.

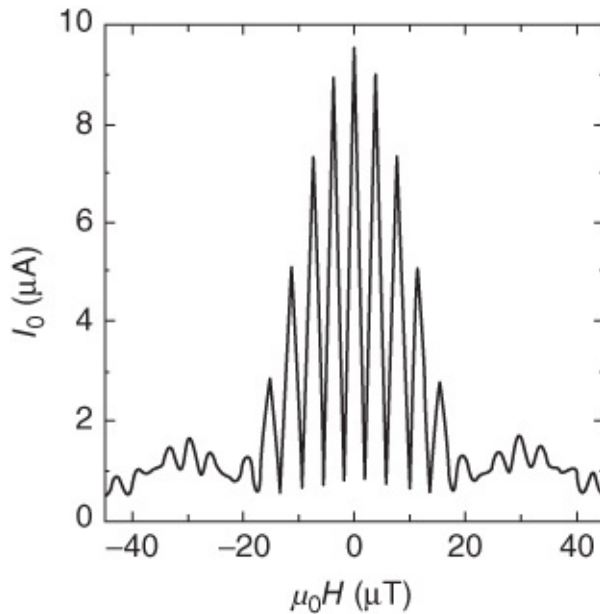


**Figure 1.30** Magnetic field dependence of the maximum supercurrent of a SQUID structure made of  $\text{YBa}_2\text{Cu}_3\text{O}_7$ . The two Josephson junctions are 9  $\mu\text{m}$  wide, such that the  $I_c$  modulation of the individual junctions appears as the envelope of the SQUID oscillations [51].

(© 2000 AIP.)

At the end of this chapter, we now turn to the question: In which form can similar interference phenomena be observed also for individual electrons? We imagine that the matter wave describing an individual electron is split into two spatially separated coherent parts, which subsequently are caused to interfere with each other. If the area enclosed by the two partial beams is penetrated by the flux  $\Phi$ , we expect a phase difference between the two partial beams. For a flux of  $h/e$ , that is, for twice the value observed in superconductors, the phase

difference will be  $2\pi$ .

Such an experiment was carried out in 1962 by Möllenstedt and coworkers using electron waves in a vacuum [51]. By means of a very thin, negatively charged wire (a so-called biprism), they split an electron beam into two partial beams, which they guided around a tiny coil (diameter about 20  $\mu\text{m}$ ) to the other side. By using additional biprisms, subsequently both beams were superimposed, yielding a system of interference stripes. Indeed, they obtained the well-known interference pattern of the double slit. Next, the system of interference stripes was studied for different magnetic fields in the coil. A change of the magnetic field affected a shift of the system of stripes, displaying the expected phase shift of  $2\pi$  for a flux change of  $h/e$ . In [Figure 1.31](#), we present a schematic of the experiment (a) and a picture of the system of stripes (b). During the change of the magnetic field, the recording film was moved parallel to the system of stripes. The shift in the system of stripes can clearly be seen. In [Figure 1.31b](#) for the total field change, the shift amounts to about three complete periods. Hence, in this experiment, the phase difference between the partial beams was changed by the magnetic field by about  $3 \times 2\pi$ .

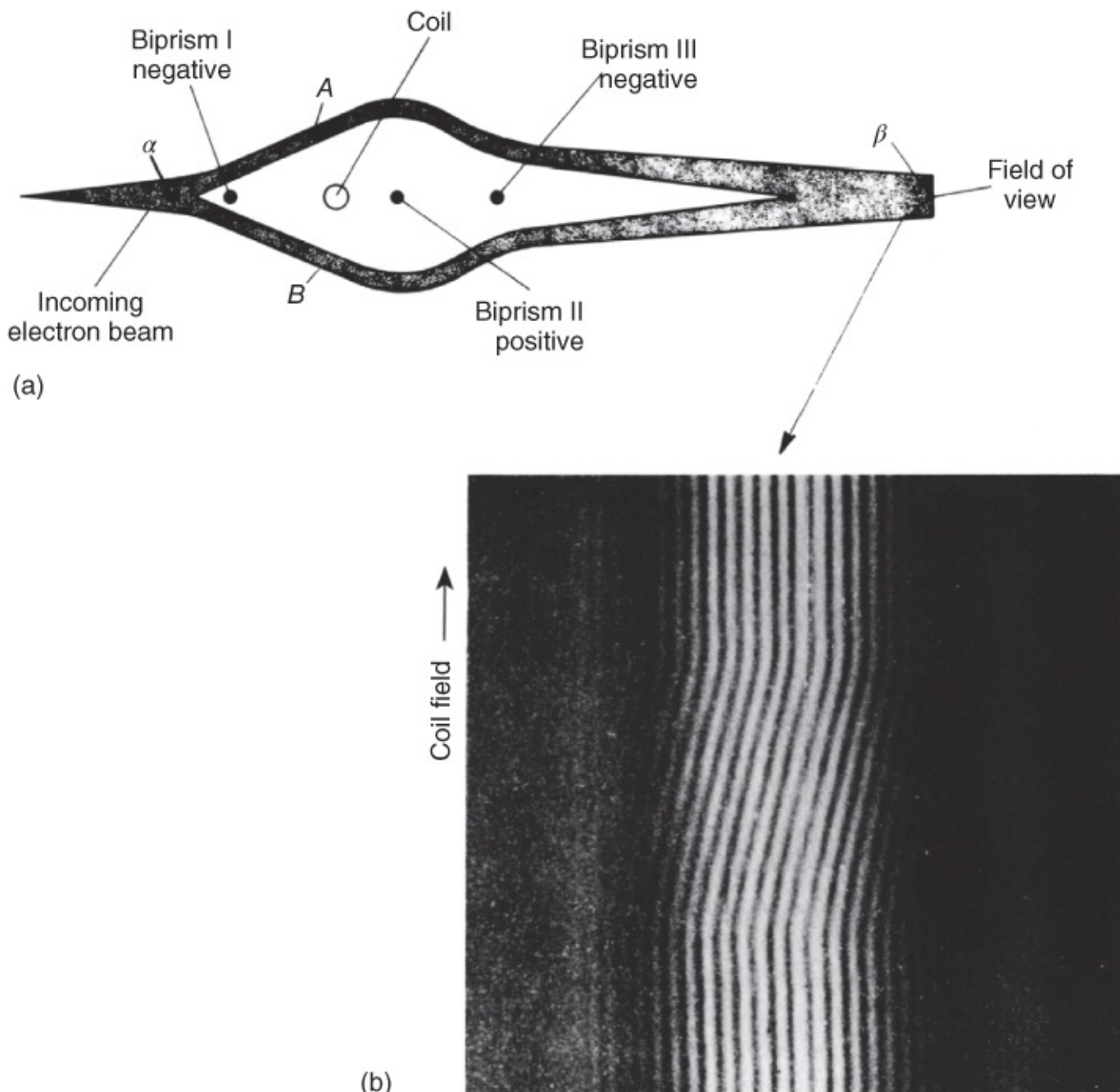


**Figure 1.31** Phase change of electron waves caused by a vector potential. (a) Beam geometry. (b) Interference pattern during a change of the magnetic field. The biprisms are quartz threads covered by a metal. The coil with 20  $\mu\text{m}$  diameter was fabricated from tungsten wire.

(From [52].)

The special feature of this experiment is the fact that the magnetic field was very carefully restricted to the interior of the coil. In this experiment, the field lines of the return flux were concentrated into a yoke made of a magnetic material and placed outside the loop area of the electron beams. The shift of the interference pattern was observed, although no Lorentz force acted on the electrons. The only forces were the constant electrostatic forces originating from the biprisms. Hence, an effect appears that cannot be explained within a classical particle concept. The interference pattern changed as a function of the magnetic flux enclosed between the two particle beams, without additional forces acting on the electron trajectory. This non-

classical effect was predicted already in 1959 by Aharonov and Bohm [53]. Subsequently, its discussion was highly controversial. However, the prediction of Aharonov and Bohm could be confirmed by means of ring-shaped magnets covered with a superconducting overlay, such that the magnetic field was completely restricted to the interior of the magnets [14].

Based on this principle of electron holography, also the flux lines shown in [Figure 1.10d](#) were imaged. In this experiment, quantum mechanics appears twofold: on the one hand, the wave nature of the electrons was utilized for imaging; on the other, it was the quantized magnetic flux of a vortex that was detected in the superconductor.

The observation of flux quantization and of quantum interference in Josephson junctions and in SQUID rings has clearly shown that the appearance of a coherent matter wave represents the key property of the superconducting state. For the amount of charge of the superconducting charge carriers, the value  $2e$  has always been found. In [Chapter 3](#), we will describe how this Cooper pairing is accomplished. However, first we will turn to the different superconducting materials.

## References

1. H. Kamerlingh-Onnes: *Commun. Leiden* **140b, c** and **141b** (1914).
2. Kamerlingh-Onnes, H. (1924) Reports and Communication 4. International Cryogenic Congress, London, p. 175;H. Kamerlingh-Onnes, W. Tuyn: *Commun. Leiden* **198** (1929) .
3. D. J. Quinn, W. B. Ittner: *J. Appl. Phys.* **33**, 748 (1962).
4. H. Kamerlingh-Onnes: *Commun. Leiden* **50a** (1924).
5. C. J. Gorter, H. Casimir: *Physica* **1**, 306 (1934).
6. W. Meißner, R. Ochsenfeld: *Naturwissenschaften* **21**, 787 (1933).
7. Geim, A. (1998) Physics Today, September 1998, p. 36.
8. D. Cribier, B. Jacrot, L. Madhav Rao, B. Farnoux: *Phys. Lett.* **9**, 106 (1964);see also: “*Progress Low Temperature Physics*”, Vol. 5, C. J. Gorter (ed.), North Holland Publishing Company, Amsterdam, p. 161 (1967).
9. J. Schelten, H. Ullmaier, W. Schmatz: *Phys. Status Solidi* **48**, 619 (1971).
10. U. Essmann, H. Träuble: *Phys. Lett.* **24 A**, 526 (1967) and *J. Sci. Instrum.* **43**, 344 (1966).
11. P. E. Goa, H. Hauglin, M. Baziljevich, E. Il'yashenko, P. L. Gammel, T. H. Johansen: *Supercond. Sci. Technol.* **14**, 729 (2001).
12. T. Matsuda, S. Hasegawa, M. Igarashi, T. Kobayashi, M. Naito, H. Kajiyama, J. Endo, N. Osakabe, A. Tonomura, R. Aoki: *Phys. Rev. Lett.* **62**, 2519 (1989)

13. R. Straub, S. Keil, R. Kleiner, D. Koelle: *Appl. Phys. Lett.* **78**, 3645 (2001)
14. A. Tonomura: “*Electron Holography*”, Springer Series in Optical Sciences Vol. **70** (1998).
15. R. Gross, D. Koelle: *Rep. Prog. Phys.* **57**, 651 (1994).
16. A. de Lozanne: *Supercond. Sci. Technol.* **12**, p. R43 (1999).
17. A. Oral, J. C. Barnard, S. J. Bending, I. I. Kaya, S. Ooi, T. Tamegai, M. Henini: *Phys. Rev. Lett.* **80**, 3610 (1998).
18. J. R. Kirtley, M. B. Ketchen, K. G. Stawiasz, J. Z. Sun, W. J. Gallagher, S. H. Blanton, S. J. Wind: *Appl. Phys. Lett.* **66**, 1138(1995); R. C. Black, F. C. Wellstood, E. Dantsker, A. H. Miklich, D. Koelle, F. Ludwig, J. Clarke: *Appl. Phys. Lett.* **66**, 1267 (1995).
19. H. F. Hess, R. B. Robinson, J. V. Waszczak: *Phys. Rev. Lett.* **64**, 2711 (1990).
20. L. Schultz, G. Krabbes, G. Fuchs, W. Pfeiffer, K.-H. Müller: *Z. Metallk.* **93**, 1057 (2002).
21. F. London: “*Superfluids*”, Vol. **1**, John Wiley & Sons, Inc., New York, p. 152 (1950).
22. R. Doll, M. Näßauer: *Phys. Rev. Lett.* **7**, 51 (1961).
23. B. S. Deaver Jr. W. M. Fairbank: *Phys. Rev. Lett.* **7**, 43 (1961).
24. F. London, H. London: *Z. Phys.* **96**, 359 (1935); F. London: “*Une Conception Nouvelle de La Supraconductivite*”, Hermann, Cie, Paris (1937).
25. J. M. Lock: *Proc. R. Soc. London, Ser. A* **208** 391 (1951).
26. T. J. Jackson, T. M. Risemann, E. M. Forgan, H. Glückler, T. Prokscha, E. Morenzoni, M. Pleines, Ch. Niedermayer, G. Schatz, H. Luetkens, J. Litterst: *Phys. Rev. Lett.* **84**, 4958 (2000).
27. A. B. Pippard: *Proc. R. Soc. London, Ser. A* **203**, 210 (1950).
28. J. S. Langer, V. Ambegaokar: *Phys. Rev.* **164**, 498 (1967).
29. D. E. McCumber, B. I. Halperin: *Phys. Rev. B* **1**, 1054 (1970).
30. J. E. Lukens, R. J. Warburton, W. W. Webb: *Phys. Rev. Lett.* **25**, 1180 (1970).
31. R. S. Newbower, M. R. Beasley, M. Tinkham: *Phys. Rev. B* **5**, 864 (1972).
32. B. D. Josephson: *Phys. Lett.* **1**, 251 (1962).
33. R.P. Feynman, R.B. Leighton, M. Sands: “*Feynman Lectures on Physics*”, Vol. **3**, Addison-Wesley Publishing Company, New York (1965).
34. L. D. Landau, E. M. Lifschitz: “*Lehrbuch der Theoretischen Physik*”, Vol. **9**, Akademie-Verlag, Berlin, 1980.

35. R. Gross: In “*Interfaces in High- $T_c$  Superconducting Systems*”, S. L. Shinde, D. A. Rudman (eds.), Springer, New York, p. 176 (1994).
36. H. Hilgenkamp, J. Mannhart: *Rev. Mod. Phys.* **74** (2002).
37. R. Kleiner, F. Steinmeyer, G. Kunkel, P. Müller: *Phys. Rev. Lett.* **68**, 2394 (1992).
38. J. S. Tsai, A. K. Jain, J. E. Lukens: *Phys. Rev. Lett.* **51**, 316 (1983).
39. D. G. McDonald: *Science* **247**, 177 (1990).
40. S. Shapiro: *Phys. Rev. Lett.* **11**, 80 (1963).
41. I. Giaever: *Phys. Rev. Lett.* **14**, 904 (1965).
42. A. H. Dayem, R. J. Martin: *Phys. Rev. Lett.* **8**, 246 (1962).
43. D. N. Langenberg, D. J. Scalapino, B. N. Taylor, R. E. Eck: *Phys. Rev. Lett.* **15**, 294 (1965).
44. I. K. Yanson, V. M. Svistunov, I. M. Dmitrenko: *Zh. Eksperim. Teor. Fiz.* **48**, 976 (1965); I. K. Yanson, V. M. Svistunov, I. M. Dmitrenko: *Sov. Phys. JETP* **21**, 650 (1966).
45. D. N. Langenberg, W. H. Parker, B. N. Taylor: *Phys. Rev.* **150**, 186 (1966); D. N. Langenberg, W. H. Parker, B. N. Taylor: *Phys. Rev. Lett.* **18**, 287 (1967).
46. R. C. Jaklevic, J. Lambe, J. E. Mercereau, A. H. Silver: *Phys. Rev.* **140 A**, 1628 (1965).
47. F. London: “*Superfluids, Macroscopic Theory of Superconductivity*”, Vol. **1**, John Wiley & Sons, Inc., New York (1950).
48. R. E. Packard, S. Vitale: *Phys. Rev. B* **46**, 3540 (1992); O. Avenel, P. Hakonen, E. Varoquaux, *Phys. Rev. Lett.* **78**, 3602 (1997); K. Schwab, N. Bruckner, R. E. Packard: *Nature* **386**, 585 (1997).
49. D. N. Langenberg, D. J. Scalapino, B. N. Taylor: *Proc. IEEE* **54**, 560 (1966).
50. C. Gürlich, S. Scharinger, M. Weides, H. Kohlstedt, R. G. MIInts, E. Goldobin, D. Koelle, R. Kleiner: *Phys. Rev. B* **81**, 094502 (2010).
51. R. R. Schulz, B. Chesca, B. Goetz, C. W. Schneider, A. Schmehl, H. Bielefeldt, H. Hilgenkamp, J. Mannhart, C. C. Tsuei: *Appl. Phys. Lett.* **76**, 912 (2000).
52. G. Möllenstedt, W. Bayh: *Phys. Bl.* **18**, 299 (1962); G. Möllenstedt, W. Bayh: *Naturwissenschaften* **49**, 81 (1962).
53. Y. Aharonov, D. Bohm: *Phys. Rev.* **115**, 485 (1959).
54. L. Ozyuzer, A. E. Koshelev, C. Kurter, N. Gopalsami, Q. Li, M. Tachiki, K. Kadowaki, T.

Yamamoto, H. Minami, H. Yamaguchi, T. Tachiki, K. E. Gray, W. K. Kwok, U. Welp: *Science* **318**, 1291 (2007).

55. H. B. Wang, S. Guénon, B. Gross, J. Yuan, Z. G. Jiang, Y. Y. Zhong, M. Grünzweig, A. Iishi, P. H. Wu, T. Hatano, D. Koelle, R. Kleiner: *Phys. Rev. Lett.* **105**, 057002 (2010).

<sup>1</sup> Throughout we will use the quantity  $\mathbf{B}$  to describe the magnetic field and, for simplicity, refer to it as “magnetic field” instead of “magnetic flux density.” Since the magnetic fields of interest (also those within the superconductor) are generated by macroscopic currents only, we do not have to distinguish between the magnetic field  $\mathbf{H}$  and the magnetic flux density  $\mathbf{B}$ , except for a few cases.

<sup>2</sup> The **self-induction coefficient  $L$**  can be defined as the proportionality factor between the induction voltage along a conductor and the temporal change of the current passing through the conductor:  $U_{\text{ind}} = -L(dI/dt)$ . The energy stored within a ring carrying a permanent current is given by  $(1/2)LI^2$ . The temporal change of this energy is exactly equal to the joule heating power  $RI^2$  dissipated within the resistance. Hence, we have  $-(d/dt)((1/2)LI^2) = RI^2$ . One obtains the differential equation  $-(dI/dt) = (R/L)I$ , the solution of which is Eq. (1.1).

<sup>3</sup> For a circular ring of radius  $r$  made from a wire of thickness  $2d$  also with circular cross-section ( $r \gg d$ ), we have  $L = \mu_0 r [\ln(8r/d) - 1.75]$  with  $\mu_0 = 4\pi \times 10^{-7} \text{ V s/A m}$ . It follows that

<sup>4</sup> Each coordinate of a system that appears quadratically in the total energy represents a thermodynamic degree of freedom, for example, the velocity  $v$  for  $E_{\text{kin}} = (1/2)mv^2$ , or the displacement  $x$  from the equilibrium position for a linear law for the force,  $E_{\text{pot}} = (1/2)Dx^2$ , where  $D$  is the force constant.

<sup>5</sup> We have an electrical insulator if the accommodation of all the electrons only leads to completely filled bands. The electrons of a filled band cannot take up energy from the electric field, since no free states are available.

<sup>6</sup> eV (electronvolt) is the standard energy unit of elementary processes:  $1 \text{ eV} = 1.6 \times 10^{-19} \text{ J}$ .

<sup>7</sup> Also non-superconducting, but diamagnetic objects, such as nuts or frogs, can levitate above magnets. However, one needs very large field gradients [7].

<sup>8</sup> We note that in this case the vortex lattice is strongly distorted. Such distorted lattices will be discussed in more detail in [Section 5.3.2](#).

<sup>9</sup> The “curl” of a vector  $\mathbf{A}$  is again a vector, the components  $(\text{curl } \mathbf{A})_x, \dots$  of which are constructed from the components  $A_i$  in the following way:

- <sup>10</sup> Notation: “div” is the divergence of a vector,  $\text{div} \mathbf{B} = \partial B_x / \partial x + \partial B_y / \partial y + \partial B_z / \partial z$ ; “grad” is the gradient,  $\text{grad} f(x, y, z) = (\partial f / \partial x, \partial f / \partial y, \partial f / \partial z)$ ; and  $\Delta$  is the Laplace operator,  $\Delta f = \partial^2 f / \partial x^2 + \partial^2 f / \partial y^2 + \partial^2 f / \partial z^2$ . In Eq. (1.16) the latter must be applied to the three components of  $\mathbf{B}$ .
- <sup>11</sup> Here, we neglect thermal fluctuations by which Cooper pairs can be generated momentarily also above  $T_c$ . We will return to this point in [Section 4.8](#).
- <sup>12</sup> The sign must be chosen according to the direction of the magnetic field.
- <sup>13</sup> Often one uses this relation for determining  $\xi_{\text{GL}}$ . Another possibility arises from the analysis of the conductivity near the transition temperature (see also [Section 4.8](#)).
- <sup>14</sup> Here, we ignore the negative sign of the electron charge. Otherwise, we would have to reverse the direction of the current and velocity vectors.
- <sup>15</sup> Again we ignore the negative sign of the electron charge.
- <sup>16</sup> These qualitative arguments treat the quantum mechanics only in a rough way, but yield the correct result.
- <sup>17</sup> This is not valid for irreversible processes. A full glass of water falling to the ground breaks into many pieces, and the water spreads over the floor. The inverse process, where the water and the broken pieces jump upon the table and reassemble to an unbroken glass filled with water, only exists in the motion picture.
- <sup>18</sup> The value given here was defined internationally in 1990 as the Josephson constant  $K_{J-90}$ , and therefore is exact.
- <sup>19</sup> For his experiments with superconducting tunnel junctions, Giaever received the Nobel Prize in 1973, together with B. D. Josephson and L. Esaki.
- <sup>20</sup> Therefore, the inductivity of the ring is slightly increased. This contribution is referred to as “kinetic inductance”  $L_{\text{kin}}$ , which must be added to the inductance  $L$  given by the geometry. Hence, we have  $L_{\text{tot}} = L + L_{\text{kin}}$ . However, since mostly the contribution  $L_{\text{kin}}$  is very small, we will not distinguish any further between  $L_{\text{tot}}$  and  $L$ .
- <sup>21</sup> This current distribution can be imaged by means of low-temperature scanning electron microscopy. Details can be found in the literature [50].

# **Chapter 2**

## **Superconducting Elements, Alloys, and Compounds**

We have already discussed a few superconducting elements and compounds in the previous chapter. Next, we will treat various materials in more detail. We will start by looking at the Periodic Table of the elements and then turn to multicomponent compounds.

Thousands of superconducting substances are presently known, and at this stage we have to ask a question: Under which criteria does a superconductor appear interesting enough to be included in a textbook? An initial more careful look at the Periodic Table appears reasonable. However, how about the immense number of superconducting alloys and compounds?

One criterion that we could use is the value of the transition temperature  $T_c$ . An important motivation for the study of new superconducting compounds certainly results from the hope of finding, one day, a room-temperature superconductor – which furthermore should also have other useful properties, such as the possibility for fabricating wires or thin films with high quality from this material.

However, another equally important criterion arises from the study of superconductors that simply show “interesting” superconducting properties. Exactly from this aspect comes the attraction of the new and the unknown. In order to classify these properties better, we briefly deal with the concepts of “conventional” and “unconventional” superconductors, before we turn to the superconducting materials themselves.

### **2.1 Introductory Remarks**

#### **2.1.1 Discovery, Preparation, and Characterization of New Superconductors**

Unfortunately, there exists no general recipe for discovering new superconductors. Often this happens by chance. Once a new material has been found, by systematically varying its components, often one succeeds to test a whole class of materials for superconductivity. The cuprate compounds or the iron pnictides are good examples.

In a first stage, often new materials are prepared in the form of powder or by sintering, and the superconducting material is often intermixed with non-superconducting wrong phases. In this case, one must find the correct phase and must identify its crystal structure, say, with X-ray diffraction. At this first stage, only relatively few superconducting parameters can be determined, such as the transition temperature  $T_c$ . If the substance turns out to be interesting, one will try to prepare single crystals in purer and purer form and also thin films. This allows to apply better and better methods for characterization. The complete characterization or even the technical application of a new superconductor can last many years or even decades.

In the subsequent sections, we will not always mention this explicitly. However, we must remember that the statement “this material is a conventional superconductor with such and such properties” resulted only after a long development.

It is only a relatively small number of materials, which is technically important. In the case of the metallic superconductors, this applies in particular to NbTi and Nb<sub>3</sub>Sn for the construction of magnets, pure Nb for resonators, sensors, and microelectronic circuits, as well as more and more also to NbN for bolometers and calorimeters. MgB<sub>2</sub> looks promising. However, for true applications, some further development work is needed. In the case of the cuprates, we mention primarily YBa<sub>2</sub>Cu<sub>3</sub>O<sub>7</sub> (sensors and cables of the second generation) and Bi<sub>2</sub>Sr<sub>2</sub>Ca<sub>2</sub>Cu<sub>3</sub>O<sub>10</sub> (cables of the first generation).

## 2.1.2 Conventional and Unconventional Superconductors

For many decades superconductivity itself was a phenomenon one could well term *unconventional*, in contrast to the “conventional” normal conducting metals. The Bardeen–Cooper–Schrieffer (BCS) theory, which we will discuss in detail in [Section 3.1.2](#), for the first time provided a satisfactory physical understanding of the properties of the superconducting materials known at the time. According to this theory, below the transition temperature the electrons form pairs, where at the same time all pairs collectively constitute a macroscopic matter wave. As far as we know, this is valid for all superconductors.

In the “conventional” superconductors, the electrons interact with each other via the vibrations of the crystal lattice. The two electrons of a Cooper pair form a state, in which the value  $S$  of the total spin as well as the value  $L$  of the total angular momentum of the pair vanishes.

Following the notation customary in atomic physics, we can denote this pair state with  $L = 0$  as an s wave. At least in first approximation this state is isotropic, that is, the superconducting wave function has the same properties along each crystallographic direction. In most substances, superconductivity is also homogeneous. Except for the case in which a barrier layer is inserted into the material (then, for instance, leading to the Josephson effect), at each location within the material the superconducting state displays essentially the same properties.

One could also add the property “non-magnetic” to the conventional list. In general, magnetic order (such as ferromagnetism or antiferromagnetism) and superconductivity represent phenomena competing against each other. Each time both phenomena are in competition, the superconducting state develops unusual properties [1]. For example, while lowering the temperature, superconductivity can set in at first, but then it is suppressed again because of the magnetic order (reentrant superconductivity). This phenomenon was predicted in 1970 by Müller-Hartmann and Zittartz [2] and was observed in 1973 for the system La<sub>1-x</sub>Ce<sub>x</sub>Al<sub>2</sub> [3].

We will come back to this point in [Section 3.1.4.2](#). Also in [Section 2.5](#) we will discuss a few other superconductors, in which reentrant superconductivity has been observed.

Which superconductors are “unconventional” in terms of spin and angular momentum? We start by looking at the possible values of  $S$  and  $L$  for a Cooper pair. With respect to the spin, the electrons, each having a spin  $\hbar/2$ , can combine to a pair with  $S = 0$  (spin singlet) or with

$S = 1 \hbar$  (spin triplet). Almost all the known superconductors prefer the first option.

In order to obtain the  $S = 0$  state, the value of the angular momentum  $L$  must attain an even multiple of  $\hbar$ . According to the rules of quantum mechanics, only in this case is the wave function of all electrons antisymmetric, that is, it changes its sign if two electrons are interchanged.<sup>1</sup> Hence, for the state with  $S = 0$ , we can have  $L = 0, 2\hbar, 4\hbar$ , and so on. These states are referred to as **s, d, g state**, and so on. However, an angular momentum different from zero always leads to rotational energy, and the superconductor avoids this if possible in order to occupy a state with the smallest possible energy. Therefore, the state with  $S = 0$  and  $L = 0$  is favored energetically and is taken up by most superconductors. However, for some superconductors and, in particular, for the high-temperature superconductors, the state with  $L = 2\hbar$  is realized. This is the first version of an “unconventional” superconductor. We will also see that other superconductors take up this state.

We must note that for an angular momentum with the value  $N\hbar$ , the z-component finds  $2N + 1$  possibilities for orienting itself, namely in integer steps from  $-N\hbar$  up to  $+N\hbar$ . In the case of  $N = 2$  (d wave), there are five possibilities. However, in the electric field of the crystal, these possibilities are not equivalent anymore. The energetic degeneracy valid for the free atom is suspended. For the high-temperature superconductors, the  $d_{x^2-y^2}$  state plays an important role, as we will see in [Section 3.2.2](#).

If, on the other hand, the Cooper pairs combine to a spin-triplet state, the angular momentum must be an odd multiple of  $\hbar$ . These states can be classified as p wave, f wave, and so on. For a state with  $S = 1\hbar$ , the z-component of the spin can have the three possible orientations  $S_z = -1\hbar, 0$ , and  $+1\hbar$ . For a p-wave state, we find that  $L_z$  also has three possibilities for orientation:  $-1\hbar, 0$ , and  $+1\hbar$ . Together with the possible orientations of the spin, this leads to nine different combinations of spin and angular momentum. However, due to the influence of the crystal field, here also only a few combinations are relevant.

Until a few years ago, p-wave pairing was known only from superfluid  ${}^3\text{He}$ . However, in the meantime, superconducting substances have been found in which spin-triplet superconductivity seems to occur. An example is the compound  $\text{Sr}_2\text{RuO}_4$ , which is an oxide material similar to the high-temperature superconductors.

In systems such as the heavy-fermion superconductors (see [Section 2.6](#)), the influence of the crystal field as well as the coupling between the spin of the charge carriers and their orbital angular momentum is very pronounced. Then one must classify the superconducting state according to the *total* angular momentum. Here, instead of spin-singlet and spin-triplet states, one often speaks of pair states with even or odd parity. States with odd parity can also appear as triplets. In the heavy-fermion superconductors, both parities can be observed.

Furthermore, for the unconventional substances, it appears likely that Cooper pairing is not accomplished by the interaction of the electrons with the crystal lattice.<sup>2</sup> Because of the unconventional Cooper pairing, in  $\mathbf{k}$ -space the superconducting state is anisotropic. However, in regular space, it is not necessarily inhomogeneous. This is exactly what distinguishes the layered superconductors. Here, similar to the case of the Josephson junction, superconducting

layers alternate with normal conducting or even insulating layers. Some high-temperature superconductors are good examples, and also are compounds such as  $\text{NbSe}_2$ , for which the Cooper pairing is conventional. In fact, these superconductors can represent atomic stacks of many Josephson junctions with a number of highly unusual properties. In this chapter, we will also discuss these materials.

Now we have discussed a few criteria that make a material particularly interesting. Next we start to look at the superconducting elements. They are all conventional superconductors and usually of type I.

## 2.2 Superconducting Elements

By looking at the elements for which superconducting phases are known today ([Figure 2.1](#) and [Table 2.1](#)), we see that superconductivity is not a rare property of metals [4]. Some elements become superconducting only in their high-pressure phases. In [Figure 2.1](#) they are shown at the dark locations, and they are listed in the second part of [Table 2.1](#). From [Figure 2.1](#), we clearly recognize two groups of superconductors:

1. *The non-transition metals* – to these belong most of the superconducting high-pressure phases.
2. *The transition metals* – with increasing element number, an inner shell (3d, 4d, and 5d levels; for the lanthanides and actinides, the 4f and 5f levels) becomes filled up within a row.

H														He			
Li	Be																
20	0,03																
Na	Mg																
K	Ca	Sc	Ti	V	Cr	Mn	Fe	Co	Ni	Cu	Zn	Ga	Ge	As	Se	Br	Kr
15	0,34	0,5	5,4	3*		2					0,9	1,1	5,4	2,7	7	1,4	
Rb	Sr	Y	Zr	Nb	Mo	Tc	Ru	Rh 3,5. $10^{-5}$	Pd	Ag	Cd	In	Sn	Sb	Te	I	Xe
4	2,8	0,6	9,2	0,9	8,2	0,5	0,5	3,2*			0,5	3,4	3,7	3,6	7,4	1,2	
Cs	Ba	La	Hf	Ta	W	Re	Os	Ir	Pt	Au	Hg	Ti	Pb	Bi	Po	At	Rn
1,7	5	6	0,4	4,4	0,01	1,7	0,7	0,1			4,15	2,4	7,2	8,7			
Fr	Ra	Ac	Ce 1,75	Pr	Nd	Pm	Sm	Eu 1,8	Gd	Tb	Dy	Ho	Er	Tm	Vb	Lu 0,1	
			Th 1,4	Pa 1,3	U 0,2	Np 0,07	Pu	Am 1	Cm	Bk	Cf	Es	Fm	Md	No	Lw	

**Figure 2.1** Distribution of the superconductors and their transition temperatures in kelvin within the Periodic Table [4]. The elements, which are superconducting only in the high-pressure phase, are shown with a dark background. (\*): C is superconducting only in the form of carbon nanotubes ( $T_C = 15$  K) or in the form of boron-doped diamond films ( $T_C = 4$  K), Cr in the form of thin films, Pd after irradiation with  $\text{He}^+$ -ions.

**Table 2.1** Selected superconducting elements, crystal structure, melting point, and some properties of the superconducting state

	Element	$T_c$ (K)	Crystal structure	Melting point (°C)	$\Theta_D$ (K)	$\lambda_L$ (nm)	$\xi_{\text{GL}}$ (nm)	$B_c$ (G)
1	Al	1.19	fcc	660	420	50	500–1600	100
2	Am [5]	0.8	hex.	994				
3	Be	0.026	hex.	1283	1160			
4	Cd	0.55	hex.	321	300	130	760	30
5	Ga	1.09 (6.5; 7.5)	orth.	29.8	317	120		59
6	Hf [6]	0.13	hex.	2220				
7	Hg	4.15	rhom.	−38.9	90	55	400	

		(3.95)	tetr.					(340)
8	In	3.40	tetr.	156	109	24–64	360–440	280
9	Ir	0.14	fcc	2450	420			19
10	La	4.8	hex.	900	140			
		(5.9)	fcc					(1600)
11	Mo	0.92	bcc	2620	460			98
12	Nb	9.2	bcc	2500	240	32–44	39–40	1950
13	Np [7]	0.075	orth.					
14	Os	0.65	hex.	2700	500			65
15	Pa	1.3						
16	Pb	7.2	fcc	327	96	32–39	51–83	800
17	Re	1.7	hex.	3180	430			190
18	Rh [8]	$3.2 \times 10^{-4}$	fcc	1966	269			
19	Ru	0.5	hex.	2500	600			66
20	Sn	3.72	tetr.	231.9	195	25–50	120–320	305
		(5.3)	tetr.					
21	Ta	4.39	bcc	3000	260	35	93	800
22	Tc	7.8	hex.		351			177
23	Th	1.37	fcc	1695	170			150
24	Ti	0.39	hex.	1670	426			100
25	Tl	2.39	hex.	303	88			170
26	U ( $\alpha$ )	0.2	orth.	1132	200			
27	V	5.3	bcc	1730	340	39.8	45	1200
28	W	0.012	bcc	3380	390			1.24
29	Zn	0.9	hex.	419	310		25–32	52
30	Zr	0.55	hex.	1855	290			47

Elements showing superconductivity only under high pressure or in high-pressure phases

	Element	$T_c$ (K)	Pressure (kbar)	Reference
31	As	0.5	120	[9]
32	B	6.0	1750	[9b]
33	Ba	5.1	>140	[10]
		(1.8)	>55	

	Element	$T_c$ (K)	Pressure (kbar)	Reference
34	Bi II	3.9	26	[11]
	Bi III	7.2	>27	
	Bi V	8.5	>78	
35	Ce	1.7	>50	[12]
36	Cs	1.5	100	[13]
37	Fe	2	150–300	[14]
38	Ge	5.4	> ca. 110	[15]
39	I	1.2	290	[16]
40	Li	20	500	[17]
41	Lu	0.02–1.1	45 to ca. 180	[18]
42	O	0.6	1000	[18]
43	P	4.6–6.1	> ca. 100	[19]
44	S	17	1600	[19]
45	Sb	3.6	>85	[20]
46	Se	6.9	> ca. 130	[21]
47	Si	6.7	> ca. 120	[15]
48	Te	4.5	>43	[22]
49	Y	1.5–2.7	120–160	[13]

Transition temperature  $T_C$ , Debye temperature  $\Theta_D$ , London penetration depth  $\lambda_L$ , Ginzburg–Landau coherence length  $\xi_{GL}$ , and critical magnetic field  $B_C$ . Many of the numerical entries are only approximate values.

fcc: face centered cubic, bcc: body centered cubic, orth.: orthorhombic, tetr: trtragonal, hex: hexagonal.

Mostly from Ref. [4, 23, 5].

In [Table 2.1](#) for a few elements, the crystal structure and the melting point are also shown to demonstrate how strongly the superconducting elements can differ in their other properties. The Debye temperature  $\Theta_D$ , which we have included in [Table 2.1](#), is a measure of the strength of the vibrations of the crystal lattice. It is connected with the characteristic “Debye frequency”  $\omega_D$  through the relation  $k_B \Theta_D = \hbar \omega_D$ . The parameters  $\Theta_D$  and  $\omega_D$  represent important quantities for conventional superconductivity, which is accomplished after all by means of the interaction of the electrons with the vibrations of the crystal lattice (phonons).

[Table 2.1](#) also includes a few properties of the superconducting state that we have discussed before: the transition temperature  $T_c$ , the London penetration depth  $\lambda_L$ , the Ginzburg–Landau coherence length  $\xi_{GL}$ , and the critical field  $B_c$  above which type-I superconductivity breaks down. The transition temperatures of the elements range between a few hundredths and 20 K. There is no correlation apparent between the value of the transition temperature and other

characteristic properties such as the crystal structure or the melting point, with which one could discriminate between the superconductors and the non-superconductors among the metals.

It remains an open question whether, in the purest state and at arbitrarily small temperatures, certain metals still would become superconducting. Theoretically, there exists no strongly binding argument for the assumption that in principle all metals must become superconducting. On the other hand, we must admit that superconductors with a very small transition temperature (say,  $T_c < 10^{-2}$  K) can be found only with great difficulty. In this case, the smallest amount of impurities, such as paramagnetic atoms (for example, Mn, Co, and so on, with concentrations smaller than 1 ppm), as well as very small magnetic fields (for example, a small fraction of the Earth's magnetic field) can completely suppress superconductivity. Therefore, one can develop the opinion that for many metals, superconductivity has not yet been discovered simply because these metals have not yet been purified sufficiently and have not yet been studied at sufficiently low temperatures. So from studies of highly dilute alloys of the noble metals with transition temperatures in the millikelvin range, it has been concluded that pure Au becomes superconducting at about 0.2 mK [24]. For Cu and Ag, such experiments yielded values of  $T_c$  of about  $10^{-6}$  mK.

The statement that “all metals become superconducting at sufficiently low temperatures” cannot, in principle, be disproved. At most, it could be confirmed, namely by demonstrating superconductivity for all metals.<sup>3</sup> Presently, this question remains open. Furthermore, we can see from [Table 2.1](#) that superconductivity strongly depends on the arrangement of the atoms. Within different crystal structures, one and the same element has different values of the transition temperature. It can happen, as, for example, in the case of bismuth (Bi) that down to very low temperatures ( $T = 10^{-2}$  K), one modification remains non-superconducting, whereas several other modifications show superconductivity.

It appears that the crystalline structure does not provide a necessary condition for superconductivity. It can also be shown that “amorphous” samples become superconducting, in some cases with a rather high transition temperature. Such amorphous samples can be prepared for some metals by condensation of the metal vapor and by freezing onto the surface of a very cold substrate.

During the more than 75 years in which superconductivity has been studied with increasing interest, there have been many attempts to find rules for the magnitude of the transition temperature. Already, early on, it was pointed out that the atomic volume, that is, the volume occupied by an atom within the metallic crystal, may be important. If this atomic volume of the elements is plotted versus the element number in the Periodic Table, one finds indeed that superconductivity appears preferentially in the region of small atomic volumes [6]. These arguments may have some importance for the understanding of the superconducting high-pressure phases. Hydrostatic pressure reduces the atomic volume. Under sufficiently high pressure, a number of elements, such as Ba and even Cs, having a particularly large atomic volume in their normal phase, turn into superconductors. However, one must take into account that under high pressure these elements may undergo phase transitions, causing a change in the

short-range order and, hence, in other parameters important for superconductivity.

A highly useful empirical rule for the magnitude of the transition temperature has been proposed by Matthias [7]. This Matthias rule indicates that the average number of valence electrons of a material represents a key to superconductivity. As valence electrons, we count all electrons in the atomic shells that are not yet closed. Hence, the number of valence electrons of an element is identical to the column number of the element in the Periodic Table. The average number of valence electrons is taken as the arithmetic average over all valence electrons. According to the Matthias rule, for the transition metals there are pronounced maxima of  $T_c$  for valence-electron numbers  $n_v$  between 3 and 8. For the value  $n_v = 5$ , this is demonstrated by the high transition temperatures of V, Nb, and Ta. Also in group 7 of the Periodic Table, a particularly high transition temperature is observed for technetium. On the other hand, the elements of groups 4 and 6 of the Periodic Table have very low transition temperatures. Within the group of the non-transition metals, an increase in the transition temperature with increasing number of valence electrons is clearly visible.

The Matthias rule turned out to be particularly useful for alloys. In [Figure 2.2](#), the transition temperature of some alloys<sup>4</sup> is plotted versus the number of valence electrons. We clearly see the two maxima of  $T_c$  for an average number of valence electrons of about 4.7 and 6.5. Also the compounds with the so-called  $\beta$ -tungsten structure and with particularly high values of  $T_c$  have average values around  $n_v = 4.7$ . We will discuss these materials in more detail in [Section 2.3.1](#).

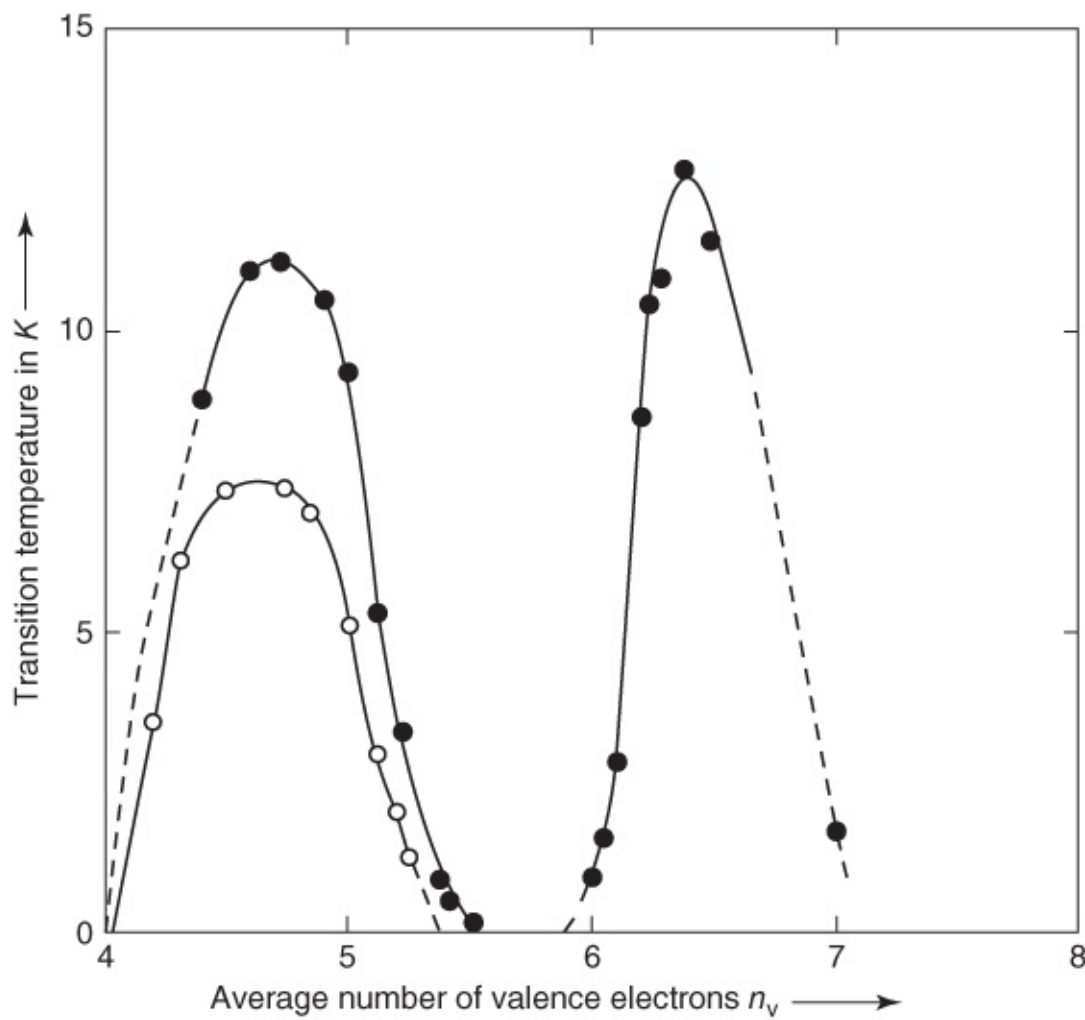


**Figure 2.2** Transition temperature of some alloys of the transition metals plotted versus the average number of valence electrons

(from Ref. [8])

: solid dots, Zr–Nb–Mo–Re and open circles, Ti–V–Cr.

## 2.3 Superconducting Alloys and Metallic Compounds

Our outlook becomes very large in scope if we include the far more than 1000 superconducting alloys and compounds into our considerations [23]. For example, it is possible to find superconducting compounds for the two components of which superconductivity is not observed. Examples are CuS with  $T_c = 1.6$  K and MgB<sub>2</sub> with  $T_c = 39$  K. Clearly, we cannot discuss all the known superconducting materials. However, we will deal with a number of substances that are or have been highly important for the basic physics or for technical applications, at least during a certain period.

### 2.3.1 The $\beta$ -Tungsten Structure

The superconductors with the  $\beta$ -tungsten structure (also A15 structure, A<sub>3</sub>B) represent a technically highly important group. These type-II superconductors can have transition

temperatures above 20 K and upper critical fields above 20 T. Before the discovery of the high-temperature superconductors, one representative of this group, namely  $\text{Nb}_3\text{Ge}$  with  $T_c = 23.2$  K [9], for more than a decade held the record of the highest transition temperature. Reviews of the properties of the A15 compounds can be found in [10–12].

In [Table 2.2](#) we present a list of the transition temperatures and some other properties of the superconducting state (London penetration depth, Ginzburg–Landau coherence length, and upper critical field<sup>5</sup>) for some of these superconductors. However, we must again note that the numbers are only given as an orientation, since they can differ strongly depending on the purity of the samples. [Figure 2.3](#) shows the crystal structure of the A15 compounds ( $\text{A}_3\text{B}$ ). The arrangement of the A atoms (Nb) along the chains parallel to the  $x$ ,  $y$ , and  $z$  axes is highly characteristic. The orthogonal chains do not intersect. Within the chains, the A atoms (Nb) have a smaller mutual distance than in the lattice of pure Nb.

**Table 2.2** Superconducting compounds with the  $\beta$ -tungsten structure [24, 13]

Compound	$T_c$ (K)	$\lambda_L$ (nm)	$\xi_{GL}$ (nm)	$B_{c2}$ (T)
$\text{V}_3\text{Ge}$	6.0	65	—	—
$\text{V}_3\text{Ga}^a$	14.2–14.6	65	4	23
$\text{V}_3\text{Si}$	17.1	70	4	23
$\text{Nb}_3\text{Sn}$	18.0	80	4	24
$\text{Nb}_3\text{Ge}$	23.2	80	3	38

<sup>a</sup> After careful annealing,  $T_c$  values around 20 K could be reached [25].

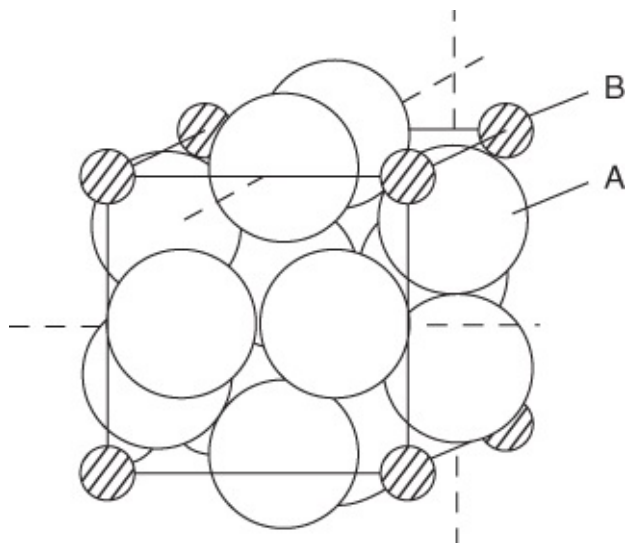


**Figure 2.3** The unit cell of the  $\beta$ -tungsten (A15) structure of the binary compounds  $\text{A}_3\text{B}$ .

Apparently, this A15 structure is highly favorable for superconductivity, although there are also other substances in this group that have very low values of  $T_c$  (e.g.,  $\text{Nb}_3\text{Os}$  with  $T_c = 1$  K), or

in which superconductivity has not been observed (e.g.,  $\text{Nb}_3\text{Sb}$ , which is not superconducting for  $T > 1 \text{ K}$  [24]).

The chains are highly important for the particular properties. If we look at the chains in terms of “one-dimensional conductors,” we obtain sharp peaks in the electronic density of states<sup>6</sup>  $N(E)$ . According to the BCS theory, this is an important quantity for the mechanism of superconductivity (see [Section 3.1](#)). If the Fermi energy is located within the region of such a peak of the density of states, we can expect two effects. On the one hand, the electron–phonon interaction can be very strong. On the other hand, the density states at the Fermi energy can be strongly temperature dependent, since a small shift of  $E_F$  due to a change in temperature also results in an appreciable change of  $N(E_F)$ .

These ideas are confirmed by the elastic behavior of some substances with high values of  $T_c$ , for example,  $\text{Nb}_3\text{Sn}$  and  $\text{V}_3\text{Si}$ . For these substances, with decreasing temperature one observes a strong decrease in the velocity of certain sound waves [15]. This means that the lattice becomes very soft with respect to certain elastic distortions. Finally, the softening can lead to an instability of the structure [16, 17]. In  $\text{Nb}_3\text{Sn}$  and  $\text{V}_3\text{Si}$  single crystals, a phase transition of the lattice can be observed at about 40 or 21 K, respectively. After the transition, the lattice, being cubic originally, shows a weak tetragonal distortion.

It has been shown in many experiments that the transition temperature of these substances depends sensitively on the degree of order within the chains. Frequently, the highest values of  $T_c$  only appear after long and careful annealing at the right temperature. Here one must pay close attention to the fact that, in addition to the  $\beta$ -tungsten structure, no other phases are formed. For choosing the proper annealing temperature, one must know the phase diagram of the substance. From our present understanding, it appears certain that for substances with the  $\beta$ -tungsten structure, the highest degree of order also yields the largest value of the transition temperature [18].

However, theoretically it also became clear that the coupling between the orthogonal systems of chains and between the chain atoms A and the atoms B within the substances  $A_3B$  must also be taken into account [19]. Only then one can understand in detail the experimental observations.

### 2.3.2 Magnesium Diboride

Early in 2001, Akimitsu and coworkers [20] discovered that below about 40 K, the compound  $\text{MgB}_2$  becomes superconducting. This was a big surprise, since intermetallic compounds had been studied for superconductivity for a long time. However, it was even more surprising, since  $\text{MgB}_2$ , with its relatively simple structure, had been known since the 1950s and was commercially available. Many properties of  $\text{MgB}_2$  are collected in the review articles [21, 22].  $\text{MgB}_2$  has a hexagonal crystal structure, in which layers of boron and layers of magnesium alternate with each other. The crystal structure is shown in [Figure 2.4](#).

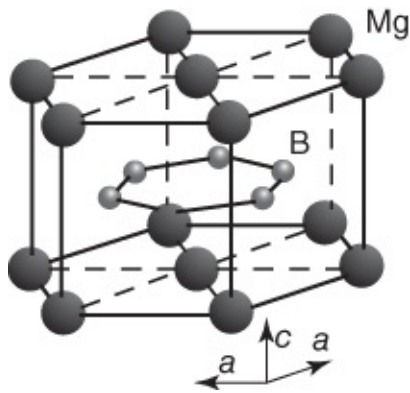


**Figure 2.4** The crystal structure of  $\text{MgB}_2$ .

(Reprinted from Ref. [26] by courtesy of IOP.)

$\text{MgB}_2$  is a type-II superconductor. In the case of pure single crystals, for the upper critical field and fields oriented parallel to the  $c$ -axis of the crystal structure, one obtains values of about 3 T, and for fields parallel to the  $a$ - or  $b$ -direction 15–20 T. (These values can be strongly increased by the controlled integration of impurities: up to about 35 T in the case of fields perpendicular to the layers and up to about 50 T in the case of parallel fields [22].) The lower critical field ranges around 0.12 T. The London penetration depth is found to be about 40 nm; from measurements of the upper critical field the Ginzburg–Landau coherence length is calculated to be 10 nm along the  $ab$ -direction and 2 nm along the  $c$ -direction.

In  $\text{MgB}_2$ , superconductivity is caused conventionally by electron–phonon interaction [22]. However, charge carriers from two different energy bands contribute quite differently to superconductivity. In some sense, one finds two kinds of Cooper pairs, which affects many characteristic properties of superconductivity (see [Section 3.2.4](#)). Therefore, the values of the penetration depth and the coherence length, indicated earlier, must be understood as averages over both kinds of Cooper pairs.

$\text{MgB}_2$  looks promising for technical applications. So far, superconducting wires and ribbons were manufactured and used for the construction of magnet coils [27].

### 2.3.3 Metal–Hydrogen Systems

Today we know many compounds that are superconducting at temperatures above 20 K. However, before the discovery of the high-temperature superconductors, the situation was very much different. Therefore, it is not surprising that superconductors with transition temperatures above 10 K generated much interest. As an example, we briefly discuss the metal–hydrogen systems, which were studied intensively in the 1970s. In these compounds the hydrogen is located at the interstitial lattice sites.

The superconductivity of palladium–hydrogen was discovered by Skoskiewicz in 1972 [28]. When he set the H/Pd ratio equal to about 0.8, he observed transition temperatures above 1 K. If he increased the hydrogen concentration to  $\text{H/Pd} \approx 0.9$ , the transition temperature increased up to about 4 K. This discovery was surprising, since the Pd–H system had been the subject of

many studies because of its other interesting properties. Furthermore, one did not expect at all to find superconductivity at this position in the Periodic Table.

The steep increase in  $T_c$  with increasing H concentration suggested that the values found by Skoskiewicz did not represent the upper limit of  $T_c$  within this system. Therefore, the hydrogen concentration was increased further by means of ion implantation at low temperatures. In this way, a maximum transition temperature  $T_c = 9$  K could be reached [29].

Replacing hydrogen by deuterium yielded an unexpected result. For a given crystal structure, the phonon frequencies of a material are inversely proportional to the square root of the mass of the lattice atoms (isotope effect, see [Section 3.1](#).3.1). Hence, for the samples containing deuterium, one would expect a smaller transition temperature. However, in this case the maximum value of  $T_c$  is about 11 K, and it appears again for the ratio D/Pd = 1. This anomalous isotope effect correlates with other anomalies for the change from H to D in palladium (for example, an increase in the diffusion constant), and indicates that the implantation of deuterium also changes the properties of the host lattice.

Another big surprise came from experiments performed with Pd–noble metal alloys [30]. In this case, after the implantation of hydrogen, transition temperatures up to 17 K were observed. These results are shown in [Figure 2.5](#). A characteristic trend from the PdAu to the PdCu alloys can clearly be seen.

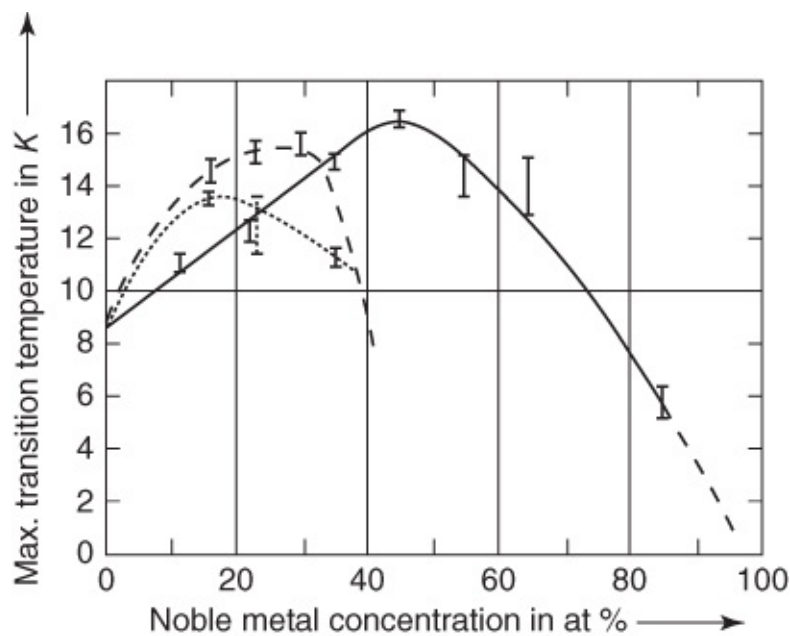
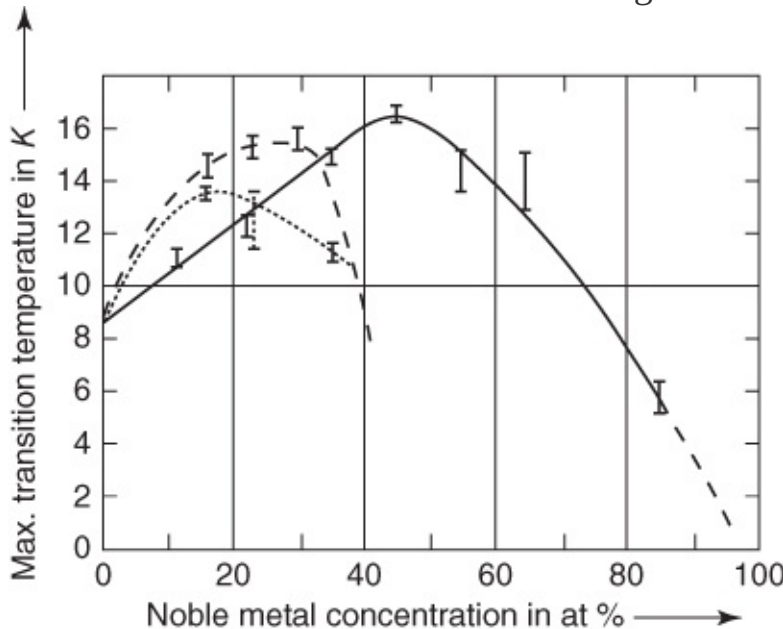


**Figure 2.5** Maximum transition temperature of Pd–noble metal alloys after charging with hydrogen by means of ion implantation at low temperatures plotted versus the noble metal concentration.

(From Ref. [30].)

Solid line: Pd–Cu–H. Dashed line: Pd–Ag–H. Dotted line: Pd–Au–H.



The superconductivity at least of pure Pd after charging with hydrogen can be reasonably well understood. The hydrogen is implanted at the interstitial lattice sites within the Pd lattice. As a result, the lattice expands slightly. The implantation of the hydrogen essentially leads to additional lattice vibrations, simply because there are more atoms per volume. These additional lattice vibrations strengthen the electron–phonon interaction and thereby favor superconductivity [31].

## 2.4 Fullerides

In 1985, R. F. Curl and R. E. Smalley, as well as H. W. Kroto, discovered one of the most peculiar carbon molecules, the  $C_{60}$  molecule ([Figure 2.6a](#)). In this molecule, termed **fullerene**, 60 carbon atoms are arranged in the form of a “soccer ball.” The name of the fullerenes goes back to the architect Buckminster Fuller, the inventor of the geodesic dome, where the construction elements are arranged like the seams of a soccer ball, similar to the  $C_{60}$  molecule. The  $C_{60}$  molecule and similar structures such as the  $C_{70}$  molecule or the carbon nanotubes belong to a class of materials that is presently rapidly conquering many areas for technical applications.

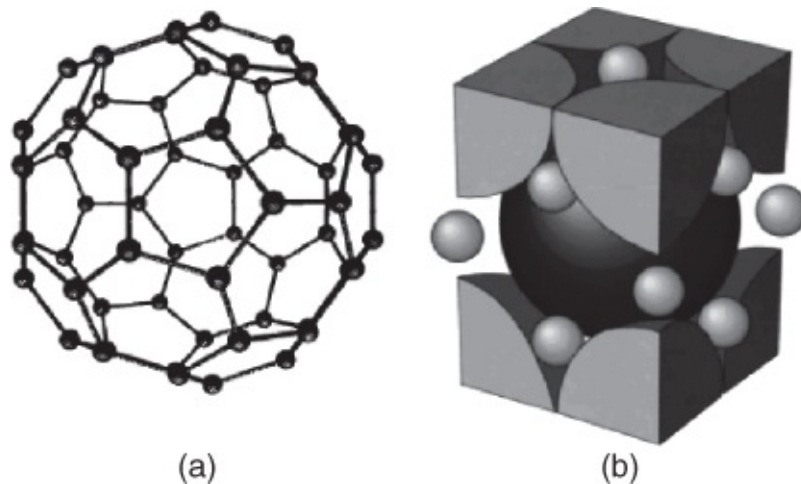


[Figure 2.6](#) (a) Fullerene molecule  $C_{60}$ . (b) Crystal structure of the fullerides [32].

The  $C_{60}$  molecules also can form crystals, which in turn can be doped with different atoms. Then one obtains the “fullerides,” which in some cases are superconducting at surprisingly high temperatures. Here superconductivity was discovered first for the compound  $K_3C_{60}$ , with a transition temperature of about 20 K [33]. In the meantime, we know a number of superconducting fullerides based on the admixture of alkali atoms or of alkaline-earth atoms. Here  $Rb_3C_{60}$  has a value of  $T_c$  of 29.5 K, and the present record under pressure is held by  $Cs_3C_{60}$  with  $T_c = 40$  K. Also for carbon nanotubes imbedded in a zeolite matrix, superconductivity could be observed with a transition temperature of about 15 K [34]. Many properties of the fullerides can be found in the review articles [32, 35, 36].

The crystal structure of the fullerides is shown in [Figure 2.6b](#). We clearly see how the alkali atoms occupy the interstitial lattice sites between the huge  $C_{60}$  molecules. The overall structure is face-centered cubic with a lattice constant of about 1.42 nm.

The fullerides mentioned above are type-II superconductors with coherence lengths near 3 nm and magnetic penetration depths of 200–800 nm. The upper critical fields are correspondingly very high, in the range of 50 T and above. The lower critical field is about 5–12 mT. The superconductivity in these materials is conventional, that is, it is based on  $S = 0, L = 0$  Cooper pairing accomplished by the electron–phonon interaction. Intramolecular vibrations of the  $C_{60}$

molecules appear to be important.

The fullerides and  $\text{MgB}_2$  demonstrate, that, after so many years in which the maximum transition temperature remained fixed at 23 K for  $\text{Nb}_3\text{Ge}$ , now “conventional” superconductors were again found with a transition temperature clearly above 30 K. Furthermore, these materials have technically highly attractive properties such as a very high upper critical field. Hence, it is not only because of the oxide materials that superconductivity is so interesting at present.

## 2.5 Chevrel Phases and Boron Carbides

The composition of the Chevrel phases is  $\text{MMo}_6\text{X}_8$ , where M denotes a metal atom (for example, Sn or Pb) or a rare-earth atom (for example, Dy, Tb, or Gd), and where X stands for sulfur or selenium. The crystal structure is hexagonal-rhombohedral, as shown in [Figure 2.7](#). The M atoms form a nearly cubic lattice, into which the  $\text{Mo}_6\text{X}_8$  units are imbedded.

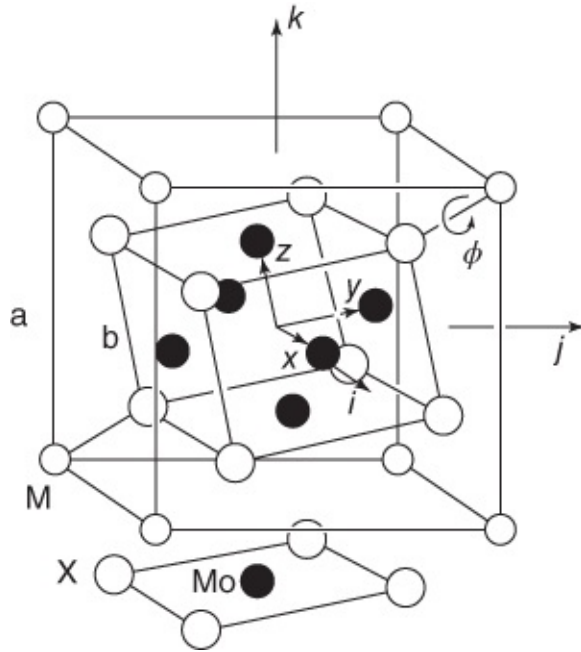


[Figure 2.7](#) The crystal structure of the Chevrel phases [37].

In [Table 2.3](#) we list the transition temperature, the upper critical field, and the characteristic lengths  $\lambda_L$  and  $\xi_{GL}$  for a few substances. A summary of the properties of the Chevrel phases can be found in [M13]. The Chevrel phases are conventional superconductors. However, they have at least two properties that make them highly interesting.

- In some compounds the upper critical field is very high. At low temperatures,  $B_{c2}$  of  $\text{PbMo}_6\text{S}_8$  has a value of 60 T. Because of such high values, the Chevrel phases are interesting for high-magnetic-field applications like the construction of magnets. Unfortunately, the materials are quite brittle. Hence, the fabrication of wires is very difficult.

- In some compounds, into which a rare-earth atom is implanted for M (for example, Dy, Er, Gd, or Tb), below the transition temperature antiferromagnetic ordering of the rare-earth ions occurs in addition to superconductivity. This weakens the superconductivity, but does not destroy it. For the conventional superconductors, the coexistence of magnetic ordering and superconductivity represents a very rare phenomenon. Usually, the (conventional) superconductivity is already destroyed due to the presence of only a few paramagnetic impurities, as we will see in [Section 3.1.4.2](#). An example of a Chevrel phase, in which antiferromagnetism and superconductivity coexist, is  $\text{TbMo}_6\text{S}_8$  with a value of  $T_c$  of 1.65 K. In this case magnetic order is observed below 0.9 K. At the onset of the magnetic order, the upper critical field is reduced, and the temperature dependence of  $B_{c2}$  shows a non-monotonic behavior.
- A further peculiarity is observed in the compound  $\text{HoMo}_6\text{S}_8$ . It becomes superconducting at 2 K. However, below 0.6 K a ferromagnetically ordered state appears in this case, which again destroys the superconductivity. This phenomenon of reentrant superconductivity can also be observed in other superconductors, for example, in the boron carbides, as we will discuss shortly. Other examples are  $\text{La}_{1-x}\text{Ce}_x\text{Al}_2$ , discussed in [Section 2.1](#), or the rhodium borides. For example,  $\text{ErRh}_4\text{B}_4$  becomes superconducting at 9 K. Below 0.93 K the rare-earth ions in this material order ferromagnetically, and the superconductivity disappears again<sup>7</sup> [40].

**Table 2.3** Superconducting properties of the Chevrel phases [[38], M7]

Composition	$T_c$ (K)	$B_{c2}$ (T)	$\lambda_L$ (nm)	$\xi_{GL}$ (nm)
$\text{PbMo}_6\text{S}_8$	15	60	240	2.3
$\text{SnMo}_6\text{S}_8$	12	34	240	3.5
$\text{LaMo}_6\text{S}_8$	7	45	—	3.1
$\text{TbMo}_6\text{S}_8$	1.65	0.2	—	45
$\text{PbMo}_6\text{Se}_8$	3.6	3.8	—	11
$\text{LaMo}_6\text{Se}_8$	11	5	—	9

Transition temperature, upper critical field for  $T = 0$ , London penetration depth, and Ginzburg–Landau coherence length.

The boron carbides [41] are compounds of the form  $\text{RM}_2\text{B}_2\text{C}$ , where R denotes a rare-earth atom (for example, Tm, Er, or Ho), and where M stands for Ni or Pd. The crystal structure of the boron carbide  $\text{LuNi}_2\text{B}_2\text{C}$  is shown in [Figure 2.8](#). Some properties of the superconducting state are listed in [Table 2.4](#). Some of these materials have transition temperatures above 15 K. For example,  $\text{YPd}_2\text{B}_2\text{C}$  and  $\text{LuNi}_2\text{B}_2\text{C}$  have a transition temperature of 23 and 16.6 K, respectively.

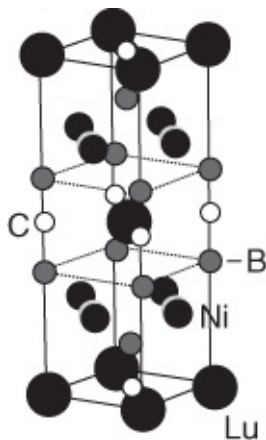


**Figure 2.8** The crystal structure of the boron carbide  $\text{LuNi}_2\text{B}_2\text{C}$ .

(Reprinted from Ref. [42] by courtesy of IOP.)

**Table 2.4** Superconducting properties of some boron carbides

Composition	$T_c$ (K)	$B_{c2}$ (T)	$\lambda_L$ (nm)	$\xi_{GL}$ (nm)	Reference
$\text{YPd}_2\text{B}_2\text{C}$	23				
$\text{LuNi}_2\text{B}_2\text{C}$	16.6	7	70–130	7	[26]
$\text{YNi}_2\text{B}_2\text{C}$	15.5	6.5	120–350	6.5	[26]
$\text{TmNi}_2\text{B}_2\text{C}$	11				
$\text{ErNi}_2\text{B}_2\text{C}$	10.5	1.4	750	15	[43]
$\text{HoNi}_2\text{B}_2\text{C}$	7.5				

Transition temperature, upper critical field for  $T = 0$ , London penetration depth, and Ginzburg–Landau coherence length.

Also for the boron carbides, which are conventional superconductors, the coexistence of superconductivity and antiferromagnetism can be observed. Similar to the case of  $\text{MgB}_2$ , different energy bands appear to contribute differently to Cooper pairing. In the case of  $\text{HoNi}_{1-x}\text{Co}_x\text{B}_2\text{C}$ , the phenomenon of reentrant superconductivity appears. In [Figure 2.9](#) this phenomenon is shown in terms of the temperature dependence of the resistivity  $\rho$ . For  $x = 0.005$ ,  $\text{HoNi}_{1-x}\text{Co}_x\text{B}_2\text{C}$  becomes superconducting at 7 K. At 5.5 K normal conductivity appears again. However, at about 5 K another transition into the superconducting state is observed, and for still lower temperatures the material remains superconducting.

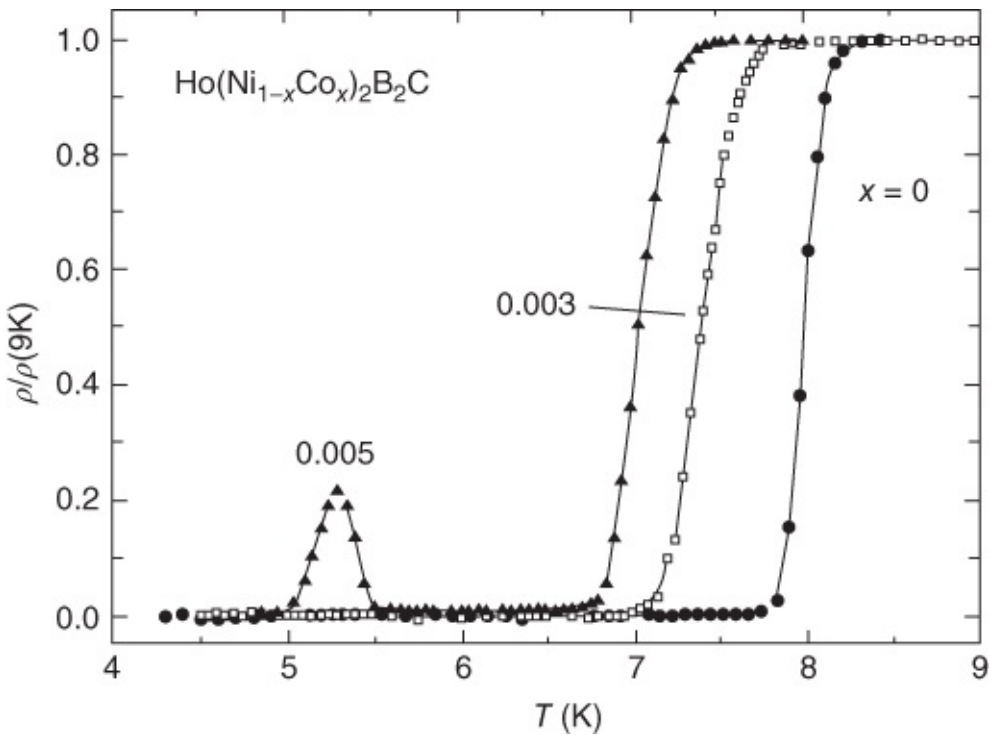


**Figure 2.9** Temperature dependence of the normalized resistivity of  $\text{HoNi}_{1-x}\text{Co}_x\text{B}_2\text{C}$ . For  $x = 0.005$  reentrant superconductivity is observed.

(Reprinted from Ref. [42] by courtesy of IOP.)

## 2.6 Heavy-Fermion Superconductors

At the end of the 1970s, a transition to superconductivity at about 0.5 K was observed for the compound  $\text{CeCu}_2\text{Si}_2$  [44]. The superconductivity of this compound was very surprising, since in this metallic conductor the effective mass of the electrons is a few hundred up to 1000 times larger than the free-electron mass. These values of the mass are obtained from the extremely large electronic density of states at the Fermi energy. It results from the interaction between the mobile electrons and the magnetic moments localized at the lattice sites. The name “heavy-fermion materials” indicates these extremely large mass values. Today we know a number of such materials. In [Table 2.5](#) we have listed the superconducting properties of a few of them.

**Table 2.5** Superconducting properties of some heavy-fermion superconductors

Composition	$T_c$ (K)	Effective mass in units of the free electron mass	$B_{c2}$ (T)	$\lambda_L$ (nm)	$\xi_{GL}$ (nm)
URu <sub>2</sub> Si	1.5 K	140	8	1000	10
CeCu <sub>2</sub> Si <sub>2</sub>	1.5	380	1.5– 2.5	500	9
UPt <sub>3</sub>	1.5	180	1.5	>1500	20
UBe <sub>13</sub>	0.85	260	10	1100	9.5
UNi <sub>2</sub> Al <sub>3</sub>	1	48	<1	330	24
UPd <sub>2</sub> Al <sub>3</sub>	2	66	2.5–3	400	8.5

Transition temperature, upper critical field for  $T = 0$ , London penetration depth, and Ginzburg–Landau coherence length.

From Ref. [45].

In our discussion of superconducting materials, the heavy-fermion superconductors represent the first class of substances with unconventional Cooper pairing [46]. Similar to the Chevrel phases and the boron carbides, discussed in the previous section, in this case also magnetic order and superconductivity appear together. However, in the former cases, the two ordered states just appear side by side. On the other hand, in the heavy-fermion superconductors, the large value of the effective mass results from magnetic interactions. Furthermore, the Cooper pairs are formed by exactly those electrons which in the case of uranium compounds predominantly originate from the 5f orbitals of uranium. At least in the case of UPd<sub>2</sub>Al<sub>3</sub>, it has been shown that the pairing is accomplished by magnetic interactions and not by the electron–phonon interaction [47].

As we have discussed already in [Section 2.1](#), in the heavy-fermion systems the interaction between the spin of the charge carriers and their orbital angular momentum is very strong. In this case, the superconducting state should be classified according to its *parity*, which can be even or odd. In the heavy-fermion superconductors, both parities can be observed.

The system most completely studied is UPt<sub>3</sub> [48]. Its hexagonal crystal structure is shown in [Figure 2.10](#). Below 5 K, UPt<sub>3</sub> is antiferromagnetic, and below 1.5 K it becomes superconducting. Here, one finds that in a temperature–magnetic field diagram, there exist three different superconducting phases with different thermodynamic properties. This fact already shows that s-wave pairing cannot occur, since in this case there would be only one possible orientation of the spin and of the angular momentum. States with even and also with odd parity are being discussed, including the spin-triplet pairing [126], if the spin-orbit coupling is neglected.

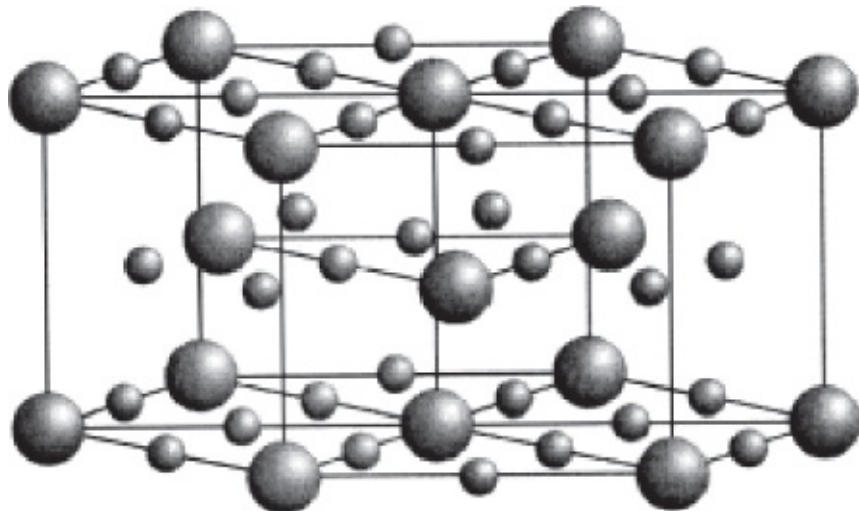


**Figure 2.10** Crystal structure of the heavy-fermion superconductor  $\text{UPt}_3$  [48].

It appears that odd parity or spin-triplet pairing also exists in  $\text{UNi}_2\text{Al}_3$  [50], and also possibly in  $\text{UBe}_{13}$  [45]. On the other hand, the compounds  $\text{CeCu}_2\text{Si}_2$  and  $\text{URu}_2\text{Si}_2$  display a strongly anisotropic superconducting state with even parity. The same is found in  $\text{UPd}_2\text{Al}_3$  although the crystal structure of this compound is the same as that of  $\text{UNi}_2\text{Al}_3$  [50]. However, the magnetic order in the two systems is different. In  $\text{UPd}_2\text{Al}_3$  there is antiferromagnetic order, which is commensurable with the lattice sites of the uranium atoms. On the other hand, in  $\text{UNi}_2\text{Al}_3$  there exists a spin density wave, which is incommensurable with the crystal structure.

$\text{UGe}_2$  and  $\text{URhGe}$  are other uranium compounds. At pressures in the range 10–15 kbar,  $\text{UGe}_2$  becomes superconducting below 1 K. Here, the magnetic moments of the uranium are ordered ferromagnetically. Hence, in this material, ferromagnetism and superconductivity coexist. It is very likely that also in  $\text{UGe}_2$  the Cooper pairs form a spin triplet [51]. The same applies to  $\text{URhGe}$  [52]. At normal pressure, this material becomes superconducting below 0.25 K. Its behavior in a magnetic field is unusual. In a magnetic field of 2 T superconductivity breaks down. However, it returns again at fields between 8 and 12.5 T, in which range transition temperatures up to 0.4 K are reached [53]. An exact explanation of this behavior is still missing.

## 2.7 Natural and Artificial Layered Superconductors

In [Section 1.5.1](#) we have discussed the layer sequence of superconductor – insulator or normal metal – superconductor in terms of the Josephson junction. By an obvious generalization we arrive at multilayers, in which different kinds of layers periodically alternate. There are a large number of possible combinations of different superconducting and non-superconducting materials. We can combine different superconductors, or we can fabricate alternating sequences of layers of superconducting and non-superconducting materials. The latter can be normal conducting metals or electrical insulators. They can also be magnetic or non-magnetic. Obviously, thin-film technology opens the door for the fabrication of many superconducting

systems with highly different properties and of strong interest for basic science. Many properties of such artificial superconducting multilayers are discussed in the review articles [54, 41]. In this book, we will also deal with some properties of these superconducting layered structures.

Materials in which the superconductivity spatially varies within the crystal structure itself represent a particularly interesting class of layered superconductors. We have already discussed magnesium diboride ( $MgB_2$ ) with its layered crystal structure. However, in this case, the Ginzburg–Landau coherence length perpendicular to the layers is much larger than the distance between the layers. Hence, the superconducting state averages over the total crystal structure, and in the final analysis we have again a spatially homogeneous, but also anisotropic, state.

However, this situation changes if the coherence length reaches the range of the layer separation or even less. Now the superconducting state starts to vary spatially, and in the extreme case we have an atomic sequence of superconducting and non-superconducting layers, in which the supercurrents flowing perpendicular to the layers represent Josephson currents. Such materials form stacks of Josephson junctions in a natural way.

The study of natural layered superconductors started in the middle of the 1960s with the dichalcogenides (compounds such as  $NbSe_2$  or  $TaS_2$ ) [55, 56]. They can be written in a general way as  $MX_2$ , where M stands for a transition metal and X for Se, S, or Te. A typical crystal structure is shown in [Figure 2.11](#).

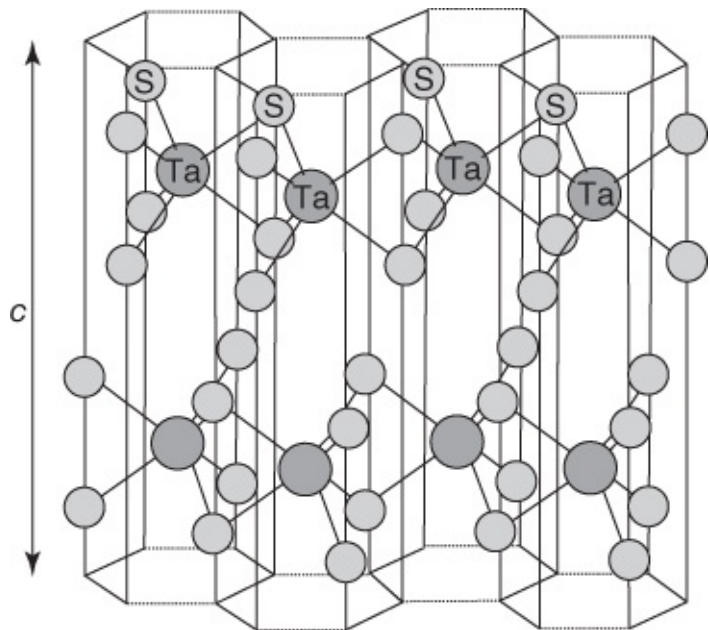
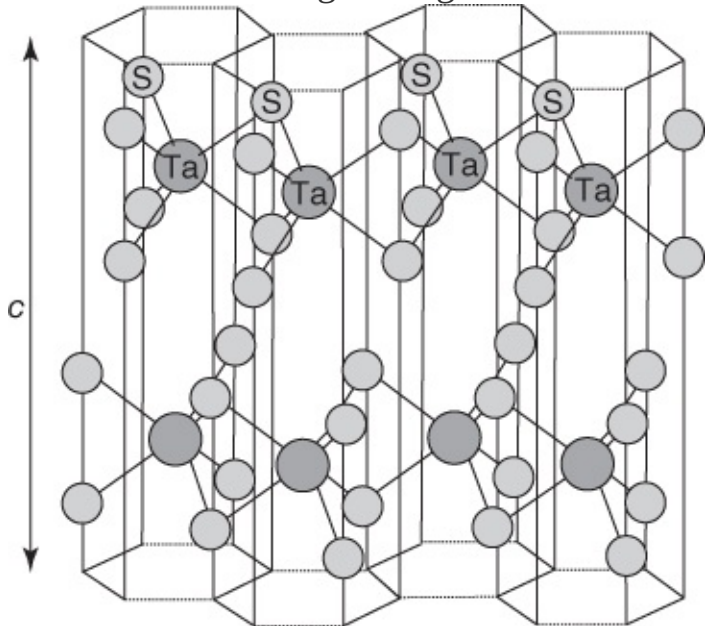


**Figure 2.11** Crystal structure of the layered superconductor 2H-TaS<sub>2</sub>.

(From Ref. [57].)

Here the “H” stands for hexagonal, and the “2” indicates that there are two different orientations of the TaS<sub>2</sub> molecules in the unit cell. The hexagonal unit cells are indicated by the dotted lines. The length along the *c*-axis is about 1.2 nm.



In the dichalcogenides, the individual MX<sub>2</sub> layers are chemically bound to each other only very weakly by means of van der Waals forces. Hence, additional atoms or molecules, including very large organic molecules such as pyridine, can be inserted (“intercalated”) between these layers. In this way, it is possible to strongly enhance the distance between the MX<sub>2</sub> layers, resulting in a reduction of the superconducting coupling between the layers and in the formation of a natural layered superconductor. In [Table 2.6](#) some properties of non-intercalated and intercalated dichalcogenides are listed.

**Table 2.6** Properties of the superconducting state of some dichalcogenides and their intercalates

Composition	$T_c$ (K)	$B_{c2\perp}$ (T)	$B_{c2\parallel}^a$ (T)	$\xi_{\parallel}$ (nm)	$\xi_{\perp}$ (nm)	$\lambda_{\parallel}$ (nm)	$\lambda_{\perp}$ ( $\mu$ m)	$s$ (nm)
$\text{NbSe}_2$	7	4	18	7–8	2.5	69–140	1.5	0.63
$\text{TaS}_1\text{Se}_1$	3.7	0.9	13	12	2	—	—	0.61
$\text{TaS}_{1.2}\text{Se}_{0.8}$	3.9	1.3	23	10	1.1	—	—	0.64
$\text{TaS}_1\text{Se}_1$ (Pyridin)	1.5	0.26	7	18	2.5	—	—	—
$\text{TaS}_2$ (Pyridin)	3.25	0.14	>16	30	0.6	130	100–500	1.18

<sup>a</sup> Extrapolated to 0 K from temperatures slightly below  $T_c$ .

Transition temperature, critical fields for field orientations perpendicular and parallel to the layers, Ginzburg–Landau coherence lengths and magnetic penetration depths for fields parallel and perpendicular to the layers, and interlayer distance  $s$ .

From Ref. [56, 58–60].

For the compound  $\text{NbSe}_2$ , the coherence length  $\xi_{\perp}$  perpendicular to the layers is about 2.5 nm, which is much larger than the interlayer distance of 0.63 nm. Similar behavior can also be seen for the non-intercalated compounds listed in the table. However, for the materials intercalated with pyridine,  $\xi_{\perp}$  is smaller than the interlayer distance. We can speak of a natural layered superconductor, in which the density of the superconducting charge carriers is spatially modulated.

In the 1970s the dichalcogenides received much interest [36], although these materials barely reached the limit of the natural layered superconductors. The large breakthrough associated with the discovery of the high-temperature superconductors also happened in the area of the natural layered superconductors. They will be discussed in the following section. Compounds such as  $\text{Bi}_2\text{Sr}_2\text{CaCu}_2\text{O}_8$  in an almost ideal way represent stacks of natural Josephson junctions, which show much interesting physics and are highly promising for applications.

In addition to the high-temperature superconductors, also a number of organic materials form layered superconductors. We will discuss these compounds in [Section 2.10](#).

## 2.8 The Superconducting Oxides

Oxides are usually understood as electrically insulating materials, and this is correct in many cases. It is even more surprising that with the cuprates it is exactly this class of materials that produced the superconductors with the highest known transition temperatures. In the following, we will concentrate on these materials. However, at the end, we will also briefly discuss additional superconducting alloys such as the bismuth oxides and the ruthenium oxides.

### 2.8.1 Cuprates

At the present time, a large number of superconducting cuprates are known. Some of these

compounds can be prepared very easily from their starting materials [61] (for example, from copper oxide, bismuth oxide, strontium oxide, and calcium carbonate in the case of  $\text{Bi}_2\text{Sr}_2\text{CaCu}_2\text{O}_8$ ). Other compounds can be formed only in reaction processes at high pressures [62–64]. In some cases only ceramics with a polycrystalline structure can be obtained. However, in many cases single crystals [65] and thin films [66] can also be produced with high quality.

The crystal structure of the cuprates goes back to that of perovskite ( $\text{CaTiO}_3$ ), shown schematically in [Figure 2.12](#). Here we have the unit  $\text{ABX}_3$ , where the B atoms are surrounded by the X atoms in the form of octahedra.

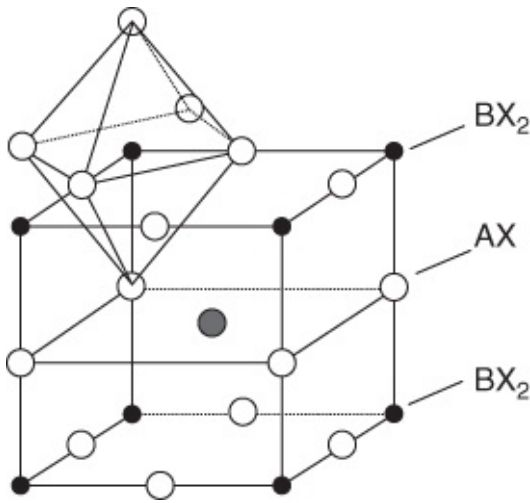


[Figure 2.12](#) General crystal structure of the perovskite compounds.

[Figure 2.13](#) presents a comparison between the crystal structures of the two cuprates  $\text{YBa}_2\text{Cu}_3\text{O}_7$  and  $\text{Bi}_2\text{Sr}_2\text{CaCu}_2\text{O}_8$ . Sometimes, the first compound is denoted as “Y123” (because of the stoichiometry of the elements) or as “YBCO” (because of the initial letters of the elements). Correspondingly, the second compound is also referred to as **Bi2212** or **BSCCO**. Both Y123 and Bi2212 form layered structures, in which layers of copper oxide alternate with intermediate layers of other elements.

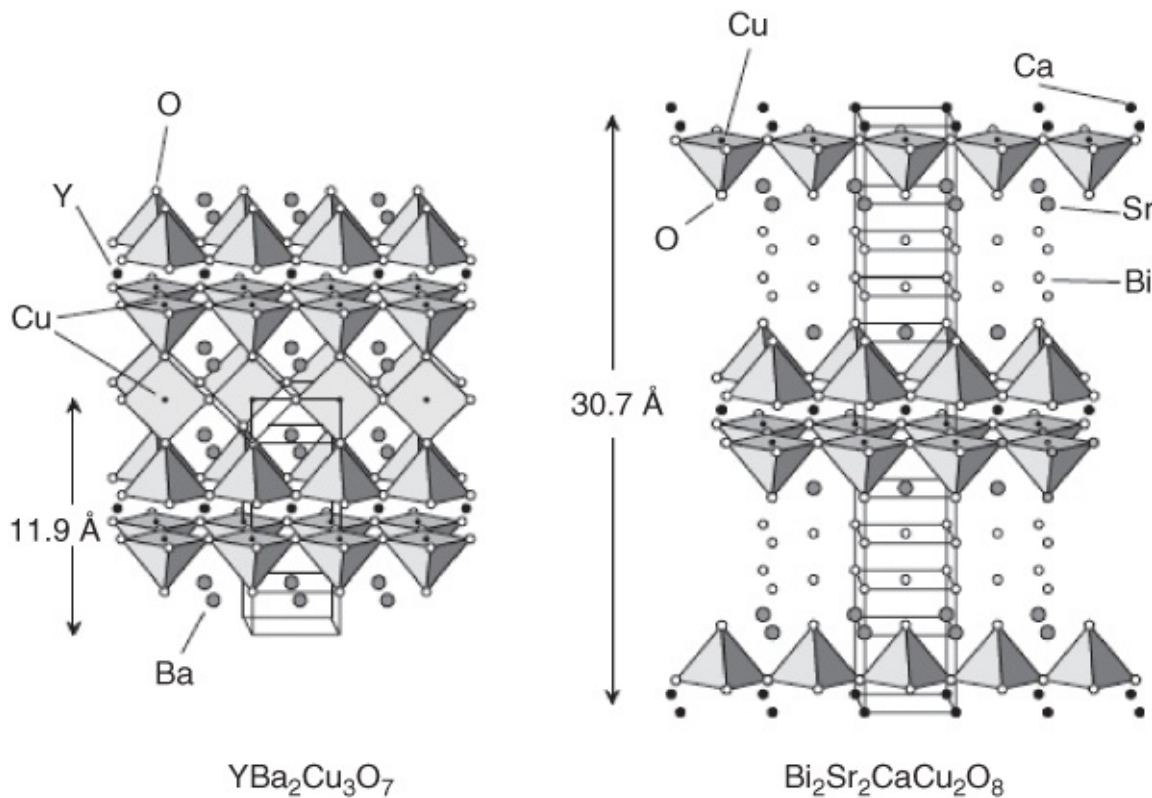


**Figure 2.13** Crystal structures of the two high-temperature superconductors  $\text{YBa}_2\text{Cu}_3\text{O}_7$  and  $\text{Bi}_2\text{Sr}_2\text{Ca}\text{Cu}_2\text{O}_8$ .

We start by looking at the copper oxide planes. In both substances, two of these planes are located close to each other, with a separation of about 0.3 nm. Within a plane, each copper ion is surrounded by a square of oxygen ions, resulting in the unit  $\text{CuO}_2$ . Perpendicular to the layers (along the crystallographic *c* direction) above each Cu ion, there exists an additional oxygen ion (so-called apex oxygen) such that each Cu together with the neighboring oxygen constitutes a tetrahedron. The tetrahedra are joined together by means of their basal planes. In the case of Y123, there is yttrium between the closely neighboring  $\text{CuO}_2$  planes, and in the case of Bi2212 there is calcium.

In the case of Y123, a  $\text{CuO}_2$  double layer is followed by a layer of barium oxide, by a layer of CuO (where a chain-like sequence Cu–O–Cu–O... is formed along the crystallographic *b*-direction; along the *a*-axis the oxygen between the copper ions is missing), and by an additional layer of BaO. In the case of Bi2212, between the  $\text{CuO}_2$  double layers, there are two layers of strontium oxide and two layers of bismuth oxide.

The crystal structure of the other high-temperature superconductors is very similar. In each case there appear planes of  $\text{CuO}_2$ , some of which can be located very close to each other. Correspondingly, we find single, double, and triple layers, and so on, of  $\text{CuO}_2$ . Here the outer layers can contain an apex oxygen ion, but not necessarily. There even exist cuprates in the form of compounds such as  $(\text{Sr},\text{Ca})\text{CuO}_2$  and  $(\text{Sr},\text{La})\text{CuO}_2$  in which all  $\text{CuO}_2$  layers have a mutual distance of about 0.35 nm (“infinite layers”) [67].

These  $\text{CuO}_2$  layers represent the important building blocks in which the high-temperature superconductivity takes place. Here the compounds containing three closely spaced  $\text{CuO}_2$  planes show the highest transition temperatures. However, the layers between the  $\text{CuO}_2$  planes not only stabilize the crystal structure but also act as the charge reservoir, supplying the charge carriers to the copper oxide, which then combine into the Cooper pairs. In this context, in particular, the oxygen content of the samples plays an important role.

Let us look at the case of YBCO, writing the oxygen content as  $6 + x$ , that is,  $\text{YBa}_2\text{Cu}_3\text{O}_{6+x}$ . The temperature versus  $x$  phase diagram is shown in [Figure 2.14](#). Compared to  $\text{YBa}_2\text{Cu}_3\text{O}_7$ , for  $x = 0$  the oxygen ions in the Cu–O chains are missing. The material turns out to be an antiferromagnetic insulator. The antiferromagnetic order sets in below the Néel temperature of about 500 K.

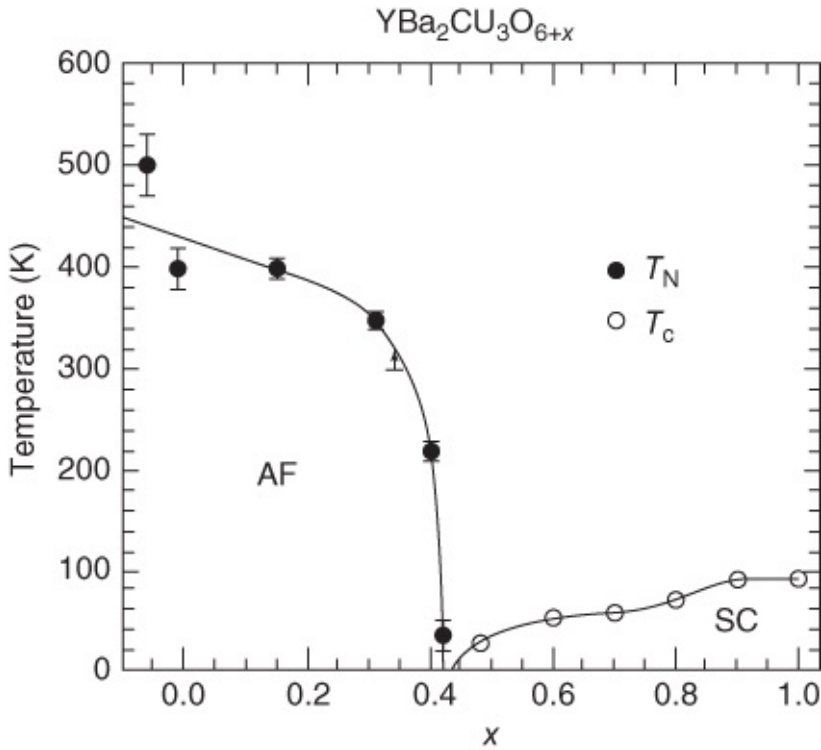


**Figure 2.14** Phase diagram (temperature vs oxygen content  $x$ ) of the cuprate  $\text{YBa}_2\text{Cu}_3\text{O}_{6+x}$ . In the state “AF,” the material is ordered antiferromagnetically and is electrically insulating. In the region “SC” the material is superconducting [49].

Already this state is by no means easy to understand. One needs to take into account the repulsive interaction between the electrons, as we will see more accurately in [Section 3.2.2](#). Here we just note that, ignoring this interaction, the material would have to be a metal. The  $d_{x^2-y^2}$  orbitals of copper are each occupied by one electron. Within the planes, these orbitals strongly overlap with the  $p_x$  and the  $p_y$  orbitals of oxygen. However, two electrons with opposite spin can be accommodated in each of these  $d_{x^2-y^2}$  orbitals. Hence, one would expect a half-filled energy band and metallic conductivity.

For example, by heating in air or oxygen, one is able to introduce additional O atoms into the

material, which then gradually build up the chains. Each oxygen atom attracts two electrons, resulting in the formation of an  $O^{2-}$  ion. Both electrons partly originate from the  $CuO_2$  planes. Hence, compared to the half-filled band at  $x = 0$ , in the  $CuO_2$  planes there are now fewer electrons than in  $YBa_2Cu_3O_6$ . In this way, we have generated holes, that is, missing electrons, in the  $CuO_2$  planes.

With increasing hole concentration, the antiferromagnetism becomes weaker and the Néel temperature decreases. At  $x \approx 0.4$ , the antiferromagnetism vanishes. With increasing hole concentration, the material becomes electrically conducting and superconductivity sets in, with the transition temperature increasing from small values up to a maximum value of about 90 K a little below  $x = 1$ . Furthermore, between  $x \approx 0.5$  and 0.75, there exists a plateau with a value of  $T_c$  of about 60 K. In this “60-K phase” the oxygen atoms of the chains are partially ordered [68]. In the case of YBCO, oxygen concentrations larger than  $x = 1$  can be achieved only with great difficulty.

In the case of  $Bi_2Sr_2CaCu_2O_8$ , very similar to  $YBa_2Cu_3O_6$ , one finds that the compound is an antiferromagnetic insulator. In this compound, one can introduce additional oxygen ions between the BiO layers. Hence, one should start from the unit  $Bi_2Sr_2CaCu_2O_{8+x}$ . Similar to the case of YBCO, with increasing  $x$  the Néel temperature at first decreases and then vanishes a little below  $x = 0.05$ . At a slightly larger oxygen content, superconductivity sets in. The transition temperature at first is very small and then increases up to about  $x = 0.16$ ,  $T_c$  reaching a value of about 90 K. For larger oxygen concentrations, the superconductivity becomes weaker again, and it vanishes again at  $x \approx 0.27$ . For larger hole concentrations,  $Bi_2Sr_2CaCu_2O_{8+x}$  is a normal conductor at all temperatures.

In BSCCO the additional oxygen atoms extract the electrons essentially from the  $CuO_2$  planes. An excess oxygen content  $x$  then corresponds to just  $x$  holes per Cu ion. Hence, for optimum doping, we have about 0.16 holes per Cu site.

The situation discussed above for YBCO and BSCCO is typical for many high-temperature superconductors. There always exists an optimum charge-carrier concentration. The transition temperature decreases if we move away from this value. The charge-carrier concentration can also be changed by substituting some constituents with elements having a different valence. For instance, in the case of the compound  $La_{2-x}Sr_xCuO_4$ , this can be done by replacing the trivalent lanthanum with the divalent strontium. In [Figure 2.15](#), we show the corresponding phase diagram. Also in this case at  $x = 0$ , one observes at first an antiferromagnetic, insulating state, in which holes are generated in the  $CuO_2$  planes by the insertion of Sr, here one hole per Sr atom. Again, for hole concentrations between 0.05 and 0.3, one finds superconductivity, where the maximum transition temperature is reached slightly above 0.15 holes per Cu site.

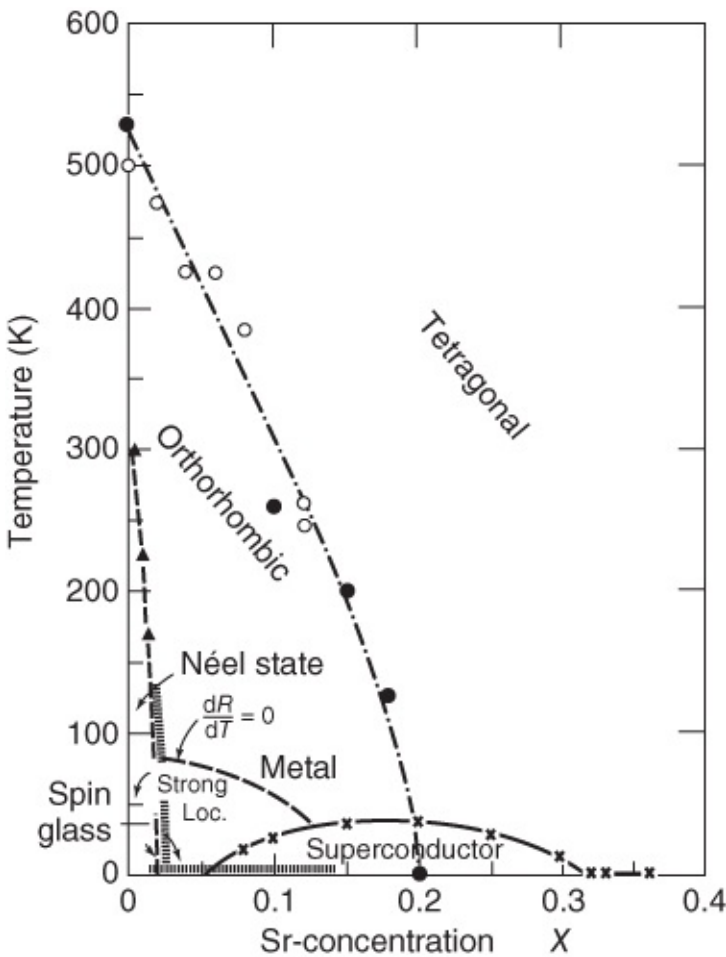


**Figure 2.15** Phase diagram (temperature vs Sr content  $x$ ) of the cuprate  $\text{La}_{2-x}\text{Sr}_x\text{CuO}_4$  [69].

In [Figure 2.15](#) a number of other properties of the material are included, such as the crystal structure, which is tetragonal for large values of  $x$  and  $T$ , and which then changes into an orthorhombic structure. At Sr concentrations slightly below  $x = 0.05$ , there is a complex magnetic order denoted as “spin glass” in the diagram. In addition, the diagram shows a dashed line, below which the resistance of the samples increases with decreasing temperature.

Whether the number of free charge carriers is regulated by oxygen concentration or by the substitution of some elements,<sup>8</sup> in all cases we can think of the high-temperature superconductors in terms of doped insulators in analogy to the doping of semiconductors. At this stage it is reasonable to ask whether there also exist electron-doped cuprates, that is, substances into which additional electrons were inserted into the  $\text{CuO}_2$  planes, compared to the half-filled band. Such compounds, indeed, do exist, where in the electron-doped case at first the antiferromagnetic state becomes weaker with increasing charge-carrier concentration, and then superconductivity appears in a certain concentration range of the charge carriers. As an example of an electron-doped high-temperature superconductor, we mention  $(\text{Nd}_{1-x}\text{Ce}_x)_2\text{CuO}_4$ , in short NCCO. In this material the maximum transition temperature of about 25 K is reached at  $x = 0.08$ . Instead of Nd, other elements such as Pr can be used. The infinite-layer materials can be either electron- or hole-doped. With  $(\text{Sr},\text{La})\text{CuO}_2$  we deal with the former case, and with  $(\text{Sr},\text{Ca})\text{CuO}_2$  we deal with the latter case.

However, one finds that the phase diagram of similar crystal structures is distinctly asymmetric with respect to electron and hole doping. In the electron-doped case, the antiferromagnetic phase is more stable and the superconducting phase is less pronounced compared to the hole-doped case. In the electron-doped case, the maximum transition temperature and the concentration interval of the charge carriers, in which superconductivity is observed, is clearly smaller. For example, with  $(\text{Sr},\text{La})\text{CuO}_2$  one reaches a maximum transition temperature of about 44 K, whereas with  $(\text{Sr},\text{Ca})\text{CuO}_2$  the maximum value is above 90 K.

In [Table 2.7](#) we list several characteristic superconducting properties of different cuprates. The cuprates are type-II superconductors with a series of highly unusual properties. At low temperatures, the Ginzburg–Landau coherence lengths parallel to the layers are 1.5–3 nm, which corresponds to about 5–10 lattice constants. However, perpendicular to the layers in many substances, the coherence length is extremely small and is about 0.3 nm or less. Hence, the superconductivity is strongly concentrated on the  $\text{CuO}_2$  layers, that is, in many cases we have natural layered superconductors (see [Section 2.7](#)). Therefore, the superconducting properties strongly depend on whether the supercurrents flow only parallel to the layers or also perpendicular to them. As a result, the magnetic penetration depth is highly anisotropic. If the magnetic field is applied perpendicular to the layers, the shielding currents flow within the layers, and the corresponding penetration depth  $\lambda_{ab}$  is typically 150–300 nm. However, for a magnetic field orientation parallel to the layers, one observes much larger values of  $\lambda_c$ . For  $\text{YBa}_2\text{Cu}_3\text{O}_7$ ,  $\lambda_c$  is about 800 nm, resulting in a ratio  $\lambda_c/\lambda_{ab}$  of 5–8. However, for the bismuth compounds, depending on the charge-carrier concentration of the samples,  $\lambda_c$  increases up to values between a few and 100  $\mu\text{m}$  or larger. Hence, one can observe a huge anisotropy ratio  $\lambda_c/\lambda_{ab}$  up to more than 1000.

**Table 2.7** Characteristic data of different cuprate superconductors

Composition	$T_{\text{c,max}}$ (K)	$\lambda_{ab}$ (nm)	$\lambda_c$ ( $\mu\text{m}$ )	$\xi_{ab}$ (nm)	$\xi_c$ (nm)	$B_{\text{c}2\perp}$ (T)	$B_{\text{c}2\parallel}$ (T)	Reference
$\text{La}_{1.83}\text{Sr}_{0.17}\text{CuO}_4$	38	100	2–5	2–3	0.3	60	—	[71]
$\text{YBa}_2\text{Cu}_3\text{O}_{7-x}$	93	150	0.8	1.6	0.3	110	240	[72]
$\text{Bi}_2\text{Sr}_2\text{CuO}_{6+x}$	13	310	0.8	3.5	1.5	16–27	43	[73]
$\text{Bi}_2\text{Sr}_2\text{CaCu}_2\text{O}_{8+x}$	94	200–300	15–150	2	0.1	>60	>250	[70]
$\text{Bi}_2\text{Sr}_2\text{Ca}_2\text{Cu}_3\text{O}_{10+x}$	107	150	>1	2.9	0.1	40	>250	[74]
$\text{Tl}_2\text{Ba}_2\text{CuO}_{6+x}$	82	80	2	3	0.2	21	300	[75–77]
$\text{Tl}_2\text{Ba}_2\text{CaCu}_2\text{O}_{8+x}$	97	200	>25	3	0.7	27	120	[74, 75, 78]
$\text{Tl}_2\text{Ba}_2\text{Ca}_2\text{Cu}_3\text{O}_{10+x}$	125	200	>20	3	0.5	28	200	[79, 80]
$\text{HgBa}_2\text{CuO}_{4+x}$	95	120–200	0.2–0.45	2	1.2	72	125	[81]
$\text{HgBa}_2\text{CaCu}_2\text{O}_{6+x}$	127	205	0.8	1.7	0.4	113	450	[81]
$\text{HgBa}_2\text{Ca}_2\text{Cu}_3\text{O}_{8+x}$	135	130–200	0.7	1.5	0.19	108	—	[81–83]
$\text{HgBa}_2\text{Ca}_3\text{Cu}_4\text{O}_{10+x}$	125	160	7	1.3–1.8	—	100	>200	[84, 85]
$\text{Sm}_{1.85}\text{Ce}_{0.15}\text{CuO}_{4-y}$	11.5	—	—	8	1.5	—	—	[86]
$\text{Nd}_{1.84}\text{Ce}_{0.16}\text{CuO}_{4-y}$	25	72–100	—	7–8	0.2–0.3	5–6	>100	[87, 88]

Maximum transition temperature, magnetic penetration depths  $\lambda_{ab}$  and  $\lambda_c$  for applied magnetic fields perpendicular and parallel to the layers, respectively, as well as the Ginzburg–Landau coherence lengths  $\xi_{ab}$  and  $\xi_c$  parallel and perpendicular to the  $\text{CuO}_2$  layers, respectively. Also the upper critical fields for field orientations perpendicular and parallel to the planes, respectively, are given. In some cases, at low temperatures the upper critical fields are extremely high, and frequently they were extrapolated to low temperatures from the slope  $dB_{\text{c}2}/dT$  near the transition temperature.

In these extremely anisotropic compounds, the transport currents perpendicular to the layers flow as Josephson currents. Therefore, these materials represent intrinsic stacks of Josephson junctions already because of their crystal structure. Parallel to the layers the coherence lengths amount to only a few lattice constants. Therefore, the superconductivity is weakened at crystal defects such as grain boundaries, and such defects can also act as Josephson junctions.

Due to the very small coherence lengths and the high transition temperatures, the ratio of the condensation energy of the superconducting phase within a coherence volume  $\xi_{ab}^2 \xi_c$  and the thermal energy  $k_B T$  can become relatively small, as we have discussed already in [Section 1.4](#).

Therefore, in high-temperature superconductors, the influence of thermal fluctuations upon the superconducting state is unusually strong, leading to a number of properties that are unknown in the classical superconductors. For example, in superconducting rings at not extremely low temperatures, the permanent currents decay as a function of time. We will return to this subject in [Section 5.3.2](#).

Finally, the Cooper pairing itself is unconventional. The pairs form spin singlets where the angular momentum assumes the value  $2\hbar$ . The exact pairing mechanism is still unknown. However, it is likely that magnetic interactions play an important role and lead to the Cooper pairing.

We see that the cuprates are distinguished by at least three highly interesting and unusual properties: their high value of  $T_c$ , the atomically small coherence lengths, and the unconventional pairing mechanism. These combinations clearly are the reason for the strong present research interest in these materials.

## 2.8.2 Bismuthates, Ruthenates, and Other Oxide Superconductors

Already in the mid-1960s, Bernd Matthias and his coworkers [89] had started a systematic study of the metallic oxides. They looked at substances based on the oxides of the transition metals, such as W, Ti, Mo, and Bi. In this context they discovered extremely interesting superconductors, such as those in the Ba–Pb–Bi–O system. However, they did not find high transition temperatures; in  $\text{BaPb}_{0.75}\text{Bi}_{0.25}\text{O}_3$  they did observe a value of  $T_c$  of 13 K [90].

Following the discovery of the cuprates, the search for oxides that do not contain copper was intensified. We mention the material  $\text{LiTiO}_2$  with  $T_c = 12$  K [91], the crystal structure of which is based on that of spinel, as well as the compound  $\text{Ba}_{1-x}\text{K}_x\text{BiO}_3$ , showing for  $x = 0.4$  a transition temperature up to 35 K [92, 93]. The crystal structure of  $\text{Ba}_{1-x}\text{K}_x\text{BiO}_3$  is derived from that of the perovskite structure, which was shown in [Figure 2.12](#) for the general structure  $\text{ABO}_3$ . In the case of the bismuthates, Bi takes up the role of the B atoms. As far as we know,  $\text{Ba}_{1-x}\text{K}_x\text{BiO}_3$  is a conventional type-II superconductor ( $\lambda_L = 220$  nm,  $\xi_{GL} = 3.7$  nm, and  $B_{c2} = 23$  T [94]), in which the Cooper pairs form a spin-singlet state with zero angular momentum.

In contrast to this, the ruthenate  $\text{Sr}_2\text{RuO}_4$ , discovered in 1994 by Maeno and coworkers [95, 96], appears to be an unconventional spin-triplet superconductor [97] with an orbital angular momentum of  $1\hbar$  (p wave) [98]. Depending on the crystal purity,  $\text{Sr}_2\text{RuO}_4$  has transition temperatures between 0.5 and 1.5 K. In spite of this low value of the transition temperature, the unconventional superconductivity in this material has generated a lot of interest and has led to a large number of publications.

$\text{Sr}_2\text{RuO}_4$  has the same crystal structure as the cuprate  $(\text{La},\text{Ba})_2\text{CuO}_4$  (see [Figure 2.16](#)). Therefore, it is well suited for a comparative study regarding the mechanism of superconductivity in these two materials. The material is a type-II superconductor with an upper critical field between 150 and 650 G, depending on the value of  $T_c$  and measured for the

field oriented perpendicular to the layers [99]. Measured parallel to the layers, the critical field is about 10 times larger. The Ginzburg–Landau coherence length derived from this is 55–150 nm parallel to the Ru layers. Perpendicular to the Ru layers, the coherence length ranges near 4 nm. Hence, it is much larger than the distance between the Ru layers [100]. For the London penetration depth, one finds values around 190 nm [101].

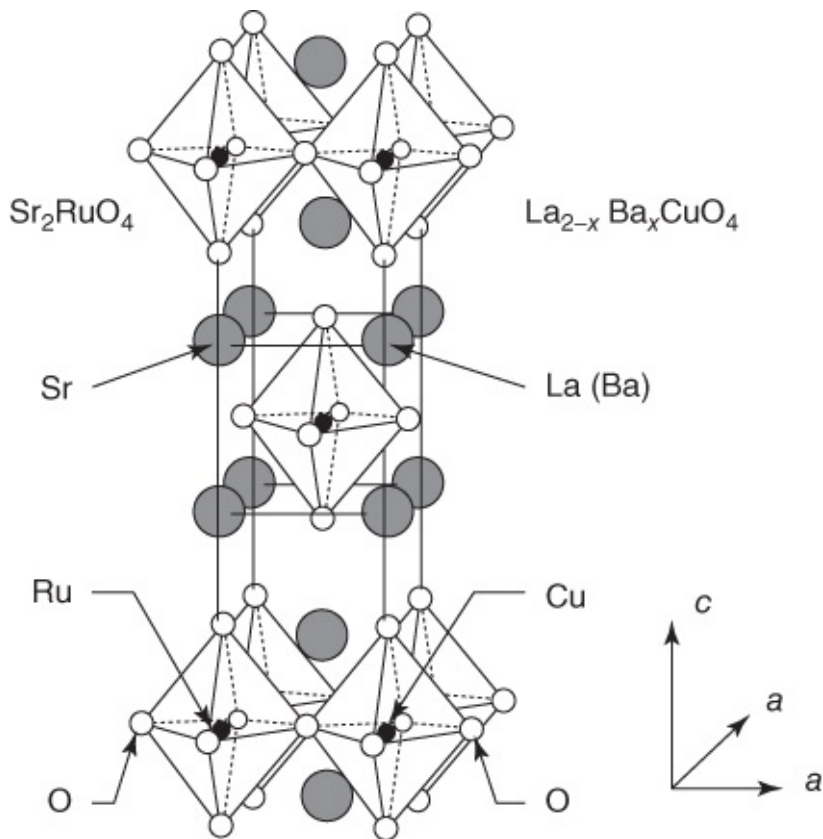


**Figure 2.16** Crystal structure of strontium ruthenate compared with the crystal structure of  $(\text{La},\text{Ba})_2\text{CuO}_4$ .

(From Ref. [95]; © 1994 Nature.)

We see that the oxide superconductors turned out to represent a real treasure-house, in terms of both their attainable transition temperatures and their unconventional properties, making them interesting for fundamental research. More surprising developments of this class of materials may lay ahead.

## 2.9 Iron Pnictides and Related Compounds

Early in 2008, Hosono and coworkers [102] from Tokyo Institute of Technology announced a new superconductor,  $\text{LaO}_{0.89}\text{F}_{0.11}\text{FeAs}$ , which becomes superconducting at 26 K. The crystal structure is shown in [Figure 2.17](#). The structure of this compound is similar to that of the cuprates. However, instead of layers of copper oxide, it contains planes of iron arsenide. Layers of lanthanum oxide, in which oxygen is replaced partly by fluorine, are located in between. These layers are doping the FeAs planes.

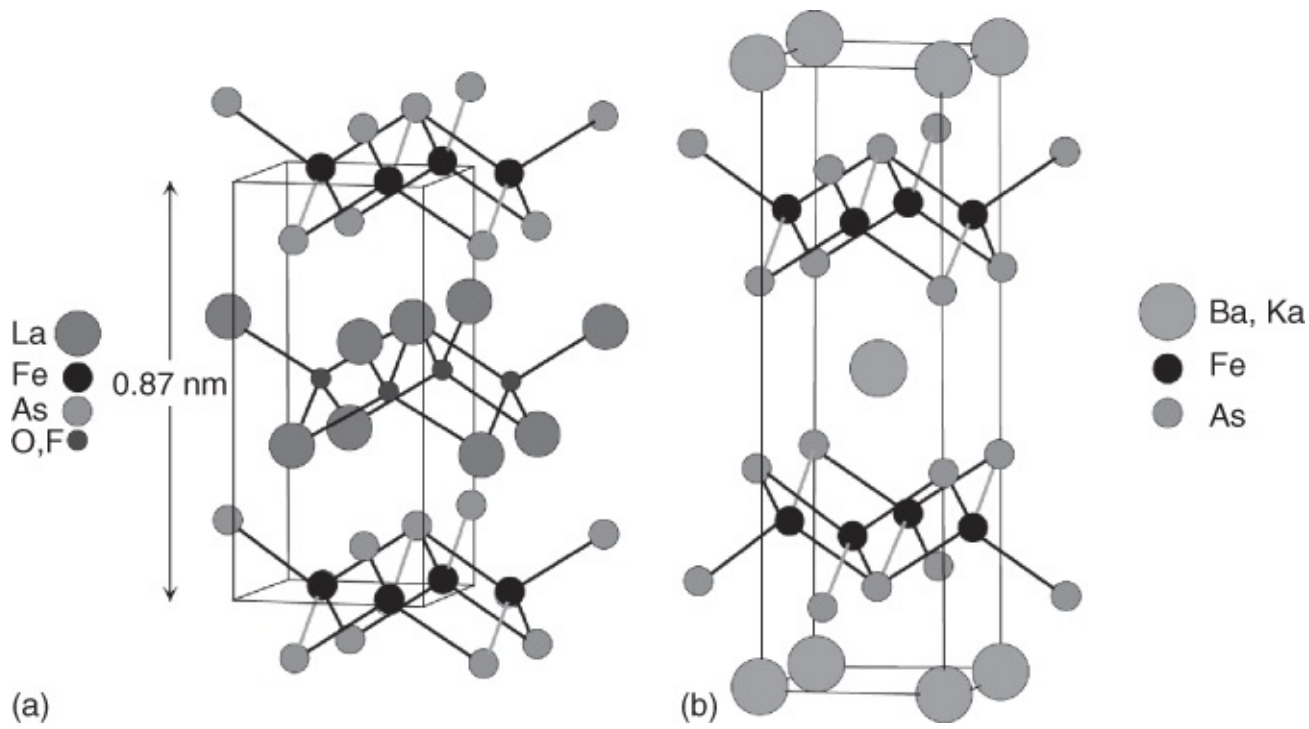


**Figure 2.17** Crystal structure of  $\text{La}(\text{O}_{1-x}\text{F}_x)\text{FeAs}$  (a) and  $\text{Ba}_{1-x}\text{K}_x\text{Fe}_2\text{As}_2$  (b).

From Ref. [103].

The similarity to the cuprate superconductors and the fact that in particular an iron compound shows a relatively high transition temperature generated an enormous interest among the physicists. The situation can be compared with the discovery of the cuprate superconductors.

Still in the same year, related compounds were discovered, the transition temperature of which can reach more than 50 K.  $\text{Sr}_{0.5}\text{Sm}_{0.5}\text{FeAs}$  ( $T_C = 56$  K) or  $\text{Ba}_{0.6}\text{K}_{0.4}\text{Fe}_2\text{As}_2$  ( $T_C = 38$  K) are examples. In the latter compound, the crystal structure of which is also shown in Figure 2.17, two FeAs layers are located within the unit cell. This class of materials, in which Ba and K can also be replaced by other elements, are also referred to as **122-compounds**, in contrast to the two former compounds, which are referred to as **111-compounds**. In addition, we mention  $\text{FeSe}$  ( $T_C \approx 8$  K, increasing under pressure up to 27 K) and  $\text{FeSe}_{0.5}\text{Te}_{0.5}$  ( $T_C \approx 15$  K). In these “11-compounds” arsenic is replaced by selenium, and there are stacks of layers of FeS at 0.55 nm distance.  $\text{FeSe}$  represents the iron-based superconductor with the simplest structure. Presently, the number of these superconductors increases explosively. A snapshot of the year 2009 is presented in [104].

Similar as in the case of the cuprates, in the undoped state, the iron pnictides are magnetically ordered. However, in contrast to the undoped cuprates, they are electrically conducting. It appears possible that magnetism and superconductivity are connected with each other. This is shown in Figure 2.18 with the example  $\text{La}(\text{O}_{1-x}\text{F}_x)\text{FeAs}$ . The electronic data are based on measurements of muon-spin-resonance ( $\mu\text{SR}$ ), magnetic susceptibility  $\chi$ , and Mößbauer spectroscopy. The crystal structure was determined by the X-ray diffractometry. In the case  $x < 0.045$  at a temperature  $T_s$ , a structural phase transition to an orthorhombic phase occurs. During further cooling, below a temperature  $T_N$  (140 K at  $x = 0$ ), a spin-density wave is observed. In

the case  $x > 0.045$  one finds superconductivity, with the superconducting transition temperature  $T_C$  reaching its maximum at  $x \approx 0.11$ .

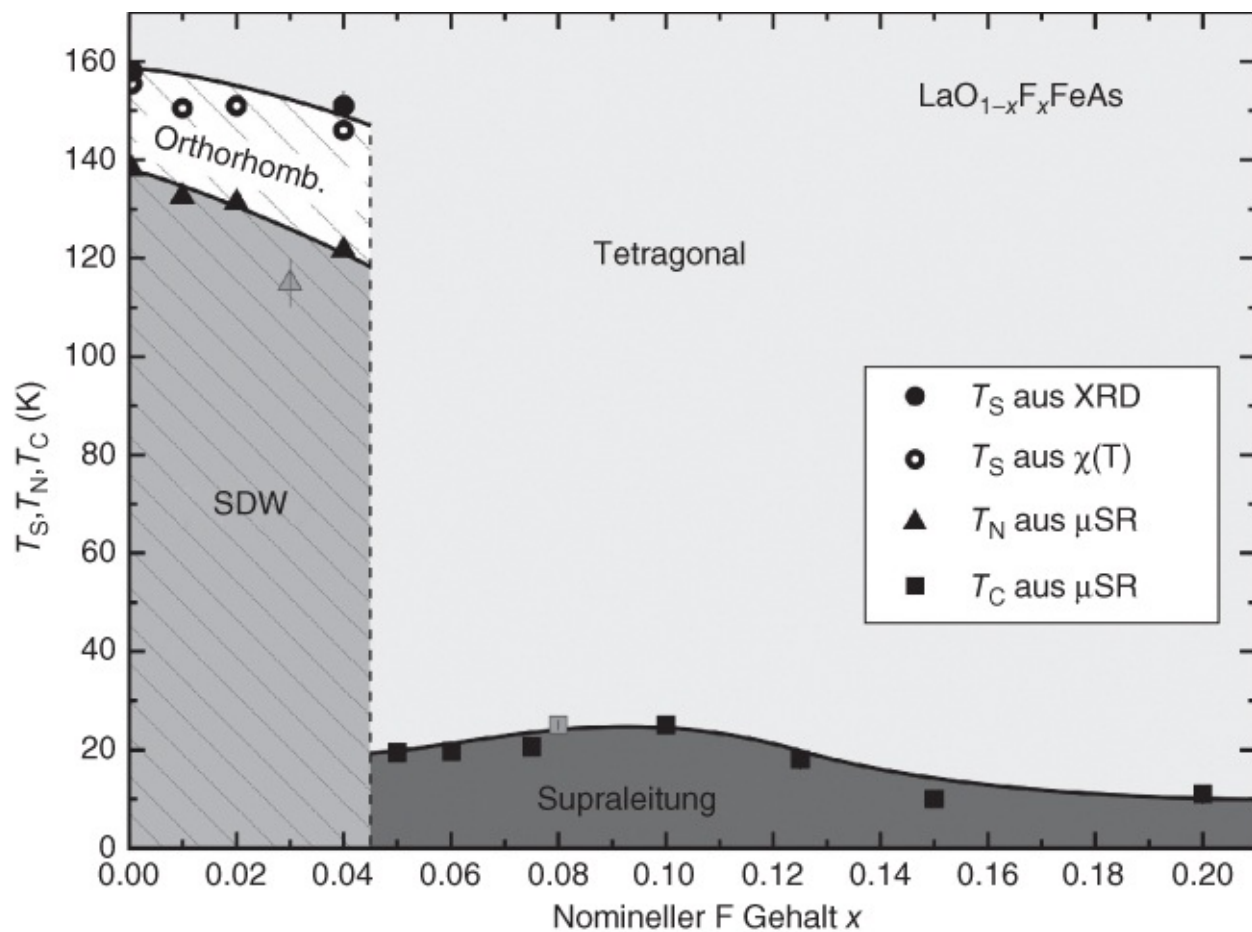


**Figure 2.18** Phase diagram of  $\text{La}(\text{O}_{1-x}\text{F}_x)\text{FeAs}$ .

(From Ref. [105].)

SDW, spin-density wave;  $\mu\text{SR}$ , muon-spin resonance;  $\chi(T)$ , magnetic susceptibility; and XRD, X-ray diffraction.

The iron pnictides are layered type-II superconductors. In [Table 2.8](#) we list data of some materials. In the case of the 1111- and the 111-compounds, the London penetration depth  $\lambda_{ab}$  ranges around 200 nm comparable to the cuprate superconductors. In the case of the 11-compounds  $\lambda_{ab}$  is about twice as large. The data of the upper critical fields show large variations. Here we must note that usually the data were extrapolated from measurements near  $T_C$  to low temperatures, and, therefore, they contain some error. However, the anisotropy ratio  $B_{c2\parallel}/B_{c2\perp}$  clearly is rather small compared to the cuprates. The 1111-compounds show the largest anisotropy of 3–5 (comparison: cuprates can reach values larger than 20). In the case of the 111-materials, the anisotropy is less than 2. The 11-compound  $\text{FeSe}_{0.5}\text{Te}_{0.5}$  appears to be nearly isotropic. The anisotropy of the coherence lengths is correspondingly small. In particular, the coherence length perpendicular to the layers,  $\xi_c$ , is comparable to or larger than the distance between the iron-containing layers. This suggests that in spite of their layered

structure, the iron pnictides behave like anisotropic three-dimensional superconductors.

**Table 2.8** Data of some iron pnictides

Material $T_c$	$T_c$ (K)	$\lambda_{ab}$ (nm)	$\xi_{ab}$ (nm)	$\xi_c$ (nm)	$B_{c2\perp}$ (T)	$B_{c2\parallel}$ (T)
LaO <sub>0.89</sub> F <sub>0.11</sub> FeAs	26	215	4.5	1.2	15	60
NdO <sub>0.82</sub> F <sub>0.18</sub> FeAs	50	190	3.7	0.9	62–70	304
Ba <sub>0.6</sub> K <sub>0.4</sub> Fe <sub>2</sub> As <sub>2</sub>	38	190	1.5	0.9	100–140	70–235
BaFe <sub>1.8</sub> Co <sub>0.2</sub> As <sub>2</sub>	25	210	2.8	—	43	—
FeSe	8	400	6	1.7	9	25
FeSe <sub>0.5</sub> Te <sub>0.5</sub>	15	560	2.6	2.6	47	47

Maximum transition temperature, London penetration depth in the case of fields perpendicular to the layer structure, coherence lengths parallel or perpendicular to the planes, and upper critical fields perpendicular and parallel to the planes.

(From Ref. [106–109].)

However, superconductivity of the iron pnictides likely is unconventional. Similar to the case of MgB<sub>2</sub>, multiband superconductivity is being discussed, where Cooper pairing differs at different Fermi surfaces. In the case of the pnictides, the s<sup>±</sup>-symmetry could be valid where (conventional) s-wave pairing is found at a given Fermi surface. However, in contrast to MgB<sub>2</sub>, in this scenario the pair-wave functions at different Fermi surfaces have different signatures. Presently it is still unclear, whether Cooper pairing is due to electron–phonon interaction or to another mechanism.

## 2.10 Organic Superconductors

In 1964, Little [110] proposed the hypothesis that it should be possible to find organic superconductors with very high transition temperatures. Here long molecular chains with conjugated double bonds along the chain and suitable ligands should be involved. Little presumed that within such structures Cooper pairs can be formed by means of the interaction of the electrons with special electronic excitations in the molecules (so-called excitons). These excitons then would take up the role of the phonons in the traditional Cooper pairing. Up to now, Little's hypothesis could not be confirmed. However, during the search for the relevant materials, other kinds of organic superconductors were discovered.<sup>9</sup>

In 1980 Jérôme *et al.* [111] discovered the first organic superconductor, namely the hexafluorophosphate of tetramethyltetraselenofulvalene (TMTSF). The material had to be kept under a hydrostatic pressure of 12 kbar, in order to suppress a metal–insulator transition. At this pressure, the organic conductor kept its metallic properties down to the lowest temperatures studied, and at  $T_c = 0.9$  K it became superconducting.

Subsequently, a number of other superconductors based on the TMTSF molecule were found. All these materials show superconductivity with transition temperatures around 1 K. For

example, we mention  $(\text{TMTSF})_2\text{ClO}_4$ , which under normal pressure remains metallic down to the lowest temperatures and becomes superconducting at 1 K [112]. In [Figure 2.19a](#) we show the structural formula of TMTSF. The general formula of the superconducting compounds is  $(\text{TMTSF})_2\text{X}$ . Here X denotes an electron acceptor. In addition to  $\text{PF}_6^-$  and  $\text{ClO}_4^-$ , this can be, for example,  $\text{AsF}_6^-$  or  $\text{TaF}_6^-$ . In these compounds, the TMTSF molecules are stacked upon each other. In the normal state, along the stacks the TMTSF compounds have a relatively large electrical conductivity. However, perpendicular to the stacks, the conductivity is small. Hence, the materials represent nearly one-dimensional conductors.

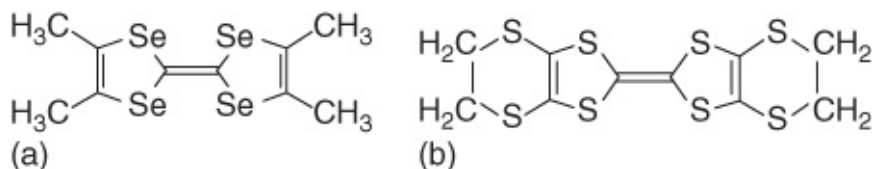


[Figure 2.19](#) Structural formulas of organic superconductors: (a) tetramethyltetraselenofulvalene (TMTSF) and (b) bis(ethylenedithia)tetra-thiafulvalene (BEDT-TTF).

The TMTSF compounds are type-II superconductors with highly anisotropic properties. For example, in  $(\text{TMTSF})_2\text{ClO}_4$  along the stacks the Ginzburg–Landau coherence length is about 80 nm, whereas along the two perpendicular directions of the crystal axes it is about 35 and 2 nm, respectively. The latter value is of the same order of magnitude as the lattice constant along the  $c$ -axis. Hence, the compound nearly represents a *two-dimensional* superconductor.

At  $T = 50$  mK, in  $(\text{TMTSF})_2\text{ClO}_4$  one finds values for the lower critical field  $B_{c1}$  of replace by 0.02, 0.1, and 1 mT along the  $a$ ,  $b$ , and  $c$  axes, respectively. The corresponding values of the upper critical field are 2.8, 2.1, and 0.16 T, respectively. The values of the London penetration depth are very large, and along the three crystal directions they are 0.5, 8, and 40  $\mu\text{m}$ , respectively [113].

In recent years, a number of organic superconductors with much higher transition temperatures have been found. Here the bis(ethylenedithia)tetra-thiafulvalene (BEDT-TTF) molecule (sometimes also denoted briefly as ET) plays an important role. Its structure is shown in [Figure 2.19b](#). For example, the compound  $(\text{BEDT-TTF})_2\text{Cu}[\text{N}(\text{CN})_2]\text{Br}$  becomes superconducting at 11.2 K [114]. The transition temperature of  $(\text{BEDT-TTF})_2\text{Cu}(\text{NCS})_2$  is 10.4 K. The crystal structure of this last compound is shown in [Figure 2.20](#).

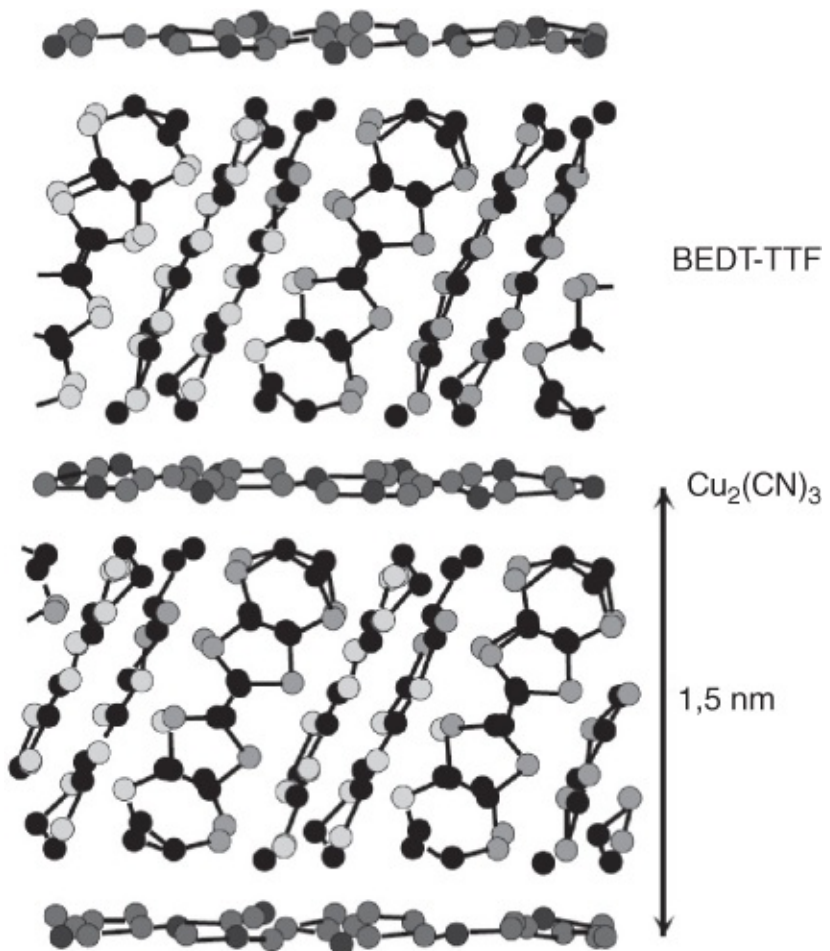


**Figure 2.20** Crystal structure of the organic superconductor  $\kappa$ -(BEDT-TTF)<sub>2</sub>Cu(NCS)<sub>2</sub>.

(From Ref. [115].)

In 2010 a new class of organic superconductors was reported based on the aromatic compound picene [116]. However, superconductivity in these materials was not yet reproduced in other laboratories. The picene molecules, with the formula C<sub>22</sub>H<sub>14</sub>, consist of five benzene rings and are stacked in a crystal by layers on top of each other (see [Figure 2.21](#)). According to [116], one obtains a superconductor if in addition one places an alkaline metal between the picene molecules. In the case of potassium, corresponding to the compound K<sub>3</sub>-picene,  $T_C$  reaches values up to 18 K, that is, a record temperature for organic superconductors. Presently, one speculates about the superconducting properties and the pairing mechanism. Some scientists see a similarity to the fullerenes discussed in [Section 2.4](#). These also show superconductivity after intercalation with alkaline atoms.

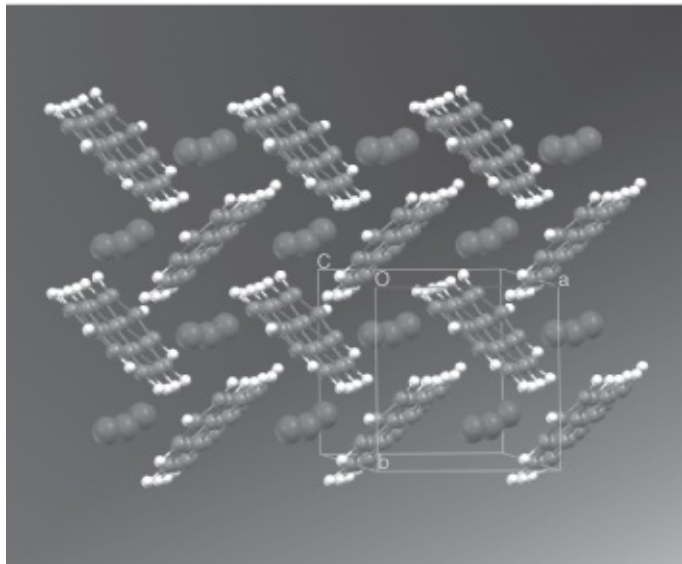
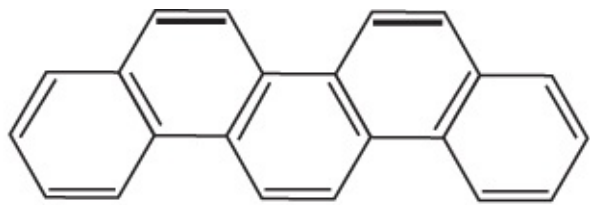


**Figure 2.21** Formula

(from Ref. [116])

and schematic crystal structure of  $K_3$ -picene. Lattice constants:  $a \approx 0.87$  nm,  $b \approx 0.59$  nm, and  $c \approx 1.3$  nm.

(reprinted by courtesy from Ref. [117], © 2011 American Physical Society)

Let us return to the superconducting properties of the ET compounds. These materials are very anisotropic. However, in contrast to the TMTSF compounds, they form two-dimensional layered structures with a high electric conductivity within two dimensions. The ET compounds are type-II superconductors.

Some of their properties are listed in [Table 2.9](#). For example, within the highly conducting layers of  $(BEDT-TTF)_2Cu(NCS)_2$ , the Ginzburg–Landau coherence length is about 10 nm. However, in the perpendicular direction it is only 0.8 nm. For a magnetic field orientation perpendicular to the layers, the London penetration depth is in the range 650–1200 nm. For field orientations parallel to the layers, one finds the very large value of about 200  $\mu$ m. For fields perpendicular to the layers, the upper critical field is about 5 T, and for parallel fields it is about 20 T.

**Table 2.9** Data of some organic superconductors based on the BEDT molecule

Composition	$T_{c,\text{max}}$ (K)	$\lambda_{\perp}$ (nm)	$\lambda_{  }$ (μm)	$\xi_{  }$ (nm)	$\xi_{\perp}$ (nm)	$B_{c2\perp}$ (T)	$B_{c2  }$ (T)
$\kappa$ -(BEDT-TTF) <sub>2</sub> Cu(NCS) <sub>2</sub>	10.4	500–2000	40–200	5–8	0.8	6	30–35
(BEDT-TTF) <sub>2</sub> Cu[N(CN) <sub>2</sub> ]Br	11.2	550–1500	40–130	2.5–6.5	0.5–1.2	8–10	80
$\beta_H$ -(BEDT-TTF) <sub>2</sub>   <sub>3</sub>	7–8 <sup>a</sup>	—	—	12.5	1	2.7	25
$\beta_L$ -(BEDT-TTF) <sub>2</sub>   <sub>3</sub>	1.5	3500	30–40	60–63	2.0	0.08	1.7–1.8
$\beta$ -(BEDT-TTF) <sub>2</sub>  Br <sub>2</sub>	2.2	550	4–5	44–46	1.9	3.3–3.6	1.5
$\beta$ -(BEDT-TTF) <sub>2</sub> Au  <sub>2</sub>	4.2	500	4	18–25	2–3	6.1–6.6	—

<sup>a</sup> At a pressure of 1.6 kbar.

Maximum transition temperature  $T_{c,\text{max}}$ , magnetic penetration depths  $\lambda_{\perp}$  and  $\lambda_{||}$  for magnetic field orientations perpendicular and parallel to the layers, respectively, and the Ginzburg–Landau coherence lengths  $\xi_{||}$  and  $\xi_{\perp}$  perpendicular and parallel to the layers, respectively. The upper critical fields for field orientations perpendicular and parallel to the layers are also indicated.

Data mostly from monograph [M12].

The organic compounds also represent superconducting layered structures. Similar to the high-temperature superconductors, they display a number of unusual properties, such as regarding the formation of magnetic vortices. Presently, the pairing mechanism of the organic superconductors remains unclear. However, similar to the cuprates, at least in some compounds the pairs appear to have an angular momentum of  $2\hbar$ . In the compound (TMTSF)<sub>2</sub>PF<sub>6</sub>, we may be dealing with a spin-triplet superconductor [118].

Up to now, the organic compounds originally proposed in Little's hypothesis could not be found. Instead, other interesting compounds have been discovered. However, the subject of the organic molecules and compounds is so rich that many new interesting superconducting materials can be expected in the future.

## 2.11 Superconductivity at Interfaces

In the previous sections of this chapter we have seen that a series of materials, above all the cuprate superconductors and the iron pnictides, only become superconducting, when they are doped with free charge carriers. Hence, one can ask whether it is also possible to achieve this effect by the accumulation of charges at an interface, whether by a transistor-like arrangement or at interfaces between materials being initially non-conducting.

First we look at the electric field effect [119, 120]. Similar to the semiconductor technology, it is the fundamental idea to generate an electric charge  $\Delta Q = CU_g$  in the electrodes by applying a voltage  $U_g$  to a gate electrode. This charge accumulates within a thin surface layer of thickness

$\lambda_{\text{el}}$ , which is inversely proportional to the square root of the charge carrier density. However, in typical metals,  $\lambda_{\text{el}}$  is only a few angstroms (here referred to as **Thomas-Fermi length**). In order that this accumulation of charge has an appreciable influence on the electric properties of a superconducting film,  $\lambda_{\text{el}}$  must be comparable to the film thickness and/or to the coherence length  $\xi_{\text{GL}}$ . At least, the induced charge density should amount to several percent of the unperturbed density of the free electrons in the material, which requires high electric fields and, hence, high breakdown fields of the gate oxide. This represents the largest experimental challenge.

Already in the 1960s in Sn-films and In-films of 7 nm thickness, the transition temperature could be raised by about 0.1–1 mK by means of the electric field effect [119]. However, for demonstrating the field effect, the high-temperature superconductors are much more promising, since in this case the concentration of charge carriers is relatively low, and on the other hand the superconducting properties vary strongly with the density of free electrons (see [Section 2.8.1](#)). Using thin films of  $\text{YBa}_2\text{Cu}_3\text{O}_{7-x}$  and also of other high-temperature superconductors, relatively large effects could be observed [120]. Using epitaxial (i.e., single-crystalline) thin films, shifts of  $T_{\text{C}}$  by 1–3 K are reached, and using polycrystalline films<sup>10</sup> shifts of 10–20 K. Using ultrathin films of  $\text{La}_{2-x}\text{Sr}_x\text{CuO}_4$ , it was even possible to change the transition temperature by 30 K [122]. Together with these shifts of  $T_{\text{C}}$ , other electronic properties also change, such as the maximum current-carrying capability of the material.

Generating superconductivity is possible at the interface between the two insulators  $\text{LaAlO}_3$  and  $\text{SrTiO}_3$ . In 2004, Ohtomo and Hwang [123] observed that at the interface between a  $\text{SrTiO}_3$  substrate and a single-crystalline thin film of  $\text{LaAlO}_3$  deposited on top of it, highly mobile electrons can be induced.  $\text{LaAlO}_3$  consists of layers of  $(\text{LaO})^+$  and  $(\text{AlO}_2)^-$  ions,  $\text{SrTiO}_3$  of neutral layers of  $(\text{SrO})$  and  $(\text{TiO}_2)$ . It is possible to generate the interfaces  $(\text{LaO})^+/\text{(TiO}_2)$  and  $(\text{AlO}_2)^-/\text{(SrO)}$ . In the first case the polarization jump at the interface leads to the accumulation of electrons, in the second case it leads to the accumulation of holes. The hole-doped interface turned out to be insulating, the electron-doped interface to be well conducting. Soon one had found superconductivity with a transition temperature of 200 mK [124], and finally it was demonstrated that superconductivity can be turned on and off by means of the electric field effect [125]. Superconductivity vanished at a gate voltage less than –150 V. The maximum of  $T_{\text{C}}$  of about 300 mK was reached at a gate voltage of +100 V.

The attained transition temperatures are rather small compared with those of many other superconductors discussed in this chapter. However, in this case we deal with a well-controllable system, which is interesting for fundamental physics. On the other hand, more and more experiments are performed at millikelvin temperatures, say, in conjunction with quantum computers. These superconducting switches could find interesting applications in this area.

## References

1. Flouquet, J. and Buzdin, A. (2002) *Ferromagnetic superconductors Physics World*, January 2002.
2. E. Müller-Hartmann, J. Zittartz: *Phys. Rev. Lett.* **26**, 428 (1970).
3. K. Winzer: *Z. Phys.* **265**, 139 (1973); G. Riblet, K. Winzer: *Solid State Commun.* **9**, 1663 (1971); M. B. Maple: *Appl. Phys.* **9**, 179 (1976).
4. C. Buzea, K. Robbie: *Supercond. Sci. Technol.* **18**, R1 (2005).
5. H. Behrens, G. Ebel (eds.) “*Superconductivity Data*”, Fachinformationszentrum Energie, Physik, Mathematik, Karlsruhe (1982).
6. Roberts, R.W. (1966) Roberts Report, General Electric port No. 63-RL-3252M and N.B.S. Technical Note 482.
7. B. T. Matthias: *Phys. Rev.* **97**, 74 (1955); B. T. Matthias: “*Progress in Low Temperature Physics*”, Vol. 2, C. J. Gorter (ed.), North Holland, Amsterdam, p. 138 (1957).
8. J. K. Hulm, R. D. Blaughter: *Phys. Rev.* **123**, 1569 (1961); V. B. Compton, E. Corenzwit, E. Maita, B. T. Matthias, F. J. Morin: *Phys. Rev.* **123**, 1567 (1961); W. Gey: *Z. Phys.* **229**, 85 (1969).
9. L. R. Testardi, J. H. Wernick, W. A. Royer: *Solid State Commun.* **15**, 1 (1974); J. R. Gavaler, M. H. Janocko, C. K. Jones: *J. Appl. Phys.* **45**, 3009 (1974).
10. A. Godeke: *Supercond. Sci. Technol.* **19**, R68 (2006).
11. L. R. Testardi: *Rev. Mod. Phys.* **47**, 637 (1975).
12. J. Muller: *Rep. Prog. Phys.* **43**, 641 (1980) (G. B.).
13. C. M. Soukoulis, D. A. Papaconstantopoulos: *Phys. Rev. B* **26**, 3673 (1982).
14. A. M. Clogston, V. Jaccarino: *Phys. Rev.* **121**, 1357 (1961); M. Weger: *Rev. Mod. Phys.* **36**, 175 (1964); J. Labbe, J. Friedel: *J. Phys. (Paris)* **27**, 153 and 303 (1966).
15. L. R. Testardi, T. B. Bateman: *Phys. Rev.* **154**, 402 (1967).
16. B. W. Batterman, C. S. Barrett: *Phys. Rev. Lett.* **13**, 390 (1964).
17. Z. W. Lu, B. M. Klein: *Phys. Rev. Lett.* **79**, 1361 (1997).
18. R. Flückiger, J. L. Staudemann, A. Treyvaud, P. Fischer: “*Proceedings of LT 14*”, Vol. 2, North Holland Publishing Company, Otaniemi, p. 1 (1975).
19. W. Weber: “*Proceedings IV Conference Superconductivity in d- and f-Band Metals*”, W. Buckel, W. Weber (eds.), Kernforschungszentrum Karlsruhe, Karlsruhe, p. 15 (1982).
20. J. Nagamatsu, N. Nakagawa, T. Muranaka, Y. Zenitani, J. Akimitsu *Nature* **410**, 63 (2001).

21. C. Buzea, T. Yamashita: *Supercond. Sci. Technol.* **14**, R115 (2001);P. C. Canfield, S. L. Bud'ko, D. K. Finnemore: *Physica C* **385**, 1 (2003);C. Canfield, G. W. Crabtree: *Phys. Today*, **56**, 34 (2003).
22. X. X. Xi: *Rep. Prog. Phys.* **71**, 116501 (2008).
23. Roberts, B.W. (1964) “Superconducting Materials and Some of Their Properties”. IV Progress in Cryogenics, and National Bureau of Standards, Technical Note 482, pp. 160–231.
24. R. F. Hoyt, A. C. Mota: *Solid State Commun.* **18**, 139 (1975);A. C. Mota, R. F. Hoyt: *Solid State Commun.* **20**, 1025 (1976);Ch. Buchal, R. M. Müller, F. Pobell, M. Kubota, H. R. Folle: *Solid State Commun.* **42**, 43 (1982).
25. G. Webb, RCA, Princeton (1971).
26. K. D. D. Rathnayaka, A. K. Bhatnagar, A. Parasiris, D. G. Naugle, P. C. Canfield, B. K. Cho: *Phys. Rev. B* **55**, 8506 (1997).
27. M. Tomsic, M. Rindfleisch, J. Yue, K. McFadden, J. Phillips: *Int. J. Appl. Ceram. Technol.* **4**, 250 (2007).
28. T. Skoskiewicz: *Phys. Status Solidi A* **11**, K 123 (1972).
29. B. Stritzker, W. Buckel: *Z. Phys.* **257**, 1 (1972).
30. B. Stritzker: *Z. Phys.* **268**, 261 (1974).
31. B. N. Ganguly: *Z. Phys.* **265**, 433 (1973);B. N. Ganguly: *Phys. Lett.* **46 A**, 23 (1973).
32. C. H. Pennington, V. A. Stenger: *Rev. Mod. Phys.* **68**, 855 (1996).
33. A. Hebard, M. J. Rosseinsky, R. C. Haddon, D. W. Murphy, S. H. Glarum, T. T. M. Palstra, A. P. Ramirez, A. R. Kortan: *Nature* **350**, 600 (1991);R. M. Fleming, A. P. Ramirez, M. J. Rosseinsky, D. W. Murphy, R. C. Haddon, S. M. Zahurak, A. V. Markhija: *Nature* **352**, 787 (1991).
34. Z. K. Tang, L. Zhang, N. Wang, X. X. Zhang, G. W. Wen, G. D. Li, J. N. Wang, C. T. Chan, P. Sheng: *Science* **292**, 2462 (2001).
35. V. Buntar, H. W. Weber: *Supercond. Sci. Technol.* **9**, 599 (1996).
36. O. Gunnarson: *Rev. Mod. Phys.* **69**, 575 (1997).
37. O. K. Andersen, W. Klose, H. Nohl: *Phys. Rev. B* **17**, 1209 (1978).
38. P. Birrer, F. N. Gygax, B. Hitti, E. Lippelt, A. Schenck, M. Weber, D. Cattani, J. Cors, M. Decroux, O. Fischer: *Phys. Rev. B* **48**, 16589 (1993).
39. S. Rehmann, T. Hermannsdörfer, F. Pobell: *Phys. Rev. Lett.* **78**, 1122 (1997).

40. D. C. Johnston, W. A. Fertig, M. B. Maple, B. T. Matthias: *Solid State Commun.* **26**, 141 (1978); H. B. Mackay, L. D. Woolf, M. B. Maple, D. C. Johnston: *Phys. Rev. Lett.* **42**, 918 (1979).
41. J.-M. Triscone, Ø. Fisher: *Rep. Prog. Phys.* **60**, 1673 (1997).
42. K.-H. Müller, V. N. Narozhnyi: *Rep. Prog. Phys.* **64**, 943 (2001).
43. P. L. Gammel, B. P. Barber, A. P. Ramirez, C. M. Varma, D. J. Bishop, P. C. Canfield, V. G. Kogan, M. R. Eskildsen, N. H. Andersen, K. Mortensen, K. Harada: *Phys. Rev. Lett.* **82**, 1756 (1999).
44. F. Steglich, J. Aarts, C. D. Bredl, W. Lieke, D. Meschede, W. Franz, H. Schäfer: *Phys. Rev. Lett.* **43**, 1892 (1979).
45. A. Amato: *Rev. Mod. Phys.* **69**, 1119 (1997).
46. R. H. Heffner, M. R. Norman: *Comments Condens. Matter Phys.* **17**, 361 (1996).
47. P. Thalmeier, M. Jourdan, M. Huth: *Phys. J.*, **6**, 51 ff (2002).
48. R. Joynt, L. Taillefer: *Rev. Mod. Phys.* **74**, 235 (2002).
49. J. M. Tranquada, A. H. Moudden, A. I. Goldman, P. Zolliker, D. E. Cox, G. Shirane, S. K. Sinha, D. Vaknin, D. C. Johnston, M. S. Alvarez, A. J. Jacobson, J. T. Lewandowski, J. M. Newsam: *Phys. Rev. B* **38**, 2477 (1988).
50. K. Ishida, D. Ozaki, T. Kamatsuka, H. Tou, M. Kyogaku, Y. Kitaoka, N. Tateiwa, N. K. Sato, N. Aso, C. Geibel, F. Steglich: *Phys. Rev. Lett.* **89**, 037002 (2002).
51. S. S. Saxena, P. Agarwai, K. Ahilan, F. M. Grosche, R. K. W. Haselwimmer, M. J. Steiner, E. Pugh, I. R. Walker, S. R. Julian, P. Monhoux, G. G. Lonzarich, A. Huxley, I. Sheikin, D. Braithwaite, J. Flouquet: *Nature* **406**, 587 (2000).
52. F. Hardy, A. D. Huxley: *Phys. Rev. Lett.* **44**, 247006 (2005).
53. F. Levy, I. Sheikin, B. Grenier, A. D. Huxley: *Science* **309**, 1343 (2005).
54. B. Y. Jin, J. B. Ketterson: *Adv. Phys.* **38**, 189 (1989).
55. J. A. Wilson, A. D. Yoffe: *Adv. Phys.* **18**, 193 (1969).
56. L. N. Bulaevskii: *Sov. Phys. Usp.* **18**, 514 (1976).
57. L. F. Mattheiss: *Phys. Rev. B* **8**, 3719 (1973).
58. S. Foner, E. J. McNiff: *Phys. Lett.* **A45**, 429 (1973).
59. R. C. Morris, R. V. Coleman: *Phys. Rev. B* **7**, 991 (1973).

60. D. E. Prober, M. R. Beasley, R. E. Schwall: *Phys. Rev. B* **15**, 5245 (1977).
61. W. E. Pickett: *Rev. Mod. Phys.* **61**, 433 (1989); W. E. Pickett: *Physica B* **296**, 112 (2001).
62. M. E. Takayama-Muromachi: *Chem. Mater.* **10**, 2686 (1998).
63. H. Yamauchi, M. Karppinen: *Supercond. Sci. Technol.* **13**, R33 (2000).
64. J. Karpinski, G. I. Meijer, H. Schwer, R. Molinski, E. Kopnin, K. Conder, M. Angst, J. Jun, S. Kazakov, A. Wisniewski, P. Puzniak, J. Hofer, V. Alyoshin, A. Sin: *Supercond. Sci. Technol.* **12**, R153 (1999).
65. A. Revcholevschi, J. Jegoudez: *Prog. Mater. Sci.* **42**, 321 (1997); W. Assmus, W. Schmidbauer: *Supercond. Sci. Technol.* **6**, 555 (1993).
66. D. G. Schlom, J. Mannhart: “*Encyclopedia of Materials: Science and Technology*”, K. H. J. Buschow, R. W. Cahn, M. C. Flemings, B. Ilschner, E. J. Kramer, S. Mahajan (eds.), Elsevier Science, Amsterdam, p. 3806 (2002); R. Wördenweber: *Supercond. Sci. Technol.* **12**, R86 (1999).
67. M. Takano, M. Azuma, Z. Hiroi, Y. Bando, Y. Takeda: *Physica C* **176**, 441 (1991); M. G. Smith, A. Manthiram, J. Zhou, J. B. Goodenough, J. T. Markert: *Nature* **351**, 549 (1991); G. Er, Y. Miyamoto, F. Kanamaru, S. Kikkawa: *Physica C* **181**, 206 (1991).
68. P. Manca, S. Sanna, G. Calestani, A. Migliori, S. Lapinskas, E. E. Tornau: *Phys. Rev. B* **63**, 134512 (2001).
69. B. Keimer, N. Belk, R. J. Birgeneau, A. Cassanho, C. Y. Chen, M. Greven, M. A. Kastner, A. Aharony, Y. Endoh, R. W. Erwin, G. Shirane: *Phys. Rev. B* **46**, 14034 (1992).
70. Y. Koval, X. Y. Jin, C. Bergmann, Y. Simsek, L. Özyüzer, P. Müller, H. B. Wang, G. Behr, B. Büchner: *Appl. Phys. Lett.* **96**, 082507 (2010).
71. Y. Ando, G. S. Boebinger, A. Passner, L. F. Schneemeyer, T. Kimura, M. Okuda, S. Watauchi, J. Shimoyama, K. Kishio, K. Tamasaku, N. Ichikawa, S. Uchida, *Phys. Rev. B* **60**, 12475 (1999).
72. T. Ishida, K. Okuda, A. I. Rykov, S. Tajima, I. Terasaki: *Phys. Rev. B* **58**, 5222 (1998); H. Nakagawa, T. Takamasu, N. Miura, Y. Enomoto: *Physica B* **246**, 429 (1998).
73. S. I. Vedeneev, A. G. M. Jansen, E. Haanappel, P. Wyder: *Phys. Rev. B* **60**, 12467 (1999).
74. I. Matsubara, H. Tanigawa, T. Ogura, H. Yamashita, M. Kinoshita, T. Kawai: *Phys. Rev. B* **45**, 7414 (1992).
75. H. Mukaida, K. Kawaguchi, M. Nakao, H. Kumakura, D. R. Dietderich, T. Togano: *Phys. Rev. B* **42**, 2659 (1990).
76. N. E. Hussey, J. R. Cooper, R. A. Doyle, C. T. Lin, W. Y. Liang, D. C. Sinclair, G.

- Balakrishnan, D. McK. Paul, A. Revcolevschi: *Phys. Rev. B* **53**, 6752 (1996).
77. A. P. Mackenzie, S. R. Julian, G. G. Lonzarich, A. Carrington, S. D. Hughes, R. S. Liu, D. C. Sinclair: *Phys. Rev. Lett.* **71**, 1238 (1993).
78. V. Vulcanescu, L. Fruchter, A. Bertinotti, D. Colson, G. Le Bras, J.-F. Marucco: *Physica C* **259**, 131 (1996).
79. K. Winzer, G. Kumm, P. Maaß, H. Thomas, E. Schwarzmann, A. Aghaie, F. Ladenberger: *Ann. Phys.* **1**, 479 (1992).
80. F. Steinmeyer, R. Kleiner, P. Müller, H. Müller, K. Winzer: *Europhys. Lett.* **25**, 459 (1994).
81. R. Puźniak, R. Usami, K. Isawa, H. Yamauchi: *Phys. Rev. B* **52**, 3756 (1995).
82. Y. C. Kim, J. R. Thompson, J. G. Ossandon, D. K. Christen, M. Paranthaman: *Phys. Rev. B* **51**, 11767 (1995).
83. M.-S. Kim, M.-K. Bae, W. C. Lee, S.-I. Lee: *Phys. Rev. B* **51**, 3261 (1995).
84. M.-S. Kim, S.-I. Lee, S.-C. Yu, I. Kuzemskaya, E. S. Itskevich, K. A. Lokshin: *Phys. Rev. B* **57**, 6121 (1998).
85. D. Zech, J. Hofer, H. Keller, C. Rossel, P. Bauer, J. Karpinski: *Phys. Rev. B* **53**, R6026 (1996).
86. Y. Dalichaouch, B. W. Lee, C. L. Seaman, J. T. Markert, M. B. Maple: *Phys. Rev. Lett.* **64**, 599 (1990).
87. S. M. Anlage, D.-H. Wu, J. Mao, S. N. Mao, X. X. Xi, T. Venkatesan, J. L. Peng, R. L. Greene: *Phys. Rev. B* **50**, 523 (1994).
88. M. Suzuki, M. Hikita: *Phys. Rev. B* **41**, 9566 (1990).
89. Ch. J. Raub: *J. Less-Common Met.* **137**, 287 (1988).
90. A. W. Sleight, J. L. Gillson, P. E. Bierstedt: *Solid State Commun.* **17**, 27 (1975).
91. S. Satpathy, R. M. Martin: *Phys. Rev. B* **36**, 7269 (1987).
92. L. F. Mattheiss, E. M. Gyorgy, D. W. Johnson, Jr.: *Phys. Rev. B* **37**, 3745 (1988).
93. R. J. Cava, B. Batlogg, J. J. Krajewski, R. Farrow, L. W. Rupp, Jr., A. E. White, K. Short, W. F. Peck, T. Kometani: *Nature* **332**, 814 (1988).
94. W. K. Kwok, U. Welp, G. W. Crabtree, K. G. Vandervoort, R. Hulscher, Y. Zheng, B. Dabrowski, D. G. Hinks: *Phys. Rev. B* **40**, 9400 (1989).
95. Y. Maeno, H. Hashimoto, K. Yoshida, S. Nishizaki, T. Fujita, J. G. Bednorz, F. Lichtenberg: *Nature* **372**, 532 (1994).

96. Y. Maeno: *Physica C* **282–287**, 206 (1997).
97. M. Sigrist, D. Agterberg, T. M. Rice, M. E. Zhitomirsky: *Physica C* **282–287**, 214 (1997).
98. Y. Maeno, T. M. Rice, M. Sigrist: *Phys. Today*, **54**, 42 (2001).
99. Z. Q. Mao, Y. Mori, Y. Maeno: *Phys. Rev. B* **60**, 610 (1999).
100. K. Yoshida, Y. Maeno, S. Nishizaki, T. Fujita: *Physica C* **263**, 519 (1996).
101. T. M. Riseman, P. G. Kealey, E. M. Forgan, A. P. Mackenzie, L. M. Galvin, A. W. Tyler, S. L. Lee, C. Ager, D. McK. Paul, C. M. Aegerter, R. Cubitt, Z. Q. Mao, T. Akima, Y. Maeno: *Nature* **396**, 242 (1998).
102. Y. Kamihara, T. Watanabe, M. Hirano, H. Hosono: *J. Am. Chem. Soc.* **130**, 3296 (2008).
103. M. Rotter, M. Tegel, D. Johrendt, I. Schellenberg, W. Hermes, R. Pöttgen: *Phys. Rev. B* **78**, 020503 (2008).
104. K. Ishida, Y. Nakai, H. Hosono: *J. Phys. Soc. Jpn.* **78**, 062001 (2009).
105. H. Luetkens, H.-H. Klauss, M. Kraken, F. J. Litterst, T. Dellmann, R. Klingeler, C. Hess, R. Khasanov, A. Amato, C. Baines, M. Kosmala, O. J. Schumann, M. Braden, J. Hamann-Borrero, N. Leps, A. Kondrat, G. Behr, J. Werner, B. Büchner: *Nat. Mater.* **8**, 305 (2009).
106. Y. Yin, M. Zech, T. L. Williams, X. F. Wang, G. Wu, X. H. Chen, J. E. Hoffman: *Phys. Rev. Lett.* **102**, 097002 (2009).
107. R. T. Gordon, N. Ni, C. Martin, M. A. Tanatar, M.D. Vannette, H. Kim, G. D. Samolyuk, J. Schmalian, S. Nandi, A. Kreyssig, A. I. Goldman, J. Q. Yan, S. L. Bud'ko, P. C. Canfield, R. Prozorov: *Phys. Rev. Lett.* **102**, 127004 (2009).
108. R. Khasanov, H. Luetkens, A. Amato, H.-H. Klauss, Z.-A. Ren, J. Yang, W. Lu, Z.-X. Zhao: *Phys. Rev. B* **78**, 092506 (2008).
109. M. Fang, J. Yang, F. F. Balakirev, Y. Kohama, J. Singleton, B. Qian, Z. Q. Mao, H. Wang, H. Q. Yuan: *Phys. Rev. B* **81**, 020509 (2010).
110. W. A. Little: *Phys. Rev.* **134A**, 1416 (1964).
111. D. Jérôme, A. Mazaud, M. Ribault, K. Bechgaard, C. R. Hebd: *Acad. Sci. Ser. B* **290**, 27 (1980).
112. K. Bechgaard, K. Carneiro, M. Olsen, R. B. Rasmussen, C. B. Jacobsen: *Phys. Rev. Lett.* **46**, 852 (1981).
113. P. A. Mansky, G. Danner, P. M. Chaikin: *Phys. Rev. B* **52**, 7554 (1995).
114. G. Saito, H. Yamochi, T. Nakamura, T. Komatsu, M. Nakashima, H. Mori, K. Oshima:

*Physica B* **169**, 372 (1991).

115. H. Seo: *J. Phys. Soc. Jpn.* Online—News and Comments June 10, (2010).  
[http://storage.ipap.jp/~jpsjoffice/jpsj.ipap.jp/news/jpsj-nc\\_69.html](http://storage.ipap.jp/~jpsjoffice/jpsj.ipap.jp/news/jpsj-nc_69.html)
116. R. Mitsuhashi, Y. Suzuki, Y. Yamanari, H. Mitamura, T. Kambe, N. Ikeda, H. Okamoto, A. Fujiwara, M. Yamaji, N. Kawasaki, Y. Maniwa, Y. Kubozono: *Nature* **464**, 76 (2010).
117. P. L. de Andres, A. Guijarro, J. A. Vergés: *Phys. Rev. B* **83**, 245113 (2011).
118. I. J. Lee, S. E. Brown, W. G. Clark, M. J. Strouse, M. J. Naughton, W. Kang, P. M. Chaikin: *Phys. Rev. Lett.* **88**, 017004 (2002).
119. R. E. Glover III, M. D. Sherill: *Phys. Rev. Lett.* **5**, 248 (1960); H. L. Stadler: *Phys. Rev. Lett.* **14**, 979 (1965).
120. C. H. Ahn, J. M. Triscone, J. Mannhart: *Nature* **424**, 1015 (2003).
121. Lucent Technologies Inc. (2002) Report of the Investigation Committee on the Possibility of Scientific Misconduct in the Work of Hendrik Schön and Coauthors; see also: *Phys. Today*(2002), p. 15, November 2002.
122. A. T. Bollinger, G. Dubuis, J. Yoon, D. Pavuna, J. Misewich, I. Bozovic: *Nature* **472**, 458 (2011).
123. A. Ohtomo, H. Y. Hwang: *Nature* **427**, 423 (2004).
124. N. Reyren, S. Thiel, A. D. Caviglia, L. F. Kourkoutis, G. Hammerl, C. Richter, C. W. Schneiter, T. Kopp, A.-S. Rüetschi, D. Jaccard, M. Gabay, D. A. Müller, J.-M. Triscone, J. Mannhart: *Science* **317**, 1196 (2007).
125. A. D. Caviglia, S. Gariglio, N. Reyren, D. Jaccard, T. Schneider, M. Gabay, S. Thiel, J. Mannhart, J.-M. Triscone: *Nature* **456**, 624 (2008).
126. H. Tou, Y. Kitaoka, K. Asayama, N. Kimura, Y. Onuki, E. Yamamoto, K. Maezawa: *Phys. Rev. Lett.* **77**, 1374 (1996).

<sup>1</sup> One finds that there are two possibilities in Nature for constructing a wave function from many quantum particles. Fermions, that is, particles with half-integer spin like electrons, form a wave function that changes its sign if two of the particles are interchanged. On the other hand, bosons, that is, particles with integer spin, form a symmetric wave function, remaining unchanged upon the interchange of two particles.

<sup>2</sup> Here one can ask the obvious question: On the one hand, does the electron–phonon interaction always leads to conventional superconductivity, and, on the other, does a different interaction always cause unconventional superconductivity? The answer is that we do not know. Theoretically, one can imagine that also unconventional superconductors can

result from the electron–phonon interaction, and that other pairing mechanisms can lead to conventional Cooper pairing. However, there are no experimental indications for this.

- <sup>3</sup> The ferromagnetic metals (e.g., Fe, Ni) must be excluded from this discussion. It appears likely that they cannot become superconducting in the ferromagnetic state. The superconducting high-pressure phase of iron, shown in [Figure 2.1](#), is non-magnetic.
- <sup>4</sup> Since, in addition to the number of valence electrons, other parameters also influence superconductivity, we can only compare alloys that have the same or similar crystal structure and whose components are located not too far from each other in the Periodic Table.
- <sup>5</sup> In this chapter we do not quote the values of the lower critical field, since the numbers often vary strongly in the literature. For orientation, the value of  $B_{c1}$  can be calculated from the expression  $B_{c1} \approx [\Phi_0 / (4\pi\lambda_L^2)] \ln(\lambda_L / \xi_{GL})$ , see [Section 4.7.1](#).
- <sup>6</sup> We see from [Figure 1.5](#) that the electronic density of states per energy interval  $dE$ , given by  $N(E) \propto dk/dE$ , can approach infinity for a single spatial direction. In the simple example of [Figure 1.5](#), the divergences are located at the band edges.
- <sup>7</sup> Another interesting superconductor we want to mention in this context of the coexistence of magnetism and superconductivity is AuIn<sub>2</sub>. This intermetallic compound is a type-I superconductor, showing superconductivity below 207 μK. The critical field increases up to 15 G at about 35 μK, and below this temperature it is reduced to about half of this value. At this temperature, nuclear ferromagnetic order sets in, and superconductivity then coexists with the ferromagnetic order of the nuclear moments [39].
- <sup>8</sup> In the case of BSCCO, this could be achieved also by current injection [70].
- <sup>9</sup> A summarizing review of the properties of organic superconductors can be found in [M12].
- <sup>10</sup> In the years 2000–2002 in a series of startling publications, scientists at the Bell Laboratories of the Company Lucent Technologies reported that by injection of charge carriers, a whole series of substances can be made superconducting, such as the organic crystals pentacene or anthracene. However, these publications turned out to be faked [121].

# Chapter 3

## Cooper Pairing

In [Chapter 1](#), we saw that superconductivity is intimately connected with the appearance of a macroscopic coherent matter wave constituted by electron pairs. Now we must ask how this pairing is accomplished, and how in the end it results in a macroscopic quantum wave with a well-defined phase. First, we will discuss conventional superconductors (see [Section 2.1](#)). In the second half of this chapter, we will turn to unconventional superconductors and in particular to high-temperature superconductors.

### 3.1 Conventional Superconductivity

#### 3.1.1 Cooper Pairing by Means of Electron–Phonon Interaction

Following our discussion in [Chapter 1](#), it appears relatively easy to arrive at a theory of superconductivity based on the microscopic interaction between the electrons themselves and between electrons and the surrounding crystal lattice. However, historically such a theory was confronted with extreme difficulties. Because of the striking change of the electrical conductivity and the magnetic effects during the onset of superconductivity, one could presume that essentially one is dealing with an ordering process within the system of conduction electrons. As we saw in [Section 1.1](#), because of the Pauli principle the conduction electrons have fairly large energies up to a few electronvolts (1 eV corresponds to thermal energy  $k_B T$  at a temperature of about 11 000 K). However, the transition into the superconducting state occurs at only a few kelvins. Hence, one had to find an interaction that could lead to ordering within the electron system in spite of the high electron energies.

There exists a multitude of possible interactions between the conduction electrons in a metal. It had been imagined [1] that Coulomb repulsion between the electrons could lead to a spatial ordering of the electrons in the form of a lattice. Also [2] a magnetic interaction seemed possible. The electrons propagating through the metal lattice with impressive velocities (electrons having energies near the Fermi energy can reach velocities near 1% of the velocity of light) generate a magnetic field because of the associated currents and can then interact with each other due to this magnetic field. Other interactions can result from the structure of the electron states (allowed energy bands, see [Section 1.1](#)) [3].

All these attempts did not lead to a satisfactory microscopic theory of superconductivity. Only in 1950/1951 was an interaction between the electrons mediated by the vibrations of the lattice discussed simultaneously and independently by Fröhlich [4] and Bardeen [5]. As it turned out later, these ideas would lead to a fundamental understanding of superconductivity in terms of established concepts about the behavior of metals. Starting from this interaction, in 1957 Bardeen *et al.* [6] were able to propose a microscopic theory of superconductivity, the *BCS*

(Bardeen–Cooper–Schrieffer) *theory*, which was able to explain quantitatively many known experimental facts, and which turned out to be extremely stimulating. Motivated by this theory, after 1957 a large number of completely new experiments were performed, which strongly expanded our ideas about superconductivity and which basically changed our underlying concepts.

Still the road from the suggestion of a new interaction (1950) to the formulation of a satisfactory theory (1957) was a very difficult one. It was thus highly favorable when, nearly simultaneously with the theoretical discussion of this new interaction and of its possible importance for superconductivity, a surprisingly clear experimental confirmation of the basic correctness of the theory reached the scene. During the study of the different isotopes of the same superconductor, it had been found that the transition temperature  $T_c$  of superconductivity depends on the mass of the lattice atoms. Furthermore, the experimentally observed dependence exactly corresponded to that expected from the theoretical concepts of Fröhlich (see [Section 3.1.3.1](#)). This has shown that apparently the theory had hit the correct point, independent of all formal difficulties. This confirmation of the basic concepts had an important influence on the subsequent development.

How can we understand the interaction between the electrons that is mediated through the lattice vibrations? In the following, we will discuss some model ideas regarding this interaction. However, we must keep in mind that these model ideas are of little value if we try to extract further conclusions.

We start with a static model. The lattice of the atomic ions, in which the conduction electrons propagate as a Fermi gas, has elastic properties. The atomic ions are not stiffly bound to their lattice sites at rest. Instead, they can be deflected from their sites. At finite temperatures, they oscillate in an irregular way around these sites, as we have discussed. If we consider just two negative charges within this lattice of atomic ions, and in an oversimplified way ignore all other electrons, the negative charge of both electrons will slightly distort the lattice by attracting the surrounding positive charges. In other words, the lattice is polarized because of the negative charge. This situation is shown schematically in [Figure 3.1](#). Compared to the uniform distribution of the positive charges, the polarization leads to an accumulation of positive charge near the polarizing negative charge. The second electron with its polarization then feels the polarization of the first electron. It experiences an attraction to the location of the polarization and, hence, to the first electron. In this way, we have described an attractive interaction between two electrons due to the polarization of the lattice.

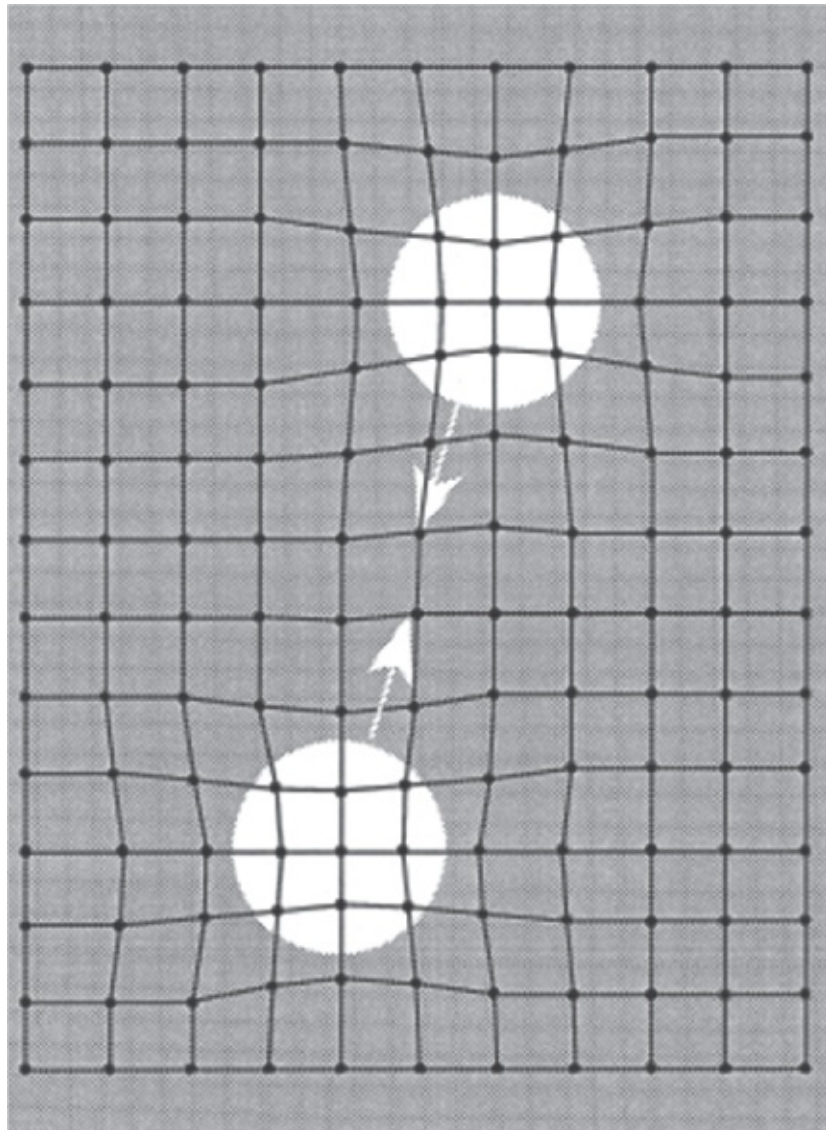


**Figure 3.1** Polarization of the lattice of atomic ions due to the electrons. Within a *static* model, this polarization cannot overcompensate the repulsion between the electrons because of their equal charge. It can only strongly reduce the repulsion.

We can present a mechanical analogy for this static, attractive interaction. We represent the elastically deformed lattice of atomic ions by an elastic membrane, say, by a thin, stretched rubber sheet or by the surface of a liquid.<sup>1</sup> Next, we place two small balls onto this membrane. In the case of the liquid, the balls must remain nonwetted. If the distance between the balls is sufficiently large because of its weight, each ball will locally deform the membrane independent of the other ([Figure 3.2a](#)).

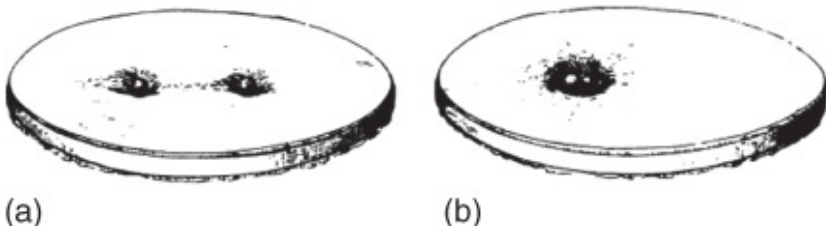


**Figure 3.2** Attraction between two small balls on an elastic membrane. The configuration (a) is unstable and changes into configuration (b).

This corresponds to the deformation of the lattice. We recognize intuitively that the energy of the total system (membrane with the two balls) can be lowered if the two small balls lie in the same hollow. They will sink in more deeply ([Figure 3.2b](#)), which corresponds to a decrease of the potential energy in the gravitational field. Hence, also the total energy of the system decreases, and the difference between the mechanical energy at the beginning and at the end is changed into heat due to frictional effects. We see that we obtain an interaction between the small balls because of the elastic membrane, resulting in a bound state, that is, in a state where the two small balls are spatially located very close to each other.

The model illustrates that an attractive interaction can be realized by means of elastic deformations, no more than that. In a metal, the electrons have impressive velocities. They do not polarize the lattice statically. One could presume that rather, during this motion through the lattice, the polarization takes place along the way, which sensitively depends on how quickly the lattice can follow the polarizing action of the electron. The time during which the lattice of atomic ions can respond to any displacements should be crucial. However, for an elastic system, this means that the characteristic internal frequencies are important. Because of this overall incorporation of a dynamical aspect, we have achieved an essential advance. Now we understand at least qualitatively that the strength of the polarization, and hence of the interaction for the same other conditions, can depend on the characteristic frequency of the lattice and, therefore, also on the mass of the atomic ions. Heavy isotopes oscillate somewhat slower, that is, they have smaller frequencies of the lattice. They can follow the polarizing action only more slowly compared to lighter isotopes. Hence, the polarization remains smaller. From this, we expect that the interaction becomes weaker and that the superconducting transition temperature is smaller. With increasing isotope mass the transition temperature decreases, in agreement with the experimental results. However, we must keep in mind that these last discussions are meaningful only in a heuristic sense and do not allow any quantitative conclusions. Only a quantum mechanical treatment can yield the frequencies of the lattice, which are essential for this interaction.

At this stage, we have introduced dynamic aspects into the interaction through the polarization of the lattice. However, we have kept the concepts of a static discussion, which yielded the energy gain of an electron due to the polarization achieved by another electron. In order to extend our dynamic model a little further, we can imagine that the second electron propagates within the polarization trail of the first electron and thereby lowers its energy, since it experiences the lattice already in a polarized state.

Basically, there are two possibilities. The first is that both electrons can propagate with the same momentum  $\mathbf{p} = \hbar\mathbf{k}$ . Then we can justifiably treat this object as a particle, namely an electron pair. However, the total momentum of this particle would be twice the momentum of a single electron. The other possibility would be that the electrons have opposite momentum. Again, one electron can propagate within the polarization trail of the other. However, in this case, the idea of a new particle, an electron pair, is more difficult. By a little abstraction, we note that in the first case the individual electrons are correlated due to the requirement that they have the same momentum, that is,  $\mathbf{p}_1 = \mathbf{p}_2$  or  $\mathbf{k}_1 = \mathbf{k}_2$ . An equally definite correlation is obtained by the requirement that  $\mathbf{p}_1 = -\mathbf{p}_2$  or  $\mathbf{k}_1 = -\mathbf{k}_2$ . We are justified to treat these strongly correlated electrons also as a pair. The latter electron pair has total momentum zero. Such pairs are referred to as **Cooper pairs**, since Cooper was the first to show that such a correlation leads to a decrease in the total energy [7]. If we take into account also the intrinsic angular momentum (spin) of the electrons, which is important for the statistical behavior of the new particles, a Cooper pair consists of two electrons with opposite momentum of equal magnitude and with opposite spins<sup>2</sup>

:

$$\text{Cooper pair : } \{\mathbf{k} \uparrow, -\mathbf{k} \downarrow\}$$

The correlation leading to Cooper pairs is energetically favored because of the lattice of positive atomic ions.

Since the possibility of a pair correlation represents the crucial key of the microscopic theory of superconductivity and, hence, for an understanding of the superconducting state, we also want to present another more general consideration. We can also understand the formation of electron pairs in a lattice from the very general formalism of the so-called *exchange interaction*.

Systems that exchange some physical quantities among themselves must experience an interaction for trivial reasons. This statement is very general. The exchange interaction of quantum mechanics deals with the fact that the exchange can lead to an attraction between two physical systems. For instance, two particles can experience an attraction because of the exchange of a third particle, leading to a state in which both particles are bound to each other.

A repulsion because of an exchange of particles can be easily understood classically. Two people, throwing a ball back and forth between themselves, experience such a repulsion. This seems obvious and can be checked easily by placing the people on two mobile platforms, which can move along the line connecting the two people. Because the ball is thrown back and forth, the two cars move away from each other. Here, it is only the exchange of the ball and the corresponding exchange of momentum that causes the repulsive interaction.

We do not attempt to construct a similarly simple model for an attractive interaction. Instead, we want to discuss an example of modern physics.

It is well known that two hydrogen atoms form a hydrogen molecule, and that the chemical bond in this molecule is very strong. In order to break this bond, one needs an energy of  $26 \times$

$10^4$  W s/mol (62.5 kcal/mol), that is, for dissociating 2 g of H<sub>2</sub>. How can we understand such a strong bond between neutral H atoms in an H<sub>2</sub> molecule? To explain the principle, we look at a slightly simpler system, namely H<sub>2</sub><sup>+</sup>, that is, a positively charged H<sub>2</sub> molecule. This ion consists of two hydrogen nuclei (two protons) and one electron. The two possible states of this system are shown in [Figure 3.3a,b](#) for a large distance between the two protons. The electron resides near one of the two protons. If we bring the protons closer together, the electron will hop from one proton to the other, with a certain probability, as we know from quantum mechanics. In our terminology, the electrons are exchanged. The probability for the exchange increases with decreasing distance. Then the electron belongs equally to both protons, as indicated in [Figure 3.3c](#). As an important result of quantum mechanics, for this problem one finds that the total energy of the system can be lowered because of the exchange. However, this means that smaller distances R are energetically more favorable. A bond between the two protons appears because of the common electron. The equilibrium distance results from the condition that the attractive force of the electron exchange is exactly balanced by the repulsive force between the two protons.

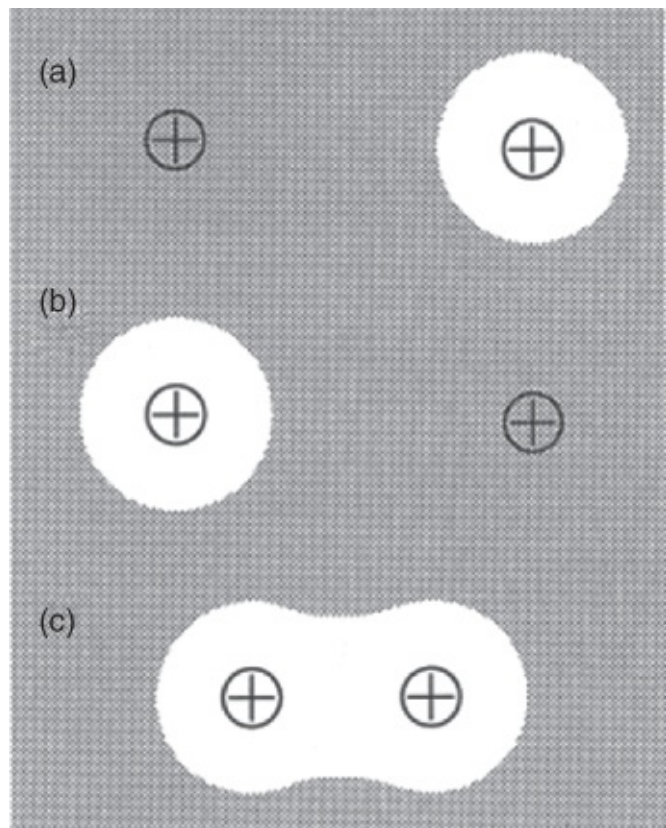


[Figure 3.3](#) Binding of the H<sub>2</sub><sup>+</sup> molecule. The scales are arbitrary. (a), (b): Two possible electron distributions for a large distance between the protons. (c) electron distribution for a small distance between the protons.

We can understand the energy gain due to the exchange of electrons in a particularly simple way, if we apply a highly fundamental principle of modern physics, namely the uncertainty principle. This principle says that both the spatial location *and* the momentum of a particle cannot simultaneously be determined exactly. The accuracy of the observation of both

quantities is limited by the famous relation

$$\Delta p_x \Delta x = \hbar$$

3.1

For our system this means that the smearing of the momentum  $\Delta p_x$  can be reduced if the electron is allowed to exist near both protons, since the smearing of its location  $\Delta x$  is enhanced in this case. As a result the energy smearing is reduced, and the energy of the electron is lowered [8].

If this energy gain is larger than the energy increase due to the Coulomb repulsion between the two protons, a net attraction is obtained. We see that the chemical bond of the  $H_2$  molecule represents a typical quantum mechanical effect. These arguments briefly outlined provide the key for the understanding of the chemical bond.

Using similar arguments, we can also understand the attractive interaction between the conduction electrons in a metal. In the metal, a new kind of particle can be exchanged, namely the phonons. The phonons are the quantized elementary vibrations of the crystal lattice. Any complex vibrational state of the lattice can be separated into normal modes, that is, into harmonic waves. This corresponds to the description in terms of a Fourier series. For a macroscopic body, the normal modes have well-defined energies. They also have definite wavelengths and, because of the relation  $p = h/\lambda$ , definite momenta. Hence, they represent particles and are referred to as **phonons** or as **quanta of sound**.

So an electron in a lattice can interact with another electron by the exchange of phonons. One speaks of the electron-electron interaction via phonons. The exchanged phonons only exist virtually during their transfer from one electron to another, since they cannot escape from the electrons into the lattice as real phonons.<sup>3</sup> Here, we note an important difference compared to the interaction within the  $H_2$  molecule. In the latter case, the exchanged electrons are real particles. This interaction via phonons is shown schematically in [Figure 3.4](#). In certain cases, namely in superconductors, it can be so strong that it becomes larger than the repulsion between the electrons due to the electrostatic forces.<sup>4</sup> Then we obtain the pair correlation we have discussed.

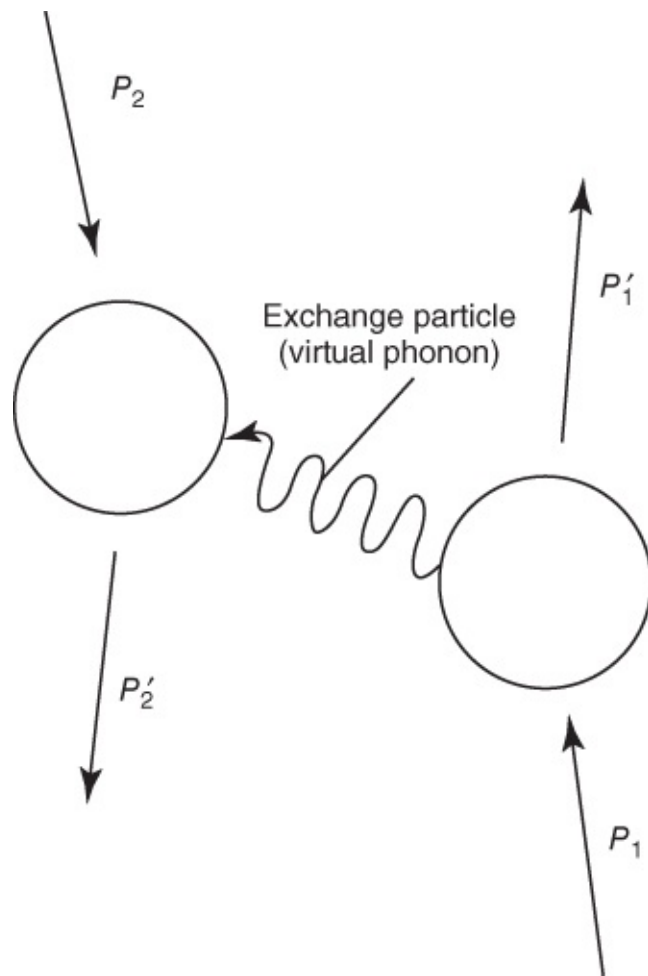


**Figure 3.4** Electron–electron interaction via phonons.

For pure superconductors, the average distance within which this pair correlation is active ranges between 100 and 1000 nm.<sup>5</sup> This length is referred to as the **BCS coherence length  $\xi_0$  of the Cooper pair**. This length must not be mixed up with the Ginzburg–Landau coherence length  $\xi_{\text{GL}}$ , which indicates the length scale within which the total system of Cooper pairs can change.

The BCS coherence length  $\xi_0$  can also be interpreted as the average size of a Cooper pair. In a highly simplified way we can say that in a pure superconductor a Cooper pair has an average size between  $10^2$  and  $10^3$  nm. This size is large compared to the average distance between two conduction electrons, which amounts to a few times  $10^{-1}$  nm. The Cooper pairs strongly overlap. Within the space of a single pair there exist  $10^6$ – $10^7$  other electrons, each being correlated in pairs. Intuitively we expect that a system of such strongly overlapping particles must have unusual properties. This will be discussed in the next section.

### 3.1.2 The Superconducting State, Quasiparticles, and BCS Theory

At least qualitatively we have seen that two electrons attract each other momentarily because of the electron–phonon interaction, and in this way they form a Cooper pair  $\{\mathbf{k}\uparrow, -\mathbf{k}\downarrow\}$ . Next we deal with the question of how these pairs collectively can occupy the same quantum state.

Here, BCS found an ingenious answer, which we want to outline for the case of zero temperature.

Let us recall first the situation of the unpaired electrons. At  $T = 0$  they occupy the lowest possible energy states. If we treat the electrons as free particles, their energy is given by

$$\varepsilon_k = \frac{1}{2m}(p_x^2 + p_y^2 + p_z^2) \quad \underline{\text{3.2a}}$$

or, with  $\mathbf{p} = \hbar\mathbf{k}$ ,

$$\varepsilon_k = \frac{\hbar^2}{2m}(k_x^2 + k_y^2 + k_z^2) \quad \underline{\text{3.2b}}$$

The possible values of  $\mathbf{k}$  are discrete (see [Section 1.2](#)), and in the simplest case in  $\mathbf{k}$ -space the electrons occupy the Fermi sphere (see [Figure 1.18](#)). All states within the Fermi sphere must be occupied by an electron, and all states outside the Fermi sphere must remain unoccupied.

The electrons near the Fermi energy will interact attractively with each other. The attractive interaction energy is taken as a negative constant  $-V$  for the electrons, with its energy range distributed over the interval  $\pm\hbar\omega_c$  near the Fermi energy.<sup>6</sup> Everywhere else the interaction is assumed to be zero. It is not necessary that the interaction energy  $V$  results from the electron–phonon interaction. However, if this is the case, it is likely that the energy  $\hbar\omega_c$  is associated with a characteristic phonon energy, or the frequency  $\omega_c$  with a characteristic phonon frequency, namely the Debye frequency.

Around the surface of the Fermi sphere, the Cooper pairs constitute a highly peculiar state, in which, within a certain interval around the Fermi energy  $E_F$ , the pair states  $\{\mathbf{k}\uparrow, -\mathbf{k}\downarrow\}$  are simultaneously unoccupied with probability  $|u_k|^2$  and occupied with probability  $|v_k|^2$ . In general, the probability amplitudes  $u_k$  and  $v_k$  are complex numbers, which depend on the wave vector  $\mathbf{k}$ . The condition  $|u_k|^2 + |v_k|^2 = 1$  must be valid, since the two probabilities must add up to 1. Classically, such a state cannot be imagined. However, in quantum mechanics such superpositions are quite possible.

Next we must determine the parameters  $u$  and  $v$ . This can be done by inserting the ansatz of the wave function of the Cooper pairs given above into the Schrödinger equation of the system. Then one calculates the energy of the system as a function of  $u$  and  $v$ , and finally one chooses  $u$  and  $v$  such that the energy reaches a minimum [M3, M4]. Then we have found the energetically optimum state consistent with the assumed wave function.

Using this procedure, for  $|v_k|^2$  one finds the expression

$$|v_k|^2 = \frac{1}{2} \left[ 1 - \frac{\varepsilon_k - E_F}{\sqrt{|\Delta|^2 + (\varepsilon_k - E_F)^2}} \right] \quad \underline{\text{3.3a}}$$

Here, the energy of the individual electrons in the absence of the interaction  $V$  is denoted by  $\epsilon_k$  as in Eqs. (3.2a) and (3.2b), and  $E_F$  is the Fermi energy. The quantity  $\Delta$  will become highly important in the following. It is given by the sum  $\Delta = -V \sum_k u_k v_k$ . Hence, it is different from zero only for values of  $\epsilon_k$  within the interval  $\pm \hbar\omega_c$ , similar to the interaction  $V$ . In general,  $\Delta$  is a complex number, which we write in the following as  $\Delta = \Delta_0 e^{i\varphi}$  with real amplitude  $\Delta_0$ . Then we have  $|\Delta|^2 = \Delta_0^2$ . For  $|u_k|^2 = 1 - |v_k|^2$ , one finds

$$|u_k|^2 = \frac{1}{2} \left[ 1 + \frac{\epsilon_k - E_F}{\sqrt{|\Delta|^2 + (\epsilon_k - E_F)^2}} \right] = \frac{1}{2} \left[ 1 + \frac{\epsilon_k - E_F}{\sqrt{\Delta_0^2 + (\epsilon_k - E_F)^2}} \right] \quad 3.3b$$

The two functions  $|u_k|^2$  and  $|v_k|^2$  are shown in [Figure 3.5](#). Here, we have assumed for  $E_F$  a value of 1 eV and for  $\Delta_0$  a value of 1 meV, which are typical for metallic superconductors. Deep within the Fermi sphere (i.e., for  $\epsilon_k \gg E_F$ ), the probability  $|v_k|^2$  of finding an electron pair in the state  $\mathbf{k}$  (or  $|\mathbf{k}|$ ) is practically equal to one, as would also be in the case for noninteracting electrons. Analogously, for energies  $\epsilon_k \ll E_F$ , the probability  $|u_k|^2$  that this state is unoccupied is nearly equal to one. However, within an interval of about  $\pm \Delta_0$  around the Fermi energy, both functions  $|u_k|^2$  and  $|v_k|^2$  strongly deviate from the value one. For independent, unpaired electrons, exactly this would not be the case. We see that the Cooper pair system shows nontrivial behavior in this energy interval. In [Figure 3.5](#), the ratio  $\Delta_0/E_F = 10^{-3}$ . Hence, we can say that only about 0.1% of all electrons, namely those near the Fermi energy, participate in the superconductivity.

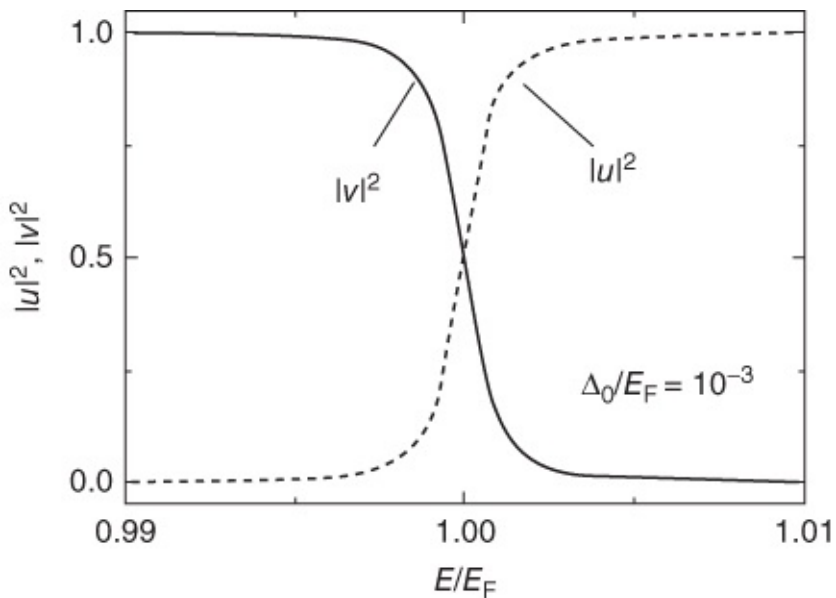


[Figure 3.5](#) The functions  $|u_k|^2$  and  $|v_k|^2$ , indicating the probability that a pair state  $\{\mathbf{k}\uparrow, -\mathbf{k}\downarrow\}$  is occupied ( $|v_k|^2$ ) or unoccupied ( $|u_k|^2$ ). For the figure, the values  $E_F = 1$  eV and  $\Delta_0 = 1$  meV were used.

The quantity  $\Delta$  depends on all states  $k$  because of the product  $u_k v_k$ . This shows that all Cooper pairs are collectively connected with each other. Contrary to this, for independent electrons,  $\Delta$  would always be zero, since either  $u_k$  or  $v_k$  always vanishes.

In the state described by the BCS theory, all pairs show the same values of all physical quantities. In particular, the motion of the center of mass is the same for all pairs. So we have arrived at the macroscopic matter wave, the properties of which we have described in detail in [Chapter 1](#). What further information is provided by the microscopic theory?

First one can calculate the energy gain because of the Cooper pairing, that is, the condensation energy. One finds that this is given by  $-N(E_F)\Delta_0^2/2$ , where  $N(E_F)$  is the density of states at the Fermi energy (see [Section 1.1](#)). In addition to  $N(E_F)$ , the condensation energy also depends on the pair interaction  $V$  because of  $\Delta_0^2$ . Apparently, it is favorable for superconductivity if both quantities become very large.

The next important question concerns the possible excitations of the superconducting ground state. As a very simple excitation we can imagine that a Cooper pair is broken, yielding two independent electrons. Here, we can look at a single unpaired electron as an “elementary process,” and we can ask how its (excitation) energy compares with the energy  $\epsilon_k$  of the same electron in the normal state. The resulting electron is referred to as ***quasiparticle***. Due to the pair interaction in the superconductor, this quasiparticle does not satisfy any longer the energy–momentum relation ([3.2b](#)).

Instead, one finds that the energy of this unpaired electron is given by [M3, M4]

$$E_k = \sqrt{(\epsilon_k - E_F)^2 + \Delta_0^2} \quad \text{3.4}$$

This function is shown in [Figure 3.6](#). If  $\Delta_0$  were zero, we would have  $E_k = \pm(\epsilon_k - E_F)$ , and we would recover the energy of the noninteracting electrons. However, for  $\Delta_0 \neq 0$ ,  $E_k$  attains a minimum value  $\Delta_0$ . This also means that at least twice this amount must be supplied, in order to break a Cooper pair and to generate two quasiparticles.

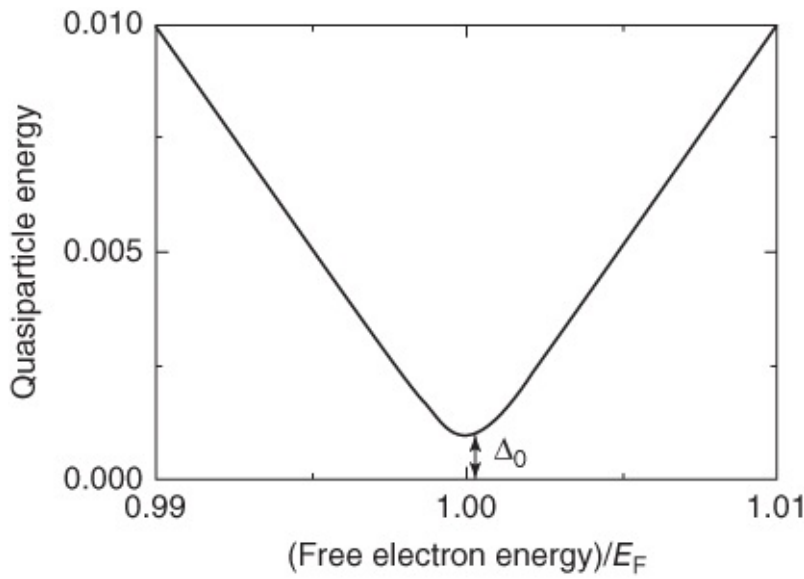


**Figure 3.6** Energy of an unpaired electron (quasiparticle) in a superconductor, plotted versus the energy the electron would have without the pair interaction.

At this stage, we can already see the influence of the Cooper pair interaction on the density of states of unpaired electrons. Even without this interaction, the density of states is in general a very complicated function depending on the crystal structure. We denote this function by  $N_n(E)$ . However, here we are concerned only with a small interval  $\pm\Delta_0$  near the Fermi energy. In this interval, we can treat the density of states of the noninteracting electrons as constant:  $N_n(E) \approx N_n(E_F)$ . In this case there are states already very close to the Fermi energy, into which the electrons can be excited. However, this is by no means possible for the quasiparticles. According to Eq. (3.4), for this the minimum energy  $\Delta_0$  is needed.

For the density of states of the quasiparticles, this means that a gap appears in an interval  $\pm\Delta_0$  at the Fermi energy. Within this gap, no states exist anymore. The exact expression for the density of states of the quasiparticles, which we want to denote by  $N_s(E)$ , is given from the BCS theory by

$$N_s(E) = N_n(E_F) \frac{|E - E_F|}{\sqrt{(E - E_F)^2 - \Delta_0^2}} \quad 3.5$$

for energies  $|E - E_F| \geq \Delta_0$ . For  $|E - E_F| < \Delta_0$ , the function  $N_s(E)$  is zero. This density of states is shown in [Figure 3.7](#). At energies  $E = E_F \pm \Delta_0$  it reaches infinity, and for large values of  $|E|$  it rapidly approaches the density of states  $N_n(E_F)$ . Within the energy interval  $E_F \pm \Delta_0$ , there are no states.<sup>7</sup> Therefore,  $2\Delta_0$  is also referred to as the **energy gap** of the superconductor.

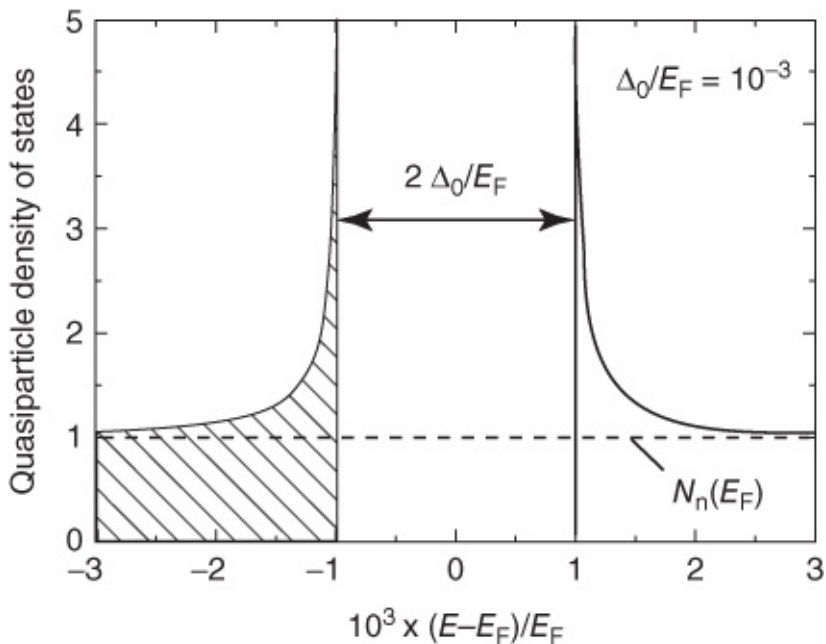


**Figure 3.7** Normalized density of states  $N_s(E)/N_n(E_F)$  of the quasiparticles in a superconductor according to the BCS theory. The ratio  $\Delta_0/E_F$  was taken as  $10^{-3}$ . At the temperature  $T = 0$ , all states below the Fermi energy are occupied (hatched region).

At this point we note that the energy states of the unpaired electrons are energetically redistributed because of the Cooper pair interaction, but they are not annihilated. If we integrate  $N_s(E)$  over all energies, we obtain the same number of states as in the normal state. Most of the states between  $E_F$  and  $E_F + \Delta_0$  in the normal conductor appear at energies slightly above  $E_F + \Delta_0$  in a superconductor.

As we will see in [Section 3.1.3](#), the energy gap in a superconductor can be observed very nicely in infrared absorption experiments and also by means of superconducting tunnel junctions. These experiments perfectly confirm our ideas about the superconducting state.

Next we turn to the properties of superconductors at finite temperatures. At  $T > 0$  some Cooper pairs are broken because of thermal fluctuations, and thermally excited quasiparticles are generated. These quasiparticles are fermions, exactly like the electrons in a normal conductor. Hence, the probability of finding a quasiparticle in a given energy state is indicated by the Fermi distribution function (1.3).

We note that a quasiparticle in the quantum state  $\mathbf{k}$  is blocking this state for the condensation of Cooper pairs, thereby affecting a reduction of the total number of Cooper pairs and also a reduction of their binding energy. One obtains a decrease in  $\Delta_0$  with increasing temperature.

For  $T \rightarrow T_c$ ,  $\Delta_0$  approaches zero.

How does the density  $n_s$  of Cooper pairs depend on  $\Delta_0$ ? One finds that  $n_s$  is proportional to  $\Delta_0^2$ . We see that, on the one hand, the quantity  $\Delta_0$  appears as (half) the “energy gap” of the superconductor. On the other hand, it also determines the number of Cooper pairs. In [Chapter 1](#), we described the Cooper pair density in terms of the absolute square of the macroscopic

wave function  $\Psi = \Psi_0 e^{i\phi}$ . One can show that  $\Delta \propto \Psi$  [9]. Hence, pair amplitude  $\Psi_0$  and  $\Delta_0$  are often used synonymously.

Finally, from the BCS theory one can derive a very simple connection between  $T_c$  and the quantities  $N_n(E_F)$ ,  $\hbar\omega_c$ , and the Cooper pair interaction  $V$ : it is [M3, M4]

$$T_c = 1.13 \frac{\hbar\omega_c}{k_B} \exp\left(-\frac{1}{N_n(E_F) V}\right) \quad \text{3.6}$$

If we identify  $\omega_c$  with the Debye frequency  $\omega_D$ , we also obtain immediately a connection between the transition temperature and the mass  $M$  of the elements building the lattice, since the frequency of the lattice vibrations is inversely proportional to the square root of  $M$ . If we substitute an isotope on a lattice site by another one, the interaction between these elements building the lattice remains unchanged. This results in the isotope effect, which we expect for Cooper pairing because of the electron–phonon interaction.

Furthermore, from the BCS theory, we can derive the following important relation between  $\Delta_0$  at zero temperature and  $T_c$ :

$$2\Delta_0(T = 0) = 3.5 k_B T_c \quad \text{3.7}$$

In the following section, we turn to the experimental results dealing with the microscopic concepts of the superconducting state.

### 3.1.3 Experimental Confirmation of Fundamental Concepts about the Superconducting State

In the previous section we have outlined a picture of the superconducting state based on the BCS theory, which represents a most successful microscopic theory of superconductivity. In principle, it is the total sum of all experimental observations explained quantitatively or at least qualitatively by the theory, which completely justifies the essential concepts. There are a few experimental results that particularly strongly illuminate certain characteristic properties of the superconducting state.

In [Chapter 1](#) we discussed results showing directly that superconductivity manifests itself in terms of a macroscopic quantum state with a well-defined phase. In the following section, we will present additional results that should strengthen our confidence in the somewhat complicated ideas about the superconducting state, and which should deepen our understanding by means of concrete experiments. Except for the isotope effect, these characteristic properties are independent of the special interaction leading to the pair correlation.

Some of the experimental facts, such as, say, the behavior of the specific heat or the isotope effect, were already known before the development of the BCS theory. Other experiments, such as, say, measurements of the tunneling effect and of the Josephson effects (discussed already in [Chapter 1](#)), were stimulated only by the microscopic theory. However, the flux quantization,

also discussed in [Chapter 1](#), is a special case, since it was already predicted by F. London long before the BCS theory arrived. On the other hand, it was experimentally observed only after the development of this theory and represents an impressive quantitative confirmation of the concept of Cooper pairing.

### 3.1.3.1 The Isotope Effect

Already in 1922, Kamerlingh-Onnes [10] studied the question of whether the nuclear mass of the lattice atoms has an influence on superconductivity, that is, if superconductivity depends on the lattice of the atomic ions, or whether it is restricted only to the system of the electrons. At the time, only the kinds of lead naturally occurring at different locations ( $M = 206$  “uranium lead” and  $M = 207.2$  “natural lead”) were at his disposal. Within his experimental accuracy, he could not detect any difference in the transition temperature. Also subsequent experiments with lead samples by Justi in 1941 [11] did not show an influence of atomic mass on  $T_c$ .

With the advent of modern nuclear physics, it was possible to produce isotopes with a larger mass difference in sufficient concentration within nuclear reactors. In 1950 in mercury a dependence of the transition temperature on nuclear mass was observed [12, 13]. Some results are listed in [Table 3.1](#).

**Table 3.1** Isotope effect in mercury [13]

Average atomic mass	199.7	200.7	202.0	203.4
Transition temperature $T_c$ (K)	4.161	4.150	4.143	4.126

We have already mentioned that these results were highly important for the development of superconductivity, since they appeared just in time to confirm perfectly the idea of the electron–phonon interaction. Already the initial rather qualitative discussions of Fröhlich or Bardeen suggested that the transition temperature  $T_c$  should be inversely proportional to the square root of the atomic mass  $M$ :

$$T_c \propto M^{-1/2} \quad \text{3.8}$$

This dependence also remained valid in the BCS theory appearing only 7 years later, as we have discussed in [Section 3.1.2](#).

The relation (3.8) is well satisfied for a series of superconductors. In [Figure 3.8](#) we show the results for tin. Tin is a favorable substance, since its possible variations of the nuclear mass are relatively large, namely from  $M = 113$  up to  $M = 123$ . In [Figure 3.8](#) the results from different laboratories are shown [14]. The dashed line corresponds to the exponent  $-1/2$  in relation (3.8). The agreement between experiment and the theoretical expectation is excellent.

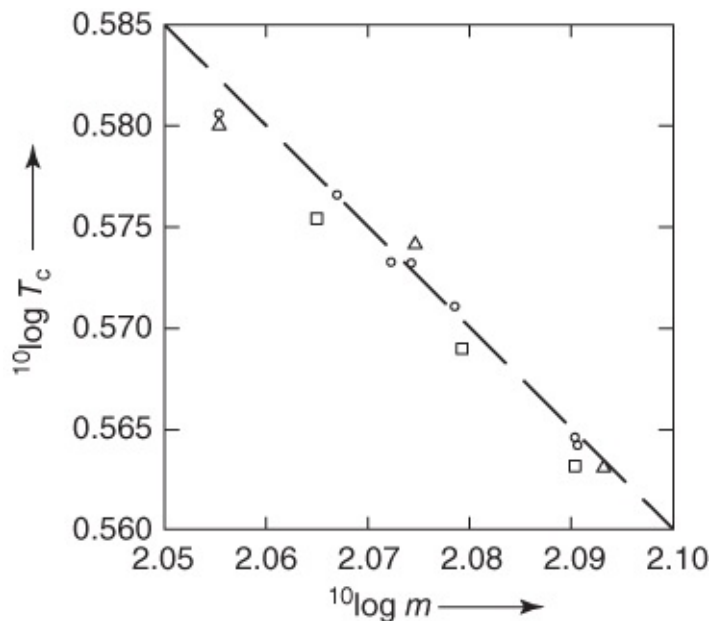


**Figure 3.8** Isotope effect in tin: ○ Maxwell; □ Lock, Pippard, and Shoenberg; and Δ Serin, Reynolds, and Lohman.

(From [14].)

From our current point of view this agreement is surprising, since the theory leading to relation (3.8) is strongly simplified. However, the agreement shows that apparently these simplifications are justified for a large number of superconductors. On the other hand, we see from [Table 3.2](#), which lists measurements of the isotope effect in different superconductors, that this is not always the case.

**Table 3.2** Isotope effect

Element	Hg	Sn	Pb	Cd	Tl	Mo	Os	Ru
Isotope exponent $\beta^a$	0.50	0.47	0.48	0.5	0.5	0.33	0.2	0.0

<sup>a</sup> The exponent  $\beta$  is obtained from experiment by fitting to the relation  $T_c \propto M^{-\beta}$ . The values shown are taken from Ref. [15].

The nontransition metals display well the exponent  $\beta = 1/2$ , the transition metals show strong deviations from this value. In spite of the great difficulties of these experiments,<sup>8</sup> the deviations are well reproduced. Measurements for uranium even indicate a value of  $\beta = -2.2$ , that is, an isotope effect with opposite sign [16].

Because of the great success of the BCS theory, one is tempted to find an explanation of the isotope exponent deviating from  $1/2$  within the framework of this theory. This is quite possible, if we closely analyze the parameter  $V$  in Eq. (3.6) characterizing the interaction. Essentially, this interaction parameter results from the difference between the *attractive* electron–phonon interaction and the *repulsive* Coulomb interaction between the electrons. If both interactions are explicitly introduced into the theory, which became possible during further development of the theory, one obtains an improved and also more complicated formula for  $T_c$  [17]:

$$T_c \propto \omega_D \exp\left(\frac{\lambda^* + 1}{\lambda^* - \mu^* (1 + \lambda^* \langle \omega \rangle / \omega_D)}\right)$$

Here, the electron–phonon interaction is characterized by  $\lambda^*$ , the Coulomb interaction by  $\mu^*$ , and  $\langle \omega \rangle$  denotes a certain average value taken over all frequencies of the crystal lattice.<sup>9</sup>

We do not want to discuss this formula in more detail. As the essential point, we note that in such a more detailed analysis the lattice frequencies also appear explicitly in the exponent, as expected. Hence, depending on the magnitude of  $\lambda^*$  and  $\mu^*$ , the influence of the factor  $\omega_D$  upon  $T_c$  (see Eq. (3.9)) is changed to a greater or lesser degree. Therefore, deviations of the quantity  $\beta$  in the relation  $T_c \propto M^{-\beta}$  from the value  $1/2$  cannot be taken as evidence against the importance of the electron–phonon interaction in these superconductors. The same applies even to the complete absence of any dependence of  $T_c$  upon  $M$ .

An important advance was achieved by tunneling experiments with superconductors, which we will discuss in the following section. The electron–phonon interaction shows up in the voltage–current characteristic of tunnel junctions, if the interaction is sufficiently strong. A careful analysis of such curves allows one to determine the quantities  $\lambda^*$  and  $\mu^*$ .

The isotope effect demonstrates most directly the influence of lattice vibrations. Because of its quantitative agreement with the theory, at least for many superconductors, it confirms the crucial role of the electron–phonon interaction. Here, the progress of nuclear physics, allowing the production of new isotopes in nuclear reactors, has strongly affected the development of superconductivity. This is one of the many examples in the field of superconductivity where different areas of physics have influenced each other during the progress that has been accomplished.

Also newly discovered superconductors have been investigated regarding the isotope effect, if possible. The results for the high-temperature superconductors will be discussed in [Section 3.2.2](#). Here, as further examples, we mention the fullerides  $K_3C_{60}$  and  $Rb_3C_{60}$  [18] as well as magnesium diboride  $MgB_2$  [19].

In the fullerides, the carbon isotope  $^{12}C$  was partly or completely replaced by the isotope  $^{13}C$ . Since carbon is a relatively light element, in this case a relatively large shift of  $T_c$  in the percent range could be observed. An isotope exponent of about 0.3 was found with a large scattering of the data. This value agrees well with the electron–phonon coupling, if we assume that the intramolecular vibrations of the  $C_{60}$  molecules provide the dominant contribution to the Cooper pairing.

For  $MgB_2$  the isotope effect was studied regarding both Mg and B. For the variation of the boron isotopes ( $^{10}B \leftrightarrow ^{11}B$ ) an exponent of about 0.3 was found, and the variation of the magnesium isotopes ( $^{26}Mg \leftrightarrow ^{27}Mg$ ) only yielded an exponent of 0.02. This indicates that the vibrations of the boron ions apparently play an important role for the Cooper pairing in  $MgB_2$ .

### 3.1.3.2 The Energy Gap

In [Figure 3.7](#) (see [Section 3.1.2](#)), we have shown the normalized density of states of unpaired electrons in the superconducting state for  $T = 0$ . The existence of a forbidden energy range (“energy gap”) has given us a simple means to understand the fact that, below a critical kinetic excitation energy, Cooper pairs cannot interact with the crystal lattice. We can use different methods for the measurement of this energy gap, which we will discuss in the following.

#### Absorption of Electromagnetic Radiation

We have already pointed out the possibility that the energy gap can be determined by measuring the absorption of electromagnetic radiation. The first experiment proving the existence of a gap in the energy spectrum of the unpaired electrons for  $T < T_c$  was reported in 1957 by Glover and Tinkham [20]. They observed the infrared transmission of thin superconducting films.

Already by the early 1930s, it had been pointed out<sup>10</sup> that electromagnetic waves of suitable frequency should serve well to break up the ordered state of a superconductor below its transition temperature. This should show up as an anomaly in the absorption. In the 1930s, such experiments could not be carried out, since the required range of electromagnetic wavelengths was not yet experimentally available. Assuming a binding energy  $E_B$  of about  $10^{-3}$  eV, for this energy we need radiation quanta with a frequency  $f = E_B/h = 2.4 \times 10^{11}$  Hz (240 GHz). These are waves with about 1 mm wavelength, for which no generation or detection methods were available in the 1930s. Only 20 years later, however, this method was applied successfully for measuring the energy gap, [20]. Today, for the range of wavelengths between about 500  $\mu\text{m}$  and 3 cm, we have sufficient, well-functioning experimental techniques for performing such measurements for quantitative determination of the energy gap.

The quantitative data analysis for this method is somewhat complicated, and we do not want to discuss it in more detail. In [Figure 3.9](#) we just show an example of such a measurement [22]. Here, the radiation was guided into a small cavity, made from the material to be studied. Within the cavity the radiation is reflected many times before it is detected. The stronger the absorption of the radiation in the cavity wall, the smaller is the detected power. For the measurement, at a fixed temperature (here about 1.4 K), the power in the superconducting and in the normal states,  $I_s$  and  $I_n$ , respectively, is determined for each wavelength. In this experiment, the superconductivity can be eliminated by a sufficiently high magnetic field. The difference between the two power values yields the difference between the reflection for both states. In [Figure 3.9](#) this difference, normalized by the power in the normal conducting state, is plotted versus the frequency. At small frequencies, we see a distinct difference between the reflection in the superconducting and in the normal conducting states. In the superconducting state the reflection is larger. At a certain frequency the difference drops abruptly, and at higher frequencies it reaches zero. Apparently, the abrupt drop sets in as soon as the quantum energy of the radiation is large enough to break up the Cooper pairs. This results in an additional absorption. For energies  $hf > 2\Delta_0$  the energy gap practically does not influence the absorption, since the electrons can be excited far beyond the energy gap by the radiation quanta. In [Table](#)

[3.3](#) we list the values of the energy gap at  $T = 0$  obtained from such measurements for different superconductors. [Table 3.4](#) presents values of the energy gap for some selected superconducting compounds and alloys.

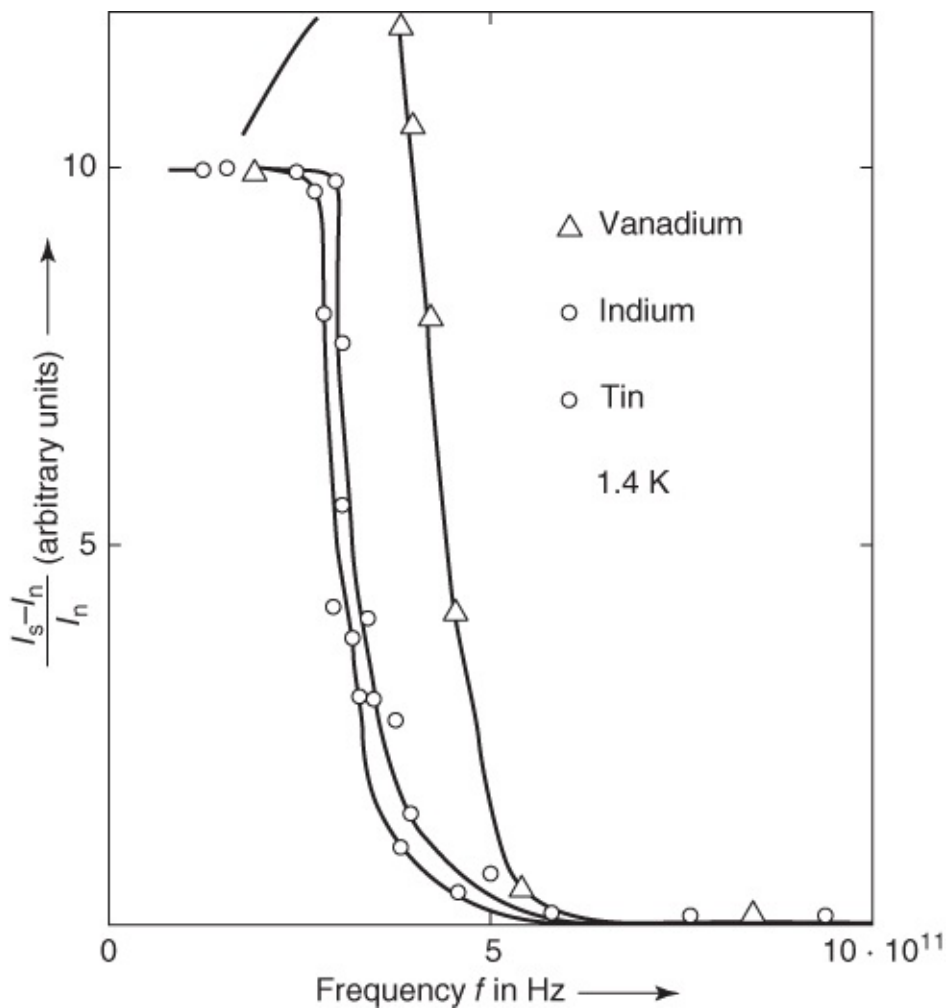


**Figure 3.9** Absorption of electromagnetic waves with frequency  $f$  in superconductors. Transition temperatures  $T_c$  are V, 5.3 K; In, 3.42 K; and Sn, 3.72 K. Measurement temperature is 1.4 K. In vanadium for  $f < 2\Delta_0/h$ , a frequency dependence is observed, the possible origin of which cannot be discussed here.

(From [22].)

**Table 3.3** Energy gap  $2\Delta_0$  in units of  $k_B T_c$  for some superconducting elements

Element	Method			
	$T_c$ (K)	Tunnel junctions	Ultrasound	Light absorption
Sn	3.72	$3.5 \pm 0.1$ (1.15)	—	3.5
In	3.4	$3.5 \pm 0.1$ (1.05)	$3.5 \pm 0.2$	$3.9 \pm 0.3$
Tl	2.39	$3.6 \pm 0.1$ (0.75)	—	—
Ta	4.29	$3.5 \pm 0.1$ (1.30)	$3.5 \pm 0.1$	3.0
Nb	9.2	3.6 (2.90)	$4.0 \pm 0.1$	$2.8 \pm 0.3$
Hg	4.15	$4.6 \pm 0.1$ (1.65)	—	$4.6 \pm 0.2$
Pb	7.2	$4.3 \pm 0.05$ (2.70)		$4.4 \pm 0.1$

The numbers in brackets indicate the energy gap in megaelectronvolts. The values are taken from Ref. [23]. For special details see Superconductivity Data, no. 19–1 (1982), Fachinformationszentrum Karlsruhe GmbH.

**Table 3.4** Energy gap  $2\Delta_0$  for selected superconducting compounds (s-wave Cooper pairing)

Material	$T_c$ (K)	$2\Delta_0$ (meV)	$2\Delta_0/k_B T_c$	References	cf. Section
$\text{Nb}_3\text{Sn}$	18	6.55	4.2	[24]	2.3.1
NbN	13	4.6	4.1	[25]	2.3.1
$\text{MgB}_2$	40	3.6–15	1.1–4.5	[19]	2.3.2
$\text{Rb}_3\text{C}_{60}$	29.5	10–13	4.0–5.1	[18]	2.4
$\text{ErRh}_4\text{B}_4$	8.5	2.7–3	3.8–4.2	[26]	2.5
$\text{PbMo}_6\text{S}_3$	12	4–5	4–5	[27]	2.5
$\text{YNi}_2\text{B}_2\text{C}$	15.5	4.7	3.5	[28]	2.5
$\text{NbSe}_2$	7	2.2	3.7	[29]	2.7
$\text{BaPb}_{0.75}\text{Bi}_{0.25}\text{O}_3$	11.5	3.5	3.5	[30]	2.8.2
$\text{Ba}_{0.6}\text{K}_{0.4}\text{BiO}_3$	25–30	8	3.5	[31]	2.8.2

Experimental methods: tunneling effect, optical methods, nuclear spin resonance, specific heat, and so on. Much data can also be found in the monograph [M14].

## Ultrasound Absorption

Sound waves also interact with the system of conduction electrons in a metal. We can look at a sound wave as a current of coherent phonons. Until recently, only sound waves with frequencies up to about 30 GHz were available. Most measurements were carried out using frequencies from a few megahertz up to 10 MHz. The energies of these frequencies are much smaller than the width of the energy gap. Only very close to  $T_c$ , where the energy gap  $2\Delta_0(T)$

approaches zero, it is possible that the sound energy of these frequencies becomes comparable to  $2\Delta_0(T)$ . Hence, in addition to other mechanisms, absorption essentially depends on the number of unpaired electrons. Below  $T_c$  this number decreases rapidly with decreasing temperature. Correspondingly, the damping of sound also decreases rapidly below  $T_c$ . In [Figure 3.10](#) we present an example of such a measurement [32]. Since for a given temperature the number of unpaired electrons depends on the width of the energy gap, the latter can be determined from such absorption measurements by means of a comparison with the theoretically expected behavior. In [Figure 3.10](#) the curve expected from the BCS theory for  $2\Delta_0(T = 0) = 3.5k_B T_c$  (Eq. (3.7)) is shown.

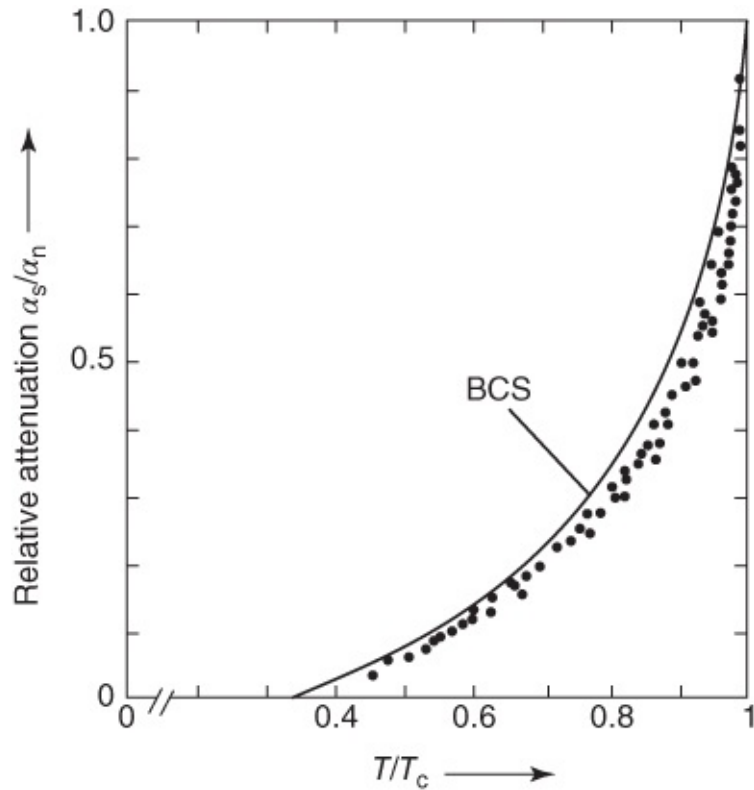


[Figure 3.10](#) Ultrasound absorption in superconducting tin and indium. The solid line indicates the behavior expected from the BCS theory for the energy gap  $2\Delta_0 = 3.5k_B T_c$ .

(From [32].)

Here, we cannot discuss in detail the analysis of such measurements, which is not quite simple. We just want to point out that, compared to electromagnetic waves, sound waves have the great advantage of penetrating more deeply into the metal, whereas high-frequency electromagnetic waves only reach a thin layer at the surface, namely within the skin depth.

## Tunneling Experiments

In 1961, Giaever pointed out the possibility of determining the energy gap by means of tunneling experiments [33, 34]. We will treat this method in some detail, since it yielded much new information far beyond just the measurement of the energy gap. The method is based on the observation of the tunneling current across a thin insulating layer between a reference sample

and the superconductor to be studied. In contrast to the Josephson current we treated in [Chapter 1](#), now we are concerned with the tunneling of the unpaired electrons.

The arrangement is shown schematically in [Figure 3.11a](#). Two metallic conductors, for instance, two aluminum layers, are separated from each other by means of a thin insulating layer, for instance,  $\text{Al}_2\text{O}_3$ . The  $\text{Al}_2\text{O}_3$  is an excellent electrical insulator, which can be fabricated nearly perfectly also with a thickness of only a few nanometers.

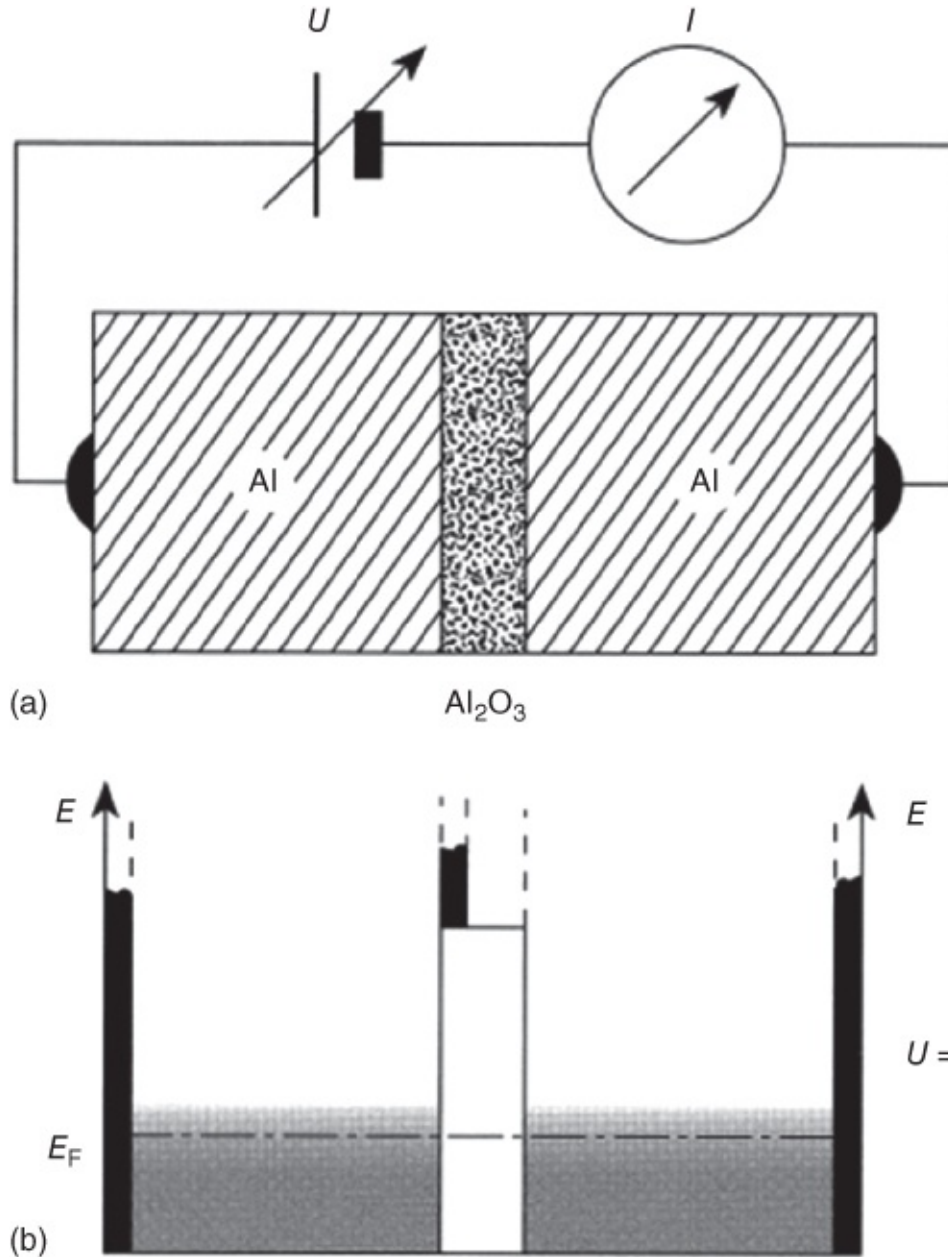


**Figure 3.11** (a) The arrangement for measuring a tunneling current. (b) The allowed energy values (black areas) and their occupation (gray shaded areas).

Because of the great importance of this tunneling effect, for instance, also in semiconductor physics, we want to look at it in more detail. Therefore, in [Figure 3.11b](#) we have indicated schematically the allowed and forbidden energy ranges near the Fermi energy for the three parts of the tunneling arrangement. The black vertical areas indicate the allowed energy bands.

The gray shaded areas show the occupation of the bands. The thermal smearing of the occupation is also indicated. In the electrical insulator the nearest allowed and unoccupied energy values are much higher.

We can also understand the tunneling effect without a detailed calculation, if we recall the wave character of our particles. If a wave encounters the surface of a medium into which it cannot enter, the wave must be *totally reflected*. Here, we recognize intuitively that the wave must penetrate a small distance into the forbidden portion. In some sense, the wave tests the possibility of whether it can exist in this medium. At the same time, its amplitude decreases exponentially, this decrease being faster, the larger the difference between the energy of the wave and an allowed energy value, that is, the higher the barrier. From this highly qualitative argument, we see immediately that for a sufficiently thin barrier there is a finite probability that the wave can extend beyond the barrier. This is always the case if the thickness of the barrier is comparable with the decay length of the wave amplitude in the forbidden regime. In this case, a finite amplitude arrives at the back side where it can exit again into the allowed regime. However, there the amplitude is very small, that is, the probability for the passage of a particle decreases rapidly with increasing barrier thickness along with the wave amplitude. We see that the tunneling probability depends on the energetic height and on the thickness of the barrier. Here, the energetic height of the barrier must be taken from the particle energy, that is, in our case of [Figure 3.11b](#) practically from  $E_F$ .

In our present discussion we are dealing with electrons, that is, with Fermi particles. They must satisfy the Pauli principle (see [Section 1.1](#)). In order to traverse the barrier, the electron must find an unoccupied state on the other side. If all states are already occupied on the other side, the passage of the electron is impossible, even for a sufficiently thin barrier. Therefore, the number of particles passing across the barrier depends on the following three quantities:

1. number of electrons reaching the barrier;
2. tunneling probability across the barrier;
3. number of unoccupied energy levels on the other side.

In a quantitative treatment of the tunneling current of electrons, all three quantities must be taken into account.

In [Figure 3.11b](#) we have shown the tunneling arrangement *without* an external voltage. If electrons can be exchanged between two systems, the equilibrium state is fixed by the fact that the Fermi energy is located at the same height, that is, the Fermi energy is displayed by a horizontal line in our schematic diagram. For this state the net exchange of particles is exactly zero. The same number of electrons tunnel to the right as to the left.

Next we apply a voltage  $U \neq 0$  to the arrangement. Practically, the voltage drop is completely restricted to the barrier layer. This means that the Fermi energies on the right and on the left of the barrier differ by the amount  $eU$ . Now the tunneling currents in both directions no longer compensate each other, and a net current  $I$  flows.

To illustrate the magnitude of the current and its dependence on the voltage  $U$ , in [Figure 3.12](#)

we present a schematic diagram that also includes the density of states. Close to the Fermi energy, within the model of free electrons, the density of states can be taken approximately as constant. In [Figure 3.12](#) the tunneling arrangement is shown for the voltages  $U = 0$ ,  $U_1$ , and  $U_2 > U_1$ . The occupation of the states is indicated by the hatched areas. For simplicity we have taken the case  $T = 0$ . On the positive side of the voltage, the energy of the electrons with their negative charge is lowered compared to the negative side. In this case, more electrons can tunnel from left to right than in the opposite direction, that is, an electron current is flowing, as shown by the horizontal arrow in [Figure 3.12b,c](#). Since we have assumed a constant density of states, the number of electrons that can tunnel from left to right increases proportional to the voltage  $U$ . Therefore, the net tunneling current  $I$  is also proportional to the applied voltage  $U$  (see [Figure 3.13](#), dashed curve 1<sup>11</sup>). At this point we emphasize again that we are only considering tunneling processes at constant energy,<sup>12</sup> that is, transitions indicated horizontally in our scheme.

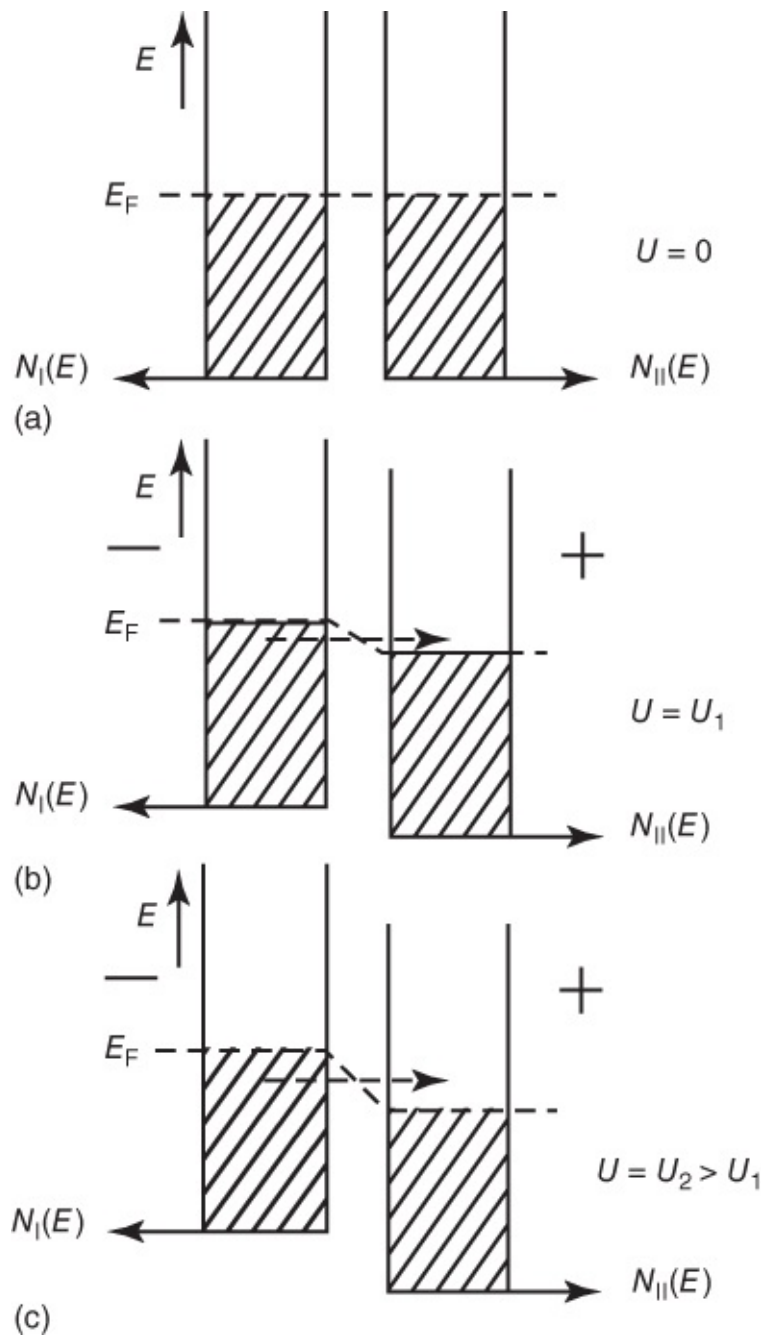


**Figure 3.12** Tunneling current between normal metals for three values of applied voltage, (a)  $U = 0$ , (b)  $U = U_1$  and (c)  $U = U_2 > U_1$ . For simplicity, the distribution for  $T = 0$  is shown. Near the energy  $E_F$  there are no states in the insulating barrier.

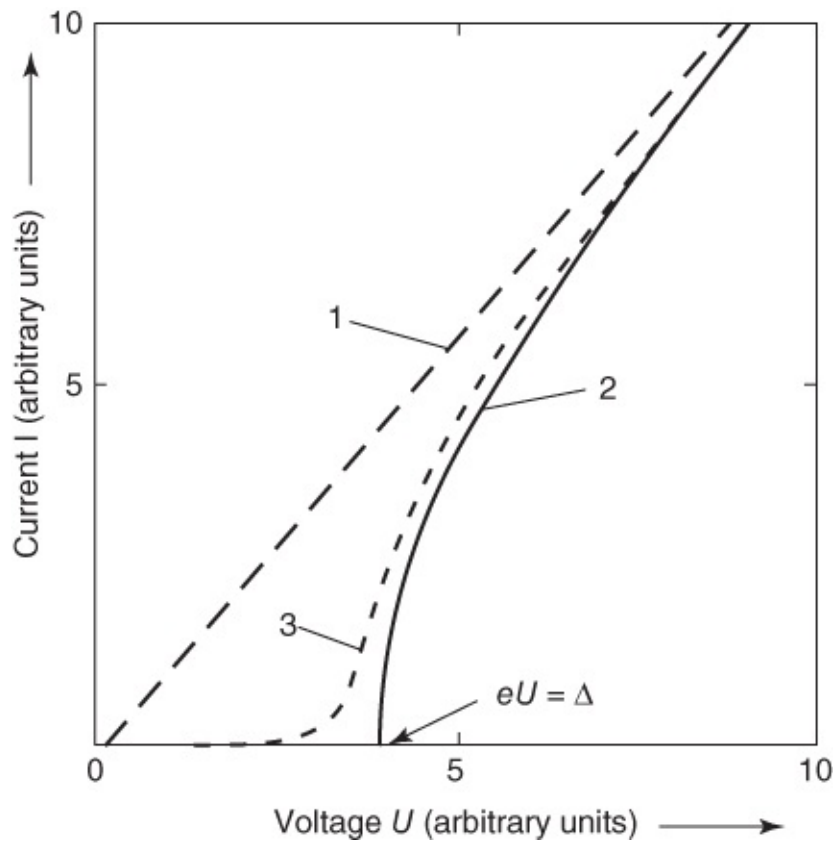


**Figure 3.13** Current–voltage characteristic of tunnel junctions: curve 1, normal conductor/normal conductor ([Figure 3.12](#)); curve 2, normal conductor/superconductor,  $T = 0$  K ([Figure 3.14](#)); and curve 3, normal conductor/superconductor,  $0 < T < T_c$ .

The current–voltage characteristic of such a tunneling arrangement changes if one or both sides are in the superconducting state. This is immediately obvious, if we recall that in the superconducting state an energy gap appears in the energy spectrum of the unpaired electrons, which strongly changes the density of states near the Fermi energy.

In [Figure 3.14](#) we show the first case, a normal conductor against a superconductor, following the scheme of [Figure 3.12](#). Again, for simplicity we take the case  $T = 0$ . The corresponding current–voltage characteristic is shown in [Figure 3.13](#) as curve 2. No tunneling current can flow up to the voltage  $U = \Delta_0/e$ , since the electrons from the normal conductor do not find any states in the superconductor. At  $U = \Delta_0/e$  the tunneling current sets in with a vertical slope. This steep rise is caused by the high density of unoccupied states in the superconductor. At higher voltages, the curve approaches the tunneling characteristic between two normal conductors (curve 1). At finite temperatures, in the normal conductor the distribution is thermally smeared, and also a few unpaired electrons exist in the superconductor above the energy gap. Furthermore, the energy gap is slightly reduced, as we have discussed in [Section 3.1.2](#). The resulting characteristic is shown schematically in [Figure 3.13](#) as curve 3.

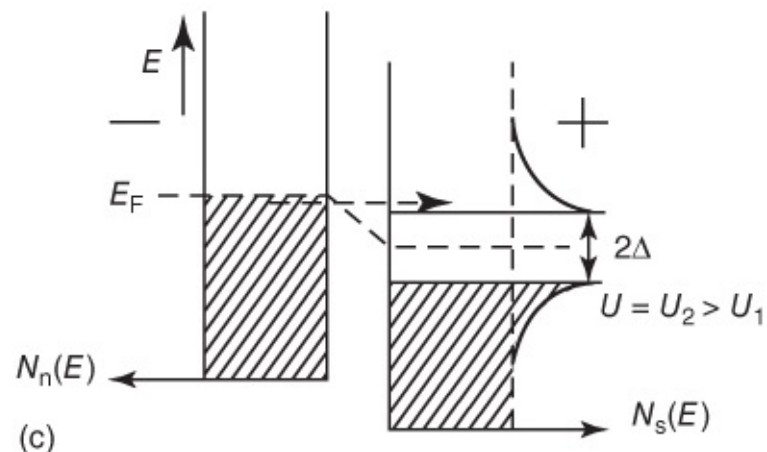
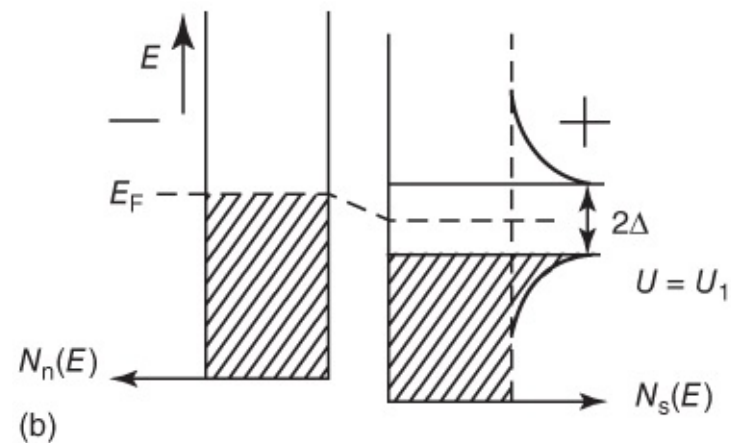
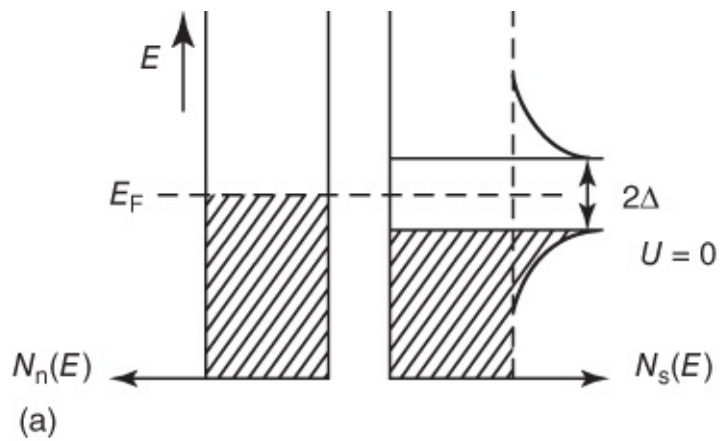


**Figure 3.14** Tunneling current between a normal conductor and a superconductor for  $T = 0$  and three values of applied voltage, (a)  $U = 0$ , (b)  $U = U_1$  and (c)  $U = U_2 > U_1$ .

From such characteristics the energy gap can be determined easily. From the function  $I(U)$ , for a given density of states of the normal conductor, we can also extract quantitative information on the energy-dependent density of states of the unpaired electrons in the superconductor. For  $T = 0$  and  $N_n(E) = \text{constant}$ , the derivative  $dI/dU$  directly yields the density of states of the unpaired electrons  $N_s(E)$ .

We note that the tunneling characteristic is independent of the direction of the voltage. During reversal of the voltage, only the role of the unoccupied and occupied states is changed. If the

superconductor is connected to the negative side, at  $U = \Delta_0/e$  the unpaired electrons can tunnel into the free states of the normal conductor. We must recall that because of the Pauli principle during the tunneling process of single electrons, in addition to the electrons of the state at the starting point (for instance, on the left side in [Figure 3.14](#)), the free energy sites at the terminal point (on the right side in [Figure 3.14](#)) must also exist.

Before we turn to case 2, namely the tunnel junction between two superconductors, we want to look at the quantitative relation between the important quantities. As we have seen, the tunneling probability depends on the height and width of the barrier. Within the small energy range near the Fermi energy with which we are concerned, we can treat this probability as a constant (independent of the energy). We denote it by  $D$ . The number of electrons tunneling per unit time at energy  $E$  from left to right is proportional to the number of *occupied* states<sup>13</sup>  $N_I(E)f(E)$  on the left side and to the number of *unoccupied* states on the right side. The probability of finding an unoccupied state at energy  $E$  is 1 minus the probability that this state is occupied, that is,  $1 - f(E)$ . In the case of a voltage drop  $U$  across the barrier, the electrons tunnel from a state with energy  $E$  on the left side into a state with energy  $E + eU$  on the right side. Hence, at the voltage  $U$ , their number is

$$N_{II}(E + eU)[1 - f(E + eU)]$$

In the following we measure the electron energy from the Fermi energy:  $\epsilon = E - E_F$ . So in a small energy interval  $d\epsilon$  at the energy  $\epsilon$ , we have the following small contribution to the tunneling current from left to right:

$$dI_{I \rightarrow II} \propto D N_I(\epsilon) f(\epsilon) N_{II}(\epsilon + eU) [1 - f(\epsilon + eU)] d\epsilon \quad 3.10$$

The total tunneling current  $I_{I \rightarrow II}$  is obtained by integration over all energies. One finds

$$I_{I \rightarrow II} \propto D \int_{-\infty}^{\infty} N_I(\epsilon) f(\epsilon) N_{II}(\epsilon + eU) [1 - f(\epsilon + eU)] d\epsilon \quad 3.11$$

Since we measure the energy from  $E_F$ , we must integrate from  $-\infty$  to  $+\infty$ . Similarly we obtain the tunneling current  $I_{II \rightarrow I}$  from right to left:

$$I_{II \rightarrow I} \propto D \int_{-\infty}^{\infty} N_{II}(\epsilon + eU) f(\epsilon + eU) N_I(\epsilon) [1 - f(\epsilon)] d\epsilon \quad 3.12$$

The difference between the two yields the net tunneling current:

$$I = I_{I \rightarrow II} - I_{II \rightarrow I} \propto D \int_{-\infty}^{\infty} N_I(\epsilon) N_{II}(\epsilon + eU) [f(\epsilon) - f(\epsilon + eU)] d\epsilon \quad 3.13$$

Here, according to Eq. (1.3), we have

$$f(\epsilon) = \frac{1}{e^{\epsilon/k_B T} + 1} \quad \text{with } \epsilon = E - E_F \quad 3.14$$

We have indicated this brief derivation, since it yields in a simple way the quantitative connection in the form of a balance equation. For the situation in [Figure 3.14](#), for example, we can assume  $N_n(\epsilon) = \text{constant}$ , and for  $N_s(\epsilon)$  we can use relation (3.5) from [Section 3.1.2](#) after changing it from  $E$  to  $\epsilon$ :

$$N_s(\epsilon) = N_n(0) \frac{|\epsilon|}{\sqrt{\epsilon^2 - \Delta_0^2}} \quad \text{for } |\epsilon| \geq \Delta_0 \quad 3.15$$

Now we can calculate the tunneling characteristic. The case of a tunnel junction between two normal conductors shown in [Figure 3.12](#) represents a very simple example for further exercise.<sup>14</sup>

$$I \propto D N_l N_n \int_{-eU}^0 1 d\epsilon \propto U$$

Next we turn to the case of a tunnel junction between two superconductors. Such a junction is shown in [Figure 3.15a,b](#) in the usual way. However, the case  $U = 0$  is omitted. In [Figure 3.15c](#) the current–voltage characteristic is presented schematically.

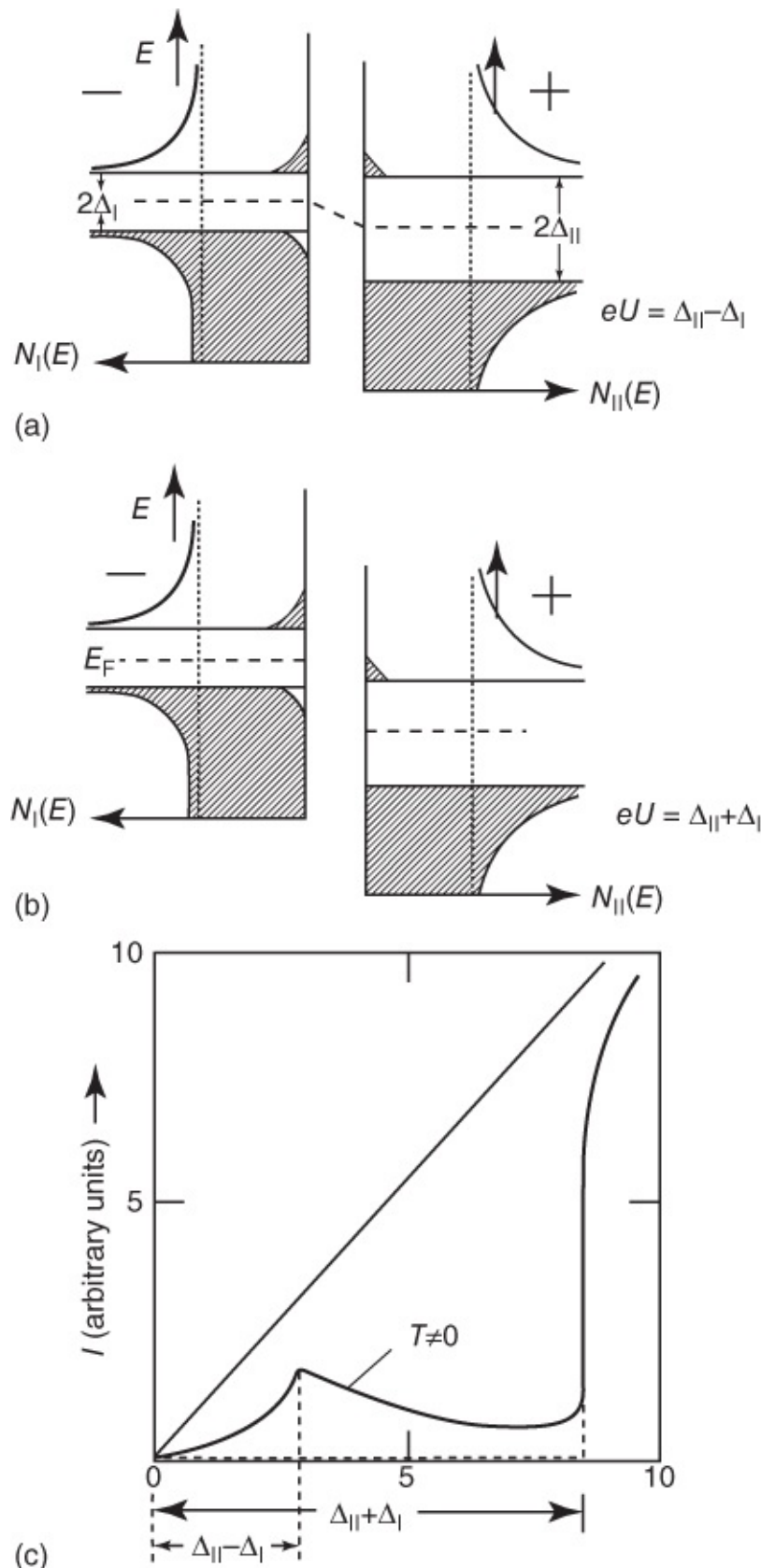


**Figure 3.15** Tunneling current between two superconductors;  $0 < T < T_c$ . (a) and (b) show the density of states and (c) displays the current voltage characteristic.

In this case the characteristic for finite temperatures differs strongly from that for  $T = 0$ . Therefore, we have assumed a distribution for  $T \neq 0$ . The dashed line in Figure 3.15c would be

obtained for  $T = 0$ . At  $eU = \Delta_{II} - \Delta_I$  a maximum of the tunneling current is reached, since now all single electrons of superconductor I can tunnel to the right, where they encounter a particularly high density of unoccupied states. Then the current decreases with a further increase in the voltage, since the density of the unoccupied states in II decreases. Finally, at  $eU = \Delta_I + \Delta_{II}$ , one observes a particularly steep increase in the current because of the high density of the occupied as well as the unoccupied states. It is this extremely steep slope that provides the important advantage of measurement using two superconductors.

Tunneling experiments have provided much important information about the energy gap. In most cases, two thin evaporated layers with an oxide layer as the barrier are used. However, also compact bulk samples can be used for studying substances that are difficult to evaporate. In the latter case, the barrier can consist also of a natural oxide layer, or it can be fabricated by the evaporation of an insulator. The study of compact bulk samples is necessary if the energy gap is to be determined in a specific crystallographic direction by using single crystals.

In [Figure 3.16](#) we present an arrangement of evaporated layers. It is advantageous to keep the tunneling area small, in order to avoid large tunneling currents and to reduce the chances for the appearance of holes in the oxide layer.

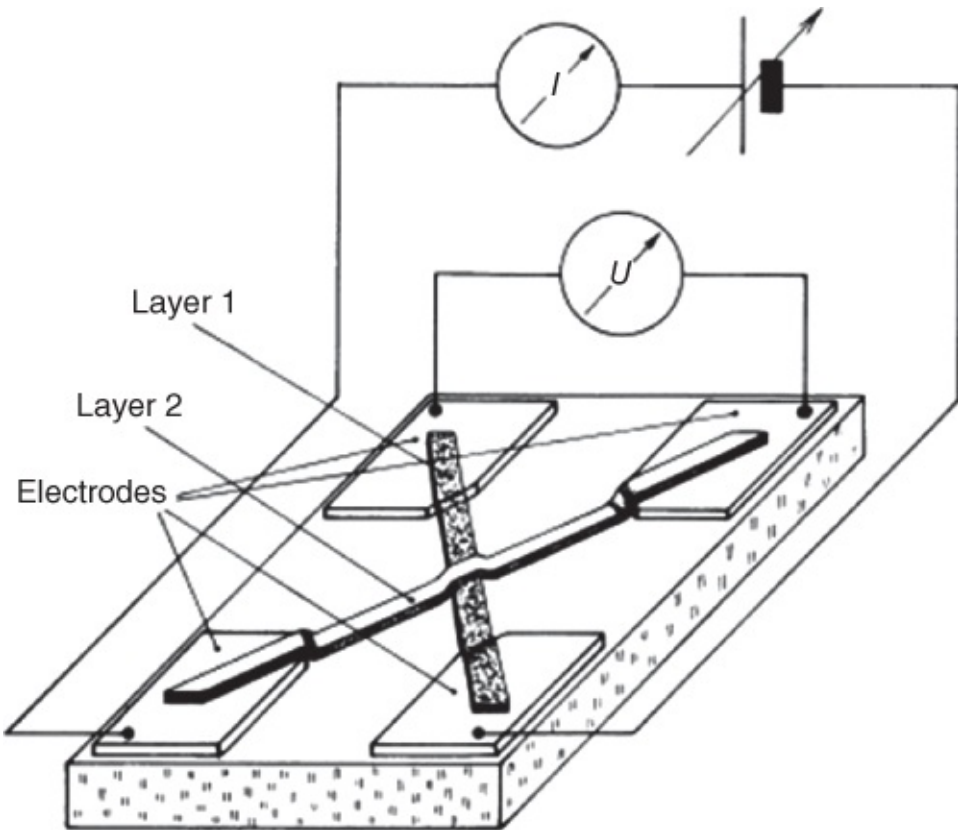


**Figure 3.16** Tunnel junction between two layers. Layer 1 was oxidized before the deposition of layer 2. The thicknesses of the layers are strongly exaggerated. Mostly they are below 1  $\mu\text{m}$ . Usually, the oxide barriers are about 3 nm thick.

[Figure 3.17](#) shows the results obtained for an Al–Al<sub>2</sub>O<sub>3</sub>–Pb tunnel junction at four different temperatures [35]. For the curves 1–3, the Al is normal conducting. Only for curve 4 do we

deal with a junction of two superconductors. However, although in the latter case the measuring temperature of 1.05 K is only slightly below the transition temperature of Al (1.2 K), the different shape of the characteristic is clearly visible.

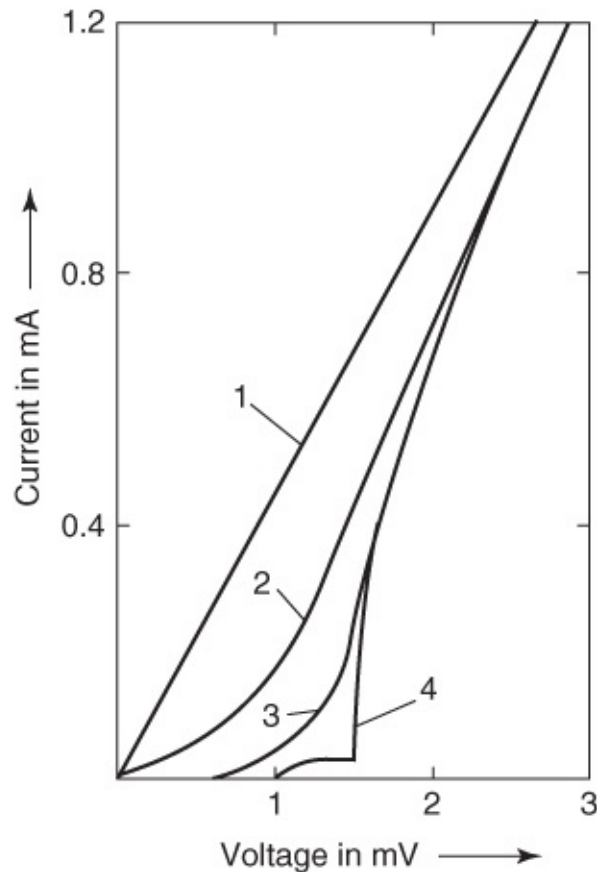


**Figure 3.17** Voltage–current characteristic of an Al–Al<sub>2</sub>O<sub>3</sub>–Pb tunnel junction. Measuring temperature: curve 1,  $T = 10$  K; curve 2,  $T = 4.2$  K; curve 3,  $T = 1.64$  K; curve 4,  $T = 1.05$  K. At 1.05 K the Al is also superconducting. The steep rise at  $eU = \Delta_I + \Delta_{II}$  can clearly be seen. Transition temperatures are: Pb, 7.2 K and Al, 1.2 K.

(From [35].)

**Figure 3.18** shows the characteristic of a typical junction between two superconductors, namely Nb–niobium oxide–Sn at 3.4 K [36]. At this temperature Nb ( $T_c = 9.3$  K) and Sn ( $T_c = 3.7$  K) are both superconducting. The solid line is the experimentally recorded result. The dots are calculated from Eq. (3.13) using proper values of the energy gaps ( $2\Delta_{\text{Sn}} = 0.74$  meV;  $2\Delta_{\text{Nb}} = 2.98$  meV).

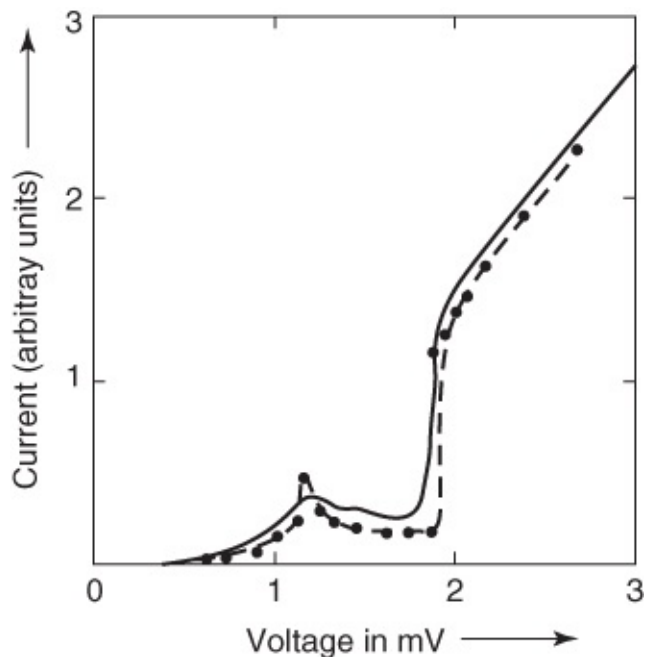


**Figure 3.18** Current–voltage characteristic of a Nb–insulator–Sn tunnel junction at  $T = 3.38$  K. The solid line is the experimentally recorded curve. The dots are calculated from Eq. (3.13) using the values  $2\Delta_{\text{Sn}} = 0.74$  meV and  $2\Delta_{\text{Nb}} = 2.98$  meV.

(From [36].)

Finally, [Figure 3.19](#) presents as an example the temperature dependence of the energy gap of tantalum [37]. The open circles show the measured data, and the solid line indicates the function  $\Delta_0(T)/\Delta_0(0)$  expected from the BCS theory. The agreement is excellent.

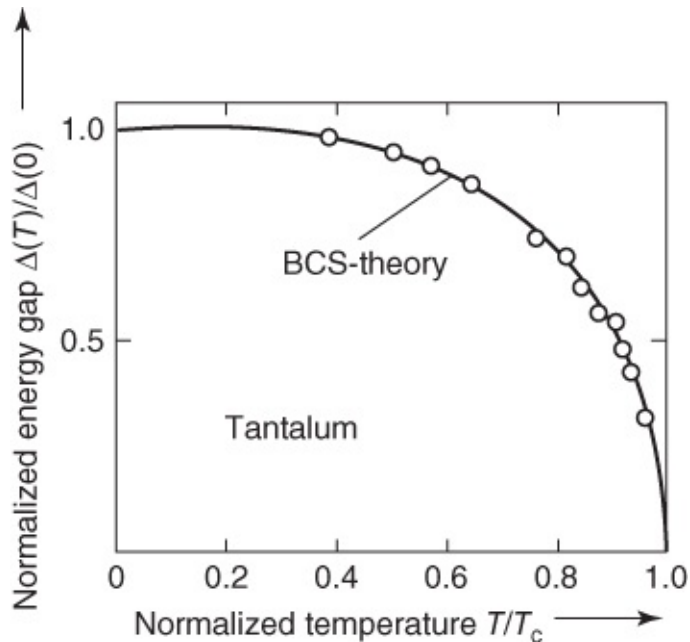


**Figure 3.19** Temperature dependence of the energy gap of tantalum;  $\Delta(0) = 1.3$  meV.

(From [37].)

We see from [Tables 3.3](#) and [3.4](#), which only contain a small part of the many possible results,

that in a series of metals the ratio  $2\Delta_0/k_B T_c$  for  $T = 0$  is close to the value 3.5 predicted by the BCS theory (Eq. (3.7)). Deviations from this value in metals such as Nb can be caused easily by impurities near the surface. For such metals it is very difficult to prepare a perfectly clean surface. The superconductors Pb and Hg show strong deviations from the values of the BCS theory. These deviations can be understood in terms of a particularly strong electron–phonon interaction in these metals.

From tunneling experiments, we can find out if the interaction leading to Cooper pairing is indeed the exchange of phonons. If the coupling between the lattice vibrations and the electron system is sufficiently strong, the density of states of the quasiparticles will be changed due to this coupling. These changes manifest themselves in the tunneling characteristic and can be measured using equipment with sufficiently high sensitivity. With some numerical work it is then possible to determine the coupling constant  $\lambda^*$  of the attractive electron–phonon interaction and the constant  $\mu^*$  of the repulsive Coulomb interaction (see Eq. (3.9)). In this way, one obtains the so-called Eliashberg function  $\alpha^2 F(\omega)$ , which is closely connected with  $\lambda^*$ . Here,  $F(\omega)$  is the density of states of the phonons. In order to avoid any confusion with the density of states of the electrons, here we denote the energy by  $\omega$ .

The tunneling measurements only deal with the phonons coupling to the electron system. On the other hand, neutron diffraction experiments can measure the density of states of the phonons independent of whether or not the latter couple to the electrons. Hence, from the comparison of both measurements, one obtains information about the coupling. [Figure 3.20](#) shows such a comparison for Pd–D samples, the properties of which we discussed in [Section 2.3.3](#) [38, 39]. In spite of the strongly different deuterium concentration, we clearly see that prominent structures appear in both measurements. In particular, the phonons with high energies, resulting from the implanted deuterium, are also visible in the tunneling measurements, indicating that these vibrations couple well to the electrons. These results explain the relatively high transition temperatures of the palladium–hydrogen system.

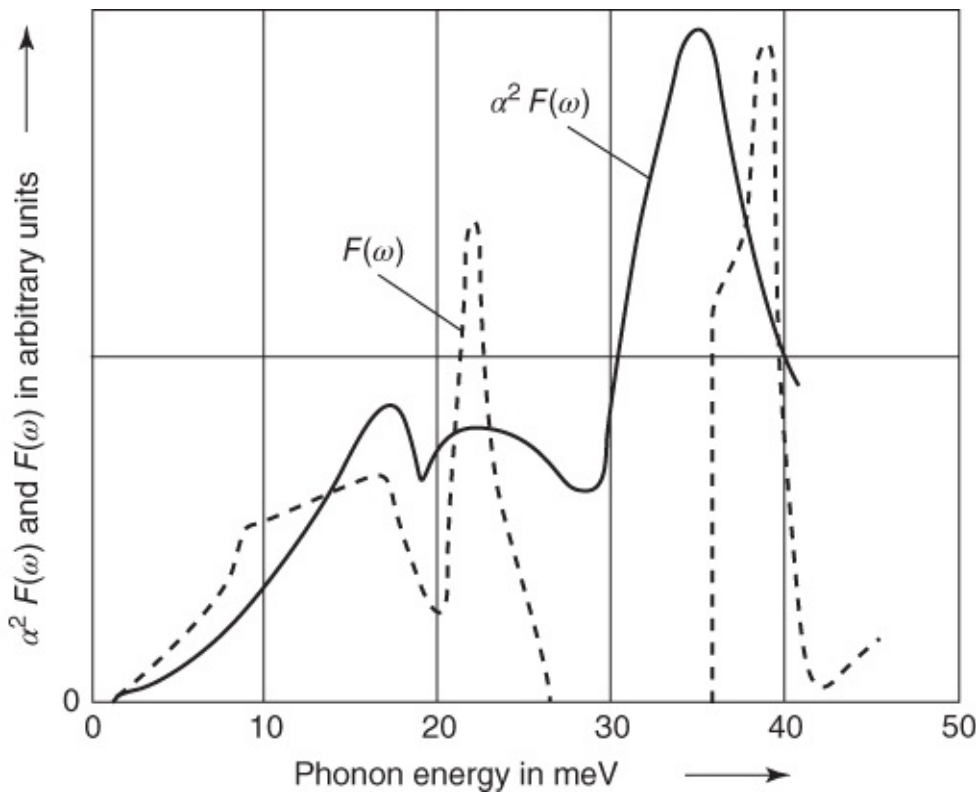


**Figure 3.20** Plot showing  $\alpha^2 F(\omega)$  obtained from tunneling measurements and  $F(\omega)$  from neutron diffraction experiments as functions of the phonon energy  $\omega$  for Pd–D samples (see [Section 2.3.3](#)).

(From [38, 39].)

The determination of the function  $\alpha^2 F(\omega)$  from the detailed structure of the tunneling conductivity and the comparison with the phonon spectrum  $F(\omega)$  obtained, say, from neutron diffraction, represented the key experiment demonstrating that in conventional superconductors Cooper pairing is due to the electron–phonon interaction.

In a similar way, for each newly discovered superconductor one can try to measure accurately the quasiparticle density of states by means of tunneling spectroscopy, if a tunnel junction with high quality can be fabricated. In the following ([Section 3.2](#)), we will see that, for high-temperature superconductors, not only tunneling spectroscopy but also other methods yield highly peculiar results, which are not yet completely understood. However, they clearly indicate that in this case the Cooper pairing is unconventional.

At this stage, we want to mention three additional aspects in context with the energy gap, which will be discussed in more detail in [Section 3.1.4](#).

1. The energy gap can have different magnitudes along different crystallographic directions. Such superconductors are referred to as **anisotropic**. This anisotropy can lead to different results in various experiments. Depending on the evaporation conditions, special crystal directions can also be distinguished in experiments performed with thin layers. Measurements with single crystals along different directions yield information about the magnitude of the anisotropy.

2. It appears that in some compounds at least two energy gaps exist. As an example we mention  $\text{SrTiO}_3$  doped with niobium, which becomes superconducting below 0.7 K [40]. Another example is  $\text{MgB}_2$  [41]. In these materials, two or more different Fermi surfaces or energy bands contribute to the superconductivity, each forming its own energy gap, respectively (“two-band superconductivity”). So in the case of  $\text{MgB}_2$  one finds one energy gap around 2 meV and another one around 7 meV.
3. In principle, the energy gap can be changed even by very small concentrations of impurities, having an atomic angular momentum and, hence, a magnetic moment (paramagnetic impurities). In this way, superconductors can be generated without an energy gap (“gapless superconductor”). However, they are still superconducting, since they display pair correlation.

So far in our discussion of the tunneling experiments with superconductors, we have only been concerned with the unpaired electrons. For the interpretation of the experimental observations, we have taken into account only the density of states of the unpaired electrons in the superconducting state. The Cooper pairs and their binding energy have never been mentioned. This also could not be expected, since within our picture of the individual electrons the total interaction was expressed in terms of the change of the density of states of the unpaired electrons.

On the other hand, since the superconducting state is based entirely on the concept of Cooper pairs, we are also interested in a picture where the Cooper pairs become distinctly visible. In the following, we will briefly discuss such a picture. However, there is a certain difficulty within this picture, since states of pairs, that is, collective states, and states of single electrons are shown in a *single* scheme.

For our discussion we take the case of a tunnel junction between two different superconductors ([Figure 3.15](#)), and for simplicity we assume  $T = 0$ . Now superconductors are characterized by showing the Cooper pairs in one state and indicating the states that are occupied by the single electrons after breaking a pair ([Figure 3.21](#)). In equilibrium without an external voltage, the Cooper pair states are shown at the same energy level. This configuration is established if we allow the exchange of particles. At an applied voltage, in the case  $T = 0$ , according to [Figure 3.15](#) we do not expect a tunneling current  $I$  in the range  $eU < \Delta_I + \Delta_{II}$ . At  $eU = \Delta_I + \Delta_{II}$ , we expect a steep rise of  $I$ . In [Figure 3.21b,c](#), we show the situation for the two possible polarities of the voltage  $U = (\Delta_I + \Delta_{II})/e$ . In our present picture, we must explain the appearance of a tunneling current at this voltage in terms of the breaking of Cooper pairs. The applied voltage must be at least large enough that a pair can decay into an electron in superconductor I and an electron in superconductor II. This is exactly the process we want to describe, namely the transfer of a particle across the insulating layer. With increasing voltage  $U$ , the possibility for such a process first appears at  $U = (\Delta_I + \Delta_{II})/e$ . If the energy of superconductor II is lowered compared to that of superconductor I by means of the voltage, at  $U = (\Delta_I + \Delta_{II})/e$ , a pair in I can be broken up. As a result, a single electron appears in the lowest state of I, whereas the other single electron tunnels into the lowest state of II. During this process the energy remains

conserved. The excitation energy of the one electron can be supplied by the transfer of the other electron in the electric field of the external voltage. The final states occupied by the two electrons are crucial for the necessary value of the voltage. At voltages  $U < (\Delta_I + \Delta_{II})/e$ , the electrons of a pair cannot be transferred into two single-electron states in I and II, respectively, at constant energy. If the superconductor II is connected to the negative side, again at  $|U| = (\Delta_I + \Delta_{II})/e$  a pair can break up, however, this time in superconductor II, and the single electrons occupy states in I and II, respectively.<sup>15</sup> Because of the extremely large density of states for single electrons at  $E = \Delta_I$ , the tunneling current sets in very steeply at  $|U| = (\Delta_I + \Delta_{II})/e$ . The argument is now similar as in the other picture. The number of processes is proportional to the number of possible final states.

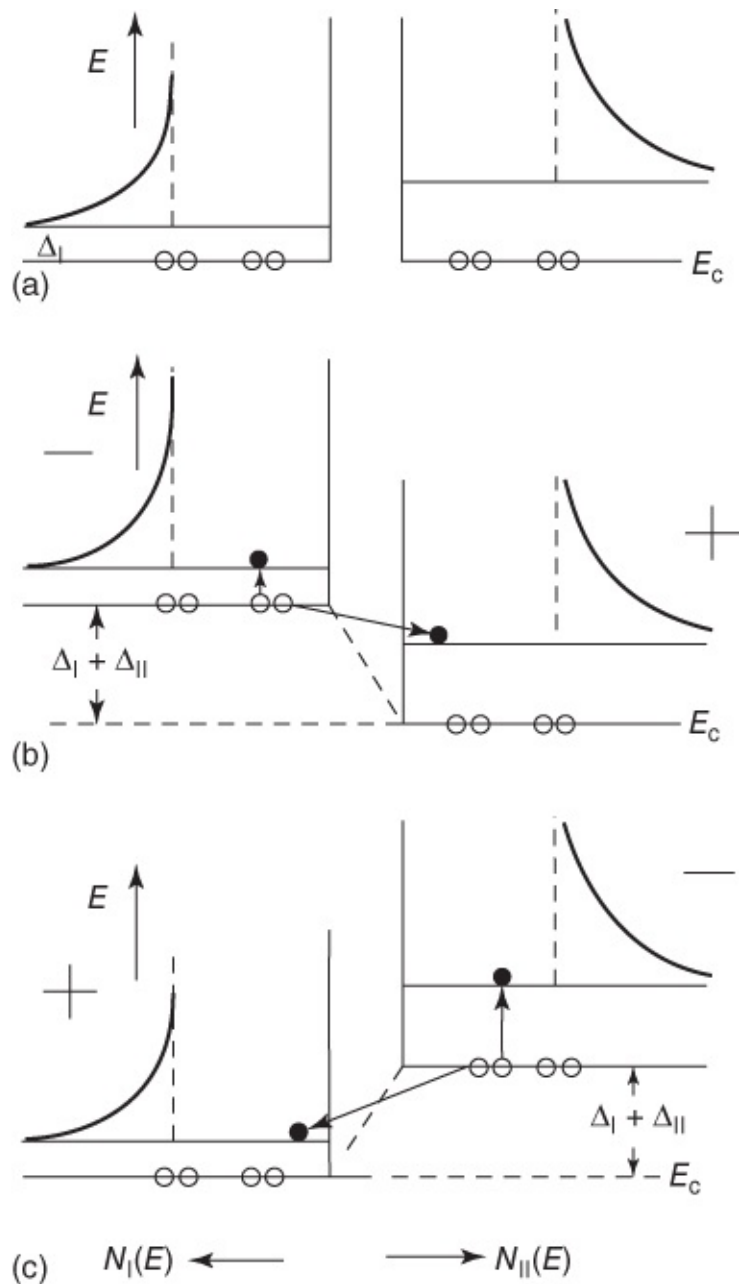


**Figure 3.21** Tunneling effect between superconductors in the picture of Cooper pairs and “excited” single electrons:  $\circ\circ$  Cooper pairs and  $\bullet$  single electrons (excitations). Graphs (a) to (c) are for different values of applied voltage.

If we want to keep this picture also for finite temperatures and to derive from it at least the qualitative form of the current–voltage characteristic, for single electrons existing in thermal equilibrium we must use the first picture discussed earlier.

In [Section 4.2](#) we will discuss another possibility for determining the energy gap in conjunction with the specific heat in the superconducting state. Furthermore, we will see in [Chapter 4](#) that, for example, the temperature dependence of the London penetration depth, being a property of the Cooper pairs, depends on the energy gap. In principle, each physical property depending on the density of states of the single electrons can be used for determining  $\Delta_0$ . We have discussed three of these possibilities, namely the absorption of light, the damping of

ultrasound, and the tunneling of single electrons. These techniques yielded many results, and the underlying physics is particularly clear.

### 3.1.4 Special Properties of Conventional Superconductors

At the end of this “microscopic” section on conventional superconductors, we want to discuss a few special properties that can enhance our understanding. Here, we emphasize in particular the influence of defects in the crystal lattice and of impurity atoms on the superconducting properties.

#### 3.1.4.1 Influence of Lattice Defects on Conventional Cooper Pairing

We use the term **defects** to denote all deviations from perfect periodicity of the crystal lattice, independent of whether they are due to the presence of foreign atoms or due to only structural perturbations, that is, displacements of the atoms from their regular sites. Primarily, such lattice defects act as scattering centers for the system of conduction electrons, reducing the electron mean free path. However, in general, the lattice defects influence all the properties of a superconductor. In this section, we will discuss some of these effects.

#### The Anisotropy Effect

The correlation of the electrons, leading to the formation of Cooper pairs, is due to the elastic vibrations of the lattice, that is, the phonons. This interaction may depend on the direction within the crystal. In the presence of such anisotropy, in a simplified way we can say that certain crystal directions are more favorable for superconductivity than others.

For example, the energy gap  $\Delta_0$  can have different values along different directions. The strength of this anisotropy is quantified in terms of the averaged square of a parameter  $\alpha$ .<sup>16</sup> A value  $\langle \alpha^2 \rangle = 0.02$ , as observed, say, for tin, means that in the different crystal directions the energy gap deviates from the average value by about  $14\% \approx 0.02^{1/2}$ . Such differences in the energy gap have been detected, for example, by means of tunneling experiments or by measurements of the absorption of ultrasound (see [Section 3.1.3.2](#)).

The transition temperature  $T_c$  is essentially determined by the more favorable spatial directions, since the transition into the superconducting state takes place when the first Cooper pairs are formed under equilibrium.<sup>17</sup> If lattice defects exist in the crystal, the electrons will be scattered at these imperfections. However, this means that the momentum of an electron quickly covers all spatial directions because of the scattering. Therefore, the interaction leading to superconductivity will be averaged. The most favorable directions will not become fully active anymore, since electrons with momentum along these directions are scattered quickly into other less favorable directions. This leads to an overall reduction of the transition temperature with an increasing concentration of the scattering centers.

The microscopic theory of superconductivity allows one to calculate this influence of the lattice defects on  $T_c$ . In [Figure 3.22](#) we show some results for tin [42]. The scattering centers are formed by impurity atoms. Since the impurity atoms have different scattering properties, for

convenience we take the residual resistance ratio  $\rho^* = R_n/(R_{273} - R_n)$  as a measure of the electron mean free path. Here,  $R_n$  is the resistance extrapolated to low temperatures, and  $R_{273}$  is the resistance at 273 K. In [Figure 3.22](#) the transition temperature is plotted versus  $\rho^*$ . The anisotropy effect is dominated by the universal, linear decrease in  $T_c$  at small impurity concentrations (see [Figure 3.22b](#)), in good agreement with the theory. For large impurity concentrations, that is, for small values of the electron mean free path, complete averaging over all spatial directions is accomplished. For the anisotropy effect alone,  $T_c$  should then approach a limiting value a small percentage below the value of the defect-free superconductor.

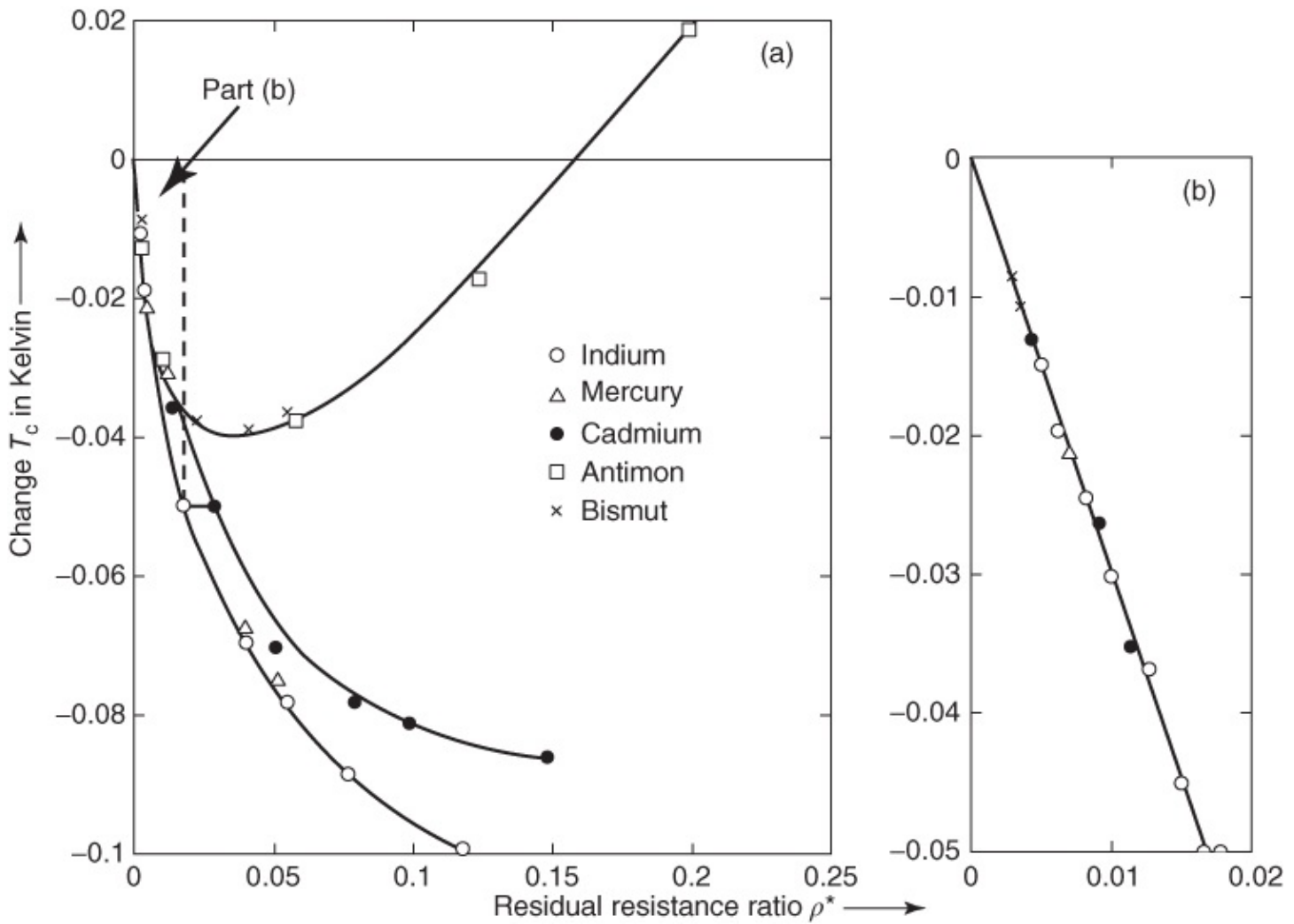


[Figure 3.22](#) Shift of the transition temperature of Sn due to impurity atoms. Graph (b) is an enlargement of the region indicated in (a).

(From [42].)

[Figure 3.22](#) indicates that this behavior is not observed anymore for large defect concentrations. Apparently, in this case, specific properties of the impurities become important, leading to various dependences of the transition temperature on the different impurity atoms. Presently we are still unable to understand these effects quantitatively in all systems. They are summarized below under the heading “valence effect.”

## The Valence Effect

The specific influence of the impurity atoms upon the transition temperature of the host metal can result from a change of the concentration of the free charge carriers or from a change of the lattice constant. For example, if we implant Bi atoms (having five electrons each in the outer shell) into tin (having four valence electrons), we expect that the number of free electrons in tin is increased. Within the model of the free-electron gas, this would lead to an increase in the density of states  $N(E_F)$  of the electrons.

Since generally the atomic volume of impurity atoms is different from that of atoms of the host lattice, mechanical strain fields are generated in the environment of the impurity atoms.

Furthermore, the lattice constant of the host metal will be changed. In general, all these effects of the lattice perturbation also cause a change of  $T_c$  (see [Section 4.6.6](#)). In order to distinguish between these effects, we must look for special alloy systems in which only a single parameter, say, the number of valence electrons or the atomic volume, varies. Up to now, a satisfactory analysis has been possible only in a few cases. For a general insight, we are still missing quantitative connections between superconductivity and other parameters of the metal. However, such quantitative information can only be obtained from experiments with selected alloy systems.

So far we have only discussed lattice defects in the form of impurity atoms. However, structural perturbations of the crystal lattice lead to similar effects. An example is shown in [Figure 3.23](#) [43]. The transition temperature of a thallium wire is plotted versus the residual resistance ratio. In this experiment, the residual resistance was increased gradually by means of plastic deformation of the T1 wire performed at liquid-helium temperatures. In principle, the change of  $T_c$  exactly corresponds to that following the implantation of chemical impurity atoms. However, in this case, the quantitative analysis is even more difficult than in the case of alloys, since the plastic deformation also generates extended defects such as grain boundaries, in addition to the statistically distributed atomic defects. Furthermore, the different scattering mechanisms add other complications to the interpretation of the data. It appears obvious that structural defects and chemical impurities result in similar effects. If during plastic deformation an atom is displaced from its regular lattice site and is relocated between other atoms at a so-called interstitial site, there it will generate a mechanical strain field exactly as a chemical impurity atom having a larger atomic volume than that of the host metal.

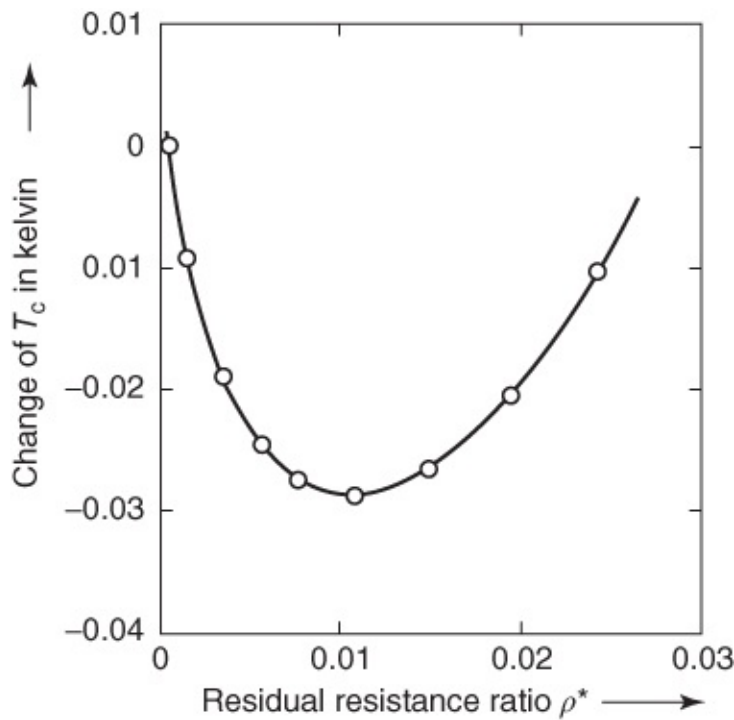


**Figure 3.23** Shift of the transition temperature of thallium due to the implantation of lattice defects. Residual resistance ratio of the defect-free sample:  $\rho^* = 0.4 \times 10^{-3}$ .

(From [43].)

At first we do not expect a change in the number of free electrons, since in the case of structural defects we are not dealing with atoms having a different number of valence electrons. However, we must recall that the structural defects change the environment of the atoms. Hence, they also change the states of the electrons and affect the density of states  $N(E_F)$ .

So far we have only considered the influence of lattice defects on the system of free electrons. However, the lattice vibrations (phonons) can also be changed, in particular, at high defect concentrations. Since the phonons constitute the interaction leading to superconductivity, we must expect that these changes of the phonon system also strongly affect the superconductivity.

## The Electron–Phonon Interaction

Extremely large perturbations of the lattice can be achieved if the sample is produced by means of the condensation of vapor upon a very cold substrate (for instance, a quartz substrate at liquid-helium temperatures). This condensation process is equivalent to an extremely rapid quench [44]. The atoms from the vapor hit the substrate in a completely statistical manner, and they lose their energy so quickly that they are frozen into totally wrong spatial configurations. Due to the attained defect structure, the superconducting transition temperature can be strongly changed.

In [Figure 3.24](#) we show the behavior of a condensed layer of tin [44]. On the left side, we see the transition curves close to  $T_c$ , and on the right side, the temperature dependence of the resistance at higher temperatures. Immediately after condensation at 4 K, the tin layer has a high resistance because of the presence of many lattice defects. The high transition temperature

of 4.6 K is surprising. It is higher by 0.9 K or 25% compared to that of regular bulk tin.

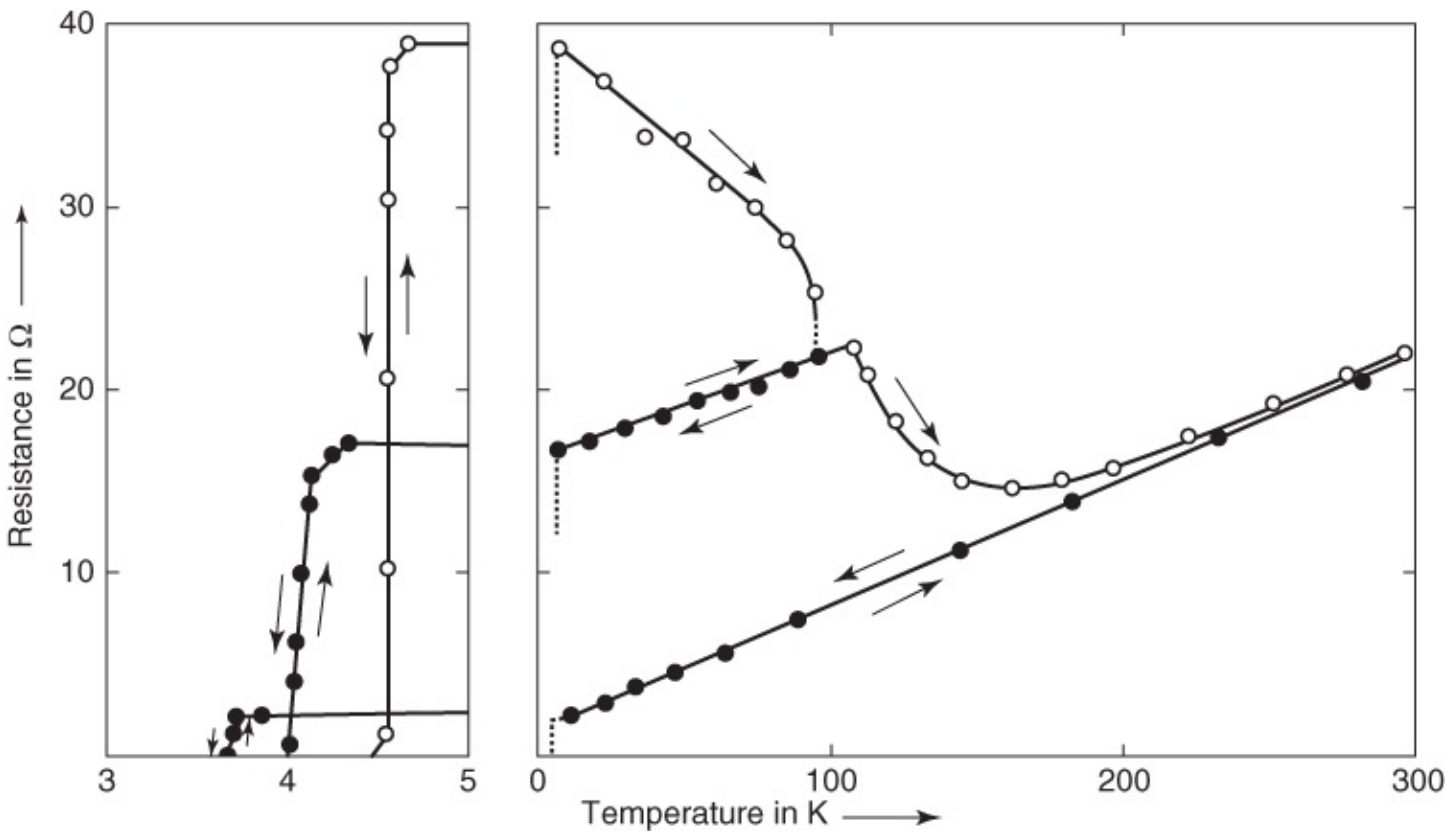


**Figure 3.24** Temperature dependence of the resistance of a tin layer produced by condensation from the vapor. Condensation temperature 4 K, layer thickness 50 nm, length 10 mm, width 1 mm. The black dots show the data observed during cooling after an annealing process.

(From [44].)

From the behavior after annealing, we see that the strong change of  $T_c$  is due to the lattice defects. During annealing at elevated temperatures, more and more atoms find the energy to move to their regular lattice sites. The perturbation of the lattice and the resistance is reduced. Simultaneously, the transition temperature is shifted to smaller values. Upon heating to about 90 K, one observes a value of  $T_c$  of about 4.1 K. After sufficiently long annealing at about 100 °C, the transition temperature of the compact bulk material is obtained.

Electron diffraction experiments with such layers produced by quench condensation indicate that these layers display a polycrystalline structure with an average size of the crystallites of about 10 nm [45].

We can suppress the crystalline order even further if, simultaneously with the Sn atoms, we also condense another substance that does not fit into the tin lattice. Here, we refer to a substance that is only slightly soluble in the host lattice, but still has some affinity to it, and, hence, is not completely precipitated [45]. In this way, one can achieve an extreme perturbation of the crystal structure.

Such an extreme perturbation also strongly affects the superconductivity. In [Figure 3.25](#) the transition curves and the annealing behavior of the resistance of a tin layer are shown. The

transition temperature is about 7 K, that is, it is increased by nearly a factor 2. Corresponding to the strong perturbation, the resistance is also very high [46]. This strongly perturbed state of the lattice is highly unstable. A pronounced ordering process already sets in at about 60 K, leading to a reduction of the resistance to about half its value. At the same time, the transition temperature is reduced to about 4.5 K. Additional annealing yields the known shift of  $T_c$  toward the value of the compact material.<sup>18</sup>

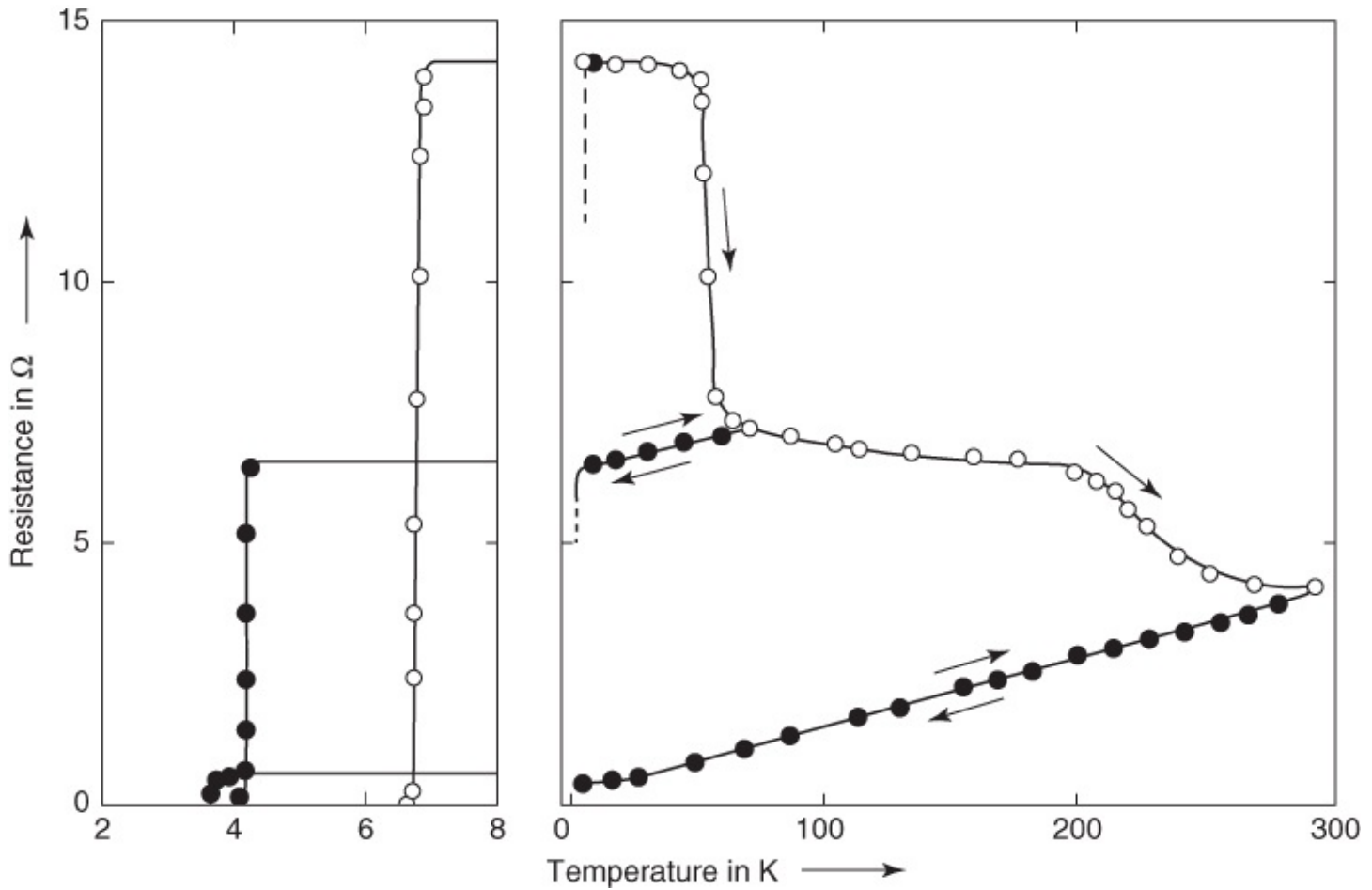


**Figure 3.25** Temperature dependence of the resistance of a tin layer produced by quench condensation together with 10 at% copper acting as impurity. Layer thickness about 50 nm, width 5 mm, length 10 mm, condensation temperature 10 K.

(From [46].)

Similar and even more pronounced changes of  $T_c$  have also been found for other superconductors [47]. The transition temperature of Al can be increased up to more than 4 K (compared to 1.2 K of the compact material) if it is condensed simultaneously together with a few atomic percent of Cu [48]. Using Ge as the impurity substance, or by means of the implantation of hydrogen, germanium, or silicon at low temperatures, the transition temperature of Al could be increased even up to the range of 7 K to more than 8 K [49]. Quench-condensed films of beryllium have a  $T_c$  of about 9.3 K [50], whereas compact Be shows a  $T_c$  of about 0.03 K.

For a long time such large changes of  $T_c$  could not be explained satisfactorily. The initial

observations go back to the early 1950s by Hilsch and coworkers. Today we have a qualitative understanding and even ideas for a quantitative interpretation of these results. Tunneling experiments and measurements of the specific heat have shown that, in the extremely disordered films,<sup>19</sup> the bond between the atoms is slightly softer than in the perfectly ordered crystal. This means that the frequencies of the lattice vibrations are lowered.<sup>20</sup> According to Eq. (3.6), this would lead to a smaller value of  $T_c$ . However, one finds that the electron–phonon interaction increases, and that  $\lambda^*$  (see Eq. (3.9)) becomes larger. This results in an *enhancement* of  $T_c$ . In this context one finds also that a reduction of the phonon frequencies more strongly affects  $T_c$ , the smaller the ratio  $T_c/\Theta_D$  (see Eq. (3.9)). In this way one can understand that in the sequence In, Sn, Zn, Al, in which  $T_c/\Theta_D$  decreases, the transition temperature is increased more and more because of the extreme disorder.<sup>21</sup>

In addition to this explanation of the change of  $T_c$ , based on a lowering of the phonon frequencies, it is also possible that scattering at lattice defects directly leads to an enhancement of the electron–phonon interaction [51]. Perhaps this mechanism causes the change of  $T_c$  at a medium degree of disorder.

At the end of this section on the influence of lattice defects, we want to also mention amorphous metals, also referred to as *metallic glasses*. As a metastable phase, they can be produced by the condensation of atoms onto a very cold substrate or by extremely rapid quenching from the melt (splat cooling) [52]. There also exist a number of superconductors among these alloys [53]. They provide the possibility of also studying in metals the low-energy excitations characteristic of amorphous materials at very low temperatures [54]. At sufficiently low temperatures in the superconducting state, the free electrons are practically completely thermally decoupled, whereby the excitations of the lattice can be measured independently [55].

### 3.1.4.2 Influence of Paramagnetic Ions on Conventional Cooper Pairing

The implantation of paramagnetic ions particularly strongly affects the superconducting transition temperature. Hence, alloys containing paramagnetic ions play a special role. Their properties will be discussed in this section.

A paramagnetic ion represents an impurity atom having a fixed magnetic moment also after its implantation into the host lattice. Such implanted magnetic moments strongly reduce the value of  $T_c$ . At first it was presumed that the strong effect is due to the magnetic moment. However, based on a systematic study of lanthanum alloys containing rare-earth elements, Matthias and coworkers [56] could show that it is the spin of the implanted ion that is crucial for the reduction of  $T_c$ . In [Figure 3.26](#) we show the change of  $T_c$  for La alloys each containing 1 at% of an admixture of a rare-earth element. The largest reduction of  $T_c$  is observed for gadolinium. Gd has the largest spin, but not the largest magnetic moment.

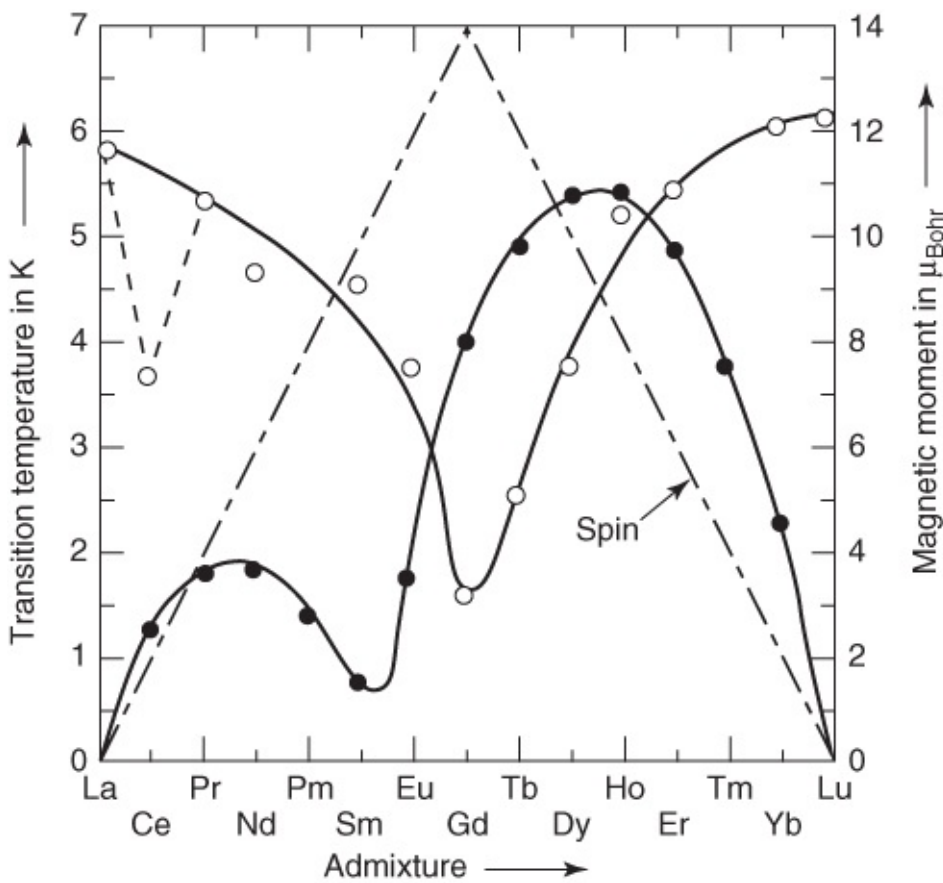


**Figure 3.26** Transition temperatures of lanthanum alloys each containing 1 at% admixture of a rare-earth element (open circles), and effective magnetic moment of the admixture (black dots).

(From [56].)

In principle, this effect of ions having a spin can be understood in a simple way. Because of the interaction between the paramagnetic ion and the conduction electrons, in the environment of the ion one spin orientation of the electron will be preferred. Depending on the kind of interaction, this can be the parallel or the antiparallel orientation. In the superconducting state, a fraction of the conduction electrons are correlated forming Cooper pairs. In conventional superconductors, the spins of the two electrons forming a Cooper pair are oriented antiparallel. If one of these two electrons approaches a paramagnetic ion, the interaction with this ion competes with the pair correlation. Independent of whether the parallel or the antiparallel orientation is preferred, the Cooper pairs can be broken up because the spin orientation of the electrons changes under the influence of the impurity atom. (We have given only a simplified, corpuscular argument, which may help to clarify the situation.)

We see that the implantation of such ions reduces the Cooper pair correlation. Hence, the transition temperature is reduced. This behavior can be understood in terms of the existing theory [57]. For small concentrations of the paramagnetic ions, the theory yields a linear reduction of  $T_c$  with increasing concentration. This linear effect has been observed in a number of systems. In [Figure 3.27](#) we show only a few examples of lead alloys. Here, one encounters the experimental difficulty that in many superconductors the solubility of paramagnetic ions practically vanishes.<sup>22</sup> In this case, a statistical distribution of the impurity atoms can be

achieved by condensing the host metal together with the paramagnetic atoms onto a cold substrate. Precipitation is suppressed because of the extremely rapid quenching process. Precipitation can then be initiated during a subsequent tempering process and can be studied by means of the change of  $T_c$ . The large scatter of the data in [Figure 3.27](#) indicates the difficulty of producing such metastable alloys.

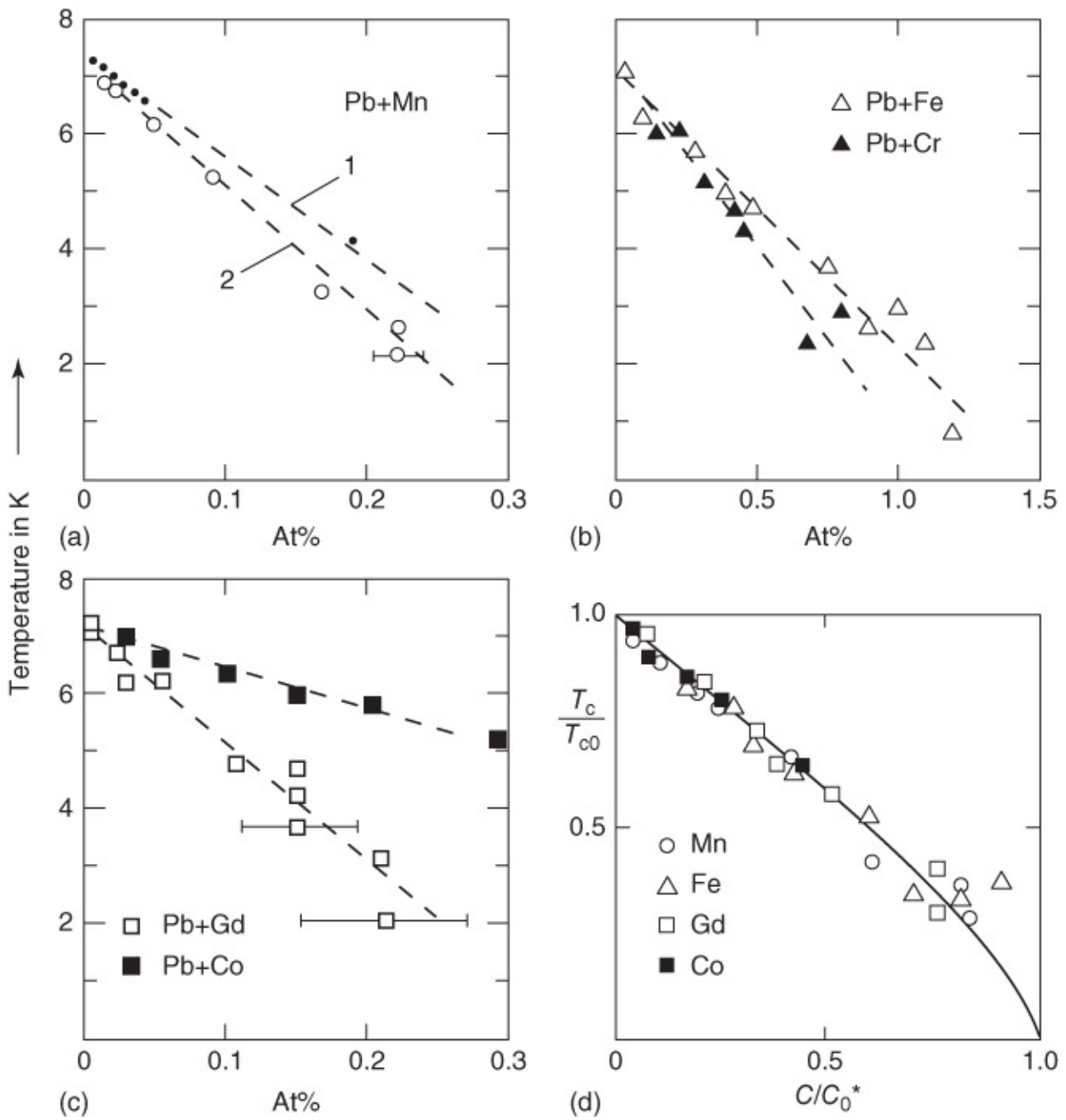


**Figure 3.27** (a) to (d): Influence of paramagnetic ions on the transition temperature of lead. In part (d) the results are plotted in reduced units. The solid line is obtained from the theory for the following critical concentrations: Mn, 0.26 at%; Fe, 1.2 at%; Cr, about 1 at%; Gd, 2.8 at%; Co, 6.3 at%. All results, except for curve 1 in part (a), were obtained with quench-condensed films. Curve 1 in part (a) was observed in alloys produced at liquid-helium temperatures by means of ion implantation. Data sources as follows: Pb + Fe, Pb + Cr, Pb + Co [58]; Pb + Mn [59–61]; and Pb + Gd [62].

Another possibility for the production of metastable alloys, in particular for small concentrations of the admixture, is provided by ion implantation (curve 1 in [Figure 3.27a](#)). Here, the paramagnetic ions are generated within an ion source. Then they are accelerated up to a few hundred kelvin electronvolts, and with this energy they are directed into a thin foil of

the host metal at low temperatures. In this way, by a suitable variation of the energy of the ions, a very homogeneous distribution of the implanted ions can be achieved.

The results shown in [Figure 3.27](#), and those of other similar experiments, can be fitted to the theory using a parameter that characterizes the strength of the interaction ([Figure 3.27d](#)). Today, a satisfactory understanding of the strength of the interaction, allowing a calculation from other parameters of the solid, is still missing. In [Table 3.5](#) we have listed the initial slope of the dependence of  $T_c$  upon the concentration  $c$  of the ions for a few systems. For high concentrations ( $c > 1$  at%) the situation becomes very complicated, since also the interaction between the paramagnetic ions can play a role. For instance, an ordering process among the spins of the ions should lead to a reduction of the destructive effect on Cooper pairs.

**Table 3.5** Reduction of the transition temperature of some superconductors due to paramagnetic ions

Superconductor	Admixture	$-dT_c/dc$ (K/at%)	References
		QC <sup>a</sup>	IP <sup>b</sup>
Pb	Mn	21	20 [59, 60]
	Cr	ca. 6	— [58]
	Fe	4.7	— [58]
	Gd	2.0	— [62]
	Co	0.8	— [58]
Sn	Mn	69	14 [60, 63]
	Cr	16	— [63]
	Fe	1.1	— [63]
	Co	0.15	— [63]
Zn	Mn	315, 285	343 [64, 65]
In	Mn	53	50 [66, 67]
La	Gd	5.1, 4.5	— [56, 68]

<sup>a</sup> Quench-condensed films.

<sup>b</sup> Ion implantation at low temperatures. A summary may be found in Ref. [69].

In conventional superconductors with a low transition temperature, the superconductivity can be completely suppressed even by very small concentrations of paramagnetic impurities. Though, so far, for a number of metals we have not yet observed superconductivity even at very low temperatures, at least in some cases this may be due to such impurities. For instance, in the case of molybdenum, superconductivity could be found only after it had been extremely purified [70].

In theoretical papers [71], it could be shown that the dependence of the transition temperature

on the concentration of the paramagnetic ions can also be very different from that originally calculated by Abrikosov and Gor'kov. Here, we are dealing with systems where the antiparallel orientation of the electron spin relative to the spin of the paramagnetic ion is energetically favored. Such alloys are referred to as **Kondo systems**.<sup>23</sup> In the normal conducting state this leads to a number of anomalies. For instance, at low temperatures the electrical resistance passes through a minimum.

For superconductors containing such paramagnetic ions, it was predicted that under certain conditions such an alloy system becomes superconducting at a temperature  $T_{c1}$ , and at a lower temperature  $T_{c2}$  it again shows normal conducting behavior [71]. At very low temperatures  $T < T_{c3}$ , superconductivity should reappear again. The reason for this surprising behavior is the temperature dependence of the interaction between the electrons and the spins of the paramagnetic ions. If at first this pair-breaking interaction strongly increases at low temperatures and then decreases again (at the so-called Kondo temperature), which is possible according to the theory for certain systems, one understands qualitatively that the correlation appearing below  $T_{c1}$  and leading to Cooper pairs is again suspended completely at still lower temperatures, because of the strongly increasing pair breaking. Finally, at very low temperatures for decreasing pair-breaking interaction, the correlation of the Cooper pairs should reappear again.

The prediction of the theory about the existence of a temperature  $T_{c2}$  discussed above could be confirmed for the system  $(\text{La}_{1-x}\text{Ce}_x)\text{Al}_2$  [72].<sup>24</sup> Pure  $\text{LaAl}_2$  has a transition temperature  $T_c = 3.26$  K. With a Ce admixture of  $x = 0.63$  at%, one finds the two transition temperatures  $T_{c1}$  and  $T_{c2}$ . In [Figure 3.28](#) we show the transition curves measured inductively (see [Section 4.6.1](#)).

The magnetic susceptibility  $\chi$  is plotted versus the temperature. In the normal conducting state  $\chi$  is practically zero, and in the superconducting state it is  $-1$ . Slightly above 1 K the sample becomes superconducting, displaying a steep transition curve. Below 0.2 K it returns to the normal conducting state. At this lower temperature, the pair-breaking effect of the Ce ions has become sufficiently strong to completely suppress the superconductivity. In La–Y–Ce alloys of suitable composition the second transition to superconductivity could also be observed at about 50 mK [73]. The transitions were also seen in resistance measurements. This represents a nice example of the combined effort of theory and experiment.

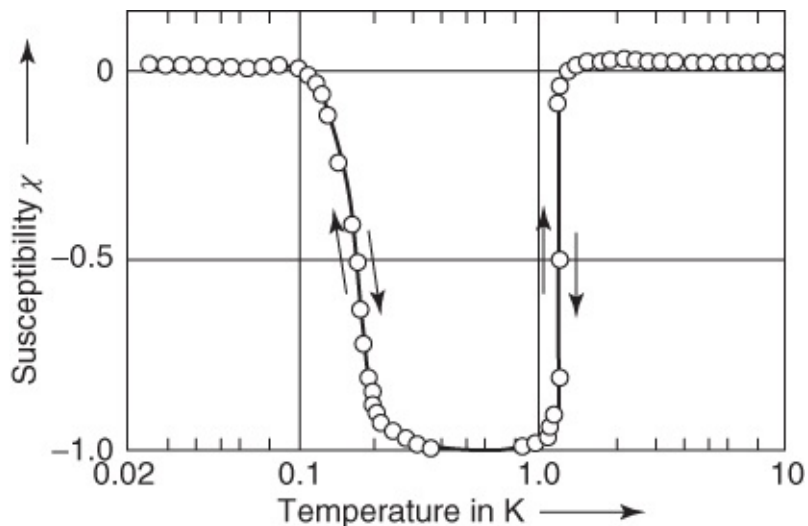


**Figure 3.28** Transition curves of  $(\text{La}_{1-x}\text{Ce}_x)\text{Al}_2$ , with  $x = 0.63$  at%.

(From [72].)

In addition to the transition temperature, the paramagnetic ions also change the energy gap of a superconductor. This effect can be understood most easily from a consideration of the lifetime of Cooper pairs. Because of the possibility of pair breaking, paramagnetic admixtures reduce this lifetime. A finite lifetime leads to an uncertainty in the energy according to  $\Delta E \Delta t \geq \hbar$  ( $\Delta t$  = average lifetime,  $\hbar$  = Planck's constant/2π). This results in a smearing of the energy gap. In [Figure 3.29](#) for the temperature  $T = 0$ , the density of states for different concentrations of the paramagnetic ions is plotted versus the normalized energy  $E/\Delta_0$ .<sup>25</sup> With increasing concentration the energy gap decreases, and simultaneously the smearing of the energy gap becomes larger. Then at a certain concentration  $c_0$ , the energy gap can vanish. However, the density of states still deviates strongly from that of the normal conducting state, and there still exists a finite concentration of Cooper pairs.

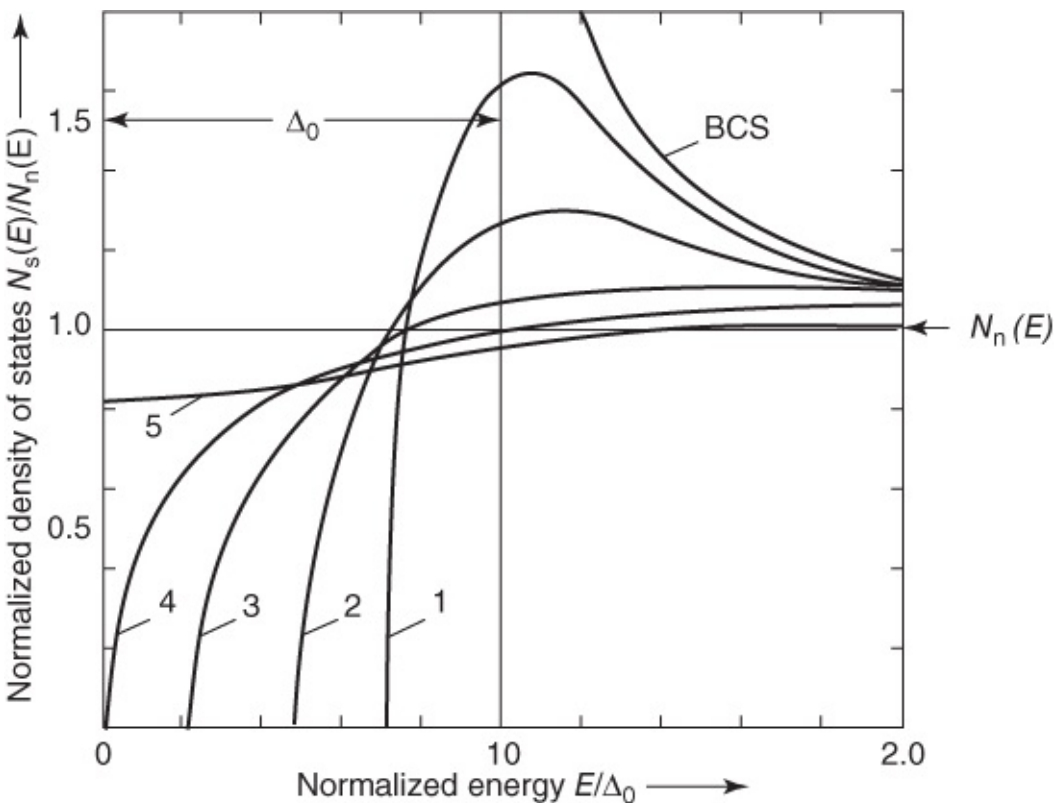


**Figure 3.29** Density of states of unpaired electrons in a superconductor containing paramagnetic ions at  $T = 0$ . The curves 1–5 correspond to increasing concentrations of the paramagnetic ions; curve 4 corresponds to the critical concentration.

(From [74].)

This state without a finite energy gap in the excitation spectrum, but still with a correlation forming Cooper pairs, is referred to as **gapless superconductivity**. Also in this state, for not too large currents, the superconductor has no measurable electrical resistance. The resistance only appears at a critical concentration  $c_0^*$ , which is larger (about 10%) than  $c_0$ . This experimental result indicates that the superconducting state does not manifest itself by the existence of a gap in the excitation spectrum, but rather by the presence of Cooper pairs.

The existence of electric current flow without resistance in the absence of a finite energy gap is also difficult to understand. In the presence of a finite energy gap, we can argue that the dissipation can only set in if the kinetic energy of the Cooper pairs is large enough to supply the finite excitation energy. However, apparently this argument does not reach to the core of the problem, since it fails for a superconductor without an energy gap. Instead, we must argue that a certain concentration of Cooper pairs is thermodynamically stable, that is, deviations from this equilibrium concentration are always compensated. If the superconductor carries an electric current, all the Cooper pairs have exactly the same momentum. If pairs disappear, with or without excitation energy, then for each pair two electrons with suitable momenta must form a Cooper pair again having exactly the same momentum as all the other pairs. The stability results from the rigid correlation among the Cooper pairs.

The effect of paramagnetic ions on the energy gap can be demonstrated experimentally by

means of tunneling measurements [75]. The improved theory [76] predicted further that discrete states should appear within the energy gap of a superconductor with paramagnetic ions. Also this prediction could be confirmed experimentally. [Figure 3.30](#) shows the normalized density of states of lead containing very small concentrations of Mn ions. Within the energy gap we clearly see two maxima in the density of states. In these experiments, paramagnetic ions were implanted into the lead film of a previously prepared Mg–MgO–Pb tunnel junction showing nearly ideal behavior.

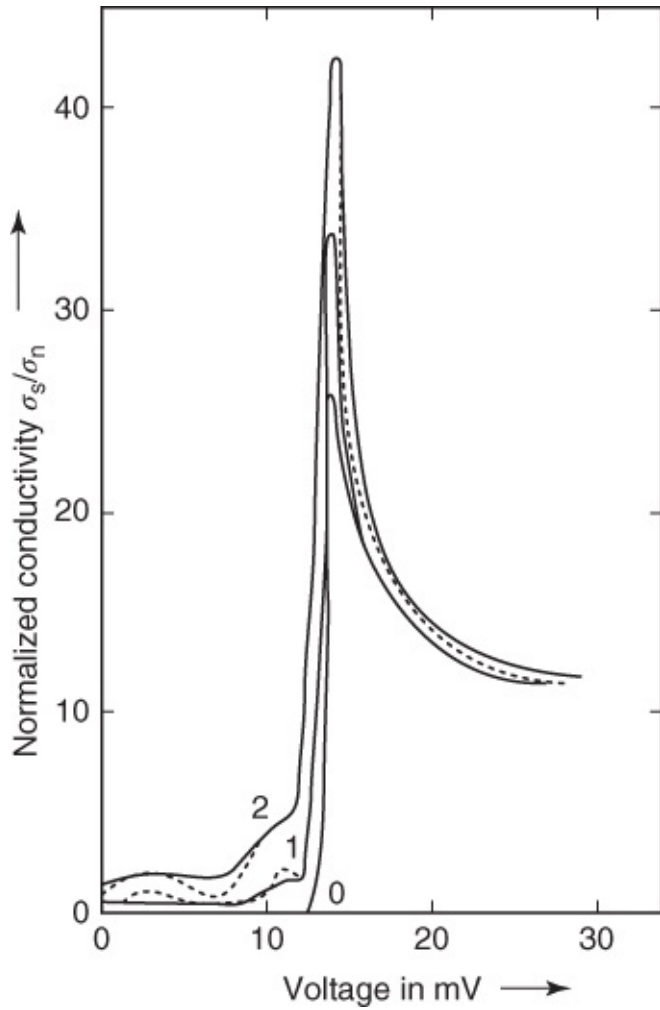


[Figure 3.30](#) Normalized conductivity  $\sigma_s/\sigma_n$  (proportional to the density of states of the electrons) of lead with an admixture of manganese. (From [61].) Temperature 200 mK. Curve 0, pure lead; curve 1, Pb + 25 ppm Mn; and curve 2, Pb + 250 ppm Mn. The dotted line is calculated from the MHZB theory [76].

Next we turn to unconventional superconductors. Here also we will see that no true gap appears in the density of states of the quasiparticles. However, the reason is very different from that discussed earlier.

## 3.2 Unconventional Superconductivity

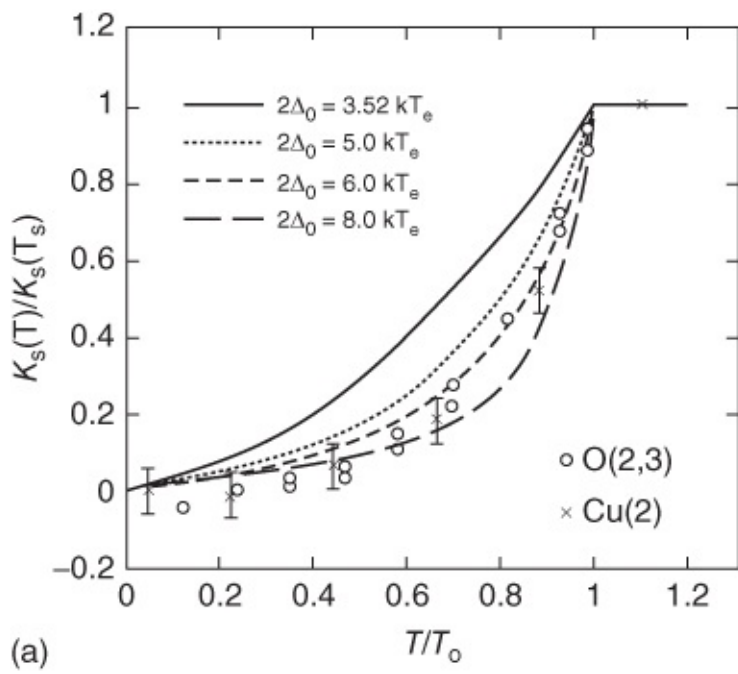
### 3.2.1 General Aspects

In the previous sections, we have presented a detailed picture of conventional superconductors. We have seen that this picture is in excellent agreement with the experimental observations. For a long time, conventional superconductors were the only superconducting materials known. They form Cooper pairs from two electrons with opposite spins by means of the electron–phonon interaction. The angular momentum of the pair as well as that of the total superconducting condensate is zero.

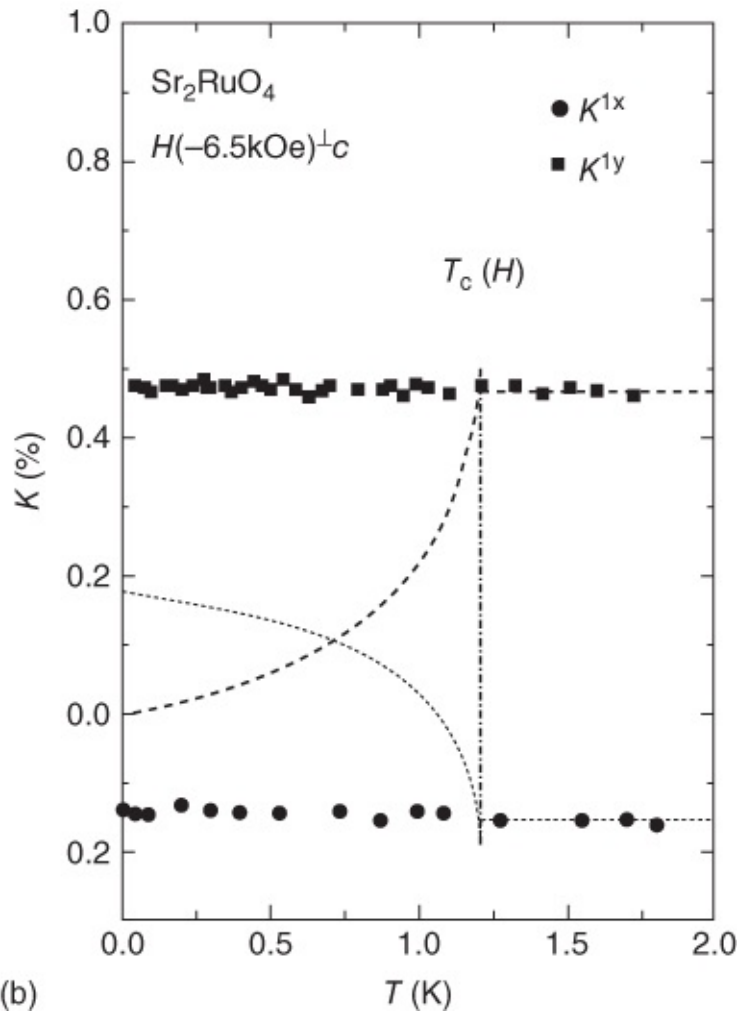
How do we recognize a superconductor with different properties? As a first characteristic signature we note that many unconventional superconductors yield a straight line if the transition temperature is plotted versus the Fermi temperature  $T_F = E_F/k_B$  (“Uemura plot”). However, most conventional superconductors are located far from this line [77].

Let us look at the electric charge  $q$ . From the observation of the flux quantization, we can directly determine  $q$ . As we have seen in [Section 1.3](#), in a superconducting ring the magnetic flux, or more accurately the fluxoid from Eq. (1.11), is quantized in units  $h/q$ . The quantity  $h/q$  also appears in the Josephson effect (see [Section 1.5](#)). For all known superconductors, these measurements yielded the value  $|q| = 2e$ . However, this does not exclude the possibility that pairs can also be formed in a different way from that found by Cooper. For example, in the context of high-temperature superconductivity, a model has been discussed in the literature predicting the formation of two different kinds of mobile particles from the system of electrons [78]. One kind carries the spin of the electrons but not the charge (“spinons”), and the other kind carries the charge  $e$  but no spin (“holons”). In analogy to Bose–Einstein condensation, the holons can form a macroscopic quantum wave consisting of charge carriers with charge  $e$ . However, holons can only move in pairs in an ingenious way such that flux quantization in units of  $h/2e$  would be observed again.

The spin of the superconducting charge carriers can also be determined relatively directly. For this purpose, one observes the precession of an atomic nucleus, say, of a copper or oxygen nucleus in the cuprates, in an applied magnetic field. This is done by means of the nuclear magnetic resonance (NMR), which is widely available today as a result of nuclear spin tomography. In a metal the precession frequency of the atomic nuclei is influenced by the spins of the conduction electrons or by the magnetic moment attached to the spin. In an applied magnetic field, the spins partly orient themselves (“Pauli paramagnetism”) and thereby generate an additional magnetic field at the location of the atomic nucleus, which changes the precession frequency of the nucleus. This effect is referred to as the ***Knight shift***. If the Cooper pairs carry zero spin, they cannot contribute anymore to the Knight shift. Then during cooling down to  $T_c$ , the Knight shift strongly decreases and approaches zero if all the electrons are paired.<sup>26</sup> [Figure 3.31](#)a shows a measurement of the Knight shift  $K_s$  for the high-temperature superconductor  $\text{YBa}_2\text{Cu}_3\text{O}_7$ . The data were taken at the oxygen and copper nuclei of the  $\text{CuO}_2$  planes [81]. Below the transition temperature we clearly see the decrease in  $K_s$ . The different lines in the figure are calculated for Cooper pairs with an angular momentum  $2 \hbar$ , or more accurately for the  $d_{x^2-y^2}$  symmetry of the pair wave function [79], which we will discuss in detail later.



(a)



(b)

**Figure 3.31** Measurement of the Knight shift: (a) for the high-temperature superconductor  $\text{YBa}_2\text{Cu}_3\text{O}_7$  [79] and (b) for  $\text{Sr}_2\text{RuO}_4$  [80]. (© 1998 Nature.) The lines indicate the expected behavior for a superconductor with spin-singlet pairing and  $d_{x^2-y^2}$  symmetry of the pair wave function.

The data shown in [Figure 3.31](#)b were obtained from the oxygen atoms in the RuO<sub>2</sub> planes of the compound Sr<sub>2</sub>RuO<sub>4</sub> [80]. For the curve denoted by  $K^{1x}$  the magnetic field was oriented along one Ru–O bond, and for the curve denoted by  $K^{1y}$  perpendicular to that. Again, the dashed line indicates the curve expected for  $d_{x^2-y^2}$  symmetry of the pair wave function. In contrast to the measurements for YBa<sub>2</sub>Cu<sub>3</sub>O<sub>7</sub>, for Sr<sub>2</sub>RuO<sub>4</sub> we do not observe any decrease in the Knight shift below  $T_c$ . This indicates that the electrons do not pair to form a spin-singlet state. Hence, for Cooper pairing only the spin-1  $\hbar$  state remains.

Next we turn to the identification of the angular momentum state. For this we must first discuss the connection between the angular momentum of a pair, the pair wave function, and the energy gap in the quasiparticle density of states.

For conventional superconductivity the pair wave function is overall isotropic, that is, it does not depend strongly on the wave vector  $\mathbf{k}$  of the electrons.<sup>27</sup> The same applies to the energy gap in the quasiparticle density of states. The generation of an unpaired electron with wave vector  $\mathbf{k}$  (or momentum  $\hbar\mathbf{k}$ ) costs energy  $\Delta_0$ , which is approximately equal for all directions of  $\mathbf{k}$ . We can illustrate this situation as shown in [Figure 3.32](#)a. Here, within the  $(k_x, k_y)$  plane of  $\mathbf{k}$ -space, the amplitude  $\Psi_0$  of the pair wave function is symbolized for a fixed value of  $|\mathbf{k}|$  by the vector describing the distance of the curve from the origin. If  $\Psi_0$  is independent of  $\mathbf{k}$ , this distance vector has the same value for all directions. Hence, in two dimensions it represents the radius of a circle, and in three dimensions the radius of a sphere. If  $\Psi_0$  depends weakly on  $\mathbf{k}$ , the circle will be slightly deformed. Similarly, we can draw the nearly  $\mathbf{k}$ -independent energy gap  $\Delta_0$  in the form of a ring around the surface of the Fermi sphere, as shown in [Figure 3.32](#)b. The energy gap  $\Delta_0$  is finite in all directions of  $\mathbf{k}$ , and it has the same value everywhere.

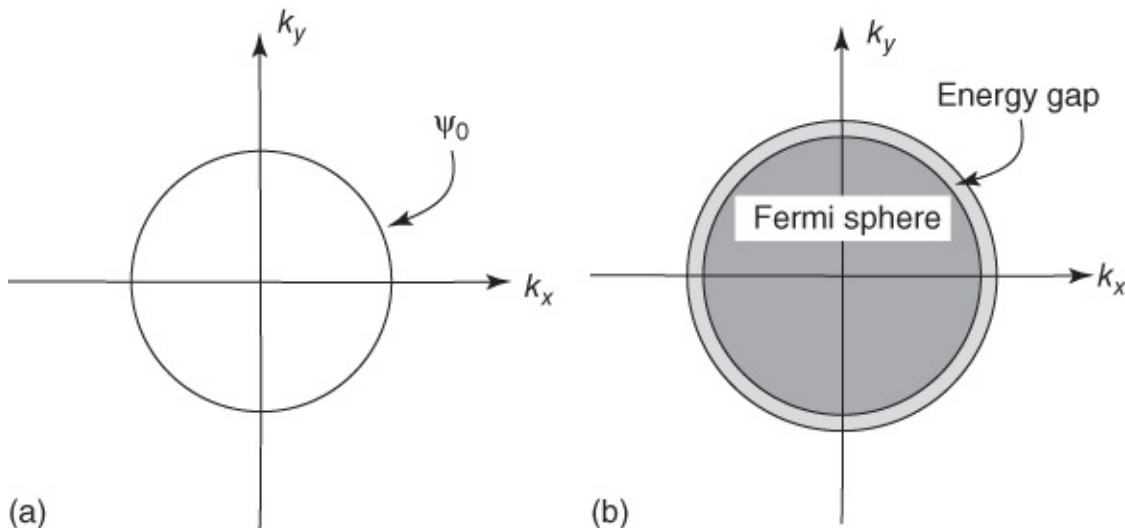


[Figure 3.32](#) Conventional superconductor with s-wave symmetry: (a) amplitude of the pair wave function in  $\mathbf{k}$ -space and (b) dependence of the magnitude of the energy gap  $\Delta_0$  upon  $\mathbf{k}$ .

The situation changes drastically if we turn to the states with finite angular momentum. First, we consider the case of spin-singlet pairing. Here, the value of the angular momentum of a pair

must be even (see [Section 2.1](#)). Hence, following the s state, we must consider  $2\hbar$  as the next lowest value.

From atomic physics, we know that for a d state there exist five different possible orientations of the z-component of the angular momentum. This leads to five different atomic orbitals, which are denoted as  $d_{xy}$ ,  $d_{yz}$ ,  $d_{xz}$ ,  $d_{x^2-y^2}$ , and  $d_{3z^2-r^2}$ . From these notations, we can find the angular dependence of the atomic orbitals. The wave function  $\Psi$  changes its value in the same way as the function indicated by the index.

For illustration we turn to the state  $d_{x^2-y^2}$  within the  $(x,y)$  plane. We look at the value of the function  $f(x,y) = x^2 - y^2$  on the unit circle with radius  $r^2 = x^2 + y^2 = 1$ . If in  $f(x,y)$  we replace  $y^2$  by  $1 - x^2$ , we obtain  $f(x,y) = 2x^2 - 1$ . This function attains its minimum value of  $-1$  on the y-axis ( $x = 0$ ), whereas on the x-axis it takes its maximum value of  $+1$ . For  $x^2 = \frac{1}{2}$ , that is, for  $x = \pm 1/\sqrt{2}$ ,  $f(x,y)$  changes sign. At these locations we have  $|x| = |y|$ , that is, the sign change occurs on the diagonal in the  $(x,y)$  plane.

We can also characterize  $f(x,y)$  by introducing the angle  $\phi$  between the y-axis and a radius vector  $\mathbf{r}$  on the unit circle. Then a point on the circle is described by  $(x,y) = (\cos\phi, \sin\phi)$ , and  $f(x,y)$  can be written as  $f(\phi) = \sin^2\phi - \cos^2\phi = -\cos(2\phi)$ . This function is shown in [Figure 3.33a](#). In [Figure 3.33b](#), we present  $|f(x,y)|$  in the  $(x,y)$  plane. Here the radius vector from the origin to the function is proportional to  $|f(x,y)|$ . The sign of  $f(x,y)$  has been indicated explicitly. We obtain a clover-leaf structure, where  $|f(x,y)|$  vanishes on the diagonals.

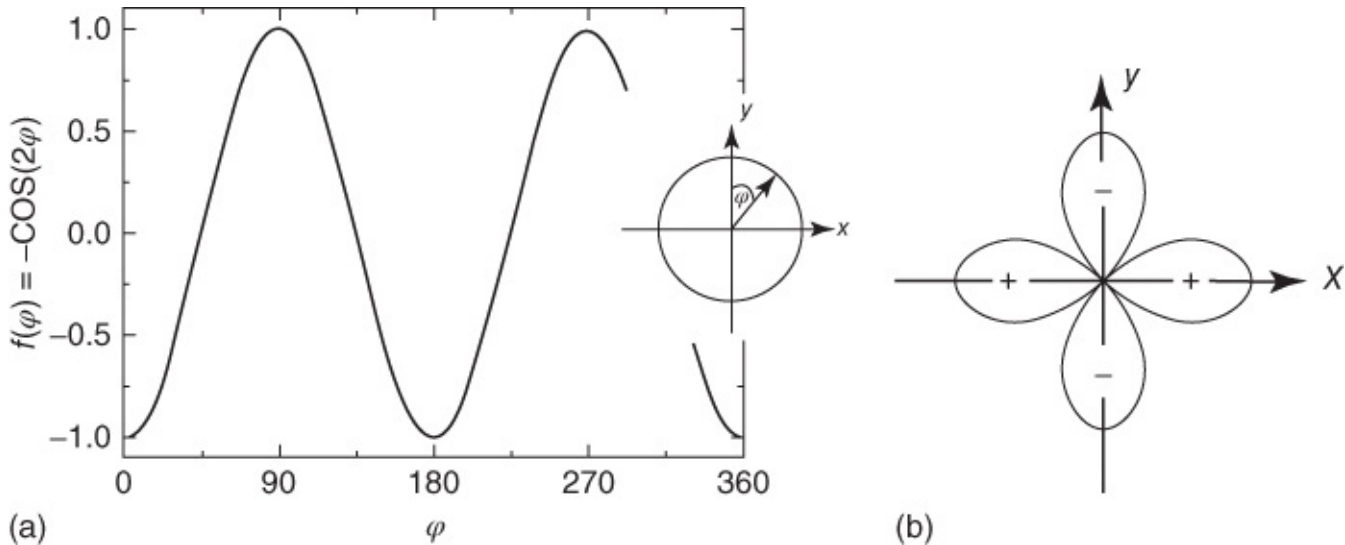


**Figure 3.33** The value of the function  $x^2 - y^2$  on the unit circle. In (a)  $f$  is plotted versus the angle  $\phi$  between the y axis and a radius vector on the unit circle:  $f(\phi) = -\cos(2\phi)$ . In (b)  $|f(x,y)|$  is plotted in the  $(x,y)$  plane. The distance vector between the origin and  $f(x,y)$  is proportional to  $|f(x,y)|$ . The sign of the function is indicated as “+” or “-.”

We could also have carried out a similar discussion in three dimensions. Then, instead of the clover-leaf of [Figure 3.33b](#), we would have found a structure of “clubs.” Analogously, for the cases  $d_{xy}$ ,  $d_{yz}$ , and  $d_{xz}$ , there would have appeared clubs, oriented spatially in a different way compared to the  $d_{x^2-y^2}$  orbital. The geometry of the  $d_{3z^2-r^2}$  orbital is more complicated.

In the case of the hydrogen atom, all the spatial directions are equivalent, and all the possible orientations of the z-component of the angular momentum are energetically equal (“degenerate”), as long as no magnetic field is applied. This is changed in the crystal. Now we must also take into account the symmetry of the crystal structure. On the one hand, this can lift the energetic degeneracy. On the other hand, it can also lead to the necessity that different orbitals must be combined with each other in order to find the energetically most favorable state.

We do not want to discuss these points in detail. Instead, we want to ask: What are the consequences of an angular momentum different from zero for the pair wave function  $\Psi$  and for the energy gap  $\Delta_0$ ? We look at these two quantities in  $\mathbf{k}$ -space.

We can write the complex function  $\Psi(k_x, k_y)$  as  $\Psi_0(k_x, k_y) e^{i\phi}$ , with a real function  $\Psi_0(k_x, k_y)$  and a phase factor  $e^{i\phi}$ . The phase factor indicates the motion of the center of mass of the Cooper pairs along a certain direction. Similar to atomic orbitals, we can classify  $\Psi_0(k_x, k_y)$  according to the angular momentum states. In the case of the  $d_{x^2-y^2}$  symmetry,  $\Psi_0(k_x, k_y)$  has the same structure as the atomic orbital shown in [Figure 3.33](#). However, we have to recall that now we are describing the state of *all Cooper pairs in  $\mathbf{k}$ -space*, that is, no longer the wave function of single electrons in regular space. Therefore, in [Figure 3.34a](#) we have displayed  $\Psi_0(k_x, k_y)$  again for the  $d_{x^2-y^2}$  symmetry.

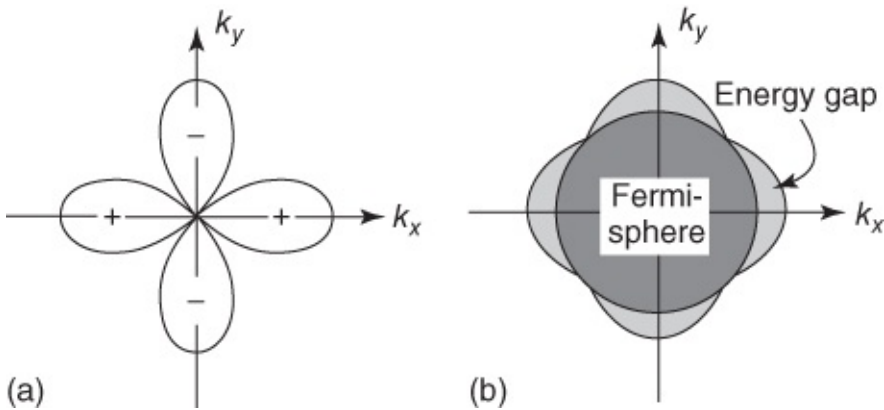


**Figure 3.34** (a) Amplitude of the pair wave function and (b) energy gap in  $\mathbf{k}$ -space for  $d_{x^2-y^2}$  symmetry. In (a) the distance from the origin to the function is proportional to  $|\Psi_0|$ . The sign of  $\Psi_0$  is indicated explicitly.

The value of the square of  $\Psi_0(k_x, k_y)$  yields the density of Cooper pairs. Obviously, this density vanishes for certain values of  $(k_x, k_y)$ . This just means that the Cooper pairs cannot move along certain crystal directions.

Analogously one finds that the energy gap  $\Delta_0$  of the quasiparticle excitations also depends on  $\mathbf{k}$ . One obtains  $\Delta_0 \propto |\Psi_0|$ . In the special case of  $d_{x^2-y^2}$  symmetry, along the directions  $k_x$  and  $k_y$  the energy gap reaches its maximum value, which we denote by  $\Delta_{\max}$  (see [Figure 3.34b](#)). Along the directions of the diagonals in the  $(k_x, k_y)$  plane we have  $\Delta_0 = 0$ . Extended to three

dimensions this means that along certain lines, namely for the angles  $45^\circ$ ,  $135^\circ$ ,  $225^\circ$ , and  $315^\circ$ ,  $\Delta_0$  vanishes. Hence, there exist certain crystal directions along which quasiparticles can be excited with zero excitation energy.

The quantities  $\Psi_0(k_x, k_y)$  and  $\Delta_0(k_x, k_y)$  must be consistent with the crystal structure. For instance, for orthorhombic crystal symmetry, the directions  $k_x$  and  $k_y$  cannot be equivalent anymore. Instead of the picture shown in [Figure 3.34a](#), then one obtains a function  $\Psi_0(k_x, k_y)$  for which the clubs, say, in the  $k_x$  direction are larger than those in the  $k_y$  direction. This can be described in terms of a mixture of a  $d_{x^2-y^2}$  state and an s state. However, here we do not want to discuss this any further.

As an important new result of our discussion, we note that for a finite angular momentum the function  $\Psi_0(k_x, k_y)$  and the energy gap  $\Delta_0(k_x, k_y)$  along certain directions can become zero, and that, furthermore,  $\Psi_0(k_x, k_y)$  can change its sign.<sup>28</sup> These two properties provide the principle for demonstrating the angular momentum state: one must detect the locations of the zero values and/or the sign change of the pair wave function. In [Sections 3.2.2](#) and [3.2.3](#), we will present a few experiments. However, first we want to discuss which new properties appear for spin-triplet pairing.

In the case of spin-triplet pairing, in addition to the finite angular momentum, which must assume an odd multiple of  $\hbar$  (see [Section 2.1](#)), we have to take into account the different possible spin orientations. As a consequence, instead of  $\Psi(\mathbf{k})$  or  $\Delta(\mathbf{k})$ , we must take  $2 \times 2$  matrices, which take into account the spin orientations of the two electrons relative to each other. Instead of these matrices, one often uses the so-called **d**-vector, the definition of which we do not want to discuss in more detail. However, similar to the case of spin-singlet pairing for  $\Psi_0$  and  $\Delta_0$ , one can find expressions also for the **d**-vector, which depend on  $\mathbf{k}$  in a relatively simple way. For instance, for the quasiparticle excitation spectrum one finds [82]

$$E_k = \sqrt{(\epsilon_k - E_F)^2 + |\mathbf{d}(\mathbf{k})|^2} \quad 3.16\text{a}$$

or for the complex **d**-vector

$$E_k = \sqrt{(\epsilon_k - E_F)^2 + |\mathbf{d}(\mathbf{k})|^2 \pm |d^*(\mathbf{k}) \times d(\mathbf{k})|} \quad 3.16\text{b}$$

instead of Eq. (3.4) for spin-singlet pairing.

Also in the case of spin-triplet pairing, the quasiparticle excitation spectrum can have zero excitation energy along certain crystal directions, which appear in  $\mathbf{k}$ -space at individual points or along extended lines. Then the **d**-vector can change its sign. Depending on the relative orientation of the spin and of the angular momentum, completely different states can be occupied. It is possible that in one and the same superconductor, transitions between these states occur, which vary with the temperature and with the magnetic field. Here, also interfaces and surfaces can play a role.

Clearly, the spin-triplet superconductors, analogous to superfluid  $^3\text{He}$ , present a rich variety of physical phenomena, which have been investigated only to a small extent up to now.

### 3.2.2 Cuprate Superconductors

At the discovery of high-temperature superconductivity in the system  $(\text{La},\text{Sr})\text{CuO}_4$ , there was no reason to assume that the mechanism of Cooper pairing would be unconventional. The high vibrational frequencies of the light oxygen ions yield a very large factor  $\omega_D$  in Eq. (3.6), such that a transition temperature in the range of 40 K seems possible. However, only a little later, with  $\text{YBa}_2\text{Cu}_3\text{O}_7$ , a superconductor with a maximum transition temperature near 90 K was found. This was difficult to understand within the established theory.

Very early also the isotope effect was measured, which appears if  $^{16}\text{O}$  is replaced by  $^{18}\text{O}$ . Here, the results for the various materials were quite different. Careful studies of nearly optimally doped  $\text{YBa}_2\text{Cu}_3\text{O}_7$ , in which about 75% of the  $^{16}\text{O}$  have been replaced by the heavy isotope, did not show any influence of the isotopic mass [83]. Based on the simple Eq. (3.6), for  $\text{YBa}_2\text{Cu}_3\text{O}_7$  one would have expected a reduction of  $T_c$  by 3.5 K. Within the experimental accuracy of about 0.1 K, the transition temperature remained unchanged. However, in  $\text{La}_{1.85}\text{Sr}_{0.15}\text{CuO}_4$  an isotope effect of the oxygen with an exponent  $\beta = 0.16$  was observed [84]. Also in compounds of  $\text{YBa}_2\text{Cu}_3\text{O}_{7-x}$ , in which Y was partly replaced by Pr, a large isotope effect was found. The transition temperature decreases with increasing Pr concentration, and it amounts to  $T_c = 30.6$  K in  $(\text{Y}_{0.5}\text{Pr}_{0.5})\text{Ba}_2\text{Cu}_3\text{O}_{7-x}$ . At the same time the isotope exponent  $\beta$  of the oxygen increases up to about 0.5 [85].

In the meantime, systematic studies have shown that the magnitude of the isotope effect depends strongly on the doping of the  $\text{CuO}_2$  planes (see [Figures 2.14](#) and [2.15](#)) [86]. In optimally doped samples, the isotope effect is small or absent. However, an appreciable isotope effect is found for underdoped as well as for overdoped cuprates, where the exponent  $\beta$  can even exceed the value 0.5. Hence, there exists a systematic influence of lattice vibrations on the transition temperature. However, it is likely that the effect occurs in an indirect way and does not indicate Cooper pairing by means of the electron–phonon coupling [87].

As another important observation we note that the implantation of paramagnetic impurities results in a much smaller change of the transition temperature than in the case of the conventional superconductors (see [Section 3.1.4.2](#)). Of course, here we must be sure that the implantation of the impurity atom does not change the concentration of the charge carriers in the  $\text{CuO}_2$  planes. In  $\text{YBa}_2\text{Cu}_3\text{O}_{7-x}$  one can substitute the nonmagnetic  $\text{Y}^{3+}$  ions by magnetic rare-earth  $^{3+}$  ions such as  $\text{Ho}^{3+}$ , and one finds that the transition temperature remains near 90 K even for complete substitution of Y [88]. On the other hand, only a small percentage of nonmagnetic  $\text{Zn}^{3+}$  ions replacing the copper can completely suppress superconductivity [89].

In this context, it is interesting to also look at the magnetic moment of the copper ions. In the undoped state, in the  $\text{CuO}_2$  planes we have  $\text{Cu}^{2+}$  ions, in which an electron resides in the two

possible locations of the atomic  $d_{x^2-y^2}$  orbital.<sup>29</sup> These  $Cu^{2+}$  ions have a spin of  $\frac{1}{2}\hbar$  and, hence, a magnetic moment. Experimentally, one finds a value of about  $0.6\mu_B$  (Bohr magnetons). This is relatively little, since we expect a value of  $1\mu_B$  if the electron were completely localized within the  $d_{x^2-y^2}$  orbital of copper. Furthermore, in the undoped state, the magnetic moments of the copper ions are ordered antiferromagnetically. If we introduce holes into the  $CuO_2$  planes, the Néel temperature  $T_N$ , at which the antiferromagnetic order sets in, decreases. The magnetic moment of the copper ions also decreases. Above a critical hole concentration the antiferromagnetism vanishes, and superconductivity sets in (see [Figures 2.14](#) and [2.15](#)). Then also the copper ions do not seem to have a *static* magnetic moment anymore.

Even the undoped, antiferromagnetic state of the  $CuO_2$  planes is highly unusual and could provide a hint for the mechanism of high-temperature superconductivity in the doped state.

As we mentioned already, in the undoped state, there exists an electron in each  $d_{x^2-y^2}$  orbital of copper. These orbitals overlap with the  $p_x$  and  $p_y$  orbitals of oxygen, as indicated in [Figure 3.35](#). If the electrons did not interact with each other except for the Pauli principle, then we would just have a half-filled energy band, and the undoped  $CuO_2$  plane would have to be metallic. However, instead, we find an electrically insulating state. The reason for this appears to be the strong electrostatic interaction between the electrons. If two electrons reside at the same Cu ion, they repel each other and they have a larger Coulomb energy. On the other hand, the electrons would like to be delocalized, since their kinetic energy would then be lower. It is just this effect that produces the binding energy in a classical metal.

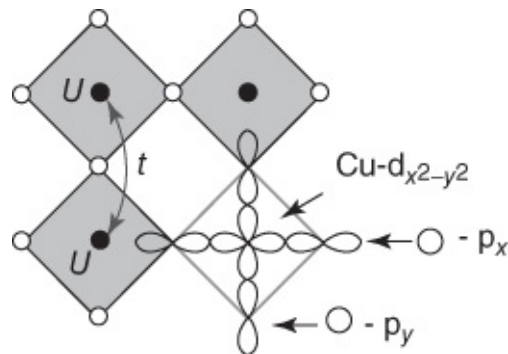


**Figure 3.35** A section of the  $CuO_2$  plane of a high-temperature superconductor consisting of four unit cells (• copper; ○ oxygen). On the lower right the relevant atomic orbitals of copper and of oxygen are sketched. The symbol “U” indicates the electrostatic repulsion between two electrons on the same copper ion; the symbol “t” (for “transfer”) indicates the kinetic energy of the electron, when it hops between neighboring copper ions.

At this stage, the important question is this: Which influence is dominant? In the case of the  $CuO_2$  planes, the repulsive effect obviously dominates and the electrons remain localized at the copper. However, they can lower their energy a little by virtually hopping back and forth between neighboring copper sites. Then the Pauli principle must also be obeyed, and the electrons must have different spin orientations in order to perform this process. In this way, we can explain at least qualitatively the antiferromagnetic/insulating state. The quantitative

treatment is based on the Hubbard model [90], which was developed in the 1950s, a long time before the discovery of the high-temperature superconductors. It leads to a splitting of the half-filled energy band appearing without the Coulomb interaction. This splitting results in two subbands, separated from each other by an energy gap. A summary of the application of the Hubbard model to high-temperature superconductors can be found, for example, in Ref. [91].

It may also be conceivable that the mechanism of high-temperature superconductivity could be understood from the Hubbard model, although the interaction between the electrons is primarily repulsive [91]. If a hole is introduced into the CuO<sub>2</sub> planes, that is, if an electron is removed, then this cancels the antiferromagnetic interaction energy<sup>30</sup> with the four nearest Cu neighbors. A second hole introduced into the CuO<sub>2</sub> plane has an energetic advantage if it occupies one of these neighboring sites, since in this case the interaction is affected only for seven instead of eight neighbors. However, similar to the electron–phonon coupling, for many holes this simple static picture would lead to an accumulation of many holes in close proximity and not to Cooper pairing. On the other hand, if we imagine that the first hole moves through the antiferromagnetic lattice, then this generates a kind of ferromagnetic trace within the antiferromagnetic lattice. The hole is moving because a neighboring electron hops to the unoccupied site. However, at its new site this electron has the wrong spin orientation, that is, its spin is oriented in the same direction as that of the neighbors. If a second hole moves along the trace of the first hole, the ferromagnetic spin configuration is changed again into an antiferromagnetic one.

These arguments demonstrate, at least qualitatively, how holes in the CuO<sub>2</sub> planes can become correlated, forming pairs. Extending this idea to many holes, we arrive at a highly dynamic system, in which the electrons are correlated by means of (antiferromagnetic) spin fluctuations.<sup>31</sup> Within this picture the short coherence lengths of the high-temperature superconductors appear in a natural way, since the interaction described is of very short range. However, up to now, a quantitative explanation of high-temperature superconductivity based on this model could not be achieved.

On the other hand, this model can explain why the resulting superconducting state should not have s-wave symmetry. The repulsion between the holes is so strong that a pair wave function is favored, for which the probability of finding two electrons at the same location is very small. This is not the case for  $L = 0$ . Hence, for  $S = 0$ , the smallest possible value of the angular momentum is  $L = 2\hbar$ .

Evidence for an unconventional symmetry of the pair wave function was obtained early. For various measured quantities, a temperature dependence was observed which was very different from that in conventional superconductors. As an example, we have already discussed the Knight shift.

An additional quantity in NMR is the decay rate with which the z-component of the nuclear spin returns to its orientation parallel to the applied static magnetic field, if it had been deflected from this orientation by a magnetic field pulse. This decay rate, the so-called spin-lattice relaxation rate  $1/T_1$ , is influenced by the interactions between the nuclear spins and the

electrons. In conventional superconductors, it has a maximum at the transition temperature. However, in the cuprates such a maximum has not been found.

Also the temperature dependence of the magnetic penetration depth is unusual. In conventional superconductors at low temperatures,  $\lambda_L$  is practically constant. However, in the cuprates, it was found that even at low temperatures in pure samples  $\lambda_L(T)$  increases linearly, and in impure samples quadratically, with increasing temperature [92].

Another example is the specific heat of the conduction electrons, which we will discuss in more detail in [Section 4.2](#). In conventional superconductors toward low temperatures it approaches zero exponentially, since the unpaired electrons must be excited beyond an energy gap. However, in the cuprates, power laws were found again [93, 94].

All these measurements indicate that the Cooper pair density as well as the energy gap in the quasiparticle excitation spectrum has zero value along certain directions in  $\mathbf{k}$ -space, as shown in [Figure 3.34](#). For illustration, we look at the case of the  $d_{x^2-y^2}$  symmetry of the quasiparticle density of states. For this, in Eq. (3.5) we must take into account the  $\mathbf{k}$  dependence of  $\Delta_0$ , and then we obtain a density of states  $N_s(E, \mathbf{k})$ , depending on the energy as well as on the wave vector  $\mathbf{k}$ . Next, we average this quantity with respect to its  $\mathbf{k}$  dependence. As a result, we obtain the density of states  $N_s(E)$  shown in [Figure 3.36](#), to be compared with [Figure 3.7](#). Now  $N_s(E)$  increases already linearly at the Fermi energy. It diverges at  $(E - E_F) = \Delta_{\max}$ , and then it rapidly approaches the value  $N_n(E_F)$  of the normal state.

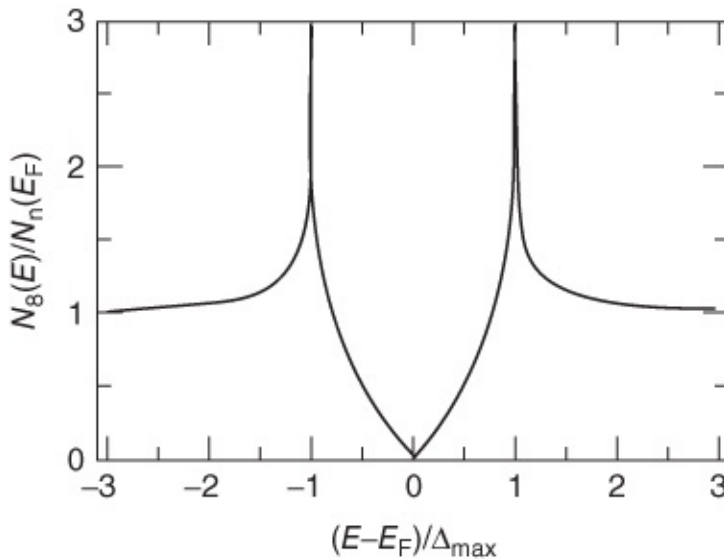


**Figure 3.36** Quasiparticle density of states  $N_s(E)$  in a superconductor with  $d_{x^2-y^2}$  symmetry of the pair wave function.

[Figure 3.37](#) shows the results of tunneling measurements at 4.2 K using the iridium tip of a scanning tunneling microscope placed onto the surface of  $\text{Bi}_2\text{Sr}_2\text{CaCu}_2\text{O}_{8+x}$  single crystals with different doping levels [95]. On average, the tunneling currents flow perpendicularly to the  $\text{CuO}_2$  planes. We clearly see that the tunneling conductivity and, hence, the quasiparticle density of states reach finite values already at small voltages.

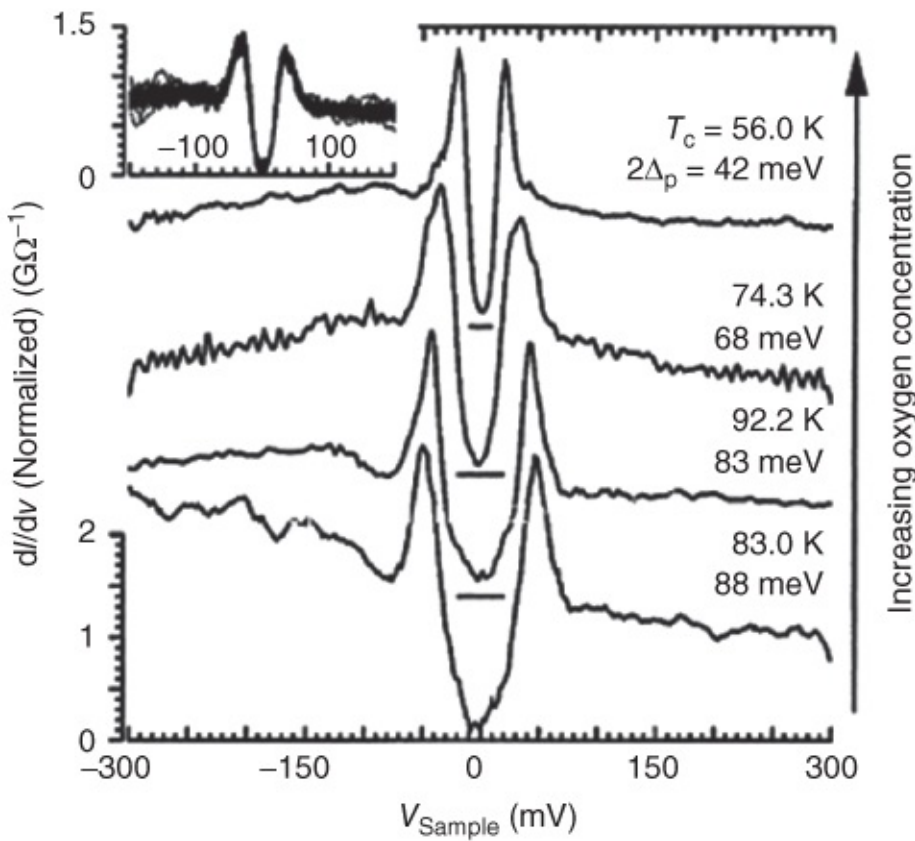


**Figure 3.37** Conductivity of tunnel junctions between the Ir tip of a scanning tunneling microscope and  $\text{Bi}_2\text{Sr}_2\text{CaCu}_2\text{O}_{8+x}$  single crystals with different doping levels. For clarity the curves are shifted vertically. The two upper curves show overdoped crystals, the third curve from the top shows an optimally doped crystal, and the curve at the bottom an underdoped crystal. The inset shows the superposition of 200 tunneling measurements for an overdoped crystal with  $T_c = 71.4 \text{ K}$ . The measurements were performed at different locations of the crystal surface [95].

It is interesting that  $\Delta_{\max}$  increases continuously with decreasing doping level, although the transition temperature passes through a maximum. Also the ratio  $2\Delta_{\max}/k_B T_c$  is by no means constant. In the case of the curves shown in Figure 3.37, it increases from 9 up to 12, which is distinctly larger than the BCS value of 3.5.

Also the density of states  $N_s(E, \mathbf{k})$  can be measured as a function of  $\mathbf{k}$ , and from this one can determine the function  $\Delta_0(\mathbf{k})$ . For this the so-called angle-resolved photoemission spectroscopy (ARPES) turned out to be highly powerful. The method is based on the photoelectric effect. For its explanation Albert Einstein had received the Nobel Prize. The photoelectric effect results if light with the frequency  $f$  is focused on the surface of a sample. If the energy  $hf$  of the photons exceeds the work function  $W$ , electrons with energy  $hf - W$  are emitted. This method can also be further improved by determining the momentum of the emitted electrons for a well-specified direction and energy of the incoming photons. Then one can calculate the energy and the momentum of the electrons within the sample and determine  $N_s(E, \mathbf{k})$  and  $\Delta_0(\mathbf{k})$  from this. These measurements clearly show that  $\Delta_0(\mathbf{k})$  vanishes, within

experimental accuracy, if the wave vector is oriented parallel to the  $\text{CuO}_2$  planes in the direction of the diagonals within the  $(k_x, k_y)$  plane [96, 97].

This is shown in [Figure 3.38](#) for the compound  $\text{Bi}_2\text{Sr}_2\text{CaCu}_2\text{O}_8$  [98]. The figure also contains the Fermi surface in the  $(k_x, k_y)$  plane. Here,  $\Gamma$  denotes the origin. The direction from  $\Gamma$  to the point marked by  $\bar{M}$  follows the copper–oxygen bonds. The direction from  $\Gamma$  to the point  $Y = (\pi/a, \pi/a)$  is diagonal to this ( $a$  is the lattice constant). In this case, the Fermi surface looks like a rounded square and is centered around the point  $Y$ .

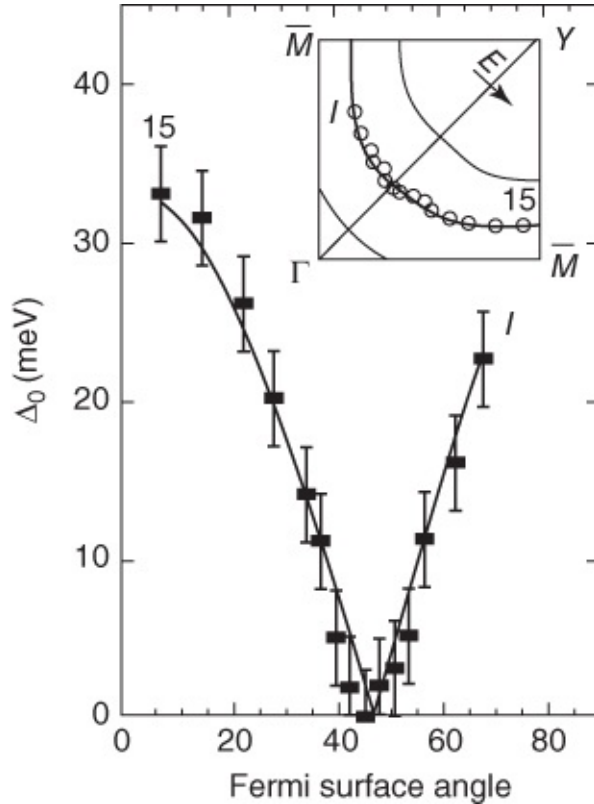


[Figure 3.38](#) ARPES measurements of the energy gap in  $\text{Bi}_2\text{Sr}_2\text{CaCu}_2\text{O}_8$  in the  $(k_x, k_y)$  plane. The main figure shows  $\Delta_0$  as a function of the angle to the Cu–O bonds. The inset shows the section of the Fermi surface for which the energy gap was determined (• raw data, ○ corrected data) [98].

The measurements mentioned so far yield information on the absolute value of the pair wave function. An additional step is achieved by phase-sensitive experiments, which directly detect the sign change of the wave function. These experiments clearly confirm that the  $d_{x^2-y^2}$  state is realized in the cuprates. For the regular space, this means that in the directions of the copper–oxygen bonds within the  $\text{CuO}_2$  planes the Cooper pair density and the energy gap reach a maximum, and they vanish diagonal to this. This particular symmetry appears likely, if we assume that the charge carriers can move easily and form pairs along these bonds.

Before we turn in detail to the phase-sensitive experiments, we want to mention another highly peculiar property of the energy gap in the cuprates. A gap can be observed even above the transition temperature. A summary of the experimental results can be found in Ref. [99].

Measurements of the Knight shift and of the spin-lattice relaxation rate  $1/T_1$  in underdoped  $\text{YBa}_2\text{Cu}_3\text{O}_{7-x}$  already showed early that spins can be “frozen out” also far above the transition temperature. This was referred to as a **spin gap**. However, subsequent measurements of the specific heat and of many other quantities indicated not only that the spin degrees of freedom are involved, but also that the density of states of the electrons is strongly reduced even at small energies. Therefore, one speaks of a pseudo-gap. This feature is highly pronounced in particular in the underdoped cuprates.

This is shown in [Figure 3.39](#) for tunneling measurements at different temperatures performed with an underdoped  $\text{Bi}_2\text{Sr}_2\text{CaCu}_2\text{O}_{8+x}$  single crystal having a transition temperature of 83 K [95]. The curve at 4.2 K has been shown already in [Figure 3.37](#). In the figure we note several features of the tunneling spectra. First, the spectra are highly nonsymmetric. There is a difference between the cases in which (for negative voltage) electrons flow out of the sample, that is, leaving holes behind, and (for positive voltage) holes flow out of the single crystal. Second, the amplitude of the conductivity maximum gradually decreases with increasing temperature. However, the voltage level indicating the value  $\Delta_{\max}$  of the maximum energy gap changes only little. In particular, at the transition temperature,  $\Delta_{\max}$  by no means approaches zero.

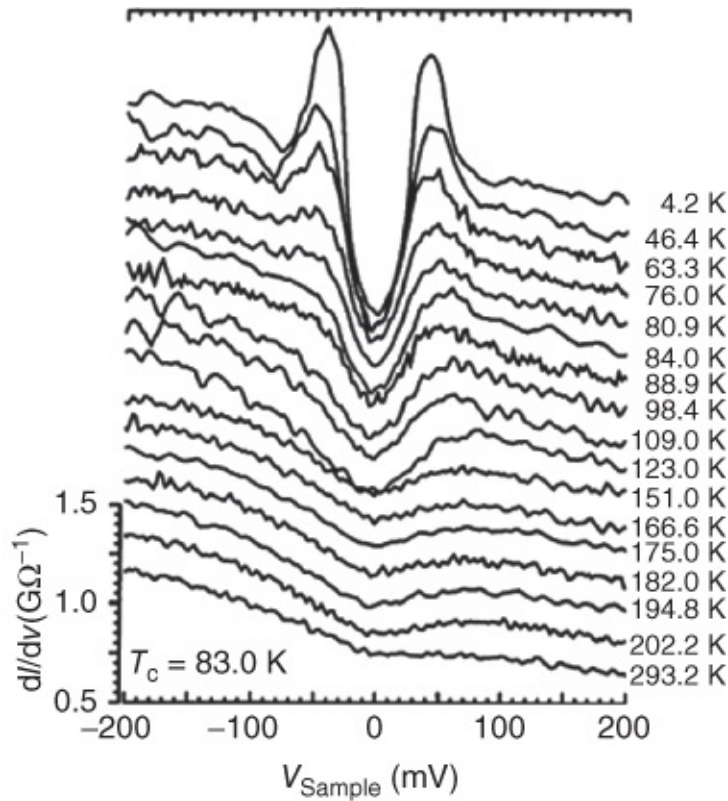


[Figure 3.39](#) Conductivity of a tunnel junction between the Ir tip of a scanning tunneling microscope and an underdoped  $\text{Bi}_2\text{Sr}_2\text{CaCu}_2\text{O}_{8+x}$  single crystal for different temperatures (see also [Figure 3.37](#)). For clarity, the experimental curves are shifted vertically [95].

Furthermore, ARPES measurements have shown that in  $\mathbf{k}$ -space above the transition temperature the pseudo-gap has the same symmetry as the energy gap in the superconducting

state, that is, the pseudo-gap also vanishes in the directions diagonal to the Cu–O bonds [100].

It is still not clear, if and how the pseudo-gap is connected with superconductivity or Cooper pairing. Possibly, the pseudo-gap could result directly from the energy gap in the superconducting state and, for example, could be caused by short-lived Cooper pairs, which exist already above  $T_C$ . However, the pseudo-gap may also arise due to a phenomenon, which is independent of the Cooper pairs, and which is competing with superconductivity. In 2010, by means of a highly sensitive scanning tunneling microscope, it could be shown that on a scale of nanometers, the pseudo-gap is accompanied by a “nematic” order of the electrons localized at the oxygen sites. In this case the translational symmetry of the crystal lattice remains, whereas the rotational symmetry is broken [101]. This numinically ordered state is weakly magnetic.

However, let us return to experiments that are directly affected by the sign change of the pair wave function. The articles [102, 103] provide a nice overview on this subject. Here, Josephson junctions, often arranged in ingenious geometries, play a crucial role.

First, let us look at a quantum interferometer between an unconventional superconductor with  $d_{x^2-y^2}$  symmetry of the pair wave function and a conventional superconductor ([Figure 3.40a](#)). The geometry is analogous to that shown in [Figure 1.24](#). However, in the present case the two halves of the interferometer, which are separated from each other by means of Josephson junctions, consist of two different superconducting materials. In [Figure 3.40](#) we have symbolized the pair wave function of the two superconductors by the clover-leaf structure of [Figure 3.34a](#) or by a circle as in [Figure 3.32a](#).<sup>32</sup> The orientation of the d-wave superconductor is taken such that the electric current direction across the Josephson junctions is along the direction of the maximum value of  $|\Psi_0|$ , that is, along a Cu–O bond in the cuprates. In [Figure 3.40](#) we have arbitrarily given the pair wave function of the conventional superconductor the positive (“+”) sign. However, we will see that this is irrelevant.

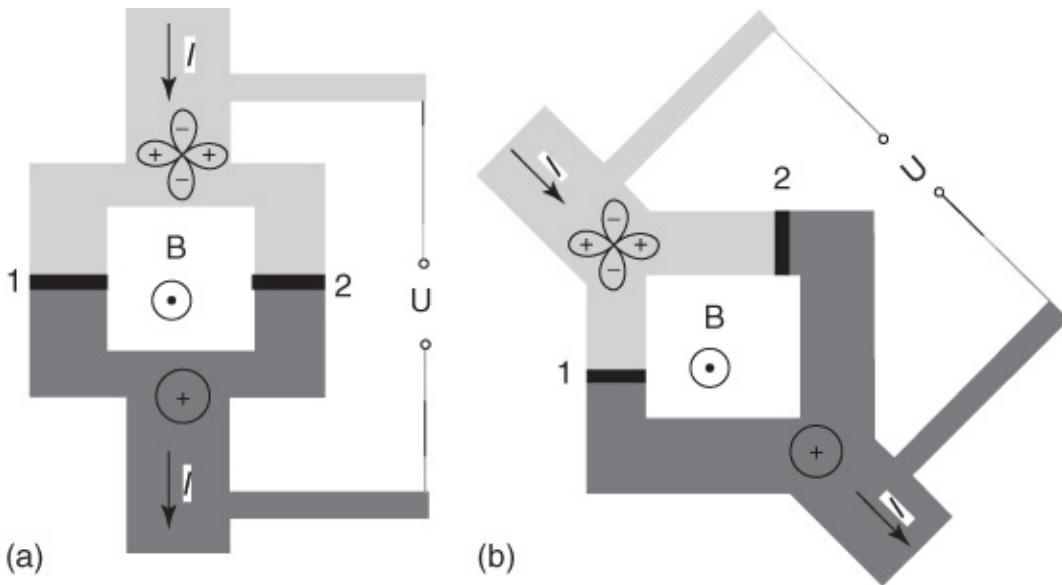


**Figure 3.40** (a), (b): Two interferometer geometries between an unconventional superconductor with  $d_{x^2-y^2}$  symmetry of the pair wave function and a conventional superconductor. The two superconductors are connected with each other by means of the Josephson junctions “1” and “2.”

Analogous to [Section 1.5.2](#), for this geometry we can calculate the maximum supercurrent across the two Josephson junctions.

We have defined the pair wave function as  $\Psi = \Psi_0(\mathbf{k})e^{i\phi}$ . Here, the real part  $\Psi_0(\mathbf{k})$  can change its sign. The remaining phase  $\phi$  must be treated in exactly the same way as in classical superconductors. In particular, as in [Section 1.5.2](#), in the two halves of the ring we can again integrate the gradient of the phases  $\phi_1$  and  $\phi_2$ , and identical to [Eq. \(1.58\)](#) we find the relation

$$\gamma_2 - \gamma_1 = \frac{2\pi}{\Phi_0} \Phi = \frac{2\pi}{\Phi_0} (\Phi_a + LJ) \quad 3.17$$

Now we must find a connection between the supercurrent across the two Josephson junctions and the phases of the pair wave function on both sides of the junction. This derivation is again perfectly analogous to that in [Section 1.5.1](#). However, now we must take into account that the pair wave function has a different sign on the two sides of the barrier. Hence, the prefactor of the Josephson current–phase relation will be negative,

$$I_s = -I_c \sin \gamma \quad 3.18$$

with  $I_c > 0$ . However, we have  $-I_c \sin \gamma = I_c \sin(\gamma + \pi)$ , and we can also say, that compared to a conventional Josephson junction, the phase of the Josephson junction has an additional phase factor of  $\pi$ . Hence, one often speaks of “ $\pi$  Josephson junctions.”

Now, analogous to [Eq. \(1.53\)](#), we can continue to write

$$\frac{I}{2} + J = -I_{c1} \sin \gamma_1 \quad 3.19a$$

$$\frac{I}{2} + J = -I_{c2} \sin \gamma_2$$

**3.19b**

Here,  $J$  is the current circulating around the ring. Here, we again note the negative sign of the sine function.

For simplicity, we now neglect the inductivity  $L$ , and we assume that both Josephson junctions have the same value of the critical current  $I_c$ . Then, analogous to Eq. (1.60), we obtain the expression

$$I = -I_c \left[ \sin \gamma_1 + \sin \left( 2\pi \frac{\Phi_a}{\Phi_0} + \gamma_1 \right) \right] \quad 3.20$$

Again we can introduce a phase  $\delta = \gamma_1 + \pi \Phi_a / \Phi_0$ , and analogous to Eqs. (1.61) and (1.62) we find

$$I_s = -I_c \left[ \sin \left( \delta - \pi \frac{\Phi_a}{\Phi_0} \right) + \sin \left( \delta + \pi \frac{\Phi_a}{\Phi_0} \right) \right] = -2I_c \sin \delta \cos \left( \pi \frac{\Phi_a}{\Phi_0} \right) \quad 3.21$$

In order to obtain the maximum supercurrent, again we must choose  $\delta$  in such a way that  $I_s$  reaches a maximum value.

We find

$$I_{s,\max} = 2I_c \left| \cos \left( \pi \frac{\Phi_a}{\Phi_0} \right) \right| \quad 3.22$$

This is the *same result* as Eq. (1.63).

We see that for the geometry we have discussed we could not find any difference compared to a conventional quantum interferometer, although we had to change the sign of the critical current of the two Josephson junctions. This would also have remained the same if on the side of the conventional superconductor we had given the pair wave function a negative sign, or if we had exchanged the “+” and “−” signs on the side of the d-wave superconductor. In each case, a sign change of the pair wave function would have appeared either at both Josephson junctions or at neither of them.

However, if we construct the interferometer as shown in [Figure 3.40b](#), a sign change only appears at *one* of the two Josephson junctions. In the figure, this is the case for the junction “1.” If we again neglect the influence of the self-inductance, we obtain

$$I_s = -I_c \left[ \sin \left( \delta - \pi \frac{\Phi_a}{\Phi_0} \right) - \sin \left( \delta + \pi \frac{\Phi_a}{\Phi_0} \right) \right] = -2I_c \sin \delta \sin \left( \pi \frac{\Phi_a}{\Phi_0} \right) \quad 3.23$$

and

$$I_{s,\max} = 2I_c \left| \sin \left( \pi \frac{\Phi_a}{\Phi_0} \right) \right| \quad 24$$

The maximum supercurrent vanishes at zero applied magnetic field. It reaches a maximum at an external magnetic flux of  $\Phi_0/2$ . Also we can say that, compared to a conventional quantum interferometer, there appears a phase shift of  $\pi/2$ , corresponding to the additional magnetic flux of half a flux quantum passing through the interferometer. In 1987, a similar geometry was proposed in conjunction with the heavy-fermion superconductors [104]. In the early 1990s, the relevant experiment was performed in Urbana using a  $\text{YBa}_2\text{Cu}_3\text{O}_7$  crystal [105]. The conventional superconductor was Pb. Within a large scatter of the data, the result Eq. (24) was obtained.

However, the geometry of [Figure 3.40b](#) leads to the problem that the results can be systematically perturbed. If during the cooling process vortices are trapped within the legs of the interferometer, either in  $\text{YBa}_2\text{Cu}_3\text{O}_7$  or in Pb, then a fraction of the magnetic flux of the vortices will be coupled into the interferometer and will result in a phase shift of the function  $I_{s,\max}(\Phi)$  in the same way as in the case of the unconventional pair wave function.

We see that we must proceed one step further, in order to demonstrate the sign change of the pair wave function in  $\text{YBa}_2\text{Cu}_3\text{O}_7$ . Another important experiment was set up similarly as the interferometer of [Figure 3.40b](#). However, now a continuous Josephson junction, fabricated by evaporation around the corner of a  $\text{YBa}_2\text{Cu}_3\text{O}_7$  single crystal, was used [106]. The geometry of this junction is shown schematically in [Figure 3.41b](#).

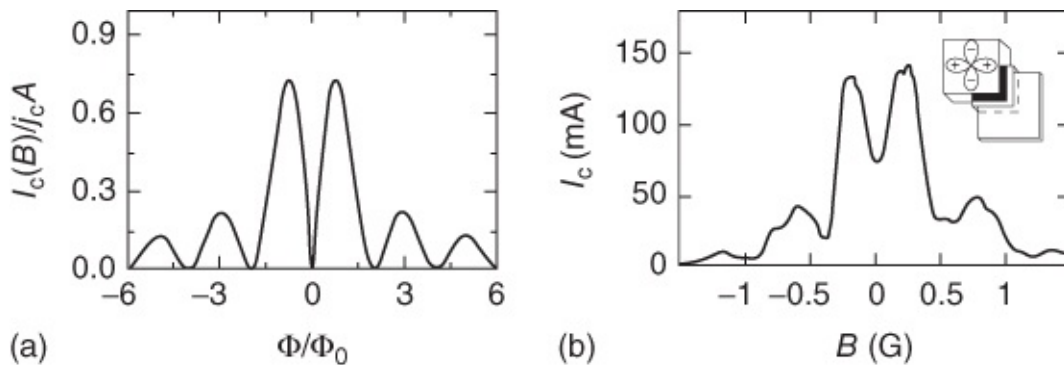


**Figure 3.41** Magnetic field or magnetic flux dependence of a Josephson junction between  $\text{YBa}_2\text{Cu}_3\text{O}_7$  and Pb for the geometry indicated in the inset in part (b). (a) The theoretical curve calculated from Eq. (25); the curve is normalized with the supercurrent  $j_c A$  expected through the junction area  $A$  in the case of homogeneous current flow. (b) The measured curve [106] (1 G =  $10^{-4}$  T).

In a conventional extended Josephson junction, the magnetic field or flux dependence of the critical current is described by the slit function (1.73). In this case, the critical current reaches a maximum value for zero magnetic flux, and with increasing flux it passes through a series of zero value of the current and of additional maxima. For the corner geometry of [Figure 3.41b](#), one obtains a drastically different result if one of the two superconductors has d-wave symmetry. In this case half of the junction has a negative value of the critical current density, whereas the other half has the usual positive value. Analogous to the derivation of Eq. (1.73), this current density can be integrated over the junction area. Then one obtains the expression

$$I_c(\Phi_J) = I_c(0) \left| \frac{\sin^2(\pi\Phi_J/2\Phi_0)}{\pi\Phi_J/2\Phi_0} \right|$$

where  $\Phi_J = B_a b t_{\text{eff}}$  is the magnetic flux through the junction as in Eq. (1.73). Here,  $B_a$  is the magnetic field applied parallel to the barrier layer,  $b$  is the total width, and  $t_{\text{eff}}$  is the effective thickness of the junction. The thickness  $t_{\text{eff}}$  is given by the thickness of the barrier layer plus the magnetic penetration depths in the two superconductors. The function is shown in [Figure 3.41a](#). [Figure 3.41b](#) shows the corresponding measurement. In spite of a few deviations, we clearly see the characteristic minimum of  $I_c$  for  $B = 0$ . Also in this case, there was the danger that magnetic vortices could be trapped in the corner of the Josephson junction and thereby could perturb the experimental result [107]. However, in this case, the result was much clearer than in the case of the ring geometry.

A completely different experiment was performed at IBM in Yorktown Heights. The magnetic flux passing through a ring made from  $\text{YBa}_2\text{Cu}_3\text{O}_7$  was detected. Several Josephson junctions were integrated into the ring. In the case of a standard solid ring fabricated from a conventional or from a d-wave superconductor, the magnetic flux  $\Phi$  through the ring would be an integer multiple of  $\Phi_0$ . In the absence of an external magnetic field, the state with the lowest energy would be the state  $\Phi = 0$ . This does not change if standard Josephson junctions are integrated into the ring. However, we must only be certain that the critical current of the Josephson junction and the inductance of the ring are large enough that the magnetic flux  $LJ$  produced by the circulating current  $J$  can supplement the externally applied flux to reach an integer multiple of  $\Phi_0$ . Therefore,  $LJ$  must amount to  $\Phi_0/2$  at least.

What happens if a  $\pi$ -Josephson junction exists within the ring? The relevant arguments were already discussed long before the discovery of high-temperature superconductivity<sup>[33](#)</sup> [108]. One finds that shielding currents can also be generated spontaneously in the ring in the absence of an applied magnetic field. Assuming that the product  $LJ$  is sufficiently large, these shielding currents then generate a magnetic flux of  $\pm\Phi_0/2$  through the ring. In this case, one also speaks of spontaneous symmetry breaking, since there are 2 equiv. states that differ only in the polarity of the shielding currents. Furthermore, one also finds that in the presence of a magnetic field the flux through the ring is quantized in units of  $(n + 1/2)\Phi_0$ , that is, always in odd multiples of *half* a flux quantum. An analogous result is obtained for any odd number of  $\pi$ -Josephson junctions in the ring. Roughly speaking, we can say that the odd number of  $\pi$  in the phase of the wave function, resulting from the  $\pi$ -Josephson junctions, is supplemented by at least one additional  $\pi$  due to the shielding currents, yielding in the end a multiple of  $2\pi$ .<sup>[34](#)</sup> We see that we have a highly characteristic effect, namely the appearance of half-integer magnetic flux quanta, which are difficult to simulate by any other means.

How can this scenario be realized with high-temperature superconductors? The secret was the fabrication of a highly special substrate, a so-called tricrystal, upon which subsequently a thin film of a high-temperature superconductor was deposited. The substrate is shown schematically in [Figure 3.42](#). It consists of three single crystalline sections of  $\text{SrTiO}_3$ , which

were rotated relative to each other, and which were then joined together again by sintering. If a  $\text{YBa}_2\text{Cu}_3\text{O}_7$  thin film is evaporated onto this substrate, the  $\text{CuO}_2$  planes orient themselves parallel to the film plane. The Cu–O bonds then point in the  $a$  and  $b$  directions of the substrate, which are indicated in [Figure 3.42](#) by (100) and (010), respectively.

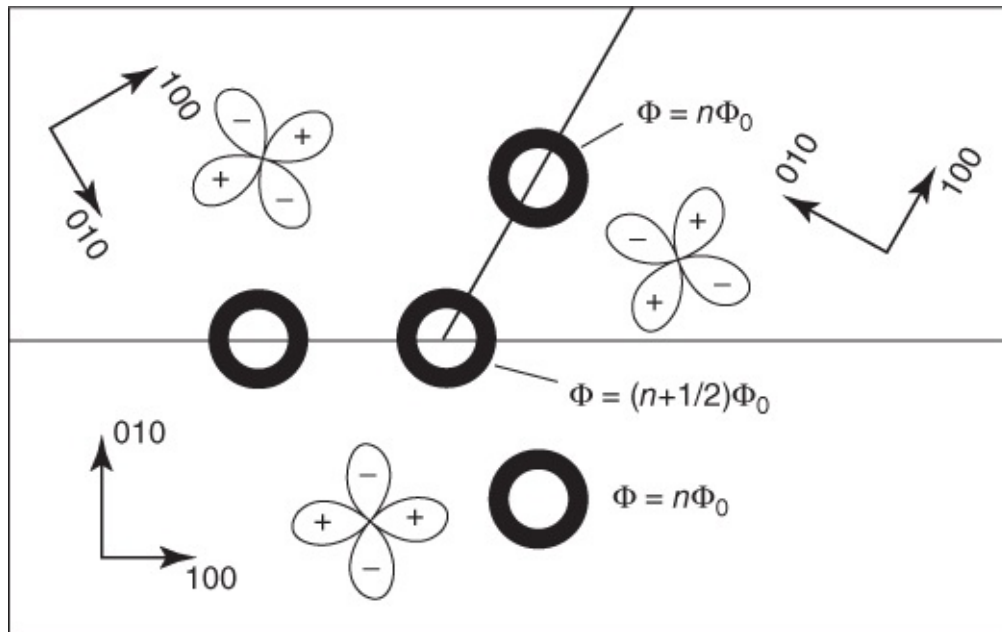


[Figure 3.42](#) Geometry of the tricrystalline experiment for detecting the half-integer magnetic flux quanta. The (100) and (010) directions indicate the directions of the crystallographic  $a$  and  $b$  axes, respectively. Inner (outer) ring diameters: 48  $\mu\text{m}$  (68  $\mu\text{m}$ ).

Next several rings were fabricated from the thin film. One ring was located wholly within one of the three sections, two rings were placed across the boundary line between two sections, and one ring cuts across all three sections. The boundary lines represent grain boundaries in the  $\text{YBa}_2\text{Cu}_3\text{O}_7$  film, and Josephson junctions appear at these locations, such that the different rings contain a different number of Josephson junctions. The ring completely placed within one section does not contain a Josephson junction. In this case, we expect that the value of the magnetic flux amounts to an integer multiple of  $\Phi_0$ . In the case of the rings cutting across a single grain boundary each, depending on the crystal orientation within the sections of the rings, we have either two conventional Josephson junctions or two  $\pi$ -Josephson junctions in the ring. In this case, we also expect an integer magnetic flux quantization.

The ring around the tricrystalline point contains three Josephson junctions. The angles between the three sections were chosen in such a way that at one of the junctions a sign change of the pair wave function appeared. In [Figure 3.42](#) this is the junction between the lower section and the section on the upper right. However, for the current flow between the two upper sections, the pair wave function has a negative sign on both sides of the corresponding junction, just as for the third Josephson junction. Hence, in the case of d-wave symmetry, we expect half-integer magnetic flux quantization for this ring.

To detect the magnetic flux passing through the rings, a superconducting quantum interference device (SQUID) was moved across the sample at low temperatures, and the flux penetrating

into this interferometer was measured. The experimental signal had to be calibrated for determining the absolute magnitude of the flux passing through the  $\text{YBa}_2\text{Cu}_3\text{O}_7$  rings. This calibration turned out to be relatively easy, since there were also three reference rings, for which an integer flux quantization was expected. By the application of a small magnetic field, flux quanta can be introduced into these rings. Even more impressive is the measurement without an applied magnetic field shown in [Figure 3.43](#). In this case, the reference rings should remain free of magnetic flux, which was also confirmed experimentally. However, in the ring around the tricrystalline point, magnetic flux always appeared. Its value, determined with high accuracy based on the calibration procedure, amounted to  $\Phi_0/2$ .

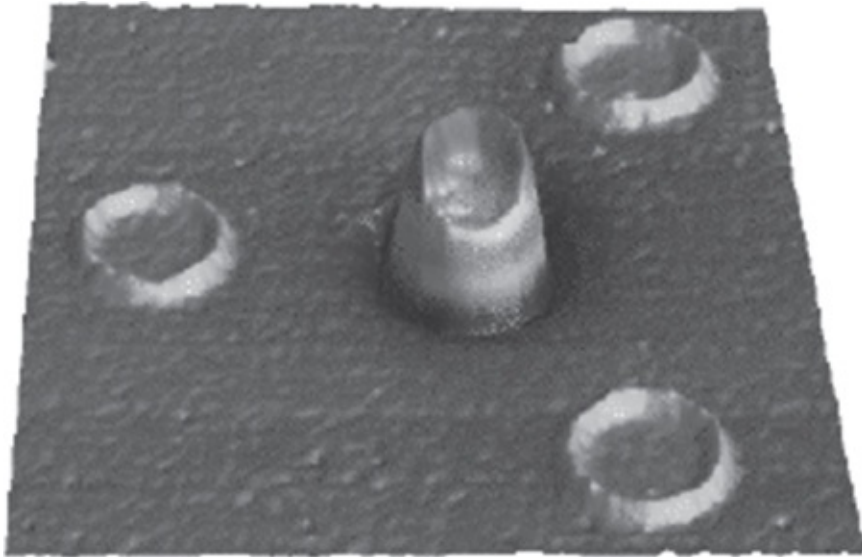


[Figure 3.43](#) Magnetic flux passing through the  $\text{YBa}_2\text{Cu}_3\text{O}_7$  rings shown in [Figure 3.42](#) in the absence of an applied magnetic field. The reference rings are free of magnetic flux, whereas the ring around the tricrystalline point carries the flux  $\Phi_0/2$  [103].

Subsequently, the half-integer magnetic flux quantization was observed in a number of hole-doped and electron-doped cuprates [103]. In this case, one refrained from fabricating the rings in the superconducting films. At the grain boundaries Josephson vortices can appear, which we will discuss in more detail in [Section 6.4](#). Regularly, they also carry the magnetic flux of  $1\Phi_0$ . However, at the tricrystalline point, a Josephson vortex appears, carrying the flux  $\Phi_0/2$ . In [Figure 3.44](#) the effect is shown for a  $\text{Bi}_2\text{Sr}_2\text{CaCu}_2\text{O}_8$  thin film.

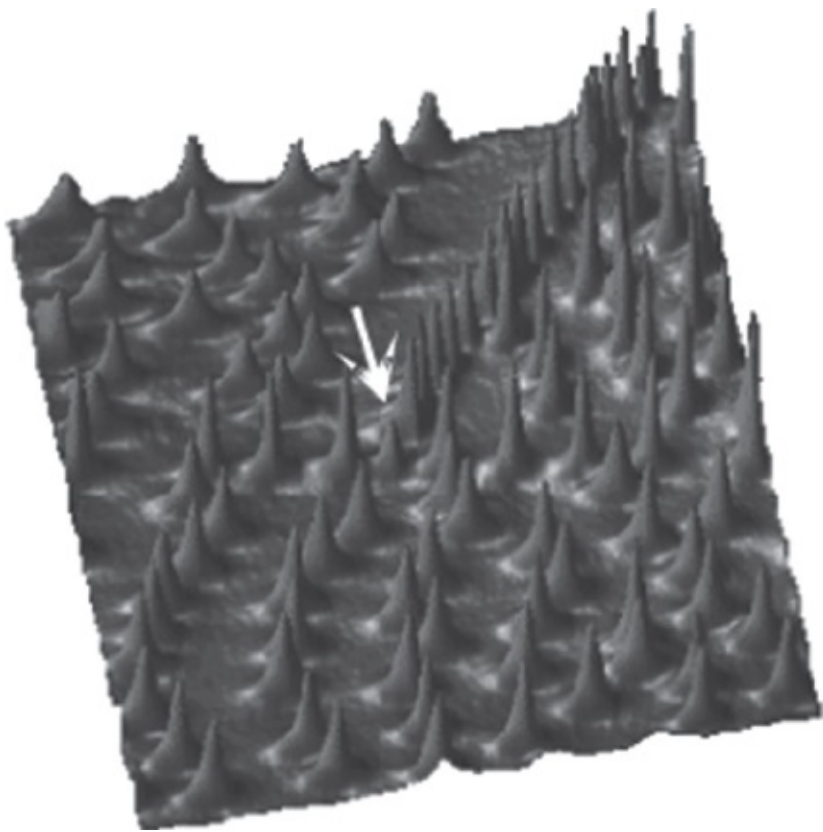


**Figure 3.44** Imaging of the magnetic flux distribution in a  $\text{Bi}_2\text{Sr}_2\text{Ca}\text{Cu}_2\text{O}_8$  thin film deposited on a tricrystal as shown in [Figure 3.42](#). Applied magnetic field:  $0.37 \mu\text{T}$ . At the tricrystalline point, indicated by the arrow, a half-integer magnetic flux quantum has appeared [109]. Image section about  $1 \text{ mm} \times 0.7 \text{ mm}$ .

In this experiment a magnetic field of  $0.37 \mu\text{T}$  was applied perpendicular to the tricrystal for generating vortices within the film. [Figure 3.44](#) was obtained again using the SQUID. One can see many integer magnetic flux quanta penetrating the film. Some are located within the compact parts of the film and some within the grain boundaries. The half-integer magnetic flux quantum is located exactly at the tricrystalline point, which lies near the center of the imaged area. One clearly sees that it has only about half the height of the other flux quanta. Similar as for the  $\text{YBa}_2\text{Cu}_3\text{O}_7$  rings of [Figure 3.43](#), in the absence of a magnetic field all vortices disappear except for this one.

It is interesting that this effect can also be observed in polycrystalline cuprate samples. In this case, the grains are arbitrarily rotated relative to each other, and some  $\pi$  rings can be generated statistically. If these samples are cooled down in a weak magnetic field, the spontaneous vortices are preferentially oriented along the magnetic field direction. As a result, one observes a paramagnetic signal instead of the diamagnetic Meissner signal. This effect is referred to as the ***paramagnetic Meissner effect*** or also as the ***Wohlleben effect*** [110, 111].

Thin-film grain-boundary junctions represent another “natural” system, where  $\pi$ -Josephson junctions play a role. In these junctions, the two halves of the bicrystal are rotated relative to each other. The actual grain-boundary meanders about the grain boundary of the substrate. In the extreme case of a bicrystal with its two halves rotated relative to each other by  $45^\circ$ , then

regions with the same and with the opposite sign of the pair wave function confront each other statistically. The magnetic field dependence of the critical current of such a grain boundary is highly complex. For example, the largest value of the critical current can only be found at high magnetic fields [112].

Subsequently, the  $d_{x^2-y^2}$  symmetry of the pair wave function was demonstrated by various groups using different experimental geometries. An example is shown in [Figure 3.45](#) [113]. In this case, the substrate consists of four sections. In the figure, the grain boundary running vertically has a misorientation angle as small as possible and appears incidentally because of the fabrication process. The two other grain boundaries are crucial. They are arranged in such a way that a  $\pi$ -Josephson junction later develops across *one* of the grain boundaries. Hence, in contrast to the interferometer geometry shown in [Figure 3.40](#), this geometry completely consists of a cuprate film. Furthermore, we note that the dimensions of both Josephson junctions are comparable to the diameter of the hole. This large width served to avoid the possibility that vortices trapped within the interferometer legs would simulate the effect of the  $\pi$ -Josephson junctions. In this case, in addition to the periodic oscillations (Eq. (24)), one can also observe the diffraction pattern of both Josephson junctions as an envelope, the symmetry or asymmetry of which immediately yields information on any trapped flux [114].

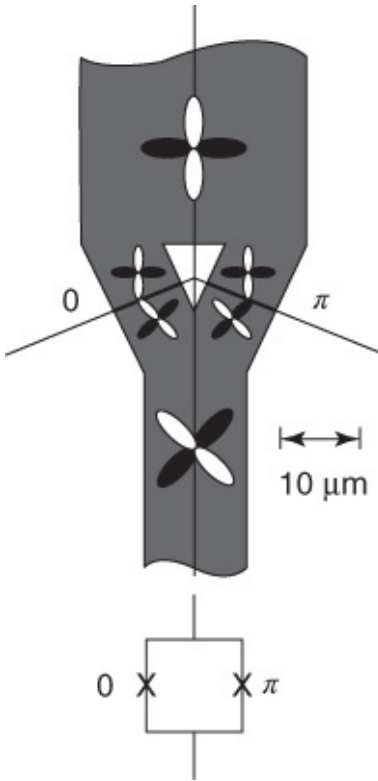


[Figure 3.45](#) Grain-boundary interferometer geometry for demonstrating the  $d_{x^2-y^2}$  symmetry in high-temperature superconductors [113].

In [Figure 3.46](#) we show measured data for  $\text{YBa}_2\text{Cu}_3\text{O}_7$ . We clearly see the highly symmetric envelope due to the two Josephson junctions ([Figure 3.46a](#)). For zero magnetic field the critical current passes through a minimum, indicating the presence of a  $\pi$ -Josephson junction ([Figure 3.46b](#)). However, if we fabricate a thin film in the same way only across a single grain

boundary, then the  $\pi$ -Josephson junction does not appear, and the critical current should display a maximum at zero magnetic field. This has also been observed. The corresponding data have already been shown in [Figure 1.30](#). Similar results could also be obtained for  $\text{Bi}_2\text{Sr}_2\text{CaCu}_2\text{O}_8$  [115], and also for the *electron-doped* compound  $(\text{La},\text{Ce})\text{CuO}_4$  [116].

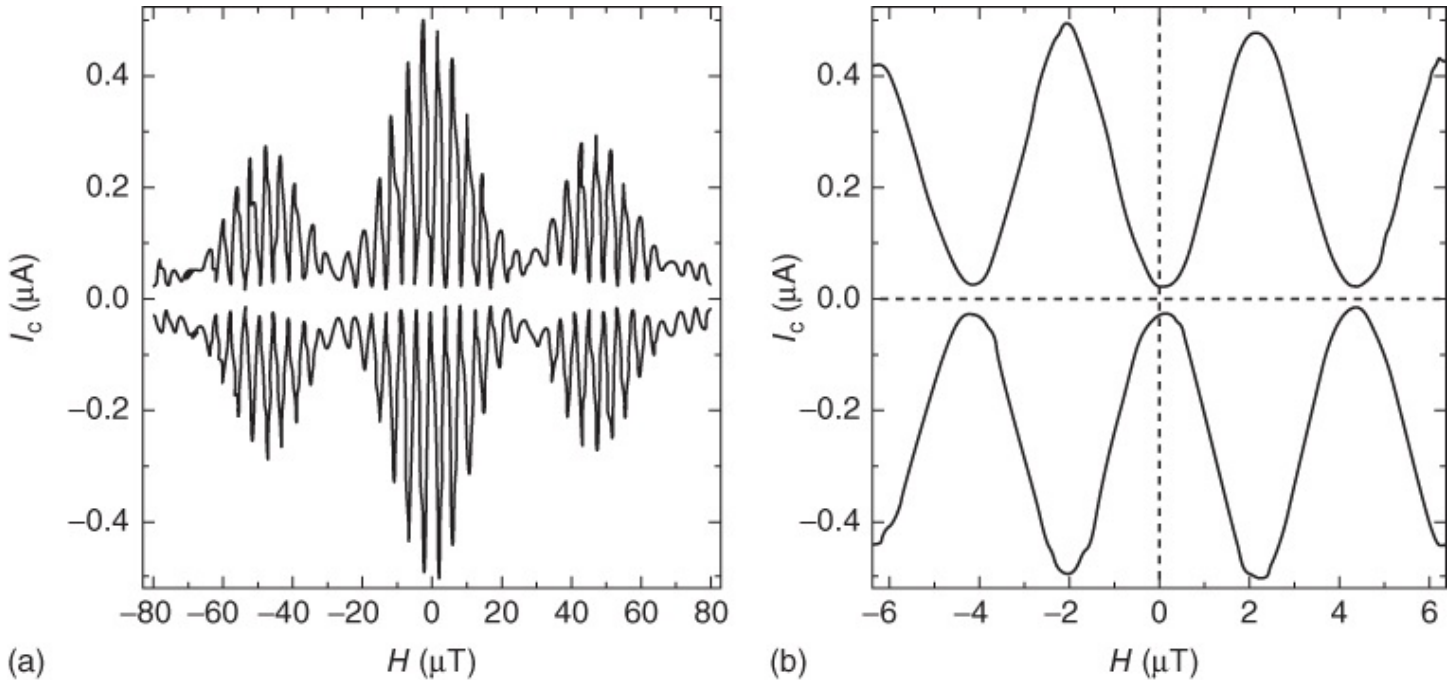


[Figure 3.46](#) Maximum supercurrent across the Josephson junctions denoted by “0” and “ $\pi$ ” in [Figure 3.45](#) plotted versus the magnetic field. Graph (b) is an enlargement of the low-field region of graph (a). The negative values of  $I_c$  were measured for a negative transport current across the interferometer [113].

(© 2000 AIP.)

In the meantime, one has gone even beyond experiments only demonstrating the  $d_{x^2-y^2}$  symmetry of the pair wave function. For example, one can fabricate a large number of  $\text{YBa}_2\text{Cu}_3\text{O}_7/\text{Nb}$  corner junctions on single-crystalline  $\text{SrTiO}_3$  substrates. In this case, the Josephson junctions are realized at ramps etched into the substrate [117]. Here the  $\pi$ -Josephson junctions can appear either at a zigzag line within a *single* junction [118], or they can also be distributed over the total substrate [119]. For example, such geometries can serve for studying the interactions between the half-integer magnetic flux quanta.

At the end of this section, we want to ask if the pair wave function has  $d_{x^2-y^2}$  symmetry in all cuprates, or if also other symmetries or at least admixtures of other symmetries may be possible.<sup>35</sup>

In the case of the electron-doped cuprates, various measurements indicate that at least within part of the doping phase diagram the s-wave symmetry could be realized [120], and that perhaps a transition between the s and the  $d_{x^2-y^2}$  symmetry happens. However, in general, a “pure”  $d_{x^2-y^2}$  state appears to prevail, perhaps with small admixtures of other symmetries. On the other hand, even very small “subdominant” components are interesting, since they can

provide further information on the nature of Cooper pairing in high-temperature superconductors.

Experiments in which a conventional superconductor (for instance, Pb or Nb) was in contact with a high-temperature superconductor in such a way that the Josephson currents were flowing perpendicular to the CuO<sub>2</sub> planes (*c*-axis junction) have indicated a small s component. In the case of a pure d<sub>x<sup>2</sup>-y<sup>2</sup></sub> symmetry of the pair wave function of the high-temperature superconductor, the contributions to the supercurrent, half of which are positive and half of which are negative, compensate each other. Hence, no overall Josephson current can appear. However, exactly such a finite Josephson current was found for YBa<sub>2</sub>Cu<sub>3</sub>O<sub>7</sub> [121], for Bi<sub>2</sub>Sr<sub>2</sub>CaCu<sub>2</sub>O<sub>8</sub> [122], and for the electron-doped cuprate (Nd,Ce)CuO<sub>4</sub> [123]. However, the critical current was very small. Its homogeneity could be demonstrated by the observation of a very clean Fraunhofer pattern. An example is shown in [Figure 3.47](#). For all three materials, quantitative analyses of the data indicated that already an s-wave component below 1% is sufficient to explain the results. We conclude that the s component is very small, but it exists.

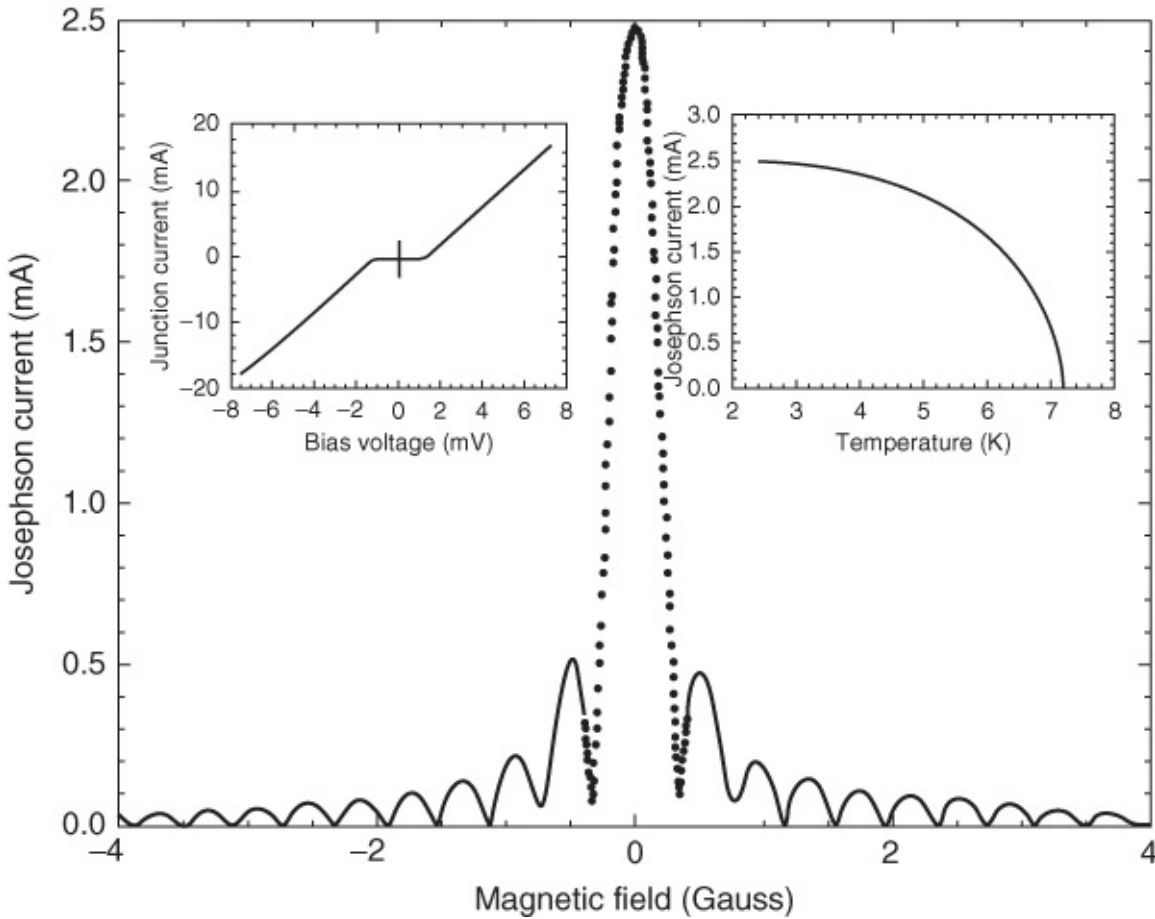


[Figure 3.47](#) Josephson junction between a YBa<sub>2</sub>Cu<sub>3</sub>O<sub>7</sub> single crystal and Pb with the current flow *perpendicular* to the CuO<sub>2</sub> planes. The observed supercurrent indicates that the pair wave function must contain a small s component. Main figure: Maximum supercurrent plotted versus the magnetic field. Inset on left: Current–voltage characteristic. Inset on right: Josephson current plotted versus the temperature. (From [102].) (1G = 10<sup>-4</sup> T).

In summary, we can say that the cuprates are perhaps the best-studied superconductors with unconventional Cooper pairing. There are many indications that the interactions between the electrons themselves lead to the Cooper pairing. However, the microscopic mechanism is not yet unequivocally identified. This is one of the remaining great challenges, if we want to understand why in this class of materials transition temperatures of 100 K and above are reached.

### 3.2.3 Heavy Fermions, Ruthenates, and Other Unconventional Superconductors

Up to now, the symmetry of the pair wave function has not been studied with such an intensity in any other superconductor as in the cuprates. However, clear indications of unconventional superconductivity have also been found in a number of other compounds. Mostly these hints were based on the observation of the signatures of locations with zero value of the energy-gap function  $\Delta_0$ .

The heavy-fermion superconductors represent a class of materials for which unconventional Cooper pairing was already discussed long before the cuprates. As mentioned in [Section 2.6](#), depending on the material, highly different symmetries of the pair wave functions are observed. We will discuss two substances in more detail, namely the extremely well-studied  $\text{UPt}_3$ , having a transition temperature of 0.5 K and  $\text{UPd}_2\text{Al}_3$ , which is superconducting below 2 K.

In the heavy fermions, the large value of the effective mass of the charge carriers results from the interaction between the electrons and localized magnetic moments, which in the case of  $\text{UPt}_3$  originate from the 5f orbitals of uranium. Hence, in these compounds magnetic interactions are essential for superconductivity, independent of how the actual pairing of the “heavy” electrons is accomplished.

In the case of  $\text{UPt}_3$ , measurements of the specific heat and also of other quantities have shown quickly that the energy-gap function must have locations with zero value. The observation of anomalies in the temperature dependence of the specific heat, of the upper critical field, or of the ultrasound absorption was even more interesting. It clearly showed that, depending on the temperature, the applied magnetic field, or the pressure, *different* superconducting pair states are developed in  $\text{UPt}_3$ . Up to then, a similar property was known only for superfluid  $^3\text{He}$ . The three phases of  $\text{UPt}_3$  are denoted as A, B, and C phase. The A and B phases can develop a Meissner state and a vortex state. However, the C phase represents a pure vortex phase, which can only be observed in external magnetic fields (see [Figure 3.48a](#)). Hence, there are a total of five superconducting phases.

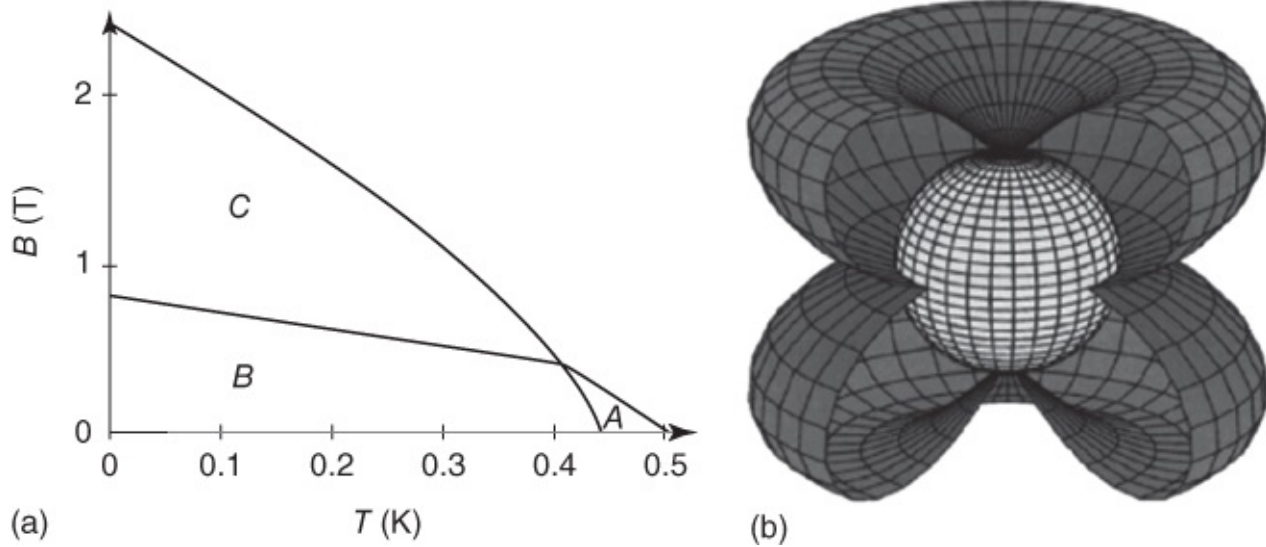


**Figure 3.48** (a) The three phases of  $\text{UPt}_3$  in a magnetic field-temperature diagram. (b) One of the discussed energy-gap functions of the B phase, plotted on a spherical Fermi surface. However, the actual Fermi surface of  $\text{UPt}_3$  is much more complicated.

(From [124].)

There exist several different phenomenological models of the structure of the A, B, and C phases. One starts with pair wave functions  $\Psi_0(\mathbf{k})$  with different symmetries, which are consistent with the hexagonal crystal structure of  $\text{UPt}_3$ . Then one constructs combinations of these, which explain the experiments as far as possible. So in the A phase,  $\Psi_0$  could be proportional to  $k_z k_x$ . On a sphere in  $\mathbf{k}$ -space, this state has zeros on the “equator”  $k_z = 0$  and at the “longitude”  $k_x = 0$ . In the C phase,  $\Psi_0$  could be proportional to  $k_z k_y$ , and the B phase could be a complex mixture  $\Psi_0 \propto k_z(k_x \pm ik_y)$  of these two pair states. The absolute value of this function (or of the energy-gap function  $\Psi_0(\mathbf{k})$ ) is shown in Figure 3.48b. Apparently, zeros appear as points at the poles (i.e., for  $k_z = 0$ ) and a zero line at the equator (i.e., for  $k_x = k_y = 0$ ).

In the case we just have discussed,  $\Psi_0(\mathbf{k})$  has even parity, that is, we have  $\Psi_0(\mathbf{k}) = \Psi_0(-\mathbf{k})$ . Correspondingly, we can also construct two-component states with odd parity, that is, with  $\Psi_0(\mathbf{k}) = -\Psi_0(-\mathbf{k})$ , which differ again in the location of the zeros. A more detailed discussion of the properties of  $\text{UPt}_3$  would exceed the aim of this book. Therefore, we refer to the review articles [124, 125].

The second heavy-fermion superconductor that we want to discuss in some detail is  $\text{UPd}_2\text{Al}_3$ . The pair wave function has even parity. For this superconductor, the nature of the pair interaction could be reasonably clarified.

The fact that for the heavy-fermion superconductors the electron–phonon interaction is not very effective as the pairing mechanism results from the large effective mass ( $70m_e$ ) of the charge carriers. In contrast to the conventional superconductors, such a heavy electron cannot escape

fast enough from a location where it has caused a lattice distortion in order to reduce the Coulomb repulsion of its partner. On the other hand, in  $\text{UPd}_2\text{Al}_3$  there exist so-called magnetic excitons, which can propagate through the crystal analogously to the phonons. They represent bosonic excitations of the 5f electrons of uranium. These excitations can interact with the “heavy” conduction electrons and in the end affect Cooper pairing.

The proof of this unconventional pairing mechanism is quite similar as for the conventional superconductors by means of a combination of tunneling spectroscopy and neutron diffraction [126]. First, a tunnel junction between  $\text{UPd}_2\text{Al}_3$  and Pb was fabricated, and its tunneling conductivity was measured. Then a magnetic field of 0.3 T was applied in order to suppress the superconductivity of Pb. Above the maximum energy gap of the  $\text{UPd}_2\text{Al}_3$ , a characteristic fine structure was observed in the measurements, which is shown in [Figure 3.49](#). This fine structure could indicate the exchange boson.

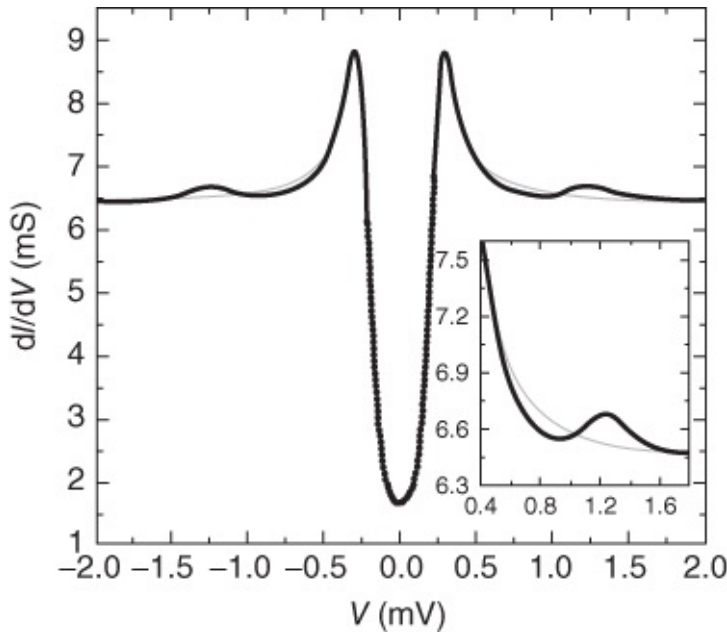


[Figure 3.49](#) Electrical conductivity of a tunnel junction between  $\text{UPd}_2\text{Al}_3$  and Pb with  $\text{AlO}_x$  as the tunneling barrier ( $T = 0.3$  K,  $B = 0.3$  T). The thinner gray line shows a theoretical fit using  $\Delta_{\max} = 235$   $\mu\text{eV}$ . The fit takes into account the finite lifetime of the quasiparticles. However, it does not contain structures due to the exchange boson [127].

(© 1999 Nature.)

A possible candidate for such a boson was identified in neutron diffraction experiments. In this case, at low temperatures, the magnetic excitons appear as characteristic excitations. [Figure 3.50](#) shows the measured spectra of the neutron intensity as a function of the energy transfer between the neutrons and  $\text{UPd}_2\text{Al}_3$ . At energies of about 1.4 meV we see an additional small maximum, which can be associated with the excitation of the exciton by the neutrons. Based on the dispersion  $\omega_E(\mathbf{q})$  of the magnetic excitons determined from these measurements, an effective potential of the pair interaction of the electrons can be formulated, and from this the tunneling density of states can be calculated. As shown in [Figure 3.51](#), the agreement with the

measured spectra is excellent. So everything strongly suggests that in  $\text{UPd}_2\text{Al}_3$  the Cooper pairing is due to the exchange of magnetic excitons.

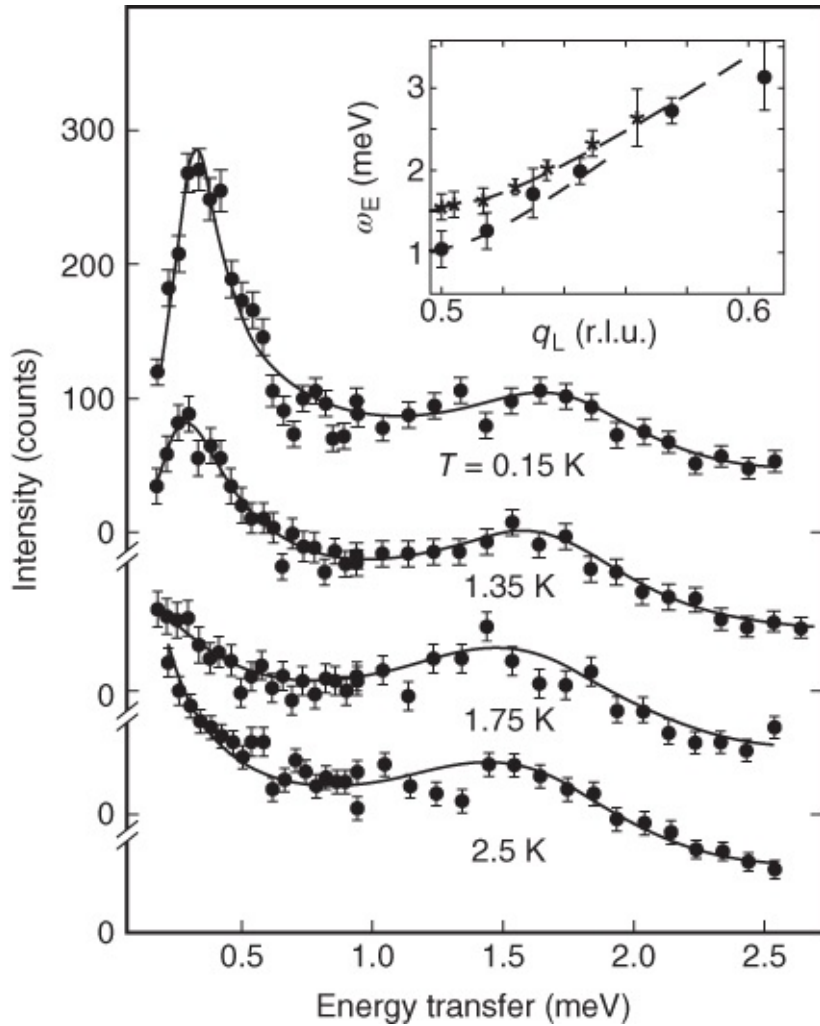


**Figure 3.50** Spectra of the neutron intensity of inelastic neutron scattering as a function of the energy transfer between the neutrons and  $\text{UPd}_2\text{Al}_3$  for different temperatures. The magnetic exciton appears as a peak at about 1.4 meV. The inset shows the resulting dependence of the frequency of the magnetic exciton upon the wave vector for  $T = 2.5 \text{ K}$  (x) and  $T = 0.15 \text{ K}$  (•) [126].

(© 2001 Nature.)

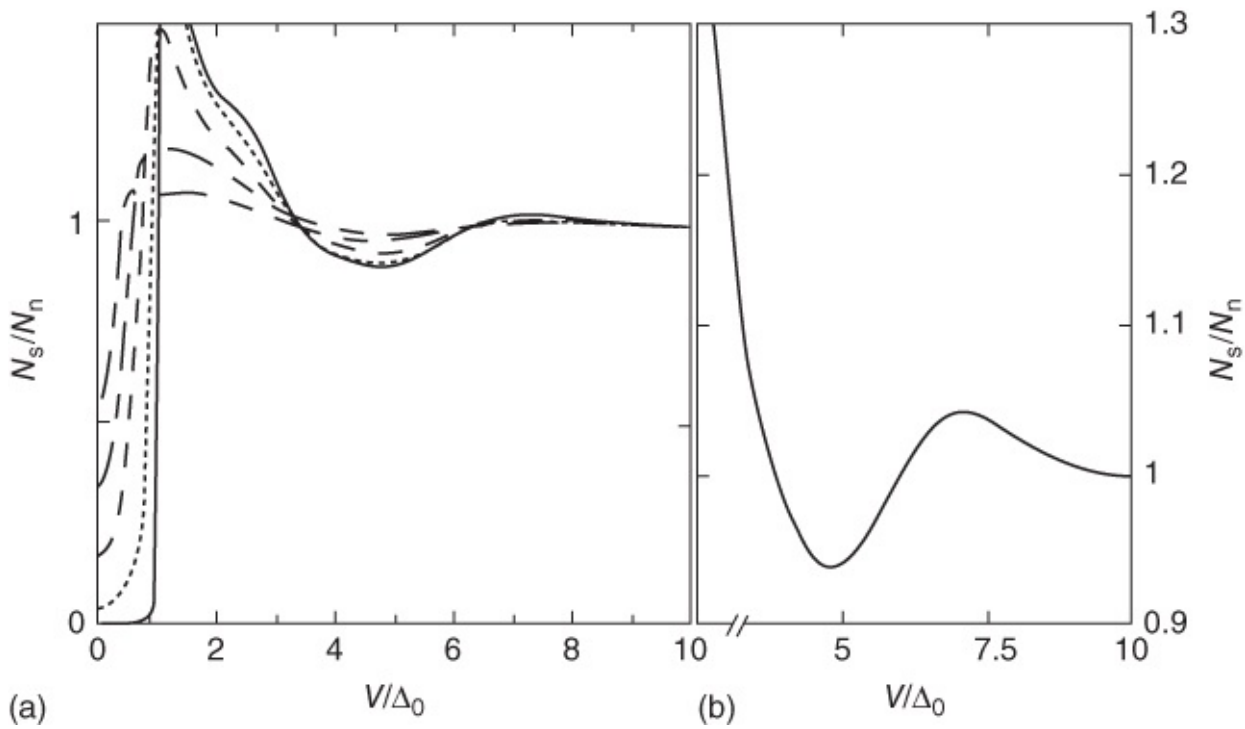


**Figure 3.51** (a) Calculated density of states of  $\text{UPd}_2\text{Al}_3$  taking into account the magnetic exciton for different temperatures. (b) An enlarged section, in which one can see the structure caused by the exciton [126].

(© 2001 Nature.)

As the third example of an unconventional superconductor, we want to discuss in some detail the strontium ruthenate  $\text{Sr}_2\text{RuO}_4$ . We have already discussed some of its properties in [Section 2.8.2](#). In [Figure 3.31b](#) we showed measurements of the Knight shift in this material, which strongly indicate that  $\text{Sr}_2\text{RuO}_4$  is a spin-triplet superconductor.<sup>36</sup> Practically,  $\text{Sr}_2\text{RuO}_4$  has the same crystal structure as the cuprate  $(\text{La},\text{Ba})\text{CuO}_4$ , which is a spin-singlet d-wave superconductor.

What is the origin of the drastic difference between the two materials? In the cuprate, the  $3\text{d}_{x^2-y^2}$  orbital of copper is crucial. We have seen that the cuprates represent antiferromagnetic insulators if we have one electron within this orbital. One has to dope this starting substance in order to obtain metallic conductivity or superconductivity. In  $\text{Sr}_2\text{RuO}_4$  we must take into account in particular the 4d orbitals. In this case ruthenium exists in the form of a  $\text{Ru}^{4+}$  ion, which has in addition four electrons in the 4d orbitals. Because of the interaction with the crystal field, the five different d orbitals are split up energetically. One obtains a subshell consisting of the two orbitals  $\text{d}_{x^2-y^2}$  or  $\text{d}_{3z^2-r^2}$ , and another one composed of the three orbitals  $\text{d}_{xy}$ ,  $\text{d}_{yz}$ , and  $\text{d}_{zx}$ , which is energetically more favorable. The conduction band of  $\text{Sr}_2\text{RuO}_4$  is formed from this subshell. Even the stoichiometric, undoped compound is electrically conducting, and below about 1.5 K it becomes superconducting. On the other hand, we know that compounds very similar to  $\text{Sr}_2\text{RuO}_4$  (for example,  $\text{SrRuO}_3$ ) are ferromagnets. Therefore, it appears that in the ruthenates the parallel spin orientation of the electrons is more favorable,

and eventually could lead to spin-triplet superconductivity. However, for  $\text{Sr}_2\text{RuO}_4$ , as well as for most other unconventional superconductors, the microscopic pairing mechanism still remains unclear.

How about the pair wave function of  $\text{Sr}_2\text{RuO}_4$ ? The most likely angular momentum state of the pair is the p state ( $L = 1\hbar$ ). In this case, we must describe the superconducting state in terms of a vector, the so-called **d**-vector, instead of a single-component function  $\Psi_0(\mathbf{k})$ . A likely form of this vector is  $\mathbf{d}(\mathbf{k}) = \hat{\mathbf{z}}(k_x + ik_y)$  or  $\mathbf{d}(\mathbf{k}) = \hat{\mathbf{z}}(p_x + ip_y)$ , if we use the notation adopted for the cuprates. The **d**-vector points along the  $\hat{\mathbf{z}}$ -direction, that is, along the crystallographic *c*-axis, and its value is complex. For this state, the z-component of the angular momentum of the Cooper pairs is  $\pm\hbar$ , and the spin of the Cooper pairs is located within the  $(x,y)$  plane. Hence, in some sense, the Cooper pairs themselves form a ferromagnetic state. We see immediately that in this state the time-reversal symmetry is broken. For time reversal, the orientation of a magnetic field must reverse. However, exactly this does not happen in a magnetically ordered state.

We would think that this ferromagnetism cannot easily be overlooked. However, we must also note the Meissner–Ochsenfeld effect. Electric shielding currents are generated immediately, which prevent homogeneous magnetization of the samples. However, at the locations where the homogeneity is interrupted, say, at impurities or at the surface, a weak magnetic field appears. Hence, in the interior of the sample there exist local fields, which vary about the average value zero. These local fields can be detected by muon-spin resonance (see [Section 1.3](#)).

Such measurements indicated that in  $\text{Sr}_2\text{RuO}_4$  local fields below 0.1 mT are, indeed, generated [128]. This represents strong evidence for the breaking of the time-reversal symmetry. A similar phenomenon has also been observed in the B phase of  $\text{UPt}_3$ , where a pair state with a complex value also exists, which breaks the time-reversal symmetry [129].

The spin-triplet superconductivity in  $\text{Sr}_2\text{RuO}_4$  has a number of unusual consequences, as one would expect. For example, there exists a vortex state, in which the vortices form a square lattice instead of a triangular lattice, if the magnetic field is oriented along the *c*-axis [130].

A second phenomenon is the appearance of a second superconducting phase with a transition temperature of about 3 K. It is observed in the form of an additional drop in the electrical resistance, occurring already above the actual superconducting transition at 1.5 K in samples that contain small inclusions of normal conducting ruthenium. Most likely this second superconducting phase is nucleated at the interfaces between the Ru inclusions and the  $\text{Sr}_2\text{RuO}_4$ . At these locations, the  $p_x$  and  $p_y$  states are no longer equivalent, and the rotational symmetry within the  $(x,y)$  plane is broken. As a consequence, a new state develops, in which the “clubs” of the p state orient themselves parallel to the interface [131]. This effect is shown schematically in [Figure 3.52a](#). This new state does not break the time-reversal symmetry anymore. Hence, it represents a second superconducting phase, in which the properties including the transition temperature differ from those in the interior of  $\text{Sr}_2\text{RuO}_4$ .

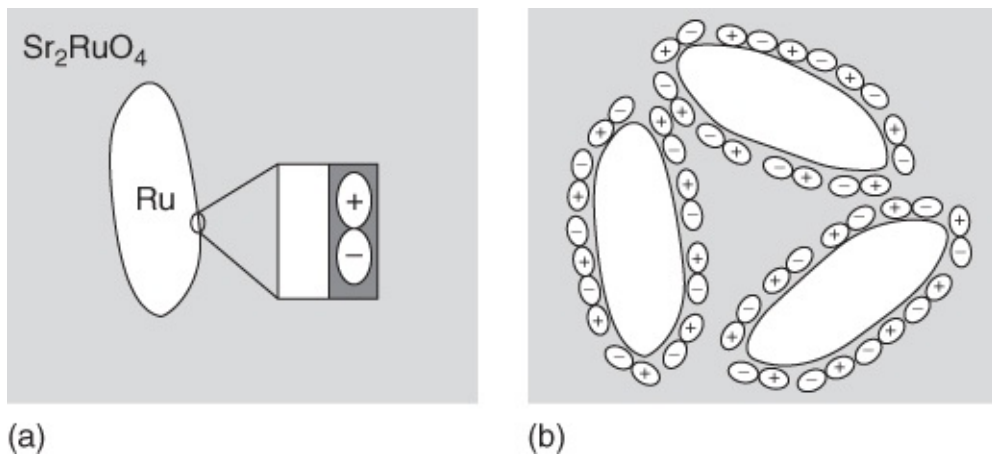


**Figure 3.52** (a) Structure of the 3K phase of  $\text{Sr}_2\text{RuO}_4$  developing at the interface with the Ru inclusions. (b) Appearance of phase jumps of  $\pi$  between three such inclusions.

(From [131]).

If several Ru inclusions are located close to each other, as shown in [Figure 3.52b](#), an interesting effect is expected. As long as the grains are independent of each other, the phases  $\phi_k$  of the pair wave functions also remain independent. However, if supercurrents can flow between the grains, the phases  $\phi_k$  will become adjusted to each other as in a Josephson junction.

If the superconducting state at the interface had s-wave symmetry, there would be no problem. However, because of the sign change of the p orbitals, the 3 K phase becomes polarized around the inclusion. In [Figure 3.52b](#) this is shown schematically by the many indicated p orbitals. If we replaced each orbital by a vector pointing in the "+" direction, these vectors would run counterclockwise around the grains in the figure [131]. If two inclusions were to get close to each other, for the same polarization of the p orbitals, two p orbitals with opposite sign would be placed next to each other. In this case the situation is very similar to that of the  $\pi$ -Josephson junctions discussed in the last section. Only for two inclusions can we shift the phase of the pair wave function of one of the two grains by  $\pi$ , and thereby remove the sign change at the contact point. For three grains this is not possible anymore. Then we have a "frustrated" situation analogous to that of the tricrystal geometry of [Figure 3.42](#). Spontaneous shielding currents develop between the three grains. By extending this to many grains, we obtain a network, which can act like a paramagnet in weak applied magnetic fields because of the spontaneous shielding currents. This effect is analogous to the Wohlleben effect, which has been observed in polycrystalline cuprate samples (see [Section 3.2.2](#)). Unconventional superconductivity is suggested also in additional compounds, such as the organic superconductors. For example, similar to the cuprates, in the layered structure  $\kappa$ -(BEDT-TTF)<sub>2</sub>Cu(NCS)<sub>2</sub> (BEDT-TTF: bis(ethylenedithia)tetra-thiafulvalene) the d-symmetry appears to be realized [132], and in the case of (TMTSF)<sub>2</sub>PF<sub>6</sub> (TMTSF: tetramethyltetraselenofulvalene) Knight-shift measurements indicate spin-triplet superconductivity [133].

### 3.2.4 FFLO-State and Multiband Superconductivity

Now we have reached nearly the end of our discussion of Cooper pairing in unconventional superconductors. Concluding this subject, we wish to take up two interesting forms of Cooper pairing, the so-called Fulde–Ferrell–Larkin–Ovchinnikov state (FFLO state, sometimes also referred to as ***LOFF state***) and multiband superconductivity.

We start with the FFLO state. Based on the BCS theory, Fulde and Ferrell [134] and independently Larkin and Ovchinnikov [135] had dealt with the question, how Cooper pairing might look in the presence of local magnetic moments in the superconductor. In this case, the magnetic moments are assumed to be ordered ferromagnetically. Now the conduction electrons and, hence, also the Cooper pairs, experience the so-called exchange interaction, which in general leads to magnetic order. This effect has a quantum mechanical origin, connected with the symmetry of the wave function of the electrons. Details can be found in textbooks on quantum mechanics or solid state physics. Here it is important that the exchange interaction contributes the amount  $E_{\text{ex}} = \mu B_{\text{ex}}$  to the energy of the electrons.  $\mu$  is the magnetic moment of the electron and  $B_{\text{ex}}$  is the so-called exchange field (which is not a real field). The latter can be as large as many 100 T. In this field, one of the electrons of the Cooper pairs experiences a reduction in energy by the amount  $E_{\text{ex}}$ . The other electron increases its energy by  $E_{\text{ex}}$ . Because of the exchange interaction, the electrons tend to orient themselves parallel to each other. On the other hand, in (conventional) superconductors the spins of both electrons are oriented antiparallel to each other. In this conflicting situation, Fulde, Ferrell, Larkin, and Ovchinnikov found stable solutions, where the Cooper pairs are not paired any longer symmetrically about the wave vector 0, but instead about the wave vector  $\mathbf{Q}$ . The condensate wave function oscillates spatially:  $\Psi \sim \cos \mathbf{Qr}$ . In the simplest case, the magnitude of the wave vector  $\mathbf{Q}$  is about equal to the coherence length. We note, that the density of the Cooper pairs, given by the squared absolute value of  $\Psi$  and, hence, proportional to  $\cos^2 \mathbf{Qr}$ , shows zeros. One obtains a lamellar sequence of areas with high and low or even vanishing Cooper pair density.

Upto now, the FFLO state has not been found in the theoretically predicted form. However, there exist related forms. We can consider superconductors in external magnetic fields near the upper critical field. Here, in most cases superconductivity breaks down by the fact, that stronger and stronger shielding currents are flowing around the vortex cores, and that eventually the superconductor assumes the normal state. Sometimes this mechanism is referred to as ***orbital effect***. We will come back to it in [Section 4.7](#). The FFLO state plays a role, if the orientation of the electron spins parallel to each other limits superconductivity. Analogous to the case considered by Fulde, Ferrell, Larkin, and Ovchinnikov, the electrons oriented parallel to the external field  $\mathbf{B}$  lower their energy by the amount  $\mu B$ , and the energy of the electrons oriented antiparallel is increased by this amount (“Zeeman splitting”). Above a certain maximum field, the parallel orientation of the electron spins wins, and superconductivity either breaks down, or assumes FFLO-like states. It appears, that this is exactly what has been found in the case of the heavy-fermion superconductor CeCoIn<sub>5</sub>, as well as of the organic superconductor  $\kappa$ -(BEDT-TTF)<sub>2</sub>Cu(NCS)<sub>2</sub> [136, 137]. In this case in addition to the upper critical field, also the specific heat was measured and analyzed. We will see, if in the future a

direct *image* of the FFLO state can be achieved.

Spatially oscillating pair wave functions play a role also at the interfaces between superconductors and ferromagnets. This will be discussed further in [Chapter 6](#).

Multiband superconductivity also starts from conventional Cooper pairing. Up to now in our discussions often we treated the conduction electrons in terms of more or less free particles, and we used concepts such as Fermi gas or Fermi sphere. Within this approximation one really does not take into account the crystal structure. Apparently, we can expect deviations, if the de Broglie wave length at least of some electrons is comparable to or smaller than the dimensions of the crystallographic unit cells. In this case one obtains energy bands for the conduction electrons, as shown in [Figure 1.5](#). Then the Fermi sphere can develop into a complex object composed of different parts. In some cases the electrons can behave as if they would carry a positive charge (referred to as **hole-like**). As an example we look at MgB<sub>2</sub> having an hexagonal crystal structure (see [Figure 2.4](#)). We can transfer crystal structures from regular space into **k**-space, and in the case of a hexagonal lattice we obtain again a hexagonal structure, indicated in [Figure 3.53](#), and which can be repeated periodically along all directions. In this structure all surfaces are shown, on which the energy of the conduction electrons is equal to the Fermi energy. In the center we see two tubes nested within each other. In this case, electrons contribute originating from the p<sub>x,y</sub>-orbitals of the boron atoms and showing hole-like behavior (“σ-band”). Practically, these electrons move exclusively within the plane of the boron atoms. The tubes in the center are surrounded by objects looking quite complex. If we repeat periodically the hexagonal cell shown in [Figure 3.53](#), these objects yield a tube-like three-dimensional network. Here, electrons contribute originating from the p<sub>z</sub>-orbitals of the boron. Partly they behave like “normal” electrons and partly like holes.

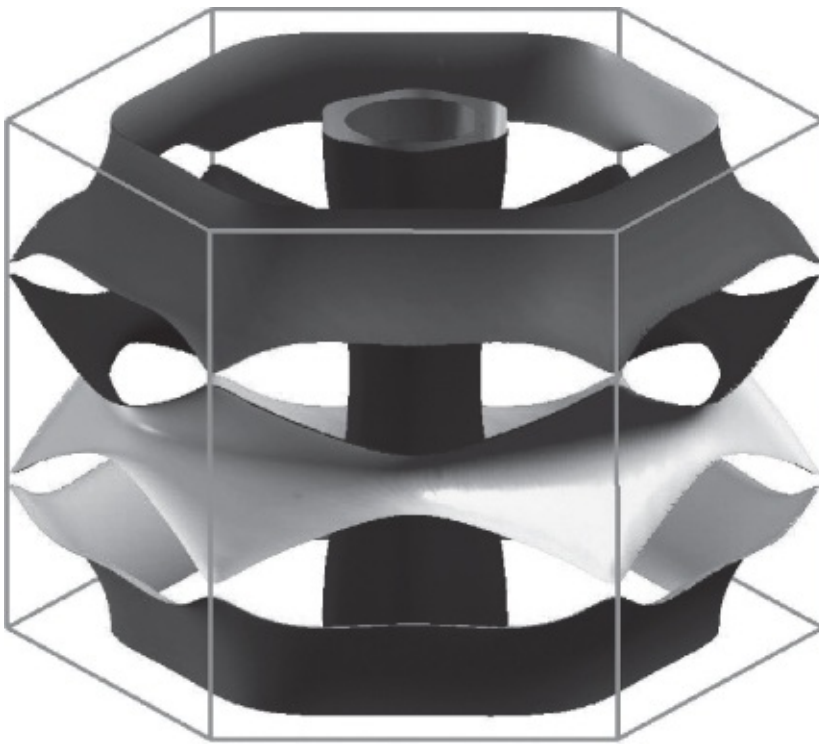


**Figure 3.53** Fermi surfaces of  $\text{MgB}_2$ . The method of calculation is described in [138].

(Courtesy by X. Quian, MIT.)

Many other metals also show similar or even more complex Fermi surfaces. So one could think that our previous discussion of the superconducting properties based on free electrons is much too simple. However, it turns out that the complex structure of the Fermi surfaces does not affect very much the properties of the superconducting state as long as the Cooper pairing on the corresponding Fermi surfaces happens about equally. Changes can be expected only, if in the case of conventional Cooper pairing, the electron–phonon interaction in different energy bands is very different.

“Two-band models” were discussed already since the 1950s. In 1980 two-band superconductivity was proposed in the case of  $\text{SrTiO}_3$  doped with niobium [40]. However, only in the case of  $\text{MgB}_2$ , a superconductor had been discovered, where two-band effects strongly showed up. So the charge carriers of the  $\sigma$ -band very strongly couple to certain phonons, forming strongly bound Cooper pairs. The pairs generated in the  $\pi$ -band are bound much weaker. As mentioned in [Section 3.1.3.2](#), correspondingly, for these two “kinds” of Cooper pairs, one finds very different energy gaps. Furthermore, the Cooper pairs arising from the  $\sigma$ -band show two-dimensional, whereas the pairs from the  $\pi$ -band show three-dimensional behavior.

This influences many characteristic quantities of superconductivity [139]. For example, with decreasing temperature the upper critical field increases more strongly than expected in the case of a one-band model. Also the anisotropy of  $B_{\text{C}2}$  with respect to different crystal directions, in the case of a one-band superconductor, is not strongly temperature dependent, whereas it is strong in a two-band superconductor. In the case of  $\text{MgB}_2$  near  $T_{\text{C}}$ , this anisotropy

is about 2, and with decreasing temperature it increases up to about 6. Also the structure of the cores of magnetic flux lines is more complicated, since near the core both subsystems are suppressed at different length scales. So the  $\pi$ -band shows a coherence length of 50 nm parallel to the layer structure, whereas the  $\sigma$ -band shows a value of about 13 nm.

Also in the case of the iron pnictides, two or more bands appear to contribute differently to superconductivity. However, in this class of materials Cooper pairing could be caused by magnetic interactions. In the case of the iron pnictides, the Fermi surfaces consist of different cylindrical objects associated with electron- and hole-like charge carriers. The experimental data suggest that s-wave Cooper pairing exists on each of these tubes. The condensate wave function appears to change its signature between neighboring cylinders. This is referred to as **s $\pm$ -symmetry**. Also in the case of this symmetry, under suitable conditions,  $\pi$ -Josephson junctions can be generated and half-integer flux quanta can be observed, analogous to the experiments discussed in [Section 3.2.2](#). This half-integer flux quantization has been experimentally demonstrated [140].

## References

1. W. Heisenberg: *Z. Naturforsch.* **2a**, 185 (1947).
2. H. Welker: *Z. Phys.* **114**, 525 (1939).
3. M. Born, K. C. Cheng: *Nature (London)* **161**, 968 and 1017 (1948).
4. H. Fröhlich: *Phys. Rev.* **79**, 845 (1950).
5. J. Bardeen: *Phys. Rev.* **80**, 567 (1950).
6. J. Bardeen, L. N. Cooper, J. R. Schrieffer: *Phys. Rev.* **108**, 1175 (1957).
7. L. N. Cooper: *Phys. Rev.* **104**, 1189 (1956).
8. R. P. Feynman: “*Feynman-Lectures on Physics*”, Vol. 3, p. 10-1 ff. Addison-Wesley Publishing Company (1965).
9. L. P. Gor'kov: *Sov. Phys.: JETP* **9**, 1364 (1960).
10. H. K. Onnes, W. Tuyt: *Commun. Leiden* **160b** (1922).
11. E. Justi: *Phys. Z.* **42**, 325 (1941).
12. E. Maxwell: *Phys. Rev.* **78**, 477 (1950).
13. C. A. Reynolds, B. Serin, W. H. Wright, L. B. Nesbitt: *Phys. Rev.* **78**, 487 (1950).
14. E. Maxwell: *Phys. Rev.* **86**, 235 (1952); B. Serin, C. A. Reynolds, C. Lohman: *Phys. Rev.* **86**, 162 (1952); J. M. Lock, A. B. Pippard, D. Shoenberg: *Proc. Cambridge Philos. Soc.* **47**, 811 (1951).

15. R. D. Parks: "Superconductivity", Marcel Dekker, New York, p. 126 (1969).
16. R. D. Fowler, J. D. G. Lindsay, R. W. White, H. H. Hill, B. T. Matthias: *Phys. Rev. Lett.* **19**, 892 (1967); W. E. Gardner, T. F. Smith: *Phys. Rev.* **154**, 309 (1967).
17. W. L. McMillan: *Phys. Rev.* **167**, 331 (1968).
18. O. Gunnarson: *Rev. Mod. Phys.* **69**, 575 (1997).
19. C. Buzea, T. Yamashita: *Supercond. Sci. Technol.* **14**, R115 (2001).
20. R. E. Glover III M. Tinkham: *Phys. Rev.* **108**, 243 (1957).
21. W. Meissner: "Handbuch der Experimentalphysik of Wien and Harms", Vol. XI, Part 2, Akademische Verlagsgesellschaft, Leipzig, p. 260 (1935).
22. P. L. Richards, M. Tinkham: *Phys. Rev.* **119**, 575 (1960).
23. R. D. Parks: "Superconductivity", Marcel Dekker, Inc., p. 14 and 16 (1969); D. H. Douglas Jr. L. M. Falicov: In: "Progress of Low Temperature Physics", Vol. 4, North-Holland, Amsterdam, p. 97 (1964)
24. D. F. Moore, R. B. Zubeck, J. M. Rowell, M. R. Beasley: *Phys. Rev. B* **20**, 2721 (1979); L. Y. L. Shen: *Phys. Rev. Lett.* **29**, 1082 (1972).
25. K. Komenov, T. Yamashita, Y. Onodera, *Phys. Lett. A* **28**, 335 (1968).
26. U. Poppe: *Physica B* **108**, 805 (1981); C. P. Umbach, L. E. Toth, E. D. Dahlberg, A. M. Goldman: *Physica B* **108**, 803 (1981).
27. U. Poppe, H. Wühl: *J. Low Temp. Phys.* **43**, 371 (1981).
28. T. Ekino, H. Fuji, M. Kosugi, Y. Zenitani, J. Akimitsu: *Phys. Rev. B* **53**, 5640 (1996).
29. B. P. Clayman, R. F. Frindt: *Solid State Commun.* **9**, 1881 (1971).
30. B. Batlogg, J. P. Remeika, R. C. Dynes, H. Barz, A. S. Cooper, J. Gano: In: "Superconductivity in d- and f-Band Metals" W. Buckel, W. Weber (eds.), Kernforschungszentrum Karlsruhe, p. 401 (1982).
31. F. Sharifi, A. Pargellis, R. C. Dynes, B. Miller, E. S. Hellman, J. Rosamilia, E. H. Hartford, Jr.: *Phys. Rev. B* **44**, 12521 (1993).
32. R. W. Morse, H. V. Bohm: *Phys. Rev.* **108**, 1094 (1957).
33. J. C. Fisher, I. Giaever: *J. Appl. Phys.* **32**, 172 (1961).
34. I. Giaever: *Phys. Rev. Lett.* **5**, 464 (1960).
35. I. Giaever, K. Megerle: *Phys. Rev.* **122**, 1101 (1961).

36. J. Sutton, P. Townsend: *Proc. LT* **8**, 182 (1963).
37. I. Giaever: *Proc. LT* **8**, 171 (1963).
38. A. Eichler, H. Wühl, B. Stritzker: *Solid State Commun.* **17**, 213 (1975).
39. J. M. Rowe, J. J. Rush, H. G. Smith, M. Mostoller, H. E. Flotow: *Phys. Rev. Lett.* **33**, 1297 (1974).
40. G. Binnig, A. Baratoff, H. E. Hoenig, J. G. Bednorz, *Phys. Rev. Lett.* **45**, 1352 (1980); M. Jourdan, N. Blümer, H. Adrian: *Eur. Phys. J. B* **33**, 25 (2003).
41. H. J. Choi, D. Roundy, H. Sun, M. L. Cohen, S. G. Louie: *Nature* **418**, 758 (2002).
42. E. A. Lynton, B. Serin, M. Zucker: *J. Phys. Chem. Solids* **3**, 165 (1957).
43. J. Hasse, K. Lüders: *Z. Phys.* **173**, 413 (1963).
44. W. Buckel, R. Hilsch: *Z. Phys.* **132**, 420 (1952).
45. W. Buckel: *Z. Phys.* **138**, 136 (1954).
46. J. Fortmann, W. Buckel: *Z. Phys.* **162**, 93 (1961).
47. W. Buckel, R. Hilsch: *Z. Phys.* **138**, 109 (1954).
48. H. Leitz, H.-J. Nowak, S. El-Dessouki, V. K. Srivastava, W. Buckel: *Z. Phys. B* **29**, 199 (1978).
49. F. Meunier, J. J. Hauser, J. P. Burger, E. Guyon, M. Hesse: *Phys. Lett.* **28 B**, 37 (1968); A. M. Lamouise, J. Chaumont, F. Meunier, H. Bernas: *J. Phys. Lett. (Orsay, Fr.)* **36**, L 271 (1975); A. M. Lamouise, J. Chaumont, F. Meunier, H. Bernas, F. Lalu: *J. Phys. Lett. (Orsay, Fr.)* **37**, L 287 (1976).
50. R. E. Glover III F. Baumann, S. Moser: “*Proceedings of the 12th International Conference on Low Temperature Physics*”, Academic Press, Kyoto, p. 337 (1970).
51. G. Bergmann: *Phys. Rev. B* **3**, 3797 (1971); *Phys. Rep.* **27 C**, 159 (1976); B. Keck, A. Schmid: *J. Low Temp. Phys.* **24**, 611 (1976).
52. H.-J. Güntherodt, H. Beck: *Top. Appl. Phys.* **46**, 1 (1981).
53. W. L. Johnston: *Top. Appl. Phys.* **46**, 191 (1981).
54. R. C. Zeller, R. O. Pohl: *Phys. Rev. B* **4**, 2029 (1971).
55. G. Kämpf, H. Selisky, W. Buckel: *Physica* **108 B**, 1263 (1981); H. von Löhneysen: *Phys. Rep.* **79**, 161 (1981).
56. B. T. Matthias, H. Suhl, E. Corenzwit: *Phys. Rev. Lett.* **1**, 92 (1958).

57. A. A. Abrikosov, L. P. Gor'kov: *Sov. Phys. JETP* **12**, 1243 (1961).
58. E. Wassermann: *Z. Phys.* **187**, 369 (1965).
59. N. Barth: *Z. Phys.* **148**, 646 (1957).
60. W. Buckel, M. Dietrich, G. Heim, J. Kessler: *Z. Phys.* **245**, 283 (1971).
61. W. Bauriedl, P. Ziemann, W. Buckel: *Phys. Rev. Lett.* **47**, 1163 (1981).
62. Kl. Schwidtal: *Z. Phys.* **158**, 563 (1960).
63. A. Schertel: *Phys. Verh.* **2**, 102 (1951).
64. G. Boato, G. Gallinaro, C. Rizutto: *Phys. Rev.* **148**, 353 (1966).
65. P. Ziemann: *Festkörperprobleme* **XXIII**, 93 (1983).
66. W. Opitz: *Z. Phys.* **141**, 263 (1955); A. W. Bjerkaas, D. M. Ginsberg, B. J. Mrstik: *Phys. Rev. B* **5**, 854 (1972).
67. A. Hofmann, W. Bauriedl, P. Ziemann: *Z. Phys. B* **46**, 117 (1982).
68. Kl. Schwidtal: *Z. Phys.* **169**, 564 (1962).
69. N. Falke, N. P. Jablonski, J. Kästner, E. Wassermann: *Z. Phys.* **220**, 6 (1969).
70. T. H. Geballe, B. T. Matthias, E. Corenzwit, G. W. Hull Jr.: *Phys. Rev. Lett.* **8**, 313 (1962).
71. E. Müller-Hartmann, J. Zittartz: *Phys. Rev. Lett.* **26**, 428 (1971).
72. K. Winzer: *Z. Phys.* **265**, 139 (1973); G. Riblet, K. Winzer: *Solid State Commun.* **9**, 1663 (1971); M. B. Maple: *Appl. Phys.* **9**, 179 (1976).
73. K. Winzer: *Solid State Commun.* **24**, 551 (1977); R. Dreyer, T. Krug, K. Winzer: *J. Low Temp. Phys.* **48**, 111 (1982).
74. V. Ambegaokar, A. Griffin: *Phys. Rev.* **137 A**, 1151 (1965).
75. M. A. Woolf, F. Reif: *Phys. Rev.* **137 A**, 557 (1965).
76. J. Zittartz, A. Bringer, E. Müller-Hartmann: *Solid State Commun.* **10**, 513 (1972).
77. Y. J. Uemura, L. P. Lee, G. M. Luke, B. J. Sternlieb, W. D. Wu, J. H. Brewer, T. M. Riseman, C. L. Seaman, M. B. Maple, M. Ishikawa, D. G. Hinks, J. D. Jorgensen, G. Saito, H. Yamochi: *Phys. Rev. Lett.* **66**, 2665 (1991).
78. P. W. Anderson: *Science* **235**, 1196 (1987); P. W. Anderson, Z. Zhu: *Phys. Rev. Lett.* **60**, 132 (1988); S. Chakravarty, P. W. Anderson: *Phys. Rev. Lett.* **72**, 3859 (1994).
79. N. Bulut, D. J. Scalapino: *Phys. Rev. B* **45**, 2371 (1992).

80. K. Ishida, H. Mukuda, Y. Kitaoka, K. Asayama, Z. Q. Mao, Y. Mori, Y. Maeno: *Nature* **396**, 658 (1998).
81. M. Takigawa, P. C. Hammel, R. H. Heffner, Z. Fisk: *Phys. Rev. B* **39**, 7371 (1989); S. E. Barrett, D. J. Durand, C. H. Pennington, C. P. Slichter, T. A. Friedman, J. P. Rice, D. M. Ginsberg: *Phys. Rev. B* **41**, 6283 (1990).
82. M. Sigrist, D. Agterberg, T. M. Rice, M. E. Zhitomirsky: *Physica C* **282**, 214 (1997).
83. B. Batlogg, R. J. Cava, A. Jayaraman, R. B. van Dover, G. A. Kourouklis, S. Sunshine, D. W. Murphy, L. W. Rupp, H. S. Chen, A. White, K. T. Short, A. M. Muisce, E. A. Rietman: *Phys. Rev. Lett.* **58**, 2333 (1987).
84. B. Batlogg, G. Kourouklis, W. Weber, J. R. Cava, A. Jayaraman, A. E. White, K. T. Short, L. W. Rupp, E. A. Rietman: *Phys. Rev. Lett.* **59**, 912 (1987).
85. J. P. Franck, J. Jung, M. A.-K. Mohamed, S. Gygax, G. I. Sproule: *Phys. Rev. B* **44**, 5318 (1991).
86. J. P. Franck: In: “*Physical Properties of High- $T_c$  Superconductors IV*”, D. M. Ginsberg (ed.), World Scientific, Singapur, p. 189 (1994).
87. T. Dahm: *Phys. Rev. B* **61**, 6381 (2000).
88. J. R. Thompson, D. K. Christen, S. T. Sekula, B. C. Sales, L. A. Boatner: *Phys. Rev. B* **36**, 836 (1987).
89. S. Uchida: *Physica C* **357**, 25 (2001).
90. J. Hubbard: *Proc. R. Soc. London, Ser. A* **243**, 336 (1957).
91. D. J. Scalapino: *Phys. Rep.* **250**, 329 (1995).
92. W. A. Hardy, D. A. Bonn, D. C. Morgan, R. Liang, K. Zhang: *Phys. Rev. Lett.* **70**, 3999 (1993); S. Kamal, R. Liang, A. Hosseini, D. A. Bonn, W. N. Hardy: *Phys. Rev. B* **58**, R8933 (1998).
93. J. W. Loram, K. A. Mirza, J. R. Cooper, W. Y. Liang, *Phys. Rev. Lett.* **71**, 1740 (1993).
94. K. A. Moler, D. J. Baar, J. S. Urbach, R. Liang, W. N. Hardy, A. Kapitulnik: *Phys. Rev. Lett.* **73**, 2744 (1994).
95. Ch. Renner, B. Revaz, J.-Y. Genoud, K. Kadowaki, Ø. Fischer: *Phys. Rev. Lett.* **80**, 149 (1998).
96. X. Z. Shen, D. S. Dessau, B. O. Wells, D. M. King, W. E. Spicer, A. J. Arko, D. Marshall, L. W. Lombardo, A. Kapitulnik, P. Diskinson, S. Doniach, J. DiCarlo, A. G. Loeser, C. H. Park: *Phys. Rev. Lett.* **70**, 1553 (1993).

97. Z. X. Shen, D. S. Dessau, *Phys. Rep.* **253**, 1 (1995); A. Damascelli, Z. Hussain, Z.-X. Shen: *Rev. Mod. Phys.* **75**, 473 (2003)
98. H. Ding, M. R. Norman, J. C. Campuzano, M. Randeria, A. F. Bellman, T. Yokoya, T. Takahashi, T. Mochiku, K. Kadowaki: *Phys. Rev. B* **54**, R9678 (1996).
99. T. Timusk, B. Statt: *Rep. Prog. Phys.* **62**, 61 (1999).
100. J. M. Harris, Z.-X. Shen, P. J. White, D. S. Marshall, M. C. Schabel, J. N. Eckstein, I. Bozović: *Phys. Rev. B* **54**, R15665 (1996).
101. M. J. Lawler, K. Fujita, J. Lee, A. R. Schmidt, Y. Kohsaka, C. K. Kim, H. Eisaki, S. Uchida, J. C. Davis, J. P. Sethna, E.-A. Kim: *Nature* **466**, 347 (2010)
102. D. J. Van Harlingen: *Rev. Mod. Phys.* **67**, 515 (1995).
103. C. C. Tsuei, J. R. Kirtley: *Rev. Mod. Phys.* **72**, 969 (2000).
104. V. B. Geshkenbein, A. I. Larkin, A. Barone: *Phys. Rev. B* **36**, 235 (1987).
105. D. A. Wollman, D. J. Van Harlingen, W. C. Lee, D. M. Ginsberg, A. J. Leggett: *Phys. Rev. Lett.* **71**, 2134 (1993).
106. D. A. Wollman, D. J. Van Harlingen, J. Giapintzakis, D. M. Ginsberg: *Phys. Rev. Lett.* **74**, 797 (1995).
107. R. A. Klemm: *Phys. Rev. Lett.* **73**, 1871 (1994); D. A. Wollman, D. J. Van Harlingen, A. J. Leggett: *Phys. Rev. Lett.* **73**, 1872 (1994).
108. L. N. Bulaevskii, V. V. Kuzii, A. A. Sobyanin: *JETP Lett.* **25**, 290 (1977); V. B. Geshkenbein, A. I. Larkin: *JETP Lett.* **43**, 395 (1986).
109. J. R. Kirtley, C. C. Tsuei, H. Raffy, Z. Z. Li, A. Gupta, J. Z. Sun, S. Megtert: *Europhys. Lett.* **36**, 707 (1996).
110. W. Braunisch, N. Knauf, G. Bauer, A. Kock, A. Becker, B. Freitag, A. Grütz, V. Kataev, S. Neuhausen, B. Boden, D. Khomskii, D. Wohlleben, J. Bock, E. Preisler: *Phys. Rev. B* **48**, 4030 (1993).
111. M. Sigrist, T. M. Rice: *Rev. Mod. Phys.* **67**, 503 (1995).
112. H. Hilgenkamp, J. Mannhart: *Rev. Mod. Phys.* **74**, 485 (2002).
113. R. R. Schulz, B. Chesca, B. Goetz, C. W. Schneider, A. Schmehl, H. Bielefeldt, H. Hilgenkamp, J. Mannhart, C. C. Tsuei: *Appl. Phys. Lett.* **76**, 912 (2000).
114. B. Chesca, *Ann. Phys.* **8**, 511 (1999).
115. J. Mannhart, H. Hilgenkamp, G. Hammerl, C. W. Schneider: *Phys. Scr.* **T102**, 107 (2002).

116. B. Chesca, K. Ehrhardt, M. Mößle, R. Straub, D. Koelle, R. Kleiner, A. Tsukada: *Phys. Rev. Lett.* **90**, 057004 (2003).
117. H. J. H. Smilde, H. Hilgenkamp, G. J. Gerritsma, D. H. A. Blank, H. Rogalla: *Physica C* **350**, 269 (2001).
118. H. J. H. Smilde, Ariando , D. H. A. Blank, G. J. Gerritsma, H. Hilgenkamp, H. Rogalla: *Phys. Rev. Lett.* **88**, 057004 (2002).
119. H. Hilgenkamp, Ariando , H.-J. Smilde, D. H. A. Blank, G. Rijnders, H. Rogalla, J. R. Kirtley, C. C. Tsuei: *Nature* **422**, 50 (2003).
120. L. Alff, S. Meyer, S. Kleefisch, U. Schoop, A. Marx, H. Sato, M. Naito, R. Gross: *Phys. Rev. Lett.* **83**, 2644 (1999);L. Alff, B. Welter, S. Kleefisch, A. Marx, R. Gross: *Physica C* **357**, 307 (2001);J. A. Skinta, T. R. Lemberger, T. Greibe, M. Naito: *Phys. Rev. Lett.* **88**, 207003 (2002);J. A. Skinta, M.-S. Kim, T. R. Lemberger, T. Greibe, M. Maito: *Phys. Rev. Lett.* **88**, 207005 (2002).
121. A. G. Sun, D. A. Gajewski, M. B. Maple, R. C. Dynes: *Phys. Rev. Lett.* **72**, 2267 (1994);A. G. Sun, A. Truscott, A. S. Katz, R. C. Dynes, B. W. Veal, C. Gu: *Phys. Rev. B* **54**, 6734 (1996);R. Kleiner, A. S. Katz, A. G. Sun, R. Summer, D. A. Gajewski, S. H. Han, S. I. Woods, E. Dantsker, B. Chen, K. Char, M. B. Maple, R. C. Dynes, J. Clarke: *Phys. Rev. Lett.* **76**, 2161 (1996).
122. M. Mößle, R. Kleiner: *Phys. Rev. B* **59**, 4486 (1999).
123. S. I. Woods, A. S. Katz, T. L. Kirk, M. C. de Andrade, M. B. Maple, R. C. Dynes: *IEEE Trans. Appl. Supercond.* **9**, 3917 (1999).
124. R. Joynt, L. Taillefer: *Rev. Mod. Phys.* **74**, 235 (2002).
125. C. Pfleiderer: *Rev. Mod. Phys.* **81**, 1551 (2009)
126. N. K. Sato, N. Aso, K. Miyake, R. Shiina, P. Thalmeier, G. Varelogiannis, C. Geibel, F. Steglich, P. Fulde, T. Komatsubara: *Nature* **410**, 340 (2001).
127. M. Jourdan, M. Huth, H. Adrian: *Nature* **398**, 47 (1999).
128. G. M. Luke, Y. Fudamoto, K. M. Kojima, M. I. Larkin, J. Merrin, B. Nachumi, Y. J. Uemura, Y. Maeno, Z. Q. Mao, Y. Mori, H. Nakamura, M. Sigrist: *Nature* **394**, 558 (1998).
129. G. M. Luke, A. Keren, L. P. Lee, W. D. Wu, Y. J. Uemura, D. A. Bonn, L. Taillefer, J. D. Garrett: *Phys. Rev. Lett.* **71**, 1466 (1993).
130. T. M. Riseman, P. G. Kealey, E. M. Forgan, A. P. Mackenzie, L. M. Galvin, A. W. Tyler, S. L. Lee, C. Ager, D. M. Paul, C. M. Aegerter, R. Cubitt, Z. Q. Mao, T. Akima, Y. Maeno: *Nature* **404**, 629 (2000); *Nature* **396**, 242 (1998);P. G. Kealey, T. M. Riseman, E. M. Forgan, L. M. Galvin, A. P. Mackenzie, S. L. Lee, D. McK. Paul, R. Cubitt, D. F. Agterberg, R. Heeb,

- Z. Q. Mao, Y. Maeno: *Phys. Rev. Lett.* **84**, 6094 (2000).
131. M. Sigrist, H. Monien: *J. Phys. Soc. Jpn.* **70**, 2409 (2001).
132. K. Izawa, H. Yamaguchi, T. Sasaki, Y. Matsuda: *Phys. Rev. Lett.* **88**, 027002 (2002).
133. I. J. Lee, S. E. Brown, W. G. Clark, M. J. Strouse, M. J. Naughton, W. Kang, P. M. Chaikin: *Phys. Rev. Lett.* **88**, 017004 (2002).
134. P. Fulde R. A. Ferrell: *Phys. Rev.* **135**, A550 (1964).
135. A. I. Larkin and Y. N. Ovchinnikov: *Zh. Eksp. Teor. Fiz.* **47**, 1136 (1964); *Sov. Phys. JETP* **20**, 762 (1965).
136. H. A. Radovan, N. A. Fortune, T. P. Murphy, S. T. Hannahs, E. C. Palm, S. W. Tozer, D. Hall: *Nature* **425**, 51 (2003); A. Bianchi, R. Movshovich, C. Capan, P. G. Pagliuso, J. L. Sarrao: *Phys. Rev. Lett.* **91**, 187004 (2003).
137. R. Lortz, Y. Wang, A. Demuer, P. H. M. Böttger, B. Bergk, G. Zwicknagl, Y. Nakazawa, J. Wosnitza: *Phys. Rev. Lett.* **99**, 187002 (2007).
138. X. Quian, J. Li, L. Qi, C.-Z. Wang, T.-L. Chan, Y.-X. Yao, K.-M. Ho, S. Yip: *Phys. Rev. B* **78**, 245112 (2008).
139. X. X. Xi: *Rep. Prog. Phys.* **71**, 116501 (2008).
140. C.-T. Chen, C. C. Tsuei, M. B. Ketchen, Z.-A. Ren, Z. X. Zhao: *Nat. Phys.* **6**, 260 (2010).

<sup>1</sup> Due to the surface tension, it costs energy to deform the equilibrium configuration of the surface of a liquid.

<sup>2</sup> The center of mass of the following Cooper pair is at rest, with a total momentum  $\mathbf{P} = \hbar\mathbf{K} = 0$ . However, if we want to describe a state in which a supercurrent flows, the Cooper pairing must be performed for  $\mathbf{K} \neq 0$ , that is, for a state  $\{\mathbf{k} + \mathbf{K}\uparrow, -\mathbf{k} + \mathbf{K}\downarrow\}$ .

<sup>3</sup> If real phonons are generated by an electron, we are dealing with a process causing electrical resistance, since energy is transferred from the electrons to the lattice in this case.

<sup>4</sup> We note that the electrostatic repulsion is highly screened by the positive charges of the atomic ions.

<sup>5</sup> The interaction via the exchange of phonons is so weak that it cannot localize the electrons of a Cooper pair more sharply than within about  $\xi_0$ . Because of the uncertainty principle, a sharper localization would result in a kinetic energy of the electrons larger than the binding energy of the pair. However, these intuitive arguments quickly run into difficulties. For instance, one can ask if the whole pair correlation is not destroyed by the high Fermi velocity. The answer is “no,” but we do not attempt to justify this. Here, we would

overextend the simple particle picture.

<sup>6</sup> In a more general way, we can also allow the interaction between the electrons to depend on the momentum or the wave vector of the electrons.

<sup>7</sup> In [Section 3.2](#) we will see that this property changes if the Cooper pairs do not form an  $L = 0$  state (see [Section 2.1](#)). In this case, quasiparticles exist for all energies.

<sup>8</sup> For small changes of  $T_c$  sufficient accuracy of the experiments cannot be achieved easily. The measurements of  $T_c$  must be performed for different samples. Hence, all other parameters affecting  $T_c$ , such as, say, internal strains, impurities, and lattice defects, must be kept sufficiently constant for all samples, in order to observe the influence of the isotopic mass alone.

<sup>9</sup> The order of magnitude of these parameters can be indicated as follows:  $\lambda^*$  varies between 0 and about 2, where the approximations become doubtful for large values of  $\lambda^*$ ;  $\mu^*$  ranges between about 0.1 and 0.2; and  $\langle\omega\rangle/\omega_D$  is about 0.6.

<sup>10</sup> See Ref. [21].

<sup>11</sup> Here, we neglect the influence of the applied voltage on the energetic height of the barrier.

<sup>12</sup> During the tunneling process, for instance, within the barrier, an electron can absorb or emit a phonon. Such processes are referred to as “**phonon-assisted tunneling**”. They are relatively rare and will be neglected initially.

<sup>13</sup> We denote the density of states in the electrodes by the indices I or II.

<sup>14</sup> In the case of [Figure 3.12](#), for all  $\epsilon > 0$ , the term in brackets  $[f(\epsilon) - f(\epsilon - eU)]$  is equal to zero, since both Fermi functions are zero. Independent of the sign of the electron charge, we have assumed  $eU > 0$ . For  $\epsilon < -eU$ , the term in brackets is zero again, since both Fermi functions have the value 1. Only in the range  $-eU < \epsilon < 0$  does the term in brackets attain the value 1. The density of states, assumed to be constant, can be taken in front of the integral. Then we obtain (see curve 1 in [Figure 3.13](#)):

<sup>15</sup> The condition  $I(U) = -I(-U)$ , which must always be valid for tunnel junctions, is satisfied.

<sup>16</sup> The averaging must be performed over all the electrons on the Fermi surface.

<sup>17</sup> As a thermodynamic quantity for the total system, the transition temperature cannot depend on the direction.

<sup>18</sup> Near 220 K, Cu forms an intermetallic compound with Sn, which results in a resistance drop. New lines of the compound appear in the diffraction image. This does not much affect the transition temperature, since the remaining almost pure tin shorts out the non-superconducting compound.

- <sup>19</sup> Often these films are referred to as ***amorphous***, but only to indicate the extreme disorder.
- <sup>20</sup> For the same mass, softer springs have smaller vibrational frequencies.
- <sup>21</sup> It is likely that the extremely large changes in Be have yet another, still not completely explained, origin. Since also alloys with cubic structure containing much Be have values of  $T_c$  above 9 K, we suspect a strong influence of the crystal structure.
- <sup>22</sup> With respect to solubility, the alloys of lanthanum with the rare earths are highly favorable.
- <sup>23</sup> J. Kondo developed the first quantitative model of such systems and could theoretically explain the observed anomalies.
- <sup>24</sup> We have discussed a few other systems showing this behavior in [Section 2.5](#).
- <sup>25</sup> Because of the normalized energy scale, the results are independent of the absolute value of the energy gap and can be used for different superconductors.
- <sup>26</sup> There exists a small, finite contribution resulting from the normal conducting vortex cores. In [Figure 3.31](#), this contribution is not included in the dotted line (A. Maeno, private communication).
- <sup>27</sup> Here, we neglect the anisotropy effect discussed in [Section 3.1.4.1](#).
- <sup>28</sup> Hence, the symmetry of the wave function is lower than the symmetry of the underlying crystal structure. The  $d_{x^2-y^2}$  symmetry could be realized in a crystal with tetragonal structure. The crystal itself reproduces its structure by means of rotations of 90° around the  $c$ -axis. However, during such rotations, the condensate wave function changes its signature. Only after rotations of 180°, it reproduces itself. Sometimes “unconventional” is defined in this way.
- <sup>29</sup> In this case, the CuO<sub>2</sub> plane is charged twofold positive.
- <sup>30</sup> In the case of a very large Coulomb repulsion, we can describe the antiferromagnetic state of the Hubbard model in terms of an “exchange energy”  $J$  as in a classical antiferromagnet. In the case of the antiferromagnet,  $J$  is negative. The system gains energy if neighboring spins orient themselves antiparallel.
- <sup>31</sup> In a similar way for electron-doped cuprates, the excess spins would locally perturb the antiferromagnetic order.
- <sup>32</sup> We note that this illustration is somewhat artificial, since the ring structure refers to the regular space and the pair wave function to  $\mathbf{k}$ -space. However, the important point is the phase difference for the two Josephson junctions.
- <sup>33</sup> Here, Josephson junctions with magnetic barriers were discussed. A  $\pi$ -Josephson junction

can also be formed in this case. We will discuss this in more detail in [Section 6.1.3](#).

- [34](#) In an accurate calculation, the energy of the system must be minimized.
- [35](#) We can imagine combinations of the form  $a\Psi_{0,1}(\mathbf{k}) \pm b\Psi_{0,2}(\mathbf{k})$  and also complex mixtures of the form  $a\Psi_{0,1}(\mathbf{k}) \pm ib\Psi_{0,2}(\mathbf{k})$ . The two functions  $\Psi_{0,1}(\mathbf{k})$  and  $\Psi_{0,2}(\mathbf{k})$  will represent pair wave functions with different symmetry. The coefficients  $a$  and  $b$  represent the relative weights of the functions. The complex mixtures violate time inversion symmetry.
- [36](#) Since the spin-orbit coupling is weak, we can again classify according to the spin and the angular momentum.

# Chapter 4

## Thermodynamics and Thermal Properties of the Superconducting State

In the last chapter we saw that a well-established theory exists for conventional superconductors. The theory explains how a coherent matter wave is constructed by means of the formation of Cooper pairs. However, we also saw that, in particular for unconventional superconductors, the microscopic details often remain unclear. On the other hand, based on only a few basic symmetry arguments, we were able to account for many properties of the pair wave function.

Next we want to treat superconductivity on a macroscopic scale. We will see that by means of a rigorous application of the general laws of thermodynamics, we can reach a deep understanding of the properties of the superconducting state. This will lead us to the Ginzburg–Landau theory [1], which was developed in the early 1950s, and which turned out to be highly powerful for the solution of many practical problems. It serves for the description of conventional as well as unconventional superconductors.

Already in 1924 Keesom [2] had tried to apply thermodynamics to superconductivity. At the time there was the difficulty that the superconducting state could not be interpreted in terms of a *single* new thermodynamic phase. Then in 1933 the discovery of the Meissner–Ochsenfeld effect brought crucial progress. At the onset of superconductivity, a magnetic field is expelled from the interior of a type-I superconductor, independent of the experimental details. This represented a clear experimental confirmation of the existence of a *single* superconducting phase. The thermodynamic equilibrium state is unequivocally determined by the specification of  $T$  and  $B$  also in the case of a type-II superconductor, where the magnetic field penetrates into the superconductor.

Before we turn to the details, we make some general remarks on the thermodynamic treatment of physical systems.

### 4.1 General Aspects of Thermodynamics

A crucial quality of the thermodynamic treatment of a macroscopic physical system arises from the fact that the immense number of independent coordinates of the individual particles is reduced to only a few macroscopic variables of the system. For instance, for the thermodynamic treatment of an ideal gas, one does not start from the  $3N$  spatial coordinates and the  $3N$  momentum coordinates of the  $N$  gas atoms. Instead, one describes the behavior by such variables as the temperature  $T$ , the volume  $V$ , the particle number  $N$ , and so on.

One is interested in the macroscopic behavior of the system, say, in the stability of the different phases, such as the solid, liquid, and gaseous phases, during the variation of one variable

while the other variables are kept constant. The thermodynamic equilibrium states of a system under specified conditions play an important role. Here, we deal with the following question. A system, say, a liquid–vapor mixture, is specified by fixing the temperature  $T$ , the volume  $V$ , and the total particle number  $N$ . We want to know the number  $N$  of atoms in the vapor in thermodynamic equilibrium, that is, in the state that is established if all other quantities can be freely adjusted under the given conditions. The system then exists in a definite state, where the particles can be freely exchanged between the vapor and the liquid, and where a definite heat exchange with a thermal bath must be possible.

At this point we mention that frequently the thermodynamic equilibrium state is not established at all or only very slowly, because the free exchange of some quantity is not possible in the particular experiment. The thermodynamic prediction on the equilibrium state is completely independent of the question of the chances for it to become realized.

All such questions are dealt with by specifying suitable thermodynamic functions, the Gibbs functions, or thermodynamic potentials. These Gibbs functions are constructed from the variables in such a way that a certain Gibbs function is associated with a definite set of independent variables. The system is completely accounted for by means of this Gibbs function.

To find the correct Gibbs function of a system is not easy. First, we must find a set of independent variables, which is sometimes difficult. Standard sets of variables are temperature  $T$ , volume  $V$ , and particle number  $N$ ; or temperature  $T$ , pressure  $p$ , and particle number  $N$ . Other variables must be added if a system is also affected, for example, by electric or magnetic fields. The behavior in a magnetic field will be highly important for superconductors.

If we have found the Gibbs function associated with a set of variables, the equilibrium states are determined by the extrema of the Gibbs function.<sup>1</sup> Two phases of a system are in equilibrium if their Gibbs functions have the same value. In principle, from this we can already answer the question of the stability of a phase. If the equilibrium state is determined by the minimum of the Gibbs function, then phase I will be unstable relative to phase II if the Gibbs function of phase I is larger than that of phase II.<sup>2</sup>

The Gibbs functions are distinguished by the fact that, for a differential variation, just the differentials of the independent variables appear. For illustration, we present a few known examples.

For the internal energy  $U$ , we have

$$dU = T dS + \delta A \quad 4.1$$

If we include only the compressional work  $\delta A^V = -pdV$ , we obtain

$$dU = T dS - p dV \quad 4.2$$

$U$  is the Gibbs function for the variables  $S$  and  $V$ . We note that these two variables change with the size of the system (“extensive state variables”), whereas this is not so in the case of the variables  $T$  and  $p$  (“intensive state variables”). In the Gibbs functions there always appear

products of extensive and intensive quantities. The negative sign of the term  $p dV$  is needed, since we define that all energies *added to* a system are counted as positive. For a reduction of the volume, that is,  $dV < 0$ , work is added to the system.<sup>3</sup> Of course, other variables, for example, the particle number  $N$ , may also appear. In the following, we always keep the particle number constant. Hence, we can ignore this variable.

The free energy  $F$  is given as

$$F = U - TS \quad 4.3$$

leading to

$$dF = dU - T dS - S dT = -S dT - p dV \quad 4.4$$

We see that  $F$  is the Gibbs function for the variables  $T$  and  $V$ .

Frequently, the arbitrary variation of the pressure  $p$  is much easier than that of  $V$  and, hence,  $p$  is introduced as the independent variable. The Gibbs function for the variables  $T$  and  $p$  is the enthalpy  $G$  with

$$G = U - TS + pV \quad 4.5$$

and

$$dG = -S dT + V dp \quad 4.6$$

In our above-mentioned discussion, we have considered only the variables pressure and temperature. For the thermodynamic treatment of the superconducting phase,<sup>4</sup> we must include an additional variable, which accounts for the behavior in a magnetic field. As the additional independent variable, we choose the magnetic field  $\mathbf{B}$ . The Gibbs function associated with the variables  $T$ ,  $p$ , and  $\mathbf{B}$  for constant particle number is

$$G = U - TS + pV - \mathbf{m} \cdot \mathbf{b} \quad 4.7$$

Here,  $\mathbf{m}$  is the magnetic moment of the superconductor.<sup>5</sup> Since here  $\mathbf{m}$  and  $\mathbf{B}$  are always parallel or antiparallel, and since we indicate this in the sign of  $\mathbf{m}$ , we can ignore the vector property in this discussion. For the variation of the internal energy, we obtain<sup>6</sup>

$$dU = T dS - p dV + B dm \quad 4.8$$

as is shown in standard textbooks on the theory of heat. Hence, one finds<sup>7</sup>

$$dG = -S dT + V dp - m dB \quad 4.9$$

For our choice of the Gibbs function  $G(T,p,B)$ , the independent variables  $T$ ,  $p$ , and  $B$  appear in the differentials, as expected.

If we know the Gibbs function of a system, we can calculate from it very easily many thermodynamic quantities by means of suitable derivatives with respect to the variables. In this

way, we find the entropy  $S$  from  $G$ :

$$S = -\left(\frac{\partial G}{\partial T}\right)_{p,B} \quad 4.10$$

Here, the symbol  $\partial/\partial T$  indicates the partial derivative with respect to temperature. At the same time, the pressure  $p$  and the magnetic field  $B$  must be kept constant. This is indicated by the subscript index  $p,B$ . In this way the dependence of the entropy on the temperature, on the magnetic field, and on the pressure is obtained:  $S = S(T,B,p)$ . If  $G$  depends on additional variables, these must also be kept constant. In this case these variables also appear in the subscript index after the bracket.

Analogously, we can also derive other thermodynamic quantities from  $G$ . From the partial derivative with respect to the pressure at constant temperature, we find the sample volume  $V$  (as a function of  $T$ ,  $B$ , and  $p$ ):

$$V = \left(\frac{\partial G}{\partial p}\right)_{T,B} \quad 4.11$$

The specific heat  $c$  is another important quantity that we will need in the following. It is defined by the relation

$$\Delta Q = cm' \Delta T \quad 4.12$$

where  $\Delta Q$  is the amount of heat we must introduce into a substance of mass  $m'$  in order to raise its temperature by  $\Delta T$ . We distinguish between different kinds of specific heat, depending on the conditions under which the addition of heat energy takes place. For example, if the pressure is kept constant, we speak of the specific heat  $c_p$  at constant pressure.

From the function  $G$  the specific heat is obtained directly by means of the expression

$$-T(\partial^2 G / \partial T^2)_{p,B} = T(\partial S / \partial T)_{p,B} = c_p \quad 4.13$$

Relations such as Eq. (4.13) are highly important for calculating the entropy from the measured temperature dependence of the specific heat. There exist specific, characteristic relations between the different thermodynamic quantities. In this chapter, we will deal with several examples.

As the last general aspect we will discuss the order of the transition between two thermodynamic phases. We have mentioned already that at a phase transition the relevant Gibbs functions have the same value. If the first derivative of the Gibbs function with respect to the temperature is discontinuous at the phase transition, one speaks of a first-order phase transition. In this case, the entropy jumps by a finite value. Analogously, if the entropy is continuous at the phase transition, but if the second derivative of the Gibbs function, which is proportional to the specific heat, shows a jump, one speaks of a second-order phase transition. For such higher-order phase transitions, L. D. Landau has developed a powerful theory [5].

Also the superconducting phase transition in the absence of a magnetic field is of second order.

The application of the concepts of the Landau theory to the superconducting phase transition will lead us to the Ginzburg–Landau theory. However, before we turn to this theory, we want to show by means of specific-heat measurements that the superconducting phase transition is, indeed, of second order. Also we want to discuss the thermal conductivity of superconductors.

## 4.2 Specific Heat

In [Figure 4.1](#) as an example we show the specific heat of tin as a function of temperature [6]. Tin is a type-I superconductor. The solid curve is observed in the absence of a magnetic field. We clearly see the jump of the specific heat at  $T_c$ , indicating a second-order phase transition. In the case of a first-order phase transition, at the transition temperature  $c_p$  would have become infinitely large.

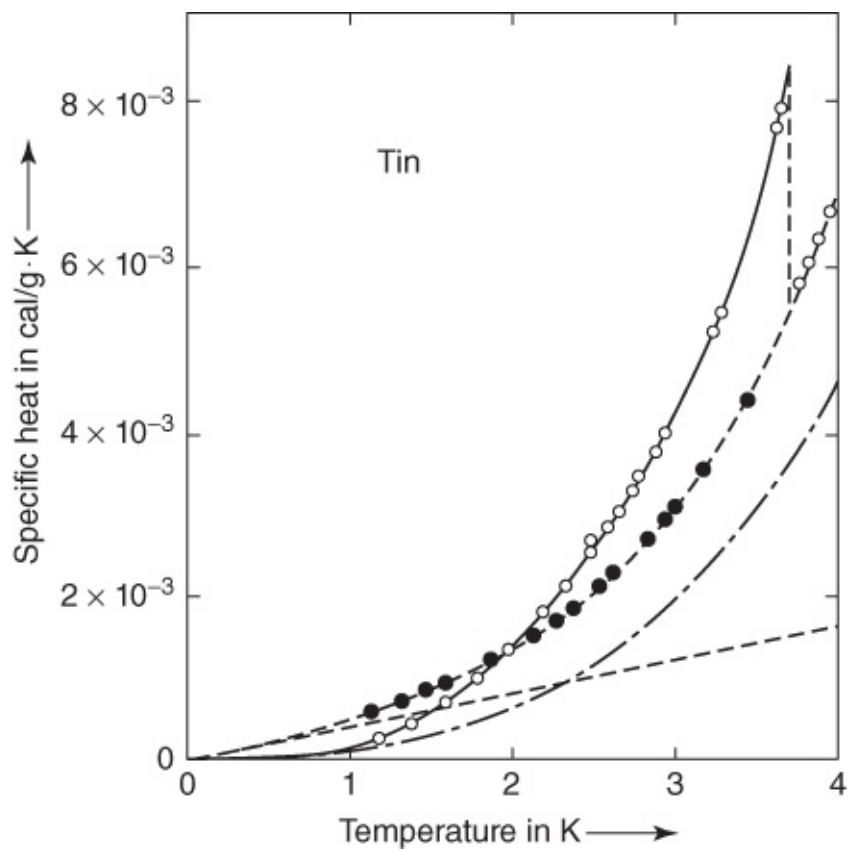


**Figure 4.1** Specific heat of tin plotted versus the temperature. Open circles: without a magnetic field; solid dots: with a magnetic field  $B > B_c$ ; dashed line: contribution of the electrons for  $B > B_c$ ; dashed-dotted line: lattice contribution for  $B > B_c$  ( $1 \text{ cal} \approx 4.18 \text{ J}$ ). (From [6].).

In magnetic fields above the critical field  $B_c$ , the specific heat  $c_n$  of the normal conducting state can also be determined for  $T < T_c$  (solid dots in [Figure 4.1](#)). In this case no discontinuity is observed, since there is no phase transition.

The specific heat of the normal conductor can be separated into two components, the contribution of the conduction electrons  $c_{nE}$  and the contribution of the lattice vibrations  $c_{nL}$ ,

thus  $c_n = c_{nE} + c_{nL}$ .

In good approximation we have

$$c_{nE} = \gamma T \quad \text{4.14}$$

$$c_{nL} = \alpha(T/\Theta_D)^3 \quad \text{4.15}$$

$\gamma$  and  $\alpha$  are constants, and  $\Theta_D$  is the Debye temperature. The Sommerfeld coefficient  $\gamma$  is proportional to the density of states of the electrons at the Fermi energy (see [Section 1.1](#)). It is given by

$$\gamma = \frac{2}{3}\pi^2 k_B^2 N(E_F) \quad \text{4.16}$$

where  $k_B = 1.38 \times 10^{-23}$  W s/K is Boltzmann's constant and  $N(E_F)$  is the density of states at the Fermi energy in (W s mol) $^{-1}$ .

In the superconducting state for medium temperatures, the temperature dependence of the specific heat is well approximated by a power law of third order. According to Eqs. ([4.14](#)) and ([4.15](#)), this means that the lattice component dominates.

Also we want to discuss briefly which temperature dependence of the specific heat in the superconducting state results from the microscopic theory. First we look at conventional superconductors.

For temperatures near  $T_c$ , the Cooper pair density and the energy gap change strongly with temperature. In this temperature range we cannot expect simple theoretical relations. However, at very low temperatures the energy gap is nearly independent of  $T$ . The introduction of energy into the electron system then essentially results in the breaking up of Cooper pairs.<sup>8</sup> For this, excitations beyond the energy gap are needed. Since the probability of such excitations should decrease following an exponential function of the kind  $\exp(-A/k_B T)$ , at very low temperatures we expect essentially an exponential decrease in the electronic component  $c_{sE}$  of the specific heat. Here,  $A$  is a constant, essentially the excitation energy.

For  $T \rightarrow 0$ , the Bardeen–Cooper–Schrieffer (BCS) theory yields for the specific heat of conventional superconductors

$$c_{sE} = 9.17 \gamma T_c \exp\left(-\frac{1.5 T_c}{T}\right) \quad \text{4.17}$$

In [Figure 4.2](#) we show an example of this exponential dependence [7]. Corresponding to Eq. ([4.17](#)),  $c_{sE}/\gamma T_c$  is plotted versus  $T_c/T$ . The straight line represents the relation ([4.17](#)). Also, before the advent of the BCS theory, highly accurate specific-heat measurements had already indicated exponential dependences at very low temperatures. This result confirmed at the time the prediction by Daunt and Mendelssohn [8] of an energy gap in the excitation spectrum of a superconductor.

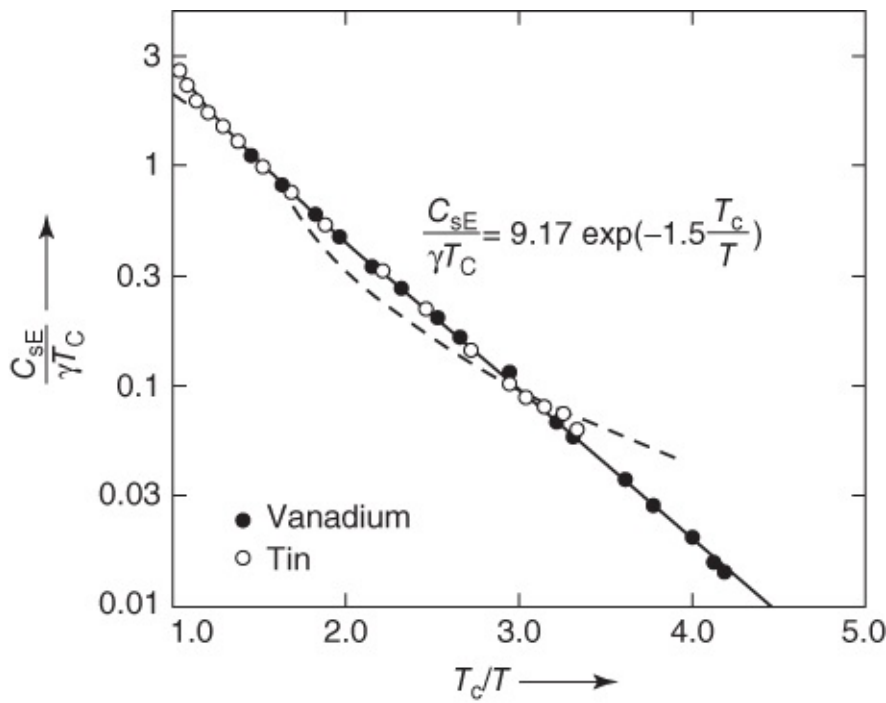


**Figure 4.2** Electronic component of the specific heat of tin and vanadium. The straight line represents the relation predicted by the BCS theory. The dashed curve indicates a  $T^3$  law according to Eq. (4.15). (From [7].)

For the relative jump of the electronic component of the specific heat,  $(c_{sE} - c_{nE})/c_{nE}$ , near  $T_c$ , the BCS theory yields the value 1.43, in excellent agreement with the experimental observations.

On the other hand, in unconventional superconductors, the excitation spectrum does not have an energy gap. Instead, the gap function  $\Delta_0(\mathbf{k})$  vanishes along certain directions in  $\mathbf{k}$ -space.

Hence, even at very low temperatures there exist an appreciable number of unpaired electrons, which contribute to the specific heat of the electron system. As we have seen in [Section 3.2](#), the function  $\Delta_0(\mathbf{k})$  can vanish at individual points or along extended lines in  $\mathbf{k}$ -space.

Therefore,  $c_{sE}(T)$  increases with temperature following a power law:  $c_{sE}(T) \propto T^a$ . Depending on the dimension of the locations with zero gap (points or lines) and on the exponents with which  $\Delta_0(\mathbf{k})$  vanishes with  $|\mathbf{k}|$  near these locations, one finds  $a = 2$  or  $a = 3$ . Also the relative magnitude of the jump  $(c_{sE} - c_{nE})/c_{nE}$  of the electronic specific heat at  $T_c$  depends on the exact behavior of  $\Delta_0(\mathbf{k})$  near the locations with zero gap. Hence, it yields information about these locations.

For the cuprates it is very difficult to determine the electronic component of the specific heat over a large temperature range, since (except for very low temperatures) the contribution of the phonons to the specific heat is relatively large [9–11]. Furthermore, it is impossible to suppress the superconductivity simply by the application of a magnetic field, because of the large values of the upper critical fields. Therefore, the difference between the specific heat in the normal and in the superconducting states cannot be extracted in the simple way shown in [Figure 4.1](#). Instead, one can use undoped samples for comparison, say, comparing  $\text{YBa}_2\text{Cu}_3\text{O}_6$

with  $\text{YBa}_2\text{Cu}_3\text{O}_7$ . In [Figure 4.3](#) we show the temperature dependence of the quantity  $\gamma = c_{\text{el}}/T$  for different levels of oxygen doping  $x$  in  $\text{YBa}_2\text{Cu}_3\text{O}_{6+x}$ . The jumps at the different transition temperatures can clearly be seen.

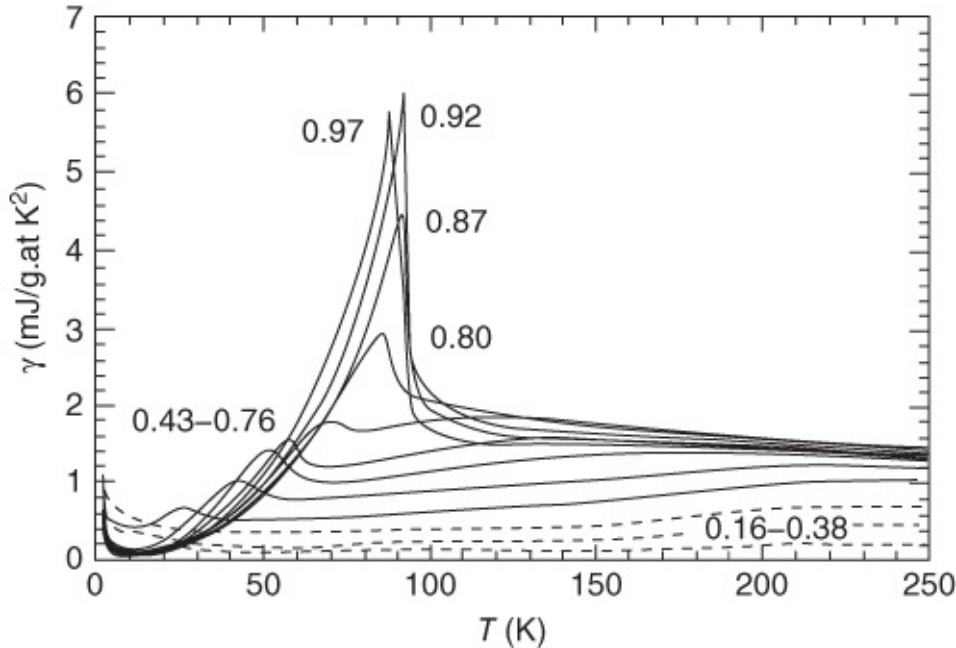


[Figure 4.3](#) Sommerfeld coefficient  $\gamma = c_{\text{el}}/T$  plotted versus temperature  $T$  for  $\text{YBa}_2\text{Cu}_3\text{O}_{6+x}$  crystals with different doping levels [12].

The specific heat  $c_{\text{SE}}$  has also been analyzed exactly in the limit of low temperatures, and a surprisingly large *linear* term has been found, that is,  $a = 1$  [13]. However, for a superconductor with  $d_{x^2-y^2}$  symmetry of the pair wave function in the absence of a magnetic field, in the simplest case one would have expected a quadratic temperature dependence of  $c_{\text{SE}}$ .<sup>9</sup> Subsequent experiments have confirmed the  $T^2$  term [14] and, on the other hand, have identified paramagnetic impurities as the origin of the linear term [15].

For the three examples of superconductors, tin, vanadium, and  $\text{YBa}_2\text{Cu}_3\text{O}_7$ , we have seen that the transition into the superconducting state represents a second-order phase transition.<sup>10</sup>

## 4.3 Thermal Conductivity

If we establish a temperature difference  $\Delta T$  along a rod of length  $l$  (taking a simple geometry), heat energy is transported from the hot end to the cold end. The thermal conductivity  $\lambda_T$  is a material parameter and is defined by the equation

$$\frac{\Delta Q}{\Delta t} = \lambda_T \frac{F}{l} \Delta T \quad 4.18$$

where  $\Delta Q/\Delta t$  is the heat energy per unit time,  $F$  and  $l$  are the cross-section and length of the rod, respectively, and  $\Delta T$  is the temperature difference. Here, we assume a linear change of  $T$

along the length of the rod.

In a metal, heat transport is due to the conduction electrons as well as lattice vibrations. In general, the contribution of the electrons is much larger than that of the lattice. In this case, from our basic understanding of the superconducting state, we can easily predict how the thermal conductivity should behave for temperatures below  $T_c$ . Below  $T_c$ , with decreasing temperature more and more conduction electrons are correlated, forming Cooper pairs, and hence are decoupled from the energy exchange. Therefore, below  $T_c$  the contribution of the electrons to the thermal conduction becomes smaller and smaller. So we expect that in the superconducting state the thermal conductivity is smaller than in the normal conducting state, as long as it is dominated by the electrons.

This behavior is shown in [Figure 4.4](#) for tin and mercury [17]. Here, we do not want to discuss the temperature dependence of the thermal conductivity in the normal conducting state. We only emphasize the fact that in the superconducting state the thermal conductivity is smaller than in the normal conducting state, as expected. At sufficiently low temperatures, at which practically no free electrons exist anymore in the superconducting state, because of the nearly complete correlation in the form of Cooper pairs, the behavior in a superconductor corresponds exactly to that in an electrically insulating crystal. The electron system is simply decoupled from the thermal behavior. If the superconductivity is suppressed by means of an overcritical magnetic field, then the metal recovers the much larger thermal conductivity of the electron system. Therefore, a superconductor can serve as a thermal switch. In the overcritical fields we have high thermal conductivity; analogous to electric circuits, the switch is closed. At zero field the thermal conductivity is much smaller, and the switch is open. Often such thermal switches represent an important feature of experiments at temperatures below 1 mK.

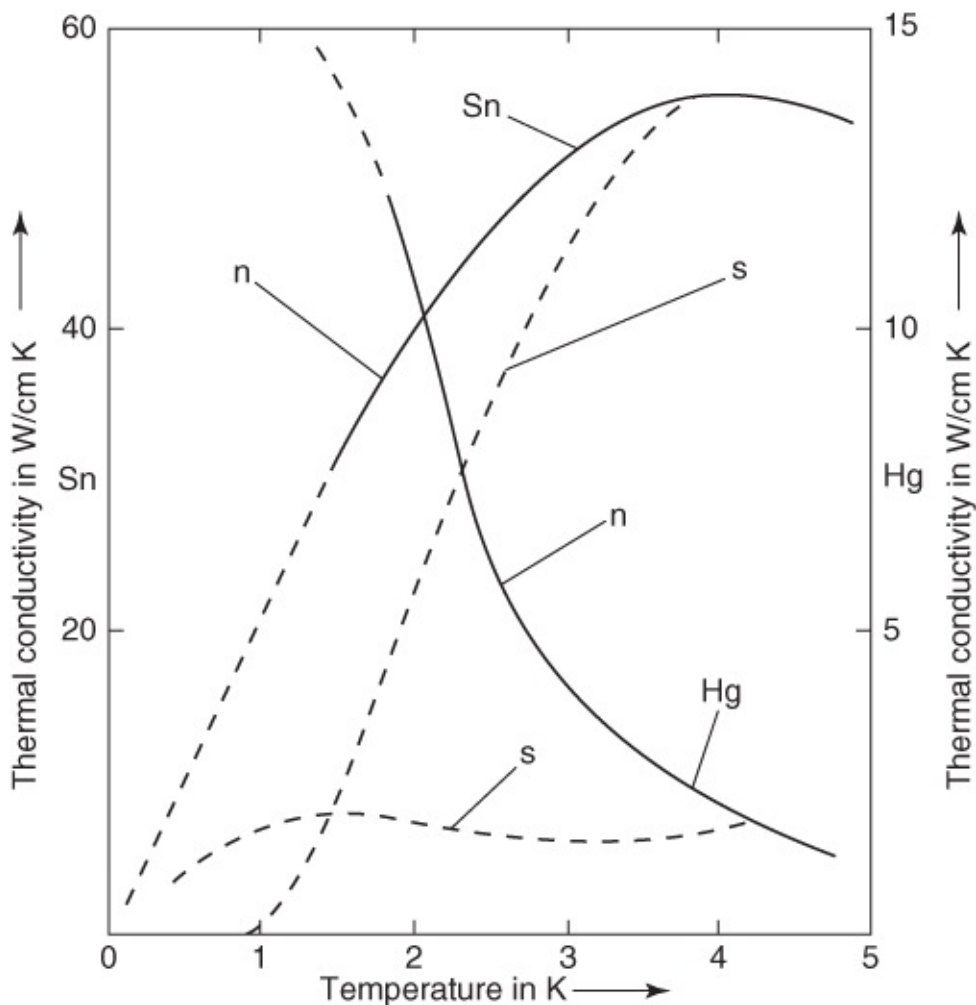


**Figure 4.4** Thermal conductivity of pure tin and mercury. (From [16].) The left scale is for Sn.

The behavior discussed earlier is characteristic of many metals. However, in alloys or highly impure metals, the situation is much more complex. If chemical impurities are introduced into a metal lattice, the electron mean free path becomes shorter due to collisions between the electrons and the impurities. At low temperatures the corresponding additional electrical resistance is observed in the form of a residual resistance. The reduction of the electron mobility also leads to an increase in the thermal resistance.

In contrast to the electrons, the lattice vibrations, the phonons, are much less hindered in their propagation by atomic lattice defects.<sup>11</sup> Therefore, the contribution of the phonons to the thermal conductivity is much less affected by such impurities. As a result, the thermal conductivity of the electrons can become smaller than that of the phonons. Then the thermal conductivities in the superconducting and in the normal conducting states differ only little from each other. As an example, we show in [Figure 4.5](#) the thermal conduction of lead–bismuth alloys containing 0.1% Bi [18].

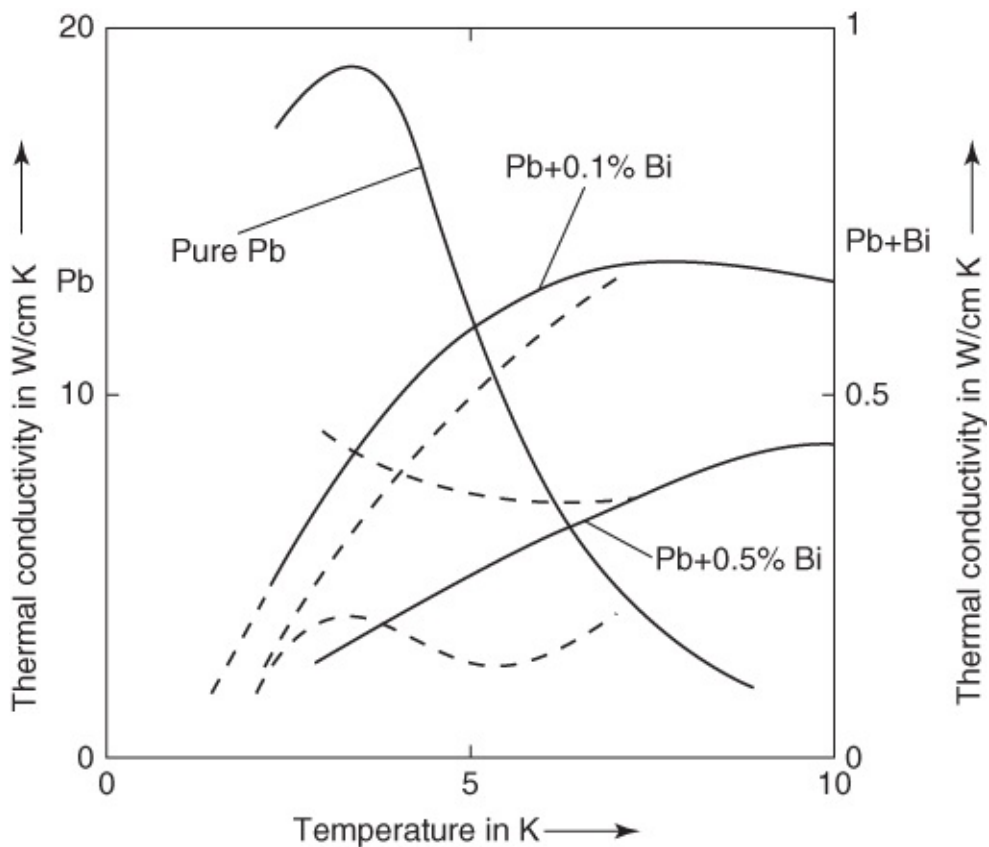


**Figure 4.5** Thermal conductivity of lead and lead–bismuth alloys. Solid lines: normal state; dashed lines: superconducting state. (From [18].)

If the electronic component of the thermal conductivity becomes much smaller than the component due to the phonons, in the superconducting state the thermal conductivity can become even larger than in the normal conducting state. This can be observed in some alloy systems. As an example of this behavior, in [Figure 4.5](#) we show the thermal conductivity of a lead–bismuth alloy containing 0.5% Bi. This behavior can be understood by noting that the electron and phonon systems can also interact with each other, that is, there are collisions between the electrons and the phonons. Such collisions of the electrons with the phonons dominate the total temperature dependence of the electrical resistance. With increasing temperature, the lattice vibrations, that is, the number of phonons, increase. As a result, the collisions of the electrons and, hence, the electrical resistance increase with increasing temperature.

In substances in which the phonons provide the dominant contribution to the thermal conduction, we must look at the electron–phonon collisions from the viewpoint of the phonons. These collisions reduce the propagation and, hence, the thermal conduction of the phonons. If the electrons are decoupled in the superconducting state, these collisions are eliminated. The thermal conductivity of the phonon system increases. In this way, we can understand why thermal conduction in the superconducting state can become larger than in the normal conducting state. This is the explanation of the results shown for the Pb–Bi alloys in [Figure 4.5](#).

Here we do not want to go any further in our discussion of thermal conductivity. We just

mention that, in unconventional superconductors, with decreasing temperature the electronic contribution vanishes much more slowly than in conventional superconductors. This results from the relatively large number of quasiparticles existing in the former also at low temperatures [19]. A similar argument applies if superconducting and normal conducting regions exist next to each other in a sample. This happens in the vortex state of type-II superconductors and also in the so-called intermediate state of type-I superconductors. The latter will be discussed in [Section 4.6.4](#) in more detail.

## 4.4 Ginzburg–Landau Theory

So far in our thermodynamic discussions we have treated the Gibbs function of the system in an integrated way, such that spatial variations of the superconducting state did not appear explicitly. Furthermore, we have not yet utilized the fact that the superconducting state can be described in terms of a macroscopic wave function with a well-defined phase.

Both aspects were incorporated by Ginzburg and Landau into their theory published in 1950. This theory represents an important extension of the London theory [20], in which a spatially constant density of the superconducting charge carriers was assumed. Surprisingly, for a long time, the Ginzburg–Landau theory did not receive the proper attention. It was only after the development of a microscopic theory that the importance of this extended phenomenological theory was generally recognized. Only gradually it has become clear that the theory accounts for important physical properties of the superconducting state. It was shown by Gor'kov that for temperatures near  $T_c$  the theory can be derived from the BCS theory [21]. One of the great successes of the theory was the prediction of the vortex state by Abrikosov [22]. Often the theory is now referred to as **GLAG theory** after the four scientists Ginzburg, Landau, Abrikosov, and Gor'kov. In 2003, A. A. Abrikosov and V. L. Ginzburg together with A. J. Leggett received the Nobel Prize in physics for the development of the theory of superconductivity and superfluidity.

The GLAG theory starts from the argument that in the normal superconducting transition in the absence of a magnetic field, we are dealing with a second-order phase transition (see [Section 4.1](#)). Landau had developed a theory exactly for such phase transitions. In the theory a parameter, the so-called order parameter, was defined, which in the new phase (here the superconducting phase) should increase continuously from zero at  $T_c$  up to the value 1 at  $T = 0$ . To describe the superconducting state, Ginzburg and Landau introduced a function  $\Psi(\mathbf{r})$  as the order parameter.<sup>12</sup> The quantity  $|\Psi(\mathbf{r})|^2$  can be interpreted as the density of the superconducting charge carriers. Since in the superconducting state  $|\Psi(\mathbf{r})|^2$  must approach zero continuously for  $T \rightarrow T_c$ , near  $T_c$  we can expand the Gibbs function<sup>13</sup>  $g_s$  of the superconducting phase in a Taylor series of the density  $|\Psi(\mathbf{r})|^2$ . Then we obtain

$$g_s = g_n + \alpha |\Psi|^2 + \frac{1}{2} \beta |\Psi|^4 + \dots \quad 4.19$$

Here, the Gibbs function  $g_n$  of the normal conducting phase appears, since for  $\Psi = 0$  the Gibbs

function  $g_s$  must be equal to  $g_n$ . Since for  $T < T_c$  we also have  $g_s < g_n$  (stability criterion), we find  $\alpha < 0$ .

Sufficiently close to  $T_c$  an approximation that includes only the first two terms of the series is satisfactory, that is, one that cuts off the series after the  $|\Psi|^4$  term. For temperatures close to the transition temperature, very general statements about the sign of the coefficients  $\alpha$  and  $\beta$  are possible:

- The coefficient  $\beta$  must be positive, otherwise a very large value of  $|\Psi|$  would always lead to a value of  $g_s$  that is smaller than  $g_n$ . The “minimum” of  $g_s$  would only be reached for  $|\Psi| \rightarrow \infty$ .
- For  $T < T_c$ , the coefficient  $\alpha$  must be negative, otherwise  $g_s$  would always be larger than  $g_n$ , since  $\beta$  is positive.
- For  $T > T_c$ ,  $\alpha$  must be positive. In this regime the normal state should have the smaller value of the Gibbs function, leading to  $|\Psi| = 0$  as the most favorable solution.

Therefore, for temperatures close to  $T_c$ , the coefficients  $\alpha$  and  $\beta$  can also be expanded in Taylor series of the temperature. Here, we include only the first nonvanishing coefficient. For  $\alpha$ , we can write

$$\alpha(T) = \alpha(0) \left( \frac{T}{T_c} - 1 \right) \quad \text{4.20a}$$

However, the coefficient  $\beta$  can be taken as constant:

$$\beta(T) = \beta = \text{const.} \quad \text{4.20b}$$

The rather abstract expansion coefficients  $\alpha$  and  $\beta$  can now be connected in a simple way with the so-called “thermodynamic critical field”  $B_{\text{cth}}$  and with the equilibrium density  $n_s$  in zero field. In the following, we will deal with  $B_{\text{cth}}$  many times. If we denote the equilibrium value of  $\Psi$  sufficiently far away from any interface by  $\Psi_\infty$ , then we have the relation  $n_s = |\Psi_\infty|^2$ . We introduce the magnetic field  $B_{\text{cth}}$  based on the difference  $g_n - g_s$ :

$$g_n - g_s = -\alpha|\Psi_\infty|^2 - \frac{1}{2}\beta|\Psi_\infty|^4 = \frac{1}{2\mu_0}B_{\text{cth}}^2 \quad \text{4.21}$$

In [Section 4.6.1](#) we will see that for a type-I superconductor under certain conditions  $B_{\text{cth}}$  exactly corresponds to the critical field  $B_c$ .

One obtains an additional equation for  $\alpha$  and  $\beta$  from the fact that at equilibrium  $g_s(|\Psi_\infty|^2)$  reaches a minimum. For the equilibrium value  $|\Psi_\infty|^2$ , we must have also  $dg_s/d|\Psi|^2 = 0$ . This yields

$$\alpha + \beta |\Psi_\infty|^2 = 0$$

4.22

From this we obtain

$$n_s = |\Psi_\infty|^2 = -\frac{\alpha}{\beta} \quad 4.23$$

and from Eq. (4.21) we find

$$B_{\text{cth}}^2 = \mu_0 \frac{\alpha^2}{\beta} \quad 4.24$$

From the temperature dependences of Eqs. (4.20a) and (4.20b) for  $\alpha$  and  $\beta$ , we see immediately that, near  $T_c$ ,  $n_s$  and  $B_{\text{cth}}$  are proportional to  $(1 - T/T_c)$ , that is, for  $T \rightarrow T_c$  they linearly approach zero. So we have<sup>14</sup>

$$n_s(T) = n_s(0)(1 - T/T_c) \quad \text{and} \quad B_{\text{cth}}(T) = B_{\text{cth}}(0)(1 - T/T_c)$$

By solving for  $\alpha$  and  $\beta$ , we find

$$\alpha = -\frac{1}{\mu_0} \frac{\beta_{\text{cth}}^2}{n_s} \quad 4.25a$$

$$\beta = -\frac{1}{\mu_0} \frac{\beta_{\text{cth}}^2}{n_s^2} \quad 4.25b$$

Now we can see directly that a second-order phase transition is described by Eq. (4.19) or (4.21):

- For  $T = T_c$  we have  $g_s = g_n$ , since  $|\Psi| = 0$ .
- The derivative  $\partial g_s / \partial T$  is

$$\frac{\partial g_s}{\partial T} = \frac{\partial g_n}{\partial T} - \frac{B_{\text{cth}}}{\mu_0} \frac{\partial B_{\text{cth}}}{\partial T} = \frac{\partial g_n}{\partial T} + \frac{B_{\text{cth}}^2(0)}{\mu_0} \left(1 - \frac{T}{T_c}\right) \frac{1}{T_c}$$

At  $T_c$  the second-term vanishes, that is,  $\partial g / \partial T$  passes through  $T_c$  continuously.

- For the second derivative  $\partial^2 g_s / \partial T^2$ , one finds

$$\frac{\partial^2 g_s}{\partial T^2} = \frac{\partial^2 g_n}{\partial T^2} - \frac{B_{\text{cth}}^2(0)}{\mu_0} \frac{1}{T_c^2}$$

We see that  $\partial^2 g / \partial T^2$  jumps by the amount  $B_{\text{cth}}^2(0)/(\mu_0 T_c^2)$ , as it must for a second-order phase transition.

We note that we can also describe a first-order phase transition in a similar way. In this case we must supplement the series expansion in Eq. (4.19) by a term  $|\Psi|^6$ , and a negative sign of  $\beta$

must be allowed.

The crucial extension of the phenomenological description is achieved by the ansatz of the Gibbs function of the superconductor in a magnetic field under the assumption of a possible spatial variation of  $\Psi$ . Hence, one uses the ansatz

$$g_s(B) = g_n + \alpha|\Psi|^2 + \frac{1}{2}\beta|\Psi|^4 + \frac{1}{2\mu_0}|\mathbf{B}_a - \mathbf{B}_i|^2 + \frac{1}{2m}\left(\left(\frac{\hbar}{i}\nabla - q\mathbf{A}\right)\Psi\right)^2 \quad 4.26$$

where  $m$  and  $q$  are the mass and charge, respectively, of the particles described by  $\Psi$ , that is,  $m = 2m_e$  and  $|q| = 2e$  for Cooper pairs, and  $\nabla$  is a differential operator, namely the gradient

$$\nabla\Psi = \text{grad}\Psi = \frac{\partial\Psi}{\partial x}\mathbf{e}_x + \frac{\partial\Psi}{\partial y}\mathbf{e}_y + \frac{\partial\Psi}{\partial z}\mathbf{e}_z$$

operating on the function  $\Psi$ .

We see that two additional terms appear. The first term refers to the energy needed to change the magnetic field from  $\mathbf{B}_a$ , the external field in the absence of the superconductor, to the value  $\mathbf{B}_i$ . For the Meissner phase with  $\mathbf{B}_i = 0$ , this term yields the total energy to be supplied for the magnetic field expulsion. The second term takes into account a possible spatial variation of  $\mathbf{B}_i$  and  $\Psi$  within the superconductor. It includes the supercurrents leading to a variation of the magnetic field. Furthermore, it contains the energy needed to establish a spatial variation of the Cooper pair density. This contribution introduces a “stiffness” of the wave function, which gains importance at the phase boundary between the superconducting and normal conducting phases. We note that this second term is constructed quite analogously to the expression in the Schrödinger equation of the kinetic energy of a particle with mass  $m$  and charge  $q$ .

One obtains the Gibbs function for the total superconducting sample from an integration of Eq. (4.26) over the volume  $V$  of the sample:

$$\int_V \left\{ g_n + \alpha|\Psi|^2 + \frac{1}{2}\beta|\Psi|^4 + \frac{1}{2\mu_0}|\mathbf{B}_a - \mathbf{B}_i|^2 + \frac{1}{2m}\left(\left(\frac{\hbar}{i}\nabla - q\mathbf{A}\right)\Psi\right)^2 \right\} \cdot dV \quad 4.27$$

This function  $G_s$  must be minimized by the variation of  $\Psi$  and  $\mathbf{A}$ . The variation then yields the two equations of the Ginzburg–Landau theory:

$$\frac{1}{2m}\left(\frac{\hbar}{i}\nabla - q\mathbf{A}\right)^2\Psi + \alpha\Psi + \beta|\Psi|^2\Psi = 0 \quad 4.28$$

$$\mathbf{j}_s = \frac{q}{2mi}(\Psi^*\nabla\Psi - \Psi\nabla\Psi^*) - \frac{q^2}{m}|\Psi|^2\mathbf{A} \quad 4.29$$

Here,  $\Psi^*$  is the complex conjugate function to  $\Psi$ .

This system of differential equations must still be supplemented by a proper boundary condition. Frequently, in this case, one applies the obvious condition that the supercurrent cannot flow out of the superconductor, that is, that the current (Eq. (4.29)) perpendicular to the

surface of the superconductor must vanish.

Next we will look in detail at the Ginzburg–Landau equations (4.28) and (4.29) or at the Gibbs function (4.27) in various limiting cases and compare the theoretical predictions with the experimental results.

## 4.5 Characteristic Lengths of the Ginzburg–Landau Theory

In the following, we will show that the Ginzburg–Landau equations contain two characteristic lengths, namely the London penetration depth  $\lambda_L$  and the Ginzburg–Landau coherence length  $\xi_{GL}$ . At this stage we cannot avoid a number of derivations and formulas. However, they are not very difficult.

We start by looking at Eq. (4.29). We want to rewrite this equation by normalizing  $\Psi$  to the value  $\Psi_\infty$ . With the notation  $\psi = \Psi/\Psi_\infty$ , we find

$$\mathbf{j}_s = \frac{q\hbar|\Psi_\infty|^2}{2mi}(\psi^*\nabla\psi - \psi\nabla\psi^*) - \frac{q^2|\Psi_\infty|^2}{m}|\psi|^2\mathbf{A} \quad 4.30a$$

With the definition (1.10) of the London penetration depth,  $\lambda_L = \sqrt{m/(\mu_0 q^2 n_s)}$ , and the relation  $n_s = |\Psi_\infty|^2$ , we find

$$\mathbf{j}_s = \frac{\hbar}{2iq}\frac{1}{\mu_0\lambda_L^2}(\psi^*\nabla\psi - \psi\nabla\psi^*) - \frac{1}{\mu_0\lambda_L^2}|\psi|^2\mathbf{A} \quad 4.30b$$

Using  $\psi = \psi_0 e^{i\phi}$  for calculating the gradient in the brackets ( $\nabla\psi = e^{i\phi}\nabla\psi_0 + \psi_0 e^{i\phi} i\nabla\phi$ ), we obtain

$$\mathbf{j}_s = \psi_0^2 \frac{\hbar}{q} \frac{1}{\mu_0\lambda_L^2} \nabla\phi - \frac{1}{\mu_0\lambda_L^2} \psi_0^2 \mathbf{A} \quad 4.30c$$

If the function  $\Psi$  is spatially constant,  $\nabla\phi$  vanishes, and  $|\psi| = 1.0$ . Then we have

$$\mathbf{j}_s = -\frac{1}{\mu_0\lambda_L^2} \mathbf{A} \quad 4.31$$

Taking the curl on both sides and using  $\text{curl } \mathbf{A} = \mathbf{B}$ , we obtain the second London equation (1.14):

$$\mathbf{B} = -\mu_0\lambda_L^2 \text{curl } \mathbf{j}_s \quad 1.14$$

We see that we recover the London theory in the case of a spatially constant Cooper pair density  $n_s$ . However, going beyond this case, the second Ginzburg–Landau equation apparently can take into account the supercurrents for a spatially varying wave function.

Let us turn to the first Ginzburg–Landau equation (4.28). Again we normalize  $\Psi$  to the value  $\Psi_\infty$ . After a short calculation we find

$$\frac{1}{2m} \left( \frac{\hbar}{i} \nabla - q \mathbf{A} \right)^2 \psi + \alpha \psi - \alpha |\psi|^2 \psi = 0 \quad 4.32\text{a}$$

Here, we must use the relation (4.23) to change the term  $\beta |\Psi_\infty|^2$ , appearing on the left-hand side, into  $-\alpha$ . We divide both sides by  $\alpha$  and obtain

$$\frac{\hbar^2}{2m\alpha} \left( \frac{1}{i} \nabla - \frac{q}{\hbar} \mathbf{A} \right)^2 \psi + \psi - |\psi|^2 \psi = 0 \quad 4.32\text{b}$$

Here, we have taken Planck's constant  $\hbar$  in front of the bracket on the left-hand side. The quantity  $-\hbar^2/(2m\alpha)$  has the dimension of [length]<sup>2</sup>. Obviously, it yields a second characteristic length of the Ginzburg–Landau theory, the Ginzburg–Landau coherence length  $\xi_{\text{GL}}$ , given by

$$\xi_{\text{GL}} = \sqrt{\frac{-\hbar^2}{2m\alpha}} \quad 4.33$$

Then the second Ginzburg–Landau equation can be written as

$$-\xi_{\text{GL}}^2 \left( \frac{\nabla}{i} - \frac{q}{\hbar} \mathbf{A} \right)^2 \psi + \psi - |\psi|^2 \psi = 0 \quad 4.34$$

With the temperature dependence of  $\alpha$  (Eq. (4.20a)), we find immediately also the temperature dependences of  $\lambda_L$  and  $\xi_{\text{GL}}$ :

$$\lambda_L(T) = \frac{\lambda_L(0)}{\sqrt{1 - T/T_c}} \quad 4.35$$

$$\xi_{\text{GL}}(T) = \frac{\xi_{\text{GL}}(0)}{\sqrt{1 - T/T_c}} \quad 4.36$$

For  $T \rightarrow T_c$  both quantities approach infinity. We note that Eqs. (4.35) and (4.36) are valid only close to  $T_c$ , although  $\lambda_L(0)$  and  $\xi_{\text{GL}}(0)$  appear in the equations. The Ginzburg–Landau theory is valid only in this limit.

Now we can introduce the ratio

$$\kappa = \frac{\lambda_L}{\xi_{\text{GL}}} \quad 4.37$$

referred to as the **Ginzburg–Landau parameter**. Within the Ginzburg–Landau equations presented earlier, it is independent of the temperature and of the magnetic field.

In Eqs. (4.30b) and (4.34) we could also have normalized the other quantities having a dimension. Then we would find that the dimensionless Ginzburg–Landau equations would

depend only on the Ginzburg–Landau parameter  $\kappa$ . Hence, this parameter is crucial for the behavior of these equations.

Which length is indicated by  $\xi_{\text{GL}}$ ? This is illustrated by a simple situation, in which the superconductor extends in the  $x$ -direction from  $x = 0$  up to  $x \rightarrow \infty$ . In the  $y$  and  $z$  directions, the superconductor is assumed to be extended infinitely. For  $x = 0$  we assume  $|\psi| = 0$ . Furthermore, we assume  $\mathbf{A} = 0$ . Then we can find a *real* solution for  $\psi$  from the equation

$$\xi_{\text{GL}}^2 \frac{d^2\psi}{dx^2} + \psi - \psi^3 = 0 \quad 4.38$$

which depends only on  $x$ . For  $x \geq 0$ , this equation has the solution

$$\psi(x) = \tanh(x/\sqrt{2}\xi_{\text{GL}}) \quad 4.39$$

shown in [Figure 4.6](#). According to Eq. (4.39),  $\psi(x)$  first increases linearly from 0, and then it approaches the limiting value 1 in the interior of the superconductor. We see that, at least in the situation we have discussed,  $\xi_{\text{GL}}$  can be interpreted as the characteristic length within which the order parameter  $\psi$  can change.

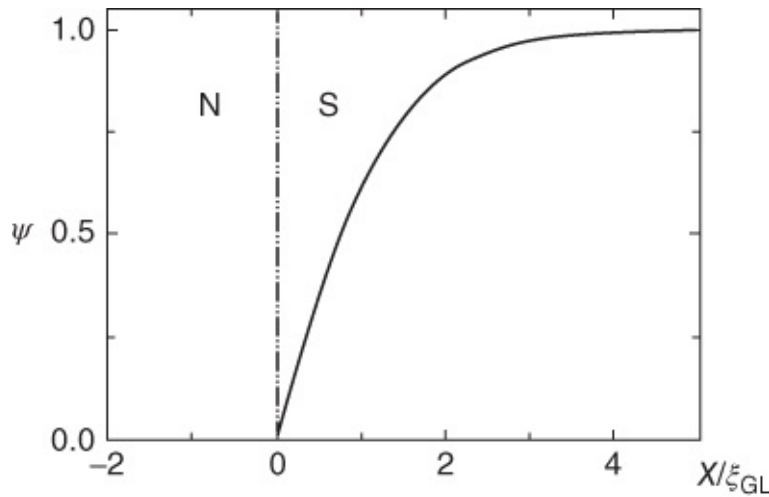


**Figure 4.6** Variation of the function  $\psi(x)$  according to Eq. (4.39) at the edge of a superconducting half-space.

Now we know the two length scales of the Ginzburg–Landau theory. The fact that the Ginzburg–Landau theory is valid only close to  $T_c$  should not diminish the importance of  $\lambda_L$  and  $\xi_{\text{GL}}$  as the characteristic length scales within which the supercurrents (or the magnetic field) and the Cooper pair density (or  $\Psi$ ) can change. Both lengths are fundamental to the superconducting state. They can be analyzed further within the microscopic theory.

At very low temperatures, in the case of conventional superconductors, one finds that  $\lambda_L$  is approximately constant. The deviation from this constant value  $\lambda_L(0)$  decreases exponentially with decreasing temperature. On the other hand, in the case of unconventional superconductors, for which the energy gap has locations with value zero along certain crystal directions, the

difference  $\Delta\lambda = \lambda_L(T) - \lambda_L(0)$  increases from zero following a power law. In the case of the  $d_{x^2-y^2}$  symmetry,  $\Delta\lambda$  is proportional to  $T$ , if the samples are sufficiently pure. For impure samples, one observes a  $T^2$  law. In [Chapter 2](#) we listed the values of  $\lambda_L(0)$  for many conventional and unconventional superconductors.

[Figure 4.7](#) shows experimental results for the temperature dependence of the penetration depth in mercury. Here,  $\lambda_L$  was determined from the magnetization of mercury colloid, that is, from small Hg balls [23]. For this material, as well as for many other conventional superconductors, the observed temperature dependence can be approximated over a wide temperature range by the empirical expression

$$\frac{\lambda_L(T)}{\lambda_L(0)} \propto \left[ 1 - \left( \frac{T}{T_c} \right)^4 \right]^{-1/2} \quad 4.40$$

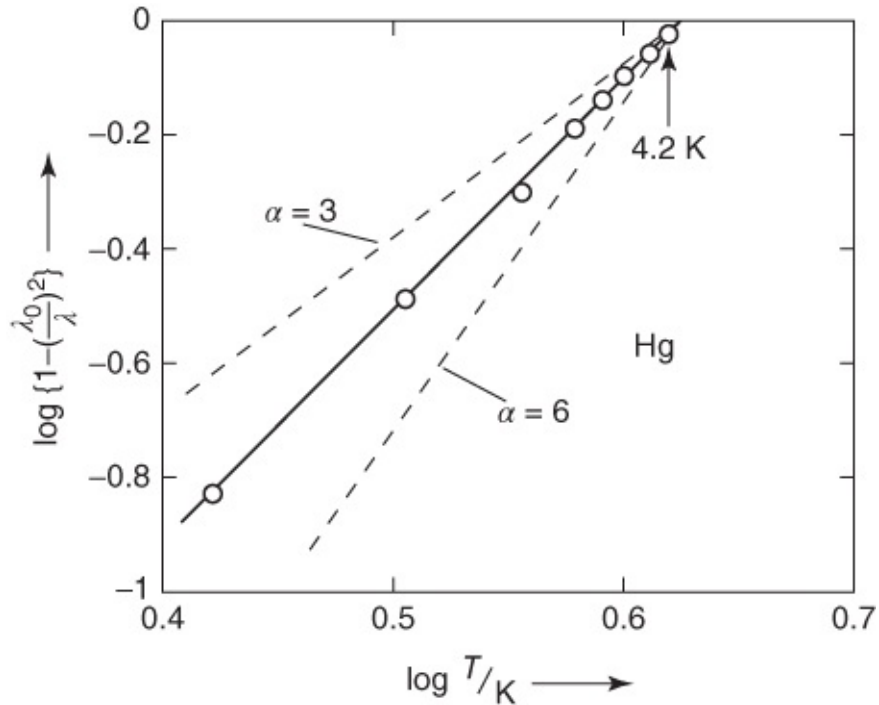


[Figure 4.7](#) Temperature dependence of the penetration depth of Hg [23]. The solid line corresponds to the exponent  $a = 4$  in the bracket of Eq. (4.40). For comparison, the cases  $a = 3$  and  $a = 6$  are also shown by the dashed curves.

For  $T \rightarrow T_c$  this relation yields Eq. (4.35), in agreement with the Ginzburg–Landau theory.<sup>15</sup> The plot in [Figure 4.7](#) allows the comparison with Eq. (4.40). The solid straight line corresponds to this equation. The agreement between the analytic expression and the experimental data is excellent.

For comparison we show in [Figure 4.8](#) the experimental results obtained for a highly pure  $\text{YBa}_2\text{Cu}_3\text{O}_7$  single crystal. The penetration depth was determined from the surface impedance of the crystal (see also [Section 7.5.1](#)). The latter was found from the frequency shift of a resonating cavity into which the crystal had been inserted. The data referring to the left vertical

axis show the ratio  $\lambda_L(0)^2/\lambda_L(T)^2$ , which is proportional to the density of Cooper pairs according to Eq. (1.10). The data referring to the right vertical axis show the difference  $\Delta\lambda = \lambda_L(T) - \lambda_L(0)$ . For each axis there are two curves, which correspond to the penetration depth along the  $a$  and  $b$  directions of the crystal, respectively. We clearly see the linear increase in  $\Delta\lambda$  over a wide temperature range.

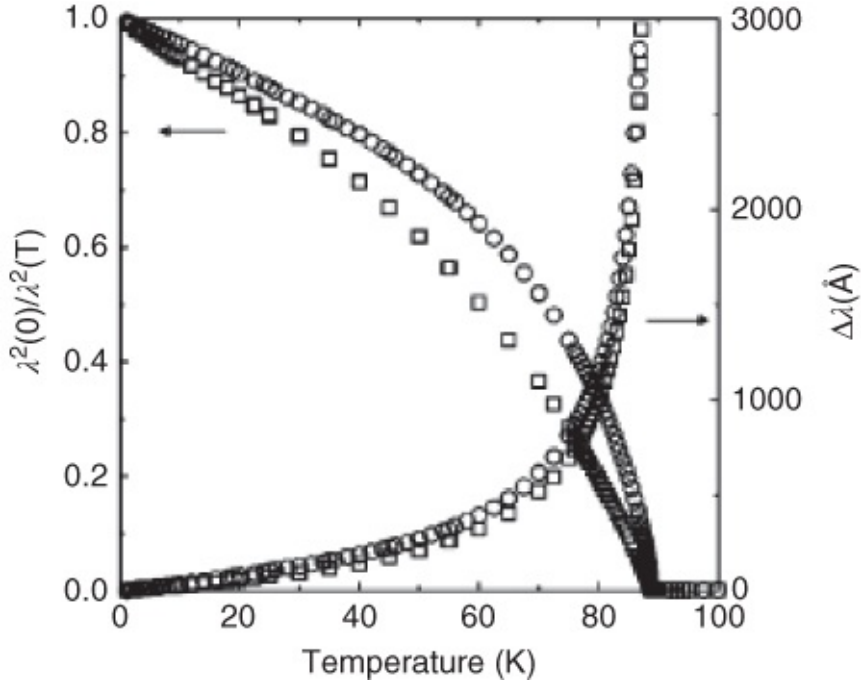


**Figure 4.8** Temperature dependence of the magnetic penetration depth in highly pure  $\text{YBa}_2\text{Cu}_3\text{O}_7$ . The circles indicate the penetration depth along the  $a$ -direction of the crystal, and the squares indicate the penetration depth along the  $b$ -direction. At low temperatures, the measurement yielded the values  $\lambda_a(0) = 160 and  $\lambda_b(0) = 80 [24].$$

The Ginzburg–Landau coherence length  $\xi_{\text{GL}}$  is much more difficult to determine experimentally than the penetration depth  $\lambda_L$ . (Numerical values of  $\xi_{\text{GL}}$  are listed in [Chapter 2](#) for a number of superconductors.) Usually one employs indirect methods. The value of  $\xi_{\text{GL}}$  is closely connected with the upper critical field of type-II superconductors, from which it can be determined (see [Section 4.7.1](#)). Another indirect method uses the analysis of the electrical conductivity above the transition temperature. Because of thermal fluctuations, superconducting small regions always appear temporarily closely above  $T_c$ , contributing to an enhanced electrical conductivity. We will return to this subject in [Section 4.8](#).

Within the Ginzburg–Landau theory,  $\lambda_L$  and  $\xi_{\text{GL}}$  represent material properties, which depend on the Cooper pair density and on the thermodynamic critical field  $B_{\text{cth}}$  because of the parameters  $\alpha$  and  $\beta$ . The microscopic theory provides us with another important relation: the dependence of  $\lambda_L$  and  $\xi_{\text{GL}}$  on the electron mean free path  $l^*$ .<sup>16</sup> For conventional superconductors in the limit  $T \rightarrow 0$ , one finds

$$\lambda_L(T=0, l^*) = \lambda_L(T=0, l^* \rightarrow \infty) \left\{ 1 + \frac{\xi_{GL}(T=0, l^* \rightarrow \infty)}{l^*} \right\}^{1/2} \quad 4.41$$

and for  $l^* = \xi_{GL}(T=0, l^* \rightarrow \infty)$  one has

$$\xi_{GL}(T=0, l^*) = \{\xi_{GL}(T=0, l^* \rightarrow \infty)l^*\}^{1/2} \quad 4.42$$

This dependence is not yet taken into account by the expressions (4.35), (4.36), and (4.40), which are valid only in the limit of very large mean free paths,  $l^* \rightarrow \infty$ . From Eqs. (4.41) and (4.42) we see that, with decreasing  $l^*$ , the length  $\lambda_L$  increases and the length  $\xi_{GL}$  decreases.

Hence, the Ginzburg–Landau parameter  $\kappa$  strongly depends on  $l^*$ . It increases with decreasing  $l^*$ .

The length  $l^*$  depends on the purity of the samples and can be controlled by the admixture of impurities. In [Section 4.7](#) we will see that by varying the degree of purity, one can change a type-I superconductor into a type-II superconductor.

Together with the BCS coherence length presented in [Section 3.1.1](#), we have introduced three different characteristic lengths of a superconductor:

1. penetration depth  $\lambda_L$  measuring the decay of the magnetic field in the interior of the superconductor;
2. average extension  $\xi_0$  of a Cooper pair as a measure of the distance within which the correlation forming Cooper pairs is active;
3. coherence length  $\xi_{GL}$  as the smallest length within which the Cooper pair density can vary – it is always larger than  $\xi_0$ , since the number density of Cooper pairs cannot vary within a distance smaller than the average extension of a Cooper pair.

The coherence length  $\xi_0$  is nearly temperature-independent, and in the limit  $l^* \rightarrow 0$  it is about equal to  $l^*$ . In different limiting cases, we can also find simple relations for this length. For example, in the BCS theory:

$$\xi_0(T=0, l^* \rightarrow \infty) = 0.18 \frac{\pi \hbar v_F}{2k_B T_c} \quad 4.43$$

$$\xi_{GL} \approx \xi_0 \frac{\lambda_L(T, l^*)}{\lambda_L(T=0, l^* \rightarrow \infty)} \quad 4.44$$

where  $v_F$  is the Fermi velocity and  $k_B$  is Boltzmann's constant. Such relations represent good approximations mostly only within specific regimes of  $T$  and  $l^*$ . In general, their mathematical derivation from the microscopic theory requires appreciable effort.

It is interesting to note that in 1951 Pippard postulated a coherence length for the interpretation of high-frequency measurements [25]. Based on this coherence length, which is closely related to  $\xi_0$ , Pippard could extend the London theory by claiming that the supercurrent density  $j_s(x, y, z)$

should depend not only on the magnetic field  $B(x,y,z)$  at the location  $(x,y,z)$  but also on the average field in a region with an extension of about the coherence length.

In the following, we return again to the thermodynamic properties of the superconducting state, and we start with type-I superconductors.

## 4.6 Type-I Superconductors in a Magnetic Field

Using the methods of thermodynamics, we look at the stability of the Meissner phase of type-I superconductors as a function of the temperature and of the applied magnetic field. We will see that in the simplest case the critical field of these superconductors, at which the transition from the Meissner phase into the normal conducting phase sets in, is identical with the thermodynamic critical field discussed in [Section 4.4](#). However, we will also see that one observes a much more complex behavior if the magnetic field at the sample edge differs from the applied field because of the shape of the sample.

We will also use thermodynamics to understand the behavior of superconductors under pressure.

### 4.6.1 Critical Field and Magnetization of Rod-Shaped Samples

[Figure 4.9](#) shows again the Meissner–Ochsenfeld effect for a rod-shaped superconductor. If the length  $l$  of the rod is much larger than the diameter, the magnetic field is slightly distorted only at the ends. Along the rod practically we have the same field  $B_a$  as in a large distance from the rod. For simple shapes of the sample (ellipsoids with principal axis parallel to the field), we can express the influence of the sample geometry by a number, the demagnetization coefficient  $N_M$ . For a long rod in a magnetic field parallel to its axis, the demagnetization coefficient is  $N_M = 0$ . In this case, the magnetic field at the surface must not be corrected, since it is identical with the external field  $B_a$  at a large distance from the sample. This illustrates the particular simplicity of this sample geometry.

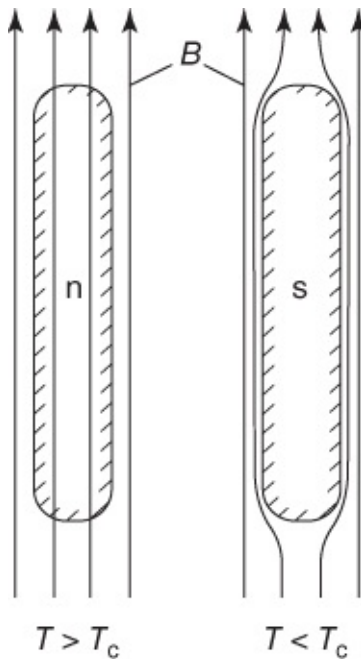


**Figure 4.9** Magnetic field expulsion for a rod-shaped sample. The sample is cooled down in the field  $B$ .

Because of its significance, we want to also present the field expulsion in the Meissner phase in a different way. Because of the shielding currents, which completely compensate the external field in the interior of the rod-shaped sample, the rod carries a magnetic moment  $m$ . Formally, we can speak of a magnetization  $M$  by writing  $M = m/V$ , where  $V$  is the sample volume. This magnetization corresponds to that of an ideal diamagnet with the susceptibility<sup>17</sup>  $\chi = -1$ .

In [Figure 4.10](#) we show this magnetization  $M$  as a function of the external field  $B_a$  for a long rod with its axis oriented parallel to the field. Following the standard custom, the *negative* magnetization is plotted versus the external magnetic field. The magnetization increases proportional to the external field. The superconductivity breaks down only if the critical field is exceeded.

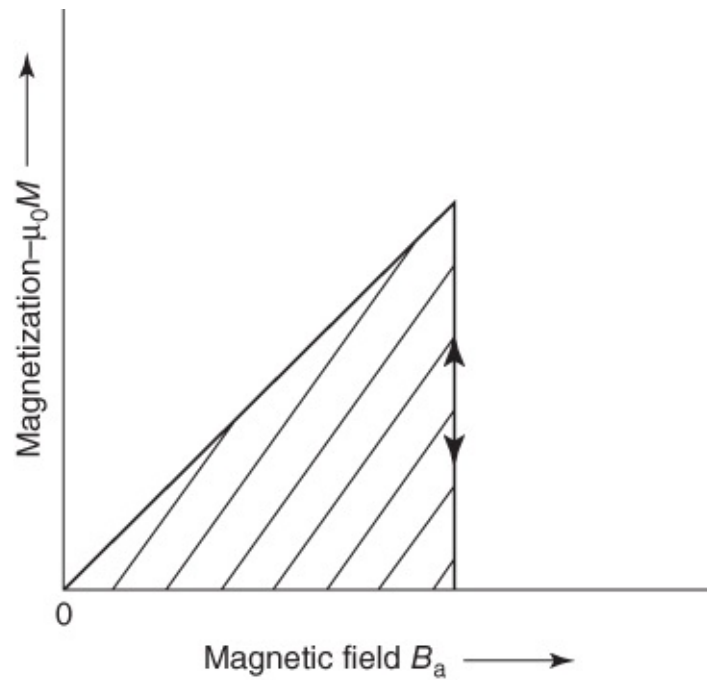


**Figure 4.10** Magnetization of a rod-shaped sample ( $N_M = 0$ ) in a magnetic field parallel to the axis. During a reversible transition, the same curve is followed for increasing and decreasing field  $B$ .

In [Figure 4.11](#) the magnetic field  $B_i$  observed in the interior of the sample, say, within a narrow channel parallel to the axis, is plotted versus the external field  $B_a$ . Because of the shielding current, the inner field  $B_i$  remains exactly zero until the critical field  $B_c$  is reached.<sup>18</sup> For all external fields  $B_a > B_c$  we have  $B_i = B_a$ , since the sample is normal conducting in this case.

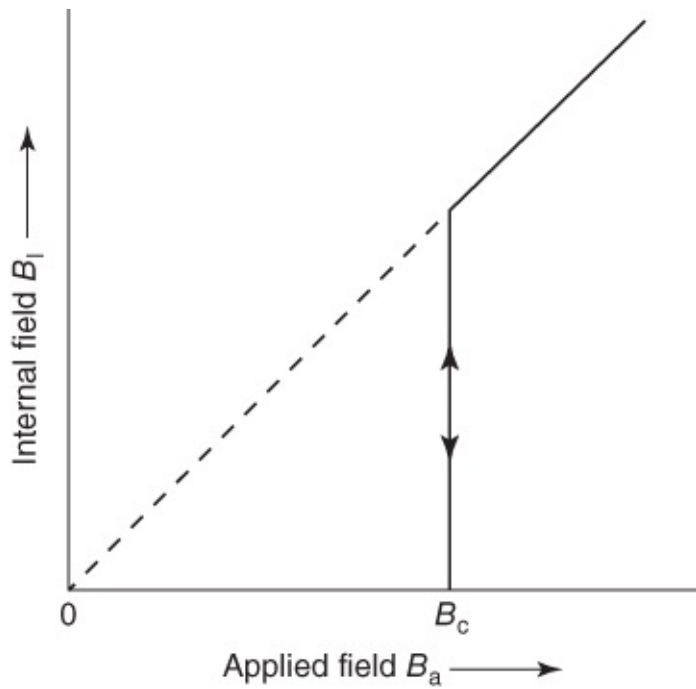


**Figure 4.11** Magnetic field in the interior of a rod-shaped sample ( $N_M = 0$ ) in a magnetic field parallel to the axis. During a reversible transition, the same curve is followed for increasing and decreasing field  $B$ .

[Figures 4.10](#) and [4.11](#) present the same information. Both plots are used frequently, and they are adjusted to different experiments: measurement of  $M$  by means of the induction or of  $B_i$ , say, by using a Hall probe.<sup>19</sup> The difference between type-I and type-II superconductors is clearly seen from the variation of  $M$  or of  $B_i$  as a function of  $B_a$  (see [Section 4.7.1](#)).

We note that the measurement of the magnetization represents a very simple method for determining the transition temperature  $T_c$ . One places the sample within an induction coil and measures the self-inductance as a function of the temperature using a small a.c. magnetic field. The self-inductance drops abruptly if superconductivity sets in. Compared to a measurement of the electrical resistance by means of a current–voltage curve (see [Section 1.1](#)), this magnetic measurement of the transition temperature has the advantage that the shielding currents must flow along the total sample surface in order to provide the shielding. Frequently, inhomogeneous samples, where the current–voltage measurement can indicate superconductivity because of a single continuous current path, do not show perfect shielding, in this way signaling the inhomogeneity.<sup>20</sup>

Now we apply the rules of thermodynamics to the Meissner state. We start from the Eq. (4.9):

$$dG = -SdT + Vdp - m dB \quad 4.9$$

First, we consider the superconducting phase in the absence of a magnetic field. Then the term  $mB$  vanishes. Furthermore, we keep the superconductor at constant pressure and only vary the temperature. For  $T < T_c$  the Gibbs function  $G_s$  of the superconductor must be smaller than  $G_n$ , the Gibbs function of the normal conductor. At  $T = T_c$ , we have  $G_s = G_n$ .

We can determine the difference  $G_n - G_s$ , which is a measure of the stability of the superconducting state, as a function of the temperature. We use the fact that the superconducting phase becomes unstable in the presence of a sufficiently strong external magnetic field. The reason for this is an increase in  $G_s$  with increasing field  $B$ , resulting in the fact that above a critical field  $G_s$  will be larger than  $G_n$  and, hence, will become unstable. Practically, the Gibbs function  $G_n$  of the normal conducting phase is independent of the magnetic field, since at least in most cases in the normal conductor the generated magnetic moments are very small.

For obtaining  $G_n - G_s$  as a function of  $T$ , we must determine the critical field  $B_c$  at different temperatures. Then the term  $\int_0^{B_c} m \, dB$  yields  $G_n - G_s$  at the corresponding temperature. We have

$$\begin{aligned} G_s(B) - G_s(0) &= - \int_0^B m \, dB & 4.45 \\ G_n(B) - G_n(0) &= 0 \\ G_n(B_c) - G_s(B_c) &= 0 \end{aligned}$$

The first equation is found by integrating Eq. (4.9) at constant temperature and constant pressure. At  $B_c$  the Gibbs functions  $G_s$  and  $G_n$  must be just equal. From these three equations, one finds

$$G_n(T) - G_s(T) = - \int_0^{B_c(T)} m \, dB \quad 4.46$$

Since in equilibrium the magnetic moment of the superconductor must always be oriented antiparallel to  $B$ , we have  $G_n(T) > G_s(T)$  for all  $T < T_c$ .

For a more quantitative statement about the difference between the Gibbs functions of the superconducting and normal conducting phases, we must know the magnetic moment  $m$  as a function of  $B$ . Now we restrict ourselves to the rod-shaped sample geometry, and we assume a spatially constant external magnetic field. In this case, the local magnetic moment  $m$  and the magnetization  $M$  are simply connected with each other:

$$m = MV \quad 4.47$$

Here,  $V$  is the sample volume, taken to be independent of the magnetic field, the pressure, and the temperature. With these conditions, we have

$$G_n - G_s = -V \int_0^{B_c} M \, dB \quad 4.48$$

For additional information, we must know the magnetization  $M$  as a function of  $B$ . For a “thick” rod of a type-I superconductor,<sup>21</sup> we have  $\chi = -1$ . Then the magnetization is in good approximation

$$M = \chi \frac{B}{\mu_0} = -\frac{B}{\mu_0} \quad 4.49$$

where  $\mu_0 = 4\pi \times 10^{-7}$  V s/A m. This yields the following simple expression for  $G_n - G_s$ :

$$G_n - G_s = \frac{V}{\mu_0} \int_0^{B_c} B dB = V \frac{B_c^2}{2\mu_0} = V \frac{B_{\text{cth}}^2}{2\mu_0} \quad 4.50$$

Now we can calculate quantitatively the difference  $G_n - G_s$ , if we have determined the critical field  $B_c$  as a function of  $T$  for our simple geometry.

For a “thick” superconductor with fully developed shielding, the critical field  $B_c$  is identical to the thermodynamic field  $B_{\text{cth}}$ . We can see this from Eq. (4.21), if we integrate the latter over the sample volume. However, for a “thin” superconductor, with dimensions comparable to the London penetration depth,  $B_c$  is larger than  $B_{\text{cth}}$  (see [Section 4.6.3](#)).

The area under the magnetization curve of the “thick,” rod-shaped type-I superconductor, multiplied by the sample volume  $V$ , yields the difference of the thermodynamic potentials,  $G_n - G_s$ , in the field  $B = 0$ . However, we also emphasize that in the case of a more complicated dependence of the magnetization on the external field, as we will see for type-II superconductors, the area under the magnetization curve  $M(B)$  always yields the difference of the Gibbs functions,  $G_n - G_s$ . The only assumption is that the magnetization is reversible, that is, it is established only by means of equilibrium states. Reversibility exists if the same magnetization curve is obtained for increasing and for decreasing external fields. In the case of the “hard superconductors,” which we will discuss in [Section 5.3.2](#), this reversibility is absent.

In [Figure 4.12](#) the critical field  $B_c$  is plotted versus the temperature for different type-I superconductors. For all temperatures  $T < T_c$ , the experimental data are well approximated by the empirical expression:

$$B_c(T) = B_c(0)[1 - (T/T_c)^2] \quad 4.51$$

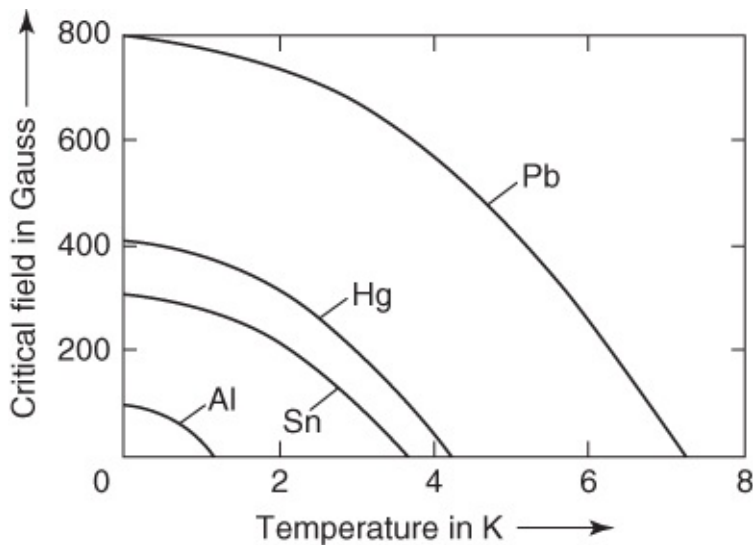


**Figure 4.12** Critical magnetic field plotted versus the temperature for different type-I superconductors ( $1 \text{ G} = 10^{-4} \text{ T}$ ).

Near  $T_c$ , this dependence approaches the linear dependence on temperature, as described by the Ginzburg–Landau theory.

#### 4.6.2 Thermodynamics of the Meissner State

In the following, we discuss the consequences for other properties of a superconductor resulting from the temperature dependence of the critical field according to Eq. (4.51). Here, we will use the strong advantage of the thermodynamic treatment, namely that all the important quantities can be obtained from the Gibbs function by means of simple differential operations.

We recall that the entropy  $S$  is found from  $G$  according to Eq. (4.10):

$$S = -\left(\frac{\partial G}{\partial T}\right)_{B,p} \quad 4.10$$

In the absence of a magnetic field, we have

$$S_n - S_s = -V \frac{B_{cth}}{\mu_0} \frac{\partial B_{cth}}{\partial T} \quad 4.52$$

Again we have neglected the  $T$  dependence of  $V$ , since it is very small. In [Section 4.6.6](#) we will return to this change of  $V$ , making the justification of our approximation more clear.

By looking at the temperature dependence of the critical field  $B_{cth}$ , as seen in [Figure 4.12](#) and as approximated by Eq. (4.51), we can immediately find the general behavior of  $S_n - S_s$ . For  $T \rightarrow T_c$  we have  $B_{cth} \rightarrow 0$ . Hence, we conclude that  $S_n - S_s \rightarrow 0$  for  $T \rightarrow T_c$ . At  $T_c$  (in the absence of a magnetic field) the entropies of the normal conducting and of the superconducting phases are equal, and no heat of transition appears at  $T_c$ . Hence, we are dealing with a second-order or higher-order phase transition. In our discussion of the specific heat (see [Section 4.2](#)), we have derived this result already in a different way.

At temperatures  $T < T_c$  the entropy difference  $S_n - S_s$  takes a positive value, since in the total range  $0 < T < T_c$  we have  $dB_{\text{cth}}/dT < 0$ . According to the third law of thermodynamics, for  $T \rightarrow 0$  also  $S_n - S_s$  must approach zero (the approximation (Eq. (4.51)) satisfies this condition). However, this means that  $S_n - S_s$  passes through a maximum. This fact has important consequences for the specific heat.

Further we note that at all temperatures  $0 < T < T_c$ , there exists a finite entropy difference  $S_n - S_s$ , that is, in this temperature range we have a first-order phase transition with a finite heat of transition.

[Figure 4.13](#) shows the temperature dependences of  $G_n$ ,  $G_s$ , and  $S_n - S_s$  plotted in arbitrary units on the vertical axis. At  $T = T_c$  the two curves  $G_n(T)$  and  $G_s(T)$  must not only take the same value but also have the same slope, as we have seen. This is the signature of a first-order phase transition. The transition to superconductivity is a second-order phase transition (as we will see explicitly in a moment), since at  $T_c$  the second derivatives of the Gibbs functions  $G_n$  and  $G_s$  are different.

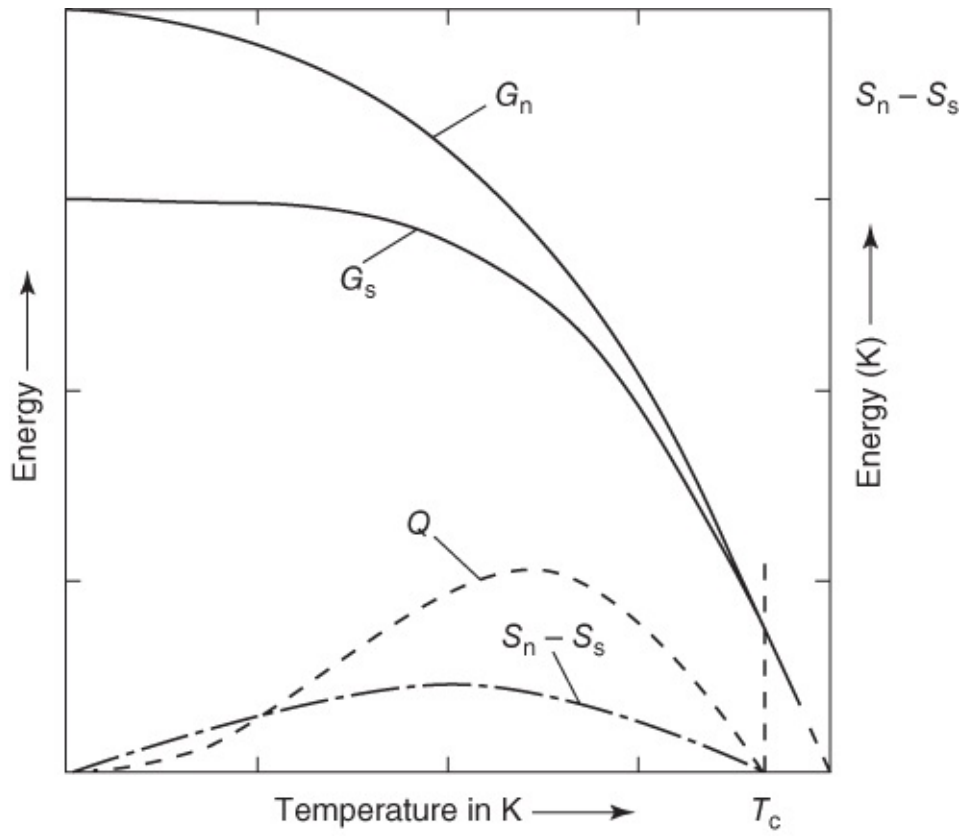


[Figure 4.13](#) Gibbs functions  $G_n$  and  $G_s$ , entropy difference  $S_n - S_s$ , and heat of transition  $Q$  plotted versus the temperature. Numerical example for 1 mol Sn:  $T_c = 3.72$  K;  $(G_n - G_s)_{T=0} = 5 \times 10^{-3}$  W s;  $(S_n - S_s)_{\text{max}} = 2.28 \times 10^{-3}$  W s/K; and  $Q_{\text{max}} = 5 \times 10^{-3}$  W s.

These results that we have derived from thermodynamics fit very well into our microscopic picture, as they should. From  $S_n - S_s > 0$ , we conclude that the superconducting phase has a

smaller entropy than the normal conducting phase. Without going into details, we recall that the entropy is a measure of the disorder of a physical system. Hence, from  $S_n > S_s$ , we conclude that the degree of order in the superconducting phase is larger than in the normal conducting phase. This higher degree of order can immediately be associated with the correlation between single electrons forming Cooper pairs and between the Cooper pairs themselves. This correlation amounts to an additional order in our system.

For  $T \rightarrow T_c$ , the Cooper pair density and the energy gap continuously approach zero. Hence, at  $T_c$  we cannot expect a heat of transition. Instead, our microscopic picture indicates that we deal with a transition of higher than first order. However, below  $T_c$  there exists a finite density of Cooper pairs. In an applied magnetic field permanent currents are generated. However, in type-I superconductors the Cooper pair density practically remains constant until the critical field is reached. At the critical field, the superconductivity breaks down, and all the Cooper pairs are broken up. This requires a finite heat of transition. At the transition from the superconducting to the normal conducting state, heat energy is consumed, namely  $(S_n - S_s)T$ . In an isothermal process this energy must be delivered to the system. However, if the transition from normal conducting to superconducting state is performed adiabatically, that is, thermally insulated with  $dQ = 0$ , the sample becomes colder, since the heat energy is extracted from the other degrees of freedom. Superconductors represent a substance that can be cooled by means of adiabatic demagnetization [26]. However, since much more effective cooling techniques have been developed, this particular method has not become an important application.

The second derivative of the Gibbs function with respect to the temperature yields the specific heat, here at constant pressure and constant  $B$  (see Eq. (4.13)). From Eq. (4.50),

$$G_n - G_s = V \frac{B_{cth}^2}{2\mu_0}$$

for the difference  $c_n - c_s$  of the specific heat in the normal state and in the superconducting state, we obtain

$$c_n - c_s = -\frac{VT}{\mu_0} \left\{ \left( \frac{\partial B_{cth}}{\partial T} \right)^2 + B_{cth} \frac{\partial^2 B_{cth}}{\partial T^2} \right\} \quad 4.53$$

or

$$c_s - c_n = \frac{VT}{\mu_0} \left\{ \left( \frac{\partial B_{cth}}{\partial T} \right)^2 + B_{cth} \frac{\partial^2 B_{cth}}{\partial T^2} \right\} \quad 4.54$$

Again we have taken the volume  $V$  as constant. Further we note that we insert here the specific volume, that is, the volume per unit mass. In this way we obtain specific quantities, here the specific heat, which refers to the amount of 1 g of the substance. The result of Eq. (4.54) was derived by Keesom [2] in 1924, but without a solid justification of the existence of a superconducting phase in the thermodynamic sense.

From Eq. (4.54) we see that at  $T = T_c$ , we have  $c_s > c_n$ . At  $T_c$  the critical field vanishes,  $B_{\text{cth}} = 0$ , and, hence,  $c_s - c_n > 0$ . At  $T_c$  the specific heat displays a jump, which is given by

$$(c_s - c_n)_{T=T_c} = \frac{VT_c}{\mu_0} \left( \frac{\partial B_{\text{cth}}}{\partial T} \right)_{T=T_c}^2 \quad 4.55$$

In the literature this important relation is referred to as **the Rutgers formula** [27]. It connects a thermal quantity, namely the jump of the specific heat, with the critical magnetic field. For a number of superconductors this relation is well satisfied. In [Table 4.1](#) we list some values of  $(c_s - c_n)_{T=T_c}$ , as obtained from thermal data and from measurements of the critical field.

**Table 4.1** Values of  $(c_s - c_n)_{T=T_c}$  obtained from thermal and magnetic data

Element	$T_c$ (K)	$(c_s - c_n)$ thermal data ( $10^{-3}$ W s/(mol K))	$(c_s - c_n)$ magnetic data ( $10^{-3}$ W s/(mol K))
Sn <sup>a</sup>	3.72	10.6	10.6
In <sup>a</sup>	3.40	9.75	9.62
Tl <sup>b</sup>	2.39	6.2	6.15
Ta <sup>a</sup>	4.39	41.5	41.6
Pb <sup>b</sup>	7.2	52.6	41.8

Test of the “Rutgers formula.”

<sup>a</sup> Ref. [28].

<sup>b</sup> Ref. [29].

Since we found  $d^2B_{\text{cth}}/dT^2 < 0$  and since  $dB_{\text{cth}}/dT$  becomes smaller and smaller with decreasing temperature, we find a temperature  $0 < T < T_c$  at which  $c_s = c_n$ . Below this temperature we have  $c_s < c_n$ . The intersection of  $c_s(T)$  and  $c_n(T)$  must appear at the temperature at which  $S_n - S_s$  reaches a maximum (see [Figure 4.13](#)).

Since the density of states represents an important quantity for superconductivity, we discuss the possibility for its determination from  $B_{\text{cth}}(T)$ . We start from Eq. (4.54). In many cases, the contribution of the lattice to the specific heat practically does not change at the onset of superconductivity. Hence, we can attribute the difference  $c_s - c_n$  completely to the electron system. So we obtain

$$c_{sE} - c_{nE} = \frac{VT}{\mu_0} \left\{ \left( \frac{\partial B_{\text{cth}}}{\partial T} \right)^2 + B_{\text{cth}} \frac{\partial^2 B_{\text{cth}}}{\partial T^2} \right\} \quad 4.56$$

According to [Figures 4.2](#) and [4.3](#) and due to the higher degree of order of the superconducting state, we can assume that in the superconducting state the specific heat of the electrons for  $T \rightarrow$

$0$  approaches zero faster than in the normal conducting state. We can express this as follows:  $c_{\text{SE}} \propto T^{1+a}$  with  $a > 0$ . This means that  $c_{\text{SE}}/T$  approaches zero for  $T \rightarrow 0$ . Then for sufficiently small temperatures, if  $c_{\text{SE}}/T$  is negligible compared to  $c_{\text{nE}}/T$ , we obtain

$$-\frac{c_{\text{nE}}}{T} = \frac{V}{\mu_0} \left\{ \left( \frac{\partial B_{\text{cth}}}{\partial T} \right)^2 + B_{\text{cth}} \frac{\partial^2 B_{\text{cth}}}{\partial T^2} \right\} \quad 4.57$$

According to Eq. (4.14), the quantity  $c_{\text{nE}}/T$  is equal to the Sommerfeld coefficient  $\gamma$ , which is proportional to  $N(E_F)$  due to Eq. (4.16). If we also assume that

$$\left( \frac{\partial B_{\text{cth}}}{\partial T} \right)^2 \ll B_{\text{cth}} \frac{\partial^2 B_{\text{cth}}}{\partial T^2}$$

which is always valid for sufficiently small temperatures, we find

$$\gamma = -\frac{V}{\mu_0} B_{\text{cth}} \frac{\partial^2 B_{\text{cth}}}{\partial T^2} \quad 4.58$$

and finally with Eq. (4.51) we get

$$\gamma = -\frac{V}{\mu_0} 2B_{\text{cth}} \frac{B_{\text{cth}}^2(0)}{T_c^2} \quad 4.59$$

We see that at sufficiently low temperatures, the observation of  $B_{\text{cth}}$  is independent of the special temperature dependence of the critical field and can serve for determining  $\gamma$  and thereby yield information about  $N(E_F)$ .

### 4.6.3 Critical Magnetic Field of Thin Films in a Field Parallel to the Surface

The behavior of thin films depends sensitively on the penetration depth, if the film thickness  $d$  becomes comparable to  $\lambda_L$ . We discussed this already in [Section 1.4](#) ([Figures 1.14](#) and [1.15](#)). As a result, we found that the magnetic field varies within the plate as given by Eq. (1.22):

$$B_z(x) = B_a \frac{\cosh(x/\lambda_L)}{\cosh(d/2\lambda_L)} \quad 4.60$$

The critical field in a thin film represents a highly important subject. As the critical field, we understand the field that must be applied to completely destroy the superconductivity, that is, to make  $G_s$  equal to  $G_n$ . With decreasing film thickness, this critical field  $B_c$  becomes larger and larger. For a thickness  $d = \lambda_L$  it can be larger by more than a factor 10 than the thermodynamic field  $B_{\text{cth}}$  we observe, when the shielding layer is fully developed.

This surprising result can be understood in a simple way. In [Section 4.1](#) we saw that the free

enthalpy of the superconducting state increases with the external field  $B_a$ . Because of Eq. (4.45) we have  $G_s(B) - G_s(0) = - \int_0^B m dB$ , where  $m$  denotes the magnetic moment of the sample, which is generated by the shielding currents. For a fully developed shielding layer, the current density  $j_s$  and its decay toward the interior of the superconductor is fixed by the external field  $B_a$  independently of the macroscopic sample dimensions. For samples that are smaller than or comparable to the penetration depth in at least one dimension, the connection between the external field and the shielding current becomes dependent on the sample geometry. With decreasing thickness, say, of our film, for constant  $B_a$ , the shielding currents become smaller and smaller. This means that for the thin superconductor, the free enthalpy increases more slowly with increasing  $B_a$  than for the “thick” superconductor. Therefore, higher fields  $B_a$  are needed to make  $G_s$  equal to  $G_n$ .

Qualitatively, we can see this very clearly from [Figure 1.16](#). The decrease in the magnetic field in the interior of the layer is a measure of the diamagnetic sample behavior. With decreasing layer thickness, the decrease in the field in the interior and, hence, the diamagnetism become smaller and smaller. In order to make  $G_s$  equal to  $G_n$  by means of an external magnetic field, with decreasing layer thickness we must apply larger and larger external magnetic fields.

We want to estimate this in the limit  $d \ll \lambda_L$ . From the general relation  $B(x) = B_a + \mu_0 M(x)$  and Eq. (1.22) or (4.60), within the adopted approximation, we find  $M(x) \approx B_a (4x^2 - d^2)/(8\mu_0 \lambda_L^2)$ . Following a simple calculation, for the magnetization averaged over the plate one finds

$$M \approx -B_a d^2/(12\mu_0 \lambda_L^2) \quad 4.61$$

which differs from expression (4.49) for the “thick” superconductor by a factor  $d^2/(12\lambda_L^2)$ . By inserting this magnetization into Eq. (4.48), we obtain a critical magnetic field that is larger than the critical field  $B_{c\text{th}}$  of the “thick” superconductor by a factor  $12^{1/2} \lambda_L/d$ .

We summarize the important result of this section: For superconductors that are comparable with the penetration depth in at least one dimension, the external field  $B_a$  needed for canceling the superconductivity is larger than the thermodynamic critical field. This result will be highly important in the following.

#### 4.6.4 The Intermediate State

Following the results of the last section, the following question comes up: Why is it possible that the superconducting state becomes unstable because of an overcritical magnetic field? From the results of [Section 4.6.3](#) we could expect that, upon reaching the critical field, the superconductor splits up into very fine domains parallel to the magnetic field and alternately consisting of superconducting and normal conducting phase. Then the superconducting domains could be thin compared to the penetration depth and could sustain a larger magnetic field without becoming unstable.

From experience we know that this is not the case. Instead, the superconducting state of a rod-

shaped sample ( $N_M = 0$ ) becomes unstable when the critical field is reached. From this, we must conclude that a separation into many fine domains is energetically unfavorable. This can be understood from a simple idea. Each interface between a normal conducting domain and a superconducting domain carries an additional energy, the wall energy. This energy does not allow the splitting of a type-I superconductor into many fine domains. The energy needed for this would make this state energetically less favorable than the normal conducting state.

This wall energy is taken into account by the gradient term in the Ginzburg–Landau theory (see Eq. (4.26)). It controls the magnetic flux structure of the so-called intermediate state. The intermediate state refers to a situation in which a homogeneous type-I superconductor is neither completely superconducting nor completely normal conducting. Such configurations can be realized very simply by means of the geometric shape of the sample.

We consider a superconducting sphere in a homogeneous external field  $B_a$  (Figure 4.14). The shielding currents flowing within a thin surface layer keep the interior of the sphere free of magnetic field. As we can see from Figure 4.14, at the surface of the sphere near the equator, this expulsion of the magnetic field results in an enhancement of the field. The actual behavior of the field is given by the superposition of the homogeneous external field  $B_a$  and the field generated by the shielding currents.

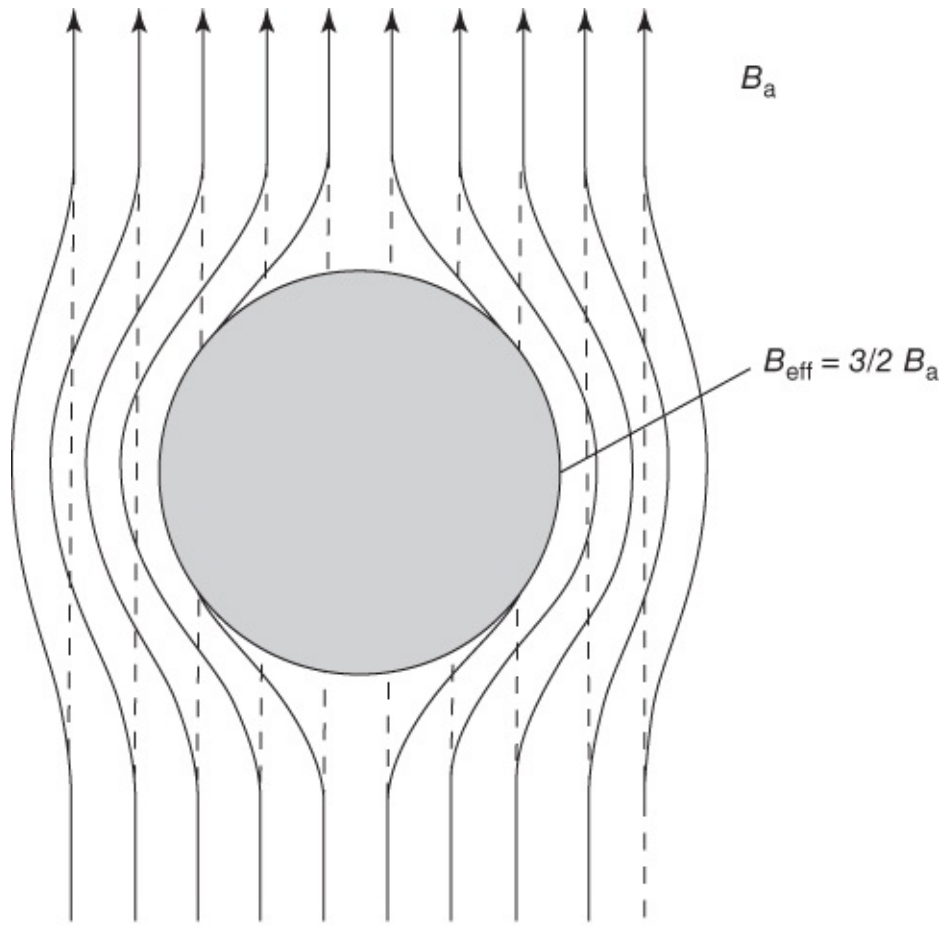


**Figure 4.14** Expulsion of magnetic field (solid field lines) from a superconducting sphere. In the absence of the sphere, the field is homogeneous (dashed field lines).

Apparently, the field enhancement results from the sample geometry. For simple geometric shapes it can be taken care of by the demagnetization coefficient (see [Section 4.6.1](#)). One can show that homogeneous samples with the shape of an ellipsoid display a homogeneous magnetization in a homogeneous external magnetic field. If one principal axis of the ellipsoid is oriented parallel to the external field, then the magnetization is also parallel to this field. This magnetization changes the magnetic field experienced by the sample. The maximum value of this field is referred to as ***the effective magnetic field  $B_{\text{eff}}$*** . It is given by

$$B_{\text{eff}} = B_a - N_M \mu_0 M \quad 4.62$$

For a superconductor with a complete Meissner effect, the magnetization  $M$  is related to the effective field  $B_{\text{eff}}$ :

$$M = -\frac{B_{\text{eff}}}{\mu_0} \quad 4.63$$

Hence, we have

$$B_{\text{eff}} = B_a + N_M B_{\text{eff}} \quad 4.64$$

or

$$B_{\text{eff}} = \frac{1}{1 - N_M} B_a \quad 4.65$$

The effective magnetic field is just the field at the equator at the surface. If the demagnetization coefficient  $N_M$  is known, the field at the equator can be calculated. For example, for a sphere we have  $N_M = 1/3$ . Hence, for the ideal diamagnetic sphere, we obtain

$$B_{\text{eff}} = \frac{3}{2} B_a \quad 4.66$$

Because of the field expulsion, for a demagnetization coefficient  $N_M > 0$  it is possible to choose a value of the external field  $B_a$  at which the superconductor is neither completely superconducting nor completely normal conducting. We look at the sphere somewhat closer. If we increase the external field  $B_a$ , at the value  $B_a = 2/3 B_{\text{eff}}$  the critical field  $B_c$  is reached at the equator. If  $B_a$  is increased further, at the equator the superconductivity must be destroyed. However, the sphere cannot become completely normal conducting, since in this case the field in the interior would be equal to the external field and, hence, would be smaller than  $B_c$ . The superconductor enters the intermediate state, that is, it splits up into superconducting and normal conducting domains.

Before we discuss this domain structure in more detail, we want to describe the behavior in the intermediate state phenomenologically. At  $B_a = B_c$  the sample must be completely superconducting. It turns out that, in the total regime  $\frac{2}{3}B_c < B_a < B_c$ , at the equator exactly  $B_c$  is

observed. With increasing  $B_a$ , the normal conducting fraction in the interior of the sphere increases exactly in such a way that the remaining field expulsion yields the value  $B_c$  at the equator.

We could say also that in the intermediate state the demagnetization coefficient  $N_M$  becomes dependent on  $B_a$ . If we measure the magnetic flux by means of an induction coil wound around the equator, then this flux  $\Phi$  increases monotonically with increasing  $B_a$ . This behavior is shown in [Figure 4.15](#).

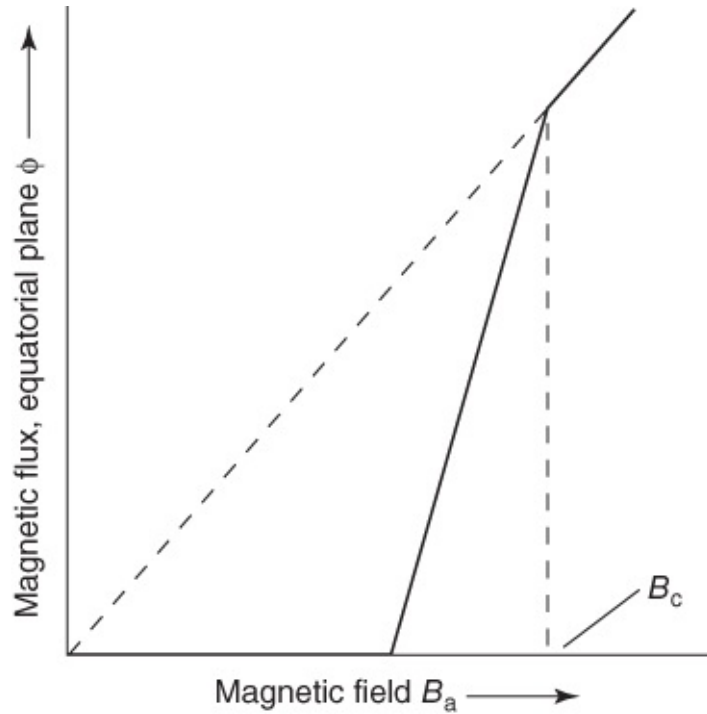


[Figure 4.15](#) Magnetic flux  $\Phi$  passing through the equatorial plane of a sphere plotted versus the external field  $B_a$ .

The magnetic flux structure of a sphere in the intermediate state has been investigated in detail [29, 30]. There exist normal conducting and superconducting domains next to each other. Hence, there are interfaces separating the normal conducting from the superconducting phase. These interfaces are stabilized because of the appearance of the critical field parallel to the external magnetic field. *For each intermediate state structure, the phase boundaries must be oriented parallel to the magnetic field.* This statement is always valid. In the case of more complicated intermediate state structures, as can appear in superconductors in an external magnetic field and for a simultaneous flow of an electric transport current (see [Section 5.2](#)), this can lead to surprising effects.

Since the development of the phase boundaries requires an amount of wall energy, the splitting into domains cannot take place on an arbitrarily fine scale. The sample must adopt a state in which larger superconducting and normal conducting domains exist next to each other. This configuration is determined by the fact that the free enthalpy of the system reaches a minimum. This requirement allows us to determine the wall energy from measurements of the

intermediate state structure.

We cannot discuss such calculations in detail. We want to mention only a few particularly simple results. In the case of a sphere, the transition into the intermediate state should happen at the field  $B_a = \frac{2}{3}B_c$ . However, this transition is accompanied by the generation of interfaces. Because of the positive wall energy, a finite amount of energy is needed for this. This energy must be supplied by the magnetic field. Therefore, the transition into the intermediate state does not occur exactly at  $B_a = \frac{2}{3}B_c$ , but at a slightly higher field instead. The field is expelled beyond the critical field until the stored field energy suffices for generating the necessary interfaces. This excess field was observed for wires in a perpendicular magnetic field and was interpreted in the way we have discussed [29].

The magnetic flux structures in the intermediate state have been investigated in detail by means of different experimental methods. Small bismuth wires were used to probe the superconducting and normal conducting domains of a sphere fabricated from tin [30]. For this purpose the sphere was cut into two halves along a plane through the equator, and subsequently the two halves were fixed together in such a way that a small opening of only a few tenths of a millimeter remained. The bismuth wires acting as magnetic field probes could be inserted into this opening. Then their electrical resistance, which for bismuth depends sensitively on the magnetic field, was measured. The normal conducting domains are detected by means of the magnetic field that they carry. On the other hand, the superconducting domains remain free of field. The small opening between the two hemispheres distorts these domains only very little, since the domain boundaries are oriented parallel to the magnetic field. With this technique the configuration of the intermediate state could be imaged [31].

Much more direct methods have since been utilized, which provide immediately a complete image of the flux structure. Among others, these are the following:<sup>22</sup>

1. the decoration of superconducting domains using a diamagnetic powder;
2. the imaging of normal conducting domains by means of the Faraday effect.

In the first method, a fine powder of a superconducting material is sprinkled onto the sample residing in the intermediate state. Mostly one uses niobium powder [32], which remains fully superconducting for the magnetic fields needed to establish the intermediate state, in the case of many superconductors with a value of  $T_c$  lower than the relatively high transition temperature of 9.2 K of Nb. The small superconducting niobium grains are ideal diamagnets. They are expelled from the regions with a high magnetic field, and they accumulate on the locations at the surface where the superconducting domains are. [Figure 4.16](#) shows such an image of the intermediate state of an indium plate [32]. Another example is presented in [Figure 5.5](#) for the case of the intermediate state in a wire carrying an electric transport current [33].

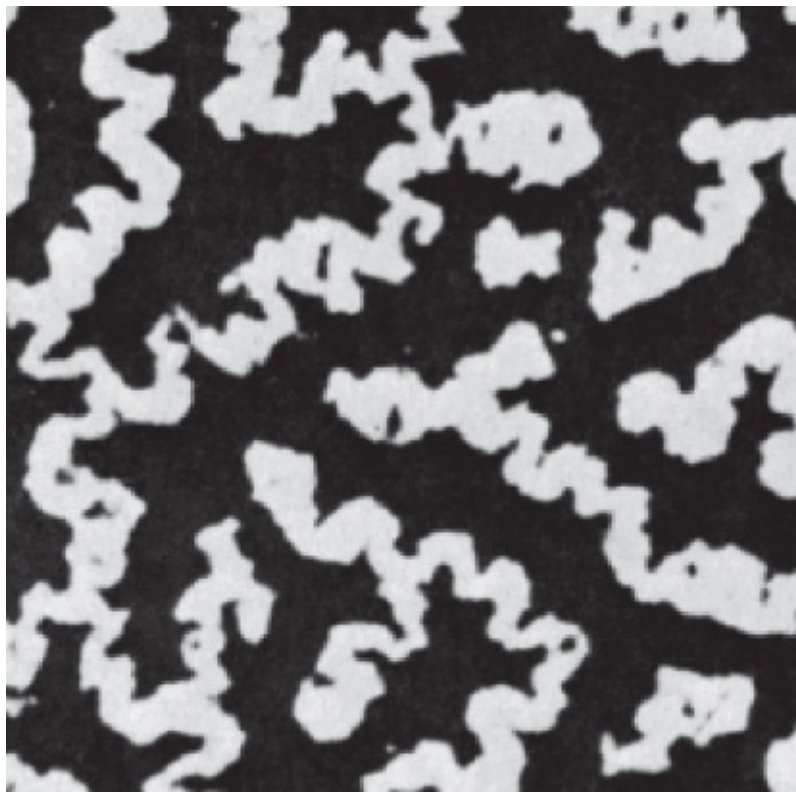


**Figure 4.16** Intermediate state structure of an indium plate. The dark regions represent the superconducting domains. In purity: 99.999 at%; thickness: 11.7 mm; diameter: 38 mm;  $B_a/B_{\text{cth}} = 0.1$ ;  $T = 1.98$  K;  $T_c$  of indium: 3.42 K; transition N → S; magnification: 5×. Because of its high demagnetization coefficient, the plate enters the intermediate state already at  $B_a/B_{\text{cth}} \approx 1$  [33].

The second method has been described already in [Section 1.2](#). Compared to the powder decoration, it has the advantage that it can also record movements, that is, temporal changes, of the intermediate state structure. Highly impressive motion pictures of the intermediate state in motion have been produced. In [Figure 4.17](#) we present an image of the intermediate state obtained in this way.

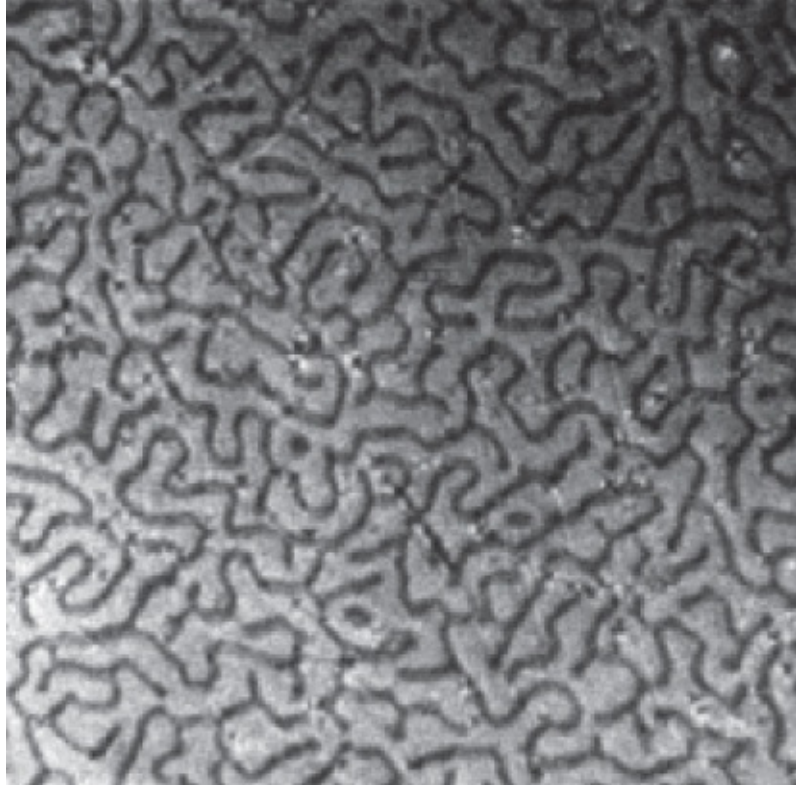


**Figure 4.17** Intermediate state structure imaged by means of the Faraday effect. Pb layer with 7  $\mu\text{m}$  thickness; thickness of the magneto-optic film of EuS and EuF<sub>2</sub>: about 100 nm; magnetic field  $B_a = 0.77 B_c$  perpendicular to the layer. The dark regions represent the superconducting domains. The imaged area is about 0.5 mm  $\times$  0.5 mm [34]. (By courtesy of Dr Kirchner, Siemens, Munich.)

#### 4.6.5 The Wall Energy

Next we want to look more closely at the wall energy associated with an interface between a normal conducting domain and a superconducting domain. This positive<sup>23</sup> wall energy has been crucial for our understanding of the intermediate state. We will find that under certain conditions the generation of an interface does not require an expense of energy. This has to do with the type-II superconductors, the properties of which will be described in [Section 4.7](#).

First we emphasize again that we assume a homogeneous material, a thickness of the superconductor much larger than  $\lambda_L$ , and a constant temperature. Under these assumptions, at an interface the magnetic field must be just equal to the critical field  $B_{\text{cth}}$ . In the normal conductor we have  $B > B_{\text{cth}}$ , and in the superconductor  $B$  vanishes within a layer thickness of about  $\lambda_L$ .

The difference between a normal conducting domain and a superconducting domain within the same material comes from the fact that in the normal state the Cooper pair density  $n_s$  is zero, whereas in the superconductor it has a definite value  $n_s(T)$  depending on the material and the temperature. We recall that it is the condensation into Cooper pairs that effects the lowering of the free enthalpy and that below  $T_c$  results in the thermodynamic stability of the superconductor instead of the normal conductor.

For our further discussion, it is crucial that at the interface the number density  $n_s(T)$  cannot drop discontinuously from  $n_s(T)$  to zero. Because of the strong correlation between the Cooper pairs, a spatial variation of  $n_s(T)$  is possible only within a distance larger than the Ginzburg–Landau coherence length  $\xi_{\text{GL}}$ .

[Figure 4.18](#) schematically indicates the situation at such an interface. In the normal domain on the left ( $x < 0$ ), the magnetic field is just  $B_{\text{cth}}$  or larger. Therefore, within this domain the normal conducting state is stabilized, since the expulsion of the magnetic field would require more free enthalpy than can be supplied by the transition into the superconducting state.<sup>24</sup> In the superconducting domain ( $x > 0$ ), the Cooper pair density increases up to the equilibrium value  $n_s(T)$  within about the coherence length. Here, we have assumed that for the superconductor we have

$$\xi_{\text{GL}} > \lambda_L$$

4.67

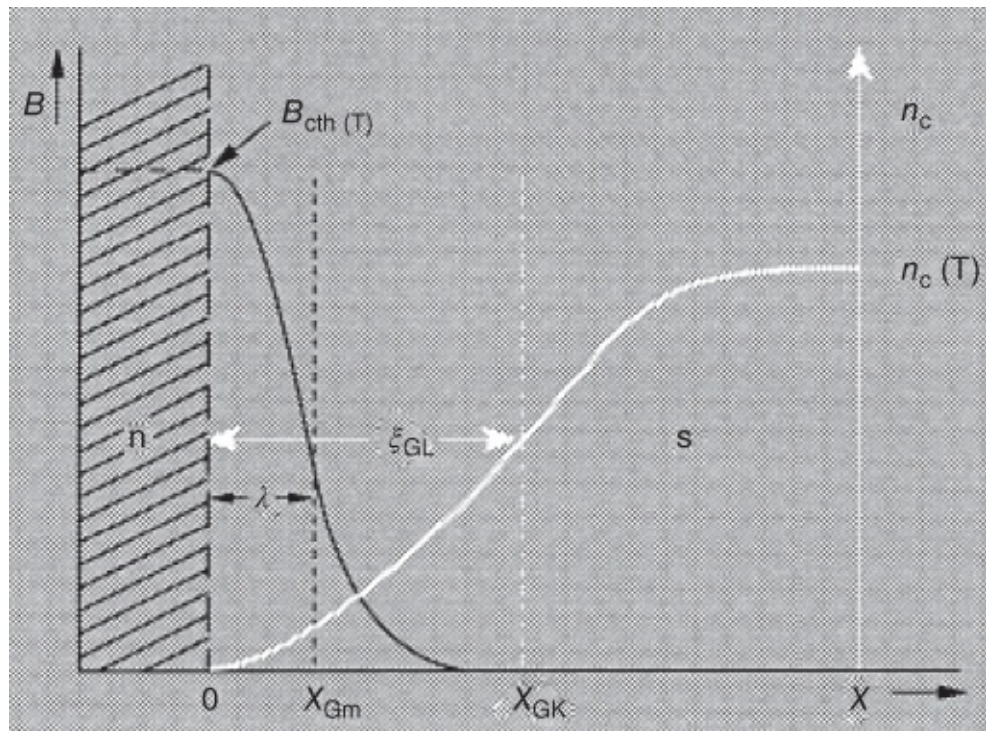


[Figure 4.18](#) Spatial variation of  $B$  and  $n_s$  at an interface between a normal conducting domain and a superconducting domain within a homogeneous material at temperature  $T$ . (Here,  $x_{\text{Gm}}$  = “magnetic boundary” and  $x_{\text{GK}}$  = “condensate boundary.”)

At the boundary layer we must compare two contributions to the energy, namely the energy  $E_B$  associated with the expulsion of the magnetic field, and the energy  $E_C$  gained because of the condensation into Cooper pairs. In the normal conductor we have  $E_B = E_C = 0$ . The magnetic field is not expelled, and no Cooper pairs exist. Deep within the interior of the superconducting domain, for the application of the critical field  $B_{\text{cth}}$ , we have at the boundary  $E_B = E_C = (1/2\mu_0)B_{\text{cth}}^2 V$  (see Eq. (4.50)). The magnitude of the full condensation energy is just

equal to the expulsion energy.

Within the boundary layer, the two energies do not have their full value. The magnetic field is not completely screened. Instead, it penetrates up to a depth  $\lambda_L$ . The expulsion energy is reduced by the amount

$$\Delta E_B = F\lambda_L \frac{1}{2\mu_0} B_{\text{cth}}^2 \quad 4.68$$

(where  $F$  is the area of the discussed boundary layer) compared to the case of complete expulsion up to the boundary line  $x = 0$  in [Figure 4.18](#). However, within the boundary layer the condensation energy is also reduced, since the number density of Cooper pairs is smaller than the equilibrium value  $n_s(T)$ . This reduction of the condensation energy is given by

$$\Delta E_C = -F\xi_{\text{GL}} \frac{1}{2\mu_0} B_{\text{cth}}^2 \quad 4.69$$

where  $F$  is the area of the discussed boundary layer and  $\xi_{\text{GL}}$  is the Ginzburg–Landau coherence length.

For simplicity, we have defined  $\lambda_L$  and  $\xi_{\text{GL}}$  in such a way that the energy values  $\Delta E_B$  and  $\Delta E_C$  are equivalent to the case in which the magnetic field penetrates completely up to the depth  $\lambda_L$  and then abruptly drops to zero and, on the other hand, the Cooper pair density abruptly jumps up to its full value  $n_s(T)$  at  $\xi_{\text{GL}}$ . In this way, we have defined a “magnetic boundary” and a “condensate boundary.” For the present case  $\xi_{\text{GL}} > \lambda_L$ , we find

$$\Delta E_C - \Delta E_B = (\xi_{\text{GL}} - \lambda_L)F \frac{1}{2\mu_0} B_{\text{cth}}^2 > 0 \quad 4.70$$

Because of relation [\(4.67\)](#), the loss in condensation energy is larger than the gain in expulsion energy. In order to generate such a boundary, we must deliver the following wall energy  $\alpha_w$  per unit area to the system:

$$\alpha_w = (\xi_{\text{GL}} - \lambda_L)F \frac{1}{2\mu_0} B_{\text{cth}}^2 \quad 4.71$$

In [Figure 4.19](#) we show the spatial variation of the energy densities  $\epsilon_B$  and  $\epsilon_C$  and their difference, which passes through a maximum.

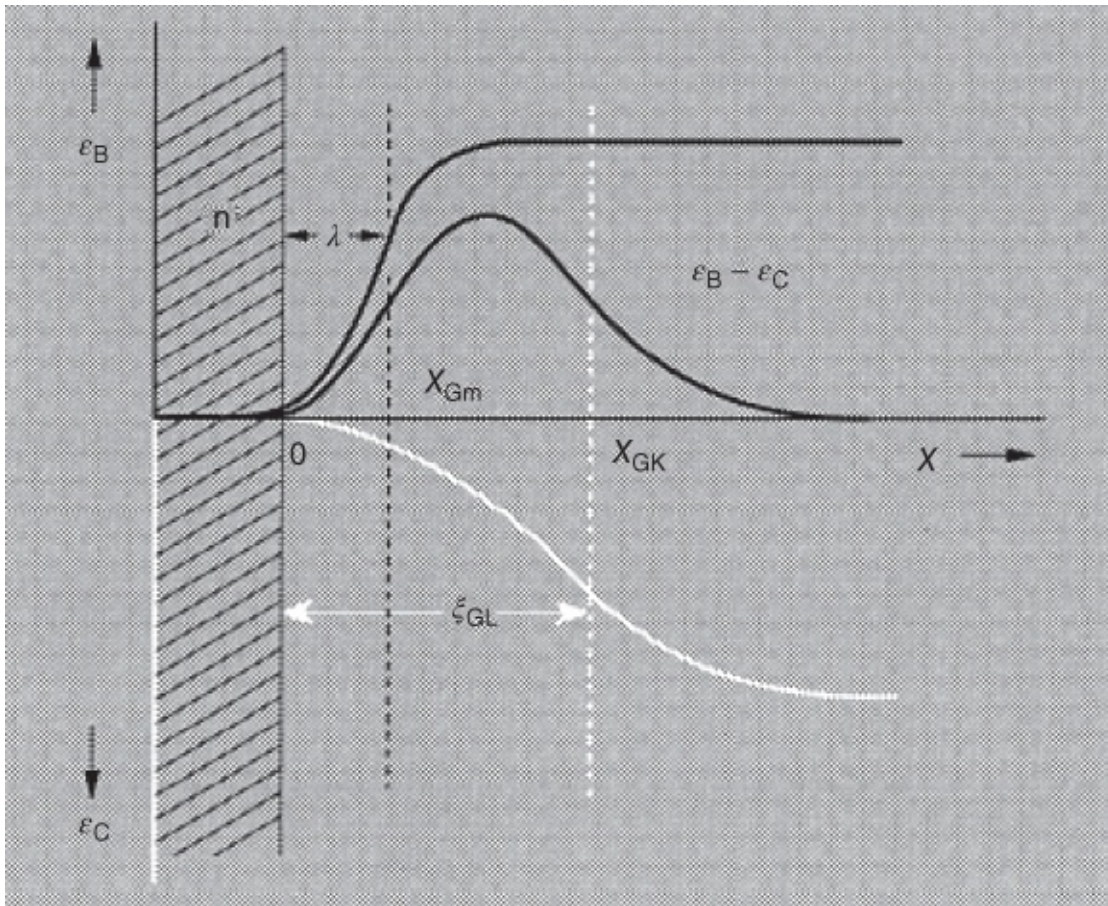


**Figure 4.19** Spatial variation of the expulsion energy  $\epsilon_B$  and of the condensation energy  $\epsilon_C$  per unit volume at the boundary. We have  $\int_0^{x \gg x_{\text{GK}}} (\epsilon_B - \epsilon_C) F dx = (\xi_{\text{GL}} - \lambda_L) F \frac{1}{2\mu_0} B_{\text{cth}}^2$ .

Here we see very clearly that the generation of a boundary layer between a normal conducting domain and a superconducting domain in a homogeneous material requires energy if  $\xi_{\text{GL}}$  is larger than  $\lambda_L$ .<sup>25</sup> In the case where  $\xi_{\text{GL}} = \lambda_L$ , that is, if the magnetic boundary and the condensate boundary coincide, we have  $\alpha_w = 0$ . In the case where  $\xi_{\text{GL}} < \lambda_L$  formally we would obtain a negative wall energy. Now a new state, the so-called mixed state, is established. However, we must emphasize that these arguments based on the Ginzburg–Landau theory are valid only close to  $T_c$ .

We will return to our discussion of the boundary between a normal conducting domain and a superconducting domain in conjunction with type-II superconductors. Next we want to discuss the pressure dependence of the superconducting state. Again we can apply the rules of thermodynamics. This section will conclude our treatment of type-I superconductors.

## 4.6.6 Influence of Pressure on the Superconducting State

In [Sections 4.6.1](#) and [4.6.2](#) we discussed the difference between the free enthalpies of the normal and the superconducting states at constant pressure as a function of the temperature. In order to simplify the formulas, for the quantitative discussion we have made three assumptions:

1. In the superconducting state, an external magnetic field should be completely expelled from

the superconducting material, that is, there should be an ideal Meissner–Ochsenfeld effect. This assumption is well satisfied for macroscopic type-I superconductors over the whole stability range. It yielded the connection between the external field and the magnetization.

2. In order to find the magnetic moment  $m$  from the magnetization  $M$ , we must know the sample volume. In this context, we have used an approximation by ignoring the dependence of the volume upon the magnetic field  $B$ . Experience indicates that this dependence is very small.
3. Finally, we have taken the temperature dependence of the critical field  $B_c$  from experiment, and we have used the parabolic dependence  $B_c(T) = B_c(0)[1 - (T/T_c)^2]$  as an analytic, satisfactory approximation.

All our discussions have been restricted to constant pressure. In this section, we take up the influence of pressure on superconductivity.

Already by 1925, Sizoo and Kamerlingh-Onnes had observed such an influence on the transition temperature  $T_c$  [35]. In [Figure 4.20](#) we show the change of the transition temperature with increasing pressure for tin in the absence of an external magnetic field [36]. The transition temperature decreases with increasing pressure. The effect is not very large. In order to change  $T_c$  in tin by 0.1 K, we must apply pressures of about 2000 bar.<sup>[26](#)</sup>

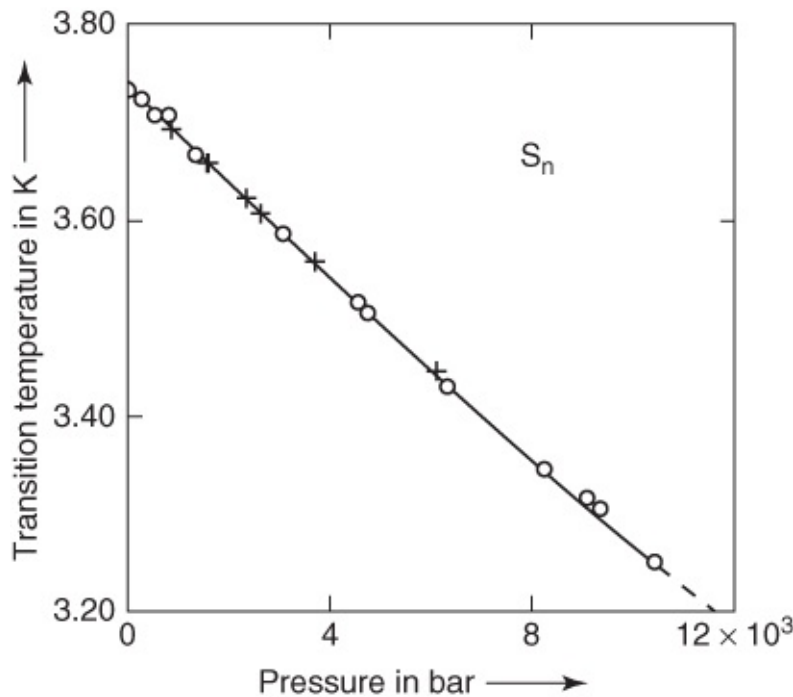


[Figure 4.20](#) Pressure dependence of the transition temperature of tin [36].

The behavior shown in [Figure 4.20](#) is typical for many superconductors. However, there are also some materials (e.g., Ti, Zr, V, La, U) whose transition temperature increases with increasing pressure [37, 38].

The change of  $T_c$  under pressure in zero magnetic field must be connected with a change of the

critical field  $B_c$  with pressure. This influence of pressure on  $B_c$  is shown in [Figure 4.21](#) for cadmium [39]. We have chosen the results for cadmium, since they represent an excellent example of highly advanced experimental techniques. The very low temperatures combined with the application of high pressures are a great challenge to the experiment.

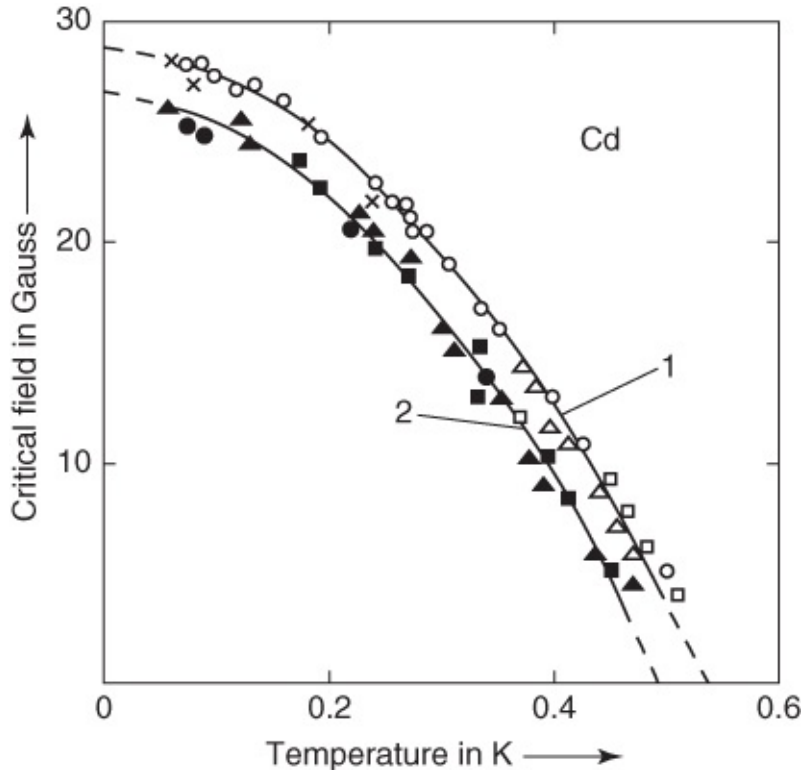


**Figure 4.21** Temperature dependence of the critical field ( $1 \text{ G} = 10^{-4} \text{ T}$ ) of cadmium at atmospheric pressure (curve 1) and at 1550 bar (curve 2). (From [39].) The original curves have many more data points than this reproduction.

The pressure was generated in a so-called “ice bomb” [40]. A steel vessel is completely filled with water. During cooling below the freezing point a pressure of about 1800 bar develops, since the volume is kept constant. At constant pressure, the freezing of water is accompanied by a volume expansion of about 10%. If the liquid–solid phase transition takes place at constant volume, the resulting ice must develop under a pressure that is sufficiently high to effect a 10% volume reduction of the ice. This ice bomb method has served for performing many experiments on the behavior under pressure.

For the studies of Cd, the ice bomb was cooled down to about  $6 \times 10^{-2} \text{ K}$  by means of so-called adiabatic demagnetization (a magnetic cooling technique), and the critical field  $B_c$  was measured down to these temperatures. In the case of Cd, the critical field  $B_c$  decreases with increasing pressure, as expected from the pressure dependence of  $T_c$  at zero magnetic field.

The reduction of the critical field under pressure means that the difference  $G_n - G_s$  decreases with increasing pressure at constant  $B$  and  $T$ . If we know the volumes of the normal conductor  $V_n$  and of the superconductor  $V_s$  as a function of our independent variables  $T$ ,  $p$ , and  $B$ , we can calculate the  $p$  dependence of  $G_n - G_s$ . However, the volume changes  $\Delta V/V$  are very small,

namely only a few  $10^{-8}$ . Therefore, it represents an experimental challenge to demonstrate these changes convincingly. The measurements of  $B_c$  under pressure are somewhat simpler, and [Figure 4.21](#) gives an example. From these measurements, we can determine the volume change during the phase transition by means of the Gibbs function  $G$ .

In general, we have the expression given in Eq. [\(4.11\)](#):

$$(\mathrm{d}G / \mathrm{d}p)_{T,B} = V$$

At the phase transition, we obtain<sup>[27](#)</sup>

$$(V_n - V_s)_{B=B_c} = V_s(B_c) \frac{\partial}{\partial p} \left( \frac{B_c^2}{2\mu_0} \right) = V_s(B_c) \frac{B_c}{\mu_0} \frac{\partial B_c}{\partial p} \quad 4.72$$

This is analogous to the expression we have indicated in [Section 4.2](#) for the entropy difference. From this expression we see that  $V_n - V_s$  vanishes at  $T_c$ , because  $B_c$  is zero. Furthermore, we see that for  $T < T_c$  we have  $V_s > V_n$ , if  $B_c$  decreases with  $p$ , that is, if  $\partial B_c / \partial p < 0$ , which is generally the case. The additional derivative with respect to  $p$  or  $T$  yields the difference of the compressibilities  $\kappa_s$  and  $\kappa_n$  or the difference of the thermal expansion coefficients  $\alpha_s$  and  $\alpha_n$  in the superconducting state and the normal state, respectively.

During the transition from the superconducting to the normal state, the volume changes have been measured directly using highly sensitive methods. Primarily, the length change of a sample in the form of a rod or a strip was determined. In [Figure 4.22](#) we show the results for tin [41]. We see that  $l_s > l_n$  for all temperatures  $T > T_c$ , as expected, where  $T_c$  denotes the transition temperature in zero magnetic field.

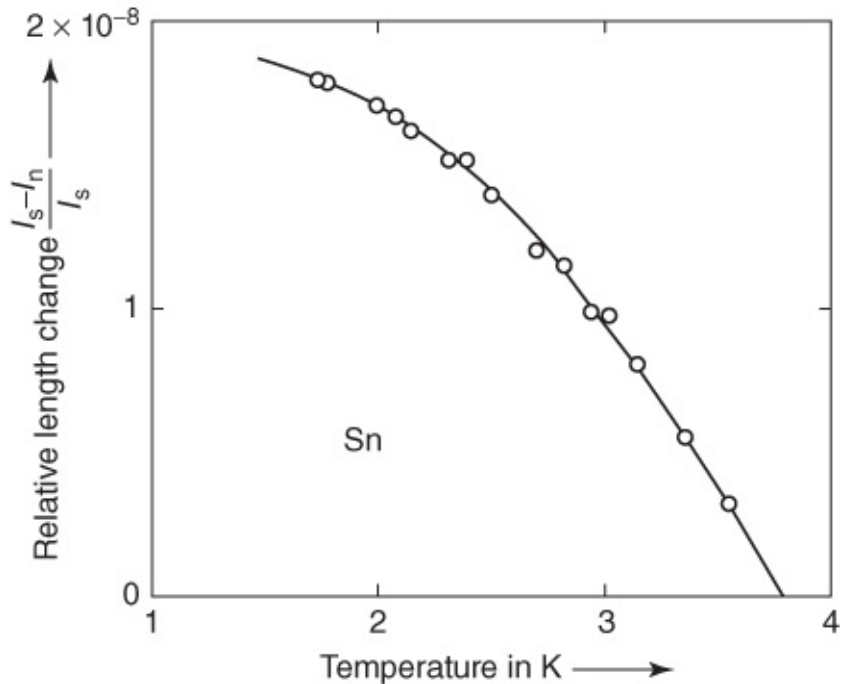


**Figure 4.22** Relative length change  $(l_s - l_n)/l_s$  of a tin rod at the transition into the superconducting state. (From [41].)

At the transition into the superconducting state, the sample expands. This is consistent with the indications of our Gibbs function, for which we had assumed a perfect expulsion of the magnetic field. We note that for a rod with 10 cm length, the measurement of this length change near  $T_c$  requires a sensitivity of the length measurement of about  $10^{-8}$  cm.

Since the development of a microscopic theory, the BCS theory, studies of the pressure dependence of the transition temperature have gained much in importance. The application of hydrostatic pressure allows the continuous variation of the lattice constant of a substance. However, the lattice constant represents an important parameter for the quantum states of the electrons as well as of the lattice vibrations, the phonons. Since both quantities are highly important for superconductivity, new information for quantitative improvements of the microscopic theory can be extracted from experiments under pressure. In [Section 1.2](#) we have seen that our knowledge about the quantitative connections between the parameters of metals and superconductivity is still highly incomplete. For the transition temperature  $T_c$  of conventional superconductors, we have from the BCS theory the relation<sup>28</sup> (see Section 3.1.2, Eq. (3.6)):

$$T_c \propto \Theta_D \exp\left(-\frac{1}{N_n(E_F) V^*}\right) \quad 4.73$$

We take the derivative with respect to  $p$  and obtain

$$\frac{\partial T_c}{\partial p} \propto \frac{\partial \Theta_D}{\partial p} \exp\left(-\frac{1}{N(E_F) V^*}\right)$$

$$+ \Theta_D \exp\left(-\frac{1}{N(E_F) V^*}\right) \left(\frac{1}{N(E_F) V^*}\right)^2 \frac{\partial(N(E_F)V^*)}{\partial p}$$

For determining the relative change of  $T_c$ , we divide by  $T_c$ :

$$\frac{1}{T_c} \frac{\partial T_c}{\partial p} = \frac{1}{\Theta_D} \frac{\partial \Theta_D}{\partial p} + \left(\frac{1}{N(E_F) V^*}\right)^2 \frac{\partial(N(E_F)V^*)}{\partial p} \quad 4.75$$

From the determination of the pressure dependence of  $T_c$  and from the Debye temperature  $\Theta_D$ , we obtain information on the pressure dependence of the quantity  $N(E_F)V^*$  [38].

The change of the transition temperature under hydrostatic pressure can also serve for the construction of a superconducting manometer. Lead is particularly suitable, since it does not have any phase transition up to about 160 kbar, and it is insensitive to lattice defects. Therefore, one can place a small lead wire into the pressure cell and determine the pressure within the cell at low temperatures from the transition temperature  $T_c$  of the wire. A calibration of this Pb manometer up to about 160 kbar has been carried out by Eichler and Wittig [42]. The insensitivity of  $T_c$  to lattice defects is important, since at the high pressures there is always a certain amount of plastic deformation, leading to the generation of lattice defects. This is even more pronounced at low temperatures.

So far we have discussed the influence of pressure within a *single-crystalline* phase. For many substances, under pressure one can obtain new crystalline phases, new modifications. Then we expect that during such a phase transition the superconducting properties are also changed. The high-pressure modification simply represents a new material.

Substances that do not show superconductivity at room pressure, but have superconducting phases at high pressure, are very interesting. In recent years, a number of such superconducting high-pressure phases have been found in semiconductors and in the transition range between metals and semiconductors (see also [Table 2.1](#) and [Figure 2.1](#)).

Frequently, newly discovered superconductors are also studied early under high pressure. So in the case of the lanthanum–barium cuprate, one found a surprisingly large increase in  $T_c$  under hydrostatic pressure [43]. Since hydrostatic pressure reduces the lattice constant, also a “chemical” reduction of the lattice constant by inserting particularly small ions into the lattice could lead to  $T_c$  enhancement. C. W. Chu and coworkers utilized this argument and replaced the lanthanum by the smaller yttrium ion. In this way, they discovered the system Y–Ba–Cu–O and prepared samples with values of  $T_c$  above 80 K [44].<sup>29</sup>

Careful studies of the thermal expansion and of the effect of pressure were performed with single crystals without twin boundaries. The thermal expansion of  $\text{YBa}_2\text{Cu}_3\text{O}_{7-x}$  was measured with a resolution of  $10^{-9}$  cm. It shows a strong anisotropy also within the Cu–O layers [45].

For a uniaxial pressure along the  $a$ -axis ([Section 2.8.1](#)), the experiments indicated a reduction of  $T_c$ , but along the  $b$ -axis an increase in  $T_c$  was found [46]. Similar results were obtained for other cuprates [47]. These observations were interpreted in terms of a change of concentration of the charge carriers in the Cu–O layers.

In the case of MgB<sub>2</sub>, with increasing pressure a linear decrease in  $T_c$  was observed, in good agreement with the behavior expected from the BCS theory [48]. In the case of the iron pnictides, depending on the doping, one finds an increase or decrease in  $T_c$  [49].

## 4.7 Type-II Superconductors in a Magnetic Field

As we have already discussed, below the lower critical magnetic field  $B_{c1}$  type-II superconductors exist in the Meissner phase, if geometric effects are ignored. However, above  $B_{c1}$  the magnetic field penetrates into the sample in the form of quantized flux lines or vortices. Above the upper critical magnetic field  $B_{c2}$ , the superconductivity vanishes. In the following, we will look in more detail at these properties from a thermodynamic point of view.<sup>[30](#)</sup>

The discussion of the boundary layer between a normal conducting domain and a superconducting domain in [Section 4.6.5](#) has shown that in the case  $\lambda_L > \xi_{GL}$  the formation of the boundary layer is accompanied by an energy gain. In this case the following condition must be (approximately) satisfied:

$$\xi_{GL} F \frac{1}{2\mu_0} B_{cth}^2 - \lambda_L F \frac{1}{2\mu_0} B^2 < 0 \quad 4.76$$

Hence,

$$\xi_{GL} B_{cth}^2 < \lambda_L B^2 \quad 4.77$$

or

$$\frac{B_{cth}^2}{B^2} < \frac{\lambda_L}{\xi_{GL}} \quad 4.78$$

Therefore, we expect that, for superconductors with  $\lambda_L > \xi_{GL}$ , the magnetic field can penetrate into the superconductor already at fields  $B$  that are smaller than  $B_{cth}$ . In this case, spatial variations of  $B$  and of the Cooper pair density  $n_s$  are expected, similar to the situation at a boundary layer. From the relations [\(4.41\)](#) and [\(4.42\)](#) in [Section 4.5](#), we see that the condition  $\xi_{GL} < \lambda_L$  can always be achieved by making the electron mean free path  $l^*$  sufficiently small. According to Eq. [\(4.41\)](#),  $\lambda_L$  increases weakly with decreasing  $l^*$ . On the other hand, according to Eq. [\(4.42\)](#),  $\xi_{GL}$  decreases with  $(l^*)^{1/2}$ . The mean free path can be reduced easily by alloying the superconductor with a small amount of impurities. The electrons are scattered at the impurities and, hence, their mean free path is reduced. Indeed, as we will see, alloys are in

general type-II superconductors.

Already in the 1930s, this particular behavior of superconducting alloys was observed experimentally. De Haas and Voogd reported [50] that in magnetic fields up to about 2 T lead–bismuth alloys still remain superconducting. These are magnetic fields that are larger by more than the factor 20 than the critical field of pure lead. There were attempts to understand such high critical fields in terms of the so-called sponge model proposed by Mendelssohn [51]. According to this model, the high critical fields should be caused by a network of fine precipitates, say, at grain boundaries. If these precipitates were assumed to be small compared to the penetration depth at least in one dimension, then the high critical fields could be understood qualitatively simply because of this geometry (see [Section 4.6.3](#)). Today we know that this sponge model may apply to many alloys, but that there exist also homogeneous superconductors, namely the type-II superconductors, which remain superconducting up to very high magnetic fields.

Qualitatively, we can understand in a simple way why a superconductor can tolerate higher magnetic fields, if at least a partial penetration of the field is possible. During the penetration of the field, the expulsion energy, which increases the free enthalpy of the superconducting state in the magnetic field, is reduced. Therefore, higher external fields are needed, in order to make the free enthalpy of the superconducting state equal to that of the normal state. Using similar arguments, we have understood the increase in the effective critical field of thin superconductors, into which the field can also penetrate.

According to [Section 4.6.5](#) we expect that, together with the penetration of the field, also the condensation energy is reduced. However, for  $\lambda_L \ll \xi_{GL}$ , the gain due to the reduction of the expulsion energy can be much larger than the loss of condensation energy. Qualitatively, this situation is well accounted for by the Ginzburg–Landau theory. The prediction of the vortex state by Abrikosov [22] was one of the great successes of this theory.

### 4.7.1 Magnetization Curve and Critical Fields

The difference between type-I and type-II superconductors is clearly seen in the form of the magnetization curve. In [Figure 4.23](#) we schematically show the magnetization curve of a type-II superconductor. Again we consider a rod-shaped sample, the demagnetization coefficient  $N_M$  of which is practically zero. At the lower critical field  $B_{c1}$ , the gain of expulsion energy due to the field penetration becomes larger than the loss of condensation energy caused by the local variation of the Cooper pair density  $n_s$ . As a result, the magnetic field penetrates into the superconductor in the form of quantized flux lines.

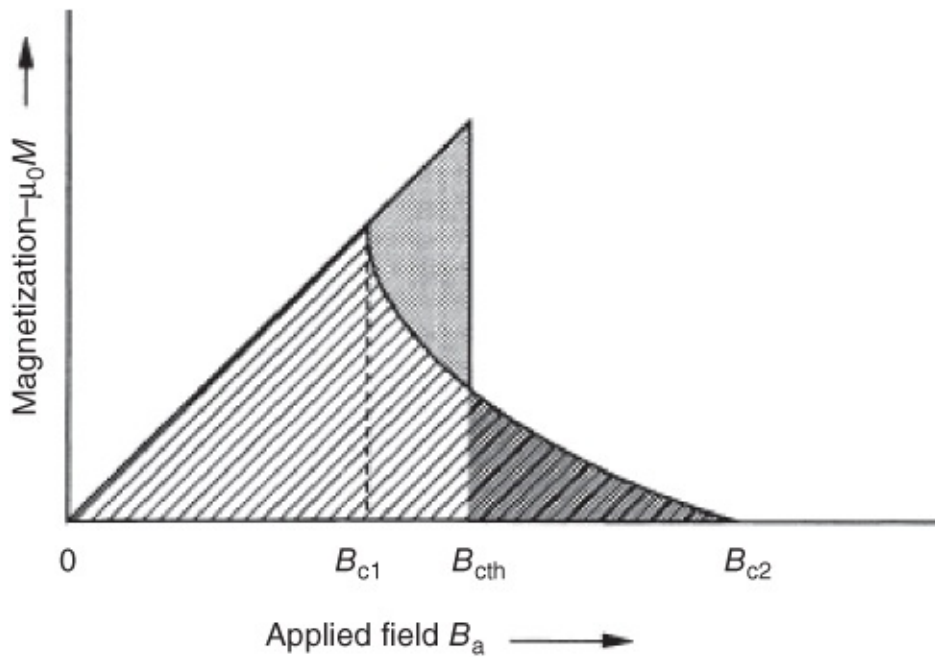


**Figure 4.23** Magnetization curve of a type-II superconductor. Rod-shaped sample with  $N_M = 0$ . Because of the definition of  $B_{c\text{th}}$ , the shaded areas must be equal.

As a result of the magnetic field penetration, with increasing field the magnetization of the superconductor decreases monotonically. At a value  $B_{c2}$ , the upper critical field, the magnetization reaches zero – the external field has canceled the superconductivity.<sup>31</sup>

From the general thermodynamic arguments (see [Sections 4.1](#) and [4.6.1](#)), at constant temperature  $T$  and constant pressure  $p$ , the difference of the free enthalpies is given by

$$G_n - G_s = - \int_0^{B_{c2}} M V \, dB \quad 4.79$$

If we ignore (as in [Section 4.6.1](#)) the very small changes of the volume  $V$  as a function of the magnetic field, we can extract  $V$  as a constant in front of the integral. The integral is proportional to the area under the magnetization curve

$$\int_0^{B_{c2}} M \, dB \propto \mu_0 F_M \quad 4.80$$

Here,  $F_M$  is the area under the magnetization curve.<sup>32</sup>

If we take a type-I superconductor for comparison, with the same difference of the free enthalpies, its magnetization curve would be given by the vertical line at  $B_{c\text{th}}$  in [Figure 4.23](#). The areas under both magnetization curves must be equal. Now we see clearly the difference between a type-I superconductor and a type-II superconductor. A type-I superconductor completely expels the field up to the thermodynamic critical field  $B_{c\text{th}}$ , that is, it stays in the Meissner phase up to this field. On the other hand, at the lower critical field  $B_{c1}$  a type-II superconductor enters a state with a penetrated field, the so-called Shubnikov phase. In the

Shubnikov phase, with increasing field the magnetization decreases monotonically and completely vanishes only at the upper critical field  $B_{c2}$ . The latter field can be much larger than the thermodynamic critical field of the corresponding type-I superconductor.

In [Figure 4.24](#) we present this important fact again. Here, the average magnetic field in the interior of the rod-shaped sample is plotted versus the external field. [Figure 4.24](#) exactly corresponds to [Figure 4.11](#) in [Section 4.6.1](#). At  $B_{c1}$  the field starts to penetrate into the superconductor. However, only at  $B_{c2}$  is the average interior field equal to the external field, or the magnetization is practically zero. Again the behavior of the corresponding type-I superconductor is indicated by the dashed line. The “corresponding” type-I superconductor denotes again one that has the same difference of the free enthalpies  $G_n - G_s$  as the type-II superconductor.

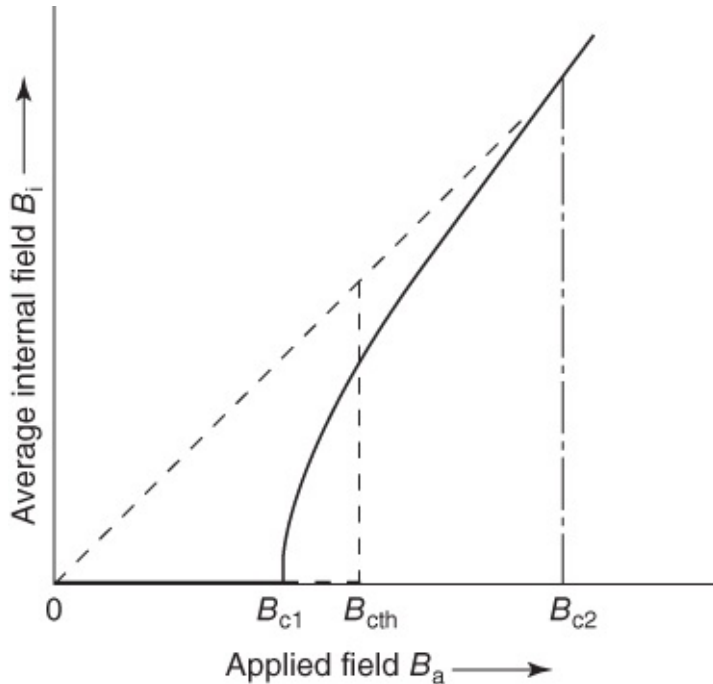


[Figure 4.24](#) Average magnetic field in the interior of a type-II superconductor plotted versus the external field.

We have already mentioned that a type-I superconductor can turn into a type-II superconductor if the electron mean free path is reduced sufficiently. This result of the Ginzburg–Landau theory has been well confirmed experimentally. By alloying with impurity atoms, which reduce the electron mean free path, all type-I superconductors can be changed into type-II superconductors. One of many examples is shown in [Figure 4.25](#). Here, the ideal magnetization curve of pure lead and the measured curve of a lead–indium alloy with 13.9 at% indium are shown [52]. Pure lead is a type-I superconductor. The alloy shows typical type-II behavior. The superconductivity of the alloy is completely canceled only at an upper critical field of about 0.24 T (2400 G). On the other hand, for the temperature of 4.2 K of this experiment, the thermodynamic field of lead is only about 0.055 T (550 G).

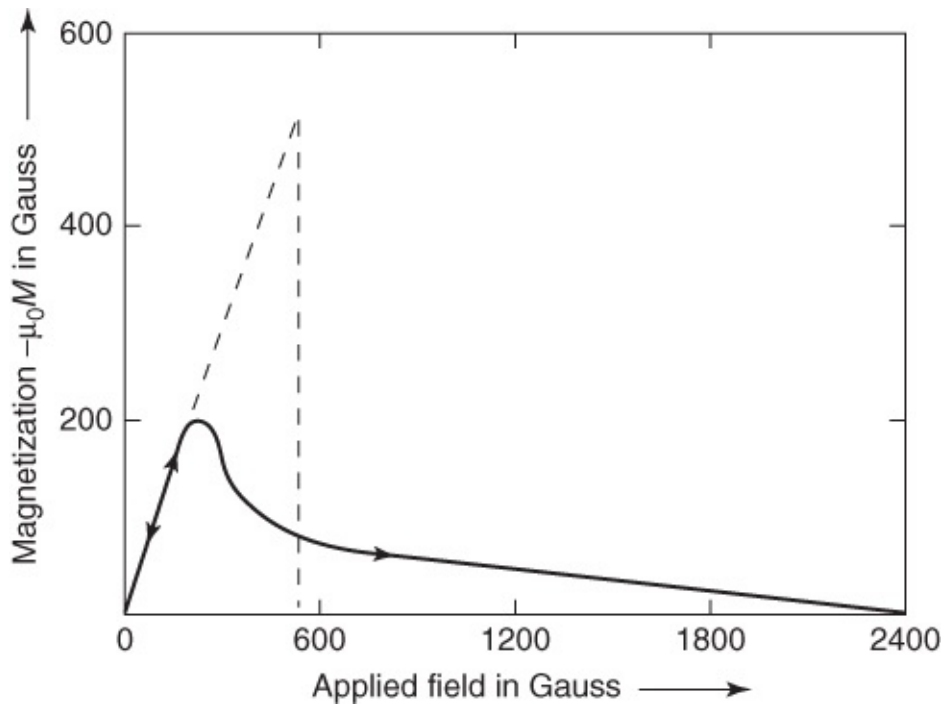


**Figure 4.25** Magnetization curve of lead with 13.9 at% of indium (solid line). Rod-shaped sample with a small demagnetization coefficient. The dashed line shows the ideal curve of pure lead ( $1 \text{ G} = 10^{-4} \text{ T}$ ). (From [52].)

Following these qualitative considerations, now we must turn to a few quantitative relations between the fields  $B_{c1}$ ,  $B_{c2}$ , and  $B_{\text{cth}}$ . All these relations are obtained from the Ginzburg–Landau theory. Here, we must keep in mind that this theory is valid only close to  $T_c$ . The crucial parameter is the Ginzburg–Landau parameter  $\kappa$ , that is, the ratio of the penetration depth  $\lambda_L$  and the coherence length  $\xi_{\text{GL}}$ .

Using the Ginzburg–Landau parameter, all the quantitative relations can be formulated in a simple way. For the upper critical field  $B_{c2}$ , one obtains

$$B_{c2} = \sqrt{2} \kappa B_{\text{cth}} \quad 4.81$$

Here, for each type-II superconductor  $B_{\text{cth}}$  is defined from the difference of the free enthalpies given by Eq. (4.50):

$$G_n - G_s = \frac{1}{2\mu_0} V B_{\text{cth}}^2$$

From the solution of the Ginzburg–Landau equations one also finds<sup>33</sup> a simple relation between the Ginzburg–Landau coherence length  $\xi_{\text{GL}}$  and  $B_{c2}$ :

$$B_{c2} = \frac{\Phi_0}{2\pi\xi_{\text{GL}}^2} \quad 4.82$$

Frequently, this relation is used for determining  $\xi_{\text{GL}}$  from the measurement of the upper critical

field. However, frequently  $B_{c2}$  is too large to be measured directly in the limit of low temperatures. In this case, one extrapolates the experimental data from temperatures near  $T_c$  down to  $T \rightarrow 0$ . For conventional superconductors, the microscopic theory yields the important relation [53]:

$$B_{c2}(0) \approx 0.7 T_c \left. \frac{dB_{c2}}{dT} \right|_{T_c} \quad 4.83$$

Furthermore, we note that Eqs. (4.82) and (4.83) are valid only for isotropic superconductors. If the superconducting properties depend strongly on the crystallographic direction, as in the high-temperature superconductors, Eq. (4.82), for example, must be replaced by  $B_{c2}^a = \Phi_0 / (2\pi\xi_b\xi_c)$ . Here, the magnetic field is applied parallel to the crystallographic  $a$  direction, and  $\xi_b$  and  $\xi_c$  are the Ginzburg–Landau coherence lengths in the directions perpendicular to the field, respectively. Analogous expressions are obtained for the field orientation along the other crystal axes. In addition, we note that the results of this section apply to single-band superconductors.

Also the lower critical field can be calculated from the Ginzburg–Landau equations. According to Abrikosov [22], in the limit  $\kappa \gg 1/\sqrt{2}$  one obtains

$$B_{c1} = \frac{1}{2\kappa} (\ln \kappa + 0.08) B_{cth} \quad 4.84$$

The value 0.08 in the bracket originates from the interaction between the vortices in the triangular lattice. We see that, with increasing  $\kappa$ ,  $B_{c1}$  decreases and  $B_{c2}$  increases. The lower critical field can also be related to the London penetration depth:

$$B_{c1} = \frac{\Phi_0}{4\pi\lambda_L^2} (\ln \kappa + 0.08) \quad 4.85$$

Equations (4.84) and (4.85) are valid for isotropic superconductors and can be modified for anisotropic superconductors analogously to Eq. (4.82). Equation (4.85) provides a simple possibility for estimating  $\lambda_L$  from the measurement of the lower critical field.

Since in alloys the mean free path  $l^*$  decreases monotonically with increasing concentration of the impurities, for each system we can indicate a specific “critical” concentration at which the host metal turns into a type-II superconductor. This transition is determined by the condition  $B_{c2} \geq B_{cth}$ . According to Eq. (4.81) this condition is equivalent to  $\kappa \geq 1/\sqrt{2}$ . We see that type-I and type-II superconductors are simply distinguished by the value of  $\kappa$ :

$$\text{type-I superconductors : } \kappa < 1/\sqrt{2} \quad 4.86a$$

$$\text{type-II superconductors : } \kappa \geq 1/\sqrt{2} \quad 4.86b$$

This discrimination is strictly valid only near  $T_c$ . For  $T < T_c$ , for  $\kappa$  values only slightly larger

than  $1/\sqrt{2}$  there exists a transition into a state in which both the Meissner phase and the Shubnikov phase appear next to each other. We will return to this point in [Section 4.7.2](#).

In [Table 4.2](#) some values of  $\kappa$  for In–Bi alloys are indicated. In this system the transition into type-II superconductivity occurs at about 1.5 at% Bi. Similar concentrations were found also for other systems. From this we see that it is very easy to obtain a type-II superconductor. The  $\kappa_1$  values in the table are obtained from measurements of the upper critical field  $B_{c2}$ . However, the  $\kappa_2$  values are calculated using a formula given by Gor'kov and Goodman. In this formula, the relation between  $\kappa$  and the electron mean free path is summarized as [55]:

$$\kappa_2 \approx \kappa_0 + 7.5 \times 10^{-4} \rho \gamma^{1/2} \quad 4.87$$

Here,  $\kappa_0$  is the Ginzburg–Landau parameter of the pure superconductor, that is, for the limiting case  $l^* \rightarrow \infty$ ,  $\gamma$  is the Sommerfeld coefficient of the specific heat of the electron system (in the unit  $J/cm^3 K^2$ ), and  $\rho$  is the resistivity in the normal conducting state (in  $\Omega cm$ ). In this formula, the electron mean free path is expressed in terms of  $\rho$  and  $\gamma$ .

**Table 4.2** The  $\kappa$  values<sup>a</sup> of In–Bi alloys

A-% Bi	1.55	1.70	1.80	2.0	2.5	4.0
$\kappa_1$ at $T_c$	0.76	0.88	0.91	1.10	1.25	1.46
$\kappa_2$ at $T_c$	0.74	0.85	0.88	1.15	1.29	1.53

$$^a \kappa_1 = \frac{B_{c2}}{\sqrt{2}B_{c\text{th}}}; \quad \kappa_2 = \kappa_0 + 7.5 \times 10^{-4} \rho \gamma^{1/2}.$$

From [54].

A comparison of lines 2 and 3 in [Table 4.2](#) indicates that the quite differently determined values of  $\kappa$  agree very well. For the application of Eq. (4.87), we must know the values of  $\kappa_0$ . These  $\kappa_0$  values can be obtained by extrapolating the  $\kappa$  values of alloys to zero concentration of the impurity atoms ([Table 4.3](#)).

**Table 4.3** The  $\kappa_0$  values<sup>a</sup> of superconducting elements

Element	Al	In	Pb	Sn	Ta	Tl	Nb	V
$\kappa_0$ at $T_c$	0.03	0.06	0.4	0.1	0.35	0.3	0.8	0.85

<sup>a</sup> See also [56].

One might ask if the constant  $\kappa_0$  for type-I superconductors has a physical meaning. Such a meaning, indeed, results from the GLAG theory. In this case, Eq. (4.81) defines a field  $B_{c2}$  which is smaller than  $B_{c\text{th}}$ . This field yields a definite lower limit for the so-called supercooling experiments.

In a magnetic field the transition from the normal conducting into the superconducting state is a

first-order phase transition (see [Section 4.1](#)). During such transitions, supercooling or superheating effects can occur. For example, water can be cooled down carefully to a few degrees below its freezing point without the formation of ice. For superconductivity this means, for example, that the magnetic field can be lowered below its critical value without the immediate appearance of the superconducting state. The magnitude of this effect depends on the detailed features of the experiment. For  $B < B_{\text{cth}}$  the normal conducting state is thermodynamically unstable. However, the new phase cannot yet form itself. First, a nucleation seed for this phase must appear, which subsequently can grow further. During such experiments, the magnetic field cannot fall below the value  $B_{c2} = (\sqrt{2})\kappa_0 B_{\text{cth}}$  without the appearance of the superconducting state. So if we have a superconductor with a  $\kappa_0$  value very close to  $1/\sqrt{2}$ , no supercooling effects can be observed. However, in superconductors like pure Al or pure In, the magnetic supercooling regimes are very large. This could be well confirmed experimentally.

Finally, we mention another possibility for determining  $\kappa$ . Also the slope of the magnetization curve near  $B_{c2}$  is determined by  $\kappa$ , and we have

$$\mu_0(dM/dB)_{B=B_{c2}} = -\frac{1}{1.16(2\kappa^2 - 1)} \quad 4.88$$

So far we have indicated four possibilities for determining  $\kappa$ : Eqs. [\(4.81\)](#), [\(4.84\)](#), [\(4.87\)](#), and [\(4.88\)](#). Near  $T_c$  all four methods yield closely similar  $\kappa$  values. However, for temperatures  $T < T_c$  the values differ from each other. This is due to the fact that the Ginzburg–Landau theory is strictly valid only close to  $T_c$ . Furthermore, beyond this range of validity,  $\kappa$  is temperature-dependent.

Because of their relation to  $B_{\text{cth}}$ , the two critical fields  $B_{c1}$  and  $B_{c2}$  are also dependent on the temperature. Neglecting all details, in [Figure 4.26](#) we show schematically the three critical fields of a type-II superconductor. We can clearly see the stability regimes of the different phases. Below  $B_{c1}$ , the Meissner phase, that is, the phase with complete field expulsion, is stable. Between  $B_{c1}$  and  $B_{c2}$  we have the mixed state, the Shubnikov phase, as the stable phase; and above  $B_{c2}$  there is normal conduction. In [Figure 4.27](#) we show this diagram for an indium–bismuth alloy (In + 4 at% Bi) [54].

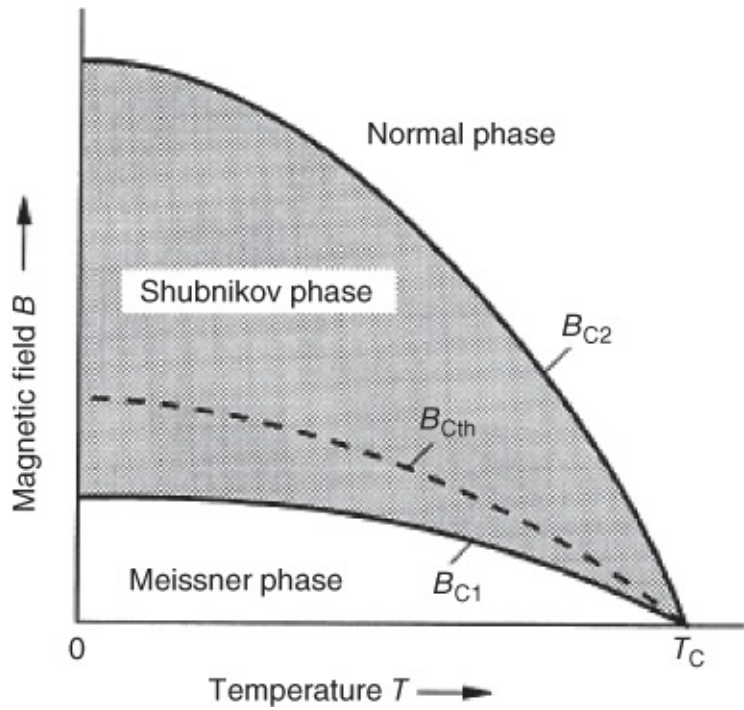


**Figure 4.26** Schematics of the phase diagram of a type-II superconductor.

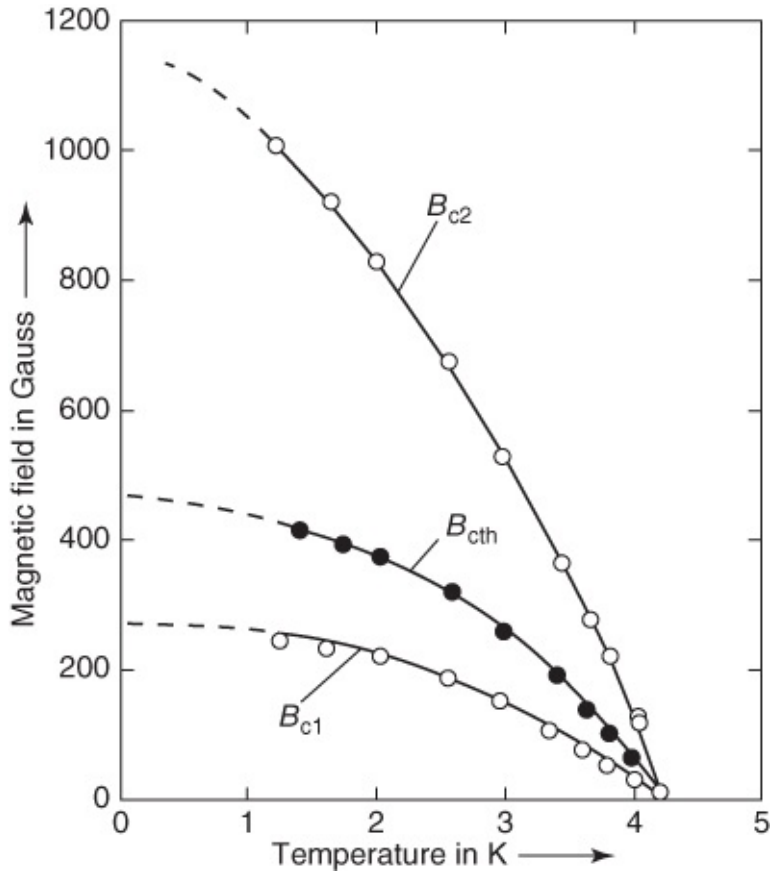


**Figure 4.27** The critical fields ( $1 \text{ G} = 10^{-4} \text{ T}$ ) of an indium bismuth alloy, In + 4 at% Bi. (From [54].)

For some substances, the upper critical field can reach rather large values (see also [Chapter 2](#)). In this case one often speaks of “high-field superconductors.” For example, the Chevrel

phases [57] (ternary molybdenum sulfides, see [Section 2.5](#)) represent materials that can tolerate extreme magnetic fields up to about 60 T without losing their superconductivity [57, 58]. In [Figure 4.28](#) we show  $B_{c2}$  plotted versus the temperature for some high-field superconductors. The critical fields of these materials can be a few hundred times larger than those of the type-I superconductors ([Figure 4.12](#)).

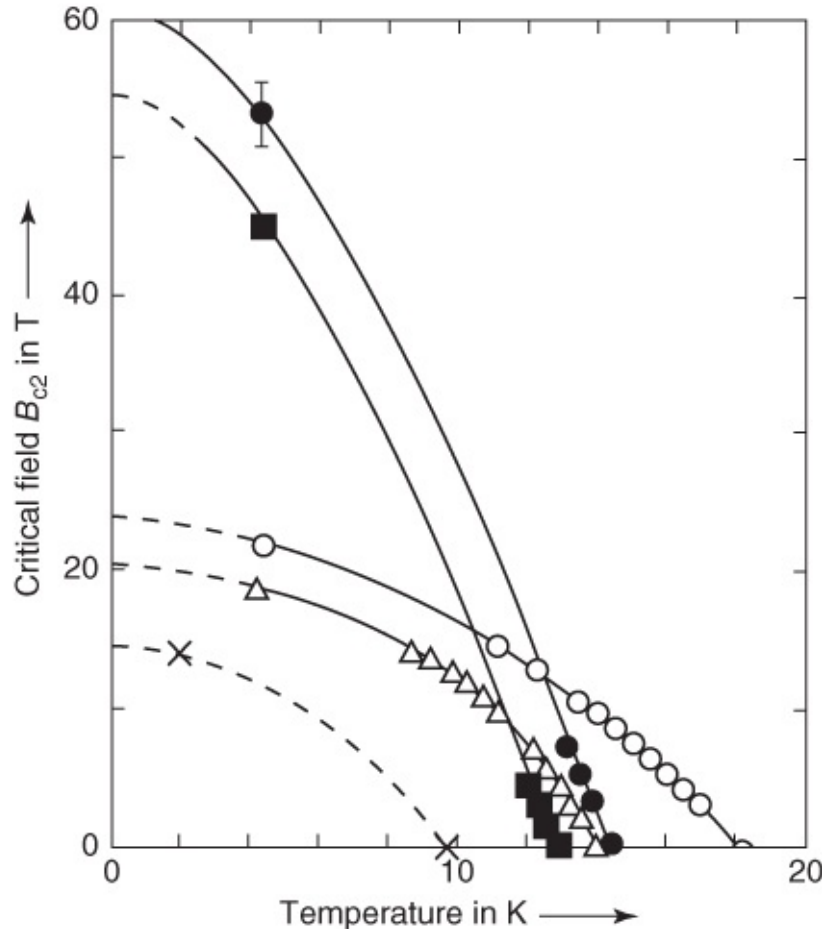


**Figure 4.28** Upper critical field of some high-field superconductors:  $\circ$  Nb<sub>3</sub>Sn, wire diameter 0.5 mm [59];  $\Delta$  V<sub>3</sub>Ga, sintered sample [59];  $\times$  Nb<sub>50</sub>Ti<sub>50</sub> [60];  $\blacksquare$  PbMo<sub>6.35</sub>S<sub>8</sub> [61];  $\bullet$  PbGd<sub>0.3</sub>Mo<sub>6</sub>S<sub>8</sub> [61]. (See also Ref. [62].)

In the high-temperature superconductors, still larger values of  $B_{c2}$  are reached. In this case the layered structure of the materials plays an important role. In order to understand this, we consider a stack of thin superconducting plates of thickness  $d$  placed in a magnetic field. The plates should represent the layers of the structure, that is, the CuO<sub>2</sub> planes in the case of the high-temperature superconductors.

If the magnetic field is oriented *perpendicular* to these layers, the supercurrents completely flow within the plates. We do not expect a particular influence of the layered structure. For the upper critical field, one finds the value

$$B_{c2\perp} = \frac{\Phi_0}{2\pi\xi_{||}^2} \quad \text{4.89}$$

which essentially is identical to the expression (4.82) for isotropic superconductors. We have only denoted the Ginzburg–Landau coherence length by  $\xi_{||}$  to indicate that in this case the change of  $\Psi$  parallel to the planes is relevant.

On the other hand, if the magnetic field is oriented *parallel* to the layers, the supercurrents are restricted to a region with the thickness  $d$  of the plates, if no supercurrents can flow between neighboring plates. If the plate thickness is smaller than the coherence length  $\xi_{\perp}$  perpendicular to the plates, we can expect that in the expression of the upper critical field the plate thickness appears instead of  $\xi_{\perp}$ . This is exactly the result one obtains. One finds [63].

$$B_{c2||}^{TP} = \sqrt{6} \frac{\Phi_0}{\pi \xi_{||} d} \quad 4.90$$

The notation “TP” indicates that we are dealing with the upper critical field of a thin plate. For  $d \ll \xi_{||}$ ,  $B_{c2||}^{TP}$  is much larger than  $B_{c2,\perp}$ .

For a single thin plate, the upper critical field can be found also in the case of an arbitrary field orientation. If we denote the angle between the magnetic field and the plane of the plate by  $\vartheta$ , the upper critical field of the plate is obtained from the quadratic equation [61]

$$B_{c2}^{TP}(\vartheta) \left| \frac{\sin \vartheta}{B_{c2,\perp}} \right| + \left[ B_{c2}^{TP}(\vartheta) \frac{\cos \vartheta}{B_{c2||}^{DP}} \right]^2 = 1 \quad 4.91$$

The quantity  $B_{c2}^{TP}(\vartheta)$  has a sharp peak at  $\vartheta = 0^\circ$ , and then decreases monotonically with increasing angle. The minimum  $B_{c2,\perp}$  is reached for  $\vartheta = 90^\circ$ . In [Figure 4.29](#) this curve is shown in comparison with experimental data of the upper critical field for the two high-temperature superconductors  $\text{YBa}_2\text{Cu}_3\text{O}_7$  and  $\text{Bi}_2\text{Sr}_2\text{CaCu}_2\text{O}_8$ . Although the measurements were performed only a few kelvins below the transition temperature, the upper critical field parallel to the layers already reaches values of 10 T and higher.<sup>34</sup> In the figure, we see that the experimental data for  $\text{Bi}_2\text{Sr}_2\text{CaCu}_2\text{O}_8$  closely follow the angle dependence expected for a thin plate (or a stack of such plates). Weak Josephson currents are flowing between the  $\text{CuO}_2$  layers of this compound (see [Sections 1.5.1](#) and [6.1.1](#)). However, they are so small that we can speak of a stack of independent plates in good approximation.

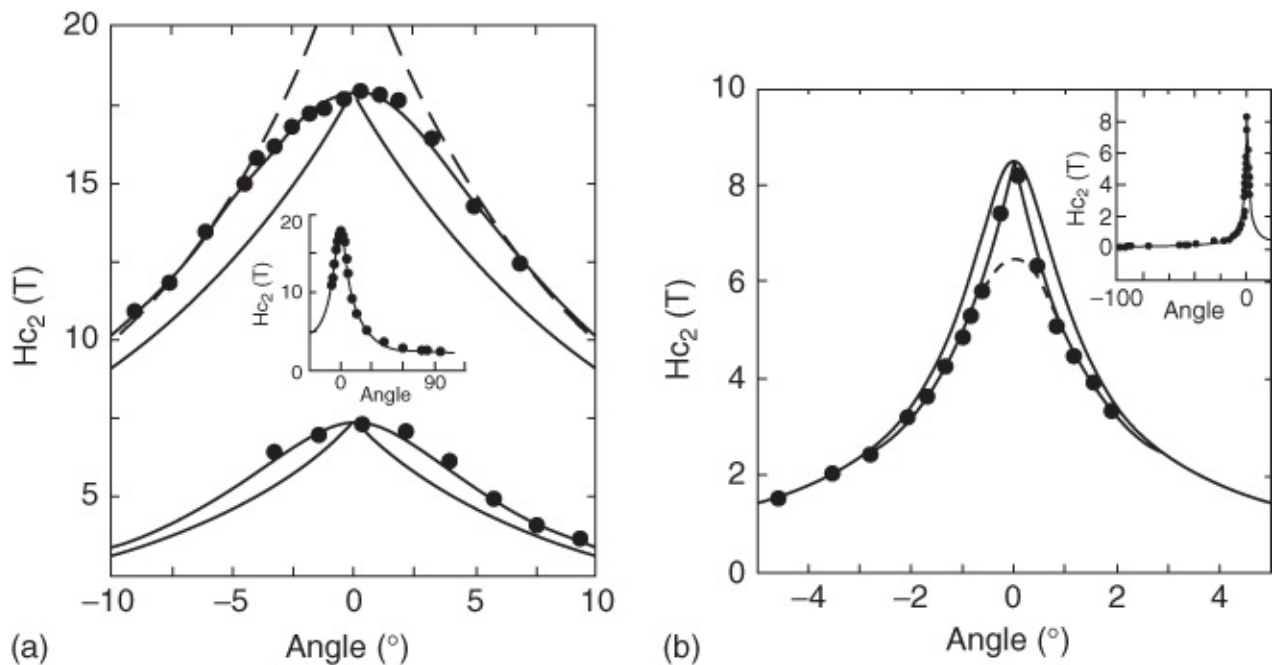


**Figure 4.29** Upper critical field  $B_{c2} = \mu_0 H_{c2}$  of the two high-temperature superconductors  $\text{YBa}_2\text{Cu}_3\text{O}_7$  ( $T_c = 91.2 \text{ K}$ , a) and  $\text{Bi}_2\text{Sr}_2\text{Ca}\text{Cu}_2\text{O}_8$  ( $T_c \approx 85 \text{ K}$ , b) obtained from resistance measurements plotted versus the angle between the  $\text{CuO}_2$  planes and the applied field. The main plots show the angles near the parallel orientation. The insets refer to the full range of angles. Measuring temperatures: for  $\text{YBa}_2\text{Cu}_3\text{O}_7$ , 89 K (upper curve) and 84.5 K (lower curve); for  $\text{Bi}_2\text{Sr}_2\text{Ca}\text{Cu}_2\text{O}_8$ , 80.4 K. The sharply peaked curves correspond to Eq. (4.91) for the angle dependence of the upper critical field of a thin plate. The rounded curves refer to Eq. (4.92) for a strongly anisotropic, but spatially homogeneous, superconductor. (From [64].)

For field orientations nearly parallel to the layers, in contrast to  $\text{Bi}_2\text{Sr}_2\text{Ca}\text{Cu}_2\text{O}_8$ , the experimental data for  $\text{YBa}_2\text{Cu}_3\text{O}_7$  follow a rounded curve. In the latter material, the coupling between the  $\text{CuO}_2$  planes is relatively strong. Hence, this compound is better described in terms of a spatially nearly homogeneous superconductor. However, the superconducting properties depend on direction. In particular, much larger supercurrents can flow within the  $\text{CuO}_2$  planes than perpendicular to the planes. This dependence on direction can be well reproduced by the Ginzburg–Landau theory if in the gradient term of the Gibbs function (4.26) one introduces different values of the effective mass for the gradients parallel and perpendicular to the planes, respectively. For the angle dependence of the upper critical field, in this “anisotropic Ginzburg–Landau theory” one obtains the expression

$$B_{c2}(\vartheta) = \frac{1}{\sqrt{(\sin \vartheta/B_{c2,\perp})^2 + (\cos \vartheta/B_{c2,\parallel})^2}} \quad 4.92$$

Here,  $B_{c2,\perp}$  is given by Eq. (4.89). For  $B_{c2,\parallel}$  one obtains

$$B_{c2,\parallel} = \frac{\Phi_0}{2\pi\xi_{\parallel}\xi_{\perp}}$$

At low temperatures, for both materials one obtains extremely high values of the upper critical field, which can be reached experimentally only in very few special laboratories. For field orientations *perpendicular* to the layers, for  $T \rightarrow 0$  in the case of  $\text{Bi}_2\text{Sr}_2\text{CaCu}_2\text{O}_8$ , for the lower limit of  $B_{c2\perp}$  one obtains a value of at least 60 T, and for  $\text{YBa}_2\text{Cu}_3\text{O}_7$  even values above 100 T. This corresponds to Ginzburg–Landau coherence lengths  $\xi_{\parallel}$  (also referred to as  $\xi_{ab}$ ) of about 1.5–3 nm. For  $\text{YBa}_2\text{Cu}_3\text{O}_7$  and for field orientations *parallel* to the layers, measurements were carried out using explosive flux-compression techniques [66]. From this it appears that this material remains superconducting up to at least 240 T. Such fields correspond to coherence lengths  $\xi_{\perp}$  (also referred to as  $\xi_c$ ) of about 0.3 nm. For  $\text{Bi}_2\text{Sr}_2\text{CaCu}_2\text{O}_8$  from such measurements near  $T_c$ , one even extrapolates critical fields in the range of 1000 T. The latter value corresponds to a “plate thickness”  $d$  of about 0.4 nm, or to a coherence length  $\xi_c \approx 0.1$  nm, if we use Eq. (4.93). These atomically small values, together with the angle dependence of the upper critical field, clearly show that in  $\text{Bi}_2\text{Sr}_2\text{CaCu}_2\text{O}_8$  the superconductivity is practically exclusively concentrated on the  $\text{CuO}_2$  planes.

So far we have discussed a number of superconductors with a very high upper critical field. From Eq. (4.90) for  $B_{c2,\parallel}$  we even conclude that the upper critical field can become arbitrarily large if the plate thickness  $d$  becomes sufficiently small. Physically, this is unreasonable. Therefore, we must look for other mechanisms that limit the superconductivity in high magnetic fields.

In the case of spin-singlet Cooper pairing a limitation is reached by the Zeeman splitting, which the two electrons of the pair experience in the magnetic field. We have discussed this in [Section 3.2.4](#). At a sufficiently high magnetic field, this energy splitting becomes so large that it is more favorable to abandon superconductivity and to orient the spins of both electrons parallel to the field. Based on these arguments, one can derive a critical field  $B_p$  that is connected with the energy gap  $\Delta_0$  via the relation [67, 68]

$$B_p = \frac{\Delta_0}{\sqrt{2}\mu_B} \approx 1.84[T/K]T_c \quad 4.94$$

Here,  $\mu_B$  denotes Bohr's magneton. This limitation of the superconducting state is also referred to as **the Clogston-Chandrasekhar-limit** or the *paramagnetic limit*. In the case of a strong coupling between the electron spin and the orbital angular momentum, this value can still be strongly increased, as well as by the Fulde–Ferrell–Larkin–Ovchinnikov (FFLO)-states discussed in [Section 3.2.4](#).

For a superconductor with a transition temperature of 10 K, from Eq. (4.94) we obtain a value of 18.4 T, and for a superconductor with  $T_c = 100$  K a value of 184 T. For most superconductors,  $B_p$  is much larger than  $B_{c2}$  according to Eq. (4.82).

At the end of our discussion of the magnetization curve and the critical fields of type-II superconductors, we emphasize that all the results presented in this section are restricted to magnetization curves that can be followed reversibly. For an increasing external magnetic field, the same curve must appear as in a decreasing field. This is only the case if the thermodynamic equilibrium state is established for each external field  $B_a$ . In [Chapter 5](#) we will see that generally this is not the case, and that, instead, all kinds of inhomogeneities hinder the spatial equilibrium distribution of the field. In this case, the form of the magnetization curve depends on the previous history of the superconductor. Only the value of  $B_{c2}$ , at which the superconductivity completely vanishes, remains unequivocally fixed.

## 4.7.2 The Shubnikov Phase

In the Shubnikov phase, which is stable in a type-II superconductor at external fields  $B_a$  in the range between  $B_{c1}$  and  $B_{c2}$ , magnetic flux penetrates into the superconductor in the form of quantized flux lines (vortices). In the case of conventional superconductors, the lowest enthalpy value is obtained for a configuration of the vortices at the corners of equilateral triangles (see [Section 1.2](#)).

In [Figure 4.30](#) the Cooper pair density, the spatial field distribution, and the supercurrent density associated with a vortex are shown schematically. In the center of the vortex the density of Cooper pairs is zero, and it reaches its equilibrium value  $n_s(T)$  at a distance of about  $\xi_{\text{GL}}$ . In the center the magnetic field has its maximum with a value of about  $2B_{C1}$ , and it decreases toward the outside. This decrease in  $B$  is controlled by the penetration depth. Superconducting circulating currents flow around the vortex core, resulting in the spatial variation of the magnetic field.

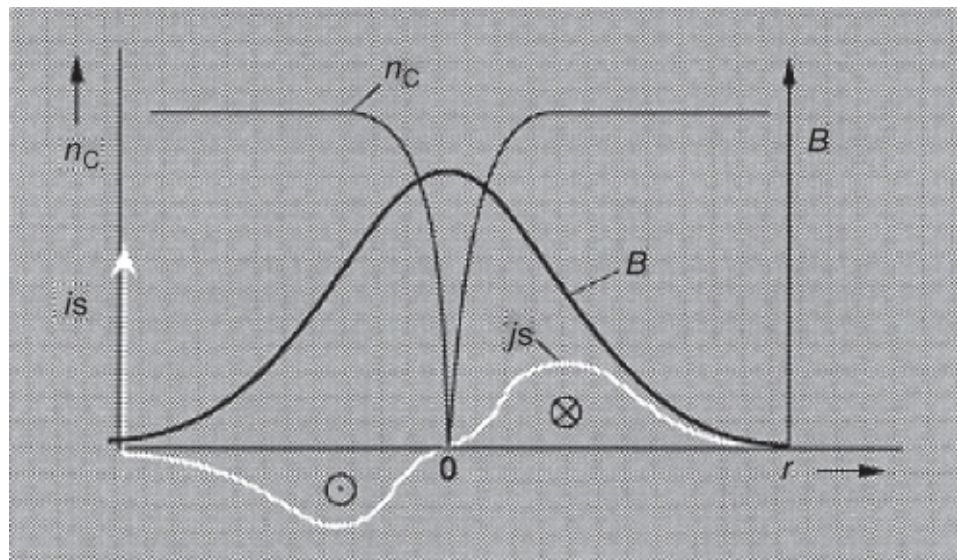


**Figure 4.30** Spatial variations of Cooper pair density, magnetic field, and supercurrent density for a planar cut across a vortex, shown schematically.

Only after a lengthy calculation can one show that the lowest enthalpy and thereby the stable state is attained for a state with a triangular vortex lattice with one flux quantum at each lattice

site. It is easy to see that only a vortex structure can appear, where each vortex contains exactly an integer multiple of the elementary flux quantum. In [Section 1.2](#) we have derived the flux quantization, or more accurately the fluxoid quantization, from the condition that, during one turn around the superconducting ring, the wave function of the Cooper pairs must just reproduce itself. This condition is also valid for the vortices of the Shubnikov phase. From this we conclude that each vortex can contain only an integer multiple of the flux quantum  $\Phi_0$ . If the configuration of a normal conducting core along the axis of a vortex is energetically favorable, we expect that each vortex contains exactly one  $\Phi_0$ , such that as many vortices can be generated as possible. However, the fact that such a vortex lattice indeed represents the state with the smallest enthalpy can only be shown by detailed calculations. In [Figure 4.31](#) we present the spatial variation of the Cooper pair density and of the magnetic field along one direction. With increasing external field  $B_a$ , the distance between the vortices becomes smaller. However, at the same time also the average Cooper pair density  $n_s$  decreases. For external fields only slightly below  $B_{c2}$ , the vortices approach each other down to a distance of about  $2 \xi_{\text{GL}}$ . In this case, because of the strong overlap of the circulating current systems, distinguishing between the individual vortices is no longer meaningful. For  $B \rightarrow B_{c2}$ , the Cooper pair density continuously approaches zero. Because of these features, the phase transition into the normal state at  $B_{c2}$  represents a second-order phase transition. On the other hand, in type-I superconductors, the phase transition in a magnetic field is of first order (see [Section 4.6.2](#)).

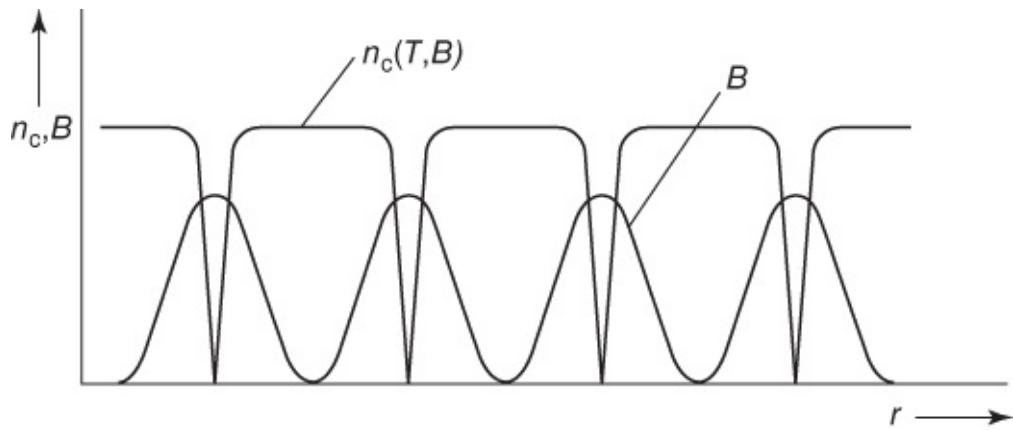


**Figure 4.31** Spatial variations of Cooper pair density and magnetic field in the Shubnikov phase, shown schematically. Between the vortices the Cooper pair density attains the equilibrium value corresponding to the given values of  $T$  and  $B$ . Since  $\lambda_L > \xi_{\text{GL}}$ , with increasing field the magnetic field between the vortices is not completely expelled any more.

Today we can investigate the Cooper pair density near a vortex with high spatial resolution using scanning tunneling microscopy [69] (see [Section 1.2](#), [Figure 1.10f](#)). With this method, for example,  $\xi_{\text{GL}}$  can be determined directly, and the density of states of the unpaired electrons within the vortex can be studied in detail. Such experiments were particularly interesting for the high-temperature superconductors. In this case,  $\xi_{\text{GL}}$  (more precisely,  $\xi_{ab}$ ) is so small that the unpaired electrons can occupy only a few discrete energy states, in contrast to many other

superconductors, where these electrons can form a continuous energy spectrum.

So far, our discussion of the vortex lattice has been restricted to samples with zero demagnetization coefficient. The magnetic flux penetration was *not* determined by the geometry as in the case of the intermediate state experiments (see [Section 4.6.4](#)). Now the question comes up, whether some kind of intermediate state also exists in a type-II superconductor, and which phases coexist in this intermediate state. As long as the type-II superconductor resides in the Meissner phase, it expels the field in the same way as a type-I superconductor. However, if the field  $B_{c1}$  is reached at the surface of the sample, flux must penetrate into the type-II superconductor. In this case, a state is established in which macroscopic domains of the Meissner phase and of the Shubnikov phase exist next to each other. An example of this new state is shown in [Figure 4.32](#). Instead of the normal phase of a type-I superconductor, for the type-II superconductor we have the Shubnikov phase.



**Figure 4.32** Coexistence of the Meissner phase and of the Shubnikov phase in a type-II superconductor with  $\kappa$  close to  $1/\sqrt{2}$ . Material: Pb + 1.89 at% Tl,  $\kappa = 0.73$ ,  $T = 1.2$  K; sample: disk with 2 mm diameter and 1 mm thickness; external field  $B_a = 36.5$  mT; magnification  $4800\times$ . This state can be established in samples with a finite value of the demagnetization coefficient. (By courtesy of Dr U. Essmann.)

Structures of this type are referred to as **intermediate-mixed state**. They are observed only for values of  $\kappa$  close to  $1/\sqrt{2}$ . Neumann and Tewordt [70] have extended the Ginzburg–Landau theory to temperatures below  $T_c$ . From this extension, one finds that there is a narrow range of  $\kappa$  values near  $1/\sqrt{2}$  where the interaction between vortices becomes attractive. Due to this attraction, domains without flux lines coexist with domains containing vortices. Further details can be found in the monograph [M17].

Turning now to the Shubnikov phase in the high-temperature superconductors, we note that several of their properties have a strong impact on this phase:

1. the atomically small Ginzburg–Landau coherence length;
2. the high transition temperature  $T_c$ ;
3. the layered structure of the superconducting state in combination with the Josephson coupling between the superconducting  $\text{CuO}_2$  layers in many cuprates.

As an additional property, we could mention the  $d_{x^2-y^2}$  symmetry of the pair wave function. However, this affects the vortex properties that we want to discuss in the following only very little.

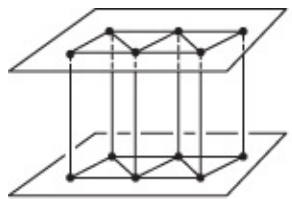
We can treat the “coherence volume”  $V_c = \xi_{ab}^{-2} \xi_c$  as the volume element<sup>35</sup> in which the Cooper pair density changes only very little, whereas large variations can appear on larger scales. In the cuprates, this volume is smaller by 2–4 orders of magnitude compared to that in conventional superconductors. We can write the condensation energy per unit volume of the superconducting state as  $E_c = B_{\text{cth}}^2 / 2\mu_0$ . In the cuprates, the value of  $B_{\text{cth}}$  can be about 1 T.

The condensation energy stored within  $V_c$  can be compared to the thermal energy  $k_B T$ . Here, we use the transition temperature  $T_c$  for an upper limit of  $k_B T$ . Obviously, the ratio  $k_B T_c / (E_c V_c)$  represents a characteristic measure indicating the sensitivity of a superconductor against thermal fluctuations. The ratio  $(k_B T_c / E_c V_c)^2 / 2$  is also referred to as the **Ginzburg number**  $G_i$ . In materials such as  $\text{YBa}_2\text{Cu}_3\text{O}_7$  or  $\text{Bi}_2\text{Sr}_2\text{CaCu}_2\text{O}_8$  it has a value of about  $10^{-2}$ . However, in conventional superconductors, one obtains values that are smaller by 5 or more orders of magnitude.<sup>36</sup> This indicates that in the cuprates thermal fluctuations play a much more important role than in conventional superconductors.

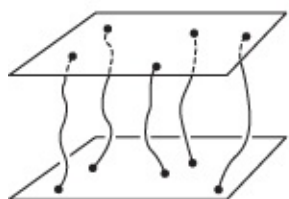
In conventional superconductors, the vortices generate a triangular lattice. Due to thermal fluctuations, the vortices can move around their equilibrium lattice site without leaving it altogether. In some sense the vortices form a crystal, which exists up to the upper critical field. However, if the fluctuations around the equilibrium site become comparable to the distance between the vortices, then the vortices will leave their lattice site, and we are dealing with a vortex liquid.

This “melting” of the vortex lattice was proposed in 1985 by Nelson and coworkers [71], and was subsequently studied in many theoretical and experimental papers, in particular for  $\text{YBa}_2\text{Cu}_3\text{O}_7$ . A summary can be found in the Refs [72–74] and in the monograph [M17]. In  $\text{YBa}_2\text{Cu}_3\text{O}_7$  the supercurrents between the  $\text{CuO}_2$  planes are relatively strong. So in this case we can speak of a highly anisotropic, but spatially nearly homogeneous, superconductor.<sup>37</sup>

In [Figure 4.33](#) we show schematically the vortex structure in the solid and liquid phases, and also a possible phase diagram. In the liquid phase there can still exist a certain amount of short-range order of the vortices (“hexatic vortex liquid”). In magnetic fields only slightly above  $B_{c1}$ , initially one expects a vortex liquid, which turns into a vortex lattice only with decreasing inter-vortex distance. At very high fields or very small distance between the vortices, the lattice melts again, and one obtains the vortex liquid. It is interesting that this melting represents a first-order phase transition, in contrast to the second-order phase transition observed in conventional type-II superconductors at  $B_{c2}$ .



Abrikosov  
flux  
lattice

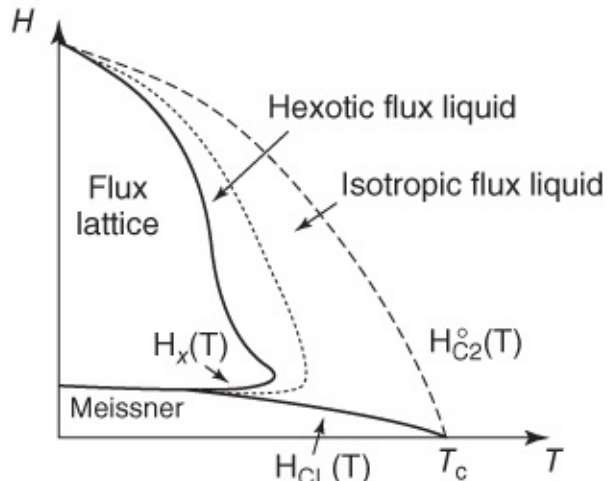


Disentangled  
flux  
liquid



Entangled  
flux  
liquid

(A)



(B)

**Figure 4.33** Possible phases of the so-called vortex matter in a spatially homogeneous superconductor in the case where thermal fluctuations play an important role [75]. (A) We see schematically different vortex configurations: (a) vortex lattice, (b) a liquid phase where the vortices still remain separated, and (c) a liquid phase with entangled vortices. (B) A schematic phase diagram is shown [76]. In the liquid phase a certain amount of short-range order is possible (“hexatic vortex liquid”). One must note also that the liquid phase is inserted between the Meissner phase and the vortex lattice.

In the early experiments, often the dissipation due to the vortex motion was studied [77], and experimental observations of the melting of the vortex lattice were discussed highly controversially for a long time. One reason is that the studied materials contain a large concentration of defects. Then, instead of the regular vortex lattice, one obtains a vortex glass. Furthermore, in the liquid phase, the vortices are not freely mobile. However, with improving quality of the crystals, the melting of the vortex lattice could be demonstrated nicely in measurements of the magnetization [78] and even of the specific heat [79]. In [Figure 4.34](#) we show a recent experimental phase diagram obtained from such measurements with  $\text{YBa}_2\text{Cu}_3\text{O}_7$  [80]. We note that the deviations from the theoretical phase diagram of [Figure 4.33](#) are still very large. In particular, there appears a glass phase caused by the defects in the vortex lattice.

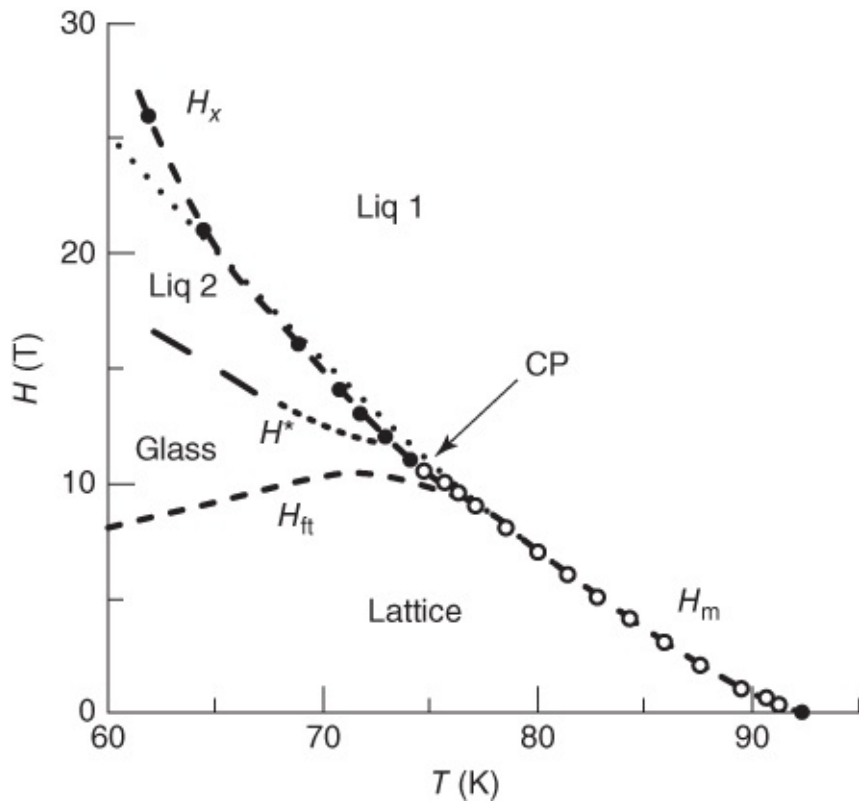


**Figure 4.34** Experimental phase diagram of the vortex state in  $\text{YBa}_2\text{Cu}_3\text{O}_7$  in magnetic fields  $\mu_0 H$  perpendicular to the  $\text{CuO}_2$  planes. The plot shows the melting line  $H_m$  ending in the critical point “CP.” The line  $H_{ft}$  separates the vortex lattice from a glassy state caused by defects in the vortex crystal. Above the line  $H^*$  the magnetization curves are reversible, and below  $H^*$  there appears hysteresis. The dashed line corresponds to a theoretical curve of the melting of the vortex lattice. (From [80], © 2001 Nature.)

Liquid vortex phases could also be detected in other anisotropic superconductors, such as  $\text{NbSe}_2$ , and also in the iron pnictide  $\text{BaCo}_x\text{Fe}_{2-x}\text{As}_2$  [81, 82]. In the case of these compounds, the Ginzburg number is about  $10^{-4}$ .

Now we turn to the superconducting, layered compounds, in which the layers are only weakly coupled with each other by means of the Josephson effect. First we consider the case  $T = 0$ , and we assume that the magnetic field is oriented perpendicular to the layered structure. Also in this case above the field  $B_{c1,\perp}$  there appear vortices each carrying one flux quantum  $\Phi_0$ . The field  $B_{c1,\perp}$  is given by

$$B_{c1,\perp} = \frac{\Phi_0}{4\pi\lambda_{ab}^2} \left( \ln \frac{\lambda_{ab}}{\xi_{ab}} + 0.08 \right) \quad 4.95$$

corresponding exactly to expression (4.85). Here, we have denoted the London penetration depth by  $\lambda_{ab}$ , since the shielding currents flow within the  $ab$  plane of the superconducting layers.

In the present case, the supercurrents flow around the vortex axis exclusively in the

superconducting layers separated from each other, that is, within the planes marked by the crystallographic  $a$  and  $b$  axes. Hence, we can speak of stacks of nearly two-dimensional vortices. In each layer the vortex can be imagined as an independent, individual object. J. R. Clem introduced the term ***pancakes*** for these vortices [83].

The case of a single thin superconducting layer of thickness  $d$  was studied by J. Pearl in 1966 [84]. It was found that within the layer the circulating currents around the vortex decay with a characteristic length  $\lambda_{\text{eff}} = \lambda_L^2/d$  from the axis toward the outside. Obviously, for  $d \ll \lambda_L$  the length  $\lambda_{\text{eff}}$  can become much larger than  $\lambda_L$ . However, also in this two-dimensional case, the vortices generate a triangular lattice within the layer.

If we have a stack of many superconducting layers, the pancakes within the different planes will interact with each other. This interaction results, on the one hand, from the magnetic field generated by each vortex, and, on the other, from the Josephson supercurrents between the planes. Two vortices in neighboring planes attract each other if they have the same sign. Hence, in a perpendicular magnetic field the pancakes order themselves on top of each other along common axes. So one again obtains essentially a triangular lattice of flux lines penetrating the whole sample.

However, now it costs only little energy to shift the individual pancakes away from their common axis. Therefore, at finite temperatures, a number of different vortex phases are possible [85]:

- the “crystalline” state, in which the pancakes form a triangular flux-line lattice;
- a flux-line liquid, in which the pancakes still form flux lines, which are freely mobile;
- a quasi-2D vortex solid, in which the pancakes form a triangular lattice within a plane, but where the lattices in different planes are freely shifted relative to each other;
- a pancake gas, in which the pancakes are freely mobile within a plane and also are not ordered any more perpendicular to it.

In [Figure 4.35](#) we show a vortex phase diagram of two  $\text{Bi}_2\text{Sr}_2\text{CaCu}_2\text{O}_{8+x}$  single crystals with different oxygen concentrations, determined from measurements of the muon-spin resonance and magnetization [86]. We can see the phases discussed above. However, we also note that the details strongly depend on the doping level of the samples. Furthermore, disorder plays an important role, similarly as in  $\text{YBa}_2\text{Cu}_3\text{O}_7$ , such that the “crystalline” phases rather represent glassy states. Similar phase diagrams were also determined using other experimental methods, say, using the vortex penetration into the crystal [87] or using the magnetic permeability [88]. Frequently, these measurements differ in a number of details, but they clearly indicate that in  $\text{Bi}_2\text{Sr}_2\text{CaCu}_2\text{O}_8$  there exist a number of different vortex states.

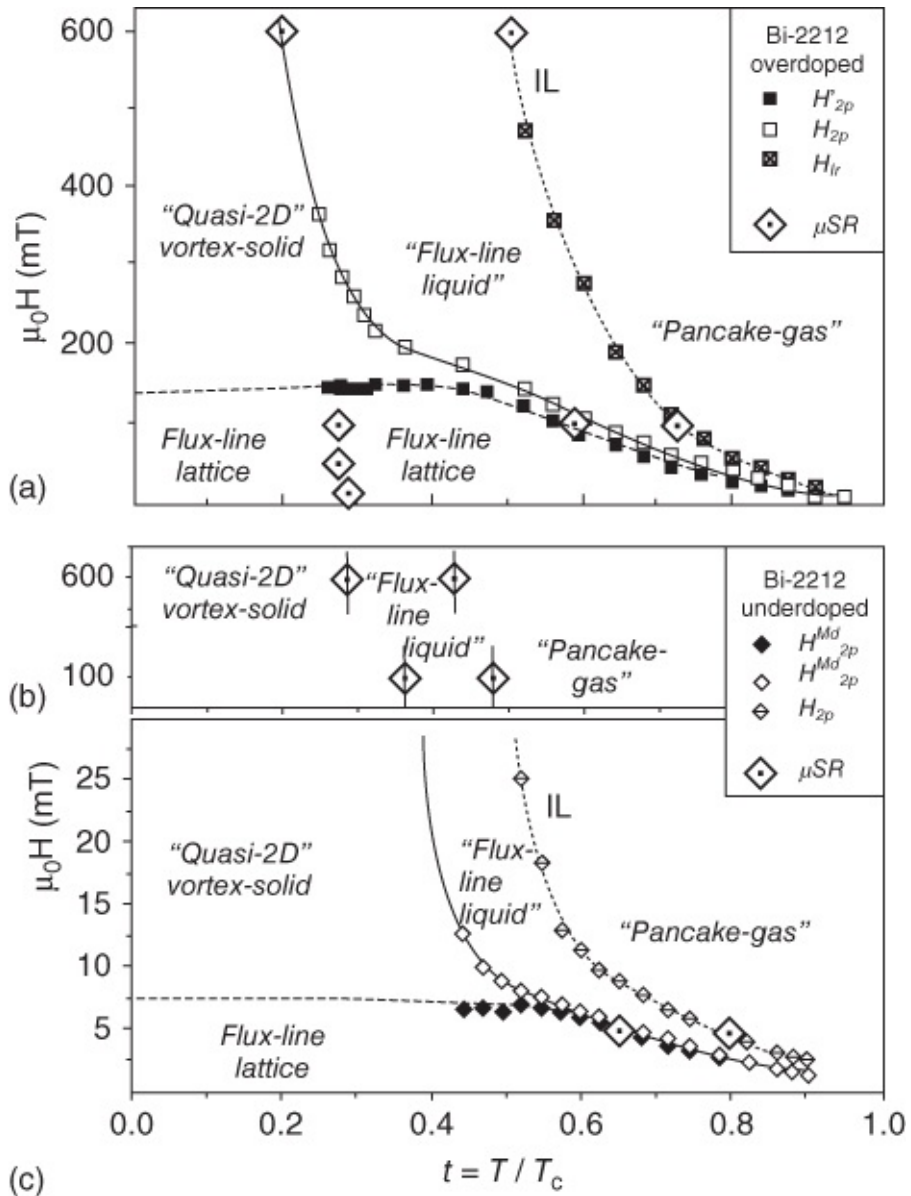


**Figure 4.35** Vortex phase diagrams of  $\text{Bi}_2\text{Sr}_2\text{CaCu}_2\text{O}_{8+x}$  single crystals with different doping. The diagrams were obtained from measurements of the muon-spin rotation ( $\mu\text{SR}$ ) and of the magnetization. (a) Over-doped crystal,  $T_c = 64$  K and (b,c) under-doped crystal,  $T_c = 77$  K [86].

Further we note that mostly a Gibbs function serves as the starting point of the theoretical calculations, which is constructed similar to Eq. (4.27) of the Ginzburg–Landau theory. This “Lawrence–Doniach model” [89] was developed in 1970. In this model one considers a stack of two-dimensional superconducting layers, which are coupled to each other by means of Josephson currents. However, the calculation of the different vortex phases is extremely difficult and can be done only using various approximations.

Let us look at the superconducting layered structure at  $T = 0$  in a magnetic field oriented parallel to the layers. If the applied field is very weak, the Meissner phase appears again. The shielding currents flow across the superconducting layers. However, the maximum value of this current is much smaller than in the case where the field is applied perpendicular to the layers.

As a result the penetration depth  $\lambda_c$  of the magnetic field parallel to the layers is much larger than perpendicular to them. The value of  $\lambda_c$  can reach up to 100  $\mu\text{m}$  or more.

Vortices can also be generated in a parallel orientation of the field, if the magnetic field exceeds a lower critical field  $B_{c1,\parallel}$ . In the Lawrence–Doniach model for  $B_{c1,\parallel}$  one finds the expression [90]

$$B_{c1,\parallel} = \frac{\Phi_0}{4\pi\lambda_{ab}\lambda_c} \left( \ln \frac{\lambda_{ab}}{s} + 1.12 \right) \quad \text{4.96}$$

Here,  $s$  is the distance between the superconducting layers. Because of the large value of  $\lambda_c$ ,  $B_{c1,\parallel}$  is smaller by a factor  $\lambda_{ab}/\lambda_c$  than the field  $B_{c1,\perp}$  for perpendicular field orientation given by Eq. (4.95). The factor  $\lambda_{ab}/\lambda_c$  can attain values of  $10^{-3}$  or smaller. Further, we note that in Eq. (4.96) compared to Eq. (4.95) the coherence length  $\xi_{ab}$  is replaced by the layer distance  $s$ .

Within the planes the vortices have a diameter of about  $2\lambda_c$  and perpendicular to the planes a diameter of about  $2\lambda_{ab}$ . Hence, they are very flat objects, extending also over many superconducting planes, since  $\lambda_{ab}$  in general is much larger than the layer distance. [Figure 4.36a](#) schematically shows the current distribution of one of these so-called “Josephson vortices.” The magnetic field distribution of such vortices can be imaged experimentally by means of scanning superconducting quantum interference device (SQUID) microscopy (see [Section 1.2](#)) [92].

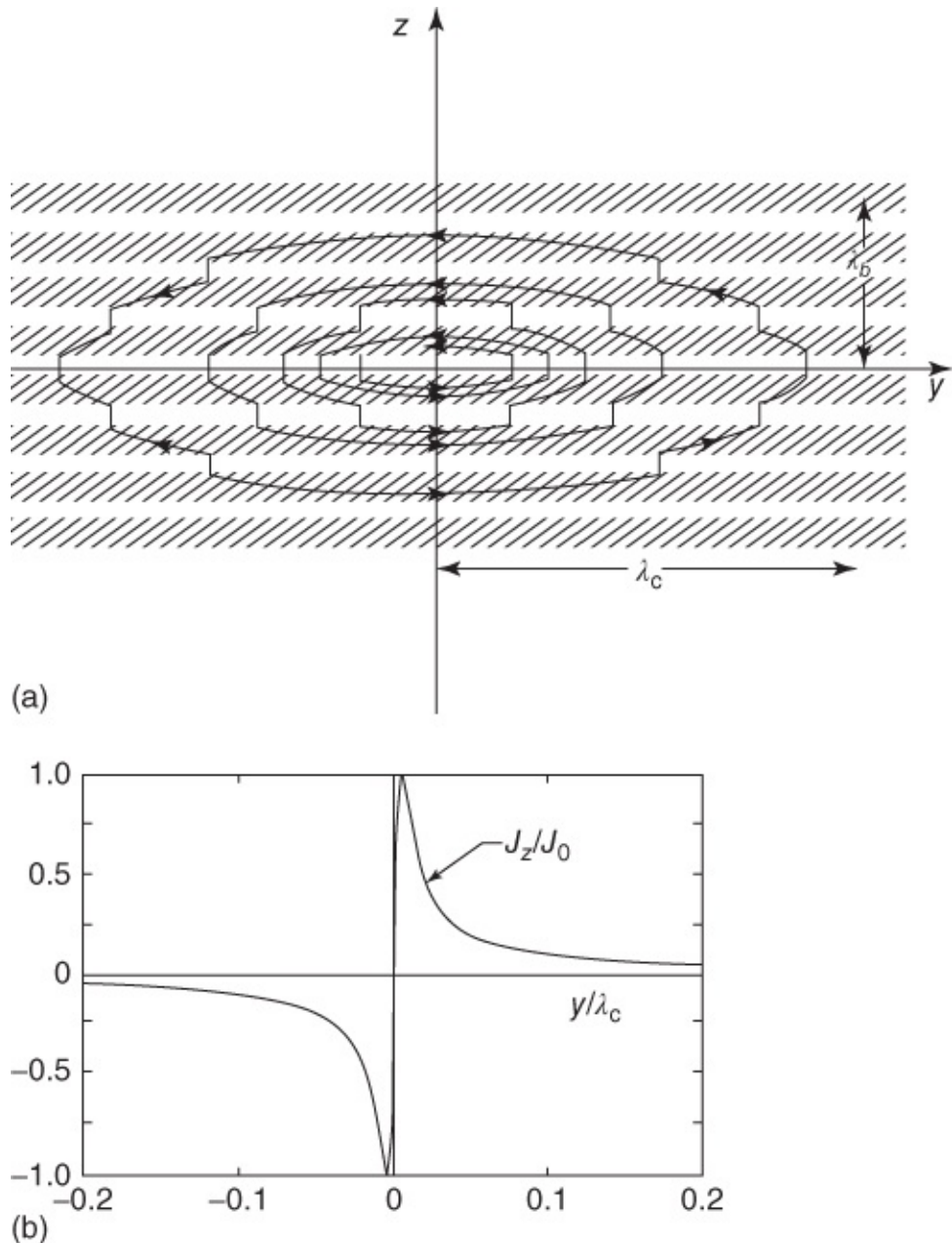


**Figure 4.36** (a) Schematic of the circulating currents around a “Josephson vortex” in a superconducting layered structure. The superconducting layers are the hatched regions extending along the  $(x,y)$  planes. The vortex axis runs along the  $x$ -direction, that is, perpendicular to the paper. (b) The supercurrent density in the  $z$ -direction between the two layers, between which the vortex axis is located. (From [91].)

Near the vortex axis the Josephson vortices differ strongly from the Abrikosov vortices in homogeneous type-II superconductors or from the pancake vortices in superconducting layered structures. In the Abrikosov vortices or pancake vortices the Cooper pair density decreases toward the vortex axis down to zero on a length scale  $\xi_{\text{GL}}$  (see [Figure 4.30](#)). On the other hand, in the Josephson vortices the axis is located within a non-superconducting layer, such that the Cooper pair density does not have to be suppressed anymore.

In [Figure 4.36b](#) we show the current density between the two superconducting layers where the vortex axis is located. The supercurrent density increases from the vortex axis toward the

outside on a length scale  $\lambda_J$ , the Josephson penetration depth (see Eq. (1.69)). It passes through a maximum value and then decreases gradually. A Josephson vortex also has a core, which is given perpendicular to the layers by the thickness of the insulating barrier and parallel to the layers by  $\lambda_J$ .

A Josephson vortex can move easily only parallel to the layers.<sup>38</sup> During a displacement in the  $z$  direction the vortex axis must cross a superconducting layer, which is only possible by suppressing the Cooper pair density within this layer at the vortex axis down to zero. However, this costs a large amount of condensation energy, and as a result the superconducting layers develop an energy barrier against the displacement of the Josephson vortex in the  $z$ -direction.

In parallel magnetic fields also the Josephson vortices generate a triangular vortex lattice [93]. If the applied magnetic field is slightly tilted away from the parallel orientation, initially the Josephson vortices cannot cross the superconducting layers [94]. We have the situation that is highly unusual for superconductors in which the magnetization generated by the circulating currents and the applied magnetic field are *not parallel* to each other. This matching effect, which can be demonstrated, for example, by the measurement of the torque trying to reorient the sample parallel to the field, is frequently used to find out if the superconductor has an internal layered structure.

Only when the magnetic field component perpendicular to the layers reaches a value corresponding to about the lower critical field  $B_{c1,\perp}$  can the magnetic field also pass through the superconducting planes. Depending on the magnitude of the maximum supercurrents that can flow between the layers, different types of vortex structures are possible. For example, independent sublattices of Josephson vortices and of pancake vortices can be formed. In the case of strong coupling between the layers, one obtains vortices that are arranged like a staircase around the direction of the applied field. This latter situation is shown schematically in [Figure 4.37](#). The flux lines cut across the superconducting planes in the form of pancake vortices. In between there appear short segments of Josephson vortices.

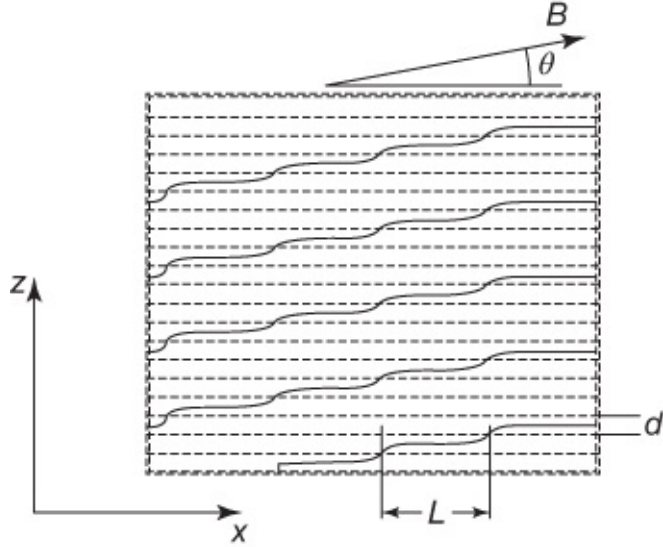


**Figure 4.37** Staircase pattern of flux lines in a magnetic field applied at an angle  $\theta$  to the superconducting layers [95]. The flux lines pass across the planes in the form of pancake vortices joined together by short segments (of length  $L$ ) of Josephson vortices.

We expect that at finite temperatures, the situation becomes even more versatile. As an example, in [Figure 4.38](#) we show the vortex phases observed for a  $\text{Bi}_2\text{Sr}_2\text{CaCu}_2\text{O}_8$  single crystal in the temperature range 77–88 K by means of Hall magnetometry [96]. The diagram indicates the different vortex phases in the  $(H_{||}, H_{\perp})$  plane. One finds a vortex liquid (VII), slightly tilted lattices from pancake vortices (II), weakly interacting crossing lattices (III), composite lattices (IV), or configurations in which the pancakes are arranged in the form of chain structures above the Josephson vortices (V, 1D chains; or VI, sublimed 1D chain state).

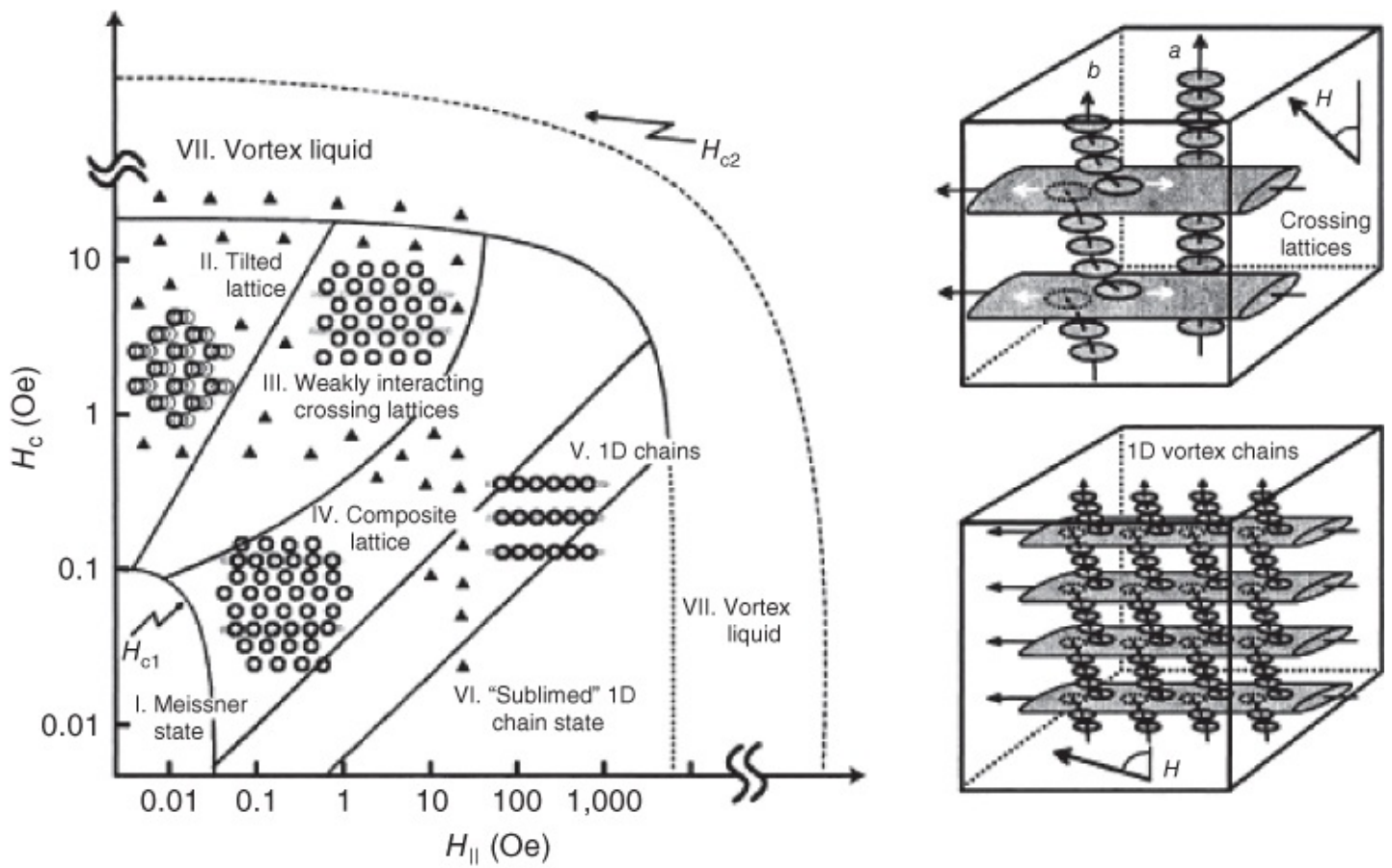


**Figure 4.38** Phase diagram of a  $\text{Bi}_2\text{Sr}_2\text{CaCu}_2\text{O}_8$  single crystal as a function of the magnetic field components  $H_c (=H_{\perp})$  and  $H_{\parallel}$ . The vortex phases were observed by means of Hall probe microscopy. Measuring temperature: 77–88 K. The two figures on the right schematically indicate two of the vortex phases (From [96], © 2001 Nature.)

We do not want to discuss the various possibilities any further. However, we emphasize that the special properties of high-temperature superconductors have resulted in a number of novel phenomena, which had not been observed previously in superconductors.

At the end of this section we briefly want to discuss what happens if we deal only with a single, very thin superconducting plane instead of a superconducting layered structure. We have already treated the case of thin plates several times in the context of the Ginzburg–Landau theory or of the critical magnetic fields, but we have ignored the influence of thermal fluctuations.

It turns out that for two-dimensional or one-dimensional systems, these fluctuations can become sufficiently large that the macroscopic wave function characterizing the superconducting state is destroyed. This result was derived by Hohenberg [97] and by Mermin and Wagner [98] in the 1960s. We can understand this easily by looking again at the coherence volume  $V_c = \xi_{ab}^2 \xi_c$ . If the superconducting layer is very thin, we must replace  $\xi_c$  by the layer thickness  $d$ . However, for  $d \rightarrow 0$  we have  $V_c \rightarrow 0$ , and the condensation energy stored in  $V_c$  vanishes. Then it costs less and less energy to generate a vortex by means of thermal fluctuations.<sup>39</sup>

In the absence of an external magnetic field, positive and negative vortices will be generated spontaneously in equal numbers such that the average magnetization of the sample vanishes. If these vortices can move independently of each other, they result in dissipation and, hence, in a finite resistance. The superconducting state is destroyed.

Berezinskii [99] as well as Kosterlitz and Thouless [100] have shown that at a somewhat lower temperature, namely at the now so-called Berezinskii–Kosterlitz–Thouless transition temperature  $T_{\text{BKT}}$ , vortex–antivortex pairs are generated. These pairs again stabilize a superconducting state, in which the Cooper pairs are not correlated with each other anymore over arbitrarily large distances.

If below  $T_{\text{BKT}}$  a magnetic field is applied perpendicular to the layer, free vortices appear with their orientation given by the applied field. At low temperatures, these vortices again form a triangular lattice. However, this lattice is also highly sensitive to thermal fluctuations. Again one can obtain a vortex liquid, perhaps having a certain hexatic short-range order [101]. Hence, also for the two-dimensional system there exists a phase diagram containing a Meissner phase, a triangular vortex lattice, and liquid vortex phases.

## 4.8 Fluctuations above the Transition Temperature

In the last section, but also briefly in [Section 1.4](#), we considered the influence of thermal fluctuations on the vortex state below the transition temperature  $T_c$ . Obviously, these fluctuations of the equilibrium state also exist above  $T_c$ . In the normal conducting state, the deviation from equilibrium can lead to the transient appearance of the superconducting state within certain regions, that is, to the formation of “puddles” of Cooper pairs. These deviations from equilibrium are not stable, and they will disappear more or less quickly. The statistical appearance of Cooper pairs will become more and more rare the higher the temperature, since with increasing temperature the normal conducting state becomes more and more stable compared to the superconducting state. Therefore, with increasing temperature, larger and larger deviations from equilibrium are needed to generate the superconducting state.

If we note further that the puddles of Cooper pairs represent perfectly conducting regions, we understand immediately that already above  $T_c$  due to the fluctuations in the normal conducting state the statistically appearing puddles of Cooper pairs result in an additional electrical conductivity, which must strongly increase on approaching  $T_c$ .

This influence of the thermal fluctuations can be clearly detected for a number of superconductors. In [Figure 4.39a](#) we show the transition curve of a bismuth film near the critical temperature  $T_c$  [102]. We see clearly that the full normal resistance is reached only at temperatures considerably above  $T_c$ . In [Figure 4.39b](#) the electrical conductance is plotted instead of the resistance. In this plot the additional conductance  $\sigma'$  of the Cooper pair puddles, statistically appearing and vanishing again, is particularly clearly visible.<sup>40</sup> We note that here and in the following we are not dealing with the specific conductance  $\sigma^*$ , but with the

conductance  $\sigma' = \sigma^* d$  ( $d$  = thickness) in the unit A/V =  $\Omega^{-1}$ .

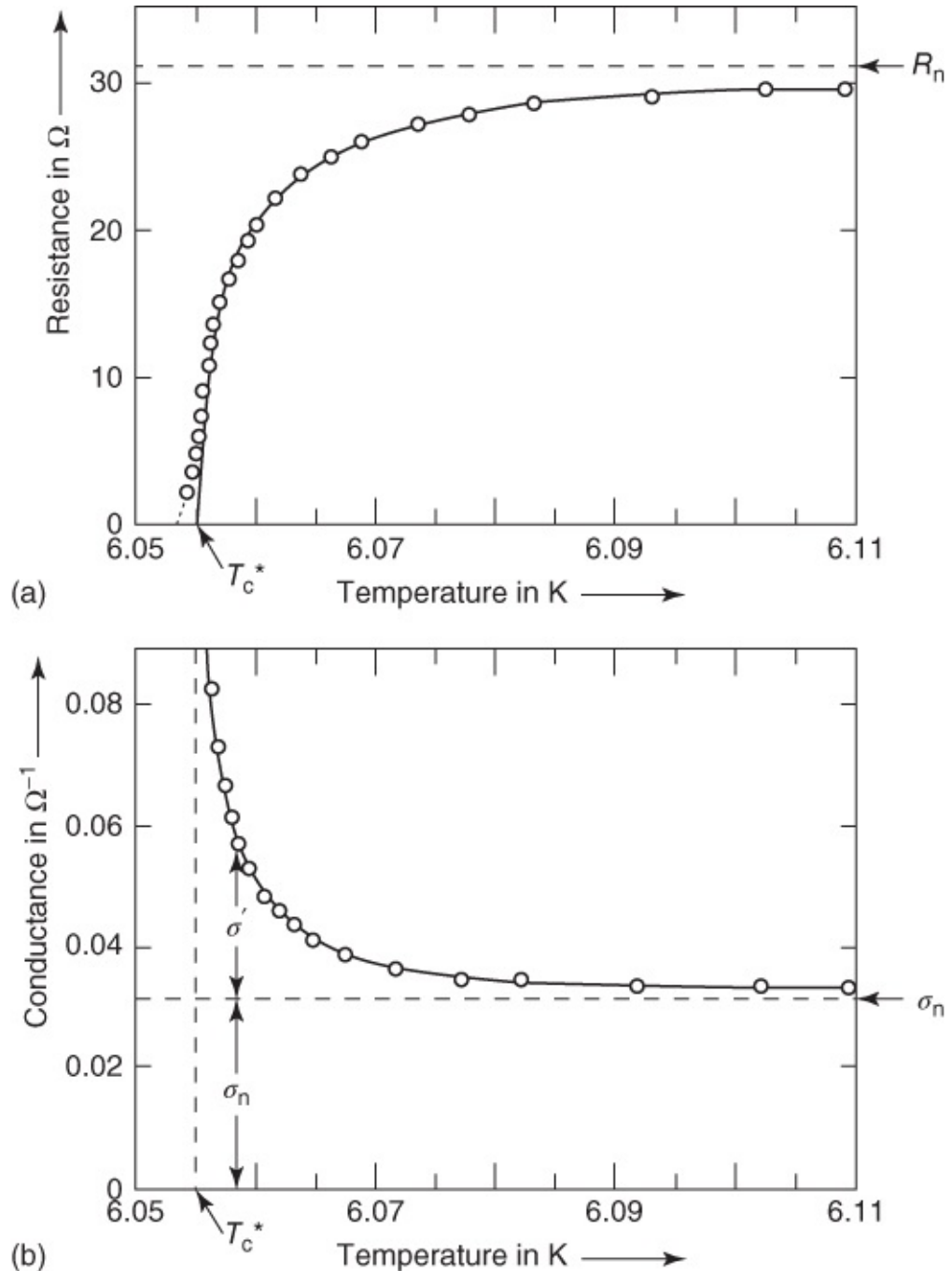


**Figure 4.39** Transition curve of an amorphous bismuth film of 47 nm thickness: (a) resistance and (b) conductance. The solid lines correspond to Eqs. (4.97) and (4.98). (From [102].)

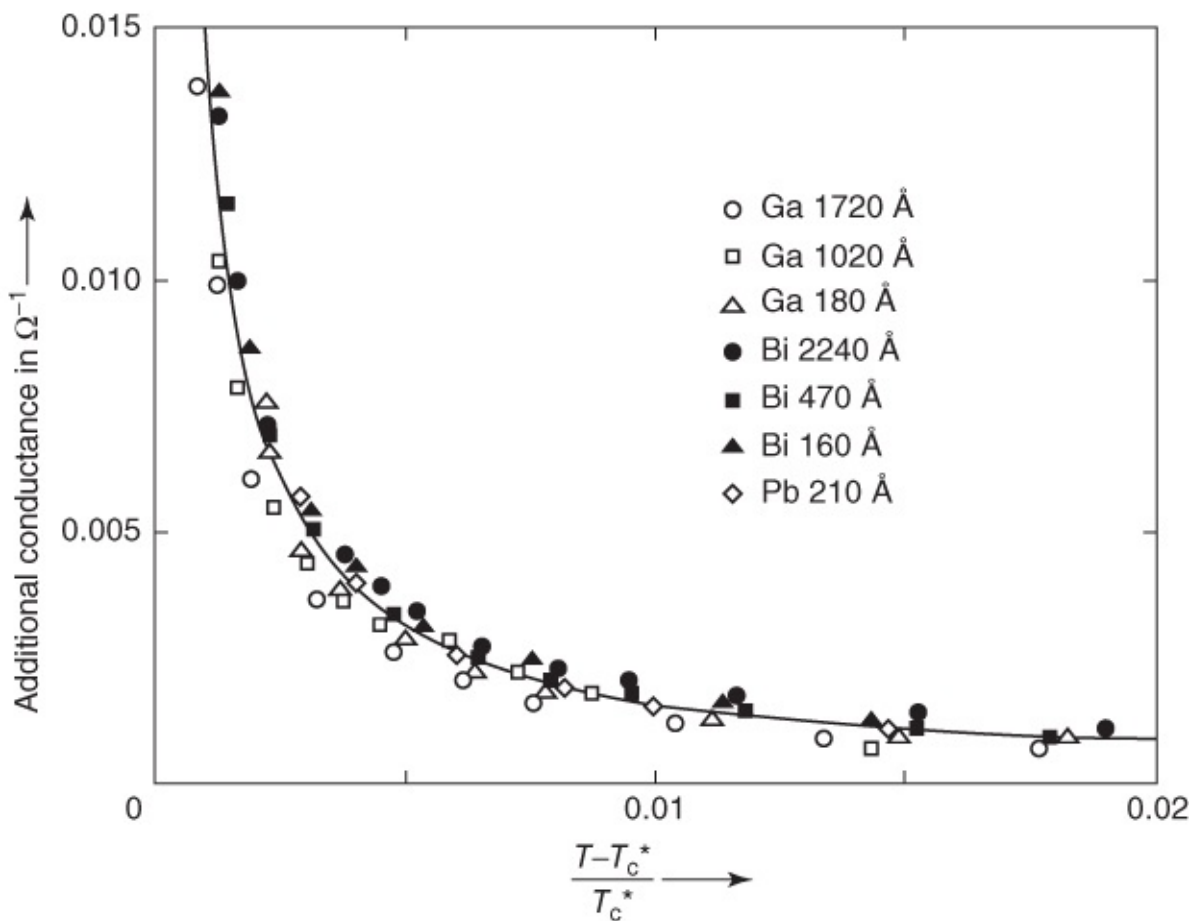


**Figure 4.40** Additional conductance for seven different films plotted versus the reduced temperature. (From [102].)

The additional conductance due to the Cooper pairs can be calculated from the existing theories of superconductivity in combination with the theory of fluctuations. For a film that is thinner than  $\xi_{\text{GL}}$ , one obtains [103]

$$\sigma'(T) = \frac{e^2}{16\hbar} \frac{T_c^*}{T - T_c^*} \frac{b}{l} \quad 4.97$$

where  $e$  is the elementary charge,  $\hbar$  is Planck's constant  $h/2\pi$ ,  $T_c^*$  is the transition temperature obtained by fitting Eq. (4.97) to the experimental data,  $b$  is the width, and  $l$  is the length of the film.

We see that the additional conductance  $\sigma'$  must be proportional to  $1/(T - T^*)$ . This theoretical result is well confirmed by experiment. The curves shown in Figure 4.39 exactly reproduce this temperature dependence. Furthermore, according to Eq. (4.97), the additional conductance  $\sigma'$  should be independent of all material properties. This result is also confirmed by experiment. In Figure 4.40 the results for seven highly different films are plotted [102]. In this case the additional conductance is normalized to the geometry of a square (width  $b$  = length  $l$ ). All films follow the general law indicated by the solid line.<sup>41</sup> The agreement even extends to the absolute magnitude of the additional conductance. For the film geometry of a square, Eq. (4.97) changes to

$$\sigma'(T) = \frac{e^2}{16\hbar} \frac{T_c^*}{T - T_c^*}$$

[4.98](#)

The constant  $e^2/16\hbar$  has the value  $1.52 \times 10^{-5} \Omega^{-1}$ . Experiments yield the value  $1.51 \times 10^{-5} \Omega^{-1}$ . This confirms that the experimentally observed additional conductance for these examples is, indeed, due to the fluctuations.

In such experiments this highly critical discussion is needed since inhomogeneities in the sample, representing regions with different transition temperatures, can also lead to similar transition curves. If, for example, in the case of tin, the transition temperature is shifted by several degrees because of the existence of such perturbations, an extension of the transition curve to higher temperatures can also be explained in terms of such perturbed regions. In this case the resistance would only decrease gradually, since more and more regions would successively become superconducting according to their transition temperature given by their degree of disorder.

In order to detect the fluctuation effects, R. E. Glover utilized amorphous films. These films have the important advantage that they are very homogeneous regarding the transition temperature because of their extreme disorder. Because of their inhomogeneity, say, due to the different strains in the individual microcrystals, crystalline films can display very large deviations from the property values determining the fluctuations.

In Eq. (4.97) we have indicated the additional conductance for two-dimensional samples. In the case of three- or one-dimensional superconductors, one finds the following dependences of the additional conductance on the temperature:

- three-dimensional,  $l$ ,  $b$ , and  $d$  large compared to  $\xi_{\text{GL}}$  [4.99](#)  $\sigma'(T) = \frac{e^2}{16\hbar} \frac{1}{2\xi_{\text{GL}}(0)} \left( \frac{T_c^*}{T - T_c^*} \right)^{1/2} \frac{db}{l}$
- one-dimensional,  $l$  large compared to  $\xi_{\text{GL}}$ ,  $b$  and  $d$  small compared to  $\xi_{\text{GL}}$

$$\sigma'(T) = \frac{e^2}{16\hbar} \pi \xi_{\text{GL}}(0) \left( \frac{T_c^*}{T - T_c^*} \right)^{3/2} \frac{1}{l} \quad [4.100](#)$$

where  $e$  is the elementary charge,  $\hbar$  is Planck's constant  $h/2\pi$ ,  $d$  is the thickness,  $b$  is the width, and  $l$  is the length of the sample.

Aside from the additional conductance due to the transient Cooper pairs, there exist still other contributions to  $\sigma'$  caused by the unpaired electrons [104], which we do not discuss any further. A detailed treatment can be found, for example, in the review article [105] or in the monograph [M3]. Furthermore, we note that in Eqs. (4.99) and (4.100) the Ginzburg–Landau coherence length enters in a relatively simple way. Hence, the measurement of  $\sigma'$  allows one to determine this quantity.

Qualitatively, we can easily understand that the sample dimensions must influence the magnitude of the fluctuations, since the Cooper pair density can vary only on a length scale of about  $\xi_{\text{GL}}$ . More rapid spatial variations require relatively high energies and, hence, practically do not appear. Within a sample that is large in all three spatial directions, the

Cooper pair density can vary spatially in all directions. All these possible configurations must be taken into account in the calculation of the additional conductance. For a two-dimensional sample, along the shortest extension the Cooper pair density is always constant spatially. Hence, averaging over all possible spatial configurations of the Cooper pair density along this direction is not necessary. For a one-dimensional sample, averaging is unnecessary along both directions in which the sample is small compared to  $\xi_{\text{GL}}$ . We see that the statistics is restricted because of the sample geometry. This results in various expressions for the additional conductance.

Experience shows that the transition curves of three-dimensional samples, say, of wires with a diameter large compared to  $\xi_{\text{GL}}$ , are very sharp, that is, the effects we have just discussed cannot be observed. The reason is not the absence of fluctuations, but rather the comparatively high residual conductance of the three-dimensional sample. For example, a tin wire of high purity with a diameter of 1 mm has a residual conductance that is at least 8 orders of magnitude larger than that of an amorphous bismuth film with 100 nm thickness and 1 mm width for the same length.<sup>42</sup> In order to enhance the additional conductance, calculated from Eq. (4.99), up to a measurable contribution compared to this high residual conductance, the factor  $T_c^*/(T - T_c^*)$  would have to attain about the value  $10^{15}$ . However, this means that such samples can display extremely sharp transition curves, and that the influence of the fluctuations on the conductance remains unobservable.

So far we have only discussed how the fluctuations affect the electrical conductance. However, if puddles of Cooper pairs appear statistically above  $T_c$ , this must be noticed also in other properties. We know that below  $T_c$  a superconductor expels small magnetic fields out of its interior, that is, it turns into an ideal diamagnet. We expect that, similar to the effect of the fluctuations on the conductance, some part of this diamagnetic property also appears above  $T_c$ .

The puddles of Cooper pairs should result in a characteristic temperature dependence of the diamagnetic behavior of the superconductor above  $T_c$ . Only a few hundredths of a degree away from  $T_c$  the additional diamagnetism is already very small and corresponds to the expulsion of just a few flux quanta. However, it has been possible to detect this effect clearly [106] by utilizing a superconducting quantum interferometer (see [Section 1.5.2](#)).

The fluctuations should also lead to an increase in the specific heat  $c$  already above  $T_c$ . This effect could also be experimentally demonstrated [107].

For the reasons we have discussed in the previous section, the fluctuation effects above  $T_c$  are also highly pronounced in high-temperature superconductors. However, often in this case a precise analysis of, say, the additional conductance over a wide temperature range is difficult since, on the one hand, also the normal conductance is strongly temperature-dependent, and, on the other hand, sample inhomogeneities can lead to a broad superconducting transition. In spite of these problems, the influence of thermal fluctuations could be observed and analyzed in many beautiful experiments [108].

## 4.9 States Outside Thermodynamic Equilibrium

Due to the fluctuations discussed in [Section 4.8](#), the superconductor spontaneously enters states outside thermodynamic equilibrium because of the uncorrelated thermal motion. From these states, the superconductor then returns to thermodynamic equilibrium by means of “relaxation processes.”

However, through the influence of external parameters, it is also possible to drive a superconductor into states that are more or less far from equilibrium. If the influence of such an external parameter is turned off abruptly,<sup>43</sup> also in this case the superconductor returns to the equilibrium state by means of relaxation processes.

We know from experience that many such relaxation processes follow an exponential law as a function of time. If the equilibrium value of a quantity  $x$  is denoted by  $x_0$ , the exponential decay of the perturbation  $(x(t) - x_0)$  is given by<sup>44</sup>

$$x(t) - x_0 = (x(0) - x_0)e^{-t/\tau} \quad 101$$

Such relaxation processes are described in terms of a constant, the decay time  $\tau$ . In order to understand the process involved, we must determine the decay time  $\tau$ .

In superconductors there are a number of such relaxation processes possible. We can drive the electron system, that is, the unpaired electrons existing at  $0 < T < T_c$ , into nonequilibrium states, for example, by irradiation with microwaves (photons of suitable energy). This possibility and the resulting phenomena will be discussed in more detail. Also we can change the Cooper pair density by irradiation with photons of energies that are larger than the energy gap (i.e., for the frequency  $f$  of the photons we must have  $hf > 2\Delta_0$ ). Finally, the phase of the Cooper pair system, which is highly important, for example, in the Josephson effect, can be driven out of equilibrium. It will return to equilibrium by means of a relaxation process after the external parameter has been switched off.

All these processes have characteristic relaxation times, for example,  $\tau_s$  for the relaxation of the system of unpaired electrons, or  $\tau_r$  for the recombination of unpaired electrons to Cooper pairs. These times are important, for example, in the use of superconducting tunnel junctions as phonon sources (see [Section 7.6.3](#)).

Also the system of the quantized lattice vibrations, the phonons, can be driven out of equilibrium, say, by irradiation with phonons of a distinct frequency, or by generating such phonons within the superconductor by the recombination of unpaired electrons into Cooper pairs. The phonon system will return to its equilibrium after the perturbation has been switched off. Depending on the relevant process  $i$ , which turns out to be important, we distinguish between different characteristic times  $\tau_i$ . For example, the excess phonons can simply leave the superconductor. In this case the relevant time is the phonon escape time  $\tau_{ph}^{esc}$ . For relaxation by means of internal scattering processes within the phonon system, the characteristic time  $\tau_{ph}^s$  is relevant. In principle, all these times can be measured.

Together with advances in the theoretical understanding of superconductivity, interest in the quantitative treatment of the nonequilibrium behavior has also increased strongly. Out of the many results, for example, in [M18], here we only want to select two simple problems. First, we want to describe the possibilities for determining the recombination time of unpaired electrons forming Cooper pairs. Second, we want to discuss a surprising result, namely the enhancement of superconductivity by means of a nonequilibrium state.

(1) In order to measure relaxation times, we must prepare a well-defined deviation of a selected quantity from equilibrium and then measure this deviation. In this case we need a high experimental time resolution because of the expected short relaxation times of the electron system. Both requirements are well satisfied by tunneling configurations (see [Section 3.1.3.2](#)). Such experiments were performed already early soon after the development of the BCS theory [109]. Here, we want to discuss only one possibility [110]. Two tunnel junctions 1 and 2 made from Al–Al<sub>2</sub>O<sub>3</sub>–Al are arranged such that the central Al layer belongs to both junctions (see [Figure 1.23](#)). A voltage  $U_1 > 2\Delta_{\text{Al}}/e$  is applied to junction 1 such that single electrons tunnel into the central Al film. As a result, in this film, the concentration of single electrons is raised above the equilibrium concentration. The established new concentration depends on the magnitude of the tunneling current transporting the electrons into the central film. However, it also depends on the lifetime of the single electrons within this film. The shorter this lifetime, that is, the faster the excess single electrons recombine into Cooper pairs, the smaller will be the resulting concentration. If we can measure the change of the concentration during the turning-on of the tunneling current across junction 1, we can determine from this the lifetime of the single electrons, that is, the recombination time in the central film.

In the central film, the changes of the concentration of the unpaired electrons can be detected using the second junction. For this purpose, one applies to this junction a voltage  $U_2 < 2\Delta_{\text{Al}}/e$ . Then only the unpaired electrons in the central film can contribute to the tunneling current across junction 2. At sufficiently low temperatures in equilibrium, there exist only very few unpaired electrons. Hence, the current  $I_2$  across junction 2 is correspondingly small. If the tunneling current  $I_1$  is switched on, with increasing concentration of the unpaired electrons in the central film also the tunneling current  $I_2$  will increase. In this way it is possible to measure the changes in the concentration.

In addition to this stationary method, also a pulse technique has been used. In this case it is sufficient to investigate only a single-tunnel junction [110]. By means of a short voltage pulse with  $U > 2\Delta_{\text{Al}}/e$ , a nonequilibrium concentration of the unpaired electrons is generated, the decay of which after the pulse can be observed directly using the tunneling current at voltage  $U < 2\Delta_{\text{Al}}/e$ .

The two methods yield the same results. In [Figure 4.41](#) we show the results of Gray *et al.* [110]. With decreasing temperature, the lifetime of the unpaired electrons, that is, the recombination time  $\tau_r$  to form Cooper pairs, essentially increases proportional to  $\exp[\Delta_0(T)/k_B T]$ . In this case  $\tau_r$  varies between about  $10^{-7}$  s at temperatures slightly below  $T_c$

up to about  $5 \times 10^{-5}$  s at 0.2 K. However, these values can serve only as an indication, since the measurement of the recombination time is influenced by several parameters, which can differ from experiment to experiment.

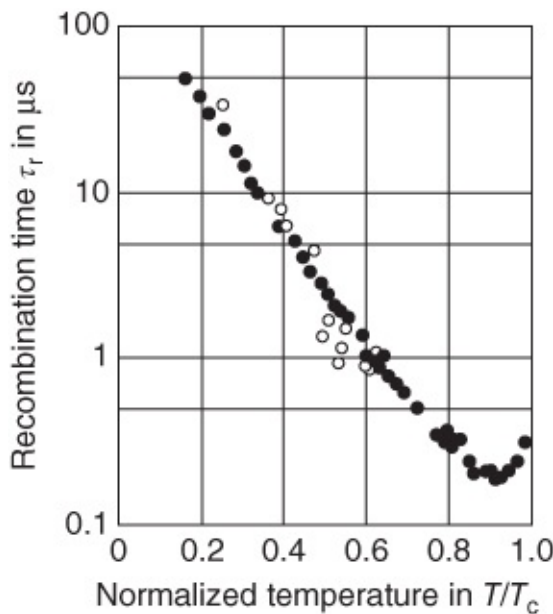


**Figure 4.41** Recombination time in Al films plotted versus the reduced temperature. Transition temperature  $T_c = 1.27$  K;  $\Delta_0(0) = 0.195$  meV; thickness values: 102, 76, and 64 nm. Full circles, stationary measurement; open circles, pulse technique. (From [110].)

For example, it is highly important whether the phonons generated during the recombination process can decay or escape quickly from the superconductor. These phonons in turn are able to break up Cooper pairs and thereby regenerate unpaired electrons. In this way the effective lifetime of the unpaired electrons can increase by a large factor. For phonon escape, the thicknesses of the studied film and the substrate are important. In the latter case, acoustic impedance matching plays a decisive role. Because of these effects, the effective recombination times can be changed by an order of magnitude or more.

In contrast to these rather complex influences, the essentially exponential increase in  $\tau_r$  with decreasing temperature can be understood easily. In conventional superconductors, with decreasing temperature the concentration of unpaired electrons decreases exponentially. Hence, the probability that an unpaired electron finds a suitable partner for the recombination to form a Cooper pair also decreases.

Finally, we mention again that a change of electron concentration can also be affected by irradiation with electromagnetic waves (photons) of suitable frequency, and that the changed concentration can be detected again using electromagnetic waves  $hf < 2\Delta_0$ , say, by measuring the reflection or the surface resistance [111]. In [Section 3.1.3.2](#), we have already discussed this possibility.

(2) In our second example, namely the enhancement of superconductivity in nonequilibrium states, we consider the case where the nonequilibrium is generated by means of irradiation with suitable photons. One can observe the surprising result that the irradiation leads to an

enhancement of the transition temperature and of the energy gap.

The experiments started with the observation that the current across a region representing a weak coupling between two superconductors, as a Josephson junction, can be influenced by irradiation with photons. Giaever [112] utilized this effect to detect the alternating Josephson current. Under favorable conditions the critical current could be enhanced considerably [113]. Eventually, Klapwijk and Mooij [114] were able to demonstrate in a beautiful experiment that this phenomenon represents a general property of the superconducting state, and that it is not just a special feature of a region of weak coupling. We want to discuss briefly this highly instructive experiment.

The experiments were performed using thin, evaporated stripes of Al (length about 3 mm, width about 3–5  $\mu\text{m}$ , thickness 0.2–1.0  $\mu\text{m}$ ). The critical current  $I_c$  and the transition temperature  $T_c$  were measured with and without high-frequency irradiation (frequency  $f$  between 10 MHz and 10 GHz). Typical results for a frequency of 3 GHz are shown in [Figure 4.42](#).

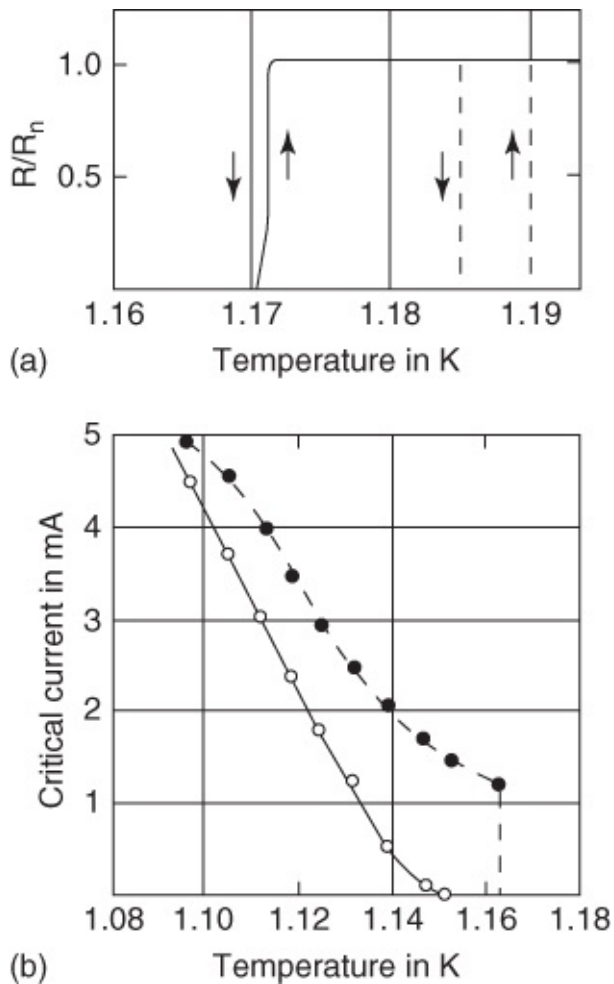


**Figure 4.42** (a) Transition curves and (b) critical currents of Al films without and with high-frequency irradiation ( $f = 3 \times 10^9 \text{ Hz}$ );  $\circ$  without irradiation (solid line) and  $\bullet$  with irradiation (dashed line). (From [114].) The dimensions of the films are as listed below:

Length $l$ (mm)	Width $b$ ( $\mu\text{m}$ )	Thickness $d$ ( $\mu\text{m}$ )
a: 2.90	3.8	0.4
b: 2.92	3.5	1.0

[Figure 4.42a](#) shows the transition into the superconducting state as detected using a simple resistance measurement. The transition temperature is clearly enhanced due to the high-frequency irradiation. Also the critical current is increased because of the high-frequency irradiation ([Figure 4.42b](#)).

This result is surprising, since one would expect that the energy supplied by the irradiation is unfavorable for superconductivity. However, at least a qualitative understanding is not too difficult and was suggested as long ago as 1961 by Parmenter [115]. A quantitative description has been given by Eliashberg and others [116]. The basic idea is the following. The Cooper pairs are bound together more strongly the more states are available to them into which they can be scattered. If there exist unpaired electrons near the Fermi energy, they obstruct scattering states for the Cooper pairs because of the Pauli principle and thereby reduce the binding energy of the pairs. In other words, the energy gap becomes smaller with increasing number of unpaired electrons.

If we are able to remove the unpaired electrons from the states near the upper edge of the energy gap, where they most effectively disturb the Cooper pairs, then this should lead to an enhancement of the energy gap, similarly as a reduction in temperature, which also results in a reduction of the concentration of unpaired electrons. It is exactly this effect that is accomplished by irradiation with photons. The unpaired electrons are energetically shifted to higher energies and thereby are removed from the upper edge of the energy gap. As a consequence, additional scattering states become available to the Cooper pairs, resulting in an enhancement of the energy gap. In this way, the enhancement of the critical current and also of the transition temperature can be understood [116]. However, the details require a quantitative treatment, since near  $T_c$  the irradiated photons can also break up Cooper pairs.

Additional nonequilibrium effects appear upon reaching the critical current in a thin superconductor, for example, in a “whisker,” that is, a very thin single crystal of only a few micrometers diameter. In this case, the transition to the normal conducting state occurs in discrete steps [117], which have been interpreted in terms of “phase-slip centers” [118]. A phase-slip center separates two superconducting regions, where the phase difference between the two Cooper pair systems increases monotonically. Analogous to the second Josephson equation (1.28), this phase change is accompanied by an electrical voltage between the two regions. A phase-slip center can also be understood as the limiting case of the flux-flow resistance (see [Section 5.3.2.3](#)) for a correspondingly small dimension of the superconductor.

Nonequilibrium processes also appear if an electric current passes across an interface between a normal conductor and a superconductor, say, between copper and tin. At the interface the normal current must be changed into a supercurrent [119]. A summary of such

nonequilibrium processes can be found in [120].

Following these discussions of the thermodynamic properties of the superconducting state in equilibrium and in nonequilibrium, we want to turn in more detail to the transport of electric current in superconductors. In this case we will find, for example, that in type-II superconductors an appreciable supercurrent can be passed through the sample only after a certain amount of defects have been introduced into the superconductor.

## References

1. V. L. Ginzburg, L. D. Landau: *Zh. Eksp. Teor. Fiz.* **20**, 1064 (1950).
2. Keesom, W.H. (1924) Rapp et Disc. IV Congress Physics Solvay, p. 288.
3. J. Custers, P. Gegenwart, H. Wilhelm, K. Neumaier, Y. Tokiwa, O. Trovarelli, C. Geibel, F. Steglich, C. Pépin, P. Coleman: *Nature* **424**, 524 (2003).
4. R. Becker, *Theorie der Wärme*, Springer, Heidelberg, p. 7 (1961).
5. L. D. Landau: *Phys. Z. Sowjet.* **11**, 545 (1937); L. D. Landau, E. M. Lifshitz: *Course of Theoretical Physics*, Vol. 5, Pergamon Press, p. 430 (1959).
6. W. H. Keesom, P. H. van Laer: *Physica* **5**, 193 (1938).
7. M. A. Biondi, A. T. Forester, M. P. Garfunkel, C. B. Satterthwaite: *Rev. Mod. Phys.* **30**, 1109 (1958).
8. J. G. Daunt, K. Mendelssohn: *Proc. R. Soc. London, Ser. A* **185**, 225 (1946).
9. A. Junod: *Physica C* **153**, 1078 (1988).
10. D. M. Ginsberg, S. E. Inderhees, M. B. Salamon, N. Goldenfeld, J. P. Rice, B. G. Pazol: *Physica C* **153**, 1082 (1988).
11. K. Kitazawa, H. Takagi, K. Kishio, T. Hasegawa, S. Uchida, S. Tajima, S. Tanaka, K. Fueki: *Physica C* **153**, 9 (1988).
12. J. W. Loram, K. A. Mirza, J. R. Cooper W. Y. Liang: *Phys. Rev. Lett.* **71**, 1740 (1993).
13. K. A. Moler, D. L. Sisson, J. S. Urbach, M. R. Beasley, A. Kapitulnik, D. J. Baar, R. Liang, W. N. Hardy: *Phys. Rev. B* **55**, 3954 (1997).
14. D. A. Wright, J. P. Emerson, B. F. Woodfield, J. E. Gordon, R. A. Fisher, N. E. Phillips: *Phys. Rev. Lett.* **82**, 1550 (1999).
15. J. P. Emerson, D. A. Wright, B. F. Woodfield, J. E. Gordon, R. A. Fisher, N. E. Phillips: *Phys. Rev. Lett.* **82**, 1546 (1999).

16. G. F. Zharkov: *J. Low Temp. Phys.* **130**, 45 (2003).
17. J. K. Hulm: *Proc. R. Soc. London, Ser. A* **204**, 98 (1950).
18. K. Mendelssohn, J. L. Olsen: *Proc. Phys. Soc. London, Sect. A* **63**, 1182 (1950).
19. M. Ausloos, M. Houssa: *Supercond. Sci. Technol.* **12**, R103 (1999).
20. F. London, H. London: *Z. Phys.* **96**, 359 (1935);F. London: *Une Conception Nouvelle De La Supraconductivite*, Hermann & Cie, Paris 1937.
21. L. P. Gor'kov: *Sov. Phys. JETP* **9**, 1364 (1960).
22. A. A. Abrikosov: *Sov. Phys. JETP* **5**, 1174 (1957).
23. D. Shoenberg: *Nature (London)* **143**, 434 (1939);D. Shoenberg: *Proc. R. Soc. London, Ser. A* **175**, 49 (1940).
24. S. Kamal, R. Liang, A. Hosseini, D. A. Bonn, W. N. Hardy: *Phys. Rev. B* **58**, R8933 (1998).
25. A. B. Pippard: *Proc. R. Soc. London, Ser. A* **216**, 547 (1953);A. B. Pippard: *Proc. Cambridge Philos. Soc.* **47**, 617 (1951).
26. K. Mendelssohn, J. R. Moore: *Nature* **133**, 413 (1934);K. Mendelssohn: “*Cyrophysics*”, Interscience Publisher Ltd. London 1960;K. Mendelssohn: *Nature (London)* **169**, 366 (1952).
27. A. J. Rutgers: *Physica* **3**, 999 (1936).
28. Mapother, D.E.: *IBM J.* **6**, 77 (1962).
29. D. Shoenberg: “*Superconductivity*”, Cambridge, Cambridge University Press (1952).
30. A. G. Meshkovsky, A. I. Shalnikov: *Zh. Eksp. Teor. Fiz.* **17**, 851 (1947).
31. A. G. Meshkovsky: *Zh. Eksp. Teor. Fiz.* **19**, 1 (1949).
32. A. L. Schawlow, B. T. Matthias, H. W. Lewis, G. E. Delvin: *Phys. Rev.* **95**, 1345 (1954).
33. F. Haenssler, L. Rinderer: *Helv. Phys. Acta* **40**, 659 (1967).
34. H. Kirchner: *Phys. Lett.* **26 A**, 651 (1968);H. Kirchner: *Phys. Status Solidi A* **4**, 531 (1971);P. B. Alers: *Phys. Rev.* **116**, 1483 (1959);W. DeSorbo: *Philos. Mag.* **11**, 853 (1965).
35. G. J. Sizoo, H. Kamerlingh-Onnes: *Commun. Leiden* **180 b**, (1925).
36. L. D. Jennings, C. A. Swenson: *Phys. Rev.* **112**, 31 (1958).
37. N. B. Brandt, N. I. Ginzburg: *Sov. Phys. USPEKHI* **12**, 344 (1969).
38. R. I. Boughton, J. L. Olsen, C. Palmy: “*Program Low Temperature Physics*”, Vol. 6, C. J.

- Gorter (ed.), North Holland, Amsterdam, p. 163 (1970).
39. N. E. Alekseevskii, Y. P. Gaidukov: *Sov. Phys. JETP* **2**, 762 (1956).
40. L. S. Kan, B. G. Lasarev, A. I. Subortzov: *Zh. Eksp. Teor. Fiz.* **18**, 825 (1948).
41. J. L. Olsen, H. Rohrer: *Helv. Phys. Acta* **30**, 49 (1957).
42. A. Eichler, J. Wittig: *Z. Angew. Phys.* **25**, 319 (1968).
43. C. W. Chu, P. H. Hor, R. L. Meng, L. Gao, Z. J. Huang: *Science* **235**, 567 (1987).
44. M. K. Wu, J. R. Ashburn, C. J. Torng, P. H. Hor, R. L. Meng, L. Gao, Z. J. Huang, C. W. Chu: *Phys. Rev. Lett.* **58**, 908 (1987).
45. C. Meingast, O. Kraut, T. Wolf, H. Wühl, A. Erb, G. Müller-Vogt: *Phys. Rev. Lett.* **67**, 1634 (1991).
46. O. Kraut, C. Meingast, G. Bräuchle, H. Claus, A. Erb, G. Müller-Vogt, H. Wühl: *Physica C* **205**, 139 (1993).
47. M. Kund, J. J. Neumeier, K. Andres, J. Markl, G. Saemann-Ischenko: *Physica C* **296**, 173 (1998).
48. B. Lorentz, R. L. Meng, C. W. Chu: *Phys. Rev. B* **64**, 012507 (2001).
49. C. W. Chu, B. Lorenz: *Physica C* **469**, 385 (2009).
50. W. J. de Haas, J. Voogd: *Commun. Leiden* **208b**, (1930) and **214b** (1931).
51. K. Mendelssohn: *Proc. R. Soc. London, Ser. A* **152**, 34 (1935).
52. J. D. Livingston: *Phys. Rev.* **129**, 1943 (1963).
53. E. Helfand, N. R. Werthamer: *Phys. Rev.* **147**, 288 (1966).
54. T. Kinsel, E. A. Lynton, B. Serin: *Rev. Mod. Phys.* **36**, 105 (1964).
55. L. P. Gor'kov: *Sov. Phys. JETP* **10**, 998 (1960).
56. H. Behrens, G. Ebel (eds) *Superconductivity Data*, Fachinformationszentrum Energie, Physik, Mathematik, Karlsruhe (1982).
57. R. Chevrel, M. Sergent, J. Prigent: *J. Solid State Chem.* **3**, 515 (1971).
58. R. Odermatt, Ø. Fischer, H. Jones, G. Bongi: *J. Phys. C* **7**, L 13 (1974); Ø. Fischer, H. Jones, G. Bongi, M. Sergent, R. Chevrel: *J. Phys. C* **7**, L 450 (1974); S. Foner, E. J. McNiff, E. J. Alexander: *Phys. Lett.* **49 A**, 269 (1974).
59. G. Otto, E. Saur, H. Witzgall: *J. Low Temp. Phys.* **1**, 19 (1969).

60. W. DeSorbo: *Phys. Rev.* **140**, A914 (1965).
61. R. Odermatt, Ø. Fischer, H. Jones, G. Bongi: *J. Phys. C* **7**, L 13 (1974).
62. Ø. Fischer: “*Proceeding of the LT14*”, Vol. 5, North-Holland, Amsterdam, Otaniemi (1975).
63. M. Tinkham: *Phys. Rev.* **129**, 2413 (1963).
64. M. J. Naughton, R. C. Yu, P. K. Davies, J. E. Fischer, R. V. Chamberlin, Z. Z. Whang, T. W. Jing, N. P. Ong, P. M. Chaikin: *Phys. Rev. B* **38**, 9280 (1988).
65. Y. Wang, S. Ono, Y. Onose, G. Gu, Y. Ando, Y. Tokura, S. Uchida, N.P. Ong: *Science* **299**, 86 (2003).
66. A. S. Dzurak, B. E. Kane, R. G. Clark, N. E. Lumpkin, J. O'Brien, G. R. Facer, R. P. Starrett, A. Skougarevsky, H. Nakagawa, N. Miura, Y. Enomoto, D. G. Rickel, J. D. Goettee, L. J. Campbell, C. M. Fowler, C. Mielke, J. C. King, W. D. Zerwekh, D. Clark, B. D. Bartram, A. I. Bykov, O. M. Tatsenko, V. V. Platonov, E. E. Mitchell, J. Herrmann, H.-H. Müller: *Phys. Rev. B* **57**, 14084 (1998).
67. B. S. Chandrasekhar: *Appl. Phys. Lett.* **1**, 7 (1962);A. M. Clogston: *Phys. Rev. Lett.* **9**, 266 (1962).
68. N. R. Werthamer, E. Helfand, P. C. Hohenberg: *Phys. Rev.* **147**, 295 (1966).
69. H. F. Hess, R. B. Robinson, J. V. Waszczak: *Phys. Rev. Lett.* **64**, 2711 (1990);Ch. Renner, A. D. Kent, Ph. Niederman, Ø. Fischer, F. Lévy: *Phys. Rev. Lett.* **67**, 1650 (1991);C. Renner, B. Revaz, K. Kadwaki, I. Maggio-Apprile, Ø. Fischer: *Phys. Rev. Lett.* **80**, 3606 (1998);S. H. Pan, E. W. Hudson, A. K. Gupta, K.-W. Ng, H. Eisaki, S. Uchida, J. D. Davis: *Phys. Rev. Lett.* **85**, 1536 (2000);J. E. Hoffman, E. W. Hudson, K. M. Lang, V. Madhavan, H. Eisaki, S. Uchida, J. C. Davis: *Science* **295**, 466 (2002).
70. L. Neumann, L. Tewordt: *Z. Phys.* **191**, 73 (1966).
71. E. Brézin, D. R. Nelson, A. Thiaville: *Phys. Rev. B* **31**, 7124 (1985).
72. G. Blatter, M. V. Feigel'man, V. B. Geshkenbein, A. I. Larkin, V. M. Vinokur: *Rev. Mod. Phys.* **66**, 1125 (1994).
73. E. H. Brandt: *Rep. Prog. Phys.* **58**, 1465 (1995).
74. J. R. Clem: *Supercond. Sci. Technol.* **11**, 909 (1998).
75. D. R. Nelson, H. S. Seung: *Phys. Rev. B* **39**, 9153 (1989).
76. M. C. Marchetti, D. R. Nelson: *Phys. Rev. B* **41**, 1910 (1990).
77. P. L. Gammel, L. F. Schneemeyer, J. V. Waszczak, D. J. Bishop: *Phys. Rev. Lett.* **61**, 1666

- (1988);P. L. Gammel, L. F. Schneemeyer, D. J. Bishop: *Phys. Rev. Lett.* **66**, 953 (1991);R. G. Beck, D. E. Farrell, J. P. Rice, D. M. Ginsberg, V. G. Kogan: *Phys. Rev. Lett.* **68**, 1594 (1992).
78. U. Welp, J. A. Fendrich, W. K. Kwok, G. W. Crabtree, B. W. Veal: *Phys. Rev. Lett.* **76**, 4809 (1996);R. Liang, D. A. Bonn, W. N. Hardy: *Phys. Rev. Lett.* **76**, 835 (1996).
79. A. Schilling, R. A. Fisher, N. E. Phillips, U. Welp, D. Dasgupta, W. K. Kwok, G. W. Crabtree: *Nature (London)* **382**, 791 (1996);M. Roulin, A. Junod, E. Walker: *Science* **273**, 1210 (1996).
80. F. Bouquet, C. Marcenat, E. Steep, R. Calemczuk, W. H. Kwok, U. Welp, G. W. Crabtree, R. A. Fisher, N. E. Phillips, A. Schilling: *Nature* **411**, 448 (2001).
81. K. Ghosh, S. Ramakrishnan, A. K. Grover, G. I. Menon, G. Chandra, T. V. C. Rao, G. Ravikumar, P. K. Mishra, V. C. Sanhi, C. V. Tomy, G. Balakrishnan, D. McK. Paul, S. Bhattacharya: *Phys. Rev. Lett.* **76**, 4600 (1996);M. Marchevsky, M. J. Higgins, S. Bhattacharya: *Nature* **409**, 591 (2001);Y. Paltiel, E. Zeldov, Y. Myasoedov, M. L. Rappaport, G. Jung, S. Bhattacharya, M. J. Higgins, Z. L. Xiao, E. J. Andrei, P. L. Gammel, D. J. Bishop: *Phys. Rev. Lett.* **85**, 3712 (2000).
82. B. Maiorov, T. Katase, S. A. Baily, H. Hiramatsu, T. G. Holesinger, H. Hosono, L. Civale: *Supercond. Sci. Technol.* **24**, 055007 (2011).
83. J. R. Clem: *Phys. Rev. B* **43**, 7837 (1991).
84. J. Pearl: *Appl. Phys. Lett.* **5**, 65 (1964).
85. A. E. Koshelev: *Phys. Rev. B* **56**, 11201 (1997);A. E. Koshelev, H. Nordborg: *Phys. Rev. B* **59**, 4358 (1999).
86. T. Blasius, Ch. Niedermayer, J. L. Tallon, D. M. Pooke, A. Golnik, C. Bernhard: *Phys. Rev. Lett.* **82**, 4926 (1999).
87. D. T. Fuchs, E. Zeldov, T. Tamegai, S. Ooi, M. Rappaport, H. Shtrikman: *Phys. Rev. Lett.* **80**, 4971 (1998).
88. M. F. Goffman, J. A. Herbsommer, F. de la Cruz, T. W. Li, P. H. Kes: *Phys. Rev. B* **57**, 3663 (1998).
89. W. Lawrence, S. Doniach: “*Proceedings of the 12th International Conference on Low Temperature Physics (LT-12), Kyoto*”, E. Kanda (ed.), Keigaku, Tokyo, p. 361 (1970).
90. J. R. Clem, M. W. Coffey, Z. Hao: *Phys. Rev. B* **44**, 2732 (1991).
91. J. R. Clem, M. W. Coffey: *Phys. Rev. B* **42**, 6209 (1990).
92. K. A. Moler, J. R. Kirtley, D. G. Hinks, T. W. Li, M. Xu: *Science* **279**, 1193 (1998).
93. L. N. Bulaevskii, J. R. Clem: *Phys. Rev. B* **44**, 10 234 (1991).

94. D. Feinberg, C. Villard: *Phys. Rev. Lett.* **65**, 919 (1990);L. N. Bulaevskii: *Phys. Rev. B* **44**, 910 (1991);S. S. Maslov, V. L. Pokrovsky: *Europhys. Lett.* **14**, 591 (1991).
95. A. E. Koshelev: *Phys. Rev. B* **48**, 1180 (1993).
96. A. Grigorenko, S. Bending, T. Tamegai, S. Ooi, M. Henini: *Nature* **414**, 728 (2001).
97. P. C. Hohenberg: *Phys. Rev.* **158**, 383 (1967).
98. N. D. Mermin, H. Wagner: *Phys. Rev. Lett.* **17**, 1133 (1966).
99. V. L. Berezinskii: *Sov. Phys. JETP* **32**, 493 (1970);V. L. Berezinskii: *Sov. Phys. JETP* **34**, 610 (1971).
100. J. M. Kosterlitz, D. J. Thouless: *J. Phys. C* **6**, 1181 (1973).
101. B. A. Huberman, S. Doniach: *Phys. Rev. Lett.* **43**, 950 (1979).
102. R. E. Glover III: “*Program Low Temperature Physics*”, Vol. 6, C. J. Gorter (ed.), North Holland Publishing Company, Amsterdam p. 291, (1961);R. E. Glover III: *Phys. Lett.* **25 A**, 542 (1967).
103. L. G. Aslamazov, A. I. Larkin: *Phys. Lett.* **26 A**, 238 (1968);H. Schmidt: *Z. Phys.* **216**, 336 (1968);A. Schmid: *Z. Phys.* **215**, 210 (1968).
104. K. Maki: *Prog. Theor. Phys.* **39**, 897 (1968);K. Maki: *Prog. Theor. Phys.* **40**, 193 (1968);R. S. Thompson: *Phys. Rev. B* **1**, 327 (1970).
105. W. J. Skocpol, M. Tinkham: *Rep. Prog. Phys.* **38**, 1049 (1975).
106. J. P. Gollub, M. R. Beasley, R. S. Newbower, M. Tinkham: *Phys. Rev. Lett.* **22**, 1288 (1969).
107. G. D. Zally, J. M. Mochel: *Phys. Rev. Lett.* **27**, 1710 (1971).
108. A. Kapitulnik: *Physica C* **153**, 520 (1988);P. P. Freitas, C. C. Tsuei, T. S. Plaskett: *Phys. Rev. B* **36**, 833 (1987);S. E. Inderhees, M. B. Salamon, J. P. Rice, D. M. Ginsberg: *Phys. Rev. Lett.* **66**, 232 (1991);E. Braun, W. Schnelle, H. Broiche, J. Harnischmacher, D. Wohlleben, C. Allgeier, W. Reith, J. S. Schilling, J. Bock, E. Preisler, G. J. Vogt: *Z. Phys. B* **84**, 333 (1991);L. B. Ioffe, A. I. Larkin, A. A. Varlamov, L. Yu: *Phys. Rev. B* **47**, 8936 (1993);V. V. Dorin, R. A. Klemm, A. A. Varlamov, A. I. Buzdin, D. V. Livanov: *Phys. Rev. B* **48**, 12951 (1993);A. S. Nygmatulin, A. A. Varlamov, D. V. Livanov, G. Balestrino, E. Milnani: *Phys. Rev. B* **53**, 3557 (1996).
109. D. M. Ginsberg: *Phys. Rev. Lett.* **8**, 204 (1962).
110. K. F. Gray, A. R. Long, C. J. Adkins: *Philos. Mag.* **20**, 273 (1969);K. F. Gray: *J. Phys. F* **1**, 290 (1971).

111. G. A. Sai-Halasz, C. C. Chi, A. Denenstein, D. N. Langenberg: *Phys. Rev. Lett.* **33**, 215 (1974).
112. I. Giaever: *Phys. Rev. Lett.* **14**, 904 (1965).
113. Yu. I. Latyshev, F. Ya. Nad': *JETP Lett.* **19**, 380 (1974); A. F. G. Wyatt, V. M. Dmitriev, W. S. Moore, F. W. Sheard: *Phys. Rev. Lett.* **16**, 1166 (1966); A. H. Dayem, J. Wiegand: *Phys. Rev.* **155**, 419 (1967).
114. T. M. Klapwijk, J. E. Mooij: *Physica* **81 B**, 132 (1976).
115. R. H. Parmenter: *Phys. Rev. Lett.* **7**, 274 (1961).
116. G. M. Eliashberg: *JETP Lett.* **11**, 114 (1970); B. I. Ivlev, S. G. Lisitsyn, G. M. Eliashberg: *J. Low Temp. Phys.* **10**, 449 (1973).
117. J. Meyer, G. V. Minnigerode: *Phys. Lett.* **38 A**, 529 (1972); J. D. Meyer: *Appl. Phys.* **2**, 303 (1973); R. Tidecks: *Springer Tracts Mod. Phys.* **121**, 1, 1990 “Current Induced Non-equilibrium Phenomena in Quasi-One-Dimensional Superconductors”.
118. W. J. Skocpol, M. R. Beasley, M. Tinkham: *J. Low Temp. Phys.* **16**, 145 (1974).
119. G. J. Dolan, L. D. Jackel: *Phys. Rev. Lett.* **39**, 1628 (1977).
120. M. Tinkham: *Festkörperprobleme* **19**, 363 (1979).

<sup>1</sup> A well-known case is the condition for the extremum of the entropy  $S$  as the Gibbs function which, in the end, is a measure of the number of “micro-states,” by which the observed macroscopic state of the system is realized. Systems having the entropy as the Gibbs function move in the direction of increasing entropy. The equilibrium state corresponds to a state with maximum entropy, of course, always under the given conditions. For equilibrium states with other Gibbs functions, the requirements of the extremum can always be related to the second law of thermodynamics.

<sup>2</sup> At this stage we should mention that phase transitions also exist at  $T = 0$ . They originate from quantum mechanics. The transition point is referred to as ***quantum-critical point***. Superconductivity can appear near a quantum-critical point between a magnetic and a nonmagnetic phase. Phase transitions of this kind are discussed in connection with the cuprate superconductors, and also in the case of materials such as the heavy fermions and many other substances [3].

<sup>3</sup> In technical thermodynamics mostly one proceeds differently. There the work that is *done by* the system is counted as positive (representing the interesting part for technology).

<sup>4</sup> Here, the terms ***superconducting state*** and ***superconducting phase*** mean the same.

<sup>5</sup> Since here the magnetic moment **m** always appears together with **B**, confusion with the mass

is unlikely.

<sup>6</sup> The differential work  $\delta A^m = B dm$  exactly corresponds to the compressional work  $\delta A^V = -p dV$ , where  $B$  and the magnetic moment  $m$  appear in place of the pressure  $p$  and the negative volume  $-V$ , respectively. We take paramagnetic materials as an example. Then  $\mathbf{m}$  is parallel to  $\mathbf{B}$ . During an increase in  $\mathbf{m}$ , that is,  $d\mathbf{m} > 0$ , work is added to the system, which appears as heat of magnetization.

<sup>7</sup> See, for example, [4].

<sup>8</sup> The density of the free, unpaired electrons has become so small that its energy absorption can be neglected.

<sup>9</sup> For d-wave superconductors in the vortex state, one expects a linear term increasing proportional to  $B^{1/2}$ . Such a term was also confirmed experimentally.

<sup>10</sup> This only applies in the absence of a magnetic field. Otherwise, the phase transition can be of first order, say, if in the case of type-I superconductors during the transition into the normal state, the magnetization changes discontinuously [16].

<sup>11</sup> The scattering of a wave at an obstacle becomes strong if the wavelength and the dimension of the obstacle are comparable. At the Fermi energy, the matter wave of the electrons has a wavelength of a few angstroms. Therefore, the electrons are strongly scattered at atomic obstacles. On the other hand, the phonons, with their much longer wavelengths, experience a much weaker interaction with the obstacle.

<sup>12</sup> Here, we describe the Ginzburg–Landau theory for an isotropic, single-component order parameter. This is adequate for conventional, homogeneous superconductors. However, the theory can be formulated similarly for unconventional superconductors, in which case usually one must consider more than one order parameter. However, in detail this can become very complicated.

<sup>13</sup> We denote the Gibbs function by the letter  $g$  to indicate that it is an energy *density*. Since the equilibrium value with respect to  $\Psi(\mathbf{r})$  can only be found from a variational calculation of the energy minimum, one should use the terminology of energy functional. However, for simplicity in the following we continue to denote  $g$  as Gibbs function.

<sup>14</sup> Note that these expressions are valid only near  $T_c$ .

<sup>15</sup> To see this we write  $[1 - (T/T_c)^4] = [1 - (T/T_c)^2][1 + (T/T_c)^2]$  and for  $T \rightarrow T_c$  replace the second factor by the factor 2. We apply the same procedure to  $[1 - (T/T_c)^2]$  and finally obtain Eq. (4.35).

<sup>16</sup> The electron mean free path  $l^*$  indicates the average distance that a conduction electron can propagate between two collisions.

- <sup>17</sup> The thin surface layer, into which the magnetic field penetrates, can be neglected for this integral look at the sample.
- <sup>18</sup> Here, we explicitly utilize the fact that the external field is compensated by the macroscopic currents flowing at the surface. To describe the magnetic fields in the interior of a substance, we must know the mechanism causing the magnetic behavior. How the magnetization is accomplished remains irrelevant only for the external magnetic field.
- <sup>19</sup> Modern Hall probes allow measurements of the magnetic field with high sensitivity. One observes the electrical voltage generated perpendicular to the electric current and to the magnetic field because of the Lorentz force. The Hall voltage is proportional to the applied magnetic field.
- <sup>20</sup> However, if the superconducting phase exists in the form of a thin network (for instance, precipitates), the measurement of the induction will indicate perfect superconductivity. Clear information on the volume fraction of the superconducting phase can be obtained from specific-heat measurements. If the sample contains normal conducting parts, according to Eq. (4.14) the specific heat of the electrons of these parts will yield the contribution  $c_{nE} = \gamma T$ , which can be observed.
- <sup>21</sup> In principle, we can also use Eq. (4.48) for a type-II superconductor. Then we must integrate up to the upper critical field  $B_{c2}$ , and the particular dependence  $M(B)$  of these superconductors must be used.
- <sup>22</sup> In [Chapter 1](#) we discussed other techniques in conjunction with the imaging of vortices.
- <sup>23</sup> This energy is positive, since energy must be supplied to the superconductor to generate the interface.
- <sup>24</sup> The boundary is only stable if a displacement to the left or to the right would lead to an increase or a decrease in the magnetic field, respectively.
- <sup>25</sup> We must note that the magnetic penetration depth at the boundary area in a metal can be slightly different from that at the boundary area in an insulator. The reason is the local variation of the Cooper pair density. Here, we have ignored this difference.
- <sup>26</sup> Pressure conversions:  $1 \text{ bar} = 10^5 \text{ Pa} = 10^5 \text{ N/m}^2 = 1 \text{ kp/cm}^2$ .
- <sup>27</sup> At the transition from the superconducting to the normal conducting state, the volume change occurs at  $B = B_c$ . On the coexistence curve, it is obtained from a differential variation of  $p$ . Here, a possible dependence  $dV_s/dp$  has been ignored.
- <sup>28</sup> Here, we denote the interaction potential between the electrons by  $V^*$ , in order to distinguish it from the volume of the superconductor.

- <sup>29</sup> Chinese scientists independently also found the system Y–Ba–Cu–O. Upon being questioned by one of the authors of this book (WB) about how they had arrived at Y, they gave the simple answer: “Since replacing Ba by Sr resulted in an enhancement of  $T_c$ , it appeared obvious to us also to replace La by Y.”
- <sup>30</sup> A more detailed discussion of the properties of vortices can be found in the monograph [M17].
- <sup>31</sup> Under certain conditions, superconductivity can survive within a thin surface layer for fields in the range  $B_{c2} < B_a \leq 1.7 B_{c3}$ . The value of  $B_{c3}$  is about  $1.7 B_{c2}$ . Here, we ignore this surface superconductivity.
- <sup>32</sup> In [Figure 4.23](#) (as in [Figure 4.10](#)) we have plotted the quantity  $-\mu_0 M$  instead of the magnetization  $M$ . For ideal field expulsion we have  $M = -B/\mu_0$  or  $-\mu_0 M = B$ . Hence, in our chosen plot for the same units of the abscissa and of the ordinate, we obtain a straight line with a  $45^\circ$  angle.
- <sup>33</sup> The details are too complicated to be presented here.
- <sup>34</sup> Actually, the measurements were limited by the fact that the vortices within the material became mobile (see [Section 4.7.2](#)). The true values of  $B_{c2}$  are much higher; for example, see [65].
- <sup>35</sup> In the case of compounds such as  $\text{Bi}_2\text{Sr}_2\text{CaCu}_2\text{O}_8$ , instead of  $\xi_c$ , we can use the thickness  $d$  of the superconducting layers.
- <sup>36</sup> We note that in some other superconducting layered structures such as the organic superconductors  $G_i$  can reach values up to  $10^{-4}$ .  $G_i$  can also become large in the case of the iron pnictides and can reach values of a few  $10^{-3}$ .
- <sup>37</sup> Occasionally, one speaks of a “weakly layered” superconductor.
- <sup>38</sup> In [Chapter 6](#) we will discuss in detail the highly interesting *dynamic* properties of moving Josephson vortices.
- <sup>39</sup> A more accurate calculation, which takes into account also the energy contribution of the shielding currents, yields an energy  $(B_{\text{cth}}^2/2\mu_0)4\pi\xi_{ab}^2 d \ln(\lambda/\xi_{ab})$  needed for this process. Here,  $\lambda = \lambda_{ab}^2/d$  is the decay length of the circulating currents in a nearly two-dimensional layer.
- <sup>40</sup> In [Figures 4.39](#) and [4.40](#), the resistance or the conductance is normalized to the film geometry of a square (length  $l$  = width  $b$ ).
- <sup>41</sup> In the discussed temperature range near  $T_c$  also the relatively thick films of Bi (224 nm) and

of Ga (172 or 102 nm) satisfy the condition  $d < \xi_{\text{GL}}$ , since  $\xi_{\text{GL}}$  approaches infinity for  $T \rightarrow T_c$ .

<sup>42</sup> The geometry yields about a factor  $10^4$  because of the thickness. Furthermore, in the residual resistance regime, the specific conductance of the amorphous material is about  $10^4$  times smaller than that in pure metals.

<sup>43</sup> By “abruptly” we mean switching times that are small compared to the times needed to establish equilibrium.

<sup>44</sup> Such an exponential law is always obtained if the rate of change of a quantity  $a(t)$  is proportional to the instantaneous value of the quantity, that is, if  $da(t)/dt \propto a(t)$ .

# Chapter 5

## Critical Currents in Type-I and Type-II Superconductors

We have already seen several times that a superconductor can carry only a limited electric current. As the first example, in [Section 1.5.1](#) we discussed the critical current in a Josephson junction. However, also in the case of homogeneous superconductors the strong correlation of the Cooper pairs leads to the existence of a critical velocity and, hence, of a critical current density  $j_c$ . If this critical value is exceeded, Cooper pairs will be broken up.

Next we want to discuss some relations resulting from the existence of a critical current density, for the maximum possible current in a superconductor. We will restrict ourselves to simple geometric situations.

Our discussions of the critical current are highly important for the technical applications of superconductivity. In type-II superconductors we have materials that can still remain superconducting also for technically interesting magnetic fields. However, for applications it is also important that these superconductors can still transport high electric currents sufficiently without resistance in high magnetic fields. As we will see, here we are confronted with another problem, which has been solved only with the so-called hard superconductors.

Before we turn in detail to the special features in type-I and type-II superconductors, we want to investigate the magnitude of the critical supercurrent density in the ideal case of a thin and homogeneous superconducting wire.

### 5.1 Limit of the Supercurrent Due to Pair Breaking

In order to determine the maximum supercurrent density that can be reached under the most favorable conditions, we consider a homogeneous superconducting wire extending along the  $x$ -direction. The diameter of the wire is assumed to be smaller than the London penetration depth  $\lambda_L$  and the Ginzburg–Landau coherence length  $\xi_{GL}$ . In this case, the Cooper pair density can be taken as constant over the cross-section of the wire, and the Ginzburg–Landau equations (4.28) and (4.29) can be solved for this problem.

In order to keep our calculation no more complicated than necessary and to uncover the underlying physics, resulting in the maximum supercurrent of our wire, we use a few simplifications. For the wave function  $\Psi$  of the superconductor, we use the ansatz

$$\Psi = \Psi_0 e^{ikx} \quad 5.1$$

Here, the amplitude  $\Psi_0$  is independent of location. This means that the Cooper pair density  $n_s = |\Psi|^2$  is spatially homogeneous. The exponential function is taken such that the wave with wavenumber  $k$  is running along the wire.

In order to see how  $\Psi$  is connected with the supercurrent or the supercurrent density along the wire, we insert Eq. (5.1) into the second Ginzburg–Landau equation (4.29):

$$j_s = \frac{q\hbar}{2mi}(\Psi^*\nabla\Psi - \Psi\nabla\Psi^*) - \frac{q^2}{m}|\Psi|^2\mathbf{A}$$

Then we obtain for the  $x$  component of the current density

$$j_{s,x} = \frac{q\hbar k}{m}\Psi_0^2 - \frac{q^2}{m}\Psi_0^2 A_x = q\Psi_0^2 \frac{\hbar k - qA_x}{m} \quad 5.2a$$

According to Eqs. (1.5) and (1.6), the ratio on the right-hand side is just the Cooper pair velocity. Hence, we have

$$j_{s,x} = q\Psi_0^2 v_x \quad 5.2b$$

This corresponds exactly to the relation  $j = qnv$  for the current density of electrically charged particles.

Next, we turn to the first Ginzburg–Landau equation (4.28):

$$\frac{1}{2m}\left(\frac{\hbar}{i}\nabla - q\mathbf{A}\right)^2\Psi + \alpha\Psi + \beta|\Psi|^2\Psi = 0$$

By inserting Eq. (5.1) and by assuming the vector potential to be also independent of  $x$ ,<sup>1</sup> we obtain

$$\frac{(\hbar k - qA_x)^2}{2m}\Psi + \alpha\Psi + \beta\Psi_0^2\Psi = 0 \quad 5.3$$

or by introducing the velocity  $v_x$  and after dividing by  $\Psi$

$$\frac{1}{2}mv_x^2 + \alpha + \beta\Psi_0^2 = 0 \quad 5.4$$

With  $\alpha < 0$ , this yields

$$\Psi_0^2 = -\frac{\alpha}{\beta}\left(1 - \frac{mv_x^2}{2|\alpha|}\right) = \Psi_\infty^2\left(1 - \frac{mv_x^2}{2|\alpha|}\right) \quad 5.5$$

Here, we have used the relation  $-\alpha/\beta = \Psi_\infty^2$  (Eq. (4.23)), and we have introduced the wave function  $\Psi_\infty$  of the homogeneous system in the absence of a supercurrent. We see that the Cooper pair density  $\Psi_0^2$  decreases with increasing kinetic energy  $1/2mv_x^2$ . It vanishes if this energy is equal to  $|\alpha|$ .

This dependence of the Cooper pair density on the velocity must also be taken into account in the expression (5.2b) for the supercurrent density. If the Cooper pair density were constant,  $j_{s,x}$  would simply increase linearly with the velocity of the charge carriers. This is exactly what

happens at small velocities. However, the larger  $v_x$ , the more pronounced is the decrease of the Cooper pair density. As soon as  $\Psi_0^2$  reaches zero,  $j_x$  vanishes. Between  $v_x = 0$  and this limiting value,  $j_x$  has a maximum as a function of  $v_x$ , which we want to determine next.

For this, we must calculate the derivative  $dj_{s,x}/dv_x$ , set it equal to zero, and find  $v_x$ . For the velocity yielding the maximum supercurrent density, we obtain

$$v_{x,p} = \sqrt{\frac{2|\alpha|}{3m}} \quad 5.6$$

According to Eq. (5.5), at this velocity the Cooper pair density attains the value  $\frac{2}{3}\Psi_\infty^2$ , and Eq. (5.2b) yields

$$j_{c,p} = q\frac{2}{3}\sqrt{\frac{2|\alpha|}{3m}}\Psi_\infty^2 \quad 5.7a$$

This current density is also referred to as the ***critical pair-breaking current density***. Using expression (4.25a), connecting  $\alpha$  with  $B_{\text{cth}}$ , and with expression (1.10) for the London penetration depth, we can write it also in the form<sup>2</sup>

$$j_{c,p} = \frac{2}{3}\sqrt{\frac{2}{3}}B_{\text{cth}}\frac{1}{\mu_0\lambda_L} \quad 5.7b$$

This critical current density can become very large. If for  $B_{\text{cth}}$  we take a value of 1 T and for  $\lambda_L$  a value of 100 nm, we obtain for  $j_{c,p}$  a value of about  $4.3 \times 10^8$  A/cm<sup>2</sup>.

In the following sections, we will see to what extent this high critical current density can be achieved in real superconductors.

## 5.2 Type-I Superconductors

As the simplest geometric example, we consider a wire with circular cross-section carrying a current  $I$ . The wire is assumed to be much thicker than the London penetration depth.

At sufficiently small currents, the superconducting wire resides in the Meissner phase. In this phase, the interior of the superconductor must remain free of magnetic flux. However, this also means that the interior cannot carry an electric current, since otherwise the magnetic field due to the current would exist. From this we also conclude that the current passing through a superconductor is restricted to the thin surface layer, into which the magnetic field can penetrate in the Meissner phase. The external currents applied to a superconductor are referred to as ***transport currents***, in contrast to the shielding currents appearing in the superconductor as circulating currents.

In [Figure 5.1](#) we show schematically the spatial distribution of a transport current in a wire with circular cross-section in a plot of the current density versus the wire radius. The total current is given by the integral of the current density over the cross-sectional area

$$I = \int_F j_s dF$$

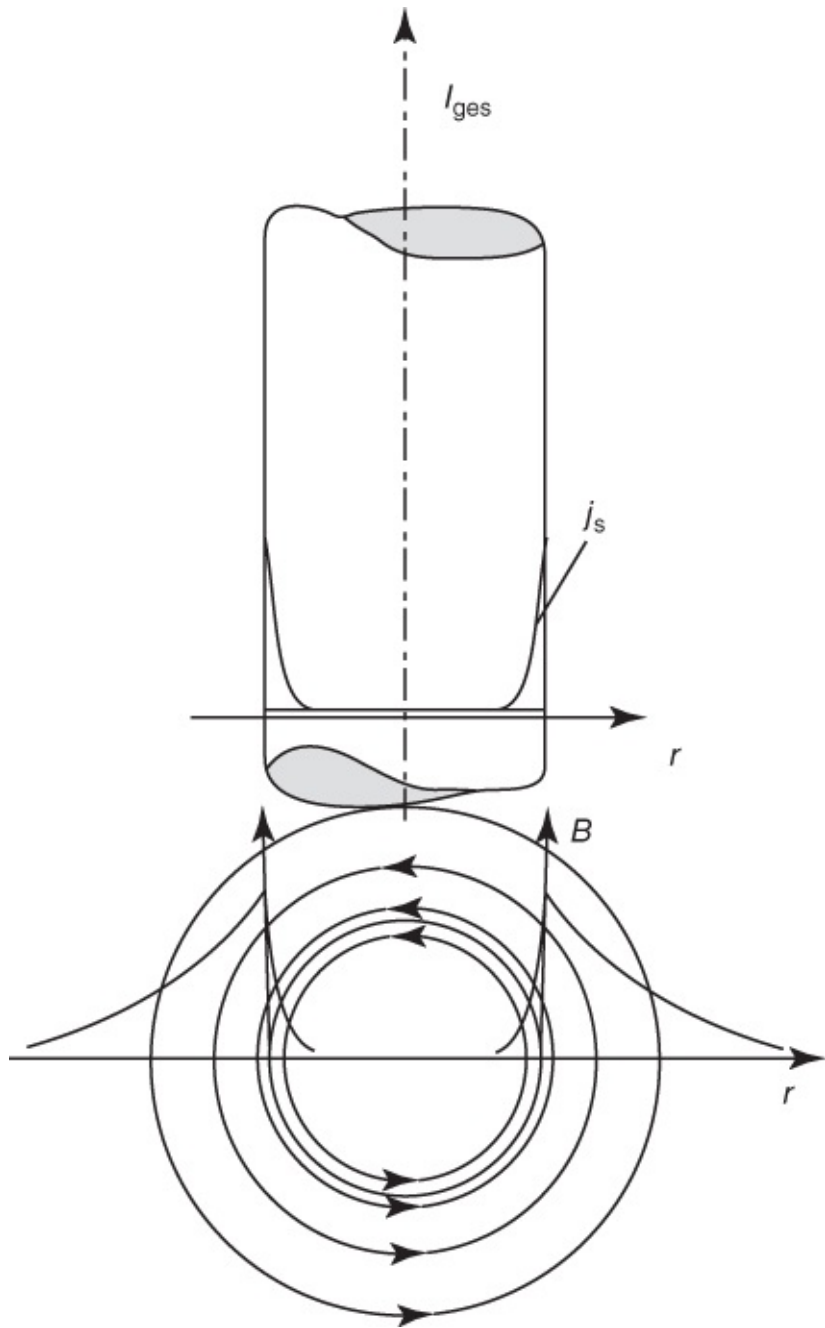


**Figure 5.1** Distribution of the current density and of the magnetic field in a current-carrying superconducting wire. The surface layer has the thickness of only the penetration depth  $\lambda_L$ .

The magnetic field of this current is also shown in [Figure 5.1](#).

Already by 1916, Silsbee [1] had proposed the hypothesis that in the case of “thick” superconductors, that is, for superconductors with a fully developed shielding layer, the critical current is reached exactly when the magnetic field of the current at the surface attains the value  $B_{\text{cth}}$ . This hypothesis has been confirmed perfectly. In other words, it means that the magnetic field and the current density at a surface with a well-developed shielding layer are strongly correlated (Eq. (4.60)). The critical value of the current density is associated with a

certain critical field, namely  $B_{\text{cth}}$ , where it is completely irrelevant whether the current density is due to shielding currents or a transport current.

Because of the validity of the Silsbee hypothesis, it is very simple to calculate the critical currents of wires with circular cross-section from the critical fields, for example, from those of [Figure 4.12](#). The magnetic field at the surface of such a wire carrying the current  $I$  is given by

$$B_0 = \mu_0 \frac{1}{2\pi R} \quad 5.9$$

where  $B_0$  is the field at the surface,  $I$  is the transport current,  $R$  is the wire radius, and  $\mu_0 = 4\pi \times 10^{-7}$  V s/A m. The only requirement is cylindrical symmetry of the current distribution. The radial dependence of the current density is arbitrary.

It follows from Eq. (5.9) that the critical current shows the same temperature dependence as the critical magnetic field (at  $I_c$  the field  $B_c$  is reached). As an example, in [Figure 5.2](#) we show the temperature dependence of the critical current for a tin wire with 1 mm diameter.

According to Eq. (5.9), the critical field of about 300 G at 0 K corresponds to a critical current  $I_{c0} = 75$  A. This critical current increases proportional to the wire radius, since the total current only flows within the thin shielding layer.

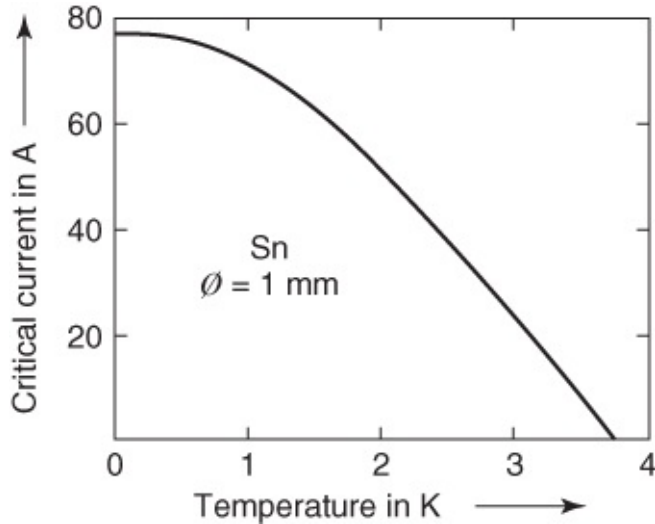


**Figure 5.2** Critical current of a tin wire with 1 mm diameter plotted versus the temperature.

We can also find an average critical *current density* at the surface. In this case we replace the exponentially decaying current density ([Figure 5.1](#)) by a distribution in which the full current density at the surface remains constant to a depth  $\lambda_L$ , the penetration depth, and then abruptly drops to zero.<sup>3</sup> Based on this argument, for the tin wire, for example, at 0 K we obtain a critical current density

$$j_{c0} = \frac{I_{c0}}{2\pi R \lambda_L(0)} = 7.9 \times 10^7 \text{ A/cm}^2 \quad 5.10$$

with  $R = 0.5$  mm,  $\lambda_L(0) = 3 \times 10^{-6}$  cm, and  $I_{c0} = 75$  A. This critical current density is similar to the critical pair-breaking current density of a thin wire treated in [Section 5.1](#). It would allow very high transport currents if the shielding effect, leading to the restriction of the current to a thin surface layer, could be avoided. Such substances have been developed in the form of the hard superconductors.

Using Silsbee's hypothesis, we can also calculate the critical currents of a superconductor in an external magnetic field. For this purpose, we only have to add the vectors of the external field and of the field of the transport current at the surface. The critical current density is reached when this resulting field attains the critical value. We consider a wire of radius  $R$  and a magnetic field  $B_a$  applied perpendicular to the wire axis. At first, no transport current is passing through the wire. Due to the Meissner effect, the field  $B_a$  is expelled from the wire, as shown in [Figure 5.3a](#). In the case of a wire in a perpendicular magnetic field, the demagnetization factor is  $\frac{1}{2}$ . Therefore, at the top and the bottom side of the wire, the effective field is  $B_{\text{eff}} = 2 B_a$ . A transport current  $I$  passing through the wire generates a magnetic field as indicated in [Figure 5.1](#). At the top side of the wire, this field is directed opposite to the applied field. At the bottom side of the wire both fields add to each other. Hence, here one observes the highest total field,  $B_{\text{ges}} = 2B_a + \mu_0 I/2\pi R$ . The critical current is reached in the case  $B_{\text{ges}} = B_{\text{cth}}$ , that is,

$$I_c = \frac{2\pi R}{\mu_0} (B_{\text{cth}} - 2B_a) \quad 5.11$$

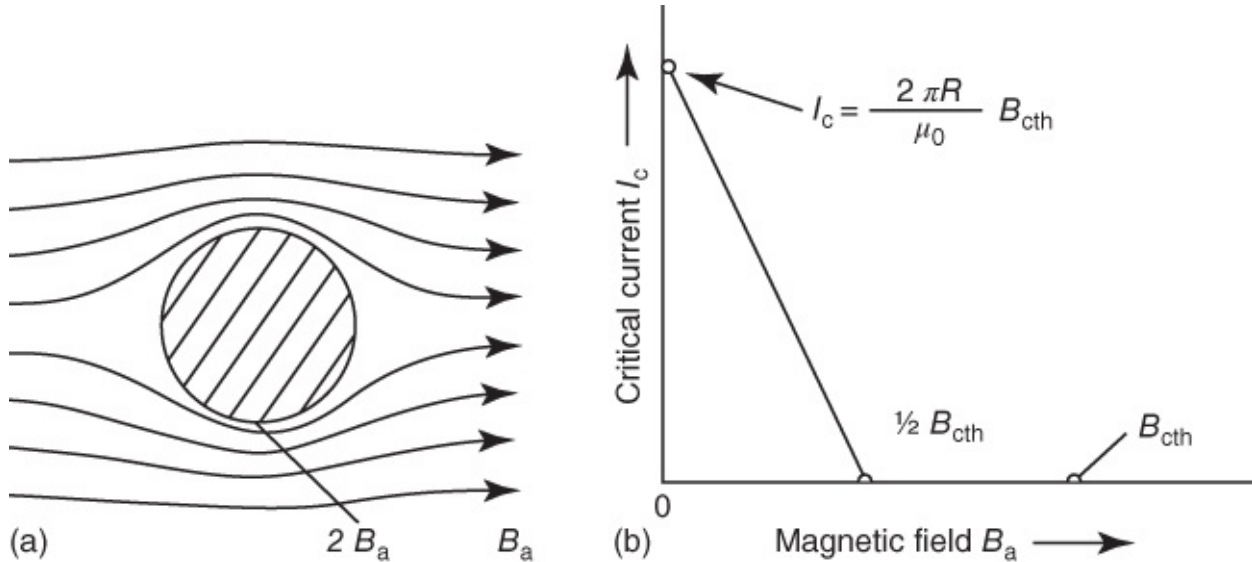


**Figure 5.3** (a) Field distribution around a superconducting wire in the Meissner phase without a transport current. (b) Critical current of a wire with circular cross-section in external field  $B_a$  oriented perpendicular to the wire axis.

This dependence is plotted in [Figure 5.3b](#).

Next we turn to the question of how the superconductor enters the normal state upon reaching the critical current. For this, we again consider a wire with circular cross-section. If the

critical current is exceeded, the Meissner phase with its complete flux expulsion must become unstable. One would expect that the superconductor becomes completely normal conducting. However, in this case the transport current would be distributed over the total cross-section. The magnetic field at the surface would remain unaffected by this redistribution. However, then everywhere in the superconductor the current density would be smaller than its critical value. Since the critical current density represents the crucial quantity for the stability of the superconducting state, we expect that the transition cannot take place in such a way that the current density is everywhere smaller than the critical value.

This assumption is confirmed by experiment. If the critical current is exceeded, the superconductor enters the intermediate state, that is, there appear normal conducting domains. Several models have been proposed to describe this intermediate state. In this case, configurations of the normal conducting or superconducting domains are sought that yield the critical field  $B_{\text{cth}}$  at all interfaces as much as possible. For the macroscopic structure of the intermediate state, this critical field value also yields the critical current density because of the fully developed shielding. A model of this kind is shown in [Figure 5.4](#) [2]. Since the magnetic field of the transport current consists of circular field lines, the phase boundaries must also run perpendicularly to the wire axis. Because of the requirement that for each radius the field must be equal to  $B_{\text{cth}}$ , the current density must increase toward the wire axis. This is accomplished also by an increase in the thickness of the superconducting domains toward the wire axis.

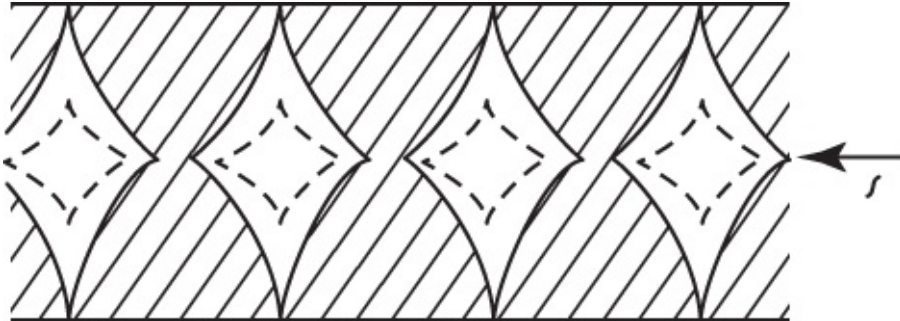


[Figure 5.4](#) Intermediate-state structure of a wire with circular cross-section at the critical current. Hatched domains are normal conducting. The structure shows rotational symmetry around the cylinder axis. For a transport current  $I > I_c$ , the superconducting domains shrink (dashed lines).

(From [2].)

The geometrical details can only be found from a calculation. In this case certain additional assumptions are necessary. The various models of this current-induced intermediate state are different because of these additional assumptions.

The domain structure of this intermediate state has been demonstrated beautifully by means of the powder decoration method (see [Section 4.6.4](#)). An example of this structure is shown in [Figure 5.5](#) [3]. Upon exceeding the critical current density, the superconducting wire jumps into a state where the superconducting domains still extend to the sample surface. Upon a further increase in the current, a normal conducting ring-shaped domain appears, which surrounds a core region residing in the intermediate state, the thickness of which increases with

increasing current.



**Figure 5.5** Intermediate-state structure of a current-carrying In cylinder. The bright stripes indicate normal conducting domains. Length 38 mm, diameter 6 mm, transport current 30 A, external field  $B_a$  perpendicular to the cylinder axis 0.01 T, temperature  $T = 2.1$  K ( $T_c$  of In: 3.42 K), normal conducting  $\rightarrow$  superconducting transition.

(From [3].)

In [Figure 5.6](#) we show the electrical resistance of the wire plotted versus the transport current [2]. At  $I_c$  the resistance jumps; however, the full normal resistance is not yet established. The latter is obtained only upon a further increase in  $I$ . Such measurements are quite difficult, since in the current-induced intermediate state at finite resistance the dissipated joule heat can easily lead to an increase in temperature and, hence, to instabilities.<sup>4</sup>

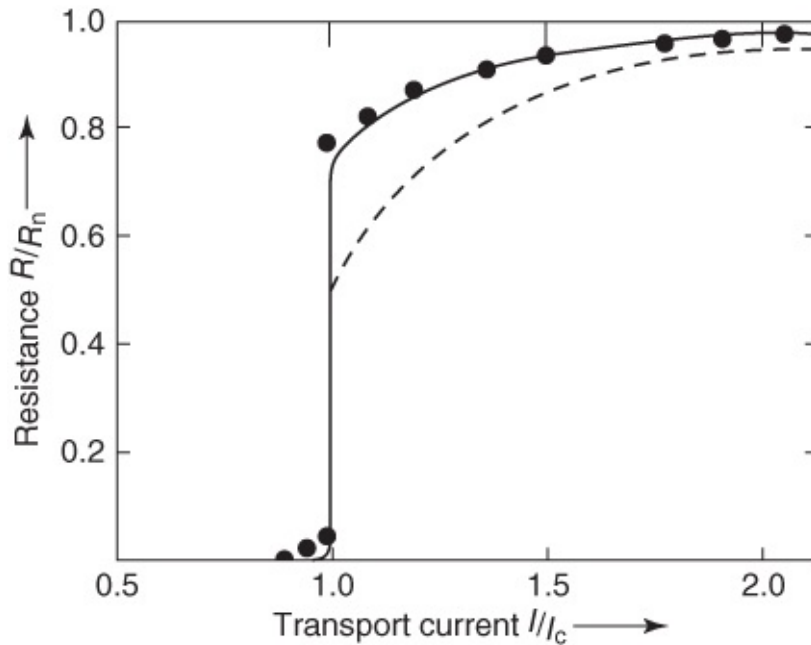


**Figure 5.6** Electrical resistance plotted against the transport current.

Solid line: model calculation from [2]; dashed line: model of London [4]; data points; from [5] (see also [6]).

Regarding the stability of the intermediate state, a “thick” wire carrying a transport current corresponds to a sample with a demagnetization coefficient different from zero in the external field (see [Section 4.6.4](#)). In both cases, by means of the transition into the intermediate state, the superconductor can respond to the constraint of the external variables (current or magnetic field) by splitting up into normal conducting and superconducting domains. In this way, the critical value can be kept constant over a range of external variables.

So far we have treated static models of the intermediate state. For a given state, the superconducting or normal conducting domains remain fixed within the sample, except for thermal fluctuations. Gorter [7] has proposed a dynamic model, according to which domain motion appears in the presence of a transport current, leading to a resistance. In this case, within this model, the interfaces are oriented parallel to the direction of the transport current. In the static model discussed earlier ([Figure 5.4](#)), they were oriented perpendicular to the current direction. Decoration experiments using Nb powder have shown that for sufficiently large transport current the domains, indeed, move across the superconductor perpendicular to the current [8].

Very complicated intermediate state structures are obtained in wires that carry large transport currents in the presence of a longitudinal magnetic field. In this case, the longitudinal external field and the circular field of the current are superimposed such that the phase boundaries, which must always be oriented parallel to the field, display a screw pattern. Therefore, the transport current is also wound in a screw pattern. In this case, unexpected effects occur. For example, field enhancement is observed in the interior of the sample, which can be understood from the structure of the intermediate state, and which demonstrates impressively the general rule (see [Section 4.6.4](#)) that the phase boundaries must always be oriented parallel to the magnetic field [9].

## 5.3 Type-II Superconductors

Next we turn to type-II superconductors, which differ in an important fundamental way from type-I superconductors. For small magnetic fields and, hence, also for small transport currents, type-II superconductors reside in the Meissner phase. In this phase they behave like type-I superconductors, that is, they expel the magnetic field and the current into a thin surface layer.

A difference from type-I superconductors first appears when the magnetic field at the surface exceeds the value  $B_{c1}$ . Then a type-II superconductor must enter the Shubnikov phase, that is, flux lines must penetrate into the superconductor. One finds that in the Shubnikov phase the ideal<sup>5</sup> type-II superconductor has a finite electrical resistance even at very small transport currents [10]. In the next section, we will treat this in detail. On the other hand, in type-II superconductors containing a large amount of defects, we can observe very large supercurrents. These “hard superconductors” will be discussed in [Section 5.3.2](#).

### 5.3.1 Ideal Type-II Superconductor

We consider a rectangular plate carrying a current parallel to the plane of the plate and kept in the Shubnikov phase due to a magnetic field  $B_a > B_{c1}$  oriented perpendicular to the plate ([Figure 5.7](#)).

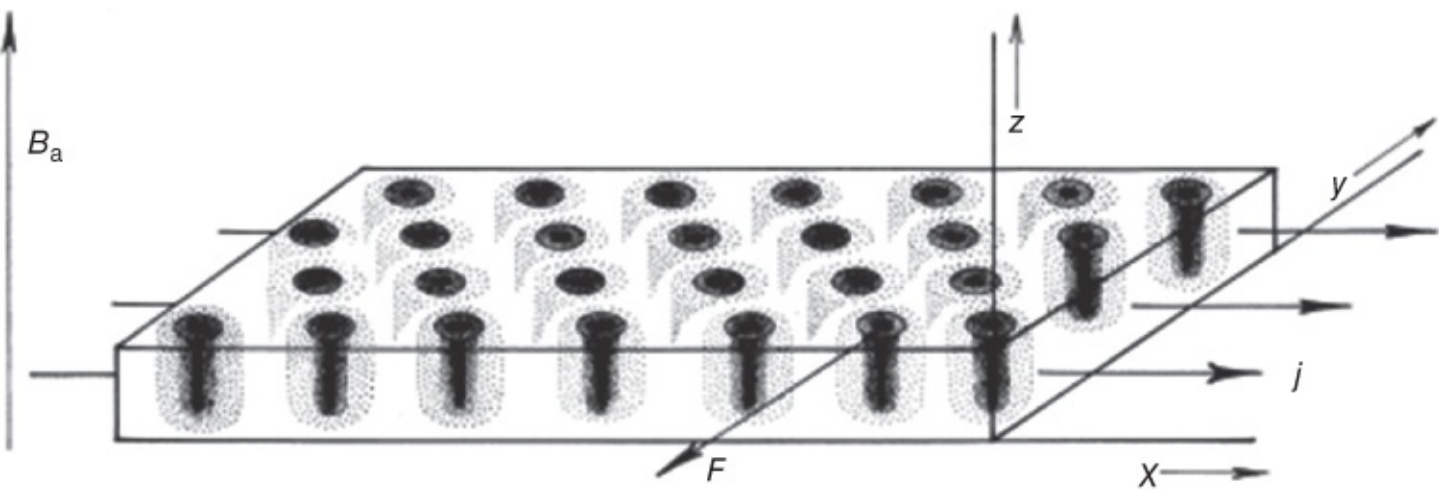


**Figure 5.7** Shubnikov phase in the presence of a transport current density  $j$ . The flux lines experience a force  $F$  driving them along the  $y$ -direction. The magnetic field distribution around the flux lines is indicated by the shading.

As the first important result of such an experiment, one finds that under these conditions the transport current  $I$  is distributed over the total cross-section of the plate, that is, it is no longer completely restricted to a thin surface layer. After the penetration of the magnetic flux into the superconducting sample, the transport current can also flow within the interior of the superconductor.

In this case there exists an important interaction between the transport current and the vortices. The transport current, say, along the  $x$ -direction, also passes through the vortices, that is, through regions where a magnetic field exists.<sup>6</sup> Between an electric current and a magnetic field, there exists the Lorentz force. In the case of a current  $I$  along a wire of length  $L$  in a perpendicular magnetic field  $B_a$ , the absolute magnitude of this force is

$$F = ILB \quad 5.12$$

This force is oriented perpendicular to  $B$  and to the current (here given by the wire axis). It is also this Lorentz force that drives our electric motors.

In the Shubnikov phase carrying a transport current, the Lorentz force acts between the vortices and the current. Since the transport current is spatially fixed by the boundaries of the plate, under the influence of the Lorentz force the vortices must move perpendicular to the current direction and to the magnetic field, that is, perpendicular to their own axis [11]. For ideal type-II superconductors, in which free motion of the vortices is possible, this vortex motion should appear already at arbitrarily small forces and, hence, at arbitrarily small transport currents.

However, the vortex motion across the superconductor causes dissipation, that is, electrical energy is changed into heat. This energy can only be taken from the transport current by means of an electrical voltage appearing along the sample. Hence, the sample shows electrical resistance.

The dissipation of electrical energy into heat during vortex motion may be due to two fundamentally different processes. The first loss mechanism is associated with the appearance

of local electric fields generated by the moving vortices. This electric field also accelerates the unpaired electrons. They can deliver their energy taken up from the electric field to the lattice and thereby generate heat.

In addition to this process for energy dissipation, associated with the spatial variation of the magnetic field in a vortex, there exists another process caused by the spatial variation of the Cooper pair density in a vortex. If a vortex moves across the location P, a temporal change of the Cooper pair density  $n_s$  also appears at this location, since  $n_s$  increases from its value zero in the vortex center toward the outside. In this case we must take into account that, following a deviation from equilibrium, this equilibrium value of  $n_s$  is re-established only after a finite time  $\tau$  (the relaxation time, see [Section 4.9](#)). If  $n_s$  changes very slowly, that is, within times much larger than  $\tau$ , the system only passes through equilibrium states. In this case, the energy consumed at the front side of the vortex during breaking up of Cooper pairs will be delivered back at the back side during pair formation. Therefore, practically no net heat is generated in this process. However, if the vortex moves sufficiently fast, such that the Cooper pair density cannot pass only through equilibrium states anymore, energy will be dissipated during the temporal change of  $n_s$ , and heat will be generated.

We can understand this in the following way. The high magnetic field within the vortex core moves sufficiently fast that the equilibrium concentration of Cooper pairs corresponding to each field value cannot be established anymore. In this case, at the front side of the vortex, the Cooper pairs are broken up in a magnetic field that is too high. On the other hand, at the back side the Cooper pairs recombine in a field that is already too small for the corresponding concentration. Since the heat of reaction of the breaking of a Cooper pair decreases with increasing magnetic field,<sup>7</sup> during the break-up process less heat energy is consumed than is delivered back during the recombination. Therefore, heat will be generated, if the temporal variation of  $n_s$  is made fast enough such that deviations from equilibrium appear between all parameters.

What we just have described for the example of the Cooper pair density is exactly the mechanism of all relaxation processes for changes of external parameters during times comparable to the relaxation time. Other well-known examples are the polarization losses of a dielectric substance in an alternating electric field or the magnetization losses of a ferromagnetic material in an alternating magnetic field.

So we summarize: As soon as the vortices in the Shubnikov phase start to move due to a transport current, we have losses and, hence, electrical resistance. Since in an ideal type-II superconductor arbitrarily small transport currents already lead to vortex motion, the critical current of such a superconductor in the Shubnikov phase is zero [10]. Therefore, such superconductors are useless for technical applications, say, for building magnets, in spite of their high critical field  $B_{c2}$ . Finite critical currents in the Shubnikov phase can only be obtained if the vortices in some way are bound to their locations. Such pinning of the vortices can, indeed, be achieved. Type-II superconductors containing such pinning centers are referred to as **hard superconductors**. Their properties will be discussed in the next section.

So far in our discussions of the critical current in type-II superconductors, we have stabilized the Shubnikov phase by means of an external magnetic field. Now we return to the question of the critical current in the absence of an external magnetic field, with which we had started. Again, we assume a wire with circular cross-section carrying the transport current  $I$ . Upon exceeding the value  $I_c = B_{c1}2\pi R/\mu_0$ , which generates just the field  $B_{c1}$  at the surface, the superconductor enters the Shubnikov phase. Since the magnetic field of the transport current circulates around the wire axis, in this geometry circular closed vortices are also generated. Under the influence of the Lorentz force they move toward the wire axis by shrinking and vanish at the axis. So for an ideal type-II superconductor with this geometry, we expect a critical current  $I_c$  determined from  $B_{c1}$  in the same way as for a type-I superconductor from  $B_{cth}$  (see [Section 5.2](#)). Since  $B_{c1}$  is smaller than  $B_{cth}$ , in ideal type-II superconductors this critical current will always be smaller than in the corresponding type-I superconductors.<sup>8</sup>

For a long time, there has been an animated discussion on the role of vortex motion in the generation of electrical voltage. Within this context many experiments were contemplated and carried out. Here, we want to treat only one example.

In 1996 Giaever [12] performed an experiment, the idea of which is illustrated with the configuration shown in [Figure 5.8](#). A thin film of a superconductor (A) is driven into the Shubnikov phase by means of an external magnetic field, and a transport current is applied. In this case, motion of the flux lines should occur. In order to detect this flux motion, on top of film A Giaever deposited a second superconducting film B, which was electrically insulated from film A by means of a thin insulating layer. In this configuration the magnetic flux lines in both films are coupled to each other.<sup>9</sup> If the vortices move across the superconductor A under the influence of the transport current, the vortices in B are dragged along because of the coupling. If, as felt by Giaever, an electrical voltage appears between the ends of the superconductor because of the vortex motion, this voltage must also be observed along the film B, which is completely separated from the primary circuit. Therefore, the arrangement represents some kind of “flux transformer.”

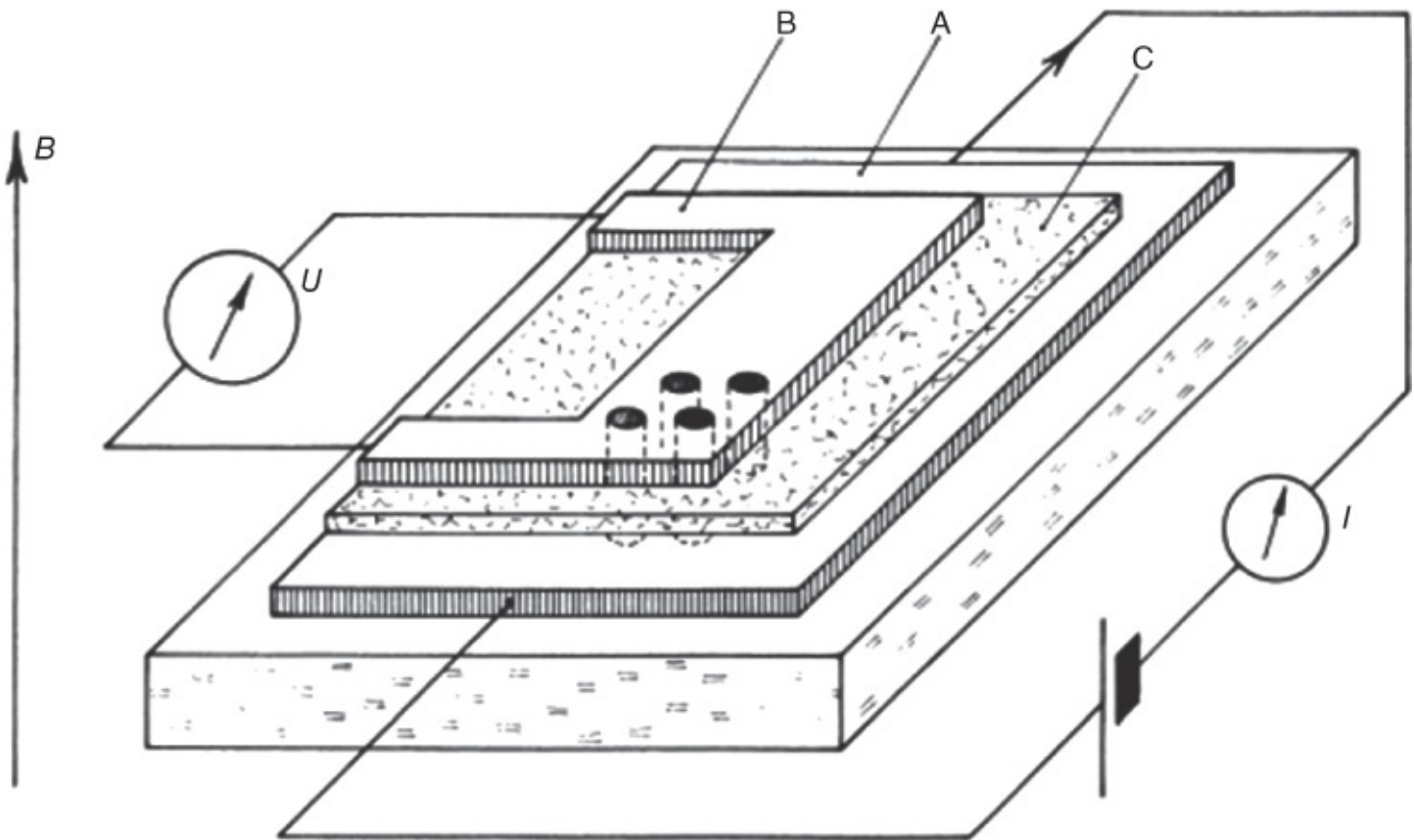


**Figure 5.8** Generation of an electrical voltage  $U$  during vortex motion. A and B are superconductors, C is an insulating layer. All layer thicknesses are strongly exaggerated.

(From [12].)

Giaever performed the experiment in the absence of an external magnetic field. Also in this case, the magnetic field of the transport current applied to film A penetrates into both films in the form of flux lines. These flux lines have opposite sign at the left and the right sides of the film, respectively, and they move from both sides of the film A to the center, where they annihilate each other. This vortex motion resulted in the expected voltage also along the electrically completely separated film B. If both films were normal conducting, no electrical voltage was observed along film B for the same conditions otherwise. This experiment clearly demonstrated the importance of vortex motion for the appearance of an electrical voltage in the Shubnikov phase.

Recently, the geometry of the flux transformer has been taken up again in order to investigate if in high-temperature superconductors the vortices can move independently of each other in the form of pancakes (see [Section 4.7.2](#)) [13]. For this purpose, at one side, for example, of a  $\text{Bi}_2\text{Sr}_2\text{CaCu}_2\text{O}_8$  single crystal a transport current is injected parallel to the layer structure, and the voltage drop is measured resulting from the vortex motion. If the vortices represent compact, continuous flux lines across the crystal, at the opposite crystal surface a voltage of equal magnitude will be induced. However, if the pancakes move independently of each other, this secondary voltage will be smaller than the primary voltage. In this way, the existence of pancake vortices in  $\text{Bi}_2\text{Sr}_2\text{CaCu}_2\text{O}_8$  could be beautifully demonstrated. On the other hand, it

turned out that the vortices in  $\text{YBa}_2\text{Cu}_3\text{O}_7$  behave more like compact, continuous flux lines.

## 5.3.2 Hard Superconductors

In [Section 4.7.1](#) we have discussed the magnetization curves of type-II superconductors ([Figure 4.23](#)). We started with ideal, homogeneous substances, that is, substances in which the vortices of the Shubnikov phase are freely mobile, having no energetically favorable locations. This discussion only represents a limiting case, which is approximated only more or less poorly by real samples.

In this section we will discuss the case in which the vortices of the Shubnikov phase are energetically strongly bound to favorable locations. These superconductors are referred to as ***hard superconductors*** and represent technically useful materials.

### 5.3.2.1 Pinning of Flux Lines

First we want to discuss how vortices in type-II superconductors can be pinned. We will deal with a series of different types of pinning centers.

In the simplest way we can understand the effect of pinning centers by means of an energy consideration. The formation of a vortex requires a certain amount of energy. This energy is contained, say, in the circulating currents flowing around the vortex core. We see that for the given conditions a vortex is associated with a certain amount of energy per unit length, that is, the longer the flux line, the larger the energy needed for its generation.

We denote this energy by  $\epsilon^*$ . It can be estimated from the lower critical field  $B_{c1}$ , above which magnetic flux starts to penetrate into a type-II superconductor. The resulting gain in expulsion energy suffices to generate vortices in the interior. For simplicity, we consider again a long cylinder in a magnetic field parallel to its axis, that is, a geometry with zero demagnetization coefficient. At  $B_{c1}$  the penetration of the magnetic flux results in  $n$  flux lines per unit area. Each flux line carries just one flux quantum  $\Phi_0$ . This requires the energy

$$\Delta E_F = n\epsilon^* LF \quad 5.13$$

where  $n$  = number of flux lines per unit area,  $\epsilon^*$  = energy per unit length of vortex,  $L$  = sample length, and  $F$  = sample cross-section. The gain in magnetic expulsion energy is

$$\Delta E_M = B_{c1} \Delta M V \quad 5.14$$

where  $\Delta M$  = change of the magnetization of the sample and  $V = LF$  = sample volume.  $\Delta M$  can be expressed in terms of the penetrated flux quanta. We have

$$\Delta M = n\Phi_0 / \mu_0 \quad 5.15$$

This yields for the gain in expulsion energy

$$\Delta E_M = \frac{1}{\mu_0} B_{c1} n \Phi_0 L F \quad 5.16$$

If the two energy changes are being set equal ( $\Delta E_F = \Delta E_M$ ), from the definition of  $B_{c1}$  we obtain

$$n\epsilon^*LF = \frac{1}{\mu_0}B_{c1}n\Phi_0LF \quad 5.17$$

and hence<sup>10</sup>

$$\epsilon^* = \frac{1}{\mu_0}(\Phi/\lambda_L)^2 \ln(\lambda_L/\xi_{GL})$$

We see that the energy  $\epsilon^*$  increases proportional to the square of the magnetic flux  $\Phi$  in a vortex. Therefore, vortices containing more than one flux quantum  $\Phi_0$  are energetically unfavorable. In a type-II superconductor or in hard superconductors, such vortices can only exist if they are strongly promoted by other conditions such as inhomogeneities in the material.

$$\epsilon^* = \frac{1}{\mu_0}B_{c1}\Phi_0 \quad 5.18$$

In the case of the estimate given above, we have considered only the field-expulsion energy. However, the loss of condensation energy on the scale of the coherence length also affects the value of  $\epsilon^*$ . From our knowledge of the vortex energy  $\epsilon^*$ , we can easily understand the pinning effect of normal precipitates. If a vortex can pass through a normal conducting inclusion, its length within the superconducting phase and thereby its energy are reduced. This is schematically indicated in [Figure 5.9](#). The hatched region indicates the normal inclusion. A vortex in location “a” has an energy smaller by the amount  $\epsilon^*l$  compared to one in location “b.” This means that we must supply the energy  $\epsilon^*l$  to the vortex in order to move it from “a” to “b.” Hence, a force is needed to effect this change in location.

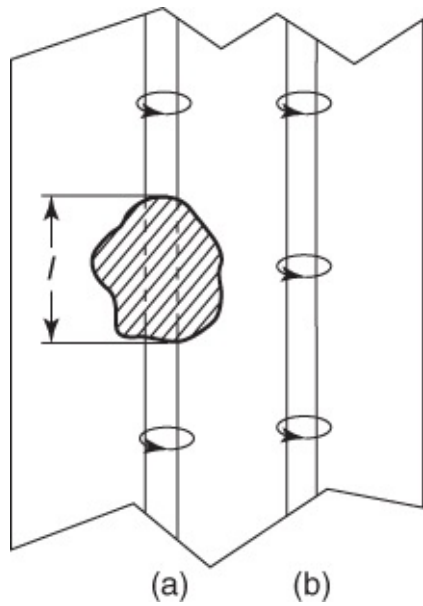


**Figure 5.9** Pinning effect of normal conducting precipitates. In location “a” the effective length of the vortex is shorter compared to that in location “b,” since there are no circulating currents in the normal conducting region.

If there are many pinning centers, the vortices will attempt to occupy the energetically most favorable locations. As shown in [Figure 5.10](#), they will also bend in order to reach the minimum value of the total energy. The length increment caused by the bending must be overcompensated by the effective shortening within the normal conducting regions. In a vortex lattice as it is generated in the Shubnikov phase, we must take into account in the total energy balance also the repulsive forces acting between the flux lines.

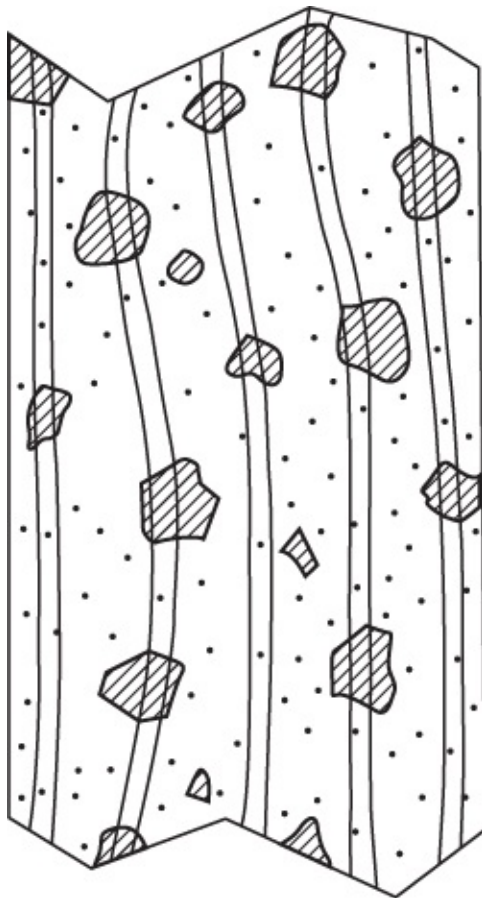


**Figure 5.10** Vortex configuration in a hard superconductor. The hatched regions represent pinning centers. The dots indicate atomic defects.

In principle, other pinning centers, say, lattice defects, can also be understood in the same way.<sup>11</sup> Every inhomogeneity of the material that is less favorable for superconductivity acts as a pinning center, with the completely normal state representing the limiting case. For example, superconducting precipitates, however, with a lower transition temperature, in general act as pinning centers.

If for a certain material the superconductivity is associated with an expansion of the crystal lattice (see [Section 4.6.6](#)), the regions with a contracted lattice will be less favorable for superconductivity and, hence, will act as pinning centers. This may be the case within grain boundaries and dislocation configurations, as they are generated during plastic deformation.

Atomic defects within the crystal lattice represent a particular issue with respect to the pinning centers. The diameter of the normal core of a vortex is about equal to the coherence length  $\xi_{\text{GL}}$ , which amounts to many lattice constants in many superconductors. Hence, one could expect that atomic defects are not effective pinning centers. However, it could be shown that the scattering of electrons at atomic defects leads to an appreciable pinning effect [14]. On the other hand, since each flux line usually covers many atomic defects, in the case of a homogeneous distribution of the atomic defects the effective pinning force vanishes, since no particular location within the material is distinguished. Such distinction only appears if the density of the atomic defects varies spatially.

In the case of superconductors with an extremely small value of the coherence length as, for example, the cuprates, the situation is completely different. Here, spatially very small defects can act as pinning centers in different ways.<sup>12</sup>

In the extreme case, even the crystal structure itself can have an effect. In [Section 4.7.2](#) we have already discussed that, in the case of the cuprates, in magnetic fields oriented parallel to the superconducting CuO<sub>2</sub> planes, there develop Josephson vortices with their axis being located in the nonsuperconducting or only weakly superconducting intermediate layers. These intermediate layers represent highly effective pinning centers against vortex motion perpendicular to the planes. One speaks of “intrinsic pinning” [15]. On the other hand, the vortices can still move easily parallel to the layer structure.

In a similar way grain boundaries or twin boundaries between single-crystalline regions act as defects, preventing vortex motion perpendicular to these defects.<sup>13</sup>

Line defects and point defects are also important. Dislocation lines represent an example. Line defects and point defects were also artificially generated by irradiating high-temperature superconductors with high-energy heavy ions or also with protons [16]. During irradiation with heavy ions, along the path of the beam particles there appears a straight, highly perturbed region across the crystal, which is referred to as a **columnar defect**. On the other hand, irradiation with protons results in accumulations of point defects.

For the generation of well-controlled pinning centers, the continuously improved techniques of nanotechnology are applied. A summary can be found in [17]. During the deposition of thin films one can incorporate nanoparticles into the superconducting matrix. Equally distributed “round” nanoparticles consisting, for example, of Y<sub>2</sub>O<sub>3</sub>, result in a nearly isotropic pinning of flux lines. On the other hand, in the case of rod-like structures, a preferential direction is obtained. As an example we mention BaZrO<sub>3</sub> nanorods, which grow on the film during its deposition by means of pulsed laser ablation [18]. In the case of pulsed laser ablation, in order to produce an YBa<sub>2</sub>Cu<sub>3</sub>O<sub>7</sub> thin film, in an oxygen atmosphere of about 0.3 mbar, highly intensive laser pulses are directed onto a “target” made of massive YBa<sub>2</sub>Cu<sub>3</sub>O<sub>7</sub>. The ablated material condenses on a single-crystalline SrTiO<sub>3</sub> substrate such that the CuO<sub>2</sub> planes of the cuprate are oriented parallel to the surface of the substrate. In order to incorporate BaZrO<sub>3</sub> nanorods in addition, one uses a target containing some BaZrO<sub>3</sub> in addition to YBa<sub>2</sub>Cu<sub>3</sub>O<sub>7</sub>. If this mixture is deposited, in addition to the YBa<sub>2</sub>Cu<sub>3</sub>O<sub>7</sub> matrix, also BaZrO<sub>3</sub> rods of about 10 nm diameter grow on the substrate, which penetrate the total thickness of the film and act as rod-shaped pinning centers.

In thin films of metallic superconductors and also in the cuprates, one can fabricate “defects” in a well-controlled way in the form of microholes within the material. In this case one often speaks of “antidots” [19]. Also the opposite of the antidots, magnetic particles placed on the film surface (“magnetic dots”), have been studied [20].

Another “defect” we want to mention is the surface of the superconductor itself. If the external magnetic field is increased (decreased), vortices enter (exit) the sample at the edge. This

process is already prevented by the flow of the shielding currents, and the vortices must traverse a surface barrier. This is also referred to as the ***Bean–Livingston barrier*** [21].

The effect of the pinning centers can also be described in terms of an energy landscape. Now the pinning center represents a potential well of depth  $E_p$ . The vortex is located at its most favorable position, similar to a ball at the lowest point of a bowl. If the ball is to be displaced from this location, one needs a force in order to supply the increase of the potential energy. To remove the ball from its most favorable location, we must supply the energy needed to lift the ball out of the bowl. Usually, in a material there are many pinning centers, which are irregularly distributed and have different energy depths  $E_p$ . If the superconductor is cooled below  $T_c$  in a magnetic field, the vortices will quickly occupy the potential wells, instead of generating a regular triangular lattice. At best, we have a distorted lattice, or in the extreme case even a glassy state [22].

The deviation of an individual vortex from its ideal location within the triangular vortex lattice depends on the depth of the potential wells, and also on the configuration of all other vortices, because of the repulsive interaction between them.

An energetically highly unfavorable arrangement of the vortices will be changed quickly because of the thermal fluctuations. These fluctuations can provide the energy difference  $\Delta E$  needed to leave the potential well, with a probability  $w = \exp(-\Delta E/k_B T)$ . In this case, the thermodynamic fluctuations can reduce the depth of the potential well, or they can supply the missing energy to the vortex. At low temperatures and for large values of  $\Delta E$ , this probability can become very small, such that the state with the lowest energy cannot be occupied any more. Furthermore, because of the interaction between the vortices,  $\Delta E$  can approach infinity. In this case we are dealing with the state of a vortex glass, which experiences no changes anymore within finite times.

A special effect occurs if two pinning centers are located very close to each other. In this case a vortex can jump very easily back and forth between the two potential wells because of thermal fluctuations. This effect is highly important in the context of superconducting quantum interferometers (SQUIDs) made from high-temperature superconductors. The magnetic field of a flux quantum located within the superconducting material of the SQUID is recorded as a measuring signal by the SQUID. If this flux quantum moves, then this (unwanted) signal changes and causes a reduction of the SQUID sensitivity for real measuring signals.<sup>14</sup> Therefore, the investigation of such pinning centers and the development of most effective and strong pinning centers are highly important.

What is the effect of the pinning centers if in the superconducting state the magnetic field is changed or a transport current is applied to the superconductor? These questions will be discussed in the next two sections. We start with the magnetization curves of hard superconductors.

### 5.3.2.2 Magnetization Curve of Hard Superconductors

If in the Shubnikov phase the vortices are attached to certain locations within the material, then

in an external field the magnetization corresponding to thermodynamic equilibrium cannot establish itself. The prerequisite for this is the free mobility of the vortices. Hence, we have to expect quite different magnetization curves. Furthermore, it represents an important difference, whether the superconductor is cooled in a field  $B_a$ , or this field is applied only after the superconducting state is established. First, we treat the properties of massive metallic superconductors, and then we turn to the high-temperature superconductors and to special thin-film structures, in which pinning centers were artificially generated.

In [Figure 5.11](#) as an example we show the behavior of a Nb–Ta alloy [23]. Niobium and tantalum can be mixed in any ratio. After careful annealing one obtains highly homogeneous mixed crystals. They yield a nearly reversible magnetization curve (curve a). After deformation of such a mixed crystal, say, by pulling for the fabrication of wires, many lattice defects exist within the crystal, acting as pinning centers for vortices. In this case the magnetization curve is completely different (curve b). First we note that a much higher magnetization is reached. This also means that in external fields much higher than  $B_{c1}$  the deformed sample can still display nearly perfect diamagnetic shielding. Furthermore, any trace of reversibility has disappeared. For decreasing field, magnetic flux remains trapped in the sample also at  $B_a = 0$ . In this case the trapped flux is oriented parallel to the previously applied external field.

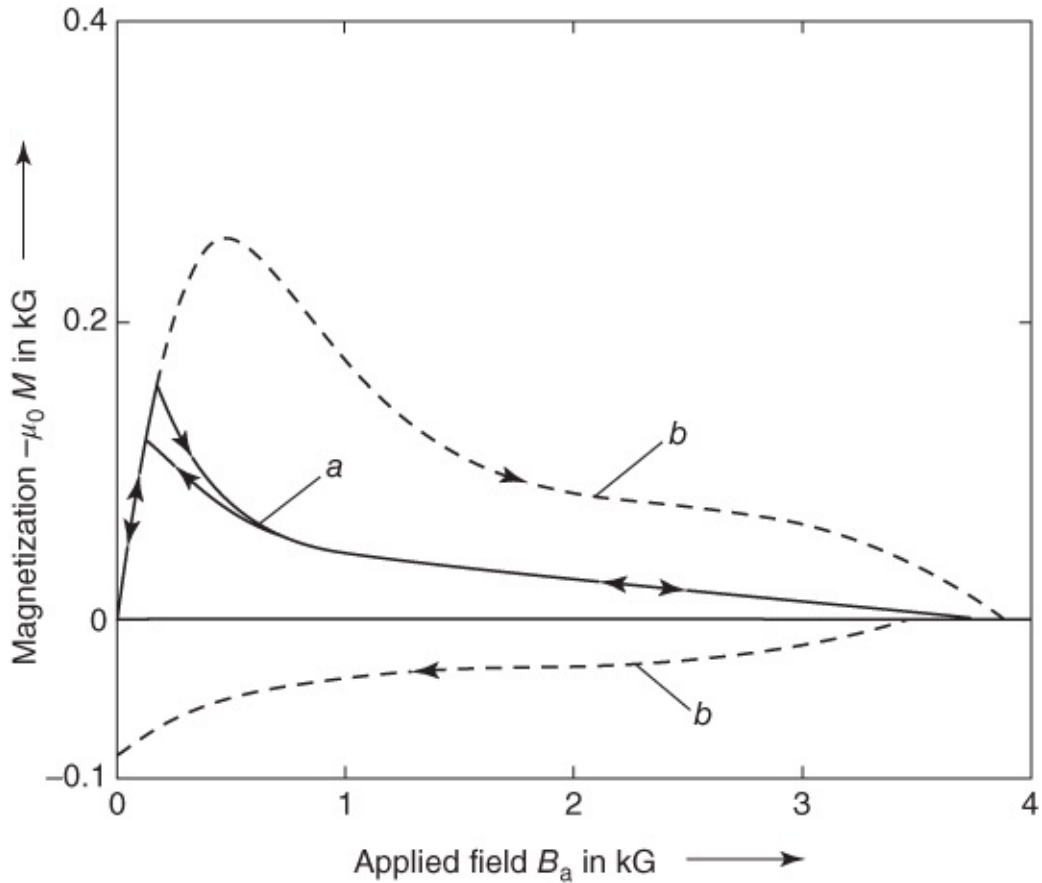


**Figure 5.11** Magnetization curves of a Nb<sub>55</sub>Ta<sub>45</sub> alloy: curve *a*, well annealed; curve *b*, with many lattice defects

(from [23]) (1 kG = 0.1 T).

Only the upper critical field  $B_{c2}$  remains unchanged. This can be understood from the fact that a mixed crystal of the alloy Nb<sub>55</sub>Ta<sub>45</sub> already has a very small mean free path  $l^*$ . Hence, the additional defects can hardly change  $\kappa$  and also  $B_{c2}$  (see [Section 4.7.1](#)) any more. If we assume that the vortices are more or less strongly pinned within the deformed material, we can easily understand this magnetization curve qualitatively. We look at the curve starting at field zero. Up to the external field  $B_{c1}$  there is no difference. The sample resides in the Meissner phase, which is hardly influenced by perturbations.<sup>[15](#)</sup>

If  $B_{c1}$  is exceeded, vortices enter the sample at the surface. At first, these vortices are attached to their locations immediately below the surface, and they cannot distribute themselves equally over the volume as in a homogeneous material. However, within the surface layer, where the pinned vortices are, shielding currents can also flow. As a result, the total shielding current, determining the diamagnetic behavior, extends further into the superconductor than in the Meissner phase, where it is restricted only to a layer with the thickness of the penetration depth. As a result, the shielding current and, hence, the diamagnetic signal in the vortex state can exceed those in the Meissner phase.

At  $B_{c2}$  the Cooper pair density is zero, and the superconductivity disappears.<sup>[16](#)</sup> The magnetic field homogeneously penetrates the superconductor. If the external field is decreased below  $B_{c2}$ , the sample again enters the Shubnikov phase. Again the magnetic flux is divided into multiples of the flux quantum  $\Phi_0$ , and the vortices are more or less strongly pinned to the perturbations in the crystal lattice. Hence, with decreasing external field they can leave the material only with difficulty. The field within the sample then becomes larger than the external field, and the magnetization of the sample becomes positive. Even at  $B_a = 0$  there remains a finite magnetic flux along the field direction trapped within the sample.<sup>[17](#)</sup>

As a second example, in [Figure 5.12](#) we show the magnetization curve of a lead–bismuth alloy containing 53 at% Bi [26]. At low fields we see abrupt changes of the magnetization, which are due to so-called flux jumps. In this case large flux-line bundles or regions of the vortex lattice tear off the pinning sites and thereby result in a jump of the magnetization toward thermodynamic equilibrium. In superconducting magnets such flux jumps are very dangerous, since, because of the generated heat energy, the superconductor can become normal conducting over its whole cross-section (see [Section 7.1.2](#)) and the magnetic field can break down.

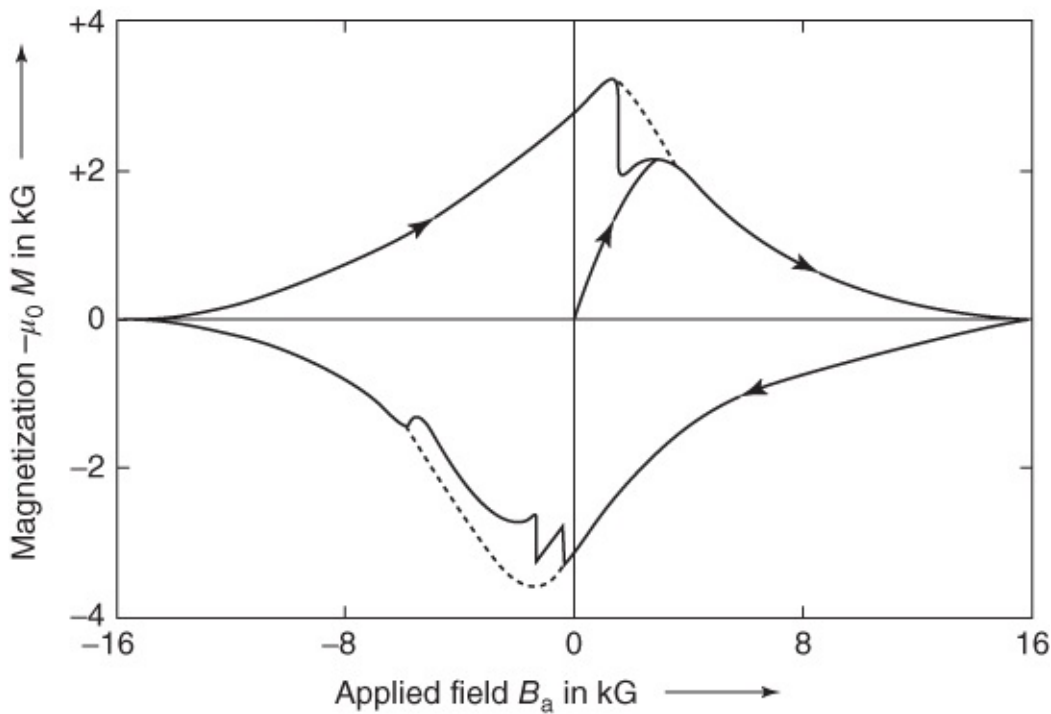


**Figure 5.12** Complete magnetization cycle of a Pb–Bi alloy (53 at% Bi). The dashed curve is expected if there are no flux jumps

(from [26]) (1 kG = 0.1 T).

Flux jumps can look spectacular and can develop into avalanches. In [Figure 5.13](#) we show an example in the case of an MgB<sub>2</sub> thin film [27]. The image was obtained by magneto-optics (see [Figure 1.10b](#)). The branching bright regions represent the locations where magnetic flux has penetrated into the sample. This is also referred to as ***dendritic flux avalanches***.

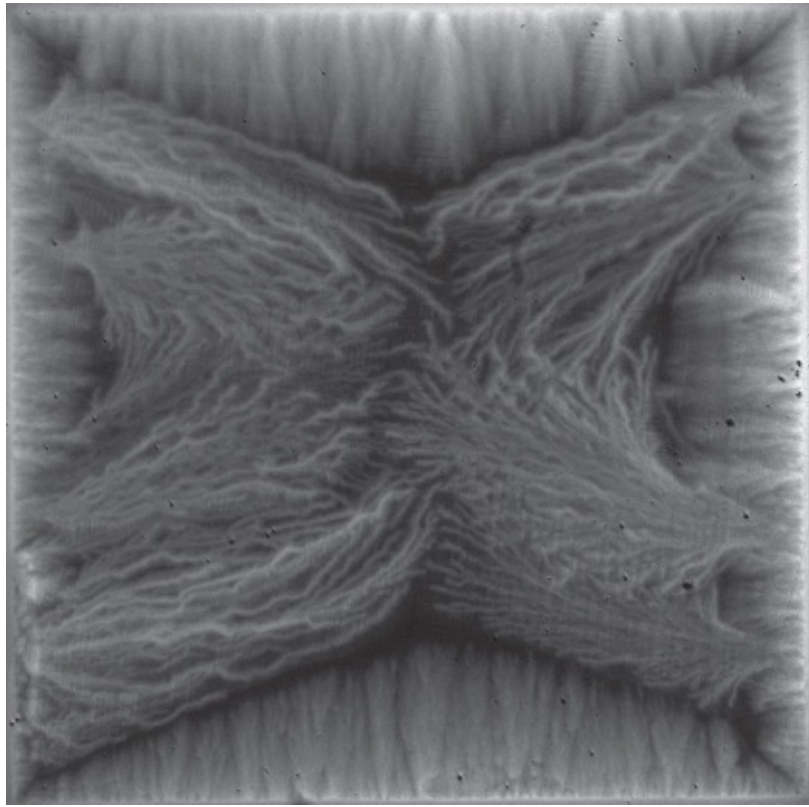


**Figure 5.13** Dendritic flux avalanches, which have penetrated into an MgB<sub>2</sub> thin film. Sample area:  $5 \times 5 \text{ mm}^2$ , film thickness: 200 nm. The magnetic field (8 mT) was applied perpendicular to the thin film. Temperature: 10 K.

(Courtesy by J. Albrecht, College Aalen.)

In high-temperature superconductors the situation is still more complicated, since a number of different vortex phases can exist even in the absence of pinning centers, as we have discussed in [Section 4.7.2](#) (see [Figures 4.33–4.38](#)). The pinning centers act differently in the different phases. Different glassy states can develop, like the amorphous vortex glass [28] or the “Bragg glass” [29]. In the latter case, at small distances the vortices are somewhat disordered. However, at large distances the vortices again approach a vortex lattice because of the interactions between them. Another example is the “Bose glass” appearing in the presence of columnar defects along a certain direction [30]. This is illustrated in [Figure 5.14](#) based on a phase diagram calculated for cuprates in magnetic fields oriented perpendicular to the layer structure [31]. Here the vortices were treated as continuous lines, that is, additional degrees of freedom due to the pancake vortices were ignored.

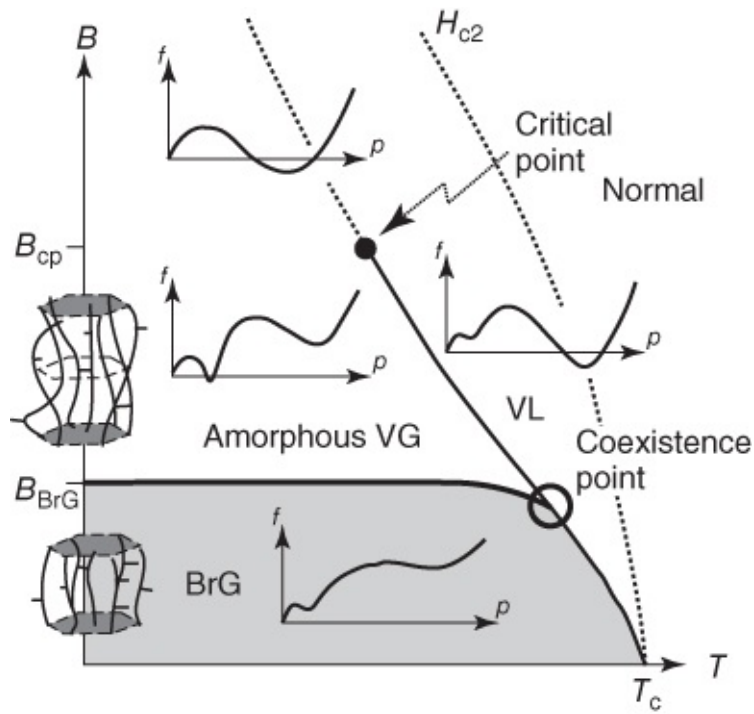


**Figure 5.14** Glass-like vortex phases in the cuprates in the presence of pinning centers [31]. BrG, Bragg glass; VG, vortex glass; VL, vortex liquid. The small insets indicate how the Gibbs energy in the corresponding phases changes as a function of the dislocation density in the vortex lattice.

In the magnetization curve, the transition between two vortex phases sometimes shows up as a maximum, which is also referred to as a **second peak** or as a **fishtail**. This is shown in [Figure 5.15](#) based on a measurement for a  $\text{YBa}_2\text{Cu}_3\text{O}_{7-\delta}$  single crystal [32]. This effect can also be well observed in  $\text{Bi}_2\text{Sr}_2\text{CaCu}_2\text{O}_8$  [33]. During the transition between the Bragg glass and the vortex glass observed here, the elastic constants of the vortex ensemble decrease, so that the vortices can adjust themselves better to the pinning centers in the material.

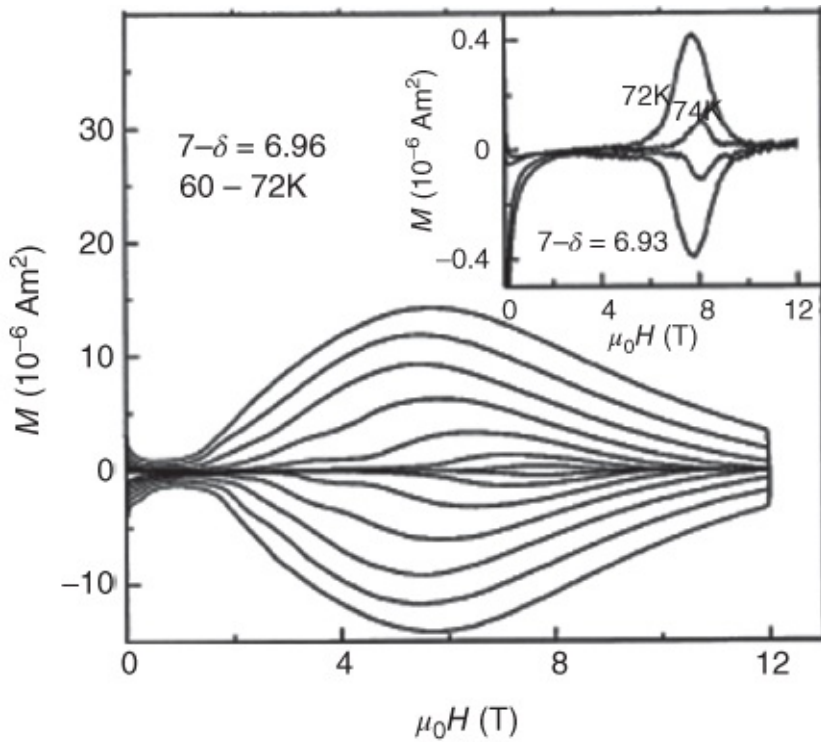


**Figure 5.15** Magnetization curve of a  $\text{YBa}_2\text{Cu}_3\text{O}_{7-\delta}$  single crystal at temperatures between 60 and 72 K. At fields above 4 T, we note a second peak [32].

As a last example of the interaction between vortices and pinning centers, in [Figure 5.16](#) we show the magnetization curve of a PbGe film, in which microholes (antidots) with a separation of 1  $\mu\text{m}$  were fabricated [34]. If a magnetic field is applied to this film, there are certain field values at which the number of vortices in the film is an integer multiple of the number of antidots. At these matching fields the vortices are distributed regularly onto the antidots. It is also possible that more than one vortex can be trapped within one antidot. In [Figure 5.15](#) in the diagram on the left the matching-field values are indicated by vertical lines. At the matching fields the vortex lattice is particularly strongly pinned.<sup>18</sup> For comparison, [Figure 5.15](#) also shows the magnetization curve of a PbGe film without antidots. In this case the magnetization curve strongly decreases already at small fields.

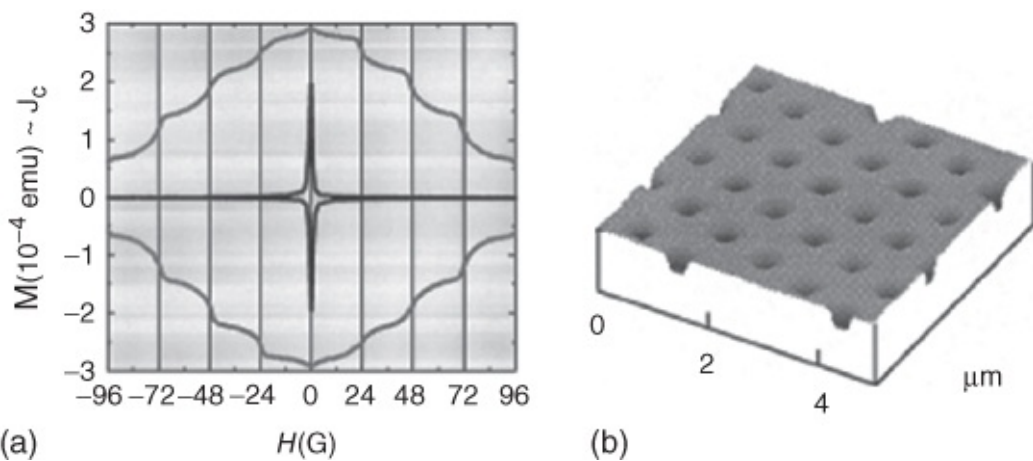


**Figure 5.16** Magnetization curve of a PbGe film (a) in which a regular lattice of microholes was fabricated (b). The magnetization (being proportional to the critical current density in the film) shows a very large hysteresis. Distinct maxima appear at the magnetic field values at which the number of vortices is an integer multiple of the number of microholes. For comparison, the magnetization curve of a PbGe film without antidots is also shown. In the latter case, the magnetization strongly decreases already at small fields. Measuring temperature: 6 K.

(Reprinted from [34] by permission of Elsevier.)

The possibility of fabricating pinning centers in thin films allows the investigation of specific models of the interaction between vortices and pinning centers. This is interesting for both the fundamental physics and technical applications. For example, in SQUID magnetometers, antidots can be placed strategically in such a way that the perturbing signals due to the vortex motion are minimized [35].

Next we want to discuss the origin of the hysteresis in the magnetization curve more quantitatively and look at the connection between the magnetization and the maximum possible supercurrent in the sample. Frequently, the direct measurement of the maximum supercurrent is difficult, since currents of 100 A or higher must be measured. Hence, it is advantageous to have a procedure for measuring the critical current without electrical contacts. This method turns out to be particularly important for the study of sintered materials, which mostly are not available in the form of wires or sheets and, hence, cannot be investigated with the standard methods.

In this context Bean [36] has proposed a model, which we want to discuss in the following in a slightly simplified version. We consider a simple geometry, namely a long, hollow cylinder (length  $L$ , diameter  $2R$ , wall thickness  $d \ll R$ ). If a circulating current  $I$  flows within this cylinder, it generates a magnetic field  $B_i = \mu_0 I/L$ , which can also be written in terms of the average current density  $j = I/(Ld)$  as  $B_i = \mu_0 j d$ .

The cylinder is assumed to be cooled in zero applied magnetic field. Upon the application of the field  $B_a$  parallel to the cylinder axis, at the outside of the superconducting cylinder a circulating current is generated shielding the interior of the cylinder (Figure 5.17). As long as the hard superconductor resides in the Meissner phase, the shielding current only flows within

the penetration depth near the surface of the cylinder. If  $B_a$  exceeds the value  $B_{c1}$ , which we can assume to be very small, magnetic flux can penetrate into the superconductor in the form of vortices. Initially, the vortices are trapped by the pinning centers below the surface. In this case, the Bean model simply assumes that the critical transport current within the region of the superconductor penetrated by the vortices just has the homogeneous critical current density  $j_c$ . For simplicity, this current density is taken as constant, that is, it is assumed to be independent of the magnetic field in the superconductor. This state carrying the critical current density is referred to as the ***critical state***.

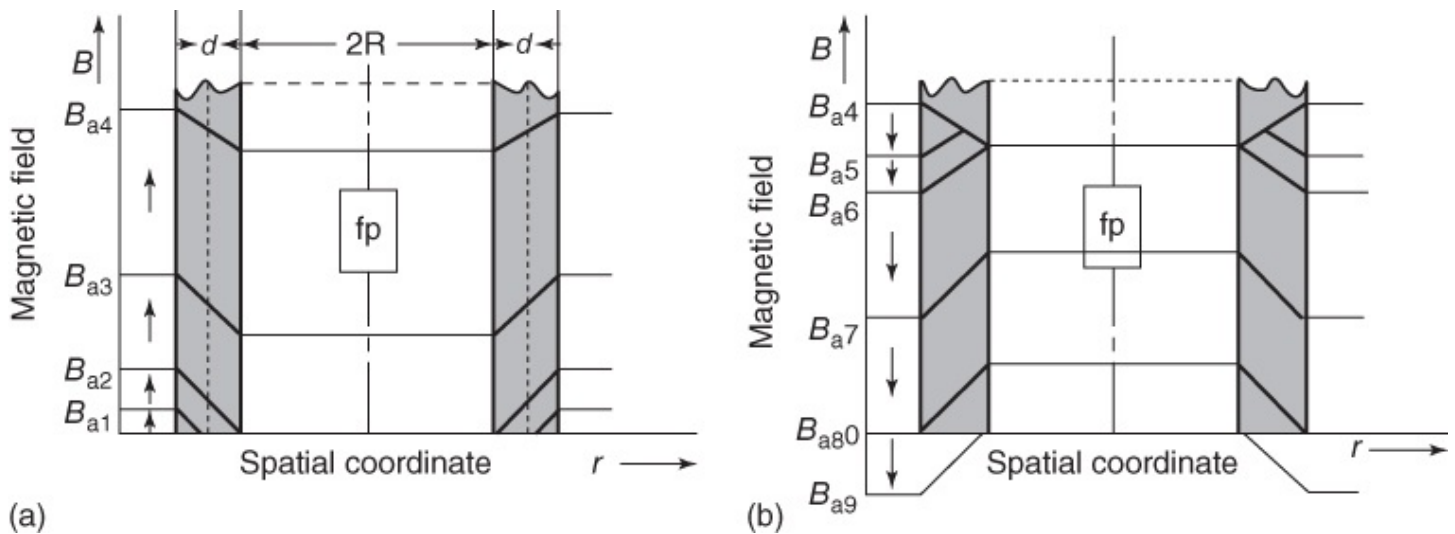


**Figure 5.17** Magnetic field distribution in a hollow cylinder of a hard superconductor for increasing (left) and decreasing (right) applied magnetic fields. At  $B_{a4}$  the decrease in  $j_c$  with increasing  $B$  is indicated by a less steep field slope [36]. fp = field probe.

If the field  $B_a$  is increased further beyond the value  $B_{c1}$ , a thicker and thicker layer below the cylinder surface is filled with vortices. The total shielding current increases proportional to the thickness of this layer which, according to our assumption, carries the constant current density  $j_c$ .<sup>19</sup> The critical state grows into the superconductor. Because of the shielding current, the magnetic field within the superconductor decreases toward the cylinder axis. If the radius  $R$  is large compared to the thickness  $d$  of the cylinder wall, we can well approximate the latter in terms of a planar layer. In this case, the magnetic field decreases linearly toward the axis.<sup>20</sup> In Figure 5.17a this field variation is indicated for different values of the external field. At  $B_{a1}$  only part of the cylinder wall is filled with vortices (dashed lines, part a). At  $B_{a2}$  the shielding current has reached its maximum value, since now the current density  $j_c$  flows homogeneously in the whole cylinder wall. However, in the interior of the cylinder, the field  $B_i$  still remains zero. Only during a further increase in  $B_a$  does a magnetic field also appear in the interior. In our simple model this field is equal to  $B_a - B_{a2}$  (with  $B_a > B_{a2}$ ).

Of course, for large fields our assumption  $j_c = \text{constant}$  cannot be valid anymore, since  $j_c$  must approach zero for  $B_a \rightarrow B_{c2}$ . So we must improve our model by requiring that  $j_c$  decreases

with increasing  $B_a$ . In this case with increasing field  $B_a$ , the difference  $B_a - B_i$  gradually approaches zero.

In [Figure 5.18](#) the field  $B_i$  in the interior of the cylinder is plotted versus the external field  $B_a$  for a  $V_3(Ga_{0.54}Al_{0.46})$  sample (high-field superconductor). Up to the value  $B_{a2}$  the field  $B_i$  remains zero. In this case, with  $j_c = \text{constant}$ , we would always have  $B_i = B_a - B_{a2}$  (dashed line). However, since  $j_c$  decreases with increasing field, the curve  $B_i(B_a)$  more and more approaches the straight line  $B_i = B_a$ . From the behavior of  $B_i(B_a)$ , or from the magnetization curve  $M(B_a) = (B_i - B_a)/\mu_0$ , within our model (which assumes the existence of a critical state) we can determine the critical current density of the material investigated. Frequently, this elegant method is applied in the study of novel superconductors. In the case of a long hollow cylinder, one obtains

$$|M(B_a)| = j_c(B_a)d \quad 5.19$$

where  $d$  is the wall thickness of the hollow cylinder. Analogously, for a solid cylinder with diameter  $2R$  one finds the magnetization  $|M| = j_c R/3$  (from, e.g., [M4]).

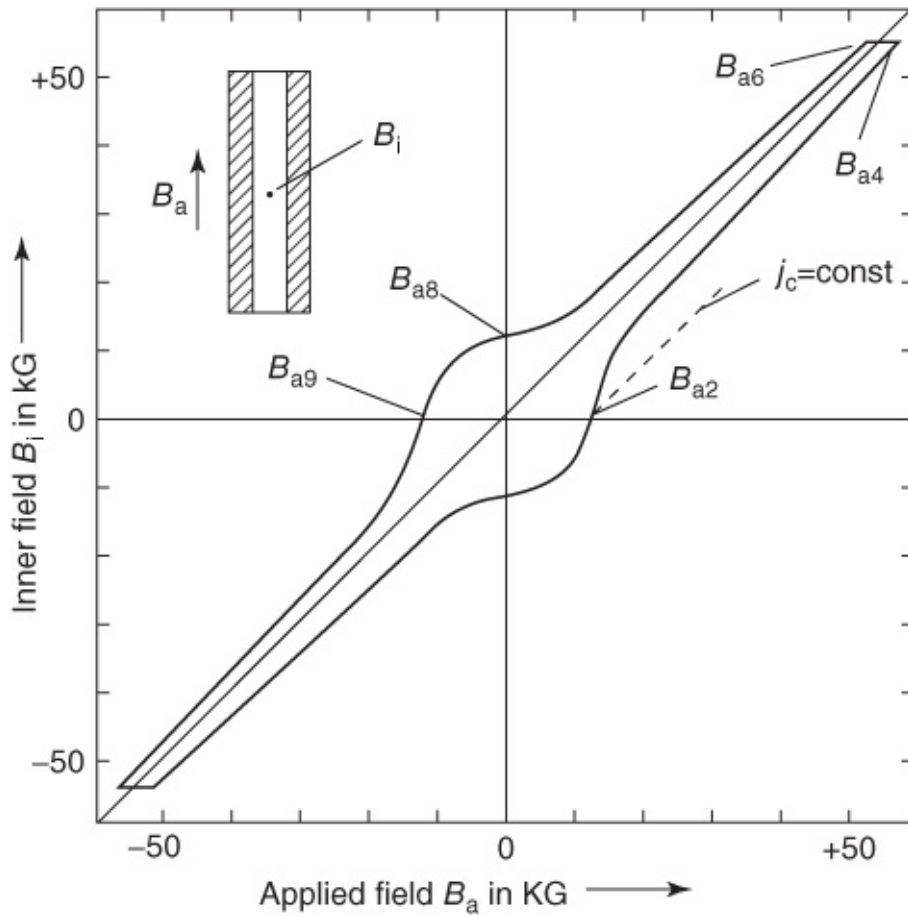


[Figure 5.18](#) Magnetic shielding of a hollow cylinder made from  $V_3(Ga_{0.54}Al_{0.46})$ . Inner field  $B_i$  plotted versus the external field  $B_a$  ( $1 \text{ kG} = 0.1 \text{ T}$ ). Measuring temperature: 4.2 K; transition temperature: 12.2 K.

(By courtesy of Dr H. Voigt, Siemens.)

We want to also discuss the case where the external field is lowered starting, say, from  $B_{a4}$ . Now, because of the negative field change ( $\Delta B < 0$ ), an induction process takes place, which slows down the shielding current flowing at the outer part of the cylinder and generates a critical current in the opposite direction. In [Figure 5.17b](#) the magnetic field variation is indicated for a few sequential values  $B_{a5}$  up to  $B_{a7}$ . Again a critical state exists in the whole cylinder. However, now the vortex density increases toward the interior. In this case the vortices appear to exit from the outer cylinder wall. Up to the value  $B_{a6}$  the field  $B_i$  remains constant. Then  $B_i$  decreases. At  $B_a = 0$  a certain magnetic flux and, hence, a field  $B_i$  is trapped. The corresponding points are indicated in [Figure 5.18](#).

If in the next step we increase the external field in the opposite direction, then at  $-B_{a9} = B_{a2}$  we just obtain the field  $B_i = 0$ . This can clearly be seen from [Figure 5.17b](#). In [Figure 5.18](#) we show the corresponding variation of  $B_i$  together with the complete hysteresis loop traversed in such an experiment. In many hard superconductors, this dependence is well described by the expression [37]

$$j_c = \frac{\alpha_c}{B + B_0} \quad 5.20$$

Here, the constants  $\alpha_c$  and  $B_0$  are characteristic for the particular material.

In samples with a more complicated shape, for example, in thin films or irregularly shaped crystals, and also in materials with an inhomogeneous structure, the penetration of magnetic flux can occur in a highly complicated way. However, in this case techniques such as magneto-optics provide the possibility to measure the spatially resolved magnetization and to derive from this the supercurrent density in the material. Here, we do not want to discuss the details and, instead, refer to the review articles [38, 39].

If, like during the measurement of the magnetization curve, the magnetic field  $B_a$  is changed, within a hard superconductor an inhomogeneous distribution of vortices develops, which by no means corresponds to thermodynamic equilibrium. Now we want to investigate what happens if the magnetic field is raised to a certain value and then is kept constant at this value. In this case we will deal with the phenomenon of flux creep.

In the critical state all locations at which magnetic flux has penetrated into the sample carry the critical current density  $j_c$ , which in turn acts with the Lorentz force on the vortices. If the applied field is kept at the value  $B_a$ , the Lorentz force is exactly compensated by the force originating from the pinning centers. Therefore, without thermal fluctuations, the vortex distribution would remain unchanged. However, because of thermal fluctuations, the energy needed to leave a pinning site can be supplied to a vortex. In this case, under the influence of the Lorentz force, the vortex will move a short distance until it is trapped again at another pinning center. Eventually, all vortices will move in this way, such that the magnetization gradually decreases and a state with lower energy is established. During this process the supercurrent density quickly falls below its critical value. This thermally activated vortex

motion is referred to as ***flux creep***.

If the supercurrent density is not too close to the critical current density, the velocity of the vortex motion will be proportional to  $\exp(-\Delta E/k_B T)$ . In general, one can show that the temporal change is then given by  $dj/dt = -j_c \exp(-\Delta E/k_B T)/t_0$ . Here,  $t_0$  denotes a characteristic time constant that depends on the material parameters. However, the height  $\Delta E$  of the energy barrier in turn depends on the supercurrent density. It must vanish when the critical current is reached, since in this case the vortices are torn off from the pinning centers. Near the critical state this behavior can be expressed by the relation

$$\Delta E(j \rightarrow j_c) \approx E_c(1 - j/j_c)^\alpha \quad 5.21$$

with a certain exponent  $\alpha$ . In the case  $\alpha = 1$ , this just leads to a reduction of the supercurrent density or of the magnetization, which is logarithmic initially:

$$|M(t)| \propto j(t) \approx j_c \left[ 1 - \frac{k_B T}{E_c} \ln(1 + t/t_0) \right] \quad 5.22$$

In [Figure 5.19](#) we show the temporal decay of the magnetization of some superconductors [40]. This decay occurs by means of flux creep. In NbTi, a classical superconductor, at about 4.2 K, that is, at about  $T_c/2$ , within more than  $10^5$  s (slightly more than 1 day) hardly any change is observed. On the other hand, in  $\text{YBa}_2\text{Cu}_3\text{O}_7$  the supercurrents clearly decrease, particularly in the single-crystalline sample. The data shown here are from the year 1990, that is, from the early period of high-temperature superconductivity. In the meantime, also  $\text{YBa}_2\text{Cu}_3\text{O}_7$  samples have been prepared in such a way that well above 15 T they can trap magnetic fields for a long time. We will discuss this subject in more detail in [Section 7.2](#).

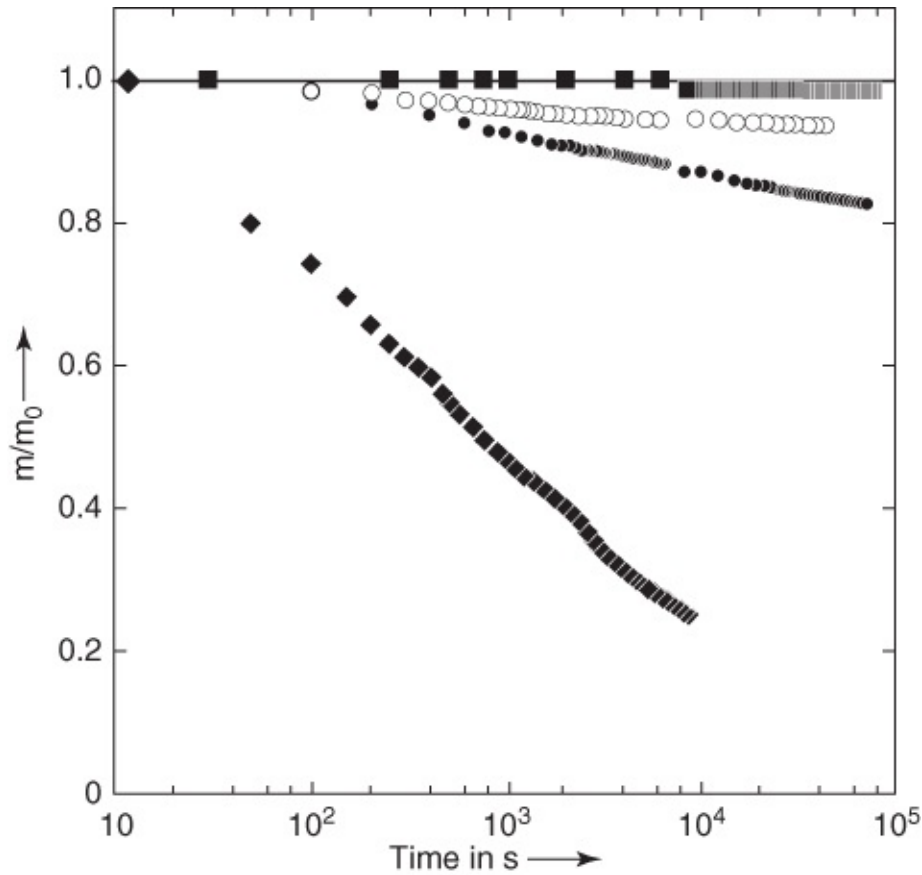


**Figure 5.19** Temporal decay of the magnetization of different superconductors. The magnetization is normalized to its value  $m_0$  observed 10 s after the supercurrents were turned on [40]. ▀ NbTi at 4.2 K; ○, •  $\text{YBa}_2\text{Cu}_3\text{O}_7$  with oriented grains at 77 K; □  $\text{YBa}_2\text{Cu}_3\text{O}_7$  single crystal at 60 K.

In the high-temperature superconductors, we must note that the different vortex phases can behave much differently. In particular, in the region of the vortex liquid one observes no or at most only a weak pinning force. In this case the magnetization curves are reversible. Therefore, the phase boundary line at the transition between the vortex liquid and the crystalline or glass-like vortex phases is referred to as the *irreversibility line*.

### 5.3.2.3 Critical Currents and Current–Voltage Characteristics

Next we want to discuss the effect of the pinning centers during current transport in superconducting wires or thin films. In [Section 5.3.1](#) we saw that an ideal type-II superconductor in the Shubnikov phase cannot carry a current perpendicular to the direction of the magnetic field without dissipation, since due to the influence of the Lorentz force the vortices start moving, resulting in dissipative processes. However, in a *real* superconductor, the vortices are never completely freely mobile. There is always a perhaps very small force necessary in order to tear the vortices off the pinning centers that are practically always present. The strength of the pinning forces acting on the individual vortices will have a certain distribution about an average value  $F_H$ . Also the whole vortex lattice will affect the pinning forces due to collective effects. However, for simplicity we will only speak of a single pinning

force  $F_H$ .

As long as the Lorentz force  $F_L$  is smaller than the pinning force  $F_H$ , the vortices cannot move. Therefore, also in every real type-II superconductor in the Shubnikov phase, we will be able to observe current flow without dissipation. If the transport current exceeds its critical value at which  $F_L = F_H$ , the vortex motion sets in, and electrical resistance appears.<sup>21</sup> We see that the critical current is a measure of the force  $F_H$  with which the vortices are pinned at energetically favored locations.

In [Figure 5.20](#) we show the current–voltage characteristics of two samples of an  $\text{Nb}_{50}\text{Ta}_{50}$  alloy with a different amount of internal disorder [41]. Both samples were cooled in the magnetic field and were measured in the Shubnikov phase. For the more strongly disordered sample 2, no electrical voltage is observed up to a transport current  $I_{c2}$  of about 1.2 A.<sup>22</sup> On the other hand, the less perturbed sample 1 shows a voltage and, hence, resistance already at about 0.2 A. The currents  $I_{c1}$  and  $I_{c2}$ , respectively, are referred to as the ***critical currents*** of both samples. An ideal sample of the same material, that is, a completely homogeneous sample, for the same conditions would display a current–voltage characteristic indicated by the dashed line.

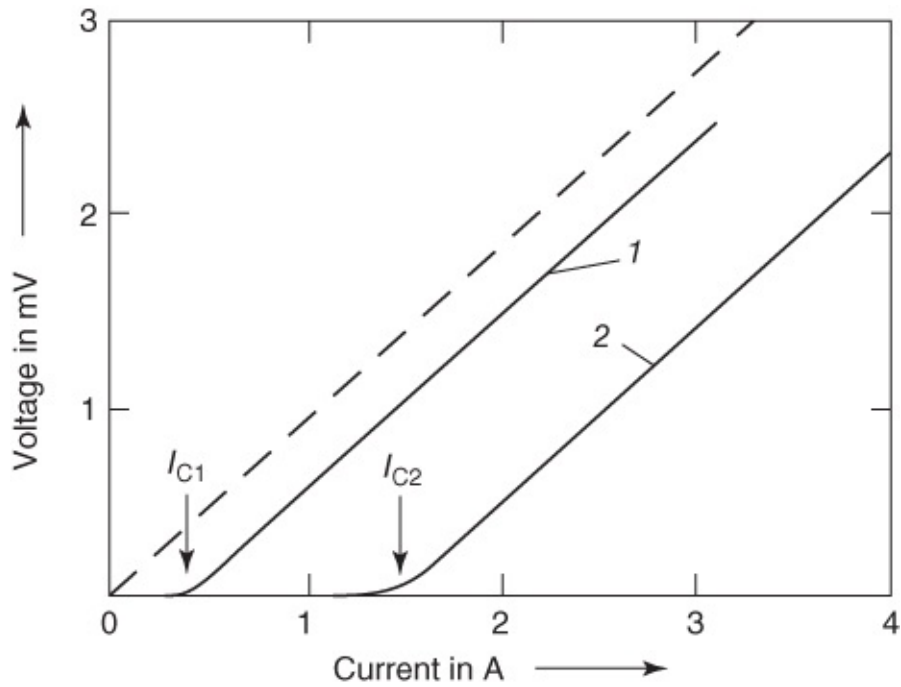


[Figure 5.20](#) Current–voltage characteristics of an  $\text{Nb}_{50}\text{Ta}_{50}$  alloy in the Shubnikov phase.  $T = 3.0$  K; external field  $B_a = 0.2$  T;  $T_c$  in zero field: 6.25 K.

(From [41].)

In hard superconductors, the pinning forces must be made particularly high in order to allow the highest possible transport currents to flow without resistance. Before we discuss a few examples of hard superconductors, we want to look at the linear part of the characteristics in [Figure 5.20](#). Also in this part of the characteristic, the voltage along the superconductor is

generated by vortex motion. The resulting differential resistance  $dU/dI = R_{\text{fl}}$ , the flux-flow resistance, clearly has the same value in both samples, that is, it is independent of the pinning centers acting on the vortices.

This observation can be understood in the following way: If the vortices are removed from the pinning centers, they move through the material under the influence of the force difference  $F^* = \mathbf{F}_L - \mathbf{F}_H$ . Because of the dissipative processes during the motion, resulting in a kind of “friction” for the vortex in the superconductor, a flux-flow velocity  $v$  develops, which is proportional to  $F^*$ . We have

$$v \propto F^* \propto (I - I_c) \quad 5.23$$

On the other hand, the electrical voltage  $U$  is proportional to  $v$ , that is, one finds

$$U \propto v \propto I - I_c \quad 5.24$$

and hence

$$dU/dI = \text{const.} \quad 5.25$$

The equal values of  $dU/dI$  for samples with different amounts of imperfections ([Figure 5.20](#)) indicate clearly that the pinning centers do not affect the relation between  $F^*$  and  $v$ . Independent of the nature of the pinning centers, the same value of  $F^*$  yields the same velocity  $v$  and, hence, the same voltage  $U$ . The characteristics are only shifted parallel to each other along the current axis.

According to these arguments, we have two components of the energy dissipation  $UI$ , namely  $UI_c$  and  $U(I - I_c)$ . We start with the component  $UI_c$ . The vortices move through the material under the influence of the Lorentz force due to a transport current. This means that they must pass through a number of potential wells. To raise a vortex out of a well costs energy. One could imagine that this energy is recovered when the vortex falls into the next (equally deep) well. In this case, there would be no net energy dissipation during vortex motion across the potential wells. However, there is the crucial fact that during their motion across the pinning centers the vortices are always elastically deformed [[42], M17]. These deformations lead to the energy losses described by the component  $UI_c$ .

Next we turn to the component  $U(I - I_c)$  of the dissipated power determining the vortex velocity according to Eq. ([5.23](#)). The most important energy losses during the vortex motion are caused by the appearance of local electric fields acting on the unpaired electrons. This means that the flux-flow resistance depends on the normal resistance of the material. One finds that  $R_{\text{fl}}$  is proportional to  $R_n$ .<sup>23</sup> Furthermore, the same dissipative effects appear at each vortex. Therefore, the dynamic (flux-flow) resistance is proportional to the vortex density. This density increases with increasing external field  $B_a$ . With increasing magnetic field, the  $U - I$  characteristics become steeper. This dependence of the flux-flow resistance on the external field is shown in [Figure 5.21](#) for a lead–indium alloy (Pb + 17 at% In) [41].

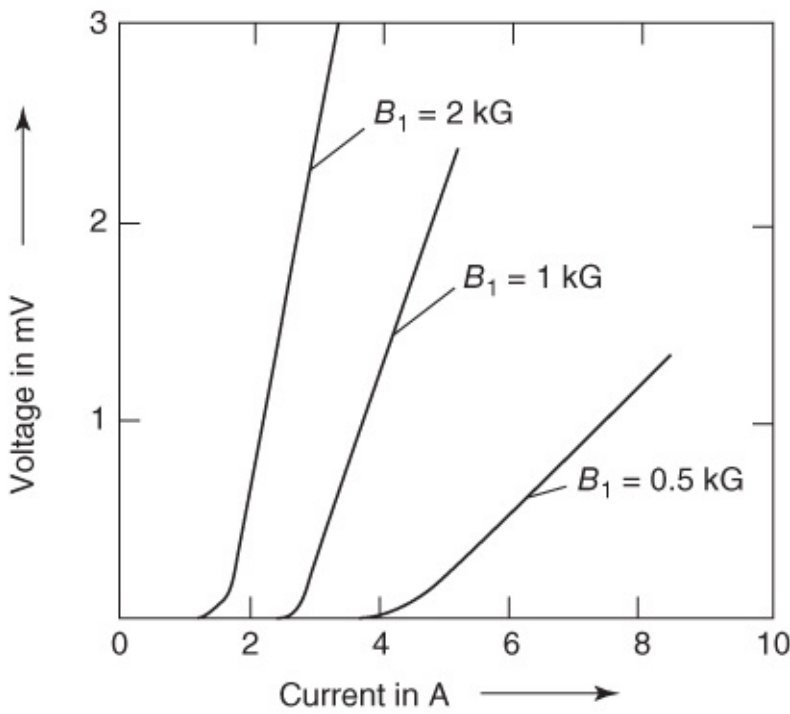


**Figure 5.21** Current–voltage characteristics of a Pb–In alloy in the Shubnikov phase. Material: Pb + 17 at% In;  $T = 2.0$  K; transition temperature in zero field: about 7.1 K.

(From [41].)

With increasing magnetic field, the critical current  $I_c$  decreases. This decrease can be caused in different ways. For increasing vortex density, not all vortices can experience the same pinning force. Hence, the average pinning force becomes smaller. On the other hand, for one and the same pinning center, with increasing external field, the pinning force decreases and approaches zero for  $B_a \rightarrow B_{c2}$ . The behavior of the critical current for increasing external field will be seen particularly clearly in a plot of the field dependence of  $I_c$  (see Figures 5.22 and 5.23).<sup>24</sup>

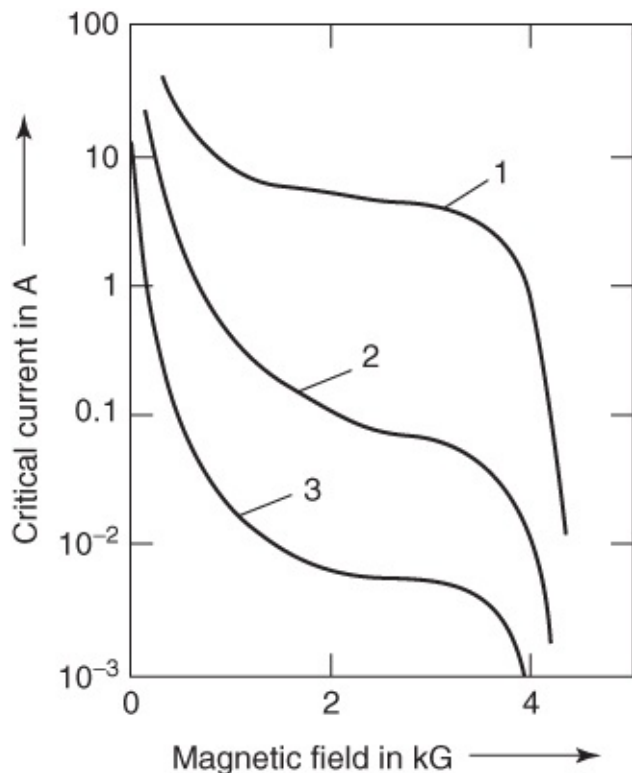


**Figure 5.22** Critical current of an  $\text{Nb}_{55}\text{Ta}_{45}$  alloy in an external magnetic field ( $1 \text{ kG} = 0.1 \text{ T}$ ) oriented perpendicular to the current. Wire diameter: 0.38 mm; measuring temperature: 4.2 K. Curve 1, immediately after cold working; curve 2, after 24 h at 1800 K; curve 3, after 48 h at 1800 K.

(From [23].)

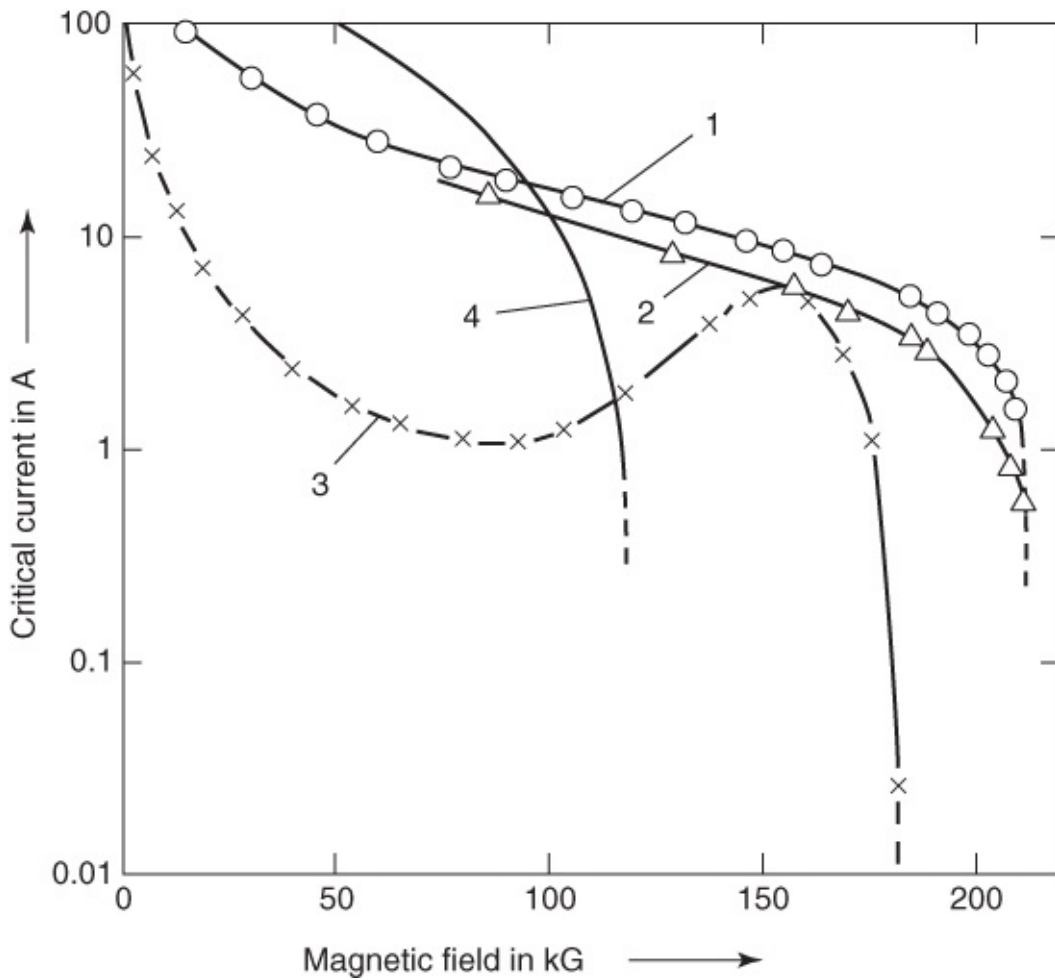


**Figure 5.23** Critical currents of thin wires of metallic high-field superconductors (1 kG = 0.1 T). Measuring temperature: 4.2 K. Curve 1: V<sub>3</sub>Si; curve 2: Nb<sub>3</sub>Sn; curve 3: V<sub>3</sub>Ga. Wire diameter of all three samples: 0.5 mm. In each case the compound exists only within a surface layer obtained by diffusion of the second component into the base material Nb or V. Curve 4, Nb–Ti; wire diameter 0.15 mm.

(From [43, 44].)

In our discussion of [Figure 5.20](#) we have already seen that the critical current  $I_c$  depends on the degree of disorder within the sample. This internal disorder

can be caused, for example, by plastic deformation. If a metal wire (such as Cu) is pulled through a die at room temperature to reduce the cross-section, many imperfections, that is, regions in which the periodic structure of the metallic lattice is strongly perturbed, are generated within the wire. Grain boundaries (i.e., transition regions between individual grains), for example, are such regions. If subsequently the metal is heated, these disordered regions gradually can be annealed out and can be transformed more and more into well-ordered regions.

If the disordered regions act as pinning sites for the vortices, a plastically deformed superconductor is expected to display a particularly high value of the critical current immediately after deformation. During heating, along with the gradual removal of the

disordered regions, the critical current should also decrease.

In [Figure 5.22](#) we clearly see this effect [23]. For an  $\text{Nb}_{55}\text{Ta}_{45}$  alloy the critical current is plotted versus the external magnetic field oriented perpendicular to the current for different degrees of disorder. Immediately after the mechanical pulling process, that is, in a state with a high degree of disorder, the critical current in the Shubnikov phase is large.<sup>25</sup> During the removal of the perturbations by means of annealing, the pinning centers disappear more and more. The critical current strongly decreases as expected. In [Figure 5.11](#) the corresponding magnetization curves are shown for the same alloy. In this case, the pinning centers lead to strong irreversibilities of the magnetization curve.

In [Figure 5.23](#) we show the values of the critical current of wires of a few metallic high-field superconductors. Since the critical current is strongly influenced by the previous treatment of the sample because of its dependence on the degree of disorder, as we have discussed, the data of [Figure 5.23](#) can serve only as a rough indication. The curves are chosen arbitrarily from a large number of examples. However, they show that suitably prepared hard superconductors, with a wire diameter of only 0.5 mm and for external fields above 10 T, can carry supercurrents of more than 10 up to 100 A without dissipation. Wires containing many thin filaments, so-called multifilamentary wires, can even carry still much higher currents. Of course, such superconductors are highly important for the construction of superconducting magnets (see [Section 7.1](#)).

In [Figure 5.23](#) we show a curve ( $\text{V}_3\text{Ga}$ ) having a maximum of the critical current near  $B_{c2}$  (the so-called peak effect, see also [Figure 5.15](#)). Apparently, with increasing external field, conditions can develop leading to a more effective pinning of the vortices. In this case the elastic properties of the vortex lattice are essential [M17]. The lattice becomes more elastic, and the vortices can adjust themselves better to the configuration of the pinning sites. Furthermore, near  $B_{c2}$  also normal conducting regions can appear, which act as additional pinning centers and cause an increase in the critical current.

By means of a systematic study of hard superconductors, it has been possible empirically to develop quite useful materials. However, the detailed dependence of the critical current on the defect structures is still by no means completely clarified.

This is even more valid for the high-temperature superconductors [45]. In this case the initial measurements of the critical currents in polycrystalline, sintered samples yielded disappointingly small values of the critical current density. At 77 K, the boiling point of liquid nitrogen, even in zero applied magnetic field, frequently the critical current density was found to be less than  $10^3 \text{ A/cm}^2$ . However, it soon became clear that to a large extent the critical current was limited by grain boundaries. In this case, the critical current of a grain boundary strongly decreases with increasing relative tilt angle between the crystal axes in the two grains. This could be demonstrated by transport measurements in thin films of  $\text{YBa}_2\text{Cu}_3\text{O}_7$  deposited onto  $\text{SrTiO}_3$  bicrystal substrates<sup>26</sup> [47].

In 2010 the details of current limitation by means of grain boundaries could be explained

theoretically [48]. Apparently, the dominating mechanism of the critical-current reduction is due to the fact that near the dislocation lines the grain boundary is electrically charged. Many additional properties of current transport across grain boundaries are summarized in the review articles [49, 50].

An additional limitation of the critical current results from the layered structure of the cuprates. Along the  $\text{CuO}_2$  planes a high value of the critical current is observed, whereas perpendicular to the planes the value is very small, and in some cases it is limited by the Josephson effect (see [Figure 1.22f](#)). Also in the case of current flow parallel to the  $\text{CuO}_2$  planes it is important, how the external magnetic field is oriented relative to the crystal structure. This effect is shown in [Figure 5.24](#) for the example of a  $\text{YBa}_2\text{Cu}_3\text{O}_7$  thin film [51]. The film was prepared by means of laser ablation. In the figure the critical current density in the case of current flow along the  $\text{CuO}_2$  planes is plotted versus the applied magnetic field for different temperatures. The field was oriented either perpendicular to the  $\text{CuO}_2$  planes (i.e., along the crystallographic  $c$ -direction) or perpendicular to the  $c$ -axis. We see that at 4.2 K critical current densities of several  $10^7 \text{ A/cm}^2$  are reached, and at 77 K still values of several  $10^6 \text{ A/cm}^2$ . As long as the magnetic field is applied parallel to the planes, these values remain also in high fields (in fact, in fields up to far above 20 T) at least at 4.2 K [52]. However, the critical current density decreases rapidly, if the magnetic field is oriented perpendicular to the layered structure. On the other hand, in the meantime (the measurements in [Figure 5.24](#) are from 1990) appreciable improvements could be achieved. Now, for example,  $\text{YBa}_2\text{Cu}_3\text{O}_7$  thin films in a field of 5 T perpendicular to the layers can carry supercurrents of several  $10^5 \text{ A/cm}^2$  also at 77 K [17].

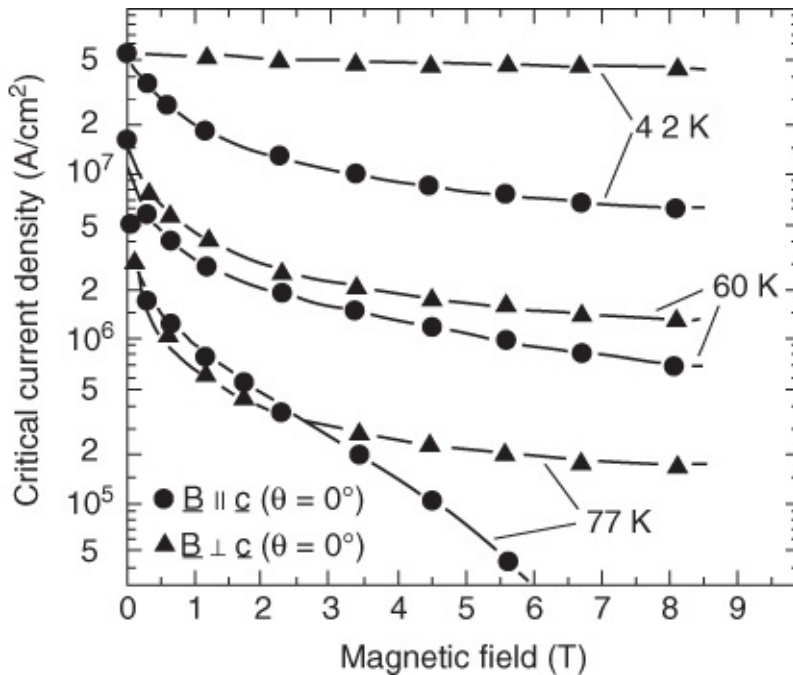


[Figure 5.24](#) Critical current density of a  $\text{YBa}_2\text{Cu}_3\text{O}_7$  thin film for three temperatures plotted versus the applied magnetic field. The field was oriented either perpendicular to the layered structure (i.e., parallel to the crystallographic  $c$ -axis) or parallel to it.

(From [51].)

In general, to achieve a high supercurrent density, in the case of the cuprates it is necessary to avoid grain boundaries, and the transport currents must flow parallel to the layered structure as much as possible. By means of thin-film technology, the corresponding epitaxial film growth can be achieved relatively easily, as long as the substrate size is not too large [53]. However, if one is interested in high-current-carrying wires or tapes fabricated from the cuprates, obviously the material must have a high critical-current value over long lengths. Furthermore, the fabrication technique should be relatively simple and not too expensive. In recent years a number of procedures have been developed, which we will discuss in [Section 7.1.2](#). Enormous progress has also been achieved in the field of massive materials, which are needed, for example, for magnetic levitation or for magnetic energy storage (see [Section 7.2](#)). These developments are by no means finished.

In addition,  $\text{MgB}_2$  and the iron pnictides can become important for the conductor development. On the one hand, the upper critical field can reach very high values. On the other hand, at least in the case of  $\text{MgB}_2$ , grain boundaries practically do not suppress the supercurrent density [54].

We want to conclude our discussion of the critical currents in superconductors with a few general remarks. We have seen that the mechanism of pair breaking results in an intrinsic maximum supercurrent density. However, in cases that are technically relevant, the critical current of a superconductor is determined by *extrinsic* properties. On the one hand, the latter properties in the form of pinning centers in the Shubnikov phase only allow a finite supercurrent, and on the other hand, for example, in the form of grain boundaries in high-temperature superconductors, they represent weak regions in the material, strongly reducing the maximum supercurrent. Whether a new material, say,  $\text{MgB}_2$ , finds interesting technical applications depends on the concrete problems, and often can be answered only after a long development period. In [Chapter 7](#), we will discuss some examples in more detail.

## References

1. F. B. Silsbee: *J. Wash. Acad. Sci.* **6**, 597 (1916).
2. B. K. Mukherjee, J. F. Allen: In: “*Proceeding of the LT 11*”, St. Andrews, p. 827 (1968); B. K. Mukherjee, D. C. Baird: *Phys. Rev. Lett.* **21**, 996 (1968).
3. F. Haensler, L. Rinderer: *Helv. Phys. Acta* **40**, 659 (1967).
4. D. Shoenberg: “*Superconductivity*”, Cambridge University Press, Cambridge (1952).
5. B. R. Scott: *J. Res. Nat. Bur. Stand.* **47**, 581 (1948).
6. L. Rinderer: *Helv. Phys. Acta* **29**, 339 (1956).
7. C. J. Gorter: *Physica* **23**, 45 (1957); C. J. Gorter, M. L. Potters: *Physica* **24**, 169 (1958); B. S. Chandrasekhar, I. J. Dinowitz, D. E. Farrell: *Phys. Lett.* **20**, 321 (1966).

8. G. J. van Gurp: *Phys. Lett.* **24 A**, 528 (1967); P. R. Solomon: *Phys. Rev.* **179**, 475 (1969).
9. H. Meissner: *Phys. Rev.* **97**, 1627 (1955); J. Stark, K. Steiner, H. Schoeneck: *Phys. Z.* **38**, 887 (1937).
10. W. Klose: *Phys. Lett.* **8**, 12 (1964).
11. C. J. Gorter: *Phys. Lett.* **1**, 69 (1962).
12. I. Giaever: *Phys. Rev. Lett.* **15**, 825 (1966).
13. R. Busch, G. Ries, H. Werthner, G. Kreiselmeyer, G. Saemann-Ischenko: *Phys. Rev. Lett.* **69**, 522 (1992); H. Safar, P. L. Gammel, D. A. Huse, S. N. Majumdar, L. F. Schneemeyer, D. J. Bishop, D. López, G. Nieva, F. de la Cruz: *Phys. Rev. Lett.* **72**, 1272 (1994); D. López, E. F. Righi, G. Nieva, F. de la Cruz: *Phys. Rev. Lett.* **76**, 4034 (1996); B. Khaykovich, D. T. Fuchs, K. Teitelbaum, Y. Myasoedov, E. Zeldov, T. Tamegai, S. Ooi, M. Konczykowski, R. A. Doyle, S. F. W. R. Rycroft: *Physica B* **284**, 685 (2000).
14. E. V. Thuneberg, J. Kurkijärvi, D. Rainer: *Phys. Rev. B* **29**, 3913 (1984).
15. M. Tachiki, S. Takahashi: *Solid State Commun.* **70**, 291 (1989).
16. L. Civale, A. D. Marwick, T. K. Worthington, M. A. Kirk, J. R. Thompson, L. Krusin-Elbaum, Y. Sun, J. R. Clem, F. Holtzberg: *Phys. Rev. Lett.* **67**, 648 (1991); M. Konczykowski, F. Rullier-Albenque, E. R. Yacoby, A. Shaulov, Y. Yesurun, P. Lejay: *Phys. Rev. B* **44**, 7167 (1991); W. Gerhäuser, G. Ries, H. W. Neumüller, W. Schmidt, O. Eibl, G. Saemann-Ischenko, S. Klaumünzer: *Phys. Rev. Lett.* **68**, 879 (1992).
17. K. Matsumoto, P. Mele: *Supercond. Sci. Technol.* **23**, 014001 (2010).
18. J. L. Macmanus-Driscoll, S. R. Foltyn, Q. X. Jia, H. Wang, A. Serquis, L. Civale, B. Maiorov, E. Hawley, D. E. Peterson: *Nat. Mater.* **3**, 439 (2004).
19. V. V. Moshchalkov, V. Bruyndoncx, L. Van Look, M. J. Van Bael, Y. Bruynseraede, A. Tonomura: In: “*Handbook of Nanostructured Materials and Nanotechnology*”, Vol. 3, H. S. Nalwa (ed.), Academic Press, San Diego, CA, p. 451 (1999).
20. J. I. Martin, M. Vélez, J. Nogués, I. K. Schuller: *Phys. Rev. Lett.* **79**, 1929 (1997).
21. C. Bean, J. Livingston: *Phys. Rev. Lett.* **12**, 14 (1964).
22. G. Blatter, M. V. Feigel'man, V. B. Geshkenbein, A. I. Larkin, V. M. Vinokur: *Rev. Mod. Phys.* **66**, 1125 (1994).
23. J. W. Heaton, A. C. Rose-Innes: *Cryogenics (G. B.)* **4**, 85 (1965).
24. J. N. Rjabinin, L. V. Shubnikov: *Phys. Z. Sowjetunion* **7**, 122 (1935).
25. K. Mendelssohn: *Proc. R. Soc. London, Ser. A* **152**, 34 (1935).

26. A. Campbell, J. E. Evetts, D. Dew Hughes: *Philos. Mag.* **10**, 333 (1964);J. E. Evetts, A. M. Campbell, D. Dew-Hughes: *Philos. Mag.* **10**, 339 (1964).
27. J. Albrecht, A. T. Matveev, J. Stremper, H.-U. Habermeier, D. V. Shantsev, Y. M. Galperin, T. H. Johansen: *Phys. Rev. Lett.* **98**, 117001 (2007).
28. M. P. A. Fisher: *Phys. Rev. Lett.* **62**, 1415 (1989);A. T. Dorsey, M. Huang, M. P. A. Fisher: *Phys. Rev. B* **45**, 523 (1992).
29. T. Nattermann: *Phys. Rev. Lett.* **64**, 2454 (1990);T. Nattermann, S. Scheidl: *Adv. Phys.* **49**, 607 (2000);S. E. Korshunov: *Phys. Rev. B* **48**, 3969 (1993);T. Giamarchi, P. Le Doussal: *Phys. Rev. Lett.* **72**, 1530 (1994); *Phys. Rev. B* **55**, 6577 (1997).
30. D. R. Nelson, V. M. Vinokur: *Phys. Rev. Lett.* **68**, 2398 (1992); *Phys. Rev. B* **48**, 13060 (1993);U. Täuber, D. R. Nelson: *Phys. Rep.* **289**, 157 (1997).
31. J. Kierfeld, V. M. Vinokur: *Phys. Rev. B* **61**, R14928 (2000).
32. K. Deligannis, P. A. J. de Groot, M. Oussena, S. Pinfold, R. Langan, R. Gagnon, L. Taillefer: *Phys. Rev. Lett.* **79**, 2121 (1997).
33. K. Kadowaki, T. Mochiku: *Physica C* **195**, 127 (1992);N. Chikumoto, M. Konczykowski, N. Motohira, A. P. Malozemov: *Phys. Rev. Lett.* **69**, 1260 (1992);E. Zeldov, D. Majer, M. Konczykowski, A. I. Larkin, V. M. Vinokur, V. B. Geshkenbein, N. Chikumoto, H. Shtrikman: *Europhys. Lett.* **30**, 367 (1995);S. Ooi, T. Shibauchi, K. Itaka, N. Okuda, T. Tamegai: *Phys. Rev. B* **63**, 020501 (2000).
34. V. V. Moshchalkov: *Physica C* **332**, 9 (2000);V. V. Moshchalkov, M. Baert, V. V. Metlushko, E. Rosseel, M. J. Van Bael, K. Temst, R. Jonckheere, Y. Bruynseraeede: *Phys. Rev. B* **54**, 7385 (1996).
35. R. Wördenweber, P. Selders: *Physica C* **366**, 135 (2002).
36. C. P. Bean: *Phys. Rev. Lett.* **8**, 250 (1962);C. P. Bean *Rev. Mod. Phys.* **36**, 31 (1964)
37. Y. B. Kim, C. F. Hempstead, A. R. Strnad: *Phys. Rev.* **129**, 528 (1963).
38. E. H. Brandt: *Rep. Prog. Phys.* **58**, 1465 (1995).
39. Ch. Joos, J. Albrecht, H. Kuhn, S. Leonhardt, H. Kronmüller: *Rep. Prog. Phys.* **65**, 651 (2002).
40. C. Keller, H. Küpfer, R. Meier-Hirmer, U. Wiech, V. Selvamanickam, K. Salama: *Cryogenics* **30**, 410 (1990).
41. A. R. Strnad, C. F. Hempstead, Y. B. Kim: *Phys. Rev. Lett.* **13**, 794 (1964).
42. K. Yamafuji, R. Irie: *Phys. Lett.* **25 A**, 387 (1967).

43. G. Otto, E. Saur, H. Wizgall: *J. Low Temp. Phys.* **1**, 19 (1969).
44. G. Bogner: *Elektrotech. Z.* **89**, 321 (1968).
45. R. Wördenweber: *Rep. Prog. Phys.* **62**, 187 (1999); T. Matsushita: *Supercond. Sci. Technol.* **13**, 730 (2000).
46. P. Chaudhari, R. H. Koch, R. B. Laibowitz, T. R. McGuire, R. J. Gambino: *Phys. Rev. Lett.* **58**, 2684 (1987).
47. D. Dimos, P. Chaudhari, J. Mannhart: *Phys. Rev. B* **41**, 4038 (1990); R. Gross, P. Chaudhari, M. Kawasaki, A. Gupta: *Phys. Rev. B* **42**, 10735 (1990).
48. S. Graser, P. J. Hirschfeld, T. Kopp, R. Gutser, B. M. Andersen, J. Mannhart: *Nat. Phys.* **6**, 609 (2010).
49. H. Hilgenkamp, J. Mannhart: *Rev. Mod. Phys.* **74**, 485 (2002).
50. R. Gross: In: “*Interfaces in High- $T_c$  Superconducting Systems*”, S. L. Shinde, D. A. Rudman (eds.), Springer, New York (1994), p. 176.
51. B. Roas, L. Schultz, G. Saemann-Ischenko: *Phys. Rev. Lett.* **64**, 479 (1990).
52. J. E. Evetts, P. H. Kes: In: “*Concise Encyclopedia of Magnetic and Superconducting Materials*”, J. Evetts (ed.), Pergamon, Oxford, p. 88 (1992).
53. For an overview, see D. G. Schlom, J. Mannhart: In: *Encyclopedia of Materials: Science and Technology*, K. H. J. Buschow, R. W. Cahn, M. C. Flemings, B. Ilschner, E. J. Kramer; S. Mahajan (eds.), Elsevier Science, Amsterdam, p. 3806 (2002); R. Wördenweber: *Supercond. Sci. Technol.* **12**, R86 (1999).
54. D. C. Larbalestier, L. D. Cooley, M. O. Rikel, A. A. Polyanskii, J. Jiang, S. Patnaik, X. Y. Cai, D. M. Feldmann, A. Gurevich, A. A. Squitieri, M. T. Naus, C. B. Eom, E. E. Hellstrom, R. J. Cava, K. A. Regan, N. Rogado, M. A. Hayward, T. He, J. S. Slusky, P. Khalifah, K. Inumaru, M. Haas: *Nature* **410**, 186 (2001).

<sup>1</sup> The calculation can also be performed using a spatially varying  $A_x$ , resulting in a more complicated calculation.

<sup>2</sup> Since Eq. (5.7b) has been obtained from an analysis of the Ginzburg–Landau equations, this expression is valid only near  $T_c$ . From the microscopic BCS theory, one finds that  $j_{c,p}$  is proportional to the energy gap  $\Delta_0$ . However, if the quantities that appear are expressed in terms of  $B_{\text{cth}}$  and  $\lambda_L$ , we obtain again  $j_{c,p} = B_{\text{cth}}/\mu_0\lambda_L$ .

<sup>3</sup> Since the penetration depth is only a few times  $10^{-6}$  cm, for macroscopic wires we always have  $R \ll \lambda_L$ . Therefore, for the problems of interest here, the surface of such wires can be

treated as a plane.

- <sup>4</sup> For sufficiently small resistance in the external circuit, the voltage–current characteristic can be traversed completely. However, the dissipated joule heat results in an increase in the average temperature.
- <sup>5</sup> In [Section 4.7.1](#), an ideal type-II superconductor was defined by the fact that its magnetization curve can be traversed reversibly for increasing and decreasing external magnetic field. In this case, the corresponding equilibrium flux-line configuration must be established arbitrarily easily, that is, arbitrarily easy flux-line motion must be possible. Hence, an ideal type-II superconductor should be perfectly homogeneous with respect to the locations of the flux lines.
- <sup>6</sup> In the illustration of the Shubnikov phase, for simplicity cylindrical vortices are presented (see, e.g., [Figures 1.8](#) and [5.7](#)). This picture could lead to the wrong conclusion that the transport current simply avoids the vortices by flowing around them, and thereby also avoids the magnetic field regions. However, in this case, because of the vortex motion, we are dealing with a complicated nonequilibrium phenomenon, and a more detailed discussion can be found in monograph [M17].
- <sup>7</sup> In the Shubnikov phase, with increasing magnetic field, the Cooper pair density and, hence, the binding energy decrease.
- <sup>8</sup> Here, “corresponding” means that the superconductors have the same geometry and the same  $B_{\text{cth}}$ .
- <sup>9</sup> The magnetic field distribution of the vortex system in superconductor A is acting across the thin insulating layer and enforces a similar flux-line distribution in superconductor B.
- <sup>10</sup> The energy per unit length,  $\epsilon^*$ , can also be obtained by integrating the circulating currents (see, e.g., [M8], [Chapter 3](#), p. 57). One obtains the expression
- <sup>11</sup> We must note, however, that often the details are difficult, and that a complete account of the effects of all pinning centers is impossible.
- <sup>12</sup> Furthermore, the vortices can form not only more or less crystalline lattices, but also liquid and even gaseous phases (see [Section 4.7.2](#)). In the latter phases the vortices can move relatively freely, the pinning forces, and, hence, the critical current  $I_c$  are small. Frequently, above  $I_c$  the electric resistance increases gradually toward the normal resistance.
- <sup>13</sup> However, we do not want to suggest that grain boundaries represent strong pinning centers. In high-temperature superconductors, for not too small tilting angles between two grains, the grain boundaries act as Josephson junctions, which can carry only a small supercurrent even in the absence of an external magnetic field. In a magnetic field this supercurrent is strongly reduced further.

- <sup>14</sup> This effect is to be compared with [Figure 1.10e](#). In this case, the displacement of flux quanta by means of an electron beam was specifically utilized for the imaging of vortices.
- <sup>15</sup> Here, we ignore the small influence of the perturbation on the penetration depth  $\lambda_L$ .
- <sup>16</sup> Here, we do not include the surface superconductivity in a thin layer near the surface, which can exist in parallel fields up to  $B_a = 1.7B_{c2}$ .
- <sup>17</sup> We note that this irreversible behavior was observed already in very early experiments with metallic alloys [24]. At the time the existence of vortices was still unknown. Therefore, a first attempt at explaining the hysteretic magnetization curves was based on the assumption of a sponge-like superconducting structure [25]. In this case magnetic flux can be trapped within the holes of the sponge similar to the superconducting hollow cylinder of [Figure 1.1](#), even if one deals with a type-I superconductor.
- <sup>18</sup> A similar but weaker effect also appears for rational values of the ratio: (number of antidots)/(number of vortices).
- <sup>19</sup> If the thickness of the cylinder wall is very small compared to the radius  $R$ , we can ignore the variation of  $r$  within the wall thickness.
- <sup>20</sup> Within the superconductor, because of the vortex structure, we have a spatial variation of the magnetic field. In our discussion of the model, the field in the superconductor is taken as the average magnetic field. A decrease in this average field means that the vortex density decreases.
- <sup>21</sup> If the pinning forces acting on the individual vortices are different, initially the most weakly pinned vortices will start moving, resulting in only a relatively small resistance. With increasing current, their number and, hence, the sample resistance will approach a certain limiting value.
- <sup>22</sup> Of course, the terminology “no voltage” represents a strong simplification. Since for currents  $I < I_c$  usually a finite and also very weak dissipation is possible, we will also observe small voltages in this case. The curves in [Figure 5.19](#) indicate this by gradually approaching the linear part.
- <sup>23</sup> Under otherwise the same conditions, with increasing  $R_n$  the vortex velocity  $v$  due to the given force  $\mathbf{F}^* = \mathbf{F}_L - \mathbf{F}_H$  (i.e., for a given current  $I = I_c + I'$ ) increases. This can be seen from a simple but instructive discussion of the dissipated power. If a vortex moves with velocity  $v$  through the material due to the force  $F^*$ , the force  $F^*$  generates the power  $P_F^* = F^*v$ . This power must be turned into heat because of the local electric fields  $E$ , thus  $P_F^* = P_{el}$ . For the resistivity  $\rho_n$  of the material in the normal state, the electrical power  $P_{el}$  is proportional to  $E^2/\rho_n$ . On the other hand, we have seen that  $E$  is proportional to  $v$ . Therefore, we have  $E^2/\rho_n \propto F^*v \propto v^2/\rho_n$  and, hence,  $F^* \propto v/\rho_n$ . For a given  $F^*$  the velocity

$v$  increases with increasing  $\rho_n$ .

- [24](#) We mention that the shape of the current–voltage characteristic in an external magnetic field also depends on the sample geometry. For example, for the same material, different characteristics are observed in a tape than in a circular disk with the current running from the center to the outer edge (“Corbino disk”).
- [25](#) The steep drop of the critical current at very small magnetic fields occurs in the Meissner phase of the superconductor at fields  $B_a < B_{c1}$  (see [Figure 5.3b](#)).
- [26](#) If  $\text{YBa}_2\text{Cu}_3\text{O}_7$  is condensed on a single-crystalline  $\text{SrTiO}_3$  substrate under low oxygen pressure (about 0.1 mbar), the thin film continues to show the crystal orientation of the substrate. In this case the substrates are mostly fabricated in such a way that the  $\text{CuO}_2$  planes of the film are oriented parallel to the surface of the substrate. This technique served in the early days for preparing  $\text{YBa}_2\text{Cu}_3\text{O}_7$  thin films with relatively high quality [46]. In a *bicrystal* substrate, two single-crystalline parts are rotated relative to each other. In this case the grain boundary of the substrate is transmitted into the thin film on top and, hence, its critical current can be studied systematically. Such grain boundaries have been discussed already in [Section 1.5](#) in the context of Josephson junctions (see [Figure 1.22e](#)).

# Chapter 6

## Josephson Junctions and Their Properties

In the previous chapter, our discussion of the critical current dealt with a property that depends strongly on the detailed structure of the materials. The physics of Josephson junctions looks much different. In this case often the details of the properties of the material only play a minor role, and many statements have very general validity. In [Chapter 1](#) we have already seen examples of this in the derivation of the Josephson equations or in the discussion of the magnetic field dependence of the maximum Josephson current across a Josephson junction. In this discussion (almost) only the fundamental properties of a coherent matter wave were relevant.

In the following, we will discuss the properties of Josephson junctions in more detail. In particular, we will focus on the dynamics of Josephson junctions. We will start with a close look at the interfaces between superconductors and normal conductors, using also the information on the superconducting state that we have gained in the previous chapters.

### 6.1 Current Transport across Interfaces in a Superconductor

#### 6.1.1 Superconductor–Insulator Interface

We start by looking at two electrical conductors that are separated from each other by an insulating intermediate layer (or even by vacuum). Initially, we assume the intermediate layer to be very thick, such that no electric charges can be exchanged between the two conductors. If we ignore the fact that the electrical properties at the surface of the superconductor may be different from those in its interior [1], the Cooper pair density and, hence, the wave function up to the geometric edge of both superconductors will be the same as in the interior.

If both superconductors approach each other down to a few nanometers, electrons can tunnel from one conductor to the other, assuming that in the second superconductor there are free, energetically suitable states (see [Section 3.1.3.2](#)). In this case, we must look at a number of different tunneling processes.

In the simplest case the tunneling process occurs directly from one conductor to the other (“direct tunneling”). In this case the tunneling probability of an electron according to the general laws of quantum mechanics depends exponentially on the height and the thickness of the energy barrier between the two superconductors.

However, frequently there is also the possibility that the electrons can stay within the barrier. There they are not freely mobile, and, instead, they are bound to an impurity atom, for example. In a general way, one speaks of localized states. If a potential difference  $eU$  is applied

between the two conductors, there is the possibility (if the process is energetically favorable) that an electron first tunnels into one of these states and then proceeds from here to the other conductor. A particularly favorable situation arises if the localized state exists just in the middle of the barrier, and if its energy is equal to that of the tunneling electron. In this case, the tunneling probability can reach nearly unity (“resonant tunneling”) [2].

The momentum or the wave vector of the tunneling electron represents another important property. In the simplest case, the electron arrives in the second metal with exactly the same wave vector with which it left the first metal. This corresponds to a “coherent” process. On the other hand, during the tunneling via localized states, there is the possibility that the momentum of the electron arriving in the second conductor has no correlation with the momentum it had when it left the first conductor. This corresponds to a “completely incoherent” tunneling process.

For *periodic* layered structures, in addition, we must look more accurately at the component of the wave vector perpendicular to the layers. If, during current transport across the layers, this component is conserved, we are dealing with a wave propagating perpendicularly to the layers or, more accurately, with a Bloch wave. In spite of the nonconducting intermediate layer, the material represents a metal. However, its conductance perpendicular to the layers will be much lower than parallel to them. If the wave vector perpendicular to the layers is not conserved, but the electron keeps its momentum parallel to the layers during tunneling between neighboring layers, frequently one speaks of “coherent tunneling” or “weakly incoherent tunneling,” in contrast to the completely incoherent tunneling process mentioned earlier.

Let us now discuss how these different processes affect the current transport between two superconductors that are separated from each other by an insulator. We must distinguish between two different charge carriers, namely Cooper pairs and unpaired electrons (quasiparticles). In [Section 3.1.3.2](#) we have already discussed the tunneling of quasiparticles, where we tacitly assumed a direct tunneling process between the two superconductors. Next we want to look a bit closer at the tunneling of Cooper pairs. In this case, we should not treat the Cooper pairs as a kind of molecule consisting of two electrons, which tunnels across the barrier as a unit. Instead, according to the microscopic theory, the supercurrent across the barrier establishes itself by a Cooper pair being broken up in the first superconductor, the two electrons then crossing the barrier independently of each other, and finally recombining again to form a pair. However, because of the interactions between the Cooper pairs, this double process has about the same probability as the tunneling of individual quasiparticles.

The flow rate of the particles across the barrier is proportional to the probability for a tunneling process to occur. In [Section 3.1.3.2](#) we have included this probability within the transmission coefficient  $D$  of the barrier layer (see, e.g., Eqs. (3.10)–(3.13)). Hence, the maximum supercurrent  $I_c$  across the barrier increases with increasing transmission coefficient. On the other hand, in the normal state, the resistance  $R_n$  experienced by the unpaired electrons increases with decreasing transmission coefficient of the barrier. Therefore, the product  $I_c R_n$  can become independent of  $D$  if we assume that the unpaired and paired electrons are tunneling in the same way.

If the two superconductors are identical and the pair wave function shows s-wave symmetry, in the case of the direct tunneling we obtain [3]

$$I_c R_n = \frac{\pi}{2e} \Delta_0(T) \tanh\left(\frac{\Delta_0(T)}{2k_B T}\right) \quad 6.1$$

where  $\Delta_0$  is the energy gap of the superconductor,  $e$  is the elementary charge, and  $k_B$  is Boltzmann's constant. This is the “Ambegaokar–Baratoff relation,” according to which the product  $I_c R_n$  only depends on the energy gap  $\Delta_0$ . The temperature dependence of the gap has already been discussed in [Section 3.1.3.2](#) (see [Figure 3.19](#)).

At temperatures far below  $T_c$ ,  $\Delta_0$  is nearly constant. In Eq. (6.1) for  $T \rightarrow 0$ , the argument of  $\tanh$  approaches infinity. In this case we have  $\tanh(\Delta_0/2k_B T) \approx 1$  and

$$I_c R_n(T \rightarrow 0) = \frac{\pi}{2e} \Delta_0(0) \quad 6.2$$

Near  $T_c$ ,  $\Delta_0$  approaches zero proportional to  $(1 - T/T_c)^{1/2}$ . Then the  $\tanh$  function can be approximated by its argument, and we find that  $I_c R_n$  is proportional to  $(1 - T/T_c)$ , that is, it approaches zero linearly.

Since  $R_n$  denotes the tunneling resistance of the electrons in the absence of the pair interaction, the question arises as to how this quantity can be determined at low temperatures. If the upper critical field of the superconductor is not too high, for example, one could apply an overcritical field to the tunnel junction and then measure  $R_n$ . With the assumption that in zero field  $R_n$  is not much different from the value determined in a field, we have found  $R_n$ .

Analogously, for superconductors with a value of  $T_c$  that is not too high, we can measure the normal resistance above the transition temperature and then find  $R_n$  at low temperatures by extrapolation.<sup>1</sup> The third and most often used possibility is to measure the current–voltage characteristic of the tunnel junction up to voltages far above  $2\Delta_0/e$ . At these voltages, the characteristic is nearly linear (see [Figure 3.18](#)). Practically, the slope  $dU/dI$  is the same measured also for electrons in the absence of the pair interaction, and, hence, it allows the determination of  $R_n$ .

Frequently, the critical current density of a tunnel junction can be tuned relatively well by means of the thickness of the barrier layer. Typical values range between  $10^2$  and a few  $10^3$  A/cm<sup>2</sup>. Hence, for a tunnel junction with  $j_c = 10^3$  A/cm<sup>2</sup> and a junction area of  $A = 10 \mu\text{m}^2$ , one obtains a critical current of 100 μA. For  $T \rightarrow 0$  the normal resistance of this junction is  $R_n = \pi\Delta_0(0)/(2eI_c)$ . If we use  $\Delta_0(0) = 2$  meV as a typical value, we find  $R_n \approx 30 \Omega$ . In this example, the resistance per square  $R_n A$  is  $3 \times 10^{-6} \Omega \text{cm}^2$ .

In [Figure 6.1](#) we show the temperature dependence of the critical current of Sn–SnO<sub>x</sub>–Sn and Pb–PbO<sub>x</sub>–Sn tunnel junctions [4]. The curve of the critical current of the Sn–SnO<sub>x</sub>–Sn junction

was calculated from Eq. (6.1). The curve for the Pb–PbO<sub>x</sub>–Sn junction was obtained from a more general formula describing tunnel junctions between different superconductors. Details can be found, for example, in the monographs [M15, M16].

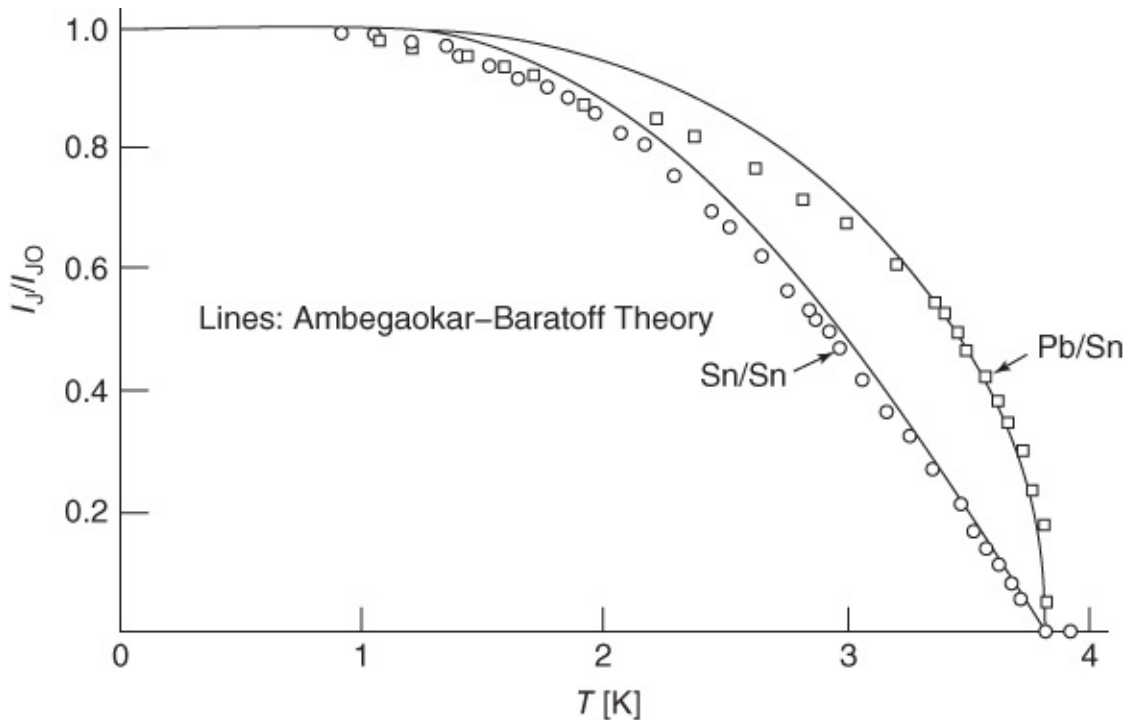


**Figure 6.1** Temperature dependence of the critical current of Sn–SnO<sub>x</sub>–Sn and Pb–PbO<sub>x</sub>–Sn tunnel junctions [4].

How does the current–voltage characteristic of a Josephson tunnel junction look? If the supercurrent across the barrier layer were absent, the quasiparticle current would lead to a characteristic similar to curve 1 in [Figure 1.23](#). On the other hand, currents smaller than  $I_c$  can flow without a voltage drop. If a direct current is applied to the junction and if we slowly increase this current starting from zero, we expect that for  $I \leq I_c$  we obtain the zero-voltage state  $U = 0$ . For  $I > I_c$  the current must be carried by the quasiparticles. According to [Figure 1.23](#), at low temperatures the transition to the linear part of the quasiparticle characteristic occurs at voltage  $U = 2\Delta_0/e$ , corresponding to the current  $I = 2\Delta_0/eR_n$ . According to Eq. (6.2), this value is larger than  $I_c$  by the factor  $4/\pi$ . We see that the voltage  $U$  should jump abruptly to a value of about  $2\Delta_0/e$ , which, indeed, is observed (see [Figure 6.2](#)). Surprisingly, in this resistive state the current can be reduced also below  $I_c$  without the tunnel junction returning to the zero-voltage state. This only happens at a much smaller current, which is often referred to as the **return current**  $I_r$ .

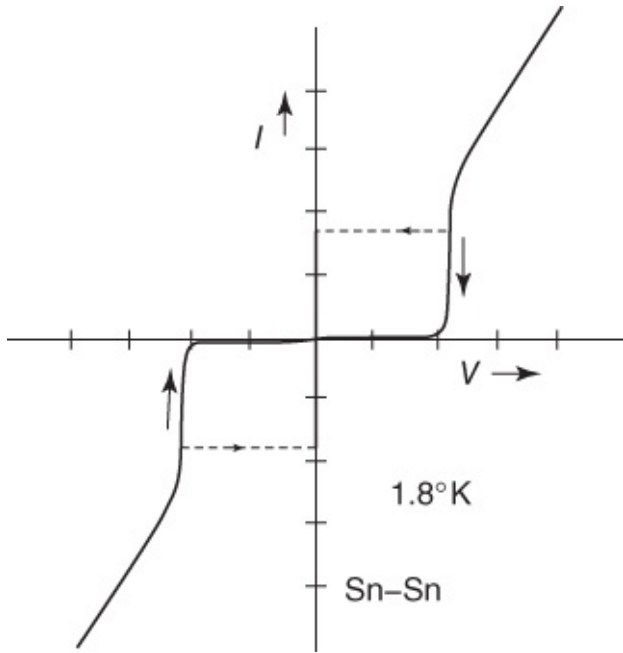


**Figure 6.2** Current–voltage characteristic of a  $\text{Sn}-\text{SnO}_x-\text{Sn}$  tunnel junction. Measuring temperature: 1.8 K; current scale: 0.5 mA/division; voltage scale: 1 mV/division.

(From Ref. [5].)

We see that for currents between  $I_r$  and  $I_c$ , we can realize two possible voltage levels:  $U = 0$  and  $U \approx 2\Delta_0/e$ . This property led to the idea of utilizing Josephson junctions as switches for the construction of logic circuits. However, in the end this idea did not turn out to be practicable. Today, superconducting digital circuits operate using the manipulation of flux quanta. We will discuss this point in more detail in [Section 7.7.2](#).

So far we have described the simplest case of direct tunneling between two s-wave superconductors. If, in addition, indirect tunneling via localized intermediate states within the barrier plays a role, the tunneling probability can depend sensitively on the potential difference  $eU$  between the two superconductors. In this case the product  $I_c R_n$  is no longer independent of the details of the barrier layer. In particular, the normal resistance above the critical current can be strongly reduced compared to Eq. (6.1).

Next we turn to tunnel junctions between superconductors with unconventional symmetry of the pair wave function  $\Psi_0$ . For the tunneling of quasiparticles, the sign of  $\Psi_0$  is irrelevant.

However, the quantity  $\Delta_0$ , which is proportional to  $|\Psi_0|$ , now depends on the tunneling direction of the quasiparticles. In [Section 3.2](#) we have discussed this point in detail. However, in this case, the Josephson currents depend on the amplitude as well as on the sign of the pair wave function of both superconductors, and also on the exact tunneling mechanism.

We illustrate this situation for the example of intrinsic tunnel junctions between neighboring  $\text{CuO}_2$  planes in high-temperature superconductors (see [Figure 1.22f](#)). During the completely *incoherent* tunneling process, the electrons lose any memory of the sign of the pair wave function. In this case we must average separately over the wave functions in both

superconducting electrodes (i.e., the CuO<sub>2</sub> planes), which yields exactly zero for a pure  $d_{x^2-y^2}$  symmetry of the pair wave function. This Josephson tunnel junction has a finite normal resistance. However, it cannot carry a supercurrent perpendicular to the layers. In the case of coherent tunneling between the CuO<sub>2</sub> layers, the electron momentum parallel to the layers remains conserved. In this case, for the calculation of the maximum Josephson current, we must integrate over products of the form  $\Psi_0^{(1)}(\mathbf{k})\Psi_0^{(2)}(\mathbf{k})$ . Here the upper indices denote the two superconducting electrodes 1 and 2, respectively. The Josephson current remains finite also for pure  $d_{x^2-y^2}$  symmetry, since the product is positive as long as  $\Psi_0^{(1)}(\mathbf{k})$  and  $\Psi_0^{(2)}(\mathbf{k})$  have the same sign. With certain approximations for low temperatures, one obtains the relation [6]

$$I_c R_n = \frac{1}{e} \Delta_{0,\max}(0). \quad 6.3$$

This differs from Eq. (6.2) by the factor  $\pi/2$ . However, generally the calculation of the (coherent) tunneling process is complicated [7], and we do not discuss it here any further. On the other hand, we must keep in mind that, compared to Eq. (6.2),  $I_c$  is always strongly reduced and is placed far below the transition of the quasiparticle characteristic into the linear regime.

In [Figure 6.3](#) we show the current–voltage characteristic of an intrinsic Josephson junction between two superconducting layers of a Bi<sub>2</sub>Sr<sub>2</sub>Ca<sub>2</sub>Cu<sub>3</sub>O<sub>10</sub> thin film [8]. In this case the CuO<sub>2</sub> planes are oriented parallel to the substrate surface. At the surface of the film, a square mesa with an edge length of 2 μm and a thickness of about 1.5 nm was fabricated. Subsequently, small wires were attached. The thickness of the mesa is chosen such that only one superconducting layer (consisting of the three closely neighboring CuO<sub>2</sub> planes of the crystal structure) exists. An electric current injected into the film at the top side of the mesa then passes exactly through a single intrinsic Josephson junction. The critical current of this junction is  $I_c \approx 160 \mu\text{A}$ . If  $I_c$  is exceeded, analogous to the junction shown in [Figure 6.2](#), the junction switches into the resistive state. Initially, the current–voltage characteristic displays a positive curvature, and for voltages above 75 mV it becomes linear.<sup>2</sup> In this regime the resistance is  $R_n = 32 \Omega$ . Hence, the value of the product  $I_c R_n$  is about 5.1 mV. The transition into the linear part of the current–voltage characteristic at 75 mV corresponds to twice the maximum energy gap  $2\Delta_{0,\max}/e$  of Bi<sub>2</sub>Sr<sub>2</sub>Ca<sub>2</sub>Cu<sub>3</sub>O<sub>10</sub>. So we find  $I_c R_n \approx 0.14\Delta_{0,\max}/e$ . Similar values were also found for Bi<sub>2</sub>Sr<sub>2</sub>CaCu<sub>2</sub>O<sub>8</sub> and for Tl<sub>2</sub>Ba<sub>2</sub>Ca<sub>2</sub>Cu<sub>3</sub>O<sub>10</sub> [9, 10].

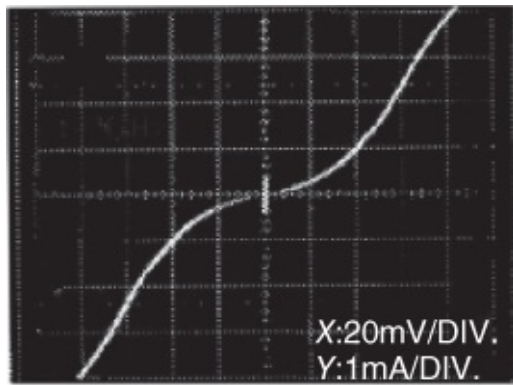


**Figure 6.3** Current–voltage characteristic of an intrinsic Josephson junction between the  $\text{CuO}_2$  planes of a  $\text{Bi}_2\text{Sr}_2\text{Ca}_2\text{Cu}_3\text{O}_{10}$  thin film. Junction area:  $2 \times 2 \mu\text{m}^2$ ; measuring temperature: 4.2 K.

(From Ref. [8], © 1999 IEEE.)

In [Figure 6.4](#) we show a current–voltage characteristic of a mesa structure with  $2 \times 2 \mu\text{m}^2$  area and about 65 nm thickness on a  $\text{Bi}_2\text{Sr}_2\text{CaCu}_2\text{O}_8$  single crystal [11]. This thickness corresponds to a sequence of 43  $\text{CuO}_2$  double layers with a barrier layer placed in between.

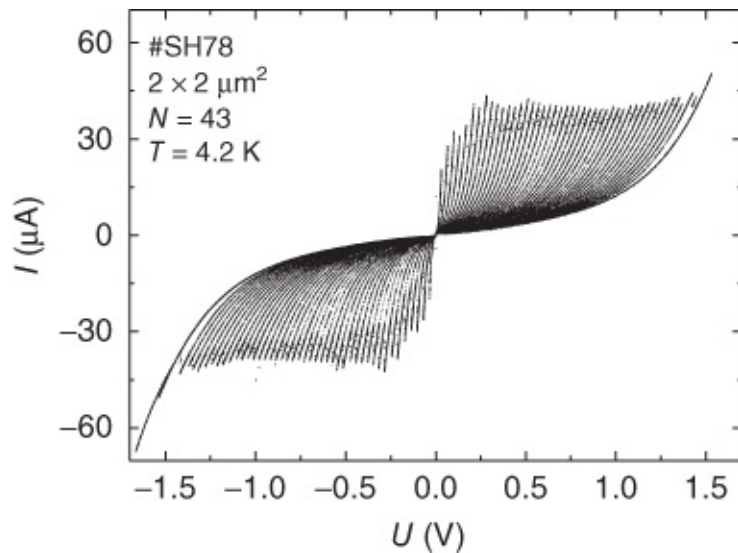


**Figure 6.4** Current–voltage characteristic of a mesa structure with  $2 \times 2 \mu\text{m}^2$  area and 65 nm thickness on a  $\text{Bi}_2\text{Sr}_2\text{CaCu}_2\text{O}_8$  single crystal. The thickness of the mesa corresponds to a stack of 43 intrinsic Josephson junctions. At higher currents, the outer branch of the characteristic continues similarly as the current–voltage characteristic shown in [Figure 6.3](#).

(From Ref. [11].)

At first sight, the characteristic looks highly complex. However, it can be understood relatively easily, if we assume that the mesa represents a stack of  $N = 43$  rather independent Josephson tunnel junctions. We must note that the *total* voltage drop  $U_{\text{tot}}$  across the mesa is measured. If all junctions are superconducting, this voltage drop is zero. If all junctions, the electrical properties of which we assume to be equal, are in the resistive state, the voltage  $U_{\text{tot}}$  is  $N$  times the value of the voltage drop of a single junction, since the voltages across the individual

junctions must be added.

In the current range between  $I_c$  and  $I_r$  a single Josephson tunnel junction shows bistability: it can exist either in the zero-voltage state ( $U = 0$ ) or in the resistive state ( $U \neq 0$ ). In the case of two junctions connected in series, which can exist in these two states independent of each other, we obtain three possible states: both junctions in the state  $U = 0$ ; one junction in the state  $U = 0$  and the other in the state  $U \neq 0$ ; or both junctions in the state  $U \neq 0$ . The current–voltage characteristic then consists of three branches, which differ in the number of resistive Josephson junctions.

Analogously, from a stack of  $N$  junctions we obtain  $N + 1$  different branches (44 branches in the case of [Figure 6.4](#)). If the individual Josephson junctions differ slightly from each other, the branch corresponding to  $M$  resistive junctions can appear at slightly different voltages, depending on *which* junctions within the stack are in the resistive state.

The structure of the current–voltage characteristic shown in [Figure 6.4](#) nearly agrees with this simple concept<sup>3</sup> of independent Josephson tunnel junctions. This indicates immediately that the transport of charge across the CuO<sub>2</sub> planes must be at least weakly incoherent, that is, no Bloch waves can develop perpendicular to the layers, which then would propagate across the whole crystal.

In high-temperature superconductors, frequently Josephson junctions are fabricated based on grain boundaries (see [Figure 1.22e](#)) [13]. The current–voltage characteristics of these junctions differ strongly from those shown in [Figures 6.2](#) and [6.3](#). In the next two sections, we will discuss these junctions in more detail.

### 6.1.2 Superconductor–Normal Conductor Interfaces

During our discussion of superconductor–insulator interfaces, we have assumed that the interface has no specific influence on the Cooper pair density  $n_s$  and that, instead, the density  $n_s$  within the interior extends up to the geometric boundary of the superconductor. Certainly, this was only an approximation, since each interface or surface causes a change of characteristic parameters such as, say, the atomic distance or the binding energy. However, if these changes are restricted to only a few atomic planes, the influences on superconductivity are correspondingly small, or become important only for extremely thin layers.

However, the assumption of a constant Cooper pair density is completely wrong in the case of the interface between a superconductor and a normal conductor, say, between Pb and Cu. In this case, electric charges can diffuse across the interface and, hence, can be practically freely exchanged.

Let us start by looking at a single superconductor–normal conductor interface. Because of the exchange of charges, in the superconductor at the interface the Cooper pair density is somewhat reduced. The pair wave function  $\Psi_0$  increases again to its full value within the length scale of the Ginzburg–Landau coherence length. In [Chapter 4](#) we have already discussed this variation in terms of the Ginzburg–Landau equations (see [Figure 4.6](#)). There we assumed

that  $\Psi_0$  vanishes at the interface. However, from the microscopic theory, one finds that a finite Cooper pair density is also induced on the side of the normal conductor, where it decays within a characteristic length scale  $\xi_N$  away from the interface<sup>4</sup> [[14], M8]. This coherence length is approximately given by

$$\xi_N(T) \approx \frac{\hbar v_F}{2\pi k_B T} \quad \text{6.4a}$$

(where  $v_F$  is the Fermi velocity,  $k_B$  is Boltzmann's constant, and  $\hbar$  is Planck's constant  $h/2\pi$ ), if the electron mean free path  $l^*$  is large compared to the extension  $\xi_0$  of a Cooper pair. In the opposite limit one finds

$$\xi_N(T) \approx \left( \frac{\hbar v_F l^*}{6\pi k_B T} \right)^{1/2} \quad \text{6.4b}$$

The quantity  $v_F l^*/3$  is just the diffusion coefficient  $D$  of the electrons in the normal conductor. Therefore, the right-hand side of Eq. (6.4b) can also be written as  $[\hbar D / (2\pi k_B T)]^{1/2}$ . We note that, for  $T \rightarrow 0$ ,  $\xi_N(T)$  diverges in both limits. Furthermore, at the interface,  $\Psi_0$  can change abruptly by a value depending on the transmission of the interface.

This situation is referred to as the ***proximity effect***. Strongly simplifying, we can describe it in the following way: Near the interface the normal conductor turns into a superconductor, and the pair correlation in the superconductor is slightly reduced.<sup>5</sup> If one of the two conductors is made sufficiently thin, these effects of the interface will appreciably change the behavior of this thin part of the whole sample.

The first observations of the influence of a normal conductor on a superconductor were reported in the 1930s for Pb films, which were electrolytically deposited on a (normal conducting) constantan wire (55% Cu + 45% Ni) [15]. With decreasing thickness, the transition temperature of these Pb films strongly decreased, and for a thickness of about 350 nm it became immeasurably small. In the late 1950s, this effect was systematically studied by Meissner [16].

In order to obtain quantitative results, a number of conditions must be satisfied that are not easy to realize experimentally. The junction between the two substances must, indeed, be metallic, and cannot be affected by any kind of oxide layers, even if they are very thin. On the other hand, interdiffusion between the two metals and the resulting formation of an alloy at the interface must be avoided. These conditions can be well satisfied using evaporated films. As an example, we discuss the behavior of double layers of Pb and Cu. In this case the influence of several parameters must be studied. For example, the thickness  $d_{\text{Pb}}$  and  $d_{\text{Cu}}$  must be varied. Furthermore, as we see from Eqs. (6.4a) and (6.4b), the electron mean free path in the layers plays a role.

In [Figure 6.5](#) we show the transition temperature plotted versus the thickness  $d_{\text{Pb}}$  of the lead [17]. In this case the Cu layer is thick compared to the coherence length  $\xi_N$ . For  $d_{\text{Pb}}$  less than

about 50 nm, the transition temperature decreases strongly. We can extrapolate a critical thickness of about 10 nm, at which  $T_c$  approaches zero. This value of the critical thickness is much smaller than the value (350 nm) observed in earlier experiments. For an explanation of this difference, we must note that the results of [Figure 6.5](#) were obtained for a double layer prepared at a substrate temperature of only 10 K. In this case both metals have a high degree of disorder and a short electron mean free path of only about 5.5 nm in Pb<sup>6</sup> and about 4.5 nm in Cu. Therefore, also the length within which the Cooper pair density can vary spatially becomes much shorter. In [Figure 6.5](#) the influence of the electron mean free path in the normal conductor is indicated by the dashed curve 2. These transition temperatures are observed for double layers, in which the copper film has been annealed prior to the evaporation of lead. In this way the electron mean free path could be increased from initially 4.0 nm up to about 80 nm. However, the Pb film was evaporated again at 10 K, that is, with nearly the same degree of disorder. We clearly see that in this way the effective depth of the proximity effect has been increased. The same decrease of  $T_c$  is also observed for thicker Pb films. A change of the mean free path in the superconductor also causes a similar effect. The shorter the mean free path, the shorter also is the effective depth of the proximity effect, since the Ginzburg–Landau coherence length decreases with decreasing mean free path (Eq. (4.42)).

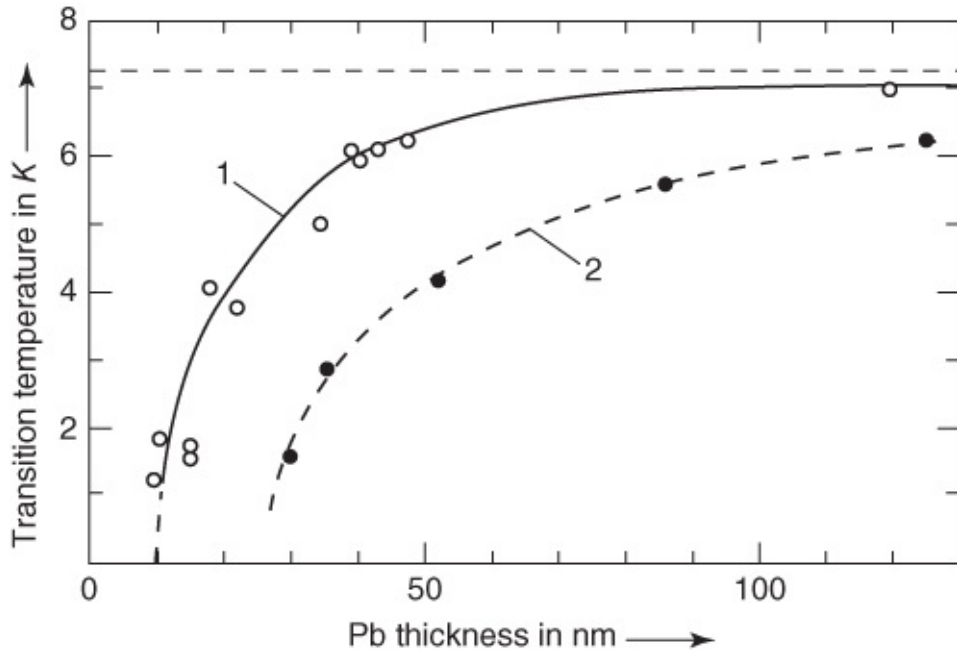


[Figure 6.5](#) Transition temperature of double layers of lead and copper. Deposition temperature: 10 K; thickness of the Cu layers  $d_{\text{Cu}} = \xi_N$ ; electron mean free path: about 5.5 nm in Pb, and about 4.5 nm (curve 1) and 80 nm (curve 2) in Cu.

(From Ref. [17].)

In [Figure 6.6](#) we show the influence of the thickness of the normal conductor [16]. The transition temperature of Pb layers with different thickness is plotted versus the thickness  $d_{\text{Cu}}$ . In this case all double layers were deposited at 10 K substrate temperature. As expected, for large thickness of the normal conductor, the transition temperature approaches a limiting value. This limit is plotted in [Figure 6.5](#).

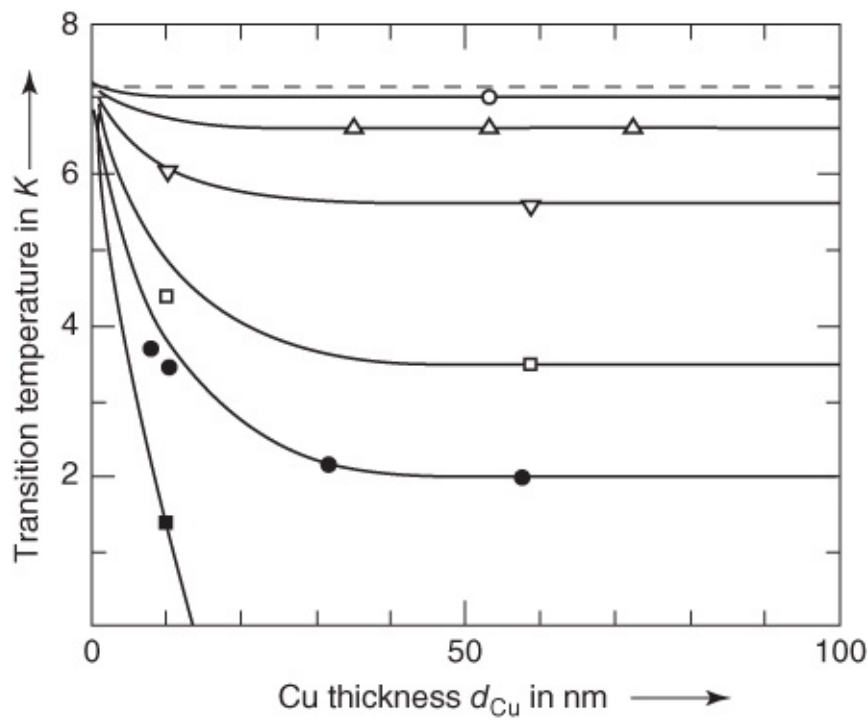


**Figure 6.6** Transition temperature of double layers of lead and copper. Deposition temperature: 10 K; thickness of the Pb films: (○) 100 nm, (Δ) 50 nm, (▽) 30 nm, (□) 15 nm, (●) 10 nm, and (■) 7 nm.

(From Ref. [17].)

The mutual influence of materials with different  $T_c$  or different strength of the electron–phonon interaction is particularly important in heterogeneous alloys. If the precipitates (say, a superconductor within a normal conductor) are very small (diameter comparable to the coherence length), the superconductivity can be suppressed. A superconducting matrix can be strongly affected in its superconducting properties by means of normal conducting precipitates. However, for the interpretation of any results in terms of interface effects, all parameters, including the mean free path, must be taken into account, in order to estimate the correct order of magnitude of the effects.

Let us look somewhat more closely at the current transport across the interface between a normal conductor and a superconductor. Together with the pair wave function  $\Psi$ , the energy gap  $\Delta_0$  decays from its maximum value  $\Delta_0(x = \infty)$  within a length scale  $\xi_{\text{GL}}$  in the superconductor and a length scale  $\xi_N$  in the normal conductor.

If an electron with energy  $E < \Delta_0(x = \infty)$  from the normal conductor arrives at the interface, it cannot penetrate very far into the superconductor, since the energy gap  $\Delta_0(x)$  rapidly increases up to values larger than  $E$ , and, hence, no states are available anymore for the electron. If the electron experiences strong inelastic scattering, it quickly reaches thermal equilibrium with the local conditions and will be accepted by the ensemble of Cooper pairs. However, what happens if the electron keeps its energy, that is, if it moves outside of the local thermal equilibrium?

On the one hand, the electron can be reflected at the interface. However, in this case, it does not contribute to the current across the interface. On the other hand, another highly interesting process also exists. If  $\Delta_0(x)$  increases slowly compared to the wavelength of the incoming electron (approximately the Fermi wavelength), the electron can form a Cooper pair with a second electron in the superconductor having an opposite momentum and spin. However, in the superconductor, the second free electron must first be created from an energy state below the Fermi energy. Then it leaves behind a hole, which in turn moves in the direction toward the normal conductor. In this case, the momentum of the outgoing hole is opposite and equal to that of the incoming electron. So we have the following situation: An electron with wave vector  $\mathbf{k}$  arrives at the interface, a Cooper pair continues this motion in the superconductor, and a hole with wave vector  $-\mathbf{k}$  moves backward in the normal conductor. Hence, a total charge of  $2e$  has moved across the interface. This process is referred to as ***Andreev reflection*** after its discoverer [18]. It is important to note that, in contrast to the usual reflection, in this case we deal with *retro-reflection*.

As a result of this Andreev reflection, a current can flow from a thin normal conducting tip into a superconductor,<sup>7</sup> which, because of the outgoing hole, at voltages below  $\Delta_0(x = \infty)/e$ , is about twice as large as would be expected if the electrons were simply to penetrate into the superconductor. Only at voltages above  $\Delta_0(x = \infty)/e$  can the electrons proceed directly into the superconductor, where they reach thermal equilibrium by means of inelastic scattering processes. In this case the return current of the holes vanishes, and the resistance of the contact increases up to the value reached in the normal state above  $T_c$ .

Next we look at a thin layer of a normal conductor placed between two superconductors. For simplicity we assume that both superconductors consist of the same material. Because of the proximity effect, a supercurrent can flow across the normal conductor still at a relatively large thickness of several nanometers. As long as the Cooper pair density induced in the normal conductor is small compared to the pair density in the interior of the two superconducting electrodes, this current satisfies the Josephson equations (1.25) and (1.28). Near  $T_c$  one finds for the product of the critical current  $I_c$  and the normal resistance  $R_n$  [M4, M8]

$$I_c R_n = \frac{3\pi}{2e} \frac{\Delta_0^2(x = 0)}{k_B T_c} \frac{d/\xi_N}{\sinh(d/\xi_N)} \quad 6.5$$

Here  $d$  is the thickness of the normal conductor and  $\Delta_0(x = 0)$  is the value of the energy gap in the superconductor near the interface, which will be reduced compared to its value in the interior of the superconductor. Near  $T_c$ ,  $\Delta_0(x = 0)$  is proportional to  $\Delta_0(x = \infty)/\xi_{GL}$ . With  $\Delta_0(x = \infty) \propto (1 - T/T_c)^{1/2}$  and  $\xi_{GL} \propto (1 - T/T_c)^{-1/2}$ , this yields a linear temperature dependence of  $\Delta_0(x = 0)$  and a quadratic temperature dependence of  $I_c R_n$ :

$$I_c R_n \propto (1 - T/T_c)^2 \quad \text{near } T_c \quad 6.6$$

Further we note that in Eq. (6.5) the properties of the barrier layer ( $d, \xi_N$ ) appear explicitly, in

contrast to the Ambegaokar–Baratoff relation (6.1) for Josephson tunnel junctions. On the one hand, due to the sinh factor, we have an exponential dependence on the thickness of the normal layer, and on the other hand, the temperature dependence of  $\xi_N$  leads to a strong increase in  $I_c R_n$  toward low temperatures.

The current–voltage characteristics of superconductor–normal metal–superconductor (SNS) junctions differ strongly from the characteristics of Josephson tunnel junctions discussed in the previous section. If the applied current is increased beyond the maximum supercurrent, the voltage mostly increases *continuously*. For large voltages the characteristic becomes linear with a slope  $dU/dI \approx R_n$ . This behavior is illustrated in [Figure 6.7](#) for the example of a Pb–(CuAl)–Pb junction [19]. In 1971 this junction was prepared by John Clarke between two crossed Pb strips with about 200  $\mu\text{m}$  width. The junction area of  $4 \times 10^4 \mu\text{m}^2$  was extremely large compared to what is customary today. Correspondingly, the junction resistance of about 1  $\mu\Omega$  was very small. Also the CuAl layer was very thick (about 0.5  $\mu\text{m}$ ), and, hence, the critical current density of the junction ( $<1 \text{ A/cm}^2$ ) and the product  $I_c R_n$  ( $<300 \text{ nV}$ ) were very small. A special measuring technique, based on superconducting quantum interferences, was needed to detect the very small voltage drop across the junction.

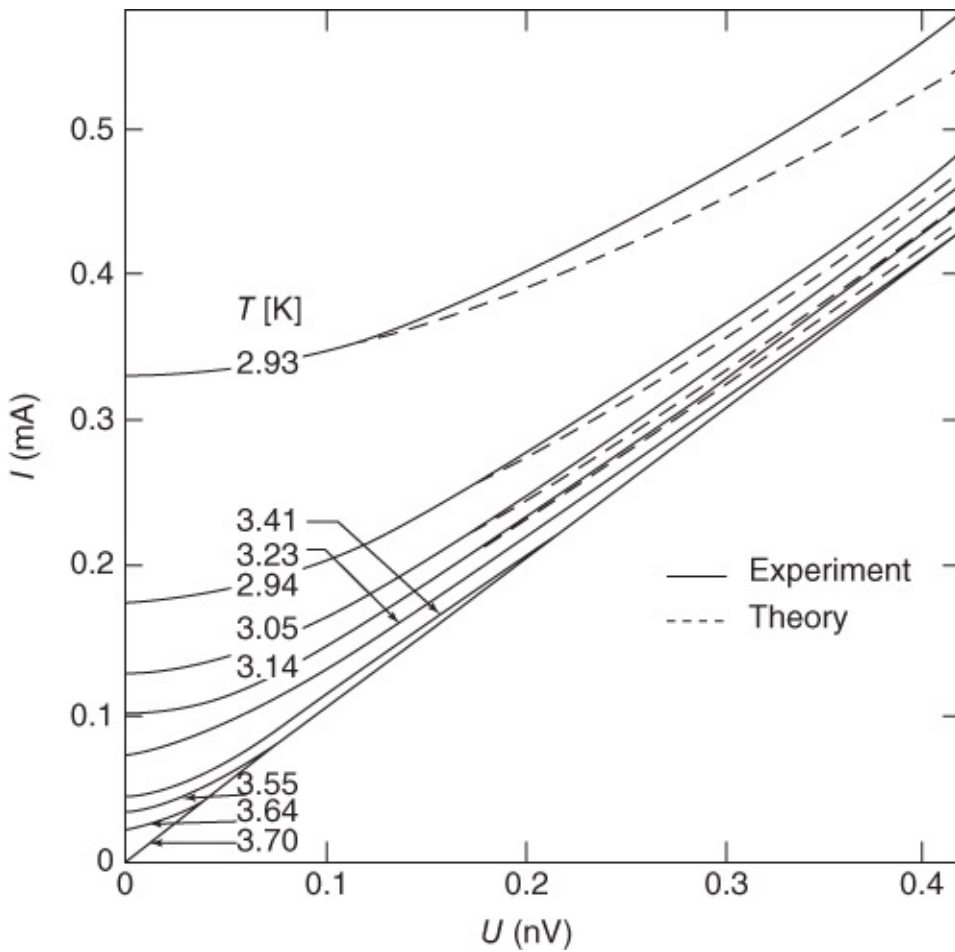


[Figure 6.7](#) Current–voltage characteristic of a Pb–(CuAl)–Pb junction for different temperatures. Junction area:  $4 \times 10^4 \mu\text{m}^2$ ; thickness of the CuAl layer: about 0.5  $\mu\text{m}$  [19].

In [Figure 6.7](#) the experimental data are compared with theoretical curves. The underlying

model, based on a current flowing through an ohmic resistance parallel to the Josephson current, will be described in the following section. At this stage, we only note that the model results in a current–voltage characteristic of the form

$$U = R_n \sqrt{I^2 - I_c^2} \quad (|I| > I_c) \quad \text{6.7a}$$

$$U = 0 \quad (|I| < I_c) \quad \text{6.7b}$$

The corresponding curves are shown in [Figure 6.7](#).

Frequently, for SNS junctions with a much thinner barrier, one observes the following properties:

1. At low temperatures there appears hysteresis similar to that in tunnel junctions. Upon exceeding the critical current, the voltage jumps to a finite value. If the current is reduced below  $I_c$ , initially the voltage drop across the junction remains finite. The junction returns to the zero-voltage state only below the value of the return current.
2. The linear extrapolation of the characteristic at large voltages back to  $U = 0$  frequently intersects the current axis at a finite, positive current value, the “excess current”  $I_{\text{ex}}$ .<sup>8</sup>
3. The excess current can be as large as half of the maximum supercurrent.
4. For very pure barrier layers, the differential resistance  $dU/dI$  frequently displays maxima at voltage values  $U_n = 2\Delta_0/(ne)$  for  $n = 1, 2, 3, \dots$  One speaks of “subharmonic” structures below the energy gap.

The property 1 will be discussed in more detail in the next section. We will see that hysteresis can be understood in a simple way, if we take into account the capacity of the Josephson junction and the resulting displacement currents.

For property 2 (the excess current), Andreev reflection again plays a special role [22]. An electron starting from the first superconductor will be reflected as a hole at the second superconductor, this in turn as an electron at the first superconductor, and so on. In the final result, this amounts to an additional current of Cooper pairs across the barrier.

Property 3 (the subharmonic structures) also originates from Andreev reflections [23]. At a voltage  $U$ , at each reflection process the electron or the hole gains energy  $eU$ . After  $n$  reflections, the electron/hole has traversed the voltage  $U$  a total of  $(n + 1)$  times. If the applied voltage has the value  $2\Delta_0/(ne)$ , then  $(n - 1)$  reflections are just enough for the electron (or the hole) to reach an allowed energy state in the opposite electrode.<sup>9</sup> At a slightly lower voltage,  $n$  reflections would still be necessary. Therefore, at voltages  $U_n = 2\Delta_0/(ne)$  the differential resistance of the junction changes.

In addition to the structures discussed earlier, there exist a number of other phenomena due to Andreev reflections [24]. As an example we discuss the appearance of a bound state of the electron and the retro-reflected hole. For this purpose, we must look a bit closer at the phase of

the wave function of the electron and of the Andreev-reflected hole. It turns out that a phase shift of  $\pi/2$  appears during Andreev reflection. After another reflection, we have a phase shift of  $\pi$  and, hence, destructive interference. However, if an *additional* phase shift of  $\pi$  can be achieved, the wave functions of the electron and of the hole interfere constructively. As a result, at the interface a bound state of the electron and the retro-reflected hole can be formed, which affects, for example, the electrical conductance across the barrier layer, and also the temperature dependence of the critical current and the current-phase relation [6].

Initially, such bound states were discussed in the context of superconductor–normal conductor double layers [25]. They play a special role in Josephson junctions consisting of at least one unconventional superconductor, say, for example, a junction between a conventional superconductor such as Pb or Nb and a high-temperature superconductor such as  $\text{YBa}_2\text{Cu}_3\text{O}_7$ . Another example is a grain-boundary junction between two single-crystalline films of a high-temperature superconductor, which are tilted relative to each other [6]. Under suitable conditions, reflection can occur in such a way that at the two reflection points the pair wave functions have a different sign. This leads exactly to the required additional phase shift of  $\pi$ . Therefore, the observation of an enhanced conductance at small voltages (zero-bias anomaly) plays an important role in the study of the symmetry of the pair wave function in high-temperature superconductors [26]. A detailed summary can be found in [27, 28].

### 6.1.3 Superconductor–Ferromagnet Interfaces

In the previous sections we had discussed the interfaces between superconductors and normal conductors and had tacitly assumed that the normal conductor is nonmagnetic. However, if we deal with a ferromagnet, analog to the case of the Fulde–Ferrell–Larkin–Ovchinnikov (FFLO) states discussed in [Section 3.2.4](#), the electrons penetrating into the ferromagnet feel the exchange interaction. This interaction increases the energy of one electron of a Cooper pair by the amount  $E_{\text{ex}}$  and reduces the energy of the other electron by the same amount. As a result, the pair wave function induced in the ferromagnetic layer oscillates. This oscillation is affected by the exponential decay discussed in the last section.

If the average mean free path of the electrons is small compared with the extension of a Cooper pair, somewhat simplified one obtains a pair wave function of the form [29]

$$\Psi \propto \exp(-x/\xi_{\text{F}1}) \cos \xi_{\text{F}2} x \quad 6.8\text{a}$$

Here, the lengths  $\xi_{\text{F}1}$  and  $\xi_{\text{F}2}$  are given by

$$\xi_{\text{F}1,2} = \sqrt{\frac{\hbar D}{[E_{\text{ex}}^2 + (\pi k_{\text{B}} T)^2]^{1/2} \pm \pi k_{\text{B}} T}} \quad 6.8\text{b}$$

$D$  is the diffusion constant, which had appeared in Eq. [\(6.4b\)](#). In Eq. [\(6.8b\)](#), the “+”-sign in front of  $k_{\text{B}} T$  refers to  $\xi_{\text{F}1}$  and the “−”-sign to  $\xi_{\text{F}2}$ .

In the case  $E_{\text{ex}} = 0$ ,  $\xi_{\text{F}1}$  would change to Eq. [\(6.4b\)](#) and  $\xi_{\text{F}2}$  would become infinite. There

would appear no oscillations, as expected in the case of a nonmagnetic superconductor/normal conductor interface. If, on the other hand,  $E_{\text{ex}}$  is large compared with  $\pi k_B T$ , we have  $\xi_{F1} \approx \xi_{F2} \approx (\hbar D/E_{\text{ex}})^{1/2}$ . If for testing we insert  $D = 10^{-2} \text{ m}^2/\text{s}$  and  $E_{\text{ex}} = 10 \text{ meV}$ , we obtain for  $\xi_{F1}$  and  $\xi_{F2}$  a value of 25 nm.

In our example, the pair wave function oscillates with a period  $2\pi \xi_{F2} = 160 \text{ nm}$ . It is interesting if we imagine superconductor–ferromagnet–superconductor Josephson contacts (hereafter referred to as **SFS-contacts**), the ferromagnetic barrier of which having a thickness of about  $\pi \xi_{F2}$ . Depending on the exact thickness of this barrier, the pair wave function in both superconducting electrodes can have the same or the opposite sign. In the first case, we deal with a standard Josephson contact, which in this context is referred to as **0-contact**. In the second case, we have a “ $\pi$ -contact,” similar to the experiments discussed in [Section 3.2.2](#). Such Josephson contacts are interesting for microelectronics. Frequently, for a desired function, circuits combining 0-contacts and  $\pi$ -contacts can be realized much simpler than based exclusively on 0-contacts.

Already in 1977, in connection with Josephson contacts having a paramagnetic barrier, the possibility of generating  $\pi$ -contacts was discussed [30]. However, it took up to 2007 when the first SFS contacts could be experimentally realized [29]. In this case, a copper–nickel alloy of composition  $\text{Cu}_{0.5}\text{Ni}_{0.5}$  was used as ferromagnetic barrier. The superconductor was niobium.

[Figure 6.8a](#) shows data in the case of a sample with a ferromagnetic barrier of 22 nm thickness. The inset shows the magnetic field dependence of the critical supercurrent across the contact for three different temperatures. Similar to the data shown in [Figure 1.28](#), in all cases a beautiful “Fraunhofer pattern” was observed. This shows that the critical supercurrent density is homogeneous along the contact. However, from these curves, one cannot conclude whether one deals with a 0-contact or a  $\pi$ -contact. This can be seen from Eq. (1.72d). Here the quantity  $\sin \delta$  had to be maximized in order to determine the critical current. This yielded the slit function Eq. (1.73), independent of the sign of  $j_c$ .

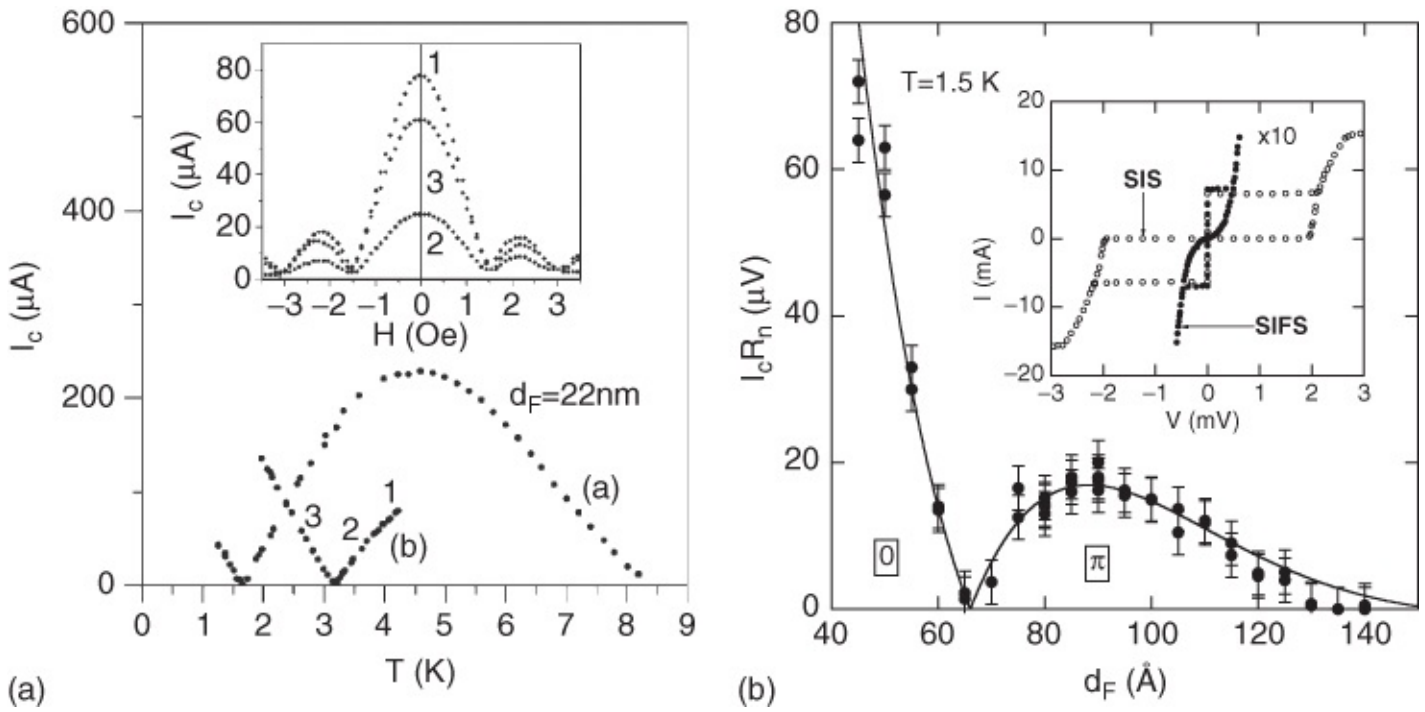


**Figure 6.8** (a) Critical current  $I_c$  of an SFS-Josephson contact (thickness of the ferromagnetic barrier: 22 nm) plotted versus the temperature for two samples (a) and (b). (Printed with permission of [29], © 2001 American Physical Society.) The inset shows the magnetic field dependence of  $I_c$ , measured at points 1, 2, and 3 of the main graph. Part (b) shows the product of the critical current  $I_c$  and the normal resistance  $R_n$  for an SIFS-Josephson contact as a function of the temperature. (Printed with permission of [31], © 2002 American Physical Society.) Solid line: Theoretical curve. Inset: Current–voltage characteristic of the SIFS-contact compared with a traditional SIS-tunnel contact. Superconducting layers: Nb, ferromagnet: PdNi, insulator:  $\text{Al}_2\text{O}_3$ .

However, it is important how the critical current  $I_c$  varies as a function of temperature in the absence of an applied magnetic field. This is shown in the main part of the figure for two samples. In the case of the curve marked with (a), we see that  $I_c$  increases with decreasing temperature between 8.5 and 5 K. However, at lower temperatures it decreases again, slightly below 2 K it reaches zero, and at still lower temperatures it increases again. Similar behavior was observed in the case of the sample marked with (b).

This behavior can be understood from the temperature dependence of  $\xi_{F2}$ . According to Eq. (6.8b),  $\xi_{F2}$  increases with increasing temperature. If, for example, at low temperatures we have a  $\pi$ -contact, at a distinct transition temperature it can turn into a 0-contact. This 0– $\pi$ -transition is connected with a sign change of the critical supercurrent density  $j_c$ . Hence,  $j_c$  and also  $I_c$  must vanish at the 0– $\pi$ -transition. This is shown exactly in Figure 6.8a.

Transitions between 0-contacts and  $\pi$ -contacts can be observed also as a function of the thickness of the ferromagnetic barrier. This is shown in Figure 6.8b. The data refer to contacts which, in addition to the ferromagnetic barrier made of NiPd, also have an insulating barrier

made of  $\text{Al}_2\text{O}_3$ , in order to increase the electric resistance  $R_n$  of the contact in the voltage-carrying state.

## 6.2 The RCSJ Model

Following the somewhat microscopic discussion in the previous two sections, now we want to introduce a very simple model, which can well describe not only the current–voltage characteristics but also the dynamics of Josephson junctions in many details. The model has been proposed by Stewart [32] and McCumber [33].

We assume that a current, which can be time-dependent, is applied to a Josephson junction. Currents smaller than the critical current  $I_c$  can flow as supercurrents across the junction. We want to describe them in terms of the Josephson equations

$$I_J = I_c \sin \gamma \quad \underline{1.25}$$

$$\dot{\gamma} = \frac{2\pi}{\Phi_0} U(t) \quad \underline{1.28}$$

Here  $\Phi_0 = h/2e$  denotes the flux quantum and  $\gamma$  the gauge-invariant phase difference (Eq. (1.26)). If  $\gamma$  is time dependent, according to Eq. (1.28), the voltage  $U(t)$  automatically is unequal to zero. Vice versa, for a voltage unequal to zero, the phase  $\gamma$  is time dependent and so also is the Josephson current  $I_J$  because of Eq. (1.25).

However, at finite voltages, quasiparticles are also flowing across the Josephson junction. Furthermore, we must keep in mind that a Josephson junction has a finite capacity  $C$ . This is particularly clear for tunnel junctions with a geometry similar to that of a plate capacitor.

In a simple approach, we treat the total current  $I$  across the junction as the sum of the Josephson current  $I_J$ , the quasiparticle current  $I_q$ , and the displacement current  $I_d$ .<sup>10</sup> Generally, the quasiparticle current  $I_q$  depends in a complicated way on the voltage  $U$ , as we have seen in our discussion of tunnel junctions. However, at not too large voltages we want to treat  $I_q(U)$  as a linear function:

$$I_q = U/R \quad \underline{6.9}$$

This means in the end that  $I_q$  is treated in terms of an ohmic resistance  $R$ . Then we obtain

$$I = I_J + I_q + I_d = I_c \sin \gamma + \frac{U}{R} + C\dot{U} \quad \underline{6.10}$$

Here we have used the relation  $I_d = C\dot{U}$  for the displacement current across a capacitor  $C$ . We can also illustrate this approach graphically by means of a parallel connection of an ohmic resistance, a capacitor, and a (nonclassical) device symbolizing the Josephson current. This circuit is shown in [Figure 6.9](#)a. Here we have indicated the Josephson current by a cross.

Because of this circuit, the model is also referred to as the **RCSJ model**.<sup>11</sup> If the capacity is neglected, one speaks of the “RSJ model.”

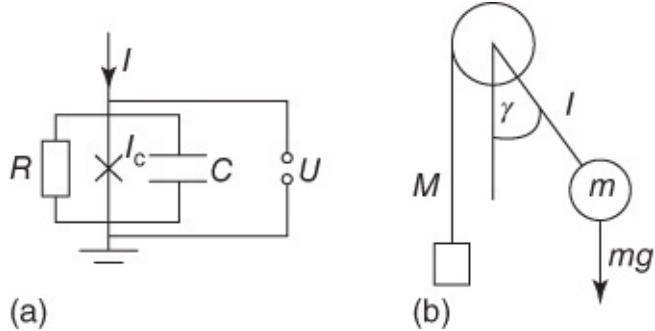


**Figure 6.9** (a) Replacement circuit of a Josephson junction carrying an applied current. (b) The pendulum as an analogous model satisfying the same equation of motion as the Josephson junction. The acting torque  $M$  is indicated by a hanging weight.

We note that frequently the treatment of the quasiparticle current in terms of an ohmic resistance in the circuit works very well. In the case of applications of Josephson tunnel junctions in the field of superconducting quantum interferometry, frequently an artificial parallel resistance, which is much smaller than the quasiparticle resistance of the junction below the energy gap, is attached to the Josephson junctions. In this case, in the RCSJ model the resistance  $R$  is given by this parallel resistance. For SNS junctions, and also for many other junction types such as grain-boundary junctions made of high-temperature superconductors, it turns out that for not too large voltages  $R$  is indeed linear. If necessary, Eq. (6.10) can be extended by using a nonlinear relation for  $I_q(U)$  (“nonlinear RCSJ model”).

In Eq. (6.10) the voltages along the Josephson current and across the resistance and the capacitor have been set equal. This follows exactly from Kirchhoff's law for the circuit of Figure 6.9a. Now we can use the second Josephson equation to eliminate either  $\gamma$  or  $U$  from Eq. (6.10). We chose the second option and obtain

$$I = I_c \sin \gamma + \frac{\Phi_0}{2\pi R} \dot{\gamma} + \frac{C\Phi_0}{2\pi} \ddot{\gamma} \quad 6.11$$

We have derived a differential equation for  $\gamma$ , which is of second order in the time and is nonlinear because of the sine term. At first, this equation does not look at all simple. It can be solved analytically only in the limit  $C = 0$ . On the other hand, it turns out that there are well-known analogous systems, the dynamics of which is also described by an equation of the form (6.11).

The pendulum (see Figure 6.9b) is such an analogous system. Its equation of motion is discussed in standard textbooks on mechanics.<sup>12</sup> We assume that the pendulum is deflected from the vertical position by the angle  $\gamma$ . The mass of the pendulum is  $m$ . An external torque  $M$ , which is oriented parallel to the rotation axis, deflects the pendulum. The restoring torque is given by the length  $l$  of the pendulum multiplied by the gravitational force  $mg \sin \gamma$ . In this case the equation of motion of the pendulum is

$$M = mgl \sin \gamma + \Gamma \dot{\gamma} + \Theta \ddot{\gamma}$$

6.12

Here  $\Theta$  is the moment of inertia of the pendulum ( $\Theta = ml^2$ , if all other masses except for the pendulum mass can be ignored). The term  $\Gamma \dot{\gamma}$  describes the damping of the pendulum with damping coefficient  $\Gamma$ . Obviously, Eq. (6.12) has the same form as Eq. (6.11), with the following correspondences:  $I \leftrightarrow M$ ,  $mgl \leftrightarrow I_c$ ,  $\Gamma \leftrightarrow \Phi_0/2\pi R$ , and  $\Theta \leftrightarrow C\Phi_0/2\pi$ . The deflection angle  $\gamma$  of the pendulum exactly corresponds to the gauge-invariant phase difference  $\gamma$  of the Josephson junction.

So instead of the Josephson junction, we can simply imagine a pendulum and look at its vibrational or rotational motion. The temporal change of the deflection angle of the pendulum, that is, the angular velocity, then corresponds exactly to the voltage  $U$  at the Josephson junction according to the second Josephson equation.

With this picture, we can predict immediately what happens if the current  $I$  through the Josephson junction is slowly increased from zero. In the pendulum model this means that we gradually apply the torque  $M$  to the pendulum. For not too large values of  $M$ , the pendulum is deflected by a certain angle  $\gamma_0$ . However, except perhaps for small oscillations about this value, the pendulum remains at rest. The time-averaged angular velocity  $\langle \dot{\gamma} \rangle$  is zero, which in the picture of the Josephson junction means that the time-averaged voltage  $\langle U \rangle$  is zero.<sup>13</sup> However, if the deflection angle of the pendulum reaches  $90^\circ$  (in the picture of the Josephson junction we have  $I = I_c$  in this case), each further increase in the torque will lead to a rotation of the pendulum. In this case, also the average angular velocity  $\langle \dot{\gamma} \rangle$  (or the average voltage at the Josephson junction) will be larger than zero.

The rotation of the pendulum depends on the mass and the damping of the pendulum. If the damping is high, for slightly overcritical values of  $M$  the pendulum will rotate very nonuniformly. Initially, it will fall down relatively quickly, and then rise again somewhat slower toward the direction  $\gamma = 90^\circ$ . This motion becomes faster and more uniform, the larger the torque. Hence,  $\langle \dot{\gamma} \rangle$  increases continuously from zero, and for large values of the torque it will become proportional to  $M$ .<sup>14</sup> This situation leads exactly to the current–voltage characteristic ( $M$  vs  $\langle \dot{\gamma} \rangle$  in the pendulum picture) shown in Figure 6.7. In this case, due to the analog, one also speaks of an overdamped Josephson junction.

In the limit of very large damping ( $m/\Gamma \rightarrow 0$  for the pendulum,  $RC \rightarrow 0$  for the Josephson junction), the time average of the voltage or of the angular velocity can be found exactly, leading to the result Eqs. (6.7a) and (6.7b).

However, if the pendulum is only weakly damped, upon exceeding the critical torque it will rotate immediately very uniformly and fast. If in the rotating state  $M$  is reduced below the critical value, the pendulum will continue to rotate because of its inertia. Only if  $M$  falls below a certain value will the pendulum come to rest. We see that we have achieved a bistable “characteristic,” for which in a certain interval of  $M$  the pendulum can either rotate or be at rest. This explains the origin of hysteretic characteristics such as that of a tunnel junction. In this case one also speaks of underdamped Josephson junctions.

The RCSJ model is often applied for the description of Josephson junctions. In particular, it reproduces well the dynamics of Josephson junctions without needing the microscopic details of current transport across the barrier. Also instead of Josephson junctions, one prefers to imagine a driven pendulum or whole systems of coupled driven pendulums, in order to have a picture of the dynamics of Josephson junctions or even complete circuits containing Josephson junctions.

Before we discuss the dynamics of Josephson junctions in more detail, we want to transform Eq. (6.11) into dimensionless form, in which we can define more accurately the meaning of “underdamped” and “overdamped.” For this purpose, the currents are measured in units of  $I_c$ , the voltages in units of  $V_c = I_c R$ , and the time in units of  $\tau_c = \Phi_0 / (2\pi I_c R)$ . The voltage  $V_c$  is also referred to as the ***characteristic voltage***, and  $f_c = 1/(2\pi\tau_c)$  as the characteristic frequency of the Josephson junction. In these units, Eq. (6.11) is reduced to

$$i = \sin \gamma + \dot{\gamma} + \beta_c \ddot{\gamma} \quad 6.13$$

This equation only contains a single material-dependent parameter, the dimensionless Stewart–McCumber parameter

$$\beta_c = \frac{2\pi I_c R^2 C}{\Phi_0} \quad 6.14$$

Obviously this parameter determines the behavior of the Josephson junction.<sup>15</sup> In the case of  $\beta_c > 1$ , one speaks of underdamped Josephson junctions, and in the case of  $\beta_c < 1$  of overdamped Josephson junctions.

In [Figure 6.10](#) we show two current–voltage characteristics numerically calculated from Eq. (6.13). We note that in this case “voltage” is understood as the time-averaged voltage across the junction. The very rapid oscillations of the Josephson current remain undetected during the recording of a characteristic. [Figure 6.10a](#) shows the characteristic for  $\beta_c = 0.5$ . The characteristic is nonhysteretic and does not deviate strongly from the relations (6.7a) and (6.7b), which one obtains for  $\beta_c = 0$ , and which is shown as a thin line in the figure. In [Figure 6.10b](#) we have  $\beta_c = 10$ . Now the characteristic is strongly hysteretic, with a return current  $I_r$  of about  $0.4I_c$ .<sup>16</sup>

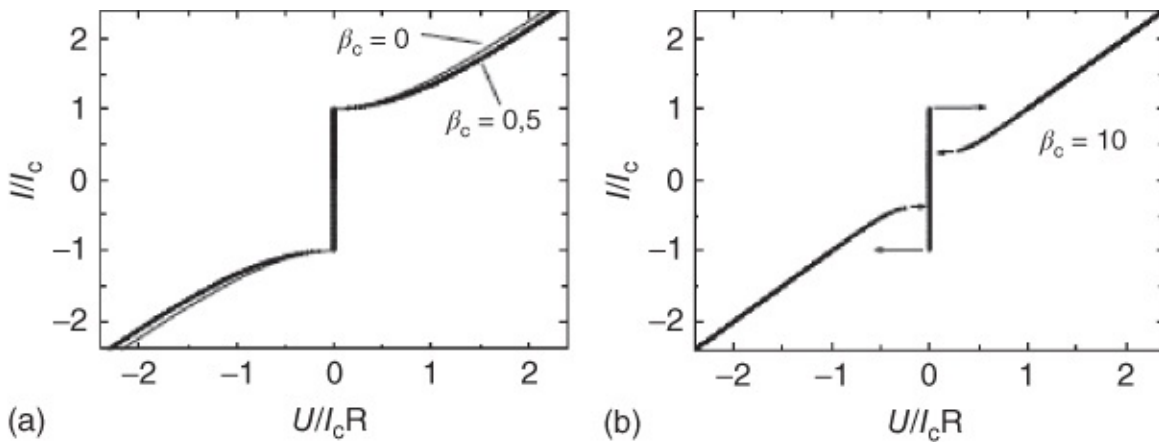


**Figure 6.10** Current–voltage characteristics of Josephson junctions calculated from the RCSJ model.

For comparison, in [Figure 6.11a](#) we show the characteristics of  $24^\circ$   $\text{YBa}_2\text{Cu}_3\text{O}_7$  grain-boundary junctions ( $a$  axes of the two halves of the substrate tilted relative to each other by  $24^\circ$ ) at 4.2 K. At 4.2 K these junctions typically show a small hysteresis, whereas at a temperature of 77 K they are nonhysteretic (see [Figure 6.11b](#)).

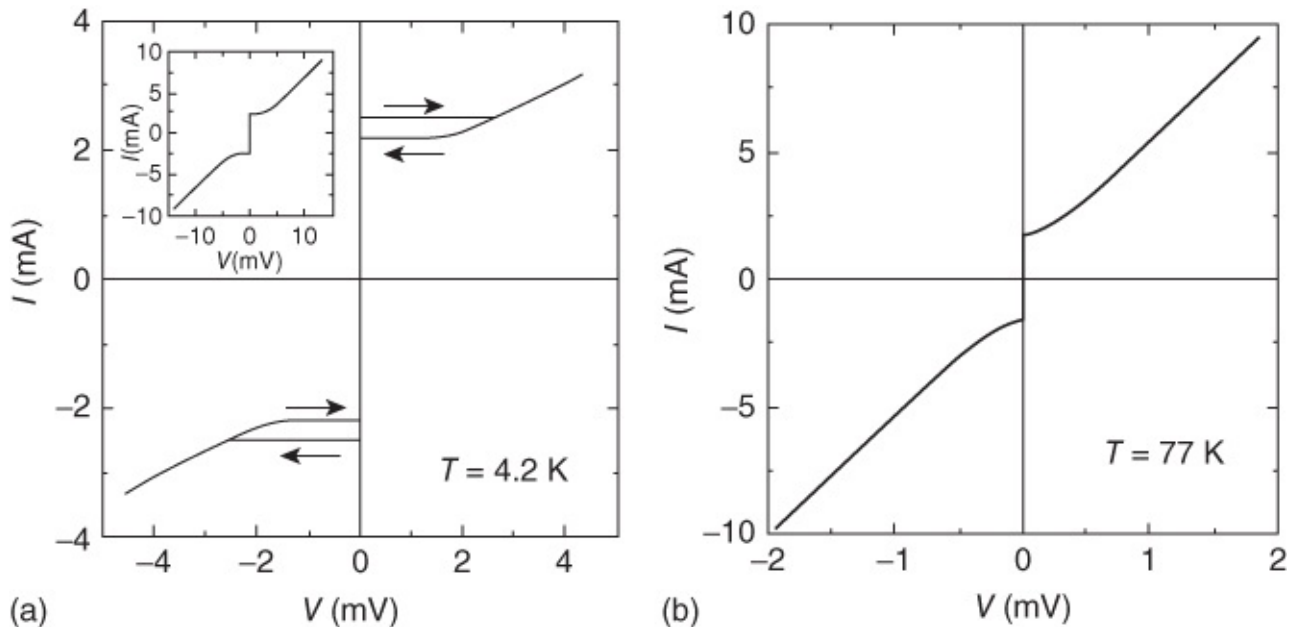


**Figure 6.11** Current–voltage characteristics of  $24^\circ$   $\text{YBa}_2\text{Cu}_3\text{O}_7$  grain-boundary junctions: (a) at 4.2 K [34] and (b) at 77 K. Junction width:  $2.3 \mu\text{m}$ ; film thickness: 120 nm.

(By courtesy of J. Mannhart and C. Schneider, University of Augsburg.)

At the end of this section, we want to discuss briefly how the current–voltage characteristics of Josephson junctions are affected by finite temperatures. With increasing temperature, on the one hand,  $I_c$  and also the product  $I_c R$  decrease, whereas, on the other hand,  $C$  remains approximately constant. However, this means that also  $\beta_c$  decreases with increasing temperature. If at low temperatures the characteristic was hysteretic, near  $T_c$  it will become nonhysteretic. However, with increasing temperature the thermal fluctuations also increase,

which results in particular from the quasiparticle currents symbolized by the resistance  $R$ .<sup>17</sup> If these fluctuations are not too large, the pendulum will only oscillate slightly about its rest position  $\gamma_0$ . However, once in a while, a very large fluctuation will cause a large deflection of the pendulum. If the characteristic is strongly hysteretic as shown in [Figure 6.10b](#), a single deflection of this kind can cause near  $I_c$  the switch of the pendulum into the rotating state, or near  $I_r$  the switch back into the zero-voltage state. We see that the hysteretic regime of the pendulum will be reduced. This reduction is more likely the longer we wait for a large fluctuation, that is, it depends on the speed with which the characteristic is recorded. Also in overdamped junctions the probability for a turnover of the pendulum is larger, the closer  $\gamma_0$  approaches the position  $90^\circ$ . However, after the turnover the pendulum comes to rest again. Therefore, near  $I_c$  a characteristic as shown in [Figure 6.10a](#) will be rounded, and we observe a finite average voltage also below  $I_c$ .

On the other hand, if the statistical fluctuations are very large, the pendulum will oscillate back and forth wildly, and the characteristic will approach more and more an ohmic straight line without any detectable Josephson current.

In the following section, we want to use the pendulum model in order to understand the behavior of Josephson junctions under microwave irradiation.

## 6.3 Josephson Junctions under Microwave Irradiation

If we irradiate a Josephson junction with microwaves of frequency  $f_{ac}$ , this microwave field causes an alternating current across the junction. In the RCSJ model this alternating current can be described as an additional applied current  $I_{ac} \cos(2\pi f_{ac} t)$ . Hence, we are dealing with the situation of the driven physical pendulum.

A harmonic oscillator would simply oscillate with a very high amplitude if  $f_{ac}$  were equal to the eigen-frequency of the oscillator. However, in the case of a nonlinear oscillator, such as the physical pendulum or the Josephson junction, its eigen-frequency decreases with increasing amplitude. We see that within certain limits the oscillator can adjust its eigen-frequency to that of the external drive.

In the case of the rotating pendulum this becomes highly interesting. In the simplest case, within a certain interval of torque values  $M$ , the pendulum will rotate with exactly the driving frequency  $f_{ac}$ . In this case on the characteristic we obtain a range of constant average angular velocity  $\langle \dot{\gamma} \rangle$ . Carried over to the characteristic of the Josephson junction, this means that there exists a certain current interval in which the average voltage is constant. According to the second Josephson equation, on this plateau of constant voltage, we have

$\langle \dot{\gamma} \rangle = 2\pi f = 2\pi f_{ac} = 2\pi \langle U \rangle / \Phi_0$  or  $\langle U \rangle = f_{ac} \Phi_0$ . In a similar way, the pendulum can also synchronize with the frequency of the external drive if its rotation frequency is near an integer multiple  $n$  of the driving frequency. In this case, we obtain steps of constant voltage at the values

$$U_n = n f_{ac} \Phi_0$$

6.15

These steps of constant voltage are referred to as **Shapiro steps** after their discoverer [35]. In his original paper Josephson had already predicted this effect [36]. He had assumed that an alternating *voltage* was applied to the junction.<sup>18</sup> In this case the Josephson equations can be solved analytically.

What is the detailed shape of the current–voltage characteristic of Josephson junctions under microwave irradiation? It turns out that a number of factors are important. This includes the damping of the junction, expressed by the Stewart–McCumber parameter  $\beta_c$ , the amplitude  $I_{ac}$  of the applied alternating current, and its frequency in particular relative to the eigen-frequency  $\omega_{pl} = 2\pi f_{pl}$  of the pendulum (the Josephson plasma frequency).

First let us look at an overdamped junction. In [Figure 6.12a](#) we show characteristics numerically calculated from Eq. (6.13). In this case we have used  $\beta_c = 0.5$  and  $f_{ac} = 0.5f_c = 0.5I_cR/\Phi_0$ , as in [Figure 6.10a](#). The applied current had a d.c. and an a.c. component. With increasing alternating current, the critical current becomes suppressed, and the Shapiro steps develop. Initially, the “step heights,” that is, the current intervals, in which the voltages have the values  $n f_{ac} \Phi_0$ , increase. In [Figure 6.12a](#) we show the corresponding characteristic for  $I_{ac}/I_c = 0.85$ . If  $I_{ac}$  is increased further, one observes that  $I_c$  as well as the height of the Shapiro steps oscillate.<sup>19</sup> This is shown in the inset of [Figure 6.12a](#), where  $I_c$  and the height of the first step ( $n = 1$ ) are plotted versus  $I_{ac}/I_c$ .

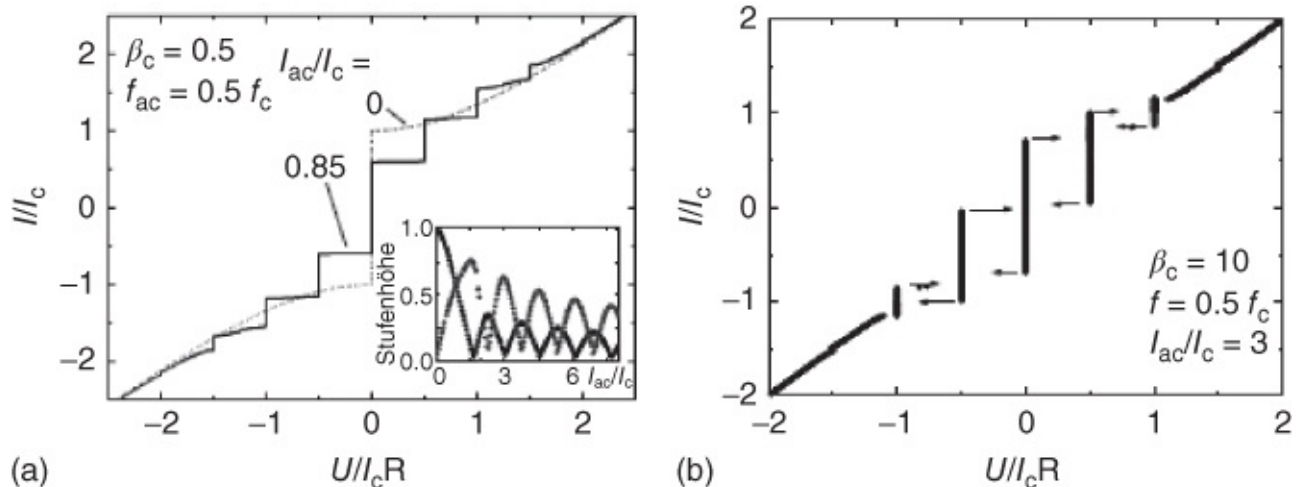


**Figure 6.12** Current–voltage characteristics of Josephson junctions under microwave irradiation calculated from the RCSJ model. (a)  $\beta_c = 0.5$  and (b)  $\beta_c = 10$ . The inset in (a) shows the critical current ( $\bullet$ ) and the height of the first Shapiro step ( $\circ$ ) plotted versus the a.c. amplitude. All currents are given in units of the critical current  $I_c$  in the absence of microwave irradiation.

In [Figure 6.12b](#) we show an analogous calculation for a junction with  $\beta_c = 10$ . We clearly see the Shapiro steps  $n = 1, 2$ , and  $3$  on the current–voltage characteristic. In contrast to [Figure 6.12a](#), now the steps are hysteretic and can only be traversed completely by increasing and

decreasing the applied current several times (see arrows in [Figure 6.12b](#)). At high values of  $\beta_c$ , we can even achieve the situation in which a number of steps cross the  $I = 0$  axis. In this case one speaks of “zero-crossing steps.” This case is highly important for the application of Josephson junctions as voltage standards, as will be discussed in more detail in [Section 7.7.1](#).

Also in this case the maximum supercurrent and the height of the Shapiro steps oscillate with increasing a.c. amplitude. The height of the  $n$ th Shapiro step is proportional to the absolute value of the  $n$ th Bessel function.<sup>20</sup> For comparison, in [Figure 6.13](#) we show measured current–voltage characteristics of an overdamped and an underdamped junction.

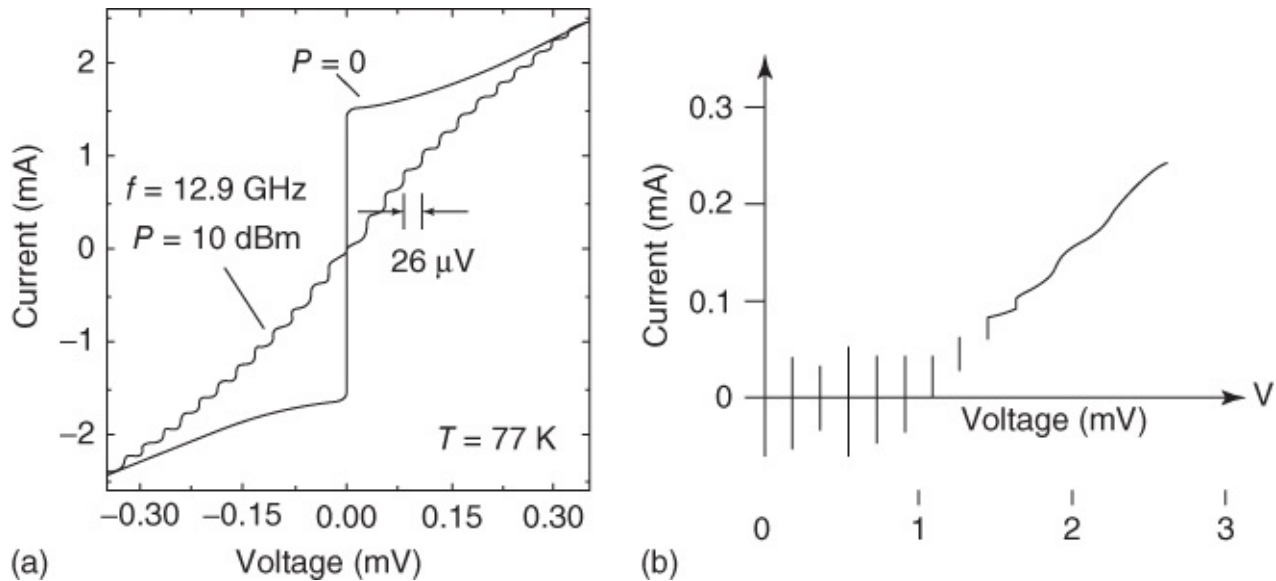


**Figure 6.13** Measured current–voltage characteristics of Josephson junctions under microwave irradiation. (a) Overdamped  $\text{YBa}_2\text{Cu}_3\text{O}_7$  grain-boundary junction [37]. (Courtesy of C. Schneider and J. Mannhart.) (b) Underdamped Nb tunnel junction [38]; microwave frequency: 94 GHz.

(© 2000 Rev. Sci. Instr.)

We note that, for unfavorable microwave frequencies and microwave powers, chaotic behavior can be observed, instead of the stable Shapiro steps. This happens in particular in underdamped junctions at microwave frequencies below the Josephson plasma frequency. In the RCSJ model, the latter can be written as  $f_{\text{pl}} = f_c/\beta_c^{1/2}$ . The appearance of chaos is a well-known phenomenon of driven nonlinear oscillators, just like the Josephson junction or the physical pendulum. A detailed discussion of chaotic phenomena in Josephson junctions can be found in [39].

Finally, we want to see the maximum frequencies up to which Shapiro steps can be observed. Based on the RCSJ model, a natural limit arises from the fact that at high frequencies larger and larger a.c. amplitudes are needed to generate Shapiro steps. The reason is the capacity of the junction, which in the end represents a short in the Josephson junction at high frequencies.

For real Josephson junctions, another natural limit is given by the energy gap of the used superconductor. In the RCSJ model we had tacitly assumed that, in the first Josephson equation

$I_J = I_c \sin \gamma$ , the amplitude  $I_c$  was independent of the oscillation frequency of the Josephson currents. However, the microscopic theory indicates that  $I_c$  strongly decreases for frequencies above  $\Delta_0/h$ . Correspondingly, for microwave frequencies above this value the amplitude of the Shapiro steps rapidly approaches zero. For conventional superconductors this leads to a restriction to frequencies below 1–2 THz. On the other hand, in high-temperature superconductors, where the maximum energy gap  $\Delta_{0,\max}$  is decisive, at least in principle the Shapiro steps should be observable up to the frequency range 10–20 THz. Indirect indications for alternating Josephson currents with such high frequencies came from the observation of resonances between the Josephson oscillations and the lattice vibrations of the system [10, 40, 41]. So far, Shapiro steps have been observed directly up to about 2.5 THz<sup>21</sup> [42].

## 6.4 Vortices in Long Josephson Junctions

In the previous two sections, we have tacitly assumed that all currents flow spatially homogeneously across the barrier of the Josephson junction. This has led us to the analog of the physical pendulum. In this section, we want to go one step further and explicitly take into account the spatial extension of the Josephson junction. We will see that also in this case we can develop an analog of the physical pendulum. However, now we must deal with a whole chain of pendulums, which are attached to a revolving (rubber) band.

For this purpose, we look at the Josephson junction shown schematically in [Figure 6.14](#). The length of the junction along the  $x$ -direction is  $L$ . A magnetic field  $B_a$  is applied along the  $y$ -direction. Furthermore, we assume that the current flow in the  $z$ -direction is homogeneous in the  $y$ -direction, that is, we only allow a spatial dependence of the Josephson currents along the  $x$ -direction.

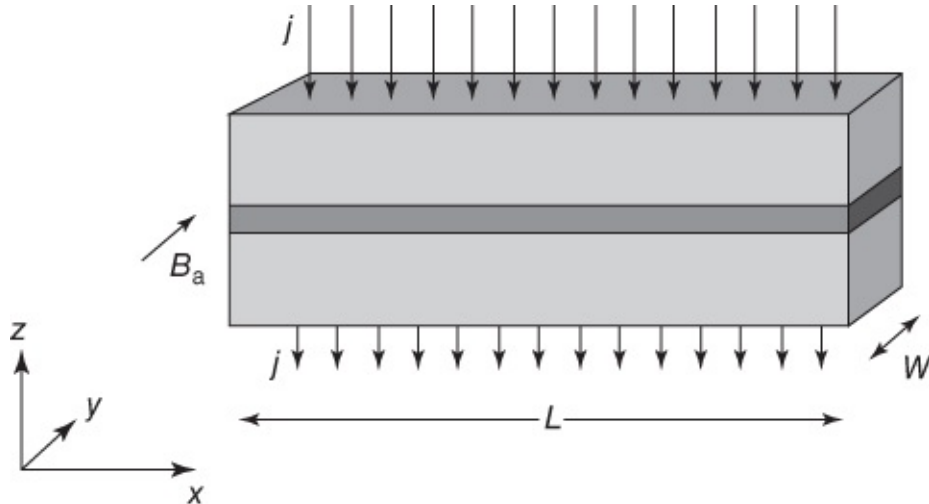


[Figure 6.14](#) Schematics of a Josephson junction extended in the  $x$  direction.

Again we describe the current density locally across the junction using the RCSJ model:

$$j_z(x) = j_c \sin \gamma + \frac{\Phi_0}{2\pi\rho t_b} \dot{\gamma} + \frac{\epsilon\epsilon_0\Phi_0}{2\pi t_b} \ddot{\gamma} \quad 6.16$$

Here, compared to Eq. (6.11), the resistance  $R$  has been replaced by the resistance  $\rho t_b$  (where  $\rho$  is the resistivity and  $t_b$  is the thickness of the barrier layer) per unit area. For  $C$  we have used the relation  $C = \epsilon\epsilon_0 A/t_b$  (where  $A$  is junction area and  $\epsilon$  is the dielectric constant); and  $j_c$  denotes the critical current density averaged over the junction.

Now we must note that currents flowing parallel to the barrier layer in the  $x$ -direction generate magnetic fields, which in turn affect the spatial variation of  $\gamma(x)$  together with the externally applied fields (see Section 1.5.2, Eq. (1.68)). Using Maxwell's equations (initially without an applied current), we obtain after a short calculation

$$\lambda_J^2 \frac{d^2\gamma}{dx^2} = \frac{j_z(x)}{j_c} \quad 6.17$$

with the Josephson penetration depth Eq. (1.69):

$$\lambda_J = \sqrt{\frac{\Phi_0}{2\pi\mu_0 j_c l_{\text{eff}}}}$$

Here  $l_{\text{eff}}$  is connected with the thickness  $d$  of the superconducting electrodes and with the London penetration depths  $\lambda_L$  of both superconductors, assumed to be identical. We have  $l_{\text{eff}} = t_{\text{eff}} + d_{\text{eff}}$ , with  $d_{\text{eff}} = \lambda_L / \sinh(d/2\lambda_L)$  and  $t_{\text{eff}} = t_b + 2\lambda_L \tanh(d/2\lambda_L)$ . For  $d \ll \lambda_L$ , this reduces to  $d_{\text{eff}} \approx 0$ ,  $t_{\text{eff}} \approx 2\lambda_L + t_b$ , and  $l_{\text{eff}} \approx t_{\text{eff}}$ . In the opposite limit  $d \gg \lambda_L$ , we have  $d_{\text{eff}} \approx 2\lambda_L^2/d$ ,  $t_{\text{eff}} \approx t_b + d$ , and  $l_{\text{eff}} \approx d_{\text{eff}}$ .

This equation must be supplemented by suitable boundary conditions for the applied magnetic field  $B_a$  and for the applied current density  $j$ . We assume that the current is injected in  $-z$ -direction into the upper electrode and is extracted from the lower electrode. The field  $B_a$  is applied in the  $y$ -direction and is spatially homogeneous. With these conditions, one obtains

$$\lambda_J^2 \frac{d^2\gamma}{dx^2} = \frac{j_z(x) - j}{j_c} \quad 6.18$$

$$\left. \frac{d\gamma}{dx} \right|_{x=0} = \left. \frac{d\gamma}{dx} \right|_{x=L} = \frac{2\pi}{\Phi_0} B_y(0) \quad t_{\text{eff}} \approx \frac{2\pi}{\Phi_0} B_a(0) \quad t_{\text{eff}} \quad 6.19$$

On the right-hand side of Eq. (6.19), the magnetic field at the edge of the junction was approximated by the applied field. If we insert Eq. (6.16) into Eq. (6.18), we obtain

$$\lambda_J^2 \frac{d^2\gamma}{dx^2} - \omega_{\text{pl}}^{-2} \frac{d^2\gamma}{dt^2} = \sin \gamma + \tau_c \frac{d\gamma}{dt} - \frac{j}{j_c} \quad 6.20$$

Here we have introduced the abbreviations  $\tau_c = \Phi_0/(2\pi j_c \rho t_b)$  and  $\omega_{\text{pl}}^{-2} = \epsilon\epsilon_0\Phi_0/(2\pi j_c t_b)$ . We easily

see that  $\omega_{\text{pl}}$  is exactly the Josephson plasma frequency rewritten in terms of the specific quantities  $\epsilon$  and  $j_c$ . We have discussed the Josephson plasma frequency already in the case of point-like junctions. The quantity  $\tau_c$  is related to the characteristic frequency  $f_c$  by  $\tau_c = 1/(2\pi f_c)$ . In the case of point-like junctions,  $\tau_c$  represents the constant by which we normalized the time.

In the case of a homogeneous current density  $j_z(x)$  the term  $d^2y/dx^2$  in Eq. (6.20) vanishes, and we recover the RCSJ Eq. (6.11), but now for the current density. In the pendulum model, this means that instead of a *single* pendulum we are dealing with a chain consisting of very many pendulums, rigidly connected to each other. If one of these pendulums is deflected by an angle  $y$ , then also all other pendulums are deflected by the same angle. The arrangement acts like a single pendulum.

Also the term  $\lambda_L^2 d^2y/dx^2$  can be interpreted within a pendulum model. We imagine that the rotation axis of the pendulum consists of a rubber band that can be twisted. Then this term corresponds to the torque from the two neighboring pendulums acting back on the pendulum at the location  $x$ , if the pendulums are twisted relative to each other.<sup>22</sup>

In the case of  $j = 0$  and negligible damping, Eq. (6.20) is also referred to as the **sine-Gordon equation**. With the additional terms<sup>23</sup>  $j/j_c$  and  $\tau_c dy/dt$ , one obtains the “perturbed sine-Gordon equation.” We have written Eq. (6.20) in a form indicating that the sine-Gordon equation represents a wave equation, which, however, is nonlinear because of the term  $\sin y$ . This equation has been studied intensively both in mathematics as well as in physics.

The pendulum model allows us to recognize immediately a number of possible “excitations” arising from Eq. (6.20):

- We can slightly deflect one of the pendulums and then let it go. In this case, the deflection will propagate like a wave along the chain. In a Josephson junction these wave-like excitations are referred to as **Josephson plasma waves**. They correspond to electromagnetic waves, propagating in the  $x$ -direction along the barrier layer and decaying gradually due to the damping term. At a given location  $x$ , one observes that  $y(x)$  oscillates about a position  $y_0$  at rest.

In the case  $j = 0$  we can set  $\sin y \approx y$  in Eq. (6.20), and with the ansatz  $y(x) \propto e^{i(kx-\omega t)}$  we can find a connection between the wave vector  $k$  and the frequency  $\omega$ . For negligible damping, one finds

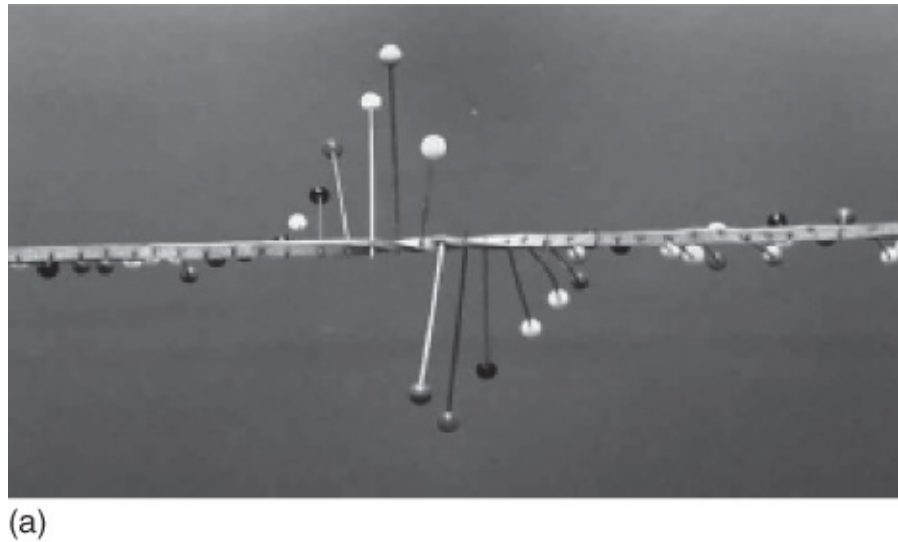
$$-\lambda_J^2 k^2 + \omega^2/\omega_{\text{pl}}^2 = 1 \quad \text{6.21a}$$

or

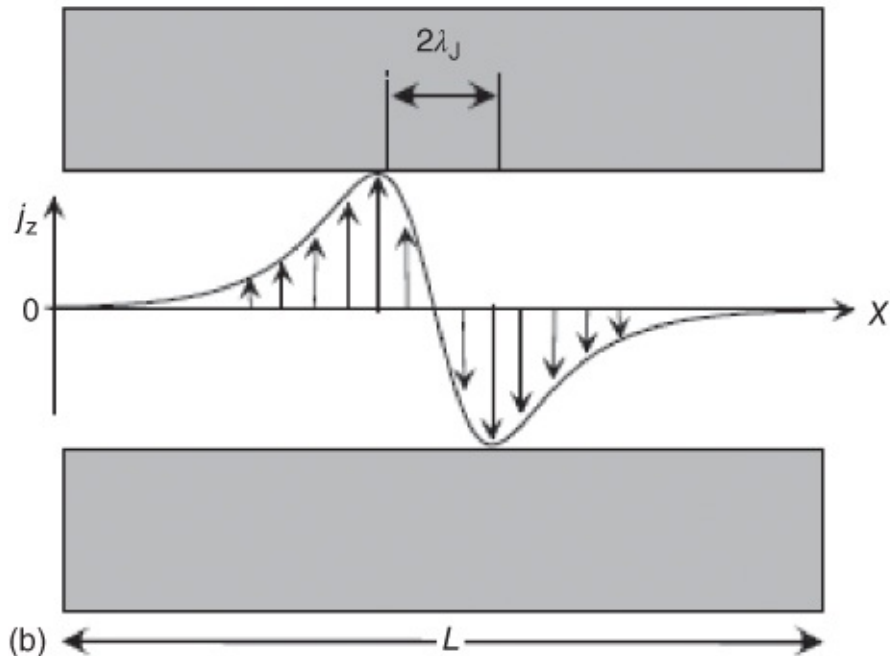
$$\omega = \sqrt{\omega_{\text{pl}}^2 + \bar{c}^2 k^2} \quad \text{6.21b}$$

with the “Swihart velocity”  $\bar{c} = \omega_{\text{pl}} \lambda_J$ . In the case  $k = 0$  we have  $\omega = \omega_{\text{pl}}$ , and for large values of  $k$  we obtain  $\omega \propto \bar{c}k$ . Comparing this with the expression  $\omega = ck$  for the

propagation of electromagnetic waves in vacuum, we see that  $\bar{c}$  plays a role quite analogous to the light velocity  $c$ . However, typically  $\bar{c}$  is only  $10^{-2}$ – $10^{-4}$  of this value. We can also discuss in a similar way the case  $j \neq 0$ , and we find an expression analogous to Eq. (6.21b), in which, however,  $\omega_{\text{pl}}$  must be replaced by  $\omega_{\text{pl}}[1 - (j/j_c)^2]^{1/4}$ . We see that for  $j \rightarrow j_c$  the minimum plasma frequency approaches zero.



(a)



(b)

**Figure 6.15** A “vortex” in a chain of pendulums (a) or in a Josephson junction (b). The chain of pendulums is realized by means of pins stuck into a rubber band. For a vortex at rest (vortex center at  $x_0$ ), the solution of the sine-Gordon equation is  $y(x) = 4 \arctan \{ \exp[-(x - x_0)/\lambda_J] \}$ .

- We can also fix one end of the chain of pendulums and twist the other end once by  $360^\circ$ . In this case one of the pendulums has completely turned over. If, starting at this pendulum, we move along the chain of pendulums, the pendulums are seen to adopt a helical arrangement, as shown in [Figure 6.15](#). If the chain of pendulums is sufficiently long, we can push the

twist along the chain without changing its shape. Obviously, this twist can only escape from the chain at its ends. It appears that the twisted pendulums collectively act like a particle moving along the chain, and which cannot be destroyed in its interior.

What are the consequences of this type of excitation for the Josephson junction? Obviously,  $\gamma(x)$  changes by  $2\pi$ , if we move over the twisted location. However, the change of  $\gamma$  is always equivalent to a change of the magnetic flux within the junction. In particular, a change by  $\pm 2\pi$  means that the flux is increased or decreased by one flux quantum  $\Phi_0$ . We see that the twisting describes a vortex. This can be seen even more clearly if we look at the supercurrent density  $j_c \sin \gamma(x)$ . If  $\gamma(x)$  increases from 0 up to  $2\pi$ , at first the current is zero, then it flows in the positive direction, at  $\gamma = \pi$  it reaches zero again, then it increases in the negative direction, and finally it vanishes again for  $\gamma \rightarrow 2\pi$ . The currents flowing “upward” across the barrier for  $\gamma(x) < \pi$  continue to flow within the upper electrode because of current conservation. Then for  $\gamma(x) > \pi$  they flow again “downward.” The supercurrents in the lower electrode complete the circulating current. In this way, we have reconstructed the current distribution around a vortex at  $\gamma(x) = \pi$ . The corresponding vortex is a “Josephson vortex” or “fluxon.” In a more general way, one also speaks of a “soliton.”

Obviously, in a Josephson junction the fluxon can be moved by an applied current because of the Lorentz force acting on the fluxon. For the chain of pendulums, a similar effect can be achieved by applying a constant torque to the whole rubber band.

It turns out that a fluxon behaves very similarly to a particle obeying the special theory of relativity, experiencing, for example, the Lorentz contraction. In this case the Swihart velocity takes the role of the light velocity. It is the maximum velocity that the fluxons can reach in a Josephson junction.<sup>24</sup> If a fluxon moves in the  $x$ -direction with velocity  $v$ , two things can happen. First, in the  $x$ -direction, it becomes shorter proportional to  $1/\sqrt{1 - v^2/c^2}$ . This exactly corresponds to the Lorentz contraction. Second, a voltage change across the junction is connected with the temporally changing phase difference  $\gamma$  (or with the temporally changing magnetic flux). The moving flux quantum electrically corresponds to a voltage pulse, where the time integral of this pulse exactly yields one  $\Phi_0$ . Of course, with increasing velocity this voltage pulse becomes sharper.

So far we have discussed two elementary excitations of the spatially extended Josephson junction: Josephson plasma waves and fluxons. One can imagine that these two excitations lead to a rich dynamics of the junction, which is also visible in the current–voltage characteristic.

Let us first discuss Josephson plasma waves. In order to excite them effectively, the external “drive” should have a frequency and also a wavelength, well adjusted to the plasma waves. In the simplest case, this is an infinitely large wavelength. Then we go back to the plasma oscillations in a homogeneous junction. For example, they can be excited by externally applied microwaves, and they can be detected by means of the high-frequency radiation emitted from the junction [43].

However, Josephson plasma oscillations can also be excited by the Josephson alternating

currents themselves or by the high-frequency electric fields induced by the currents. As in every driven oscillator, during the variation of the frequency of the alternating Josephson current one traverses a resonance curve, where the width and the height of the resonance depend on the damping, more exactly on the quality, of the oscillator. However, in the case of nonlinear oscillators, we must take into account that, at high amplitudes of the resonance, instabilities appear, which cause a breakdown of the resonance. In the case of a small underdamped Josephson junction, the junction simply switches back to the zero-voltage state.

The Josephson current can be spatially modulated by an applied magnetic field, as we have already seen in [Section 1.5.2](#) in our discussion of the magnetic field dependence of the maximum supercurrent of the “short” Josephson junction. In this way, plasma waves with finite wavelength can be excited. Now the finite extension of the junction must still be taken into account. This preferably causes the excitation of standing waves, where the largest allowed wavelength along the barrier corresponds to a half-wave within the junction satisfying the condition<sup>25</sup>  $L = \lambda/2 = \pi/k$ . The additional resonances correspond to  $n$  half-waves along the barrier, that is, they obey the condition  $L = n\lambda/2 = n\pi/k$ . In short junctions the “wavelength” of the Josephson current in the  $x$ -direction is proportional to the applied magnetic field or to the magnetic flux within the junction. The condition  $L = n\lambda/2$  means that the magnetic flux should amount to  $n\Phi_0/2$ , that is, it should correspond to magnetic fields at which the critical supercurrent across the junction attains a minimum. If the alternating Josephson currents have excited one of the standing waves, they remain locked to the standing wave during not too large variations of the applied current.

Analogous to the Shapiro steps during microwave irradiation, in this case we observe “Fiske steps” on the current–voltage characteristic, at which the voltage changes only little<sup>26</sup> [44]. The small change of the voltage results from the finite width of the corresponding resonance curves. An accurate analysis of these resonances was given by Kulik [45]. For a more detailed discussion, see also [M15]. In [Figure 6.16](#)a we show the corresponding structures on the current–voltage characteristic of a Sn–SnO–Sn junction [44].

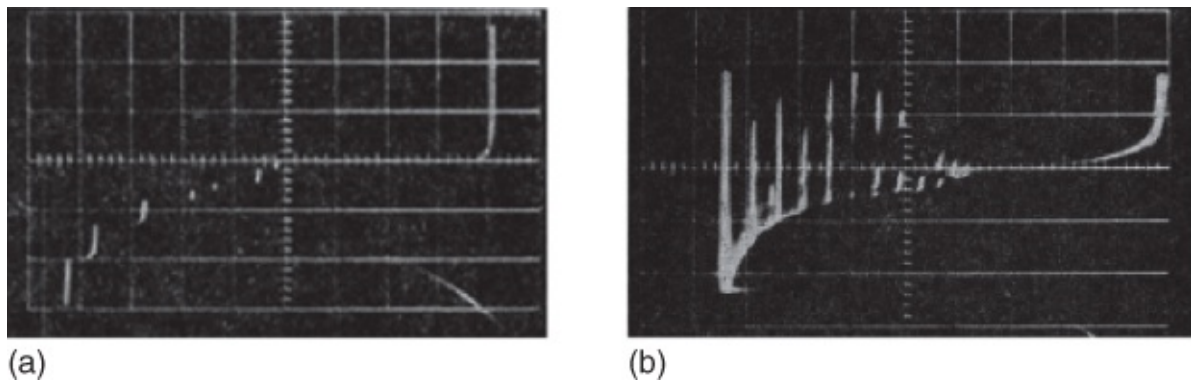


**Figure 6.16** (a) Current–voltage characteristic of a Sn–SnO–Sn junction in a magnetic field of 0.52 mT parallel to the barrier layer. (b) Superposition of current–voltage characteristics for magnetic fields between 0 and 0.8 mT. Vertical scale: 200  $\mu\text{A}/\text{cm}$ ; horizontal scale: 100  $\mu\text{V}/\text{cm}$ . Measuring temperature: 1.93 K [44].

In this case a magnetic field of 0.52 mT was applied parallel to the barrier layer. The zero

point of the coordinate system is in the lower left corner of the figure. In this particular magnetic field, we see a number of vertical branches before the energy gap  $2\Delta_{\text{Sn}}/e$  is reached (on the right side of the figure). At other values of the magnetic field, these vertical branches appear with another amplitude and perhaps at another voltage level. If many characteristics for different fields are superimposed, we obtain a pattern such as shown in [Figure 6.16b](#). In this case, the magnetic field was varied between 0 and 0.8 mT. We clearly see a number of equidistant and nearly perpendicular branches, the Fiske resonances.

Next let us turn to the second form of excitations, the fluxons. The spatial extension of a fluxon at rest is about  $2\lambda_J$  (see [Figure 6.15](#)). Therefore, in order to observe phenomena of fluxon dynamics, we need a Josephson junction whose length  $L$  is much larger than  $\lambda_J$ . Typically, the Josephson penetration depth is in the range of a few micrometers. Hence, the above condition can be achieved easily. On the other hand, sophisticated fabrication techniques are needed to prepare a short Josephson junction with dimensions comparable to or smaller than  $\lambda_J$ . (In the latter case, we return to the physics of Josephson junctions we have already discussed in [Section 1.5.2](#)).

If two fluxons of opposite sign (a fluxon and an antifluxon) approach each other, they can either annihilate each other or simply pass through each other if their velocity is sufficiently high. If the fluxons arrive at the edge of a Josephson junction (or of a chain of pendulums), they can either leave the junction or, again for sufficiently high velocity, they can be reflected and move back with the opposite sign. If a fluxon–antifluxon pair annihilates itself, Josephson plasma waves are generated during this process. The same happens if a fluxon leaves the junction. In this case, electromagnetic waves are emitted into the external space: the junction emits microwaves.

Now we must answer the question of how fluxons or antifluxons can enter a Josephson junction. Interestingly, this is also possible without the application of an external magnetic field. Just in this case we observe phenomena such as the reflection of rapidly moving fluxons at the edges of the junction. If the current across a Josephson tunnel junction, which initially contains no fluxons, is increased starting from zero, upon exceeding the critical current the junction will enter the resistive state, in which the currents flow across the barrier more or less homogeneously. In this case the currents have an alternating current component, the frequency of which is given by the Josephson relation:  $\omega_J = 2\pi f_J = 2\pi \langle U \rangle / \Phi_0$ . If, starting from this state, we reduce the applied current and, hence, the (average) voltage  $\langle U \rangle$  across the junction, at some stage the frequency  $\omega_J$  will become equal to the frequency of the Josephson plasma waves (Eqs. [\(6.21a\)](#) and [\(6.21b\)](#)) such that a standing wave with a specific wave vector  $k$  can develop. In this case the supercurrents experience a spatial modulation. Since in tunnel junctions below the energy gap the damping is very small, the standing wave may reach a very high amplitude. If this amplitude becomes equal to  $j_c$ , the standing wave cannot remain stable. Instead, fluxon–antifluxon pairs are generated spontaneously. Because of the Lorentz force exerted by the applied current, the fluxons and antifluxons move through the junction and are reflected at the edges.

In this new state, the average voltage across the junction changes. We assume that there are  $n$  fluxons within the junction. These fluxons move with a certain velocity  $v$ . A given fluxon needs time  $T = 2L/v$  to be reflected back and forth once. If we determined the phase difference  $\gamma(t)$  at a fixed location, we would find that, at each of the two passages of the fluxon,  $\gamma$  would have changed by the amount  $\Delta\gamma = 2\pi$ . So we have  $\Delta\gamma/T = 4\pi/T = 4\pi/(2L/v) = 2\pi v/L = 2\pi \langle U \rangle / \Phi_0$ , or  $\langle U \rangle = \Phi_0 v / L$ . According to the induction law, this means that during time  $T$  the flux has changed by  $2\Phi_0$ . This is correct since one flux quantum moved in one direction and another flux quantum in the other direction.

If there are  $n$  fluxons within the junction, this results in an average voltage  $\langle U_n \rangle = n\Phi_0 v / L$ . The fluxon velocity is determined from the balance between the Lorentz force and the damping force. However, we must remember that fluxons behave like relativistic particles, the velocity of which cannot exceed  $\bar{c}$ . Hence, we obtain the maximum voltage

$$\langle U_{n,ZFS} \rangle = n\Phi_0 \bar{c} / L \quad \text{6.22}$$

Following the spontaneous generation of the vortex–antivortex pairs at a certain applied current, which then move with velocity  $v < \bar{c}$ , we can reduce the current and, hence, reduce also  $v$  and the voltage. However, below a certain limiting voltage, the pairs annihilate themselves or are no longer reflected at the junction edge. In this case one finds another state that consists of a smaller number of fluxons, or the junction returns to the zero-voltage state. On the other hand, if we increase the current again, the velocity  $v$  will approach the velocity limit  $\bar{c}$ , and the average voltage will approach the limit (Eq. (6.22)). Above a maximum current, which is smaller than  $I_c$ , the junction switches back to the quasiparticle characteristic.

In this way we obtain a whole number of branches, the so-called zero-field steps, on the current–voltage characteristic. The branches differ in the number of fluxons moving back and forth in the junction [46]. We note that in the relativistic regime neighboring branches differ by  $\Delta U = \Phi_0 \bar{c} / L$ . This is exactly twice the voltage distance between neighboring Fiske resonances. In [Figure 6.17](#) we show a corresponding measurement [47].

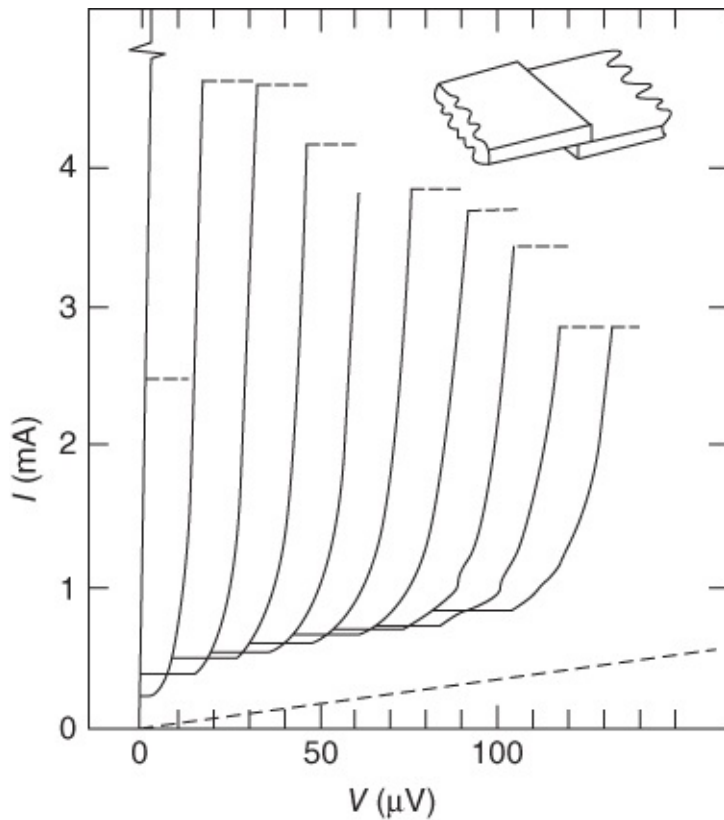


**Figure 6.17** Fluxons that are reflected back and forth cause zero-field steps in an Nb–Pb tunnel junction. Length of the junction: 1 mm, width: 15  $\mu\text{m}$ . Josephson penetration depth: about 29  $\mu\text{m}$ . Measuring temperature: 4.2 K. Neighboring branches each correspond to one additional fluxon [47].

The motion of fluxons can be observed very nicely if the two ends of a Josephson junction are joined together, that is, if we have ring-shaped junctions. If we can inject fluxons with only a *single* polarity into such a junction, these fluxons can neither annihilate each other anymore nor escape from the junction, as long as the electrodes remain superconducting. For the pendulum model, this corresponds to the situation where the pendulum chain, being open initially, is twisted by  $n$  revolutions, and where the ends of the chain are then joined together. Obviously, the twisting of the chain then cannot be removed as long as the rubber band remains intact.

A number of methods have been developed for trapping fluxons within a ring. In the simplest case the junction is cooled below  $T_c$ , perhaps under a small applied magnetic field gradient, hoping that fluxons are nucleated. To generate fluxons directly below  $T_c$  is much more reproducible. In the pendulum model we could imagine that the rubber band is cut at a certain location, then twisted by  $360^\circ$ , and finally joined together again. This can be achieved exactly by means of an electron beam or a laser beam, which is focused on the junction and is scanned radially from the outside to the inside across one of the two superconducting electrodes in the presence of a small magnetic field. During this process the electrode is locally heated above  $T_c$  [48].

In a third highly elegant and reproducible method, which was only recently demonstrated, in the language of the pendulum model, two neighboring pendulums are twisted relative to each

other by  $360^\circ$  and then joined together again. During this twisting, an opposite twisting, that is, an antifluxon, is generated, which can move freely in contrast to the rotation between the two pendulums joined together. In a Josephson junction this twisting and joining together is achieved by means of a control current, which generates a flux quantum  $\Phi_0$  in the barrier at a certain location of the junction [49].

In [Figure 6.18](#) we show the superposition of current–voltage characteristics of a ring-shaped Nb–Pb Josephson tunnel junction, into which nine fluxons were injected sequentially by means of an electron beam [48]. We see a total of nine branches, each of which starts linearly at small voltages (fluxon velocities) and then, with a nearly vertical slope, approaches a voltage limit, which is proportional to the number of fluxons within the ring.

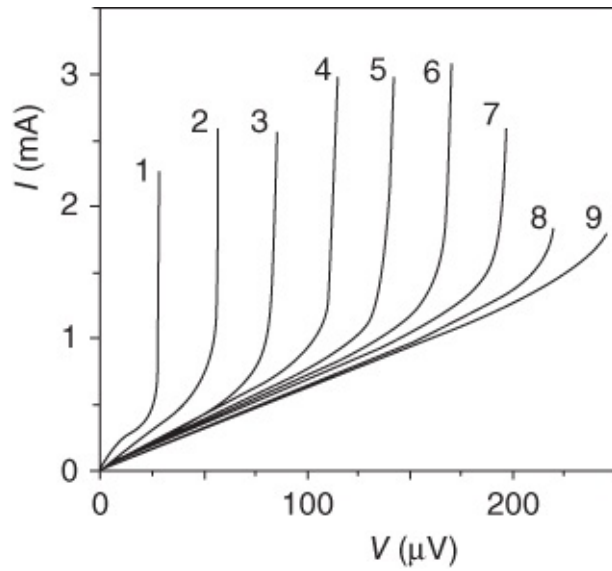


**Figure 6.18** Superimposed current–voltage characteristics of a ring-shaped Nb–Pb Josephson tunnel junction, into which nine fluxons were injected sequentially by means of an electron beam. The numbers indicate the number of fluxons within the ring. Inner diameter of the ring: 100  $\mu\text{m}$ ; outer diameter: 150  $\mu\text{m}$  [48].

If a ring-shaped Josephson junction (and correspondingly also a junction with another geometry) is locally heated with an electron beam, the electrical properties of the junction change at this location. For example, moving fluxons are slowed down somewhat resulting in a reduced voltage drop across the junction. The observed voltage changes are particularly high if a location is heated where a fluxon collides with another object, for example, with a fluxon at rest [50] or with an antifluxon moving in the opposite direction. This property can be utilized to obtain spatially resolved images of these collisions. In [Figure 6.19](#) we show the example of a ring-shaped Nb–Pb tunnel junction, in which two fluxon–antifluxon pairs existed [51]. [Figure 6.19a](#) indicates the geometry. Due to the applied current, the fluxons and the antifluxons move in opposite directions. Hence, during each revolution, the two fluxons collide with the two antifluxons. In this case during the various revolutions the collisions always happen at the same location. Therefore, one observes a relatively large change of the voltage drop across the sample as soon as the electron beam is focused on the collision zone. In [Figure 6.19b,c](#) we see the beam-induced voltage change as a function of the location of the beam focus on the sample.

In both images the collision zones are indicated by the bright regions. In [Figure 6.19](#)b the applied current was small, and the fluxons moved only with a nonrelativistic velocity. In this case the collision zones are relatively long. However, in the case of [Figure 6.19](#)c the fluxon–antifluxon pairs moved with nearly the Swihart velocity  $\bar{c}$  and, therefore, they appear strongly contracted relativistically (Lorentz contraction). Now the collision regions are much sharper.

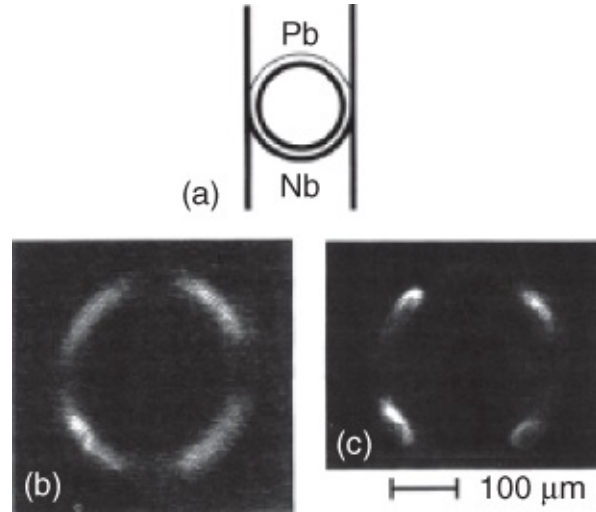


**Figure 6.19** Imaging of fluxons in a ring-shaped Josephson tunnel junction by means of low-temperature scanning electron microscopy. (a) Geometry of the ring (inner diameter: 100  $\mu\text{m}$ ; outer diameter: 120  $\mu\text{m}$ ; circumference in units of  $\lambda_J$ : 5.8). Measuring temperature: 5 K. In the ring there are two moving fluxon–antifluxon pairs. The locations where the collisions between the fluxons and the antifluxons happen are indicated by the bright signal. Image (b) shows the collisions for a small bias current and a low fluxon velocity. Image (c) refers to a fluxon velocity near the Swihart velocity  $\bar{c}$  [51].

Now we return again to long, open Josephson junctions. So far we have discussed these junctions only in the absence of an external magnetic field. If we slowly increase the external field starting from zero at first without an applied current, the Josephson junction generates a diamagnetic shielding current, that is, it behaves similarly to a homogeneous superconductor in the Meissner state.<sup>27</sup> However, these Josephson shielding currents decay away from the edge on the length scale  $\lambda_J$ , that is, much slower than the shielding currents in a homogeneous superconductor, which decay on the length scale  $\lambda_L$ . This can be seen mathematically if in Eq. (6.20) initially we set all time-dependent terms and the applied current equal to zero and then use  $\sin \gamma \approx \gamma$ . Then we obtain  $\lambda_J^2 d^2 \gamma / dx^2 = \gamma$ , and together with the boundary condition (6.19) we find the exponential decay of  $\gamma(x)$  and, hence, also of the Josephson current. If the field is increased further and further, at some stage fluxons enter the junction from both edges. If now a current is also applied, these fluxons start moving as soon as the pinning forces are exceeded. In this case the fluxons move through the junction in one direction, and new vortices are continuously supplied at one end. If the distance between the vortices is  $l$  and if they move with a velocity  $v$ , obviously the vortices arrive at the edge of the junction with the frequency  $f = v/l$ . Each vortex passing a location  $x_0$  increases the phase difference  $\gamma$  there by  $2\pi$ . Hence, according to the second Josephson equation, we also have an average voltage of  $\Phi_0 f = \Phi_0 v/l$ .

Now we can express the distance  $l$  in terms of the applied field  $B_a$  and the effective thickness  $t_{\text{eff}}$  of the junction. The magnetic flux in the junction is  $B_a t_{\text{eff}} L$ . If this just corresponds to  $n$  flux quanta, we have  $n\Phi_0 = B_a t_{\text{eff}} L$ , or  $\Phi_0 = B_a t_{\text{eff}} L/n$ . We have exactly one flux quantum within the length  $l = L/n$ . The voltage across the junction can be written as  $U_{\text{FF}} = B_a t_{\text{eff}} v$ . Also in this case  $\bar{c}$  is the velocity limit of the fluxon motion. Hence, we obtain a voltage limit  $U_{\text{FFS}} = B_a t_{\text{eff}} \bar{c}$ , which is slowly approached by the voltage across the junction with increasing applied current.

This structure of the current–voltage characteristic is referred to as **a flux-flow step**. In [Figure 6.20](#) this is shown for the case of a numerical simulation, in which the sine-Gordon equation ([6.20](#)) was used. We see the steep parts of the characteristic up to currents of about 0.65 of the maximum supercurrent in zero field. At higher currents the junction switches into the resistive state corresponding to the quasiparticle branch of a tunnel junction. We note that a fine structure is superimposed on this coarse structure. These are the Fiske resonances, which can also be excited in long Josephson junctions.

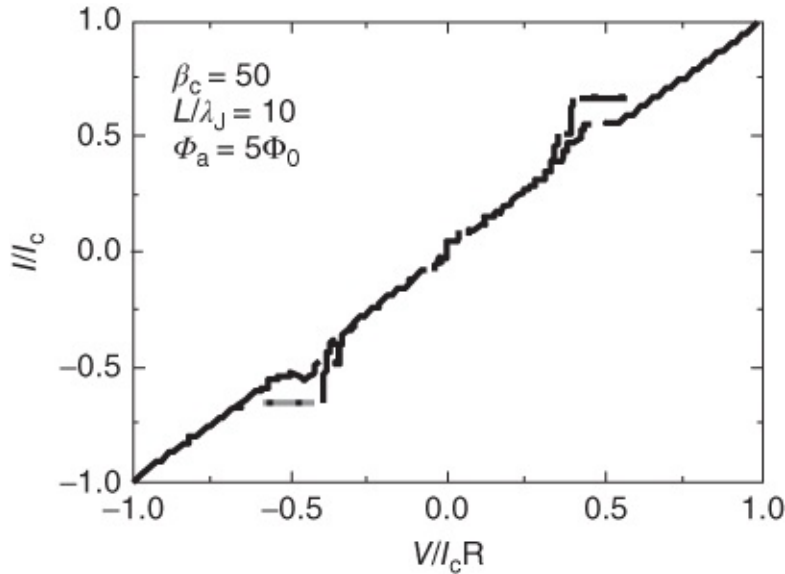


**Figure 6.20** Current–voltage characteristic of a long Josephson junction in an external magnetic field calculated from Eq. ([6.20](#)) (applied magnetic flux:  $5\Phi_0$ ). Junction length:  $10\lambda_J$ . Damping parameter  $\beta_c = (f_c/f_{\text{pl}})^{1/2} = 50$ .

In this and the previous section, we have discussed a whole number of dynamic properties of Josephson junctions, which affect the current–voltage characteristic in the form of Shapiro steps, Fiske resonances, zero-field steps, or flux-flow steps. We have discussed these properties in some detail, not only because they are interesting from the point of view of nonlinear dynamics, but also because they represent the foundation for the application of Josephson junctions at high frequencies, say, as voltage standards or as flux-flow oscillators. We will return to these subjects in [Chapter 7](#).

A large number of additional phenomena appear already in single Josephson junctions, the discussion of which would go far beyond the scope of this book. For example, one can prepare SFS-Josephson contacts having  $0$ -coupled and  $\pi$ -coupled regions within the same contact [52].

At the locations of the  $0-\pi$ -transition there can appear Josephson vortices carrying only half a flux quantum and behaving very peculiarly. Similar behavior can be observed in the case of hybrid contacts consisting of conventional superconductors and cuprates [53]. In systems having many alternating  $0-\pi$ -transition regions, as well as in conventional Josephson contacts having special current injectors, even “fractional” flux quanta can be generated carrying an arbitrary fraction of a flux quantum [54]. Correspondingly much richer is the behavior of coupled Josephson junctions, say, in vertically stacked junctions or in planar networks. For further details, we refer to the monographs [M3, M15, M16] and to the articles [55].

## 6.5 Quantum Properties of Superconducting Tunnel Junctions

So far we have described Josephson junctions as objects in which a small Cooper pair current flows across the junction because of the coupling between the macroscopic wave functions in both superconducting electrodes. The properties of the Cooper pair current are determined by the two Josephson equations. Our further discussion was completely classical and has led us to the analogy between Josephson junctions and physical pendulums. Another analogy was point masses gliding down an undulating surface (washboard potential). Now we want to look in more detail into the quantum properties of Josephson junctions. We first focus more closely on the junction capacity.

### 6.5.1 Coulomb Blockade and Single-Electron Tunneling

We start by looking at a capacitor carrying the charges  $\pm Q$  on its (normal conducting) electrodes. The capacitor has the capacity  $C = \epsilon\epsilon_0 A/t_B$ , where  $A$  is the capacitor area,  $t_B$  is the distance between the plates, and  $\epsilon$  is the dielectric constant. In this case the voltage between the plates is  $U = Q/C$ . The energy of the capacitor is  $E_{c,1} = Q^2/2C$ . Now an electron (charge  $-e$ ) tunnels between the plates, so that the charges of both electrodes are reduced to  $+Q - e$  or to  $-Q + e$ . Following the tunneling process, the electrostatic energy of the junction is  $E_{c,2} = (Q - e)^2/2C$ . We must assume that  $E_{c,2} < E_{c,1}$  in order for the process to be possible. This yields the condition<sup>28</sup>  $|Q| > e/2$  or  $|U| > e/2C$  as the prerequisite that an electron can tunnel to the other plate. This effect is referred to as the **Coulomb blockade** [56].

However, at finite temperatures, thermal fluctuations will cause the electrons to tunnel back and forth as long as the thermal energy  $k_B T$  is comparable to or larger than  $E_c$ . In order to develop a better feel for this influence, we compare the Coulomb energy  $E_c = e^2/2C$  of the capacitor charged with one electron with  $k_B T$ . In this case the capacity should be smaller than  $e^2/2k_B T$ . If we insert  $T = 1$  K, we obtain  $C < 0.9 \times 10^{-15}$  F. If we further assume  $\epsilon = 5$  and  $t_B = 1$  nm, this corresponds to a capacitor area of about  $0.02 \mu\text{m}^2$ , that is, to a length of the edge of about  $0.15 \mu\text{m}$ . So we need very small devices and low temperatures, in order that this effect is not completely wiped out by thermal fluctuations.

Furthermore, also the quantum fluctuations should be small. We can estimate their influence from the uncertainty relation  $\Delta E \Delta t > \hbar/2$ , connecting the uncertainty of the energy  $\Delta E$  with that of the time  $\Delta t$ . The value of  $\Delta E$  should be smaller than  $E_c$ . A charge fluctuation will be removed from a tunnel junction within a characteristic time constant  $\Delta t = RC$ . Inserting this into the uncertainty relation, we obtain  $e^2 RC / 2C > \hbar/2$  or  $R > \hbar/e^2 = R_Q/2\pi$ . Here we have introduced the quantum resistance  $R_Q = \hbar/e^2 = 24.6 \text{ k}\Omega$ . For a tunnel junction with  $0.1 \mu\text{m}$  length of its edge, this means that its resistance per square must be larger than a few  $\mu\Omega \text{ cm}^2$ , which generally is the case.

We see that the Coulomb blockade will be important in tunnel junctions with edge lengths far below  $1 \mu\text{m}$  and for temperatures far below  $1 \text{ K}$ . However, we cannot simply attach a current or voltage source to capacitors or tunnel junctions, so far treated as being isolated, since in this case the much larger capacity of the wiring, appearing parallel to the tunnel junction, would destroy this effect again. This is no longer the case if two tunnel junctions are connected in series. The common electrode between the two tunnel junctions then represents an island that is connected with the environment (i.e., with a current or voltage source) through the tunneling barriers. Furthermore, we can control the charge on the island by means of another capacity, the “gate.” In this case we have a transistor-like arrangement, in which initially without a gate voltage we can observe the Coulomb blockade. Below a limiting voltage  $U_c = e/2C_\Sigma$  the current is practically zero (here  $C_\Sigma$  is the total capacity of the island to the environment). For somewhat higher voltages, first a single electron tunnels to the island, which is then charged up. The next electron can tunnel only after the first electron has left the island. So we have a controlled flow of single electrons, which tunnel across the island with a frequency  $f_e$ . The current is

$$I = dQ/dt = ef_e \quad 6.23$$

This relation connects the current with the elementary charge and with the frequency  $f_e$ .

Only at higher limiting voltages can two, three, and so on, additional electrons occupy the island simultaneously. Corresponding to these limiting voltages, there appear step-like structures on the current–voltage characteristic, which are also referred to as a **Coulomb staircase** [56]. Here the current values are<sup>29</sup>  $I_n = nef_e$  ( $n = 1, 2, 3, \dots$ ).

The voltage  $U_c$  can be varied between zero and its maximum value by means of the gate electrode. Analogous to the classical transistor, one obtains a device that controls the flow of individual electrons, a single-electron transistor. Vice versa, this device can also serve for accurately measuring charges on the island. In this case we have an electrometer, analogous to the superconducting magnetometer. In particular, in the single-electron electrometer, the voltage  $U_c$  varies periodically with the gate voltage  $U_g$ , where the period is given by one elementary charge.

In [Figure 6.21](#) we show an early measurement of the Coulomb blockade and the Coulomb staircase. In this case the current flow between the Pt–Ir tip of a tunneling microscope and a

granular Au film was measured [57]. One of the Au grains represented the island. The charge on the island was not yet controlled by means of a gate voltage, but instead the *capacity* of the arrangement was varied by means of the distance between the tip and the gold surface. This produces a very similar effect and also leads to a modulation of  $U_c$ .

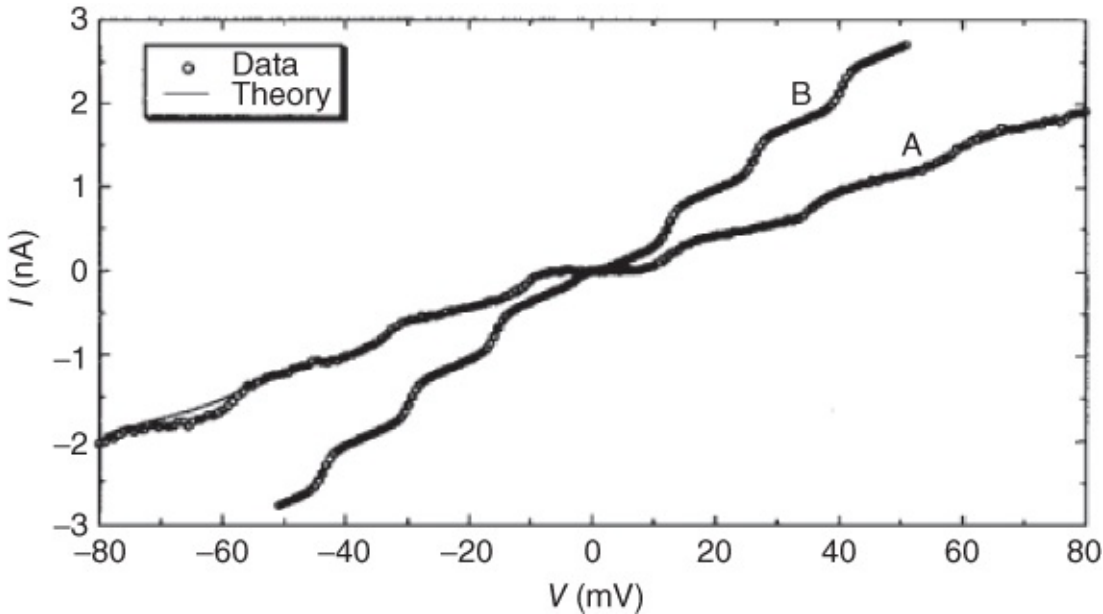


**Figure 6.21** Coulomb blockade and Coulomb staircase shown for the example of the current–voltage characteristic of a tunnel junction with an extremely small capacity between a Pt–Ir tip and the surface of a granular Au film. Measuring temperature: 4.2 K. Curve A: large distance between tip and surface; curve B: short distance between tip and surface [57].

So far we have discussed the *normal conducting* tunnel junction. Turning now to superconductors, charging effects are also expected to play a role. In the simplest case we just have to replace  $e$  by the charge  $2e$ .<sup>30</sup> For example, the voltage  $U_c$  varies periodically with  $2e$  instead of  $e$ , as was demonstrated experimentally [58].

Now the implications of this result must be discussed in more detail. In the case of the Josephson tunnel junction, we were dealing with a current of Cooper pairs without an external voltage. In the wave picture, the pair wave function of the superconductor was spread over both electrodes. Because of the Coulomb effect, exactly this current flow is interrupted. In other words, the superconducting wave function remains localized within the two electrodes. In contrast to the Josephson case, now the number of charge carriers in each electrode is fixed. However, the rigid phase coherence between the wave functions in both electrodes is destroyed.

Actually, this result arises from a deep origin. One can show that there is an uncertainty relation between the number  $N$  of Cooper pairs and the phase  $\phi$  of the pair wave function. One finds

$$\Delta N \Delta \phi > 1$$

6.24

If the phase  $\phi$  is defined exactly, then the particle number remains undefined, and vice versa.

Applied to the Josephson junction, this means that we can have either a well-defined phase difference  $\gamma$  (in which case the Cooper pairs are delocalized over both electrodes) or a well-defined particle number in the electrode (but then we lose the Josephson effect).

In order to decide which regime is valid, we must compare the Coulomb energy  $E_{c,p} = (2e)^2/2C$  with the energy associated with the Josephson coupling between the two superconductors. In analogy to the potential energy of the physical pendulum, the Josephson coupling energy is  $-E_J \cos \gamma$ , with  $E_J = \Phi_0 I_c / 2\pi$ . In the case  $\gamma = 0$ , this energy is just equal to  $-E_J$ . If  $E_J > E_c$ , the Josephson effect will dominate; and for  $E_J < E_c$ , the Coulomb effect will be dominant. However, for comparable energies one observes a highly complex behavior (see, e.g., [59]). Because  $E_J/E_{c,p} \propto I_c C \propto A^2$ , the ratio  $E_J/E_{c,p}$  increases quadratically with the area of the tunnel junction. For typical values of  $j_c$ ,  $\epsilon$ , and so on, the transition between the two limits happens at dimensions of the structure in the very low sub-micrometer range.

The Coulomb blockade in superconductors finds an application in the “Cooper pair box” (see [Figure 6.22](#)) [60]. In this case a small superconducting island is coupled to a superconducting reservoir by means of a superconducting tunnel junction, analogous to the single-electron transistor. Due to the Coulomb blockade the number of electrons is fixed and can be controlled by means of a gate electrode.

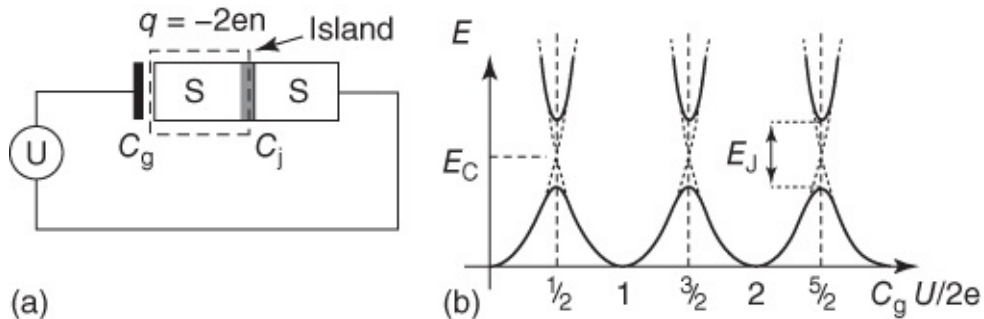


**Figure 6.22** Schematics of the “Cooper pair box.” (a) A superconducting island is connected with a superconducting counter-electrode by means of a tunnel junction (capacity  $C_j$ ). The number of electrons on the island can be controlled by means of a gate electrode (capacity  $C_g$ ). (b) Charging energy of the island plotted versus the charge  $C_g U$  induced by the gate electrode.

(Reprinted from Ref. [60] by permission of Physica Scripta.)

In the case of  $U_g = 0$ , we denote the pair wave function by  $|0\rangle$ . If the charge on the island is changed by  $n \cdot 2e$ , one obtains a new pair wave function  $|n\rangle$ , containing  $n$  additional Cooper pairs. If the Cooper pairs behave like independent particles, the electrostatic energy of the island would take the form  $(Q - 2ne)^2/2C_\Sigma$ . As a function of  $Q$ , this corresponds to a series of parabolas with their extrema at  $2ne$ . In [Figure 6.22](#)b these are shown as thin lines. However, according to the laws of quantum mechanics, near the crossing points of the parabolas, that is, for the charges  $Q = (n + 1/2)2e$ , a wave function will appear representing a coherent superposition  $a|n+1\rangle + b/n\rangle$  of the two states  $|n+1\rangle$  and  $|n\rangle$ . Here  $a$  and  $b$  denote complex numbers. As a consequence, at the crossing points the charging energy splits up (thick lines in

[Figure 6.22b](#)). The calculation shows that the splitting is just equal to  $E_J$ .

The charge in the Cooper pair box can be detected by means of a single-electron electrometer. In [Figure 6.23](#) we show a corresponding experimental result. Indeed, one observes a stair-like increase of the charge  $\langle n \rangle$  on the island averaged over the thermal fluctuations. The charge  $\langle n \rangle$  increases in units of  $2e$ . However, it is crucial that the experimental curve is continuous also between the integer values of  $\langle n \rangle$  and very well corresponds to the quantum mechanical expectations.

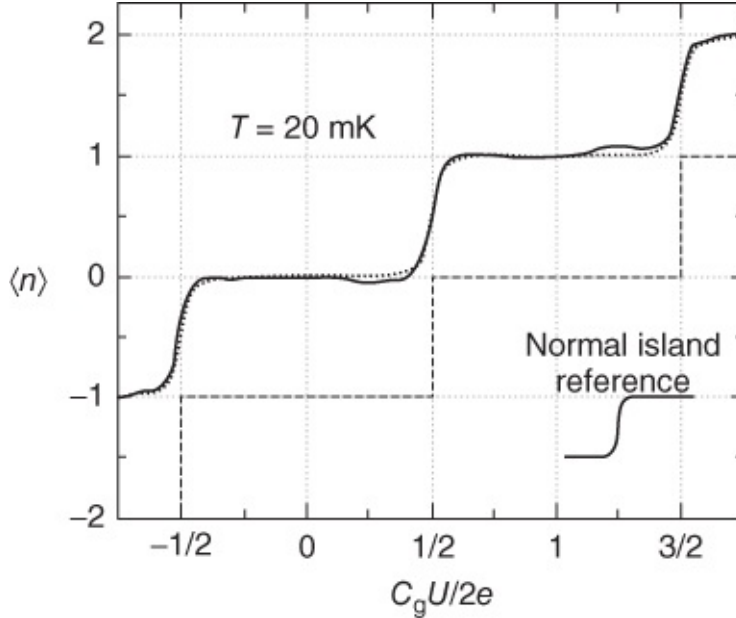


[Figure 6.23](#) Measurement of the time-averaged charge  $\langle n \rangle$  induced by the gate electrode shown in [Figure 6.21](#) plotted versus the gate voltage. The superconductor is Al. The dashed line indicates the behavior of  $\langle n \rangle$  in the absence of the quantum mechanical interaction between neighboring states  $|n\rangle$  and  $|n+1\rangle$ . The behavior of  $\langle n \rangle$  of a normal conducting reference island, where the charge varies in units of  $e$ , is also shown.

(Reprinted from Ref. [60] by permission of Physica Scripta.)

The effect of the quantum mechanical superposition has been demonstrated by Nakamura *et al.* [61] in an elegant experiment. By means of a rapidly pulsed gate voltage, these researchers transferred the Cooper pair box for a short time  $\Delta t$  from an integer value  $n = 0$  into the superimposed state. According to the laws of quantum mechanics, there the wave function oscillates with frequency  $f = E_J/h$  between the states  $|0\rangle$  and  $|1\rangle$ . If the gate voltage is switched off again, with a certain probability  $|w|^2$  the system then exists in the state  $|1\rangle$ , which depends on the pulse width, and which varies periodically between  $|w|^2 = 0$  and  $|w|^2 = 1$  (“Rabi oscillations”). The “excess” Cooper pair in the state  $|1\rangle$  can flow off via a second tunnel junction in the form of two quasiparticles. Hence, the current across this tunnel junction as a function of the pulse width directly indicates the probability  $|w|^2$ . The energy scheme of this process and the experimental result is shown in [Figure 6.24](#). It demonstrates unequivocally that a coherent superposition of the states  $|0\rangle$  and  $|1\rangle$  could be achieved. In the experiment the superconducting tunnel junction was prepared in the form of a superconducting quantum

interference device (SQUID)-like annular structure, which allows one to control the Josephson coupling energy  $E_J$  by means of a relatively small magnetic field or flux  $\Phi_a$ .

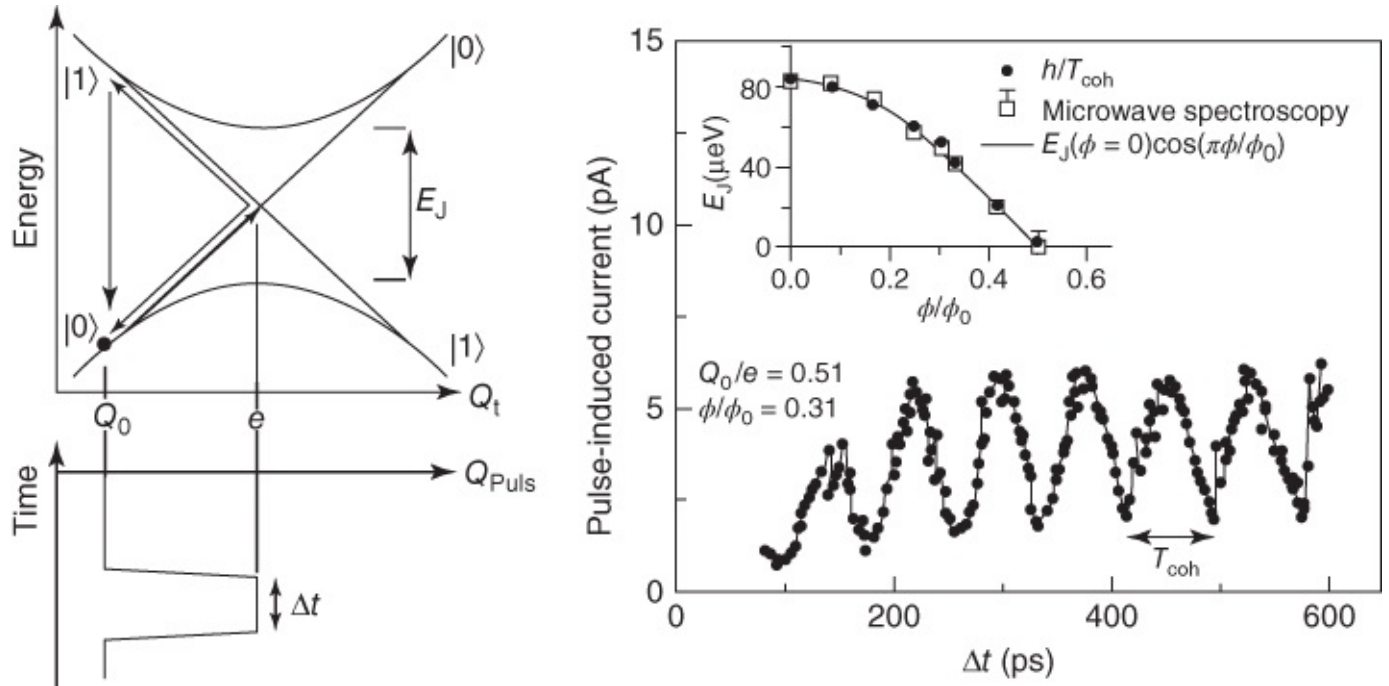


**Figure 6.24** Observation of Rabi oscillations by means of a Cooper pair box. Used superconductor: Al; measuring temperature: 30 mK. The two states differing by one Cooper pair are denoted by  $|0\rangle$  and  $|1\rangle$ . In the upper left diagram, the electrostatic energies of these states are shown as crossing dotted lines as a function of the charge  $Q_t$  induced on the island by the gate voltage. The crossing point is located at  $Q_t = e$ . The quantum mechanical coupling due to the Josephson effect splits the energetically degenerate states (parabolic solid lines), and at  $Q_t = e$  the splitting takes the value  $E_J$  (Josephson coupling energy). Initially, at  $Q_t = Q_0$  the system is in the state  $|0\rangle$ . By means of a short pulse (see the lower left graph) the gate voltage and, hence,  $Q_t$  is raised up to the value  $e$  within a few picoseconds. Now the system oscillates for a time  $\Delta t$  with frequency  $f = E_J/h = 1/T_{coh}$  between  $|0\rangle$  and  $|1\rangle$ . Subsequently  $Q_t$  is reduced very quickly again to its starting value. Depending on the pulse width  $\Delta t$ , with a certain probability the Cooper pair box exists either in the state  $|0\rangle$  or in the state  $|1\rangle$ . The state  $|1\rangle$  with the higher energy is unstable. The excess charge  $2 - e$  flows off in the form of two quasiparticles via the tunnel junction. If  $\Delta t$  is varied, this tunneling current oscillates as a function of  $\Delta t$  with the period being just  $T_{coh}$ . The experimental result is shown in the graph on the right-hand side. In the experiment the Josephson coupling energy could be controlled by a magnetic field or a flux  $\Phi$ . The inset of this graph shows the value of  $E_J$  determined from  $T_{coh} = h/E_J$  for various values of  $\Phi$  and compares these values with measurements from independent studies (“microwave spectroscopy”).

(From Ref. [61]. © 1999 Nature.)

There is hope that one day a new kind of logic device will be realized based on the quantum mechanical superposition of two states  $|0\rangle$  and  $|1\rangle$ , and that such devices will be able to

manipulate the quantum mechanically superimposed “qubits” instead of the classical bits 0 and 1. Here we note that the quantum mechanical probability  $w$  is a *complex* number, the phase of which represents an additional property not known in classical logic. Presently the possibility of such quantum computers is being investigated theoretically and experimentally by many scientists (not only physicists of different disciplines, but also mathematicians and information scientists). An overview can be found in Refs. [62]. The review articles [63] deal especially with superconducting qubits. These quantum computers could solve a number of problems for which classical computers would need an extremely long time. Of course, at the moment we cannot know whether such a computer will ever be produced and what kind of hardware will be used.

However, in any case the attempt to reach this highly ambitious goal is expected to yield many new insights into quantum mechanical systems and, last but not least, to yield measurement techniques and applications that are still unknown today. Therefore, quantum properties are also the subject of the concluding section of this chapter. We will see that also magnetic flux quanta or the phase differences across Josephson junctions can be used as qubits.

## 6.5.2 Flux Quanta and Macroscopic Quantum Coherence

In the previous section, we have seen that Cooper pair states with different numbers  $n$  of Cooper pairs can be superimposed quantum mechanically. We can ask if a similar process is also possible for flux quanta. More generally, we can ask if a point mass sliding down a “washboard,” representing an analogous system for the description of the Josephson junction in the RCSJ model (see [Section 6.2](#)), also follows the laws of quantum mechanics [64].

The answer to both these questions is “yes.” Let us look again at the RCSJ Eq. ([6.11](#)):

$$C \cdot \left( \frac{\Phi_0}{2\pi} \right)^2 \ddot{\gamma} = \frac{\Phi_0}{2\pi} I - \frac{\Phi_0 I_c}{2\pi} \sin \gamma - \frac{\Phi_0^2}{(2\pi)^2 R} \dot{\gamma}$$

Here it has been multiplied by  $\Phi_0/2\pi$  and solved for the ***inertia term***. In the following, we assume that the damping is very small. In this case we neglect the ***friction term*** ( $\propto \dot{\gamma}$ ). If we interpret  $\gamma$  as a kind of spatial coordinate, the right-hand side of Eq. ([6.11](#)) can be interpreted as a force, which can be derived from a potential

$$U(\gamma) = -\frac{\Phi_0 I_c}{2\pi} \cos \gamma - \frac{\Phi_0 I}{2\pi} \gamma \tag{6.25}$$

using  $F = -dU/dy$ . This is the washboard potential along which the point mass is moving. Obviously, the washboard is tilted from the horizontal position because of the current  $I$ . Classically, the point mass starts to move if the potential is tilted enough that  $U$  does not display any minima anymore, or if for a smaller tilting angle the thermal fluctuations can heave the point mass over the maxima.

Quantum mechanically it should be possible that the point mass tunnels through the potential barrier ([Figure 6.25](#)). However, this process can be observed only if the thermal fluctuations

are sufficiently small, that is, at very low temperatures. An exact calculation yields the condition  $k_B T < \hbar\omega_{pl}(I)/2\pi$ , with the Josephson plasma frequency

$$\omega_{pl}(I) = (2\pi I_c / \Phi_0 C)^{1/2} [1 - (I/I_c)^2]^{1/4}$$

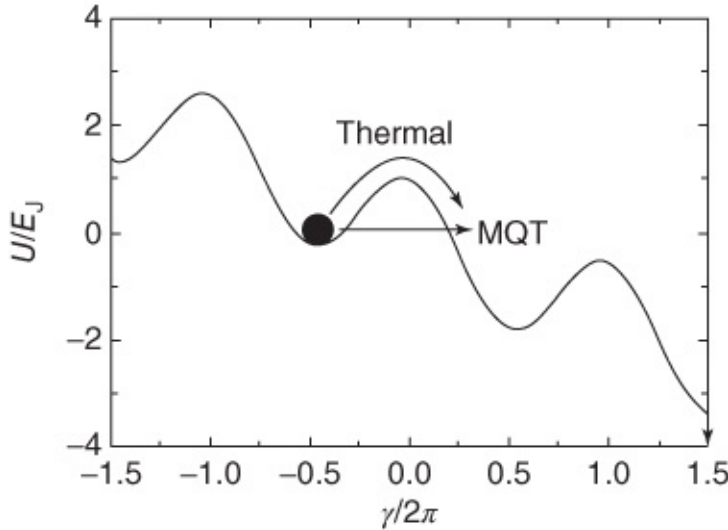


**Figure 6.25** Macroscopic quantum tunneling (MQT) in a Josephson junction. The potential normalized to  $E_J$  (Eq. (6.25)) is shown for  $I/I_c = 1/4$ .

Obviously,  $\omega_{pl}(I)$  must be as large as possible, and, hence,  $C$  as small as possible. In the case  $I = 0$  and  $\omega_{pl}(0) = 10^{11} \text{ s}^{-1}$ , one obtains  $T < 0.1 \text{ K}$ , which is not too difficult to realize.

If the point mass has tunneled through the potential barrier, it will slide down the washboard because of the small damping. For the Josephson junction, this means that the junction switches from the zero-voltage state into the resistive state. The macroscopic quantum tunneling (MQT) can be studied experimentally by recording the distribution of the current values at which the junction switches into the resistive state. In the end, this yields the probability for surmounting the potential barrier. Such studies were performed in the 1980s, and they clearly confirmed the process of MQT [65]. In a similar way, Josephson fluxons can tunnel through a potential barrier [66].

The situation becomes particularly interesting if the potential  $U(\gamma)$  has the shape of a double well, as indicated in [Figure 6.26a](#). According to quantum mechanics, in this potential the energy states must take up discrete values  $E_n$ , some of which are indicated schematically in [Figure 6.26](#) by horizontal lines. In the symmetric case of [Figure 6.26a](#), the states in the right and left wells are the same. In particular there exist two ground states, which differ in the figure by the sign of  $\gamma$ . If the potential can be tilted ([Figure 6.26b](#)), this degeneracy is lifted.

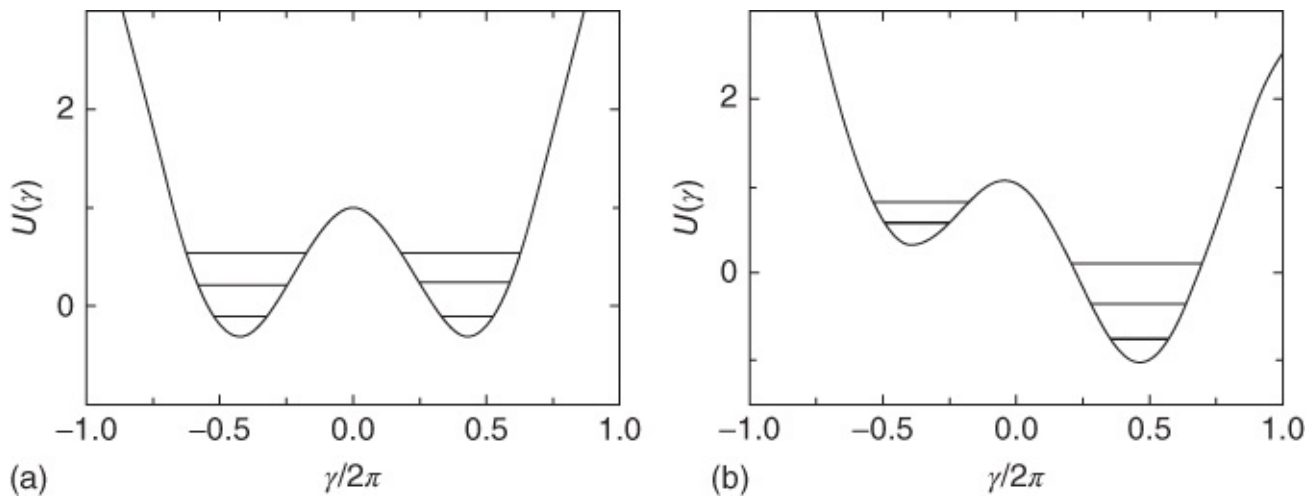


**Figure 6.26** Double-well potential for the generation of quantum mechanically superimposed states: (a) symmetric potential with energetically degenerate energy levels (horizontal lines; only a few levels are shown schematically) and (b) tilted potential with nondegenerate ground state.

Potential shapes of this kind can be achieved with Josephson junctions. An example is a Josephson junction that is integrated into a superconducting ring<sup>31</sup> [67]. The magnetic flux through the ring is  $\Phi = \Phi_a + LJ$ , where  $\Phi_a$  denotes the externally applied flux and  $LJ$  the flux generated by the ring current  $J$ , which is proportional to the ring inductance  $L$ . The current  $J$  also passes through the Josephson junction, and we have  $J = I_c \sin \gamma$ . The phase difference  $\gamma$  in turn is proportional to  $\Phi$  (see [Section 1.5](#)):  $\gamma = 2\pi\Phi/\Phi_0$ . The energy of the ring is the sum of the magnetic energy  $LJ^2/2 = (\Phi - \Phi_a)^2/2L$  and the energy of the Josephson junction. Hence, we have

$$U(\Phi) = \frac{(\Phi - \Phi_a)^2}{2L} - \frac{I_c \Phi_0}{2\pi} \cos \frac{2\pi\Phi}{\Phi_0} \quad 6.26$$

This potential has the form shown in [Figure 6.26](#), where the symmetric case (modulo  $\Phi_0$ ) is obtained for  $\Phi_a = \Phi_0/2$  and the nonsymmetric case for  $\Phi_a \neq \Phi_0/2$ . Now the system can be prepared by an applied magnetic field in such a way that the ground state is close to  $\Phi = +\Phi_0/2$ . In this case the ring current  $J$  is assumed to flow clockwise. We denote this state by  $|+\rangle$ . Correspondingly, we denote the state with the counter-clockwise current flow by  $|-\rangle$ . If the field is reduced to  $\Phi_0/2$ , the system adopts a superposition of the two degenerate states  $|+\rangle$  and  $|-\rangle$ . In this case the ring current simultaneously flows clockwise and counter-clockwise. If we go back again to the original flux, analogous to the Cooper pair box described in [Section 6.5.1](#), with a certain probability the system is in the state  $|-\rangle$ . This probability oscillates proportional to the time during which the ring resided in the degenerate state.<sup>32</sup>

In 2000, experimental evidence of this quantum mechanical superposition was reported by scientists at Stony Brook [68], although the Rabi oscillations could not yet be detected directly. In 1999 and 2000, a similar design with three Josephson junctions integrated into a ring was

investigated in Delft and in Cambridge, Massachusetts [69]. Also in this case initially only indirect evidence for the superposition of two flux states was obtained. Finally, in 2003, the direct detection of the Rabi oscillations was achieved by the Delft group [70]. In the previous year, Rabi oscillations could be observed in single Josephson junctions<sup>33</sup> [71], as well as in a sophisticated combination of a Cooper pair box and a SQUID ring [72].

Presently, the development progresses rapidly.<sup>34</sup> The design of the qubits and of the electronic circuits are varied and improved, in order, for example, to sustain the macroscopic quantum coherence over times as long as possible. In the case of the experiments shown in [Figure 6.24](#), the Rabi oscillations could be observed only for a few nanoseconds. In the meantime, the corresponding times reach a few microseconds. Also one achieved the coupling of qubits and the generation of so-called entangled states, which are highly important for the realization of quantum circuits [73]. For example, these are states of the type  $(|0\rangle_A|1\rangle_B - |1\rangle_A|0\rangle_B)/\sqrt{2}$ , where the indices refer to the two qubits A and B.

In the case of the systems discussed so far, the microwaves irradiating the superconductors consisted of many photons. One further step is carried out by experiments coupling the superconducting qubits with single photons, which are reflected back and forth in a resonator. For some time, such systems are investigated in atomic physics and are referred to as **cavity quantum electrodynamics**. One irradiates the resonator with photons, which interact with the atom for a certain time, and eventually escape from the resonator and can be measured. At the Yale University quite analogously one achieved the coupling of a Cooper-pair box with a microwave resonator [74, 75]. Frequently, this is referred to as **circuit quantum electrodynamics**. In the following, we want to discuss one of the first experiments in more detail.

[Figure 6.27](#) shows schematically the layout of the superconducting chip made from niobium and subsequently measured at a temperature of 15 mK. The resonator consists of a superconducting strip, along which standing waves can be generated. The figure shows a situation where the length  $L$  of the resonator corresponds to one wavelength  $\lambda$ . The electric field is directed toward both outer conductors. The qubit is located in the middle of the resonator. Without the coupling with the qubit, the resonator can be described in terms of an harmonic oscillator and, according to the rules of quantum mechanics, possesses an energy spectrum  $E_n = \hbar\omega_r(n + 1/2)$ . Here  $n \geq 0$  is an integer number, which indicates how many photons are in the resonator, and  $\omega_r$  is the resonance frequency of the resonator. In the following, the energy levels belonging to a given value of  $n$  are denoted by  $|0\rangle$ ,  $|1\rangle$ ,  $|2\rangle$ , and so on. We note that the distances between neighboring energy levels are equidistant. We only consider two energy levels of the qubit, which we denote  $|\uparrow\rangle$  and  $|\downarrow\rangle$ . In general, the qubit has more than two energy levels. However, the energy distances of the qubit are not equidistant, such that one can excite with photons specifically transitions between two energy levels. In contrast to atomic physics, one can control very well the position of the energy levels of the qubit and, in addition, one can couple the resonator much stronger with the qubit than it would be possible in the case of real atoms.

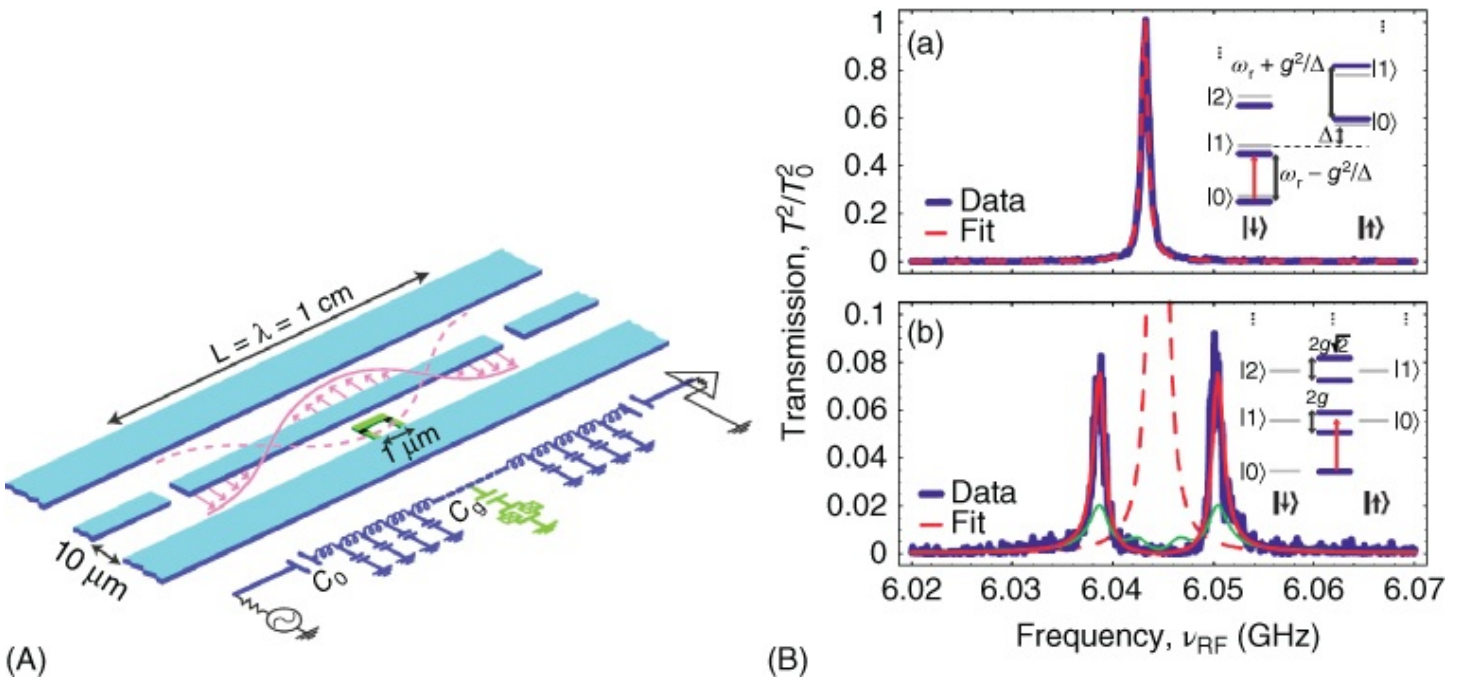


**Figure 6.27** Circuit quantum electrodynamics based on a Cooper-pair box coupled to a superconducting resonator. A: Scheme of the superconducting chip. (Reprinted with permission of [74], © 2004 American Physical Society.) B: Measurements of the transmission probability of a microwave through the circuit ([75], © 2004 Nature). In the upper part, the energy levels of the Cooper-pair box are adjusted such that they are far from the energy levels of the resonator. In the lower part, both qubit levels coincide with the energy levels of the resonator. The dashed curve in part (b) is the theoretical curve in the uncoupled case.

In the coupled system, the states of the qubit and of the photons in the resonator superimpose and form new energy levels. If in this case the original energy states of the qubit and of the resonator strongly differ from each other, the coupling is weak, and one obtains, for example, the energy scheme shown in Figure 6.27(B,a). Here it is assumed that the distance between both energy levels of the qubit differs by the amount  $\Delta$  from the energy difference  $E_n = \hbar\omega_r$  of the photons in the resonator. The energy levels are indicated in the right half of the figure. There on the left the energy levels are shown when the qubit resides in the ground state  $|1\rangle$  and when 0, 1, or 2 photons exist in the resonator. The thick lines correspond to the uncoupled system, the thin lines to the coupled system. In the figure the coupling strength is denoted by  $g$ , where  $\hbar g$  is the corresponding coupling energy. In the right scheme, the qubit resides in the energetically higher state  $|1\rangle$ , and the levels with 0 or 1 photon in the resonator are correspondingly shifted up. In the figure the transmission probability of the microwaves through the superconducting resonator, as the measured quantity, is plotted versus the irradiated microwave frequency. The measurement shown refers to a qubit in state  $|1\rangle$ , and the transition from  $|0\rangle$  to  $|1\rangle$  was observed. One obtains a resonance curve with its maximum at the frequency  $\omega_r - g^2/\Delta$ . If the qubit had been in state  $|1\rangle$ , the maximum of the resonance curve would be at  $\omega_r + g^2/\Delta$ . Hence, from the measurement, one can decide which state was occupied by the qubit.

The effects of the coupling become much stronger if the energies of the resonator and of the qubit are equal. This case is shown in the lower part of Figure 6.27(B). Again on the left, the

energy levels of the uncoupled system of the state  $|1\rangle$  of the qubit are shown, and on the right for the state  $|1\rangle$ . In the coupled case, these states are completely mixed. One cannot distinguish any longer between the photons and the qubit. The resulting energy levels are shown in the middle. We see doublets with the splitting  $2g\sqrt{n}$ , which increases with increasing number of photons in the resonator. If the resonator is irradiated by photons, and the transmission of the resonator is measured, we see two resonance peaks, which are shifted by the amount  $2g$  during the transition from  $|0\rangle$  to  $|1\rangle$ .

The measurements of [Figure 6.27\(B\)](#) are compared with theoretical curves, and the agreement is excellent. The arrangement is functioning. This allowed the Yale group, and subsequently many other groups, to perform many fundamental experiments of quantum mechanics.

Bell's inequality could be tested by means of two phase-qubits entangled via a resonator [76]. Based on this inequality, John Bell had demonstrated the way to distinguish clearly between classical and quantum mechanical behavior. The measurement showed that, in spite of their macroscopic size, both qubits represent a true quantum system.

Now it is possible to control qubits as well as photons at the level of single quanta. Hence, this offers an ideal construction kit for the developments toward a quantum computer.

## References

1. D. G. Naugle, R. E. Glover: *Phys. Lett.* **28 A**, 611 (1969); W. Kessel, W. Rühl: *PTB-Mitteilungen* **79**, 258 (1969).
2. D. Bohm, “*Quantum Theory*”, Prentice Hall, New York (1951).
3. V. Ambegaokar, A. Baratoff: *Phys. Rev. Lett.* **10**, 486 (1963); Erratum: *Phys. Rev. Lett.* **11**, 104 (1963).
4. M. D. Fiske: *Rev. Mod. Phys.* **36**, 221 (1964).
5. R. C. Jaklevic, J. Lambe, J. E. Mercereau, A. H. Silver: *Phys. Rev.* **140 A**, 1628 (1965).
6. Y. Tanaka, S. Kashiwaya: *Phys. Rev. B* **56**, 892 (1997).
7. G. B. Arnold, R. A. Klemm: *Phys. Rev. B* **62**, 661 (2000).
8. A. Odagawa, M. Sakai, H. Adachi, K. Setsune: *IEEE Trans. Appl. Supercond.* **9**, 3012 (1999).
9. K. Tanabe, Y. Hidaka, S. Karimoto, M. Suzuki: *Phys. Rev. B* **53**, 9348 (1996); M. Itoh, S.-I. Karimoto, K. Namekawa, M. Suzuki: *Phys. Rev. B* **55**, R12001 (1997).
10. K. Schlenga, R. Kleiner, G. Hechtfischer, M. Mößle, S. Schmitt, P. Müller, Ch. Helm, Ch. Preis, F. Forsthofer, J. Keller, H. L. Johnson, M. Veith, E. Steinbeiß: *Phys. Rev. B* **57**, 14518 (1998).

11. Heim, S. (2002) Fluxonen und Quasiteilchen in mikrostrukturierten intrinsischen Josephsonkontakten auf  $\text{Bi}_2\text{Sr}_2\text{CaCu}_2\text{O}_{8+\delta}$  Einkristallen. PhD thesis. University of Tübingen.
12. T. Koyama, M. Tachiki: *Phys. Rev. B* **54**, 16183 (1996); S. N. Artemenko, A. G. Kobel'kov: *Phys. Rev. Lett.* **78**, 3551 (1997); D. A. Ryndyk, J. Keller, C. Helm: *J. Phys. Condens. Matter* **14**, 815 (2002).
13. K. A. Delin, A. W. Kleinsasser: *Supercond. Sci. Technol.* **9**, 227 (1996).
14. P. de Gennes: *Rev. Mod. Phys.* **36**, 225 (1964).
15. A. D. Misener, H. Grayson Smith, J. O. Wilhelm: *Trans. R. Soc. Can.* **29**, (III) 13 (1935).
16. H. Meissner: *Phys. Rev.* **109**, 686 (1958); *Phys. Rev. Lett.* **2**, 458 (1959); *Phys. Rev.* **117**, 672 (1960)
17. P. Hilsch, R. Hilsch, G. v. Minnigerode: “*Proceedings of the 8th International Conference on Low Temperature Physics (LT 8)*”, Butterworth, London, p. 381 (1963); P. Hilsch: *Z. Phys.* **167**, 511 (1962).
18. A. F. Andreev: *Sov. Phys. JETP* **19**, 1228 (1964); for an overview, see also B. Pannetier, H. Courtois: *J. Low Temp. Phys.* **118**, 599 (2000).
19. J. Clarke: *Phys. Rev. B* **4**, 2963 (1971).
20. B. N. Taylor, E. Burstein: *Phys. Rev. Lett.* **10**, 14 (1963)
21. J. M. Rowell, W. L. Feldmann, *Phys. Rev.* **172**, 393 (1968)
22. G. E. Blonder, M. Tinkham, T. M. Klapwijk: *Phys. Rev. B* **25**, 4515 (1982).
23. T. M. Klapwijk, G. E. Blonder, M. Tinkham: *Physica B* **109**, 1657 (1982).
24. W. J. Tomasch: *Phys. Rev. Lett.* **15**, 672 (1965); J. M. Rowell, W. L. McMillan: *Phys. Rev. Lett.* **16**, 453 (1966); W. L. McMillan, P. W. Anderson: *Phys. Rev. Lett.* **16**, 85 (1966).
25. P. de Gennes, D. Saint James: *Phys. Lett.* **4**, 151 (1963).
26. L. Alff, H. Takashima, S. Kashiwaya, N. Terada, H. Ihara, Y. Tanaka, M. Koyanagi, K. Kajimura: *Phys. Rev. B* **55**, R 14757 (1997); M. Covington, M. Aprili, E. Paraoanu, L. H. Greene, F. Xu, J. Zhu, C. A. Mirkin: *Phys. Rev. Lett.* **79**, 277 (1997); H. Aubin, L. H. Greene, S. Jian, D. G. Hinks: *Phys. Rev. Lett.* **89**, 177001 (2002).
27. T. Löfwander, V. S. Shumeiko, G. Wendin: *Supercond. Sci. Technol.* **14**, R53 (2001).
28. S. Kashiwaya, Y. Tanaka: *Rep. Prog. Phys.* **63**, 1641 (2000).
29. V. V. Ryazanov, V. A. Oboznov, A. Yu. Rusanov, A. V. Veretennikov, A. A. Golubov J., Aarts: *Phys. Rev. Lett.* **86**, 2427 (2001).

30. L. N. Bulaevskii, V. V. Kuzii, A. A. Sobyanin: *JETP Lett.* **25**, 290 (1977).
31. T. Kontos, M. Aprili, J. Lesueur, F. Genêt, B. Stephanidis, R. Boursier: *Phys. Rev. Lett.* **89**, 137007 (2002).
32. W.C. Stewart: *Appl. Phys. Lett.* **12**, 277 (1968).
33. D.E. McCumber, *J. Appl. Phys.* **39**, 3113 (1968)
34. H. Hilgenkamp, J. Mannhart: *Rev. Mod. Phys.* **74** (2002).
35. S. Shapiro: *Phys. Rev. Lett.* **11**, 80 (1963).
36. B. D. Josephson: *Phys. Lett.* **1**, 251 (1962).
37. S. B. Kaplan: *Supercond. Ind. Spring*, 25 (1995).
38. C. A. Hamilton, *Rev. Sci. Instrum.* **71**, 3611 (2000).
39. R. L. Kautz, R. Monaco: *J. Appl. Phys.* **57**, 875 (1985).
40. Ch. Helm, Ch. Preis, F. Forsthofer, J. Keller, K. Schlenga, R. Kleiner, P. Müller: *Phys. Rev. Lett.* **79**, 737 (1997).
41. P. Seidel, A. Pfuch, U. Hübner, F. Schmidl, H. Schneidewind, J. Scherbel: *Physica C* **293**, 49 (1997).
42. S. Rother, Y. Koval, P. Müller, R. Kleiner, Y. Kasai, K. Nakajima, M. Darula: *IEEE Trans. Appl. Supercond.* **11**, 1191 (2001); H. B. Wang, P. H. Wu, T. Yamashita: *Phys. Rev. Lett.* **87**, 107002 (2001).
43. A. J. Dahm, A. Denenstein, T. F. Finnegan, D. N. Langenberg, D. J. Scalapino: *Phys. Rev. Lett.* **20**, 859 (1968); N. F. Pedersen, T. F. Finnegan, D. N. Langenberg: *Phys. Rev. B* **6**, 4151 (1972); A. J. Dahm, D. N. Langenberg: *J. Low Temp. Phys.* **19**, 145 (1975).
44. D. D. Coon, M. D. Fiske, *Phys. Rev.* **138**, A744 (1965).
45. I. O. Kulik: *Sov. Tech. Phys.* **12**, 111 (1967).
46. T. A. Fulton, R. C. Dynes: *Solid State Commun.* **12**, 57 (1973).
47. N. F. Pedersen, D. Welner: *Phys. Rev. B* **29**, 2551 (1984).
48. A. V. Ustinov, T. Doderer, R. P. Huebener, N. F. Pedersen, B. Mayer, V. A. Obozov: *Phys. Rev. Lett.* **69**, 1815 (1992); see also Th. Doderer: *Int. J. Mod. Phys. B* **11**, 1979 (1997).
49. A. V. Ustinov: *Appl. Phys. Lett.* (2002) **80**, 3153; B. A. Malomed, A. V. Ustinov: *Phys. Rev. B* (2004) **69**, 064502.
50. S. Keil, I. V. Vernik, T. Doderer, A. Laub, H. Preßler, R. P. Huebener, N. Thyssen, A. V.

- Ustinov, H. Kohlstedt: *Phys. Rev. B* **54**, 14948 (1996);S. G. Lachenmann, T. Doderer, R. P. Huebener, D. Quenter, J. Niemeyer, R. Pöpel, *Phys. Rev. B* **48**, 3295 (1993).
51. A. Laub, T. Doderer, S. G. Lachenmann, R. P. Huebener, V. A. Obozov: *Phys. Rev. Lett.* **75**, 1372 (1995).
52. M. Weides, M. Kemmler, E. Goldobin, H. Kohlstedt, R. Waser, D. Koelle, R. Kleiner: *Phys. Rev. Lett.* **97**, 247001 (2006).
53. H. Hilgenkamp, Ariando , H.-J. H. Smilde, D. H. A. Blank, G. Rijnders, H. Rogalla, J. R., Kirtley, C. C. Tsuei: *Nature* **422**, 50 (2003).
54. R. G. Mints, *Phys. Rev. B* **57**, R3221 (1998);R. G. Mints, I. Papiashvili, J.R. Kirtley, H., Hilgenkamp, G. Hammerl, J. Mannhart: *Phys. Rev. Lett.* **89**, 067004 (2002);E. Goldobin, D. Koelle, R. Kleiner: *Phys. Rev. B* **70**, 174519 (2004);K. Buckenmaier, T. Gaber, M. Siegel, D. Koelle, R. Kleiner, E. Goldobin: *Phys. Rev. Lett.* **98**, 117006 (2007).
55. J. Bindslev Hansen, P.E. Lindelof: *Rev. Mod. Phys.* **56**, 431 (1981);M. Darula, T. Doderer, S. Beuven: *Supercond. Sci. Technol.* **12**, R1 (1999);N. F. Pedersen, A. V. Ustinov: *Supercond. Sci. Technol.* **8**, 389 (1995);A. V. Ustinov: *Physica D* **123**, 315 (1998).
56. D. V. Averin, K. K. Likharev: *J. Low Temp. Phys.* **62**, 345 (1986);T. A. Fulton, G. J. Dolan: *Phys. Rev. Lett.* **59**, 109 (1987);D. V. Averin, K. K. Likharev: In: “*Mesoscopic Phenomena in Solids*” (eds B. L. Altshuler, P.A. Lee and R.A. Webb) Elsevier, Amsterdam, p. 173 (1991);For information about networks of ultrasmall Josephson tunneling processes, see P. Delsing, C. D. Chen, D. B. Haviland, T. Bergsten, T. Claeson: *AIP Conf. Proc.* **427**, 313 (1997).
57. A. E. Hanna, M. Tinkham: *Phys. Rev. B* **44**, 5919 (1991).
58. M. T. Tuominen, J. M. Hergenrother, T. S. Tighe, M. Tinkham: *Phys. Rev. Lett.* **69**, 1997 (1992); *Phys. Rev. B* **47**, 11599 (1993).
59. P. Joyez, P. Lafarge, A. Filipe, D. Esteve, M. H. Devoret: *Phys. Rev. Lett.* **72**, 2458 (1994).
60. V. Bouchiat, D. Vion, P. Joyez, D. Esteve, M. H. Devoret: *Phys. Scr. T* **76**, 165 (1998).
61. Y. Nakamura, Yu. A. Pashkin, J. S. Tsai: *Nature* **398**, 786 (1999);see also Y. Nakamura, Yu. A. Pashkin, J. S. Tsai: *Physica B* **280**, 405 (2000); *Physica C* **357**, 1 (2001); *Phys. Rev. Lett.* **87**, 246601 (2001); *Physica C* **367**, 191 (2002)
62. Physics World, March 1998 Issue on “Quantum Information”;see also C. Bennet, *Phys. Today* **48**, 24 (1995);A. Steane, *Rep. Prog. Phys.* **61**, 117 (1998).
63. Yu. Makhlin, G. Schön, A. Shnirman: *Rev. Mod. Phys.* **73**, 357 (2001);J. Clarke, F. K. Wilhelm: *Nature* **453**, 1031 (2008)

64. A. O. Caldeira, A. J. Leggett: *Ann. Phys. (New York)* **149**, 374 (1983);A. J. Leggett, A. Garg: *Phys. Rev. Lett.* **54**, 857 (1985).
65. R. F. Voss, R. A. Webb: *Phys. Rev. Lett.* **47**, 265 (1981);J. M. Martinis, M. H. Devoret, J. Clarke: *Phys. Rev. B* **35**, 4682 (1987);J. Clarke, A. N. Cleland, M. H. Devoret, D. Esteve, *Science* **239**, 992 (1988).
66. A. Kemp, A. Wallraff, A. V. Ustinov: *Phys. Status Solidi* **233**, 472 (2002);A. Wallraff, J. Lisenfeld, A. Lukashenko, A. Kemp, M. Fistul, Y. Koval, A. V. Ustinov: *Nature* **425**, 155 (2003).
67. R. Rouse, S. Han, J. E. Lukens: *Phys. Rev. Lett.* **75**, 1614 (1995).
68. J. R. Friedman, V. Patel, W. Chen, S. K. Tolpygo, J. E. Lukens: *Nature* **406**, 43 (2000).
69. J. E. Mooji, T. P. Orlando, L. Levitov, L. Tian, C.H. van der Wal, S. Lloyd: *Science* **285**, 1036 (1999);C. H. van der Wal, A. C. J. ter Haar, F. K. Wilhelm, R. N. Schouten, C. J. P. M. Harmans, T. P. Orlando, S. Lloyd, J. E. Mooji: *Science* **290**, 773 (2000).
70. I. Chiorescu, Y. Nakamura, C. J. P. M. Harmans, J. E. Mooji: *Science* **299**, 1869 (2003);see also: J. Clarke: *Science* **299**, 1850 (2003).
71. Y. Yu, S. Han, X. Chu, S.-I. Chu, Z. Wang: *Science* **296**, 889 (2002).
72. D. Vion, A. Aassime, A. Cottet, P. Joyez, H. Pothier, C. Urbina, D. Esteve, M. H. Devoret: *Science* **296**, 886 (2002).
73. M. Steffen, M. Ansmann, R. C. Bialczak, N. Katz, E. Lucero, R. McDermott, M. Neeley, E. M. Weig, A. N. Cleland, J.M. Martinis: *Science* **313**, 1423 (2006).
74. A. Blais, R.-S. Huang, A. Wallraff, S. M. Girvin, and R. J. Schoelkopf: *Phys. Rev. A* **69**, 062320 (2004).
75. A. Wallraff, D. I. Schuster, A. Blais, L. Frunzio, R.- S. Huang, J. Majer, S. Kumar, S. M. Girvin, R. J. Schoelkopf: *Nature* **431**, 162 (2004).
76. M. Ansmann, H. Wang, R. C. Bialczak, M. Hofheinz, E. Lucero, M. Neeley, A. D., O'Connell, D. Sank, M. Weides, J. Wenner, A. N. Cleland, J. M. Martinis: *Nature* **461**, 504, (2009).

<sup>1</sup> We note that for a temperature-independent  $R_n$ , Eq. (6.1) simply indicates the temperature dependence of the critical current.

<sup>2</sup> We note that, in contrast to the tunnel junction shown in [Figure 6.2](#), the conductance  $dI/dU$  is relatively large also for small voltages. This indicates that quasiparticle states also exist at small energies, as expected for a superconductor with d-wave symmetry of the pair wave function.

<sup>3</sup> Later in this chapter, we will see that interactions between the junctions exist, for example, if vortices are present. Another interaction results from nonequilibrium charging (charge fluctuations) of the CuO<sub>2</sub> planes [12]. However, these interactions practically do not affect the current–voltage characteristic.

<sup>4</sup> This effect can also be included in the Ginzburg–Landau equations. In this case one extrapolates the decay of  $\Psi_0$  in the superconductor linearly into the normal conductor. This extrapolated length is then used as an additional parameter for the boundary condition of the Ginzburg–Landau equations.

<sup>5</sup> Correspondingly, the transition temperature of a superconductor with a low value of  $T_c$  increases if it is in contact with a superconductor with a higher transition temperature.

<sup>6</sup> The disorder also has a very small influence on the transition temperature of Pb and reduces it slightly. In the limit  $d_{\text{Pb}} \rightarrow \infty$ , a  $T_c$  of 7 K is reached.

<sup>7</sup> This arrangement is referred to as “Sharvin contact.”

<sup>8</sup> Such excess currents were first observed for tunnel junctions with a thin barrier layer [20]. However, in this case the barrier layer very likely contained metallic shorts [21], such that actually an SNS junction was studied.

<sup>9</sup> We assume that no inelastic scattering process occurs during this time.

<sup>10</sup> Actually, there is also a contribution due to the interference of the Cooper pairs and the quasiparticles, which is proportional to  $\cos \gamma$ . However, this contribution can be neglected in particular at voltages below  $2\Delta_0/e$ .

<sup>11</sup> Resistively and capacitively shunted junction.

<sup>12</sup> Another analogous system that is frequently discussed consists of a mass moving down an inclined undulating plane (“washboard potential”). As long as one assumes that the mass stays in contact with the plane, this also leads to an equation of motion of the form (6.11), where the spatial coordinate  $x$  takes over the role of  $\gamma$ .

<sup>13</sup> We note that we have allowed small oscillations of the pendulum about its position  $\gamma_0$  at rest. For the Josephson junction such “motion” exists and is referred to as Josephson plasma oscillation. If the pendulum oscillates about  $\gamma_0 = 0$ , then the frequency of this oscillation is  $\omega_{\text{pl}} = (mgl/\Theta)^{1/2} = (g/l)^{1/2}$ . For the Josephson junction we obtain  $\omega_{\text{pl}} = (2\pi I_c/\Phi_0 C)^{1/2}$ . If with increasing torque (or current  $I$ ) the pendulum oscillates about  $\gamma_0 \neq 0$ , this frequency decreases and reaches zero at  $\gamma_0 = 90^\circ$ .

<sup>14</sup> If the pendulum rotates nearly harmonically, the time average of the sine term and also the inertia term are very small and can be neglected. Hence, Eq. (6.12) yields the time average

$M = \Gamma \langle \dot{\gamma} \rangle$ , and from (6.11) we have  $I = \frac{\Phi_0}{2\pi R} \langle \dot{\gamma} \rangle = \frac{\langle U \rangle}{R}$ .

- 15 For pendulums or (nonlinear) electronic circuits, at this stage one would rather introduce the quality factor  $Q$ , which is proportional to  $\beta_c^{1/2}$ .
- 16 One can show that for large values of  $\beta_c$  the return current  $I_r$  is about  $4I_c/(\pi\beta_c^{1/2})$  [M16].
- 17 The “white noise” of a resistance  $R$  is indicated by the Nyquist formula. According to this formula, in frequency space the spectral power of the voltage noise  $S_v$  per frequency interval  $df$  is for all frequencies  $f$  given by  $4k_B T R$ .
- 18 However, this case is very difficult to realize in practice, since usually Josephson junctions have a very low impedance, and since, for example, the resistances of the circuit wires also make an ideal voltage source look like a current source.
- 19 At frequencies comparable to or larger than the characteristic frequency  $f_c$ , one finds that the height  $I_n$  of the  $n$ th step is approximately given by  $2I_c|J_n(x)|$ . Here  $J_n(x)$  is the  $n$ th Bessel function ( $n = 0$  describes the critical current itself). The argument  $x$  is proportional to the ratio  $I_{ac}/I_c$ . However, at frequencies much below  $f_c$  the step height is only  $I_c f_{ac}/f_c$ , that is, it approaches zero at low frequencies. Further details can be found, for example, in the monographs [M15, M16].
- 20 The same dependence is found for applied voltages  $U(t) = U_0 + U_{ac} \cos(\omega_{ac}t)$ , instead of the applied direct and alternating currents. In this case the second Josephson equation can easily be solved analytically. The resulting Josephson alternating current can be expressed as a series of Bessel functions and finally yields the steps with constant voltage at voltages  $U_n = nf_{ac}\Phi_0$ .
- 21 The difficulty of measurements in the terahertz range arises from the problem of inducing sufficiently strong alternating currents within the Josephson junction.
- 22 However, with the pendulum model we are dealing with a discrete system, in which the second derivative  $d^2y/dx^2$  must be replaced by the expression  $(y_{n+1} + y_{n-1} - 2y_n)/\Delta x^2$ . In this case the index  $n$  refers to the pendulums, and  $\Delta x$  is the distance between neighboring pendulums.
- 23 If damping effects in the superconducting layers are taken into account, one can obtain another (small) term, which is proportional to  $d^3y/dx^2dt$ . Here we ignore this term.
- 24 This is correct as long as no any additional terms appear in Eq. (6.19).
- 25 For simplicity, here we only discuss standing waves in the  $x$ -direction. Of course, standing waves also appear analogously in the  $y$ -direction.

- [26](#) The voltage values are  $U_n = \Phi_0 \omega_n / 2\pi = \Phi_0 \bar{c}n / 2L$ , with integer  $n$  and  $\omega_n = \bar{c}k = \bar{c}n\pi / L$ .
- [27](#) The effect of an applied field can also be simulated in the pendulum model. The boundary condition (6.19) only means a twisting of the ends of the pendulum chain, where the angle by which the ends of the chain are twisted relative to each other increases proportional to the applied field.
- [28](#) Here we look at the charge as being continuous. This does not represent a contradiction to the quantization of the elementary charge in units of  $e$ , since each arbitrary value of  $Q$  can be obtained by shifting the electrons relative to the positive background charge of the ions.
- [29](#) We note that this relation looks very similar to the relation  $U_n = n\Phi_0 f$ , indicating the voltages of the Shapiro steps on the characteristic of a Josephson junction under microwave irradiation. In this case we have the correspondences  $I \leftrightarrow U$  and  $e \leftrightarrow \Phi_0$ . This “duality” between the Coulomb effect and the Josephson effect can be extended further. For example, we also have the correspondences conductance  $\leftrightarrow$  resistance and capacity  $\leftrightarrow$  inductance.
- [30](#) Here we ignore the role of the unpaired quasiparticles and their interactions with the pair state. Details can be found in the monograph [M3].
- [31](#) We will return again to this arrangement in [Section 7.6.4.1](#) in form of the “rf-SQUID.”
- [32](#) However, we note that in this case magnetic flux or circulating currents are superimposed, in contrast to the superposition of charges in the Cooper pair box.
- [33](#) In this case states with different phase differences  $\gamma$  are superimposed. One speaks of phase qubits.
- [34](#) This applies not only to superconductivity. Qubits are investigated in different areas of physics, for example, based on ions, atoms, or semiconducting quantum dots.

# Chapter 7

## Applications of Superconductivity

Attempts at technical applications of superconductivity are as old as the studies of this fascinating phenomenon. Kamerlingh-Onnes hoped that it would be possible to generate magnetic fields in a highly economic way by means of electrical conductors without resistance. Today, the operation of superconducting magnets is standard in many different fields of scientific research, and also in medical technology, for example, in nuclear spin tomography. Similarly spectacular are applications of superconductivity in electronic measuring techniques. Here they provide us with the possibility to increase the sensitivity in many cases by orders of magnitude compared to techniques based on normal conducting circuits.

However, at this point we must emphasize that the requirement for a superconductor to perform a given task reliably is a necessary, but by no means sufficient, condition. It is at least equally important that the superconductors can perform the task economically, and that there exist no alternative procedures that can be operated more simply and more favorably. Furthermore, superconductors are not expected to replace well-established techniques unless the new technique yields *important* advantages.

For illustration we look at two examples. In the field of electrical power distribution, one could imagine employing superconducting cables over the total distance between the power station and private consumers. In this case, losses in the cable network<sup>1</sup> would be reduced. On the other hand, superconducting cables are expensive,<sup>2</sup> and the cooling technology must be taken into account. However, even if superconducting cables could be installed everywhere, we must compare the advantages of the superconductor with those of copper cables *cooled to the same low temperature*, where they have a much lower resistance than at room temperature. On the other hand, the installation of a superconducting cable may become worthwhile if larger and larger currents must be carried by a given cross-section, say, within the existing cable pits from a power station to a big city. In this case, it may be more favorable to install a superconducting cable instead of digging new cable pits for conventional cables.

As a second example, we look at the application of superconducting devices in digital electronics. We can imagine large circuits of superconductors operating at frequencies of 100 GHz or above and simultaneously consuming very little power. It is just this latter point that is highly problematic in the application of semiconductors. On the other hand, conventional technology is continually improving. In the end, a superconducting circuit that may be available within a decade must be compared with the semiconductor technology also expected within 10 years. For example, in the 1980s, superconducting circuits were discussed operating at frequencies of about 1 GHz, which was spectacularly high at that time. Today even higher frequencies are achieved in every conventional PC. However, also in the field of digital circuits, it will be economically interesting to use superconductors perhaps in combination with semiconductors for performing tasks that are impossible or highly difficult with

conventional techniques.

We see that every time we must look at the whole system and at the already existing field, in order to find out where and when a superconducting technique offers advantages. The advantages of superconductors are quite obvious if applications can be realized that are impossible with conventional technology. This is the case with the generation of high magnetic fields in large volumes, the detection of magnetic fields down to the range below  $10^{-15}$  T, or the free floating and stable positioning of objects by means of levitation. We will also discuss a number of other examples.

Within the scope of this book, we will try to provide a first impression of the applications of superconductivity and of the associated problems.<sup>3</sup> Many details cannot be mentioned. For a wide overview, we refer the reader to the monographs [M19–M31]. However, in this chapter, we want to present examples indicating that even today our technology cannot be imagined without superconductivity, and that many possible new applications can be expected in the future.

## 7.1 Superconducting Magnetic Coils

### 7.1.1 General Aspects

The generation of high magnetic fields represents a necessary prerequisite in many fields of research and technology. In the previous chapters, we have seen how important high magnetic fields are for the study of superconductivity itself. As another example of solid-state physics we mention the quantum Hall effect [3], which among other things serves for the definition of the ohm. In this case, semiconducting structures are operated at low temperatures at magnetic fields of 10 T and above.

These experiments can be carried out in small volumes of only a few cubic centimeters. On the other hand, in the field of high-energy physics or nuclear fusion research, we need magnetic fields of 5–10 T in enormously large volumes of many cubic meters. The requirements of nuclear spin tomography have their place between these two extreme cases. Here, patients are exposed to magnetic fields of 1–3 T. However, the bore of the magnet must be large enough to accommodate the patient.

As the last example we mention nuclear spin resonance spectroscopy, which today represents the crucial equipment for studying the structure of proteins. In this case the magnetic fields can hardly be high enough. On the one hand, the sample volumes are usually small (in the range of cubic centimeters), but on the other hand, the homogeneity of the field must be extremely high. This latter requirement can only be fulfilled by building large magnets.

Even in the field of small magnets for research purposes, one can be convinced quickly that superconductivity provides a distinct advantage. Let us assume, for example, that we want to generate a field of 10 T in a copper coil (Bitter magnet) with an inner bore of 4 cm diameter and 10 cm length. To sustain this field we need at least 5000 kW of electrical power; the heat

generated must be completely removed by cooling water. In this case at least  $1 \text{ m}^3$  of cooling water per minute must be pumped through the magnet and subsequently must be passed through a cooling tower. On the other hand, in principle,<sup>4</sup> a superconducting magnet no longer consumes electrical power after the magnetic field has been generated. One only needs the cooling power to cool the magnet to low temperatures and to keep it at these temperatures. However, compared to the power consumption of the Bitter magnet, the latter is negligibly small.<sup>5</sup>

## 7.1.2 Superconducting Cables and Tapes

Next we discuss the features of the superconducting cables or tapes that must carry the current required by the magnet.

At the projected maximum magnetic field, the maximum possible current density must still be reasonably high to allow currents of 100 A and above (hard superconductors, see [Section 5.3.2](#)). In any case, current densities above  $10^4 \text{ A/cm}^2$  must be reached. These current densities must be calculated for the total cross-section of the conductor, including all nonsuperconducting parts such as the insulating layers and the normal conducting matrix surrounding the superconductor. As we will see in a moment, the latter matrix represents a highly important feature.

During the construction of superconducting coils, the disappointing result has been observed that the critical current values measured with short wire samples by far could not be achieved. This phenomenon is referred to as the **degradation effect**. Even at current values that are smaller than the expected critical current by a factor of 2 and more, there appear instabilities that can lead to the completely normal conducting state of the coil. In particular, for large coils, there is the danger of complete destruction if the energy stored in the magnetic field could not be removed properly. Since for large coils safe operation must be guaranteed by any means, the only option that remains is to keep the currents sufficiently small and to use a larger amount of superconducting material to reach the desired fields. In the beginning of the development of superconducting magnets, the degradation effect represented a serious handicap, in particular in the case of magnets for high fields.

Only in 1965 could these difficulties be overcome to a large extent by using “stabilized” wires [4]. It was recognized that the instabilities were caused by flux jumps. In this case, whole flux bundles tear away from their pinning sites because of such influences as temperature fluctuations or mechanical shocks. Subsequently, under the influence of the Lorentz force, these flux bundles move through the material in an abrupt jump (see [Figures 5.12](#) and [5.13](#)). During this rapid motion of whole flux bundles, a large amount of heat is generated. If this heat cannot be removed sufficiently fast, a temperature rise appears and sections of the superconductor can become normal conducting. This normal resistance then leads to additional heating, and the normal conducting region expands. In this way, the whole coil becomes unstable and, perhaps very quickly, enters the normal conducting state (“quench”).<sup>6</sup>

Stabilization can be achieved by surrounding the superconductor with a normal conductor

having a resistance as low as possible, such as copper or aluminum. In the case of a good electrical contact to this surrounding normal conductor, the current passing through the coil can find a low-ohmic short nearby if a section of the coil becomes normal conducting. Now heating due to the appearance of normal conduction remains small. Therefore, such a combination of conducting materials provides the opportunity to cool down and become superconducting again following a flux jump.

Following these qualitative arguments, in the case of stationary currents, we want to look at this situation in some detail. Additional details can be found in [M20a].

We start by looking at a superconducting wire without a matrix according to [M20a]. A current having a density near the critical current density  $j_c$  is assumed to pass through the wire with the cross-section  $A$ , and a small normal conducting region of length  $l$  is assumed to exist. The temperature rise amounts to  $\Delta T = T_c - T_0$  above the bath temperature  $T_0$ . Cooling is by means of liquid helium, that is,  $T_0 = 4.2$  K.  $T_c$  denotes the critical temperature of the superconductor in a given magnetic field. The specific resistance of this region is denoted by  $\rho$ , and the thermal conductivity of the wire by  $k$ . Now it is the question, whether this perturbation is expanding, or if it collapses again after a certain time. With the assumptions given earlier, in the normal conducting region the thermal power  $j_c^2 \rho A l$  is generated, which must be discharged at both ends of the normal conducting region into the wire. Thermal conductance can discharge approximately the power  $2kA\Delta T/l$ . By equating the expressions for the generated and the discharged power, one obtains a critical length  $l_c \approx [2k\Delta T/j_c^2 \rho]^{1/2}$ . If the original length of the region was smaller than  $l_c$ , the region will collapse, in the opposite case it will grow. If we insert typical values for the case of Nb–Ti, which are valid, for example, at a field of 6 T ( $j_c = 2 \times 10^5$  A/cm<sup>2</sup>,  $\rho = 6.5 \times 10^{-5}$  Ω cm,  $k = 10^{-3}$ /cm K,  $T_0 = 4.2$  K,  $T_c = 6.5$  K), one finds  $l_c \approx 0.4$  μm. Hence, at a given wire cross-section  $A \approx 3 \times 10^{-3}$  cm<sup>2</sup>, one must heat up only a volume of  $1.2 \times 10^{-7}$  cm<sup>3</sup>, in order to cause a quench. This is accomplished by injected energies in the range of nanojoules. Using a normal conducting matrix of Cu results in a substantial reduction of the average specific resistance and in an increase in  $k$ . The ratio  $k/\rho$  can increase by 5 orders of magnitude or more, and  $l_c$  increases correspondingly by more than a factor of 100. However, injected energies of a few microjoules are sufficient to cause a quench.

Therefore, the conductor must be cooled at a part of its surface as large as possible, in order to achieve an effective protection against a quench (cryogenic stability). In this case, stability criteria can be formulated, which must be satisfied by the conductor. In the simplest case we can imagine a rectangular section of length  $l$  of the conductor, its cross-section  $A$  consisting of a fraction  $\lambda$  of a superconductor, and of a fraction  $(1 - \lambda)$  of a normal conductor. For simplicity we assume that this section is heated by  $\Delta T$  from the bath temperature to the transition temperature  $T_c$ . Then the applied current ( $\approx I_c$ ; current density  $j_c = I_c/\lambda A$ ) passes through the normal conductor and generates a voltage  $V$ . The dissipated power amounts to  $I_c V$ , which can be written as  $\lambda^2 \rho j_c^2 A l / (1 - \lambda)$ . The maximum power, which can be discharged through the conductor surface, is  $h \Delta T P$ , where  $h$  denotes the heat transfer coefficient (cooling power per area =  $h \Delta T$ ) and  $P$  denotes the cooled part of the conductor surface. From the

ratio of these two power values, one obtains the criterion [5]

$$\alpha = \frac{\lambda^2 j_c^2 \rho A}{(1 - \lambda) Ph \Delta T} < 1 \quad 7.1$$

for the thermal stability of the arrangement.

Furthermore, in the case of short perturbations, the temporal temperature behavior and the maximum temperature increment must be determined. The analysis can be improved further by indicating the spatial extension of the perturbation. In this way one obtains the information, whether a perturbation of given energy density can be discharged sufficiently rapidly [M20a].

Equation (7.1) shows that it will be safe by choosing a small filling factor, that is, a small value of  $\lambda$ . This can be important, for example, in the case of very large coils. These coils are referred to as **overstabilized**. They can also be operated if a significant part of the current passes through both the superconductor and the normal conductor. Then a voltage develops along the coil, that is, electrical power must be supplied for the operation of the magnet. This mode of operation is reasonable in particular for the temporary generation of magnetic field peaks.

A special problem, which had been investigated intensively, concerns the appearance of flux jumps. According to Bean's model (see [Section 5.3](#)), exactly the critical current density flows within the regions of a type-II superconductor into which magnetic flux has penetrated. If flux jumps happen in this situation, the superconductor will heat up, the critical current density decreases, perhaps additional motion of flux lines occurs, more heating takes place, that is, the process builds up more and more. However, there exist criteria under which the magnet remains stable against this effect. One can calculate the heat energy per volume generated in a plate-shaped part of a conductor of thickness  $2a$  because of the current redistribution, and one finds  $\mu_0 j_c \Delta j_c a^2 / 3$ . Here,  $\Delta j_c$  denotes the change of the critical current density. Assuming a linear relation for the temperature dependence of  $j_c$ , we have  $\Delta j_c = -j_c(T - T_0)/(T_c - T_0)$ . Now we imagine that the plate is decoupled from its environment and that the heat energy  $\Delta Q_s$  is injected into it. We write the total heat energy per volume generated in the plate in the form  $\gamma C(T - T_0)$ , where  $\gamma$  denotes the density of the material and  $C$  the specific heat. This heat energy is obtained from  $\Delta Q_s$  and the heat energy generated by the current redistribution:

$\gamma C(T - T_0) = \Delta Q_s + \mu_0 j_c \Delta j_c a^2 (T - T_0) / 3(T_c - T_0)$ . If the second term on the right-hand side is equal to the first, the system becomes unstable. (Then we could inject again this heat energy as the amount  $\Delta Q_s$  into the plate, resulting in a still larger heat development, etc.). With the definition

$$\beta = \frac{\mu_0 j_c^2 a^2}{\gamma c \Delta T} \quad 7.2$$

( $\Delta T$  again denotes the difference between critical temperature and bath temperature) we see that in this case stability is reached for  $\beta < 3$ . We note that this yields a maximum value of  $a$ , which typically falls in the region of 100  $\mu\text{m}$ . Of course, in the case of multifilamentary conductors, detailed calculations go beyond these simple estimates. In particular, one must take

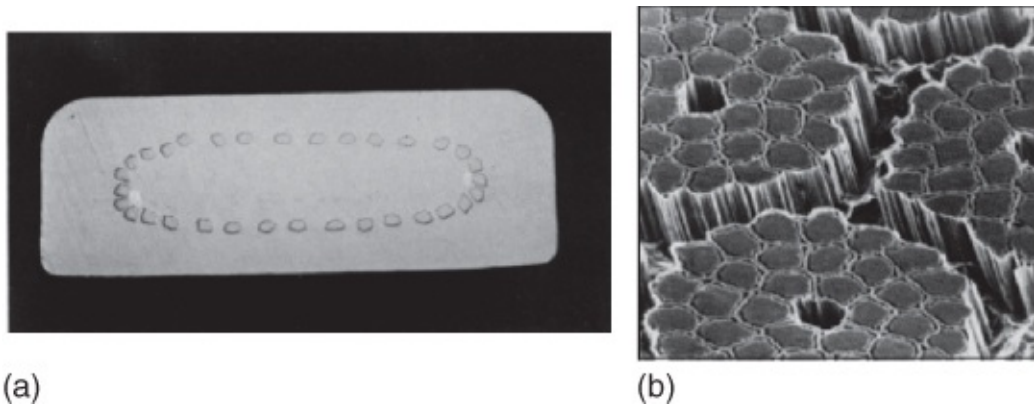
into account also the self-field of the current. However, also in this case the stability is reached, when  $\beta$  falls below a certain value, which depends on the geometry of the conductor and on the applied current. In the case of a round wire of radius  $a$  and an applied current of 50% of the critical current,  $\beta$  must be smaller than about 60. At 90% of the critical current,  $\beta$  must be smaller than about 4.

Another important criterion deals with the filament radius itself: this must fall below a certain value, in order to achieve stability. One introduces a parameter  $d$  according to

$$d^2 = \frac{k\Delta T(1 - \lambda)}{\lambda j_c^2 \rho} \quad 7.3$$

Here,  $k$  denotes the thermal conductivity of the wire. The other quantities were defined already in Eqs. (7.1) and (7.2). In the case of a filament, the radius must be smaller than  $\sqrt{8d}$ , in order that the conductor remains stable against flux jumps. Using typical numerical values, one finds filament radii in the range of 50  $\mu\text{m}$ , which is technically feasible. However, a problem develops as soon as the magnetic flux changes within the conductor, an induction voltage perpendicular to the filaments is generated, currents flow within the normal conducting matrix, and thereby couple the filaments again. In this case, instead of the filament radius, one must consider the radius of the total wire, which in general is much larger. Partly one can improve the situation by twisting the filaments, since in this case the voltages induced across the normal conductor at least partly compensate each other. At the end of this section, we return again to this subject.

Of course, in addition to these considerations, we must take into account the mechanical stability of the magnet, since at high magnetic fields the generated Lorentz forces are quite strong. In this case, the stability requirements result in completely new criteria for the technical feasibility of superconducting materials. During the early period of the development of superconducting magnets, niobium–zirconium alloys with a transition temperature around 10 K were used nearly exclusively. Then these alloys were replaced by niobium–titanium alloys with a composition of roughly Nb + 50 at% Ti (see [Figure 5.22](#)). Today, this material represents the standard material in the case of the construction of coils. In addition to a somewhat larger critical field of about 13 T, it had important metallurgical advantages [6]. The composite conductor can be fabricated by inserting a thick Nb–Ti rod into a copper block of suitable dimensions and by pulling the whole piece down to wire size. In this way, an excellent contact between the superconductor and the copper is achieved. The ratio of the cross-sections of copper and Nb–Ti ranges from 1.3 : 1 up to 10 : 1. [Figure 7.1](#) shows a cross-section of a few types of conductors.



(a)

(b)

**Figure 7.1** (a) Strongly overstabilized Nb–Ti conductor in a Cu matrix. Seven such tapes were electron-beam-welded together along their flat surface, and then were used as the conductor material in the bubble chamber magnet at CERN (see [Figure 7.4](#)). At 5 T,  $I_c$  amounts to 110 A. (b) Scanning electron microscope image of a multifilamentary conductor made of Nb–Ti. The superconducting material is embedded into a matrix made from Cu and CuNi. To obtain the image, the Cu was removed by etching.

(Courtesy of Dr Hillmann, Vacuumschmelze GmbH, Hanau; see also [7].)

For feasible current values up to fields of about 10 T, coils can be fabricated from Nb–Ti. In [Figure 7.2](#) we show a few small research magnets as they are used mainly in solid-state physics.

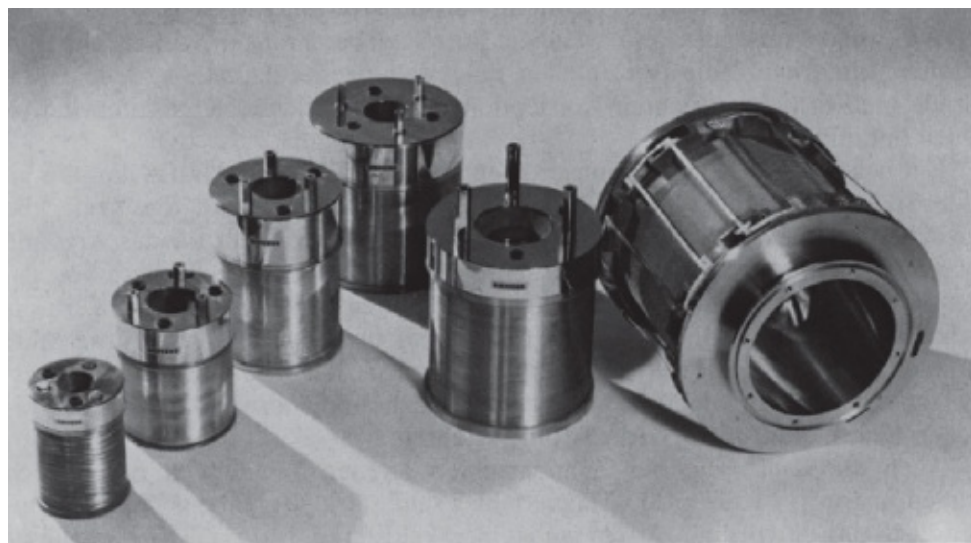


**Figure 7.2** Superconducting laboratory magnets. The coil diameter ranges from a few centimeters up to decimeters.

(By courtesy of Siemens, Research Laboratory, Erlangen.)

The bubble chamber magnet<sup>[7]</sup> at European Nuclear Research Center (CERN) with a diameter of about 4 m represented one of the first large superconducting systems. It started its operation in the mid-1970s and operated for about 15 years without major interruptions. The magnet consisted of two coils, which in turn were composed of 20 pancake coils each. In [Figure 7.3](#) we show the construction of one of these coils. The magnetic field was 3.5 T. The force acting

between the coils reached 9000 tons. The total weight of the overstabilized conductor with a length of 60 km was 100 tons. The coils were operated with a current of 5700 A.

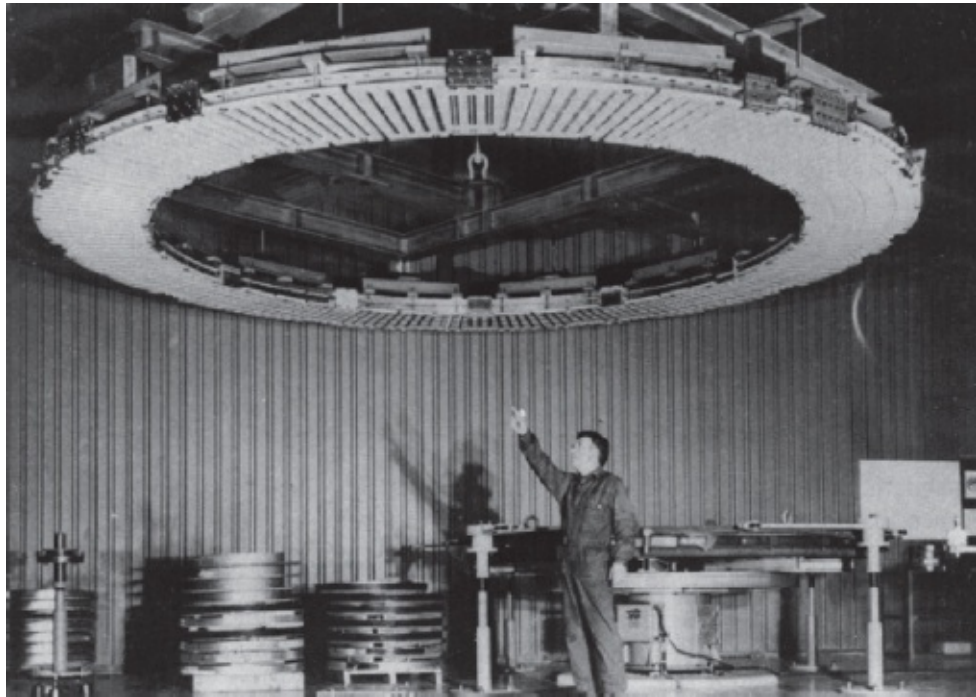


**Figure 7.3** Pancake coil of the superconducting bubble chamber magnet of the European Nuclear Research Center (CERN) in Geneva.

Today  $\text{Nb}_3\text{Sn}$  is used as the material for the fabrication of high-magnetic field coils. Magnetic fields higher than 20 T can be realized with this superconductor<sup>8</sup> [8]. Although  $\text{Nb}_3\text{Sn}$  is very brittle, it has been possible to develop wires that contain, within a wire diameter of about 1 mm, several thousand very fine  $\text{Nb}_3\text{Sn}$  filaments embedded in a metal matrix. In this case, Nb rods are stuck into a tin bronze ( $\text{Cu} + \text{Sn}$ ), and at the same time the whole bundle is pulled down to the desired diameter. The  $\text{Nb}_3\text{Sn}$  is produced during a subsequent tempering process (heating up to a temperature between 700 and 800 °C) by means of the reaction of the Sn from the bronze with the Nb. Pictures of the cross-section of these multifilamentary conductors look similar to that shown in [Figure 7.1b](#) of a  $\text{Nb}-\text{Ti}$  conductor.

If extremely large currents must pass through the coil, multifilamentary conductors can be combined to larger bundles, which in turn can be placed within suitable tubes (“cable in conduit”). In this way they can be electrically insulated from neighboring conductors, and also they can be cooled internally by cold helium gas. In [Figure 7.4](#) we show the example of a cable as it is tested for the nuclear fusion reactor International Thermonuclear Experimental Reactor (ITER) (see [Section 7.3.4](#)) [10]. Currents up to more than 60 000 A in fields above 10 T can flow through this cable.

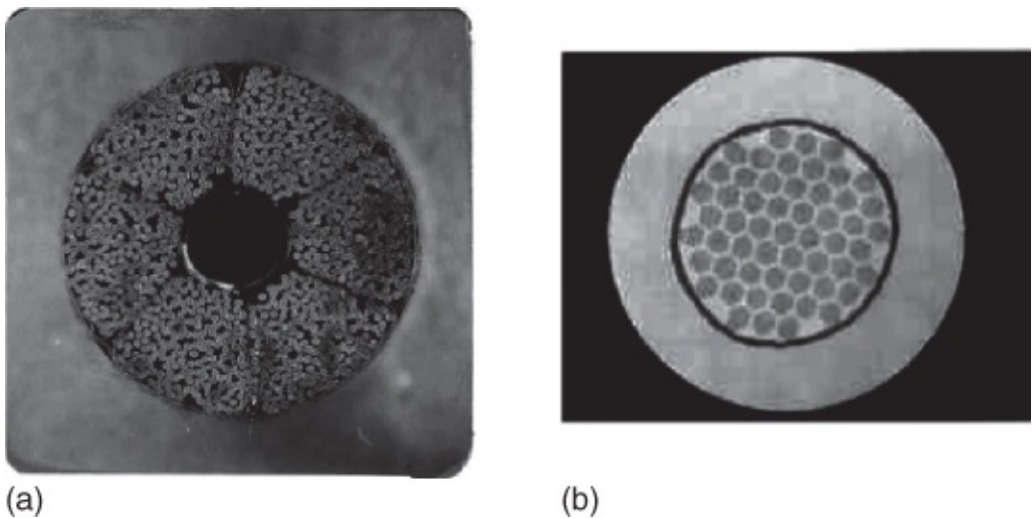


**Figure 7.4** Cross-section of a “cable in conduit.” (a) Whole cable; the individual wires are grouped around a central opening of 1 cm diameter. (b) Individual wire (diameter 0.81 mm) consisting of Nb<sub>3</sub>Sn filaments within a Cu matrix.

(From [9] with permission of IOP.)

Presently Nb<sub>3</sub>Al [11] is also being studied intensively as a metallic superconductor regarding its use for the construction of magnets. In this material the upper critical field is somewhat higher than in Nb<sub>3</sub>Sn. A summary of different materials and procedures can be found in [9].

Because of their high upper critical fields, the cuprate superconductors, MgB<sub>2</sub>, and perhaps also the iron pnictides are particularly interesting for the generation of high magnetic fields. For example, in the case of Bi<sub>2</sub>Sr<sub>2</sub>CaCu<sub>2</sub>O<sub>8</sub>-tape conductors above 30 T, the critical current density is still high enough to allow, at least in principle, the construction of magnets [12, 13] (see [Figure 7.5](#)). So far one could not fabricate superconducting coils, which generate such high fields. However, coils were constructed already which, in a background field of 31 T, could generate in addition up to 2.8 T [14]. Regarding these materials, a second important aspect is the possibility to operate magnetic coils at temperatures far above 4.2 K. In the case of cuprates, cooling can be done with liquid nitrogen (at 77 K) or by cryo-coolers, which were continuously improved parallel to the superconductor technology and can generate temperatures around 20 K without any problem [13].

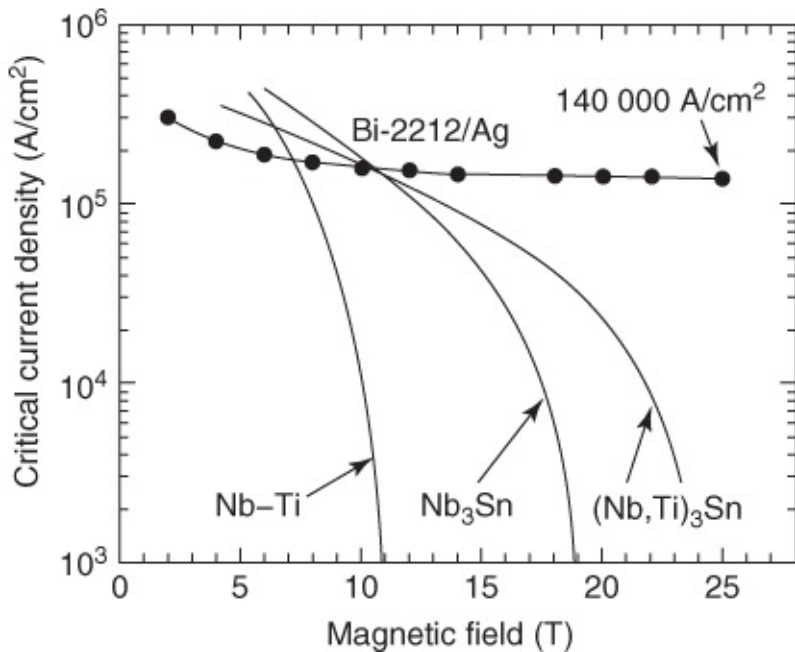


**Figure 7.5** Critical current densities at 4.2 K of Nb–Ti, Nb<sub>3</sub>Sn, and Bi<sub>2</sub>Sr<sub>2</sub>CaCu<sub>2</sub>O<sub>8</sub> conductor tapes plotted versus the magnetic field.

(From [12] with permission of IOP.)

In the case of MgB<sub>2</sub>, with increasing magnetic field the critical current density decreases rapidly. However, also in this case magnetic coils can be realized, which generate fields of 1–2 T and are operated by means of cryo-coolers [15].

If high-temperature superconductors are used, the stability behavior against quenching changes. In the case of liquid-nitrogen-cooled coils made of cuprate superconductors one deals with a large distance to the transition temperature. Then one must not consider any longer the stability of the magnet against the growth of small regions heated above  $T_c$ , but instead the heating of the complete magnet [16].

During the use of cryo-coolers, the magnet is operated in vacuum. Therefore, the stability arguments described at the beginning of this section, based on the cooling with liquid helium, cannot directly be applied. One finds that in the case of cryo-cooling a low-temperature superconductor such as Nb<sub>3</sub>Sn, frequently a quench occurs already if, at a given local temperature rise, the critical current of the superconductor is reduced sufficiently that the transport current is split between superconductor and normal conductor [17]. This can happen already much before reaching the transition temperature  $T_c$ . Therefore, the operating temperature of the cooler must be chosen sufficiently low that this effect does not occur. In the case of the high-temperature superconductors and also of MgB<sub>2</sub>, one should analyze again the behavior of the complete magnet [18].

In the case of the cuprates, as well as of MgB<sub>2</sub>, it is still more difficult to fabricate good conductors than in the case of Nb<sub>3</sub>Sn [[19], M22]. However, during the years important advances were achieved. For example, we look at the cuprates. The “powder-in-tube” method

is used frequently for the fabrication of tapes or round wires made of  $\text{Bi}_2\text{Sr}_2\text{CaCu}_2\text{O}_8$  or  $\text{Bi}_2\text{Sr}_2\text{Ca}_2\text{Cu}_3\text{O}_{10}$ . In this case, suitable starting materials (“precursors”) were filled into silver tubes, and then the latter, in a complex sequence of pulling, rolling, and glowing steps, were brought to their final form and composition. [Figure 7.6a](#) shows a cross-section of a  $\text{Bi}_2\text{Sr}_2\text{Ca}_2\text{Cu}_3\text{O}_{10}$ -tape conductor.

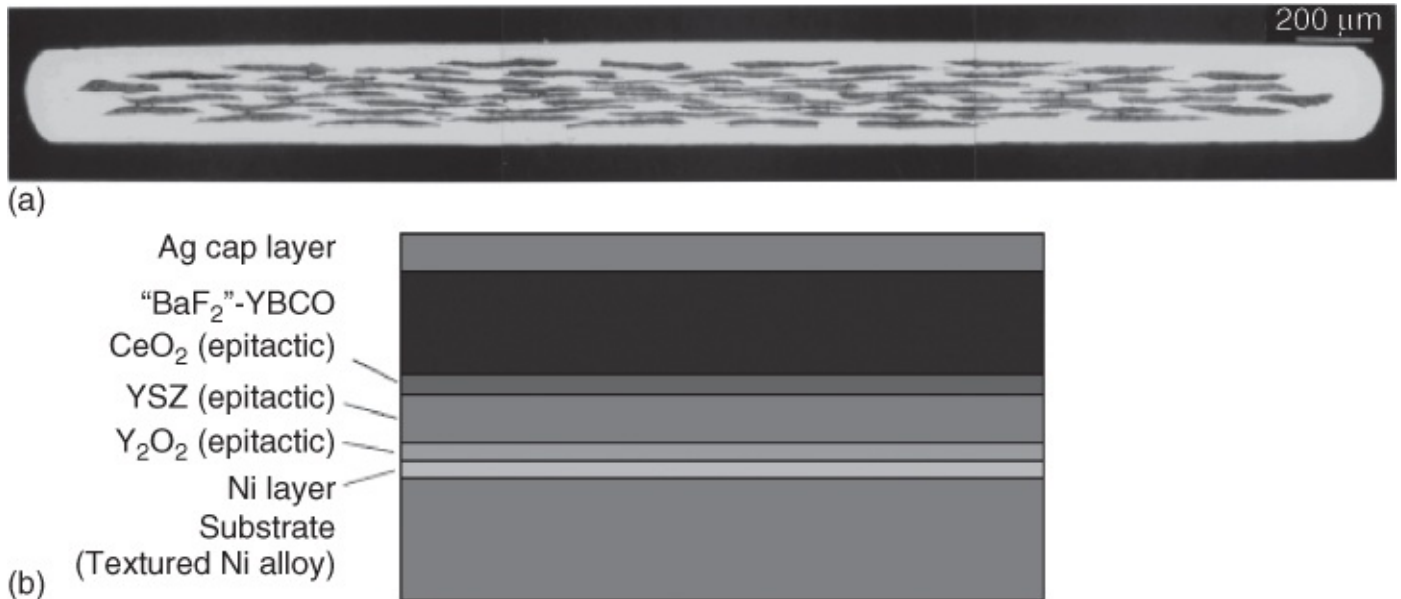


[Figure 7.6](#) (a) Cross-section of a  $(\text{Bi},\text{Pb})_2\text{Sr}_2\text{Ca}_2\text{Cu}_3\text{O}_{10}$  conductor tape. (By courtesy of O. Eibl, University of Tübingen.) (b) Schematic of a  $\text{YBa}_2\text{Cu}_3\text{O}_7$  film prepared using the RABiTS/MOD process on a nickel alloy substrate.

(From [20].)

Conductors fabricated in this way are expensive, not the least because of the silver matrix. Hence, also other fabrication methods are needed. In one concept strongly pursued during the last years, tapes, say, of Ni or Ni–Cu are coated with  $\text{YBa}_2\text{Cu}_3\text{O}_7$  in such a way, that on the one hand the superconductor grows epitaxially with almost perfect crystallographic orientation, and on the other hand the procedure remains feasible and cheap also in the case of large tape lengths. Frequently, this is referred to as **wires** or **tapes** of the second generation. Presently, tapes are fabricated with more than 1 km length, carrying currents of 100 A or more. [Figure 7.7](#) shows an example.

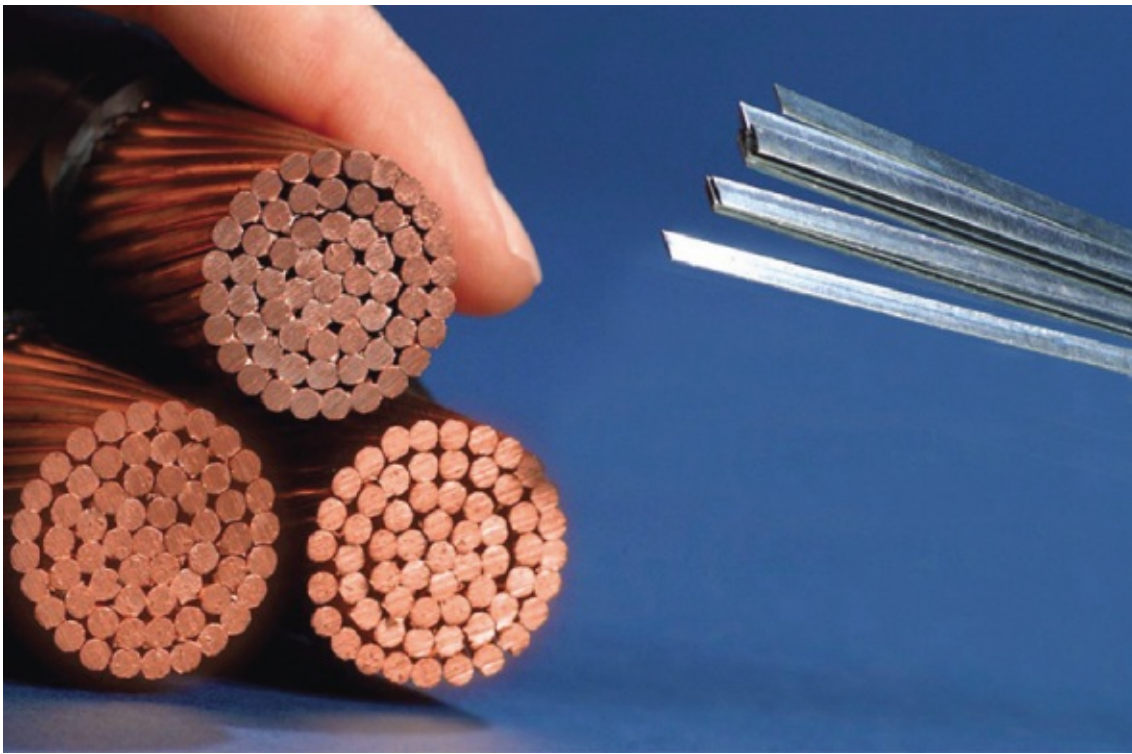


**Figure 7.7** Superconducting tapes made of  $\text{YBa}_2\text{Cu}_3\text{O}_7$  (right) compared with a copper cable (left), which can carry the same amount of current.

(Courtesy of AMC.)

Important fabrication methods are “RABiTS” (rolling assisted biaxially textured substrate) [21] and “IBAD” (ion-beam-assisted deposition) [22]. In the case of RABiTS, initially for adjusting the lattice structure, a number of buffer layers and finally nearly single-crystalline  $\text{YBa}_2\text{Cu}_3\text{O}_7$  are evaporated onto a Ni substrate well oriented along two crystallographic directions (i.e., biaxially textured) in a relatively low vacuum (see [Figure 7.6b](#)). In another method,  $\text{YBa}_2\text{Cu}_3\text{O}_7$  is also precipitated out of organic solutions (MOD, metal-organic deposition) [23]. In the case of IBAD, during the thin-film deposition of buffer layers, for example, onto nickel (usually the laser deposition technique is used), an ion beam is employed in addition for partly removing the buffer layers again and thereby suppressing the growth of crystallites having the wrong orientation. The critical current of the remaining grain boundaries can be increased further by means of a Ca-doped  $(\text{Y,Ca})\text{Ba}_2\text{Cu}_3\text{O}_7$  covering layer [24]. This covering layer compensates the charging effects at the grain boundary.

Conductors made from high-temperature superconductors and also from  $\text{MgB}_2$  are highly interesting for their use as current feeding lines connecting the temperatures near 77 K with the Nb–Ti or the  $\text{Nb}_3\text{Sn}$  magnets operated at 4.2 K. These feeding lines carry a high current, and at the same time they are poor heat conductors. Hence, they provide a considerable reduction of the heat input into the cryostat. In the area of superconducting magnet systems, such current feeding lines were among the first commercial applications of high-temperature superconductors [25].

The last general aspect we want to discuss in the context of superconducting materials deals

with the question of power losses that are dissipated if the field is changed in a magnet, or if a cable is operated with alternating current. Such losses must be minimized as far as possible.

One loss mechanism, which is nearly independent of the rate at which the field changes, results from the fact that in the case of changing magnetic fields the flux lines within the superconductor redistribute themselves irreversibly [M20a]. If the field changes periodically by  $\pm B_{ac}$  around an average value  $B_0$ , one obtains a hysteresis loop in the magnetization curve  $M(B)$ . The area enclosed by this loop yields the energy loss per cycle.

During this cycle, magnetic flux lines enter the superconductor and leave it again, according to [Figure 5.16](#). During this process energy is dissipated. If  $B_{ac}$  is sufficiently small, the flux lines will stay only near the surface of the superconductor, and the loss is relatively small. If  $B_{ac}$  increases, eventually the flux lines will move to the center of the superconductor and back again. This results in maximum losses. At still higher  $B_{ac}$ , the power losses become smaller again, since during most of the time the field completely penetrates the superconductor, and the flux lines only move over relatively small distances. For a given  $B_{ac}$ , one can reach this case also by making the superconducting filaments very thin.

However, in this case we have neglected the fact that in general these filaments are surrounded by an electrically good conducting matrix. According to Maxwell's equation  $\text{curl } \vec{E} = -\dot{\vec{B}}$ , temporally changing magnetic fields result in electric fields and, hence, in lossy eddy currents within the matrix. Furthermore, the latter couple the filaments again. This effect is larger the more rapid the magnetic field changes. Also the effect increases with the conductor surface penetrated by the field. If the magnetic field is oriented perpendicular to the transport current, this results in specific requirements about the length of a conductor piece. For example, we look at a piece of a tape conductor made of superconducting and normal conducting layers [M20a]. The magnetic field is oriented perpendicular to the broad side of the conductor and changes with the rate  $\dot{B}$ . In this case one finds a critical length  $l_c = 4(a\rho j_c/\dot{B})^2$  of the conductor piece, above which the superconducting layers are coupled practically completely by currents within the normal conductor. Here,  $j_c$  denotes the critical current density of the superconductor,  $a$  half of the thickness of the superconducting layers, and  $\rho$  the resistivity of the normal conductor. If we insert typical numerical values, depending on the value of  $\dot{B}$ , we find critical lengths of the order of a few millimeters or centimeters. The trick to divide the filament conductor into small pieces consists of twisting it, as is shown in [Figure 7.8](#). In such arrangements, the induced fields or currents compensate each other to a large extent.

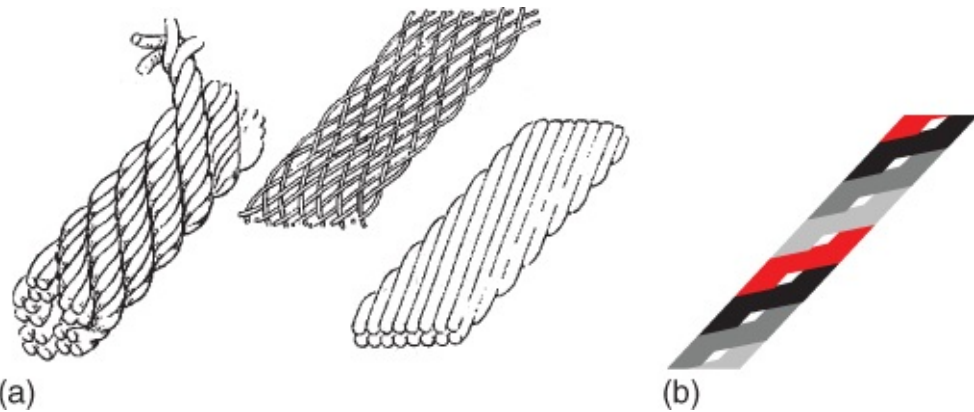


**Figure 7.8** Schematics of a twisted superconducting cable for applications in the case of temporally changing currents and fields. The three arrangements (a) rope, braid, and Rutherford design – require a flexible wire. ([26], © IEEE.) The schematics (b) (Röbel-design) is suitable also in the case of tape conductors made of high-temperature superconductors.

The exact treatment of the eddy-current losses is relatively complicated because in addition to the external field, all conductor elements also affect a given conductor piece. Details can be found in [M20a, [27]].

Now we return to the superconducting magnets and discuss the questions dealing with the protection of the coil.

### 7.1.3 Coil Protection

Even with the use of fully stabilized materials and perfect construction of the coil, events (e.g., gas breaking into the vacuum of the cryostat) can happen that lead to the coil becoming normal conducting. In this case the magnetic field breaks down, and the total energy stored in the magnetic field is abruptly turned into heat. In large coils this energy is large. For example, a magnetic field of 5 T within a volume of  $1 \text{ m}^3$  represents a stored field energy of 10 MJ (about 2.8 kWh). If upon entering the normal conducting state this energy is turned into heat in an uncontrolled way, the complete destruction of the magnet is possible.

In this case several processes can happen. The abrupt heating can cause local melting of the coil material, because very high currents are generated by induction during the breakdown of the field. We mention also that the induction processes can also endanger the whole cryostat. If large eddy currents are generated in the metal walls of the cryostat, there also appear large forces, which can possibly exceed the mechanical load limit. All these problems must be carefully noted during the construction of superconducting magnets.

If in the normal conducting state the electrical resistance of the coil is large, the generated currents will remain small, and destruction due to joule heating can be avoided. However, in this case during the decay of the magnetic field there appear very large voltages, which can cause electric discharges between the windings of the coil.

In order to avoid such catastrophic consequences of an abrupt unintended transition of the coil into the normal conducting state, in particular for large coils, protective devices must be

incorporated that allow the stored energy to be removed from the magnet coil as fast as possible. In principle, this can be done in several ways. In [Figure 7.9](#) we show three possible forms of the corresponding equivalent circuits [28].

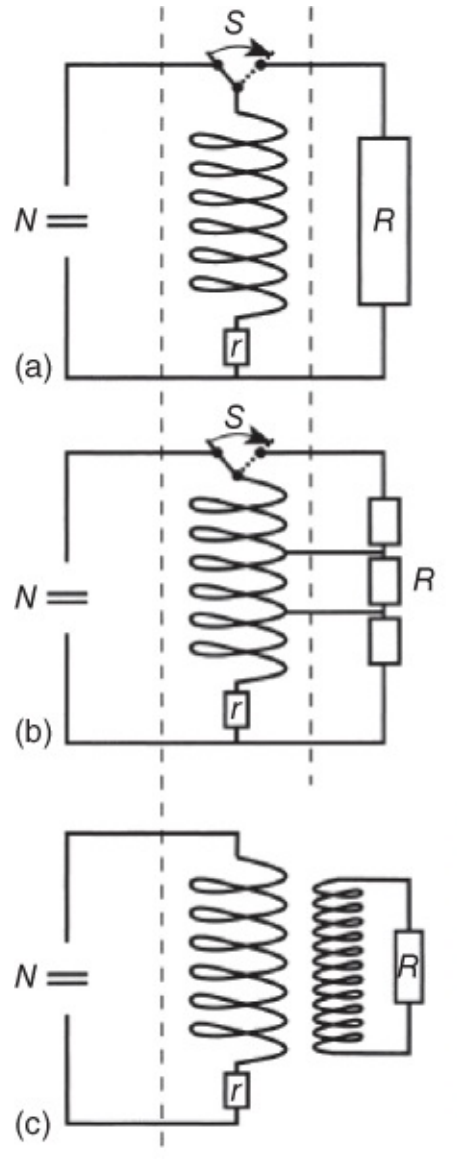


**Figure 7.9** Three examples (a),(b) and (c) of electric coil protection:  $N$  = current supply;  $r$  = internal resistance of the coil;  $R$  = protective resistance;  $S$  = switch, which is automatically activated at a disturbance. The dashed lines surround the parts located within the He bath.

An obvious possibility is shown in [Figure 7.9a](#). In this case the magnet coil is connected with an external resistance  $R$ . If this resistance  $R$  is large compared to the internal resistance  $r$  of the coil, during the decay of the magnetic field the dominant part of the stored energy  $E$ , namely the fraction  $ER/(R + r)$ , will be dissipated in the external resistance in the form of heat. This method has the advantage that only a small amount of liquid helium evaporates within the cryostat. The disadvantage of this solution results from the high electrical voltages generated during the decay of the field, since  $R$  must be large compared to  $r$ . Hence, coils that are protected with this system must be particularly carefully insulated against internal discharges.

A better variant of this procedure is shown in [Figure 7.9b](#). In this case the coil is separated into

different sections, each of which is connected with its own protective resistance. In this way any voltage that appears is also divided up, and extreme voltage peaks can be avoided.

In special cases it can also be advantageous to remove the stored energy inductively from the magnet coil ([Figure 7.9c](#)). For this purpose, the coil must be surrounded by a closed conductor having a small self-inductance. Then during the decay of the magnetic field the dominant energy dissipation will take place within this conductor, say, a copper cylinder. However, this conductor must be placed very close to the coil, that is, within the He bath, in order to achieve good inductive coupling. The disadvantage is that the whole energy is transferred into the liquid-He bath, resulting in a very strong evaporation of the liquid. Per kilowatt-second of dissipated energy of about 250 l of helium gas at normal conditions is generated. This corresponds to the evaporation of about 0.35 l of the liquid. This inductive energy removal will not be used for large coils with a stored energy of a few megajoules. The advantage of this method comes from the fact that no large voltages appear between the windings.

We restrict ourselves to these few examples, since only the principal issues are to be outlined. Every large coil must be individually optimized regarding its whole concept including the cryostat.

The large forces developed at the coils for high magnetic fields represent an important construction problem. Frequently this needs massive supporting structures, which in turn must be designed such that they are not exposed to overcritical forces, say, due to eddy currents, during breakdown of the magnetic field. The force acting on the windings of cylindrical coils radially toward the outside is very strong for high magnetic fields. The magnetic pressure of a field  $B$  stored within the coil amounts to  $p \approx B^2/2 \mu_0$ . At 1 T this yields already about 4 bar. At 20 T the pressure reaches 1.6 kbar, which is high enough for plastically deforming copper. The coil construction must be able to withstand these forces, and in turn the latter also must not influence the magnetic field. As long as the mechanical supporting elements can be placed completely within the cryostat, the construction solutions are not too difficult. However, there are large problems if the application of the magnet requires that the supporting elements must reach the outside of the cryostat. The mechanical construction must be very massive because of the large forces and, hence, it results in a large heat input into the cryostat. If possible, all supporting structures are designed in such a way that the materials predominantly experience tension in order to keep the cross-sections as small as possible.

These few examples should provide an impression about which engineering tasks are confronted during the construction of a reliable superconducting magnet for high magnetic fields, and which must be solved.

## 7.2 Superconducting Permanent Magnets

So far we have discussed the generation of magnetic fields by means of coils carrying high electric currents. However, “hard superconductors,” that is, superconductors containing strong pinning centers (see [Section 5.3.2](#)), provide the possibility to store magnetic fields permanently.<sup>9</sup> The principle can be taken, for example, from [Figure 5.12](#). After the external

field has been raised to a high value and then has been returned again to zero, a remanent field remains trapped in the interior of the superconductor. In the case of the Pb–Bi alloy shown in [Figure 5.12](#), this remanent field is about 0.35 T. The superconductor also could have been cooled down in the applied magnetic field. After the external field has been switched off, the superconductor would have remained magnetized.<sup>[10](#)</sup>

In contrast to a standard permanent magnet, and in contrast to ideal type-I or type-II superconductors, a hard superconductor will try to keep the field in its interior at the value at which it was cooled down. As a result, a hard superconductor can hang firmly underneath a magnet, or it can be positioned askew (see the hanging levitated train of [Figure 1.11](#)). This toy demonstrates the potential of superconducting magnets. One can imagine superconducting bearings, gyroscopes,<sup>[11](#)</sup> flywheels for energy storage, motors, and much more [[29], M23]. However, in this case, we must consider the balance between the costs and the benefits.

In this case, the high-temperature superconductors again have the advantage that the cooling requirement is less expensive. With these materials during cooling down to 77 K, one can trap already fields of about 1 T. At a temperature of 29 K about 17 T were trapped in such materials. This exceeds the strongest standard magnets (alloys of Nd, Fe, and B) by a factor of 10 [30–32]. In this case the limit is not determined by the pinning centers, but instead by the mechanical strength of the material. At these fields, the magnetic forces pointing toward the outside become so large that they simply tear apart the high-temperature superconductors. Already in the case of the field values achieved presently the superconductors must be surrounded by special steel supports in order to at least compensate the magnetic pressure.

The results discussed above were obtained using melt-textured  $\text{YBa}_2\text{Cu}_3\text{O}_7$  [33]. In this fabrication process, first polycrystalline compressed  $\text{YBa}_2\text{Cu}_3\text{O}_7$  cylinders with a diameter of a few centimeters are prepared. During this step the grains within the cylinder are arbitrarily oriented. In this form the material could transport only relatively small supercurrents. The main reason is the fact that the grain boundaries between the grains are strongly tilted relative to each other and act like Josephson junctions, even if they are sintered together very well. Even in the absence of an applied magnetic field, the critical current of these junctions is small and rapidly approaches zero in the presence of a magnetic field. If we want to obtain a massive material with a large value of the critical current, we must orient the grains as much as possible, such that the  $\text{CuO}_2$  planes all have nearly the same orientation. In this case large supercurrents can flow parallel to these planes. At the same time, highly effective pinning centers trapping the vortices must be introduced into the material.

Both of these conditions are satisfied by the melt-texturing technique. In a simplified description, the polycrystalline compressed cylinders are heated initially up to above 1000 °C so that they melt. Additional seed crystals with a higher melting point ( $\text{MgO}$ ,  $\text{SrTiO}_3$ , or  $\text{SmBa}_2\text{Cu}_3\text{O}_7$ ) are attached to the compressed cylinders. During the subsequent cooling process, these seed crystals cause a nearly single-domain recrystallization of the superconductor.

Furthermore, admixtures, such as  $\text{Y}_2\text{O}_3$ , which reacts during the tempering process, yielding

nonsuperconducting  $\text{Y}_2\text{BaCuO}_5$ , are added to the compressed cylinders.  $\text{Y}_2\text{BaCuO}_5$  is finely dispersed within the cylinder and forms highly effective pinning centers trapping the vortices. In this way, finally one obtains a material that can carry very high supercurrents parallel to the  $\text{CuO}_2$  planes.

The procedure we have just described is one of several possibilities to produce well-textured, massive materials from high-temperature superconductors. A summary of the different methods can be found in [34].

## 7.3 Applications of Superconducting Magnets

### 7.3.1 Nuclear Magnetic Resonance

Nuclear magnetic resonance (NMR) represents an important tool for investigating the structure of organic molecules. In this case the material to be studied is placed within a magnetic field. In the field, because of the quantization of the direction, the hydrogen nuclei can occupy only two orientations of their magnetic moment relative to the magnetic field, namely parallel or antiparallel. These two orientations differ in their potential energy. The parallel orientation has the smaller potential energy, that is, energy must be supplied in order to turn the moments away from the parallel orientation. The energy difference between the two orientations is proportional to the magnetic field, which is assumed to be oriented along the z-direction:  $\Delta E = 2\mu_z B_z$ . Here,  $\mu_z$  is the magnetic moment in the z-direction.

The hydrogen nuclei of an organic molecule are distributed over these states. In this case the more favorable energy level is occupied somewhat more strongly. This distribution is shown schematically in [Figure 7.10a](#). If this system is irradiated with an electromagnetic wave having the quantum energy  $hf = \Delta E$ , transitions between the levels  $E_1$  and  $E_2$  are caused by this radiation. Since the lower level is occupied more strongly, more transitions per unit time take place from the bottom up than in the opposite direction, that is, the radiation is absorbed. If we vary the frequency  $f$  of the radiation at constant magnetic field, we observe a typical absorption signal at the resonance frequency  $f_r = \Delta E/h$  ([Figure 7.10b](#)).

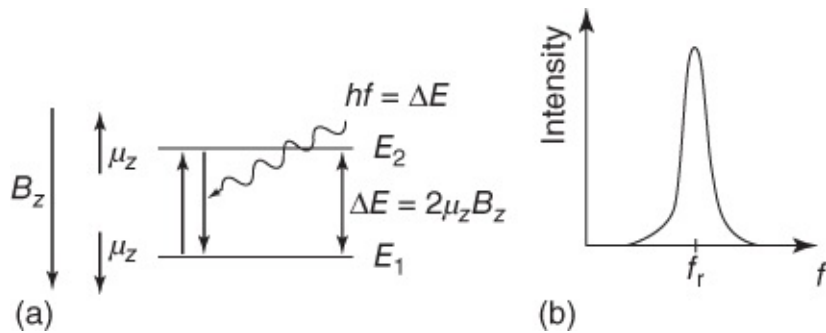


[Figure 7.10](#) Schematic diagram of nuclear magnetic resonance: (a) energy levels and (b) absorption signal.

The hydrogen nuclei sense not only the external field  $B_z$ , but also their (chemical) environment.

This is highly crucial. It results in the fact that the resonance frequency of the hydrogen nuclei is slightly different in different chemical environments, for example, within the CH<sub>3</sub> or CH<sub>3</sub>O groups of an organic molecule. This frequency change is referred to as the ***chemical shift***. We see that NMR allows one to identify the chemical environment of a hydrogen nucleus. This possibility is extremely important for clarifying the structure of organic molecules.

The resolution of the individual lines becomes difficult or impossible if the line width is larger than their mutual distance on the frequency axis. In this case one only observes a large unresolved signal. In addition to the features of the apparatus (e.g., the homogeneity of the magnetic field), the width of individual lines is determined by the interaction of the specific nucleus with the more distant groups of the molecule. Because of this interaction, the absorption line of a specific group of protons again consists of a whole number of narrower lines, and, hence, displays a distinct half-width.

In this case an important improvement of the resolution can be achieved by means of high magnetic fields. The chemical shift is proportional to the external magnetic field, that is, the lines from the different groups of protons move further apart with increasing field. However, the line separation due to the interaction with neighboring groups is independent of the external field  $B_z$ , that is, the half-width due to this interaction remains constant also in high fields.

Hence, in high fields it is possible to separate such lines of the different groups, which still overlap with each other at smaller fields, and to measure precisely the chemical shift and the coupling between the nuclear spins. In [Figure 7.11](#) this is shown by means of the comparison of NMR measurements performed at 9.4 T (400 MHz), 14.1 T (600 MHz), and 21.1 T (900 MHz).

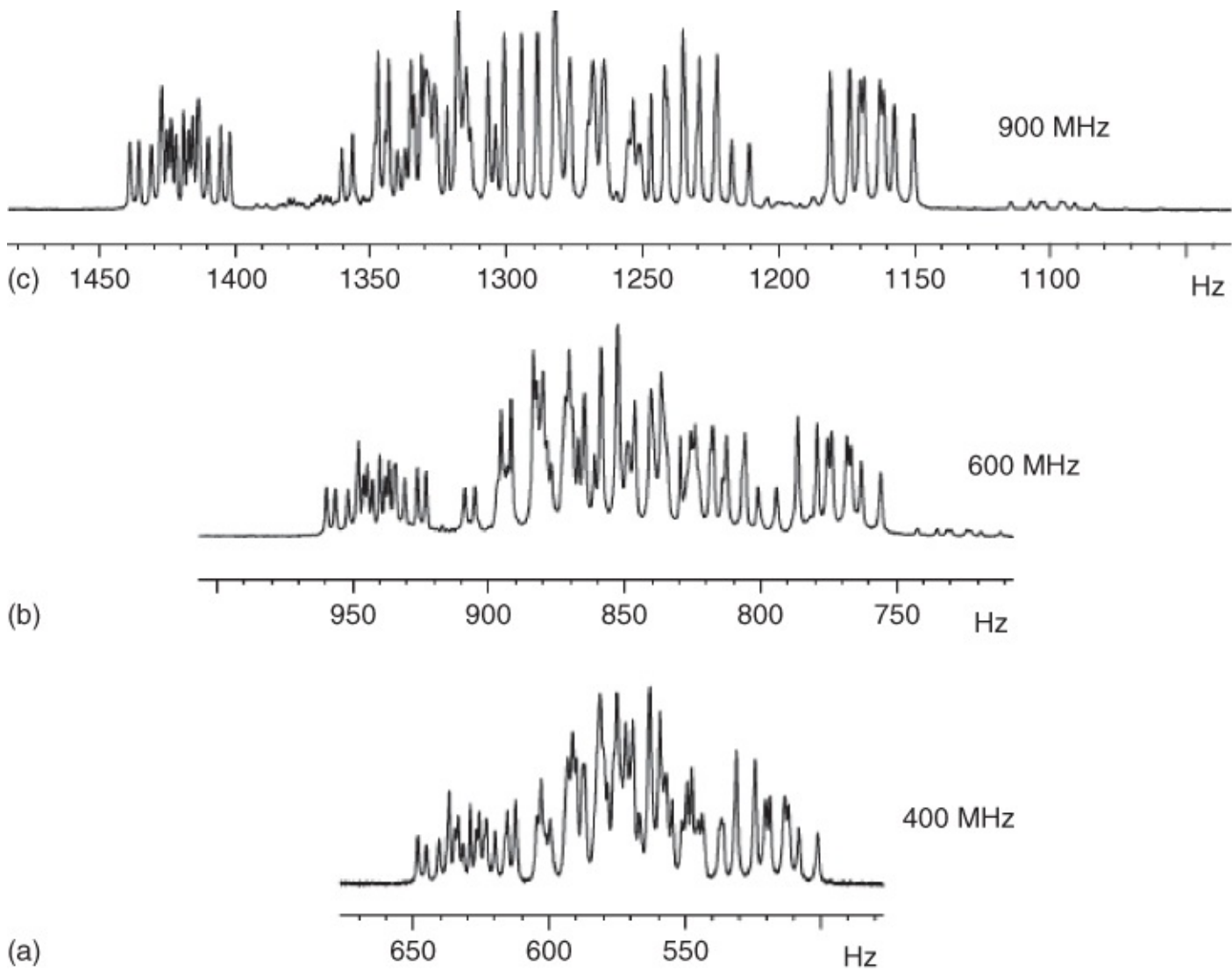


**Figure 7.11** Comparison between the NMR spectra of estradiol acetate in fields of 9.4 T (a), 14.1 T (b), and 21.1 T (c).

(Courtesy of Bruker BioSpin Inc.)

The large and temporally stable fields of superconducting magnets provide an important advantage. However, for these high-resolution resonance spectrometers, it is necessary to have extremely homogeneous fields at the location of the sample. Each field inhomogeneity increases the half-width of the lines.

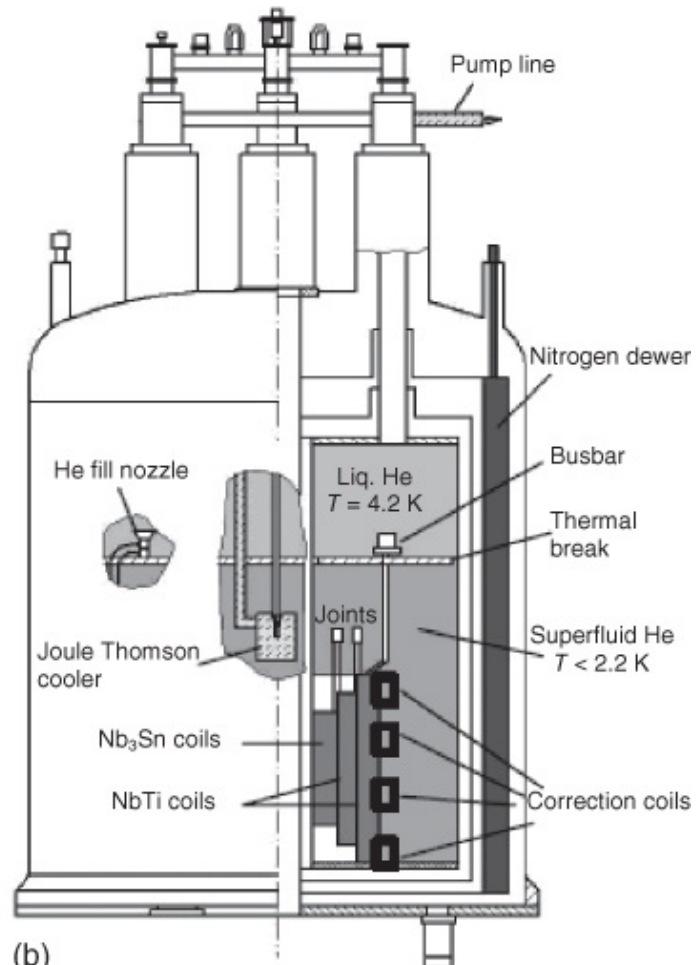
In the early 1970s, there were systems that were operated at 7.5 T and had a field homogeneity (relative field deviation) of better than  $2 \times 10^{-7}$  within the sample volume (sphere with 1 cm diameter) [35]. It was possible to resolve NMR lines that differed in their frequency only by  $\delta = 0.05$  Hz at a measuring frequency of 270 MHz. Today, the field of superconducting NMR magnets ranges from 4.7 T (corresponding to a proton spin resonance frequency of 300 MHz) up to 23.5 T (1 GHz) with a typical bore at room temperature of 54 mm. The field homogeneity<sup>12</sup> amounts to  $10^{-10}$  within a sample volume of  $5 \times 5 \times 20$  mm<sup>3</sup>. The standard frequency resolution of such systems is 0.2 Hz.

The photograph in [Figure 7.12a](#) shows a modern 1000 MHz NMR spectrometer with its

superconducting magnet system of about 4 m in height, representing presently the limit of a technically feasible NMR apparatus. The principles of the construction of such a magnet system are shown in [Figure 7.12b](#).



(a)



(b)

**Figure 7.12** NMR spectrometer: (a) modern 1000 MHz NMR spectrometer with a highly homogeneous 21.1 T magnetic field and (b) principle of construction of an NMR magnet system cooled with superfluid helium.

(Courtesy of Bruker BioSpin Inc., Karlsruhe.)

Usually the superconducting magnet consists of different shells. In the region with the highest field near the central bore of the magnet, Nb<sub>3</sub>Sn conductors are used because of their higher critical field compared to Nb–Ti. In the external parts with a smaller field, the material Nb–Ti is used because of its better properties in this case and its more favorable cost factor. The individual conductor sections must be connected by superconducting joints. The superconducting correction coils needed to homogenize the field are mounted on the outside around the main magnet.

The superconducting wires are surrounded by superfluid helium. For this purpose about 250 ml/h liquid helium are permanently pumped off using a Joule–Thomson cooling unit. Every 2 months the helium reservoir must be refilled. The helium tank is surrounded by another tank filled with liquid nitrogen and acting as a radiation shield. The liquid nitrogen must be refilled about every 3 weeks.

A maximum-field NMR magnet such as shown in [Figure 7.12](#) is charged stepwise up to its full field. At the end it stores a magnetic field energy of more than 10 MJ. Then the magnet is shorted by closing a superconducting switch, and the persistent-mode operation is established. Finally, to minimize the heat input, the massive current feeding lines are removed from the magnet. In the shorted state the magnetic field changes only by less than 10 ppm per year, and the magnet can be operated for many years without intervention from the outside. The extremely small resistive losses in the superconducting wires or joints are due to vortex motion.

As we have indicated already in [Section 7.1.1](#), in the area of maximum-field NMR the use of high-temperature superconductors will be crucial. Therefore, it is intended to use conductors made of  $\text{YBa}_2\text{Cu}_3\text{O}_7$ ,  $\text{Bi}_2\text{Sr}_2\text{CaCu}_2\text{O}_8$ , or  $\text{Bi}_2\text{Sr}_2\text{Ca}_2\text{Cu}_3\text{O}_{10}$  for the inner shells of the magnet where the field is highest. In this way the magnetic field can be raised to the required value at the location of the sample.

In recent years NMR spectroscopy has experienced enormous growth, in particular because of the advances achieved in the study of large molecules, such as proteins and prions. In order to cover the strongly increasing demand of maximum-field NMR equipment in Europe, the United States, and Japan, there is a large effort to set up powerful NMR laboratories. Presently, the worldwide annual investment in superconducting NMR spectrometers amounts to about US\$ 250 million.

### 7.3.2 Magnetic Resonance Imaging

With magnetic resonance imaging (MRI), NMR has found a medical application, without which modern medicine could not be imagined any longer. In this case the method presented in [Figure 7.12a](#) is used for studying human tissue.

In the field of structural chemistry, high-resolution nuclear spin resonance essentially utilizes the shift of the resonance frequency of protons (and also of other nuclei) due to their different chemical environments (chemical shift) as well as the coupling between the nuclear spins. On the other hand, in MRI the strength of the resonance signal is used as a measure of proton density. However, also the relaxation times of the nuclear spins are used as the measurement signal. We distinguish between two relaxation times,  $T_1$  and  $T_2$ :  $T_1$  is a measure of the time it takes for a system of nuclear moments to reach equilibrium orientation in a magnetic field and  $T_2$  is associated with the phase of the precessing nuclear moments. Both relaxation times can be used diagnostically.

To generate the required magnetic fields, in the larger systems superconducting Nb–Ti coils are used. Since the 1980s instruments have been constructed in which the whole body of a patient can be studied. For routine applications fields amount up to 3 T. For scientific and medical research, fields up to 9 T are used. This technique is particularly promising for the investigation of the functional behavior of the human brain (fMRI). In [Figure 7.13](#) we show one of the most advanced whole-body nuclear spin tomographs, operating with a static field of 3 T. The system includes an active cooling device, and helium must be refilled only once every

year.

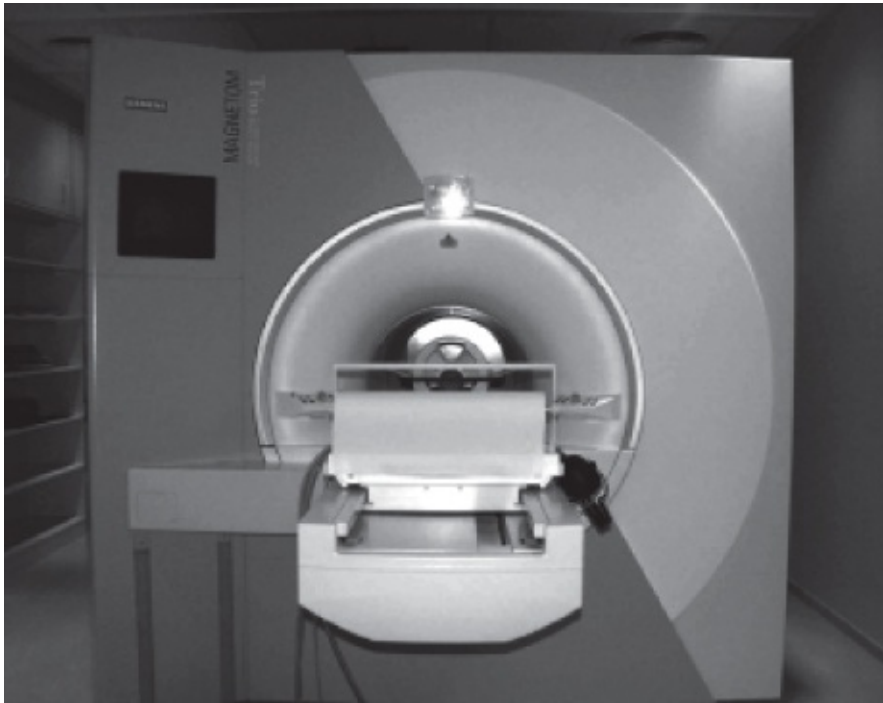


**Figure 7.13** View into the 3 T whole-body nuclear spin tomography with a superconducting magnet, installed in the Radiology Clinic at the University of Tübingen (Siemens Magnetom Trio). In the foreground we see the table that is moved into the tube of the tomography.

(Courtesy of Radiology Clinic, University of Tübingen.)

In order to correlate the nuclear spin signals with the spatial coordinates, that is, to obtain a map of the signal height or of the relaxation times, a spatially varying magnetic field, for example, a field increasing linearly along the  $x$ -direction with the slope  $dB_z/dx$ , is superimposed onto the constant magnetic field  $B_z$ . Then the location of the detected nuclei along the  $x$ -axis can be determined according to the resonance frequency. Within this layer, by means of short applied gradient fields, one selects signals according to frequency and phase. In this way in  $\mathbf{k}$ -space one obtains a spatially resolved representation of the layer. From this, the spatial image is finally calculated. In [Figure 7.14](#) we show the image of a human head and brain obtained in this way.

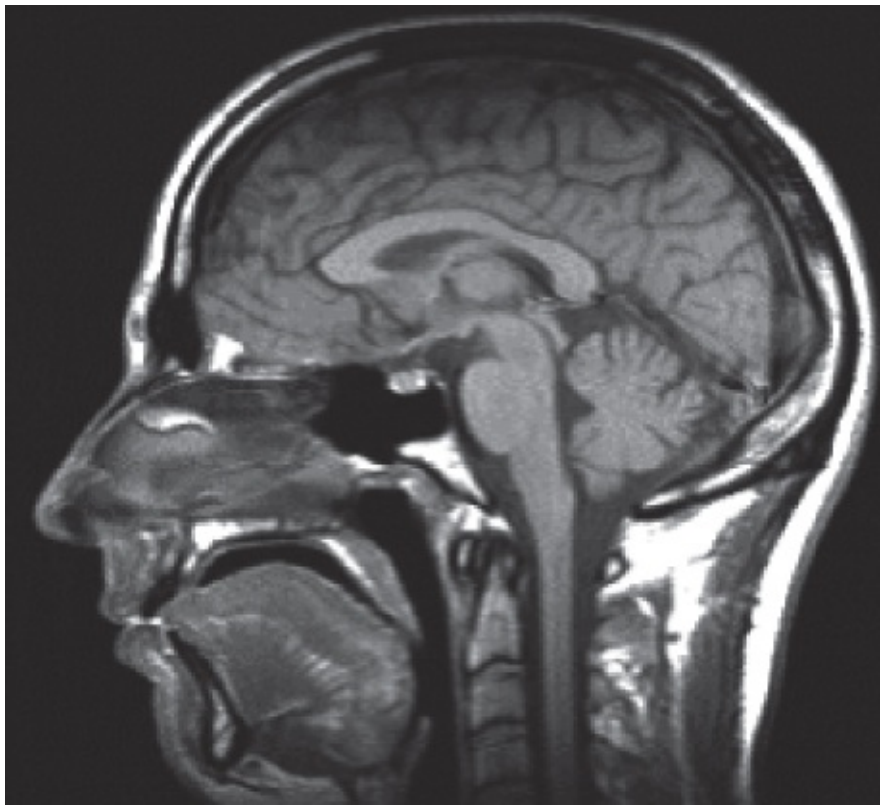


**Figure 7.14** Magnetic resonance image of a human head and brain.

(Courtesy of Radiology Clinic, University of Tübingen.)

### 7.3.3 Particle Accelerators

Another large field of applications of superconducting magnets, in particular also of very large magnets, has developed in the area of high-energy physics [36, 37]. Today, particles are accelerated up to energies in the tera-electronvolt range ( $1 \text{ TeV} = 10^{12} \text{ eV}$ ) [26]. These particles with high energies, for example, protons or electrons, must be kept on their trajectories by means of suitable magnetic fields. In a simplified description, this is easier the stronger the available magnetic fields. In particular, at constant energy, with increasing magnetic field, the diameter of the circular accelerator can be made smaller. On the other hand, for the same diameter, with increasing magnetic field, higher particle energies can be reached. Superconducting magnets can also be used for guiding the particle beams after they have left the accelerator.

Early generations of particle accelerators have been equipped with conventional magnets. However, presently these facilities cannot be imagined any longer without superconducting magnets (mostly made of Nb–Ti). The largest facility today, the Large Hadron Collider (LHC) at CERN, contains 1232 large dipole magnets, which generate a magnetic field of 8.3 T with a current of 11 850 A. Each magnet is 14.3 m long, and cooling is by superfluid helium. In addition, 7000 further magnets are used for beam guidance and beam corrections. The huge detector systems ATLAS and CMS also contain large magnets [38]. [Figure 7.15](#) shows a view on some of the dipole magnets of the LHC within the storage ring of 26 km circumference. In [Figure 7.16](#) we see how two of these magnets are joined together. These figures provide an

impression of the immense technical effort, which the application of superconductivity has reached.



**Figure 7.15** View of the dipole magnets within the LHC circular tunnel.

(Courtesy of CERN.)

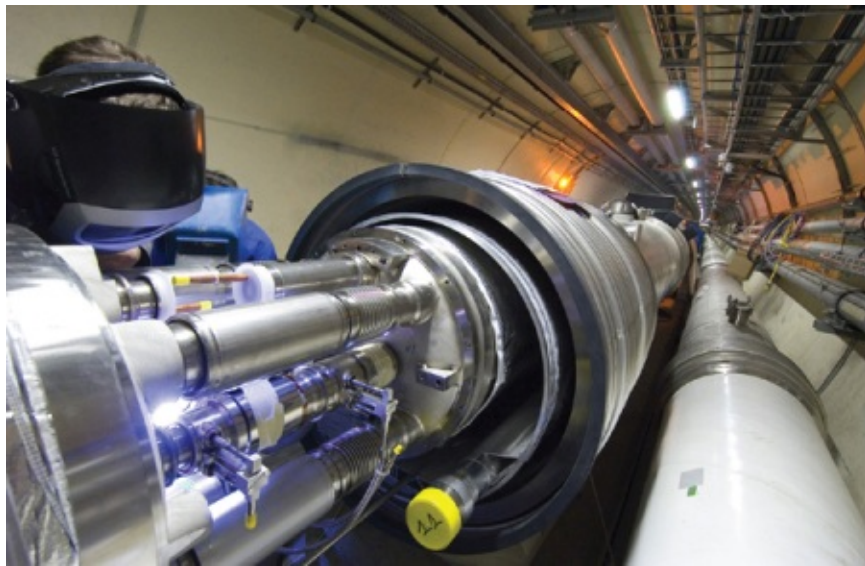


**Figure 7.16** Two dipole magnets of the LHC are joined together.

(Courtesy of CERN.)

In addition to these large facilities, we should not forget that smaller systems are also very important [36]. For example, electron storage rings become important for the fabrication of semiconductor devices. In order to fabricate structures in the deep submicrometer range, the wafers must be irradiated with soft X-rays, which are generated with high intensity in the form of synchrotron radiation in storage rings. Due to the use of superconducting magnets, such instruments can be built in a relatively compact way. Cyclotrons are also used in medicine, for

example, for the generation of short-lived radioisotopes for positron emission tomography (PET). In this case Oxford Instruments has made a compact system commercially available, which uses superconducting magnets [36].

Finally, we point out that superconducting resonant cavities represent another important component of accelerator physics. We will return to this subject in [Section 7.5.2](#).

### 7.3.4 Nuclear Fusion

At present a large effort is being made to achieve controlled nuclear fusion, that is, the fusion of two hydrogen nuclei to forming a helium nucleus, a process that occurs spontaneously in the hydrogen bomb. The energy gain of this process is very large. Since there is an almost unlimited supply of hydrogen on Earth, this thermonuclear process could become an important energy source in the future. Presently, work on fusion is still at the level of fundamental research. On the way to controlled nuclear fusion, very large difficulties must be overcome. In order to start the energy delivering processes, hydrogen gas must be heated up to temperatures of at least a few ten million degrees. This hot plasma practically consists only of hydrogen nuclei<sup>13</sup> and electrons, and, of course, cannot be kept simply in some material container. However, since we are dealing with charged particles, the particle trajectories can be bent by means of a magnetic field. Therefore, it is possible to keep the particles within a suitable reaction chamber in spite of their high velocity using sufficiently high magnetic fields of suitable geometry. However, the required magnetic fields are so high that they can be generated economically only with superconducting magnets.

In recent years, research has concentrated on two types of reactors, the stellarator and the tokamak [39]. In Germany the stellarator “Wendelstein” is under construction [40], and in Japan the Large Helical Device (LHD) [41, 42]. Here, we want to describe briefly the project ITER, a reactor of the tokamak type presently in Cadarache under construction. ITER represents a cooperation between the European Union, Japan, Russia, China, South Korea, India, and the United States. The goal is to build a 500 MW fusion reactor with an energy amplification of 10.

In [Figure 7.17](#) we show a schematic diagram of the projected reactor [10]. Within the reactor there are a number of different coils, which provide, for example, the magnetic enclosure of the toroidal fusion plasma and also the generation of a heating current in the plasma. The person shown at the bottom indicates the immense dimensions of the system. In this case, magnetic fields up to 13 T are generated in the interior of the fusion region.

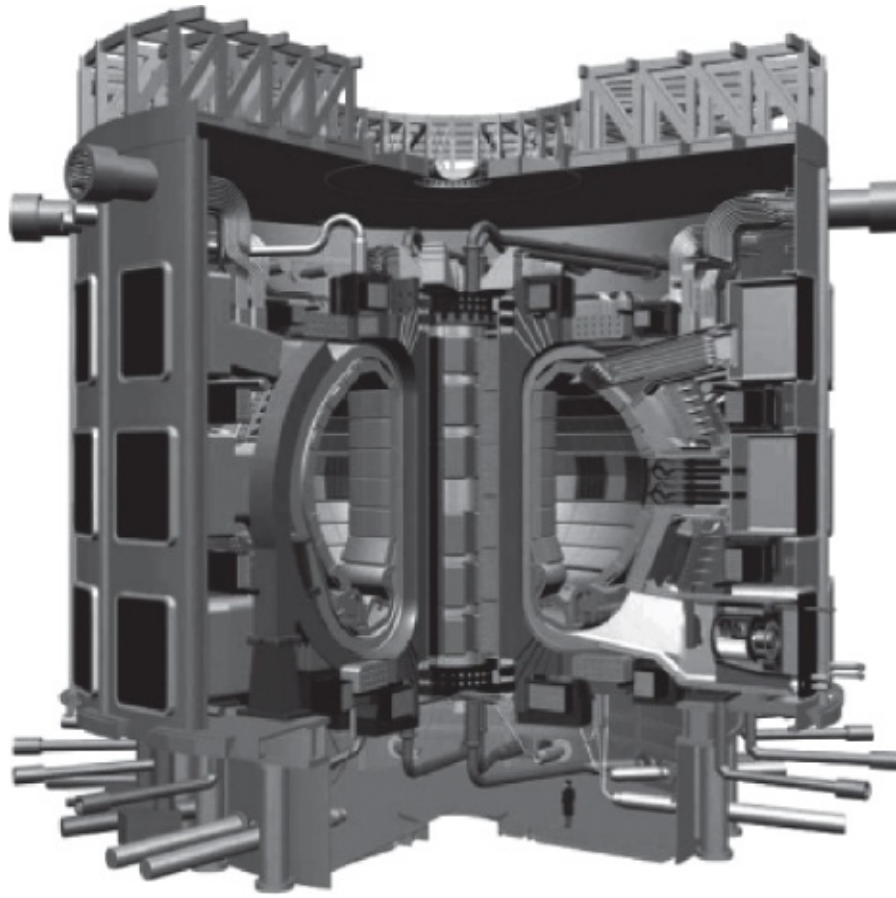


**Figure 7.17** Schematic of the fusion reactor ITER, which is presently under construction. The toroidal plasma chamber (with a kidney-shaped cross-section) is enclosed by 18 field coils (each 14 m high and 8 m wide). At the torus axis (center of the picture), the central coil (12 m high, 4 m diameter) is placed vertically. The torus is surrounded by six poloidal coils and by smaller correcting coils.

(Reprinted from [10] with permission of IOP.)

### 7.3.5 Energy Storage Devices

Energy storage represents another area in which superconducting magnets could become very important in the future. In the early years, projects dealt with extremely large coils for storing energy in the form of magnetic fields.<sup>14</sup> On the other hand, the projects and the experimental studies of today concentrate on medium-sized or smaller systems [43], which store energies in the range of 1–100 MJ very effectively, and also deliver it back very fast with powers in the range of a few megavolt amperes.<sup>15</sup> The purpose of this energy storage is essentially to stabilize the supply of power in times of peak consumption or after a disruption [44]. Frequently, there occur fluctuations in the range of seconds or even milliseconds. In contrast to, say, pump storage facilities, magnetic coils can supply their stored energy sufficiently fast.

In the case of  $B = 1$  T, the magnetic energy density  $B^2/2 \mu_0$  amounts to 0.4 MJ/m<sup>3</sup>. If we want to store 10 MJ at 5 T, we need this (average) field in a volume of about 1 m<sup>3</sup>, which is not an extreme requirement. Furthermore, the magnetic field should be kept within a closed volume as much as possible. The stray field should be kept small because of environmental aspects and

also to keep the mechanical forces small, which are acting on the coil. Also the eddy-current losses within the range of the stray field would make the storage less effective. Therefore, frequently toroidal field configurations are preferred. As we have mentioned, the energies stored in the magnet must be available very fast. In this case high induction voltages appear, which, for example, in the SMES system planned for the fusion reactor ITER, can amount to nearly 5 kV. (In this case 1 GJ is supposed to be stored with a maximum delivered power of 150 MVA). Because of these high specifications, at present larger systems based on conventional superconductors are developed. However, small energy storage devices based on high-temperature superconductors have been realized already [45]. In this case, the attractive feature results from the possibility of achieving a very simple operation at temperatures in the range of 25–70 K by means of cryo-coolers.

In [Figure 7.18](#) for illustration we show a relatively small 80 kVA system storing 200 kJ at a current of 300 A [46]. In this case a torus configuration with an inductance of 4.37 H is formed by 10 Nb–Ti magnet coils (diameter 36 cm). The current can be increased briefly up to 430 A, and then about 420 kJ can be stored.

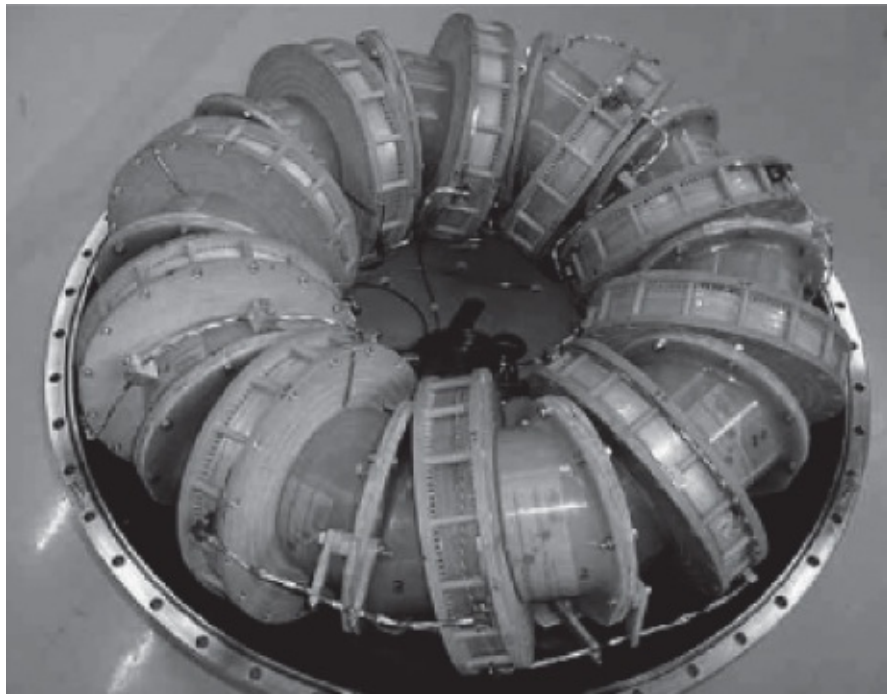


**Figure 7.18** Magnetic energy storage device consisting of 10 Nb–Ti coils (diameter of each coil: 36 cm). Up to 420 kJ can be stored.

(Courtesy of Dr K.-P. Jüngst, Research Center, Karlsruhe.)

In addition to the superconducting coil and the cooling arrangement, the whole SMES system consists of an energy preparation system, which represents the interface between the power grid to be stabilized and the coil. Here, the alternating current of the grid is transformed into the direct current within the coil, and if the grid must be stabilized, back again at only small energy loss. In addition, the electronic control is needed. Using Nb–Ti, for the cooling the cost only amounts to about 15% of the total cost of the system [44]. So they do not represent an important factor.

The second possibility for energy storage or stabilization of the power grid is rapidly rotating flywheels. This technique is particularly interesting for the use of high-temperature superconductors. Typical energies that are stored range between kilojoules and megajoules. In the case of a homogeneous, disk-shaped flywheel, the rotation energy is  $mr^2\omega^2/4$ . It increases quadratically with the angular frequency  $\omega$  and linearly with the mass of the disk. A rotating disk with a diameter of 0.5 m, a mass of 1 kg, and an angular frequency  $\omega = 1000$  Hz (about 10 000 rpm) already contains an energy of more than 15 kJ.

Many commercial flywheels are made of steel, placed on an air-cushion bearing, and rotate with a relatively low angular velocity. Alternatively, using glass-fiber-reinforced plastic materials, high rotation speeds in the range of 50 000 r.p.m and more are being used. In this case the stored energy per kilogram of active mass is larger by more than an order of magnitude than in the case of SMES or of flywheels made of steel [47]. Typical power values to be delivered by flywheels range between kilovolt amperes and megavolt amperes, and these energies should be stored over several hours.

For example, with melt-textured  $\text{YBa}_2\text{Cu}_3\text{O}_7$  (see [Section 7.2](#)), standard permanent magnets can be levitated in a stable way. In this case the magnets can also rotate or carry a load, for example, a flywheel. This provides the possibility to construct highly stable flywheels with low losses based on superconducting bearings. It should be possible to achieve storage times of 100 h and more [48]. At present different designs are being studied. The flywheels should store energies between a few kilowatt-hours and a few hundred kilowatt-hours. For example, relatively light and small flywheels (a few kilograms mass, about 50 cm diameter), which operate at rotation speeds of 10 000 r.p.m. and more [49, 50], have been studied. But systems as heavy as tons rotating at speeds of a few thousand revolutions per minute have also been investigated [51]. In this case various problems must still be solved, such as the avoidance of flux jumps in the superconductor, which result in a lowering of the flywheel with time.

In the case of a flywheel presently developed at Boeing [50], [Figure 7.19a](#) shows the rotating part of the magnetic bearing carrying the rotor consisting of aluminum and carbon fibers. In the figure we see several concentric rings. The outer ring made of fiber-reinforced composite material holds the structure together. Then follow alternately rings made of permanent magnets and ferromagnetic steel. The arrangement generates an axial magnetic field with a high-field gradient near the surface. In the actual construction, the side shown in the figure is pointing down and rotates closely above a layer consisting of melt-textured  $\text{YBa}_2\text{Cu}_3\text{O}_7$ -pellets ([Figure 7.19b](#)). The total rotor has a mass of 132 kg, and at about 22 000 rpm it can store an energy of 18 MJ (5 kWh).

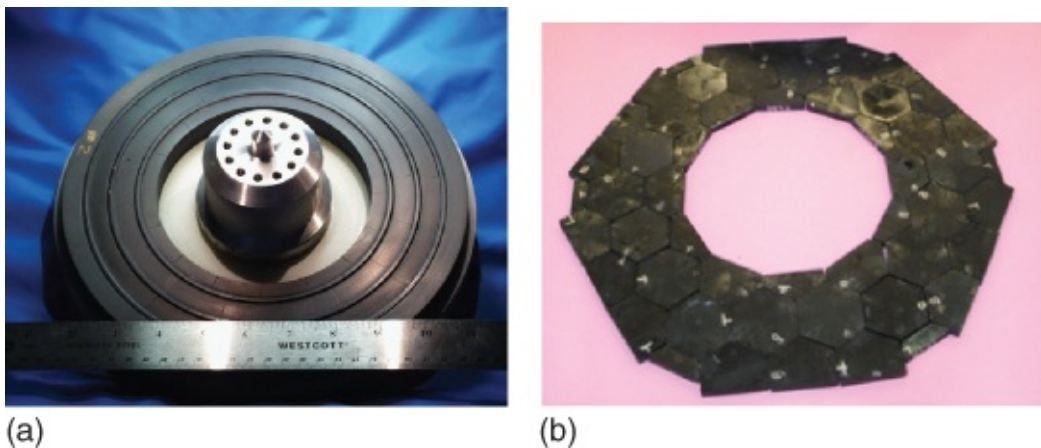


**Figure 7.19** The rotating part of the magnetic bearing of a flywheel (a). Courtesy of IOP. The layer made of  $\text{YBa}_2\text{Cu}_3\text{O}_7$ -pellets, above which the flywheel rotates (b).

Courtesy of M. Strasik, Copyright © 2011 Boeing, all rights reserved.

### 7.3.6 Motors and Generators

In the case of electric motors basically one uses the fact that in an external magnetic field moving electrons experience the Lorentz force directed perpendicular to the direction of the field and of the electric current. In particular, this results in a torque acting on the magnetic moment associated with circular currents, pulling the latter moment in the direction parallel to the field.

In the simplest arrangement, the unipolar motor, the current in the rotor mostly flows parallel to the rotational axis. If the external magnetic field is oriented in radial direction, the Lorentz force leads to a rotation of the rotor. The first electric motors were of this type.

More advanced are motors where the magnetic coils of a “stator” generate a temporally changing magnetic field, which rotates around its axis at constant field amplitude. This field causes a torque acting on the rotor within the stator and results in the rotation of the former. In the case of the synchronous motor, the rotor carries a constant magnetization and consists of permanent magnets or magnetic coils operated with a constant current. In the case of the asynchronous motor, eddy currents are induced within the rotor resulting in its rotation.

On the other hand in the case of the generator, permanent magnets or magnetic coils are rotated mechanically, and the ac voltage generated in the stator is utilized. Also the unipolar principle can be used for the generation of (direct) currents.

In conventional electric motors and generators, for the generation of the required magnetic fields, coils having an iron core are used. This fixes the technically feasible magnetic field. At a given value of the power, the magnitude of the magnetic field in turn determines the volume of the unit. The efficiency of the motor or generator is limited by the hysteresis losses in the iron cores and the eddy-current losses in the electrically conducting parts.

Superconducting magnets allow the generation of much larger magnetic fields than conventional coils having an iron core. Therefore, for the same power value, the

superconducting units turn out to be much smaller. This can represent an important advantage for many applications. Perhaps it is even more important that eddy-current losses and hysteresis losses are minimized or avoided. Of course, in an estimate of the cost-effectiveness, the costs of the cryogenics for the superconducting units must be taken into account. In particular, the higher requirements regarding maintenance (handling of liquid helium) represent problems in the case of conventional superconductors such as Nb–Ti. If the rotor contains superconducting coils, the cooling of a rotating part adds another technical complication. However, in the case of high-temperature superconductors, the competitiveness is much less limited.

An electric motor – an unipolar motor [52], in which the fixed, field-generating superconducting coils made of Nb–Ti were supplied with direct current – having a power of about 2500 kW (3250 hp), already in 1969 was completed, tested, and used for driving a cooling-water pump of the Fawley Power Station, England [35]. In the 1970s, designs were realized where the superconducting coil rotates [53].

Also today unipolar motors having fixed Nb–Ti coils are up to date. Motors of this type at a power level of a few tens of megawatts for ship propulsion are being constructed [54]. However, the developments are particularly intensive in the case of high-temperature superconductors. Based on  $\text{Bi}_2\text{Sr}_2\text{CaCu}_2\text{O}_{10}$  – wires of the first generation, in 2007 the company American Superconductor has fabricated a ship's engine of 36.5 MW power, which is about 5 m long and weighs 75 tons. (For comparison: a conventional ship's engine of similar power would be three times larger and three times heavier.) In this case it is a synchronous motor having superconducting coils of the rotor [55]. The rotor rotates at 120 r.p.m. and is cooled to about 30 K by means of cold He-gas. Because of the high and temporally changing stray fields, the coils of the stator are normal conducting.

Also smaller ship's engines for power levels in the range 4–10 MW are being developed or have been fabricated already [55]. [Figure 7.20](#) shows the schematics of a motor having 5 MW power and 230 r.p.m. together with the real motor.

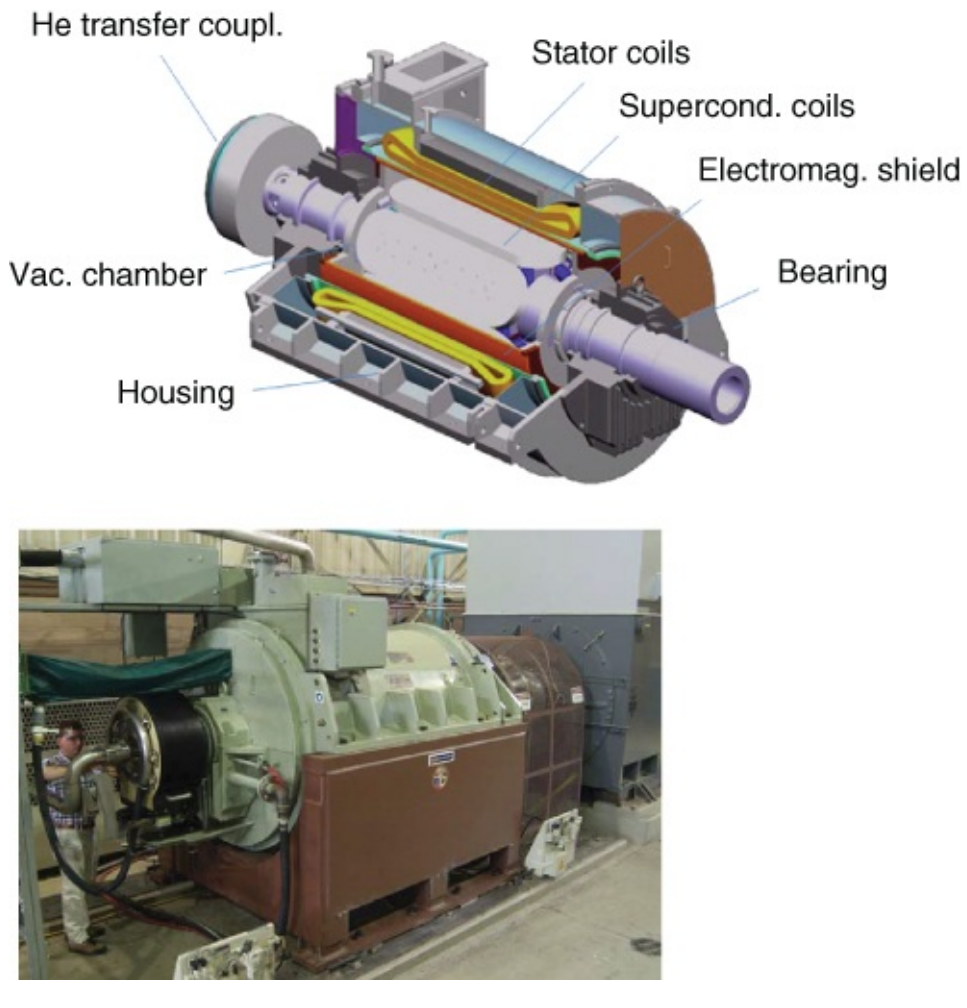


**Figure 7.20** A 5 MW ship's engine having superconducting rotor coils [55].

(Illustration at the top and photo below by courtesy of AMSC.)

Next we turn to generators. On the one hand, large generators of the 100 MVA range and above are in preparation. Smaller units based on high-temperature superconductors are always interesting if, in addition to the energy efficiency, also the savings in size and weight are important. This applies to ship's engines [54], but also to generators of wind power plants [56]. Presently, wind power plants operate with (conventional) turbines at power values of about 2 MVA. To be used particularly in off-shore wind parks, more powerful but still compact and not too heavy turbines would be desirable. Presently, such superconducting prototypes are being developed, at power levels up to 10 MVA. [Figure 7.21](#) shows schematically the construction of the generator, which is similar to the synchronous motor of [Figure 7.20](#). In this case the various parts are stretched along the rotational axis. The superconducting coils of the rotor, which induce an alternating electric voltage within the windings of the stator (three phases, made of copper), are the essential components. The iron rings are meant to restrict the magnetic flux to the space between stator and rotor.

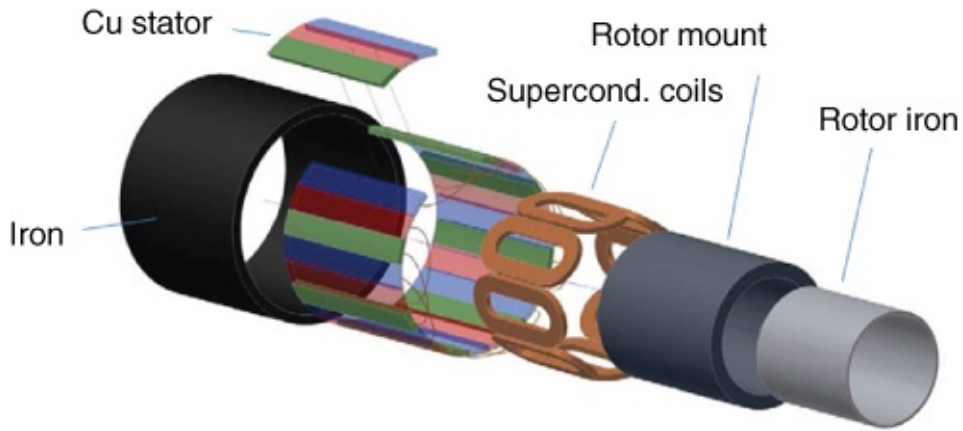


**Figure 7.21** Schematics of the construction of a current generator in the case of a wind power plant [56].

(Courtesy of IOP.)

Superconducting generators are interesting also in the case of hydroelectric power stations. In Germany, Zenergy, Converteam UK Ltd, and E.ON developed a 1.75 MVA generator consisting of 28 superconducting coils, which is tested in the hydroelectric power station Hirschaid. [Figure 7.22](#) shows its rotor rotating at about 200 r.p.m. The weight of the rotor plus the surrounding vacuum chamber is about 16 tons. The total generator has a diameter of about 5 m. At equal size, it yields about 30% more power compared with the earlier conventional system.



**Figure 7.22** 1.75 MVA generator for operation in a hydroelectric power plant.

(Courtesy of Converteam UK Ltd.)

### 7.3.7 Magnetic Separation and Induction Heaters

Additional possible applications of superconducting magnets, which should be mentioned briefly, concern magnetic separation [57] and induction heating of metallic materials [58]. For a long time, the technology of magnetic separation based on conventional magnets is utilized. The separation of ferromagnetic material from ores by means of strong magnetic fields is a well known procedure. In [Figure 7.23](#) we show schematically the apparatus used for the separation of magnetic particles from liquids. The liquid passes through an electromagnet containing a matrix made of steel wool, for example. Near the surface of the steel wool there develop strong field gradients, which separate the magnetic particles.

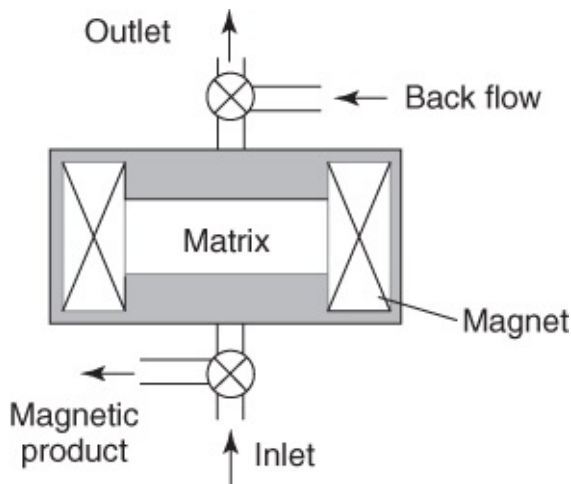


**Figure 7.23** Schematic construction of a magnetic separator [57].

Superconducting magnets allow the generation of much higher fields and very high-field gradients. This provides the possibility to effectively separate materials, which differ only little in their magnetic properties. This is important, say, for water desalination or for the separation of blood cells. Up to fields of 8.5 T industry uses Nb–Ti magnets. Especially in the case of small systems, the use of high-temperature superconductors, in form of magnetic coils or also of permanent magnets, as described in [Section 7.2](#), is feasible [59].

Also induction heating is an important and established procedure within the metalworking industry. For example, during the construction of car bodies, frequently metal blocks of aluminum or copper must be heated before further processing, in order to achieve the necessary ductility. This can be done by eddy-current heating. For this purpose, the work-piece is rotated in the field of a strong magnet. Here, a superconducting magnet shows clear advantages compared with a conventional electromagnet. The energy consumption is much smaller, and the work-piece can be heated more rapidly. In 2007 suitable eddy-current heaters were introduced, and superconductor technology entered a widespread small-business sector. [Figure 7.24](#) shows such a facility (magnetic block-heating facility) developed by Zenergy Power together with the company Bültmann, which is active in mechanical engineering [58]. The frequency of the eddy currents ranges between 4 and 12 Hz, and is much lower than the frequency of conventional facilities (50–60 Hz). Therefore, the eddy currents penetrate much further into the work-piece, and the material is heated much more uniformly. An efficiency of more than 80% is achieved, which is more than two times higher than the efficiency of conventional induction furnaces.



**Figure 7.24** Magnetic block-heating facility (induction heater) containing superconducting HTS-magnets.

(Courtesy of Zenergy Power GmbH.)

### 7.3.8 Levitated Trains

We have already discussed several times the contactless placement of an object by means of superconductors (see, e.g., [Figure 1.11](#)). In this case the placement was also stable statically, that is, without relative motion between magnet and superconductor. A somewhat different concept is applied in the case of magnetically levitated (Maglev) trains. In this case strong magnets are mounted within the train, generating a sufficiently strong magnetic field directed downward. The gliding track of the train consists of a sequence of loops made of a good conductor, for example, Al wire. Without motion, there are no repulsive forces between the magnets in the train and the gliding track.

Initially, the train must be accelerated up to a certain speed in a conventional way. During the motion, repulsive forces develop between the magnets in the train and the conductor loops of the gliding track. Eddy currents are induced in the conductor loops, which according to Lenz's rule generate a magnetic field oriented so as to oppose the primary field (here the field of the magnets in the train). This field results in a repulsive force and causes the train to float above the track as soon as the required velocity is reached. The forward drive is achieved by means of a coil system actively operated within the track.

The magnets in the train can be conventional, as in the Transrapid, which started operation 2002 in Shanghai, and also superconducting magnet coils have been tested. In particular, in Japan and in Germany such studies were initiated early [60]. Germany has gone back to conventional technology, whereas in Japan the concept of superconducting coils is favored. The superconducting magnet coils mounted in the trains generate fields of about 5 T. In 2003 the fastest test train reached a speed of about 580 km/h. There are plans to connect Osaka, Nagoya, and Tokyo with the Maglev. In [Figure 7.25](#) we show a photograph of the Maglev MLX

01. The superconducting coils including the helium liquefier are mounted behind the gray-shaded sections on the side of the train.

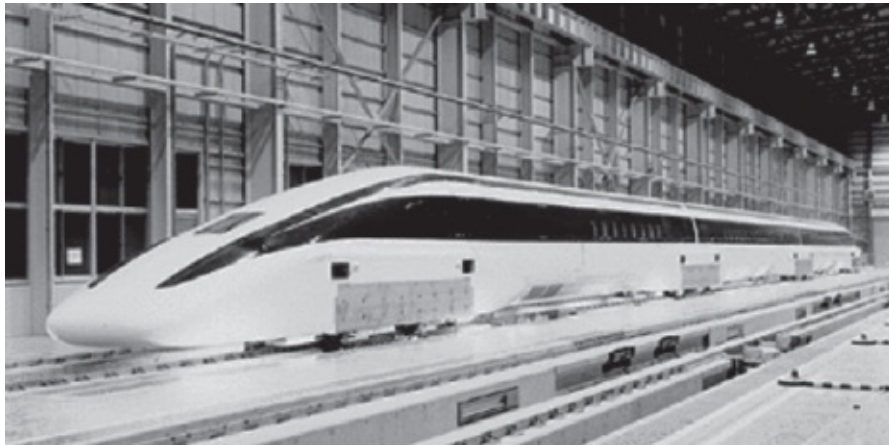


**Figure 7.25** Magnetically levitated Maglev MLX 01 train on the test track near Tokyo.

(Courtesy of the Railway Technical Research Institute, Japan.)

## 7.4 Superconductors for Power Transmission: Cables, Transformers, and Current Fault Limiters

Cables, transformers, and current limiting devices are important components of the power distribution between power station and consumer. In a power station, electrical power in the gigawatt range is generated at high operating voltages, and this is then transported to the consumer via underground cables or by free long-distance power lines. In this case the voltage is reduced stepwise by means of transformers from its starting level near 380 kV to the standard household value. The distribution system is protected against shorts by means of current fault limiters.

Under the proper conditions, the use of superconductors in electrical power transmission can be highly favorable. Already in the 1960s superconducting cables, transformers, and current fault limiters were investigated. However, for conventional superconductors the expensive refrigeration technique represents a severe hurdle. With high-temperature superconductors, the criteria of economics have become much easier. Presently, in government as well as industrial laboratories test systems are being developed, which in some cases are already undergoing field tests.

### 7.4.1 Superconducting Cables

The use of superconducting cables appears particularly obvious, since in this case the electrical losses are small. However, the issues of economics, reliability, and ease of maintenance must be carefully evaluated. In terms of the long-distance power grid, the power distribution by means of superconducting cables would be too expensive. On the other hand, in the case of metropolitan areas, there exists a demand for transporting large amounts of power over relatively short distances. When the existing cable pits are used up, further increasing

demand for power will require new pits to be prepared, leading possibly to large costs. If the normal conducting cables are replaced by superconductors, the capacity of the existing pits can be increased. In this case the use of superconductors becomes interesting. In the case of a leak, such cables also have the advantage (for operation using high-temperature superconductors) that only nitrogen gas is emitted instead of the environmentally dangerous oils that are used for cooling the normal conducting high-power cables.

Perhaps the first published proposal for a superconducting cable was made in 1962 by McFee [61]. He discussed a single-phase a.c. cable for a power of 750 MVA at 200 kV. He proposed lead for the conductor. It was planned that the current value would be increased by the subdivision of the conductor into many parallel lines in such a way that for an equal amount of power the voltage would be reduced down to the generator voltage. The many parallel lines would be arranged within a helium-cooled tube. In this way transformation up to a higher voltage for power transmission would be avoided.

In this case we must note that residual losses always appear in an a.c. cable, which must be taken care of by the cooling medium. In the alternating electric field also the normal electrons are accelerated. Furthermore, the temporally changing magnetic flux induces eddy currents and losses, which, however, can be kept small by a suitable twisting of the conductor (see [Section 7.1.2](#)).

In the case of direct current, the power transmission can be carried out practically without losses. Very small losses appear only due to load fluctuations and perhaps due to a remaining residual waviness. In 1962 a cable had been reported consisting of two separate lines that could transport a total power of 104 MVA over a distance of 1600 km with a current of 67 kA in each line [62]. The construction of this cable was very simple. The cable consisted of concentric tubes. The niobium conductor was carried by a tube acting as a substrate and cooled on the inside by a flow of liquid helium. The tube in turn was vacuum-insulated and enclosed by a hollow tube cooled with liquid nitrogen.

During the 1960s up to the 1980s, superconducting d.c. and a.c. cables based on conventional superconductors were intensively investigated worldwide [63, 64]. However, they were never used commercially partly because of the expensive cooling technology with liquid helium. Another reason was the reduced demand for electrical power because of the energy crisis.

After 1986 the developments concentrated on the high-temperature superconductors. In industry, companies such as American Superconductor, BICC, Nexans Pirelli, Siemens, Southwire, or Sumitomo became heavily involved. Commercially, nitrogen-cooled cables are much more interesting than helium-cooled cables. The latter would have become competitive at power levels above 5–10 GVA. In the case of nitrogen-cooled cables, this level ranges about 300–500 MVA.

The current projects concentrate on a.c. cables, since they can easily replace the existing cables. However, in the future also superconducting d.c. cables could become interesting for long transport lines, say, from the power station to a distant area of high population density [48].

In the case of a.c. cables several designs are used. In the simplest case, one deals only with a superconducting layer, which is cooled by liquid nitrogen. Then the “cryostat,” consisting of concentric, evacuated, and flexible corrugated tubes, is located directly above the conductor. The outer corrugated tube is surrounded by a warm dielectric. However, in the case of this construction, high stray fields are generated, and the electric losses are high. Therefore, improved versions have a coaxial superconducting return conductor. In this geometry, also the dielectric intermediate layers are cold. However, this does not allow any longer the use of established dielectrics (e.g., oil-impregnated, laminated paper insulation). [Figure 7.26](#) shows such a cable, fabricated by the companies Nexans and American Superconductor. It is in operation in a pilot project on Long Island, where current is fed into the power grid since 2008 [65] (see [Figure 7.27](#)). The current connection is 600 m long and consists of three individual cables for the three phases. At a transmission voltage of 138 kV, it can carry average currents of 2400 A.



**Figure 7.26** Superconducting cable as it is operated in the Long Island project. Around an inner core made of copper, two layers of  $\text{Bi}_2\text{Sr}_2\text{Ca}_2\text{Cu}_3\text{O}_{10}$ -tape conductors, which are separated from each other by dielectric layers, are wound in a spiral. The outer spiral layer is made of copper and serves for stabilization. The corrugated tubes constitute the cryostat system. Liquid nitrogen passes through the inner tube. The space between both corrugated tubes is evacuated and contains insulating layers.

(Courtesy of Nexans.)



**Figure 7.27** The cable system of the Long Island project.

(Courtesy of Nexans.)

### 7.4.2 Transformers

Transformers represent an important component of our power grid. They transform the alternating voltages of the generator output of a few ten kilovolts up to values in the range 200–400 kV and back again to the voltage levels of the various distribution grids. Depending on the task, these transformers can transmit power levels of a few megavolt amperes up to more than 1000 MVA.

The operation of transformers made of superconducting windings could become very attractive [66]. In a transformer the relative losses only amount to about 1%. However, summed over all the transformers that are operating, these losses become quite appreciable. In the distribution of electrical power about one-quarter of the total losses of 5–10% are generated by the transformers. Furthermore, in a transformer with superconducting windings, much higher current densities are possible than in a conventional transformer. Hence, for the same amount of power, a superconducting transformer can be built more compact and lighter. In the case of stationary transformers, this aspect may represent only a very small advantage. However, it can become crucial for mobile systems, such as electric trains [67]. In the case of an accident, liquid-nitrogen-cooled superconducting transformers are much less harmful to the environment than their normal conducting, oil-cooled counterparts.

However, another advantage of superconducting transformers arises from the fact that, in the extreme case, they can be operated for hours at twice the regular power level. On the other hand, with normal conducting transformers this is impossible. Hence, the latter must be strongly oversized.

In addition to these basic advantages, there are high requirements regarding the

superconducting windings. The a.c. losses must be kept as small as possible, which requires twisting (see [Figure 7.8](#)). Because of the same reason, the magnetic fields acting on the individual windings must be as small as possible. Typically, the windings of the transformer carry currents of a few hundred amperes. However, in case of a short they can reach a multiple of this value. Therefore, the designs must withstand this value. Alternatively, the maximum current must be properly limited.

Transformers having superconducting windings have been investigated since the 1960s. In the 1980s, a few units with power values around 100 MVA were tested successfully. The conductors were made of Nb–Ti multifilamentary wires. Following the discovery of the cuprate superconductors, initially in laboratories of many companies transformers based on  $\text{Bi}_2\text{Sr}_2\text{CaCu}_2\text{O}_8$ -tape conductors were fabricated at power levels up to a few megavolt amperes [68]. Some of these transformers were successfully tested in the power grid. However, using  $\text{Bi}_2\text{Sr}_2\text{CaCu}_2\text{O}_8$ -tape conductors, so far the transformers could not yet be made competitive against the conventional systems.

More recent developments are based on  $\text{YBa}_2\text{Cu}_3\text{O}_7$ -tape conductors of the second generation [68]. The requirements needed for an operation in the power grid are almost within reach. At least transformers at the power level of a few tens of megavolt amperes should be realized in the near future.

### 7.4.3 Current Fault Limiters

In the case of shorts within a transformer system at high-power levels, the current must be limited quickly and reliably. The current fault limiters should be reusable many times. Exactly this can be achieved with superconductors. In this case several techniques can be employed. A detailed overview can be found in [69]. Here we present a strongly simplified summary.

For example, a superconducting wire or thin film can be directly included in the circuit. During regular operation the superconductor does not affect the current flow. However, if the current increases strongly in the case of a short, the critical current of the superconductor will be exceeded, and the current will be limited because of the resistance now appearing in the circuit (“resistive current fault limiters”). In this case, in particular the fast switching time is advantageous, which guarantees that the short-circuit current cannot increase much before the switch is activated. Therefore, also all the other components within the circuit can be scaled down for a reduced excess current. In order to keep the power dissipated because of the short from destroying the superconductor, after a short time the current passing through the superconductor is switched off by means of a power switch. After the current fault limiters has cooled down again within the liquid-nitrogen bath, it returns to the superconducting state and is ready again after the disturbance has been eliminated.

In the case of the “inductive current fault limiters” [70, 71], a coil, which surrounds an iron core as in a transformer, is inserted into the circuit. Because of this inductance, the current increases only slowly with time. Now we must prevent this inductance from appearing also during regular operation. For this purpose, the coil is wound around a superconducting hollow

cylinder carrying an iron core in its interior. The hollow cylinder corresponds to the shorted secondary winding of a transformer. Instead of a simple hollow cylinder, a series of shorted superconducting rings can be used. At not too large current values, the cylinder keeps the magnetic flux in its interior constant and, hence, it shields the iron core against the magnetic fields generated in the circuit. If in the case of a short the magnetic field generated by the circuit becomes too large, the cylinder enters the normal conducting state, the magnetic field couples to the iron core, and the inductance of the current fault limiters abruptly jumps to a higher value.

Current fault limiters based on high-temperature superconductors must be able to handle a power of 20 MVA or more in order to be economically competitive. However, then they open up a large potential market for superconductivity. Until about 2007, superconducting current fault limiters up to the 10 MVA range were tested [69]. Present developments reach the 20 MVA level or even distinctly higher. Siemens, American Superconductor, and Nexans developed a resistive 42 MVA to 31 kV current fault limiters based on  $\text{YBa}_2\text{Cu}_3\text{O}_7$ -tape conductors, which were wound to a total of 63 bifilar coils. At a time three of these coils were operated in parallel, and 21 of these triplets in series. [Figure 7.28](#) shows the whole system. The two vertical “towers” are the current leads into the cryostat, which contains the superconducting coils in its interior. [Figure 7.28b](#) shows the coil system. The diameter of the coils is 0.6 m.

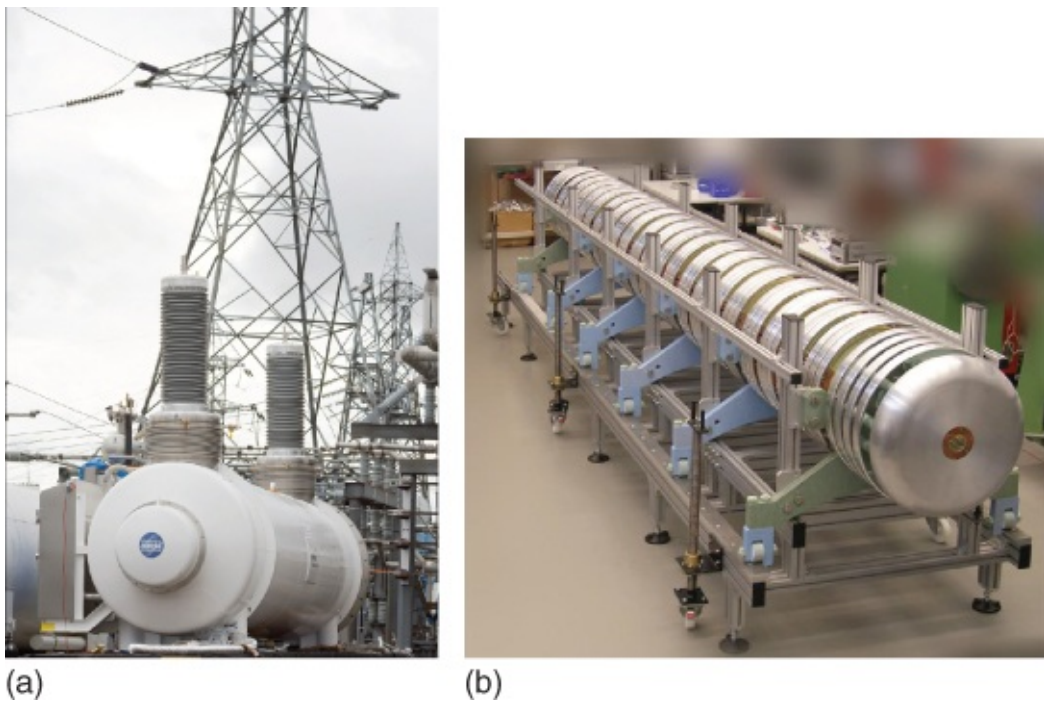


[Figure 7.28](#) A resistive 42 MVA to 31 kV current fault limiter. (a) Whole system and (b) coil system.

(Courtesy of Siemens AG.)

[Figure 7.29](#) shows an inductive current fault limiters. This is a test system toward a 15 MVA to 10 kV device as it is developed presently by Bruker together with two German utility companies. The superconducting rings of the secondary coil consist of  $\text{YBa}_2\text{Cu}_3\text{O}_7$ -tape

conductors of 4 cm width. The average operating current will be 817 A. During a short, the current fault limiters is expected to limit the initial current rise to less than 5 kA within 1 ms, and subsequently to about 2 kA during a maximum of 500 ms.

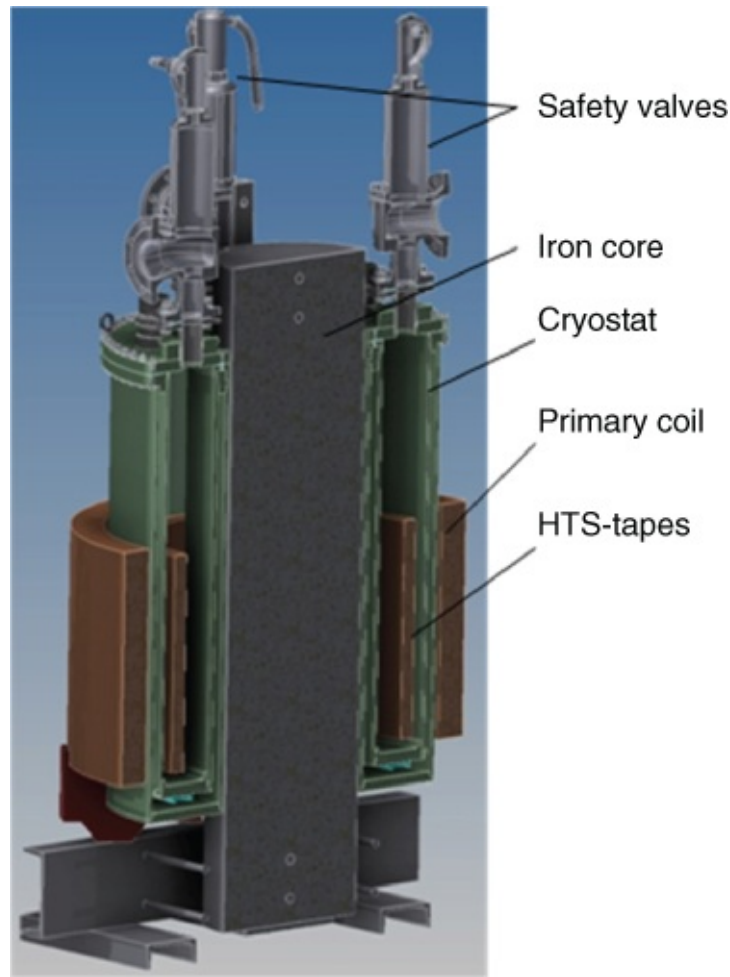


**Figure 7.29** Sectional view of an inductive 15 MVA to 10 kV current fault limiters

(Courtesy of Mr Henning, Bruker ASC.)

## 7.5 Superconducting Resonators and Filters

In [Sections 7.1, 7.2, 7.3, 7.4](#), in the case of magnets and cables for power transmission, we have discussed large-scale applications of superconductivity. Next we will discuss the possible applications of superconductors at microwave frequencies from a few tens of megahertz up to above 100 GHz. The resonating cavities of particle accelerators represent another large-scale application that we will discuss. However, in [Section 7.5.3](#) in our discussion of the resonator and filter structures in the telecommunications field we will deal with much smaller systems. In some sense, these “passive” microwave devices also represent the transition to the sensors and active devices of the subsequent [Sections 7.6](#) and [7.7](#), in which the typical dimensions are in the range of micrometers to millimeters.

Before we discuss in detail selected passive microwave devices, in [Section 7.5.1](#) we will present a brief introduction into the basic physics of the high-frequency behavior of

superconductors. In this frequency range superconductors have a finite resistance. However, at not too high frequencies the resistance is still much smaller than that of a normal conductor such as copper. This feature allows highly compact devices, which can also be much better in quality than their normal conducting counterparts.

### 7.5.1 High-Frequency Behavior of Superconductors

If an electromagnetic wave is focused on a superconductor, it penetrates into the superconductor over a certain distance and “shakes” the Cooper pairs as well as the unpaired quasiparticles. As a result, the superconductor displays a finite resistance.

In order to become acquainted with the problem and to introduce a number of important concepts in the area of the high-frequency behavior [72], we start by looking at a *normal conducting* metal exposed to a planar electromagnetic wave arriving in z-direction.<sup>16</sup> The metal is assumed to be very thick. If the wavelength of the incoming radiation is large compared to the electron mean free path, one can use Ohm's law to obtain the connection between the current density  $\mathbf{j}_n$  in the metal and the electric field  $\mathbf{E}$  of the incoming radiation,  $\mathbf{j}_n = \sigma_n \mathbf{E}$ . Here  $\sigma_n$  is the conductivity.<sup>17</sup> We have added the index “*n*” in order to distinguish between normal conducting currents and supercurrents, which will be discussed further below. If Maxwell's equations are solved, we find that the wave decays according to  $\exp(-z/\delta)$ , where

$$\delta = \sqrt{\frac{2}{\omega \mu_0 \sigma_n}} \quad 7.3$$

denotes the so-called skin depth. For example, in the case of copper at room temperature and at a frequency  $f = \omega/2\pi$  of 10 GHz, the skin depth is about 0.66 μm.

In the case of much higher frequencies or higher conductivities, at some point  $\delta$  becomes comparable to or smaller than the electron mean free path  $l^*$ . Then the current density and the electric field are no longer connected by a *local* relation as in Ohm's law, but instead by a complicated integral, which averages the electric field over about one mean free path. In the case of  $l^* \gg \delta$ , one finds that  $\delta$  is approximately proportional to  $(\sigma_n \omega)^{-1/3}$  (“anomalous skin effect”). For details see, for example, Refs [M4, M24].

The surface impedance  $Z_S$  represents an important quantity in the microwave technique. It is defined as the ratio between the electric and magnetic field strengths. In general, it is a complex number, which can be written as

$$Z_S = R_S + iX_S = \sqrt{\frac{i\omega \mu_0}{\sigma_n}} = \frac{1}{\delta \sigma_n} (1 + i) \quad 7.4$$

where  $R_S$  is the surface resistance<sup>18</sup> and  $X_S$  is the surface reactance. In our case we have  $R_S = X_S$ . In the regime of the regular skin effect, both quantities are proportional to  $f^{1/2}$ . In copper at room temperature and a frequency  $f = 10$  GHz, one finds a value  $R_S = 26$  mΩ.

Turning from the normal conductor to the superconductor, the situation becomes complicated, since there are a number of different length scales, for example, the extension  $\xi_0$  of the Cooper pairs (i.e., the BCS (Bardeen–Cooper–Schrieffer) coherence length), the London penetration depth  $\lambda_L$ , the skin depth  $\delta$ , or the electron mean free path  $l^*$ . In particular, in the case when  $\delta$  becomes smaller than the “electromagnetic coherence length”  $\xi_{\text{em}} = [\xi_0^{-1} + (l^*)^{-1}]^{-1}$ , a complicated nonlocal equation must be solved [73, 74].

As an example, in [Figure 7.30](#) we show the surface resistance of Al as a function of temperature for different microwave frequencies in the range between 15.7 and 94.5 GHz [75]. All curves are normalized to their value at  $T_c$ . At constant frequency,  $R_S$  decreases with decreasing temperature. At constant temperature,  $R_S$  increases with increasing microwave frequency. The two effects can be easily understood qualitatively. Since the concentration of the unpaired electrons decreases with decreasing temperature, at constant frequency the resistance must decrease with decreasing temperature. On the other hand, at constant temperature the contribution of the unpaired electrons to the alternating current increases with increasing frequency compared to that of the Cooper pairs, and one obtains an increase in  $R_S$ .

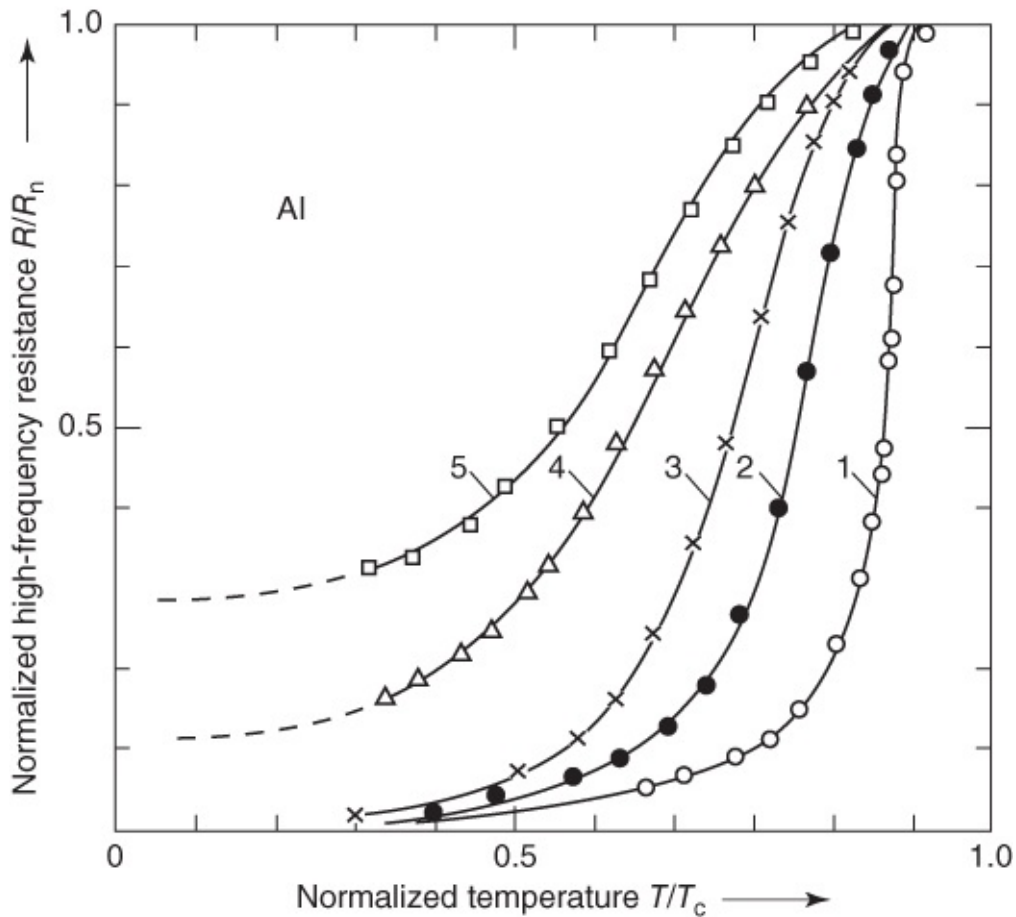


**Figure 7.30** Surface resistance of aluminum plotted versus the reduced temperature. (From [68].) Curve 1:  $f = 15.7$  GHz,  $hf = 0.64k_B T_c$ ; Curve 2:  $f = 60$  GHz,  $hf = 2.46k_B T_c$ ; Curve 3:  $f = 76$  GHz,  $hf = 3.08k_B T_c$ ; Curve 4:  $f = 89$  GHz,  $hf = 3.63k_B T_c$ ; and Curve 5:  $f = 94.5$  GHz,  $hf = 3.91k_B T_c$ .

At frequencies  $f > 10$  GHz, below  $T_c$  the resistance becomes appreciable. At frequencies larger than the energy gap, the behavior is more and more similar to that of a normal conductor. If the energy gap  $2\Delta_0$  is small compared to the energy of the electromagnetic quanta  $E = hf$ , it will affect only little the excitation processes leading to an energy exchange. For distinctly higher frequencies, like we encounter, say, in the visible range ( $f \approx 10^{15}$  Hz), there is practically no difference between the superconducting and the normal conducting states. In this case the energies of the quanta are a few electronvolts, and, hence, they are much larger than the energy gap of typically a few  $10^{-3}$  eV.

Curves such as shown in [Figure 7.30](#) can be understood in detail from the microscopic theory [M4]. For conventional superconductors at temperatures below about  $0.5T_c$ , approximately one finds the dependence [76].

$$R_S \propto \frac{\omega^2}{T} e^{-\Delta_0/k_B T} + R_{\text{res}} \quad 7.5$$

A simple description of the high-frequency properties of superconductors is possible in the local limit, in which the electron mean free path  $l^*$  is much smaller than the BCS coherence length  $\xi_0$ , and the latter is much smaller than the London penetration depth  $\lambda_L$ . Under these conditions, which, however, are not satisfied in the case of Al, the supercurrents can be expressed in terms of the London equations (1.14) and (1.24):

$$\mathbf{B} = -\mu_0 \lambda_L^2 \operatorname{curl} \mathbf{j}_s$$

$$\mathbf{E} = \mu_0 \lambda_L^2 \dot{\mathbf{j}}_s$$

We assume that for the unpaired electrons Ohm's law,  $\mathbf{j}_n = \sigma_n \mathbf{E}$ , is valid, and that the total current density  $\mathbf{j}$  is given by the sum of the quasiparticle current and the Cooper pair current:

$$\mathbf{j} = \mathbf{j}_n + \dot{\mathbf{j}}_s$$

With  $\mathbf{E} \propto \exp(-i\omega t)$  and  $\mathbf{j} \propto \exp(-i\omega t)$ , we can write  $\mathbf{j} = \sigma \mathbf{E}$ . Here  $\sigma$  is a complex number:

$$\sigma = \sigma_1 - i\sigma_2 = \sigma_n - i\frac{1}{\omega \mu_0 \lambda_L^2} \quad 7.6$$

At typical microwave frequencies we have  $\sigma_1 \ll \sigma_2$ . In this case we obtain

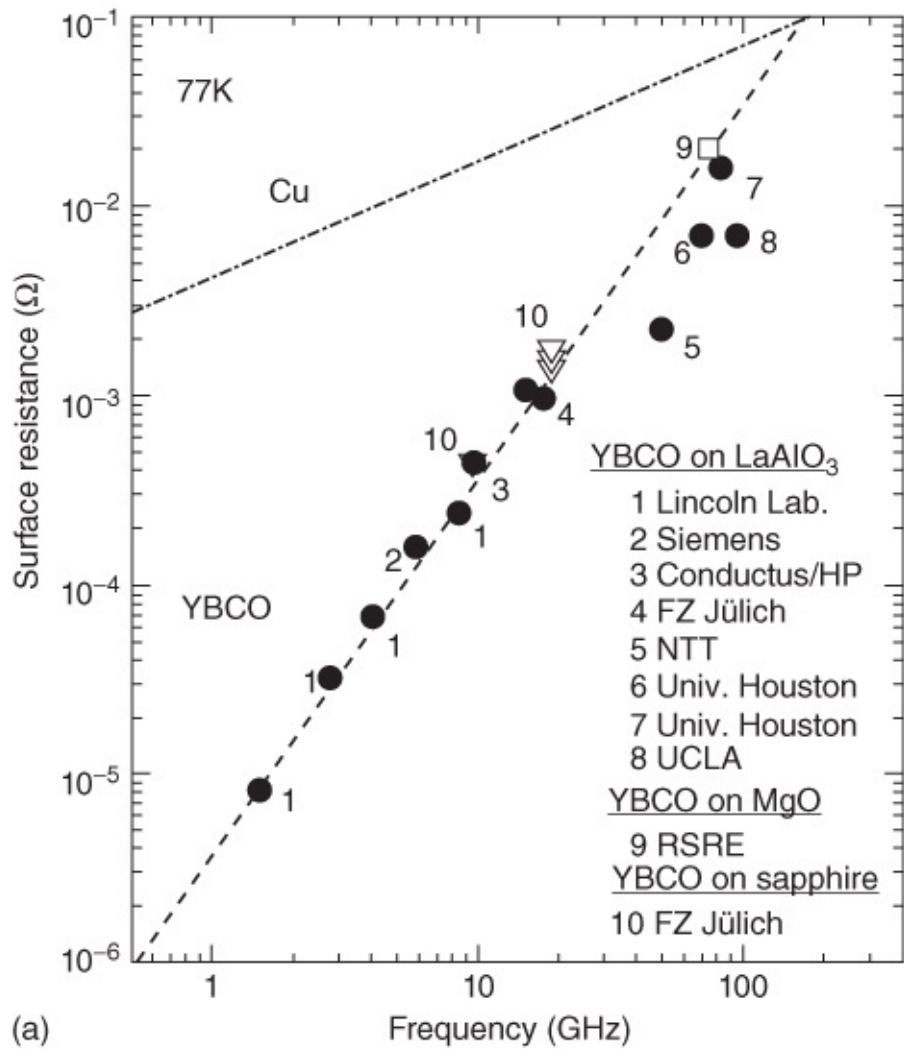
$$R_S = \frac{1}{2} \omega^2 \mu_0^2 \sigma_n \lambda_L^3 \quad 7.7$$

$$X_S = \omega \mu_0 \lambda_L^2 \quad 7.8$$

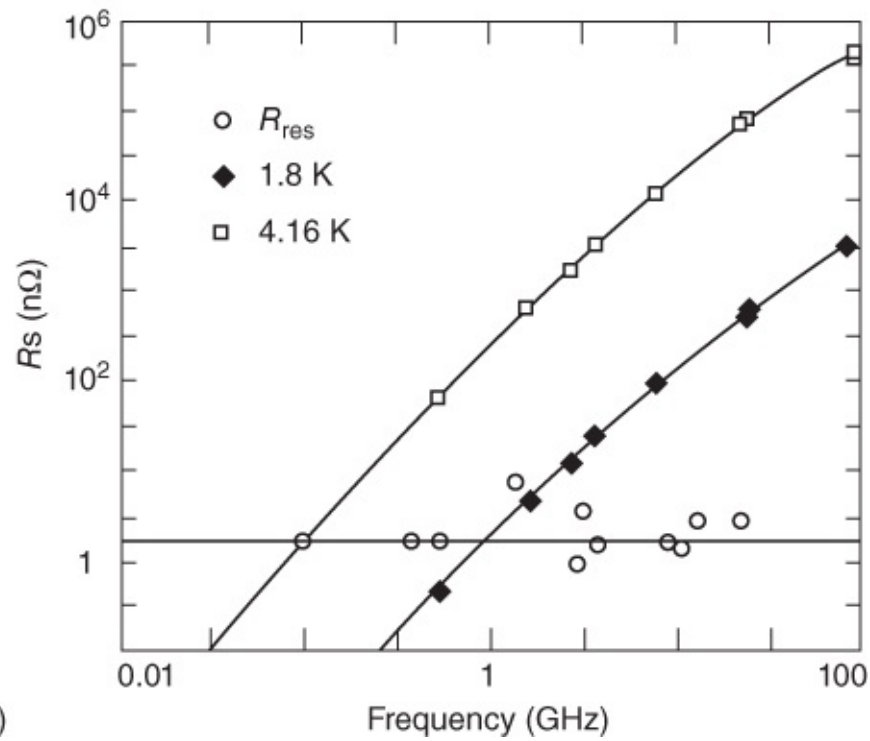
We note that  $R_S$  increases quadratically with frequency. Furthermore,  $R_S$  and  $X_S$  are temperature dependent due to  $\sigma_n$  and  $\lambda_L$ .

For  $T \rightarrow T_c$  the length  $\lambda_L$  diverges and, hence, also the expressions (7.7) and (7.8) diverge. However, this divergence is an artifact due to the approximations made. In fact, both quantities approach the corresponding expressions (7.4) for the normal conductor. Further we note that in a superconductor the skin depth  $\delta$  is simply limited by the London penetration depth  $\lambda_L$ . Therefore, at not too high frequencies, we have  $\delta \approx \lambda_L$ .

In [Figure 7.31a](#) we show the surface resistance of  $\text{YBa}_2\text{Cu}_3\text{O}_7$  compared to that of Cu at  $T = 77$  K plotted versus the microwave frequency [72]. In the case of  $\text{YBa}_2\text{Cu}_3\text{O}_7$  and also of most other high-temperature superconductors, the local limit is valid. We note that well above 150 GHz the superconductor does not provide an advantage compared to Cu and can become even worse. In [Figure 7.31b](#) we show the surface resistance of Nb at frequencies between 10 MHz and 100 GHz at  $T = 1.8$  and  $4.16$  K [78]. At 1.8 K the resistance  $R_S$  is smaller than that in  $\text{YBa}_2\text{Cu}_3\text{O}_7$  by more than 2 orders of magnitude (in  $\text{YBa}_2\text{Cu}_3\text{O}_7$  at low temperatures  $R_S$  is not much smaller than at 77 K). In [Figure 7.31b](#) we also show the residual resistance at very low temperatures, which is nearly constant in the frequency interval discussed. However, generally it depends on the surface quality of the material.



(a)



(b)

**Figure 7.31** Surface resistance of (a)  $\text{YBa}_2\text{Cu}_3\text{O}_7$  compared to Cu at 77 K [72] and (b) Nb at 1.8 and 4.16 K. The residual resistance at low temperatures is also shown [77].

(From [72, 77] with permission of IOP.)

So far we have tacitly assumed that the high-frequency fields are sufficiently weak that the induced currents can be carried by the superconductor. Also we have assumed that in the case of type-II superconductors there are no vortices. However, in some applications, such as the resonating cavities of particle accelerators discussed in the next section, the high-frequency fields can reach large amplitudes [77, 79]. In the case of type-I superconductors such as high-purity Nb, presently the best material for high-frequency applications at high-power levels, the magnetic field component can reach the critical field  $B_c$ . On the other hand, at high frequencies the superconducting state can be slightly “overheated,” and  $B_c$  can even be exceeded by a small percentage, before the superconductivity breaks down. This effect is shown in [Figure 7.32](#), where the critical high-frequency field, above which the surface resistance strongly increases, is plotted versus the reduced temperature.

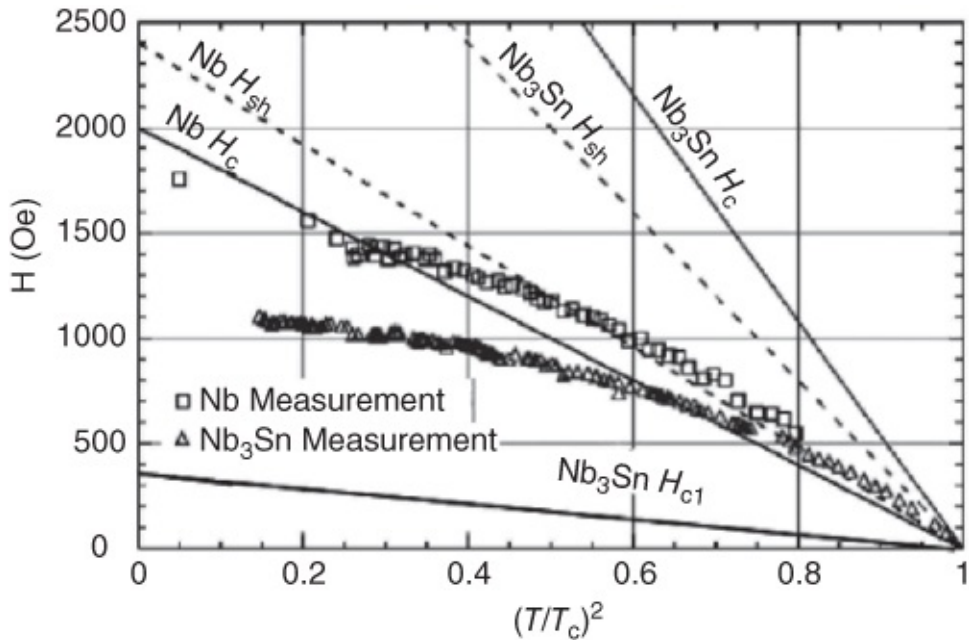


**Figure 7.32** Critical high-frequency fields  $H = B/\mu_0$  in the superconductors Nb and  $\text{Nb}_3\text{Sn}$  plotted versus the temperature. Above this field the surface resistance strongly increases. The thermodynamic critical fields  $H_c$  and the superheating fields  $H_{sh}$  are also shown. In the case of  $\text{Nb}_3\text{Sn}$ ,  $H_{c1}$  is also indicated.

(From [77] with permission of IOP.)

In the case of conventional type-II superconductors  $B_{c1}$  is the essential quantity.<sup>19</sup> However, in this case the Meissner phase can be “overheated,” as is shown in [Figure 7.32](#) for  $\text{Nb}_3\text{Sn}$ . As soon as vortices have penetrated into the material, they oscillate in the high-frequency field, leading to a strong increase in the surface resistance. Therefore, high-frequency devices made from type-II superconductors must be well shielded against external fields in order to avoid the

possibility that during the cooling process too many vortices are trapped within the superconductor.

## 7.5.2 Resonators for Particle Accelerators

Resonating cavities placed in series and traversed with nearly light velocity by charged particles represent one of the most important components of linear accelerators and storage rings [77, 80]. Resonators are cavities with electrically highly conducting walls. They oscillate with frequencies between 50 MHz and 3 GHz. In this case different oscillatory modes (standing waves) can be excited, which differ in their resonance frequency, in the number of the nodes and antinodes, and in the direction of the electric and magnetic fields.

The principle of the acceleration can be explained in the simplest way in terms of a cylindrical accelerator where the particles propagate (in the z-direction) along its axis ([Figure 7.33](#)). We assume that the resonator is excited in the “ $\text{TM}_{010}$  mode” (transverse magnetic).<sup>20</sup> The electric alternating field in the resonator is oriented parallel to the z-axis and, hence, parallel to the particle trajectory. It is constant along z, and in the radial direction it decreases down to zero at the cavity wall. The magnetic field component is oriented in the azimuthal direction and reaches its maximum at the cylinder wall.

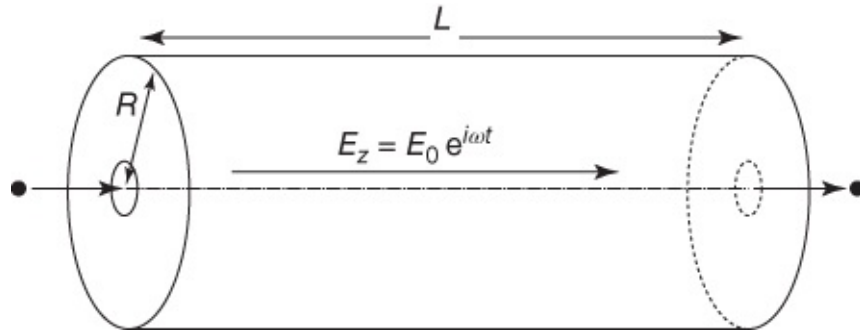


[Figure 7.33](#) Principle of the acceleration of charged particles in a cylindrical resonating cavity. The resonator is excited in the “ $\text{TM}_{010}$  mode,” in which the electric field is oriented parallel to the z-axis, and the magnetic field in azimuthal direction.

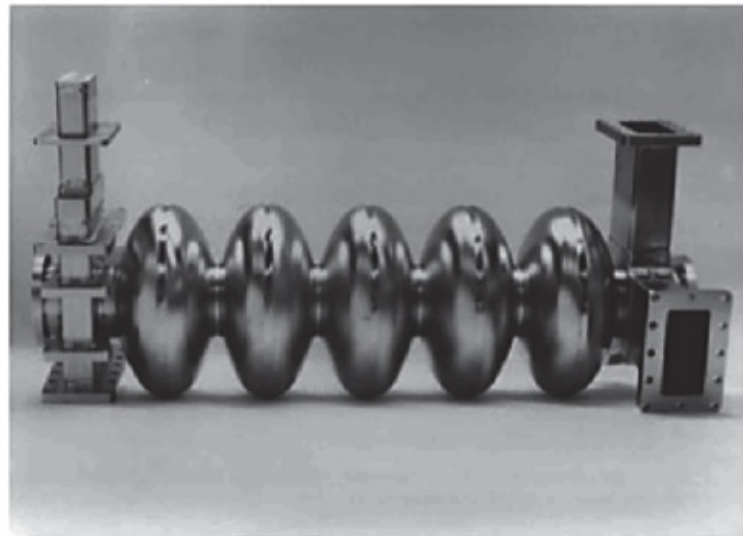
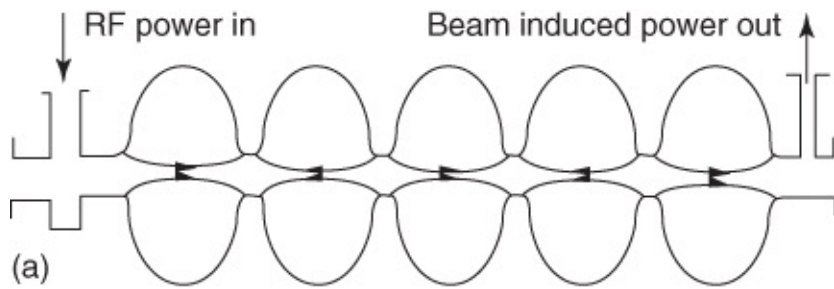
In the ideal case a particle should enter the resonator at the beginning of a half-wave and should exit the resonator again at the end of the half-wave. In this case it always experiences an acceleration in the same direction. For a resonator of length  $L$ , the transit time of the electron is  $t = L/c$ , assuming that its velocity is practically the velocity of light. This transit time must correspond to half the resonator period. Hence, we have  $f = c/2L$ . At a frequency of 1.5 GHz, this corresponds to a resonator length of 10 cm. The accelerating voltage experienced by the electrons during their passage through the resonator is about  $V = (2/\pi)L E_0$ , where  $E_0$  is the maximum field in the resonator along the cylinder axis [77].

The frequency with which the  $\text{TM}_{010}$  mode oscillates is given by  $2.405c/(2\pi R)$ , where  $R$  is the cylinder radius. At 1.5 GHz,  $R$  must be about 7.7 cm. In the  $\text{TM}_{010}$  mode the magnetic field component is oriented in the azimuthal direction and reaches its maximum at the cylinder wall.

There its maximum value is  $B_0 \approx 0.58(\mu_0\epsilon_0)^{1/2}E_0$ , leading to a ratio  $B_0/E_0$  of about 19 G/(MV/m). At an electric field  $E_0$  of 20 MV/m,  $B_0$  amounts to about 380 G.

In the TM<sub>010</sub> mode the quality factor of the cylindrical resonator is  $Q = 257 \Omega/R_S$ . Here, we recognize the advantage of a superconducting resonator. At 1.5 GHz, values of the surface resistance  $R_S$  in the range of milliohms in the case of Cu can be reached, whereas they are in the range of 20 nΩ in the case of Nb. Hence, values of the quality factor larger than  $10^{10}$  become possible. At a typical stored energy in the resonator of about 0.85 J based on the numbers given above, this yields a power loss of only about 0.6 W.

In [Figure 7.34](#) we show a real resonator element, which was operated at the Jefferson Laboratory of CEBAF [77]. At CEBAF electrons are accelerated up to energies of 5 GeV. The effective acceleration fields per resonator amount to about 5–7 MV/m. Similar acceleration fields are also used in LEP-II at CERN. In the latter case electron-positron collisions occur at energies up to 200 GeV.



(b)

**Figure 7.34** Resonator structure for the acceleration of electrons at CEBAF (Jefferson Laboratory, Newport News, Virginia, USA). (a) Cross-sectional drawing. (b) Real structure. The structure consists of five resonators covered with a Nb layer and placed in series. Its active length is 50 cm. The resonance frequency is 1.5 GHz. The electron beam traverses the resonator during one half-wave, whereas it traverses the opening between the resonators during the second half-wave. Therefore, within the resonators the electrons always experience an electric field that accelerates them in the forward direction.

(From [77] with permission of IOP.)

The International Linear Collider (ILC) represents one of the largest projects, which is planned presently. It will accelerate electrons and positrons at least up to 500 GeV [81]. The accelerator is 31 km long and contains 16 000 resonators made of pure niobium. The individual resonators are expected to operate at acceleration fields of about 31.5 MV/m.

### 7.5.3 Resonators and Filters for Communications Technology

Modern communications technology is based on the transfer of data at frequencies of a few gigahertz. In a simplified description, the signal originating from a cell-phone, having a certain bandwidth around a carrier frequency, is received by the base station, amplified, transmitted to another station on the ground or in a satellite, amplified again and, perhaps via another intermediate station, transmitted to the receiver. If ideal amplifiers existed, we would have essentially covered the task of the signal transmission. However, amplifiers do not operate perfectly linearly. As a result, during amplification of a signal, which differs from the carrier

frequency  $f$  by  $\Delta f$ , signals at the frequencies  $f \pm 2\Delta f$ , and so on, are also generated.

Today, the frequency spectrum available for the transmission of information is covered very densely by the emitting channels. Therefore, if a signal appears outside the allowed frequency band, it is very likely that another emitting channel operates at these frequencies and, hence, processes this perturbing signal. In order to avoid this effect, bandpass filters must be attached to the input and to the output of an amplifier. At the input the still wideband signal should be divided into a larger number of well-separated frequency intervals, which are then amplified separately and finally are emitted again at the proper emission frequency. Also at this stage, the unwanted sidebands should be cut off by filters. An ideal bandpass filter allows the transmission of the full signal only in a well-defined frequency interval, whereas it shuts off all other frequencies (rectangular filter). In order to come close to this ideal performance, sophisticated arrangements are frequently employed.

A resonator represents the basic element of a filter. It has exactly the ability to oscillate with high amplitude close to its resonance frequency. The width of the resonance is determined by its quality factor. One distinguishes between the quality factor  $Q_0$  without a load, that is, without the connection of the resonator to other devices, and the quality factor  $Q_L$  with a load. We have

$$Q_L^{-1} = Q_0^{-1} + Q_{\text{ext1}}^{-1} + Q_{\text{ext2}}^{-1} \quad 7.9$$

Here,  $Q_{\text{ext1}}$  and  $Q_{\text{ext2}}$  denote the quality factors of the input and output devices, respectively. The quality factor  $Q_L$  is directly connected with the frequency interval  $\Delta f_{3\text{dB}}$  about the resonance frequency  $f_0$  at which the resonator amplitude has dropped by 3 dB (i.e., down to half of its value):<sup>21</sup>

$$f_{3\text{dB}} = f_0 / Q_L \quad 7.10$$

The higher the quality factor, the sharper is the resonance curve.

However, the resonance curve of a single resonator is still far from the ideal rectangular shape. Hence, one uses an arrangement consisting of a whole series of resonating elements (a multipole filter) [82]. The simplest example is a “Chebyshev filter,” consisting of a chain of  $N$  resonators, where two neighboring resonators are coupled to each other. The first and the  $N$ th resonators are coupled to the input and to the output, respectively. A second example is an “elliptical filter.” In this case all resonators are coupled to each other.

In the case of large values of  $N$  (e.g., 10–20), the transmission curves of these multipole filters can display very steep rising and falling edges and can closely approach the rectangular shape. As a typical feature of the filters one observes that the transmission curves oscillate slightly as a function of frequency within as well as outside the transmitted frequency range. The more resonator elements are used and the better their quality factor, the better is the filter quality.

This brings us nicely to the advantages of superconductors. In the case of normal conducting metals, the  $Q$ -factor can be increased by using a three-dimensional resonator structure with a

large ratio volume/surface area. The stored energy of the resonator is proportional to its volume, and the losses are proportional to its surface area, since the dissipative currents are carried at the surface.

However, superconductors can also serve for fabricating thin-film resonator structures with a large quality factor. For a given number of resonators and a given quality, a superconducting device can be much smaller than its normal conducting counterpart. This is particularly interesting for satellite operations, as long as the total system consisting of filter and refrigerator remains smaller and lighter than the normal conducting system. The second and probably the more important advantage of the superconductor arises from the fact that a larger number of resonators with higher quality can be coupled with each other compared to the normal conducting case. Hence, simply *better* filters are possible.

However, also in this case the advantages of the superconductor and the cooling effort must be evaluated together. Therefore, at least for the moment the use of conventional superconductors is not of interest. However, in the case of high-temperature superconductors, small and simply operating cryo-coolers<sup>22</sup> can be employed, which cool the filter base stations down to 60–70 K [72, 83]. For this application,  $\text{YBa}_2\text{Cu}_3\text{O}_7$  is highly important. Today, thousands of base stations contain superconducting filters, and this number is expected to grow rapidly. Satellite systems are in the test phase [84].

In [Figure 7.35](#) we show different designs of planar resonator structures [65]. Mostly these designs are fabricated from  $\text{YBa}_2\text{Cu}_3\text{O}_7$  on a substrate for which the losses<sup>23</sup> are as small as possible [85]. For example,  $\text{MgO}$  or  $\text{LaAlO}_3$  are suitable for this purpose. In addition to  $\text{YBa}_2\text{Cu}_3\text{O}_7$ , also thin films of  $\text{Tl}_2\text{Ba}_2\text{CaCu}_2\text{O}_8$  are applied in form of passive microwave devices [83].

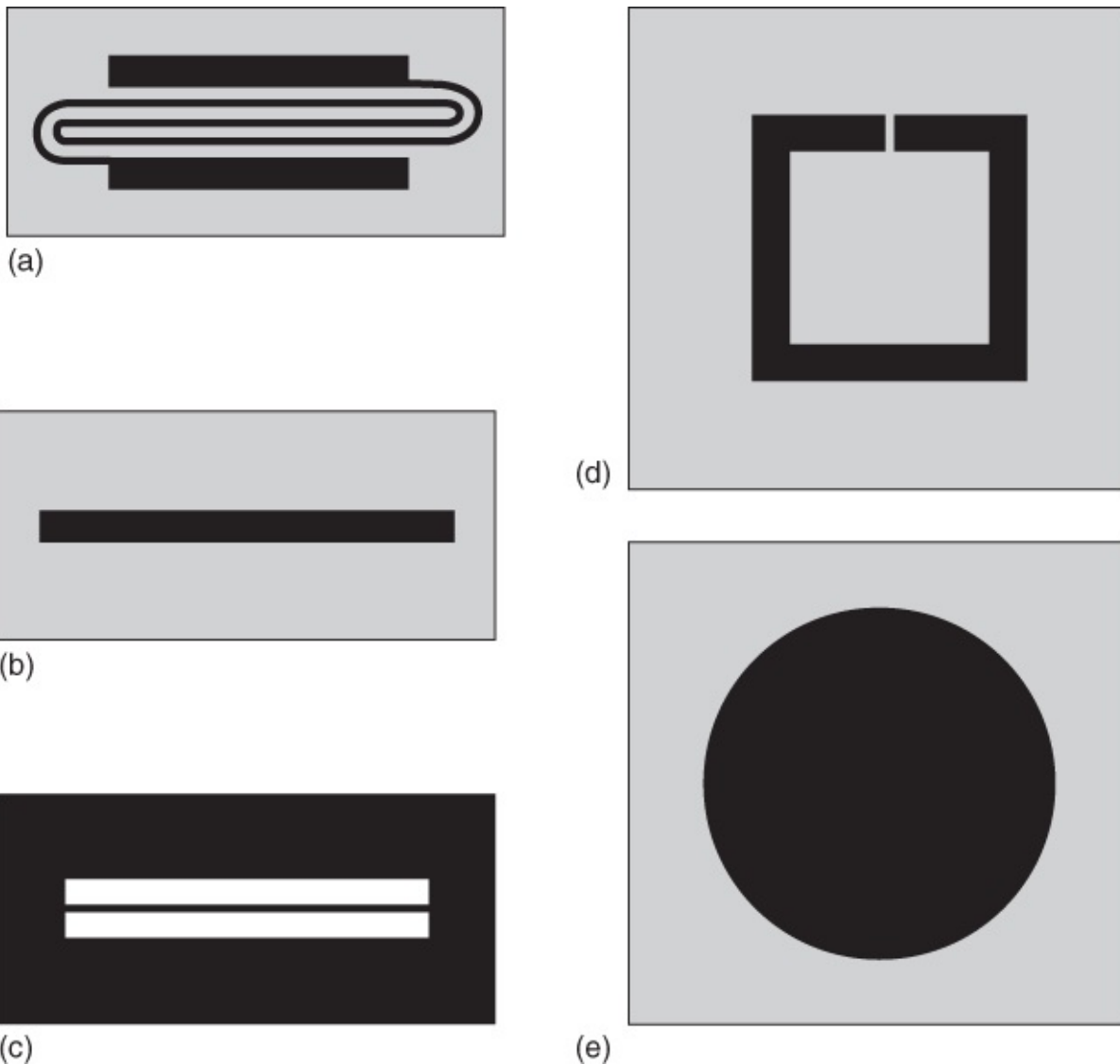


**Figure 7.35** Different designs of planar resonator structures: (a) quasilumped element, (b) microstrip, (c) coplanar waveguide, (d) folded microstrip with integrated capacitors, and (e) ring resonator.

(From [65] with permission of IOP.)

In the structure shown in [Figure 7.35a](#), the two thick stripes act as a capacitor, whereas the meandering stripe in between represents the inductance of an *LC* tank circuit. The simple design of [Figure 7.35b](#) is referred to as a **microstrip resonator**. Alternating electric fields applied parallel to the stripe cause the stripe to oscillate, and resonances appear if the strip length is a multiple of half the wavelength of the irradiating microwave. The structure in [Figure 7.35c](#) is a coplanar waveguide. The resonator of [Figure 7.35d](#) is just a bent micro-waveguide with an integrated capacity (slit at the upper end of the structure). Finally, the structure shown in [Figure 7.35e](#) is referred to as a **ring resonator**.

In these configurations, electric fields are generated relative to a ground plane, which is a second superconducting thin film on the back side of the substrate. Without going into the details, it is obvious that the fabrication of thin films of the highest quality on both sides of the substrate using a complex material such as  $\text{YBa}_2\text{Cu}_3\text{O}_7$  represents an impressive feat.

However, the required technology is more and more under control [86].

As an example, in [Figure 7.36](#) we show an eight-pole quasi-elliptic filter made from  $\text{YBa}_2\text{Cu}_3\text{O}_7$  together with the measured transmission curve [87]. This design represents only one of many possible options. The basic device is a meandering resonator, which is equivalent to the structure shown in [Figure 7.35d](#). Eight such resonators in the form of thin films are placed on a  $\text{MgO}$  substrate and mounted within a high-frequency box. The filter transmits nearly without attenuation signals at frequencies between 1.73 and 1.745 GHz, and outside of this frequency band it reduces the signals by 40 dB and more. The filter is part of a larger system, containing also a cryo-cooler down to temperatures of about 60 K as well as other superconducting and normal conducting microwave components. The module served for operation in mobile-receiving stations of the Universal Mobile Telecommunications System (UMTS).

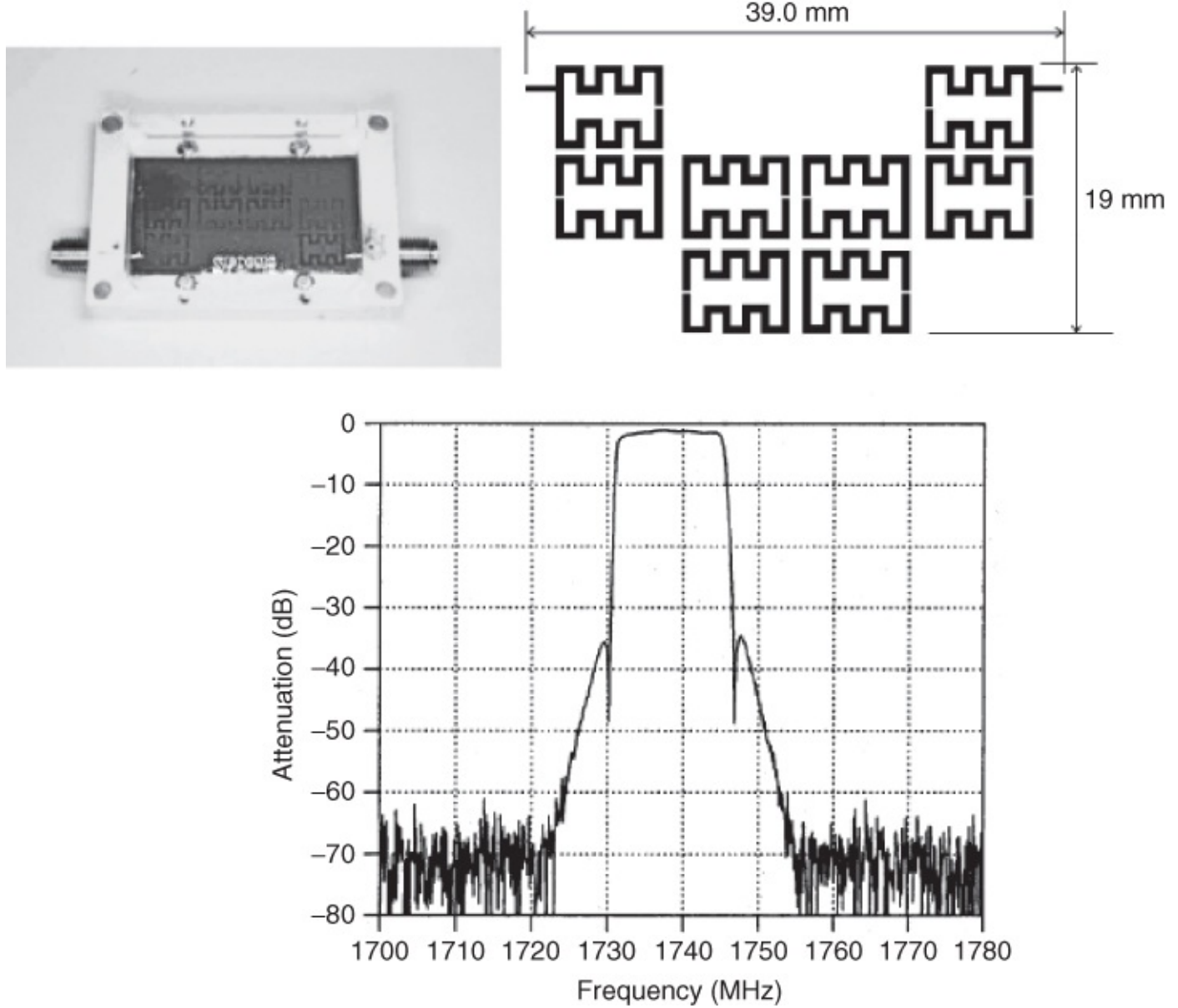


**Figure 7.36** Eight-pole elliptic bandpass filter consisting of meandering  $\text{YBa}_2\text{Cu}_3\text{O}_7$  resonators on a  $\text{MgO}$  substrate and the transmission curve [87].

(© 1999 IEEE.)

The detailed design not only of a filter but also of any other superconducting microwave component depends, in addition to the ingenuity of the inventor, on the special function to be performed (e.g., bandpass filter, bandstop filter), on the frequency range, and most importantly on the microwave power the filter must be able to handle. At high-power levels, as they appear, say, in output filters, large currents flow within the superconductor. At least upon reaching the critical current value the response of the filter is nonlinear (i.e., it depends on the amplitude of the microwave fields). Then the filter cannot fulfill its function any longer, if it is not suitably designed [83].

We do not want to go too deeply into the details of passive microwave components. However, we point out that in addition to filters there are a number of other components that strongly benefit from the use of (high-temperature) superconductors [72]. For example, highly compact

and well-functioning antennas can be designed. This is advantageous for radar systems [88], but is also interesting for nuclear spin resonance and nuclear spin tomography (see [Sections 7.3.1](#) and [7.3.2](#)) [89]. The better the antennas (here, mostly planar induction coils) detecting the signals from the spins precessing within the human body, the faster the measurements can be carried out and the higher is the contrast of the images.

Antennas represent just the first example of the application of superconductivity in a *measuring technique*. Further such examples will be discussed in the following section.

## 7.6 Superconducting Detectors

Superconductors are applied for the detection of many quantities to be measured. In this case we must distinguish between the physical quantity to which the detector primarily responds and the physical property to be derived from this.

In the case of bolometers, primarily the heating of the sensor, caused by irradiation with electromagnetic waves or with highly energetic particles, is utilized. Then in general this heating is transformed into an electrical voltage and is detected. Superconducting quantum interferometers (SQUIDs) primarily respond to changes of the magnetic flux penetrating the interferometer. The quantity to be measured (in the simplest case, the external magnetic field) must cause a change of this flux, which again is transformed into a voltage change. In the case of Josephson junctions, the alternating Josephson currents interact with external alternating fields, leading to structures (Shapiro steps) in the current–voltage characteristic that can be detected easily. In the case of tunnel junctions, quasiparticles are excited beyond the energy gap primarily due to the absorption of energy quanta (e.g., photons). Then the conductivity of the tunnel junction below the energy gap increases and can be detected.

The quantity to be measured can be detected either statically or within a well-defined frequency interval, which is more often the case. Therefore, the detector sensitivity at a given frequency represents an important aspect characterizing the detector.

In this chapter we will see that superconducting detectors are among the most sensitive sensors and in some cases reach the ultimate measuring sensitivity limited by quantum mechanics. Exactly this represents the particular importance of these devices.

### 7.6.1 Sensitivity, Thermal Noise, and Environmental Noise

In the absence of an external signal, the quantity measured by a sensor (e.g., an electrical voltage  $U$ ) will fluctuate about an average value. This noise can be described more accurately by recording  $U(t)$  over a certain time  $t$  and then by expressing it in terms of its Fourier transform in frequency space. In this case one obtains the spectral distribution of the amplitude  $U(\omega)$  or of the spectral power  $S_\omega = dU^2(\omega)/d\omega$ . The dimension of  $S_\omega$  is  $(V^2/\text{Hz})$ . In general, the quantity to be measured (e.g., a magnetic field) is proportional to  $U$ . We can transform  $S_\omega$  into a noise power  $S_B$  in  $(\text{T}^2/\text{Hz})$  or into a noise amplitude  $S_B^{1/2}$  in  $(\text{T}/\text{Hz}^{1/2})$ .

In the simplest case  $S_\omega$  is independent of frequency. This is referred to as **white noise**. It is connected with the statistical thermal fluctuations of the atoms and of the atomic building blocks.<sup>24</sup> Furthermore, in most cases one observes that at low frequencies  $S_\omega$  varies approximately proportional to  $1/\omega$  or  $1/f$ . Frequently, a number of different stochastic processes contribute to this  $1/f$  noise.

In principle, a measured curve  $U(t)$  can be smoothed by averaging the measured values over a certain time interval  $\Delta t$ . In the case of white noise, the amplitude of the fluctuations of  $U(t)$  about its average value is inversely proportional to the square root of the averaging time interval. Hence, the integration time must be quadrupled in order to reduce the fluctuations to one-half.

Frequently one deals with periodic signals, for example, electromagnetic radiation having a fixed frequency  $f_s$  and a certain bandwidth  $\Delta f_s$ , or signals that can be generated with a certain repetition frequency. In this case, contributions to the detector signal  $U(t)$  that differ from this frequency can be filtered out by means of suitable modulation techniques. In terms of frequency space, in this case one measures only within a certain frequency interval  $\Delta f_m$  about the frequency  $f_m \approx f_s$ . In this case only the noise contributions close to  $f_m$  are relevant, and the detector is characterized by its noise power at exactly this frequency.

Furthermore, the signal shape  $U_s(t)$  can be highly characteristic (e.g., the temporal behavior of the electric and magnetic fields generated by a beating heart). Also if the signals arrive in a nonperiodic sequence, the frequency spectrum displays quite characteristic structures corresponding to the Fourier spectrum of the signal. In this case it is meaningful to detect only selected frequency intervals.

In order to be able to measure a signal, obviously the signal must be larger than the background noise. In this case the voltage change effected by the signal to be measured should be at least as large as the noise amplitude. A quantity that is often used to characterize detectors is the noise-equivalent power ( $NEP$ ) in  $\text{W}/\text{Hz}^{1/2}$ . This indicates the power that a signal must have within a bandwidth  $\Delta f$  of 1 Hz in order to generate the same power within the detector as the noise contribution. A signal with this power results in a signal-to-noise ratio of unity. If the  $NEP$  measured within a bandwidth of 1 Hz is divided by  $k_B$ , the noise temperature  $T_N$  is obtained. In some cases one also uses the detectivity  $D = (NEP)^{-1}$ , or the specific detectivity  $D^* = D/(\text{detector area})^{1/2}$ , in order to characterize the detector.

Another quantity that is often used to compare different detectors is the energy resolution (in  $\text{J}/\text{Hz}$ ). It indicates which energy is associated with the detector noise in a bandwidth of 1 Hz.

Ideally, the noise temperature and the energy resolution are limited by quantum fluctuations of the radiation field. If one measures over a time interval  $\Delta t = 1/\Delta f$ , the energy smearing  $\Delta E/\Delta f$  must amount to at least  $\hbar/2$ . If a radiation field with frequency  $\omega$  is detected within this bandwidth, then this corresponds to a minimum noise energy  $\hbar\omega/2$ , or to a minimum noise temperature  $T_q = hf/2k_B$  (quantum limit). In this case the minimum energy that can be resolved is  $\hbar/2$ .

So far our discussion has been restricted to the noise properties of the detector. However, in addition, the noise contributions of the whole measuring system must be considered, and also the contributions from unwanted signals (environmental noise). Frequently, it is a difficult task to distinguish between these perturbations and the real signals. This task can require more effort than optimizing the detector itself. In the following sections we will discuss a number of examples.

## 7.6.2 Incoherent Radiation and Particle Detection: Bolometers and Calorimeters

Bolometers and calorimeters are detectors having a relatively simple construction, and which are heated by the radiation source to be detected. The radiation can be heavy particles, but also photons from the far-infrared to the X-ray or even  $\gamma$ -ray range [90–92].

Usually, the temperature rise in the sensor is translated into an electrical quantity. If the response time of the detector is short compared to the rate at which the particles arrive at the detector, one speaks of a calorimeter – in the opposite case of a bolometer. Hence, a bolometer responds to the energy flux of the incoming radiation. By a temporal integration of the heat pulse, the calorimeter allows one to determine the energy of a single quantum.

The three most important components of the detector are the absorber of the heat energy, a thermometer, and a thermal coupling to the heat bath. The heat capacity of the absorber should be as small as possible, in order to yield the largest possible temperature rise due to the deposited energy. The absorber should be coupled to a bath via the smallest possible thermal connection (mounting). Both conditions demand a low operating temperature, since at low temperatures the specific heat and the thermal conductivity are small. Finally, the thermometer must indicate the temperature rise in the absorber very rapidly and with high sensitivity.

The detection of radiation by means of superconductors was discussed very early [93]. In this case the superconductors can be used as a thermometer in different ways. One can use the large resistance increase at the transition temperature. In this case the superconductor is attached to the absorber in the form of a thin strip. This thermometer is part of a circuit with a current supply and a small resistance connected in parallel. During a temperature change the resistance change in the thermometer leads to a change of the current flowing through the resistance, which in turn will be detected by a SQUID (see [Section 7.6.4](#)).

Extremely sensitive experiments are performed at very low temperatures below 100 mK. In this case one must choose a superconductor with a transition temperature exactly at the operating temperature of the experiment. For this purpose, materials such as Al, W, Ir, or Ta are used, where in addition the transition temperature can be tuned using the contact of the superconductor with a normal conducting layer (see [Section 6.1.2](#)). In the case of these transition thermometers, the operating temperature of the experiment must be kept very accurately at its optimum value.

More recently, more and more magnetic calorimeters are used, where the heating leads to a change of the susceptibility of paramagnetic ions in the absorber. This change can be detected

directly by means of SQUIDs [94].

An example of a calorimeter experiment in fundamental research is CRESST (Cryogenic Rare Event Search with Superconducting Thermometers), a detector installed in the Grand Sasso underground laboratory [95]. The purpose of this detector is the search for weakly interacting massive particles (WIMPs) [91]. From astronomical observations, we know that the visible matter in the Universe only amounts to a small fraction of the total mass. The missing mass can be accounted for partly by neutrinos. However, for a large part of the missing mass, a still unknown kind of heavy elementary particle is presumed, denoted by “WIMP.” The main construction of CRESST consists of a cryostat, which is several meters high, and in the well-shielded center of which an absorber consisting of several calcium-tungstate crystals of 300 g weight each are mounted at 15 mK. A tungsten transition thermometer is used, which is read off by a SQUID.

Particularly suitable for the detection of X-rays are microcalorimeters, in which thin films (e.g., Bi or Si) with an area of  $0.1\text{--}1 \text{ mm}^2$  suitable for X-ray absorption are used as absorber. Therefore, absorbers and thermometers (generally transition thermometers) are thermally coupled to the outside via thin Si,  $\text{SiO}_x$ , or  $\text{Si}_3\text{N}_4$  membranes fabricated lithographically. Such and similar detectors can resolve energies of about 2 eV in the case of 1–2 keV X-rays with count rates up to  $500 \text{ s}^{-1}$  [96]. With increasing energy, the resolution decreases slightly, and at 60 keV reaches values of about 120 eV [97]. In addition to individual detectors, planar arrays are already developed, in order to increase the detector area.

In [Figure 7.37](#) we show a scanning electron micrograph of an  $8 \times 8$  microcalorimeter array fabricated at the National Bureau of Standards and Technology, Boulder. The magnified detail of the freely hanging support made of  $\text{Si}_3\text{N}_4$  is also shown [98]. The individual calorimeters have an area of  $0.4 \times 0.4 \text{ mm}^2$  and use a Bi layer as absorber and a Mo/Cu double layer as transition thermometer at 175 mK.

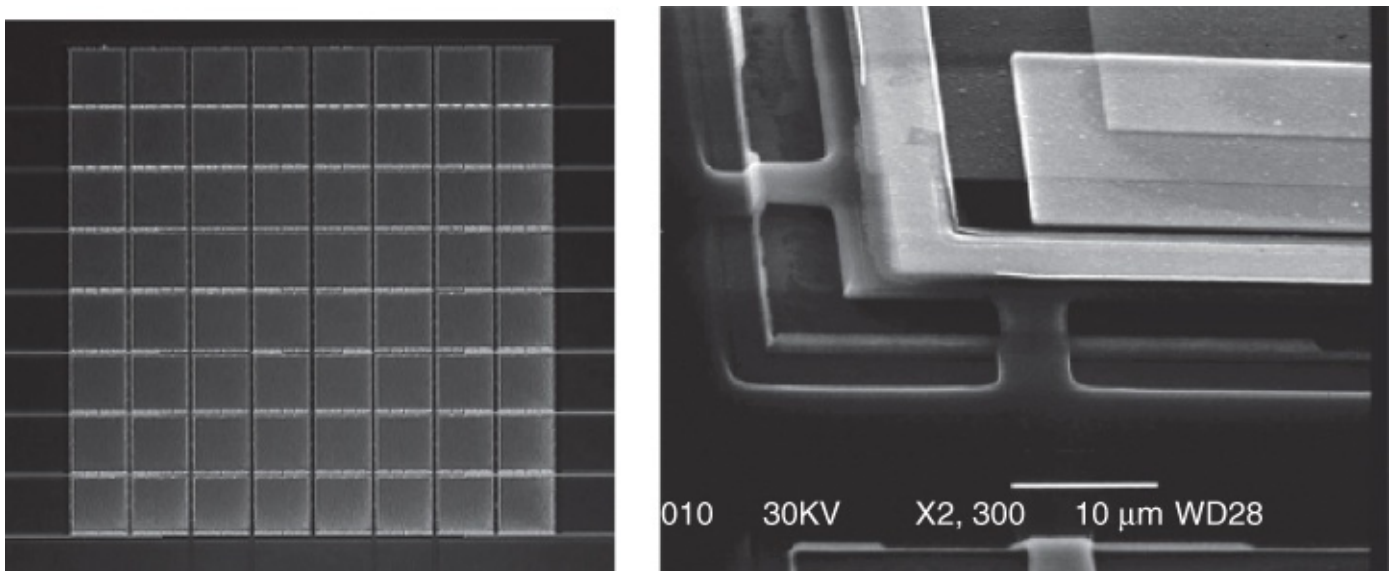


**Figure 7.37** SEM image of an  $8 \times 8$  microcalorimeter array and a magnified detail of the  $\text{Si}_3\text{N}_4$  membranes, which allow a freely hanging mount of each calorimeter. The magnified detail also shows part of the thermometer [98].

(© 2003 IEEE.)

In addition to their use in, say, X-ray satellites, the detection of X-rays also finds many applications on the ground. For example, in scanning electron microscopes the X-rays emitted from the sample because of the impinging electrons are used to perform spatially resolved chemical analysis. Today superconducting bolometers have reached an energy resolution with a short response time, which is only exceeded by the wavelength-dispersive X-ray spectrometers (“WDX,” resolution 2–20 eV at energies below 10 keV). The standard energy-dispersive X-ray analysis (“EDX spectrometer”) with a resolution of 100–140 eV is much worse.

Other properties of superconductors can also be utilized for thermometry, such as, for example, the temperature dependence of the critical Josephson current of superconductor-normal conductor–superconductor junctions (see [Section 6.1.2](#)) [90] or the strongly temperature-dependent quasiparticle conductance of superconductor–insulator–normal conductor junctions (see [Section 3.1.3.2](#)) [92].

In particular, using superconductor–insulator–superconductor tunnel junctions (SIS junctions), detectors or detector arrays for X-rays or for low-energy photons can be fabricated, in which the energy resolution gets close to that of the transition calorimeters. In this case one of the two electrodes serves as the absorber layer. Photons with energies far above the energy gap of this superconductor there break up Cooper pairs. The resulting quasiparticles diffuse to the counter-electrode(s), and there are detected as an additional quasiparticle current [99, 100]. The advantage of these detectors is the much higher stability against thermal drift compared to the transition thermometers, since the high sensitivity of the SIS junctions is not restricted only to a very small temperature range. SIS detectors are very fast and can reach count rates up to  $10^4 \text{ s}^{-1}$  [101].

In the case of SIS detectors for X-rays, nonequilibrium effects in the superconductor (generation of “hot electrons”) play an important role. Such nonequilibrium effects are systematically utilized in “hot-electron bolometers” (HEBs) [102]. One uses the effect that the electron system can be heated very fast. In this case the typical response times can be in the range of some picoseconds. Only after much longer timescales reach the electrons equilibrium with the phonons and, hence, with the crystal lattice. In a normal metal this rapid effect would not lead to a large change of the resistance. However, in superconductors it can be clearly resolved because of the mutual interrelation between the quasiparticles and the Cooper pairs.

Hot-electron effects are utilized in the case of bolometers as well as of calorimeters. For detection one can use ultra-thin superconducting films, SNS (superconductor–normal conductor–superconductor)-contacts, or SIS-contacts. During operation as bolometers, NHP values of better than  $10^{-16}$  W/Hz $^{1/2}$  were achieved. Values down to  $10^{-20}$  W/Hz $^{1/2}$  should be possible.

In the 1980s, detectors with a time-resolution of about 5 ns could be fabricated using ultra-thin Nb-films [103]. In 2001, response times in the range of 30 ps were reached based on niobium-nitride films of only 5 nm thickness [102]. A very small strip was prepared, which covered an area of a few square micrometers in form of a meander. This structure carries an applied current slightly below the critical current. Due to an incoming photon, the strip locally becomes resistive, and the resulting voltage drop can be measured. Later the fabrication method was improved again. Now one can produce “nano-wires” having a width of 30 nm or less [104]. These detectors allow the registration of single photons, from the ultra-violet to the near infrared.<sup>25</sup> They are interesting also in connection with circuits which transform light signals into electric voltages.

Finally we turn to (electromagnetic) radiation detectors for microwaves up to medium infrared frequencies. In the medium infrared range, the radiation detectors are based on the heating of an absorber and the subsequent thermometric detection of the signal as described above. Here, a number of excellent conventional methods exist for radiation detection. Golay-cells use the expansion of a gas volume and still belong to the most sensitive detectors operated at room temperature. Using semiconductor detectors such as HgCdTe, at 77 K sensitivities  $D^*$  around  $10^{11}$  cm Hz $^{1/2}$ /W represent the state of the art, and record values are still much higher. Bolometers made of high-temperature superconductors reach these values. However, presently they are not much better [105].

On the other hand, in the far-infrared, superconducting detectors are much better than other detectors. For example, for the detection of wavelengths of about 400 μm, bolometers were fabricated in which an Al strip on a sapphire substrate served as a transition thermometer at 1.25 K, and a Bi layer on the opposite side served as absorber [106]. In this case a detector sensitivity  $D^*$  of about  $10^{14}$  cm Hz $^{1/2}$ /W and a NEP of about  $2 \times 10^{-15}$  W/Hz $^{1/2}$  were achieved. Based on an array of transition sensors, even a camera operating in the far-infrared was developed [107]. It operates at frequencies around 0.35 THz. In the far-infrared, also bolometers made of high-temperature superconductors are of interest, say, for the satellite-based detection of the 84.43 mm emission of OH<sup>-</sup> ions in the atmosphere. Using

$\text{GdBa}_2\text{Cu}_3\text{O}_{7-x}$  transition thermometers at 85 K for wavelengths in the range between 70 and 200  $\mu\text{m}$ , a value of  $D^*$  of  $3 \times 10^{10} \text{ cm Hz}^{1/2}/\text{W}$  ( $NEP = 3 \text{ pW/Hz}^{1/2}$ ) could be reached, which is adequate for such observations [108].

Detectors coupling a very thin and narrow superconducting strip to a wave guide and operating this as a resonator (“kinetic inductance detectors”) are relatively new [109]. In addition to its geometry, the inductance  $L$  of the strip also depends on the kinetic energy of the Cooper pairs and, hence, on their density  $n$ . We have  $L = L_{\text{kin}} + L_g$ , where  $L_g$  denotes the geometric inductance and  $L_{\text{kin}}$  the “kinetic inductance.” If the strip is very small and thin,  $L_{\text{kin}}$  is large compared to  $L_g$ . If Cooper pairs are broken up due to irradiation with photons or other particles,  $n$  and  $L_{\text{kin}}$  change and, hence, also the resonance frequency and the quality of the resonator. The arrangement can be operated as a highly sensitive detector with the additional advantage, that many resonators of different frequencies can be utilized by a *single* wave guide (“multiplexing”). Therefore, these detectors are well suitable for the construction of large arrays.

In the case of still larger wavelengths, the dimensions of the detectors become comparable to or smaller than the wavelength. In this case, by means of suitable antennas, high-frequency currents can be induced in the detectors, and the radiation can be observed directly in frequency space or after mixing it down to lower frequencies. This will be discussed in more detail in the following section.

### 7.6.3 Coherent Detection and Generation of Radiation: Mixers, Local Oscillators, and Integrated Receivers

The radiation detectors discussed in [Section 7.6.2](#) were based predominantly on the energy deposition of the incoming radiation in an absorber and its resulting heating. On the other hand, electromagnetic radiation with wavelengths larger than a few hundred micrometers can be detected by means of the alternating voltages or currents induced in the detector.

The most direct form of detection would be to record the time dependence of the incoming signal and then to process it further in some way. However, at frequencies above a few gigahertz such a procedure would not be very practicable. In the opposite extreme the incoming radiation would generate (incoherently) a quasistatic signal nearly independent of its frequency, which can be detected. Basically, bolometers and calorimeters follow this latter principle. In this case the incoming radiation initially generates lattice vibrations or hot electrons, which then heat up a thermometer.

A device with a nonlinear current–voltage characteristic like a diode can also rectify an incoming alternating field. An alternating voltage harmonically oscillating about  $U = 0$  generates a current flow through the diode only in the forward direction. Hence, the temporally averaged current is different from zero. A dependence on the frequency of the incoming radiation can arise, since, on the one hand, the amplitude of the alternating voltage coupled into the diode via an antenna is frequency-dependent and, on the other hand, the dynamic properties of the diode depend on the frequency.

The next step is a frequency-selective detection of the incoming radiation. This can be achieved by probing or multiplying the signal arriving at the detector with frequency  $f_S$  synchronously in phase with the frequency  $f_D$ . In this case the detector delivers a signal proportional to the temporal average of the product  $\cos(2\pi f_S t)\cos(2\pi f_D t)$ . In the case  $f_S = f_D$ , this average yields the value 1/2, and otherwise the value 0.

Josephson junctions also follow this principle, although the details require an analysis of the nonlinear dynamics in the junction (see [Section 6.3](#)). The high-frequency radiation arriving at the junction interacts with the alternating Josephson currents and generates steps of constant voltage on the current–voltage characteristic. The steps appear at the d.c. voltages  $U_n = nhf_S/2e$  ( $n = 0, 1, 2, \dots$ ). The current interval  $\Delta I$  in which a given step is stable (the step height) depends on the microwave amplitude. Hence, in the case  $n \neq 0$ , the Shapiro steps can be used to analyze the frequency as well as the power of the incoming high-frequency radiation.<sup>[26](#)</sup>

The microwave-induced or the far-infrared-induced change of the current–voltage characteristic is utilized in the “Hilbert spectrometer” to obtain a spectrum of the incoming radiation. For this purpose, prototypes operated with cryo-coolers were developed, which use grain-boundary Josephson junctions made of  $\text{YBa}_2\text{Cu}_3\text{O}_7$  including an integrated high-frequency antenna as detectors [110]. At frequencies between 1 and 4 THz a relative frequency resolution of about  $10^{-3}$  could be achieved.

The detectors just described represent “homodyne” receivers, which process the signal at the frequency at which it arrives. However, “heterodyne” receivers are used much more frequently. In this case initially the signal is transformed into a signal of lower frequency (intermediate frequency  $\omega_{\text{IF}} = 2\pi f_{\text{IF}}$ ), and then it is processed further. This principle is used, for example, by satellite receivers for radio and television.

The conversion of the signal frequency to the intermediate frequency is performed by mixers. These mixers are devices with a nonlinear current–voltage characteristic  $I(U)$  or  $U(I)$ . We assume that a time-dependent current  $I(t)$  is induced in the device. In this case at not too large current amplitudes the voltage  $U(t)$  can be expanded in a power series (Taylor series)

$$U(t) = U_0 + aI + bI^2 + cI^3 + \dots \quad \underline{\text{7.11}}$$

If  $I(t)$  has the form  $I_{\text{ac}} \cos(\omega_S t)$ , the linear term is proportional to  $\cos(\omega_S t)$  and the square term is proportional to  $\cos^2(\omega_S t) = [1 - \cos(2\omega_S t)]/2$ . We see that the square term yields a *static* contribution to  $U$  and also a contribution at frequency  $2\omega_S$ . The cubic term yields contributions at  $\omega_S$  and  $3\omega_S$ , and so on. We see that the nonlinear terms yield higher harmonics of the incoming radiation.

We couple two frequencies  $\omega_S$  and  $\omega_{\text{LO}}$ , which are not too different from each other, into the mixer. In this case  $\omega_{\text{LO}}$  is generated by a local oscillator. In general the latter is located close to the mixer. In the series expansion (Eq. (7.11)) the square term results in a contribution of the

form

$$\cos(\omega_s t) \cos(\omega_{\text{LO}} t) = \{\cos[(\omega_s - \omega_{\text{LO}})t] + \cos[(\omega_s + \omega_{\text{LO}})t]\}/2$$

that is, it contains frequency contributions at  $\omega_{\text{LO}} \pm \omega_s$ . In the case  $\omega_{\text{LO}} \approx \omega_s$  the difference frequency  $\omega_{\text{IF}} = |\omega_{\text{LO}} - \omega_s|$  is much smaller than  $\omega_{\text{LO}}$  and  $\omega_s$ . The signal is mixed down. Analogously, the higher terms in Eq. (7.11) yield frequency components at  $|2\omega_{\text{LO}} - \omega_s|$ ,  $|\omega_{\text{LO}} - 2\omega_s|$ ,  $|3\omega_{\text{LO}} - \omega_s|$ , and so on.

It is important to convert the signal at  $f_s = \omega_s/2\pi$  to the intermediate frequency  $f_{\text{IF}}$  as effectively and with as little noise as possible. In this case both the signal frequency  $f_s = f_{\text{LO}} - f_{\text{IF}}$  and its mirror frequency  $f_s = f_{\text{LO}} + f_{\text{IF}}$  can contribute. Depending on whether both frequencies are admitted or one of them is filtered out, one speaks of single-sideband (SSB) or double-sideband (DSB), and one indicates this notation among the quantities characterizing the mixer. These quantities include the conversion gain  $\alpha = (\text{power at } f_{\text{IF}})/(\text{power at } f_s)$  or the noise temperature of the mixer only or of the whole detector system.

The signal conversion is larger, the more nonlinear is the current–voltage characteristic of the mixer. An almost jump-like change of the conductance would be ideal. One of the best conventional mixers is the Schottky diode, which is operated at room temperature, and at 500 GHz has a DSB noise temperature of about 1000 K. At 500 GHz the minimum noise temperature based on the radiation fluctuations due to the uncertainty relation,  $T_q = hf/2k_B$ , is about 11 K. We see that the Schottky mixers are much above this value.

Using Josephson junctions and in particular SIS tunnel junctions as mixers, one can get much closer to the quantum limit. Furthermore, the local oscillator requires only very small amounts of power in the range of 1  $\mu\text{W}$  or less, whereas, for example, the Schottky mixer must be supplied with a few milliwatts.

The details of the theory of Josephson and SIS-mixers are relatively complicated, and can be found in the review article [111]. Here, we only present an outline.

The Josephson mixer is based on an overdamped Josephson junction with a nonhysteretic current–voltage characteristic (see [Section 6.3](#)). In a simplified discussion, a local oscillator generates Shapiro steps on the current–voltage characteristic. If the signal having a frequency not much different from  $f_{\text{LO}}$  is superimposed, a beat is obtained. The total amplitude and, hence, the total microwave power are pumping with the difference frequency  $f_{\text{IF}}$ . Therefore, the height of the Shapiro steps and the voltage varying continuously between the steps change periodically with the intermediate frequency  $f_{\text{IF}}$ . Between the steps the differential resistance of the characteristic reaches a maximum (see [Figure 6.12a](#)). Here, the pumping of the characteristic at constant current yields the maximum alternating voltage amplitude, which can be even larger than the signal amplitude. The conversion gain  $\alpha$  can reach values larger than 1. However, because of the nonlinear oscillations in the Josephson junction, also noise contributions from a large frequency range are mixed down to the intermediate frequency.

Therefore, in spite of the large conversion gain, one only reaches noise temperatures of about 40–50 times the quantum limit.

On the other hand, the quantum limit can almost be reached using SIS tunnel junctions.<sup>27</sup> In this case basically one uses the extreme nonlinearity of the quasiparticle characteristic<sup>28</sup> at the gap voltage<sup>29</sup>  $2\Delta_0/e$ . However, we must also take into account that the quasiparticle characteristic is modified again during microwave irradiation (see [Figure 1.24](#)). The quasiparticles can take up energy from the radiation field in multiples of  $\hbar\omega$ , and in this way can tunnel to the counter-electrode already at voltages below  $2\Delta_0/e$ . There appear maxima of the differential conductance at the voltage levels  $(2\Delta_0 - n\hbar\omega)/e$  (with  $n = 1, 2, 3, \dots$ ). Similar to the Josephson mixer, also in the case of the SIS-mixer the characteristic is pumped back and forth between two extremes at the intermediate frequency. For example, if the signal amplitude were equal to the amplitude of the local oscillator, in [Figure 1.24](#) these extremes would just be given by the two curves 1 and 2.

A rise of the quasiparticle conductance at the energy gap that is as large as possible is a prerequisite of a high sensitivity of an SIS-mixer. This requires a tunnel junction with a nearly perfect tunneling barrier as well as very low operating temperatures.

Today, SIS-mixers as they are routinely operated in radio telescopes or in the Herschel space telescope, are based on Nb–(Al/AlO<sub>x</sub>)–Nb tunnel junctions [112]. These junctions can be operated extremely well up to about 700 GHz. Higher frequencies or energies  $\hbar\omega$  exceed the energy gap  $\Delta_0$  of Nb. Then, in the whole superconducting circuit, also fabricated from Nb, large damping sets in, and the mixer no longer functions.<sup>30</sup> As an alternative material for higher frequencies, for example, NbN can be used up to a maximum frequency of 1.2 THz. However, at present one cannot yet fabricate sufficiently good tunneling barriers for this material. Highly promising results are presently achieved using SIS junctions with the composition NbTiN–MgO–NbTiN or Nb–(Al/AlN<sub>x</sub>)–NbTiN. These junctions can be operated up to maximum frequencies of about 1 THz. Possibly here an application for the superconductor MgB<sub>2</sub> may also develop. However, for this, it is necessary to prepare excellent tunneling barriers.

On the other hand, it appears that the high-temperature superconductors cannot be used as SIS-mixers. In this case, because of the  $d_{x^2-y^2}$  symmetry of the pair wave function (see [Section 3.2.2](#)), the tunneling characteristics are highly rounded (see, e.g., [Figure 6.3](#)). However, the high-temperature superconductors could be suitable as Josephson mixers operating up to frequencies of a few terahertz.

The Atacama Large Millimeter/Sub-Millimeter-Array (ALMA) is an example of the application of SIS-mixers in a large research project [112]. Presently, it is under construction in the Atacama desert in Chile and shall become operating in 2013. ALMA consists of a total of 65 synchronously operated radio telescopes, their size ranging between 7 and 12 m. The detection range of the telescopes extends to frequencies between 30 and 950 GHz, divided into 10 bands. Superconducting SIS-mixer based on Nb are used as detectors at frequencies above 84 GHz. The cryostat containing the detectors has a diameter of about 1 m and is cooled by

means of a cryo-cooler. Each frequency band is separately placed within the cryostat in form of an independent sub-unit (cartridge). [Figure 7.38](#) shows one of these cartridges (seventh frequency band; 275–373 GHz). The upper third of the cartridge is cooled to 4 K. The incoming radiation first reaches mirror 2, and from there it is directed toward mirror 1. The polarization grating consists of many thin wires. The fraction of the radiation, which is polarized parallel to the wires, passes through the grating and is focused via mirror 1 on a horn antenna and from there on a SIS-mixer. The fraction of the radiation polarized perpendicular to the wires is reflected at the grating and reaches the other SIS-mixer via mirror 1. In the warm part of the cartridge there is a microwave oscillator. Its reference frequency, synchronized over all telescopes of the array, at first is multiplied and subsequently is applied to the SIS-mixer. The difference frequency coming from the mixers, ranging between 4 and 12 GHz, is amplified in the subsequent stages and processed further.

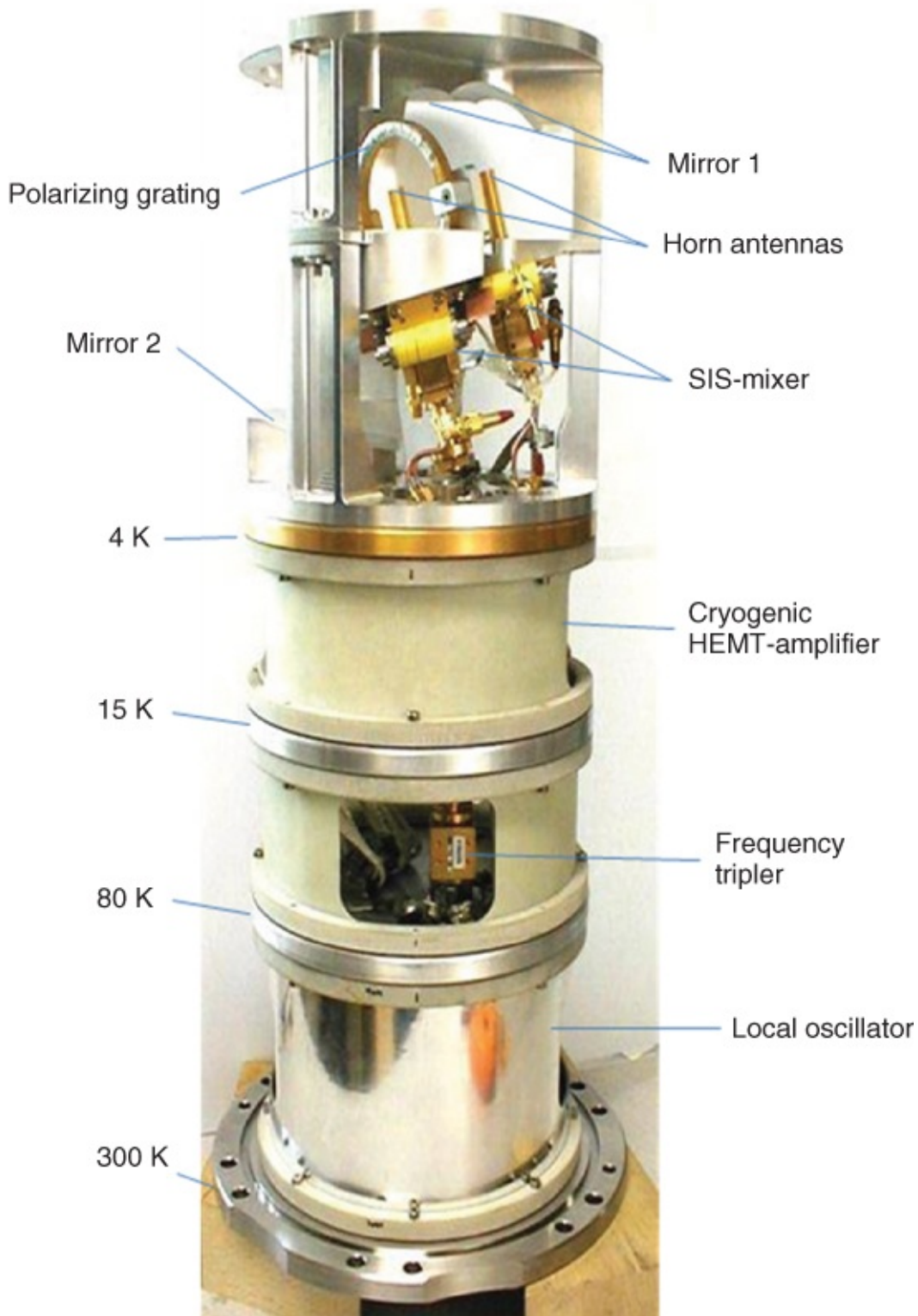


**Figure 7.38** The cartridge of the seventh frequency band of the ALMA telescope.

(Courtesy of S. Mahieu, IRAM.)

A completely different mixing principle is used in the HEB mixer, which can be operated up to frequencies of several terahertz. In [Section 7.6.2](#) we have already discussed the basic principle of the HEB. In order to apply these devices as mixers, very thin Nb or NbN microbridges are integrated into the structure of an antenna and are coupled to a heat bath. A

typical structure is shown in [Figure 7.39](#) together with the current–voltage characteristic of the mixer. Typically, one works with a bath temperature of 4.2 K. Upon exceeding the critical current, a hotspot develops in the bridge. In this hotspot the temperature is only slightly above  $T_c$ . During irradiation of the bridge, the heated region expands. The bridge cannot respond directly to the high-frequency amplitude of the local oscillator or of the signal. However, the size of the hotspot and, hence, the bolometer resistance or the current–voltage characteristic can be modulated with the intermediate frequency. A small direct voltage is applied to the bridge – in the case of [Figure 7.39](#), about 0.5 mV. During irradiation with the local oscillator and with the signal, an alternating voltage is generated about this bias point.

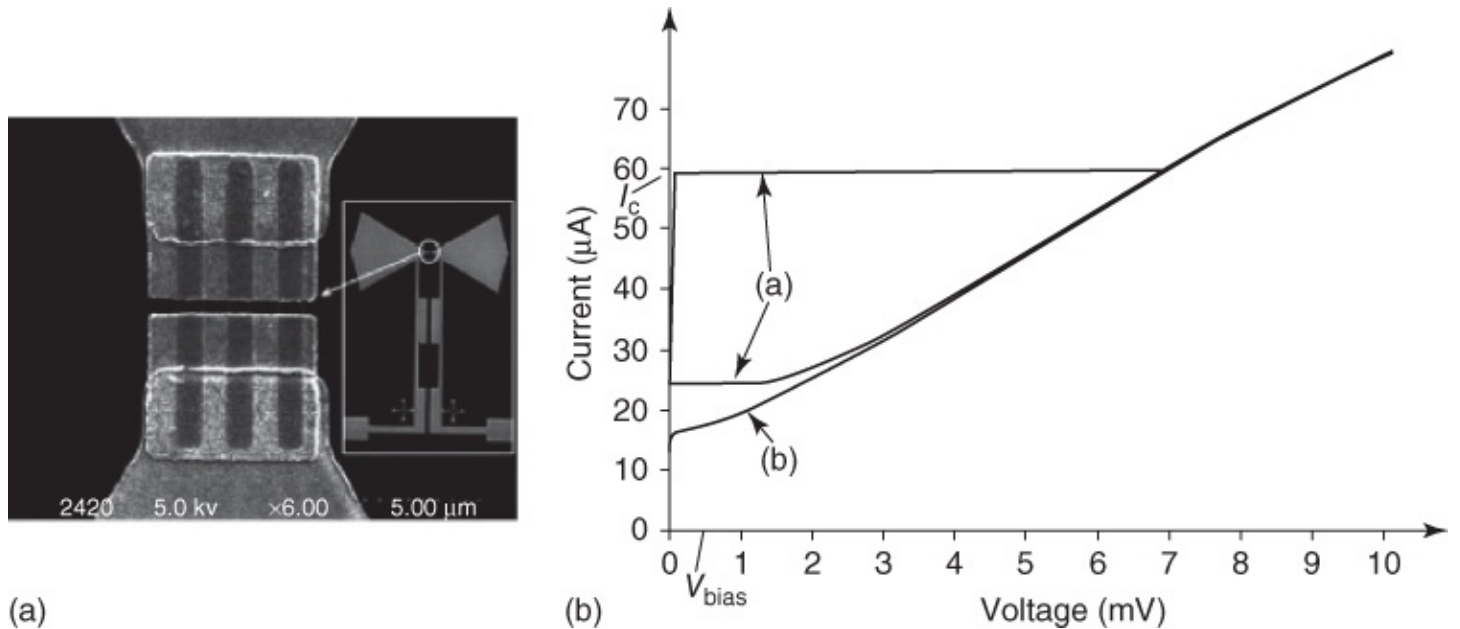


**Figure 7.39** HEB mixer made from NbN. Scanning electron microscope image of three microbridges integrated into a dipole antenna ((A) the bridges can just be seen in the form of very narrow lines in the slit between the wide contact areas) and the current–voltage characteristic of a bridge (a) without and (b) with high-frequency irradiation with a local oscillator. The bridges are 0.4  $\mu$ m long and 0.8  $\mu$ m wide [113].

(Reprinted from [113] with permission of IOP.)

At 800 GHz the receiver operating with the mixer shown in [Figure 7.39](#) had a DSB noise temperature of about 900 K. In the frequency band between 1.4 and 1.9 THz NbN-mixers are used in the Herschel space telescope. Other HEB mixers have already been applied at a few terahertz. However, the (at least so far) relatively small bandwidth is a disadvantage of the HEB bolometers. Intermediate frequencies above about 4 GHz can only be processed very poorly.

So far we have discussed only the mixer, but not its periphery. First, the mixer must be integrated into a structure, adjusting its impedance to that of the antenna. The antenna itself can either have a planar design as in [Figure 7.39](#) or be constructed as a 3D structure. In this case more or less standard high-frequency designs (waveguides, mixer blocks, horn antennas) are used, which we cannot discuss in more detail. In general also the local oscillator is a

conventional Gunn oscillator.

However, an integrated superconducting receiver, developed by V. P. Koshelets and S. V. Shitov, deserves special mention [114]. As local oscillator, it contains a long Josephson tunnel junction made from Nb–(Al/AlO<sub>x</sub>)–Nb, which utilizes the motion of the Josephson fluxons along the tunneling barrier to generate the high frequency (fluxon oscillator, see also [Section 6.4](#)). A Nb–(Al/AlO<sub>x</sub>)–Nb tunnel junction also serves as SIS-mixer. In [Figure 7.40](#) we show a photograph of the central part of the chip containing the superconducting components. In addition, among other things, also a high-electron-mobility transistor (HEMT) amplifier for the intermediate frequency of 400 MHz, a feedback loop effecting the extreme narrow-band emission of the fluxon oscillator, as well as an Si lens focusing the incoming radiation on the mixer or the integrated H-antenna, are all kept at low temperatures. At 500 GHz the receiver reaches its minimum noise temperature below 100 K, and it can be applied in the frequency range 400–600 GHz.

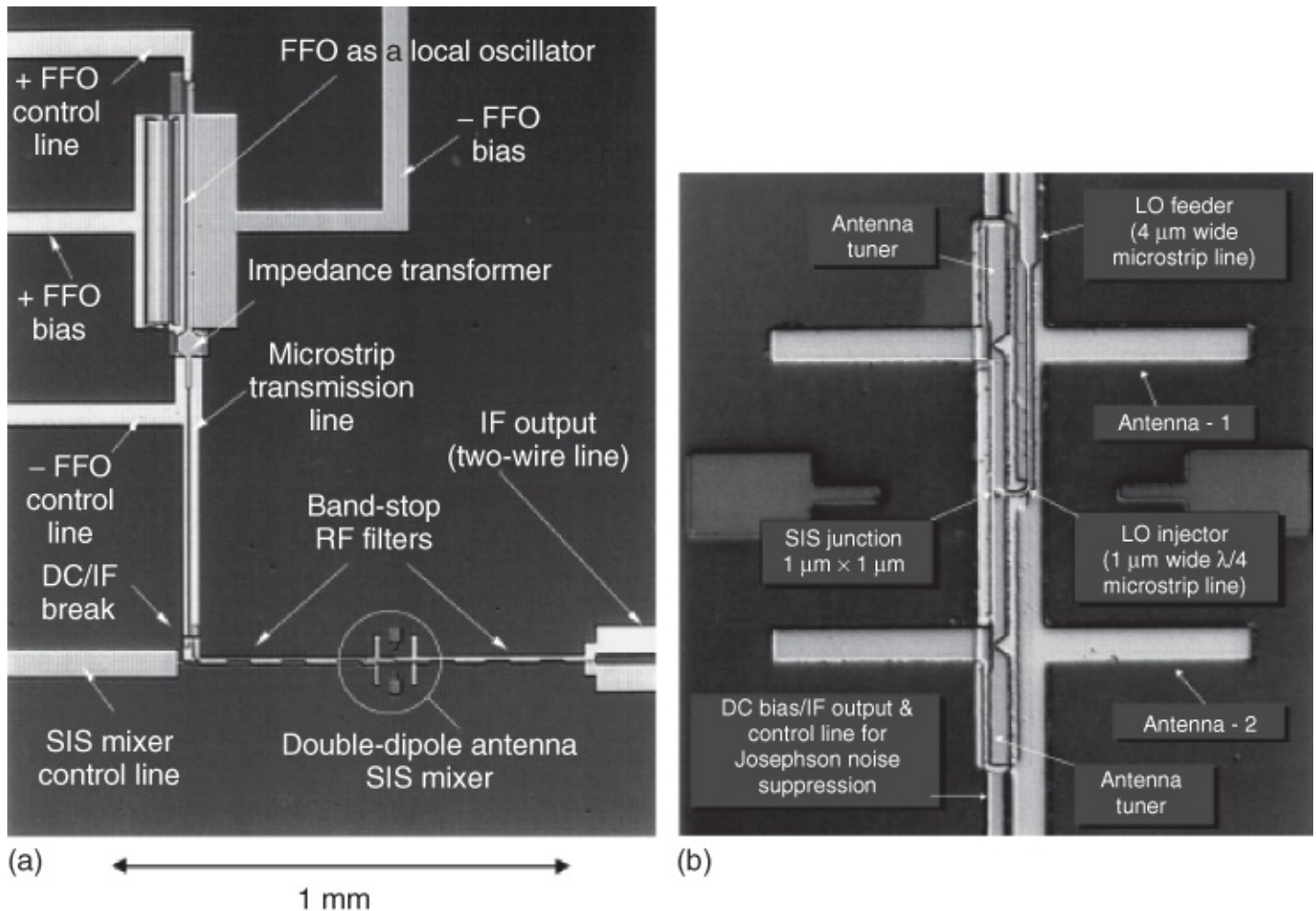


**Figure 7.40** Integrated superconducting receiver for frequencies up to 600 GHz. (a) Photograph of the central part of the chip with  $4 \times 4 \text{ mm}^2$  total area. (b) Magnification of the part with the SIS-mixer. The section shown represents an area of about  $100 \times 150 \mu\text{m}^2$  and is rotated by  $90^\circ$  relative to the photograph (a).

(Reprinted from [114] with permission of IOP.)

The fluxon oscillator of the integrated receiver represents a first example of the *generation* of high-frequency radiation using superconductors. This oscillator can reliably generate power levels near  $1 \mu\text{W}$ . Another much studied method uses arrays of coupled Josephson junctions, where the dimensions of the junctions are smaller than the extension of a fluxon. These junctions are made to oscillate synchronously in phase by means of suitable interactions, and in this way a relatively high emission intensity can be achieved. For this purpose, one can mount series configurations of Josephson junctions into microwave resonators or strip lines in such a way that the radiation emitted by the junctions acts back on them with a synchronizing effect. Using such arrays, it has been possible to couple power values of about  $0.4 \text{ mW}$  at  $410 \text{ GHz}$  into detector Josephson junctions integrated on the chip [115]. In this case  $498$  overdamped Nb–(Al/AlO<sub>x</sub>)–Nb tunnel junctions (dimensions  $2 \times 80 \mu\text{m}^2$ ) in groups of six junctions each were integrated into a meandering strip line. Using a somewhat smaller array and a planar antenna connected with the strip line, about  $0.5 \mu\text{W}$  could be recorded off-chip [115]. Recently, coherent far-infrared radiation at frequencies between  $0.4 \text{ THz}$  and about  $1 \text{ THz}$  could be extracted from staples of more than  $600$  intrinsic Josephson contacts (see [Figure 1.22f](#)) [116, 117]. The emitted power ranged about a few microwatts, and is likely to be increased much further.

Also two-dimensional arrays yielded highly promising results [118, 119]. A comprehensive overview about the different kinds of radiation sources can be found in the articles [120].

The synchronization of many Josephson junctions is very difficult. Therefore, a large amount of research still must be done in order to achieve stable and if possible tunable high-frequency sources at a power level above a few microwatts at frequencies up to the terahertz range.

A completely different kind of generation of radiation, namely that of phonons (i.e., ultrasound), has turned out to be highly successful in particular in fundamental research. The phonons are generated by means of superconducting tunnel junctions, which at the same time can be used also as phonon detectors. Compared to other sources of ultrasound, SIS tunnel junctions distinguish themselves because of their ability to generate phonons at extremely high frequencies [121].

The effect can be explained using [Figure 3.21b](#). A voltage much above the energy gap is applied to the tunnel junction. As a result an appreciable tunneling current flows across the junction, which increases the concentration of unpaired electrons in the counter-electrode beyond the equilibrium level. Delivering energy to the lattice (i.e., due to the generation of phonons), these electrons reduce their energy from  $E = eU - \Delta_0$  down to the lower edge of the excitation spectrum, that is, to the energy  $E' = \Delta_0$ . This process is relatively fast, taking about  $10^{-9} \text{ s}$ . During this process, a continuous phonon spectrum is generated, but with a sharp edge at the energy  $hf = eU - 2\Delta_0$ . This sharp edge appears because, at the lower edge of the excitation, the density of states is very high and, hence, the number of transitions is particularly large, which in a *single step* leads from  $E = eU - \Delta_0$  to  $E' = \Delta_0$ . At the same time the energy  $eU - 2\Delta_0$  is emitted as a phonon.

The next step, which takes a much longer time  $\tau > 10^{-7} \text{ s}$  at low temperatures, is the

recombination of the unpaired electrons to Cooper pairs. During this process, phonons with energy  $2\Delta_0$  are generated. Assuming the energy gap of Sn with  $2\Delta_{\text{Sn}} = 1.1 \times 10^{-3}$  eV, then we obtain for these recombination phonons the frequency  $f = 2\Delta_{\text{Sn}}/h = 280$  GHz.

Also the detection of such high-frequency phonons can be accomplished with superconducting tunnel junctions. For this purpose in the detector junction we choose a bias point  $U < 2\Delta_0$ . The tunneling current is very small, since it can be carried only by the unpaired electrons existing at the chosen temperature. However, if phonon radiation with energy  $2\Delta_0$  arrives, these phonons can break up Cooper pairs. As a result, the tunneling current increases. This increase in the current is proportional to the phonon current, that is, to the number of phonons absorbed per second within the tunnel junction.

In addition to the monochromatic phonons with  $hf = 2\Delta_0$ , in principle also the continuous spectrum can be utilized spectroscopically because of the quite sharp edge at  $hf = eU - 2\Delta_0$  [122]. This edge can be shifted by varying the voltage  $U$  applied to the tunnel junction. If an excitation energy is covered by this process, a particularly strong absorption of phonons will appear in a narrow range of voltage  $U$ .

The Josephson alternating current across an SIS junction offers another highly efficient source of high-frequency, monochromatic phonons [123]. In addition to photons, this current also generates monochromatic phonons with frequency  $f = 2eU/h$ , which can then be used for spectroscopic purposes.

Finally, we mention that superconducting tunnel junctions can also serve for studying solids using polarized electrons with extremely small energy. If a tunnel junction is placed in a magnetic field oriented parallel to the junction interface, the states of the unpaired electrons with magnetic moment parallel or antiparallel to the magnetic field are energetically separated. (We just discuss the tunneling of the unpaired electrons.) If in the magnetic field a voltage is applied to such a junction between a normal conductor and a superconductor, initially the electrons with one orientation of their magnetic moment, that is, with one spin direction, will be able to tunnel. In this way, for example, one can study directly the direction of the moments of the electrons in a ferromagnet [124].

#### 7.6.4 Quantum Interferometers as Magnetic Field Sensors

The wave property of the superconducting state is very nicely demonstrated in SQUIDs. In [Section 1.5.2](#) we discussed this in detail. We saw that the maximum supercurrent within a ring structure, into which two Josephson junctions are integrated, is periodically modulated according to the flux penetrating the ring. The period was given by the flux quantum  $\Phi_0 = h/2e$ . The operation of the d.c. SQUID (direct current superconducting quantum interference device) is based on this geometry. In this section we will discuss also another type of interferometer, the r.f. SQUID (r.f. = radio frequency), which contains only one Josephson junction within the ring.

In order to fabricate highly sensitive measuring instruments from SQUIDs, some optimization

procedures are needed, which we will discuss in the following two sections.

### 7.6.4.1 SQUID Magnetometer: Basic Concepts

We start with d.c. SQUIDs. If we want to operate these as magnetometers, it appears advantageous to make the ring area  $A$  as large as possible, such that a small change  $\Delta B_a$  of the applied magnetic field results in the largest possible flux change  $\Delta\Phi_a = A\Delta B_a$ . On the other hand, one finds that the modulation depth of the maximum supercurrent decreases with increasing ring inductance  $L$ . In this case the crucial quantity is the dimensionless inductance parameter (see [Section 1.5.2](#)) given by Eq. (1.59):

$$\beta_L = \frac{2LI_c}{\Phi_0}$$

Here,  $I_c$  is the critical current of the two Josephson junctions in the ring, assumed to be identical. The quantity  $\beta_L$ , except for a factor  $\pi/2$ , can be interpreted as the ratio of the coupling energy  $I_c\Phi_0/2\pi$  stored in a Josephson junction and the magnetic energy  $\Phi^2/2L$  stored within the ring, with  $\Phi = \Phi_0/2$ .

Accurate analyses of the noise properties of SQUIDs caused by thermal fluctuations indicate that  $\beta_L$  should be approximately unity [125] (the ratio of the coupling energy of a Josephson junction and the maximum magnetic energy in the ring is approximately  $2/\pi$ ). The noise parameter

$$\Gamma = \frac{2\pi k_B T}{I_c \Phi_0} \quad 7.12$$

indicating the ratio of the thermal energy  $k_B T$  and the Josephson coupling energy, is another important quantity appearing in the noise analysis. This parameter should be as small as possible and also should not exceed a value of about unity. Hence, for a given temperature we obtain a condition for the critical current of a Josephson junction. It should not fall much below the value  $2\pi k_B T/\Phi_0$ . At 4.2 K, from this we find a minimum value of about 0.17  $\mu\text{A}$ , and at 77 K a value of 3.2  $\mu\text{A}$ .

Also the product  $\Gamma\beta_L = (4\pi k_B T/\Phi_0^2)L \equiv L/L_{\text{th}}$  obviously should not be much larger than unity. Hence, at 4.2 K the inductance should not greatly exceed a value of about 6 nH, and correspondingly at 77 K a value of 320 pH.<sup>[31](#)</sup>

Since the inductance of a ring increases in proportion to its circumference, obviously we have a conflicting situation, since at the same time the ring area should be large, but the ring inductance should be small. This situation results in many different concepts for the design of SQUIDs. In particular, in the 1970s and 1980s, three-dimensional cylinder geometries were often chosen, in which, for example, a cylinder including the Josephson junctions was evaporated onto a quartz thread. Alternatively, two half-cylinders made of massive material were combined electrically insulated from each other, and the Josephson junctions were

realized by means of screw connections. The same technique was applied in particular also for r.f. SQUIDs, which contained only one Josephson junction [126].

Modern SQUIDs are fabricated by means of thin-film technology. In order to achieve a small inductance together with a large SQUID area, one can utilize the diamagnetic behavior of superconductors and, instead of a thin ring structure, one can use a superconductor with a large area as shown in [Figure 7.41](#). These large-area structures are also referred to as **washer SQUIDs** or, because of the inventor, as Ketchen SQUIDs [126]. The structures shown in [Figure 7.41](#) are used for d.c. SQUIDs made of high-temperature superconductors, in which the Josephson junctions are prepared in the form of grain-boundary junctions (see [Figure 1.22e](#)).

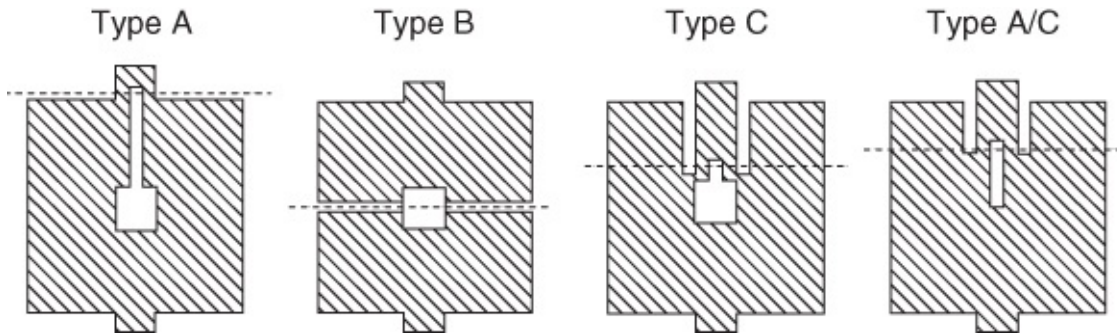


[Figure 7.41](#) Realized geometries of planar d.c. SQUIDs made of high-temperature superconductors (mainly from  $\text{YBa}_2\text{Cu}_3\text{O}_7$ ). The Josephson junctions are generated at the grain boundary within the substrate (often  $\text{SrTiO}_3$ ), indicated by the dashed line. The current input is located at the upper or lower edges of the structures indicated as the extensions [125].

The ring currents circulate around the inner opening (hole or slit) which, hence, determines the inductance of the SQUID. In the case of SQUIDs operated at 77 K, a typical hole diameter is in the range of about 10  $\mu\text{m}$ . If a magnetic field is applied perpendicular to the film plane, shielding currents flow in the superconducting film (in the washer), which focus the field into the inner opening. One can show that in the case of a quadratic structure with an outer diameter  $D$  and a hole diameter  $d$ , the effective area of the SQUID is  $A_{\text{eff}} = Dd$ , that is, it increases in proportion to the outer dimension of the washer. However,  $D$  cannot be made arbitrarily large, because otherwise during the cooling process vortices are trapped in the superconductor, even in cryostats where the Earth's magnetic field is strongly suppressed by means of suitable shielding.<sup>32</sup>

In order to increase the effective area of the SQUID further still, one needs to use flux transformers. Such a flux transformer consists of a closed superconducting loop, the receiving end of which represents a coil with  $N_1$  turns.<sup>33</sup> In a closed superconducting loop, the total magnetic flux remains constant. If the external field through the coil changes, a shielding current  $J_T$  is generated in the whole loop, which compensates the magnetic flux associated with the field change. The secondary part of the flux transformer (the coupling coil) is arranged in the form of several superconducting windings (winding number  $N_2$ ) around the SQUID hole. In this way the shielding current  $J_T$  generates a magnetic field at the location of the SQUID, which can again increase the field sensitivity of the SQUID appreciably for a suitable configuration.

of the transformer.<sup>34</sup>

The total inductance  $L_T$  of the transformer is given by the sum of the inductance  $L_1$  of the receiving coil, the inductance  $L_2$  of the coil directly above the SQUID, and the residual inductance  $L_3$  of the lines connecting the two coils. We assume that the field  $B_a$  to be detected only penetrates the receiving coil. In this case the flux change through the transformer is given by

$$\Delta\Phi = N_1 A_1 B_a + L_{\text{tot}} J_T \quad 7.13$$

Here,  $A_1$  is the area of the cross-section of the receiving coil. Because of flux conservation we have  $\Delta\Phi = 0$  and, hence,  $J_T = -N_1 A_1 B_a / L_{\text{tot}}$ . Via the receiver coil, the latter current generates a magnetic flux  $MJ_T$  in the SQUID, where  $M$  is the mutual inductance between the SQUID and the secondary coil. We can express  $M$  in terms of the inductance of this coil and the inductance  $L_s$  of the SQUID:  $M = \alpha(L_2 L_s)^{1/2}$  with the coupling constant  $\alpha$ , which in the case of good coupling can reach values close to  $\alpha = 1$ .

Finally, the magnetic field  $B_s = MJ_T / A_{\text{eff},s}$  is coupled into the SQUID, where  $A_{\text{eff},s}$  is the effective SQUID area without the transformer. One finds

$$B_s = -B_a N_1 \frac{A_1}{A_{\text{eff},s}} \alpha \frac{\sqrt{L_s L_2}}{L_1 + L_2 + L_3} \quad 7.14$$

The inductance  $L_1$  is proportional to  $N_1^2 A_1^{1/2}$ . If we neglect the residual inductance  $L_3$ , then  $B_s$  is proportional to  $(L_1 L_2)^{1/2} / (L_1 + L_2)$ . This expression attains its maximum if  $L_1 = L_2$ . Under this condition, one obtains

$$B_s = -B_a N_1 \frac{A_1}{A_{\text{eff},s}} \alpha \sqrt{\frac{L_s}{4L_1}} \propto A_1^{3/4} \quad 7.15$$

We see that the sensitivity of the magnetometer can be increased by choosing a large value of  $A_1$ . However, then one must take into account that a spatially strongly varying signal is averaged over this area. If possible, the SQUID is surrounded by 10–20 windings of the transformer, and  $A_1$  is chosen in the range of 1 cm<sup>2</sup>. In this way the magnetic field sensitivity of the SQUID is increased by 2 orders of magnitude, and in the end one obtains an effective SQUID area (including the transformer) in the range of a few square millimeters. Optimized SQUID magnetometers are able to resolve flux values of about  $10^{-6}\Phi_0$  within a bandwidth of 1 Hz. This yields a magnetic field sensitivity of about  $10^{-15}$  T/Hz<sup>1/2</sup>, which is better by orders of magnitude than the sensitivity of conventional magnetometers.

If the SQUID is operated at 4.2 K or below, the flux transformers can be wound easily from Nb wire. Also Nb thin-film technology allows the fabrication of superconducting multilayers, which are separated from each other by insulating layers. In this case one can fabricate the

coupling coil in the form of a planar spiral directly above the SQUID washer, and one can bond the part of the transformer made from the wire to the spiral.

However, so far no flexible wire made of high-temperature superconductors, which even can be bonded, is available. Hence, in this case one must work completely with planar structures. And also the fabrication of superconducting multilayers is not easy. Therefore, in the simplest case the transformer is directly connected with the SQUID within a single superconducting layer (see [Figures 7.42a,b](#)); in [Figure 7.41](#) this corresponds to an additional large superconducting loop, which increases the lower half of the SQUID to the form of a figure of “8.” In this case we have  $N_1 = N_2 = 1$ , which results in a not particularly good coupling, but has the advantage of a simple thin-film technology.

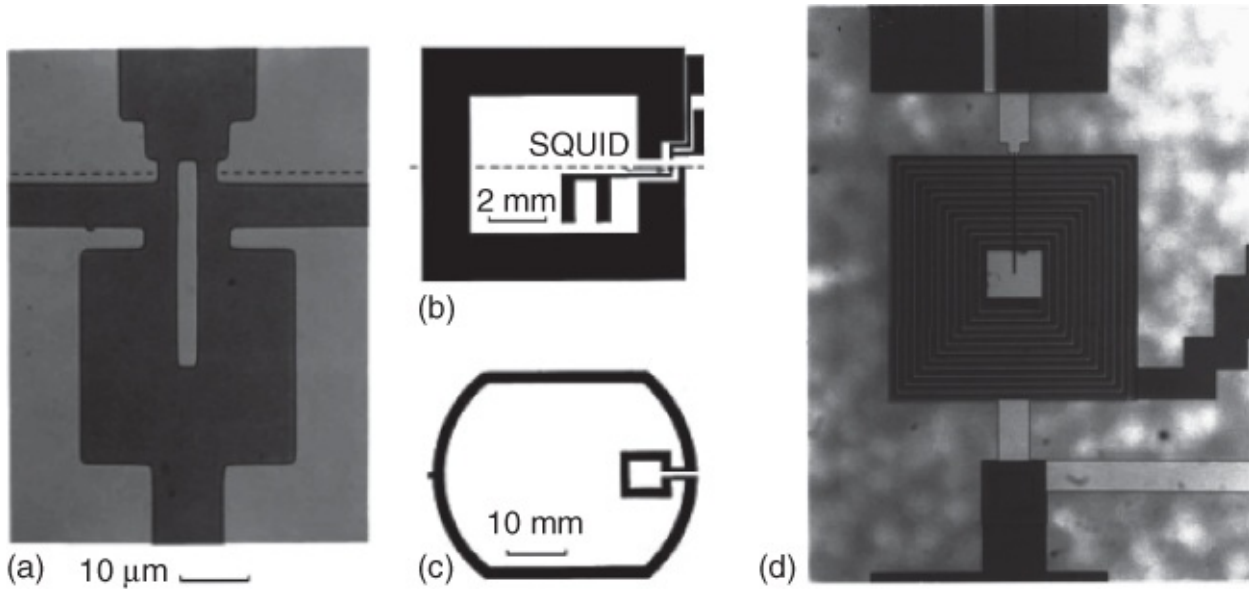


**Figure 7.42** Different  $\text{YBa}_2\text{Cu}_3\text{O}_7$  SQUID magnetometer designs together with a flux transformer. (a) and (b) Show a directly coupled magnetometer, in which a large input loop (b) within a single superconducting layer is connected with the SQUID (a). (c) Shows a single-layer transformer fabricated on a separate substrate, placed on top of the SQUID in the flip-chip technology. (d) Shows a magnetometer in which the transformer and the SQUID are integrated on the same chip using a two-layer technology. The input coil of the transformer consists of 12 windings, and the washer SQUID located below has an edge length of 0.5 mm [125].

Alternatively, the flux transformer is fabricated on a separate substrate, and this is coupled mechanically to the substrate carrying the SQUID ([Figure 7.42c](#)). If two superconducting layers are used, the input coil of the transformer can have several windings. In this case the inner end of the spiral must be connected with the outside by an insulated line. This can be achieved by means of a short connecting line within a second superconducting layer. In principle, magnetometers can also be fabricated using a two-layer technique, in which the SQUID and a flux transformer containing several windings are integrated on a chip ([Figure 7.42d](#)). However, in this case for high-temperature superconductors the yield of well-functioning magnetometers is still low.

A completely different concept is applied in the case of the multiloop SQUID magnetometer introduced in the early 1970s by Zimmerman [127]. Its principle is shown in [Figure 7.43a](#). The magnetometer consists of  $N$  loops connected in parallel, which are closed by a pair of Josephson junctions common to all loops. Essentially, the effective area of the magnetometer is given by the area of a partial loop (i.e.,  $1/N$  of the total area), whereas the inductance is reduced by the factor  $1/N^2$  compared to the inductance of a circular loop with the diameter of the magnetometer, because of the interaction among the loops. With this geometry, effective areas in the range of a few square millimeters can be realized without the need for additional flux transformers. Today the multiloop magnetometer is used more and more, in particular, in the Nb version, for example, for studying biomagnetic signals at the Physikalisch Technische Bundesanstalt (PTB) in Berlin [130] (see [Figure 7.43c](#)). Such magnetometers have been fabricated also from  $\text{YBa}_2\text{Cu}_3\text{O}_7$  (see [Figure 7.43b](#)).

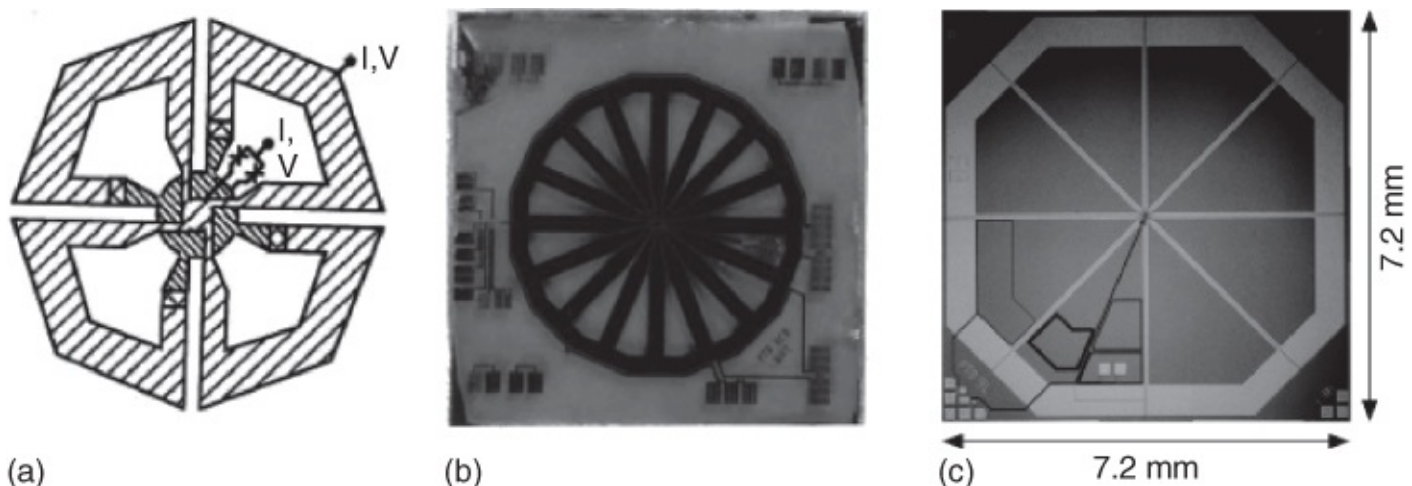


**Figure 7.43** Multiloop or “cartwheel” SQUID magnetometer: (a) schematic representation; (b) 16-loop magnetometer made of  $\text{YBa}_2\text{Cu}_3\text{O}_7$  on a bicrystal substrate with  $1 \times 1 \text{ cm}^2$  area [125, 128]; and (c) 8-loop magnetometer made of Nb [129]. The two differently hatched areas in (a) indicate two different superconducting layers. The two Josephson junctions in each loop are indicated by crosses.

(Reproduction of (c) with permission of Elsevier.)

Next we must discuss the signal-reading technique of the d.c. SQUID magnetometers, cf. Figs. [7.43\(a\)](#) to [\(c\)](#). First, one needs overdamped Josephson junctions with a single-valued current–voltage characteristic<sup>35</sup> (see [Figure 6.10](#)). In this case also the characteristic of the SQUID, that is, the parallel connection of both junctions, is nonhysteretic. As soon as a voltage different from zero appears at the Josephson junctions, alternating currents flow. In the case of not too large voltages, these currents are highly nonharmonic,<sup>36</sup> such that the temporal average of the alternating Josephson currents remains finite and is modulated periodically with the flux penetrating the ring, like the static Josephson current. Therefore, the whole current–voltage characteristic of the SQUID varies with applied flux, as shown in [Figure 7.44b](#). If a slightly overcritical constant current  $I_B$  (bias current) is applied to the SQUID, also the temporally averaged voltage is modulated periodically with the applied flux or magnetic field (see [Figure](#)

[7.44c](#)). This voltage modulation is detected as the signal. We see that the d.c. SQUID transforms the applied flux into a voltage.

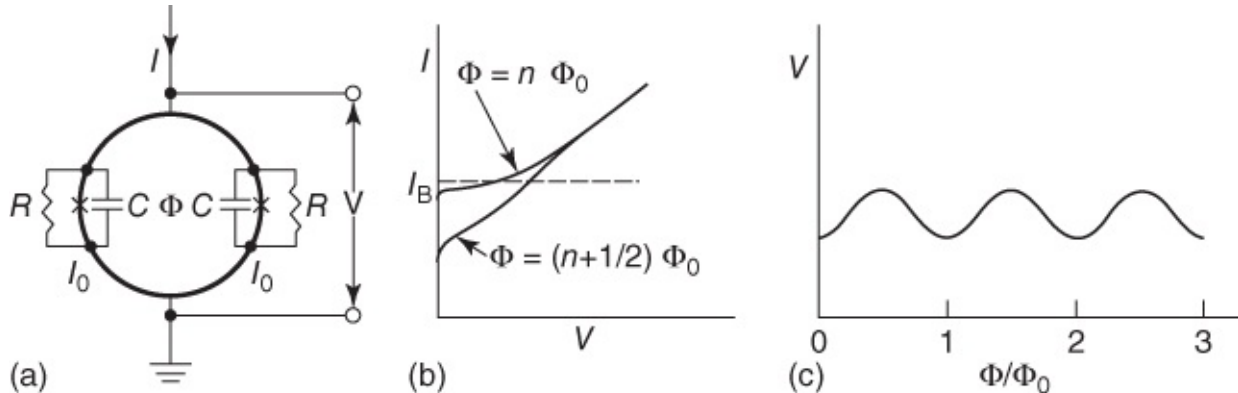


**Figure 7.44** Signal-reading principle of the d.c. SQUID: (a) equivalent circuit of the SQUID; (b) schematic current–voltage characteristic; and (c) voltage modulation at constant applied current [125].

From [Figure 7.44b](#) we see that the amplitude of the voltage modulation is not the same for all values of the applied current. Far above the critical current the rectified fraction of the Josephson current and, hence, also the voltage modulation is very small. In the case of slightly undercritical currents, thermal fluctuations again and again cause a short current or voltage pulse and, hence, a small voltage.<sup>37</sup> Therefore, at small voltages the characteristic looks rounded. We see that there exists an optimum current value applied to the SQUID.

Even now the SQUID signal  $V(\Phi_a)$  has a number of bad features, which must be corrected:

1.  $V(\Phi_a)$  changes because of fluctuations in particular of the critical currents of both Josephson junctions. A frequency analysis of this noise, caused, for example, by redistributions of the charges in the barrier layer, indicates that the noise increases toward small frequencies ( $1/f$  noise).
2. The voltage changes  $\Delta V(\Phi_a)$  are relatively small (in the range of a few tens up to  $100 \mu\text{V}$ ), and the impedance of the SQUID is only in the range of a few ohms. However, a voltage detection using semiconductor devices requires large impedances and voltage amplitudes.
3. The curve  $V(\Phi_a)$  varies periodically with the flux quantum  $\Phi_0$ . However, a good detector should deliver a signal that changes as linearly as possible with the quantity to be measured. At any rate the detector response should be unequivocal.

Solutions have been found for all three of the above problems.

The fluctuations in point 1 above can be eliminated to a large extent by means of suitable modulation techniques. The fluctuations of the critical currents of the two Josephson junctions are independent of each other. However, they can always be decomposed into a symmetric part (equal sign of the fluctuations of both critical currents) and an antisymmetric part (opposite sign of the fluctuations of both critical currents). The symmetric part leads to a shift of  $V(\Phi_a)$  along the voltage axis, that is, to a temporal fluctuation of the mean value  $V_0$  of the curve

$V(\Phi_a)$ . The flux penetrating through the SQUID is modulated by means of a small alternating field (amplitude  $\approx \Phi_0/2$ ). In this case the modulation frequency  $f_m$  is in the range of a few hundred kilohertz up to megahertz. Hence,  $V(\Phi_a)$  is also modulated at this frequency. This signal is fed into a normal conducting, but cooled, tank circuit (transformer) which, furthermore, increases the impedance up to the values needed by the signal-reading electronics. The signal detected at  $f_m$  is independent of the mean value  $V_0$ , such that the fluctuation of this quantity is eliminated. The antisymmetric part of the fluctuations of the critical currents effectively represents a ring current around the SQUID hole. The magnetic flux generated by these fluctuations leads to a shift of  $V(\Phi_a)$  along the  $\Phi_a$  axis. If the applied current is quickly reversed, one obtains a shift of  $V(\Phi_a)$  in the opposite direction. If one averages the values of the voltages measured repeatedly for the two polarities (typically the reversal is carried out at frequencies of a few kilohertz), then also the antisymmetric fluctuation is eliminated.

The combination of the two techniques, flux modulation and bias reversal, is also referred to as **double modulation**. Together with the transformer technique, it solves the problems of the fluctuations in points 1 and 2 above, which are slower than the frequency of the corresponding modulations. In [Figure 7.45](#) we show the result of both modulation techniques for the example of a d.c. SQUID made of  $\text{YBa}_2\text{Cu}_3\text{O}_7$  operated at 77 K. In this case first the time-dependent signal  $V(t)$  at constant external flux was recorded and then Fourier-transformed and calibrated. On the right vertical axis the intensity of the flux noise is plotted in units  $\Phi_0^2/\text{Hz}$ , and on the left vertical axis the energy resolution (see [Section 7.6.1](#)) is given in units joules per hertz. If only the magnetic flux is modulated, in the case of SQUIDs made of high-temperature superconductors, frequently the noise strongly increases at frequencies below 1 kHz. However, in combination with the bias reversal, one can reach sensitivities of a few  $10^{-12} \Phi_0^2/\text{Hz}$  or  $10^{-30} \text{J}/\text{Hz}$  down to frequencies of about 1 Hz.

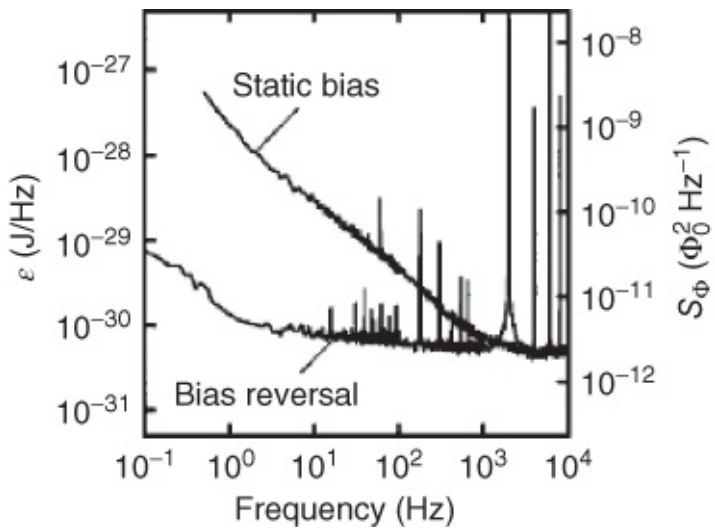


**Figure 7.45** Flux noise and energy resolution of a  $\text{YBa}_2\text{Cu}_3\text{O}_7$  SQUID operated at 77 K for the application only of the flux modulation technique (static bias) and of the double modulation technique (bias reversal). The peaks visible above 1 kHz are caused by the bias reversal technique itself. At low frequencies perturbing signals caused by the a.c. environment (at harmonics of 60 Hz) and due to other sources can be seen [125].

In addition to the technique we have just described, there also exist a number of alternatives such as the additional positive feedback (APF) procedure. In this case a fraction of the applied current is used to generate a very steep slope of  $V(\Phi_a)$ , which is then amplified directly by means of conventional electronics and recorded. Further details can be found in Refs [129, 131].

Using the techniques discussed so far, a number of noise sources can be eliminated. There remains the thermal white noise, which can be minimized but not eliminated by a suitable choice of parameters such as  $\beta_L$  or  $\Gamma$ . Also the noise due to the statistical movements of the vortices trapped within the SQUID washer remains, as well as the influence of environmental noise. These sources act as signals for the magnetometer and, hence, they cannot be eliminated just by suitable signal-handling techniques.

Therefore, trapped vortices must be avoided or must be pinned strongly enough at suitable pinning centers in the film so that, if possible, they do not move. In the case of SQUIDs made of metallic superconductors such as Nb,<sup>38</sup> the trapping of vortices during the cooling process is not an important issue, since in most cases it can be avoided by careful cooling in a magnetically shielded environment. This also applies to  $\text{YBa}_2\text{Cu}_3\text{O}_7$  SQUIDs, as long as one operates in a magnetically shielded environment. However, in some applications these SQUIDs must be operated in the field. In this case one can introduce holes or slits into the SQUID washer. Then the magnetic flux at least in part is pushed into these holes, instead of generating vortices in the superconducting material [132, 133].

In another trick, a Josephson junction is integrated into the flux transformer (vortex barrier) [134]. In this way one avoids the currents in the transformer becoming too large and generating additional noise, say, during movements of the magnetometer.

The influence of external noise sources can be minimized in part by means of suitable shielding. If the spatial or temporal behavior of the true signal is different from that of the environmental noise, then the latter can be suppressed also by means of special gradiometer techniques. We will return to this point in [Section 7.6.4.2](#).

Now the problem in point 3 above still remains, that is, we must answer the following question: How can an unequivocal signal be generated from the periodic voltage response  $V(\Phi_a)$  of the d.c. SQUID? For this purpose one uses the method of feedback of flux (flux-locked mode). First one turns to the steepest part of the  $V(\Phi_a)$  curve, and then the detected and amplified voltage signal is fed into a feedback coil. If  $V(\Phi_a)$  is moving away from the bias point due to a signal  $\Phi_s$  to be detected, the feedback coil generates an additional amount of flux that exactly compensates  $\Phi_s$ . In this case one measures a voltage signal  $V_F$ , which is proportional to the current through the feedback coil and, hence, proportional to the flux signal  $\Phi_s$ .

Possibly, very *large* flux changes  $\Phi_s$  cannot be compensated any more. However, in this case, the periodic curve  $V(\Phi_a)$  provides the possibility to jump over some periods and perhaps even to count these periods. In this way the SQUID attains a very large dynamic range in which it can measure signals.

Also very *fast* flux changes can hamper the feedback. These must be avoided, since otherwise the value of the field at which the magnetometer performs its measurement upon re-establishing the feedback remains unclear. In some cases the maximum slew rate must be very high. We assume a field change of  $100 \mu\text{T}$  within  $10 \text{ ms}$ , which can happen easily, say, during a thunderstorm. In the case of a magnetometer area of  $2 \text{ mm}^2$ , this corresponds to a change of about  $10^5$  flux quanta. Hence, the electronics must be able to compensate  $10^7 \Phi_0/\text{s}$ . However, such values can be reached with modern electronics.

Now we leave d.c. SQUIDs and turn to the functional principles of r.f. SQUIDs. This SQUID was developed in the early 1970s [135] and is still used frequently today. As we have discussed already, basically an r.f. SQUID consists of a superconducting ring, into which a single Josephson junction is integrated. This ring is then inductively coupled to a tank circuit driven near its resonance. The driving frequencies  $f_{\text{rf}}$  are in the range of a few hundred megahertz up to a few gigahertz. For example, the alternating voltage at the  $LC$  circuit serves as the read-out signal.

In order to understand the properties of the r.f. SQUID, we consider the total flux  $\Phi$  through the ring as a function of the applied flux  $\Phi_a$ . Initially we have  $\Phi = \Phi_a + LJ$ , where  $L$  is the ring inductance and  $J$  is the ring current. This current flows across the Josephson junction. Hence, according to the first Josephson equation (1.25) we have  $J = I_c \sin \gamma$ . Analogous to Eq. (1.58), describing the connection between the phase difference of both Josephson junctions and the magnetic flux in the ring in the case of the d.c. SQUID, in the case of the r.f. SQUID we find  $\gamma = -2\pi\Phi/\Phi_0$ . Hence, we have

$$\Phi = \Phi_a - LI_c \sin(2\pi\Phi/\Phi_0)$$

**7.16a**

If both sides are divided by the flux quantum, and writing  $\Phi/\Phi_0 = \phi$ , we obtain

$$\varphi = \varphi_a - \frac{\beta}{2\pi} \sin(2\pi\varphi) \quad \text{7.16b}$$

with  $\beta = 2\pi LI_c/\Phi_0$ . Except for a factor  $\pi$ , the quantity  $\beta$  corresponds to the inductivity parameter  $\beta_L$  that we have discussed in conjunction with the d.c. SQUID. In [Figure 7.46](#) we show the curve  $\Phi(\Phi_a)$  calculated from Eq. (7.16b) for three values of  $\beta$ . In the case  $\beta < 1$ ,  $\Phi(\Phi_a)$  is single-valued, whereas in the case  $\beta > 1$ , it displays hysteresis for certain values of  $\Phi_a$ . Both types of curves can be used in magnetometry.

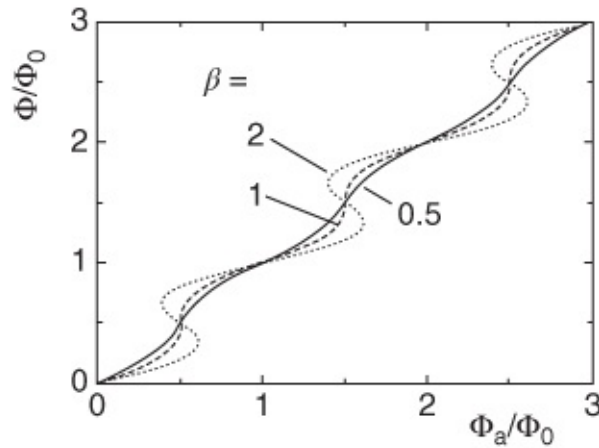


**Figure 7.46** Functional principle of the r.f. SQUID: total flux through the ring plotted versus the external flux.

In the case  $\beta < 1$  in the end the r.f. SQUID corresponds to a nonlinear inductance, which periodically modulates the resonance frequency  $1/(L_{\text{eff}}C)^{1/2}$  of the tank circuit with the applied flux. If the tank circuit is driven with a constant frequency near resonance, this change in the resonance causes a large change of the a.c. amplitude at which the tank circuit oscillates.

In the case  $\beta > 1$  the flux  $\Phi(\Phi_a)$  jumps as soon as the external flux, composed of a static part  $\Phi_{\text{St}}$  and an alternating part  $\Phi_{\text{rf}} \sin(2\pi f_{\text{ac}} t)$  caused by the tank circuit, reaches a critical point with an infinite slope  $d\Phi/d\Phi_a$ . This causes a damping of the tank circuit, and its quality factor decreases. This damping is minimal (maximal) if  $\Phi_{\text{St}}$  attains a half-integer (integer) value of  $\Phi_0$ .

We see that, exactly like the d.c. SQUID, the r.f. SQUID also shows a response function oscillating with period  $\Phi_0$ . Analogous to the d.c. SQUID, in the case of the r.f. SQUID the quantity  $\beta$  should be approximately unity, and the parameter  $\Gamma$  should not greatly exceed the value unity. This results in similar requirements in the design and read-out technique, such that also in this case washer geometries and feedback techniques can be employed.

The r.f. SQUID has the advantage that, in contrast to the d.c. SQUID, no transport current must

be applied to the Josephson junction. Therefore, the operation is much more reliable. Bond wires can break, and unwanted current peaks can destroy the Josephson junctions. On the other hand, in the case of the d.c. SQUID, the read-out technique is much less noisy, at least during operation at 4.2 K. In contrast to the r.f. SQUID, well-constructed arrangements are limited by the noise properties of the SQUID and not by the measuring electronics. However, during operation at 77 K, the noise properties of the d.c. SQUID and of the r.f. SQUID are not much different any more, such that many measurements can also be performed by r.f. SQUIDs.

Interferometer configurations with more than two Josephson junctions have been and continue to be investigated. In principle, analogous to the optical lattice, one can imagine that a parallel connection of many Josephson junctions yields a very high sensitivity. However, the fabrication of many identical Josephson junctions is highly problematic. If in a parallel connection of many Josephson junctions the junction parameters or also the loop areas between the junctions vary, the interference pattern is highly irregular and in the end useless. However, recently relatively homogeneous arrangements have been demonstrated [136].

Alternatively, one can use strongly varying loop sizes and contact parameters. In the case of these arrangements, in zero field the critical supercurrent has a maximum value and then decreases rapidly to a very small value. It is the idea to use the distinct peak of the maximum supercurrent as a sensitive field sensor. [Figure 7.47](#) shows schematically such an interferometer (SQIF, superconducting quantum interference filter) together with the measured  $V(\Phi_a)$ -characteristic [137]. The interferometer consisted of 30 Nb-contacts in parallel. Similar arrangements based on  $\text{YBa}_2\text{Cu}_3\text{O}_7$  are also investigated [138]. For comparison, the figure also shows the signal of a dc SQUID of the same size, which shows a much smaller voltage amplitude. In addition to irregular arrays in parallel, also irregular arrangements of d.c. SQUIDs in series or two-dimensional configurations of loops are investigated [139]. SQIFs are tested also regarding their usefulness in microelectronic circuits, as we will discuss in [Section 7.7](#) [140].

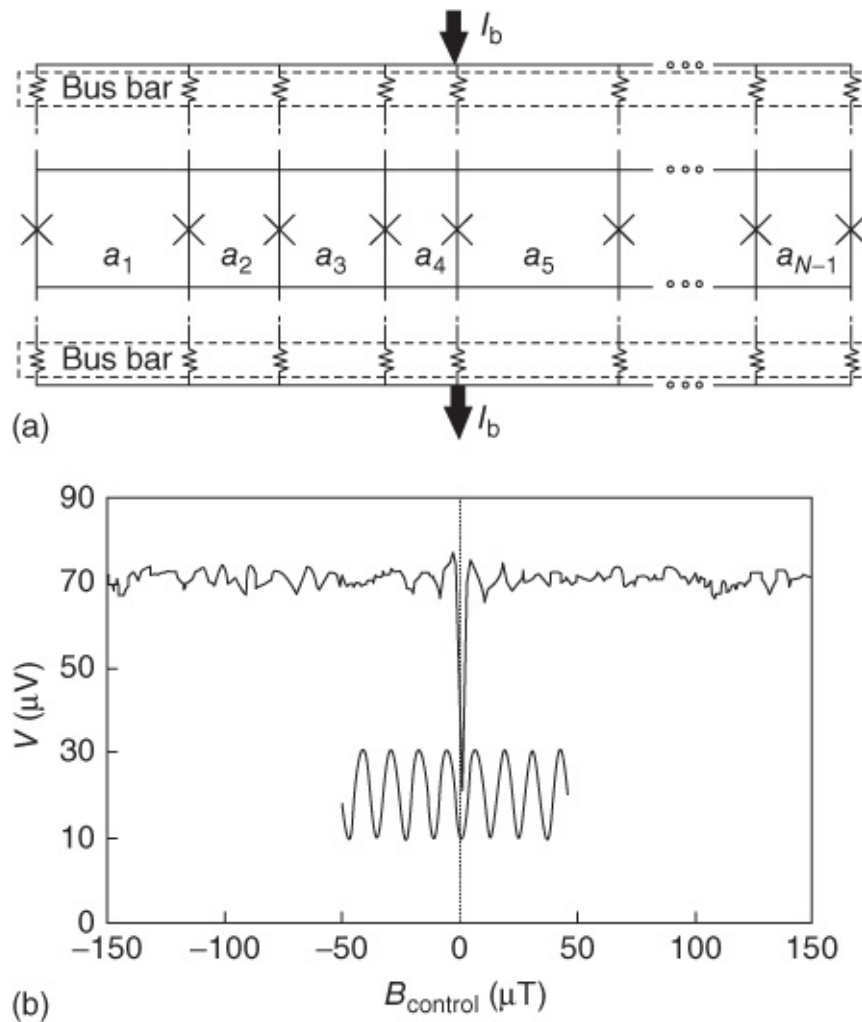


**Figure 7.47** Superconducting quantum interference filter (SQIF). (a) Equivalent circuit and (b) voltage response of a 30-junction interferometer compared with a d.c. SQUID of the same size.

(Reproduced from [137] with permission of Elsevier.)

#### 7.6.4.2 Environmental Noise, Gradiometers, and Shielding

Because of the extreme sensitivity of SQUID magnetometers, a point has been reached at which almost any arbitrary external signal can be larger than the signal to be measured. For illustration, in [Figure 7.48](#) we present a comparison between the magnitude of “interesting” signals and environmental noise sources [141]. For example, a screwdriver at a distance of 5 m generates a much higher field than the human heart! The signals generated in the human brain have a magnitude similar to the magnetic fields generated by a car passing at 2 km distance!

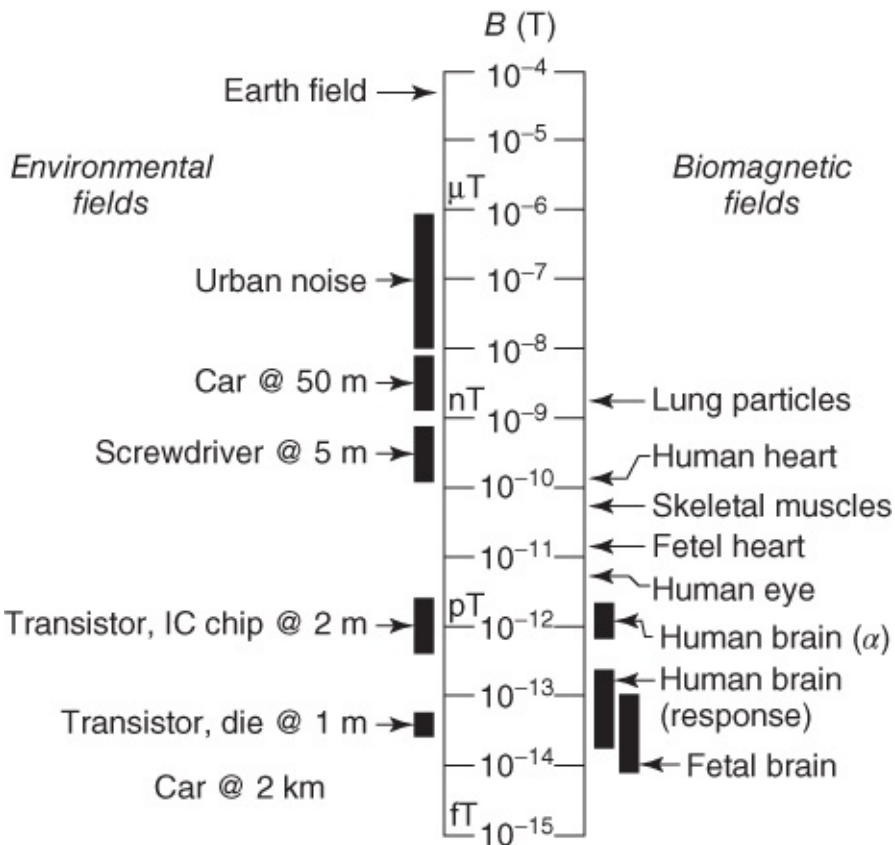


**Figure 7.48** Comparison between environmental noise sources and important biomagnetic fields.

(Reproduced from [141] with permission of Elsevier.)

As a first step for suppressing such perturbations, one uses magnetic shielding procedures. A soft magnetic shielding around a cryostat already can suppress static or low-frequency magnetic fields by 3–4 orders of magnitude. Furthermore, one can mount the SQUID and the sample to be studied within a superconducting cavity. This cavity does not reduce the magnetic field, but it keeps the magnetic flux in its interior constant. Therefore, magnetic field *changes* hardly affect the field within the shielded volume.<sup>39</sup> On a larger scale, whole chambers are surrounded by magnetic shields. So far, the best magnetically shielded chamber is installed at the PTB in Berlin [143]. The chamber is 2.9 m in size and is surrounded by seven layers of Mumetal, as well as by a thick aluminum cover, in order to shield against high-frequency electromagnetic fields. In addition to these passive shields, compensation coils serve for active field suppression. Together with the active shield, at 0.01 Hz the chamber achieves a field suppression up to a factor  $2 \times 10^6$ , and at a frequency of 5 Hz up to more than  $2 \times 10^8$ .

If one wants to measure within a less shielded or even an unshielded environment, other techniques for the suppression of environmental noise fields are necessary. The same applies to a shielded chamber, if one is interested, for example, in the signal of the human brain, which is superimposed by the thousand times stronger signal of the beating heart.

However, frequently sources of environmental noise are much further away from the SQUID than the source to be measured. Therefore, near the interferometer the perturbing signal is *spatially* nearly constant, whereas frequently the signal to be detected strongly decreases.

Therefore, the *gradient* of the magnetic field is dominated by the parts due to the signal.

Gradiometers can be constructed analogously to flux transformers for determining such spatial variations. The simplest example is a planar arrangement in the form of a figure of “8.” The two loops of this “8” are oriented in opposite directions, such that a homogeneous field change does not change the total flux through the two loops and, hence, does not generate a shielding current. However, if a different flux is generated within both loops, a shielding current proportional to the flux difference in both loops is generated, which then couples into the SQUID. If the vertical axis of the “8” is oriented in the  $y$ -direction and the normal vector of the loops in the  $z$ -direction, the arrangement measures the difference  $\Delta B_z/\Delta y$  averaged over the loop areas. In the following we denote this difference as the gradient  $dB_z/dy$ . In [Figure 7.49](#) we show two versions of such a gradiometer.

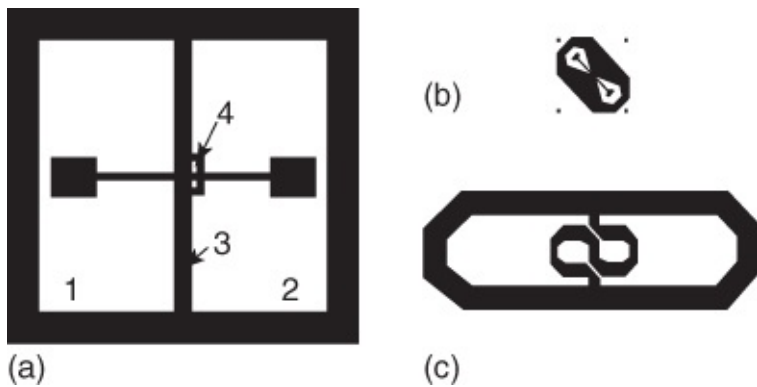


[Figure 7.49](#) Realizations of single-layer planar gradiometers measuring the gradient  $dB_z/dy$  [124]. In (a) the field gradient generates a current in strip “3,” which is coupled to the SQUID “4” [144]. The gradiometer of  $1 \times 1 \text{ cm}^2$  area shown in (b) is coupled to the SQUID in the center and, in turn, is coupled to the larger gradiometer (c) [145].

In a similar way, gradiometers can be generated for all kinds of gradients,  $dB_x/dz$ ,  $dB_z/dx$ , and so on.<sup>40</sup> Also one can construct different kinds of gradiometers, which measure second derivatives,  $d^2B_z/dx^2$ , and so on, or also higher derivatives ( $n$ th-order gradiometers). In [Figure 7.50](#) we show some examples constructed from wires [146]. Such gradiometers are mainly used in magneto-encephalography (MEG), that is, the study of the brain's magnetism. In this case several hundred SQUIDs are sometimes combined.

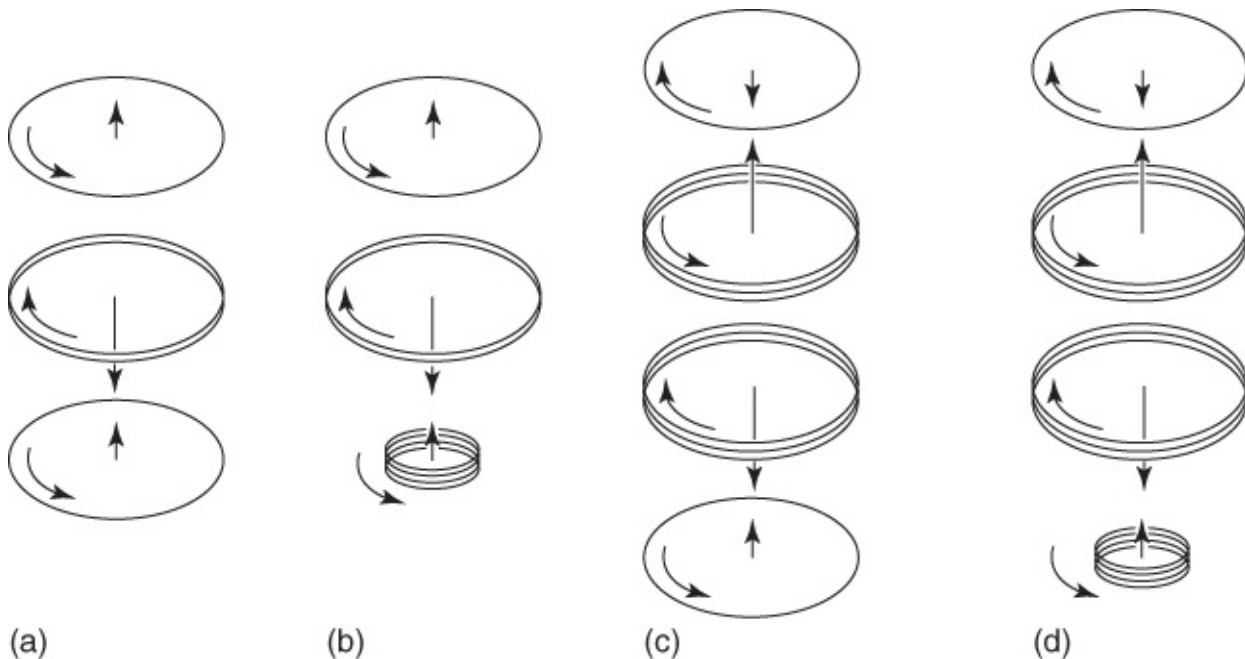


**Figure 7.50** Different gradiometers constructed from wires. The wire connections between the windings are not shown. (a,b) Symmetric or antisymmetric gradiometer of second order for  $d^2B_z/dz^2$ . (c,d) Symmetric or antisymmetric gradiometer of third order for  $d^3B_z/dz^3$ . The curved arrows indicate the current direction in the gradiometer; the straight arrows show the direction of the magnetic fields generated by the currents.

(Reproduced from [146] with permission of IOP.)

In addition to these hardware gradiometers, more and more applications have also been developed in which a number of magnetometers or gradiometers of relatively low order are combined by computer, and which in this way realize various gradiometers of higher order [146]. In addition to these gradient techniques, frequently sophisticated methods of signal analysis are employed, which utilize special temporal features of the signal and in this way can separate the signal from the environmental noise.

#### 7.6.4.3 Applications of SQUIDs

Because of the high sensitivity of SQUIDs, there are many possibilities for applications. SQUID susceptometers are particularly simple systems, which are routinely operated in many laboratories. They are commercially available from a number of companies. The magnetic susceptibility  $\chi$  of the sample in a static field is the quantity of interest. The magnitude of the field can be a few tesla. The field is applied to the sample, which is located within the oppositely wound compensation coil of the gradiometer. The current flowing in the transformer is proportional to the flux difference through both coils which, in turn, is proportional to the magnetization of the sample and, hence, proportional to  $\chi$ . The SQUID is located at some distance from the sample volume, in order to avoid too large fields at the location of the SQUID. Frequently, Nb r.f. SQUIDs are used. The sample is thermally insulated from the transformer, such that the sample temperature can be varied between room temperature and a few kelvin.

At the other end of the scale of complexity are the SQUID multichannel systems for MEG. Modern instruments operated at 4.2 K contain up to several hundred SQUID magnetometers or gradiometers. In [Figure 7.51](#) we show a system of CTF Inc. With such multichannel systems, the magnetic fields generated by the brain just above the skull can be measured with high resolution. The signals predominantly arise from the gray cells of the cerebral cortex. In this case the field of a single active neuron of less than 0.1 fT would be too small to be detected directly. Instead, one measures the signal of a few ten thousand neurons firing simultaneously.

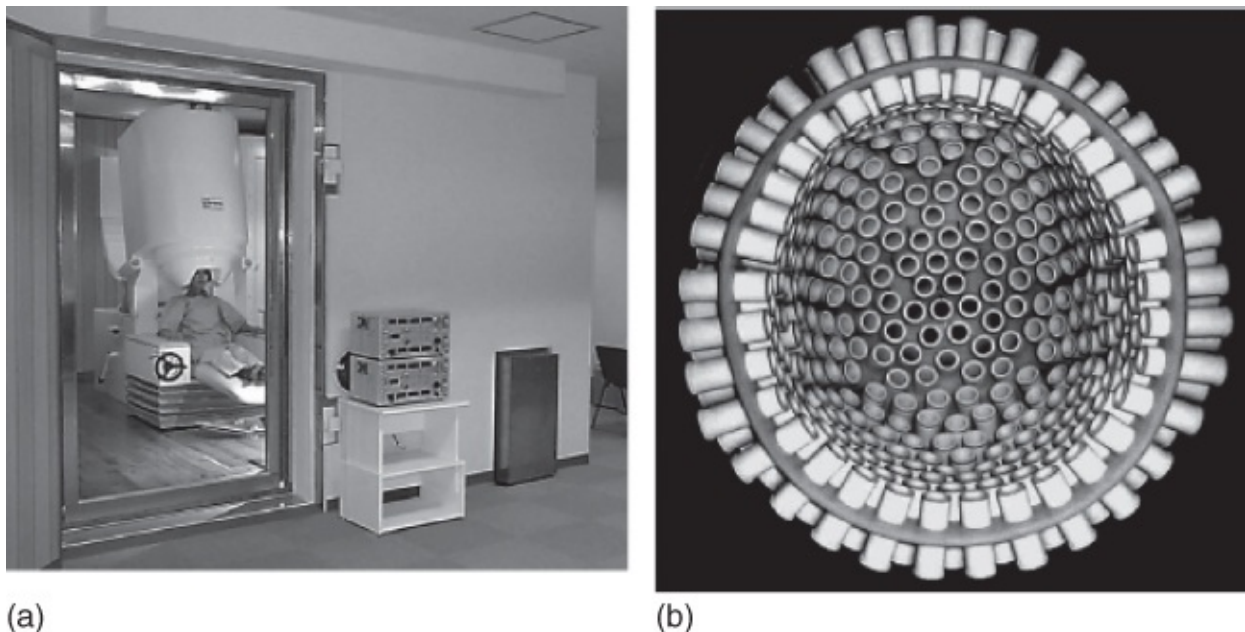


**Figure 7.51** SQUID multichannel system for magneto-encephalography. (a) Whole system with a test person within a magnetically shielded chamber (CTF MEG system, installed at Riken, Japan). (b) View into the helmet-like SQUID arrangement of 275 sensors in the form of radial gradiometers.

(Reproduced from [141] with permission of IOP; left photograph by courtesy of CTF Systems Inc.)

A detailed discussion of the multichannel systems presently available or even of the medically relevant questions would be far beyond the scope of this book. Instead, we refer to the review articles [146–148]. However, we address briefly a few aspects.

First there is the question of the analysis of the magnetic signals. The really interesting subject is the distribution of the currents within the brain generating these signals. One can show that the backward calculation of the currents from the detected fields is not possible unequivocally (the inverse problem), even if the field of these currents could be measured arbitrarily accurately. Therefore, additional assumptions must be used, which can be justified mostly from medical background knowledge. Frequently, a signal originates from just a few well-localized regions in the brain. In this case one models the current flow in terms of several short conductor segments (current dipoles), the location and orientation of which are then calculated from the magnetic field signal. One finds, for example, the coordinates of the regions in the brain that are active during an epileptic seizure. These active regions can then be superimposed with an image of the brain obtained from MRI.

A second question we want to mention is the usefulness of MEG. The procedure represents a relatively large effort. However, it supplements in a very meaningful way the existing methods such as nuclear spin tomography, computer tomography, and PET. In the end, these methods image the processes of the metabolism in the brain. On the other hand, MEG images the much faster electromagnetic processes in the brain. Frequently, it is complementary to electro-encephalography (EEG), and, hence, it is used in combination with the measurement of the EEG signals. Maxwell's equations are not symmetric with respect to the electric and magnetic signals. There exist current distributions that are visible either only in the EEG or only in the MEG. Even if the information is the same, the MEG has the advantage that it is perfectly noninvasive (one just measures with a helmet-like arrangement around the skull). Furthermore, frequently it is difficult to obtain electrical signals with good spatial resolution, since above the brain there exist several insulating or also better conducting layers (skull bone, skin, etc.), which distort the electric potentials.<sup>41</sup> On the other hand, magnetic signals reach the outside without difficulty and there can be analyzed rapidly and with high spatial accuracy.

Signals from the heart of about  $10^{-10}$  T are much larger than signals from the brain (see [Figure 7.48](#)). However, fine structures with amplitudes of a few picoteslas are clinically highly relevant. There are two important aspects. On the one hand, one wants to localize the sources of a (pathological) signal as accurately as possible in all three spatial directions. This can be achieved by measuring the magnetic field at the chest and at the back in all three spatial directions, and also by sophisticated techniques of reconstruction [149]. On the other hand, rapid examinations with rather simple SQUID systems are interesting, in order to detect rapidly pathological changes, say, in the case of a heart attack. In this case, (perhaps mobile) high- $T_c$  systems, which can be operated in an unshielded environment, are attractive [150]. At present, clinical studies are being performed regarding not only these but also many other questions.

The SQUID-based nuclear spin resonance systems represent a very interesting development during the last years. An overview is found in article [151]. Conventionally, nuclear spin resonance is performed in very high magnetic fields (see [Sections 7.3.1](#) and [7.3.2](#)). In this case the magnetization  $M$ , generated by the spins precessing at the Larmor frequency  $\omega_L$ , is detected by means of resonantly operated induction coils. The induced voltage is given by the temporal change of the magnetic flux passing through the coil, and, hence, is proportional to the product  $\omega_L M$ . The magnetization, in turn, is proportional to the applied magnetic field  $B$  and thereby also to  $\omega_L$ . Hence, the voltage signal is proportional to  $B^2$  and decreases rapidly with decreasing field. On the other hand, SQUIDs directly detect the magnetic flux, and the signal is proportional to  $\omega_L$  and to  $B$ . In principle, in the case of small fields SQUIDs show an advantage. However, if one would not apply some additional tricks, at fields of a few microteslas the generated signal would be far too small for allowing a reasonable detection. Initially, highly polarized noble gases such as  $^{129}\text{Xe}$  or  $^3\text{He}$  were used as contrast agent [152]. Polarization of the noble gases is achieved by optical pumping. At a field of 2 mT, the NMR spectroscopy of mineral oil was possible even without contrast agent [153]. In the meantime the detection of protons could be improved much by applying a “strong” magnetic field  $B_p$  of a

few milliteslas to the sample before the actual measurement. Then the measurement is carried out after this field had been switched off, and a much smaller measurement field  $B_m$  of a few microteslas had been applied oriented perpendicular to  $B_p$  [154]. In this case  $B_p$  is switched off sufficiently slowly, such that the proton spins can rotate into the direction of the measurement field. [Figure 7.52](#) shows measurements performed using a pepper–vegetable [155]. The sample was polarized in fields between 40 and 100 mT. The actual measurement was carried out at 66 µT. At this field, the proton spins rotate only at 2.8 kHz, and the signals can easily penetrate an aluminum can without distortion. However, in the case of the traditional nuclear spin-tomography, metallic objects within the body of a patient distort the images. Aside from the high costs of a high-field magnet, this is one of the advantages of the low-field nuclear spin tomography. Without large problems, this technique can be combined with, say, the SQUID-encephalography. It could be shown, that tumor tissue could be imaged with a much higher contrast than in the case of the traditional method [151].

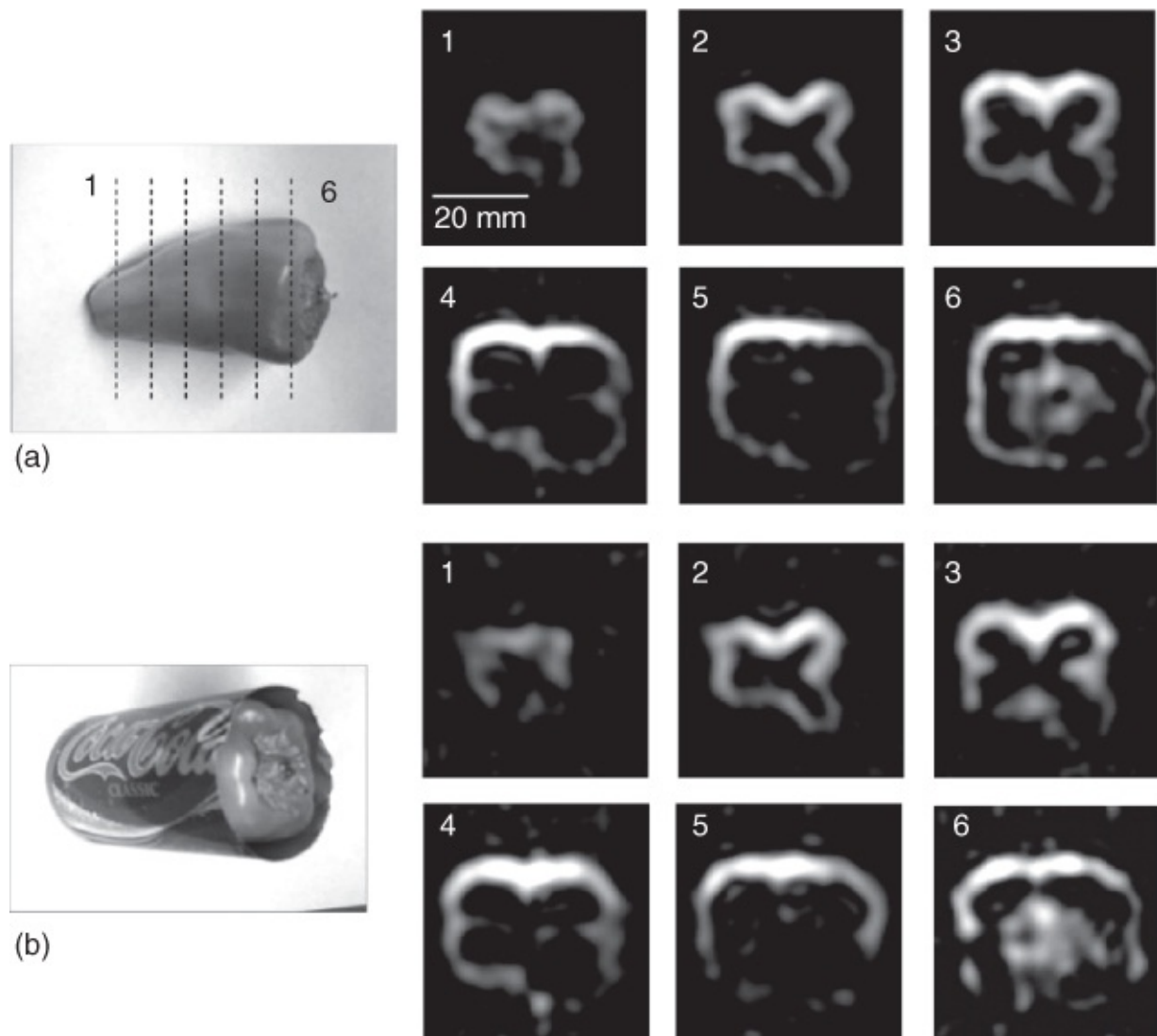


[Figure 7.52](#) Low-field nuclear spin tomography of a pepper–vegetable. (a) “Free” sample. (b) The pepper–vegetable was kept in an aluminum can.

(Reprinted from [155] with permission by Elsevier.)

In the systems just described, magnetic fields are detected by means of SQUIDs that do not move relative to the object to be studied. In another method, the SQUID is moved relative to the sample with high spatial resolution [156, 157]. These SQUID microscopes can reach a spatial resolution in the micrometer range. A number of different techniques have been reported, some of which are shown schematically in [Figure 7.53](#).

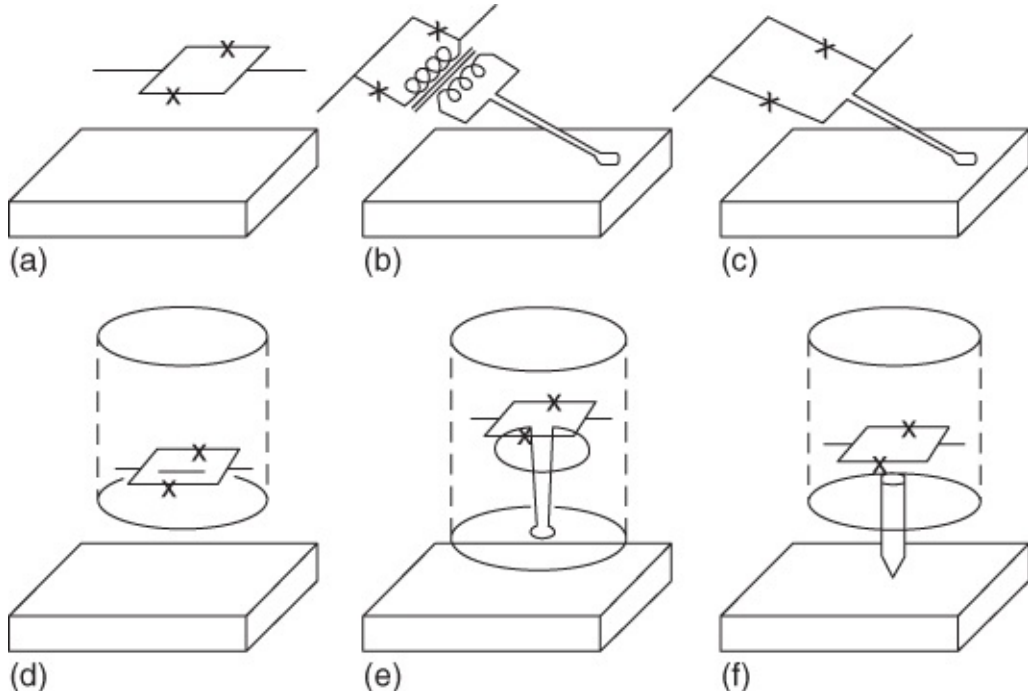


**Figure 7.53** Different types of SQUID microscopes: (a–c) The SQUID including the flux transformer is scanned over the surface of the cooled sample. (d–f) The SQUID and the sample are thermally insulated from each other, where the sample perhaps can remain in air at room temperature. (f) The magnetic field signal is coupled into the SQUID by means of a ferromagnetic tip.

(Reproduced from [156] with permission by Elsevier.)

Instruments have been constructed based on metallic superconductors as well as on high-temperature superconductors. The applications of these SQUID microscopes range from studies, say, of the vortex structure in superconductors (see [Figure 3.44](#)), the analysis of chips or wafers in microelectronics [158, 159], to the detection of biological signals of cell tissues [160] or magnetically active bacteria [161]. For illustration, in [Figure 7.54](#) we show a section of the portrait of George Washington on a \$1 bill [162]. The printing paint is weakly magnetic and can be well detected by the SQUID.



**Figure 7.54** Section of the portrait of George Washington on a \$1 bill imaged with the SQUID microscope [162].

(By courtesy of R. C. Black, Y. Gim, A. Mathai, and F. C. Wellstood.)

Also SQUIDs are scanned over the surface of the sample in the nondestructive evaluation (NDE) of materials. Within this field of application, the procedures aim at the detection of hidden defects in the material, such as cracks in various components. The investigation of the rivets in the fuselage of airplanes [163] or of the steel reinforcement of concrete bridges [164] represent typical examples.

In these measurements eddy currents are induced, by means of induction coils, within the component to be investigated. Defects in the material then change the current flow in the component, and, hence, also change the magnetic field generated by these currents. In the case of conventional detectors, these alternating fields are detected by additional induction coils. However, because of the skin effect (Eq. (7.3)), the alternating fields penetrate less and less far into the material, the higher its conductivity and the higher the frequency. It is at this point that the advantage of SQUIDs arises, since, compared to conventional detectors, much lower frequencies can be used and, therefore, defects can be detected also at large depth. Depending on the object to be tested, the excitation frequencies range from a few hertz up to a few kilohertz.

For the NDE procedures, the use of high- $T_c$  SQUIDs is particularly interesting, since in most cases the tests must be performed in the field, using systems that can be transported easily. In special cases, such as for the examination of the surface of superconducting Nb cavity resonators [165], also the use of low- $T_c$  SQUIDs can be interesting.

In general, materials testing must be performed in a very noisy and magnetically unshielded environment (e.g., an aircraft hangar), where in addition the sensor must be moved in a magnetic field. Therefore, severe requirements are imposed on the suppression of environmental noise, and on the speed at which the feedback electronics can respond to signal changes. In recent years the necessary technique has been developed, and SQUID systems can reliably detect defects that cannot be detected (or only with much less accuracy) using conventional eddy-current procedures.<sup>42</sup>

In addition to the examples discussed in this section, SQUIDs are applied in many other fields, which we cannot cover in detail. For example, in [Section 7.6](#) we mentioned that SQUIDs are used for reading the thermometers in calorimetry. SQUIDs are used to investigate the equivalence of gravitational and inertial mass in drop experiments [166]. SQUIDs can also be designed as extremely sensitive high-frequency amplifiers up into the gigahertz range [167], in order to detect new elementary particles [168]. SQUIDs have also been evaluated in the search for minerals or for mine-fields from airplanes [169]. Most recently, SQUIDs were fabricated on a nano-scale in order to detect the magnetic field of just a few atoms [170].

These examples are meant to demonstrate again the multiple use of SQUIDs, and with this we want to conclude our discussion of quantum interferometers. Many additional aspects can be found in the summaries [M26, M27].

## 7.7 Superconductors in Microelectronics

Now we return to the applications of superconductors at high frequencies. Here, we will emphasize the Josephson alternating current. First we discuss voltage standards, which utilize the Josephson frequency–voltage relation (1.27),  $f_J = U/\Phi_0$ . Subsequently we will see how fast and low-power digital circuits can be realized based on the Josephson junction.

### 7.7.1 Voltage Standards

In [Section 6.3](#) we saw that, during microwave irradiation (frequency  $f_{ac}$ ), constant-voltage steps (Shapiro steps) develop in the current–voltage characteristic of a Josephson junction at the voltage levels  $U_n = n f_{ac} \Phi_0$ , with  $n = 0, \pm 1$ , and so on. In overdamped (nonhysteretic) Josephson junctions, the voltage levels between the steps can also be traversed continuously, whereas in strongly underdamped (hysteretic) junctions the Shapiro steps are also hysteretic. Even in the absence of an applied current, a number of discrete voltage levels can be obtained (zero-current steps, see [Figures 6.12](#) and [6.13](#)).

These Shapiro steps are ideally suited for realizing a voltage standard, since they connect the voltage with the irradiated frequency via the fundamental constant  $\Phi_0$ . On the one hand, microwave frequencies can be measured with an enormous accuracy, and on the other, they can be kept extremely stable by means of feedback circuits. Conventional voltage standards (Weston cells, that is, Cd(Hg)/CdSO<sub>4</sub>(aq), Hg<sub>2</sub>S<sub>4</sub>/Hg batteries producing a voltage of 1.0183 V), which yielded the definition of the volt up to the 1970s, show relative deviations of about

$10^{-6}$ , which is too large for the requirements of today [171, 172]. However, using Josephson junctions, accuracies of a few  $10^{-10}$  can be reached today.

In 1990 the quantity  $K_J = 1/\Phi_0$  (Josephson constant) was fixed internationally to the value 483.5979 GHz/mV ( $K_{J90}$ ) and in this way defines the volt. In the years prior to that, slightly different values of  $K_J$  were used by different laboratories.

At an irradiation frequency of, say, 75 GHz, one obtains Shapiro steps at multiples of about 155  $\mu$ V. If one wants to realize a standard for 1 V, at this irradiation frequency, one needs about 6500 series-connected Josephson junctions, which are operated at the first Shapiro step ( $n = 1$ ). If one chooses  $n = 5$ , one still needs about 1300 junctions.

There is a difficulty in fabricating so many junctions with nearly identical properties, and, at the same time, in distributing the irradiated microwave power uniformly over these junctions. The problems that appear if these conditions are not satisfied are quite obvious in the case of nonhysteretic junctions. If all junctions carry the same current, at some junctions, the parameters of which deviate too much from the mean value, or which receive the “wrong” microwave power, voltage values appear *between* the Shapiro steps. In this case the total voltage is no longer a multiple of  $f_{ac}\Phi_0$ , and the voltage standard does not function.

The problem of the homogeneous input of microwave power can be solved by arranging the chain of Josephson junctions in a meandering form and by irradiating the microwaves onto the parallel windings of the meander ([Figure 7.55](#)). In this case at the end of each winding there is a suitably sized resistive closure in order to avoid microwave reflection at the ends.

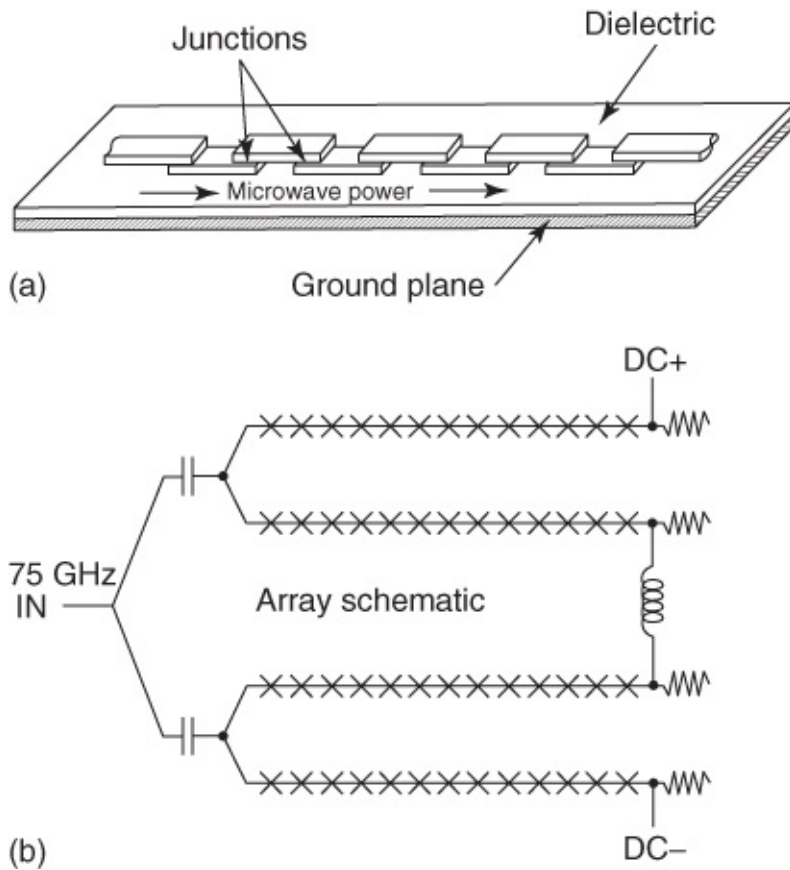


**Figure 7.55** Schematic diagram of the arrangement of Josephson junctions and of the microwave input in a voltage standard [171].(a) layout, (b) array schematic.

(© 2000 Rev. Sci. Instr.)

The second problem, namely the exactly reproducible fabrication of the individual junctions, initially could only be solved by means of strongly underdamped junctions [173]. Since in this case the Shapiro steps can appear as zero-crossing steps, the quantized voltages can be measured also in the absence of an applied current. Any additional resistors in the chain of Josephson junctions then do not contribute to the total voltage. However, also in the case of these Josephson junctions, parameters such as the junction dimension, the Josephson plasma frequency, or the Stewart–McCumber parameter (Eq. (6.14)) must be chosen with high accuracy, in order to avoid, say, chaotic behavior, or the excitation of electromagnetic standing waves in the junction [174].

In the 1980s, in a collaboration between the PTB in Braunschweig and the National Institute of Standards and Technology in Boulder, larger and larger series-connected circuits were developed. In the late 1980s chips with about 15 000 junctions had been fabricated, which under microwave irradiation generated a total of more than 150 000 Shapiro steps at voltages between  $-10$  and  $10$  V [171]. In [Figure 7.56](#) we show the realization of a still somewhat larger 10 V standard. It consists of 20 208 Nb tunnel junctions. In each of the 16 meanders, there are 1263 junctions.

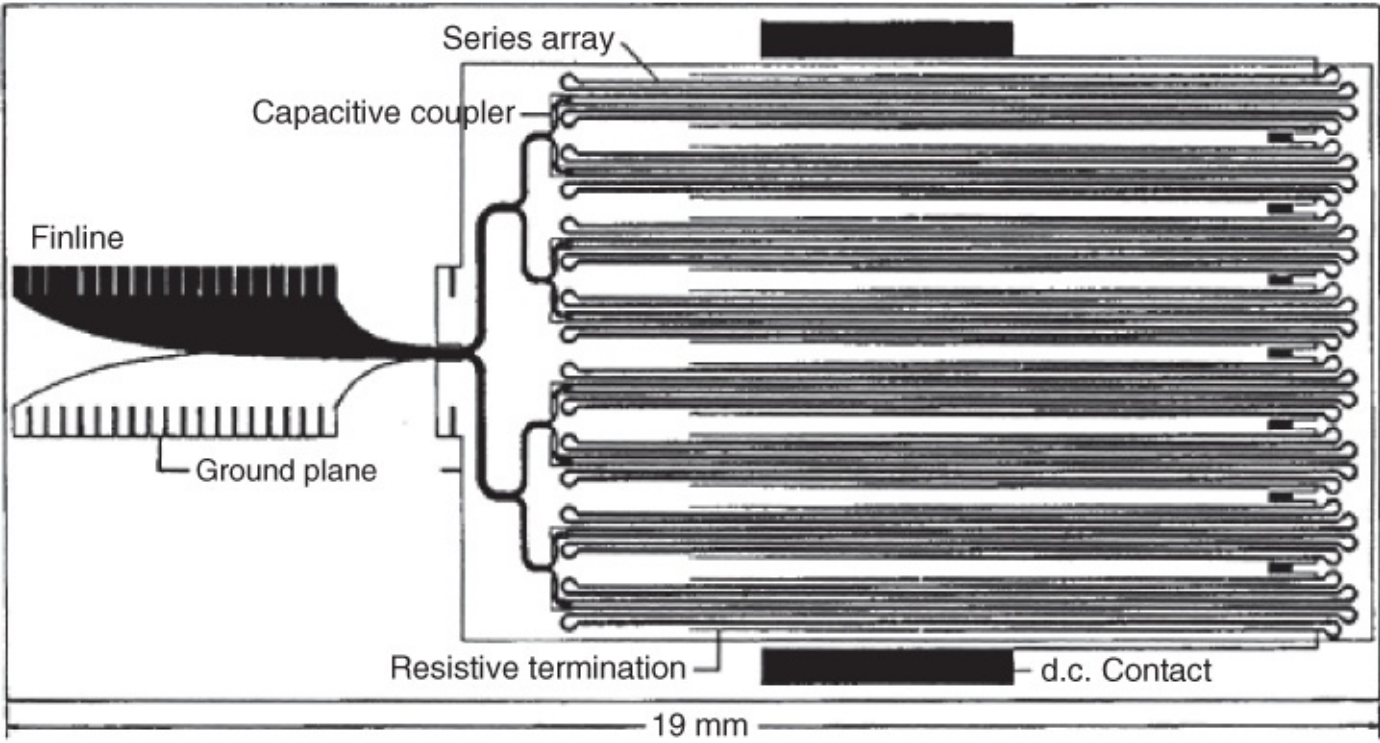


**Figure 7.56** The 10 V voltage standard consisting of 20 208 Josephson tunnel junctions. The series-connected junctions are supplied with direct current. The microwaves (75 GHz) are coupled into the chip via a finline antenna and there are distributed to the branches of the meander [171].

(© 2000 Rev. Sci. Instr.)

If in such a series-connected circuit at a microwave irradiation of 75 GHz one wants to establish, for example, a voltage level of 10.0 V, one must pick the Shapiro step number 64 480. In this case at some junctions the voltage  $3f_{ac}\Phi_0$  and at some other junctions the voltage  $4f_{ac}\Phi_0$  is generated. This operation is quite tedious, since, because of the finite resistance of the wiring leading to the chip, a given battery voltage along a load line can distribute itself in different ways over the wiring and the Josephson junctions, as is illustrated in [Figure 7.57](#). If the desired step is finally established, its voltage level can be compared with the voltage signal to be calibrated.<sup>43</sup>

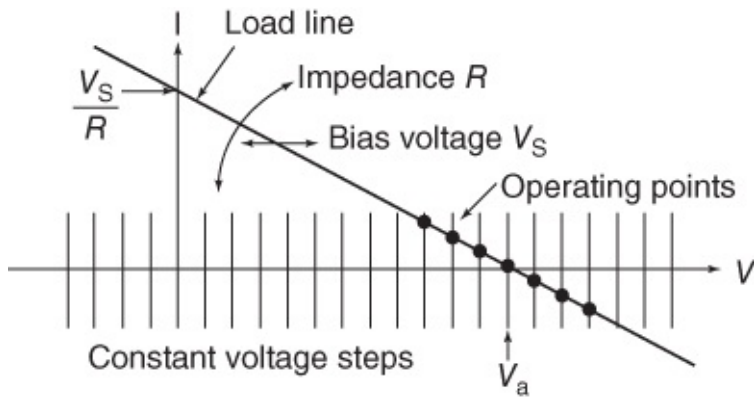


**Figure 7.57** Establishing a quantized voltage level on the characteristic of a voltage standard. A given voltage  $V_s$  can distribute itself along the load line  $V_s/R$  in different ways over the Josephson junctions and the resistors  $R$  inserted in the circuit [171].

(© 2000 Rev. Sci. Instr.)

Using the niobium thin-film technologies available today, one can also fabricate nonhysteretic Josephson junctions with good reproducibility. On the one hand, one uses SIS junctions, which are supplied with a parallel resistance of suitable dimension. On the other hand, SNS or SINIS junctions are used. In this case, the barrier layer contains an additional normal conducting layer. In principle, also  $\text{YBa}_2\text{Cu}_3\text{O}_7$  grain-boundary junctions can be used [175]. However, in this case at present the scatter of the parameters is still too large to realize series-connected circuits consisting of many junctions.

In the case of series-connected circuits of nonhysteretic Josephson junctions, the current-voltage characteristic is single-valued also under microwave irradiation. At the optimum current, each of the  $N$  junctions resides on the same Shapiro step  $n$ , such that the total voltage amounts to  $Nn f_{ac} \Phi_0$ . In order to pick up an arbitrary voltage value from this series-connected circuit, current-input lines are attached within distances of  $2^k$  junctions, as shown in [Figure 7.58](#). This arrangement is also referred to as a **programmable voltage standard**. By now, 1 V standards are fabricated routinely, and 10 V standards are in preparation [176].

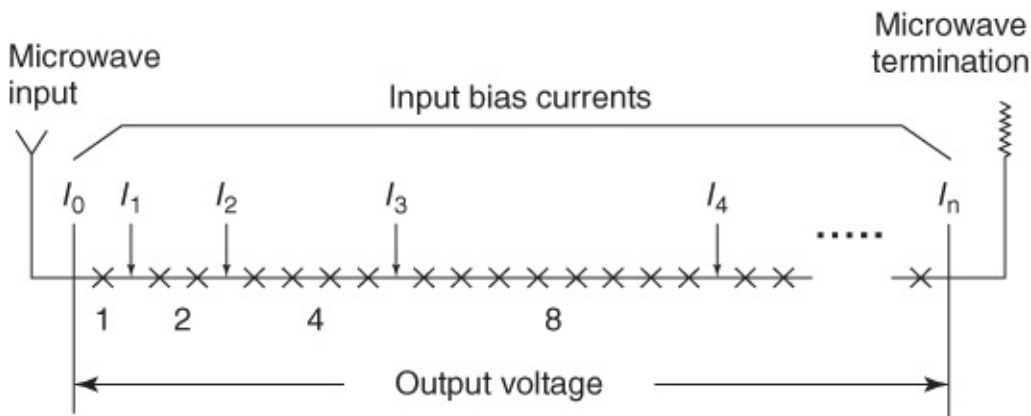


**Figure 7.58** Locations of the current input at a programmable voltage standard containing nonhysteretic Josephson junctions [171].

(© 2000 Rev. Sci. Instr.)

At present voltage standards for a.c. voltages and synthesizers for arbitrary wave forms have also been developed [171, 176]. In this case voltage pulses generated by the Josephson junctions are processed digitally. In the next section we discuss the basic principles of such digital circuits, concluding our treatment of the applications of superconductivity.

## 7.7.2 Digital Electronics Based on Josephson Junctions

In digital circuits signals are processed and stored in binary form. The processing is done by means of many simple circuits (gates), which apply elementary logic operations to a sequence of zeros and ones. The processing should be performed as fast as possible, with very little power consumption, and free of errors. Furthermore, it should be possible to write the data as fast as possible and reliably into a storage device and to read them again. In this case the required devices also must be accommodated on a chip in very large numbers.

One of the big advantages of a superconducting circuit is the fact that during a switching event only very little power is dissipated.<sup>44</sup> Furthermore, superconductors can process signals extremely fast. Cycle frequencies far above 100 GHz are possible [177]. Superconducting rings are suitable for the storage of binary information, in which the information can be carried by neighboring quantized flux states (0 or  $1 \Phi_0$ ). The first designs were developed in the 1950s for constructing active digital circuits or storage devices based on superconductors [178]. In this case the superconductor should be switched back and forth between the superconducting and normal states by means of an applied magnetic field.

Since the mid-1960s circuits based on Josephson junctions have been investigated [179]. The first attempts tried to use underdamped Josephson tunnel junctions and their hysteretic characteristic as a binary switch between the superconducting and resistive states. In particular at IBM until the early 1980s, a very large effort was spent to develop a “Josephson computer” at clock frequencies up into the gigahertz range [180]. However, the Pb tunnel junctions used initially in this case turned out to be unreliable. Another severe problem arose from the fact that at high clock frequencies the switching process was not stable. In the superconducting state a current below the critical current is applied to the junction. A received signal renders the junction overcritical, such that it switches into the resistive state. However, in order to return back to the superconducting state, the applied current first must be switched off,<sup>45</sup> which in principle can happen at cycles in the gigahertz range. But in this case zero-current steps, which are so important in the voltage standard, develop on the current–voltage characteristic, and the voltage across the junction can change to a negative voltage level as well as to zero. Because of this switching behavior, this type of Josephson junction is not suitable for operation at frequencies above some gigahertz.

In later years, mainly in Japan, the technology of Josephson junctions was strongly improved, such that circuits containing more than 20 000 Josephson junctions with clock frequencies up to above 3 GHz could be fabricated [181]. Also transistor-like devices for signal amplification were developed with metallic as well as with oxide superconductors [182].

A totally different approach is used in the rapid single flux quantum (RSFQ) logic. In this case

one starts with overdamped Josephson junctions. If a slightly overcritical current is applied to an overdamped junction, the Josephson alternating currents flow across the junction in the form of short pulses. In this case the width of the pulse is about  $\frac{46}{\Phi_0/(I_c R)}$ , where  $I_c$  is the critical current of the junction and  $R$  its normal resistance. In the case  $I_c R = 1$  mV, one obtains a pulse width of about 2 ps. During a pulse, the phase difference  $\gamma$  changes by  $2\pi$ . According to the second Josephson equation,  $\gamma = (2\pi/\Phi_0) U$ , this change leads to a voltage pulse. The area under the pulse, integrated over time, exactly amounts to  $\Phi_0$ . In [Figure 7.59](#) we show such a pulse sequence as calculated from the RCSJ model (Eq. (6.13)).

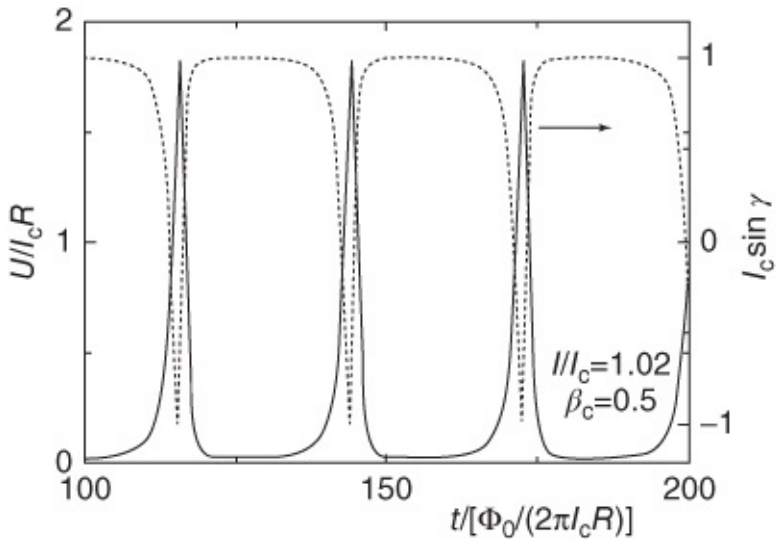


[Figure 7.59](#) Sequence of voltage or current pulses across a Josephson junction. Numerical calculation based on Eq. (6.13), RCSJ model.

The idea is to use individual voltage pulses as numerical units<sup>47</sup> [177]. The basic principle is shown in [Figure 7.60](#). In an elementary numerical cell, indicated as a box, there arrive  $n$  signal channels  $S_1, S_2, \dots, S_n$ , which are processed into  $m$  signal channels  $S'_1, S'_2, \dots, S'_m$ . A clock T controls the cell. If a pulse arrives within a cycle given by the clock, then this corresponds to “1.” If no pulse arrives, this corresponds to “0.” The next pulse of the clock reads the result of the logic operation. The scheme shown in [Figure 7.60b](#) would correspond to an “or” gate, in which an output pulse is generated, if within a clock cycle a pulse arrives either in  $S_1$  or in  $S_2$ .

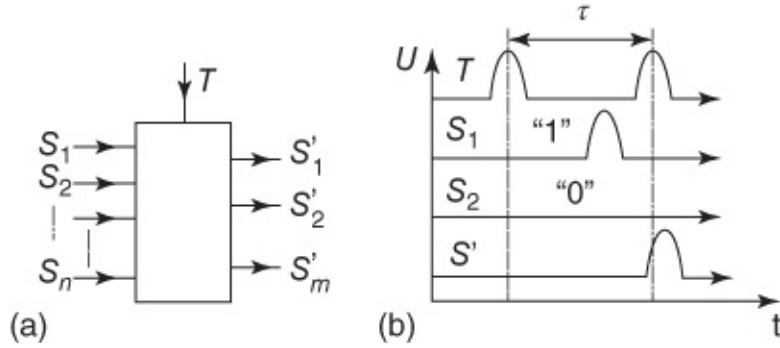


**Figure 7.60** Basic principle of the RSFQ logic. (a) elementary numerical call, (b) scheme of an “or” gate.

(After [177].)

All the necessary logic components can be generated by means of sophisticated circuits with Josephson junctions. Many basic concepts are presented in Ref. [177].<sup>48</sup> The transmission, amplification, and multiplication of pulses between the cells can be performed by active lines containing Josephson junctions. Data storage is carried out by means of SQUID-like rings, in which a pulse is written, stored, and read in the form of a flux quantum. In Figure 7.61 we show two structures (pulse-splitter and set-reset flip-flop) as examples. The pulse-splitter is based on three Josephson junctions  $J_1-J_3$ , to which an undercritical current is applied. A pulse arriving from the left side via the line A briefly generates an overcritical current in junction  $J_1$ . This current then causes a voltage pulse in this junction. As a result, voltage pulses propagate along both lines B and C, which, in turn, briefly make the junctions  $J_2$  and  $J_3$  resistive. After the “firing” of these junctions, obviously the input pulse is doubled.

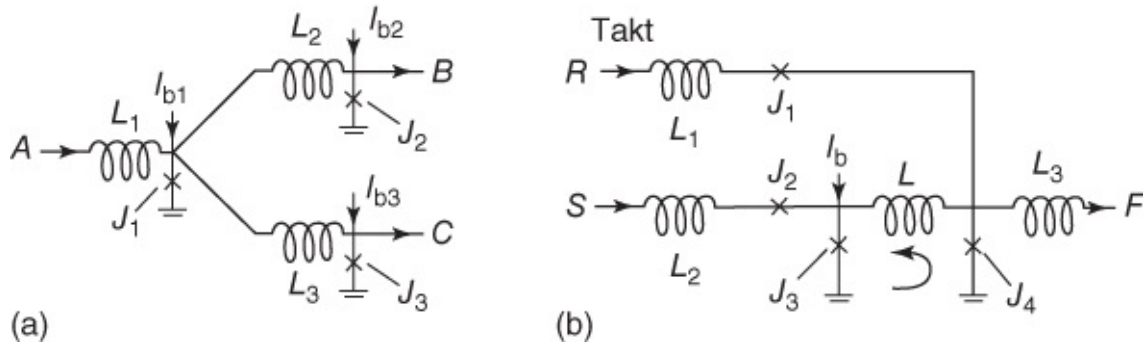


**Figure 7.61** Basic circuits from the RSFQ logic: (a) pulse-splitter and (b) set-reset flip-flop.

(After [177].)

In the case of the set-reset flip-flop, the junctions  $J_3$  and  $J_4$  are located within a SQUID ring that can store exactly one flux quantum. The current  $I_b$  is chosen such that the two flux states correspond to a circulating current flowing clockwise or counter-clockwise, respectively. If the current flows counter-clockwise (“0”), then it passes through junction  $J_3$ . Then a pulse arriving via  $S$  switches just this junction. The phase change of  $2\pi$  is written into the SQUID ring as a flux quantum, and the circulating current changes its sign (“1”). Now the circulating current flows clockwise and passes through junction  $J_4$ . A cycle pulse arriving subsequently

via the reset line  $R$  shifts the junction  $J_4$  into the overcritical state, such that, on the one hand, the SQUID ring is returned back into the state “0,” and on the other, a pulse is forwarded into line  $F$ . However, if a pulse arrives via  $S$  while the SQUID resides in state “1,” then  $J_3$  does not become overcritical. In this case the pulse switches the correspondingly designed junction  $J_2$  and escapes from the circuit. Analogously, a pulse via  $R$  switches the junction  $J_1$  in the case of the “0” state. The pulse escapes again, and no signal is forwarded to  $F$ .

The pulse-splitter and set-reset flip-flop were meant to illustrate the basic principle of the processing of RSFQ pulses. In fact, the real circuits are a little more sophisticated, in order to allow a higher error tolerance in the fabrication process. In the meantime a large number of different digital circuits has been realized [183]. One of the fastest demonstrated circuits is a so-called  $T$  flip-flop fabricated in Nb technology, which operated up to a cycle frequency of 770 GHz<sup>49</sup> [186]. In [Figure 7.62](#) we show a microprocessor developed 2002 in Stony Brook together with TRW, which contained about 65 000 Josephson junctions and operates at a clock frequency of 20 GHz. The power consumption is only a few milliwatts [187].

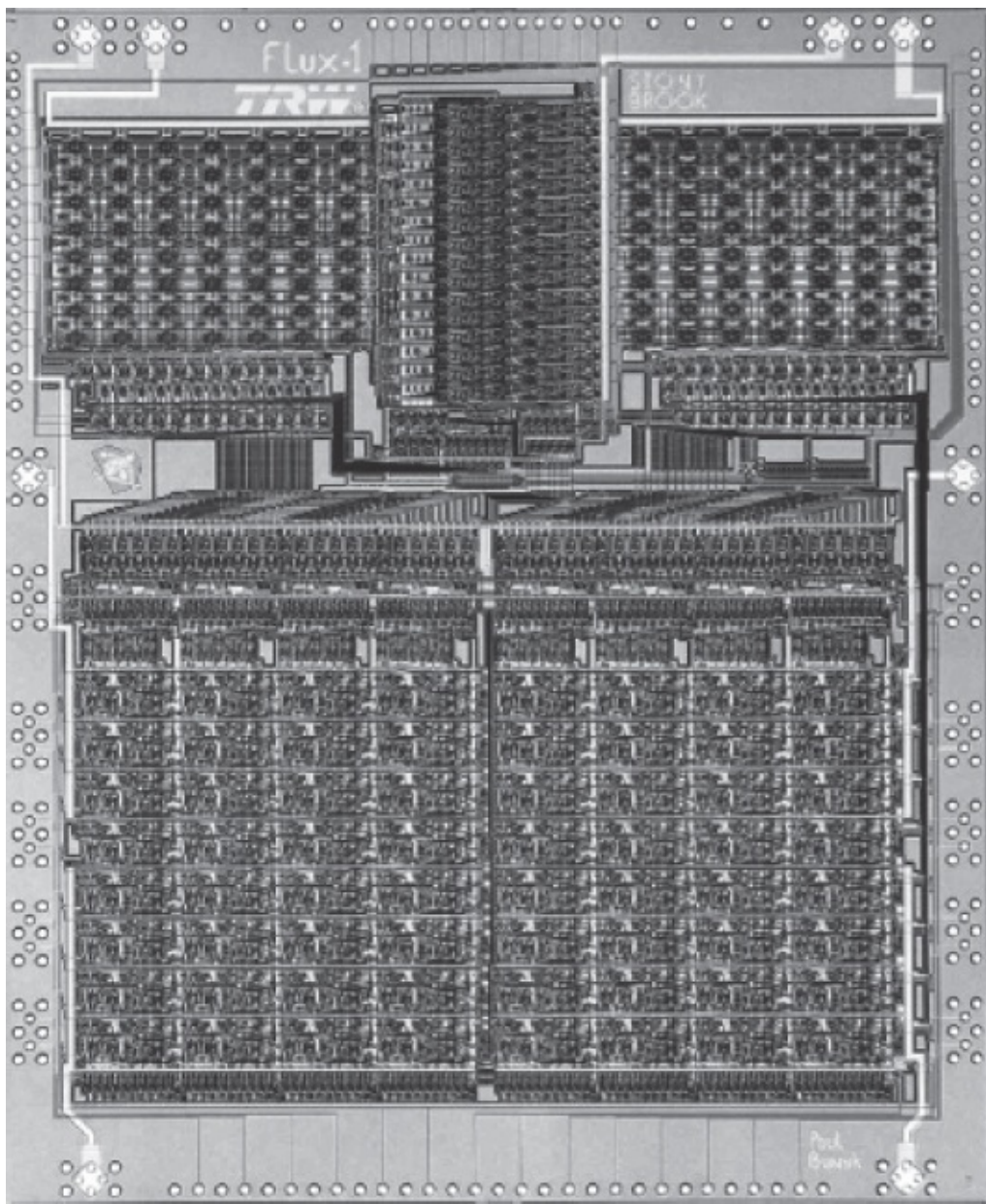


**Figure 7.62** A 20 GHz microprocessor containing about 65 000 Nb Josephson junctions [187].

(© 2002 IEEE.)

Compared with semiconductor processors, the number of active elements integrated on the chip is not yet very impressive, and it is a long way to really large-scale circuits. Therefore, it is difficult to predict to what extent the Josephson electronics will enter daily life. Also semiconductor technology progresses rapidly. Today in modern PCs, processors are installed, having clock speeds which could not be imagined in the 1980s. However, the power consumption represents an important issue. In the case of superconducting circuits it is much smaller than in the case of semiconductor chips. Therefore, one can expect that superconducting technologies become attractive, when the cooling effort of conventional technology becomes too big. Also applications can be imagined in a situation, where low temperatures are already available as, say, in the case of the digital read-out of a voltage standard.

In any case, further exciting developments can be expected in this field as well as in the applications of superconductivity. We are thinking of the area of qubits we have discussed in [Section 6.5](#), which presently is actively investigated. As our final example, [Figure 7.63](#) shows a circuit where 4 qubits are coupled together [188]. Three of these qubits are entangled with each other, in order to generate, say, a “Greenberger–Horn–Zeilinger”-wave function of the form  $|\text{GHZ}\rangle = (|000\rangle + |111\rangle)/\sqrt{2}$ . Here, we have used the bra and ket notation of the wave function, which is used in quantum mechanics. The three numbers 000 or 111 indicate the binary states of the three qubits. Logic gates consisting of three qubits are highly important for a future quantum computer, the realization of which seems very likely, however, only in the far future.

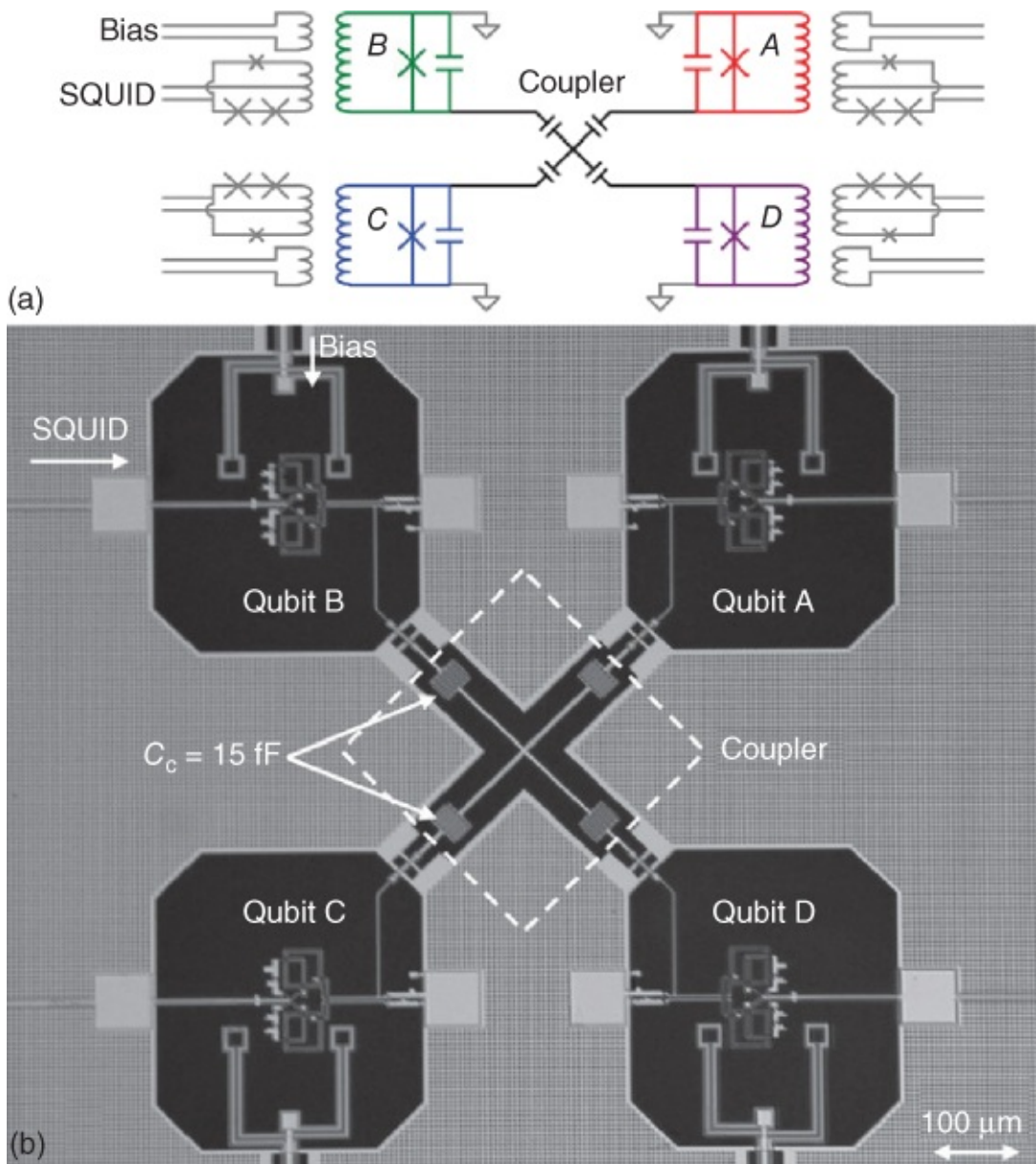


**Figure 7.63** Circuit consisting of four qubits coupled together. (a) schematic circuit, (b) image of chip. The capacitive coupling structure is located within the dashed square. The qubits are located in the center of the dark regions and are inductively coupled to the bias connections and the read-out SQUIDs.

([188], © 2010 Nature.)

## References

1. S. Morozumi: *Physica C* **357**, 20 (2001).
2. J. Clarke, D. C. Larbalestier, *Nat. Phys.* **2**, 497 (2006).
3. K. von Klitzing: *Rev. Mod. Phys.* **58**, 519 (1986); H. L. Stormer: *Rev. Mod. Phys.* **71**, 875 (1999); R. B. Laughlin: *Rev. Mod. Phys.* **71**, 863 (1999).

4. A. R. Kantrowitz, Z. J. Stekly: *Appl. Phys. Lett.* **6**, 56 (1965); D. B. Montgomery, L. Rinderer: *Cryogenics* **8**, S. 221 (1968).
5. Z. J. J. Stekly, R. Thome, B. Strauss: *J. Appl. Phys.* **40**, 2238 (1969).
6. L. D. Cooley, L. R. Motowidlo: *Supercond. Sci. Technol.* **12**, R135 (1999).
7. "Ullmanns Encyklopädie der technischen Chemie", 4th edn, Vol. **22**, p. 349, Verlag Chemie, Weinheim, (1982).
8. S. W. Van Sciver, K. R. Marken: *Phys. Today* **55**, 37 (2002).
9. R. Flükiger: *Supercond. Sci. Technol.* **10**, 872 (1997).
10. J.-L. Duchateau, M. Spadoni, E. Salpietro, D. Ciazynski, M. Ricci, P. Libeyre, A. della Corte: *Supercond. Sci. Technol.* **15**, R17 (2002).
11. T. Takeuchi: *Supercond. Sci. Technol.* **13**, R101 (2000).
12. H. Kumakura: *Supercond. Sci. Technol.* **13**, 34 (2000).
13. T. Matsushita: *Supercond. Sci. Technol.* **13**, 51 (2000).
14. H. W. Weijers, U. P. Trocietitz, W. D. Markiewicz, J. Jiang, D. Myers, E. E. Helstrom, A. Xu, J. Jaroszynski, P. Noyes, Y. Viouchkov, D. C. Larbalestier: *IEEE Trans. Appl. Supercond.* **20**, 576 (2010).
15. K. Vinod, R. G. Abilash Kumar, U. Syamaprasad: *Supercond. Sci. Technol.* **20**, R1 (2007).
16. J. Lehtonen, R. Mikkonen, J. Paasi: *Supercond. Sci. Technol.* **13**, 251 (2000).
17. K. Watanabe, S. Awaji: *J. Low Temp. Phys.* **133**, 17 (2003).
18. A. Korpela, J. Lehtonen, R. Mikkonen: *Supercond. Sci. Technol.* **16**, 355 (2003).
19. P. Vase, R. Flükiger, M. Leghissa, B. Glowacki: *Supercond. Sci. Technol.* **13**, R71 (2000).
20. M. W. Rupich, U. Schoop, D. T. Verebelyi, C. Thieme, W. Zhang, X. Li, T. Kodenkandath, N. Nguyen, E. Siegal, D. Buczek, J. Lynch, M. Jowett, E. Thompson, J.-S. Wang, J. Scudiere, A. P. Malozemoff, Q. Li, S. Annavarapu, S. Cui, L. Fritzemeier, B. Aldrich, C. Craven, F. Niu, A. Goyal, M. Paranthaman: *IEEE Trans. Appl. Supercond.* **13**, 2458 (2003).
21. A. Goyal, D. P. Norton, J. D. Budai, M. Paranthaman, E. D. Specht, D. M. Kroeger, D. K. Christen, Q. He, B. Saffian, F. A. List, D. F. Lee, P. M. Martin, C. E. Klabunde, E. Hartfield, V. K. Sikka: *Appl. Phys. Lett.* **69**, 1795 (1996).
22. Y. Iijima, K. Matsumoto: *Supercond. Sci. Technol.* **13**, 68 (2000); K. Kim, M. Paranthaman, D. P. Norton, T. Aytug, C. Cantoni, A. A. Gapud, A. Goyal, D. K. Christen: *Supercond. Sci. Technol.* **19**, R23 (2006).

23. M. S. Bhuiyan, M. Paranthaman, K. Salama: *Supercond. Sci. Technol.* **19**, R1 (2006).
24. A. Weber, G. Hammerl, A. Schmehl, C. W. Schneider, J. Mannhart, B. Schey, M. Kuhn, R. Nies, B. Utz, H.-W. Neumüller: *Appl. Phys. Lett.* **82**, 772 (2003); G. Hammerl, A. Schmehl, R. R. Schulz, B. Goetz, H. Bielefeldt, C. W. Schneider, H. Hilgenkamp, J. Mannhart: *Nature* **407**, 162 (2000).
25. P. F. Herrmann, E. Beghin, G. Bottini, C. Cottevielle, A. Leriche, T. Verhaege, J. Bock: *Cryogenics* **34**, 543 (1994).
26. W. K. H. Panofsky, M. Breidenbach: *Rev. Mod. Phys.* **71**, S121 (1999).
27. S. Takács: *Supercond. Sci. Technol.* **10**, 733 (1997).
28. P. F. Smith: “The Technology of Large Magnets”, In: “A Guide to Superconductivity”, D. Fishlock (ed.), McDonald & Co. Ltd. (1969).
29. J. R. Hull: *Supercond. Sci. Technol.* **13**, R1 (2000).
30. L. Schultz, G. Krabbes, G. Fuchs, W. Pfeiffer, K.-H. Müller: *Z. Metallkd.* **93**, 1057 (2002).
31. G. Krabbes, G. Fuchs, P. Verges, P. Diko, G. Stöver, S. Gruss: *Physica C* **378**, 636 (2002); G. Fuchs, P. Schätzle, G. Krabbes, S. Gruß, P. Verges, K.-H. Müller, J. Fink, L. Schulz: *Appl. Phys. Lett.* **76**, 2107 (2000); H. Ikuta, T. Hosokawa, M. Yoshikawa, U. Mizutani: *Supercond. Sci. Technol.* **13**, 1559 (2000).
32. M. Tomita, M. Murakami: *Nature* **421**, 517 (2003).
33. M. Murakami, M. Morita, K. Doi, K. Miyamoto: *Jpn. J. Appl. Phys.* **28**, 1189 (1989); R. L. Meng, L. Gao, P. Gautier-Picard, D. Ramirez, Y. Y. Sun, C. W. Chu: *Physica C* **232**, 337 (1994); M. Morita, M. Sawamura, S. Takebayashi, K. Kimura, H. Teshima, M. Tanaka, K. Miyamoto, M. Hashimoto: *Physica C* **235**, 209 (1994); G. Krabbes, P. Schätzle, W. Bieger, U. Wiesner, G. Stöver, M. Wu, T. Strasser, A. Köhler, D. Litzkendorf, K. Fischer, P. Görnert, *Physica C* **244**, 145 (1995).
34. G. Desgardin, I. Monot, B. Raveau: *Supercond. Sci. Technol.* **12**, R115 (1999).
35. (1970) Cryophysics Newsletter, Vol. **8**, January 1970.
36. M. N. Wilson: *IEEE Trans. Appl. Supercond.* **7**, 727 (1997).
37. P. Schmüser: *Rep. Prog. Phys.* **54**, 683 (1991).
38. N. Siegel for the LHC Magnet Team: *IEEE Trans. Appl. Supercond.* **7**, 252 (1997); F. Kircher, B. Levesy, Y. Pabot, D. Campi, B. Curé, A. Hervé, I. L. Horvath, P. Fabbricatore, R. Musenich: *IEEE Trans. Appl. Supercond.* **9**, 837 (1999); H. H. J. ten Kate for the ATLAS Collaboration: *IEEE Trans. Appl. Supercond.* **9**, 841 (1999).
39. P. Bruzzone: *Supercond. Sci. Technol.* **10**, 919 (1997).

40. R. Heller, W. Maurer and the W-7-X Team: *IEEE Trans. Appl. Supercond.* **10**, 614 (2000).
41. T. Satow, S. Imagawa, N. Yanagi, K. Takahata, T. Mito, S. Yamada, H. Chikaraishi, A. Nishimura, S. Satoh, O. Motojima: *IEEE Trans. Appl. Supercond.* **10**, 600 (2000).
42. D. Normile: *Science* **279**, 1846 (1998).
43. W. V. Hassenzahl, *IEEE Power Eng. Rev.* **20**, 4 (2000).
44. X. D. Xue, K.W.E. Cheng, D. Sutanto: *Supercond. Sci. Technol.* **19**, R31 (2006).
45. S. S. Kalsi, D. Aized, B. Connor, G. Snitchler, J. Campbell, R. E. Schwall, J. Kellers, Th. Stephanblome, A. Tromm, P. Winn: *IEEE Trans. Appl. Supercond.* **7**, 971 (1997); R. Kreutz, H. Salbut, D. Krischel, A. Hobl, C. Rademacher, N. Blacha, P. Behrens, K. Duetsch: *IEEE Trans. Appl. Supercond.* **13**, 1860 (2003).
46. K.-P. Juengst, R. Gehring, A. Kudymow, H.-J. Pfisterer, E. Suess: *IEEE Trans. Appl. Supercond.* **12**, 754 (2002).
47. G. Ries, H.-W. Neumueller: *Physica C* **357**, 1306 (2001).
48. W. V. Hassenzahl, *IEEE Trans. Appl. Supercond.* **11**, 1447 (2001).
49. T. Ichihara, K. Matsunaga, M. Kita, I. Hirabayashi, M. Isono, M. Hirose, K. Yoshii, K. Kurihara, O. Saito, S. Saito, M. Murakami, H. Takabayashi, M. Natsumeda, N. Koshizuka: *IEEE Trans. Appl. Supercond.* **15**, 2245 (2005); F. Werfel, U. Floegel-Delor, T. Riedel, R. Rothfield, D. Wippich, B. Goebel, G. Reiner, N. Wehlau: *IEEE Trans. Appl. Supercond.* **17**, 2138 (2007).
50. M. Strasik, J. R. Hull, J. A. Mittleider, J. F. Gonder, P. E. Johnson, K. E. McCrary, C R. McIver: *Supercond. Sci. Technol.* **23**, 034021 (2010).
51. H. J. Bornemann, M. Sander: *IEEE Trans. Appl. Supercond.* **7**, 398 (1997).
52. A. D. Appleton: “Superconductors in Motion” in “*A Guide to Superconductivity*”, D. Fislock (ed.), McDonald & Co. Ltd., p. S. 78 (1969).
53. J. S. Edmonds: *IEEE Trans. Mag. Mag.* **15**, 673 (1979).
54. D. U. Gubser: *Physica C* **392**, 1192 (2003).
55. S. S. Kalsi, N. Henderson, J. Voccio: “*Superconductor Motors for High Speed Ship Propulsion*”, American Superconductor Corporation (0000)
56. A. B. Abrahamsen, N. Mijatovic, E. Seiler, T. Zirngibl, C. Træholt, P. B. Nørgård, N. F. Pedersen, N. H. Andersen, J. Østergård: *Supercond. Sci. Technol.* **23**, 034019 (2010).
57. J. X. Jin, S. X. Dou, H. K. Liu: *Supercond. Sci. Technol.* **11**, 1071 (1998).

58. Zenergy Power und Bültmann GmbH (2007).
59. H. Hayashi, K. Tsutsumi, N. Saho, N. Nishizima, K. Asano: *Physica C* **392**, 745 (2003).
60. Lichtenberg, A. (1942) Verkehrstechnik/Der Verkehrsingenieur, 26, p. 73; Albrecht, C., Elsel, W., Franksen, H., Parsch, C.P., and Wilhelm, K. (1974) Superconducting levitated systems: first results with the experimental facility in Erlangen. ICEC 5 International Cryogenic Engineering Conference, May 1974, Kyoto, paper B 2.
61. R. McFee: *Elect. Eng. (N.Y.)* **81**, 122 (1962).
62. Gauster, W.F., Freeman, D.C., and Long, H.M. (1964) Proceedings of *World Power Conference 1964*, Paper 56, p. 1954.
63. R. L. Garwin, J. Matisoo: *Proc. IEEE* **55**, 538 (1967).
64. P. Klaudy, I. Gerold, A. Beck, P. Rohner, E. Scheffler, G. Ziemeck: *IEEE Trans. Magn. MAG-17*, 153 (1981).
65. J.F. Maguire, J. Yuan: *Physica C* **469**, 874 (2009).
66. B. W. McConnell, S. P. Mehta, M. S. Walker: *IEEE Power Eng. Rev.* **20**, 7 (2000).
67. M. Leghissa, B. Gromoll, J. Rieger, M. Oomen, H.-W. Neumüller, R. Schlosser, H. Schmidt, W. Knorr, M. Meinert, U. Henning, *Physica C* **372**, 1688 (2002).
68. E. F. Pleva, V. Mehrota, S. W. Schwenterly: *Supercond. Sci. Technol.* **23**, 014025 (2019); X. Chen, J. Jin: *Res. Com.* **1**, P2.1 (2007).
69. M. Noe, M. Steurer: *Supercond. Sci. Technol.* **20**, R15 (2007).
70. W. Paul, M. Lakner, J. Rhyner, P. Unternährer, Th. Baumann, M. Chen, L. Widenhorn, A. Guérig: *Supercond. Sci. Technol.* **10**, 914 (1997).
71. M. Chen, W. Paul, M. Lakner, L. Donzel, M. Hoidis, P. Unternaehrer, R. Weder, M. Mendik: *Physica C* **372**, 1657 (2002).
72. N. Klein: *Rep. Prog. Phys.* **65**, 1387 (2002).
73. A. B. Pippard: *Proc. R. Soc. A* **216**, 547 (1953).
74. D. C. Mattis, J. Bardeen, *Phys. Rev.* **111**, 412 (1958).
75. M. A. Biondi, M. P. Garfunkel: *Phys. Rev.* **116**, 853 and 862 (1959); D. C. Mattis, J. Bardeen: *Phys. Rev. Lett.* **2**, 143 (1959)
76. Passow, C. (1970) Eletrotechniky Casopis, XXI, p. 419.
77. H. Padamsee: *Supercond. Sci. Technol.* **14**, R28 (2001).

78. W. Weingarten: “*Frontiers of Accelerator Technology*”, S. I. Kutokawa *et al.* (eds.), World Scientific, Singapore, p. 363.
79. A. V. Velichko, M. J. Lancaster, A. Porch: *Supercond. Sci. Technol.* **18**, R24 (2005).
80. D. Proch: *Rep. Prog. Phys.* **61**, 431 (1998).
81. A. Cho: *Science* **315**, 746 (2007).
82. D. M. Pozar: “*Microwave Engineering*”, John Wiley & Sons, Inc., New York (1998).
83. R. W. Simon, R. B. Hammond, S. J. Berkowitz, B. A. Willemsen: *Proc. IEEE* **92**, 1585 (2004).
84. You, M. and Mirafthab, V. (2008) IEEE Microwave Magazine, Oktober.
85. E. K. Hollmann, O. G. Vendik, A. G. Zaitsev, B. T. Melekh: *Supercond. Sci. Technol.* **7**, 609 (1994).
86. G. Schlom, J. Mannhart: In: “*Encyclopedia of Materials: Science and Technology*”, K. H. J. Buschow, R. W. Cahn, M. C. Flemings, B. Ilschner, E. J. Kramer, S. Mahajan (Hrsg.), Elsevier Science, Amsterdam, p. 3806 (2002); R. Wördenweber: *Supercond. Sci. Technol.* **12**, R86 (1999).
87. J. S. Hong, M. J. Lancaster, R. B. Greed, D. Voyce, D. Jedamzik, J. A. Holland, H. J. Chaloupka, J.-C. Mage: *IEEE Trans. Appl. Supercond.* **9**, 3893 (1999); R. B. Greed, D. C. Voyce, D. Jedamzik, J. S. Hong, M. J. Lancaster, M. Reppel, H. J. Chaloupka, J. C. Mage, B. Marcilhac, R. Mistry, H. U. Häfner, G. Auger, W. Rebernak: *IEEE Trans. Appl. Supercond.* **9**, 4002 (1999).
88. H. Chaloupka: in *Microwave Superconductivity*, H. Weinstock and M. Nisenoff (eds.), NATO Science Series E: Applied Sciences, Vol. **375**, Kluwer Academic Publishers, Dordrecht/Boston/London, 1999, p. 337.
89. S. M. Anlage: in *Microwave Superconductivity*, H. Weinstock and M. Nisenoff (eds.), NATO Science Series E: Applied Sciences, Vol. **375**, Kluwer Academic Publishers, Dordrecht/Boston/London, p. 353 (1999).
90. C. K. Stahle, D. McCammon, K. D. Irwin: *Phys. Today* **52**, 32 (1999).
91. D. Twerenbold, *Rep. Prog. Phys.* **59**, 349 (1996); H. Kraus: *Supercond. Sci. Technol.* **9**, 827 (1996).
92. J. Zmuidzinas, P. L. Richards: *Proc. IEEE* **92**, 1597 (2004).
93. G. Aschermann, E. Friedrich, E. Justi, J. Kramer: *Phys. Z.* **42**, 349 (1941).
94. C. Enss, A. Fleischmann, K. Horst, J. Schönenfeld, J. Sollner, J. S. Adams, Y. H. Huang, Y. H. Kim, G. M. Seidel: *J. Low Temp. Phys.* **121**, 137 (2000).

95. G. Angloher, M. Bauer, I. Bavykina, A. Bento, C. Bucci, C. Ciemniak, G. Deuter, F. von Feilitzsch, D. Hauff, P. Huff, C. Isaila, J. Jochum, M. Kiefer, M. Kimmerle, J.-C. Lanfranchi, F. Petricca, S. Pfister, W. Potzel, F. Pröbst, F. Reindl, S. Roth, K. Rottler, C. Sailer, K. Schäffner, J. Schmaler, S. Scholl, W. Seidel, M. v. Sivers, L. Stodolsky, C. Strandhagen, R. Strauß, A. Tanzke, I. Usherov, S. Wawoczny, M. Willers, A. Zöller: *Eur. Phys. J. C*, **72**, 1971 (2012).
96. G. C. Hilton, J. M. Martinis, K. D. Irwin, N. F. Bergren, D. A. Wollman, M. E. Huber, S. Deiker, S. W. Nam: *IEEE Trans. Appl. Phys.* **11**, 739 (2001); D. A. Wollman, K. D. Irwin, G. C. Hilton, L. L. Dulcie, D. E. Newbury, J. M. Martinis: *J. Microsc.* **188**, 196 (1997).
97. D. T. Chow, M. L. van den Berg, A. Loshak, M. Frank, T. W. Barbee, Jr. S. E. Labov: *IEEE Trans. Appl. Supercond.* **11**, 743 (2001).
98. G. C. Hilton, J. A. Beall, S. Deiker, J. Beyer, L. R. Vale, C. D. Reintsema, J. N. Ullom, K. D. Irwin, *IEEE Trans. Appl. Supercond.* **13**, 664 (2003).
99. L. Li, L. Frunzio, C. Wilson, K. Segall, D. E. Prober, A. E. Szymkowiak, S. H. Moseley: *IEEE Trans. Appl. Supercond.* **11**, 685 (2001).
100. H. Pressler, M. Ohkubo, M. Koike, T. Zama, D. Fukuda, N. Kobayashi: *IEEE Trans. Appl. Supercond.* **11**, 696 (2001).
101. M. Frank, L. J. Hiller, J. B. le Grand, C. A. Mears, S. E. Labov, M. A. Lindeman, H. Netel, D. Chow, A. T. Barfknecht: *Rev. Sci. Instrum.* **69**, 25 (1998).
102. A. D. Semenov, G. N. Gol'tsman, R. Sobolewski: *Supercond. Sci. Technol.* **15**, R1 (2002).
103. E. M. Gershenson, M. E. Gershenson, G. N. Gol'tsman, A. D. Semenov, A. V. Sergeev: *JETP Lett.* **34**, 268 (1981).
104. F. Marsili, F. Najafi, E. Dauler, F. Bellei, X. Hu, M. Csete, R. J. Molnar, K. K. Berggren: *Nano Lett.* **11**, 2048 (2011).
105. A. J. Kreisler, A. Gaugue: *Supercond. Sci. Technol.* **13**, 1235 (2000).
106. J. Clarke, P. L. Richards, N.-H. Yeh: *Appl. Phys. Lett.* **30**, 664 (1977).
107. E. Heinz, T. May, G. Zieger, D. Born, S. Aders, G. Torwirth, V. Zakosarenko, M. Schubert, T. Krause, M. Starkloff, A. Krüger, M. Schulz, F. Bauer, H.-G. Meyer: *J. Infrared Milli Terahz Waves* **31**, 1355 (2010).
108. M. J. M. E. de Nivelle, M. P. Bruijn, R. de Vries, J. J. Wijnbergen, P. A. J. de Korte, S. Sánchez, M. Elwenspoek, T. Heidenblut, B. Schwierzi, W. Michalke, E. Steinbeiss: *J. Appl. Phys.* **82**, 4719 (1997).
109. P. K. Day, H. G. LeDuc, B. A. Mazin, A. Vayonakis, J. Zmuidzinas: *Nature* **425**, 817 (2003).

110. Y. Y. Divin, O. Volkov, V. Pavlovskii, U. Poppe, K. Urban: *IEEE Trans. Appl. Supercond.* **11**, 582 (2001);F. Ludwig, J. Menzel, A. Kaestner, M. Volk, M. Schilling: *IEEE Trans. Appl. Supercond.* **11**, 586 (2001).
111. J. R. Tucker, M. J. Feldman: *Rev. Mod. Phys.* **57**, 1055 (1985).
112. Rudolf, H. (2006) The ALMA front end. German Microwave Conference, Karlsruhe, Germany, March 28–30.
113. K. H. Gundlach, M. Schicke: *Supercond. Sci. Technol.* **13**, R171 (2000).
114. V. P. Koshelets, S. V. Shitov: *Supercond. Sci. Technol.* **13**, R53 (2000).
115. S. Kiryu, W. Zhang, S. Han, S. Deus, J. E. Lukens: *IEEE Trans. Appl. Supercond.* **7**, 3107 (1997).
116. L. Ozyuzer, A. E. Koshelev, C. Kurter, N. Gopalsami, Q. Li, M. Tachiki, K. Kadowaki, T. Yamamoto, H. Minami, H. Yamaguchi, T. Tachiki, K. E. Gray, W.-K. Kwok, U. Welp: *Science* **318**, 1291 (2007).
117. H. B. Wang, S. Guénon, B. Gross, J. Yuan, Z. G. Jiang, Y. Y. Zhong, M. Grünzweig, A. Iishi, P. H. Wu, T. Hatano, D. Koelle, R. Kleiner, *Phys. Rev. Lett.* **105**, 057002 (2010).
118. P. Barbara, A. B. Cawthorne, S. V. Shitov, C. J. Lobb: *Phys. Rev. Lett.* **82**, 1963 (1999);J. Oppenländer, W. Güttinger, T. Traeuble, M. Keck, T. Doderer, R. P. Huebener: *IEEE Trans. Appl. Supercond.* **9**, 4337 (1999).
119. F. Song, F. Müller, R. Behr, A. M. Klushin: *Appl. Phys. Lett.* **95**, 172501 (2009).
120. M. Darula, T. Doderer, S. Beuven: *Supercond. Sci. Technol.* **12**, R1 (1999);X. Hu, S. Z. Lin: *Supercond. Sci. Technol.* **23**, 053001 (2010).
121. W. Eisenmenger, A. H. Dayem: *Phys. Rev. Lett.* **18**, 125 (1967).
122. H. Kinder, K. Laszmann, W. Eisenmenger: *Phys. Lett.* **31 A**, 475 (1970);H. Kinder: *Phys. Rev. Lett.* **28**, 1564 (1972).
123. P. Berberich, R. Buemann, H. Kinder: *Phys. Rev. Lett.* **49**, 1500 (1982).
124. M. Osofsky: *J. Supercond.* **13**, 209 (2000);R. Meservey, P. M. Tedrow: *Phys. Rep.* **238**, 173 (1994);P. Fulde: *Adv. Phys.* **22**, 667 (1973).
125. For an overview, see D. Koelle, R. Kleiner, F. Ludwig, E. Dantsker, J. Clarke: *Rev. Mod. Phys.* **71**, 631 and 1249 (1999).
126. A. H. Silver, J. E. Zimmerman: *Phys. Rev.* **157**, 317 (1967).
127. J. E. Zimmerman: *J. Appl. Phys.* **42**, 4483 (1971).

128. F. Ludwig, E. Dantsker, D. Koelle, R. Kleiner, A. H. Miklich, D. T. Nemeth, J. Clarke, D. Drung, J. Knappe, H. Koch: *IEEE Trans. Appl. Supercond.* **5**, 2919 (1995).
129. D. Drung: *Physica C* **368**, 134 (2001).
130. D. Drung, R. Cantor, M. Peters, H. J. Scheer, R. Koch: *Appl. Phys. Lett.* **57**, 406 (1991); D. Drung, H. Koch: *IEEE Trans. Appl. Supercond.* **3**, 2594 (1993).
131. D. Drung: In: “*SQUID Sensors: Fundamentals, Fabrication and Applications*”, H. Weinstock (ed.), NATO ASI Series E329, Kluwer, Dordrecht, p. 63 (1996).
132. E. Dantsker, S. Tanaka, J. Clarke: *Appl. Phys. Lett.* **70**, 2037 (1997); E. Dantsker, S. Tanaka, P. Å. Nilsson, R. Kleiner, J. Clarke: *Appl. Phys. Lett.* **69**, 4099 (1996).
133. H.-J. Barthelmess, B. Schiefenhöfel, M. Schilling: *Physica C* **368**, 37 (2002).
134. R. H. Koch, J. Z. Sun, V. Foglietti, W. J. Gallagher: *Appl. Phys. Lett.* **67**, 709 (1995); F. P. Milliken, S. L. Brown, R. H. Koch: *Appl. Phys. Lett.* **71**, 1857 (1997).
135. J. E. Mercereau: *Rev. Phys. Appl.* **5**, 13 (1970); M. Nisenoff: *Rev. Phys. Appl.* **5**, 21 (1970); J. E. Zimmerman, P. Thiene, J. T. Harding: *J. Appl. Phys.* **41**, 1572 (1970).
136. S. Krey, O. Brügmann, M. Schilling: *Appl. Phys. Lett.* **74**, 293 (1999).
137. J. Oppenländer, Ch. Häussler, T. Träuble, N. Schopohl: *Physica C* **368**, 119 (2002).
138. V. Schultze, R. I. IJsselsteijn, H.-G. Meyer, J. Oppenländer, Ch. Häussler, N. Schopohl, *IEEE Trans. Appl. Supercond.* **13**, 775 (2003).
139. J. Oppenländer, P. Caputo, Ch. Häussler, T. Träuble, J. Tomes, A. Friesch, N. Schopohl: *Appl. Phys. Lett.* **83**, 969 (2003) and *IEEE Trans. Appl. Supercond.* **13**, 771 (2003).
140. V. K. Kornev, I. I. Soloviev, N. V. Klenov, O. A. Mukhanov: *IEEE Trans. Appl. Supercond.* **17**, 569 (2007).
141. J. Vrba: *Physica C* **368**, 1 (2002).
142. W. O. Hamilton: *Rev. Phys. Appl.* **5**, 41 (1970).
143. J. Bork, H.-D. Hahlbohm, R. Klein, A. Schnabel: “*Biomag2000, Proceedings of the 12th International Conference on Biomagnetism*”, J. Nenonen, R. J. Ilmoniemi, T. Katila (eds.), Helsinki University of Technology, Espoo, p. 970 (2001).
144. G. Daalmans: *Appl. Supercond.* **3**, 399 (1995).
145. M. I. Faley, U. Poppe, K. Urban, H. J. Krause, H. Soltner, R. Hohmann, D. Lomparski, R. Kutzner, R. Wördenweber, H. Bousack, A. I. Braginski, V. Y. Slobodchikov, A. V. Gapelyuk, V. V. Khanin, Y. V. Maslenikov: *IEEE Trans. Appl. Supercond.* **7**, 3702 (1997).

146. J. Vrba, S. E. Robinson: *Supercond. Sci. Technol.* **15**, R51 (2002).
147. V. Pizzella, S. Della Penna, C. Del Gratta, G. L. Romani: *Supercond. Sci. Technol.* **14**, R79 (2001).
148. H.-C. Yang, H. E. Hong, S. Y. Yang, S.-H. Liao: *Supercond. Sci. Technol.* **22**, 093001 (2009).
149. V. Jazbinšek, O. Kosch, P. Meindl, U. Steinhoff, Z. Trontelj, L. Trahms: *Biomag2000, Proceedings of the 12th International Conference on Biomagnetism*, J. Nenonen, R. J. Ilmoniemi, T. Katila (eds.), Helsinki University of Technology, Espoo, p. 583 (2001).
150. R. Weidl, L. Dörrer, F. Schmidl, P. Seidel, G. Schwarz, U. Leder, H. R. Figulla, R. Schüler, O. Solbrig, H. Nowak: *Recent Advances in Biomagnetism, Proceedings of the 11th International Conference on Biomagnestim*, T. Yoshimoto (ed.), Tohoku University Press, Sendai, p. 113 (1999); P. Seidel, F. Schmidl, S. Wunderlich, L. Dörrer, T. Vogt, H. Schneidewind, R. Weidl, S. Lösche, U. Leder, O. Solbrig, H. Nowak: *IEEE Trans. Appl. Supercond.* **9**, 4077 (1999).
151. J. Clarke, M. Hatridge, M. Mößle: *Annu. Rev. Biomed. Eng.* **9**, 389 (2007).
152. Dinh M. TonThat, M. Ziegeweid, Y.-Q. Song, E.J. Munson, S. Appelt, A. Pines, J. Clarke: *Chem. Phys. Lett.* **272**, 245 (1997); M. P. Augustine, A. Wong-Foy, J. L. Yarger, M. Tomaselli, A. Pines, D. M. TonThat, J. Clarke: *Appl. Phys. Lett.* **72**, 1908 (1998).
153. K. Schlenga, R. McDermott, J. Clarke, R. E. de Souza, A. Wong-Foy, A. Pines: *Appl. Phys. Lett.* **75**, 3695 (1999).
154. R. McDermott, A. H. Trabesinger, M. Mück, E. L. Hahn, A. Pines, J. Clarke: *Science* **295**, 2247 (2002).
155. M. Mößle, S.-I. Han, W. R. Myers, S.-K. Lee, N. Kelso, M. Hatridge, A. Pines, J. Clarke: *J. Magn. Reson.* **179**, 146 (2006).
156. J. R. Kirtley, J. P. Wikswo, Jr.: *Annu. Rev. Mater. Sci.* **29**, 117 (1999).
157. J. R. Kirtley: *Physica C* **368**, 55 (2002).
158. S. Chatraphorn, E. F. Fleet, F. C. Wellstood: *J. Appl. Phys.* **92**, 4731 (2002).
159. J. Beyer, H. Matz, D. Drung, Th. Schurig: *Appl. Phys. Lett.* **74**, 2863 (1999).
160. F. Baudenbacher, N. T. Peters, P. Baudenbacher, J. P. Wikswo: *Physica C* **368**, 24 (2002).
161. T. S. Lee, Y. R. Chemla, E. Dantsker, J. Clarke, *IEEE Trans. Appl. Supercond.* **7**, 3147 (1997).
162. Clarke, J. (1994) Scientific American, August 1994, p. 36 (Spektrum der Wissenschaften, Oktober 1994, p. 58).

163. M. V. Kreutzbruck, K. Allweins, G. Gierelt, H.-J. Krause, S. Gärtner, W. Wolf: *Physica C* **368**, 85 (2002).
164. H.-J. Krause, W. Wolf, W. Glaas, E. Zimmermann, M. I. Faley, G. Sawade, R. Mattheus, G. Neudert, U. Gampe, J. Krieger: *Physica C* **368**, 91 (2002).
165. M. Mück, C. Welzel, F. Gruhl, M. V. Kreutzbruck, A. Farr, F. Schölz: *Physica C* **368**, 96 (2002).
166. W. Vodel, S. Nietzsche, R. Neubert, H. Dittus: *Physica C* **372**, 154 (2002).
167. C. Hilbert, J. Clarke: *J. Low Temp. Phys.* **61**, 263 (1985); M. Mück, J. B. Kycia, J. Clarke: *Appl. Phys. Lett.* **78**, 967 (2001); M. Mück: *Physica C* **368**, 141 (2002).
168. C. Hagman, D. Kinion, W. Stoeffl, K. Van Bibber, E. Daw, H. Peng, L. J. Rosenberg, J. LaVeigne, P. Sikivie, N. S. Sullivan, D. B. Tanner, F. Nezrik, M. S. Turner, D. M. Moltz, J. Powell, N. A. Golbev: *Phys. Rev. Lett.* **80**, 2043 (1998).
169. C. P. Foley, K. E. Leslie, R. A. Binks, S. H. K. Lam, J. Du, D. L. Tilbrook, E. E. Mitchell, J. C. Macfarlane, J. B. Lee, R. Turner, M. Downey, A. Maddever: *Supercond. Sci. Technol.* **15**, 1641 (2002).
170. W. Wernsdorfer: *Supercond. Sci. Technol.* **22**, 064013 (2009).
171. C. A. Hamilton: *Rev. Sci. Instrum.* **71**, 3611 (2000).
172. J. Niemeyer: *PTB-Mitteilungen* **110**, 169 (2000); B. Seeber (ed.) “*Handbook of Applied Superconductivity*”, Institut of Physics Publishing, Bristol, p. 1813 (1998).
173. M. T. Levinsen, R. Y. Chiao, M. J. Feldman, B. A. Tucker: *Appl. Phys. Lett.* **31**, 776 (1977).
174. R. L. Kautz, *Rep. Prog. Phys.* **59**, 935 (1996).
175. A. M. Klushin, S. I. Borovitskii, C. Weber, E. Sodtke, R. Semerad, W. Prusseit, V. D. Gelikonova, H. Kohlstedt: *Appl. Supercond.* **158**, 587 (1997).
176. S. P. Benz, C. A. Hamilton, C. J. Burroughs, T. E. Harvey, L. A. Christian: *Appl. Phys. Lett.* **71**, 1866 (1997); J. Kohlmann, R. Behr: In: “*Superconductivity-Theory and Applications*”, A. M. Luiz (Hrsg.), InTech (2011).
177. K. K. Likharev, V. K. Semenov: *IEEE Trans. Appl. Supercond.* **1**, 3 (1991).
178. D. A. Buck: *Proc. IRE* **44**, 482 (1956).
179. J. Matisoo: *Appl. Phys. Lett.* **9**, 167 (1966).
180. W. Anacker: *IBM J. Res. Dev.* **24**, 107 (1980).

181. T. Nishino: *Supercond. Sci. Technol.* **10**, 1 (1997); S. Kotani, A. Inoue, H. Suzuki, S. Hasuo, T. Takenouchi, K. Fukase, F. Miyagawa, S. Yoshida, T. Sano, Y. Kamioka: *IEEE Trans. Appl. Supercond.* **1**, 164 (1991); M. Hosoya, T. Nishino, W. Hioe, S. Kominami, K. Takagi: *IEEE Trans. Appl. Supercond.* **5**, 3316 (1995).
182. S. Faris, S. Raider, W. Gallagher, R. Drake: *IEEE Trans. Magn.* **MAG-19**, 1293 (1983); J. Mannhart: *Supercond. Sci. Technol.* **9**, 49 (1996).
183. A. H. Silver: *IEEE Trans. Appl. Supercond.* **7**, 69 (1997); T. Van Duzer, *IEEE Trans. Appl. Supercond.* **7**, 98 (1997); K. K. Likharev: *Czech. J. Phys.* **46**, 3331 (1996).
184. T. Ortlepp, Ariando, O. Mielke, C. J. M. Verwijs, K. F. K. Foo, H. Rogalla, F. H. Uhlmann, H. Hilgenkampp: *Science* **312**, 1483 (2006).
185. A. K. Feofanov, V. A. Oboznov, V. V. Bol'ginov, J. Lisenfeld, S. Poletto, V. V. Ryazanov, N. Rossolenko, M. Khabipov, D. Balashov, A. B. Zorin, P. N. Dmitriev, V. P. Koshelets, A. V. Ustinov: *Nat. Phys.* **6**, 593 (2011).
186. W. Chen, V. Rylyakov, V. Patel, J. E. Lukens, K. K. Likharev: *IEEE Trans. Appl. Supercond.* **9**, 3212 (1999).
187. M. Dorojevets: *Physica C* **378**, 1446 (2002); M. Dorojevets, P. Bunyk, D. Zinoviev: *IEEE Trans. Appl. Supercond.* **11**, 326 (2001).
188. M. Neeley, R. C. Bialczak, M. Lenander, E. Lucero, M. Mariantoni, A. D. O'Connell, D. Sank, H. Wang, M. Weides, J. Wenner, Y. Yin, T. Yamamoto, A. N. Cleland, J. M. Martinis: *Nature* **467**, 570 (2010).
189. M. B. Ketchen: *IEEE Trans. Magn.* **MAG-17**, 387 (1980).

<sup>1</sup> For Japan it was estimated that the application of superconducting technology projected to the year 2010 would yield an annual energy saving up to 100 tWh and simultaneously would reduce CO<sub>2</sub> emissions by 100 million tons per annum. Interestingly, the largest energy saving would result from the use of superconductors in computers [1].

<sup>2</sup> In the case of copper cables, the costs are 20–30 \$ per kA and meter. In the case of nitrogen-cooled wires of Bi<sub>2</sub>Sr<sub>2</sub>CaCu<sub>2</sub>O<sub>10</sub> the corresponding costs are 100–200 \$. In the case of tapes of YBa<sub>2</sub>Cu<sub>3</sub>O<sub>7</sub> and also for MgB<sub>2</sub>, one hopes to reach or even get below the price of copper cables [2].

<sup>3</sup> Usually we will not distinguish much between industrial and scientific applications. Also, because of space limitations, we will discuss the conventional alternative techniques only in a few cases.

<sup>4</sup> Here, we ignore the power consumption in the normal conducting current-feeding lines of the magnet or in any other normal conducting connections. However, the two ends of the coil

can also be joined together to form a closed superconducting circuit, in which case the field is maintained without any external power consumption (“persistent mode”).

- <sup>5</sup> This is particularly the case if liquid nitrogen can be used for the cooling. Cooling with liquid nitrogen is at least 50 times cheaper than cooling with liquid helium. Furthermore, the cryostats are simpler and, hence, cheaper. Therefore, magnets fabricated from high-temperature superconductors are highly interesting.
  - <sup>6</sup> By repeated quenching, a magnet can be “trained.” During several quenches, the superconducting wires rearrange themselves into a more stable position, such that finally higher magnetic fields can be reached.
  - <sup>7</sup> In a bubble chamber, the trace of a highly energetic particle is made visible by the fact that along the track small bubbles are formed in a liquid because of the local heating affected by the ionization processes. The track of the charged particles is curved because of the Lorentz force in an applied magnetic field. From the curvature, the sign of the charge as well as the momentum of the particle for known charge can be determined. In the case of very large momenta of highly energetic particles, large magnetic fields must be used in order to achieve detectable curvatures of the tracks. Today bubble chambers are no longer used for particle detection. However, in modern detector systems, huge superconducting magnets serve for producing the curvature of the particle tracks.
  - <sup>8</sup> Today hybrid magnets are used in special high-field laboratories. In this case the external magnet is made from NbTi, followed by an Nb<sub>3</sub>Sn coil. In addition, in the center, there is a conventional Bitter magnet. With such magnet systems presently 45 T can be generated for continuous operation [Reports of the National High Magnetic Field Laboratory, Florida/Los Alamos, Vol. 7 (2000)]. Fields up to about 100 T can be generated with normal conducting magnets in a pulsed operation. For still higher fields, explosive methods must be used.
- <sup>9</sup> Here “permanent” means as long as the transition temperature is not exceeded.
- <sup>10</sup> A similar behavior can be achieved also with superconducting hollow cylinders. As soon as the cylinder is cooled down below  $T_c$ , it keeps the magnetic flux in its interior constant. This principle is used for stabilizing experimental setups against temporally changing magnetic fields.
  - <sup>11</sup> In fields with rotational symmetry, the superconductor can rotate fast relative to the field.
  - <sup>12</sup> In this case up to 40 partly superconducting correcting coils (“shims”) with optimized field profiles and currents must be used for homogenizing the main superconducting magnet. In addition, the sample rotates in order to achieve spatial averaging of the local fields.
  - <sup>13</sup> One uses the isotope tritium, the nuclei of which consist of one proton and two neutrons.
  - <sup>14</sup> This principle of energy storage is often referred to as **SMES** (superconducting magnetic

energy storage).

- <sup>15</sup> In this connection, power is usually given in VA (volt ampere) instead of watt:  $1 \text{ VA} = 1 \text{ W}$ .
- <sup>16</sup> Usually the wave is described by a complex expression, which is proportional to  $\exp[i(kz - \omega t)]$ . If the amplitude of the wave decays with increasing  $z$ , then  $k$  itself is a complex number.
- <sup>17</sup> If the displacement currents also play a role, instead of  $\sigma_n$  a complex function  $\sigma = \sigma_1 + i\sigma_2$  can be used.
- <sup>18</sup> The power  $P_d$  dissipated in a high-frequency resonator is proportional to  $R_S$ . The **quality factor  $Q$**  is defined as  $Q = \omega U / P_d$ , where  $U$  is the energy stored in the resonator, and it is inversely proportional to  $R_S$ . Obviously, one tries to keep  $R_S$  as small as possible. Exactly this can be achieved with superconductors.
- <sup>19</sup> In the case of high-temperature superconductors, frequently defect structures such as grain boundaries play a role [79].
- <sup>20</sup> The electromagnetic standing waves in a resonator are classified with the notation “ $\text{TM}_{hkl}$ ” or “ $\text{TE}_{hkl}$ .” In the case of the “ $\text{TM}$ ” modes, the magnetic field has no component in the  $z$ -direction. The integer numbers  $hkl$  indicate the nodes of the electric field in the resonator in azimuthal ( $h$ ), radial ( $k$ ), and  $z$ -direction ( $l$ ). In the case of the transverse electric (“ $\text{TE}$ ”) modes, essentially the electric and magnetic fields are exchanged.
- <sup>21</sup> **One decibel (1 dB)** is defined as  $10 \log(A/A_0)$ , where  $A/A_0$  is the signal amplitude normalized by the amplitude  $A_0$ . Hence, a reduction of 3 dB corresponds to a decrease by a factor  $10^{0.3} \approx 2$ .
- <sup>22</sup> The use of liquid nitrogen would require far too much maintenance and, hence, is not practicable.
- <sup>23</sup> Frequently, these losses, which determine the quality factor of the resonator, are expressed in form of the “loss angle”  $\delta$ . The quantity  $\tan \delta$  is equal to the ratio between the imaginary and real parts of the complex dielectric constant  $\epsilon(\omega)$ .
- <sup>24</sup> In the case of the electrical resistance  $R$ , this noise is generated by the statistical thermal motion of the electrons in the metal (Nyquist noise).
- <sup>25</sup> As near-infrared one denotes the range of wave lengths between 0.8 and 3  $\mu\text{m}$ , as medium-infrared the range between 0.8 and 20  $\mu\text{m}$ . The far-infrared includes wavelengths between 20 and 1 mm, or frequencies between 300 GHz and 15 THz.
- <sup>26</sup> The maximum supercurrent through the junction (i.e.,  $n = 0$ ) varies nearly independent of the frequency.

- [27](#) The noise temperature of the *total* receiver is about 10 times this value.
- [28](#) Possible Josephson currents across the junction are suppressed by the application of a magnetic field.
- [29](#) For simplicity we assume that both superconductors are identical; otherwise,  $2\Delta_0/e$  must be replaced by  $(\Delta_I + \Delta_{II})/e$ .
- [30](#) In principle, the mixer itself can operate up to  $2\Delta_0$ , that is, in the case of Nb up to about 1.4 THz. Therefore, one also tries to use a normal metal such as Al in the periphery instead of Nb. At these frequencies, Al still has a relatively acceptable surface resistance.
- [31](#) These values are only an indication. In principle, a SQUID can still function up to  $L/L_{th} \approx 2\pi$ .
- [32](#) During any motion of these vortices, perturbing signals are generated, which reduce the sensitivity of the SQUID.
- [33](#) Frequently, one uses  $N_1 = 1$ , that is, the receiver coil is only a single loop (“pickup loop”).
- [34](#) The sensor coil may perhaps be located relatively far from the SQUID. This is particularly advantageous if the measurements are to be performed in large external fields.
- [35](#) This requirement is satisfied intrinsically at 77 K by  $\text{YBa}_2\text{Cu}_3\text{O}_7$  grain-boundary junctions. However, Nb junctions must be supplied with a parallel resistance.
- [36](#) They consist of a series of short pulses, which appear phase-shifted at the two Josephson junctions; the phase shift changes periodically according to the flux penetrating the ring.
- [37](#) Within the pendulum model (see [Section 6.2](#)), this means that again and again one of the driven pendulums turns over statistically. Then the angular velocity of the pendulums attains a finite value.
- [38](#) High-purity Nb is a type-I superconductor (see [Section 2.2](#)). However, thin films of Nb contain enough atomic defects to change Nb into a type-II superconductor.
- [39](#) Because of the quantum condition for the magnetic flux in a superconducting cylinder, in principle, it is also possible to generate a completely field-free volume. Practically, a field reduction down to  $10^{-11}$  T has been achieved [142].
- [40](#) For the gradients  $dB_z/dz$ ,  $dB_y/dy$ , and  $dB_x/dx$ , one needs three-dimensional arrangements as shown in [Figure 7.49a](#). The other gradients can be detected already by a suitable orientation of planar arrangements.
- [41](#) This is particularly valid if one is interested in the brain signals of a fetus within the mother

(see [Figure 7.48](#)).

- [42](#) Therefore, in this case the bolts in airplanes had to be removed for maintenance, tested, and mounted again, which is very time-consuming.
- [43](#) In this case initially the voltage value must be measured sufficiently accurately using a well-calibrated voltmeter, in order to distinguish between neighboring quantum numbers  $n \pm 1$ .
- [44](#) In the case of semiconductor circuits, the heat dissipation, in particular in large computers, is highly problematic.
- [45](#) Hence, this kind of circuit is also referred to as ***latching logic***.
- [46](#) We note that the unit of flux or of the flux quantum can be written as  $T \text{ m}^2$  as well as  $\text{V s}$ .
- [47](#) Within the pendulum picture (see [Section 6.2](#)), this means to process the individual overturns of the pendulum.
- [48](#) In the meantime large computer programs also exist for the layout of different cells. Special programs allow the simulation also of highly complex circuits.
- [49](#) Josephson junctions made of high-temperature superconductors could increase the switching speed again by 1 order of magnitude. However, presently these junctions cannot be fabricated yet with sufficient reproducibility. Also  $\pi$ -Josephson contacts are interesting for the RSFQ-technique. They allow the fabrication of simpler circuits which require a smaller number of current sources [184, 185].

# Monographs and Article Collections

## History of Superconductivity

[M1] P. F. Dahl (1992), *Superconductivity. Its Historical Roots and Development from Mercury to the Ceramic Oxides*, American Institute of Physics, New York.

## General Books

[M2a] R. D. Parks (Hrsg.), *Superconductivity*, 2 Vols. Marcel Dekker, Inc., New York, 1969.

[M2b] K.-H. Bennemann and J. B. Ketterson (eds) (2003) *The Physics of Superconductors*, 2 Vols. Springer-Verlag Berlin, Intensive survey of superconductivity by several authors.

[M3] M. Tinkham (1996), *Introduction to Superconductivity*, McGraw-Hill Book Company, New York, Introduction into the theory of superconductivity.

[M4] J. R. Waldram, (1996). *Superconductivity of Metals and Cuprates*, Institute of Physics Publishing, Bristol and Philadelphia, PA, Superconductivity in theory and experiment.

[M5] J. B. Ketterson and S. N. Song (1999) *Superconductivity* Cambridge University Press, Cambridge, Introduction into the theory of superconductivity.

[M6] V.V. Schmidt (1997). *The Physics of Superconductors – Introduction to Fundamentals and Applications* (eds P. Müller, A.V. Ustinov) Springer-Verlag, Berlin, Heidelberg, New York, Revised edition of a classic of the Russian literature.

[M7] M. Cyrot and D. Pavuna, (1992). *Introduction to Superconductivity and High- $T_c$  Materials*, World Scientific Publishing Co., Short introduction to superconductivity.

[M8] P.-G. de Gennes (1966) *Superconductivity of Metals and Alloys*. W. A. Benjamin, Inc., New York, Introduction into the theory of superconductivity.

[M9] D.-R. Tilley and J. Tilley, *Superfluidity and Superconductivity*, Van Nostrand Reinhold Co., New York, 1974. Introduction into the physics of both superconductors and superfluids.

## Special Materials

[M10] H. Ullmaier, *Irreversible Properties of Type II Superconductors*, Springer Tracts in Modern Physics, vol. 76, Springer-Verlag, Berlin, Heidelberg, New York, 1975. Short monograph on hard superconductors.

[M11] V. L. Ginsburg and D. A. Kirzhuits, *High Temperature Superconductivity*, Consultants Bureau, New York and London, 1982.

- [M12] T. Ishiguro and K. Yamaji, *Organic Superconductors*, Springer Series in Solid-State Sciences, vol. 88, 1990.
- [M13] *Superconductivity in Ternary Compounds*, (eds O. Fischer and M. B. Maple), vol. 32, Topics in Current Physics, Springer-Verlag, Berlin, 1982.

## Tunnel Junctions, Josephson Junctions, and Vortices

- [M14] E. L. Wolf, *Principles of Electron Tunneling Spectroscopy*, Oxford University Press, New York, 1985.
- [M15] A. Barone and G. Paterno, *Physics and Applications of the Josephson Effect*, John Wiley & Sons, Inc., New York, 1982.
- [M16] K. K. Likharev, *Dynamics of Josephson Junctions and Circuits*, Gordon and Breach Science Publishers, Philadelphia, PA, 1991.
- [M17] R. P. Huebener, *Magnetic Flux Structures in Superconductors*, 2nd edn, Springer Series in Solid-State Sciences, vol. 6, Springer, New York, 2001.

## Nonequilibrium Superconductivity

- [M18] *Nonequilibrium Superconductivity*, Elsevier Science Publishers, Amsterdam, (1986), Modern Problems in Condensed Matter Sciences, vol. 12, (eds D. N. Langenberg and A. I. Larkin).

## Applications of Superconductivity

### General Overview

- [M19] T. P. Orlando and K. A. Delin, *Foundations of Applied Superconductivity*, Addison-Wesley Publishing Company, Inc., Reading, MA, 1991.

## Magnets, Cables, Power Applications

- [M20a] M. N. Wilson, *Superconducting Magnets*, Oxford University Press, New York, 1983.
- [M20b] Y. Iwasa, *Case Studies in Superconducting Magnets*, Plenum Press, New York, 1994.
- [M21] P. Komarek, *Hochstromanwendungen der Supraleitung*, Teubner Studienbücher, Stuttgart, 1995.
- [M22] B. R. Lehdorff, *High- $T_c$  Superconductors for Magnet and Energy Technology*, Springer Tracts in Modern Physics, vol. 171, Springer-Verlag, Berlin, Heidelberg, 2001.

[M23] F. C. Moon, *Superconducting Levitation*, John Wiley & Sons, Inc., New York, 1994.

## Microwaves, Magnetic Field Sensors, Electronics

[M24] M. Hein, *High-Temperature Superconductor Thin Films at Microwave Frequencies*, Springer Tracts in Modern Physics, vol. 155, Springer-Verlag, Berlin, Heidelberg, 1999.

[M25] H. Weinstock and M. Nisenoff (eds), *Microwave Superconductivity* NATO Science Series E: Applied Sciences, vol. 375, Kluwer Academic Publishers, Dordrecht/Boston, MA/London, 1999.

[M26] *SQUID Sensors: Fundamentals, Fabrication and Applications*, H. Weinstock (ed.), NATO ASI Series E: Applied Sciences, vol. 329, Kluwer Academic Publishers, Dordrecht, 1996.

[M27] *SQUID Handbook*, J. Clarke and A. Braginski (eds), Wiley-VCH Verlag GmbH, Berlin, 2003.

[M28] *Superconducting Devices*, S. T. Ruggiero and D. A. Rudman (eds), Academic Press Inc., San Diego, CA, 1990.

[M29] *The New Superconducting Electronics*, H. Weinstock and R. W. Ralston (eds), NATO Science Series E: Applied Sciences, Vol. 251, Kluwer Academic Publishers, Dordrecht/Boston, MA/London, p. 387, 1999.

[M30] J. Hinken, *Supraleiter-Elektronik, Grundlagen – Anwendungen in der Elektronik*, Springer-Verlag, Heidelberg, 1988.

[M31] V. Kose, *Superconducting Quantum Electronics*, Springer-Verlag, Heidelberg, 1989.

## Low Temperature Physics and Technology

[M32] Ch. Enss and S. Hunklinger, *Tieftemperaturphysik*, Springer-Verlag, Heidelberg, 2000.

[M33] O. V Lounasmaa, *Experimental Principles and Methods below 1 K*, Academic Press, London and New York, 1974.

# Index

## **a**

*Abrikosov, A. A.*,

Abrikosov vortex, *see* flux line

ac Josephson current, *see* Josephson effect

ALMA

Ambegaokar Baratoff relation

amorphous superconductor

Andreev bound states

Andreev reflection

antenna, superconducting

antidot

APF

ARPES

A15 structure, *see*  $\beta$  tungsten structure

## **b**

(Ba,Ka)BiO<sub>3</sub>

*Bardeen, J.*

BCS coherence length

dependence on mean free path

BCS theory

Bean Livingston barrier

Bean model

bearing, superconducting

*Bednorz, J. G.*

BEDT-TTF compounds

Berezinskii-Kosterlitz-Thouless Transition

$\beta$  tungsten structure

Bi2212, *see*  $\text{Bi}_2\text{Sr}_2\text{Ca}\text{Cu}_2\text{O}_8$

bias reversal

bismuthates

$\text{Bi}_2\text{Sr}_2\text{Ca}\text{Cu}_2\text{O}_8$

Bitter magnet

*Bohr, N.*

Boltzmann's constant

boron carbides

Bose Einstein Condensation

Bose glas

Bragg glas

BSCCO, *see*  $\text{Bi}_2\text{Sr}_2\text{Ca}\text{Cu}_2\text{O}_8$

bubble chamber

**c**

cable

superconducting

twist

cable in conduit

calorimeter

canonical momentum

cartwheel SQUID, *see* multiloop SQUID magnetometer

characteristic frequency

characteristic voltage

chemical shift

Chevrel phases

Circuit QED

Clogston-Chandrasekhar limit

coherence length, *see also* BCS coherence length and Ginzburg Landau coherence length

BCS

Ginzburg Landau

coherent matter wave, *see* matter wave

columnar defect

computer tomography

condensation energy

conventional superconductivity

*Cooper, L. N.*

Cooper pair

collective pair function

pair density and energy gap

Cooper pair box

Cooper pairing

anisotropy effect

early models

effect of lattice deformations

effect of paramagnetic ions

valence effect

via antiferromagnetic spin fluctuations

via electron phonon interaction

via magnetic excitons

Coulomb blockade

Coulomb staircase

CRESST

critical current

depinning

grain boundary Josephson junction

Josephson junction

pair breaking

Silsbee Rule

SIS Josephson junction  
SNS Josephson junction  
SQUID  
type I superconductor  
type II superconductor  
critical current density, thin plate  
critical field, thermodynamic  
critical magnetic field  
critical magnetic field, thin plate  
critical state  
critical temperature  
BCS formula  
McMillan formula  
cuprates  
antiferromagnetic state  
discovery  
heat capacity  
magnetic penetration depth  
material properties  
phase sensitive measurements of pair wave function  
pseudo gap  
quasiparticle density of states  
spin lattice relaxation rate  
current limiting devices  
current voltage characteristic  
intrinsic Josephson junction  
Josephson junction under microwave irradiation  
Josephson tunnel junction  
NbTi  
Pb-In

RCSJ model  
SFS junction  
SIS tunnel junction  
SNS junction  
subharmonic structures

***d***

dc SQUIDs  
*de Broglie, L.*  
de Broglie relation  
decay length  
decoration  
Debye frequency  
Debye temperature  
demagnetization factor  
density of states  
detectivity  
diamagnetism, effect of fluctuations  
dichalcogenides  
digital electronics  
directly coupled magnetometer  
*d* orbitals  
*Drude, P*  
*d* vector  
*d* wave superconductivity

***e***

EDX spectrometer  
EEG  
*Einstein, A.*

electrical resistance, Drude model  
electrical resistance, temperature dependence  
electron gas, *see* free electron gas  
electron holography  
Eliashberg function  
energy gap  
    anisotropy  
    infrared absorption  
    tables  
    tunnel experiments  
energy-momentum relation, electrons in periodic potential  
energy resolution  
energy storage, superconducting  
entropy  
ET salts, *see* BEDT-TTF compounds  
excess current  
exchange interaction

## **f**

Fermi energy

Fermi function

Fermi sphere

*Feynman, R.*

FFLO state

field effect, electric

filter

    Chebyshev

    elliptic

    superconducting

fishtail, *see* second peak

Fiske steps

flow resistance

fluctuation conductance

flux creep

flux flow resistance, *see* flow resistance

flux flow step

flux jumps

flux line lattice

flux line lattice, melting

flux lines

hopping

imaging techniques

motion, dissipation of energy

flux-locked mode

flux modulation

flux noise

fluxoid

fluxoid quantization

fluxon

fluxon dynamics

flux quantization

Doll-Nä bauer experiment

Deaver-Fairbanks experiment

flux quantum

half integer

flux transformer

fly-wheels

Fraunhofer pattern

free electron gas

free energy, definition

free enthalpy, definition

*Fröhlich, H.*

fullerides

fusion reactor

***g***

gapless superconductivity

gauge invariance

gauge invariant phase difference

generators, superconducting

*Giaever, I.*,

Gibbs energies

*Ginzburg, V. L.*

Ginzburg Landau coherence length

dependence on mean free path

Ginzburg Landau equations

Ginzburg Landau parameter

Ginzburg Landau theory

free energy

Ginzburg number

GLAG theory, *see* Ginzburg Landau theory

Golay cell

*Gorkov, L. P.*

gradiometer

grain boundary

grain boundary Josephson junction, *see* Josephson junction

***h***

hard superconductor

heavy fermion superconductors

material properties  
order parameter symmetry  
HEB bolometer  
HEB mixer  
helium, boiling point  
heterodyne receiver  
high field superconductor  
high temperature superconductor, *see* cuprate  
Hilbert spectrometer  
holon  
homodyne receiver  
hot electron bolometer, *see* HEB  
Hubbard model  
hybrid magnets, *see* magnets  
hysteresis, magnetization

*i*

IBAD  
 $I_c R_n$  Product, SIS junction  
 $I_c R_n$ -Produkt, SNS junction  
ideal diamagnetism, *see* Meissner Ochsenfeld Effect  
inductance parameter  
induction heater  
intermediate state  
internal energy, definition  
intrinsic Josephson junction, *see* Josephson junctions  
intrinsic pinning  
inverse problem, MEG  
iron pnictides  
irreversibility line

isotope effect

cuprates

elements

experiments

fullerides

$\text{MgB}_2$

*j*

*Josephson, B. D.*

Josephson constant

Josephson coupling energy

Josephson current, *see* Josephson effect

Josephson effect

ac Josephson current

dc Josephson current

Josephson equations

Josephson junctions

bridges

Fraunhofer pattern

grain boundaries

intrinsic

pendulum model

SINIS

SIS

SNS

overdamped

underdamped

Josephson mixer

Josephson penetration depth

Josephson plasma frequency

Josephson plasma oscillations

Josephson plasma waves

standing waves

Josephson vortex, *see* fluxon

## **k**

*Kamerlingh-Onnes, H.*

Knight shift

Kondo effect

Kosterlitz Thouless Transition, *see* Berezinskii Kosterlitz Thouless transition

## **l**

*Landau, L. D.*

LaO/STO

Large Hadron Collider

laser ablation

latching logic

Lawrence Doniach model

layered superconductors

levitated train

levitation

load line

local oscillator

lock in transition

LOFF state, *see* FFLO state

*London, F.*

*London, H.*

London equations

London penetration depth

*Lorentz, H. A.*

Lorentz contraction

Lorentz microscopy

lower critical field

layered superconductors

Low Temperature Scanning Electron Microscopy

**m**

macroscopic wave function, siehe matter wave

MAGLEV, *see* levitating train

magnetic flux, definition

magnetic penetration depth, *see also* London penetration depth

dependence on mean free path

conventional superconductors

unconventional superconductors

magnetic resonance imaging

magnetization

of hard superconductors

magnetization curve, type II superconductor

magneto cardiography, *see* MCG

magneto encephalography, *see* MEG

magneto-optics

magnets

coil protection

current feeding

energy storage

high temperature superconductor

hybrid

levitated trains

magnetic resonance imaging

magnetic separation

motors and generators  
NbTi  
 $\text{Nb}_3\text{Sn}$   
nuclear fusion  
nuclear magnetic resonance  
particle accelerators  
permanent  
stability  
wires

manometer, superconducting  
matching  
matter wave  
    coherent

Matthias rule

McCumber parameter, *see* Stewart-McCumber parameter

MEG

*Meissner, W.*

Meissner effect, paramagnetic

Meissner Ochsenfeld Effect

Meissner phase, *siehe* Meissner state

Meissner state, stability

melt texturing

$\text{MgB}_2$

micro calorimeter

mixer

MOD

motors, superconducting

MRI, *see* magnetic resonance imaging

*Müller, K. A.*

multiband superconductivity

multifilament wire  
multiloop SQUID magnetometer  
multipole filter  
muon spin resonance ( $\mu$ SR)

***n***

NbN

NbSe<sub>2</sub>

Nb<sub>3</sub>Sn

NbTi

NDE

NEP

neutron scattering

nitrogen, boiling point

NMR, *see* nuclear magnetic resonance

noise 1/f, 426, 446, *see also* thermal noise

noise parameter

noise temperature

noise, white

non-destructive evaluation, *see* NDE

non-equilibrium processes

nuclear magnetic resonance

Nyquist noise, *see* thermal noise

***o***

Ochsenfeld, R.

order parameter, *see* pair wave function

organic superconductors

oscillator, superconducting

**p**

pair breaking

pair breaking critical current

pair wave function

*d* symmetry

*s* symmetry

phase sensitive measurements

sub-dominant components

Palladium-Hydrogen

pancake vortex

paramagnetic limit

paramagnetic Meissner effect

parity

particle-wave duality

*Pauli, W.*

Pauli limiting field, *see* paramagnetic limit

Pauli principle

peak effect

permantent current, *see* persistent current

persistent current

persistent mode

PET

phase slip center

phase transition, order of

phonon detection

phonon generation

phonons

photo effect

picene

pickup loop

$\pi$  Josephson junction

pinning

pinning center

pinning force

*Planck, M.*

Planck's constant

pnictide, *see* iron pnictide

pressure, effect on superconducting state

proximity effect

pseudo gap

powder-in-tube method

*p* wave superconductivity

## **q**

quality factor

quantum computer

quantum fluctuations

quantum hall effect

quantum interference

quantum interference filter, *see* SQIF

quantum resistance

quantum tunneling, macroscopic

quasiparticle

density of states, *s*wave pairing

density of states, *d*wave pairing

energy-momentum relation, *p* wave pairing

energy-momentum relation, *s* wave pairing

recombination time

qubit

quench

**r**

Rabi oscillations

RABiTS

Rapid single flux quantum logic, *see* RSFQ

RCSJ model

receiver, integrated

recombination time

reentrant superconductivity

relaxation processes

resistance, *see* electrical resistance

resonators

particle accelerators

communication technology

rf SQUID

RSFQ

RSJ model

return current

Rutgers formula

Ruthenates

**s**

Sagnac interferometer

scanning tunneling microscopy

*Schrieffer, J. R.*

Schrödinger equation

screen room, magnetic

second peak

sensitivity, *see* detectivity

sensors, sensitivity

Shapiro steps  
shield, superconducting  
Shubnikov phase  
signal-to-noise ratio  
Silsbee rule  
Sine Gordon equation  
single electron electrometer  
single electron transistor  
single electron tunneling  
SINIS junction, *see* Josephson junction  
SIS junction, *see* Josephson junction  
SIS mixer  
skin effect  
skin depth  
slew rate  
SMES  
SNS junction, *see* Josephson junction  
soliton  
*Sommerfeld, A.*  
Sommerfeld coefficient  
specific heat  
conventional superconductors  
Sn  
Rutgers formula  
unconventional superconductors  
spinon  
splat cooling  
sponge model  
SQUID  
SQUID, applications

SQUID magnetometer, designs

SQUID magnetometer, readout

SQUID microscope

SQUID multichannel systems

SQUID susceptometer

SQIF

$\text{Sr}_2\text{RuO}_4$

flux line lattice

pair wave symmetry

3K phase

stability parameter (against quench)

Stewart McCumber parameter

superconducting elements

superconducting quantum interferometer, *see* SQUID

superconductivity

discovery

conventional, *see* conventional superconductivity

improvement at non-equilibrium

unconventional, *see* unconventional superconductivity

superconductor-ferromagnet interface

superconductor, hanging

superconductor, high frequency behavior

superconductor-insulator interface

superconductor-normal conductor interface

superconductor of first kind, *see* type I superconductor

superconductor of second kind, *see* type II superconductor

supercooling

superfluidity

surface impedance

surface reactance

surface resistance

s wave superconductivity

Swihart velocity

**t**

tapes, superconducting

TaS<sub>2</sub>

thermal conductivity

thermal noise

thermal switch

thermodynamic potentials, *see* Gibbs functions

thermodynamics, general relations

thermometer, superconducting

time reversal symmetry

TMTSF compounds

transformer, superconducting

transition edge thermometer

transition temperature, *see* critical temperature

tricrystals

tunnel diode

tunnel effect

tunnel junction

    normal conductor - normal conductor

    normal conductor - superconductor

    superconductor - superconductor

tunneling

    direct

    via localized states

    resonant

    incoherent

coherent  
spin polarized

tunneling spectroscopy

cuprates

Pd-D

$\text{UPd}_2\text{Al}_3$

tunnel resistance

two-band superconductivity

type I superconductors

dependence on  $\kappa$

type II superconductors

phase diagram

dependence on  $\kappa$

## ***u***

Uemura plot

UMTS

uncertainty principle

space-momentum

energy – time

particle number-phase

unconventional superconductivity

$\text{UPd}_2\text{Al}_3$

upper critical magnetic field

anisotropic superconductors

cuprates

layered superconductors

thin plate

$\text{UPt}_3$

$\text{URhGe}$

**v**

vector potential

voltage standard

programmable

vortex, *see* flux line

vortex gas

vortex glass

vortex liquid

vortex phases, layered superconductors

vortex structure, layered superconductor

**w**

wall energy

washboard potential

washer SQUID

wave vector

WDX spectrometer

Weston cell

WIMP

Wohlleben effect, *see* paramagnetic Meissner effect

**y**

Y123, *see*  $\text{YBa}_2\text{Cu}_3\text{O}_7$

$\text{YBa}_2\text{Cu}_3\text{O}_7$

YBCO, *see*  $\text{YBa}_2\text{Cu}_3\text{O}_7$

**z**

zero bias anomaly

zero field steps



# **WILEY END USER LICENSE AGREEMENT**

Go to [www.wiley.com/go/eula](http://www.wiley.com/go/eula) to access Wiley's ebook EULA.



Reinhold Kleiner and Werner Buckel

# Superconductivity

An Introduction

Third Updated Edition

